FNIRS IN NEUROSCIENCE AND ITS EMERGING APPLICATIONS

EDITED BY: Ning Liu, Meryem Ayse Yücel, Yunjie Tong, Yasuyo Minagawa, Fenghua Tian and Xianchun Li

PUBLISHED IN: Frontiers in Neuroscience and Frontiers in Human Neuroscience

frontiers Research Topics

frontiers

Frontiers eBook Copyright Statement

The copyright in the text of individual articles in this eBook is the property of their respective authors or their respective institutions or funders. The copyright in graphics and images within each article may be subject to copyright of other parties. In both cases this is subject to a license granted to Frontiers.

The compilation of articles constituting this eBook is the property of Frontiers.

Each article within this eBook, and the eBook itself, are published under the most recent version of the Creative Commons CC-BY licence. The version current at the date of publication of this eBook is CC-BY 4.0. If the CC-BY licence is updated, the licence granted by Frontiers is automatically updated to the new version.

When exercising any right under the CC-BY licence, Frontiers must be attributed as the original publisher of the article or eBook, as applicable.

Authors have the responsibility of ensuring that any graphics or other materials which are the property of others may be included in the CC-BY licence, but this should be checked before relying on the CC-BY licence to reproduce those materials. Any copyright notices relating to those materials must be complied with.

Copyright and source acknowledgement notices may not be removed and must be displayed in any copy, derivative work or partial copy which includes the elements in question.

All copyright, and all rights therein, are protected by national and international copyright laws. The above represents a summary only. For further information please read Frontiers' Conditions for Website Use and Copyright Statement, and the applicable CC-BY licence.

ISSN 1664-8714
ISBN 978-2-88976-953-7
DOI 10.3389/978-2-88976-953-7

About Frontiers

Frontiers is more than just an open-access publisher of scholarly articles: it is a pioneering approach to the world of academia, radically improving the way scholarly research is managed. The grand vision of Frontiers is a world where all people have an equal opportunity to seek, share and generate knowledge. Frontiers provides immediate and permanent online open access to all its publications, but this alone is not enough to realize our grand goals.

Frontiers Journal Series

The Frontiers Journal Series is a multi-tier and interdisciplinary set of open-access, online journals, promising a paradigm shift from the current review, selection and dissemination processes in academic publishing. All Frontiers journals are driven by researchers for researchers; therefore, they constitute a service to the scholarly community. At the same time, the Frontiers Journal Series operates on a revolutionary invention, the tiered publishing system, initially addressing specific communities of scholars, and gradually climbing up to broader public understanding, thus serving the interests of the lay society, too.

Dedication to Quality

Each Frontiers article is a landmark of the highest quality, thanks to genuinely collaborative interactions between authors and review editors, who include some of the world's best academicians. Research must be certified by peers before entering a stream of knowledge that may eventually reach the public - and shape society; therefore, Frontiers only applies the most rigorous and unbiased reviews.
Frontiers revolutionizes research publishing by freely delivering the most outstanding research, evaluated with no bias from both the academic and social point of view. By applying the most advanced information technologies, Frontiers is catapulting scholarly publishing into a new generation.

What are Frontiers Research Topics?

Frontiers Research Topics are very popular trademarks of the Frontiers Journals Series: they are collections of at least ten articles, all centered on a particular subject. With their unique mix of varied contributions from Original Research to Review Articles, Frontiers Research Topics unify the most influential researchers, the latest key findings and historical advances in a hot research area! Find out more on how to host your own Frontiers Research Topic or contribute to one as an author by contacting the Frontiers Editorial Office: frontiersin.org/about/contact

FNIRS IN NEUROSCIENCE AND ITS EMERGING APPLICATIONS

Topic Editors:
Ning Liu, Stanford University, United States
Meryem Ayse Yücel, Boston University, United States
Yunjie Tong, Purdue University, United States
Yasuyo Minagawa, Keio University, Japan
Fenghua Tian, University of Texas at Arlington, United States
Xianchun Li, East China Normal University, China

Citation: Liu, N., Yücel, M. A., Tong, Y., Minagawa, Y., Tian, F., Li, X., eds. (2022). FNIRS in Neuroscience and its Emerging Applications. Lausanne: Frontiers Media SA. doi: 10.3389/978-2-88976-953-7

Table of Contents

06 ***Editorial: FNIRS in neuroscience and its emerging applications***
Ning Liu, Meryem Ayşe Yücel, Yunjie Tong, Yasuyo Minagawa, Fenghua Tian and Xianchun Li

09 ***Coordination Elicits Synchronous Brain Activity Between Co-actors: Frequency Ratio Matters***
Xiaojun Cheng, Yafeng Pan, Yinying Hu and Yi Hu

19 ***Cognitive Enhancement by Transcranial Photobiomodulation Is Associated With Cerebrovascular Oxygenation of the Prefrontal Cortex***
Emma Holmes, Douglas W. Barrett, Celeste L. Saucedo, Patrick O'Connor, Hanli Liu and F. Gonzalez-Lima

29 ***Enhancing Attention by Synchronizing Respiration and Fingertip Pressure: A Pilot Study Using Functional Near-Infrared Spectroscopy***
Yi-Lei Zheng, Dang-Xiao Wang, Yu-Ru Zhang and Yi-Yuan Tang

47 ***Performance Monitoring via Functional Near Infrared Spectroscopy for Virtual Reality Based Basic Life Support Training***
Emin Aksoy, Kurtulus Izzetoglu, Engin Baysoy, Atahan Agrali, Dilek Kitapcioglu and Banu Onaral

55 ***Reality Status Judgments of Real and Fantastical Events in Children's Prefrontal Cortex: An fNIRS Study***
Hui Li, Tao Liu, Jacqueline D. Woolley and Peng Zhang

64 ***Effects of Tai Chi Chuan on Inhibitory Control in Elderly Women: An fNIRS Study***
Yuan Yang, Tingting Chen, Mingming Shao, Shoufu Yan, Guang H. Yue and Changhao Jiang

75 ***Assessing Brain Networks by Resting-State Dynamic Functional Connectivity: An fNIRS-EEG Study***
Yujin Zhang and Chaozhe Zhu

87 ***Resting-State Functional Connectivity Estimated With Hierarchical Bayesian Diffuse Optical Tomography***
Takatsugu Aihara, Takeaki Shimokawa, Takeshi Ogawa, Yuto Okada, Akihiro Ishikawa, Yoshihiro Inoue and Okito Yamashita

102 ***Atypical Dynamic-Connectivity Recruitment in Attention-Deficit/Hyperactivity Disorder Children: An Insight Into Task-Based Dynamic Connectivity Through an fNIRS Study***
Stephanie Sutoko, Yukifumi Monden, Tatsuya Tokuda, Takahiro Ikeda, Masako Nagashima, Tsukasa Funane, Hirokazu Atsumori, Masashi Kiguchi, Atsushi Maki, Takanori Yamagata and Ippeita Dan

116 ***Altered Functional Connectivity in the Motor and Prefrontal Cortex for Children With Down's Syndrome: An fNIRS Study***
Shi-Yang Xu, Feng-Mei Lu, Meng-Yun Wang, Zhi-Shan Hu, Juan Zhang, Zhi-Yi Chen, Paulo A. S. Armada-da-Silva and Zhen Yuan

126 ***Assessing Time-Resolved fNIRS for Brain-Computer Interface Applications of Mental Communication***
Androu Abdalmalak, Daniel Milej, Lawrence C. M. Yip, Ali R. Khan, Mamadou Diop, Adrian M. Owen and Keith St. Lawrence

136 ***Using the General Linear Model to Improve Performance in fNIRS Single Trial Analysis and Classification: A Perspective***
Alexander von Lühmann, Antonio Ortega-Martinez, David A. Boas and Meryem Ayşe Yücel

153 ***Performance Improvement of Near-Infrared Spectroscopy-Based Brain-Computer Interface Using Regularized Linear Discriminant Analysis Ensemble Classifier Based on Bootstrap Aggregating***
Jaeyoung Shin and Chang-Hwan Im

164 ***Differences in Net Information Flow and Dynamic Connectivity Metrics Between Physically Active and Inactive Subjects Measured by Functional Near-Infrared Spectroscopy (fNIRS) During a Fatiguing Handgrip Task***
Elizabeth L. Urquhart, Xinlong Wang, Hanli Liu, Paul J. Fadel and George Alexandrakis

180 ***Frequency-Domain Techniques for Cerebral and Functional Near-Infrared Spectroscopy***
Sergio Fantini and Angelo Sassaroli

198 ***Brain-Based Binary Communication Using Spatiotemporal Features of fNIRS Responses***
Laurien Nagels-Coune, Amaia Benitez-Andonegui, Niels Reuter, Michael Lührs, Rainer Goebel, Peter De Weerd, Lars Riecke and Bettina Sorger

218 ***Sleep State Modulates Resting-State Functional Connectivity in Neonates***
Chuen Wai Lee, Borja Blanco, Laura Dempsey, Maria Chalia, Jeremy C. Hebden, César Caballero-Gaudes, Topun Austin and Robert J. Cooper

230 ***Cerebral Hemodynamic Responses to the Sensory Conflict Between Visual and Rotary Vestibular Stimuli: An Analysis With a Multichannel Near-Infrared Spectroscopy (NIRS) System***
Nghia Trong Nguyen, Hiromasa Takakura, Hisao Nishijo, Naoko Ueda, Shinsuke Ito, Michiro Fujisaka, Katsuichi Akaogi and Hideo Shojaku

244 ***Cortical Activation Patterns of Different Masking Noises and Correlation With Their Masking Efficacy, Determined by Functional Near-Infrared Spectroscopy***
Qiyang Sun, Xianren Wang, Bixue Huang, JinCangjian Sun, Jiahui Li, Huiwen Zhuang and Guanxia Xiong

254 ***An Augmented-Reality fNIRS-Based Brain-Computer Interface: A Proof-of-Concept Study***
Amaia Benitez-Andonegui, Rodion Burden, Richard Benning, Rico Möckel, Michael Lührs and Bettina Sorger

275 ***Joint Attention During Live Person-to-Person Contact Activates rTPJ, Including a Sub-Component Associated With Spontaneous Eye-to-Eye Contact***
Swethasri Dravida, J. Adam Noah, Xian Zhang and Joy Hirsch

294 ***Applications of Resting-State fNIRS in the Developing Brain: A Review From the Connectome Perspective***
Zhishan Hu, Guangfang Liu, Qi Dong and Haijing Niu

306 ***Interpersonal Neural Synchronization During Cooperative Behavior of Basketball Players: A fNIRS-Based Hyperscanning Study***
Lin Li, Huiling Wang, Huiyu Luo, Xiaoyou Zhang, Ruqian Zhang and Xianchun Li

314 ***Functional Near-Infrared Spectroscopy Indicates That Asymmetric Right Hemispheric Activation in Mental Rotation of a Jigsaw Puzzle Decreases With Task Difficulty***
Murat Can Mutlu, Sinem Burcu Erdoğan, Ozan Cem Öztürk, Reşit Canbeyli and Hale Saybaşılı

326 ***Using a Data-Driven Approach to Estimate Second-Language Proficiency From Brain Activation: A Functional Near-Infrared Spectroscopy Study***
Miaomei Lei, Toshinori Miyoshi, Ippeita Dan and Hiroki Sato

337 ***Integration of Spatial Information Increases Reproducibility in Functional Near-Infrared Spectroscopy***
Sergio Luiz Novi, Edwin Johan Forero, Jose Angel Ivan Rubianes Silva, Nicolas Gabriel S. R. de Souza, Giovani Grisotti Martins, Andres Quiroga, Shin-Ting Wu and Rickson C. Mesquita

349 ***Prefrontal Responses to Odors in Individuals With Autism Spectrum Disorders: Functional NIRS Measurement Combined With a Fragrance Pulse Ejection System***
Mingdi Xu, Yasuyo Minagawa, Hirokazu Kumazaki, Ken-ichi Okada and Nozomi Naoi

366 ***Acute Effects of Two Types of Dumbbell Exercise on Oxygenated Hemodynamic Concentration of Cerebral Activation in Healthy Young Male Adults: A Functional Near-Infrared Spectroscopy Study***
Yana Wang, Jiaojiao Lü, Jifeng Rong, Linjie Song, Wei Wang, Yifan Jiang, Yu Liu and Lingyan Huang

frontiers | Frontiers in Neuroscience

TYPE Editorial
PUBLISHED 03 August 2022
DOI 10.3389/fnins.2022.960591

Check for updates

OPEN ACCESS

EDITED AND REVIEWED BY
Xiaolin Zhou,
Peking University, China

*CORRESPONDENCE
Ning Liu
ningl@stanford.edu

SPECIALTY SECTION
This article was submitted to Brain Imaging Methods, a section of the journal Frontiers in Neuroscience

RECEIVED 03 June 2022
ACCEPTED 30 June 2022
PUBLISHED 03 August 2022

CITATION
Liu N, Yücel MA, Tong Y, Minagawa Y, Tian F and Li X (2022) Editorial: FNIRS in neuroscience and its emerging applications.
Front. Neurosci. 16:960591.
doi: 10.3389/fnins.2022.960591

COPYRIGHT
© 2022 Liu, Yücel, Tong, Minagawa, Tian and Li. This is an open-access article distributed under the terms of the Creative Commons Attribution License (CC BY). The use, distribution or reproduction in other forums is permitted, provided the original author(s) and the copyright owner(s) are credited and that the original publication in this journal is cited, in accordance with accepted academic practice. No use, distribution or reproduction is permitted which does not comply with these terms.

Editorial: FNIRS in neuroscience and its emerging applications

Ning Liu[1]*, Meryem Ayşe Yücel[2], Yunjie Tong[3], Yasuyo Minagawa[4], Fenghua Tian[5] and Xianchun Li[6,7,8]

[1]Department of Psychiatry and Behavioral Sciences, Stanford University, Stanford, CA, United States, [2]Neurophotonics Center, Biomedical Engineering, Boston University, Boston, MA, United States, [3]Weldon School of Biomedical Engineering, Purdue University, West Lafayette, IN, United States, [4]Department of Psychology, Faculty of Letters, Keio University, Tokyo, Japan, [5]Department of Bioengineering, University of Texas at Arlington, Arlington, TX, United States, [6]Shanghai Key Laboratory of Mental Health and Psychological Crisis Intervention, Affiliated Mental Health Center (ECNU), School of Psychology and Cognitive Science, East China Normal University, Shanghai, China, [7]Shanghai Changning Mental Health Center, Shanghai, China, [8]Institute of Wisdom in China, East China Normal University, Shanghai, China

KEYWORDS

functional near-infrared spectroscopy (fNIRS), methodology, Brain Computer Interfaces (BCI), hyperscanning, multi-modal imaging, frequency-domain fNIRS, resting-state connectivity

Editorial on the Research Topic
FNIRS in neuroscience and its emerging applications

This Research Topic focused on recent developments in methodologies and applications of functional near-infrared spectroscopy (fNIRS). It consists of 28 articles on various aspects that were contributed by more than 150 authors. It includes original research articles (24), clinical trials (1), hypothesis and theory (1), and reviews (2).

Near-infrared spectroscopy has been used to study the function of the brain for more than three decades. In recent years, significant progress has been made in methodologies and applications of this technique because of its competitive advantages, such as non-invasiveness, cost-effectiveness, and portability. In this Research Topic, we saw a wide range of novel fNIRS applications among which are the neural mechanism of fantasy (Li et al.), Tai chi chuan (Yang et al.), Haptics-assisted mediation (Zheng et al.), sensory conflict (Nguyen et al.), mental rotation (Mutlu et al.), fatiguing handgrip (Urquhart et al.), and dumbbell exercise (Wang et al.). For instance, Yang et al. reported that Tai chi chuan intervention for 8 weeks could improve ability of inhibitory control in older adults, which was associated with increased prefrontal activation. The findings suggest that Tai chi chuan exercise could be an effective, suitable intervention for improving executive function in elderly people. Zheng et al. reported that haptics-assisted mediation could reduce mind-wandering and enhance attention after a 5-day practice. Moreover, such improvement was related to enhanced activity in the right prefrontal activation and significant changes in the functional connectivity between the brain regions related to the attention networks. The study by Urquhart et al. investigated the effect of motor task fatigue on brain hemodynamics at different frequency bands (endothelial, neurogenic, and myogenic). One strength of this study is that four different types of functional connectivity metrics were applied to the fNIRS signals. Their methods were feasible and

revealed that physical activity has an effect on the cortical networks at different frequency bands. Although this study involved healthy adults, these methods were revealed to be applied to older populations and those with impaired cardiovascular health.

The technique was also used to classify second-language proficiency (Lei et al.), monitor virtual reality (VR) based training (Aksoy et al.), monitor transcranial infrared laser stimulation (TILS) (Holmes et al.), and improve acoustic therapy (Sun et al.). Additionally, multiple fNIRS applications on atypical populations have also emerged, including attention deficit hyperactivity disorder (ADHD) (Sutoko et al.), children with Down's syndrome (Xu et al.) and autism spectrum disorder (ASD) (Xu et al.). In the study by Xu et al. fNIRS was used to probe the olfactory function in teenagers with ASD. Measurements of the olfactory function, including odor sensitivity, were conducted by using a fragrance pulse ejection system that not only provides precise amount of odor stimuli, but also motivates and helps individuals with ASD to complete the odor perception task. The use of this system that is exclusively compatible with fNIRS made functional measurement of olfaction possible in individuals with ASD and yielded valuable results. They found significantly weaker activation in the right dorsolateral prefrontal cortex (rDLPFC) in the ASD group than in the neuro-typical group, and the strength of the rDLPFC activity significantly correlated with odor sensitivity. These findings indicate possible impairments in the higher order functions of olfaction, such as olfactory working memory, in individuals with ASD.

FNIRS-based Brain Computer Interfaces (BCI) have gained significant momentum in recent decades. Some notable new developments in this field are the GLM improvement in BCI (von Lühmann et al.), time-resolved fNIRS for BCI (Abdalmalak et al.), and ensemble classifiers for fNIRS-based BCI (Shin and Im). In addition, Nagels-Coune et al. tried to help people with "locked-in" syndrome to communicate with the help of fNIRS-based binary communication paradigm. They have successfully tested the paradigm on healthy participants performing two mental imagery tasks. The study shows the potential of answer encoding using spatiotemporal fNIRS signal features or spatial fNIRS signal features only. Also, Benitez-Andonegui et al. examined an augmented-reality (AR) fNIRS-based BCI on healthy participants that performing motor-imagery tasks. They demonstrated for the first time that by using AR feedback and flexible choice encoding in form of search trees, they can increase the degrees of freedom of a BCI system.

FNIRS-based hyperscanning shows interbrain neural synchrony during social interaction. The field has increased dramatically in the recent decade (Gvirts and Perlmutter, 2019; Balters et al., 2020). Because of its unique data analysis algorithm (Cui et al., 2012), it allows researchers to design tasks with greater flexibility and in more naturalistic settings than typical single-person cognitive studies. In this topic, Dravida et al. investigated joint attention hyperscanning, and they found that social joint attention task induced greater activity in right temporoparietal junction than the non-social condition. Meanwhile, eye-contact frequency could modulate the joint attention activity. More interestingly, cross-brain coherence analysis revealed greater coherence between high eye contact dyads than low eye contact dyads. Cheng et al. studied how the interpersonal coordination pattern modulates coordination outcome and the related brain-to-brain connectivity in dyads that performed a co-drew task. They found that interpersonal multifrequency coordination pattern facilitates the coordination efficiency, which was associated with the enhanced brain-to-brain connectivity. Li et al. reported hyperscanning study of basketball players, and they found that significant interpersonal neural synchronization (INS) was observed in the dorsolateral prefrontal area only in dyads of basketball players when they performed joint-drawing task, which provided the inter-brain evidence for enhanced cooperative behavior in the individuals with team-based sports training.

Multi-modal brain imaging can supplement drawbacks of using a single modality by extracting complementary features. In this topic, Lee et al. examined how the sleeping state influences the resting-state networks (RSNs) in the neonate population using fNIRS-EEG combined method. Neuroimaging for neonates is usually performed when they are asleep; however, RSNs depending on the sleeping state, i.e., quiet sleep (QS) and active sleep (AS), remain unknown. The authors found sleeping state-dependent RSNs with strong long-range connectivity during AS and enhanced short-range connectivity during QS. This finding can significantly contribute to future neuroimaging studies in neonates. Aihara et al. applied their recently developed Hierarchical Bayesian (HB) algorithm on resting state data collected by fNIRS. They evaluated and compared the reconstruction performances of their algorithm with two current algorithms for diffuse optical tomography using fMRI signals as a reference. They showed that their HB algorithm outperformed the prevailing algorithms with higher similarity to the resting state connectivity results from fMRI. Furthermore, Zhang and Zhu reported multimodal fNIRS-EEG recording to study dynamic resting-state connectivity.

In methodological development, Novi et al. revisited the reproducibility of the fNIRS signal during a finger-tapping task, and described a method to increase reproducibility in fNIRS by applying an MRI-based neuronavigation approach. As an emerging neuroimaging technique, the reproducibility of fNIRS signal is still a subject of debate. Earlier studies suggest that fNIRS signal is reproducible over group analysis, but the inter-subject and within-subject reproducibility remains low. Novi et al. revisited this subject and presented a real-time neuronavigation protocol to guide probe positioning. Based on this protocol, consistent, and robust activation of primary motor cortex was obtained at the intra-subject level. Overall, their

findings support that integration of spatial information could increases the reproducibility of fNIRS signal.

Lastly, this special issue includes two review articles. Fantini and Sassaroli reviewed Frequency-Domain fNIRS (FD-NIRS) from the basic principles to some most recent developments. They reviewed the absolute optical properties and hemoglobin concentration values reported in the literature for animal models and for the human brain. They also reviewed the application of FD-NIRS on studying hemodynamic responses to brain activity (slow signals) and on studying neuronal activation (fast signals). Furthermore, the authors reported some recent developments of FD-NIRS to maximize the sensitivity to cortical brain tissue relative to the superficial extracerebral tissue (scalp, skull, etc.). Hu et al. reviewed the recent fNIRS studies in brain connectome and resting-state connectivity, with a focus on developing brain. Early brain development from infancy through childhood is closely related to the development of cognition and behavior in later life. Resting-state functional near-infrared spectroscopy (fNIRS) has shown valuable potential in exploring brain network architecture and its changes during the development. They reviewed recent neural developmental research using resting-state fNIRS, both in typical and atypical development of brain connectome. The remaining challenges and future directions in this field were also discussed.

To summarize, the series of research, clinical and review articles that compose this Research Topic covered a wide range of applications and methodologies in fNIRS technique. We hope that this Research Topic will inspire the scientific community with more potential applications, overcome some shortcomings, and promote the technique into more scenarios that could improve the quality of life that span from neonates to elderly adults for both neuro-typical and atypical populations.

Author contributions

All authors listed have made a substantial, direct, and intellectual contribution to the work and approved it for publication.

Acknowledgments

To the helpful Frontiers team whose organizational skills and understanding made this Research Topic possible.

Conflict of interest

The authors declare that the research was conducted in the absence of any commercial or financial relationships that could be construed as a potential conflict of interest.

Publisher's note

All claims expressed in this article are solely those of the authors and do not necessarily represent those of their affiliated organizations, or those of the publisher, the editors and the reviewers. Any product that may be evaluated in this article, or claim that may be made by its manufacturer, is not guaranteed or endorsed by the publisher.

References

Balters, S., Baker, J. M., Hawthorne, G., and Reiss, A. L. (2020). Capturing human interaction in the virtual age: a perspective on the future of fNIRS hyperscanning. *Front. Hum. Neurosci.* 14, 588494. doi: 10.3389/fnhum.2020.588494

Cui, X., Bryant, D. M., and Reiss, A. L. (2012). NIRS-based hyperscanning reveals increased interpersonal coherence in superior frontal cortex during cooperation. *NeuorImage* 59, 2430–2437. doi: 10.1016/j.neuroimage.2011.09.003

Gvirts, H. Z., and Perlmutter, R. (2019). What guides us to neutrally and behaviorally align with anyone specific? A neurobiological model based on fNIRS hyperscanning studies. *Neuroscientist* 26, 108–116. doi: 10.1177/1073858419861912

frontiers in Neuroscience

ORIGINAL RESEARCH
published: 15 October 2019
doi: 10.3389/fnins.2019.01071

Coordination Elicits Synchronous Brain Activity Between Co-actors: Frequency Ratio Matters

Xiaojun Cheng[1], *Yafeng Pan*[2], *Yinying Hu*[2] *and Yi Hu*[2]*

[1] School of Psychology, Shenzhen University, Shenzhen, China, [2] School of Psychology and Cognitive Science, East China Normal University, Shanghai, China

People could behave in two different ways when engaging in interpersonal coordination activities: moving at the same frequency (isofrequency pattern, IP; the movement frequency ratio is 1:1) or at different frequencies (multifrequency pattern, MP; the movement frequency ratio is non 1:1). However, how the interpersonal coordination pattern modulates coordination outcome and the related brain-to-brain connectivity is not fully understood. Here, we adopted a continuous joint drawing task in which two participants co-drew parallelogram shapes according to two coordination patterns (i.e., IP vs. MP) while their brain activities were simultaneously recorded by the functional near-infrared spectroscopy (fNIRS) based hyperscanning technique. Dyads showed better coordination performance, as well as relatively greater interpersonal brain synchronization (IBS) at the left frontopolar area, in the MP condition compared to the IP condition. Granger causality analyses further disclosed the bidirectional influences between the brains of the coordinating individuals. Such interpersonal influences were enhanced when individuals coordinated in the MP condition. Finally, the IBS during coordination was related to the dyadic self-control level. Taken together, our study revealed that interpersonal multifrequency coordination pattern facilitates the coordination efficiency, which was associated with the enhanced brain-to-brain connectivity. Our work also suggests the potentially positive role of self-control during the interpersonal coordination process.

Keywords: interpersonal brain synchronization, interpersonal coordination, multifrequency pattern, fNIRS-based hyperscanning, frontopolar

OPEN ACCESS

Edited by:
Ning Liu,
Stanford University, United States

Reviewed by:
Aiping Liu,
University of British Columbia, Canada
Xin Di,
New Jersey Institute of Technology, United States
Chenbo Wang,
East China Normal University, China

***Correspondence:**
Yi Hu
yhu@psy.ecnu.edu.cn

Specialty section:
This article was submitted to Brain Imaging Methods, a section of the journal Frontiers in Neuroscience

Received: *12 April 2019*
Accepted: *24 September 2019*
Published: *15 October 2019*

Citation:
Cheng X, Pan Y, Hu Y and Hu Y (2019) Coordination Elicits Synchronous Brain Activity Between Co-actors: Frequency Ratio Matters. Front. Neurosci. 13:1071. doi: 10.3389/fnins.2019.01071

INTRODUCTION

People frequently engaged in social interactions, the achievement of which are largely relied on our capacity to coordinate behaviors with others in space and time (Sebanz et al., 2006; Richardson et al., 2007; Nessler and Gilliland, 2009). In some coordination activities, we just perform movements at the same frequency (i.e., *isofrequency pattern, IP*), or mirroring, such as side-by-side walking or together singing/humming. In some other activities, however, we are required to perform non-mirroring pattern—acting at different frequencies (i.e., *multifrequency pattern, MP),* such as dancing or sports. Various interpersonal coordination tasks based on either MP or IP are developed and studied for different researching purposes separately. However, in real life people sometimes need to balance different coordination strategies to achieve the goal more effectively (Skewes et al., 2015). Thus, it would be important for us to understand how the interpersonal coordination pattern (IP vs. MP) modulates the coordination outcome and the related brain-to-brain connectivity.

The essential distinction between the IP and MP is the relative frequency with which the actions of interacting individuals occur—IP has the movement frequency ratio of 1:1 while MP has the movement frequency ratios of non 1:1. According to the frequency-locking dynamics model, higher order frequency ratios were more difficult for individuals to perform or maintain than lower order frequency ratios (Treffner and Turvey, 1993; Peper et al., 1995). Related studies have provided evidence that when the frequency differences increased, the coordination of the group became less stable (Zhang et al., 2018), and more challenging (Gorman et al., 2017), which suggested that the MP would harm the coordination performance. However, it was found that team performance could also benefit from the asymmetry interpersonal relations in some complex social interactions (Wallot et al., 2016). In order to complete interpersonal coordination, individuals would use available information to predict another person's actions and then adjust their own actions (Knoblich and Jordan, 2003; Vesper et al., 2013). During this process, individuals might spontaneously form specific coordination strategies, for example, one person led the task and the other one followed ("leader-follower" relationship) (Davidson and Good, 2002; Goebl and Palmer, 2009; Richardson et al., 2015), or two persons equally adapted their behavior to each other ("hyper-leaders/followers" relationship) (Konvalinka et al., 2010; Pecenka and Keller, 2011). In MP condition, individuals moved at different frequencies, so that the partner's action could serve as a reference for individuals to adjust their action, which could facilitate the development of specific strategies and improve the interpersonal coordination performance.

In order to better understand the neural activities during social interaction, researchers have proposed a "two-person neuroscience" approach to study the physiological basis of human social interaction (Hari and Kujala, 2009). By recording the brain activities of two or more interacting individuals (i.e., hyperscanning), related studies have demonstrated that social interactions are associated with enhanced interpersonal brain synchronization (IBS), as measured by EEG (e.g., Jahng et al., 2017; Hu et al., 2018), fNIRS (e.g., Cui et al., 2012; Cheng et al., 2015; Liu et al., 2015; Hu et al., 2017), or fMRI (e.g., Schippers et al., 2010; Stolk et al., 2014). Specifically, the IBSs were found in various interpersonal coordination tasks. For example, studies have found inter-brain coherence when individuals moved at the same frequency, such as together key pressing (Cui et al., 2012; Cheng et al., 2015; Pan et al., 2017), coordinated group walking (Ikeda et al., 2017), and cooperative singing/humming (Osaka et al., 2014, 2015). Also, a related study has revealed synchronous oscillatory activities across individuals in a more complicated task in which a captain and a co-pilot coordinately operated the flight mission of plane takeoff and landing (Astolfi et al., 2012). By using a neuroimaging approach, studies have further observed the emergence of specific coordination strategies (e.g., leader-follower relationship) in terms of brain activities during individuals' interaction, demonstrating the greater information flow from the leader/sender to the follower/receiver (Schippers et al., 2010; Holper et al., 2012). Note that in these studies individuals were assigned with the dominant or secondary roles in the interaction tasks. If there are no such assigned roles, will individuals gradually form specific strategies during a continuous coordination activity? Moreover, will the brain-to-brain connectivity be varied by different coordination patterns?

Here, we explored how the coordination pattern (MP vs. IP) modulated the coordination outcome and the related brain-to-brain connectivity. We adopted a two-person complementary continuous joint drawing task to simulate the complex interpersonal coordination context in our real life. In the task, participants co-drew shapes of parallelograms on the computer by using a marker (one participant controlled the horizontal movement of the marker, while the other controlled the vertical movement of the marker), either at the same frequency (IP) or different frequencies (MP). Dyadic coordination performance in both IP and MP condition were calculated for comparison. Further, we recorded the brain activities from interacting individuals by simultaneously using the functional near-infrared spectroscopy (fNIRS) based hyperscanning technique. The prior region of interest was the frontopolar cortex, as it played an essential role in social interactions (especially in interpersonal coordination), where synchronous activities across brains were identified in previous fNIRS-based studies (Cheng et al., 2015; Nozawa et al., 2016; Ikeda et al., 2017). We would focus on the IBS during the interpersonal coordination. Further, Granger causality analysis (GCA) was used to provide a neurobiological suggestion of coupling directionality, i.e., which individual was more actively driving the other. In the study, we also collected participants' evaluations of self-control level, which was found to be related to the leadership (Fairhurst et al., 2014). Previous study has revealed that, compared to the followers, leaders would be generally associated with a stronger internal locus of control (self-control) and, therefore, a greater belief that outcomes were contingent on their behavior (Anderson and Schneier, 1978). Individuals' self-control bias could further modulate the degree of their adaptation to the partner when coordinating (Fairhurst et al., 2014). Collecting the participants' evaluations of self-control level and exploring their relationship with coordination performance and brain-to-brain connectivity would help us better understand the interpersonal coordination processes.

METHODS

Participants

Sixty-two graduate and undergraduate students (age: 21.39 ± 2.36 years, 15 males) took part in this study. All participants were right-handed and had normal or corrected-to-normal vision. They were randomly assigned into pairs with an unacquainted partner, and then 31 dyads (15 female-male dyads and 16 female-female dyads) were created. All participants provided written informed consent before the experiment. Each participant would be compensated 40 *yuan* for his/her participation. The experimental procedures were approved by the University Committee on Human Research Protection of East China Normal University, and carried out in accordance with the recommendations in the Methods.

Tasks and Procedures

Two participants, randomly assigned as participant #1 and participant #2, were seated in front of a computer monitor separately (at the distance of 50 cm approximately), separated by a thick partition (**Figure 1A**). They would first have a 3-min resting phase, during which both of them were asked to relax and to remain still (Jiang et al., 2015). The resting phase served as the baseline in the current study.

Participants then performed a computerized complementary continuous joint drawing task adapted from the children's drawing game "Etch-a-Sketch" (Arueti et al., 2013; Gooijers et al., 2013). Their goal was to trace the lines of the target shapes on the screen (resolution: 1,920 × 1,080) by using a marker. The movement of the marker was controlled by two participants jointly, participant #1 controlled the horizontal movement (with the "A" and "S" keys) and participant #2 controlled the vertical movement (with the "↑" and "↓" keys). A total of eight drawing blocks were included in the task. Each drawing block began with a 2-s fixation ("+") in the center of the screen, followed by a target shape in red (**Figure 1D**). The shape had the line width of 4 pixels. After 5 s, a blue marker (i.e., a filled circle with a diameter of 4 pixels) appeared randomly at one of the four vertexes of the target shape. Then participants could move the marker jointly by pressing specific keys (i.e., "A"/"S" and "↑"/"↓"). The gain of each key-pressing was set to 2 pixels. Participants were required to trace the lines of the shape precisely in a clockwise manner. When the marker went back to the start point, the drawing period ended. During the task, participants were not allowed to communicate with each other verbally. They could adjust their actions according to the real-time tracing path displayed on the screen.

Two coordination patterns (i.e., IP and MP) were arranged in the task. In the IP condition, the target shapes contained diagonal lines with the slope of 1 (the upper panel of **Figure 1C**); two participants needed to move at the same frequency to get better performance. In the MP condition, the target shapes contained diagonal lines with the slopes of 1/3 or 3 (the lower panel of **Figure 1C**). In this case, one participant (participant #1 or #2, randomly assigned) needed to move three times faster than the other one. Such a design was adopted in order to keep participants' actions as similar as possible across two conditions while the coordination pattern was manipulated. In MP condition, the participant who, relatively, moved a given drawing block faster would be regarded as the "higher-frequency participant," and the other one as the "lower-frequency participant." It was noted that an individual would possibly be the high-frequency participant in some drawing blocks and the low-frequency participant in others. Eight shapes (four in the IP condition and four in MP condition) used in the current study were equal in area, and their circumferences varied from 1,778 (MP condition) to 2,291 (IP condition) pixels. In the task, the eight shapes were presented in a random order.

Before the task, the participants completed a questionnaire of the locus of control (LOC) (Levenson, 1981). The questionnaire assessed the individual's general beliefs about the factors that have influenced one's own life. Three independent sub-scales included in the questionnaire measured the extent to which people believe that their lives are controlled by themselves (self-control), powerful others (other-control), or chance (chance-control). Each sub-scale included eight items. The questionnaire used a Likert response format (1–6 points, disagreement to agreement). In the current study, we mainly focused on the measurement of the self-control (Fairhurst et al., 2014).

NIRS Data Acquisition

An ETG-7100 optical topography system (Hitachi Medical Corporation, Japan) was employed to simultaneously measure participants' concentrations of oxygenated hemoglobin (oxy-Hb) and deoxygenated hemoglobin (deoxy-Hb) during the experiment. The sampling rate was 10 Hz. Each participant had 2 × 5 probe patches (with a 3 cm distance between emitter probes and detector probes), forming a total of 13 recording channels (CHs). The patch was placed over the participant's forehead, covering the frontopolar cortex (FPC) and part of the dorsal lateral prefrontal cortex (DLPFC). The placement of the patch followed the International 10–20 system. The lowest probe row of the patch was aligned with the horizontal reference curve, with the middle optode located on the frontal pole midline point (Fpz) (see **Figure 1B**). Meanwhile, the middle probe column of patches was aligned along the sagittal reference curve. The correspondence between the NIRS channels and the measurement points on the cerebral cortex was determined using the virtual registration method (Lancaster et al., 2000; Tzourio-Mazoyer et al., 2002; Singh et al., 2005; Tsuzuki et al., 2007), which has been validated by a multi-subject study of anatomical craniocerebral correlation (Okamoto et al., 2004).

Data Analyses

Behavior Performance

We recorded the coordinates of the marker's movements so that we could obtain dyads' tracing path by simple computation (Arueti et al., 2013). For each shape, we first calculated the deviation index of participants' drawings. It was determined by the number of pixels that the traced shape created by the participants (the blue line) deviated from the original shape (the red line) (Pink area, **Figure 1E**). For a given drawing block, the lower the deviation score indicated a more accurate precision by which the two participants drew. Since the circumferences of the eight shapes were not perfectly matched, which might have an impact on the deviation score, the original deviation scores were further divided by the circumference to eliminate the potential effect of the varying circumferences. The output deviation scores ranged between 0, representing a perfect score (flawless tracing), and tens of thousands, representing poor accuracy and a large deviation from the original shape. Given the inverse relationship between the deviation score and the accuracy performance, we took the reciprocal of deviation score as the accuracy performance. Lastly, accuracy performance per unit time, namely the coordination efficacy, was calculated as the behavior performance index in the current study. A high coordination efficacy value indicated a good coordination performance.

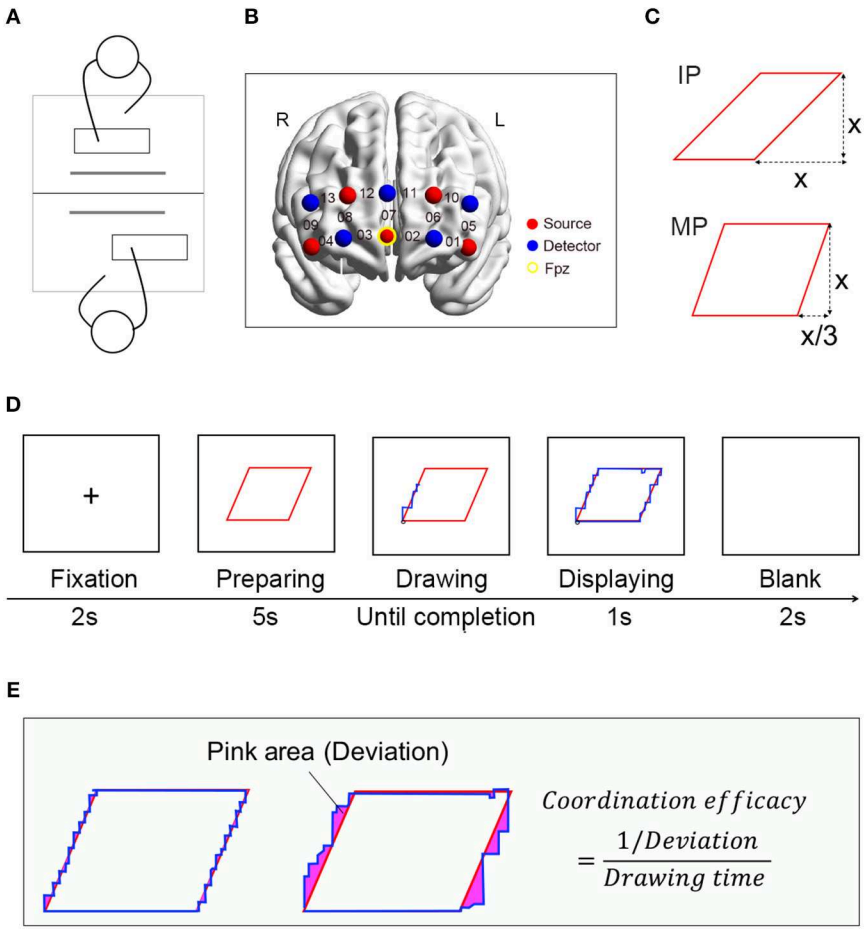

FIGURE 1 | Experimental design for the coordination task. **(A)** Experimental setup. Participants co-drew shapes of parallelogram jointly. **(B)** Probe configuration. The integers on the cerebral cortex indicate the measuring channels. **(C)** Examples of target shapes for the IP and MP conditions. **(D)** Events and time flow in a drawing block. **(E)** The calculation for coordination performance (i.e., coordination efficacy). The deviation scores were determined by the amounts of pixels that traced shape deviated from the original shape (the pink area).

Self-Control Level

We calculated dyadic self-control level by averaging the rating scores of two participants according to previous studies (Bilek et al., 2015; Hu et al., 2017; Pan et al., 2017). Additionally, we calculated the differences between the two participants in self-control scores. Specifically, in a dyad, the participant who had a relatively higher self-control score was labeled as the high-self-control participant, while the other one was labeled as the low-self-control participant.

Interpersonal Brain Synchronization (IBS)

Both oxy-Hb and deoxy-Hb signals were automatically exported from the ETG-7100 system. Only the oxy-Hb signals were analyzed in the current study since the oxygenated hemoglobin is the most sensitive parameter of regional cerebral blood flow and provides the robust correlation with the BOLD signal (Hoshi, 2003). We employed the method of spline interpolation to detect the possible motion artifacts (Scholkmann et al., 2010) (by using the function hmrMotionArtifactByChannel from the Homer2 NIRS Processing package, Huppert et al., 2009). Then, the oxy-Hb data were high-pass filtered with the cut-off frequency of 0.01 Hz to remove longitudinal signal drift and noise from the instrument. After the preprocessing, the wavelet transform coherence (WTC) analysis of the two time series derived from two participants in dyad was conducted to assess the IBS for each dyad and each channel (Grinsted et al., 2004). The WTC toolbox used in this study was from Grinsted et al. (2004). According to previous studies (Cui et al., 2012; Hu et al., 2017), a larger coherence value would be observed when two persons interact, compared with that during the resting state. As participants continuously coordinated with each other, and they needed approximately 7 seconds to trace a single line, we mainly focused on the period from 3.2 to 12.8 s (frequency band: 0.08∼0.31 Hz). Adopting this frequency band could also remove the high- and low-frequency noise as well. We then calculated the WTC values in our interested frequency band (i.e., 0.08∼0.31 Hz) for each participant dyad during the resting phase and the drawing periods. Task-related

IBS was defined as the increased IBS during the drawing periods compared to the resting phase (i.e., drawing period—resting phase). The false discovery rate (FDR) correction was applied for all 13 channels to control multiple comparisons, and the alpha-level was set to $p < 0.05$. Finally, the visualization of the IBS results was performed by BrainNet Viewer (Xia et al., 2013).

Directional Coupling

We conducted Granger causality analyses (GCA) to provide a neurobiological suggestion of coupling directionality, i.e., which individual was more actively driving the other, to explore whether there were specific coordination strategies developed during the interpersonal coordination. The Matlab Multivariate Granger Causality Toolbox (MVGC) was used to estimate the magnitude of Granger causality (i.e., GC) between two time series. GC is a statistical estimation of how much one time series is predicted by the history of another time series, taking into account how much it is predicted by its own previous history, in the form of a log-likelihood ratio (see more details in Barnett and Seth, 2014).

Our GCA was based on the preprocessed oxy-Hb signals during the drawing periods. Further, we converted the preprocessed signals into z-scores using the mean and the standard deviation of the signals recorded during the rest (baseline) session (Liu et al., 2015; Yang et al., 2016; Pan et al., 2018). In our study, we focused on the information flow between the high-self-control participant and the low-self-control participant (i.e., high-self-control participant → low-self-control participant, and low-self-control participant → high-self-control participant) in both MP and IP conditions. Additionally, we would also explore the information flow between the high-frequency participant and the low-frequency participant (i.e., high-frequency participant → low-frequency participant, and low-frequency participant → high-frequency participant) in only the MP condition, as there was no such a role of high- or low-frequency in the IP condition as two participants acted at the same frequency. Specifically, the GC was estimated at each direction for each dyad during MP and IP condition separately, and then one-sample *t*-tests were used to examine which direction differed from zero (Bonferroni adjusted). Independent-samples *t*-tests and repeated-measure ANOVA were further used to estimate the effects of direction and coordination pattern on the information flow.

RESULTS

Behavioral Performance

Participant dyads took approximately 27 s to complete drawing a shape. A pair-sample *t*-test was performed on the coordination performance, with the coordination pattern (MP vs. IP) as the within-subject independent variable. The result revealed a significant effect of coordination pattern, $t_{(30)} = 4.53$, $p < 0.001$, Cohen's $d = 0.81$, with the better coordination performance at the MP condition (0.0121 ± 0.0043) compared to the IP condition (0.0094 ± 0.0039) (**Figure 2**).

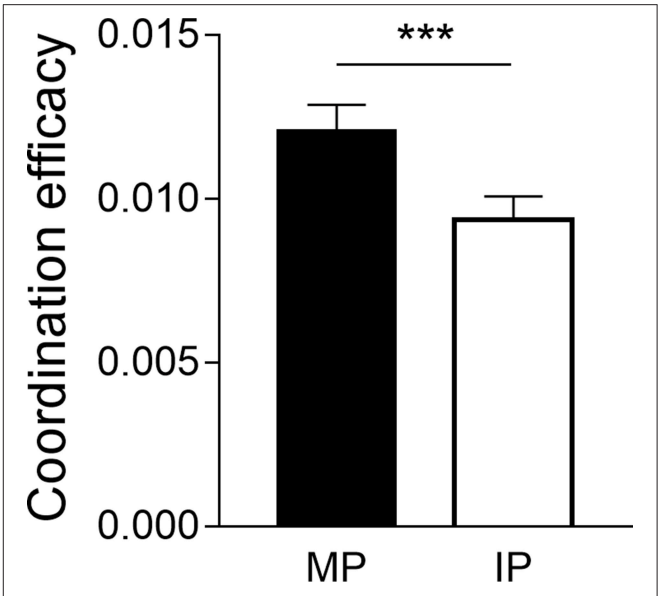

FIGURE 2 | Behavioral performance. Better coordination performance was found in the MP condition compared to the IP condition. Error bars indicated standard errors. ***$p < 0.001$.

The IBS During Interpersonal Coordination

We first examined whether there were increased task-related IBS during the interpersonal coordination. A series of one-sample *t*-tests were conducted on the task-related IBS for each channel. Channels 1∼8 demonstrated significant task-related IBS ($ts \geq 2.24$, $ps < 0.05$, Cohen's $ds \geq 0.40$, **Figure 3A**) during interpersonal coordination. All the above channels except CH 5 were survived after FDR correction. These channels were located at the bilateral FPC. We further examined the relationship between the IBS and the coordination efficacy for each channel. However, only the IBS at CH 1, which was located at the left FPC, showed the correlation with the coordination efficacy, $r = 0.43$, $p < 0.05$ (**Figure 3B**, FDR uncorrelated). This channel had also displayed significant increased task-related IBS during the coordination tasks. These findings indicated that the bilateral FPC was generally engaging in interpersonal coordination, and specifically, the IBS at the left FPC predicted the coordination outcome. Further, the IBS at the CH 1 was closely related to the dyadic self-control level, $r = 0.45$, $p < 0.05$ (**Figure 3B**).

We then performed a series of one-sample *t*-tests on the task-related IBS for the two conditions separately to find the IBS elicited by the specific coordination pattern. For the MP coordination, significant IBS was found at CHs 1∼7 ($ts \geq 2.20$, $ps < 0.05$, Cohen's $ds \geq 0.39$, **Figure 3C**), which were located at the bilateral FPC. Channels 1, 2, 3, 4, and 6 survived after FDR correction. Particularly, the IBS at the left FPC was associated with the coordination efficacy: CH 1, $r = 0.47$, $p < 0.01$. For the IP condition, significant IBS was found at CHs 2, 3, 4, 6, and 8 ($ts \geq 2.50$, $ps < 0.05$, Cohen's $ds \geq 0.45$, **Figure 3C**). The IBSs did not show their correlations with the coordination performance.

Direct comparisons between the IBS of these two coordination patterns were conducted. Pair-samples *t*-tests showed that the

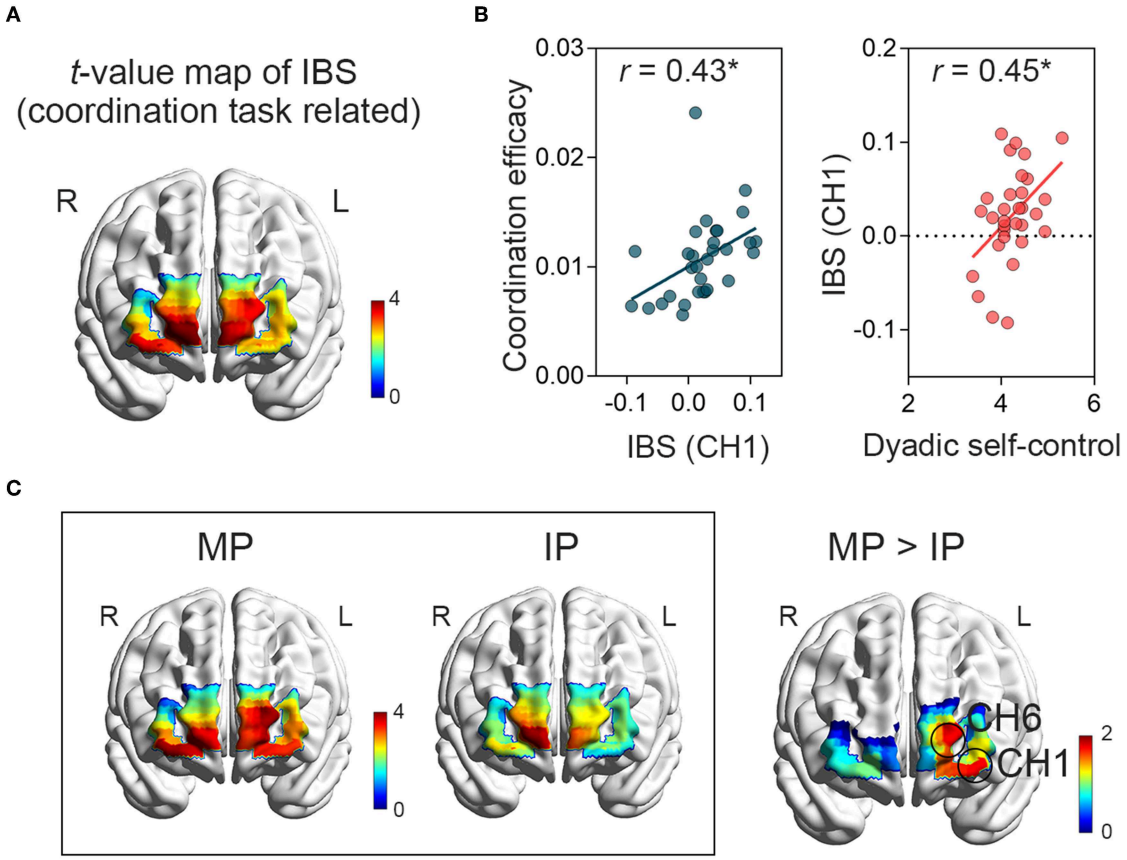

FIGURE 3 | The IBS. **(A)** Dyads showed significant IBS at the bilateral FPC when coordinating. **(B)** The IBS at the left FPC (CH 1) was positively correlated with the coordination efficacy. Further, the detected IBS was related to dyadic self-control level. *$p < 0.05$. **(C)** The IBS in the MP condition tended to be greater than that in the IP condition at left FPC (CH 1).

IBS in the MP condition tended to be greater than that in the IP condition at the left FPC (**Figure 3C**): CH 1, $t_{(30)} = 1.75$, $p < 0.05$ (one-tailed, FDR uncontrolled), Cohen's $d = 0.31$. CH 6, $t_{(30)} = 1.78$, $p < 0.05$ (one-tailed, FDR uncontrolled), Cohen's $d = 0.32$. However, no greater IBS was found in IP condition compared to the MP condition, $ps > 0.05$.

Coupling Directionality

We carried out Granger causality analyses (GCA) to explore the directionality of the coupling during interpersonal coordination. As CH 1 was engaged in the interpersonal coordination performance, we would mainly focus on the signals of CH 1. The results showed that all directions being examined (i.e., "high-self-control participant → low-self-control participant" and "low-self-control participant → high-self-control participant" in both MP and IP conditions, as well as "high-frequency participant → low-frequency participant" and "low-frequency participant → high-frequency participant" in the MP condition) yielded significant increases in the GC relative to zero, $ps < 0.05$ (Bonferroni adjusted).

Further, we performed a repeated measured ANOVA on the GC, with the direction ("high-self-control participant → low-self-control participant" and "low-self-control participant → high-self-control participant") as the between-subject variable and the coordination pattern (MP vs. IP) as the within-subject variable. The results revealed a significant main effect of coordination pattern, $F_{(1, 60)} = 4.14$, $p < 0.05$, $\eta^2_{\text{partial}} = 0.06$, with the larger GC in the MP condition (0.049 ± 0.005) compared to the IP condition (0.044 ± 0.004) (**Figure 4A**), suggesting the stronger interpersonal influence between coordinating individuals in the MP condition. However, we did not find a significant effect of the direction, $F_{(1, 60)} = 0.19$, $p > 0.05$, or the interaction between the direction and the coordination pattern, $F_{(1, 60)} = 0.93$, $p > 0.05$. Instead, we found a significantly positive correlation between the GCs of the two directions (**Figure 4B**), both in MP condition, $r = 0.52$, $p < 0.01$, and in the IP condition, $r = 0.58$, $p < 0.001$. Additionally, we examined the interpersonal influence between the high-frequency participant and low-frequency condition participant in the MP condition. The GCs of the two directions showed positive correlation (**Figure 4C**), $r = 0.43$, $p < 0.01$, and no evidence of coupling directionality was found, $t_{(60)} = 0.54$, $p > 0.05$. These findings indicated that two participants in dyad might not develop a leader-follower relationship during the coordination.

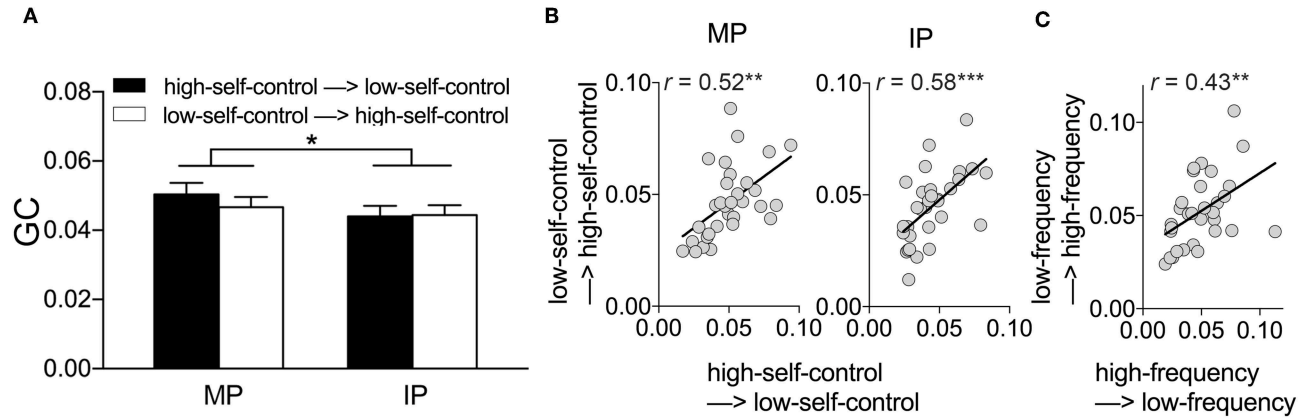

FIGURE 4 | GCA results (CH 1). **(A)** Larger GC was found in the MP condition compared to the IP condition. Error bars indicate standard errors. $^{*}p < 0.05$. **(B)** The GC from the high-self-control participant to the low-self-control participants was correlated with that from the low-self-control participant to the high-self-control participant in both the MP condition and IP condition. $^{***}p < 0.001$, $^{**}p < 0.01$. **(C)** In MP condition, the GC from the high-frequency participant to the low-frequency participants was correlated with that from the low-frequency participant to the high-frequency participant. $^{**}p < 0.01$.

DISCUSSION

In the current study, we arranged a complementary continuous joint drawing task in both MP and IP conditions and measured the brain activities of the coordinating individuals simultaneously. We found better coordination performance, as well as the relatively greater task-related IBS, in the MP condition compared to the IP condition. GCA analyses further revealed that there were mutually interpersonal influences (i.e., information flow from one participant to the other) between coordinating individual. Such a kind of interpersonal influence was generally stronger in the MP condition compared to the IP condition. Finally, the detected IBS had a linkage to the dyadic self-control level. To our knowledge, this is the first fNIRS-based hyperscanning study directly exploring how interpersonal coordination pattern modulated coordination outcome and the related brain-to-brain connectivity.

In this study, significant IBS was observed during the interpersonal coordination at the FPC as expected. Specifically, we found the close relationship between the degree of increased IBS at the left PFC and the coordination efficacy. These findings highlighted the engagement of FPC in interpersonal coordination, which was consistent with the previous studies (Suda et al., 2010; Funane et al., 2011; Cheng et al., 2015; Ikeda et al., 2017). The measured frontopolar brain signals might indeed reflect functions involved in social interaction and coordination. The IBS at FPC induced by the interpersonal coordination could be possibly related to the temporally aligned recruitment of coordination-related cognitive processes, such as mentalizing and predicting each other's states (Frith and Frith, 2003; Amodio and Frith, 2006) and monitoring outcomes and maintaining meta-cognitive representations (Amodio and Frith, 2006; Rushworth et al., 2011).

The better coordination performance, as well as the relatively greater brain-to-brain connectivity (i.e., IBS and GC), was found in the multifrequency coordination pattern in the current study. It would be likely that the coordination between individuals might not simply follow the frequency-locking dynamics model that suggesting coordination performance would be damaged in the MP condition. Instead, MP settings might facilitate the information exchange between co-actors when they needed to perform quickly continuous movements and they could hardly see each other and were not allowed to communicate with each other directly. According to participants' informally oral reports (obtained after they completed the task), they generally felt difficult to maintain the actions, especially in the IP pattern condition as they could not well-predict their partner's action. In the MP condition, individuals did not need to move at the same time, so that they could observe and predict their partner's actions, and then adjust their own actions easily. Making correct predictions could be crucial for successfully performing joint actions (Vesper et al., 2013, 2017). Thus, the information exchange might be more efficient in the MP condition. The possibility was supported by the greater brain-to-brain connectivity, i.e., increased IBS and enhanced interpersonal information flow, during individuals' coordination in the MP condition. The brain-to-brain coupling between interacting individuals was found to mark the emergence of meaning and mutual understanding (Stolk et al., 2014). It was noted that participants' subjectively perceived different difficulty level in maintaining the two coordination patterns might also moderate the results to some extent; future studies could employ objective measurements or formal subjective ratings to clarify this issue.

With respect to the IP condition, we did not find significant correlations between the detected IBS (at CHs 2/3/4/6) and the coordination efficacy. It should be noted that interpersonal coordination activity generally involves multiple cognitive processes, such as mental representing, information sharing, and action monitoring (Vesper et al., 2017). It might be possible that the CHs (i.e., 2/3/4/6) were engaging in some cognitive processes during the interpersonal coordination, so that the IBS could be induced by the coordination activity but could not well-predict

the overall degree of coordination efficacy. In the current study, only the IBS at CH 1 showed its correlation with the coordination efficacy during interpersonal coordination, which suggested that the IBS at CH 1 could be a predictor for the interpersonal coordination efficacy. We found the relationship of IBS at CH 1 and the coordination efficacy in the MP condition. Also, the IBS at CH 1 tended to show its correlation with the coordination efficacy in IP condition, $r = 0.30$, $p < 0.05$ (one-tailed). Given that in the IP condition the coordination efficacy was damaged, we speculate that the coordinating actions between two participants did not achieve success, so that the IBS at CH 1 did not reach a significant level, and the correlation of IBS and coordination efficacy was relatively weak.

During interpersonal coordination, two potential coordination strategies have been found in previous studies: the "leader-follower" relationship (Davidson and Good, 2002; Goebl and Palmer, 2009; Richardson et al., 2015) and the "hyper-leader/follower" relationship (Konvalinka et al., 2010; Pecenka and Keller, 2011). In the current study, we did not observe the difference in the GC between the related directions (e.g., "high-self-control participant → low-self-control participant" vs. "low-self-control participant → high-self-control participant"; "high-frequency participant → low-frequency participant" vs. "low-frequency participant→ high-frequency participant"), indicating that individuals might not develop the primary or secondary roles. Instead, our GCA results showed the information flow from the high-self-control participant to the low-self-control participant was correlated with that from the low-self-control participant to the high-self-control participant, which suggested that the two participants influenced (or adapted) to each other mutually. Thus, we argued that participants performing the coordination task may form the "hyper-leader/follower" relationship in our study. Given that individuals could change their collaboration strategies and find a proper interaction mode to better achieve the goal (Skewes et al., 2015), it might also be possible that individuals were planning to form a "leader-follower" relationship at the beginning, and both of them happened to consider themselves being leaders or followers, forming a "hyper-leaders/followers" relationship. Future studies could further explore the development of coordination strategies during social interactions over time.

The present study pointed to a connection between the IBS during interpersonal coordination and the dyadic self-control level, which was consistent with the previous findings that the IBS was related to real-world social functioning (Bilek et al., 2015). Noted that we did not find a significant correlation between the self-control and the coordination efficacy ($r = 0.15$, $p = 0.43$), which suggested that the self-control level might modulate the interpersonal coordination processes but not directly contribute to the coordination outcome. The association between the IBS and self-control in the current study could reflect the mutual adaptation to some extent. We did not find the association between the detected IBS and two participants' difference in self-control. It indicated that the conception difference among individuals did not influence the IBS. These results provided additional evidence for a potential "hyper-leaders/followers" rather than "leader-follower" relationship between interacting individuals.

Several limitations should be addressed. First, only one frequency ratio (i.e., 1:3) was arranged in the MP condition in the present study. Related study has found that the in non 1:1 frequency ratios, the types of frequency ratios, such as integer (e.g., 1:3, 1:2) or not (e.g., 2:3, 3:5), could also affect coordination performance (Gooijers et al., 2013). Additional frequency ratios could be included in future studies. Besides, in the current task, two participants were not allowed to communicate with each other directly. Previous studies have revealed the roles of gaze or gesture communications in the joint action (Chen et al., 2013; Bilek et al., 2015). It would be worth exploring the effect of coordination pattern when two participants could see or hear each other. Second, we could not exclude the potential effect of task difficulty level on the establishment of IBS and coordination efficacy. Future studies could further manipulate or control the difficulty level of different coordination patterns. At last, we measured the FPC and DLPFC in the current study, however, other areas, such as right temporal parietal junction and superior frontal cortex, were also found to play an important role in social interaction (Cui et al., 2012; Liu et al., 2016; Pan et al., 2017). It could be possible that the significant IBS would be found in other regions in IP condition. The roles of the related brain regions during interpersonal coordination (including both MP and IP conditions) could be further examined by measuring the entire brain.

In summary, our work explored the effect of coordination pattern (MP vs. IP) on interpersonal coordination outcome and the related brain-to-brain connectivity. Compared to the IP condition, the MP condition could elicit better coordination performance and relatively greater brain-to-brain connectivity (i.e., IBS and interpersonal influence) between coordinating individuals. Finally, the IBS during the interpersonal coordination was related to dyadic self-control level. Taken together, our study revealed that the multifrequency pattern favors for the interpersonal coordination, which was associate with the enhanced brain-to-brain connectivity between coordinating individuals. These findings provide valuable insights for real-world teamwork, during which two or more individuals are required to coordinate in both space and time. Future studies can explore whether the effect is seen here with the bidirectional interaction also holds for the unidirectional interaction, as well as this effect in those with disorders of social cognition and behavior.

DATA AVAILABILITY STATEMENT

The datasets generated for this study are available on request to the corresponding author.

ETHICS STATEMENT

This study was carried out in accordance with the recommendations of the University Committee on Human

Research Protection of East China Normal University with written informed consent from all subjects. All subjects gave written informed consent in accordance with the Declaration of Helsinki. The protocol was approved by the University Committee on Human Research Protection of East China Normal University.

AUTHOR CONTRIBUTIONS

XC and YiH designed experiments. YP and YinH carried out experiments. XC, YiH, and YP analyzed experimental results. XC and YiH wrote the manuscript.

FUNDING

This work was supported by National Natural Science Foundation of China (31800951 and 31872783), the Natural Science Foundation of Guangdong (2018A030310431), the Guangdong Provincial Key Platform and Major Scientific Research Projects (2017KQNCX172), and the Natural Science Foundation of SZU (2018053).

ACKNOWLEDGMENTS

The authors would like to thank Zixuan Wang and Yujiao Zhu for their assistance in data acquisition.

REFERENCES

Amodio, D. M., and Frith, C. D. (2006). Meeting of minds: the medial frontal cortex and social cognition. *Nat. Rev. Neurosci.* 7, 268–277. doi: 10.1038/nrn1884

Anderson, C. R., and Schneier, C. E. (1978). Locus of control, leader behavior and leader performance among management students. *J. Acad. Manag.* 21, 690–698. doi: 10.2307/255709

Arueti, M., Perachbarzilay, N., Tsoory, M. M., Berger, B., Getter, N., and Shamaytsoory, S. G. (2013). When two become one: the role of oxytocin in interpersonal coordination and cooperation. *J. Cogn. Neurosci.* 25, 1418–1427. doi: 10.1162/jocn_a_00400

Astolfi, L., Toppi, J., Borghini, G., Vecchiato, G., He, E. J., Roy, A., et al. (2012). Cortical activity and functional hyperconnectivity by simultaneous EEG recordings from interacting couples of professional pilots. *Conf. Proc. IEEE Eng. Med. Biol. Soc.* 2012, 4752–4755. doi: 10.1109/EMBC.2012.6347029

Barnett, L., and Seth, A. K. (2014). The mvgc multivariate granger causality toolbox: a new approach to granger-causal inference. *J. Neurosci. Methods* 223, 50–68. doi: 10.1016/j.jneumeth.2013.10.018

Bilek, E., Ruf, M., Schäfer, A., Akdeniz, C., Calhoun, V. D., Schmahl, C., et al. (2015). Information flow between interacting human brains: identification, validation, and relationship to social expertise. *Proc. Natl Acad. Sci. U.S.A.* 112, 5207–5212. doi: 10.1073/pnas.1421831112

Chen, Y., Smith, L. B., and Andrew, B. (2013). Joint attention without gaze following: human infants and their parents coordinate visual attention to objects through eye-hand coordination. *PLoS ONE* 8:e79659. doi: 10.1371/journal.pone.0079659

Cheng, X., Li, X., and Hu, Y. (2015). Synchronous brain activity during cooperative exchange depends on gender of partner: a fNIRS based hyperscanning study. *Hum. Brain Mapp.* 36, 2039–2048. doi: 10.1002/hbm.22754

Cui, X., Bryant, D. M., and Reiss, A. L. (2012). NIRS-based hyperscanning reveals increased interpersonal coherence in superior frontal cortex during cooperation. *Neuroimage* 59, 2430–2437. doi: 10.1016/j.neuroimage.2011.09.003

Davidson, J. W., and Good, J. M. M. (2002). Social and musical coordination between members of a string quartet: an exploratory study. *Psychol. Music* 30, 186–201. doi: 10.1177/0305735602302005

Fairhurst, M. T., Janata, P., and Keller, P. E. (2014). Leading the follower: an fMRI investigation of dynamic cooperativity and leader-follower strategies in synchronization with an adaptive virtual partner. *Neuroimage* 84:688. doi: 10.1016/j.neuroimage.2013.09.027

Frith, U., and Frith, C. D. (2003). Development and neurophysiology of mentalising. *Philos. Transac. R. Soc. Lond. B* 358, 459–473. doi: 10.1098/rstb.2002.1218

Funane, T., Kiguchi, M., Atsumori, H., Sato, H., Kubota, K., and Koizumi, H. (2011). Synchronous activity of two people's prefrontal cortices during a cooperative task measured by simultaneous nearinfrared spectroscopy. *J. Biomed. Opt.* 16:077011. doi: 10.1117/1.3602853

Goebl, W., and Palmer, C. (2009). Synchronization of timing and motion among performing musicians. *Music Percept.* 26, 427–438. doi: 10.1525/mp.2009.26.5.427

Gooijers, J., Caeyenberghs, K., Sisti, H. M., Geurts, M., Heitger, M. H., Leemans, A., et al. (2013). Diffusion tensor imaging metrics of the corpus callosum in relation to bimanual coordination: effect of task complexity and sensory feedback. *Hum. Brain Mapp.* 34, 241–252. doi: 10.1002/hbm.21429

Gorman, C., Amazeen, P. G., Crites, M. J., and Gipson, C. L. (2017). Deviations from mirroring in interpersonal multifrequency coordination when visual information is occluded. *Exp. Brain Res.* 235, 1209–1221. doi: 10.1007/s00221-017-4888-5

Grinsted, A., Moore, J. C., and Jevrejeva, S. (2004). Application of the cross wavelet transform and wavelet coherence to geophysical time series. *Nonlinear Processes Geophys.* 11, 561–566. doi: 10.5194/npg-11-561-2004

Hari, R., and Kujala, M. V. (2009). Brain basis of human social interaction: from concepts to brain imaging. *Physiol. Rev.* 89, 453–479. doi: 10.1152/physrev.00041.2007

Holper, L., Scholkmann, F., and Wolf, M. (2012). Between-brain connectivity during imitation measured by fNIRS. *Neuroimage* 63, 212–222. doi: 10.1016/j.neuroimage.2012.06.028

Hoshi, Y. (2003). Functional near-infrared optical imaging: utility and limitations in human brain mapping. *Psychophysiology* 40, 511–520. doi: 10.1111/1469-8986.00053

Hu, Y., Hu, Y., Li, X., Pan, Y., and Cheng, X. (2017). Brain-to-brain synchronization across two persons predicts mutual prosociality. *Soc. Cogn. Affect. Neurosci.* 2017, 1835–1844. doi: 10.1093/scan/nsx118

Hu, Y., Pan, Y., Shi, X., Cai, Q., Li, X., and Cheng, X. (2018). Inter-brain synchrony and cooperation context in interactive decision making. *Biol. Psychol.* 133, 54–62. doi: 10.1016/j.biopsycho.2017.12.005

Huppert, T. J., Diamond, S. G., Franceschini, M. A., and Boas, D. A. (2009). Homer: a review of time-series analysis methods for near-infrared spectroscopy of the brain. *Appl. Opt.* 48, D280–D298. doi: 10.1364/AO.48.00D280

Ikeda, S., Nozawa, T., Yokoyama, R., Miyazaki, A., Sasaki, Y., Sakaki, K., et al. (2017). Steady beat sound facilitates both coordinated group walking and inter-subject neural synchrony. *Front. Hum. Neurosci.* 11:147. doi: 10.3389/fnhum.2017.00147

Jahng, J., Kralik, J. D., Hwang, D. U., and Jeong, J. (2017). Neural dynamics of two players when using nonverbal cues to gauge intentions to cooperate during the prisoner's dilemma game. *Neuroimage* 157, 263–274. doi: 10.1016/j.neuroimage.2017.06.024

Jiang, J., Chen, C., Dai, B., Shi, G., Ding, G., Liu, L., et al. (2015). Leader emergence through interpersonal neural synchronization. *Proc. Natl. Acad. Sci. U.S.A.* 112, 4274. doi: 10.1073/pnas.1422930112

Knoblich, G., and Jordan, J. S. (2003). Action coordination in groups and individuals: learning anticipatory control. *J. Exp. Psychol. Learn. Memory Cogn.* 29, 1006–1016. doi: 10.1037/0278-7393.29.5.1006

Konvalinka, I., Vuust, P., Roepstorff, A., and Frith, C. D. (2010). Follow you, follow me: continuous mutual prediction and adaptation in joint tapping. *Q. J. Exp. Psychol.* 63:2220. doi: 10.1080/17470218.2010.497843

Lancaster, J. L., Woldorff, M. G., Parsons, L. M., Liotti, M., Freitas, E. S., and Rainey, L., et al. (2000). Automated Talairach Atlas labels for functional brain mapping. *Hum. Brain Mapp.* 10, 120–131. doi: 10.1002/1097-0193(200007)10:3<120::AID-HBM30>3.0.CO;2-8

Levenson, H. (1981). "Differentiating among internality, powerful others, and chance," in *Research with the Locus of Control Construct, Assessment Methods, Vol. 1*, ed H. M. Lefcourt (London: Academic), 15–63. doi: 10.1016/B978-0-12-443201-7.50006-3

Liu, N., Mok, C., Witt, E. E., Pradhan, A. H., Chen, J. E., and Reiss, A. L. (2016). NIRS-based hyperscanning reveals inter-brain neural synchronization during cooperative Jenga game with face-to-face communication. *Front. Hum. Neurosci.* 10:82. doi: 10.3389/fnhum.2016.00082

Liu, T., Saito, H., and Oi, M. (2015). Role of the right inferior frontal gyrus in turn-based cooperation and competition: a near-infrared spectroscopy study. *Brain Cogn.* 99, 17–23. doi: 10.1016/j.bandc.2015.07.001

Nessler, J. A., and Gilliland, S. J. (2009). Interpersonal synchronization during side by side treadmill walking is influenced by leg length differential and altered sensory feedback. *Hum. Move. Sci.* 28, 772–785. doi: 10.1016/j.humov.2009.04.007

Nozawa, T., Sasaki, Y., Sakaki, K., Yokoyama, R., and Kawashima, R. (2016). Interpersonal frontopolar neural synchronization in group communication: an exploration toward fNIRS hyperscanning of natural interactions. *Neuroimage* 133, 484–497. doi: 10.1016/j.neuroimage.2016.03.059

Okamoto, M., Dan, H., Sakamoto, K., Takeo, K., Shimizu, K., Kohno, S., et al. (2004). Three dimensional probabilistic anatomical cranio-cerebral correlation via the international 10–20 system oriented for transcranial functional brain mapping. *Neuroimage* 21, 99–111. doi: 10.1016/j.neuroimage.2003.08.026

Osaka, N., Minamoto, T., Yaoi, K., Azuma, M., and Osaka, M. (2014). Neural synchronization during cooperated humming: a hyperscanning study using fNIRS. *Procedia Soc. Behav. Sci.* 126, 241–243. doi: 10.1016/j.sbspro.2014.02.395

Osaka, N., Minamoto, T., Yaoi, K., Azuma, M., Shimada, Y. M., and Osaka, M. (2015). How two brains make one synchronized mind in the inferior frontal cortex: fNIRS-Based hyperscanning during cooperative singing. *Front. Psychol.* 6:1811. doi: 10.3389/fpsyg.2015.01811

Pan, Y., Cheng, X., Zhang, Z., Li, X., and Hu, Y. (2017). Cooperation in lovers: an fNIRS-based hyperscanning study. *Hum. Brain Mapp.* 38, 831–841. doi: 10.1002/hbm.23421

Pan, Y., Novembre, G., Song, B., Li, X., and Hu, Y. (2018). Interpersonal synchronization of inferior frontal cortices tracks social interactive learning of a song. *Neuroimage* 183, 280–290. doi: 10.1016/j.neuroimage.2018.08.005

Pecenka, N., and Keller, P. E. (2011). The role of temporal prediction abilities in interpersonal sensorimotor synchronization. *Exp. Brain Res.* 211, 505–515. doi: 10.1007/s00221-011-2616-0

Peper, C. E., Beek, P. J., and van Wieringen, P. C. W. (1995). Multifrequency coordination in bimanual tapping: asymmetrical coupling and signs of supercriticality. *J. Exp. Psychol. Hum. Percept. Perform.* 21, 1117–1138. doi: 10.1037/0096-1523.21.5.1117

Richardson, M. J., Harrison, S. J., Kallen, R. W., Walton, A., Eiler, B. A., Saltzman, E., et al. (2015). Self-organized complementary joint action: behavioral dynamics of an interpersonal collision-avoidance task. *J. Exp. Psychol. Hum. Percept. Perform.* 41:665. doi: 10.1037/xhp0000041

Richardson, M. J., Marsh, K. L., Isenhower, R. W., Goodman, J. R., and Schmidt, R. C. (2007). Rocking together: dynamics of intentional and unintentional interpersonal coordination. *Hum. Move. Sci.* 26,867–891. doi: 10.1016/j.humov.2007.07.002

Rushworth, M. F. S., Noonan, M. P., Boorman, E. D., Walton, M. E., and Behrens, T. E. (2011). Frontal cortex and reward-guided learning and decision-making. *Neuron* 70, 1054–1069. doi: 10.1016/j.neuron.2011.05.014

Schippers, M. B., Roebroeck, A., Renken, R., Nanetti, L., and Keysers, C. (2010). Mapping the information flow from one brain to another during gestural communication. *Proc. Natl. Acad. Sci. U.S.A.* 107, 9388–9393. doi: 10.1073/pnas.1001791107

Scholkmann, F., Spichtig, S., Muehlemann, T., and Wolf, M. (2010). How to detect and reduce movement artifacts in near-infrared imaging using moving standard deviation and spline interpolation. *Physiol. Measurement* 31, 649–662. doi: 10.1088/0967-3334/31/5/004

Sebanz, N., Bekkering, H., and Knoblich, G. (2006). Joint action: bodies and minds moving together. *Trends Cogn. Sci.* 10, 70–76. doi: 10.1016/j.tics.2005.12.009

Singh, A. K., Okamoto, M., Dan, H., Jurcak, V., and Dan, I. (2005). Spatial registration of multichannel multi-subject fNIRS data to MNI space without MRI. *Neuroimage* 27, 842–851. doi: 10.1016/j.neuroimage.2005.05.019

Skewes, J. C., Skewes, L., Michael, J., and Konvalinka, I. (2015). Synchronised and complementary coordination mechanisms in an asymmetric joint aiming task. *Exp. Brain Res.* 233, 551–565. doi: 10.1007/s00221-014-4135-2

Stolk, A., Noordzij, M. L., Verhagen, L., Volman, I., Schoffelen, J.-M., Oostenveld, R., et al. (2014). Cerebral coherence between communicators marks the emergence of meaning. *Proc. Natl. Acad. Sci. U.S.A.* 111, 18183–18188. doi: 10.1073/pnas.1414886111

Suda, M., Takei, Y., Aoyama, Y., Narita, K., Sato, T., Fukuda, M., et al. (2010). Frontopolar activation during face-to-face conversation: an in situ, study using near-infrared spectroscopy. *Neuropsychologia* 48, 441–447. doi: 10.1016/j.neuropsychologia.2009.09.036

Treffner, P. J., and Turvey, M. T. (1993). Resonance constraints on rhythmic movement. *J. Exp. Psychol. Hum. Percept. Perform.* 19, 1221–1237. doi: 10.1037/0096-1523.19.6.1221

Tsuzuki, D., Jurcak, V., Singh, A. K., Okamoto, M., Watanabe, E., and Dan, I. (2007). Virtual spatial registration of stand-alone MRS data to MNI space. *Neuroimage* 34, 1506–1518. doi: 10.1016/j.neuroimage.2006.10.043

Tzourio-Mazoyer, N., Landeau, B., Papathanassiou, D., Crivello, F., Etard, O., Delcroix, N., et al. (2002). Automated anatomical labeling of activations in SPM using a macroscopic anatomical parcellation of the MNI MRI single-subject brain. *Neuroimage* 15, 273–289. doi: 10.1006/nimg.2001.0978

Vesper, C., Abramova, E., Bütepage, J., Ciardo, F., Crossey, B., Effenberg, A., et al. (2017). Joint action: mental representations, shared information and general mechanisms for coordinating with others. *Front. Psychol.* 7:254. doi: 10.3389/fpsyg.2016.02039

Vesper, C., van der Wel, R., Knoblich, G., and Sebanz, N. (2013). Are you ready to jump? Predictive mechanisms in interpersonal coordination. *J. Exp. Psychol. Hum. Percept. Perform.* 39, 48–61. doi: 10.1037/a0028066

Wallot, S., Mitkidis, P., McGraw, J. J., and Roepstorff, A. (2016). Beyond synchrony: joint action in a complex production task reveals beneficial effects of decreased interpersonal synchrony. *PLoS ONE* 11:e0168306. doi: 10.1371/journal.pone.0168306

Xia, M., Wang, J., and He, Y. (2013). BrainNet viewer: a network visualization tool for human brain connectomics. *PLoS ONE* 8:e68910. doi: 10.1371/journal.pone.0068910

Yang, J., Kanazawa, S., Yamaguchi, M. K., and Kuriki, I. (2016). Cortical response to categorical color perception in infants investigated by near-infrared spectroscopy. *Proc. Natl. Acad. Sci. U.S.A.* 113, 2370–2375. doi: 10.1073/pnas.1512044113

Zhang, M., Kelso, J. A. S., and Tognoli, E. (2018). Critical diversity: divided or united states of social coordination. *PLoS ONE* 13:e0193843. doi: 10.1371/journal.pone.0193843

Conflict of Interest: The authors declare that the research was conducted in the absence of any commercial or financial relationships that could be construed as a potential conflict of interest.

Copyright © 2019 Cheng, Pan, Hu and Hu. This is an open-access article distributed under the terms of the Creative Commons Attribution License (CC BY). The use, distribution or reproduction in other forums is permitted, provided the original author(s) and the copyright owner(s) are credited and that the original publication in this journal is cited, in accordance with accepted academic practice. No use, distribution or reproduction is permitted which does not comply with these terms.

frontiers in Neuroscience

ORIGINAL RESEARCH
published: 18 October 2019
doi: 10.3389/fnins.2019.01129

Cognitive Enhancement by Transcranial Photobiomodulation Is Associated With Cerebrovascular Oxygenation of the Prefrontal Cortex

*Emma Holmes[1], Douglas W. Barrett[1], Celeste L. Saucedo[1], Patrick O'Connor[1], Hanli Liu[2] and F. Gonzalez-Lima[1]**

[1] Department of Psychology, Institute for Neuroscience, University of Texas at Austin, Austin, TX, United States, [2] Department of Bioengineering, University of Texas at Arlington, Arlington, TX, United States

OPEN ACCESS

Edited by:
Vince D. Calhoun,
Georgia State University,
United States

Reviewed by:
Juanita J. Anders,
Uniformed Services University of the Health Sciences, United States
Paolo Cassano,
Massachusetts General Hospital and Harvard Medical School,
United States

***Correspondence:**
F. Gonzalez-Lima
gonzalezlima@utexas.edu

Specialty section:
This article was submitted to Brain Imaging Methods, a section of the journal Frontiers in Neuroscience

Received: 12 April 2019
Accepted: 04 October 2019
Published: 18 October 2019

Citation:
Holmes E, Barrett DW, Saucedo CL, O'Connor P, Liu H and Gonzalez-Lima F (2019) Cognitive Enhancement by Transcranial Photobiomodulation Is Associated With Cerebrovascular Oxygenation of the Prefrontal Cortex. Front. Neurosci. 13:1129. doi: 10.3389/fnins.2019.01129

Transcranial infrared laser stimulation (TILS) is a novel, safe, non-invasive method of brain photobiomodulation. Laser stimulation of the human prefrontal cortex causes cognitive enhancement. To investigate the hemodynamic effects in prefrontal cortex by which this cognitive enhancement occurs, we used functional near-infrared spectroscopy (fNIRS), which is a safe, non-invasive method of monitoring hemodynamics. We measured concentration changes in oxygenated and deoxygenated hemoglobin, total hemoglobin and differential effects in 18 healthy adults during sustained attention and working memory performance, before and after laser of the right prefrontal cortex. We also measured 16 sham controls without photobiomodulation. fNIRS revealed large effects on prefrontal oxygenation during cognitive enhancement post-laser and provided the first demonstration that cognitive enhancement by transcranial photobiomodulation is associated with cerebrovascular oxygenation of the prefrontal cortex. Sham control data served to rule out that the laser effects were due to pre-post task repetition or other non-specific effects. A laser-fNIRS combination may be useful to stimulate and monitor cerebrovascular oxygenation associated with neurocognitive enhancement in healthy individuals and in those with prefrontal hypometabolism, such as in cognitive aging, dementia and many neuropsychiatric disorders.

Keywords: photobiomodulation, near-infrared spectroscopy, prefrontal cortex, cognitive enhancement, cerebrovascular oxygenation

INTRODUCTION

Photobiomodulation techniques using lasers or LEDs in the far-red to near-infrared spectrum, also called low-level light/laser therapy, have been widely used for wound healing, musculoskeletal pain, arthritis, and other conditions (Brosseau et al., 2004; Hopkins et al., 2004; Cotler et al., 2015). Brain cells are highly dependent on oxygen supply for energy metabolism. Various forms of photobiomodulation of the nervous system are currently being tested for applications in aging-related neurocognitive decline (Vargas et al., 2017), depression and anxiety (Disner et al., 2016; Caldieraro and Cassano, 2019) as well as various neurological disorders (Naeser and Hamblin, 2011; Holanda et al., 2017). Recently, transcranial infrared laser stimulation (TILS) by 1064-nm laser has

been introduced as a possible means of human cognitive enhancement (Barrett and Gonzalez-Lima, 2013; Gonzalez-Lima and Barrett, 2014; Hwang et al., 2016; Blanco et al., 2017a,b).

This experiment attempted to elucidate the hemodynamic effects of TILS of the human prefrontal cortex at the wavelength, energy and power density used in previous cognitive augmentation studies. The goal was to provide further support for the proposed mechanism of cerebral oxygenation of this treatment (Tian et al., 2016; Wang et al., 2017) by gathering real-time hemodynamic data from around the prefrontal site of laser administration during cognitive performance. A better understanding of the hemodynamic effects of this new method for cognitive enhancement may allow progress toward its use as a clinical treatment.

Photobiomodulation techniques influence mitochondrial respiration and promote beneficial cellular functions in multiple tissues, including nervous tissue (Eells et al., 2004; Wong-Riley et al., 2005). It has been suggested that brain photobiomodulation has a photonic action on cytochrome-c-oxidase (CCO) that leads to hemodynamic effects (Rojas and Gonzalez-Lima, 2011; Gonzalez-Lima and Barrett, 2014). Near infrared photons pass through the forehead (Tedford et al., 2015) to affect the functioning of tissue on the cortical surface, upregulating the enzymatic activity of CCO, the final and rate-limiting step in the mitochondrial electron transport chain. CCO is responsible for oxygen consumption at the cellular level, which is vital in oxidative phosphorylation for the production of ATP, the primary source of biochemical energy in the body. Mitochondrial respiration driven by neural activation leads to higher demand for energy production that needs to be maintained by increasing the supply of oxygenated blood from the circulation. Alternatively, the laser stimulation might produce transcranial effects due to the heat produced by the laser or the LEDs (Ito et al., 2000). However, it has recently been confirmed that the effects of TILS are due to the effect of the photons themselves that photo-oxidize CCO to a conformation that has more affinity for oxygen consumption, rather than the effects of heat on increasing metabolism or circulation (Wang et al., 2018). This further supports the hypothesis that photons from TILS are acting by upregulating CCO and therefore having an enhancing effect on mitochondrial energy metabolism and cerebral hemodynamics (Wang et al., 2017).

Functional near-infrared spectroscopy (fNIRS) is an optical method that usually maps the transient hemodynamic responses in the cerebral cortex during functional tasks, including cognitive tasks such as working memory (Tian et al., 2014). However, a different application of fNIRS with two source-detector channels served to investigate longer time (minutes) cerebral hemodynamic effects during TILS (Tian et al., 2016). In our present application of fNIRS, we combined cognitive tasks with 20 source-detector channels to measure longer time effects before and after TILS. The head was fitted with a close cap covered in grommets with positions consistent with the 10–20 EEG mapping system. These grommets served as housings for a montage of 20 channels of optical emitters and detectors, spaced 3-cm apart. In dual-wavelength fNIRS, emitters serve as sources for two wavelengths of light, each on either side of the isosbestic point of hemoglobin at 810 nm. One wavelength is primarily absorbed by oxygenated hemoglobin (HbO_2), whereas the other wavelength is primarily absorbed by deoxygenated hemoglobin (Hb). The detectors use fiber optic cables to extract photons not absorbed by hemoglobin and transmit them into the spectroscopy system. The computational system is then able to determine the relative change (Δ) in concentrations of oxygenated hemoglobin [HbO_2] and deoxygenated hemoglobin [Hb]. Dual-wavelength fNIRS has already been used to show the longer time effects of TILS on cerebral oxygenation in humans who were not performing cognitive tasks (Tian et al., 2016).

Previously, TILS using a 1064 nm wavelength was used to augment cognitive functioning and behavioral data revealed statistically significant improvements in performance on the psychomotor vigilance task (PVT) and the delayed match-to-sample task (DMS) in healthy young adults (Barrett and Gonzalez-Lima, 2013; Hwang et al., 2016). The purpose of the present study was to use fNIRS to map hemodynamic responses during cognitive activation before and after TILS to the prefrontal cortex, under conditions that included these cognitive tasks. A greater understanding of the physiological effects of TILS on prefrontal cognitive enhancement may facilitate its use in clinical settings.

MATERIALS AND METHODS

Subjects

A total of 34 healthy adult participants (16 male, 18 female; average age: 31, standard error: 2.5) were recruited from the University of Texas at Austin. The 18 experimental group participants (9 male, 9 female) received full laser stimulation and completed all tasks using a within-subject control design. They performed the cognitive tasks before and after TILS, with concomitant fNIRS recordings, to reflect the hemodynamic effects of TILS on cognitive performance. Another 16 participants (7 male, 9 female) were matched blind to treatment as sham controls without photobiomodulation (TILS procedure used with light off). Cognitive data was measured in seven of the sham participants (3 male, 4 female) as previously described (Barrett and Gonzalez-Lima, 2013). Hemodynamic data was measured in nine of the sham participants (4 male, 5 female) as previously described (Wang et al., 2017). The protocol was approved by the University of Texas at Austin's Institutional Review Board and complied with all applicable federal and NIH guidelines. All subjects gave written informed consent in accordance with the Declaration of Helsinki.

Functional Near-Infrared Spectroscopy

Figure 1A illustrates the experimental timeline. **Figure 1B** illustrates the position of fNIRS channels relative to brain areas and the separate collection of measurements of [Hb] and [HbO_2]. The fNIRS system used for this experiment was a NIRScout Standard system outfitted with LED light sources and Avalanche Photodiode Detectors (the most sensitive light detectors offered by NIRx Medical Technologies, LLC; Minneapolis, MN, United States). An fNIRS cap was fitted based

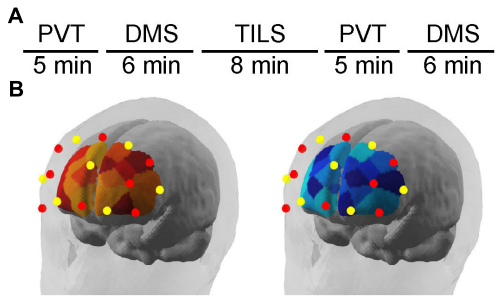

FIGURE 1 | (A) Experimental design timeline to obtain the fNIRS results during cognitive testing with the psychomotor vigilance task (PVT) and delayed match-to-sample task (DMS), before and after transcranial infrared laser stimulation (TILS). **(B)** Illustrates the position of fNIRS channels relative to brain areas and the separate monitoring of changes in [Hb] and [HbO_2] using a dual-wavelength fNIRS system. Schematic location of fNIRS map of frontal cortex hemodynamics as illustrated by the NirSTAR software (NIRx Medical Technologies, LLC; Minneapolis, MN, United States). Red dots represent emitters; yellow dots represent detectors. Relative changes in oxygenated hemoglobin (left) and deoxygenated hemoglobin (right) were quantified as illustrated in the brain schematic diagrams.

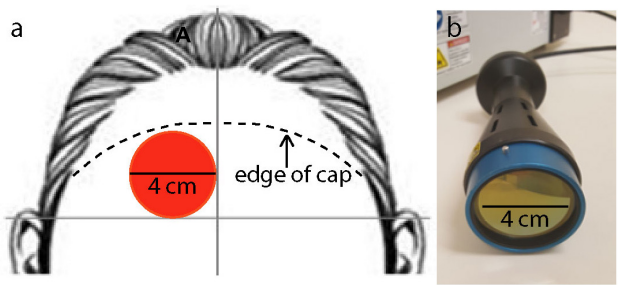

FIGURE 2 | (a) Location of laser stimulation treatment on the right forehead: 4-cm diameter site (red circle) in the corner lateral to the midline of the forehead and superior to a horizontal line above the two ears. Laser treatment location was not moved throughout the full 8 min of treatment. The figure also illustrates where the approximate edge of the cap was relative to the 4-cm laser spot (segmented lines). **(b)** Laser instrument used to administer the laser treatment with a collimation optical device of 4 cm aperture diameter.

on the circumference of the head (ranging 54–58 cm). Using the cotton end on a stick, the hair was moved out of the way within the grommets to be used in the montage. The caps were then fitted with a montage of eight emitters and seven detectors arrayed on the head above the frontal bone. **Figure 2** illustrates where the approximate edge of the cap was relative to the 4-cm laser spot. An overcap was then placed on top of the full montage to reduce extraneous effects due to ambient light. The fNIRS system was connected to the NirSTAR operating program on a separate computer. The system was then calibrated and automatically adjusted until there was a stable signal detected within each emitter-detector paired channel. During recording epochs, the system recorded at a sampling rate of 7.8125 Hz, or about eight measurements per second. Each emitter/detector pair corresponded to one channel, with 20 channels in total, with 3-cm source-detector distances.

After calibration, the fNIRS system collected data for 2 min while the participant was inactive and maintained normal respiratory and blinking rates. These data provided the zero baseline from which changes in the hemoglobin dependent variables were calculated as described below. The participant then began the PVT task while the fNIRS system took measurements throughout the task (5 min). The same was done during the administration of the DMS task (6 min). The fNIRS system was not gathering data during the laser treatment (8 min), to prevent the laser from possibly interfering with the optodes; however, the placement of the cap, emitters, detectors, and overcap remained unchanged throughout administration of the laser. The same procedure for the PVT and DMS was repeated post-TILS. The post-TILS tasks and fNIRS started within 2 min after laser irradiation.

Following the post-treatment tasks, the fNIRS system was turned off and the apparatus was removed from the participant. The fNIRS system automatically used the modified Beer-Lambert law in order to calculate the relative concentrations of oxygenated hemoglobin [HbO_2] and deoxygenated hemoglobin [Hb].

Transcranial Infrared Laser Stimulation

This study used a collimated laser diode with a wavelength of 1064 nm supplied by Cell Gen Therapeutics, LLC (Model CG-5000 laser, HD Laser Center; Dallas, TX, United States). The wavelength used in this and other studies from this lab is longer than is typically used (Rojas and Gonzalez-Lima, 2011). This longer wavelength was used to improve transmission through the cortical surface and to reduce light scattering as compared to shorter wavelengths. Light scattering is the dominant light-tissue interaction, but scattering decreases with longer wavelengths (Jacques, 2013).

This device has been cleared as safe for human use by the Food and Drug Administration (FDA) for indications of muscle or joint pain, improving circulation, improving muscle aches, and wound healing. This device has not been evaluated or approved by the FDA for the specific uses in this study. The power density of the treatment was 250 mW/cm^2, and the energy density of the treatment was 120 J/cm^2. These parameters were chosen because they showed significant cognitive benefits in our previous studies (Barrett and Gonzalez-Lima, 2013; Blanco et al., 2017a; Vargas et al., 2017). Approximately 1–2% of the laser treatment applied to the forehead at a wavelength of 1064 nm passes through the frontal bone (Barrett and Gonzalez-Lima, 2013); therefore approximately 1.2–2.4 J/cm^2 reaches the cortical surface. The aperture of the laser extended in a 4 cm diameter circle. **Figure 2b** illustrates the laser device and aperture used in this study.

All participants received TILS once, on the day of cognitive testing. The laser treatment was applied to the right side of the forehead, targeting the right prefrontal cortex, which is the brain region showing the most effective cognitive-enhancing effect in our PVT and DMS studies (Barrett and Gonzalez-Lima, 2013; Hwang et al., 2016; Vargas et al., 2017). Previous studies in the lab have alternated placement of laser application between different sites in the forehead; however, because of constraints due to the fNIRS cap, there was only room on the participant's right forehead for treatment in a single site. **Figure 2a** illustrates the

forehead placement (target) of the laser stimulation. Concerning the 10–20 electrode mapping system used in EEG, the laser aperture was just below the Fp2 point (right frontal pole). The laser treatment was delivered for 8 min from a distance of approximately 10 inches.

The researcher and participant were locked in a non-reflective room with a sign on the outer door indicating that the laser was in use. All participants and lab personnel present wore protective eyewear guarding against the 1064-nm wavelength (900–1000 nm: 5 +, 1000–2400 nm: 7+; 2900–10600 nm: 7+) in accordance with safety operating procedures for this machine, and the participants had their eyes closed at all times while the laser treatment was being administered.

Laser stimulation parameters

Center wavelength (nm): 1064
Spectral bandwidth (nm): 5 (FWHM)
Operating mode: CW
Average radiant power (mW): 3400
Polarization: No (after fiber transmission)
Aperture diameter (cm): 4
Irradiance at aperture (mW/cm^2): 250
Beam divergence: Near zero (well-collimated beam)
Beam shape: Circular
Beam profile: Top Hat
Beam spot size at forehead target (cm^2): 13.6
Irradiance at forehead target (mW/cm^2): 250
Exposure duration (s): 480
Radiant exposure (J/cm^2): 120
Radiant energy (J): 1632
Number of points irradiated: One
Forehead area irradiated (cm^2): 13.6
Delivery mode: Non-contact; 10 inches distance of the beam source to the forehead target
Number and frequency of treatment sessions: One session; delivered in 8 min
Total radiant energy (J): 1632

Cognitive Testing

The PVT was administered to participants as the first cognitive task to measure reaction times before and after TILS. At both time points, the fNIRS system was run continuously during the task. The PVT is a computer-based task originally developed by Dinges and Powell (1985) as a visual reaction time task. This task was originally used to test reaction time under sustained operations; however, it has now been modified to test general sustained attention and vigilance in healthy individuals. This task has been shown to be a reliable indicator of frontal cortex function (Drummond et al., 2005). In this task, participants attend to a white fixation cross in the middle of a black background. After a short period of time, the fixation cross disappears and there is a variable period of delay where the screen remains black. After the delay, white numbers begin counting up in the middle of the screen in milliseconds. The participants are instructed to press the space bar as soon as they see the numbers appear. The counter briefly stops to display the final reaction time before moving on to the next trial. If participants press the space bar before the appearance of the numbers, a message of "Too Soon!" is briefly displayed on the screen. If the participants take too long to respond (greater than 500 ms), the trial is recorded as a lapse in attention. The PVT consisted of 40 trials, and the delay period between the presentation of the fixation cross and the stimulus varied pseudo randomly between 2, 4, and 6 s. The duration of the PVT was approximately 5 min. The two dependent variables recorded by the computer are reaction time (in msec) and the number of "correct" trials. If the participant responded too soon (before the onset of the stimulus) or too late (after 500 ms have elapsed), the trial was coded as incorrect.

The DMS was administered to participants directly following their completion of the PVT to measure working memory both pre-treatment and post-treatment. Performance on this working memory task has previously been shown to be mediated by a frontoparietal network (Nieder and Miller, 2004). In this task, participants are presented with a 6 × 6 grid of red and yellow squares in a random pattern presented on a plain gray background. A delay of 6 s follows, during which only the gray background is shown. After the delay period, two 6 × 6 grids are presented side by side. One grid (the "match") is identical to the original grid, and the second grid (the "foil") is slightly different. The participant must respond with either the left or right SHIFT key to indicate which grid is the match. Following the choice, either "Correct" or "Incorrect" are briefly displayed onscreen based on the participant's choice. If the participant does not answer within 4 s, the trial times out and the feedback given is "Timeout." The DMS consisted of 30 trials, and the duration of the DMS was approximately 6 min. The two dependent variables recorded by the computer were response time (in ms) during the choice part of the task and the number of correct trials.

Data Analysis

The data from the optical signal obtained from the fNIRS apparatus was processed using the software NirsLAB (v2017.6) provided by NIRx Optical Neuroimaging. All epochs/channels were checked to ensure that at no time there were any channels saturated; no saturated intervals were found. Each recording epoch was checked for data quality in all 20 channels, and if the gain provided by the initial calibration step was not within the recommended range, that data was discarded. Out of 20 channels × 18 participants = 360 time series of data for all participants, eight were removed from the analysis. The data was then processed using a band-pass filter, with a low cut-off frequency of 0.01 Hz (to remove the widely observed slow baseline drift) and a high cut-off frequency of 0.2 Hz (to remove electronic noise and fast-oscillating cardiac waves) (Tian et al., 2010; Piper et al., 2014). The modified Beer-Lambert Law was used to calculate changes in oxygenated hemoglobin concentration ($\Delta[HbO_2]$) and deoxygenated hemoglobin concentration ($\Delta[Hb]$) relative to the initial baseline set as zero (Tian et al., 2016; Wang et al., 2016). Total hemoglobin ($\Delta[HbT]$) was calculated with a sum ($\Delta[HbO_2] + \Delta[Hb]$) and differential concentrations of hemoglobin ($\Delta[HbD]$) were calculated using a difference score ($\Delta[HbD] = \Delta[HbO_2] - \Delta[Hb]$) as in Tian et al. (2016) and Wang et al. (2017). This value ($\Delta[HbD]$) is an indicator of changes in tissue oxygen saturation (Tian et al., 2016) which is

closely correlated with changes in cerebral blood flow (Wang et al., 2017). These values were calculated and averaged for each recording epoch for each subject. The fNIRS system gives only relative values (not absolute values) of these measures; therefore, the first fNIRS readings (taken before the first PVT session) were used as a zero-point by subtracting those values for each subject/channel from each subsequent measurement, to standardize the data and create a common zero-point baseline shared by all subjects.

To evaluate the effect of the TILS treatment, all 20 channels were averaged together to create an index of global cerebral blood flow (across the entire range of frontal cortex sampled, including both hemispheres) for each subject/epoch. These "all-channels" averages for the values of HbO_2, Hb, HbT, and HbD were compared between pre-TILS and post-TILS measures using paired *t*-tests with a two-tailed level of significance with $p \leq 0.01$.

For each subject's cognitive performance in both sessions of the PVT and DMS, an overall cognitive score was calculated, incorporating both speed (reaction time) and accuracy (number of correct responses), using the rate correct score or RCS (Woltz and Was, 2006). This overall cognitive score was equal to the number of correct responses divided by the sum of all reaction times. The PVT and DMS behavioral results were analyzed with paired *t*-tests comparing performance on these tasks before and after TILS with a two-tailed level of significance with $p \leq 0.01$.

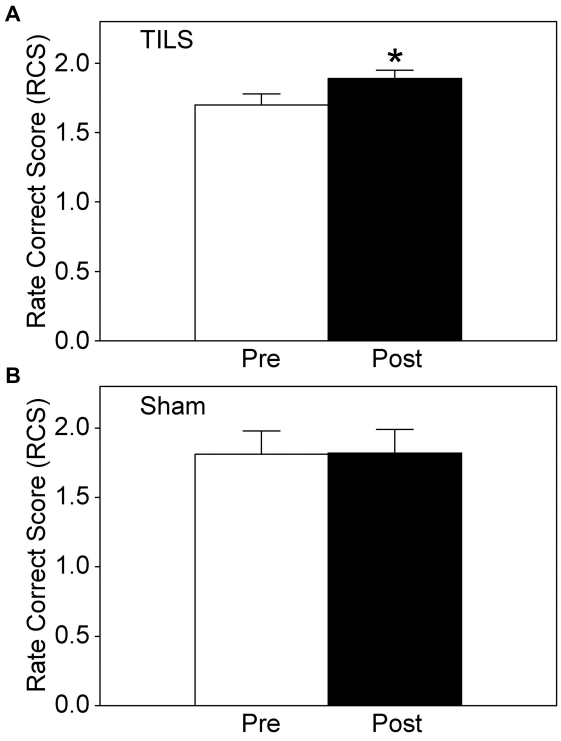

FIGURE 3 | Rate correct score (RCS) for cognitive performance before and after TILS **(A)** and Sham **(B)**. Mean ± S.E., * = Significant mean difference between Pre- vs. Post- TILS scores, $p \leq 0.01$. *No randomization occurred for sham, since we used a within-subject design in which the same subjects are their own control by directly comparing pre- vs post- measures statistically. There were no significant pre-post differences in the sham subjects.

RESULTS

Cognitive Effects of TILS and Sham

Cognitive results from the PVT and DMS were obtained before and after TILS and sham. As expected, overall cognitive processing improved after TILS, as indicated by the significantly higher rate correct score (**Figure 3A**), whereas there were no significant differences after sham (**Figure 3B**). This score reflects the speed and accuracy of cognitive processing. The overall rate correct score effect size (Cohen's *d*) after TILS was $|d| = 0.62$, indicating a medium effect size, given that $|d| < 0.2$ = small effect; $0.2 < |d| < 0.8$ = medium effect; $|d| > 0.8$ = large effect (Cohen, 1988).

Table 1 summarizes the details of all the individual scores for TILS and sham. On average, the DMS contributed stronger effect sizes as compared to the PVT. Average performance in the DMS improved after TILS, with significant improvements in both number of correct answers and memory retrieval time (i.e., time to make a choice between the match and foil grids) as assessed by paired *t*-tests. Performance on the PVT tended to improve, in terms of faster reaction times after the TILS treatment, as well as an increase in the number of correct trials (where a correct trial is defined as neither a "too-fast" trial nor a "lapse" with a reaction time greater than 500 ms), but this improvement was not significant at $p \leq 0.01$.

Sham cognitive data analyses showed no significant differences in any of the pre-post comparisons, using the same methods as in the TILS group (**Table 1**). As expected from two previous sham-controlled studies using the same PVT and DMS tasks (Barrett and Gonzalez-Lima, 2013; Hwang et al., 2016), cognitive processing did not improve significantly after sham, as shown by nearly identical pre-post rate correct scores. Mean ±SE for sham, pre: 1.81 ±0.17. Mean ±SE for sham, post: 1.82 ±0.17. The value of *t* is 0.077143. The value of *p* is 0.94102. The result is *not* significant at $p \leq 0.05$.

Hemodynamic Effects of TILS and Sham

There was a significant effect of TILS on three of the dependent variables: $\Delta[HbO_2]$, $\Delta[HbT]$, and $\Delta[HbD]$ all showed significant increases at $p \leq 0.01$ after TILS but not after sham. Deoxygenated hemoglobin $\Delta[Hb]$ did not show a significant difference after TILS. The significant hemodynamic effects of TILS showed large effect sizes ($|d| = 0.94$–1.02). **Tables 2**, **3** shows means ± standard errors and the values of *t* and *p* across all channels during the PVT and DMS pre-post comparisons, respectively. No single channel was driving the significant effect, as all channels were highly co-linear with each other. There were no other significant differences between PVT and DMS besides the TILS main effect on the hemodynamic response.

Sham hemodynamic data analyses showed no significant differences in any of the pre-post comparisons. As expected from a previous hemodynamic study of TILS and sham effects (Wang et al., 2017), none of the hemodynamic

TABLE 1 | Results of cognitive tests before (Pre) and after (Post) TILS and Sham.

Dependent variable	Pre-TILS	Post-TILS			
	Mean ± S.E.	Mean ± S.E.	*t*-Score	*p*-value	Cohen's *d*
A. LASER					
PVT reaction time (ms)	331.6 ± 6.10	329.2 ± 6.73	−0.53	0.60	0.09
PVT correct trials (out of 40)	38.5 ± 0.43	39.3 ± 0.23	1.74	0.10	0.52
DMS response time (s)*	2.03 ± 0.07	1.83 ± 0.07	−3.17	0.01	0.64
DMS correct trials (out of 30)*	22.3 ± 0.82	24.7 ± 0.61	2.85	0.01	0.73
Dependent variable	**Pre-Sham**	**Post-Sham**			
	Mean ± S.E.	Mean ± S.E.	*t*-Score	*p*-value	Cohen's *d*
B. SHAM					
PVT reaction time (ms)	316.1 ± 14.9	326.4 ± 20.6	1.57	0.17	0.22
PVT correct trials (out of 40)	39.0 ± 0.53	38.4 ± 0.57	−0.83	0.44	0.39
DMS response time (s)	2.1 ± 0.14	2.0 ± 0.12	−0.67	0.53	0.00
DMS correct trials (out of 30)	22.4 ± 1.38	23.0 ± 1.07	0.40	0.70	0.18

**No randomization occurred for sham, since we used a within-subject design in which the same subjects are their own control by directly comparing pre- vs. post-measures statistically. There were no significant pre-post differences in the sham subjects (Mean ± S.E., * = Significant mean difference between Pre- vs. Post- TILS scores, $p \leq 0.01$).*

TABLE 2 | Cerebral hemodynamic changes before (Pre) and after (Post) TILS averaged across all 20 channels during the PVT.

PVT	Pre-TILS	Post-TILS			
	Mean ± S.E.	Mean ± S.E.	*t*-score	*p*-value	Cohen's *d*
HbO_2*	0.0412 ± 0.0194	0.2199 ± 0.0489	4.28	0.001	0.99
Hb	−0.0095 ± 0.0027	−0.0066 ± 0.0062	0.45	0.665	0.14
HbT*	0.0316 ± 0.0191	0.2134 ± 0.0478	4.27	0.001	1.02
HbD*	0.0507 ± 0.0201	0.2265 ± 0.0507	4.18	0.002	0.95

*(μM; Mean ± S.E., * = Post-TILS scores significantly greater than Pre-TILS scores, $p \leq 0.01$).*

TABLE 3 | Cerebral hemodynamic changes before (Pre) and after (Post) TILS averaged across all 20 channels during the DMS.

DMS	Pre-TILS	Post-TILS			
	Mean ± S.E.	Mean ± S.E.	*t*-score	*p*-value	Cohen's *d*
HbO_2*	0.0390 ± 0.0201	0.2162 ± 0.0494	4.17	0.001	0.97
Hb	−0.0095 ± 0.0029	−0.0076 ± 0.0061	0.30	0.768	0.10
HbT*	0.0295 ± 0.0196	0.2086 ± 0.0484	4.14	0.001	1.00
HbD*	0.0485 ± 0.0210	0.2237 ± 0.0512	4.11	0.001	0.94

*(μM; Mean ± S.E., * = Post-TILS scores significantly greater than Pre-TILS scores, $p \leq 0.01$).*

measures changed significantly after sham. $\Delta[HbO_2]$: The value of t is 1.7928. The value of p is 0.11076. The result is *not* significant at $p \leq 0.05$. $\Delta[Hb]$: The value of t is 0.945994. The value of p is 0.37184. The result is *not* significant at $p < 0.05$. $\Delta[HbT]$: The value of t is 2.272126. The value of p is 0.05772. The result is *not* significant at $p < 0.05$. $\Delta[HbD]$: The value of t is 1.351153. The value of p is 0.21361. The result is *not* significant at $p < 0.05$.

Since significant effects were found only after TILS, we further analyzed all the TILS data in terms of temporal and spatial effects as described below. No further analysis of the negative sham data was done because there were no significant hemodynamic sham effects to analyze.

Temporal and Spatial Hemodynamic Effects of TILS

The effects of TILS on the fNIRS signal are depicted in **Figures 4**, **5**, in terms of the temporal and spatial effects of TILS, respectively. The level of oxygenated hemoglobin rose significantly after TILS and maintained a higher level throughout the post-TILS period (**Figure 4**). We made an additional statistical comparison because the relative temporal pattern of $\Delta[HbO_2]$ during PVT appeared to change from before to after TILS regardless of baseline, and we determined whether this was a significant difference. We verified that this was not a significant difference. We performed repeated measures ANOVA on $\Delta[HbO_2]$ during the 5 min of PVT, minute by minute, pre-TILS vs. post-TILS. Therefore, there were two within-subject variables. We were interested in the interaction between pre-post and minutes. In other words, was the shape of the curve during those 5 min statistically different between pre-TILS and post-TILS. That interaction was not significant: Pre-post × Minutes: $F(4,68) = 0.991$, $p = 0.419$.

Comparing differences between pre- and post-TILS in terms of spatial effects, the anterior channels in the fNIRS frontal montage (**Figure 5A**) registered higher levels of oxygenated hemoglobin than the posterior channels during cognitive processing of PVT (**Figure 5B**) and DMS (**Figure 5C**). To verify that the significant effects within

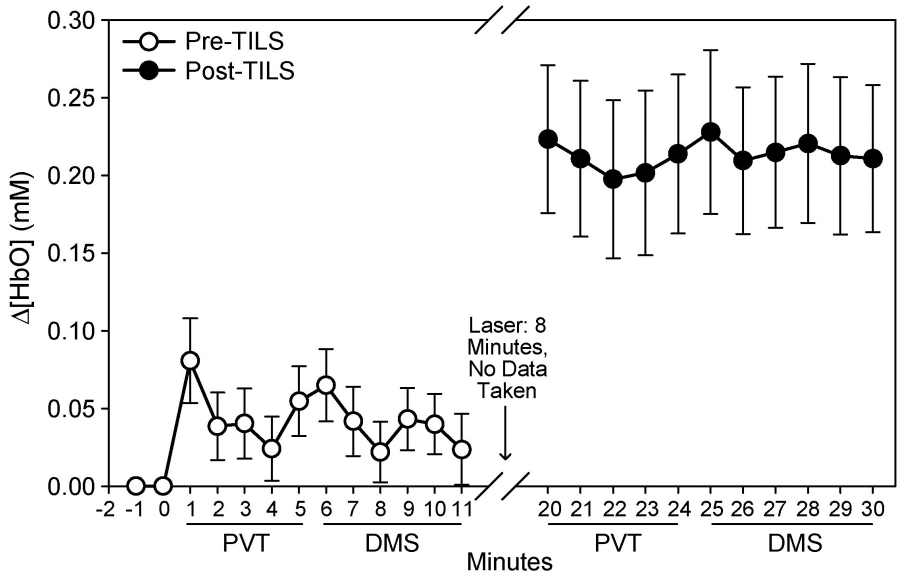

FIGURE 4 | Temporal sequence of changes in oxygenated hemoglobin (μM), pre- and post-TILS during cognitive processing in the PVT and DMS tasks. Mean ± S.E.

individual channels was not due to multiple statistical comparisons, the "Sharper Bonferroni" correction was used (Hochberg, 1988), in which *p*-values are corrected for multiple comparisons using multiplication according to ranked order; with 20 comparisons (one for each channel), the strongest effect is multiplied by 20, the next-strongest by 19, etc. The channels that still showed significant pre-to-post-TILS increases in HbO_2 during both the PVT and DMS epochs, with corrected values of $p \leq 0.01$, were channels 4, 6, 9, 11, 14, 16, and 19. These are also the channels with the highest *T*-values (red in **Figures 5B,C**) in the anterior part of the frontal montage.

DISCUSSION

This study is the first to demonstrate that cognitive enhancement by transcranial photobiomodulation is associated with cerebrovascular oxygenation of the prefrontal cortex. The control group (sham) behavioral data and hemodynamic data (with no photobiomodulation) showed no significant differences in any of the pre-post comparisons. These sham control data served to rule out that the laser effects were due to pre-post task repetition or other non-specific effects.

The main finding was the highly significant hemodynamic effect of TILS on $\Delta[HbO_2]$, $\Delta[HbT]$, and $\Delta[HbD]$ on the anterior frontal cortex during cognitive processing. The laser treatment resulted in a large increase in oxygenated hemoglobin in the anterior frontal region measured by the fNIRS apparatus, corresponding to the prefrontal cortex region engaged during the PVT and DMS tasks (Nieder and Miller, 2004; Drummond et al., 2005). This large hemodynamic response was about five times greater than in the pre-TILS condition and it was sustained for more than 10 min of cognitive processing after TILS.

The concern that heating might cause non-specific fNIRS changes rather than the neurophotonic stimulation has been addressed directly in our recently published paper (Wang et al., 2018) that compares the effects of heating vs. TILS on the cerebral hemodynamic responses. The results showed that thermal stimulation of the forehead does not produce the effects of TILS on $\Delta[HbO_2]$, $\Delta[HbT]$, and $\Delta[HbD]$ (e.g., Figure 6 of Wang et al., 2018). These results served to rule out the concern that heating from our cold laser might be responsible for any signal changes that could explain the cerebral hemodynamic effects measured by fNIRS.

The improvement in overall cognitive performance following TILS was much smaller as compared to the hemodynamic response. To interpret this finding we considered the results from another previous study (Wang et al., 2017) comparing hemodynamic effects on superficial tissues and brain to address how reflective the fNIRS measure is of brain changes and how much is this measure contaminated by changes in oxygenation from superficial tissues. The results showed that laser-induced superficial skin and tissue changes (measured at 1.5 cm source-detector distance) are about 5% above baseline whereas brain changes (measured at 3 cm source-detector distance) are about 20% when compared using metabolic/hemodynamic ratios (e.g., Figure 5 of Wang et al., 2017). Therefore, TILS-induced cerebral hemodynamic changes do not appear to receive a heavy contribution from superficial tissues that could account for our findings that fNIRS brain changes are much greater than changes in cognition. This is consistent with the general finding that hemodynamic responses are several times greater than observable cognitive differences and levels of tissue oxygen consumption (Fox, 2012; Beishon et al., 2018).

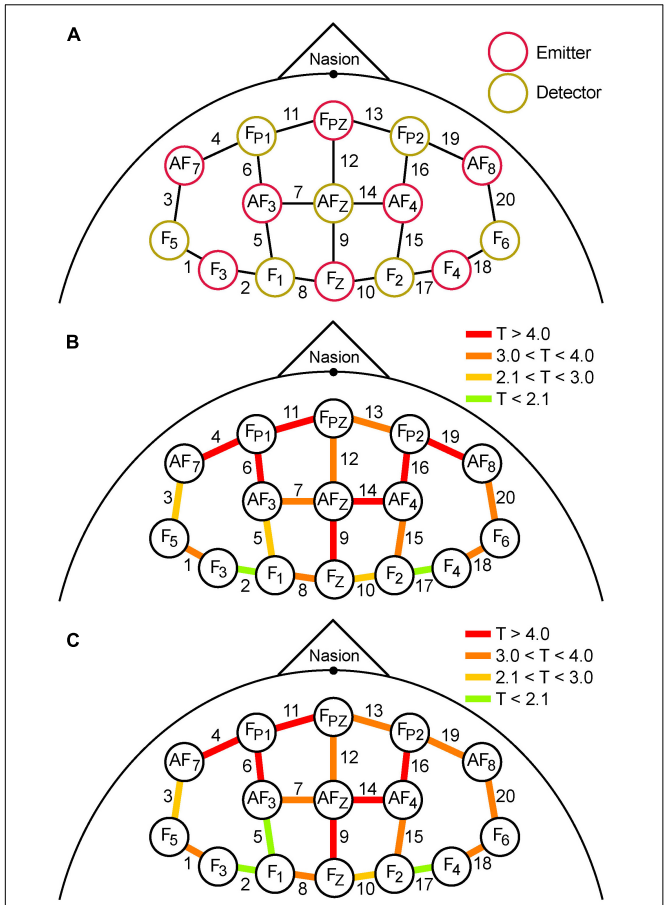

FIGURE 5 | (A) Schematic spatial layout of the frontal montage used for fNIRS recording. Red and yellow circles correspond to emitters and detectors, respectively. The labels inside the circles correspond to the 10–20 EEG system locations used for each emitter and detector. Each adjacent emitter/detector pair formed a channel that gathered fNIRS data (20 labeled lines). **(B)** Colored lines represent the magnitude of T-scores from the analysis of mean differences between pre- and post-TILS PVT epochs. **(C)** The magnitude of T-scores comparing the pre- and post-TILS DMS epochs. The affected channels are almost identical, with two exceptions (channels 5 and 19).

The behavioral sham data comparing pre-post tasks without TILS served to confirm the lack of learning/placebo effects for repeated testing of our specific DMS and PVT tasks, and replicated the same sham findings from our published studies. The cognitive effects are consistent with our previous two studies in which we compared TILS with sham/placebo groups in the same PVT and DMS tasks (Barrett and Gonzalez-Lima, 2013; Hwang et al., 2016). Indeed, pre-post testing of these PVT and DMS tasks in a single session without laser stimulation do not lead to improved cognitive scores (Barrett and Gonzalez-Lima, 2013). Therefore, placebo or practice effects cannot explain the cognitive improvement produced by TILS. The fact that the improvement in PVT performance was not statistically significant at the $p \leq 0.01$ level may be based on the single treatment given because repeated TILS leads to a significant increase in PVT scores (Vargas et al., 2017). In addition, we have previously found significant improvements caused by TILS as compared to sham in other prefrontal-dependent cognitive tasks, such as the Wisconsin card sorting task (Blanco et al., 2017a) and rule-based category learning (Blanco et al., 2017b).

The main limitation of the study was the lack of data acquired during the TILS administration, which was implemented to avoid the possibility of damage to the fNIRS system's photodetectors by the laser. Other fNIRS systems contain a shutter system to maintain the recording during TILS without damaging the photodetectors. Also, the system only returns the relative changes in HbO_2 and Hb, with no absolute "zero" point, making it difficult to compare across subjects; this issue necessitated the use of the initial recording period as a zero-point by subtracting it from subsequent data points within the time series.

In the future, an event-related design will be implemented, using event markers during the different phases of the PVT and DMS to examine hemodynamic changes within each stage of the task (e.g., encoding vs. maintenance vs. retrieval of the visuospatial memory during the DMS) as done in our previous fNIRS study of working memory in post-traumatic stress disorder (Tian et al., 2014). Prefrontal neurons associated with working memory are selectively active during the maintenance phase of the DMS (Sawaguchi and Yamane, 1999); synchronizing the different phases of the task with simultaneous fNIRS readings may yield more task-specific temporal results.

Transcranial infrared laser stimulation may be useful as a safe, non-invasive, non-pharmacological and cost-effective approach to increasing cognitive function. The scope of the hemodynamic effect of TILS on human brains may be monitored in real time using fNIRS. This combined TILS-fNIRS system could be a tool for titrating the dose of laser treatment for each individual based on their own particular cerebrovascular oxygenation response. Additionally, this system might help identify good candidates for therapeutic intervention with laser stimulation prior to presentation of symptoms based on hypofrontality. In the future, this laser treatment could be used for populations presenting with prefrontal hypometabolism, such as in cognitive aging, mild cognitive impairment, Alzheimer's disease, and many other neurological and psychiatric conditions that lead to cognitive decline (Rojas and Gonzalez-Lima, 2013).

CONCLUSION

In conclusion, TILS at 1064 nm wavelength enhanced cognitive performance and fNIRS response in human prefrontal cortex. Together the results of this study and our previous studies suggest that TILS is a form of photobiomodulation that can successfully augment cerebrovascular oxygenation and thereby improve human cognitive brain functions.

DATA AVAILABILITY STATEMENT

The raw data supporting the conclusion of this manuscript will be made available by the authors, without undue reservation, to any qualified researcher.

ETHICS STATEMENT

The protocol was approved by the University of Texas at Austin's Institutional Review Board and complied with all applicable federal and NIH guidelines. All subjects gave written informed consent in accordance with the Declaration of Helsinki.

AUTHOR CONTRIBUTIONS

EH, DB, and FG-L designed the experiment. EH, DB, CS, and PO'C collected the data. DB and FG-L performed the statistical analysis. EH, DB, HL, and FG-L interpreted the results. EH wrote the first draft of the manuscript. DB prepared the figures. All authors contributed to the manuscript revision, read, and approved the submitted version.

FUNDING

This study was supported by the Oskar Fischer Project Fund.

ACKNOWLEDGMENTS

We thank Dr. Benjamin Zinszer and the Multimodal Neuroimaging Initiative at UT Austin for guidance and the use of the fNIRS system.

REFERENCES

Barrett, D. W., and Gonzalez-Lima, F. (2013). Transcranial infrared laser stimulation produces beneficial cognitive and emotional effects in humans. *Neuroscience* 230, 13–23. doi: 10.1016/j.neuroscience.2012.11.016

Beishon, L., Williams, C. A. L., Robinson, T. G., Haunton, V. J., and Panerai, R. B. (2018). Neurovascular coupling response to cognitive examination in healthy controls: a multivariate analysis. *Physiol. Rep.* 6:e13803. doi: 10.14814/phy2.13803

Blanco, N. J., Maddox, W. T., and Gonzalez-Lima, F. (2017a). Improving executive function using transcranial infrared laser stimulation. *J. Neuropsychol.* 11, 14–25. doi: 10.1111/jnp.12074

Blanco, N. J., Saucedo, C. L., and Gonzalez-Lima, F. (2017b). Transcranial infrared laser stimulation improves rule-based, but not information-integration, category learning in humans. *Neurobiol. Learn. Mem.* 139, 69–75. doi: 10.1016/j.nlm.2016.12.016

Brosseau, L., Welch, V., Wells, G., DeBie, R., Gam, A., Harman, K., et al. (2004). Low level laser therapy (classes I, II and III) for the treatment of osteoarthritis. *Cochrane Database Syst. Rev.* 3:CD002046. doi: 10.1002/14651858.CD002046.pub2

Caldieraro, M. A., and Cassano, P. (2019). Transcranial and systemic photobiomodulation for major depressive disorder: a systematic review of efficacy, tolerability and biological mechanisms. *J. Affect. Disord.* 243, 262–273. doi: 10.1016/j.jad.2018.09.048

Cohen, J. (1988). *Statistical Power Analysis for the Behavioural Sciences*, 2nd Edn. New York, NY: Lawrence Erlbaum Associates.

Cotler, H. B., Chow, R. T., Hamblin, M. R., and Carroll, J. (2015). The use of low level laser therapy (LLLT) for musculoskeletal pain. *MOJ Orthop. Rheumatol.* 2:00068. doi: 10.15406/mojor.2015.02.00068

Dinges, D., and Powell, J. (1985). Microcomputer analyses of performance on a portable, simple visual RT task during sustained operations. *Behav. Res. Methods Instr. Comput.* 17, 652–655. doi: 10.3758/BF03200977

Disner, S. G., Beevers, C. G., and Gonzalez-Lima, F. (2016). Transcranial laser stimulation as neuroenhancement for attention bias modification in adults with elevated depression symptoms. *Brain Stimul.* 9, 780–787. doi: 10.1016/j.brs.2016.05.009

Drummond, S., Bischoff-Grethe, A., Dinges, D. F., Ayalon, L., Mednick, S. C., and Meloy, M. J. (2005). The neural basis of the psychomotor vigilance task. *Sleep* 28, 1059–1068.

Eells, J. T., Wong-Riley, M. T., VerHoeve, J., Henry, M., Buchman, E. V., Kane, M. P., et al. (2004). Mitochondrial signal transduction in accelerated wound and retinal healing by near-infrared light therapy. *Mitochondrion* 4, 559–567. doi: 10.1016/j.mito.2004.07.033

Fox, P. T. (2012). The coupling controversy. *Neuroimage* 62, 594–601. doi: 10.1016/j.neuroimage.2012.01.103

Gonzalez-Lima, F., and Barrett, D. W. (2014). Augmentation of cognitive brain functions with transcranial lasers. *Front. Syst. Neurosci.* 8:36. doi: 10.3389/fnsys.2014.00036

Hochberg, Y. (1988). A sharper Bonferroni procedure for multiple tests of significance. *Biometrika* 75, 800–802. doi: 10.1093/biomet/75.4.800

Holanda, V. M., Chavantes, M. C., Wu, X., and Anders, J. J. (2017). The mechanistic basis for photobiomodulation therapy of neuropathic pain by near infrared laser light. *Lasers Surg. Med.* 49, 516–524. doi: 10.1002/lsm.22628

Hopkins, J. T., McLoda, T. A., Seegmiller, J. G., and Baxter, D. G. (2004). Low-level laser therapy facilitates superficial wound healing in humans: a triple-blind, sham-controlled study. *J. Athl. Train.* 39, 223–229.

Hwang, J., Castelli, D. M., and Gonzalez-Lima, F. (2016). Cognitive enhancement by transcranial laser stimulation and acute aerobic exercise. *Lasers Med. Sci.* 31, 1151–1160. doi: 10.1007/s10103-016-1962-3

Ito, Y., Kennan, R., Watanabe, E., and Koizumi, H. (2000). Assessment of heating effects in skin during continuous wave near infrared spectroscopy. *J. Biomed. Opt.* 5, 383–390. doi: 10.1117/1.1287730

Jacques, S. L. (2013). Optical properties of biological tissues: a review. *Phys. Med. Biol.* 58, R37–R61. doi: 10.1088/0031-9155/58/11/R37

Naeser, M. A., and Hamblin, M. R. (2011). Potential for transcranial laser or LED therapy to treat stroke, traumatic brain injury, and neurodegenerative disease. *Photomed. Laser Surg.* 29, 443–446. doi: 10.1089/pho.2011.9908

Nieder, A., and Miller, E. (2004). A parieto-frontal network for visual numerical information in the monkey. *Proc. Natl. Acad. Sci. U.S.A.* 101, 7457–7462. doi: 10.1073/pnas.0402239101

Piper, S. K., Krueger, A., Koch, S. P., Mehnert, J., Habermehl, C., Steinbrink, J., et al. (2014). A wearable multi-channel fNIRS system for brain imaging in freely moving subjects. *Neuroimage* 85, 64–71. doi: 10.1016/j.neuroimage.2013.06.062

Rojas, J. C., and Gonzalez-Lima, F. (2011). Low-level light therapy of the eye and brain. *Eye Brain* 3, 49–67. doi: 10.2147/EB.S21391

Rojas, J. C., and Gonzalez-Lima, F. (2013). Neurological and psychological applications of transcranial lasers and LEDs. *Biochem. Pharmacol.* 86, 447–457. doi: 10.1016/j.bcp.2013.06.012

Sawaguchi, T., and Yamane, I. (1999). Properties of delay-period neuronal activity in the monkey dorsolateral prefrontal cortex during a spatial delayed matching-to-sample task. *J. Neurophysiol.* 82, 2070–2080. doi: 10.1152/jn.1999.82.5.2070

Tedford, C. E., DeLapp, S., Jacques, S., and Anders, J. (2015). Quantitative analysis of transcranial and intraparenchymal light penetration in human cadaver brain tissue. *Lasers Surg. Med.* 47, 312–322. doi: 10.1002/lsm.22343

Tian, F., Delgado, M. R., Dhamne, S. C., Khan, B., Alexandrakis, G., Romero, M. I., et al. (2010). Quantification of functional near infrared spectroscopy to assess cortical reorganization in children with cerebral palsy. *Opt. Express* 18, 25973–25986. doi: 10.1364/OE.18.025973

Tian, F., Hase, S. N., Gonzalez-Lima, F., and Liu, H. (2016). Transcranial laser stimulation improves human cerebral oxygenation. *Lasers Surg. Med.* 48, 343–349. doi: 10.1002/lsm.22471

Tian, F., Yennu, A., Smith-Osborne, A., Gonzalez-Lima, F., North, C. S., and Liu, H. (2014). Prefrontal responses to digit span memory phases in patients with post-traumatic stress disorder (PTSD): a functional near infrared

spectroscopy study. *Neuroimage Clin.* 4, 808–819. doi: 10.1016/j.nicl.2014.05.005

Vargas, E., Barrett, D. W., Saucedo, C. L., Huang, L. D., Abraham, J. A., Tanaka, H., et al. (2017). Beneficial neurocognitive effects of transcranial laser in older adults. *Lasers Med. Sci.* 32, 1153–1162. doi: 10.1007/s10103-017-2221-y

Wang, X., Reddy, D. D., Nalawade, S. S., Pal, S., Gonzalez-Lima, F., and Liu, H. (2018). Impact of heat on metabolic and hemodynamic changes in transcranial infrared laser stimulation measured by broadband near-infrared spectroscopy. *Neurophotonics* 5:011004. doi: 10.1117/1.NPh.5.1.011004

Wang, X., Tian, F., Reddy, D. D., Nalawade, S. S., Barrett, D. W., Gonzalez-Lima, F., et al. (2017). Up-regulation of cerebral cytochrome-c-oxidase and hemodynamics by transcranial infrared laser stimulation: a broadband near-infrared spectroscopy study. *J. Cereb. Blood Flow Metab.* 37, 3789–3802. doi: 10.1177/0271678X17691783

Wang, X., Tian, F., Soni, S. S., Gonzalez-Lima, F., and Liu, H. (2016). Interplay between up-regulation of cytochrome-c-oxidase and hemoglobin oxygenation induced by near-infrared laser. *Sci. Rep.* 6:30540. doi: 10.1038/srep30540

Woltz, D. J., and Was, C. A. (2006). Availability of related long-term memory during and after attention focus in working memory. *Mem. Cognit.* 34, 668–684. doi: 10.3758/BF03193587

Wong-Riley, M. T., Liang, H. L., Eells, J. T., Chance, B., Henry, M. M., Buchmann, E., et al. (2005). Photobiomodulation directly benefits primary neurons functionally inactivated by toxins: role of cytochrome c oxidase. *J. Biol. Chem.* 280, 4761–4771. doi: 10.1074/jbc.M409650200

Conflict of Interest: The authors declare that the research was conducted in the absence of any commercial or financial relationships that could be construed as a potential conflict of interest.

Copyright © 2019 Holmes, Barrett, Saucedo, O'Connor, Liu and Gonzalez-Lima. This is an open-access article distributed under the terms of the Creative Commons Attribution License (CC BY). The use, distribution or reproduction in other forums is permitted, provided the original author(s) and the copyright owner(s) are credited and that the original publication in this journal is cited, in accordance with accepted academic practice. No use, distribution or reproduction is permitted which does not comply with these terms.

frontiers in Neuroscience

ORIGINAL RESEARCH
published: 12 November 2019
doi: 10.3389/fnins.2019.01209

Enhancing Attention by Synchronizing Respiration and Fingertip Pressure: A Pilot Study Using Functional Near-Infrared Spectroscopy

Yi-Lei Zheng[1,2], Dang-Xiao Wang[1,2,3], Yu-Ru Zhang[1,3] and Yi-Yuan Tang[4]*

[1] State Key Laboratory of Virtual Reality Technology and Systems, Beihang University, Beijing, China, [2] Peng Cheng Laboratory, Shenzhen, China, [3] Beijing Advanced Innovation Center for Biomedical Engineering, Beihang University, Beijing, China, [4] Department of Psychological Sciences, Texas Tech University, Lubbock, TX, United States

Sustained attention is a fundamental ability ensuring effective cognitive processing and can be enhanced by meditation practice. However, keeping a focused meditative state is challenging for novices because involuntary mind-wandering frequently occurs during their practice. Inspired by the potential of force-control tasks in invoking internal somatic attention, we proposed a haptics-assisted meditation (HAM) to help reduce mind-wandering and enhance attention. During HAM, participants were instructed to maintain awareness on the respiration and meanwhile adjust bimanual fingertip pressures to keep synchronized with the respiration. This paradigm required somatosensory attention as a physiological foundation, aiming to help novices meditate starting with the body and gradually gain essential meditation skills. A cross-sectional study on 12 novices indicated that the participants reported less mind-wandering during HAM compared with the classic breath-counting meditation (BCM). In a further longitudinal study, the experimental group with 10 novices showed significantly improved performance in several attentional tests after 5 days' practice of HAM. They tended to show more significant improvements in a few tests than did the control group performing the 5-day BCM practice. To investigate the brain activities related to HAM, we applied functional near-infrared spectroscopy (fNIRS) to record cerebral hemodynamic responses from the prefrontal and sensorimotor cortices when performing HAM, and we assessed the changes in cerebral activation and functional connectivity (FC) after the 5-day HAM practice. The prefrontal and sensorimotor regions demonstrated a uniform activation when performing HAM, and there was a significant increase in the right prefrontal activation after the practice. We also observed significant changes in the FC between the brain regions related to the attention networks. These behavioral and neural findings together provided preliminary evidence for the effectiveness of HAM on attention enhancement in the early stage of meditation learning.

Keywords: sustained attention, cognitive improvement, meditation, functional near-infrared spectroscopy, respiration, fingertip pressure

OPEN ACCESS

Edited by:
Xianchun Li,
East China Normal University, China

Reviewed by:
Jack Adam Noah,
Yale University, United States
Dan Zhang,
Tsinghua University, China

****Correspondence:***
Dang-Xiao Wang
hapticwang@buaa.edu.cn

Specialty section:
This article was submitted to Brain Imaging Methods, a section of the journal Frontiers in Neuroscience

Received: *12 April 2019*
Accepted: *25 October 2019*
Published: *12 November 2019*

Citation:
Zheng Y-L, Wang D-X, Zhang Y-R and Tang Y-Y (2019) Enhancing Attention by Synchronizing Respiration and Fingertip Pressure: A Pilot Study Using Functional Near-Infrared Spectroscopy. Front. Neurosci. 13:1209. doi: 10.3389/fnins.2019.01209

INTRODUCTION

Maintaining attention on a current undertaking and resisting the occurrence of unrelated thoughts are vital aspects of human behaviors. Considerable literature has indicated the broad benefits of intensive meditation practice on attentional performance, mainly including better control over the distribution of limited attentional resources (Van Leeuwen et al., 2009; Slagter et al., 2011), improvement in executive control (Tang et al., 2007; Van den Hurk et al., 2018), and reduced mind-wandering (Mrazek et al., 2013). These findings provide evidence for the claim that meditation benefits the cognitive process, particularly the features of conflict monitoring and attention control (Lutz et al., 2008; Malinowski, 2013; Posner et al., 2015; Tang et al., 2015).

Meditation encompasses a family of practices, and currently, focused attention meditation (FAM) is one of the most widely used and investigated types (Tang and Posner, 2013; Lippelt et al., 2014). FAM is usually the starting point for novice meditators. During this meditation, practitioners are required to maintain attention on specific content such as breathing or a candle flame (Vago and Silbersweig, 2012). In the breath-counting meditation (BCM), for example, practitioners focus on the breathing constantly and count each respiratory cycle silently from 1 to 10 and then start again from 1. Meanwhile, they are instructed to let intervening thoughts pass by and keep concentration on respiration (Levinson et al., 2014; Milz et al., 2014). However, BCM is not as simple as it sounds, because involuntary mind-wandering frequently happens, especially for novices. They often report that they stopped counting, counted over 10, or had to reflect intensively to figure out what was the next count during the BCM practice. Given that mind-wandering is a naturally occurring phenomenon, novices are generally unaware of mind-wandering at the moment it occurs. Consequently, keeping concentration continuously on the breathing is so hard that the sufficient meditative time is short in the early stage of meditation. Besides, practitioners' attentional states are evaluated solely by themselves, and this limits the ability of meditation coaches to provide a timely reminder when the practitioners' attention shifts away from their breathing.

Human's haptic channel is a unique sensory modality in terms of combining sensory perception and motor output. Compared with typical attentional tasks using visual stimuli, haptic-related tasks could invoke internal somatic attention and help participants control the focused spotlight of attention spontaneously. There existed but a few attempts that investigated the effects of somatosensory signals on attention and the possibility of enhancing attention through haptic tasks (Bauer et al., 2006; Dvorkin et al., 2013; Sanchez-Lopez et al., 2014). Our previous work indicated that a 5-day training of force-control tasks with pure haptic feedback could promote short-term attention (Wang et al., 2014). Driven by the beneficial effects of meditation on various attention functions, in this paper, we proposed a *haptics-assisted meditation* (HAM) by incorporating force control and meditation practice. We further hypothesized that this novel paradigm (i) could help novices reduce mind-wandering during the meditation practice and (ii) has the potential in attention enhancement.

To validate the first hypothesis, 12 participants without meditation experience conducted HAM and the traditional BCM for the same duration. Self-reports for the mind-wandering during the two meditation practices were recorded. Furthermore, another 20 novices engaged in a longitudinal experiment aiming to address the second hypothesis. In the experiment, an experimental group and a control group performed a 5-day training of HAM and BCM, respectively. A battery of tests was conducted to assess attentional performance of the two groups before and after the training. In addition, brain hemodynamic responses of the experimental group were measured by functional near-infrared spectroscopy (fNIRS) to explore the possible effects of the short-term HAM training on brain attentional functions.

Functional near-infrared spectroscopy allows for non-invasive monitoring of cerebral concentration changes in oxygenated (oxy-Hb) and deoxygenated (deoxy-Hb) hemoglobin without severe restrictions on body movements and physical environment (Boas et al., 2014). These features make fNIRS well suited for monitoring the neural activity during HAM where natural movements of hands and metallic sensors are necessary. fNIRS has been used to investigate neural activities related to meditation in recent years and indicated a consistent enhancement in the activation of the prefrontal area after meditation practice. The increased activation in the prefrontal cortex (PFC) tended to correlate with better performance in the cognitive tests (Endo et al., 2013; Ji et al., 2019). Meditation practitioners and non-practitioners showed a significant difference in the prefrontal activation during meditation. An increase in oxy-Hb and a decrease in deoxy-Hb were observed in practitioners as compared with non-practitioners (Cheng et al., 2010). Similar hemodynamic differences were also found in the auditory cortex of meditation experts and controls (Gundel et al., 2018). Their findings showed that experts had an increased activation in auditory areas during meditation and also had a more widespread activation pattern beyond the meditative task itself, such as resting state, indicating possible long-term effects on the brain. A longitudinal study further demonstrated that a 6-week practice significantly improved the oxy-Hb at all parts of the PFC in meditation novices as compared with controls who conducted relaxation training for the same duration (Gagrani et al., 2018). For participants with some meditation experience, a 20-min meditation practice increased cerebral oxygenation and enhanced their performance during the Stroop color–word task (Deepeshwar et al., 2015). These findings uniformly suggested an enhanced activation related to meditation practice and provided evidences for the feasibility of fNIRS in meditation research.

With this background, the present study employed fNIRS to assess the effects of the proposed HAM on cerebral hemodynamic responses. Given that the PFC is a crucial structure for cognitive functions, and the sensorimotor cortex (SMC) mainly involves in body sensation and force control, we recorded fNIRS signals from these regions and investigated how HAM affected the cerebral activation in this study. Besides, functional connectivity (FC) is defined as a robust temporal dependency among neural activation patterns, which could indicate coordinated

activities between distinct cerebral regions and provide valuable information about the brain communication network (Friston, 2011). For this, we also investigated the FC between the bilateral PFC and SMC to better understand how these regions interacted with each other during HAM.

MATERIALS AND METHODS

Participants

Twelve students without meditation experience from Beihang University participated in experiment 1. They were randomly assigned to group A and B. Group A carried out BCM on the first day and HAM at the same time of the second day, whereas group B carried out HAM on the first day and BCM on the second day. Another 20 naive students from Beihang University who were not involved in experiment 1 were recruited for experiment 2. They were assigned to an experimental or control group randomly with the restriction that gender composition was matched between groups. Experimental participants attended HAM for 5 days for 60 min/day. The controlled participants were given the same number and length of training sessions but attended BCM. There was no significant difference in gender, age, and years of education across groups for both experiments (independent-samples *t*-tests on age and years of education; see **Table 1**).

All participants in the experiments were right-handed and meditation naive without any previous meditation experience and have normal or corrected-to-normal visual acuity. All of them were confirmed having no history of mental health problems and not receiving any psychopharmacological treatments. Written informed consent was obtained from all participants before the study, and this study was approved by the State Key Laboratory of Virtual Reality Technology and Systems of China.

Procedures

Figure 1 illustrates the experiment procedures. Prior to formal experiments, participants were provided with written instructions and sufficient practice to make sure they were thoroughly familiar with the requirements. In experiment 1, participants performed the HAM and BCM practices separately at the same time for two consecutive days. Each practice lasted 75 min, split into four sessions of 15 min with 5-min breaks between two adjacent sessions. For each participant, the number of reported mind-wandering episodes during the HAM and BCM practices was recorded separately.

In experiment 2, the experimental and control groups conducted a 5-day training of HAM and BCM, respectively. Both groups performed a 60-min training each day, including three sessions of 20 min with a 5-min break following each session. The two groups were given a battery of tests before training and immediately after the final training session. These tests were arranged in two consecutive days to avoid fatigue. Specifically, the Blink, Stroop, Reading, and Gabor tasks were performed on the first day, and the attention network task (ANT), sustained attention to response task (SART), and Math task were on the second day. There was a 10-min break after each test. Besides, fNIRS measurements were conducted when the experimental participants performed ANT and SART in pretests and posttests. fNIRS signals during the last training session were also recorded from all experimental participants.

Haptics-Assisted Meditation

Figure 2 shows the procedure of HAM during which participants sat in a chair in front of a fixed force-sensor plate and tied a respiration sensor to their abdomen. They also wore an eyeshade for eliminating visual disturbance and a pair of head-mounted earmuffs for eliminating noise. Because deep breathing practice was proved to be beneficial for a variety of cognitive functions and widely used in meditation, participants were instructed to keep a constant, slow, and deep diaphragmatic breathing during the task (Brown and Gerbarg, 2009). More specific requirements for breathing were described in our previous study (Zheng et al., 2019).

Each 20-min session of HAM consisted of four 5-min blocks. During block 1, participants conducted the breath-counting task that is the same as what the control group did. During block 2, "positive mapping," participants pressed two force sensors using their left and right index fingertips synchronously, increasing the fingertip forces when inhaling and decreasing the forces when exhaling. They were asked to try their best to control the change of fingertip forces to match with their respiratory rhythm. Block 3, "negative mapping," was similar to block 2 with the difference that participants were required to decrease the forces when inhaling and increase the forces when exhaling. During block 4, "hybrid mapping," participants performed positive mapping or negative mapping every 10 respiratory cycles and then switched to another mapping mode. The participants, therefore, needed to

TABLE 1 | Demographics of participants.

	Experiment 1			Experiment 2		
	Group A	**Group B**	***p*-values**	**HAM group**	**BCM group**	***p*-values**
Gender	2 F, 4 M	2 F, 4 M	\	4 F, 6 M	4 F, 6 M	\
Mean age (SD)	24.2 (1.7)	23.7 (1.6)	0.62	23.1 (1.7)	23.1 (2.3)	1.00
Mean years of education (SD)	17.7 (1.8)	17.2 (0.8)	0.54	16.5 (1.3)	17.2 (1.9)	0.35

F denotes females, and M denotes males. Years of education indicate the number of academic years a person completed in a formal program provided by elementary and secondary schools, universities, colleges, or other formal postsecondary institutions.

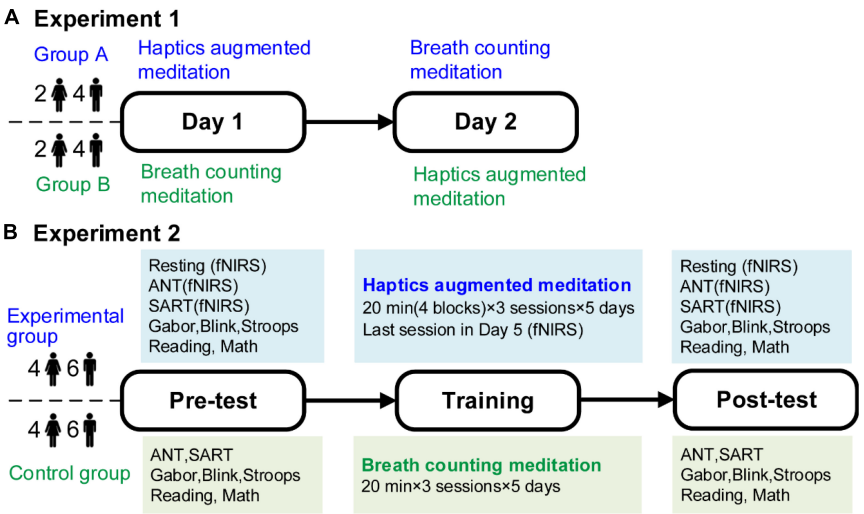

FIGURE 1 | Experimental procedures. **(A)** Experiment 1. Twelve participants carried out HAM and BCM on two consecutive days. **(B)** Experiment 2. Twenty participants were allocated randomly to the experimental or control group who conducted 5-day training of HAM or BCM, respectively. Both groups conducted a battery of tests before and after the training. For the experimental group, fNIRS signals during ANT and SART before and after the training, and during the last training session were recorded. HAM, haptics-assisted meditation; BCM, breath-counting meditation; fNIRS, functional near-infrared spectroscopy; ANT, attention network task; SART, sustained attention to response task.

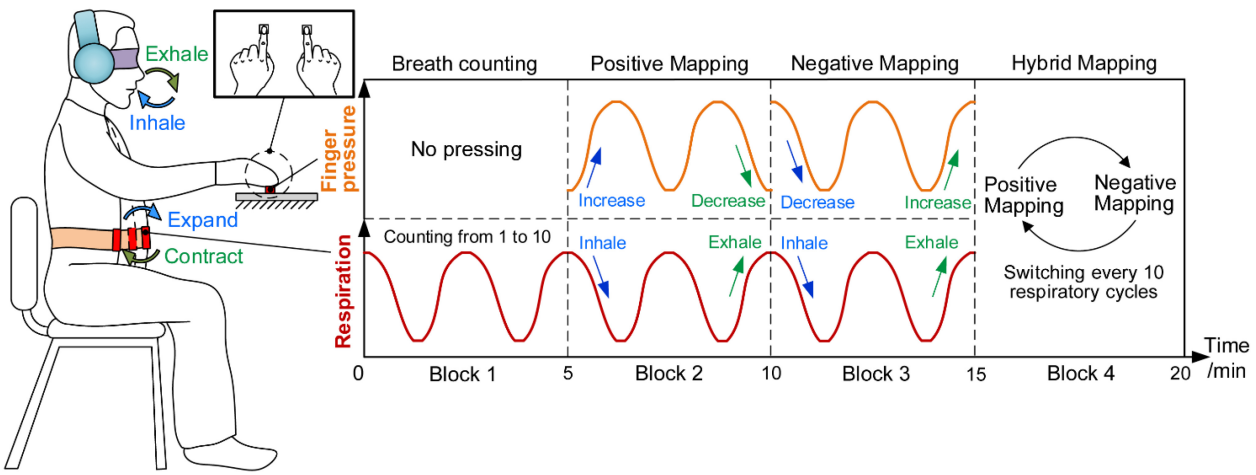

FIGURE 2 | Haptics-assisted meditation. Participants conducted the breath-counting task in block 1. In block 2, "positive mapping" mode, participants were required to increase the fingertip pressure when inhaling and decrease when exhaling. Block 3, "negative mapping" mode, is similar to block 2 with the difference that participants decreased the fingertip pressure when inhaling and increased when exhaling. In block 4, "hybrid mapping" mode, participants performed the positive mapping or negative mapping mode every 10 respiratory cycles.

perform the breath counting simultaneously to ensure the correct switch between the two mapping modes. At the end of each block, participants would hear a short music to remind them to enter into the next block.

It should be noted that a simplified HAM was performed in experiment 1. While pressing with bilateral index fingers in experiment 2, participants were only required to press one force sensor using their right index fingers in the simplified task and thus were allowed to report mind-wandering using left hands conveniently. During experiment 1, participants performed two sessions of positive mapping and two sessions of negative mapping in the sequence of positive, negative, positive, and negative. They were instructed to immediately report whenever they became aware of mind-wandering by clicking a digital counter (GSQ100, Paulone Inc., China) in their left hands and then refocused on the task. Mind-wandering here was defined as "forgetting to press the sensor when breathing in or out," "performing the wrong mapping mode," or "being aware that thoughts had drifted away from breathing or pressing." These guidelines were instructed to all participants before the experiment. Besides, participants were not required to report mind-wandering in experiment 2.

Data of respiration and fingertip force were recorded at a sample rate of 200 Hz. A respiration sensor belt (used in combination with NeXus-10 Mark II, Mindmedia Inc., Netherlands) was tied to the participant's abdomen to record respiratory signals. Two force sensors (FSG15N1A, Honeywell Inc., United States) were mounted on a fixed plate to measure the fingertip pressures exerted by two index fingers.

Breath-Counting Meditation

During BCM, participants sat in a spacious and silent room and held a digital counter in their left hands. They were instructed to sit on a chair comfortably, close eyes, and silently count each respiratory cycle from 1 to 10 and then repeat from 1. The requirements for the breathing here were consistent with the requirements in HAM. The participants were also asked to concentrate entirely on the task and press the counter immediately to report the mind-wandering whenever they became aware of losing track of the task. Specifically, mind-wandering here refers to "stopping counting," "counting over 10," or "had to reflect intensively to figure out what was the next count." Following the report, participants should bring the focus back to the breathing and count again from 1.

When performing BCM, participants followed a compact disc with body posture adjustment and relaxed practice accompanied by a music background. Instructions on the compact disc were from standard guided audio recordings. A coach observed facial and body cues to identify those who were struggling with the practice and gave proper instructions immediately after the training session. At the end of each session, the counters' number of all participants was recorded and reset to zero. The number of subjective mind-wandering reports was recorded using digital counters (GSQ100, Paulone Inc., China) from all participants.

Test Tasks

Five computerized attentional tasks (ANT, SART, Blink, Gabor, and Stroop) and two real-world tasks (Reading and Math) were used to assess the changes of attentional performance from pretests to posttests. We increased the difficulty of these tasks because all participants in this study were healthy graduate students. Thus, some parameters of these tasks such as the number of trials, duration of stimulus, and time limit for response were modified based on the parameters used in previous studies.

Attention network task has been used to assess the effects of meditation on three basic aspects of attention including alerting, orienting, and executive control (Fan et al., 2002; Tang et al., 2007). In each trial of the task, first, there was a fixation cross at the center of the screen for 500 ms. Then, a cue was presented for 100 ms to inform the target would occur right now and to provide information on where the target would be. Following the cue, there was a fixation period for 300 ms, and then the target and flankers appeared simultaneously. Participants needed to respond to the direction (left or right) of the arrow target by clicking the corresponding buttons on the keyboard as fast and accurately as possible. The arrow target was surrounded by flankers that pointed in either the same or opposite direction. The target and flankers were presented until the participant responded, but for no longer than 1,000 ms. After participants made a response, the target and flankers disappeared immediately, and there would be a short resting period for 1,500 ms. Following this period, participants received the next trial until completing 108 trials. The whole task lasted for about 6 min. The average accuracy and response time (RT) were also calculated to assess the overall performance of the task. Subtraction of RTs was used to obtain scores for the performance in alerting, orienting, and executive control, as described by Fan et al. (2002).

Sustained attention to response task is a go/no-go continuous performance task that requires participants to respond to the go stimuli as quickly as possible, and no response to no-go stimulus appears infrequently (Helton et al., 2009; Levinson et al., 2014). In this task, participants received 240 trials corresponding to 240 single digits (24 each from 0 to 9). In each trial, a random digit was presented for 500 ms at the center of the computer screen and followed by a fixation cross for 500 ms. Participants were instructed to respond to each digit via a key press as fast as possible when the digit appeared but to withhold their response when that digit was a 3. The digit would disappear, and the next digit would appear no matter the participant responded or not. The duration from digit to digit lasted for 1,000 ms, and thus, the whole task took 4 min. The RT and accuracy were calculated for all trials. The accuracy indicated the whole proportion of trials successfully responding to go stimuli and not responding to no-go stimuli.

Attentional blink task (Blink) is a classic test to assess the level of the attentional-blink deficit (Van Leeuwen et al., 2009). The deficit indicates that when two targets (T1 and T2) embedded in a rapid stream of events are presented in close temporal proximity, the second target is often not seen and is believed to result from competition between the two targets for limited attentional resources. A recent study has found a smaller attentional blink and reduced brain-resource allocation to the first target after 3 months of meditation training (Slagter et al., 2007). In this study, we also used this task to assess the possible effects of HAM on the distribution of attentional resources. Each trial started with a 1,780-ms fixation cross, followed by a rapid serial stream of 15 or 19 letters. The letters were from the alphabet except B, I, O, Q, and S, because these letters are likely to be confused with numbers. Each letter was presented randomly for 25 ms, followed by a 34-ms blank. For each trial, one or two letters were replaced by a random number between 2 and 9. When only one letter was replaced by a number, a second letter was replaced with a blank screen (T2-absent trial). There could be short (336 ms) or long (672 ms) interval between the first (T1, a number) and second target (T2, a number or the blank screen). Participants were asked to report T1 and T2 by typing the numbers in order on a keyboard after the stream ended. If participants were sure no T2 was presented, they entered zero for this number, whereas they had to guess T2 if they thought T2 had been presented but could not ensure which number it was. They were informed to report as accurately as possible, and there was no time limit for response. The next trial began after the second response. Participants performed 102 trials of the task, consisting of 48 short-interval/T2-present trials, 18 long-interval/T2-present trials, 18 short-interval/T2-absent trials, and 18 long-interval/T2-absent trials with a random

order. The proportion of the correct trials (T1 and T2 were both reported correctly) was calculated as task accuracy.

Stroop words task has been used to investigate the effects of meditation practice on executive functions and has revealed significant differences between meditators and non-meditators (Moore and Malinowski, 2009; Moore et al., 2012). Stimuli in the task were the four words RED, BLUE, GREEN, and YELLOW, presented in the same color as the written word in congruent trials (e.g., RED presented in red) or in different colors in incongruent trials (e.g., RED presented in blue). Participants were instructed to indicate the color of each word while ignoring the semantic meaning of the word. These words in the task were presented in Chinese characters, given that all participants engaging in this study are Chinese. In each trial, a fixation cross was first presented at the center of the screen for 500 ms, followed by the color word that was presented for 1,000 ms. Participants were required to enter their responses by pressing the corresponding keys as fast and accurately as possible when the word appeared. Four keys on the keyboard were color coded and used to provide comfort for the participant when responding, including the keys "a" (red, left middle finger), "." (yellow, left index finger), "x" (green, right index finger), and " ' " (blue, right middle finger). The whole test consisted of 96 trials that included 64 incongruent trials and 32 congruent trials. These trials were presented in a random order. Each incongruent stimulus appeared in each of the three other colors with equal frequency. After the test, the accuracy for all trials and the RT for incongruent trials were calculated for each participant.

The Gabor patch discrimination task (Gabor) in the present study was modified from a task in the study of Wang et al. (2014). The task consisted of 100 trials. In each trial, four pictures with different angles of stripes were presented on the center of the computer screen for 300 ms, and each picture was followed by a 300-ms blank (see **Figure 3**). The fifth picture was then displayed for 300 ms after a 3-s blank. Participants were provided 3 s to report whether the final picture had appeared in the previous four pictures via key pressing. The next trial began after the response. There could be 18 pictures with a minimum angle difference of 10° in this task, as shown in **Figure 3B**. The five pictures presented in each trial were assigned randomly from the 18 pictures with a restriction that the minimum angle difference across the five pictures was not less than 30°. For example, the pictures of 0°, 20°, and 30° would not appear in the following four pictures if the picture of 10° had been presented first. This restriction aimed to ensure clear discrimination for the presented pictures for all participants in each trial. Accuracy of the task was calculated to assess the performance of sustained attention and working memory.

The five tests mentioned above were all presented on a 21-in. cathode-ray tube (CRT) monitor (100-Hz refresh rate, 1,024 × 768 resolution) and were developed in the C programing environment. The fixation cross and stimulus in these tasks always appeared centrally on the screen. Before each test, participants performed 20 practice trials at least to get familiar with the test.

We also conducted two non-computerized but more real-world tasks (Math computation and Reading task as follows) to assess the possible transfer effect of HAM on attention enhancement to activities in real life. A similar math computation task has been used in our previous study and revealed significant enhancement of performance after a 5-day training of force-control tasks (Wang et al., 2014). In this test, 32 lines of Arabic numbers (the font of Times New Roman, size 16 pt) were printed on a piece of A4 paper, and each line included 30 numbers with a range of 0–9. Participants were required to mark the pairs of two adjacent numbers whose sum equaled to 10 as many as possible within the time limit of 8 min. They were informed to mark the numbers line by line with a pen and were not allowed to go back to previous lines to change their answers. The score of the test was computed manually by subtracting the number of wrongly marked pairs from the number of correctly marked pairs. In addition, the sequences of digits were modified for the posttest, but the total number of pairs summing to 10 was the same as the pretest.

In the Reading task, four passages were selected from the texts with the same difficulty level in the Nelson-Denny Reading Comprehension Tests (Feng et al., 2013). These passages were all related to history with similar numbers of words (approximately 450 words) and were modified to develop an easier version considering all participants are not native speakers of English. The modification was done by translating and marking difficult or low-frequency English words with Chinese. The four passages were then assigned to two sets. The two sets were tested as the pretest and posttest with a balanced order across participants. Ten single-choice comprehension questions and 20 misspelled words were designed for each set. The questions were closely related to the content of the passages. The misspelled word was done by exchanging the order of two adjacent letters, but the meaning of the word was not easy to be misunderstood; for example, "young" was written as "yuong." Participants were required to answer the questions, mark the misspelled words they found with circles, and mark "/" in the position they were reading whenever they became aware of mind-wandering. Participants would be stopped when the test duration exceeded 40 min. The task score was computed as S1 + S2 − S3 − S4 with the presence of four components: number of right answers of the single-choice comprehension questions (S1), number of the misspelled words that were found accurately (S2), number of right-spelled words but marked as misspelled (S3), and number of mind-wandering self-reports (S4).

Temporal Synchronization

Figure 4 shows the example data of respiration and fingertip forces during the HAM practice. Descent of the black curve in the figure represents inhalation, and the curve's ascent represents exhalation. The rise of the red and blue curves represents the increase of the left and right index fingertip forces, respectively. Similarly, the going down of the curves represents the decrease of the forces.

The temporal synchronization (Δ_{TS}) was defined as the time difference between the moment that respiration signals and fingertip forces begin to change. Δ_{TS} for the left and right hands was computed separately, considering that there could exist a difference between the dominant and non-dominant hands. Four

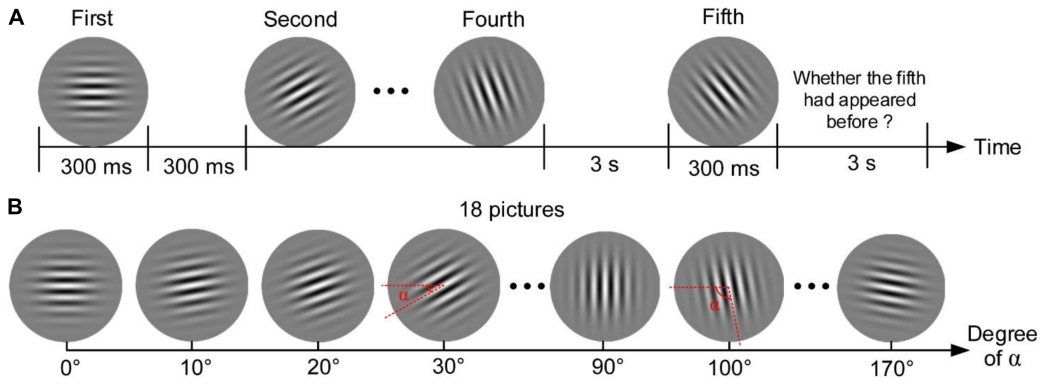

FIGURE 3 | Gabor patch discrimination task. **(A)** Procedure of one trial. **(B)** Eighteen pictures that could be presented in the task.

Δ_{TS} values can be computed in one respiratory cycle as listed in **Table 2**. With Δ_{TS} in block 2 taken as an example, the four Δ_{TS} values include the time difference (i) between the moment of beginning to inhale and beginning to increase the fingertip forces, (ii) between the moment of inhalation end and the moment of the forces reaching the maximum, (iii) between the moment of beginning to exhale and beginning to decrease the forces, and (iv) between the moment of exhalation end and the moment of the forces reaching the minimum. The B1, B2, B3, and B4 denote the data points of beginning to inhale, inhalation ending, beginning to exhale, and exhalation ending, respectively. The L1, L2, L3, and L4 (R1, R2, R3, and R4) denote the data points of left (right) index fingertip force beginning to increase, reaching a maximum, beginning to decrease, and reaching a minimum, respectively. Considering that the respiratory and fingertip force signals reached a plateau near the peak and valley, calculating those start and end data points of the plateaus was the key to the algorithm for computing Δ_{TS}.

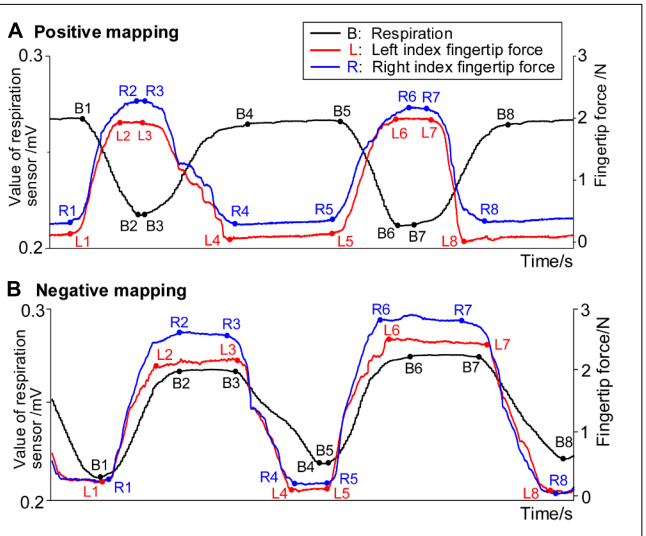

FIGURE 4 | Example data of respiration signals and forces from bilateral index fingers in **(A)** positive mapping and **(B)** negative mapping.

We developed the algorithm in MATLAB (2018b, MathWorks, Inc., United States) and stated the steps as follows. First, a bandpass filter (0.5–100 Hz) and moving average filtering were used to remove apparent noise. Second, we segmented the filtered dataset into segments of each respiratory cycle by setting the minimum interval among two adjacent peaks and the minimum amplitude of peaks. So the moments of the maximum points and minimum points in each data segment can be obtained. Last, for each data segment, the least square method was used to obtain a straight line that passed the maximum or minimum point to fit the plateaus of peak or valley. The intersections of this straight line with the filtered signals were then calculated. Generally, more than one intersection would be obtained. The intersection with the minimum abscissa (i.e., the corresponding moment) was the start point of the peak or valley plateau, and the intersection with the maximum abscissa was the end of the plateau.

Near-Infrared Spectroscopy

An fNIRS system (NirScan, DanYang HuiChuang Medical Equipment Inc., China) with three wavelengths (740, 808, and 850 nm) of near-infrared light was used to record cerebral hemodynamic changes with a sampling rate of 17 Hz. Twenty-two emitters and 24 detector probes were plugged into a soft cap with an inter-optode distance of 30 mm. The measurement channels were located midway between each emitter–detector pair. A total of 64 channels were symmetrically distributed in bilateral hemispheres and were positioned over the PFC and SMC in accordance with the international 10–20 electrode placement system (Jasper, 1958). The emitter R marked in **Figure 5** was placed in Cz.

We measured fNIRS signals from all participants when they performed ANT and SART in the pretest and posttest and when they conducted the last session of HAM practice. We also recorded 5 min of fNIRS signals during resting state before each fNIRS measurement. For the fNIRS data, variables of interest were relative changes in the concentration of oxy-Hb and deoxy-Hb compared with that at baseline. The baseline was defined as 1 min at rest before the ANT and SART, as well as before

TABLE 2 | Definition of temporal synchronization in positive and negative mapping.

Mode	Definition of Δ_{TS} (time difference between the moment of event A and B)		Calculation of Δ_{TS}	
	Event A	Event B	Left hand	Right hand
Positive mapping	Starting to inhale	Starting to increase force	$\lvert T(B1) - T(L1)\rvert$	$\lvert T(B1) - T(R1)\rvert$
	Inhalation end	Force reaching the maximum	$\lvert T(B2) - T(L2)\rvert$	$\lvert T(B2) - T(R2)\rvert$
	Starting to exhale	Starting to decrease force	$\lvert T(B3) - T(L3)\rvert$	$\lvert T(B3) - T(R3)\rvert$
	Exhalation end	Force reaching the minimum	$\lvert T(B4) - T(L4)\rvert$	$\lvert T(B4) - T(R4)\rvert$
Negative mapping	Starting to exhale	Starting to increase force	$\lvert T(B1) - T(L1)\rvert$	$\lvert T(B1) - T(R1)\rvert$
	Exhalation end	Force reaching the maximum	$\lvert T(B2) - T(L2)\rvert$	$\lvert T(B2) - T(R2)\rvert$
	Starting to inhale	Starting to decrease force	$\lvert T(B3) - T(L3)\rvert$	$\lvert T(B3) - T(R3)\rvert$
	Inhalation end	Force reaching the minimum	$\lvert T(B4) - T(L4)\rvert$	$\lvert T(B4) - T(R4)\rvert$

each block of HAM. We should note that there was no 1-min rest before each block for those HAM sessions without fNIRS measurements. During the resting state and baseline periods, participants were instructed just to rest and relax without a specific focus.

Data Analysis and Statistics

All analyses for behavioral and fNIRS data were completed by MATLAB (2016b, MathWorks, Inc., United States). For the self-reports in experiment 1, we conducted paired *t*-tests to compare the number of mind-wandering reported in HAM and BCM. We also used paired *t*-tests to compare the performance in the pretests and posttests within the HAM or BCM group in experiment 2. In order to assess the difference in the performance changes between the two groups, we first calculated the change of performance by subtracting the performance in pretests from the performance in posttests for each group, and then we compared the performance changes between the two groups by independent-samples *t*-tests.

For fNIRS data, the preprocessing was conducted using the open-source software HOMER2[1] implemented in MATLAB. All recorded signals were first processed by the principal component analysis approach to remove signal contamination, such as systematic artifacts (Tak and Ye, 2014). The motion artifact segments greater than five standard deviations from the mean were detected and replaced with their spline interpolation on the basis of neighboring signals. The corrected signals were then bandpass filtered between 0.01 and 0.2 Hz to remove baseline drift and physiological noises. The filtered optical data were finally converted into hemoglobin signals in accordance with the modified Beer–Lambert law (Cope and Delpy, 1988).

Data of oxy-Hb and deoxy-Hb were individually averaged according to the task condition (ANT_pre, ANT_post, SART_pre, SART_post, and Block1, 2, 3, and 4 in HAM) for each channel. The first 60 s of all these conditions was discarded from the analysis to give participants enough time to reach a steady state. The analysis for the HAM period was performed by the block, resulting in a 240-s average for each participant and each block. The fNIRS analyses for the conditions of ANT_pre, ANT_post, SART_pre, and SART_post were performed by task excluding wrong trials (i.e., only including all correct trials). Then, the values of oxy-Hb and deoxy-Hb were converted into *z*-scores by a Fisher *z*-statistics before statistical tests.

We further analyzed FC using the Pearson correlation coefficient and a seed-based approach (Tak and Ye, 2014). The hemoglobin data during the task period (discarding the first 60 s as described above) were used to compute the Pearson correlation coefficients between the seed channel and all the other channels, generating a 64 × 64 *r*-value correlation matrix for each participant and each condition. These individual-level correlation coefficients were then converted to *z*-values via Fisher's *r*-to-*z* transformation to improve normality, resulting in eight 64 × 64 *z*-value FC matrices corresponding to the eight conditions for each participant. To perform a group-averaged FC comparison, we first averaged these individual *z*-value FC matrices within each condition and then converted the group-level *z*-value matrix into an *r*-value matrix via Fisher's *z*-to-*r* transformation for each condition. For reasons of conciseness, only the FC analysis of oxy-Hb data was reported in this study, although the deoxy-Hb data had gone through the same analysis.

Statistical analyses were applied to the values of oxy-Hb, deoxy-Hb, and the FC matrices separately in a channel-wise manner. Paired *t*-tests were conducted for each channel to test whether there were significant differences before and after the HAM training ($p < 0.05$). We also performed paired *t*-tests for each channel to identify the channels showing significant changes in each block of HAM as compared with those during the resting state. Here, the method of false discovery rate (FDR) was applied to each channel to control the family-wise error rate (Singh and Dan, 2006). Significance values reported in this study were those that survived the FDR.

RESULTS

Behavioral Results

Performance Changes After Haptics-Assisted Meditation and Breath-Counting Meditation Training

Figure 6A presents the number of mind-wandering self-reports in experiment 1. The paired *t*-test indicated significantly less mind-wandering ($p = 0.003$) in HAM (1–7, mean 3.27 ± 2.195) than in BCM (3–28, mean 13.09 ± 7.981). One participant

[1]http://homer-fnirs.org/

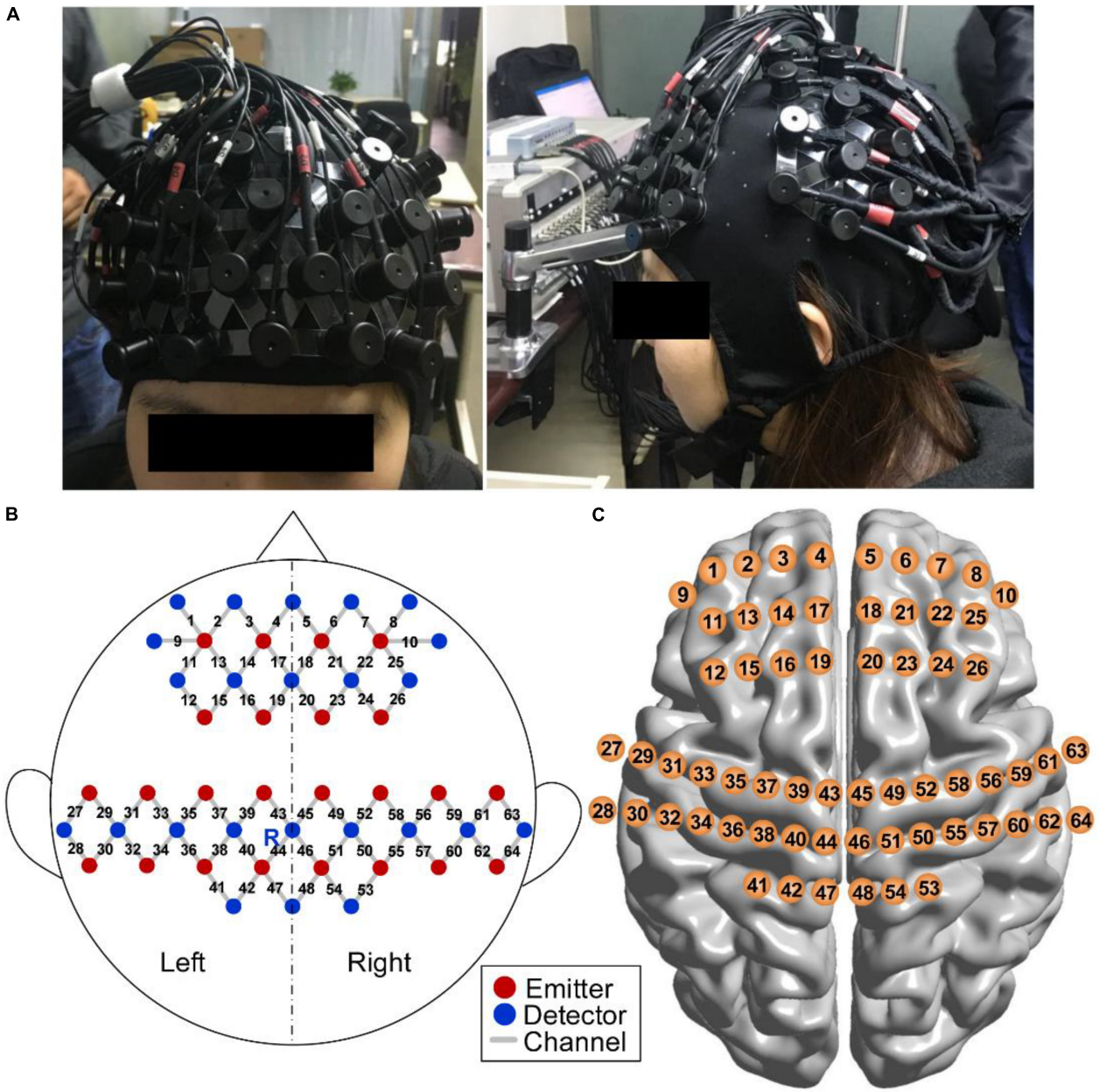

FIGURE 5 | fNIRS measurement. **(A)** Photograph of fNIRS measurement on a participant. **(B)** Schematic of imaging pad. Twenty-two emitters (red dots) and 24 detectors (blue dots) were symmetrically placed on the bilateral hemispheres and constituted 64 measurement channels (gray lines), allowing for the prefrontal and sensorimotor cortices to be measured. The emitter R was placed in Cz of the international 10–20 system. **(C)** Anatomical position of each measurement channel.

was excluded from the analysis because he reported drowsiness during the experiment.

For experiment 2, we compared the attentional performance in the pretests and posttests using paired *t*-tests. After the HAM training, significant improvements were observed in the accuracy of the Gabor test ($p = 0.034$), and in the scores of Reading ($p = 0.031$) and Math tests ($p = 0.002$), as shown in **Table 3**. The performance of the Stroop task also improved significantly ($p = 0.003$), indicated by a decrease in the mean RT. Besides, the accuracy in Blink, ANT, SART, and Stroop also increased, although these improvements were statistically insignificant. The mean RT of SART and the orienting time, executive time, and mean RT of ANT were slightly shorter than those in the pretests. For the BCM group, we found significantly improved performance in Math (higher scores, $p = 0.006$) and Stroop (shorter RT, $p = 0.028$). However, the mean RT of SART became longer ($p = 0.006$) after the training.

Moreover, we computed the changes of performance for HAM and BCM group separately and then compared the difference in the changes between the two groups by

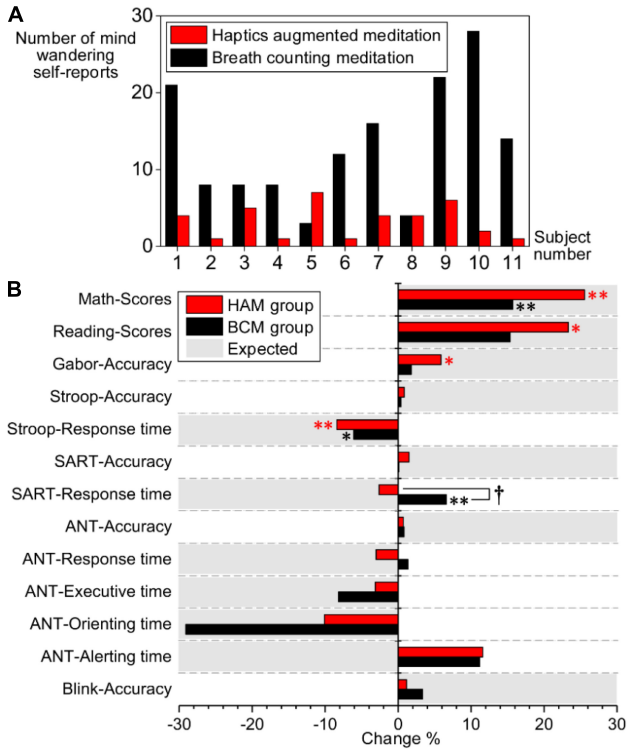

FIGURE 6 | (A) Number of mind-wandering self-reports during HAM (red bars) and BCM (black bars). **(B)** Comparison of performance changes between the HAM (red bars) and BCM groups (black bars). The vertical axis indicates the task performance. The horizontal axis indicates the percentage of performance change after training [i.e., (Post – Pre)/Pre × 100%]. The positive values marked in gray represent that increased performance is expected for the task; the negative values marked in gray represent that decreased performance is expected. * and ** denote significant changes of performance within the HAM or BCM group; *, $p < 0.05$; **, $p < 0.01$. †denotes a significant difference in the performance changes between the HAM and BCM groups ($p < 0.05$). HAM, haptics-assisted meditation; BCM, breath-counting meditation.

independent-samples *t*-tests (see **Figure 6B**). A significant difference was observed only in the mean RT of SART (2.62% decrease in HAM group and 6.60% increase in BCM group, $p = 0.006$). Nevertheless, for HAM group, we found (i) greater improvements in the accuracy of SART ($p = 0.334$), Stroop ($p = 0.722$), and Gabor ($p = 0.332$); (ii) greater improvements in the scores of Math ($p = 0.180$) and Reading ($p = 0.553$); and (iii) greater decrease in the mean RT of Stroop ($p = 0.414$) and ANT ($p = 0.104$) than those for BCM group. These findings suggested that the HAM group showed greater improvements in several tests than did the BCM group, although none of these improvements were statistically significant.

Behavioral Performance During Haptics-Assisted Meditation Training

We used the temporal synchronization (Δ_{TS}) to assess the attentional performance during HAM. The decrease in Δ_{TS} indicates improved performance. **Figure 7A** shows the mean Δ_{TS} values in blocks 2, 3, and 4 from all sessions. Because all participants engaged in this study were right-handed, and there could exist a difference in Δ_{TS} between the dominant and non-dominant hands, we computed the Δ_{TS} for the left and right hands separately. The mean Δ_{TS} derived from the left and right hands both remained around 400 ms, and there was no significant difference between the bilateral hands, although the Δ_{TS} performed by the left hand seemed to be more stable. Besides, we did not find a significant difference of Δ_{TS} across the three blocks, but the variability of Δ_{TS} across subjects in block 2 (positive mapping) tended to be smaller than that in the other two blocks (negative and hybrid mapping).

Furthermore, participants evaluated their attentional level using a score of 1–10, with 10 being the highest level of attention at the end of each HAM session. **Figures 7B,C** present the average attentional scores for the whole session and each block, respectively. The subjective attentional scores for the session and the block both showed a trend of increase as the practice

TABLE 3 | Performance of HAM group in pretoup separately and then compasests and posttests.

Tasks	Index	Pre (mean ± SD)	Post (mean ± SD)	Change %	*t*-value	*p*-value
Blink	Accuracy	0.86 ± 0.67	0.87 ± 0.08	1.16	0.515	0.619
ANT	Alerting time (ms)	36.89 ± 17.32	41.16 ± 15.87	11.58	0.895	0.394
	Orienting time (ms)	21.87 ± 12.91	19.66 ± 9.37	−10.11	−0.35	0.734
	Executive time (ms)	64.06 ± 19.43	62.05 ± 14.10	−3.13	−0.308	0.765
	Response time (ms)	510.58 ± 32.94	495.14 ± 28.00	−3.02	−1.814	0.103
	Accuracy	0.98 ± 0.02	0.99 ± 0.01	0.71	1.397	0.196
SART	Response time (ms)	308.55 ± 39.30	300.45 ± 29.24	−2.62	−1.126	0.289
	Accuracy	0.95 ± 0.05	0.96 ± 0.03	1.48	1.155	0.278
Stroop	Response time (ms)	820.12 ± 98.24	751.25 ± 101.44	−8.40	−3.927	0.003**
	Accuracy	0.97 ± 0.02	0.98 ± 0.02	0.83	1.000	0.343
Gabor	Accuracy	0.65 ± 0.06	0.69 ± 0.07	5.87	2.493	0.034*
Reading	Scores	19.30 ± 6.20	23.80 ± 4.21	23.32	2.558	0.031*
Math	Scores	162.40 ± 27.76	203.90 ± 34.13	25.55	4.432	0.002**

*Change = (Post − Pre)/Pre × 100%. *p < 0.05. **p < 0.01. ANT, attention network task; SART, sustained attention to response task.*

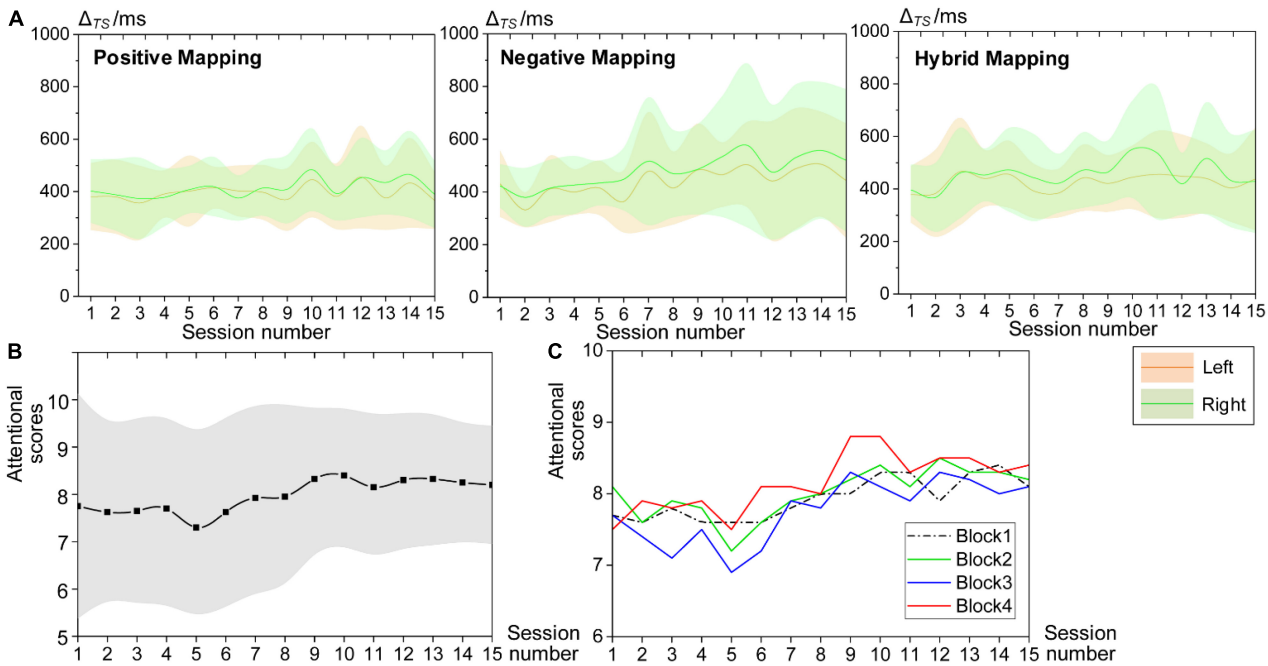

FIGURE 7 | Behavioral performance during HAM training. **(A)** Mean Δ_{TS} values of all sessions for block 2 (positive mapping), block 3 (negative mapping), and block 4 (hybrid mapping). The green patterns represent Δ_{TS} computed from the right, and the yellow patterns represent Δ_{TS} from the left. **(B)** Mean attentional scores for the whole session reported by all participants. **(C)** Mean attentional scores for each block. HAM, haptics-assisted meditation.

sessions increased. The variability of the scores for the whole session between participants also tended to be smaller over time. These findings suggested that HAM enhanced sustained attention ability from subjective judgment.

Neural Results

Hemodynamic Changes After Haptics-Assisted Meditation Training

Mean concentrations of oxy-Hb and deoxy-Hb when performing ANT and SART in the posttests compared with the pretests by paired *t*-tests with FDR thresholding. **Figure 8** presents a visual depiction of changes in oxy-Hb and deoxy-Hb concerning various cortical regions. Data from oxy-Hb showed a significant increase in the post-ANT in several channels over the PFC (channels 1, 20, and 25; $p = 0.021$, 0.003, and 0.008, respectively), as well as in the left SMC (channels 27, 30, and 40; $p = 0.009$, 0.032, and 0.017, respectively) and the right SMC (channels 52 and 58; $p = 0.026$ and 0.015, respectively) when compared with the pre-ANT. For the deoxy-Hb, we observed a significant decrease in channels 1, 2, and 20 ($p = 0.032$, 0.039, and 0.040, respectively) over the PFC in the post-ANT. Besides, there was a significant increase in oxy-Hb over the right PFC (channel 25, $p = 0.031$) in the post-SART. A significant decrease in deoxy-Hb was also observed in this channel ($p = 0.022$) when compared with the pre-SART. Additionally, after the HAM training, we also found an increase in oxy-Hb and a decrease in deoxy-Hb over the right PFC during the resting state. However, no significant changes were observed following thresholding by FDR.

Furthermore, the changes in FC matrices across all channels after the HAM training are shown in **Figure 9A**. Each pixel value in the 64 × 64 correlation matrix corresponds to the value of the change in the group-average Pearson correlation coefficients for oxy-Hb. Paired *t*-tests with the FDR adjustments indicated that there was a significant increase in FC between several channels of the medial PFC and the SMC during resting state. In the posttest, a significantly decreased FC between the left PFC and the right SMC was observed during ANT as compared with the pre-ANT. There was also a uniformly decreased FC between the PFC and SMC in the post-SART. These channel–pairs that increased or decreased significantly ($p < 0.05$) after the training are presented in **Figure 9B** with red or blue lines, respectively.

Hemodynamic Responses During Haptics-Assisted Meditation Sessions

We performed paired *t*-tests with FDR correction for each channel to identify the channels that changed significantly in each block of HAM when compared with those at its baseline (resting state before the block). In block 1, data from oxy-Hb suggested a trend of increase in most parts of the PFC and SMC. The results from paired *t*-tests showed a significant increase in channels 12 and 26 ($p = 0.046$ and 0.043); however, the significant values did not survive after the FDR thresholding. The deoxy-Hb data also demonstrated a trend of decrease in part of the PFC and the medial SMC, although there was no statistical significance.

Although a slight increase in oxy-Hb and a decrease in deoxy-Hb were observed in block 1, we found a uniform and widespread

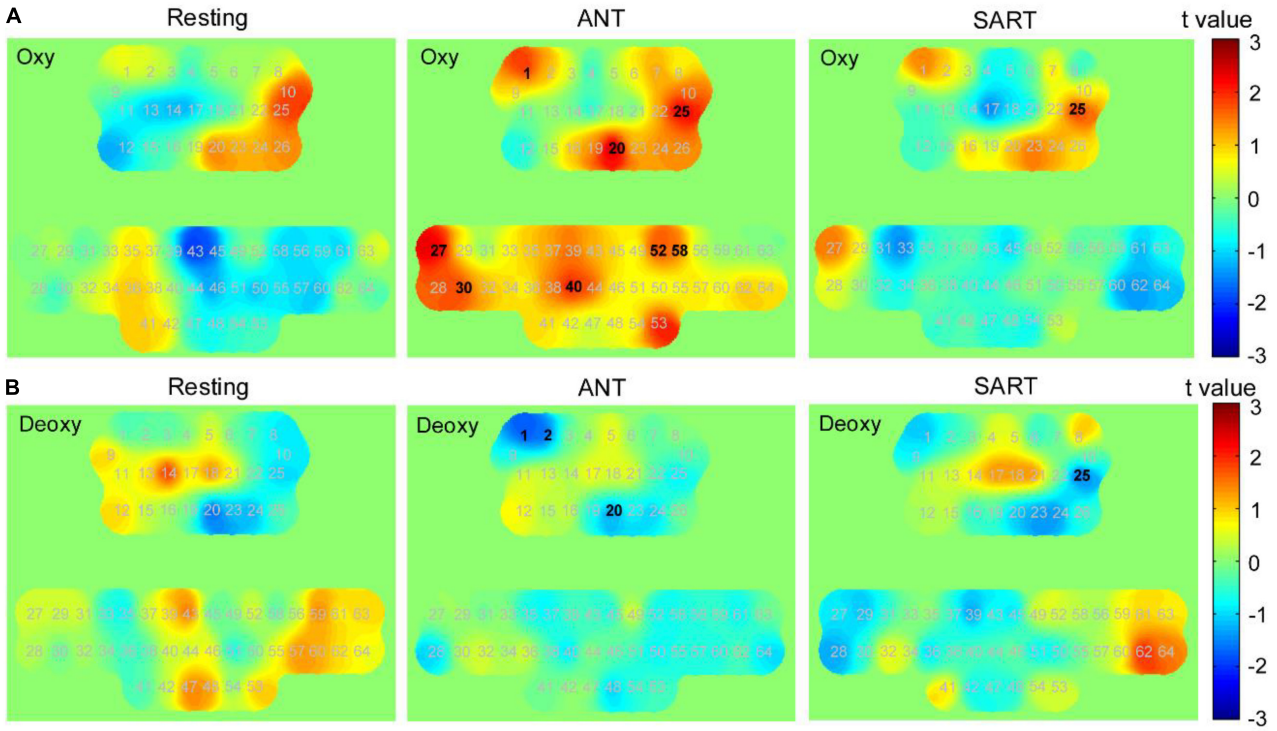

FIGURE 8 | Changes in the concentration of oxy-Hb and deoxy-Hb after training (post minus pre). *t*-value maps obtained by paired *t*-tests on **(A)** oxy-Hb and **(B)** deoxy-Hb. Each number in these maps denotes the numbering of optical channels. The numbers marked in bold denote that the changes in these channels were significant statistically. The positive *t*-values in the color bar represent higher concentration in posttests than in pretests, and the negative values represent lower concentration than in the pretests.

activation pattern when participants performed blocks 2, 3, and 4, indicated by increased oxy-Hb and decreased deoxy-Hb in most regions of the bilateral PFC and SMC. During block 2, participants showed a significant increase in oxy-Hb in channel 26 located in the right PFC and a decrease in deoxy-Hb in this channel. We also observed the decreased deoxy-Hb in the left PFC (channels 1 and 9). Over the SMC, there was significantly increased oxy-Hb in channels 30, 40, 41, 53, and 55 and decreased deoxy-Hb in channels 30, 40, 51, and 53. For block 3, we observed a similar but more widespread activation in the PFC relative to block 2, including significantly increased oxy-Hb in channels 9, 12, 25, and 26 and decreased deoxy-Hb in channels 1, 7, 9, and 26. There was also a significant increase in oxy-Hb in the medial SMC (channels 40, 41, 46, 47, 53, and 54) and the right SMC (channels 63 and 64), as well as a significant decrease in deoxy-Hb in channels 27, 51, and 53.

When performing block 4, participants also showed significantly increased oxy-Hb in the PFC including channels 1, 9, 15, 25, and 26. Although there was also a widespread increase in oxy-Hb over most regions of SMC, only the channels 53 and 54 showed a statistically significant increase following the FDR thresholding. The deoxy-Hb data demonstrated a significant decrease in channels 1 and 9 located in the left PFC, as well as in channels 30, 51, 53, and 64 located in the SMC. **Figure 10** presents the *t*-value maps of oxy-Hb and deoxy-Hb for each block, and **Table 4** summarizes these statistical results.

We further compared the differences in FC between each block and its baseline. **Figure 11A** shows the group-level FC across all channels for each block, and **Figure 11B** marks those channel–pairs that significantly increased or decreased compared with those at baseline (paired *t*-tests with FDR thresholding, $p < 0.05$) by red or blue lines, respectively. When performing block 1, participants showed a significant decrease in the FC between the PFC (left PFC in particular) and the right SMC. Block 2 and block 3 demonstrated a similar finding that FC within the PFC and the SMC became stronger than during resting state, and only several channels showed weaker coupling between the PFC and SMC. For block 4, although a few channels within the PFC and SMC demonstrated enhanced connectivity, FC between most channels in the PFC and SMC tended to decrease when performing the task.

DISCUSSION

The present study proposed and implemented a HAM paradigm for attention enhancement. A series of behavioral performance and fNIRS findings suggested an improvement of the proposed paradigm as compared with a classical BCM paradigm. In terms of the behavioral performance, participants reported less mind-wandering in HAM than in BCM. Furthermore, the experimental group performing the 5-day HAM training showed

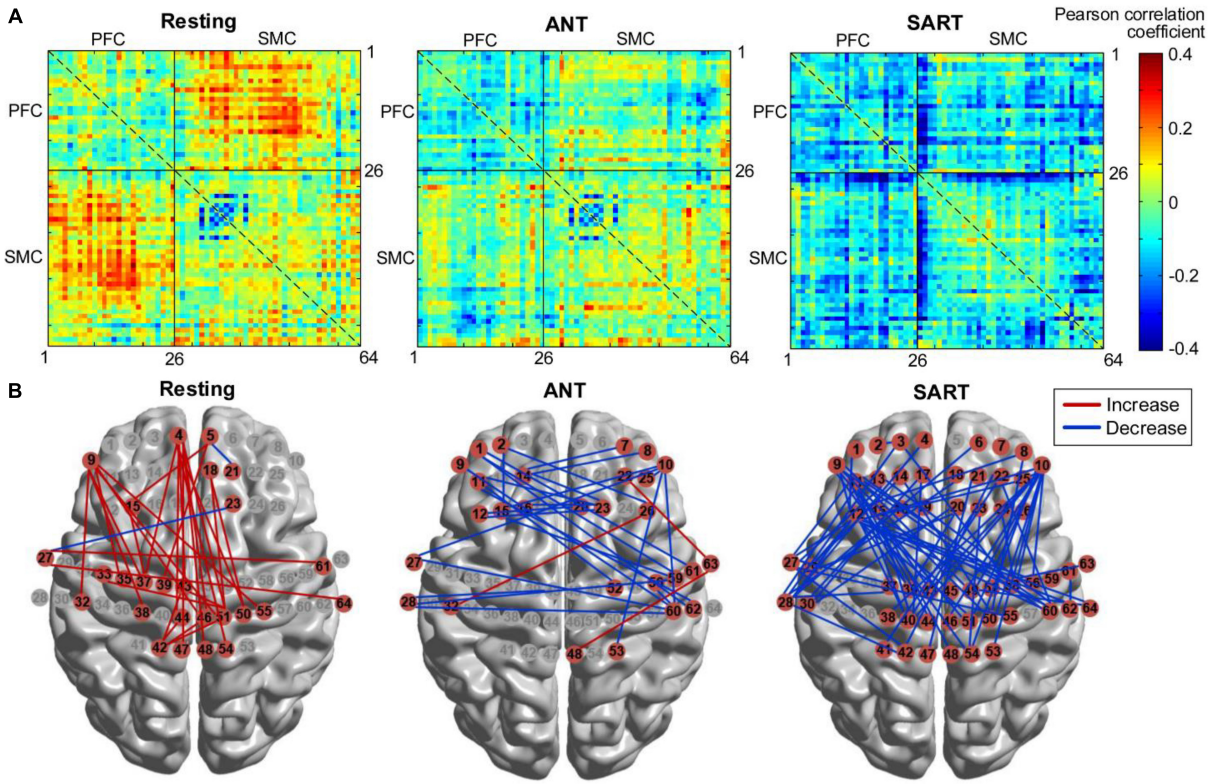

FIGURE 9 | Changes in FC after training (post minus pre). **(A)** FC matrices across all channels. Each number (1–64) in the *x*- or *y*-axis denotes the numbering of optical channels. The color bar indicates the value of the Pearson correlation coefficient. **(B)** FC that increased or decreased significantly ($p < 0.05$) after the training, marked with red or blue lines, respectively. FC, functional connectivity.

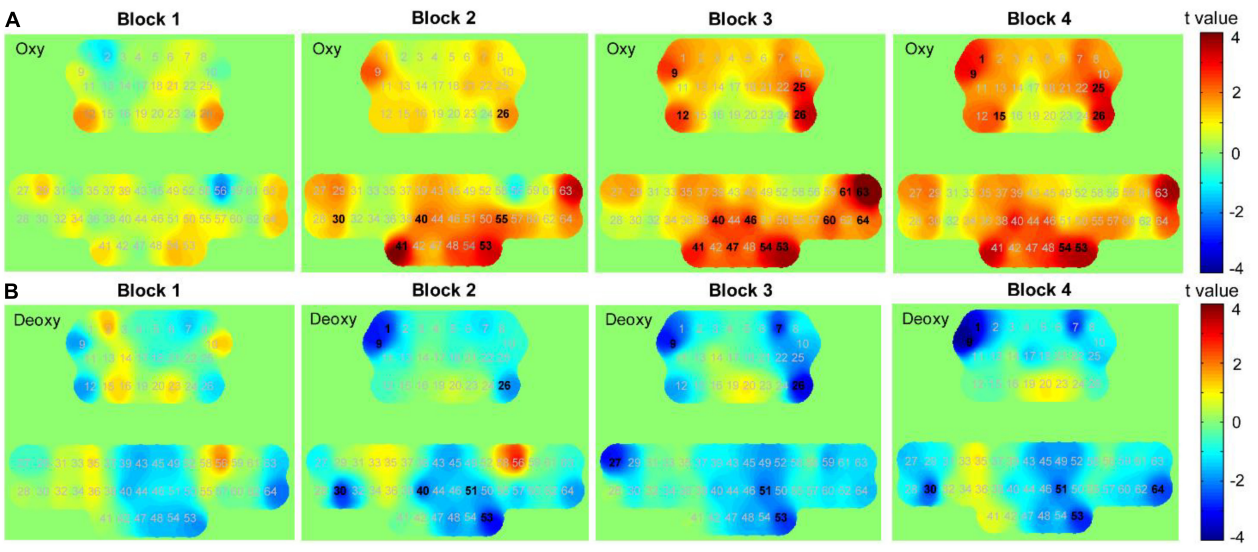

FIGURE 10 | *t*-value maps obtained by paired *t*-tests on **(A)** oxy-Hb and **(B)** deoxy-Hb for each block. The numbers marked in bold denote that these channels showed significant changes than during resting state.

significant improvements in the performance of Stroop, Gabor, Reading, and Math tests after the training. Although there was uniform enhancement in the performance of these tests observed among the HAM group, the control group just had significant improvements in the Math and Stroop tests and even a reduction in the SART performance after the 5-day BCM

TABLE 4 | Summary of the *t*-test results of oxy-Hb and deoxy-Hb.

Comparison	Variable	Brain region	Channel number	*p*-values
Block 2 – Resting	Oxy-Hb	PFC	26	0.021
		SMC	30, 40, 41, 53, 55	0.023, 0.015, 0.002, 0.006, 0.013
	Deoxy-Hb	PFC	1, 9, 26	0.010, 0.008, 0.027
		SMC	30, 40, 51, 53	0.013, 0.007, 0.020, 0.033
Block 3 – Resting	Oxy-Hb	PFC	9, 12, 25, 26	0.028, 0.015, 0.008, 0.012
		SMC	40, 41, 46, 47, 53, 54, 63, 64	0.002, 0.017, 0.014, 0.004, 0.003, 0.001, 0.023
	Deoxy-Hb	PFC	1, 7, 9, 26	0.027, 0.005, 0.007, 0.003
		SMC	27, 51, 53	0.003, 0.03, 0.02
Block 4 – Resting	Oxy-Hb	PFC	1, 9, 15, 25, 26	0.011, 0.015, 0.019, 0.021, 0.017
		SMC	53, 54	0.023, 0.013
	Deoxy-Hb	PFC	1, 9	0.007, 0.007
		SMC	30, 51, 53, 64	0.013, 0.023, 0.030, 0.023

PFC, prefrontal cortex; SMC, sensorimotor cortex.

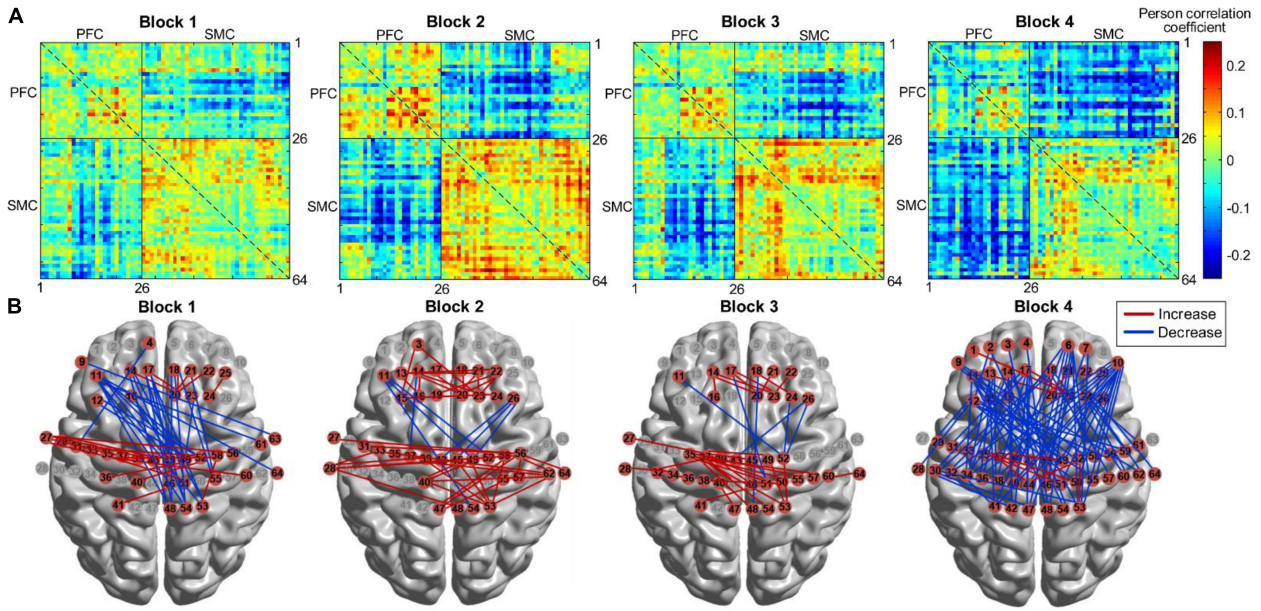

FIGURE 11 | FC for four HAM blocks. **(A)** FC matrices across all channels. **(B)** FC that increased or decreased significantly ($p < 0.05$) marked by red or blue lines, respectively. FC, functional connectivity; HAM, haptics-assisted meditation.

training. The experimental group showed significantly greater improvement in the SART after 5 days of HAM than did the controlled BCM group. The HAM group tended to show greater improvements in the Stroop, Gabor, Math, and Reading tests than did the BCM group, although these improvements were not significant statistically. These outcomes after only 5 days of training suggested the potential of HAM for more considerable improvement in attention performance as the training sessions increased.

The desired meditative state stresses a balanced state of relaxation while focusing on attention, and this state is considered an essential factor in improving the efficacy of exercise on cognitive function (Walsh and Shapiro, 2006; Macdonald et al., 2013). The HAM paradigm was designed to help novices maintain this balanced state in terms of the following aspects. First, the paradigm integrated several vital components of meditation, including deep breathing, mental imagery, body sensations, and mindfulness training. These components have shown broad positive effects on attention control and emotion regulation in previous studies (Tang et al., 2015). When performing HAM, practitioners breathed deeply, slowly, and stably and needed to focus attention on their fingers to keep synchronized with respiration. Such a process was expected to induce a state of restful alertness. Besides, the design of the two-hand response was also introduced to allow a comfortable and relaxed posture because most participants had reported unnatural posture for the one-hand response in the preliminary experiment.

Second, single focus is considered a critical factor that facilitates the efficacy of attention training (Lippelt et al., 2014).

However, this factor might be at risk in the proposed paradigm, as HAM was a dual task of breath awareness and force control, and participants might need to switch attention between the two subtasks. Nevertheless, participants in this study scarcely reported that their attention on the breathing was distracted by the force control. Instead, they tended to report the breath focusing and the force control as one integrated task. For example, they reported in their post-questionnaires that "These two tasks seem to be one, and it is very natural," "I imaged an energy flow circulating between my abdomen and fingertips," and "I felt my body as a whole when performing the task." Therefore, the dual-task design of HAM did not prevent practitioners from maintaining the desired state of relaxation and focusing. The improvement in the performance of attentional tests after the HAM training also supported that the design did not risk the effectiveness of HAM on attention enhancement.

Finally, we designed a relatively complicated paradigm for HAM. Precisely, participants needed to perform four progressive blocks (i.e., breath counting, positive mapping, negative mapping, and hybrid mapping) in each session. The breath-counting block first provided participants a brief relaxed period to help them get into the desired state gradually. The following three blocks were similar but had differences in the mapping mode, which was designed to improve the participant's engagement in the practice. Besides, the paradigm of block 4 required to count and retain the number of respiratory cycles and thus combined meditation practice with working memory training. Given that working memory training also benefits attentional functions (Klingberg, 2010; Spencer Smith and Klingberg, 2015), this combination was expected to amplify the training effect over the use of only one of these components for novice meditators.

Many styles of meditation practice rely on thought control, such as focusing on the breath and paying attention to the present moment. However, the approach of controlling thoughts might be not optimal for novices because they have to struggle to control their thoughts from mind-wandering in the early stage of meditation. Compared with the traditional meditation practice stressing thought control, HAM required concentration on a specific response from the body, while reducing reliance on the control of thoughts, which may be more accessible for novices. Besides, compared with BCM, HAM required a higher cognitive load and thus inhibited participants from spontaneous and frequent mind-wandering. Considering that a high cognitive demand might be a potential factor that influences the efficacy of exercise on cognitive function (Ji et al., 2017, 2019), the higher cognitive load in HAM suggested a stronger training dose than pure breath awareness meditation and thus may accelerate the practitioner's access to meditative states.

Because the HAM paradigm is suitable for novices and raises the possibility of amplifying the training effect, we hypothesized that a short period of training might benefit the self-regulation of attention networks. Although 5 days of training was indeed short for novices, we have reasons to expect that the 5-day HAM practice could lead to improvements in attention functions. Previous findings indicated that the 5-day meditation practice with the integrative body–mind training method induced significantly better attention and control of stress than in a control group given relaxation training (Tang et al., 2007). Our previous work also demonstrated that 5 days of training with a force-control task improved the efficiency of the executive attention networks (Wang et al., 2014). Raz et al. (2005) found changed brain processes even after a single meditation session. Besides, there existed viewpoints that the amount of time participants spent meditating each day, rather than the total number of hours of meditative practice over their lifetime, affects performance on attentional tasks (Chan and Woollacott, 2007). Taken together, a short (5 days) but intensive (1 h/day) training was conducted in this study. Nevertheless, we should note that for a short period of training, the high-quality practice was necessary for every session, and the experimental process needed to guarantee that each practice session achieved a good result. A longer period of practice is still needed in future research to investigate the long-term effect of HAM on attention functions.

Our previous study has validated that the synchronization between the force and respiration signals can be used as an objective marker of attentional state (Zheng et al., 2019). Thus, another advantage of the HAM paradigm might lie in the possibility of real-time monitoring of the attentional state. The monitoring allows novices to obtain real-time feedback of their brain state and, therefore, could promote the training by proper intervention or guidance. In the present study, the algorithm for computing Δ_{TS} had an average error of about 50 ms and indicated an overall accuracy of 87.5% because participants performed an approximately 400-ms Δ_{TS} during the training. The accuracy met the requirements for assessing the changes in attentional performance over time in this study. It should be noted that the current algorithm was executed offline, and how to improve the accuracy and speed of the algorithm for online calculation is needed to be investigated in further research.

Functional near-infrared spectroscopy findings in this study suggested that an increased brain activation could occur after the practice, which was consistent with most previous literature. We found significantly increased oxy-Hb and decreased deoxy-Hb over the right PFC when performing ANT and SART in the posttests. There was also an increasing trend of oxy-Hb in the right PFC during the resting state. These findings support the assumption that meditation beginners who need to overcome habitual ways of internally reacting to one's unrelated thoughts might show a greater prefrontal activation (Allen et al., 2012). Achieving the focused meditative state involves the attentional control effort in the early stage of meditation, thus activating the prefrontal regions. It should be noted that this study used the task-level (block-level) design for the fNIRS data analysis. Future research is advised to investigate event-related responses within trials of the testing task, as well as during the meditation practice, which might provide more information regarding brain attention functions. Neural recordings for the control group are also necessary to understand the differences between HAM and traditional meditation types.

Moreover, although the FC analyses were limited in terms of the small sample size, this study suggested consistent findings

with previous studies showing that meditation increased certain synchronous activities within default mode network (DMN) (Jang et al., 2011). Following the training, we observed a stronger FC between the medial PFC and SMC at resting state. Given that the medial PFC and inferior parietal lobule are considered key regions of the DMN involved in self-referential processing (Northoff et al., 2006; Sajonz et al., 2010), the stronger connectivity may be interpreted as increased self-monitoring and cognitive control over the DMN function (Brewer et al., 2011). Besides, we observed a reduced FC between most channels over the PFC and SMC in the post-SART, as well as between some channels of the PFC and temporal cortex in the post-ANT. Similar findings were shown in previous fMRI studies. For example, one cross-sectional study on pain processing demonstrated decreased connectivity of executive and pain-related brain regions in meditators (Grant et al., 2011). We accordingly speculated that the reduced coupling at the tasking state might be associated with increased attentional control because participants did not have to pay so much effort for the stimulus monitoring and response inhibition after the training. Nevertheless, whether reduced coupling between these brain regions indicates improved attentional regulation needs further investigation with a larger number of subjects. Besides, the current fNIRS system did not provide the accurate neuro-navigation information corresponding to the brain anatomical structure; thus, findings regarding more precision regions of interest were not discussed in this study. Further FC analysis for more precision brain regions such as the dorsolateral PFC might provide additional information.

On the basis of these behavioral and fNIRS results, we surmised that HAM affected brain attentional functions positively by activating the attention network, SMC, and the regions related to working memory. The effective activations were obtained by the specific design of the HAM paradigm that involved body sensations, muscle control, attention switching within the internal body, and working memory practice. HAM incorporated respiratory perception with force control, requiring somatosensory attention as a physiological foundation and thus provided a useful way for novices to obtain a series of key meditation skills, including (i) how to feel directly when mind has wandered from its sensory focus, (ii) how to control somatic attention to compete with internally focused rumination, (iii) how to obtain familiarity with the fluctuations of sensations of breathing and forces, and (iv) how to control the attentional spotlight to shift from one to another flexibly. Together, these enhanced skills might become a crucial early stage of attention enhancement (Kerr et al., 2013).

CONCLUSION

This study adds to the literature demonstrating the potential value of human haptic channels in cognitive training. Preliminary results demonstrate the improvements in behavioral performance and brain activation following 5 days of practice, which provides evidence for the effectiveness of HAM on attention enhancement in the early stage of meditation learning. On the basis of the present work, future longitudinal studies with larger subject populations and controlled neural recordings will be necessary to validate the conclusions further. Another possible place for future research is assessing the moment-to-moment attentional state during the practice by online computing of the synchronization between breathing and force signals. The online method can be used to link fNIRS measurements to attentional performance and possibly develop a real-time neurofeedback paradigm.

DATA AVAILABILITY STATEMENT

The raw data supporting the conclusions of this manuscript will be made available by the authors, without undue reservation, to any qualified researcher.

ETHICS STATEMENT

Experiments were approved by the State Key Laboratory of Virtual Reality Technology and Systems of China. Written informed consents were obtained from all participants.

AUTHOR CONTRIBUTIONS

Y-LZ and D-XW designed the research plan, organized the study, and wrote the manuscript. Y-RZ and D-XW administered the experiments. All authors coordinated the data analysis, interpreted the data, discussed the results, and edited the manuscript.

FUNDING

This work was supported by the National Key Research and Development Program under grant no. 2017YFB1002803 and the National Natural Science Foundation of China under grant no. 61572055.

REFERENCES

Allen, M., Dietz, M., Blair, K. S., van Beek, M., Rees, G., Vestergaard-Poulsen, P., et al. (2012). Cognitive-affective neural plasticity following active-controlled mindfulness intervention. *J. Neurosci.* 32, 15601–15610. doi: 10.1523/JNEUROSCI.2957-12.2012

Bauer, M., Oostenveld, R., Peeters, M., and Fries, P. (2006). Tactile spatial attention enhances gamma-band activity in somatosensory cortex and reduces low-frequency activity in parieto-occipital areas. *J. Neurosci.* 26, 490–501. doi: 10.1523/JNEUROSCI.5228-04.2006

Boas, D. A., Elwell, C. E., Ferrari, M., and Taga, G. (2014). Twenty years of functional near-infrared spectroscopy: introduction for the special issue. *Neuroimage* 85, 1–5. doi: 10.1016/j.neuroimage.2013.11.033

Brewer, J. A., Worhunsky, P. D., Gray, J. R., Tang, Y. Y., Weber, J., and Kober, H. (2011). Meditation experience is associated with differences in default

mode network activity and connectivity. *Proc. Natl. Acad. Sci. U.S.A.* 108, 20254–20259. doi: 10.1073/pnas.1112029108

Brown, R. P., and Gerbarg, P. L. (2009). Yoga breathing, meditation, and longevity. *Ann. N. Y. Acad. Sci.* 1172, 54–62. doi: 10.1111/j.1749-6632.2009.04394.x

Chan, D., and Woollacott, M. (2007). Effects of level of meditation experience on attentional focus: is the efficiency of executive or orientation networks improved? *J. Altern. Complement. Med.* 13, 651–658. doi: 10.1089/acm.2007.7022

Cheng, R. W. F., Borrett, D. S., Cheng, W., Kwan, H. C., and Cheng, R. S. S. (2010). Human prefrontal cortical response to the meditative state: a spectroscopy study. *Int. J. Neurosci.* 120, 483–488. doi: 10.3109/00207454.2010.483650

Cope, M., and Delpy, D. T. (1988). System for long-term measurement of cerebral blood and tissue oxygenation on newborn infants by near infrared transillumination. *Med. Biol. Eng. Comput.* 26, 289–294. doi: 10.1007/BF02447083

Deepeshwar, S., Vinchurkar, S. A., Visweswaraiah, N. K., and Nagendra, H. R. (2015). Hemodynamic responses on prefrontal cortex related to meditation and attentional task. *Front. Syst. Neurosci.* 8:252. doi: 10.3389/fnsys.2014.00252

Dvorkin, A. Y., Ramaiya, M., Larson, E. B., Zollman, F. S., Hsu, N., Pacini, S., et al. (2013). A virtually minimal visuo-haptic training of attention in severe traumatic brain injury. *J. Neuroeng. Rehabil.* 10:92. doi: 10.1186/1743-0003-10-92

Endo, K., Matsukawa, K., Liang, N., Nakatsuka, C., Tsuchimochi, H., Okamura, H., et al. (2013). Dynamic exercise improves cognitive function in association with increased prefrontal oxygenation. *J. Physiol. Sci.* 63, 287–298. doi: 10.1007/s12576-013-0267-266

Fan, J., McCandliss, B. D., Sommer, T., Raz, A., and Posner, M. I. (2002). Testing the efficiency and independence of attentional networks. *J. Cogn. Neurosci.* 14, 340–347. doi: 10.1162/089892902317361886

Feng, S., D'Mello, S., and Graesser, A. C. (2013). Mind wandering while reading easy and difficult texts. *Psychon. Bull. Rev.* 20, 586–592. doi: 10.3758/s13423-012-0367-y

Friston, K. J. (2011). Functional and effective connectivity: a review. *Brain Connect.* 1, 13–36. doi: 10.1089/brain.2011.0008

Gagrani, M., Faiq, M. A., Sidhu, T., Dada, R., Yadav, R. K., Sihota, R., et al. (2018). Meditation enhances brain oxygenation, upregulates BDNF and improves quality of life in patients with primary open angle glaucoma: a randomized controlled trial. *Restor. Neurol. Neurosci.* 36, 741–753. doi: 10.3233/RNN-180857

Grant, J. A., Courtemanche, J., and Rainville, P. (2011). A non-elaborative mental stance and decoupling of executive and pain-related cortices predicts low pain sensitivity in zen meditators. *Pain* 152, 150–156. doi: 10.1016/j.pain.2010.10.006

Gundel, F., von Spee, J., Schneider, S., Haeussinger, F. B., Hautzinger, M., Erb, M., et al. (2018). Meditation and the brain - neuronal correlates of mindfulness as assessed with near-infrared spectroscopy. *Psychiatry Res. Neuroimaging* 271, 24–33. doi: 10.1016/j.pscychresns.2017.04.002

Helton, W. S., Kern, R. P., and Walker, D. R. (2009). Conscious thought and the sustained attention to response task. *Conscious. Cogn.* 18, 600–607. doi: 10.1016/j.concog.2009.06.002

Jang, J. H., Jung, W. H., Kang, D., Byun, M. S., Kwon, S. J., Choi, C., et al. (2011). Increased default mode network connectivity associated with meditation. *Neurosci. Lett.* 487, 358–362. doi: 10.1016/j.neulet.2010.10.056

Jasper, H. H. (1958). The ten-twenty electrode system of the international federation. *Electroencephalogr. Clin. Neurophysiol.* 10, 367–380.

Ji, Z., Feng, T., Mei, L., Li, A., and Zhang, C. (2019). Influence of acute combined physical and cognitive exercise on cognitive function: an NIRS study. *PeerJ* 7:e7418. doi: 10.7717/peerj.7418

Ji, Z., Li, A., Feng, T., Liu, X., You, Y., Meng, F., et al. (2017). The benefits of tai chi and brisk walking for cognitive function and fitness in older adults. *PeerJ* 5:e3943. doi: 10.7717/peerj.3943

Kerr, C. E., Sacchet, M. D., Lazar, S. W., Moore, C. I., and Jones, S. R. (2013). Mindfulness starts with the body: somatosensory attention and top-down modulation of cortical alpha rhythms in mindfulness meditation. *Front. Hum. Neurosci.* 7:12. doi: 10.3389/fnhum.2013.00012

Klingberg, T. (2010). Training and plasticity of working memory. *Trends Cogn. Sci.* 14, 317–324. doi: 10.1016/j.tics.2010.05.002

Levinson, D. B., Stoll, E. L., Kindy, S. D., Merry, H. L., and Davidson, R. J. (2014). A mind you can count on: validating breath counting as a behavioral measure of mindfulness. *Front. Psychol.* 5:1202. doi: 10.3389/fpsyg.2014.01202

Lippelt, D. P., Hommel, B., and Colzato, L. S. (2014). Focused attention, open monitoring and loving kindness meditation: effects on attention, conflict monitoring, and creativity: a review. *Front. Psychol.* 5:1083. doi: 10.3389/fpsyg.2014.01083

Lutz, A., Slagter, H. A., Dunne, J. D., and Davidson, R. J. (2008). Attention regulation and monitoring in meditation. *Trends Cogn. Sci.* 12, 163–169. doi: 10.1016/j.tics.2008.01.005

Macdonald, D. A., Walsh, R., and Shapiro, S. L. (2013). "Meditation: empirical research and future directions," in *The Wiley-Blackwell Handbook of Transpersonal Psychology*, eds G. Hartelius, and H. L. Friedman, (Chichester: Wiley), 433–458. doi: 10.1002/9781118591277.ch24

Malinowski, P. (2013). Neural mechanisms of attentional control in mindfulness meditation. *Front. Neurosci.* 7:8. doi: 10.3389/fnins.2013.00008

Milz, P., Faber, P. L., Lehmann, D., Kochi, K., and Pascual-Marqui, R. D. (2014). sLORETA intracortical lagged coherence during breath counting in meditation-naive participants. *Front. Hum. Neurosci.* 8:303. doi: 10.3389/fnhum.2014.00303

Moore, A., Gruber, T., Derose, J., and Malinowski, P. (2012). Regular, brief mindfulness meditation practice improves electrophysiological markers of attentional control. *Front. Hum. Neurosci.* 6:18. doi: 10.3389/fnhum.2012.00018

Moore, A., and Malinowski, P. (2009). Meditation, mindfulness and cognitive flexibility. *Conscious. Cogn.* 18, 176–186. doi: 10.1016/j.concog.2008.12.008

Mrazek, M. D., Franklin, M. S., Phillips, D. T., Baird, B., and Schooler, J. W. (2013). Mindfulness training improves working memory capacity and GRE performance while reducing mind wandering. *Psychol. Sci.* 24, 776–781. doi: 10.1177/0956797612459659

Northoff, G., Heinzel, A., de Greck, M., Bermpohl, F., Dobrowolny, H., and Panksepp, J. (2006). Self-referential processing in our brain - a meta-analysis of imaging studies on the self. *Neuroimage* 31, 440–457. doi: 10.1016/j.neuroimage.2005.12.002

Posner, M. I., Rothbart, M. K., and Tang, Y. (2015). Enhancing attention through training. *Curr. Opin. Behav. Sci.* 4, 1–5. doi: 10.1016/j.cobeha.2014.12.008

Raz, A., Fan, J., and Posner, M. I. (2005). Hypnotic suggestion reduces conflict in the human brain. *Proc. Natl. Acad. Sci. U.S.A.* 102, 9978–9983. doi: 10.1073/pnas.0503064102

Sajonz, B., Kahnt, T., Margulies, D. S., Park, S. Q., Wittmann, A., Stoy, M., et al. (2010). Delineating self-referential processing from episodic memory retrieval: common and dissociable networks. *Neuroimage* 50, 1606–1617. doi: 10.1016/j.neuroimage.2010.01.087

Sanchez-Lopez, J., Fernandez, T., Silva-Pereyra, J., Martinez Mesa, J. A., and Di Russo, F. (2014). Differences in visuo-motor control in skilled vs. novice martial arts athletes during sustained and transient attention tasks: a motor-related cortical potential study. *PLoS One* 9:e91112. doi: 10.1371/journal.pone.0091112

Singh, A. K., and Dan, I. (2006). Exploring the false discovery rate in multichannel NIRS. *Neuroimage* 33, 542–549. doi: 10.1016/j.neuroimage.2006.06.047

Slagter, H. A., Davidson, R. J., and Lutz, A. (2011). Mental training as a tool in the neuroscientific study of brain and cognitive plasticity. *Front. Hum. Neurosci.* 5:17. doi: 10.3389/fnhum.2011.00017

Slagter, H. A., Lutz, A., Greischar, L. L., Francis, A. D., Nieuwenhuis, S., Davis, J. M., et al. (2007). Mental training affects distribution of limited brain resources. *PLoS Biol.* 5:e138. doi: 10.1371/journal.pbio.0050138

Spencer Smith, M., and Klingberg, T. (2015). Benefits of a working memory training program for inattention in daily life: a systematic review and meta-analysis. *PLoS One* 10:e0119522. doi: 10.1371/journal.pone.0119522

Tak, S., and Ye, J. C. (2014). Statistical analysis of fNIRS data: a comprehensive review. *Neuroimage* 85, 72–91. doi: 10.1016/j.neuroimage.2013.06.016

Tang, Y., Hölzel, B. K., and Posner, M. I. (2015). The neuroscience of mindfulness meditation. *Nat. Rev. Neurosci.* 16, 213–225. doi: 10.1038/nrn3916

Tang, Y., and Posner, M. I. (2013). Tools of the trade: theory and method in mindfulness neuroscience. *Soc. Cogn. Affect. Neurosci.* 8, 118–120. doi: 10.1093/scan/nss112

Tang, Y. Y., Ma, Y., Wang, J., Fan, Y., Feng, S., Lu, Q., et al. (2007). Short-term meditation training improves attention and self-regulation. *Proc. Natl. Acad. Sci. U.S.A.* 104, 17152–17156. doi: 10.1073/pnas.0707678104

Vago, D. R., and Silbersweig, D. A. (2012). Self-awareness, self-regulation, and self-transcendence (S-ART): a framework for understanding the neurobiological mechanisms of mindfulness. *Front. Hum. Neurosci.* 6:296. doi: 10.3389/fnhum.2012.00296

Van den Hurk, P. A. M., Giommi, F., Gielen, S. C., Speckens, A. E. M., and Barendregt, H. P. (2018). Greater efficiency in attentional processing related to mindfulness meditation. *Q. J. Exp. Psychol.* 63, 1168–1180. doi: 10.1080/17470210903249365

Van Leeuwen, S., Müller, N. G., and Melloni, L. (2009). Age effects on attentional blink performance in meditation. *Conscious. Cogn.* 18, 593–599. doi: 10.1016/j.concog.2009.05.001

Walsh, R., and Shapiro, S. L. (2006). The meeting of meditative disciplines and western psychology: a mutually enriching dialogue. *Am. Psychol.* 61, 227–239. doi: 10.1037/0003-066X.61.3.227

Wang, D., Zhang, Y., Yang, X., Yang, G., and Yang, Y. (2014). Force control tasks with pure haptic feedback promote short-term focused attention. *IEEE Trans. Haptic.* 7, 467–476. doi: 10.1109/TOH.2014.2359007

Zheng, Y., Wang, D., Zhang, Y., and Xu, W. (2019). Detecting mind wandering: an objective method via simultaneous control of respiration and fingertip pressure. *Front. Psychol.* 10:216. doi: 10.3389/fpsyg.2019.00216

Conflict of Interest: The authors declare that the research was conducted in the absence of any commercial or financial relationships that could be construed as a potential conflict of interest.

Copyright © 2019 Zheng, Wang, Zhang and Tang. This is an open-access article distributed under the terms of the Creative Commons Attribution License (CC BY). The use, distribution or reproduction in other forums is permitted, provided the original author(s) and the copyright owner(s) are credited and that the original publication in this journal is cited, in accordance with accepted academic practice. No use, distribution or reproduction is permitted which does not comply with these terms.

frontiers in Neuroscience

ORIGINAL RESEARCH
published: 12 December 2019
doi: 10.3389/fnins.2019.01336

Performance Monitoring via Functional Near Infrared Spectroscopy for Virtual Reality Based Basic Life Support Training

Emin Aksoy[1,2], Kurtulus Izzetoglu[3], Engin Baysoy[1], Atahan Agrali[1], Dilek Kitapcioglu[2] and Banu Onaral[3]*

[1] Department of Biomedical Device Technology, Acıbadem Mehmet Ali Aydınlar University, Istanbul, Turkey, [2] Center of Advanced Simulation and Education, Acıbadem Mehmet Ali Aydınlar University, Istanbul, Turkey, [3] School of Biomedical Engineering, Science and Health Systems, Drexel University, Philadelphia, PA, United States

The use of serious game tools in training of medical professions is steadily growing. However, there is a lack of reliable performance assessment methods to evaluate learner's outcome. The aim of this study is to determine whether functional near infrared spectroscopy (fNIRS) can be used as an additional tool for assessing the learning outcome of virtual reality (VR) based learning modules. The hypothesis is that together with an improvement in learning outcome there would be a decrease in the participants' cerebral oxygenation levels measured from the prefrontal cortex (PFC) region and an increase of participants' serious gaming results. To test this hypothesis, the subjects were recruited and divided into four groups with different combinations of prior virtual reality experience and prior Basic Life Support (BLS) knowledge levels. A VR based serious gaming module for teaching BLS and 16-Channel fNIRS system were used to collect data from the participants. Results of the participants' scores acquired from the serious gaming module were compared with fNIRS measures on the initial and final training sessions. Kruskal Wallis test was run to determine any significant statistical difference between the groups and Mann–Whitney *U* test was utilized to obtain pairwise comparisons. BLS training scores of the participants acquired from VR based serious game's the learning management system and fNIRS measurements revealed decrease in use of resources from the PFC, but increase in behavioral performance. Importantly, brain-based measures can provide an additional quantitative metric for trainee's expertise development and can assist the medical simulation instructors.

Keywords: functional near infrared spectroscopy, basic life support, medical training, virtual reality, medical simulator

OPEN ACCESS

Edited by:
Fenghua Tian,
University of Texas at Arlington,
United States

Reviewed by:
Tao Liu,
Zhejiang University, China
George Alexandrakis,
University of Texas at Arlington,
United States

****Correspondence:***
Emin Aksoy
emin.aksoy@acibadem.edu.tr;
dreminaksoy@gmail.com

Specialty section:
This article was submitted to Brain Imaging Methods, a section of the journal Frontiers in Neuroscience

Received: *05 September 2019*
Accepted: *27 November 2019*
Published: *12 December 2019*

Citation:
Aksoy E, Izzetoglu K, Baysoy E, Agrali A, Kitapcioglu D and Onaral B (2019) Performance Monitoring via Functional Near Infrared Spectroscopy for Virtual Reality Based Basic Life Support Training. Front. Neurosci. 13:1336. doi: 10.3389/fnins.2019.01336

INTRODUCTION

Advances in new technologies allowed many domains to fulfill their changing needs with a new set of tools. Education is also one of those domains in which educators and learners are now using various serious gaming modules to meet different training requirements. Medical training professionals adopted these serious game based learning modules as medical simulation trainings

and they have utilized it as a part of their curriculum. Previous studies have shown the advantages of interactive media tools over standard textbook lessons such as game based learning (Holzinger et al., 2008; Prensky, 2012; Deterding, 2013). Serious games also provide considerably positive effects on subject understanding, diligence and motivation (Pellas et al., 2018). Serious gaming modules can benefit different display technologies such as virtual reality (VR) head mounted displays, PC monitors and tablet PCs. Because of its high immersion levels, VR head mounted displays have attracted more interest for medical content development. Many instructors began to utilize VR-based approach in their teaching activities, due to the capacity of VR technologies to highly engage trainees through virtual environments and dynamic conditions (Hanson and Shelton, 2008; Holzinger et al., 2008; Prensky, 2012; Deterding, 2013). Serious gaming modules exploit scoring methods such as accuracy, task completion, and response times to assess the effectiveness of the serious gaming module and performance of the learner. However there is a need for an additional tool, enabling instructors to measure the efficacy of the modules and providing them an increased accuracy while assessing the real performance of the trainee.

It is well studied that task–specific activation of prefrontal cortex (PFC), is related with sensory, motor skills, and cognitive processes in human brain (Kelly and Garavan, 2005). These neural activities and mental workload during learning and practicing were successfully measured and quantified by using functional near infrared spectroscopy (fNIRS) over the last decade. fNIRS has been utilized as a functional brain activity monitoring technique in various field settings since it provides a safe, non-invasive, and practical method which measures the real time hemodynamic responses associated with brain activity changes. It is shown that, a particular amount of near infrared light can be transmitted for long distances throughout biological materials between the range of 700 and 1300 nm and additionally concentration differences of oxyhemoglobin (HbO_2) and de-oxyhemoglobin (HHb) molecules (changes as small as 0.05–0.10 μM in tissues) in biological molecules shows different absorption amount of emitted infrared light (Jöbsis, 1977; Villringer, 1997; Maria et al., 2000).

Measured absorption and scattered amount of photons can be interpreted and assessed by using modified Beer–Lambert Law (Cope and Delpy, 1988; Chen et al., 1999; Rolfe, 2000). We have used the Oxy [oxygenation = OxyHb − deOxyH] and the localized activity changes which are known to be associated with working memory for this study (Bunce et al., 2006; Sato et al., 2011, 2013).

To date, fNIRS was exploited for assessment of operator's cognitive performance different disciplines ranging from aviation to medical domain (Ayaz et al., 2012; Armstrong et al., 2018). In clinical settings, measurements of PFC activation by fNIRS while performing various surgical tasks (open surgical knot tying, navigational task, laparoscopic localization task, laparoscopic surgery task, robot assisted tasks, and etc.) were reported in many studies (Leff et al., 2007, 2008; Mylonas et al., 2008; Ohuchida et al., 2009; James et al., 2010, 2011; Shetty et al., 2016; Modi et al., 2017; Nemani et al., 2018).

As for the medical profession training, Basic Life Support (BLS) is a healthcare training course that assures responding to a patient correctly during cardiac and respiratory arrest. Smith et al. investigated major decline of BLS skills retention in 3, 6, 9, and 12 months, because of that, BLS courses are organized more frequently in most of the medical training centers (Smith et al., 2008). In this study, a VR based serious game module, 3D Medsim (Bochum/Germany), was run for teaching the algorithm of "BLS" training compatible with ERC (European Resuscitation Council) 2015 Guidelines (Perkins et al., 2015). Training induced mental workload and PFC activation of participants were quantified through fNIRS system while the participants are using the VR based BLS serious gaming module. Hypothesis of this study is to determine whether there is any decline in Oxy data as the participants learn and become familiar with both VR and BLS protocols. A significant reduction in the amount of PFC activation is expected with increased task familiarity and skill acquisition.

MATERIALS AND METHODS

Participants

A total of 22 right handed subjects participated in this study classified into four different groups based on their knowledge level in BLS procedure and familiarization with VR games. These groups and number of participants within each group are listed on **Table 1**. This study has been reviewed and approved by the Ethical Committee of Acıbadem Mehmet Ali Aydinlar University. All participants gave written informed consent in accordance with the Declaration of Helsinki (World Medical Association, 2013).

Experimental Protocol

3DMedsim VR based BLS serious gaming software compatible with ERC 2015 BLS algorithm was used for the study (Perkins et al., 2015). The knowledge levels of the participants were assessed by the scoring system provided by the serious gaming software (Smith et al., 2008; Perkins et al., 2015; Aksoy, 2019). Following scores of the gaming module, denoted in **Table 2**, revealed the knowledge levels of the participants. Head mounted displays (HTC Vive) with high flickering rate and resolution were used in this study in order to minimize the potential risk of dizziness. The participants were also informed about this potential risk. At the beginning of the VR test, the subjects were asked to check around in VR platform in order to provide

TABLE 1 | Groups and number of participants.

	VR experience	BLS knowledge	Healthcare professional	*N*	%
Group 1	−	−	No	7	31.8
Group 2	+	−	No	5	22.7
Group 3	+	−	Yes	5	22.7
Group 4	−	+	Yes	5	22.7
		Total		22	100.0

TABLE 2 | Scoring criteria of the VR based serious game.

Criteria	Points
Checking consciousness	10
Head tilting	10
Checking breathing	10
Telling someone to call 911	10
Sending someone to fetch an AED (Automated External Defibrillator)	10
Controlling carotid pulse	10
Effective chest compression	10
Opening AED Device	10
Placement of AED pads	10
Defibrillation with AED	10
Total	100

TABLE 3 | Basic life support algorithm based on ERC 2015 criteria.

Criteria
Ensure that the scene is safe
Check responsiveness by shaking gently and shouting loudly
Open the airway using the head tilt and chin lift technique
Telling someone to call 911
Sending someone to fetch an AED
Starting and continuing high-quality CPR in 30 compressions and 2 ventilations sequence
Attaching the AED pads when it arrives
Following the instructions are given by the AED
Delivering shock when advised by the AED
Continue with CPR for another 2 min or until the patient starts breathing

a transition moment for getting used to virtual environment. Following that the subjects were instructed about the correct actions to be taken and played the rescuer role interactively.

Unlike tutorial module, in self-training tasks without hints or instructions to follow, subjects were expected to perform proper steps in an order within a correct timing. Self-training tasks were integrated with a Learning Management (LMS) scoring system providing assessment scores at the end of the session. BLS training protocol was based on 10 subsequent criteria as tabulated in **Table 3** (Aksoy and Sayali, 2019).

Experimental protocol delineated in **Figure 1** starts with a lobby environment in VR, where participants are informed not to move for 10 s for the initial fNIRS baseline recording. Participants who had no prior VR experience had a VR familiarization session for 120 s. Familiarization session consist of basics tasks such as browsing within the software and using HTC Vive controller in VR environment. Participants who had completed the familiarization session directed to lobby screen. Participants who did not require a VR familiarization session started the game from lobby screen. Experiment had three blocks: "tutorial," "seaside," and "subway station." After the completion of each block participants directed to lobby and rest for 15 s before starting the next block. "Tutorial," which utilized a visual assistant, acted as an orientation and aimed to make users more familiar on how to perform BLS tasks. Upon completion of the "tutorial," participants performed "seaside" and "subway station" blocks. Both "seaside" and "subway station" blocks had the same scenario workflow in different environments.

Functional Near Infrared Spectroscopy

A continuous wave fNIRS system (fNIR Devices, LLC, Potomac, MD, United States) was used in this study to monitor the hemodynamic response from PFC. The fNIRS system consists of three modules: a 16 channel sensor pad, a control box and a computer running data acquisition software. The sensor pad has four light emitting diodes (LED) used as light sources, 10 detectors. Entire 16 optode (channel) measurement locations are illustrated in **Figure 2**.

The sensor pad was positioned on the PFC region of the participants (**Figure 3**). 730 and 850 nm wavelengths of lights were acquired continuously at the sampling rate of 2 Hz (Izzetoglu et al., 2007). fNIRS signal can be corrupted by instrument noise, physiological noise, and motion artifacts. Hence, to improve the sensitivity and spatial specificity of brain activity measures, a finite impulse response low pass filter was applied to hamper physiological confounding signals, such as respiration and heart beat oscillations. A linear phase low-pass FIR filter with cut-off frequency between 0.1 and 0.15 Hz has been used. The high deviations and motion artifact per channel were removed using the sliding-window motion artifact rejection reported in Ayaz et al. (2010). The filtered light intensity data were processed with the Modified Beer Lambert Law to calculate oxygenated (oxyHb) and deoxygenated hemoglobin (deoxyHb) values for each channel. Using these values, oxygenation measures (Oxy = OxyHb − DeoxyH) were derived, and left PFC region (Channel 3), known to be associated with working memory, was used within the scope of this study (Kelly and Garavan, 2005; Leff et al., 2008; Ayaz et al., 2012). Therefore, channel 3 was defined as the region of interest in this study. Since the sample size is limited, normality assumption cannot be provided and parametric methods cannot be used. Standard non-parametric tests have been used when assumptions of parametric tests cannot be

FIGURE 1 | Experimental protocol work flow (* indicates starting point for people who had prior VR experience).

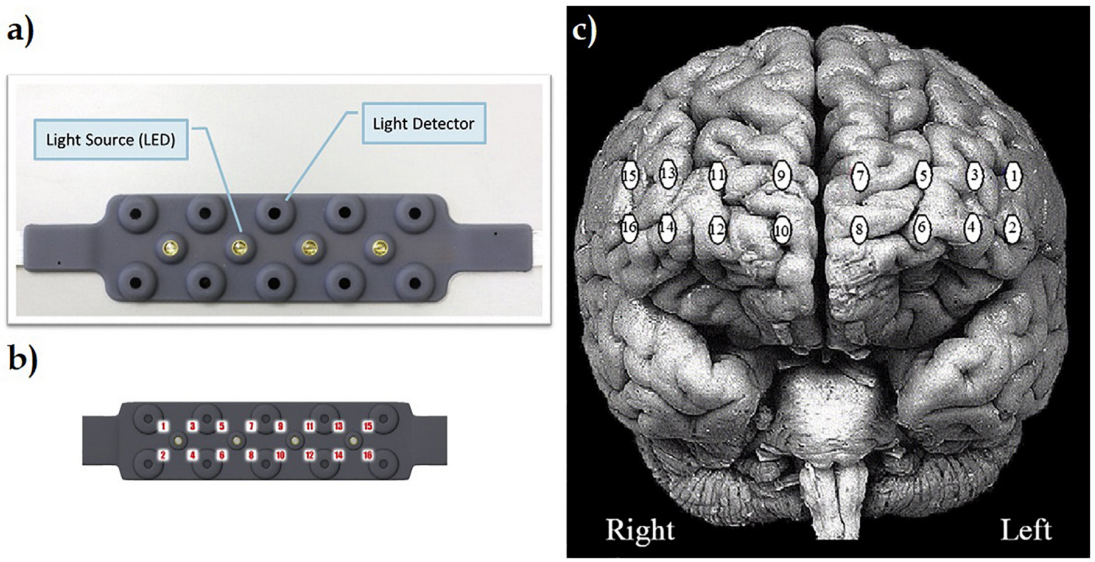

FIGURE 2 | (a) fNIR sensor incorporates four light emitting diodes (LED) used as light sources, 10 light detectors. **(b)** Specific locations of entire 16 optode (channel) measurements over sensor pad. **(c)** Registration of 16 channels through PFC of brain surface (Ayaz et al., 2012).

achieved or the sample size is limited. One of the most common non-parametric test is Kruskal–Wallis test. Kruskal Wallis non-parametric method compare the distributions between groups. Significant result of a non-parametric test does not differentiate whether the difference is between the location and shape of the distributions. Thus, it limits the use of non-parametric tests especially where the shape of distribution between groups is very different (Dwivedi et al., 2017). In addition, the Shapiro Wilk test p value for each group was found to be greater than 0.05 in terms of OXY levels and game scores. All statistical analysis was carried out by using MedCalc Statistical Software version 12.7.7 (MedCalc Software bvba, Ostend, Belgium) (Schoonjans et al., 1995).

RESULTS

Behavioral Performances

Basic life support scores for each group and sessions were calculated by the scoring system of the VR based serious gaming module (**Figure 4**). In all groups except group 3 (With Prior VR experience/prior BLS Knowledge) there is a statistically significant difference between groups for score in the first day (Kruskal Wallis $p < 0.05$). The improvement of BLS scores between the first and seventh day for all the groups can be seen on **Figure 4**. There is a significant improvement of BLS scores in group 1 (+72.68%) and group 2 (+67.42%), whereas there was no significant improvement of BLS scores in group 3 (+ 3.53%) and group 4 (+11.67%) (**Table 4**).

fNIRS Results

Mean Oxy values per channel were calculated for each group to conduct a correlational analysis between subject's training performances and cognitive workload assessed via the changes in blood oxygenation levels from the PFC region of human brain.

FIGURE 3 | A subject wearing fNIRS pad and HMD.

The oxy values of the healthcare professionals with prior VR experience remains almost the same in the first and seventh day

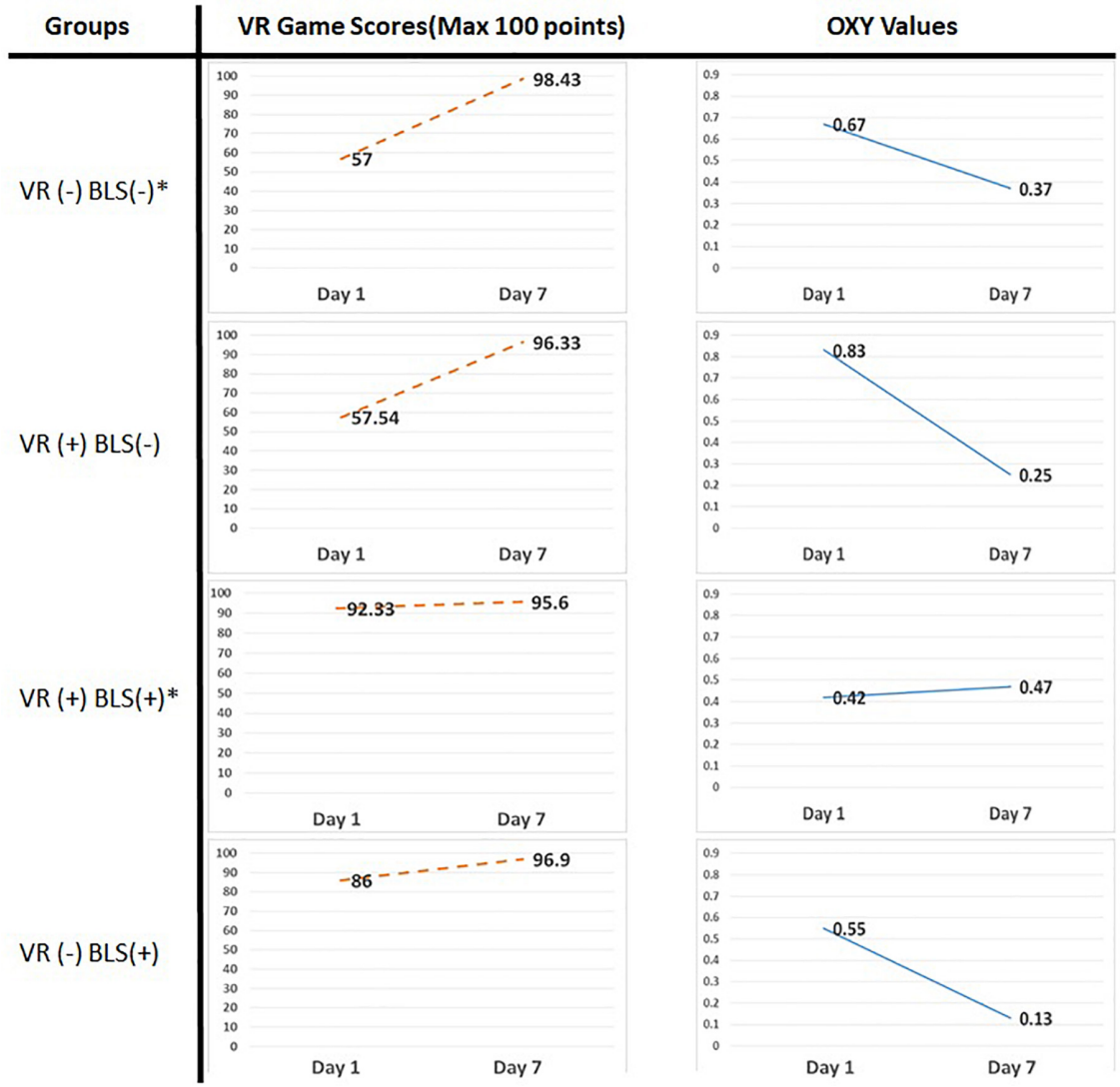

FIGURE 4 | Serious gaming scores (column 1) of the subjects acquired from the learning management system of the game module on the first and seventh day and mean oxy values (column 2) from four groups on the first and seventh day of the study (* indicates statistical significant values) (**Supplementary Table S1**).

(**Figure 4**). On the contrary, significant decreases of fNIRS oxy values can be seen in all other groups on the seventh day. The significant decreases of fNIRS Oxy levels on the seventh day were calculated by 54.90% in group 1, 30.47% in group 2, and 22.81% in Group 4.

Kruskal Wallis test was utilized to determine any significant difference between the groups and Mann–Whitney *U* test was utilized to obtain pairwise comparisons. The statistical analysis results are shown on **Tables 5**, **6**.

As shown on **Table 5**, there is statistically significant difference between groups for score in the first day (Kruskal Wallis $p < 0.05$). According to the *post hoc* test results, there is significant difference between all pairwise comparisons except VR−, BLS− and VR+, BLS− (Bonferroni correction $p < 0.008$ Mann–Whitney *U*). These statistical data reveal that prior VR experience had no additional positive effect on gaming scores.

TABLE 4 | Basic life support scores of four groups.

Groups	VR−BLS−	VR+ BLS−	VR+ BLS+	VR− BLS+
Day 1 Mean BLS Score	57.00	57.54	92.33	86.00
Day 7 Mean BLS Score	98.43	96.33	95.60	96.90
Improvements (%)	+ %72.68	+ %67.42	+ %3.54	+ %12.67

DISCUSSION

The positive effect of tablet based and VR based serious gaming modules for healthcare was shown in various studies. Virtual gaming is becoming a part of the existing trainings programs for healthcare. Utilizing serious gaming as a self-learning strategy is time saving for both learners and educators, as serious gaming

TABLE 5 | Statistical analysis of fNIRS data and serious gaming scores (100/100) by using Kruskal Wallis test.

	Groups				
	VR−, BLS−	**VR+, BLS−**	**VR+, BLS+**	**VR−, BLS+**	***p***
	Mean ± SS	**Mean ± SS**	**Mean ± SS**	**Mean ± SS**	
fNIRS OXY Level Day 1	0.67 ± 1.18	0.82 ± 1.38	0.41 ± 1.09	0.55 ± 1.1	0.898
fNIRS OXY Level Day 7	0.37 ± 0.81	0.25 ± 0.38	0.47 ± 0.86	0.13 ± 0.49	0.879
Serious Game Day 1 Score	57 ± 21.7	54.2 ± 26.3	92.9 ± 7.3	85.9 ± 10.5	<0.001
Serious Game Day 7 Score	98.3 ± 2.9	96.4 ± 2.9	96.2 ± 47	96.9 ± 3.4	0.176

TABLE 6 | *Post hoc* test results between pairwise comparisons of scores on day 1 by using Mann–Whitney *U* test (**Supplementary Table S2**).

	VR− BLS− VS. VR+ BLS−	**VR− BLS− VS. VR+ BLS+**	**VR− BLS− VS. VR− BLS+**	**VR+ BLS− VS. VR+ BLS+**	**VR+ BLS− VS. VR− BLS+**	**VR+ BLS+ VS. VR− BLS+**
Pairwise comparison of performance scores (*p* values)	0.835	<0.001	<0.001	<0.001	<0.001	0.037

modules can be available by learners at any time or anywhere. The other advantages provided by serious gaming is that it improves decision making capabilities of learners in complex situations and self-learning capabilities by providing the learners with the opportunity to practice as much as they can (Johnson et al., 2016; Verkuyl et al., 2017; Kinder and Kurz, 2018).

The gaming module used for this study has a scoring system linked with a dedicated learning management system, allowing us to assess learners' results in an objective manner. In current use of VR based gaming modules, there are still challenges about the technology of assessment including high-stakes assessment in medical education (Christopoulos et al., 2018). Due to similar needs for assessment, we were in a search for an additional tool for the assessment of VR based gaming modules.

To date, fNIRS was used in clinics for examination of many neuronal activities of infants and adults suffer from visual, auditory, olfactory, and mental diseases (Meek et al., 1998; Sakatani et al., 1999; Bartocci et al., 2000; Zaramella et al., 2001; Peña et al., 2003; Wilcox et al., 2005; Arenth et al., 2007). Psychiatric applications also benefit fNIRS imaging for examination of task-dependent abnormalities in PFC of patients with schizophrenia, depression and Alzheimer's diseases (Fallgatter et al., 1997; Fallgatter and Strik, 2000; Matsuo et al., 2002; Suto et al., 2004; Kuwabara et al., 2006). fNIRS imparts a novel objective metric for better understanding of task specific motor skill assessment during surgical training certification as well. Based on these studies, fNIRS was chosen in this study as the tool for measuring the PFC activities and cognitive workload of the participants.

In our study, it has been found out that prior BLS knowledge had positive effects on both BLS scores and fNIRS values. There was a statistically significant difference in gaming scores between the groups on the first day. The improvement of BLS gaming scores for groups 1 and 2 (without prior BLS knowledge) between the first and seventh day was detected. These values reveal that the VR based serious gaming module used for this study had a positive effect on learning the content of BLS for the groups without prior BLS knowledge. Because of the tutorial session with VR equipment at the initial phase of the study, it is observed that having no prior VR experience did not have a significant effect on the gaming scores and fNIRS results. Limitations in this study were the risk of dizziness due to HMD displays and discomfort during the training sessions caused by the cables of both HMD displays and the fNIRS head pad. For future studies, we plan to benefit wireless HMD displays with the same or higher resolution of the ones used and wireless fNIRS systems allowing the operators to move more freely with less discomfort during the trainings. A limitation of this study was the limited number of subjects but this study focuses on the overall effect measurement, and within the scope of this exploratory study, total number of subjects (n = 22) is considered sufficient for the effect size. It is also important that it is difficult to have an access to professional healthcare staff with prior VR experience and BLS knowledge for an exploratory research study.

The decrease of mean fNIRS levels in all groups except the expert group (Group 3) may indicate that the cognitive workload of the participants were decreased once they became familiar with the task and had enough practices at the seventh day of the study. These findings are in agreement and supported by the previous studies (Ayaz et al., 2012). The correlation between the fNIRS data and gaming scores reveal that fNIRS can be used as a complementary technological tool for assessment in addition to the behavioral performance via serious gaming modules.

CONCLUSION

Emergency situations are encountered frequently in the healthcare environment and it is crucial for the expert healthcare providers to be ready for the distraction factors caused by potential emergency situations. Besides scores acquired from simulators' or serious gaming modules' embedded scoring systems, measuring mental/cognitive workload during these trainings can be a complimentary tool to assess the readiness

of healthcare workers to perform their duties during emergency situations. Training scores acquired from VR based BLS serious game and fNIRS Oxy level measurements of the participants reveal that fNIRS can be used as an additional tool for assessment supporting medical simulation educators by monitoring cognitive workload during training. Utilizing fNIRS measurements, we were able to reveal a significant reduction in the amount of PFC activation with increased task familiarity and skill acquisition. Due to these promising results, we plan to combine fNIRS measurements with scoring algorithms of other serious gaming modules and medical simulation modalities in our future studies.

DATA AVAILABILITY STATEMENT

All datasets generated for this study are included in the article/**Supplementary Material**.

ETHICS STATEMENT

The studies involving human participants were reviewed and approved by the Acıbadem Mehmet Ali Aydınlar University Ethical Committee (ATADEK). The patients/participants provided their written informed consent to participate in this study.

AUTHOR CONTRIBUTIONS

EA: study design, VR module creation, and assessment. KI and BO: study design and analysis of results. AA: fNIRS measurements. EB: data collection. DK: analysis of results.

ACKNOWLEDGMENTS

We would like to thank Center of Advanced Simulation and Education (CASE) and Acıbadem Mehmet Ali Aydınlar University for their hosting and valuable support in particular for the fNIRS data acquisition and analyses.

SUPPLEMENTARY MATERIAL

The Supplementary Material for this article can be found online at: https://www.frontiersin.org/articles/10.3389/fnins.2019.01336/full#supplementary-material

TABLE S1 | Mean oxy values of channel 3 and serious gaming scores of the subjects acquired from the learning management system of the game module.

TABLE S2 | Pairwise comparison (*p* values) between groups.

REFERENCES

Aksoy, E. (2019). Comparing the effects on learning outcomes of tablet-based and virtual reality-based serious gaming modules for basic life support training: randomized trial. *JMIR Serious Games.* 7:e13442. doi: 10.2196/13442

Aksoy, E., and Sayali, E. (2019). Serious gaming as an additional learning tool for medical education. *In. J. Educ. Technol.* 5, 52–59. doi: 10.20448/2003.52.52.59

Arenth, P. M., Ricker, J. H., and Schultheis, M. T. (2007). Applications of functional near-infrared spectroscopy (fNIRS) to neurorehabilitation of cognitive disabilities. *Clin. Neuropsychol.* 21, 38–57. doi: 10.1080/13854040600878785

Armstrong, J., Izzetoglu, K., and Richards, D. (2018). "Using functional near infrared spectroscopy to assess cognitive performance of UAV sensor operators during route scanning," in *Proceedings of the 11th International Joint Conference on Biomedical Engineering Systems and Technologies*, Vol. 3, (Madeira: SciTePress.), 286–293.

Ayaz, H., Izzetoglu, M., Shewokis, P. A., and Onaral, B. (2010). Sliding-window motion artifact rejection for functional near-infrared spectroscopy, conf. proc. *IEEE Eng. Med. Biol. Soc. Buenos Aires, Argentina* 2010, 6567–6570. doi: 10.1109/IEMBS.2010.5627113

Ayaz, H., Shewokis, P., Bunce, S., Izzetoglu, K., Willems, B., and Onaral, B. (2012). Optical brain monitoring for operator training and mental workload assessment. *Neuroimage* 59, 36–47. doi: 10.1016/j.neuroimage.2011.06.023

Bartocci, M., Winberg, J., Ruggiero, C., Bergqvist, L. L., Serra, G., and Lagercrantz, H. (2000). Activation of olfactory cortex in newborn infants after odor stimulation: a functional near-infrared spectroscopy study. *Pediatr. Res.* 48, 18–23. doi: 10.1203/00006450-200007000-00006

Bunce, S. C., Izzetoglu, M., Izzetoglu, K., Onaral, B., and Pourrezaei, K. (2006). Functional near-infrared spectroscopy. *IEEE Eng. Med. Biol. Mag.* 25, 54–62. doi: 10.1109/MEMB.2006.1657788

Chen, W. G., Zeng, S. Q., Luo, Q. M., Gong, H., Yang, Z. Z., Guan, L. C., et al. (1999). Monitoring of mental work and pattern recognition of human brain with functional near infrared imager. in proceedings saratov fall meeting 98: light scattering technologies for mechanics. *Biomed. Mater. Sci.* 3726, 545–549.

Christopoulos, A., Conrad, M., and Shukla, M. (2018). Increasing student engagement through virtual interactions: how? *Virtual Real.* 22, 353–369. doi: 10.1007/s10055-017-0330-3

Cope, M., and Delpy, D. T. (1988). System for long-term measurement of cerebral blood and tissue oxygenation on newborn infants by near infra-red transillumination. *Med. Biol. Eng. Comput.* 26, 289–294. doi: 10.1007/bf02447083

Deterding, S. (2013). Gameful design for learning. *T+D* 67, 60–63.

Dwivedi, A. K., Mallawaarachchi, I., and Alvarado, L. A. (2017). Analysis of Small sample size studies using nonparametric bootstrap test with pooled resampling method. *Stat. Med.* 36, 2187–2205. doi: 10.1002/sim.7263

Fallgatter, A. J., Roesler, M., Sitzmann, L., Heidrich, A., Mueller, T. J., and Strik, W. K. (1997). Loss of functional hemispheric asymmetry in Alzheimer's dementia assessed with near-infrared spectroscopy. *Brain Res. Cogn. Brain Res.* 6, 67–72. doi: 10.1016/s0926-6410(97)00016-5

Fallgatter, A. J., and Strik, W. K. (2000). Reduced frontal functional asymmetry in schizophrenia during a cued continuous performance test assessed with near-infrared spectroscopy. *Schizophr Bull.* 26, 913–919. doi: 10.1093/oxfordjournals.schbul.a033505

Hanson, K., and Shelton, B. (2008). Design and development of virtual reality: analysis of challenges faced by educators. *Educ. Technol. Soc.* 11, 118–131.

Holzinger, A., Kickmeier, M., and Albert, D. (2008). Dynamic media in computer science education; content complexity and learning performance: is less more? *Educa. Technol. Soc.* 11, 279–290.

Izzetoglu, M., Bunce, S., Izzetoglu, K., Onaral, B., and Pourrezaei, K. (2007). Functional brain imaging using near-infrared technology. *IEEE Eng. Med. Biol. Mag.* 26, 38–46. doi: 10.1109/MEMB.2007.384094

James, D. R., Orihuela-Espina, F., Leff, D. R., Sodergren, M. H., Athanasiou, T., Darzi, A. W., et al. (2011). The ergonomics of natural orifice translumenal endoscopic surgery (NOTES) navigation in terms of performance, stress, and cognitive behavior. *Surgery* 149, 525–533. doi: 10.1016/j.surg.2010.11.019

James, D. R. C., Orihuela-Espina, F., Leff, D., Mylonas, G., Kwok, K. W., Darzi, A. W., et al. (2010). "Cognitive burden estimation for visuomotor learning with fNIRS," in *Medical Image Computing and Computer-Assisted Intervention –*

MICCAI 2010, eds D. Hutchison, et al. (Berlin: Springer Press), 319–326. doi: 10.1007/978-3-642-15711-0_40

Jöbsis, F. F. (1977). Noninvasive, infrared monitoring of cerebral and myocardial oxygen sufficiency and circulatory parameters. *Science* 198, 1264–1267. doi: 10.1126/science.929199

Johnson, D., Deterding, S., Kuhn, K., Staneva, A., Stoyanov, S., and Hides, L. (2016). Gamification for health and wellbeing: a systematic review of the literature. *Internet Interv.* 6, 89–106. doi: 10.1016/j.invent.2016.10.002

Kelly, A. M., and Garavan, H. (2005). Human functional neuroimaging of brain changes associated with practice. *Cereb. Cortex.* 15, 1089–1102. doi: 10.1093/cercor/bhi005

Kinder, F. D., and Kurz, J. M. (2018). Gaming strategies in nursing education. *Teach. Learn. Nurs.* 13, 212–214. doi: 10.1016/j.teln.2018.05.001

Kuwabara, H., Kasai, K., Takizawa, R., Kawakubo, Y., Yamasue, H., Rogers, M. A., et al. (2006). Decreased prefrontal activation during letter fluency task in adults with pervasive developmental disorders: a near-infrared spectroscopy study. *Behav. Brain Res.* 172, 272–277. doi: 10.1016/j.bbr.2006.05.020

Leff, D., Orihuela-Espina, F., Atallah, L., Athanasiou, T., Leong, J., Darzi, A. W., et al. (2008). Functional prefrontal reorganization accompanies learning-associated refinements in surgery: a manifold embedding approach. *Comput. Aided Surg.* 13, 325–339. doi: 10.3109/10929080802531482

Leff, D., Orihuela-Espina, F., Atallah, L., Darzi, A., and Yang, G. Z. (2007). Functional near infrared spectroscopy in novice and expert surgeons – A Manifold embedding approach. *Med. Image Comput. Comput. Assist. Interv.* 10, 270–277. doi: 10.1007/978-3-540-75759-7_33

Maria, A. F., Fantini, S., Toronov, V., Filiaci, M. E., and Gratton, E. (2000). "Cerebral hemodynamics measured by near-infrared spectroscopy at rest and during motor activation. Proceedings of the Optical Society of America," in *Vivo Optical Imaging Workshop*, (Washington).

Matsuo, K., Kato, N., and Kato, T. (2002). Decreased cerebral haemodynamic response to cognitive and physiological tasks in mood disorders as shown by near-infrared spectroscopy. *Psychol. Med.* 32, 1029–1037. doi: 10.1017/s0033291702005974

Meek, J. H., Firbank, M., Elwell, C. E., Atkinson, J., Braddick, O., and Wyatt, J. S. (1998). Regional hemodynamic responses to visual stimulation in awake infants. *Pediatr. Res.* 43, 840–843. doi: 10.1203/00006450-199806000-00019

Modi, H., Singh, H., Yang, G. Z., Darzi, A., and Leff, D. (2017). A decade of imaging surgeons' brain function (part I): terminology, techniques, and clinical translation. *Surgery* 162, 1121–1130. doi: 10.1016/j.surg.2017.05.021

Mylonas, G. P., Kwok, K. W., Darzi, A., and Yang, G. Z. (2008). Gaze-contingent motor channelling and haptic constraints for minimally invasive robotic surgery. *Med. Image Comput. Comput. Assist. Interv.* 11, 676–683. doi: 10.1007/978-3-540-85990-1_81

Nemani, A., Yucel, M. A., Kruger, U., Gee, D. W., Cooper, C., Schwaitzberg, S. D., et al. (2018). Assessing bimanual motor skills with optical neuroimaging. *Sci. Adv.* 4:eaat3807. doi: 10.1126/sciadv.aat3807

Ohuchida, K., Kenmotsu, H., Yamamoto, A., Sawada, K., Hayami, T., Morooka, K., et al. (2009). The frontal cortex is activated during learning of endoscopic procedures. *S. Endosc.* 23, 2296–2301. doi: 10.1007/s00464-008-0316-z

Pellas, N., Fotaris, P., Kazanidis, I., and Wells, D. (2018). Augmenting the learning experience in Primary and Secondary school education: a systematic review of recent trends in augmented reality game-based learning. *Virtual Real.* 23, 329–346. doi: 10.1007/s10055-018-0347-2

Peña, M., Maki, A., Kovačić, D., Dehaene-Lambertz, G., Koizumi, H., Bouquet, F., et al. (2003). Sounds and silence: an optical topography study of language recognition at birth. *Proc. Natl. Acad. Sci. U.S.A.* 100, 11702–11705. doi: 10.1073/pnas.1934290100

Perkins, G. D., Handley, A. J., Koster, R. W., Castren, M., Smyth, M. A., Olasveengen, T., et al. (2015). European resuscitation council guidelines for resuscitation 2015: section 2. Adult basic life support and automated external defibrillation. *Resuscitation* 95, 81–99. doi: 10.1016/j.resuscitation.2015.07.015

Prensky, M. (2012). *From Digital Natives to Digital Wisdom: Hopeful Essays for 21st Century Learning*. Thousand Oaks Calif, CA: Corwin press.

Rolfe, P. (2000). In vivo near-infrared spectroscopy. *Annu. Rev. Biomed. Eng.* 2, 715–754. doi: 10.1146/annurev.bioeng.2.1.715

Sakatani, K., Chen, S., Lichty, W., Zuo, H., and Wang, Y. P. (1999). Cerebral blood oxygenation changes induced by auditory stimulation in newborn infants measured by near infrared spectroscopy. *Early. Hum. Dev* 55, 229–236. doi: 10.1016/s0378-3782(99)00019-5

Sato, H., Aoki, R., Katura, T., Matsuda, R., and Koizumi, H. (2011). Correlation of within-individual fluctuation of depressed mood with prefrontal cortex activity during verbal working memory task: optical topography study. *J. Biomed Opt.* 16:126007. doi: 10.1117/1.3662448

Sato, H., Yahata, N., Funane, T., Takizawa, R., Katura, T., Atsumori, H., et al. (2013). A NIRS-fMRI investigation of prefrontal cortex activity during a working memory task. *Neuroimage* 83, 158–173. doi: 10.1016/j.neuroimage.2013.06.043

Schoonjans, F., Zalata, A., Depuydt, C. E., and Comhaire, F. H. (1995). MedCalc: a new computer program for medical statistics. *Comput. Methods Programs Biomed.* 48, 257–262. doi: 10.1016/0169-2607(95)01703-8

Shetty, K., Leff, D. R., Orihuela-Espina, F., Yang, G. Z., and Darzi, A. (2016). Persistent prefrontal engagement despite improvements in laparoscopic technical skill. *JAMA Surg.* 151, 682–684. doi: 10.1001/jamasurg.2016.0050

Smith, K. K., Gilcreast, D., and Pierce, K. (2008). Evaluation of staff's retention of ACLS and BLS skills. *Resuscitation* 78, 59–65. doi: 10.1016/j.resuscitation.2008.02.007

Suto, T., Fukuda, M., Ito, M., Uehara, T., and Mikuni, M. (2004). Multichannel near-infrared spectroscopy in depression and schizophrenia: cognitive brain activation study. *Biol. Psychiatry* 55, 501–511. doi: 10.1016/j.biopsych.2003.09.008

Verkuyl, M., Romaniuk, D., Atack, L., and Mastrilli, P. (2017). Virtual gaming simulation for nursing education: an experiment. *Clin. Simul. Nurs.* 13, 238–244. doi: 10.1016/j.ecns.2017.02.004

Villringer, A. (1997). Functional neuroimaging. Optical approaches. *Adv. Exp. Med. Biol.* 413, 1–18. doi: 10.1007/978-1-4899-0056-2_1

Wilcox, T., Bortfeld, H., Woods, R., Wruck, E., and Boas, D. A. (2005). Using near-infrared spectroscopy to assess neural activation during object processing in infants. *J. Biomed. Opt.* 10:11010. doi: 10.1117/1.1852551

World Medical Association (2013). World medical association declaration of helsinki: ethical principles for medical research involving human subjects. *JAMA* 310, 2191–2194. doi: 10.1001/jama.2013.281053

Zaramella, P., Freato, F., Amigoni, A., Salvadori, S., Marangoni, P., Suppjei, A., et al. (2001). Brain auditory activation measured by near-infrared spectroscopy (NIRS) in neonates. *Pediatr. Res.* 49, 213–219. doi: 10.1203/00006450-200102000-00014

Conflict of Interest: fNIR Devices, LLC manufacturers the optical brain imaging instrument and licensed IP and know-how from Drexel University. KI and BO were involved in the technology development and thus offered a minor share in the startup firm, fNIR Devices, LLC.

The remaining authors declare that the research was conducted in the absence of any commercial or financial relationships that could be construed as a potential conflict of interest.

Copyright © 2019 Aksoy, Izzetoglu, Baysoy, Agrali, Kitapcioglu and Onaral. This is an open-access article distributed under the terms of the Creative Commons Attribution License (CC BY). The use, distribution or reproduction in other forums is permitted, provided the original author(s) and the copyright owner(s) are credited and that the original publication in this journal is cited, in accordance with accepted academic practice. No use, distribution or reproduction is permitted which does not comply with these terms.

frontiers in Human Neuroscience

ORIGINAL RESEARCH
published: 20 December 2019
doi: 10.3389/fnhum.2019.00444

Reality Status Judgments of Real and Fantastical Events in Children's Prefrontal Cortex: An fNIRS Study

Hui Li[1], Tao Liu[2], Jacqueline D. Woolley[3]* and Peng Zhang[4]*

[1] School of Education, Central China Normal University, Wuhan, China, [2] School of Management, Zhejiang University, Hangzhou, China, [3] Department of Psychology, The University of Texas at Austin, Austin, TX, United States, [4] Faculty of Psychology and Behavior, Tianjin Normal University, Tianjin, China

The present study aimed to examine neural mechanisms underlying the ability to differentiate reality from fantasy. Using functional near-infrared spectroscopy (fNIRS), we measured prefrontal activations in children and adults while they performed a reality judgment task. Participants' task was to judge the reality status of events in fantastical and realistic videos. Behavioral data revealed that, although there was no accuracy difference, children showed significantly longer reaction times in making the judgments than did adults. The fNIRS data consistently revealed higher prefrontal activations in children than in adults when watching the videos and judging the reality of the events. These results suggest that when making judgments of event reality, children may require more cognitive resources and also mainly rely on their own personal experiences.

Keywords: reality judgment, fantasy, child development, fNIRS, PFC

OPEN ACCESS

Edited by:
Fenghua Tian,
The University of Texas at Arlington, United States

Reviewed by:
Yujin Zhang,
Institute of Automation (CAS), China
Han Zhang,
The University of North Carolina at Chapel Hill, United States
Kurtulus Izzetoglu,
Drexel University, United States

****Correspondence:***
Tao Liu
liu_tao@zju.edu.cn;
tao_luoma@aliyun.com
Jacqueline D. Woolley
woolley@austin.utexas.edu

Specialty section:
This article was submitted to Brain Imaging and Stimulation, a section of the journal Frontiers in Human Neuroscience

Received: *20 August 2019*
Accepted: *03 December 2019*
Published: *20 December 2019*

Citation:
Li H, Liu T, Woolley JD and Zhang P (2019) Reality Status Judgments of Real and Fantastical Events in Children's Prefrontal Cortex: An fNIRS Study. Front. Hum. Neurosci. 13:444. doi: 10.3389/fnhum.2019.00444

INTRODUCTION

Television, movie, and video viewing have become a staple of children's daily lives. Two-thirds of children under age 7 in the United States watch television every day, usually for around 2 h (Rideout and Hamel, 2006). Similar patterns are found in other countries; for example, in China, 93% of Chinese preschoolers watch television every day for about an hour and half (Li et al., 2014). Young children are also increasingly becoming Internet consumers; video sharing sites are one of the first sites that young children visit on the Internet, and these sites are especially popular with younger children (Holloway et al., 2013).

Children's television, movies, and videos often contain a mix of real and fantastical events. For example, "Elmo" teaches children about what it means to be alive, and "Dora the Explorer" teaches children about animals while playing with a magic stick. In addition, animated cartoons can easily violate the laws of nature; characters can appear and disappear, or turn into something else entirely. This raises the important question of how we ensure that children learn what we expect them to learn from this arguably confusing content (Hopkins and Weisberg, 2017). An inability to distinguish real from not-real could limit the amount and type of real-world learning that takes place, and could also potentially generate misconceptions.

What do we know about children's ability to judge the reality status of real and fantastical events in videos? More generally, the ability to differentiate reality from fantasy emerges early in development, with children beginning to use words like "real" and "pretend" by age 2 (Woolley and Wellman, 1990). Research by Flavell et al. (1990) indicates that 3-year-old children do not always understand that television is representational, and sometimes think that real objects are

actually inside the television. Goldstein and Bloom (2015) observed a similar pattern – preschool-age children judged actors on videos to really be experiencing the emotions they were portraying. Yet other studies show the reverse pattern – children incorrectly judge video and television content to be unreal. Wright et al. (1994) observed a bias in children aged 5 and younger to incorrectly assume that all television content was fictional. Work by Li et al. (2015) similarly indicates that young 4-year-olds often underestimate the reality status of real events in videos. They showed children real and fantastical events and asked them to judge their reality status. Although children performed well when asked to judge the reality of fantastical events, they often claimed that real events could not actually happen in real life. Li et al. suggest that, in judging the reality of events on television and video, children rely heavily on their personal experience.

Although previous behavioral studies have consistently documented these sorts of errors in young children, the neural correlates underlying them are still not understood. The goal of the present research is thus to investigate the neural underpinnings of children's ability to make the fantasy-reality distinction for video content, and to determine whether the same neural structures are involved for both children and adults. Research by Abraham et al. (2008) found selective activations of the anterior prefrontal cortex (PFC) and the precuneus/posterior cingulate when adult participants evaluated whether it was possible to interact with real people vs. with fictional characters. They suggest that real people activate more autobiographical memory retrieval, and propose that whether or not character-type information is coded in self-relevant terms is a key factor in differentiating reality from non-reality. Altmann et al. (2014) examined the neurocognitive processes when adults read purportedly real or invented narratives; results indicated that participants had faster reaction times (RTs) when a story was believed to be real vs. fictional. In addition, fMRI data indicated that the factual and the fictional contexts reflected different levels of simulation: they propose that reading factual texts mostly involves thinking about actions and their outcomes, as reflected in increased activations mainly in social-brain areas such as the temporo-parietal junction (TPJ), whereas reading fiction normally increases activation in cognitive control areas such as the dorsolateral prefrontal cortex (dlPFC).

Woolley (1997) argues that children are not "fundamentally different" from adults in their ability to distinguish fantasy and reality. Han et al. (2007) provide initial evidence that the underlying mental processes may differ. Using fMRI, Han et al. (2007) recorded 10-year-old children's activations while viewing both silent movies showing humans in real-life situations and cartoon clips with non-human characters. The results showed that children's medial prefrontal cortex (mPFC) was activated when watching both real and cartoon characters. In contrast, previous research with adults had revealed that the mPFC was only activated in processing the mental activity of real characters in movie clips (Han et al., 2005). The authors suggest that adults respond differently to real and fictional worlds – automatically attributing mental states to characters in the former but not the latter, whereas children do not.

Due to the technical limitations of fMRI, it is difficult to examine brain activation in younger children, who cannot keep their body motionless for long periods of time. Functional near-infrared spectroscopy (fNIRS) is non-invasive brain imaging technique that has relatively high temporal resolution, places few physical constraints, and is tolerant to motion artifact and electromagnetic noise (for review, see Scholkmann et al., 2014). Therefore, it is ideal for use with young children (Perlman et al., 2014; Liu et al., 2017). One recent study with fNIRS revealed that watching fantastical events performed by cartoon characters leads to increased activation in children's dlPFC relative to playing with them using a touch screen (Li et al., 2018). This study established the feasibility of using this method to address children's fantasy-reality distinction; however, the neural correlates underlying the ability to discriminate fantasy from reality in children remain largely unknown. To address this question, the present study used fNIRS to examine activation patterns in the PFC of children and adults while they performed a real-fantastical judgment task.

MATERIALS AND METHODS

Thirty-five participants, 16 children (78.54 ± 7.40 months, six girls) and 19 adults (257.53 ± 28.94 months, 10 women) viewed videos varying by character (real vs. fantastical) and event (real vs. fantastical) type in a mixed design, forming four conditions, i.e., fantastical character fantastical event (FF), fantastical character real event (FR), real character fantastical event (RF), and real character real event (RR). Three children's behavioral data were missing due to mis-manipulation of the presentation software, leaving 32 participants in the final data analyses. All children's parents signed informed consent forms and were paid 200 RMB (30.8 USD) for their participation. This study was approved by the Institutional Review Board of Central China Normal University.

Each participant was shown 40 short video clips, each of which portrayed a central event lasting about 4000 ms. All the clips were taken from the popular cartoons *SpongeBob* and *Happy Satellite* (see **Appendix A** for the list of clip descriptions) (Skolnick and Bloom, 2006). Videos were displayed in the pre-determined random order indicated in **Appendix A** across 40 trials. Each video clip was followed by one question. Participants' task was to judge the reality of the events (e.g., "Do you think it is possible for two people to take a boat ride in real life?") by pressing "1" on a keypad for "Yes" and "0" for "No" (see **Figure 1**).

Each trial began with a fixation cross (duration: 2000 ms), which was followed by a single video clip for 4000 ms. Each video clip was accompanied by a taped verbal description of the event. After each event, a question cue (a ringing sound) was presented to ready the participant for the test question. Variable jitter times were inserted before the video clips (4000–9000 ms) to help maintaining participants' attention on the task. Prior to and after all trials, participants were respectively given 30 s to rest.

A multichannel fNIRS system (LABNIRS; Shimadzu, Japan) was used to record hemodynamic changes in the prefrontal cortices covered by 22 channels (see **Figure 2**). The bottom channels covered the Fp1–Fp2 line and the bottom central

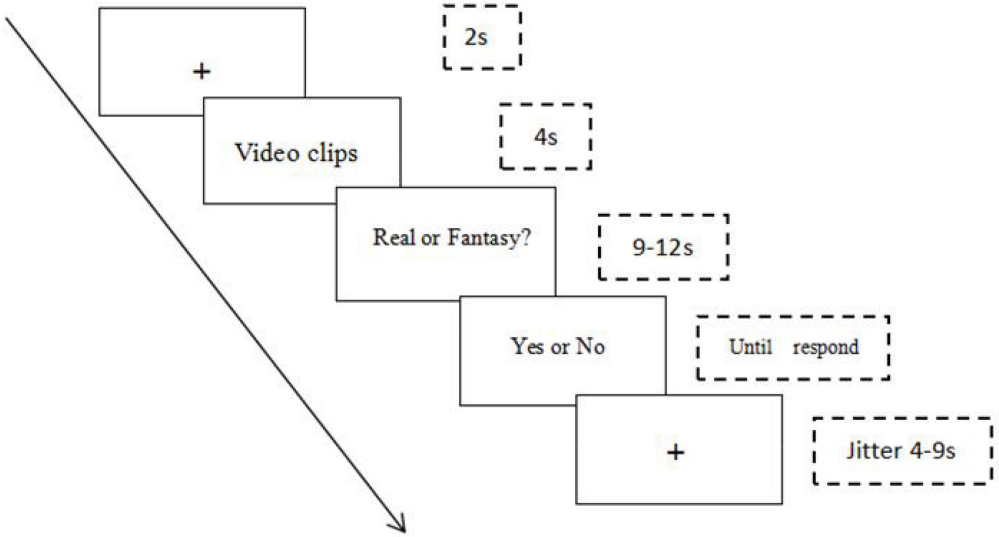

FIGURE 1 | Procedure for a reality judgment trial.

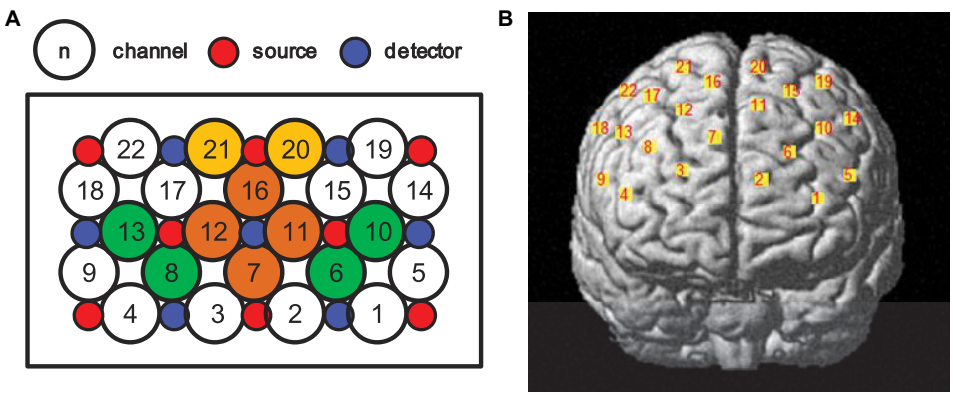

FIGURE 2 | (A) Channel arrangement, and **(B)** positions of fNIRS channels. Circles in orange covered the medial part of prefrontal cortex (mPFC), circles in green covered the left and right prefrontal cortex (lPFC and rPFC), circles in yellow covered the dorsolateral prefrontal cortex (dlPFC).

probe covered the Fpz point according to the international 10–10 system (Vespignani and Braun, 2009). We mainly analyzed oxygenated hemoglobin (HbO), since it is the most sensitive parameter of regional cerebral blood flow and provides a robust correlation with the BOLD signal (Hoshi et al., 2001; Huppert et al., 2006). The duration for each trial ranged approximately from 10 to 17 s, that is, 0.06–0.1 Hz. To remove global trends and systematic noise such as heartbeats and breath, and to include more task-related cortical activations, the raw HbO data were preprocessed by a band-pass filter (0.01–0.1 Hz). A baseline correction was then conducted by subtracting the mean value of the last 15 s resting period prior the first trial from the filtered HbO data. Since the fNIRS measures relative but not absolute hemodynamic concentrations like fMRI, the HbO data was further converted into *z* scores using the mean value and standard deviation from the same 15 s baseline period (Matsuda and Hiraki, 2006). To increase signal-to-noise ratio, the HbO data belonging to the same region of interest (ROI) were averaged. Finally, group-averaged data were obtained across all trials for both the video watching and reality judgment periods.

Positions of the fNIRS channels were measured using a 3D electromagnetic tracking device (FASTRAK; Polhemus, Colchester, VT, United States), and then a probabilistic registration method was used to estimate each channel's corresponding position in the Montreal Neurological Institute (MNI) space via NIRS-SPM. Because the MNI space was established for adults but not children, the estimated channel positions may be not accurate. To avoid potential deviations in children, we intentionally neglected the peripheral channels and also the ones with low registration probabilities (i.e., <0.60). **Table 1** shows positions of all fNIRS channels. Finally, we focused on four ROIs, that is, the mPFC (Ch 7, 11, 12, and 16), the left prefrontal cortex (lPFC; Ch 6 and 10), the right prefrontal cortex (rPFC; Ch 8 and 13), and the dlPFC (Ch 20 and 21).

TABLE 1 | Positions of all fNIRS channels.

Channel	Anatomical label	Percentage of Overlap
CH01	11 – Orbitofrontal area	0.50
CH02	10 – Frontopolar area	0.70
CH03	10 – Frontopolar area	0.75
CH04	11 – Orbitofrontal area	0.57
CH05	10 – Frontopolar area	0.57
CH06	10 – Frontopolar area*	0.96
CH07	10 – Frontopolar area*	1.00
CH08	10 – Frontopolar area*	0.94
CH09	10 – Frontopolar area	0.57
CH10	10 – Frontopolar area*	0.69
CH11	10 – Frontopolar area*	1.00
CH12	10 – Frontopolar area*	1.00
CH13	10 – Frontopolar area*	0.64
CH14	46 – Dorsolateral prefrontal cortex	0.86
CH15	10 – Frontopolar area	0.59
CH16	10 – Frontopolar area*	0.78
CH17	10 – Frontopolar area	0.55
CH18	46 – Dorsolateral prefrontal cortex	0.76
CH19	9 – Dorsolateral prefrontal cortex	0.56
CH20	9 – Dorsolateral prefrontal cortex*	0.88
CH21	9 – Dorsolateral prefrontal cortex*	0.90
CH22	9 – Dorsolateral prefrontal cortex	0.55

**Indicates region of interest in the present study.*

RESULTS

To examine differences between children and adults in their judgments of event reality, we conducted mixed ANOVAs (Age [2] × Character [2] × Event [2]) on the behavioral and fNIRS data independently. The statistical analyses were conducted using the Statistical Package for the Social Sciences 19 (SPSS), and the significance level was set at $p < 0.05$. To control for false positives, all *p*-values were corrected by false discovery rate (FDR = 0.05).

Behavioral Data

We calculated RT and accuracy as performance indices. Concerning RT, there was a significant main effect of Age [$F(1,30) = 19.89$, $p < 0.001$, $\eta_p^2 = 0.40$], with longer RT in children ($M \pm SE$: 1953.34 ± 190.65 ms) than in adults (849.78 ± 150.70 ms). Although the main effect of Character was not significant [$F(1,30) = 3.29$, $p = 0.08$, $\eta_p^2 = 0.10$], participants tended to show longer RT on real (1511.39 ± 161.43 ms) than on fantastical (1197.68 ± 80.85 ms) characters. There was also a significant main effect of Event [$F(1,30) = 9.85$, $p < 0.01$, $\eta_p^2 = 0.25$], with longer RT on real (1607.45 ± 174.45 ms) than on fantastical (1195.66 ± 93.71 ms) events.

There was also a significant interaction between Age and Character [$F(1,30) = 3.62$, $p = 0.06$, $\eta_p^2 = 0.11$]. Simple effects tests and multiple comparisons revealed that for real characters, children's RT (2235.25 ± 257.69 ms) was longer than adults' (843.03 ± 213.16 ms) [$F(1,30) = 17.33$, $p < 0.001$, $\eta_p^2 = 0.37$], and for fantastical characters, children's RT (1671.44 ± 183.43 ms) was also longer than adults' (856.52 ± 151.72 ms) [$F(1,30) = 11.72$, $p < 0.001$, $\eta_p^2 = 0.28$]. In addition, children's RT was longer when events were performed by real than by fantastical characters [$F(1,30) = 5.81$, $p < 0.05$, $\eta_p^2 = 0.16$].

The analyses also revealed a significant interaction between Age and Event [$F(1,30) = 7.24$, $p < 0.05$, $\eta_p^2 = 0.19$]. Simple effects tests and multiple comparisons (Bonferroni correction) revealed that for real events, children's RT (2335.76 ± 268.85 ms) was longer than adults' (879.15 ± 222.39 ms) [$F(1,30) = 17.43$, $p < 0.001$, $\eta_p^2 = 0.37$], and for fantastical events, children's RT (1570.93 ± 144.42 ms) was also longer than adults' (820.40 ± 119.46 ms) [$F(1,30) = 16.04$, $p < 0.001$, $\eta_p^2 = 0.35$]. In addition, children's RT was longer in judging the reality status of real than fantastical events [$F(1,30) = 14.31$, $p < 0.001$, $\eta_p^2 = 0.32$], whereas no RT differences were revealed between judgments of real and fantastical events in adults. No RT differences were observed between judgments involving real and fantastical characters in adults. There were no significant differences between children and adults in accuracy. **Figure 3** illustrates the behavioral results of RT and accuracy.

Taken together, children consistently showed longer RT than adults. Furthermore, children needed more time to make a decision when faced with real events and characters relative to when they judged fictional events and characters, whereas adults spent equivalent amounts of time judging both.

fNIRS Data

Intra-Brain Activation

We first examined the cortical activations involved in the judgment task, and applied one-sample *t*-tests on preprocessed HbO data during the video watching and reality judgment periods for both the adult and child participants. **Figure 4** shows heat maps of the *t* values. For adults, no ROI areas were activated compared with the resting baseline (*p*s > 0.111) while watching videos, but there was a tendency to show decreased activations in the mPFC [-1.15 ± 0.56; $t(18) = -2.183$, $p = 0.043$, uncorrected and not significant after FDR correction] while judging the reality of the events (*p*s > 0.173 for the other ROIs).

By contrast, for children, when watching the videos they showed increased activations in the lPFC [0.96 ± 0.32; $t(18) = 3.525$, $p = 0.003$, FDR corrected], the rPFC [1.38 ± 0.60; $t(18) = 2.561$, $p = 0.022$, FDR corrected], and also showed the same tendency in the mPFC [0.76 ± 0.45; $t(18) = 1.941$, $p = 0.071$, uncorrected]. No ROI areas were significantly activated when judging the reality of the events in children (*p*s > 0.095).

In addition, we also analyzed the Deoxy data to verify the results found by the Oxy data. The Deoxy data were preprocessed in the same way as the Oxy data, and the *t*-test revealed significantly decreased activations compared with the resting baseline regardless of watching or judging periods in adults (*p*s < 0.005, FDR corrected). The children also showed the same trend of decreasing of prefrontal activations, especially in the dlPFC, the lPFC and the rPFC during the video watching period (*p*s < 0.05, FDR corrected; $p = 0.099$ in mPFC uncorrected),

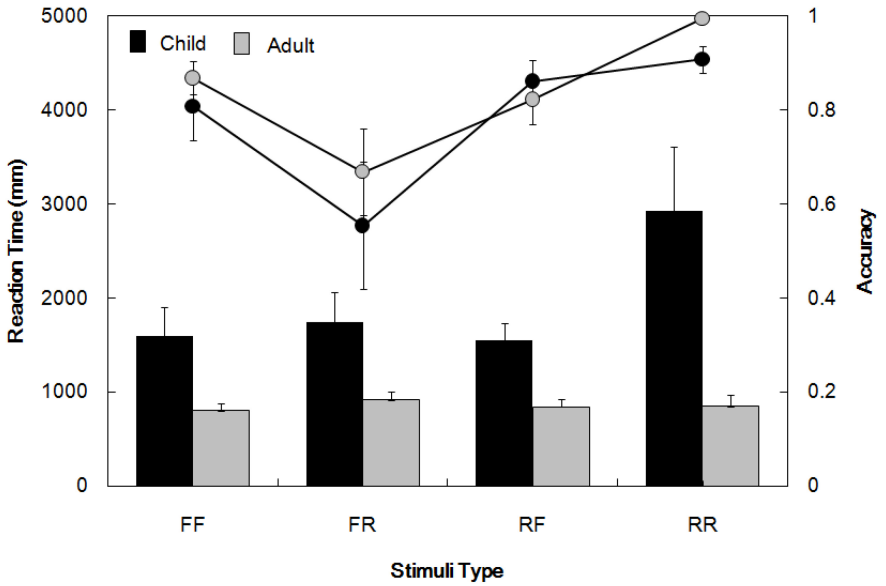

FIGURE 3 | Behavioral performance yielded by children and adults. FF, FR, RF, and RR represent fantastical character with fantastical event, fantastical character with real event, real character with fantastical event, and real character with real event. The bar graphs represent reaction time, while the line graphs represent accuracy. Bars indicate standard errors.

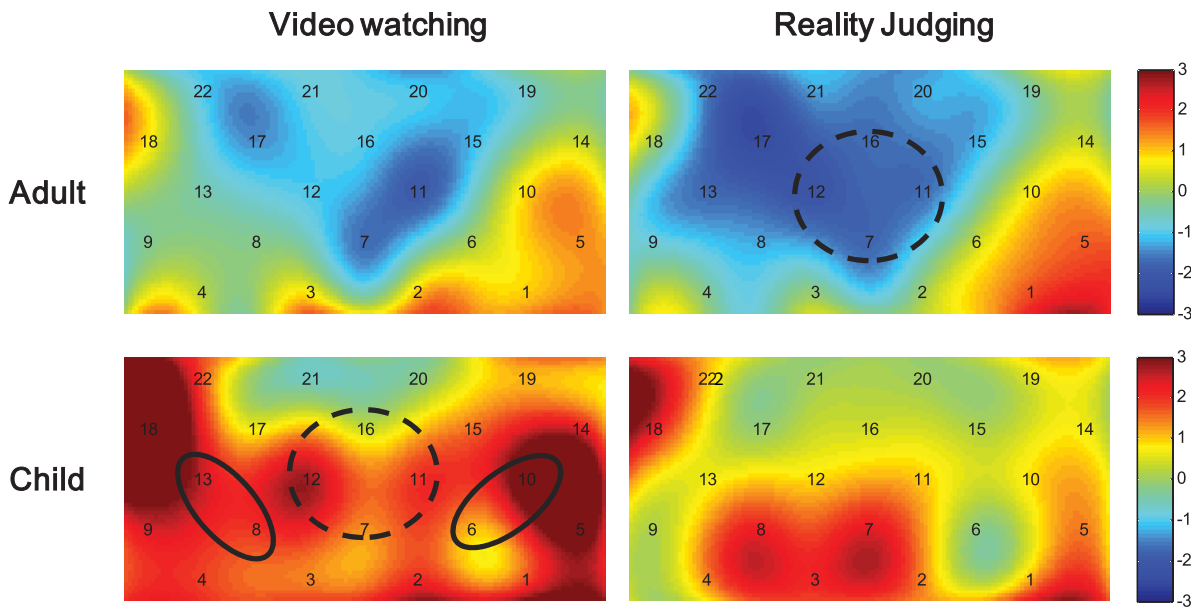

FIGURE 4 | Heap maps of *t* values comparing activations during the video watching and reality judgment periods to the resting baseline in both the child and adult participants. Solid circles indicate the ROIs that showed significantly increased activations ($p < 0.05$ FDR corrected), whereas the dashed circles indicate $p < 0.05$ uncorrected.

and in the left and right PFC during the reality judgment period (*p*s < 0.05, FDR corrected).

Activation Differences

We then compared the activation differences between the adult and child participants using the same Age [2] × Character [2] × Event [2] ANOVA. While watching the event videos, the analysis revealed significant main effects of Age in the mPFC [$F(1,33) = 6.516$, $p < 0.05$, $\eta_p^2 = 0.17$] and the rPFC [$F(1,33) = 4.573$, $p < 0.05$, $\eta_p^2 = 0.12$], and also an Age by Character interaction in the rPFC [$F(1,33) = 5.112$, $p < 0.05$, $\eta_p^2 = 0.13$]. No other main effects and interactions were demonstrated. Simple effects tests and multiple comparisons (Bonferroni correction) revealed that children showed higher

activations than adults in the mPFC. In the rPFC, the same trend of increased activation in children compared with adults was revealed, especially while watching events performed by fantastical characters ($p < 0.05$; $p = 0.080$ while watching real characters).

When judging the reality of events, the ANOVA consistently revealed significant main effects of Age in the mPFC [$F(1,33) = 6.128$, $p < 0.05$, $\eta_p^2 = 0.17$] and the rPFC [$F(1,33) = 4.650$, $p < 0.05$, $\eta_p^2 = 0.12$] and a main effect of Character in the mPFC [$F(1,33) = 7.700$, $p < 0.01$, $\eta_p^2 = 0.19$]. The Age by Event interaction was also significant in the rPFC [$F(1,33) = 5.728$, $p < 0.05$, $\eta_p^2 = 0.15$]. No other significant main effects or interactions were revealed. Simple effects tests and multiple comparisons (Bonferroni correction) revealed higher mPFC activations in the children compared with the adults ($p < 0.05$). In addition, the mPFC also showed higher activations while judging the events performed by real characters than those performed by fantastical characters ($p < 0.01$). Importantly, the children tended to show higher rPFC activations when judging the real events than the fantastical events ($p = 0.055$), and the rPFC activation differences between children and adults were mainly revealed when judging the real events ($p < 0.05$). **Figure 5** shows heap maps of F values for the main effects of Age (child vs. adult) during the video watching and reality judgment periods.

The same mixed three-way ANOVA revealed no significant main effects and interactions in both the video watching ($ps > 0.099$) and reality judgment periods ($ps > 0.080$), except for a main effect of Age in the mPFC when judging the reality of events [$F(1,33) = 7.185$, $p < 0.05$, $\eta_p^2 = 0.18$]. During the video watching and reality judgment periods, children tended to showed decreased Deoxy but increased Oxy, confirming that the present findings revealed by the Oxy data resulted from cognitive processing involved in the reality judgment task.

Behavioral-Activation Relation

We then directly examined relations between participants' behavioral performance and their prefrontal activations. There was no significant relation between the prefrontal activations and RT while judging the reality of the events in children or adults ($ps > 0.10$). Concerning the ACC, children tended to show a positive correlation between their judgment accuracy on RR events and the mPFC activation in the reality judging period ($r = 0.544$, $p = 0.054$). For adults, the same trend was revealed between their mPFC activation and both the general judgment accuracy (watching period: $r = 0.443$, $p = 0.057$; judging period: $r = 0.411$, $p = 0.081$) and accuracy on FR events (watching period: $r = 0.488$, $p = 0.034$; judging period: $r = 0.497$, $p = 0.030$).

DISCUSSION

The present study aimed to examine neural differences between children and adults in judging the reality of an event. To achieve this goal, we measured both children's and adults' prefrontal activations using fNIRS in an event-reality-judgment task. The present study provides preliminary evidence regarding the neural structures involved for both children and adults in making reality judgments, thus may contribute to the literature on the development of an understanding of reality and fantasy.

The main findings of the present results are two-fold. First, the behavioral data suggest that children required more cognitive resources (Heekeren et al., 2004; Yang et al., 2009) to judge the real events with real characters than to judge all the other events. Adults, on the other hand, needed significantly fewer resources to judge all events, and used equal amounts of cognitive resources across all four types of events.

Second, consistent with behavioral data, the fNIRS data also revealed higher prefrontal activations in children than in adults while watching and judging the reality of events, especially in the mPFC and rPFC. More importantly, when judging the real events or the events performed by real characters, the children showed higher prefrontal activations, confirming the behavioral findings. In addition, positive correlations were revealed between children's mPFC activations and their judgment accuracy on RR events. The medial part of PFC has been indicated in self referential thinking and autobiographical memory retrieval (Ramnani and Owen, 2004; Cavanna and Trimble, 2006; Gilbert et al., 2006; Svoboda et al., 2006), and

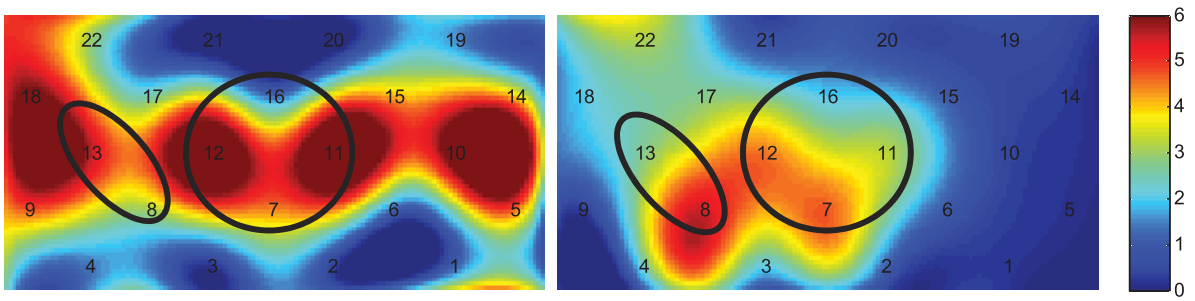

FIGURE 5 | Heap maps of F values for the main effect of Age (child vs. adult) during the video watching and reality judgment periods. Solid circles indicate the ROIs that showed significantly different activations ($p < 0.05$ FDR corrected).

is selectively engaged when processing contexts containing real entities (Abraham and von Cramon, 2009). Thus, children may mainly rely on their self-referential experience to judge the reality of events. This finding is consistent with Han et al.'s (2007) research showing that adults' mPFC was not activated during viewing cartoon clips with fantastical characters, whereas children's mPFC was activated when viewing events with both real and fantastical characters.

In addition, the left anterior of PFC is closely associated with verbal working memory (Hartley et al., 2000), memory retrieval (Wolf et al., 2006) and mental simulations (Altmann et al., 2014). Thus, in making judgments of real events, it appears that children may need additional cognitive resources from memory (Liu et al., 2012). Taken together, these results may support theoretical claims made by Woolley and Ghossainy (2013) that children rely on personal experience in making reality status judgments.

The present study focuses only on the PFC. Future research should explore more social-brain areas, such as the inferior frontal gyrus and the temporal parietal junction, since reality judgment involves aspects of social cognition, and the mirror neuron system connects one's own experience with social stimuli yielded by other persons. Additionally, Shtulman and Carey (2007) suggest that children and adults may use different criteria to distinguish between possible and impossible events. Exploring the neural bases of children's and adults' understanding of possible, impossible, and improbable events in the media would inform this hypothesis, and thus is an additional important topic for future research. Third, the present study only recruited children between 78.54 ± 7.40 months of age; more younger and older children should be examined in future studies to confirm the present findings.

DATA AVAILABILITY STATEMENT

The datasets generated for this study are available on request to the corresponding author.

ETHICS STATEMENT

The studies involving human participants were reviewed and approved by the Institutional Review Board of Central China Normal University. Written informed consent to participate in this study was provided by the participants' legal guardian/next of kin.

AUTHOR CONTRIBUTIONS

HL and JW: conceptualization. TL and PZ: methodology. HL, TL, and JW: writing original draft and review and editing.

FUNDING

This research was supported by the National Natural Science Foundation of China Grants (31700968, 61503421, and 31771236).

REFERENCES

Abraham, A., and von Cramon, D. Y. (2009). Reality = relevance? Insights from spontaneous modulations of the brain's default network when telling apart reality from fiction. *PloS One* 4:e4741. doi: 10.1371/journal.pone.0004741

Abraham, A., Von Cramon, D. Y., and Schubotz, R. I. (2008). Meeting george bush versus meeting cinderella: the neural response when telling apart what is real from what is fictional in the context of our reality. *J. Cogn. Neurosci.* 20, 965–976. doi: 10.1162/jocn.2008.20059

Altmann, U., Bohrn, I. C., Lubrich, O., Menninghaus, W., and Jacobs, A. M. (2014). Fact vs fiction–how paratextual information shapes our reading processes. *Soc. Cogn. Affect. Neurosci.* 9, 22–29. doi: 10.1093/scan/nss098

Cavanna, A. E., and Trimble, M. R. (2006). The precuneus: a review of its functional anatomy and behavioural correlates. *Brain* 129, 564–583. doi: 10.1093/brain/awl004

Flavell, J. H., Flavell, E. R., Green, F. L., and Korfmacher, J. E. (1990). Do young children think of television images as pictures or real objects? *J. Broadcast. Electron. Media* 34, 399–419. doi: 10.1080/08838159009386752

Gilbert, S. J., Spengler, S., Simons, J. S., Steele, J. D., Lawrie, S. M., Frith, C. D., et al. (2006). Functional specialization within rostral prefrontal cortex (Area 10): a meta-analysis. *J. Cogn. Neurosci.* 18, 932–948. doi: 10.1162/jocn.2006.18.6.932

Goldstein, T. R., and Bloom, P. (2015). Characterizing characters: how children make sense of realistic acting. *Cogn. Dev.* 34, 39–50. doi: 10.1016/j.cogdev.2014.12.001

Han, S., Jiang, Y., and Humphreys, G. W. (2007). Watching cartoons activates the medial prefrontal cortex in children. *Chin. Sci. Bull.* 52, 3371–3375. doi: 10.1007/s11434-007-0505-5

Han, S., Jiang, Y., Humphreys, G. W., Zhou, T., and Cai, P. (2005). Distinct neural substrates for the perception of real and virtual visual worlds. *Neuroimage* 2005, 928–935. doi: 10.1016/j.neuroimage.2004.09.046

Hartley, A., Reuter-Lorenz, P. A., Jonides, J., Smith, E. E., Miller, A., Marshuetz, C., et al. (2000). Age differences in the frontal lateralization of verbal and spatial working memory revealed by PET. *J. Cogn. Neurosci.* 12, 174–187. doi: 10.1162/089892900561814

Heekeren, H. R., Marrett, S., Bandettini, P. A., and Ungerleider, L. G. (2004). A general mechanism for perceptual decision-making in the human brain. *Nature* 431, 859–862. doi: 10.1038/nature02966

Holloway, D., Green, L., and Livingstone, S. (2013). *Zero to Eight. Young Children and Their Internet Use*. London: LSE.

Hopkins, E. J., and Weisberg, D. S. (2017). The youngest readers' dilemma: a review of children's learning from fictional sources. *Dev. Rev.* 43, 48–70. doi: 10.1016/j.dr.2016.11.001

Hoshi, Y., Kobayashi, N., and Tamura, M. (2001). Interpretation of near-infrared spectroscopy signals: a study with a newly developed perfused rat brain model. *J. Appl. Physiol.* 90, 1657–1662. doi: 10.1152/jappl.2001.90.5.1657

Huppert, T. J., Hoge, R. D., Diamond, S. G., Franceschini, M. A., and Boas, D. A. (2006). A temporal comparison of BOLD, ASL, and NIRS hemodynamic responses to motor stimuli in adult humans. *Neuroimage* 29, 368–382. doi: 10.1016/j.neuroimage.2005.08.065

Li, H., Boguszewski, K., and Lillard, A. S. (2015). Can that really happen? Children's knowledge about the reality status of fantastical events in television. *J. Exp. Child Psychol.* 139, 99–114. doi: 10.1016/j.jecp.2015.05.007

Li, H., Subrahmanyam, K., Bai, X., Xie, X., and Liu, T. (2018). Viewing fantastical events versus touching fantastical events: short-term effects on children's inhibitory control. *Child Dev.* 89, 48–57. doi: 10.1111/cdev.12820

Li, H., Wu, X. K., and Zhou, Z. K. (2014). 3 ˜ 6 years old children's media use. *Shanghai Res. Educ.* 5, 57–59.

Liu, T., Liu, X., Yi, L., Zhu, C., Markey, P. S., and Pelowski, M. (2017). Assessing autism at its social and developmental roots: a review of autism spectrum disorder studies using functional near-infrared spectroscopy. *Neuroimage* 185, 955–967. doi: 10.1016/j.neuroimage.2017.09.044

Liu, T., Saito, H., and Oi, M. (2012). Distinctive activation patterns under intrinsically versus extrinsically driven cognitive loads in prefrontal cortex: a near-infrared spectroscopy study using a driving video game. *Neurosci. Lett.* 506, 220–224. doi: 10.1016/j.neulet.2011.11.009

Matsuda, G., and Hiraki, K. (2006). Sustained decrease in oxygenated hemoglobin during video games in the dorsal prefrontal cortex: a NIRS study of children. *NeuroImage* 29, 706–711. doi: 10.1016/j.neuroimage.2005.08.019

Perlman, S. B., Luna, B., Hein, T. C., and Huppert, T. J. (2014). fNIRS evidence of prefrontal regulation of frustration in early childhood. *Neuroimage* 85, 326–334. doi: 10.1117/1.1854672

Ramnani, N., and Owen, A. M. (2004). Anterior prefrontal cortex: insights into function from anatomy and neuroimaging. *Nat. Rev. Neurosci.* 5, 184–194. doi: 10.1038/nrn1343

Rideout, V., and Hamel, E. (2006). *The Media Family: electronic Media in the Lives of Infants, Toddlers, Preschoolers and their Parents*. Menlo Park, CA: The Henry J. Kaiser Family Foundation.

Scholkmann, F., Kleiser, S., Metz, A. J., Zimmermann, R., Meta Pavia, J., Wolf, U., et al. (2014). A review on continuous wave functional near-infrared spectroscopy and imaging instrumentation and methodology. *Neuroimage* 85, 6–27. doi: 10.1016/j.neuroimage.2013.05.004

Shtulman, A., and Carey, S. (2007). Improbable of impossible? How children reason about the possibility of extraordinary events. *Child Dev.* 78, 1015–1032. doi: 10.1111/j.1467-8624.2007.01047.x

Skolnick, D., and Bloom, P. (2006). What does Batman think about SpongeBob? Children's understanding of the fantasy/fantasy distinction. *Cognition* 101, B9–B18. doi: 10.1016/j.cognition.2005.10.001

Svoboda, E., McKinnon, M. C., and Levine, B. (2006). The functional neuroanatomy of autobiographical memory: a meta-analysis. *Neuropsychologia* 44, 2189–2208. doi: 10.1016/j.neuropsychologia.2006.05.023

Vespignani, H., and Braun, M. (2009). Automated cortical projection of EEG sensors: anatomical correlation via the international 10–10 system. *Neuroimage* 46, 64–72. doi: 10.1016/j.neuroimage.2009.02.006

Wolf, R. C., Vasic, N., and Walter, H. (2006). Differential activation of ventrolateral prefrontal cortex during working memory retrieval. *Neuropsychologia* 44, 2558–2563. doi: 10.1016/j.neuropsychologia.2006.05.015

Woolley, J. D. (1997). Thinking about fantasy: are children fundamentally different thinkers and believers from adults? *Child Dev.* 68, 991–1011. doi: 10.1111/j.1467-8624.1997.tb01975.x

Woolley, J. D., and Ghossainy, M. (2013). Revisiting the fantasy–reality distinction: children as naïve skeptics. *Child Dev.* 84, 1496–1510. doi: 10.1111/cdev.12081

Woolley, J. D., and Wellman, H. M. (1990). Young children's understanding of realities, nonrealities, and appearances. *Child Dev.* 61, 946–961. doi: 10.1111/j.1467-8624.1990.tb02833.x

Wright, J. C., Huston, A. C., Reitz, A. L., and Piemyat, S. (1994). Young children's perceptions of television reality: determinants and developmental differences. *Dev. Psychol.* 30, 229–239. doi: 10.1037/0012-1649.30.2.229

Yang, Y., Liang, P., Lu, S., Li, K., and Zhong, N. (2009). The role of the DLPFC in inductive reasoning of MCI patients and normal agings: an fMRI study. *Sci. China Ser. C Life Sci.* 52, 789–795. doi: 10.1007/s11427-009-0089-1

Conflict of Interest: The authors declare that the research was conducted in the absence of any commercial or financial relationships that could be construed as a potential conflict of interest.

Copyright © 2019 Li, Liu, Woolley and Zhang. This is an open-access article distributed under the terms of the Creative Commons Attribution License (CC BY). The use, distribution or reproduction in other forums is permitted, provided the original author(s) and the copyright owner(s) are credited and that the original publication in this journal is cited, in accordance with accepted academic practice. No use, distribution or reproduction is permitted which does not comply with these terms.

APPENDIX A

List of stimulus item descriptions.

Categorization	Real character	Fantastical character
Real event	4. A boy and a girl are talking as they walk.	3. SpongeBob is singing a song with his friend.
	6. Students are saying hi to their teacher.	21. SpongeBob is asking to unfold a chair.
	8. A boy is waiting for his friend to get out of the car.	23. SpongeBob is watching TV with his friend.
	10. A boy is calling his friend on the phone.	27. SpongeBob is taking a boat ride with his friend.
	11. Two children are arm wrestling.	33. SpongeBob is receiving a package.
	12. The doctor is giving the students their check-ups.	34. SpongeBob is saying hi to his friend.
	15. A teacher is teaching a class.	35. SpongeBob is crying.
	16. A boy is having dinner with his mother.	36. SpongeBob is talking on the intercom.
	28. Boys are running around on the playground.	37. SpongeBob is going to sleep.
	40. Boys are eating.	39. SpongeBob is making a hamburger.
Fantastical event	5. A boy is hiding behind a magic shield.	1. SpongeBob is going into a container that is smaller than his body.
	9. A boy is flying on a broom.	2. SpongeBob and his friend are flying out of the house.
	14. A girl is moving a man by magic.	7. SpongeBob and his friend are rotating in the sky.
	17. A boy is jumping out of the computer.	13. SpongeBob is transforming his body after absorbing water.
	18. A boy is stuck in a blast of light.	24. SpongeBob is flying like a rocket.
	19. A boy is flying to chase adults.	25. SpongeBob is running on the wall.
	20. Two boys are flying in the sky.	29. SpongeBob is putting Patrick Star into his mouth.
	22. A girl is making two men stand still with light.	31. SpongeBob is twisting his body while floating in the air.
	26. A boy made two girls appear by pressing a button.	32. SpongeBob is transforming his arms.
	30. Two adults are shaking hands to generate current.	38. SpongeBob is elongating his mouth to drink water.

frontiers in Human Neuroscience

CLINICAL TRIAL
published: 22 January 2020
doi: 10.3389/fnhum.2019.00476

Effects of Tai Chi Chuan on Inhibitory Control in Elderly Women: An fNIRS Study

*Yuan Yang[1,2], Tingting Chen[4], Mingming Shao[1,2], Shoufu Yan[3], Guang H. Yue[5,6] and Changhao Jiang[1,2,3]**

[1] Beijing Key Laboratory of Physical Fitness Evaluation and Technical Analysis, Capital University of Physical Education and Sports, Beijing, China, [2] The Center of Neuroscience and Sports, Capital University of Physical Education and Sports, Beijing, China, [3] School of Kinesiology and Health, Capital University of Physical Education and Sports, Beijing, China, [4] School of Education, Beijing Dance Academy, Beijing, China, [5] Center for Mobility and Rehabilitation Engineering, Kessler Foundation, West Orange, NJ, United States, [6] Rutgers New Jersey Medical School, Rutgers, The State University of New Jersey, Newark, NJ, United States

Background: Inhibitory control is a sub-ability of executive function and plays an important role in the entire cognitive process. However, declines in inhibitory control during aging significantly impair the quality of life of elderly people. Investigating methods to delay the decline of inhibitory control has become a focal point in current research. Tai Chi Chuan (TCC) is one effective method used to delay cognitive declines in older adults. However, the specific effects of TCC on inhibitory control and the mechanisms through which TCC may improve cognition in older adults have not been comprehensively investigated.

Objective: The study explores possible neurological mechanisms related to the effects of TCC interventions on inhibitory control in older people using a functional near-infrared spectroscopy (fNIRS) technique and reaction times (RTs).

Methods: A total of 26 healthy, elderly people who had not received TCC training completed all study procedures. The subjects were randomized to either the TCC group or the control group. Subjects in the TCC group were taught TCC by a certified instructor and trained for 8 weeks. The control group continued to perform general daily activities. The Flanker task was administered to every participant to evaluate inhibitory control pre- and post-intervention. While participants were performing the Flanker task, fNIRS data were collected.

Results: Post-intervention, significant differences for incongruent flankers were found only for the TCC intervention group. Faster RTs were observed for the incongruent flankers in the TCC group than in the control group ($p < 0.05$). Analysis of the fNIRS data revealed an increase in oxy-Hb in the prefrontal cortex during the incongruent flankers after the TCC exercise intervention.

Conclusion: The TCC intervention significantly improved inhibitory control in older adults, suggesting that TCC is an effective, suitable exercise for improving executive function and neurological health in elderly people.

Clinical Trial Registration: Chinese Clinical Trial Register, ChiCTR1900028457.

Keywords: inhibitory control, Tai Chi Chuan, elderly women, fNIRS (functional near-infrared spectroscopy), Flanker

OPEN ACCESS

Edited by:
Xianchun Li,
East China Normal University, China

Reviewed by:
Nazareth Castellanos,
Complutense University of Madrid, Spain
Xu Cui,
Stanford University, United States

***Correspondence:**
Changhao Jiang
jiangchanghao@cupes.edu.cn

Specialty section:
This article was submitted to Health, a section of the journal Frontiers in Human Neuroscience

Received: *22 September 2019*
Accepted: *31 December 2019*
Published: *22 January 2020*

Citation:
Yang Y, Chen T, Shao M, Yan S, Yue GH and Jiang C (2020) Effects of Tai Chi Chuan on Inhibitory Control in Elderly Women: An fNIRS Study. Front. Hum. Neurosci. 13:476. doi: 10.3389/fnhum.2019.00476

INTRODUCTION

The cognitive functioning of adults declines with advancing age. This decline increases the prevalence of cognitive impairment, and is currently a topic of focus in cognitive neuroscience research (Anderson and McConnell, 2007). Cognitive decline can reduce quality of life and social competence in the elderly population. Further, cognitive declines may result in adverse physiological and psychological consequences (Wu et al., 2013). Therefore, techniques to maintain the cognitive functioning of older people are of considerable significance and require further study. Maintenance strategies should focus on both physiological impact and psychological benefits.

Aerobic exercise is a type of endurance exercise that has aerobic metabolism as its primary component. Some researchers have utilized aerobic exercise as a method of preventing cognitive decline (Groot et al., 2016; Panza et al., 2018). However, existing studies have resulted in equivocal findings. A study investigating the effects of 30-min sessions of moderate-intensity, bicycle-based exercise found that the aerobic exercise improved cognitive function (Song and Yu, 2019). However, a 12-week intervention study, conducted by Kimura et al. (2010), did not reveal a significant change in the reaction times (RTs) or accuracy rate (AR) of older people in a switching task post-intervention. Furthermore, no evidence emerged from this study supporting the notion of exercise sessions improving cognitive functioning in older adults. These findings are, thus, inconsistent, potentially due to discrepant intervention methods. Therefore, it is important to investigate effective methods of maintaining cognitive function in older adults.

In recent years, researchers have utilized mind-body exercises to delay cognitive function declines in the elderly population (Lam et al., 2009, 2011; Fong et al., 2014; Zhang et al., 2014; Ikudome et al., 2016). Mind-body exercises are defined as aerobic exercises that improve balance and flexibility by concentrating on physical movements and controlling breathing. Such mind-body exercises include Tai Chi Chuan (TCC), Baduanjin, and Wuqinxi (Zheng et al., 2015). Mind-body exercises are known to improve the individual's cardiopulmonary function as well as cognitive abilities (Miller and Taylor-Piliae, 2014). Nguyen and Kruse (2012) randomly assigned 102 healthy older participants to a TCC group or a control group. The TCC group trained for 6 months, whereas the control group maintained their normal daily activities. The cognitive functioning of the participants was tested using the Trail Making Test (TMT) at baseline and post-intervention. The results suggested that, after the TCC intervention, the older adults' TMT scores were significantly improved. These findings support the hypothesis that long-term TCC exercise can improve cognitive functioning in older people.

Although mind-body exercises are beneficial to cognitive functioning in the elderly population, most current studies have focused on general cognitive functions. Few studies have examined the differential effects of mind-body exercise on specific cognitive functions. Research has demonstrated that the effect of exercise on executive functions is more significant than its effect on general cognitive functioning (Colcombe and Kramer, 2003). Executive function is an advanced cognitive function primarily characterized by inhibition, shifting, updating, and other cognitive subcomponents (Perner and Lang, 1999). Inhibitory control is a subclass of specific cognitive control functions and is defined as the ability to inhibit the activation of irrelevant information during cognitive processing, in this way, inhibitory control is important for all cognitive processes (Smith, 1999).

The Flanker task (Eriksen and Eriksen, 1974) is used to measure inhibitory control in older adults and requires the participant to identify a directional response to the central target stimulus presented between a series of lateral distractors (flankers). The flankers can be consistent with the central stimulus, representing the same directional response (< < < < <); alternatively, flankers can be inconsistent with the central stimulus, representing an incongruent, or opposite, directional response (> > < > >). Therefore, perception and responses must be allocated to the central target, for which processing of the flanking stimulus must be suppressed using inhibitory control. The suppression of response to the flanking stimuli is required to reduce the possibility of disturbance in the perceptually evoked response, while dominant perceptual cues activate the action schema (Amanda et al., 2019). In inconsistent arrays, where the target and flanking stimuli are mapped to opposite directional modes, there will be greater interference between the correct and incorrect responses. Thus, increased response inhibition is required to suppress the impact of interference. This is closely related to inhibitory control (Collette et al., 2009; Gothe et al., 2014; Chen K.C. et al., 2017; Guarino et al., 2019). Research has demonstrated that older people do not perform as well as younger people on inhibition tasks. This may be because older people are required to mobilize more cognitive resources to deal with conflicting information. This apparent decline implies that maintaining inhibitory control abilities with advancing age is critical (Zelazo et al., 2004; Kawai et al., 2012).

Prior studies on the cognitive benefits of mind-body exercises have not generally focused on neurological mechanisms, but those which did have primarily utilized electroencephalography (EEG) and functional magnetic resonance imaging (fMRI) (Chang et al., 2017; Tao et al., 2017b). Functional near-infrared spectroscopy (fNIRS) is a neuroimaging technique for investigating cortical hemodynamic responses (Chen T.T. et al., 2017). Since oxygenated hemoglobin (oxy-Hb) and deoxygenated hemoglobin (deoxy-Hb) have different absorption spectra in the infrared range, fNIRS imaging quantifies the levels of oxy-Hb and deoxy-Hb by evaluating changes in near-infrared light intensity migrating from the source to a detector. Signals reflecting changes in oxy-Hb and deoxy-Hb concentrations are calculated based on the modified Beer-Lambert's law to infer local brain activation (Obrig and Villringer, 2003; Renata et al., 2019). The advantage of fNIRS is that the equipment is relatively stable, avoiding motion artifacts and making it suitable for the study of cortical responses during complex motor stimulation. Thus, fNIRS imaging can be used in sports and motion studies with high ecological validity.

Abbreviations: ANOVA, analysis of variance; EEG, electroencephalography; fMRI, functional magnetic resonance imaging; fNIRS, functional near-infrared spectroscopy; Oxy-Hb, oxygenated hemoglobin; ROIs, regions of interest; RTs, reaction times.

For example, the prefrontal cortex supports the cognitive control needed for complex motor learning and motor control, and data regarding activation of this area can be readily obtained using fNIRS (Leff et al., 2011). Due to these factors, fNIRS is more suitable than other imaging methods for the study of the cognitive benefits of sports (Tsujii and Watanabe, 2009).

To address the aforementioned knowledge gaps and equivocal research findings, we conducted a randomized controlled trial to investigate the effects of mind-body exercise (a TCC intervention) on specific cognitive functions in healthy older people and examined the relevant neurological mechanisms. Eight weeks of TCC exercises were performed and we employed the Flanker task as a cognitive experiment concomitant with fNIRS monitoring to evaluate whether the TCC exercises would significantly improve the inhibitory control of older adults. We hypothesized that 8 weeks of TCC practice could significantly modulate inhibitory control and improve neurological functioning in older adults.

METHODS

Study Design and Participants

Participants were recruited from the local community in the Haidian District, Beijing, China. The eligibility criteria were being over the age of 60–75 and having a Mini-Mental State Examination score ≥24. The exclusion criteria were the presence of neurological conditions, depressive symptoms, or vision problems.

The participants were randomly assigned to either the TCC group or the control group. Participants in the experimental group learned TCC from a certified instructor and trained for 8 weeks (45 min per session for 3 days per week). Participants in the control group were instructed to maintain their original physical activity habits during the 8-week period. Each participant was administered the Flanker task (Eriksen and Eriksen, 1974) to evaluate their inhibitory control at baseline and post-intervention. The Flanker task was inspired by the classical paradigm of Eriksen and Eriksen (see section "Instruments") (Eriksen and Eriksen, 1974). While performing the Flanker task, fNIRS data were collected from each participant. The primary outcome variable was changes in the oxy-Hb levels. The secondary outcome was the RTs for the incongruent flankers indicative of inhibitory control.

The Institutional Ethics Committee of Capital University of Physical Education and Sports approved the study. All participants signed an informed consent document prior to the intervention. A researcher who was not involved in the study used a serial number generator software program to randomly allocate the participants to the two groups.

Intervention

Before starting the 8-week TCC intervention (45 min per session for 3 days per week), the participants in the TCC group learned 24-form simplified TCC over six sessions (3 times per week for 2 weeks). Based on a compilation document from the General Administration of Sports of China, a number of studies on healthy elderly people have utilized 24-form simplified TCC (Chang et al., 2014). The TCC class was taught at a stadium in the Capital University of Physical Education and Sports by one instructor and two inspectors. After six classes, participants in the TCC group took part in the formal TCC intervention for 8 weeks. The formal TCC intervention comprised sessions of 45 min each, 3 days per week. Each 45-min session included a 5-min warm-up (muscle stretching), a 35-min TCC session, and a 5-min relaxation activity (breathing exercise). Participants were instructed to complete the Ratings of Perceived Exertion Scale after the TCC session to control the exercise intensity at a medium aerobic level. Participants in the control group did not undergo the TCC intervention and only performed their normal, general daily activities. The flow of the TCC exercise intervention program is shown in **Figure 1**.

To minimize confounding factors affecting cognitive function, the two groups were asked to maintain their normal daily lifestyle throughout the study and to inform the researchers of any lifestyle changes or emerging health-related events. In addition, all participants received weekly calls from a researcher involved in the study to monitor their health and any daily lifestyle changes, as well as to monitor their participation in other sports.

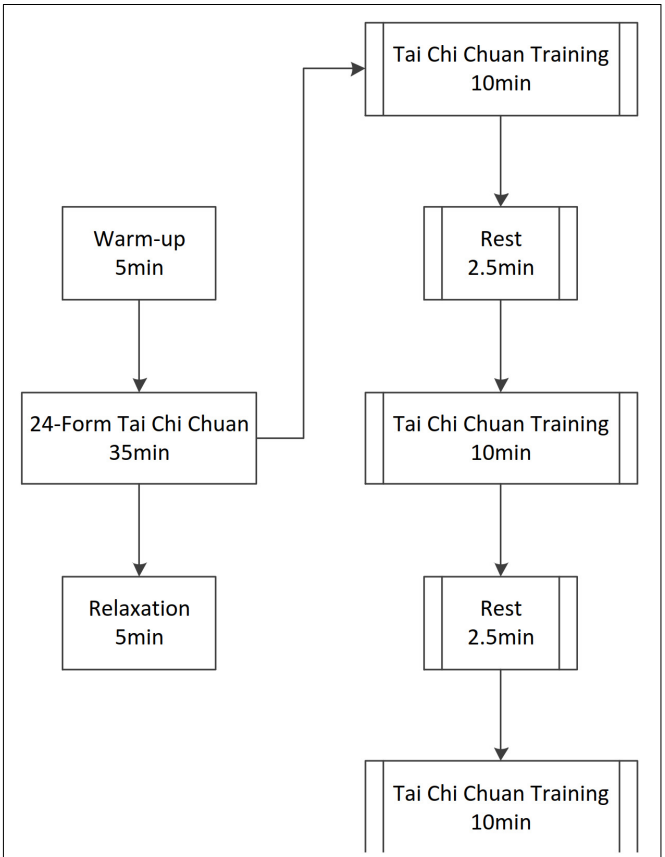

FIGURE 1 | The TCC intervention lasted for 45 min per session. Each 45-min session included a 5-min warm-up, a 35-min TCC session, and a 5-min relaxation activity.

Instruments

Neuroimaging

The results were assessed by experienced researchers at baseline and after the 8-week intervention. The researchers were blind to the participants' group allocation. The primary outcome investigated was the fNIRS data, which included changes in oxy-Hb. The ETG-4000 system (Hitachi Ltd., Tokyo, Japan) was used for monitoring oxy-Hb levels. Participants' oxy-Hb was monitored while performing the behavioral task. During monitoring, the light in the room was dimmed and the indoor environment was quiet. During the assessment, participants were asked to keep their posture stable and remain as still as possible. The fNIRS equipment was placed symmetrically over the frontal region of the participant's head. The optical cap used consists of two measuring panels, each of which contains 22 channels. The arrangement of the optical poles is a 3 × 5 array and covers an area of 12 cm × 6 cm. The lowest detection point on the EEG 10–20 system was located at Fp1–Fp2. The absorption of near-infrared light was calculated using a time resolution of 0.1 s. In total, 44 channels of fNIRS data were obtained.

Cognitive Task

The second outcome studied was performance on the Flanker task. The classic arrow Flanker task paradigm was used to test inhibitory control. Before the assessment began, the participants were instructed to complete the training segment. The formal assessment began at the end of the training segment. The entire Flanker task consists of four blocks, which included two congruent flanker tasks and two incongruent flanker tasks. Each block comprised 30 trials. The stimulus was randomly presented in the center of the computer screen. The stimuli included congruent flanker conditions (e.g., > > > > > and < < < < <) and incongruent flanker conditions (e.g., > > < > > and < < > < <). In each block, the target marker (+) was first presented in the center of the screen, followed by the stimulus. Next, a blank screen was shown for up to 1,000 ms during the participant's response window. The participants were required to react to the stimulus during the black screen time, after which the target marker appeared again and the next trial commenced. During the task, the background of the screen was black, and the stimuli were white. Blocks had a 30 s rest period between them. The participants were required to remain silent and to maintain a stable posture. The total time for the formal testing was approximately 5-min. During the test, the participants were required to judge the direction of the middle target arrow among the five arrows as quickly and accurately as possible. This required the participant to avoid false interference stimuli. Responses were recorded by choosing the correct key on the keypad (F key or J key representing left or right). After pressing the key, the computer recorded the participant's AR and RTs. The Flanker task was conducted using E-Prime (version 2.0.10.182; Psychology Software Tools, Sharpsburg, PA, United States) on a 14-inch notebook computer with a 1,024 × 768 resolution screen. The E-Prime software was used to compile the Flanker task performance data. The Flanker task procedure is shown in **Figure 2**.

Statistical Analysis

A mixed-model experiment was conducted with a 2 (group: TCC group vs. control group) × 2 (time: pre-test vs. post-test) × 2 (task: congruent vs. incongruent) design. The IBM SPSS software (version 23.0; IBM Corp., Armonk, NY, United States) was used for the statistical analysis. The RTs of the behavioral data were analyzed using repeated-measures analysis of variance (ANOVA) with a 2 (group: TCC group vs. control group) × 2 (time: pre-test vs. post-test) × 2 (task: congruent vs. incongruent) design. If there was a statistically significant interaction, a simple-effects analysis was used for further statistical analysis. The p-value was corrected with the Greenhouse-Geisser method, and the α significance level was set at 0.05.

We selected the frontal and temporal points of the brain because the fNIRS (ETG-4000 system) can only cover these two regions. Previous studies have shown that, as a key region of the cognitive control network, the dorsolateral prefrontal cortex (DLPFC) plays an important role in cognitive control processes (Miller and Cohen, 2001; Tao et al., 2017a). Thus, this choice of points was suitable. Four regions of interest (ROIs) were identified (Kameyama et al., 2004; Suto et al., 2004): the frontal superior left area (Frontal_Sup_L, which contained channels 9, 13, and 18), the frontal inferior left area (Frontal_Inf_L, which contained channels 3, 7, and 12), the frontal superior right area (Frontal_Sup_R, which contained channels 5, 10, and 14), and the frontal inferior area right (Frontal_Inf_R, which contained channels 2, 7, and 11). The ROIs were classified according to the existing anatomical calibration system, the Automated Anatomical Labeling software (Tzourio-Mazoyer et al., 2002), and related research results (**Figure 3**).

The data from the fNIRS were pre-processed by the xTopo software (version 2.08; Hitachi Ltd., Tokyo, Japan and Xu Cui, Stanford, CA, United States). The components with frequencies of less than 0.04 Hertz and more than 0.50 Hertz were filtered out. This decision was based on previous studies (Yanagisawa et al., 2010; Byun et al., 2014). Baseline correction was performed using a linear fitting function (Zhang et al., 2000). To this end, a linear fit was performed in the 10 s baseline before all of the active task segments and during the post-task baseline. The post-task baseline was determined as the average over the last 10 s of the resting period between active blocks (Ehlis et al., 2016). The mean values of the oxy-Hb signals of the four ROIs were calculated by averaging the same-condition blocks for each participant under each channel and then averaging the channels of the ROIs. The mean values of the oxy-Hb signals were analyzed using a repeated-measures ANOVA as a 2 (time: pre-test vs. post-test) × 2 (group: TCC group vs. control group) × 2 (task: congruent vs. incongruent) × 4 (ROI: Frontal_Sup_L vs. Frontal_Inf_L vs. Frontal_Sup_R vs. Frontal_Inf_R) design.

RESULTS

A total of 30 healthy older people who had not previously received TCC training participated in this study (mean age = 66.12 ± 3.81 years). Of the 30 participants, 26 (13 in the TCC group, 13 in the control group) completed all study

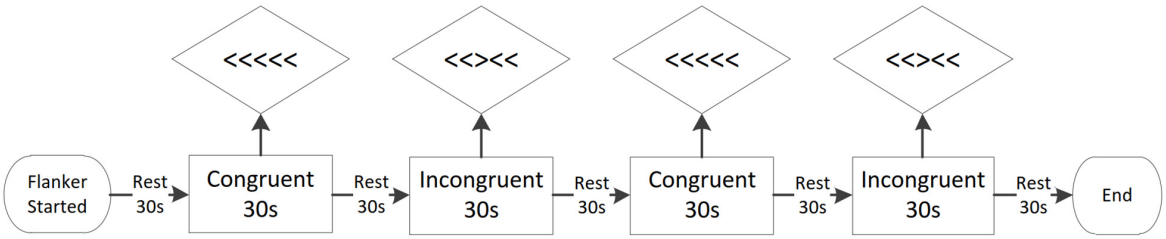

FIGURE 2 | The full Flanker task consists of four blocks of 30 trials each, which include two congruent flanker tasks and two incongruent flanker tasks. The stimuli are randomly presented in the center of the computer screen. The stimuli include congruent flanker conditions (e.g., > > > > > and < < < < <) and incongruent flanker conditions (e.g., > > < > > and < < > < <) conditions. Each block has a 30 s rest period.

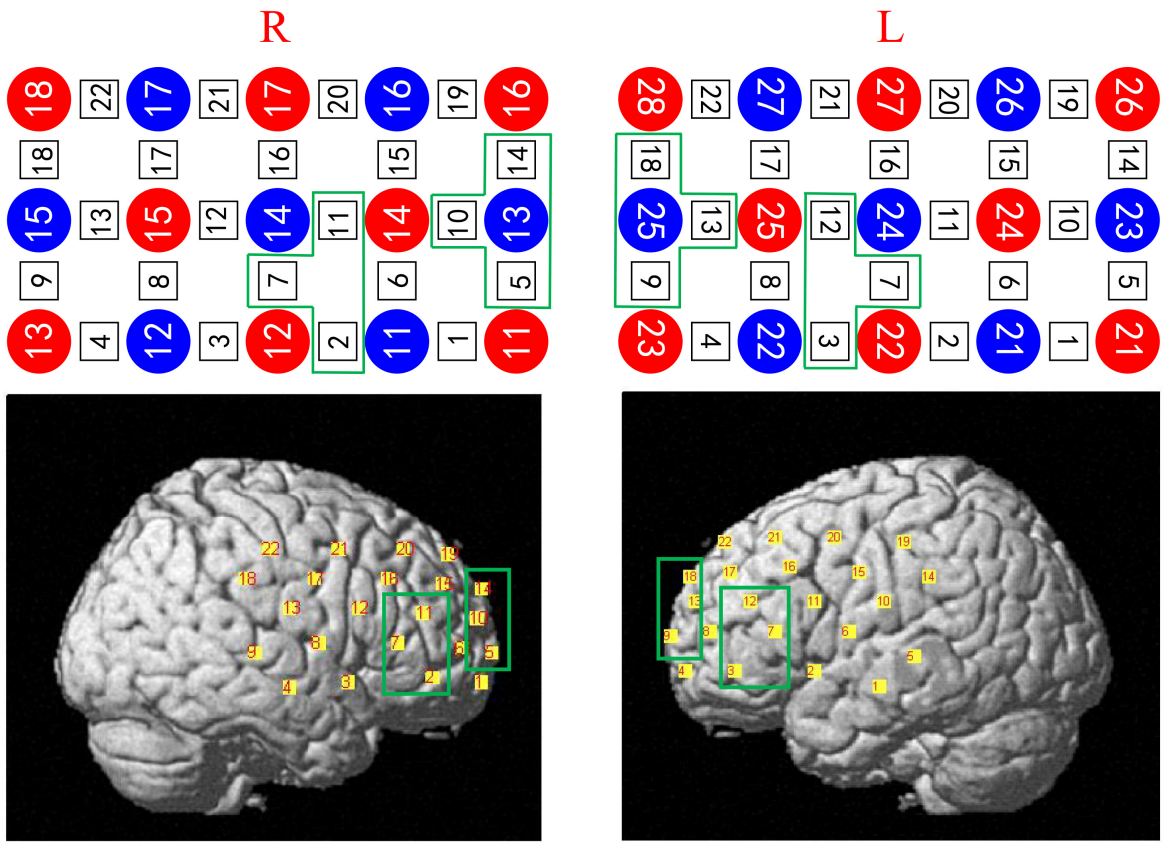

FIGURE 3 | Four regions of interest (ROIs): the frontal superior left area (Frontal_Sup_L, which contains channels 9, 13, and 18), the frontal inferior left area (Frontal_Inf_L, which contains channels 3, 7, and 12), the frontal superior right area (Frontal_Sup_R, which contains channels 5, 10, and 14), and the frontal inferior area right (Frontal_Inf_R, which contains channels 2, 7, and 11) were classified according to the existing anatomical calibration system, and related research results. L: **left**. R: **right**.

procedures. Two participants dropped out of the TCC group owing to scheduling conflicts and two participants dropped out of the control group, one owing to an inability to perform to the Flanker task and one owing to scheduling conflicts.

Demographic Data

Before the intervention, the demographic variables of the two groups were analyzed (**Table 1**). There were no significant differences ($p > 0.05$) between the groups in terms of age, height, weight, years of education, Mini-Mental State Examination score, average exercise levels (days per week), or body mass index. These findings indicated that the demographic characteristics of the two groups were sufficiently homogeneous.

Homogeneity Test on the Baseline Flanker Task Scores

A homogeneity test was conducted on the baseline (pre-intervention) Flanker task scores for the TCC and control

TABLE 1 | Demographic variables and MMSE scores (M ± SD, n = 26).

Factor	TCC Group	Control Group	t	p
Age (years)	66.31 ± 4.25	65.92 ± 3.48	0.25	0.80
Height (m)	1.61 ± 0.06	1.60 ± 0.05	0.39	0.70
Weight (kg)	62.15 ± 7.65	64.38 ± 7.57	−0.75	0.46
BMI	23.91 ± 2.88	25.02 ± 2.80	−0.99	0.33
Education (years)	13.46 ± 2.11	13.77 ± 2.17	−0.37	0.72
Exercise time (days/week)	3.69 ± 0.75	3.77 ± 0.83	−0.28	0.81
MMSE score	26.73 ± 2.63	27.47 ± 1.69	−0.91	0.37

TABLE 2 | Significance analysis of the Flanker task pre-intervention.

	Congruent		Incongruent	
	F	p	F	p
Group	0.001	0.98	0.78	0.39

groups. The selected significance level was 0.05 (**Table 2**). The baseline flanker task scores did not differ significantly between the control group and the TCC group for the congruent flankers ($F(1,24) = 0.001$, $p = 0.98 > 0.05$) or incongruent flankers ($F(1,24) = 0.78$, $p = 0.39 > 0.05$).

Flanker Task RTs

The Flanker task RTs were analyzed using a repeated-measures ANOVA (**Table 3** and **Figure 4**) with a 2 (group: TCC group vs. control group) × 2 (time: pre-test vs. post-test) × 2 (task: congruent vs. incongruent) design. The interaction of time by group was not statistically significant for congruent flankers ($F(1,24) = 0.01$, $p = 0.92 > 0.05$). The main effect of time was statistically significant for incongruent flankers ($F(1,24) = 91.03$, $p < 0.05$). The main effect of group was statistically significant ($F(1,24) = 4.91$, $p = 0.04 < 0.05$) and the interaction of time by group was statistically significant ($F(1,24) = 38.25$, $p < 0.05$).

Further, the simple-effects analysis showed that under incongruent task conditions, the TCC group was significantly different. The RTs at the post-test was faster than that at the pre-test, and the difference was significant ($p < 0.05$). There was no significant change in the control group ($p > 0.05$). The RTs in the TCC group when performing the incongruent task before the intervention was higher than that in the control group, but the difference was not significant ($p > 0.05$). The incongruent task RTs in the TCC group after the intervention was faster than that in the control group, and the difference was significant ($p < 0.05$) (**Figure 5**). Therefore, the TCC intervention had a positive impact on the inhibitory control ability of the elderly participants.

TABLE 3 | RTs (ms) on the Flanker test (M ± SD).

Task	Type	TCC Group		Control Group	
		Pre	Post	Pre	Post
Flanker	Congruent	374.0 ± 59.0	323.7 ± 51.3	373.5 ± 45.9	321.2 ± 53.0
	Incongruent	391.1 ± 54.8	270.8 ± 30.0*	377.5 ± 46.2	351.8 ± 38.9

*$p < 0.05$, significant difference.

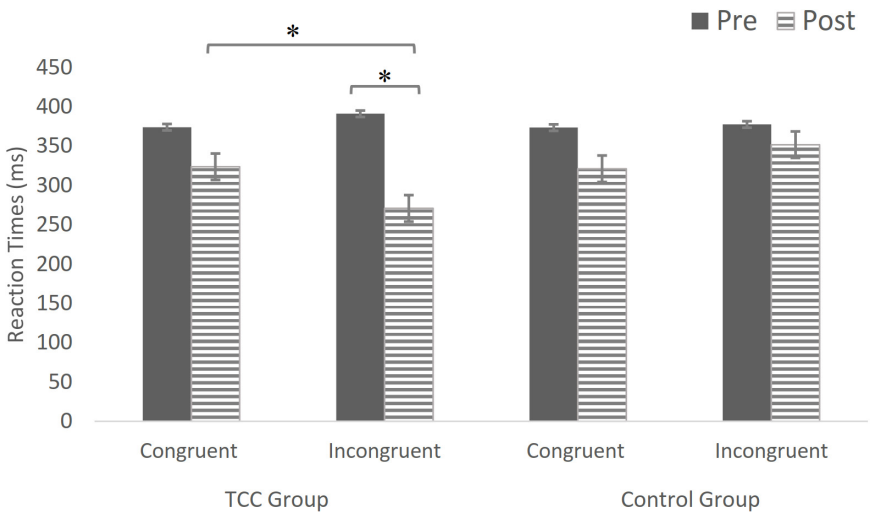

FIGURE 4 | In the incongruent flanker task for the TCC group, the RTs at post-test was faster than those at pre-test. The difference was statistically significant. The incongruent flanker task RTs for the TCC group post-intervention were significantly faster than for the control group. There was no statistically significant change in the control group. *$p < 0.05$, significant difference; Bars indicate standard errors.

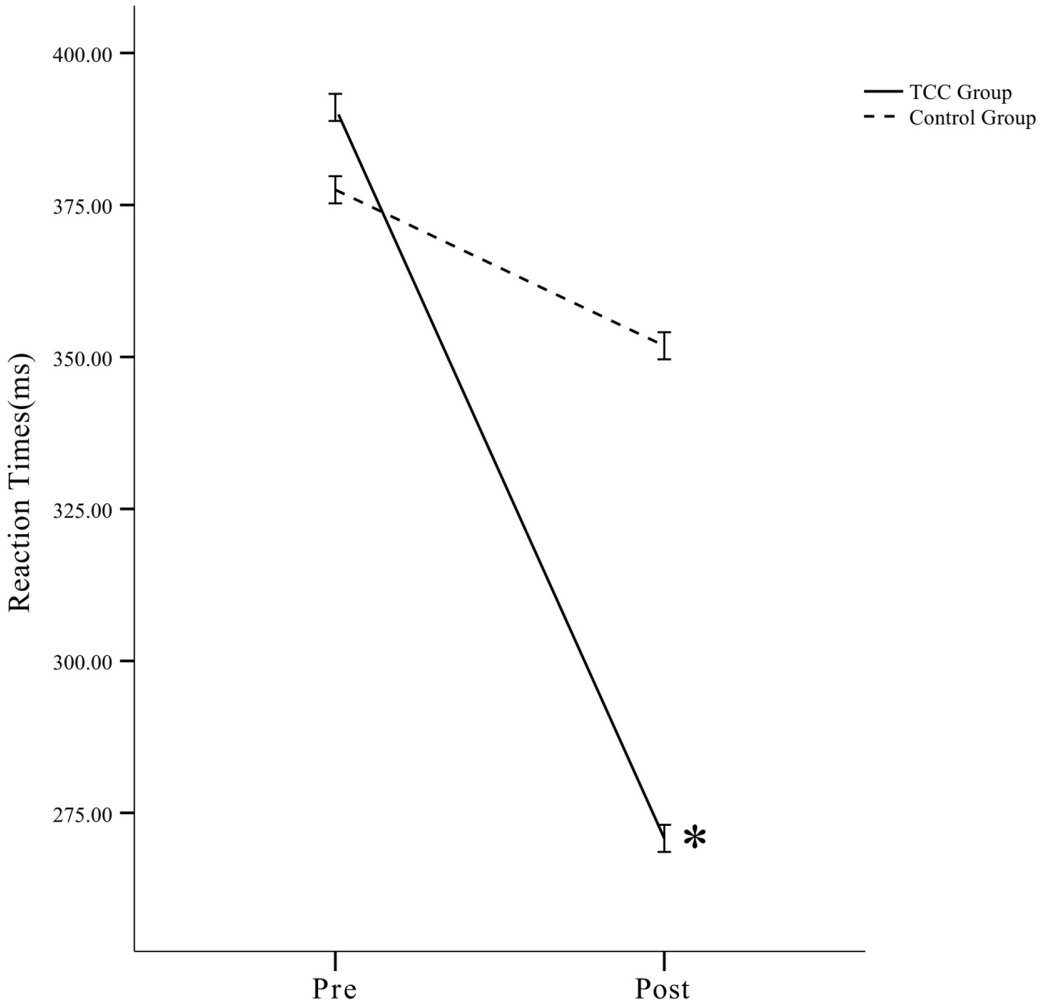

FIGURE 5 | The RTs of the TCC and control groups in the incongruent task were lower than those before the intervention, whereas the reduction in the TCC group was significantly different. *$p < 0.05$, significant difference; Bars indicate standard errors.

Figure 5 shows that, after the intervention, the RTs of the TCC and control groups in the incongruent flanker task were faster than those recorded before the intervention. The reduction in RTs in the TCC group was statistically significant.

fNIRS Results

The oxy-Hb signal was analyzed using repeated-measures ANOVA with a 2 (time: pre-test vs. post-test) × 2 (group: TCC group vs. control group) × 2 (task: congruent vs. incongruent) × 4 (ROIs: Frontal_Sup_L vs. Frontal_Inf_L vs. Frontal_Sup_R vs. Frontal_Inf_R) design. The results showed that, in the incongruent flanker task, the main effect of time was statistically significant ($F(1,24) = 4.683$, $p = 0.041 < 0.05$). The interaction of time by group by ROI was also statistically significant ($F(3,22) = 4.492$, $p = 0.012 < 0.05$), which indicates that there were significant differences in the ROIs between the different groups pre- and post-intervention. The oxy-Hb signals in ROIs under different task conditions pre- and post-intervention are presented in **Tables 4**, **5**.

A simple-effects analysis was conducted on the three-way interaction of time by group by ROIs to explore the effects of the TCC intervention on the different ROIs in the two groups of participants. The results showed that the Frontal_Sup_L oxy-Hb signal in the TCC group was higher at post-test than at pre-test for the incongruent flanker task, and that there was a statistically significant difference ($p < 0.05$). However, there was no significant difference in the control group ($p > 0.05$). There was no significant difference in the oxy-Hb signal between the two groups pre-intervention ($p > 0.05$). Post-intervention, the oxy-Hb signal in the TCC group was higher than that in the control group ($p < 0.05$). The Frontal_Inf_L oxy-Hb signal in the TCC group was higher than that at pre-test when performing the incongruent flanker task post-intervention ($p < 0.05$). However, there was no statistically significant change in the control group ($p > 0.05$). There were no significant difference in the oxy-Hb signal between the two groups pre-intervention ($p > 0.05$). Post-intervention, the oxy-Hb signal in the TCC group was higher than that in the control group and the difference was borderline

TABLE 4 | Oxy-Hb signal in ROIs under different task conditions pre-intervention (M ± SD).

ROIs	TCC Group		Control Group	
	Congruent	Incongruent	Congruent	Incongruent
Frontal_Sup_L	−0.013 ± 0.091	−0.013 ± 0.105	−0.028 ± 0.059	−0.013 ± 0.017
Frontal_Inf_L	−0.012 ± 0.107	0.003 ± 0.075	−0.024 ± 0.001	0.008 ± 0.003
Frontal_Sup_R	0.061 ± 1.902	−0.040 ± 0.044	0.091 ± 0.015	−0.024 ± 0.003
Frontal_Inf_R	−0.009 ± 0.010	−0.002 ± 0.778	−0.009 ± 0.001	−0.007 ± 0.003

TABLE 5 | Oxy-Hb signal in ROIs under different task conditions post-intervention (M ± SD).

ROIs	TCC Group		Control Group	
	Congruent	Incongruent	Congruent	Incongruent
Frontal_Sup_L	0.041 ± 0.021	0.116 ± 0.143*	−0.032 ± 0.058	−0.003 ± 0.071
Frontal_Inf_L	0.049 ± 0.030	0.093 ± 0.114*	−0.016 ± 0.080	0.002 ± 0.120
Frontal_Sup_R	0.041 ± 0.015	−0.050 ± 0.037	0.089 ± 0.106	−0.002 ± 0.540
Frontal_Inf_R	−0.003 ± 0.008	−0.006 ± 0.004	0.003 ± 0.087	−0.006 ± 0.098

*$p < 0.05$, significant difference.

significant ($p = 0.057$). The changes in the other ROIs were not statistically significant (**Figure 6**).

DISCUSSION

Eight weeks of a TCC intervention can improve older people's performance on the Flanker task and enhance brain activation in the left frontal lobe during an inhibition task (incongruent flankers). This indicates that TCC can improve the inhibitory control of older adults and enhance the activation of the brain regions related to inhibition. The results from the Flanker task showed that, in the incongruent flanker task, the RTs of the TCC group post-intervention were significantly faster than those pre-intervention, while the changes for the control group were not statistically significant. Post-intervention, the RTs for the TCC group were faster than those of the control group, and there were statistically significant differences. This finding suggests that the TCC exercise program improved Flanker task performance in older people. This result is consistent with those of previous studies. Ji et al. (2017) used a conflict control task to investigate the effects of different exercises on the executive function of older adults. Eighty-four, healthy, older participants were randomly divided into a TCC group, a fast walking group, and a control group. The participants were tested pre- and post-intervention, and the results showed that the test scores of the exercise group participants were significantly higher than those in the control group. In addition, the scores for the TCC group were significantly higher than those for the control group, and the ARs and RTs of the TCC group were higher than those of the fast walking group. Ji et al.'s (2017) findings indicate that their TCC intervention had a stronger positive effect on inhibition control in older people.

The Flanker task involves a cognitive component used in suppressing conflicting information (Kopp et al., 1996). The results of this study showed that, pre-intervention, the RTs on the incongruent flanker task were higher than in the congruent flanker task. With the increase in task difficulty, the RTs became slower. This finding indicates that participants were required to mobilize more cognitive resources to deal with more complex conflicting information. The results of this study confirm that these cognitive functions can be improved through using TCC exercises.

TCC is a mind-body exercise that integrates flexibility and coordination. Its spatial orientation changes greatly. The mental state of the participant undertaking TCC is concentrated, but relaxed, and the technique itself is closely related to restraint and control. The practice of TCC requires the integration of mental concentration and breathing control into physical motions to achieve a harmonious balance between body and mind (Lan et al., 2004, 2013). This combination produces psychological benefits, including improvements in attentiveness and reductions in stress and anxiety (Zhou et al., 2018). Moreover, TCC involves visual information processing that occurs simultaneously with the physical movements. This visual processing may improve the information processing abilities related to tasks involving cognitive processing and activities. The spatial orientation and action of TCC practice changes greatly. Elderly people frequently deal with the conflicting information as their spatial orientations and action directions are inconsistent when they perform the different exercises during TCC, and they are required to select the correct action. This physical process requires the individual to perform cognitive activities, including motor recall and task switching. Further, TCC involves the integration of the motor system and cognitive nervous system through two components: aerobic exercise and cognitive training. Previous studies have shown that both aerobic exercise and cognitive training can improve cognitive performance (Chang et al., 2010). Therefore, TCC can improve older people's ability to deal with conflicting information as this study demonstrated.

The fNIRS results demonstrated that, compared with the control group, the participants who received 8 weeks of the

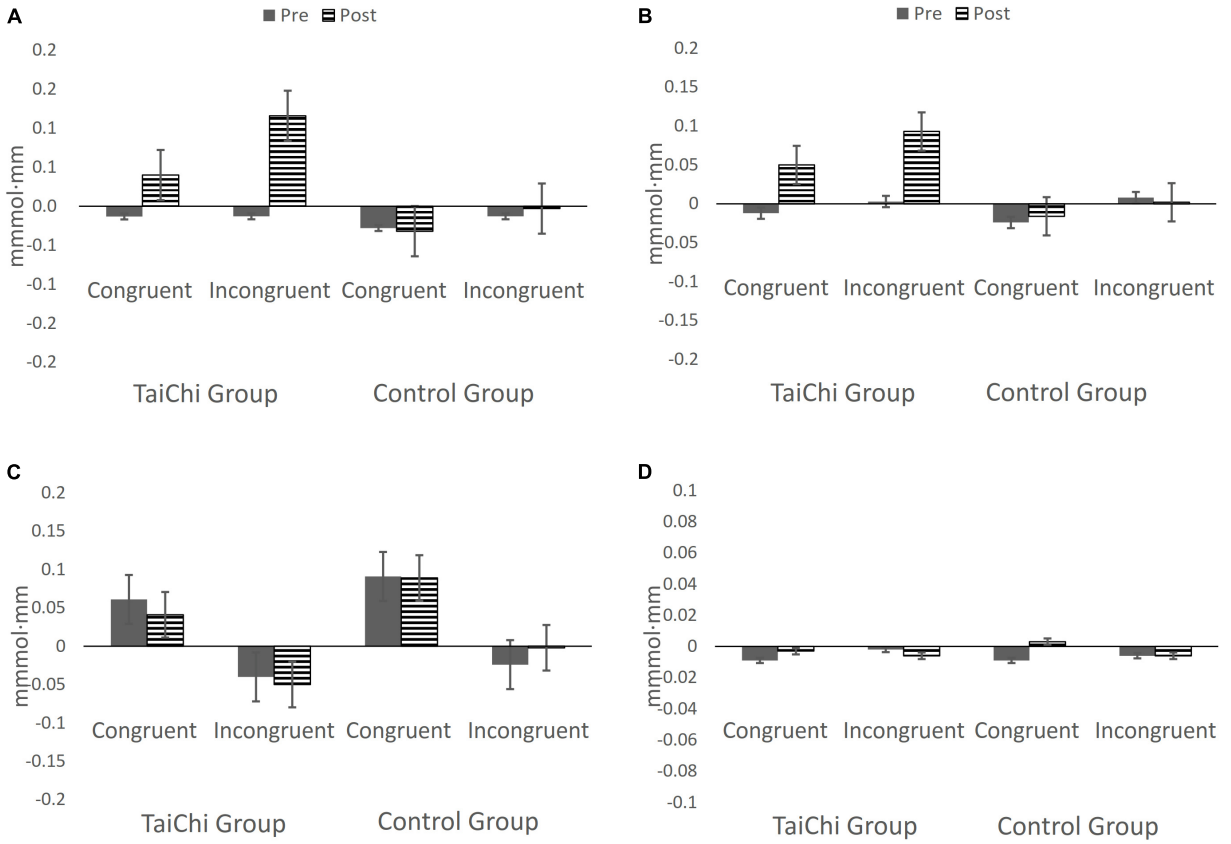

FIGURE 6 | The oxy-Hb concentration change in ROIs during the incongruent flanker task. **(A)** The Frontal_Sup_L oxy-Hb signals for the TCC group performing the incongruent flanker task post-intervention were significantly higher than at pre-test. There was no statistically significant change for the control group. Post-intervention, the oxy-Hb signals for the TCC group were higher than for the control group. **(B)** The Frontal_Inf_L oxy-Hb signals for the TCC group were higher than that at pre-test when performing the incongruent flanker task post-intervention. There was no significant change for the control group. Post-intervention, the oxy-Hb signals for the TCC group were higher than for the control group and the difference was marginally significant. **(C)** The changes in the Frontal_Sup_R were not statistically significant. **(D)** The changes in the Frontal_Inf_R were not statistically significant. Bars indicate standard errors.

TCC intervention had higher oxy-Hb concentrations in the Frontal_Inf_L and Frontal_Sup_L when they completed the Flanker task. The increase in oxy-Hb concentration reflects an increase in regional cerebral blood flow caused by the activation of cortical neurons. This finding suggests that the cortical activation was stronger in these areas (Byun et al., 2014). Therefore, TCC exercise evidently enhanced the activation of the left frontal lobe during the Flanker task. This finding is consistent with the conclusions of previous research. For example, Wei et al. (2013) used fMRI to compare the brain structures of 40 older people who had long-term experience practicing TCC in comparison to participants who did not practice TCC. The researchers found that the middle frontal sulcus and other brain regions were significantly thicker in the participants who practiced TCC long-term. Their results demonstrate that the practice of TCC long-term can result in changes to the local structures of the brain, and these changes are reflected in better executive control ability.

The frontal lobe is an important brain region for controlling executive function. Research has found that mind-body exercises can enhance activation in the frontal lobe when completing control tasks. Chen T.T. et al. (2017) used the Flanker task to examine the effect of a mind-body exercise intervention on executive control. The researchers found that 8 weeks of mind-body exercises enhanced activation in the prefrontal lobe and as well as executive functions. The frontal lobe is also associated with inhibitory control, which is strongly susceptible to brain aging. Compared with younger people, the activation of the frontal lobe differs in older people when they undergo the Flanker task (Zhu et al., 2010). Since frontal lobe dysfunction is associated with multiple diseases, strengthening activation through training can enhance self-regulation and used as a tool for treating, or preventing, related diseases. The results of this study are helpful in understanding how mind-body exercises influence brain activation and behavioral performance. The findings of this, and other, research suggest that mind-body exercises may induce these effects over time and are a useful tool for disease prevention and treatment.

After 8 weeks of TCC intervention, we found that activation in the left frontal lobe was significantly altered, but no changes were found in other brain regions. One possible explanation is that the spatial resolution of the fNIRS was limited. The spectral

probe used in this study covered only the prefrontal and temporal lobes. Important subcortical areas, such as the hippocampus, are difficult to detect. In addition, different TCC exercise programs may lead to the activation of different brain regions. Therefore, these differences should be examined in future studies. There were also specific methodological limitations in this study. First, since all our participants were older women, the conclusions of this study may not reflect the changes experienced by older men. Second, the sample size was limited, thus affecting the statistical analyses. Sample sizes should be increased in future research.

CONCLUSION

Tai Chi Chuan has a positive impact on the inhibitory control and regional brain activation of older adults. This was indicated by improved Flanker task performance and enhanced activation of the left frontal lobe-related brain areas in participants undergoing an 8-week TCC intervention. Tai Chi Chuan is easy to learn and a safe exercise, even for older adults. The results of this study are instructive for designing exercise programs for older adults.

DATA AVAILABILITY STATEMENT

The raw data supporting the conclusions of this article will be made available by the authors, without undue reservation, to any qualified researcher.

ETHICS STATEMENT

The experiments were approved by the Capital University of Physical Education and Sports. All participants gave written informed consent in accordance with the Declaration of Helsinki. The experiments comply with the current laws of the country in which they were performed.

AUTHOR CONTRIBUTIONS

YY, SY, and CJ: conceptualization and formal analysis. YY, SY, TC, GY, and CJ: writing – review and editing. MS: software. CJ: resources, project administration, and funding acquisition. YY and MS: data curation. YY: writing – original draft preparation. TC: fNIRS data analysis.

FUNDING

This work was supported by the National Natural Science Foundation (NNSF) of China under Grant No. 31771244.

ACKNOWLEDGMENTS

This work was an open manuscript to be reviewed Research Fund of the State Key Laboratory of Cognitive Neuroscience and Learning to CJ. Thanks for the help of Taijiliao (China) Culture Development Co., Limited in the recruitment and coordination of participants.

REFERENCES

Amanda, L. M., Abigail, C. B., Jennifer, L. S., Savage, K. M. P., Tracey, C., and Matthew, B. P. (2019). Acute and protracted disruptions to inhibitory control following sports related concussion. *Neuropsychologia* 131, 223–232. doi: 10.1016/j.neuropsychologia.2019.05.026

Anderson, L. A., and McConnell, S. R. (2007). Cognitive health: an emerging public health issue. *Alzheimers Dement.* 3, s70–s73. doi: 10.1016/j.jalz.2007.01.018

Byun, K., Hyodo, K., Suwabe, K., Ochi, G., Sakairi, Y., Kato, M., et al. (2014). Positive effect of acute mild exercise on executive function via arousal-related prefrontal activations: an fNIRS study. *Neuroimage* 98, 336–345. doi: 10.1016/j.neuroimage.2014.04.067

Chang, Y. K., Chu, I. H., Liu, J. H., Wu, C. H., Chu, C. H., Yang, K. T., et al. (2017). Exercise modality is differentially associated with neurocognition in older adults. *Neural Plast.* 2017, 1–11. doi: 10.1155/2017/3480413

Chang, Y. K., Nien, Y. H., Chen, A. G., and Yan, J. (2014). Tai ji quan, the brain, and cognition in older adults. *J. Sport Health Sci.* 3, 36–42. doi: 10.1016/j.jshs.2013.09.003

Chang, Y. K., Nien, Y. H., Tsai, C. L., and Etnier, J. L. (2010). Physical activity and cognition in older adults: the potential of Tai chi chuan. *J. Aging Phys. Act.* 18, 451–472. doi: 10.1123/japa.18.4.451

Chen, K. C., Weng, C. Y., Hsiao, S., Tsao, W. L., and Koo, M. (2017). Cognitive decline and slower reaction time in elderly individuals with mild cognitive impairment. *Psychogeriatrics* 17, 364–370. doi: 10.1111/psyg.12247

Chen, T. T., Yue, G. H., Tian, Y. X., and Jiang, C. H. (2017). Baduanjin mind-body intervention improves the executive control function. *Front. Psychol.* 7:2015. doi: 10.3389/fpsyg.2016.02015

Colcombe, S., and Kramer, A. F. (2003). Fitness effects on the cognitive function of older adults: a meta-analytic study. *Psychol. Sci.* 14, 125–130. doi: 10.1177/1745691617707316

Collette, F., Schmidt, C., Scherrer, C., Adam, S., and Salmon, E. (2009). Specificity of inhibitory deficits in normal aging and Alzheimer's disease. *Neurobiol. Aging* 30, 875–889. doi: 10.1016/j.neurobiolaging.2007.09.007

Ehlis, A. C., Haeussinger, F. B., Gastel, A., Fallgatter, A. J., and Plewnia, C. (2016). Task-dependent and polarity-specific effects of prefrontal transcranial direct current stimulation on cortical activation during word fluency. *Neuroimage* 140, 134–140. doi: 10.1016/j.neuroimage.2015.12.047

Eriksen, B. A., and Eriksen, C. W. (1974). Effects of noise letters upon the identification of a target letter in a nonsearch task. *Percept. Psychophys.* 16, 143–149. doi: 10.3758/BF03203267

Fong, D. Y., Chi, L. K., Li, F., and Chang, Y. K. (2014). The benefits of endurance exercise and Tai Chi Chuan for the task-switching aspect of executive function in older adults: an ERP study. *Front. Aging Neurosci.* 6:295. doi: 10.3389/fnagi.2014.00295

Gothe, N. P., Fanning, J., Awick, E., Chung, D., Wójcicki, T. R., Olson, E. A., et al. (2014). Executive function processes predict mobility outcomes in older adults. *J. Am. Geriatr. Soc.* 62, 285–290. doi: 10.1111/jgs.12654

Groot, C., Hooghiemstra, A. M., Raijmakers, P. G., Berckel, B. N., Scheltens, P., Scherder, E. J., et al. (2016). The effect of physical activity on cognitive function in patients with dementia: a meta-analysis of randomized control trials. *Ageing Res. Rev.* 25, 13–23. doi: 10.1016/j.arr.2015.11.005

Guarino, A., Favieri, F., and Boncompagni, I. (2019). Executive functions in Alzheimer disease: a systematic review. *Front. Aging Neurosci.* 10:437. doi: 10.3389/fnagi.2018.00437

Ikudome, S., Mori, S., Unenaka, S., Kawanishi, M., Kitamura, T., and Nakamoto, H. (2016). Effect of long-term body-mass-based resistance exercise on cognitive

function in elderly people. *J. Appl. Gerontol.* 36, 1519–1533. doi: 10.1177/0733464815625834

Ji, Z., Li, A., Feng, T., Liu, X., You, Y., Meng, F., et al. (2017). The benefits of tai chi and brisk walking for cognitive function and fitness in older adults. *PeerJ* 5:e3943. doi: 10.7717/peerj.3943

Kameyama, M., Fukuda, M., Uehara, T., and Mikuni, M. (2004). Sex and age dependencies of cerebral blood volume changes during cognitive activation: a multichannel near-infrared spectroscopy study. *Neuroimage* 22, 1715–1721. doi: 10.1016/j.neuroimage.2004.03.050

Kawai, N., Kubo-Kawai, N., Kubo, K., Terazawa, T., and Masataka, N. (2012). Distinct aging effects for two types of inhibition in older adults: a near-infrared spectroscopy study on the Simon task and the flanker task. *Neuroreport* 23, 819–824. doi: 10.1097/WNR.0b013e3283578032

Kimura, K., Obuchi, S., Arai, T., Nagasawa, H., Shiba, Y., Watanabe, S., et al. (2010). The influence of short-term strength training on health-related quality of life and executive cognitive function. *J. Physiol. Anthropol.* 29, 95–101. doi: 10.2114/jpa2.29.95

Kopp, B., Rist, F., and Mattler, U. (1996). N200 in the flanker task as a neurobehavioral tool for investigating executive control. *Psychophysiology* 33, 282–294. doi: 10.1111/j.1469-8986.1996.tb00425.x

Lam, L., Tam, C., Lui, V., Chan, W., Chan, S., Chiu, H., et al. (2009). Modality of physical exercise and cognitive function in Hong Kong older Chinese community. *Int. J. Geriatr. Psychiatry* 24, 48–53. doi: 10.1002/gps.2072

Lam, L. C., Chau, R. C., Wong, B. M., Fung, A. W., Liu, V. W., Tam, C. C., et al. (2011). Interim follow-up of a randomized controlled trial comparing Chinese style mind body (Tai Chi) and stretching exercises on cognitive function in subjects at risk of progressive cognitive decline. *Int. J. Geriatr. Psychiatry* 26, 733–740. doi: 10.1002/gps.2602

Lan, C., Chen, S. Y., and Lai, J. S. (2004). Relative exercise intensity of tai chi chuan is similar in different ages and gender. *Am. J. Chin. Med.* 32, 151–160. doi: 10.1142/S0192415X04001746

Lan, C., Chen, S. Y., Lai, J. S., and Wong, M. K. (2013). Tai chi chuan in medicine and health promotion. *Evid. Based Complementary Altern. Med.* 2013, 1–17. doi: 10.1155/2013/502131

Leff, D. R., Orihuela-Espina, F., Elwell, C. E., Athanasiou, T., Delpy, D. T., Darzi, A. W., et al. (2011). Assessment of the cerebral cortex during motor task behaviours in adults: a systematic review of functional near infrared spectroscopy (fNIRS) studies. *Neuroimage* 54, 2922–2936. doi: 10.1016/j.neuroimage.2010.10.058

Miller, E. K., and Cohen, J. D. (2001). An integrative theory of prefrontal cortex function. *Annu. Rev. Neurosci.* 24, 167–202. doi: 10.1146/annurev.neuro.24.1.167

Miller, S. M., and Taylor-Piliae, R. E. (2014). Effects of tai chi on cognitive function in community-dwelling older adults: a review. *Geriatr. Nursing* 35, 9–19. doi: 10.1016/j.gerinurse.2013.10.013

Nguyen, M. H., and Kruse, A. (2012). A randomized controlled trial of Tai chi for balance, sleep quality and cognitive performance in elderly Vietnamese. *Clin. Intervent. Aging* 7, 185–190. doi: 10.2147/CIA.S32600

Obrig, H., and Villringer, A. (2003). Beyond the visible - imaging the human brain with light. *J. Cereb. Blood Flow Metab.* 23, 1–18. doi: 10.1097/01.wcb.0000043472.45775.29

Panza, G. A., Taylor, B. A., Macdonald, H. V., Johnson, B. T., Zaleski, A. L., Livingston, J., et al. (2018). Can exercise improve cognitive symptoms of Alzheimer's disease? *J. Am. Geriatr. Soc.* 66, 487–495. doi: 10.1111/jgs.15241

Perner, J., and Lang, B. (1999). Development of theory of mind and executive control. *Trends Cogn. Sci.* 3, 337–344. doi: 10.1016/S1364-6613(99)01362-5

Renata, D. L., Laura, P., Anna, B., Chiara, B., Yoko, H., Yasuyo, M., et al. (2019). Recommendations for motion correction of infant fNIRS data applicable to multiple data sets and acquisition systems. *Neuroimage* 200, 511–527. doi: 10.1016/j.neuroimage.2019.06.056

Smith, E. E. (1999). Storage and executive processes in the frontal lobes. *Science* 283, 1657–1661. doi: 10.1126/science.283.5408.1657

Song, D., and Yu, D. S. F. (2019). Effects of a moderate-intensity aerobic exercise programme on the cognitive function and quality of life of community-dwelling elderly people with mild cognitive impairment: a randomised controlled trial. *Int. J. Nurs. Stud.* 93, 97–105. doi: 10.1016/j.ijnurstu.2019.02.019

Suto, T., Fukuda, M., Ito, M., Uehara, T., and Mikuni, M. (2004). Multichannel near-infrared spectroscopy in depression and schizophrenia: cognitive brain activation study. *Biol. Psychiatry* 55, 501–511. doi: 10.1016/j.biopsych.2003.09.008

Tao, J., Chen, X., Egorova, N., Liu, J., Xue, X., Wang, Q., et al. (2017a). Tai chi chuan and baduanjin practice modulates functional connectivity of the cognitive control network in older adults. *Sci. Rep.* 7:41581. doi: 10.1038/srep41581

Tao, J., Liu, J., Liu, W., Huang, J., and Kong, J. (2017b). Tai chi chuan and Baduanjin increase grey matter volume in older adults: a brain imaging study. *J. Alzheimers Dis.* 60, 1–12. doi: 10.3233/JAD-170477

Tsujii, T., and Watanabe, S. (2009). Neural correlates of dual-task effect on belief-bias syllogistic reasoning: a near-infrared spectroscopy study. *Brain Res.* 1287, 118–125. doi: 10.1016/j.brainres.2009.06.080

Tzourio-Mazoyer, N., Landeau, B., Papathanassiou, D., Crivello, F., Etard, O., Delcroix, N., et al. (2002). Automated anatomical labeling of activations in SPM using a macroscopic anatomical parcellation of the MNI MRI single-subject brain. *Neuroimage* 15, 273–289. doi: 10.1006/nimg.2001.0978

Wei, G. X., Xu, T., Fan, F. M., Dong, H. M., Jiang, L. L., Li, H. J., et al. (2013). Can TaiChi reshape the brain? a brain morphometry study. *PLoS One* 8:e61038. doi: 10.1371/journal.pone.0061038

Wu, Y., Wang, Y., Burgess, E. O., and Wu, J. (2013). The effects of Tai Chi exercise on cognitive function in older adults: a meta-analysis. *J. Sport Health Sci.* 2, 193–203. doi: 10.1016/j.jshs.2013.09.001

Yanagisawa, H., Dan, I., Tsuzuki, D., Kato, M., Okamoto, M., Kyutoku, Y., et al. (2010). Acute moderate exercise elicits increased dorsolateral prefrontal activation and improves cognitive performance with stroop test. *Neuroimage* 50, 1702–1710. doi: 10.1016/j.neuroimage.2009.12.023

Zelazo, P. D., Craik, F. I. M., and Booth, L. (2004). Executive function across the life span. *Acta Psychol.* 115, 167–183. doi: 10.1016/j.actpsy.2003.12.005

Zhang, R., Zuckerman, J. H., and Levine, B. D. (2000). Spontaneous fluctuations in cerebral blood flow: insights from extended-duration recordings in humans. *Am. J. Physiol. Heart Circ. Physiol.* 278, H1848–H1855. doi: 10.1046/j.1365-201X.2000.00727.x

Zhang, X., Ni, X., and Chen, P. (2014). Study about the effects of different fitness sports on cognitive function and emotion of the aged. *Cell Biochem. Biophys.* 70, 1591–1596. doi: 10.1007/s12013-014-0100-8

Zheng, G., Liu, F., Li, S., Huang, M., Tao, J., and Chen, L. (2015). Tai chi and the protection of cognitive ability: a systematic review of prospective studies in healthy adults. *Am. J. Prev. Med.* 49, 89–97. doi: 10.1016/j.amepre.2015.01.002

Zhou, M., Liao, H., Sreepada, L. P., Ladner, J. R., Balschi, J. A., and Lin, A. P. (2018). Tai chi improves brain metabolism and muscle energetics in older adults. *J. Neuroimaging* 28, 359–364. doi: 10.1111/jon.12515

Zhu, D. C., Zacks, R. T., and Slade, J. M. (2010). Brain activation during interference resolution in young and older adults: an fMRI study. *Neuroimage* 50, 810–817. doi: 10.1016/j.neuroimage.2009.12.087

Conflict of Interest: The authors declare that the research was conducted in the absence of any commercial or financial relationships that could be construed as a potential conflict of interest.

Copyright © 2020 Yang, Chen, Shao, Yan, Yue and Jiang. This is an open-access article distributed under the terms of the Creative Commons Attribution License (CC BY). The use, distribution or reproduction in other forums is permitted, provided the original author(s) and the copyright owner(s) are credited and that the original publication in this journal is cited, in accordance with accepted academic practice. No use, distribution or reproduction is permitted which does not comply with these terms.

frontiers in Neuroscience

ORIGINAL RESEARCH
published: 24 January 2020
doi: 10.3389/fnins.2019.01430

Assessing Brain Networks by Resting-State Dynamic Functional Connectivity: An fNIRS-EEG Study

Yujin Zhang[1,2] *and Chaozhe Zhu*[3]*

[1] *Brainnetome Center, Institute of Automation, Chinese Academy of Sciences, Beijing, China,* [2] *National Laboratory of Pattern Recognition, Institute of Automation, Chinese Academy of Sciences, Beijing, China,* [3] *State Key Laboratory of Cognitive Neuroscience and Learning, Beijing Normal University, Beijing, China*

The coordination of brain activity between disparate neural populations is highly dynamic. Investigations into intrinsic brain organization by evaluating dynamic resting-state functional connectivity (dRSFC) have attracted great attention in recent years. However, there are few dRSFC studies based on functional near-infrared spectroscopy (fNIRS) even though it has some advantages for studying the temporal evolution of brain function. In this research, we recruited 20 young adults and measured their resting-state brain fluctuations in several areas of the frontal, parietal, temporal, and occipital lobes using fNIRS-electroencephalography (EEG) simultaneous recording. Based on a sliding-window approach, we found that the variability of the dRSFC within any region of interest was significantly lower than the connections between region of interests but noticeably greater than the correlation between the channels with a short interoptode distance, which mainly consist of physiological fluctuations occurring in the superficial layers. Furthermore, based on a time-resolved *k*-means clustering analysis, the temporal evolution was extracted for three dominant functional networks. These networks were roughly consistent between different subject subgroups and in varying sliding time window lengths of 20, 30, and 60 s. Between these three functional networks, there were obvious time-varied and system-specific synchronous relationships. In addition, the oscillation of the frontal-parietal-temporal network showed significant correlation with the switching of one EEG microstate, a finding which is consistent with a previous functional MRI-EEG study. All this evidence implies the functional significance of fNIRS-dRSFC and demonstrates the feasibility of fNIRS for extracting the dominant functional networks based on RSFC dynamics.

Keywords: functional connectivity, resting state, dynamic, functional near-infrared spectroscopy, electroencephalogram

OPEN ACCESS

Edited by:
Fenghua Tian,
University of Texas at Arlington, United States

Reviewed by:
Stavros I. Dimitriadis,
Cardiff University, United Kingdom
Zhen Yuan,
University of Macau, China

***Correspondence:**
Chaozhe Zhu
czzhu@bnu.edu.cn

Specialty section:
This article was submitted to Brain Imaging Methods, a section of the journal Frontiers in Neuroscience

Received: *11 September 2019*
Accepted: *18 December 2019*
Published: *24 January 2020*

Citation:
Zhang Y and Zhu C (2020) Assessing Brain Networks by Resting-State Dynamic Functional Connectivity: An fNIRS-EEG Study. Front. Neurosci. 13:1430. doi: 10.3389/fnins.2019.01430

INTRODUCTION

The human brain is a highly complex network with dynamic and context-dependent coordination between disparate neural populations. Functional connectivity, which refers to the neural synchronization between brain areas, has been shown to reflect the information interactions between disparate neural populations. Based on the functional connectivity during the resting state

(RSFC), researchers have produced a wealth of literature and revealed a great deal of information about the large-scale organization of the brain.

Although most RSFC studies are based on an implicit assumption that the brain functional connectivity is temporally stationary throughout the measurement period, rich evidence has amply confirmed that RSFC is highly non-stationary (Chang and Glover, 2010; Hutchison et al., 2013a; Mueller et al., 2013; Allen et al., 2014; Damaraju et al., 2014; Kucyi et al., 2017). In some cases, RSFC varies greatly between strongly positive and strongly negative correlations within time scales of seconds to minutes. Such temporal fluctuations of the dynamic RSFC (dRSFC) have been shown to be an essential property that can unveil flexibility in the dynamic functional coordination between different neural systems (Allen et al., 2014) and are not exclusive to humans (Majeed et al., 2011; Hutchison et al., 2013b; Keilholz et al., 2013). Furthermore, disruptions in RSFC dynamic characteristics are evidence of abnormal brain activity in mental disorders, such as schizophrenia (Damaraju et al., 2014; Zhang et al., 2016; Sanfratello et al., 2019), depression (Demirtas et al., 2016), attention deficit hyperactivity disorder (Zhang et al., 2016), and Alzheimer's disease (Jones et al., 2011; Fu et al., 2019). Some disease-related abnormalities have not been found using stationary RSFC. Therefore, the characteristics of dRSFC have great functional significance and should be able to provide new perspectives on brain function.

Functional near-infrared spectroscopy (fNIRS) is an emerging non-invasive brain imaging technique that has great potential for evaluating the dynamic characteristics of the intrinsic brain organization. First, the time sampling rate of fNIRS can reach milliseconds (57 ms in the current study), much higher than conventional functional MRI (fMRI). In theory, better temporal resolution enables a richer temporal characterization of dRSFC with greater degrees of freedom (Zalesky et al., 2014). Second, fNIRS is not disturbed by electromagnetic fields, making it possible to be synchronously used with electroencephalography (EEG)/magnetoencephalography/fMRI technologies and allowing researchers to investigate the neural fundamentals of dRSFC. Furthermore, fNIRS can be portable, comfortable, and quiet. This facilitates fNIRS-based dRSFC applications in almost all human subjects, especially infants, various in-bed patients, and in conditions where fMRI-based dRSFC is difficult to apply (Bunce et al., 2006; Hoshi, 2007). Recently, in addition to the large number of fNIRS-based stationary RSFC studies (White et al., 2009; Lu et al., 2010; Mesquita et al., 2010; Zhang H. et al., 2010; Zhang Y. J. et al., 2010; Zhang et al., 2011; Homae et al., 2011; Duan et al., 2012; Niu and He, 2014), the feasibility of fNIRS-based dRSFC has been validated by two prior studies (Li et al., 2015; Niu et al., 2019). Specifically, based on a sliding-window correlation analysis, the variability (Q) of the fNIRS-based dRSFC between long-distance intrahemispheric areas (>10 cm) was found to be significantly greater than that between homotopic areas or between short-distance intrahemispheric areas (<10 cm) (Li et al., 2015), findings which are consistent with those from fMRI studies. In addition, compared with healthy subjects, it has been found that not only the global Q value increased in both patients with amnestic mild cognitive impairment and patients with Alzheimer's disorder, but also there were two abnormal brain RSFC states in patients with Alzheimer's disorder (Niu et al., 2019). However, these prior investigations of fNIRS-based dRSFC just scratched the surface. Based on fNIRS-based dRSFC, the possibility of evaluating a credible temporal evolution of a specific functional system is not very clear. With the exception of the Q value, other time-resolved characteristics of dRSFC, such as time-varied synchronous and antisynchronous changes between different networks, have not been investigated.

In the present study, we measured the resting-state brain fluctuations of several parts of the frontal, parietal, temporal, and occipital lobes using fNIRS. Based on a sliding-window approach and time-resolved k-means clustering, we extracted the evolution of dominant functional networks among these measured brain areas. We also evaluated the dynamic characteristics within a functional network, as well as the dynamic relationship between networks. Furthermore, we tried to support the credibility of fNIRS-based dRSFC analysis by exploring the relationship between the dynamic fluctuations in dRSFC networks and the switching of electrophysiological microstates based on fNIRS-EEG simultaneously recorded datasets.

MATERIALS AND METHODS

Participants

Twenty young adults (mean age = 25.3, SD = 1.49, 11 male) were recruited from Beijing Normal University to participate in this study. No subjects had motor or other neurological diseases. Before the experiment, informed consent was obtained according to the procedure approved by the Review Board at State Key Laboratory of Cognitive Neuroscience and Learning, Beijing Normal University.

Data Acquisition

All subjects underwent two successive resting-state sessions of fNIRS-EEG simultaneous measurements. One session was scanned with eyes closed; another was scanned with eyes open. Both resting-state sessions had a duration of 8 min. During the experiments, the subjects were seated in a chair in a silent room with dim lighting. The subjects were instructed to keep still with their eyes closed/open, relax their mind, and remain motionless as much as possible. The trigger and the terminal signs of the experiments were presented and synchronized with the fNIRS and EEG equipment using E-prime software (v.1.2, Psychological Software Tools, Pittsburgh, PA, United States). The subjects participated in these two experiments in random order. In the present study, to avoid interference from the RSFC difference between the eyes-closed and eyes-open state (Zou et al., 2009; Wong et al., 2015), we only used the eyes-closed resting-state session data to perform the dRSFC analysis.

fNIRS measurements were conducted with the LABNIRS fNIRS System for Research (Shimadzu Co., Kyoto, Japan). The

absorption of near-infrared light at three wavelengths of 780, 805, and 830 nm was measured with a sampling time of 57 ms. The 18 emitters and 20 detector probes were plugged into a homemade holder that could combine fNIRS optodes and EEG electrodes together. The holder resulted in 40 measurement channels, including 36 standard-distance channels (interoptode distance = 30 mm) and 4 short-distance channels (interoptode distance = 15 mm). To make sure the channels could cover the regions of interest that we had previously defined, we adjusted the arrangement of the emitters and the detectors using a 3D digitizer and the registration function in NIRS-SPM software (Ye et al., 2009). With their help, we captured 3D coordinates from all the standard-distance measurement channels, transformed them to coordinates of the Montreal Neurological Institute standard template, and probabilistically estimated the structural labels as Brodmann areas according to the channels' coordinates. Finally, we set five regions of interest (ROIs), as shown in **Figure 1A**. Furthermore, the four short-distance channels were located above the bilateral frontal area (near channels 4 and 22) and the temporoparietal junction (near channels 9 and 27). While considering the needs of the group analysis, the locations of the emitters and the detectors were marked according to the international 10–20 system (Jasper, 1958).

Electroencephalography data were acquired simultaneously with a 32-channel Ag–AgCl electrode cap (Neuroscan, Inc.) (international 10–20 montage and the vertical and horizontal electrooculograms). All the electrodes were referenced to the linked electrodes placed on the right mastoid. The EEG sampling rate was 1,000 Hz.

fNIRS Data Preprocessing

For the fNIRS raw dataset, we first removed the optical density time courses before and after the experiments according to the start and the end markers set by the E-prime software. The data from one subject was removed because it lacked start/end markers (these markers were necessary for the subsequent analysis of the combined fNIRS and EEG). The concentration changes in HbO and HbR for each channel were then calculated according to the modified Beer–Lambert law (Cope and Delpy, 1988). Because several previous studies (Hoshi, 2007; Lu et al., 2010) showed that the signal/noise ratio of HbO was much higher than that of HbR, this study focused on the HbO concentration changes.

A temporal low-pass filter (<1.5 Hz) and a high-pass filter (>0.01 Hz) were applied to remove the high-frequency noise fluctuations and the ultralow frequency trends. To further remove the systemic physiological interferences arising from the superficial layer (that is, the scalp and skull), such as the vascular fluctuations arising from the cardiac pulsations, respiration, Mayer waves, and other very low-frequency fluctuations, a linear regression analysis was performed. Specifically, for each standard-distance channel, the time course was regressed the average time course for all the short-distance channels. The residual time course after regression was finally filtered again by a low-pass filter (<0.15 Hz) to eliminate the remaining high-frequency noises and retain the spontaneous brain fluctuations.

dRSFC Calculation

For each individual, as the pipeline shown in **Figures 1B,C**, we estimated the dRSFC between any two measurement channels using a sliding-window correlation approach. Specifically, a 20-s time window was selected and then shifted along the entire time course in steps of one 0.057-s time point each. Within each time window, the Pearson correlation was calculated for each pair of measurement channels. Therefore, all the 36 measurement channels had an 8-min measurement duration and a 20-s sliding time window, resulting in $C_{36}^{2} = 630$ pairs with 8,076 time points of dRSFC.

To compare with previous studies that focused on the spatial distribution of the variability of dRSFC, we first quantitatively estimated the variance in the dRSFC fluctuations for each pair of channels. Then, according to the five predefined ROIs, which were described above and are shown in **Figure 1A**, we classified the dRSFC into 15 categories, of which 5 were within ROIs and 10 were between ROIs. The mean value, as well as the standard deviation, of the variability of the dRSFC of each category was calculated. Finally, we compared the mean variability of the dRSFC between two connection groups: within the ROIs and between the ROIs, by a two-sample *t*-test.

For comparison, we also calculated the static RSFC (sRSFC). As shown in **Figures 1B,D**, it was proposed for each subject using a Pearson correlation analysis between any two measurement channels over the whole length of the time series. Then, to assess the sRSFC results at group level, a pair-by-pair one-sample *t*-test was performed across all the subjects and corrected by false discovery rate (FDR).

Clustering Analysis of the dRSFC Fluctuations

To assess the temporal relationship of dRSFC between different connections, we applied a *k*-means clustering algorithm to the temporal fluctuations in the dRSFC. For each individual, we used the L2 (Euclidean) distance function during *k*-means clustering with random initialization of the centroid positions. The number of clusters (k) varied from 2 to 10. To eliminate the influence of random centroid positions, we repeated the clustering analyses 100 times with centroid positions updates. Then, for each k, a ratio (A) between the between-cluster distance and the within-cluster distance for each subject was computed. In our hypothesis, an acceptable value of k should yield greater mean values of A for all individuals with relatively low variance. Therefore, the final k was determined at the group level using the elbow criterion of the cluster validity index, defined as the ratio between the standard deviation of A and the mean value of A across all the subjects. Finally, as shown in **Figure 1E**, the temporal fluctuations in the dRSFC from $C_{36}^{2} = 630$ pairs were classified into k clusters for each subject, of which the centroid positions were the time courses representing the most typical fluctuations in the dRSFC.

Because brain activity during the resting state is not time locked, the fluctuations in the RSFC (temporal structure) could not be directly compared between subjects, but their spatial distribution (spatial structure) could. Therefore, as shown in **Figure 1E**, we collected all the spatial distribution matrices

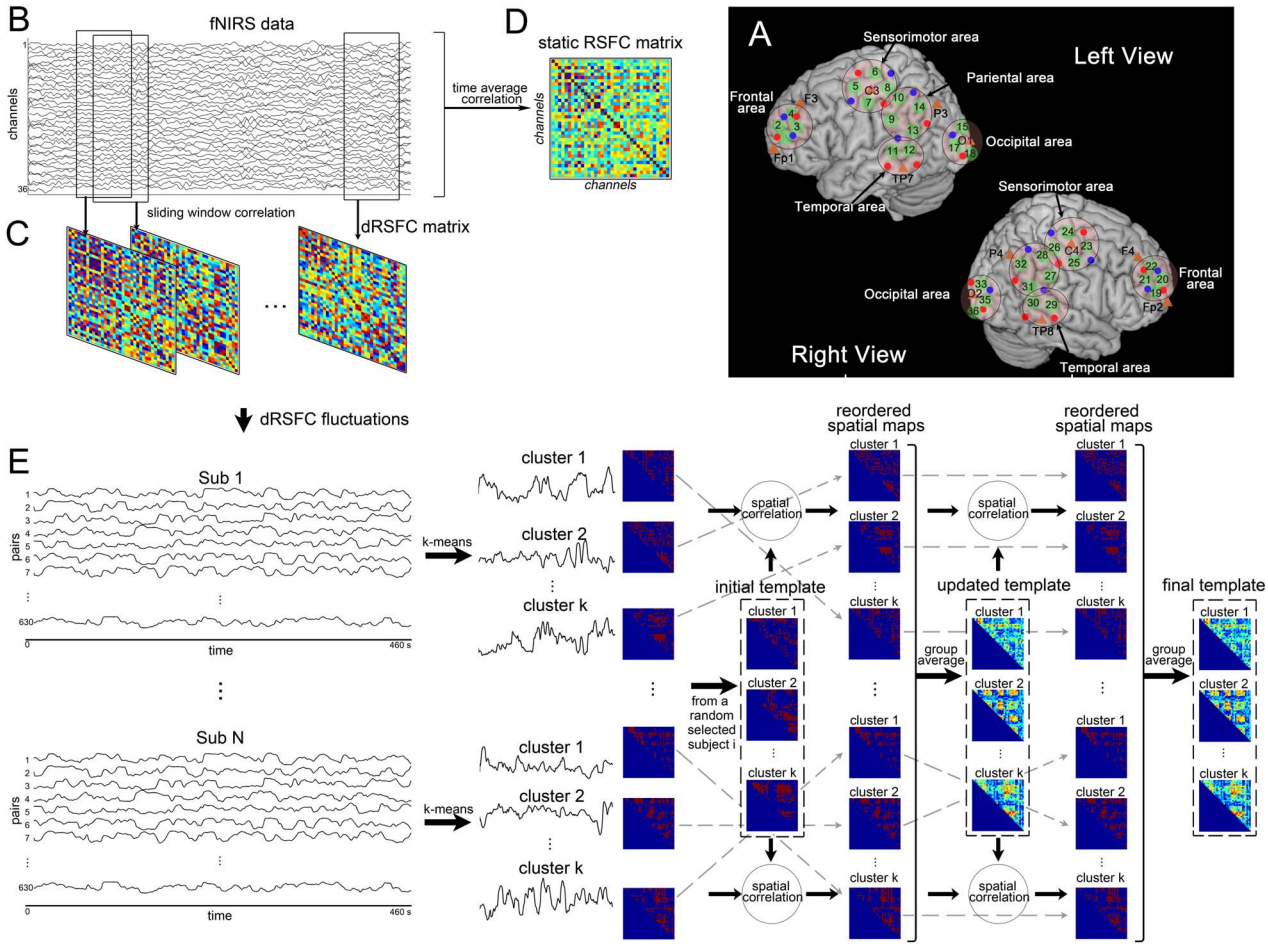

FIGURE 1 | Illustration of functional near-infrared spectroscopy (fNIRS)-based dynamic resting-state functional connectivity (dRSFC) analysis. **(A)** Anatomical positions of the fNIRS standard-distance channels. Green represents the 36 fNIRS measurement channels. Red and blue dots represent the fNIRS emitters and detectors, respectively. The five ROIs were marked by black circles in the left and right views. The short-distance channels are not demonstrated here; two of these were near channels 4 and 22, and the other two were near channels 9 and 27. **(B)** An example of fNIRS data from a random selected subject. **(C)** Static RSFC analysis. The static RSFC was calculated from the time courses of the entire scanning between any two channels. **(D)** Dynamic RSFC analysis. The dRSFC was calculated between any two measurement channels using a sliding-window correlation approach. In this approach, a time window with a fixed length was selected and then shifted along the entire time course in a fixed step. Within each time window, the RSFC was calculated for each pair of measurement channels using the Pearson correlation method. This process results in quantification of time-varying dRSFC over the whole scanning. Owing to the connectivity matrix is symmetric, the effective number of connection pairs among all the 36 measurement channels is $C_{36}^{2} = 630$. **(E)** Pipeline of clustering analysis of the dRSFC fluctuations.

identified for each individual subject and reordered them by two loops so we could use the same labels for the subsequent group analysis. Specifically, for the first loop, we set the k spatial matrices of a random selected subject as the initial template. Then, we computed a spatial correlation of the template with the individual matrices and labeled each individual matrix with the template it best corresponded to. For the second loop, the mean matrix of each cluster was calculated at the group level and set as the updated template. After repeating the above process, the individual spatial matrix was relabeled and unified at the group level.

Furthermore, to assess the transient relationship between the centroid time courses of different clusters, we quantified the instantaneous phases of each time course by a wavelet transform and calculated the time-varied phase difference between them. Specifically, we computed the convolution of the individual centroid time course of dRSFC with a complex Gabor wavelet centered at frequency f:

$$G(t, f) = e^{-\frac{t^2}{2\sigma_t^2}} e^{-j2\pi ft}$$

Here, we set $f = 0.08$ Hz, $\sigma_t = 10$ s. The phase for this convolution was extracted for all time bins t:

$$\theta(t) = \text{angle}(G(t) * x(t))$$

The phase difference between each of the two time courses (x and y) was defined as:

$$\Delta\theta(t) = \theta_x(t) - \theta_y(t)$$

EEG Data Processing

First, we checked the data to remove the redundant time courses before and after the experiments according to the start and the end markers set by the E-prime software. After band-pass filtering from 1 to 100 Hz with a 50-Hz notch filter, the continuous EEG data was re-referenced with the average time course of all the effective channels. The channels with the great noise whose amplitudes were higher than five times the standard deviation of the entire time course were removed.

The EEG microstate was extracted according to the pipeline (introduced in Van de Ville et al., 2010). In general, we first down-sampled the EEG data to 125 Hz to reduce the computational complexity. Then, as shown in **Figure 2A**, we calculated the global field power index, which is the standard deviation of the potentials at all electrodes, for each time point (Brunet et al., 2011). All the time points that contained EEG global field power maxima were determined. These time points were considered to having relatively high signal/noise ratio (Brunet et al., 2011). Therefore, the momentary EEG maps at those time points were extracted as the best representative topographies. Next, using the Cartool software (v 3.55, developed by Functional Brain Mapping Lab, Geneva, Switzerland), a modified spatial cluster analysis applying the atomize-agglomerate hierarchical clustering method was used to identify the most dominant map (i.e., microstates) topographies at the individual level and at the group level. During this process, the optimal number of microstates was determined to be 3 based on a cross-validation criterion, which is derived by dividing the global explained variance by the degrees of freedom (Brunet et al., 2011). To assess the switching time course of the microstates, we calculated the spatial correlation between each instantaneous EEG map and the three group-level template maps. For each time point, the dominant microstate was selected as the one with the greatest spatial correlation. The binary time series corresponding to each microstate was considered to represent the microstate activities.

Correlating With fNIRS-dRSFC and EEG Microstates

Some previous studies have been found that, after convolution with the hemodynamic response function, the prototypical EEG microstates during rest may have ability to explain hemodynamic activities in some specific large-scale resting state networks (Britz et al., 2010; Musso et al., 2010). Therefore, here we evaluated the relationship between the temporal fluctuations of each fNIRS-based dRSFC (the centroid time course for each cluster) and the time course of the EEG microstate switching for each subject. Specifically, as shown in **Figure 2B**, we first convoluted the binary time series of each EEG microstate with the canonical hemodynamic response function, which was generated by SPM toolbox. Then, the resultant smooth microstate time course was down-sampled to 17.5439 Hz, the same as the sampling rate of the fNIRS data, and correlated with the centroid time course for each fNIRS-based dRSFC cluster using the Pearson correlation index (Britz et al., 2010). Hence, we obtained a correlation matrix between all the fNIRS-based dRSFC clusters and all the EEG microstates for each subject. Using the Fisher Z transformation, we got a z-score matrix from the correlation matrix. Finally, we checked the z-scores at the group level using a one-sample t-test.

RESULTS

The sRSFCs between all the fNIRS channels with a standard interoptode distance are demonstrated in **Figure 3**. For clarity, the ROI-level sRSFCs are also shown in connectivity map form and matrix form. Obviously, all the connectivities between the homogeneous interhemispheric areas were significant ($p < 0.01$, FDR corrected). There were also several significant connectivities across the heterogeneous areas, but the connectivities of the occipital area were very limited.

As shown in **Figure 4A**, the dRSFCs between any two ROIs were highly non-stationary. Specifically, the variability of the dRSFCs within the frontal ROIs was generally great and positive at most time points. Such high values are consistent with the results from the sRSFC over the whole measurement time period (sRSFC = 0.649). By contrast, the dRSFC between the heterogeneous regions (F-P and F-O in **Figure 4A**) were relatively lower and exhibited both strongly positive and strongly negative correlations. The sRSFCs in these connectivities were obviously lower than those within the frontal ROIs (sRSFC = 0.208 for the F-P connectivity, and sRSFC = −0.135 for the F-O connectivity).

For the quantitative analysis, we evaluated the dRSFC variability of the connectivities within and between the ROIs. As shown in **Figure 4B**, the variability of the dRSFC within the ROIs was significantly lower than that between the ROIs ($p < 0.001$, Bonferroni corrected); this is consistent with the findings in previous studies (Allen et al., 2014; Li et al., 2015). In addition, by comparison with the variability in the correlation between the channels with a short interoptode distance, the variability in the dRSFC between channels with standard interoptode distances was significantly greater both within and between ROIs ($p < 0.001$, Bonferroni corrected). This implies that the dRSFC oscillations between the channels with a standard distance have some functional significance, rather than being caused by physiological noise. Specific to the connectivities between ROIs, as shown in **Figure 4C**, the connectivities with the greatest variability were primarily related to the frontal area, especially occurring between the frontal and the temporal areas.

After the temporal clustering analysis, four dRSFC clusters were extracted, and the probability of occurrence of each connectivity across the subjects was calculated for each cluster. For clarity, the connections for which the probability of occurrence was more than 50% are shown in the channel-level connectivity map (**Figure 5**). Furthermore, we averaged the probability of occurrence according to the regions to which the two nodes belong and drew the ROI-level group consistency matrix for each cluster. Obviously, cluster 1 was primarily concentrated in the connectivities between the bilateral frontal, parietal, and temporal areas. Cluster 2 was concentrated in the connections with the occipital area. Clusters 3 and 4 were primarily concentrated in the connections with the sensorimotor area, in which the first one was bilaterally symmetrical and the latter one was obviously lateralized to the left. It should be noted

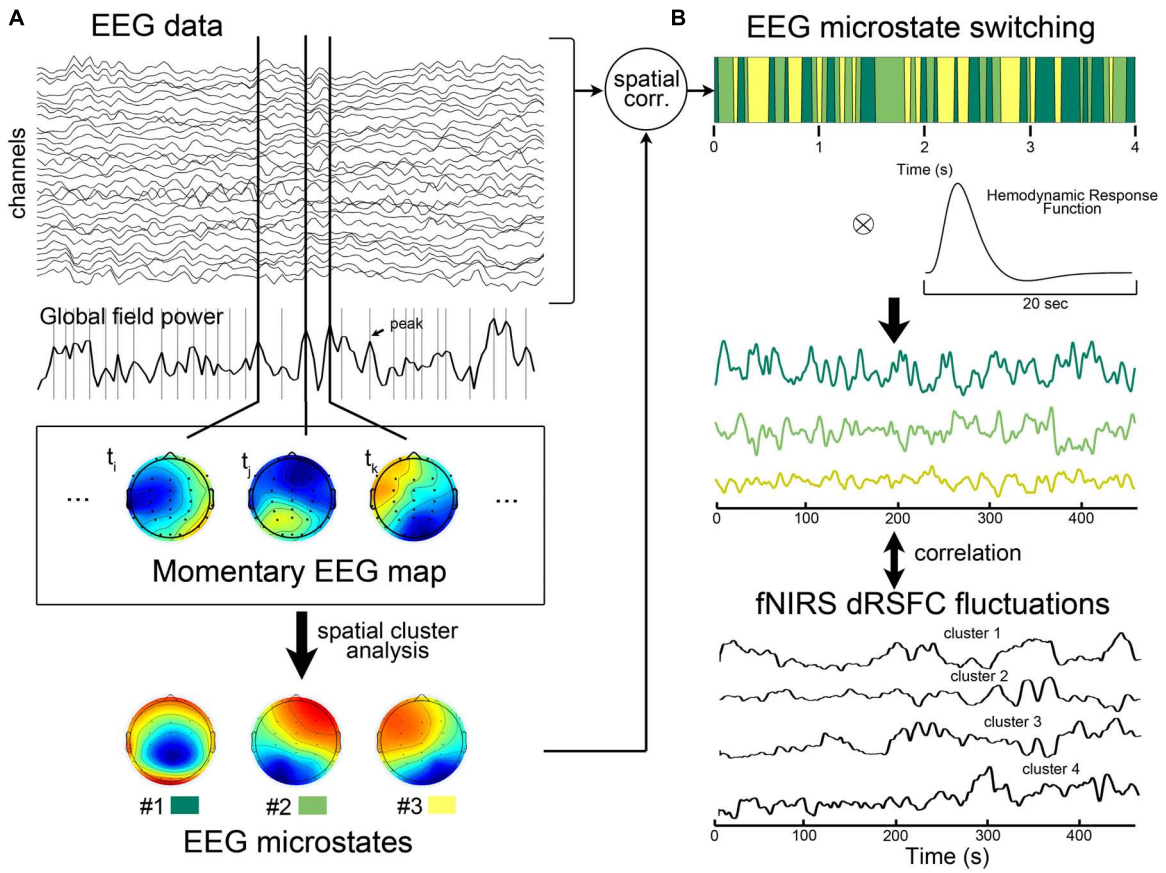

FIGURE 2 | Illustration of electroencephalography (EEG)-microstate analysis and the correlation analysis between EEG microstates and fNIRS-based dRSFC fluctuations. **(A)** EEG microstate analysis. The EEG microstate was identified by a modified spatial cluster analysis from all the individual momentary EEG maps with the maxima global field powers. During this process, the optimal number of microstates was determined to be 3 based on a cross-validation criterion, which is derived by dividing the global explained variance by the degrees of freedom. **(B)** After calculating the spatial correlation between each instantaneous EEG map and the three group-level template maps, the dominant microstate was identified as the one with the greatest spatial correlation at that time point. The previous studies have shown that after the convolution of the binary time course of a EEG microstate with the hemodynamic response function, the resultant temporal smoothed signal correlated with hemodynamic fluctuations of the large-scale functional networks. Therefore, we proposed the correlation analysis between the smoothed microstate-switching signals with fNIRS-dRSFC fluctuations.

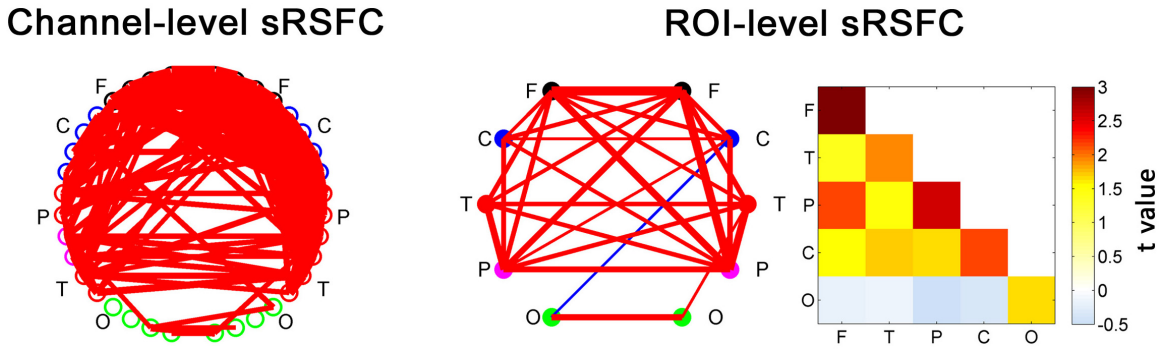

FIGURE 3 | The static RSFC (sRSFC) between all the fNIRS channels with a standard interoptode distance. The sRSFCs, which are significantly greater/lower than zero at the group level ($p < 0.01$, FDR corrected), are indicated by the red/blue lines, respectively. The width of the line represents the strength of the *t*-value (one-sample *t*-test at the group level). For clarity, the ROI-level sRSFCs are shown in two forms: connectivity network map and matrix. They are the group-level statistic results after categorizing and averaging the connection edges according to an ROI partition of the nodes for each individual. F, frontal area; C, sensorimotor area; P, parietal area; T, temporal area; O, occipital area.

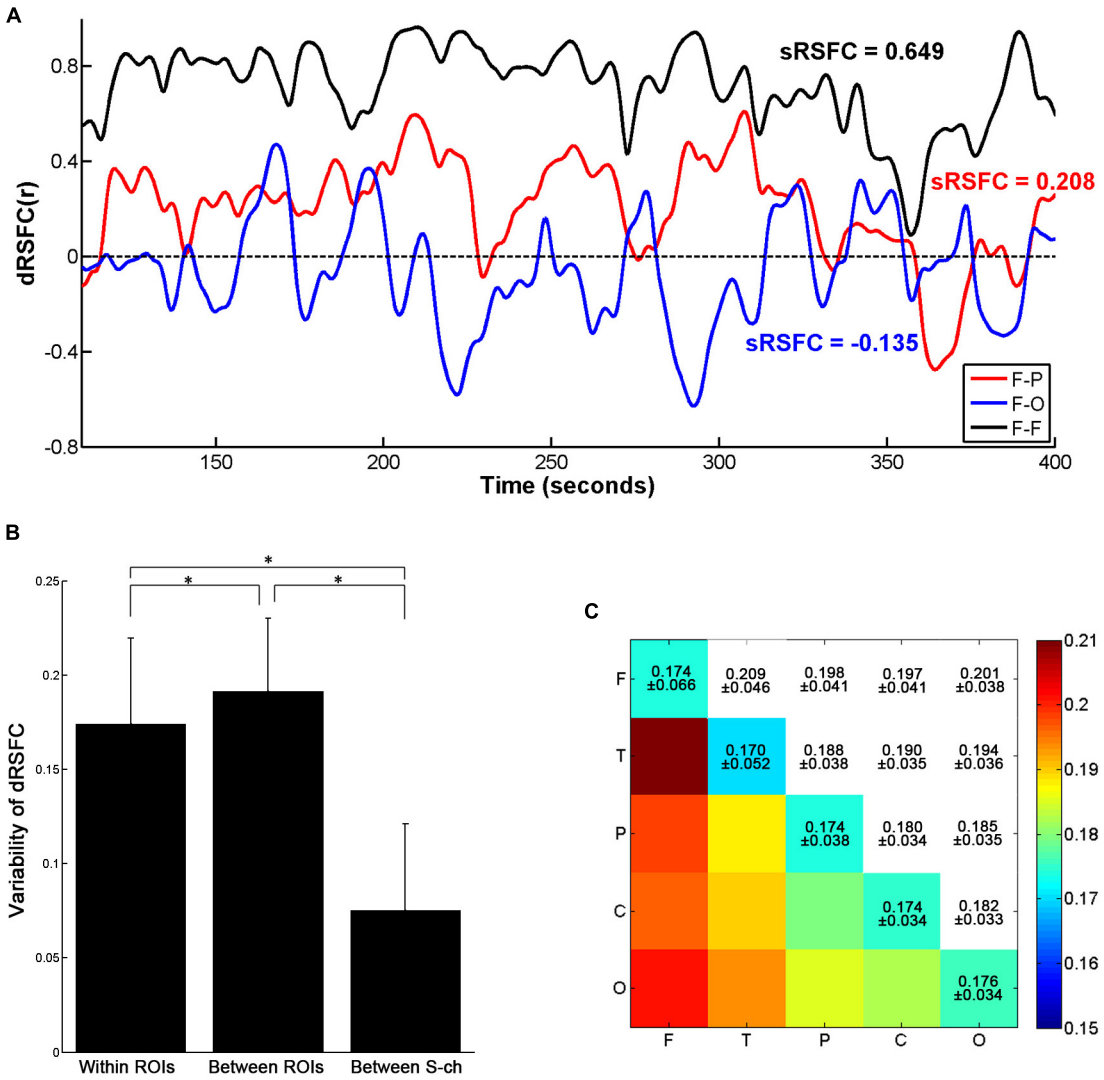

FIGURE 4 | Variability of the dRSFCs. **(A)** Examples of dRSFC fluctuations for a representative subject (subject 1). The black line indicates the dRSFC between the bilateral frontal ROIs; the red line indicates the dRSFC between the frontal and the parietal ROIs; and the blue line indicates the connectivity between the frontal and the occipital ROIs. F, frontal area; P, parietal area; T, temporal area; O, occipital area. **(B)** Group comparison of variability of the dRSFC within and between ROIs and between channels with a short interoptode distance (S-ch). Error bars indicate standard deviations. Asterisks represent significant group differences with a *t*-test at $p < 0.001$ (Bonferroni corrected). **(C)** The means and standard deviations of the dRSFC variability between different ROIs at the group level.

that, as shown in the probability of the occurrence matrix, cluster 4 had a relatively low consistency across the subjects compared with the other three clusters.

By a Gaber wavelet transform, we calculated the instantaneous phase difference between the centroid time courses of the four clusters. As shown in **Figure 6**, they constantly switched between positive correlation, negative correlation, and anticorrelation, accompanied by some system-specific preferences. For example, cluster 1 was positively synchronized with cluster 3/4 most of the time, but sometimes this was reversed. In contrast, cluster 1 was primarily negatively synchronized with cluster 2 most of the time.

Figure 7 presents the topographies of the EEG microstates and the relationship between the temporal fluctuations of each fNIRS-based dRSFC (the centroid time course for each cluster) and the switching time course of the EEG microstates. The oscillation of cluster 1 was significantly correlated with the switching of the EEG microstate 1 ($p = 0.031$, uncorrected), but the other clusters did not demonstrate a significant correlation with the switching between EEG microstates.

We also evaluated the reproducibility of the primary findings in this study. First, based on a sliding time window size of 20 s, we randomly divided the subjects into two subgroups and repeated the analysis to examine the impact of varying the subject datasets. As shown in **Figure 8A**, the main results, e.g., based on the temporal dRSFC clustering analysis, show that three kinds of functional networks could be extracted: the frontal-parietal-temporal network (cluster 1), the occipital network (cluster 2), and the sensorimotor network (cluster 3), keeping good

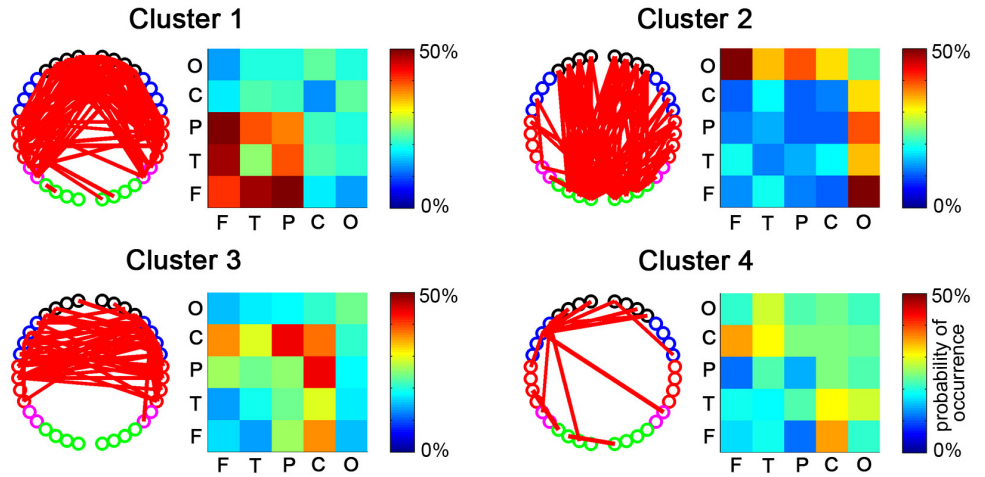

FIGURE 5 | The spatial distributions of dRSFC clusters. For each cluster, the connectivity map with the dominant channel-level connectivity (left) and the ROI-level group consistency matrix (right) are demonstrated. The red lines in the left maps represent the dominant connectivity that occurred in this cluster in more than half of the participants. The values in the right matrix represent the average probability of occurrence at the group level.

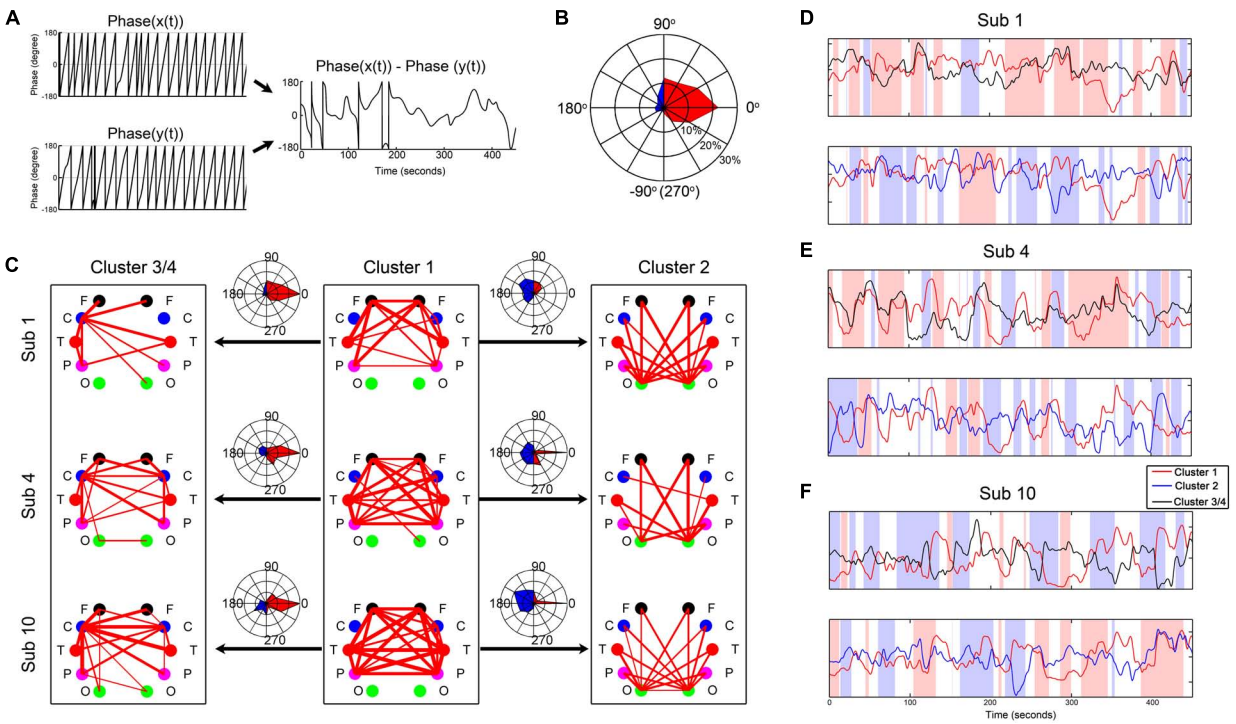

FIGURE 6 | Demonstration of the instantaneous phase difference between the centroid time courses of the clusters from three representative subjects. **(A)** Illustration of the instantaneous phase difference calculation. **(B)** An example of the fingerprint map which intuitively displays the result of phase difference in **(A)**. The fingerprint map refers to the percentage of each phase difference across the whole measurement time. The three concentric circles represent 10, 20, and 30%, respectively. **(C)** Demonstration of the instantaneous phase difference between the centroid time courses of the clusters from three representative subjects. **(D–F)** The corresponding centroid time courses of the clusters from the three subjects. The pink background represents the moments with positive synchronization (−45–45°), and the blue background shows the moments with reverse synchronization (135–225°).

consistency with the results from the entire subject groups. However, we also found that cluster 4, which had a relatively lower consistency in the entire subject group (as shown in the probability matrix of occurrence in **Figure 5**), also had relatively low consistency between the different subgroups. Second, using the entire subject group, we also separately used sliding time window sizes of 20, 30, and 60 s to examine the impact of varying the window lengths on the dynamic RSFC findings. The

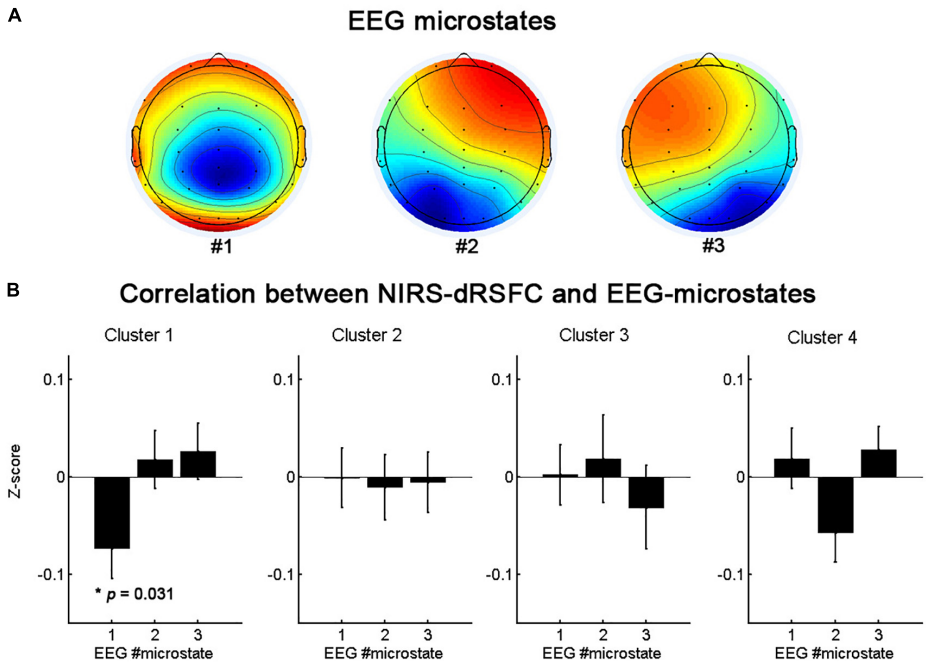

FIGURE 7 | The topographies of the EEG microstates **(A)** and the statistical analysis results **(B)** for the correlation between the temporal fluctuations of fNIRS-based dRSFC clusters and the switching time course of the EEG microstates.

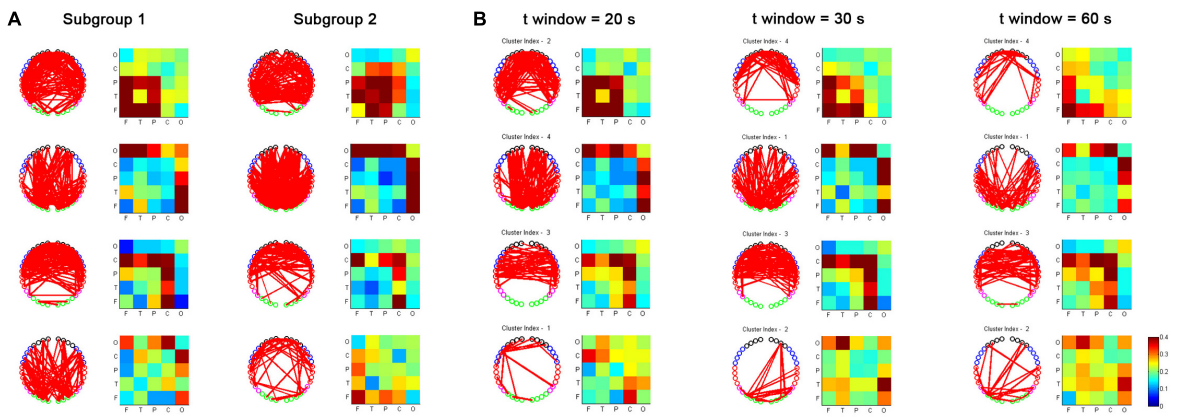

FIGURE 8 | Reproducibility of fNIRS-based dRSFC from two randomly selected subgroups of subjects **(A)** and fNIRS-based dRSFC with different time window lengths (20, 30, and 60 s) **(B)**.

cluster results (**Figure 8B**) were generally consistent with the investigations reported above.

DISCUSSION

In this study, we first extracted the dynamic fluctuations of fNIRS-based RSFC over specific regions in the frontal, temporal, parietal, and occipital areas. Consistent with the findings in previous studies (Li et al., 2015), the variability of the dRSFC within the ROIs was significantly lower than that between the ROIs ($p < 0.001$, Bonferroni corrected), possibly resulting from relatively stable information interactions within a local region (Allen et al., 2014; Zalesky et al., 2014). The variability of the dRSFC, not only between ROIs but also within ROIs, was significantly greater than the variability in the correlation between the fNIRS channels with a short interoptode distance, an area which is located above the bilateral frontal area and the temporoparietal junction. It is known that channels with a short distance primarily consist of physiological fluctuations in the superficial layers. Therefore, this evidence implies that our fNIRS-based dRSFC oscillations have some functional significance, rather than being caused by physiological noise.

Second, by using time-resolved k-means clustering, we extracted dRSFC clusters, which were primarily focused in the three dominant functional systems. These were the frontal-parietal-temporal network, the occipital network, and the sensorimotor network. These networks are very consistent between different subject subgroups and in varying sliding time window lengths of 20, 30, and 60 s. These results confirm that the dominant functional networks could be well identified and extracted based on the time-resolved clustering of fNIRS-based dRSFC. Most importantly, we reproducibly identified the occipital network, as well as the connectivities between the occipital area and anterior regions (such as the frontal area). Such connections are critical for visual object processing (Sehatpour et al., 2008) and consciousness (Giacino et al., 2014; Koch et al., 2016) but may not be revealed by static fNIRS-based RSFC (Mesquita et al., 2010). As reported in previous works, the most dynamic connections always correspond to the weakest stationary RSFC (Li et al., 2015) because the dynamic RSFCs are near zero in the time averages. Thus, it is apparent that, since analyses using the stationary assumption reduce the information about RSFC fluctuations to time averages, these convenient RSFC analyses may have led to an oversimplified characterization of the brain's functional networks. The successful extraction of the occipital network in the present study suggests that assessing functional connectivity from their dynamic characteristics could rectify the deficiency of the static fNIRS-based RSFC by identifying some "hidden" functional connectivity/system.

We also evaluated the synchrony between the different functional networks and found how the synchrony varied through time. The networks constantly switch between positive correlation, negative correlation, and anticorrelation, accompanied by some system-specific preferences. The frontal-parietal-temporal network (cluster 1), for example, was primarily positively synchronized with the sensorimotor network (cluster 3/4) and negatively synchronized with the occipital network (cluster 2) during most of the time intervals, but sometimes this was reversed. This finding is consistent with a previous fMRI-based dynamic RSFC analysis that found that the temporal fluctuations of the dRSFC were an essential property that can unveil flexibility in the dynamic functional coordination between different neural systems (Allen et al., 2014). In particular, based on time-resolved methodologies for analyzing the variability of the dRSFC, most dynamic connectivities were found to be intermodular (i.e., to link elements from the separable subsystems) and localized to known hubs, such as the default mode regions, superior occipital networks, and fronto-parietal systems (Allen et al., 2014; Zalesky et al., 2014). Their alternating pattern of correlations and anticorrelations implies that these intermodular regions may be connected with specific systems for a fraction of the time. That is, the multiple functional associations among these systems are realized through a dynamic process of time-division multiplexing (Zalesky et al., 2014).

Similar to the dynamic functional connectivity of brain hemodynamic activation, the momentary global state of the neurophysiological activities does not change randomly and continuously over time (Lehmann et al., 1987; Van de Ville et al., 2010). These momentary global states, termed "EEG microstates," remain stable for ∼80–120 ms and can be assessed by analyzing the temporal evolution of the EEG scalp topography. With a limited number of prototypical configurations, EEG microstates are persistently identified across the entire life span (Keilholz et al., 2013). The changing of the EEG microstates in the resting state indicates that rapid switching between the activities of the neural assemblies of the brain occurs. Research has showed that, after convolution with the hemodynamic response function, the rapidly fluctuating EEG microstates correlate significantly with the slow oscillations of fMRI resting-state networks (Britz et al., 2010; Musso et al., 2010; Yuan et al., 2012). In the present study, to further support the credibility of the dRSFC data and to explore the neural basis of the RSFC dynamic fluctuation, we evaluated the relationship between the temporal fluctuations of each fNIRS-based dRSFC (the centroid time course of each cluster) and the switching time course of EEG microstates based on simultaneous recording fNIRS-EEG datasets. We found that the oscillation of the frontal-parietal-temporal network (cluster 1) was significantly correlated with the switching of the EEG microstate 1. The spatial distributions of the these three EEG microstates are generally consistent with the map in the previous EEG microstate studies (Britz et al., 2010; Khanna et al., 2015). EEG microstate 1 roughly corresponded to map 4 in Britz et al., 2010, which was found to be significantly correlated with the hemodynamic activity in a right-lateralized dorsal frontoparietal network, mainly contributing to switching and reorienting attention. It is consistent with the findings in the present study, implying the credibility of fNIRS-based dRSFC networks.

In previous fMRI-based dRSFC studies, the dorsal attention areas and default-mode regions were consistently assigned to the partition with a more variable connectivity (Allen et al., 2014; Zalesky et al., 2014). In our study, however, the connections with the greatest variability were primarily related to the frontal area, especially between the frontal and the temporal areas. We guess that this discrepancy may have result from the relatively better signal/noise ratio in the frontal area during the fNIRS data acquisition. This finding reminds us that the variability analysis in fNIRS-based dRSFC could be influenced by the signal/noise ratio of the data. Future research needs to be careful to avoid this disruptive factor.

In this study, although clusters 1–3 were highly consistent; cluster 4 had a relatively lower consistency between the different subject subgroups, within any subject group, or across different time window lengths. We are not sure about the exact reason but speculate that this may have been due to uncontrollable behavior and mental diversity between individuals and at different time points. This may also have resulted from the diversity of the spatial localization of the fNIRS measurement channels between subjects. This needs to be further investigated in future studies with a larger sample size and repeated measurements.

CONCLUSION

In conclusion, this study demonstrated the functional significance of fNIRS-dRSFC and the feasibility of fNIRS for

extracting the dominant functional networks based on RSFC dynamics. Because of the advantages of fNIRS in clinical applications, fNIRS-based dRSFC research could help researchers gain insight into the relationship between time-varying brain activity patterns and critical aspects of cognition and behavior by making up for the deficiencies of stable RSFC research.

DATA AVAILABILITY STATEMENT

The datasets generated for this study are available on request to the corresponding author.

ETHICS STATEMENT

The studies involving human participants were reviewed and approved by the Review Board at State Key Laboratory of Cognitive Neuroscience and Learning, Beijing Normal University. The participants provided their written informed consent to participate in this study.

AUTHOR CONTRIBUTIONS

YZ and CZ contributed to the conception and design of the study. YZ organized the database, performed the analysis, and wrote the first draft of the manuscript. CZ contributed to the manuscript revision.

FUNDING

This work was supported by the National Key Research and Development Program of China (2017YFB1002502), the National Natural Science Foundation of China (Grant nos. 81871398 and 61431002), and Open Research Fund of the State Key Laboratory of Cognitive Neuroscience and Learning.

ACKNOWLEDGMENTS

We thank Edmund F. Perozzi and Rhoda E. Perozzi, Ph.Ds. for editing and English language assistance.

REFERENCES

Allen, E. A., Damaraju, E., Plis, S. M., Erhardt, E. B., Eichele, T., and Calhoun, V. D. (2014). Tracking whole-brain connectivity dynamics in the resting state. *Cereb. Cortex* 24, 663–676. doi: 10.1093/cercor/bhs352

Britz, J., Van De Ville, D., and Michel, C. M. (2010). BOLD correlates of EEG topography reveal rapid resting-state network dynamics. *Neuroimage* 52, 1162–1170. doi: 10.1016/j.neuroimage.2010.02.052

Brunet, D., Murray, M. M., and Michel, C. M. (2011). Spatiotemporal analysis of multichannel EEG: CARTOOL. *Comput. Intell. Neurosci.* 2011:813870. doi: 10.1155/2011/813870

Bunce, S. C., Izzetoglu, M., Izzetoglu, K., Onaral, B., and Pourrezaei, K. (2006). Functional near-infrared spectroscopy. *IEEE Eng. Med. Biol. Mag.* 25, 54–62.

Chang, C., and Glover, G. H. (2010). Time-frequency dynamics of resting-state brain connectivity measured with fMRI. *Neuroimage* 50, 81–98. doi: 10.1016/j.neuroimage.2009.12.011

Cope, M., and Delpy, D. T. (1988). System for long-term measurement of cerebral blood and tissue oxygenation on newborn infants by near infrared transillumination. *Med. Biol. Eng. Comput.* 26, 289–294. doi: 10.1007/bf02447083

Damaraju, E., Allen, E. A., Belger, A., Ford, J. M., McEwen, S., Mathalon, D. H., et al. (2014). Dynamic functional connectivity analysis reveals transient states of dysconnectivity in schizophrenia. *Neuroimage Clin.* 5, 298–308. doi: 10.1016/j.nicl.2014.07.003

Demirtas, M., Tornador, C., Falcon, C., Lopez-Sola, M., Hernandez-Ribas, R., Pujol, J., et al. (2016). Dynamic functional connectivity reveals altered variability in functional connectivity among patients with major depressive disorder. *Hum. Brain Mapp.* 37, 2918–2930. doi: 10.1002/hbm.23215

Duan, L., Zhang, Y. J., and Zhu, C. Z. (2012). Quantitative comparison of resting-state functional connectivity derived from fNIRS and fMRI: a simultaneous recording study. *Neuroimage* 60, 2008–2018. doi: 10.1016/j.neuroimage.2012.02.014

Fu, Z., Caprihan, A., Chen, J., Du, Y., Adair, J. C., Sui, J., et al. (2019). Altered static and dynamic functional network connectivity in Alzheimer's disease and subcortical ischemic vascular disease: shared and specific brain connectivity abnormalities. *Hum. Brain Mapp.* 40, 3203–3221. doi: 10.1002/hbm.24591

Giacino, J. T., Fins, J. J., Laureys, S., and Schiff, N. D. (2014). Disorders of consciousness after acquired brain injury: the state of the science. *Nat. Rev. Neurol.* 10, 99–114. doi: 10.1038/nrneurol.2013.279

Homae, F., Watanabe, H., Nakano, T., and Taga, G. (2011). Large-scale brain networks underlying language acquisition in early infancy. *Front. Psychol.* 2:93. doi: 10.3389/fpsyg.2011.00093

Hoshi, Y. (2007). Functional near-infrared spectroscopy: current status and future prospects. *J. Biomed. Opt.* 12:062106. doi: 10.1117/1.2804911

Hutchison, R. M., Womelsdorf, T., Allen, E. A., Bandettini, P. A., Calhoun, V. D., Corbetta, M., et al. (2013a). Dynamic functional connectivity: promise, issues, and interpretations. *Neuroimage* 80, 360–378. doi: 10.1016/j.neuroimage.2013.05.079

Hutchison, R. M., Womelsdorf, T., Gati, J. S., Everling, S., and Menon, R. S. (2013b). Resting-state networks show dynamic functional connectivity in awake humans and anesthetized macaques. *Hum. Brain Mapp.* 34, 2154–2177. doi: 10.1002/hbm.22058

Jasper, H. H. (1958). The ten-twenty electrode system of the international federation. *Electroencephalogr. Clin. Neurophysiol.* 10, 371–375.

Jones, D. T., Machulda, M. M., Vemuri, P., McDade, E. M., Zeng, G., Senjem, M. L., et al. (2011). Age-related changes in the default mode network are more advanced in Alzheimer disease. *Neurology* 77, 1524–1531. doi: 10.1212/WNL.0b013e318233b33d

Keilholz, S. D., Magnuson, M. E., Pan, W. J., Willis, M., and Thompson, G. J. (2013). Dynamic properties of functional connectivity in the rodent. *Brain Connect* 3, 31–40. doi: 10.1089/brain.2012.0115

Khanna, A., Pascual-Leone, A., Michel, C. M., and Farzan, F. (2015). Microstates in resting-state EEG: current status and future directions. *Neurosci. Biobehav. Rev.* 49, 105–113. doi: 10.1016/j.neubiorev.2014.12.010

Koch, C., Massimini, M., Boly, M., and Tononi, G. (2016). Neural correlates of consciousness: progress and problems. *Nat. Rev. Neurosci.* 17, 307–321. doi: 10.1038/nrn.2016.22

Kucyi, A., Hove, M. J., Esterman, M., Hutchison, R. M., and Valera, E. M. (2017). Dynamic brain network correlates of spontaneous fluctuations in attention. *Cereb. Cortex* 27, 1831–1840. doi: 10.1093/cercor/bhw029

Lehmann, D., Ozaki, H., and Pal, I. (1987). EEG alpha map series: brain micro-states by space-oriented adaptive segmentation. *Electroencephalogr. Clin. Neurophysiol.* 67, 271–288. doi: 10.1016/0013-4694(87)90025-3

Li, Z., Liu, H., Liao, X., Xu, J., Liu, W., Tian, F., et al. (2015). Dynamic functional connectivity revealed by resting-state functional near-infrared spectroscopy. *Biomed. Opt. Express* 6, 2337–2352. doi: 10.1364/BOE.6.002337

Lu, C. M., Zhang, Y. J., Biswal, B. B., Zang, Y. F., Peng, D. L., and Zhu, C. Z. (2010). Use of fNIRS to assess resting state functional connectivity. *J. Neurosci. Methods* 186, 242–249. doi: 10.1016/j.jneumeth.2009.11.010

Majeed, W., Magnuson, M., Hasenkamp, W., Schwarb, H., Schumacher, E. H., Barsalou, L., et al. (2011). Spatiotemporal dynamics of low frequency BOLD fluctuations in rats and humans. *Neuroimage* 54, 1140–1150. doi: 10.1016/j.neuroimage.2010.08.030

Mesquita, R. C., Franceschini, M. A., and Boas, D. A. (2010). Resting state functional connectivity of the whole head with near-infrared spectroscopy. *Biomed. Opt. Express* 1, 324–336.

Mueller, S., Wang, D., Fox, M. D., Yeo, B. T., Sepulcre, J., Sabuncu, M. R., et al. (2013). Individual variability in functional connectivity architecture of the human brain. *Neuron* 77, 586–595. doi: 10.1016/j.neuron.2012.12.028

Musso, F., Brinkmeyer, J., Mobascher, A., Warbrick, T., and Winterer, G. (2010). Spontaneous brain activity and EEG microstates. A novel EEG/fMRI analysis approach to explore resting-state networks. *Neuroimage* 52, 1149–1161. doi: 10.1016/j.neuroimage.2010.01.093

Niu, H., and He, Y. (2014). Resting-state functional brain connectivity: lessons from functional near-infrared spectroscopy. *Neuroscientist* 20, 173–188. doi: 10.1177/1073858413502707

Niu, H., Zhu, Z., Wang, M., Li, X., Yuan, Z., Sun, Y., et al. (2019). Abnormal dynamic functional connectivity and brain states in Alzheimer's diseases: functional near-infrared spectroscopy study. *Neurophotonics* 6:025010. doi: 10.1117/1.NPh.6.2.025010

Sanfratello, L., Houck, J. M., and Calhoun, V. D. (2019). Dynamic functional network connectivity in schizophrenia with magnetoencephalography and functional magnetic resonance imaging: do different timescales tell a different story? *Brain Connect* 9, 251–262. doi: 10.1089/brain.2018.0608

Sehatpour, P., Molholm, S., Schwartz, T. H., Mahoney, J. R., Mehta, A. D., Javitt, D. C., et al. (2008). A human intracranial study of long-range oscillatory coherence across a frontal-occipital-hippocampal brain network during visual object processing. *Proc. Natl. Acad. Sci. U.S.A.* 105, 4399–4404. doi: 10.1073/pnas.0708418105

Van de Ville, D., Britz, J., and Michel, C. M. (2010). EEG microstate sequences in healthy humans at rest reveal scale-free dynamics. *Proc. Natl. Acad. Sci. U.S.A.* 107, 18179–18184. doi: 10.1073/pnas.1007841107

White, B. R., Snyder, A. Z., Cohen, A. L., Petersen, S. E., Raichle, M. E., Schlaggar, B. L., et al. (2009). Resting-state functional connectivity in the human brain revealed with diffuse optical tomography. *Neuroimage* 47, 148–156. doi: 10.1016/j.neuroimage.2009.03.058

Wong, C. W., DeYoung, P. N., and Liu, T. T. (2015). Differences in the resting-state fMRI global signal amplitude between the eyes open and eyes closed states are related to changes in EEG vigilance. *Neuroimage* 124(Pt A), 24–31. doi: 10.1016/j.neuroimage.2015.08.053

Ye, J. C., Tak, S., Jang, K. E., Jung, J., and Jang, J. (2009). NIRS-SPM: statistical parametric mapping for near-infrared spectroscopy. *Neuroimage* 44, 428–447. doi: 10.1016/j.neuroimage.2008.08.036

Yuan, H., Zotev, V., Phillips, R., Drevets, W. C., and Bodurka, J. (2012). Spatiotemporal dynamics of the brain at rest–exploring EEG microstates as electrophysiological signatures of BOLD resting state networks. *Neuroimage* 60, 2062–2072. doi: 10.1016/j.neuroimage.2012.02.031

Zalesky, A., Fornito, A., Cocchi, L., Gollo, L. L., and Breakspear, M. (2014). Time-resolved resting-state brain networks. *Proc. Natl. Acad. Sci. U.S.A.* 111, 10341–10346. doi: 10.1073/pnas.1400181111

Zhang, H., Zhang, Y. J., Duan, L., Ma, S. Y., Lu, C. M., and Zhu, C. Z. (2011). Is resting-state functional connectivity revealed by functional near-infrared spectroscopy test-retest reliable? *J. Biomed. Opt.* 16:067008. doi: 10.1117/1.3591020

Zhang, H., Zhang, Y. J., Lu, C. M., Ma, S. Y., Zang, Y. F., and Zhu, C. Z. (2010). Functional connectivity as revealed by independent component analysis of resting-state fNIRS measurements. *Neuroimage* 51, 1150–1161. doi: 10.1016/j.neuroimage.2010.02.080

Zhang, J., Cheng, W., Liu, Z., Zhang, K., Lei, X., Yao, Y., et al. (2016). Neural, electrophysiological and anatomical basis of brain-network variability and its characteristic changes in mental disorders. *Brain* 139(Pt 8), 2307–2321. doi: 10.1093/brain/aww143

Zhang, Y. J., Lu, C. M., Biswal, B. B., Zang, Y. F., Peng, D. L., and Zhu, C. Z. (2010). Detecting resting-state functional connectivity in the language system using functional near-infrared spectroscopy. *J. Biomed. Opt.* 15:047003. doi: 10.1117/1.3462973

Zou, Q., Long, X., Zuo, X., Yan, C., Zhu, C., Yang, Y., et al. (2009). Functional connectivity between the thalamus and visual cortex under eyes closed and eyes open conditions: a resting-state fMRI study. *Hum. Brain. Mapp.* 30, 3066–3078. doi: 10.1002/hbm.20728

Conflict of Interest: The authors declare that the research was conducted in the absence of any commercial or financial relationships that could be construed as a potential conflict of interest.

Copyright © 2020 Zhang and Zhu. This is an open-access article distributed under the terms of the Creative Commons Attribution License (CC BY). The use, distribution or reproduction in other forums is permitted, provided the original author(s) and the copyright owner(s) are credited and that the original publication in this journal is cited, in accordance with accepted academic practice. No use, distribution or reproduction is permitted which does not comply with these terms.

frontiers in Neuroscience

ORIGINAL RESEARCH
published: 31 January 2020
doi: 10.3389/fnins.2020.00032

Resting-State Functional Connectivity Estimated With Hierarchical Bayesian Diffuse Optical Tomography

Takatsugu Aihara[1,2], Takeaki Shimokawa[2], Takeshi Ogawa[3], Yuto Okada[4], Akihiro Ishikawa[5], Yoshihiro Inoue[5] and Okito Yamashita[2,6]*

[1] Graduate School of Human and Environmental Studies, Kyoto University, Kyoto, Japan, [2] Neural Information Analysis Laboratories, Advanced Telecommunications Research Institute International, Kyoto, Japan, [3] Cognitive Mechanisms Laboratories, Advanced Telecommunications Research Institute International, Kyoto, Japan, [4] Graduate School of Information Science, Nara Institute of Science and Technology, Nara, Japan, [5] Medical Systems Division, Research and Development Department, Shimadzu Corporation, Kyoto, Japan, [6] RIKEN Center for Advanced Intelligence Project, Tokyo, Japan

OPEN ACCESS

Edited by:
Yunjie Tong, Purdue University, United States

Reviewed by:
Han Zhang, University of North Carolina at Chapel Hill, United States
Shijie Zhao, Northwestern Polytechnical University, China

***Correspondence:**
Takatsugu Aihara
aihara@atr.jp

Specialty section:
This article was submitted to Brain Imaging Methods, a section of the journal Frontiers in Neuroscience

Received: *20 October 2019*
Accepted: *13 January 2020*
Published: *31 January 2020*

Citation:
Aihara T, Shimokawa T, Ogawa T, Okada Y, Ishikawa A, Inoue Y and Yamashita O (2020) Resting-State Functional Connectivity Estimated With Hierarchical Bayesian Diffuse Optical Tomography. Front. Neurosci. 14:32. doi: 10.3389/fnins.2020.00032

Resting-state functional connectivity (RSFC) has been generally assessed with functional magnetic resonance imaging (fMRI) thanks to its high spatial resolution. However, fMRI has several disadvantages such as high cost and low portability. In addition, fMRI may not be appropriate for people with metal or electronic implants in their bodies, with claustrophobia and who are pregnant. Diffuse optical tomography (DOT), a method of neuroimaging using functional near-infrared spectroscopy (fNIRS) to reconstruct three-dimensional brain activity images, offers a non-invasive alternative, because fNIRS as well as fMRI measures changes in deoxygenated hemoglobin concentrations and, in addition, fNIRS is free of above disadvantages. We recently proposed a hierarchical Bayesian (HB) DOT algorithm and verified its performance in terms of task-related brain responses. In this study, we attempted to evaluate the HB DOT in terms of estimating RSFC. In 20 healthy males (21–38 years old), 10 min of resting-state data was acquired with 3T MRI scanner or high-density NIRS on different days. The NIRS channels consisted of 96 long (29-mm) source-detector (SD) channels and 56 short (13-mm) SD channels, which covered bilateral frontal and parietal areas. There were one and two resting-state runs in the fMRI and fNIRS experiments, respectively. The reconstruction performances of our algorithm and the two currently prevailing algorithms for DOT were evaluated using fMRI signals as a reference. Compared with the currently prevailing algorithms, our HB algorithm showed better performances in both the similarity to fMRI data and inter-run reproducibility, in terms of estimating the RSFC.

Keywords: resting-state functional connectivity (RSFC), near-infrared spectroscopy (NIRS), diffuse optical tomography (DOT), hierarchical Bayesian estimation algorithm, minimum norm algorithm

INTRODUCTION

Brain consists of spatially distributed regions that have their own function, but these regions are functionally connected, that is, they continuously send information to each other. Recent progress in the acquisition and analysis of functional neuroimaging data has made it possible to explore functional connectivity in the human brain. Functional connectivity is defined as a temporal correlation of neuronal activation patterns between anatomically distant brain regions and has been assessed using various non-invasive functional neuroimaging modalities including functional magnetic resonance imaging (fMRI), magnetoencephalography (MEG) and electroencephalography (EEG). In particular, functional connectivity under resting conditions (resting-state functional connectivity, RSFC) has attracted widespread attention in neuroscience (Biswal et al., 1995; Greicius et al., 2003). One of the reasons for this might be that a growing body of studies has reported altered levels of functional connectivity in neurological and psychiatric brain disorders, including Alzheimer's disease, depression, dementia and schizophrenia (van den Heuvel and Hulshoff Pol, 2010).

Most RSFC studies use fMRI because of its high spatial resolution. For example, the first direct evidence for the default mode network (DMN) was demonstrated using resting-state fMRI data based on seed-based correlation analysis (Greicius et al., 2003). The dorsal attention network (DAN), the resting-state network antagonistically coupled with the DMN, were also identified using resting-state fMRI data with the seed-based approach (Fox et al., 2005). There is a more sophisticated approach than the seed-based correlation analysis, the use of spatial independent component analysis (ICA). Spatial ICA is a widely used method for decomposing fMRI data into signal and noise components and was implemented using the Group ICA of fMRI Toolbox (GIFT)[1]. Multiple resting-state networks including DMN can be easily identified by applying spatial ICA to resting-state fMRI data (Jafri et al., 2008), and therefore the use of this approach is increasing. Despite growing use of fMRI in RSFC studies, fMRI has dis-advantages of high cost and low portability. In addition, fMRI may not be safe or appropriate for people (1) with metal or electronic implants in their bodies (such as pacemakers, cochlear implants, metallic tattoos, etc.) because MRI involves exposure to strong magnetic fields and induced electric fields, (2) with claustrophobia because subjects are required to enter narrow scanner tube and (3) who are or may be pregnant because the risk of exposure to magnetic fields for the fetus is still unknown.

Functional near-infrared spectroscopy (fNIRS) is a non-invasive optical imaging technique that measures changes in both oxygenated (oxy-) and deoxygenated (deoxy-) hemoglobin (Hb) concentrations based on changes in light absorption at multiple wavelengths, whereas fMRI mainly measures changes in deoxy-Hb concentrations, referred to as the blood-oxygen-level-dependent (BOLD) signals. Because fNIRS is free of above disadvantages in fMRI, it can be used as an alternative human brain mapping technique for situations in which fMRI is contraindicated. Rather than an alternative to fMRI, fNIRS would provide even additional information, because fNIRS creates images of both oxy- and deoxy-Hb simultaneously (as described above, the BOLD signal is mostly sensitive to deoxy-Hb) and has a higher sampling rate than fMRI does (>10 Hz with fNIRS, whereas $\sim$0.5 Hz with fMRI). Thanks to these advantages, fNIRS has been used to investigate RSFC. Lu et al. (2010), one of the earliest resting-state fNIRS studies, demonstrated that, using seed-based correlation analysis, RSFC maps over the sensorimotor and auditory cortexes were consistent with those of previous fMRI findings. Furthermore, Duan et al. (2012) and Sasai et al. (2012) examined relationship of RSFCs between fNIRS and fMRI by simultaneously recording these signals and demonstrated that fNIRS can be used to collect information regarding RSFC defined in fMRI. As for the approach to estimate RSFC, Zhang et al. (2010) compared a spatial ICA with the conventional seed-based correlation approach with respect to the estimation of RSFC from fNIRS data and demonstrated the superior performance of spatial ICA with higher sensitivity and specificity, especially in the case of higher noise level (Zhang et al., 2010). Despite the success these resting-state fNIRS studies achieved, current standard fNIRS imaging (i.e., optical topography that is two-dimensional image based on the spatial interpolation method) has several disadvantages. First, fNIRS imaging uses sparse arrangements of source and detector optodes (and therefore measurement channels are also sparsely arranged) and therefore the positions of the measurement channels do not always overlap the real activation foci. Therefore, the spatial resolution of fNIRS imaging is low compared to fMRI. Second, the positions of the measurement channels relative to brain anatomy vary among subjects, and also among runs within the same subjects when the runs were performed on different days, resulting in reduced reliability of comparison among subjects and runs. Third, fNIRS signals are, in most cases, degraded by the hemodynamic changes in the scalp layer. Changes in scalp hemodynamics sometimes exceed those in cortical hemodynamics (Takahashi et al., 2011). In these three problems, the third one was dealt with by several studies that succeeded to reduce scalp artifacts with the use of principal component analysis (PCA) (Zhang et al., 2005), independent component analysis (ICA) (Kohno et al., 2007), short-distance channel regression (Zeff et al., 2007; Eggebrecht et al., 2014) or combination of PCA and multi-distance probe arrangement (Sato et al., 2016). However, there is a way to solve all the three problems at once, a method called diffuse optical tomography (DOT).

Diffuse optical tomography is an advanced technique to reconstruct three-dimensional images showing changes in cerebral hemodynamics. The technique follows the strategy to use high-density DOT grids, which bring about overlapping measurements at multiple source-detector separation distances. The use of overlapping measurements improves spatial resolution in the head surface direction. In addition, different measurement distances provide information about different depths. This is because the penetration depth of the light increases with the source-detector separation distance. Depending on the source-detector distance and the subject's

[1] http://trendscenter.org/software/gift/

scalp/skull thickness, the light may or may not sufficiently penetrate through the superficial layers (scalp) to the deeper layers (brain tissue) (Rupawala et al., 2018). There are two stages to obtain DOT images. The first stage is forward modeling where the measurement process is simulated using a head model and physical laws. The second stage is image reconstruction where the hemodynamic changes inside the head medium are estimated from fNIRS signals by inverting the forward model. The image reconstruction problem is formulated as a linear inverse problem (Boas et al., 2004), which is ill-posed and therefore requires *a priori* information to constrain possible solutions. One approach to solve the inverse problem is the regularization. In the DOT algorithm based on the regularization (Zeff et al., 2007; Eggebrecht et al., 2014), a DOT image is obtained by minimizing a cost function consisting of the data fitting term and constraint terms representing *a priori* information. Another is the Bayesian approach, which uses a probabilistic model of observations and constraints called the likelihood function and prior distribution, respectively (Guven et al., 2005; Shimokawa et al., 2012).

Although there were a variety of image reconstruction algorithms, no research had proposed a DOT algorithm to accurately reconstruct both the scalp and cortical activities simultaneously. Most studies took a two-process approach: (1) hemodynamic changes in the superficial layers, including scalp and skull, were removed from all measurements and (2) a DOT image reconstruction method was applied to the denoised data in order to estimate only the cortical activity. Most artifact-removal methods used in the first process were based on an assumption that the temporal patters in the hemodynamic changes of the superficial layers are homogeneous over the whole head (e.g., Kohno et al., 2007) or they are similar to those of short-distance channels (Eggebrecht et al., 2014). However, the artifact-removal methods based on the above assumption would not work well if the systemic interference occurring in the superficial layers of the human head is inhomogeneous across the surface of the scalp as reported in Gagnon et al. (2012, 2014) or if hemodynamic changes in the superficial layers are highly correlated with those in the cortex (though see Kirilina et al., 2012; Funane et al., 2014; for methods to overcome this). To avoid these weak points in the artifact-removal methods based on temporal information, we recently proposed a method that uses the spatial information of the optical paths of all observation channels, which are not affected by temporal inhomogeneity or correlation, in order to remove the scalp hemodynamics (Shimokawa et al., 2013). The method is an expanded version of the previously proposed hierarchical Bayesian (HB) DOT algorithm (Shimokawa et al., 2012) and is able to reconstruct both the scalp and cortical activities simultaneously.

In the first version of our Bayesian DOT algorithm (Shimokawa et al., 2012), we introduced sparse regularization to improve the depth accuracy and the spatial resolution and verified its performance with phantom experiments. Then, in the expanded version (Shimokawa et al., 2013), we introduced different types of regularization for the cortex and the scalp, sparse and smooth regularization to cortical and scalp's hemodynamic changes, respectively, and validated the proposed method through both two-layer phantom experiments and MRI-based head-model simulations. Furthermore, we have conducted real human experiments with movement tasks and confirmed the performance of the HB DOT on imaging task-related functional responses (Yamashita et al., 2016). The present study therefore aims to investigate whether the HB DOT is used successfully to estimate spontaneous changes in cortical hemodynamics instead of task-related changes. We conducted real human experiments to record resting-state fNIRS signals from bilateral frontal and parietal areas using high-density probe array with multiple-distance channels, which required a major improvement of measurement (i.e., development of a custom-made holder that stably fits to the scalp). Then, we calculated the RSFC from the estimates of cortical hemodynamic changes with HB DOT. We also acquired resting-state fMRI data and used it as a reference in order to validate the performance of our algorithm. In addition, we compared the performance of our method with that of the two-process approach, which is the currently prevailing method for DOT. As for the DOT algorithms used in the two-process approach, we adopted the modified depth-compensation minimum-norm algorithm (abbreviated as MN) and the current standard method developed in Washington University (named in this study as MN-WU) (Eggebrecht et al., 2014), in line with our previous study on imaging task-related activities (Yamashita et al., 2016). Because there are still few studies on RSFC using DOT (White et al., 2009; Eggebrecht et al., 2014), the present study will provide important information to the relevant research areas.

MATERIALS AND METHODS

To obtain resting-state brain activity, fMRI and fNIRS data were recorded during resting state on different days. fMRI data was used as a reference. fNIRS signals were passed through DOT analyses to reconstruct three-dimensional images of changes in cerebral hemodynamics. Three different DOT algorithms, HB, MN and MN-WU were compared in terms of resting-state connectivity. Schematic of the processing stream for fNIRS and fMRI data are shown in **Figure 1**.

Subjects

Twenty healthy male subjects aged between 21 and 38 participated in both fMRI and fNIRS experiments on different days. All of the subjects, except for one subject who is one of the authors, were paid for their participation. None reported history of neurological or psychiatric disorders. All subjects gave written informed consent to participate in the experimental procedures, which were approved by the ATR Review Board Ethics Committee.

Tasks

In the fMRI experiment, each subject undergone a 10 min resting state condition in which he/she was instructed to stay still, to stay awake, to fixate on the crosshair, and not to think about specific things.

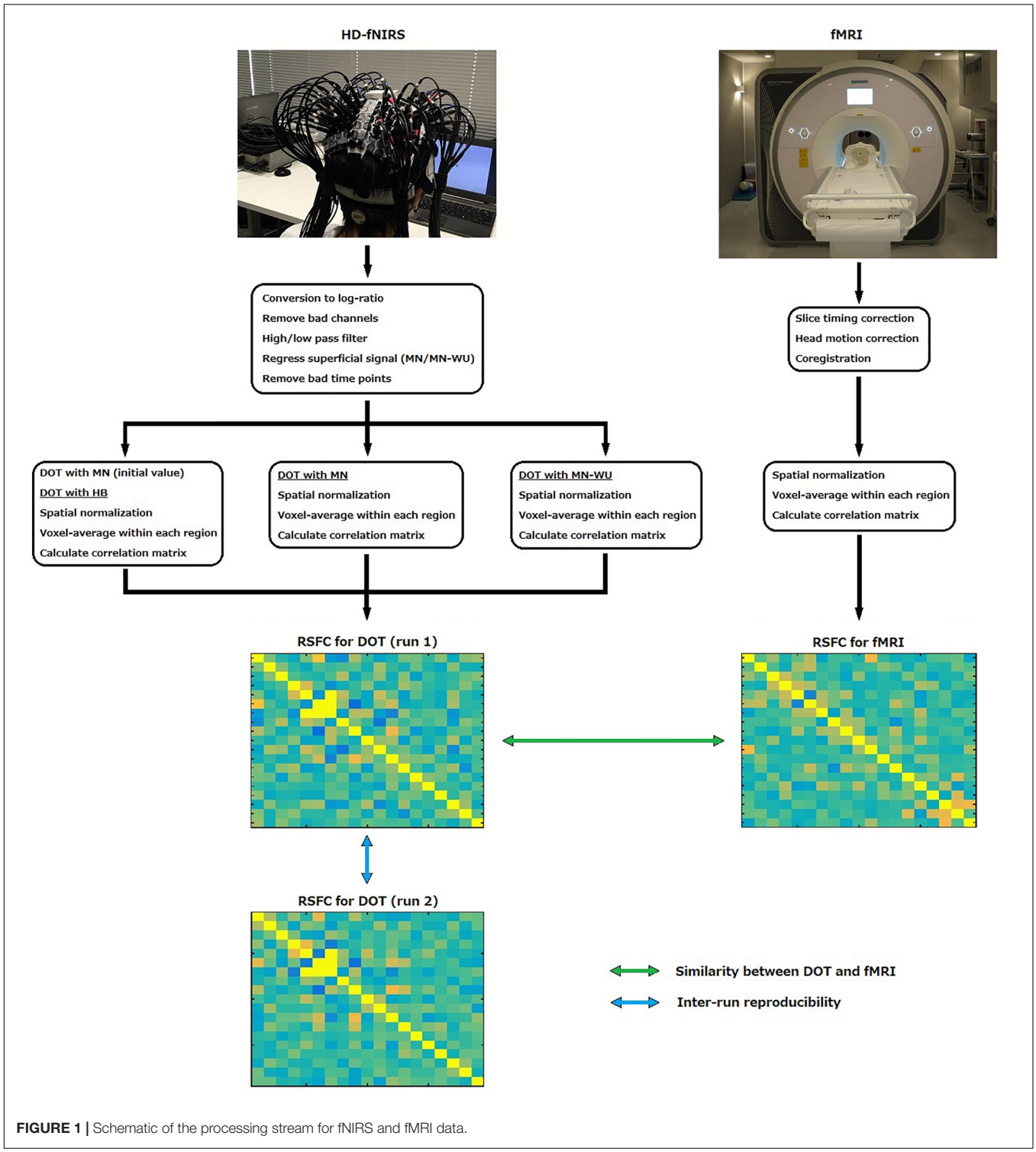

FIGURE 1 | Schematic of the processing stream for fNIRS and fMRI data.

In the fNIRS experiment, each subject undergone a two-back working memory task (took about 15 min) and two 10 min resting state conditions similar to that in the fMRI experiment. The resting state conditions were undergone before and after the WM task condition. We did not use the WM data in the present study.

MRI and fMRI Data Acquisition

Subjects lay down in an MRI scanner. Structural MR images were acquired for construction of individual head models, and functional images were acquired for evaluation of the reconstructed DOT images. All MRI data were recorded using a 3T MRI scanners, MAGNETOM Trio Tim, MAGNETOM Verio,

MAGNETOM Prisma (Siemens Medical Systems, Erlangen, Germany). The acquisition parameters for T1-weighted images were as follows: repetition time (TR) = 2,300 ms, time of echo (TE) = 2.98 ms, flip angle = 9°, slice thickness = 1 mm, field of view (FOV) = 256 mm, imaging matrix = 256 × 256, inversion time (TI) = 900 ms. The acquisition parameters for echo-planar images (EPIs) were as follows: TR = 2,500 ms, TE = 30 ms, flip angle = 80°, slice thickness = 3.2 mm, FOV = 212 mm, imaging matrix = 64 × 64 mm.

NIRS Data Acquisition

Subjects were seated in a comfortable reclining armchair. fNIRS data were acquired using commercial NIRS equipment (SMARTNIRS, Shimadzu Corp., Japan) with probes whose shapes were customized for high-density (HD) measurements. Using a custom-made holder, 32 source and 32 detector probes were placed on the scalp to cover bilateral frontal and parietal areas. We adopted four 4 × 4 square arrays (**Figures 2A,B**), where the first- and second-shortest distances between source and detector probes were 13 and 29 mm, respectively. We used all of the first- and second-nearest neighbor measurement pairs, which provided 56 'first' and 96 'second' channels, respectively, resulting in a total of 152 measurement channels.

Just after the fNIRS recording, the surface image of the subject's face, the positions of the three fiducial markers (nasion, left and right preauricular points) and the probe positions were acquired with a hand-held laser scanner and a stylus marker (FastSCAN; Polhemus, United States), for the co-registration of the fNIRS data to the T1-MRI.

Three near-infrared beams (wavelength 780, 805, and 830 nm) were irradiated and detection beams sampled at 18.5 Hz were used to calculate Δ[oxy-Hb] and Δ[deoxy-Hb].

fMRI Data Processing

fMRI signals were processed using SPM12 (the Wellcome Centre for Human Neuroimaging). The first four volumes were discarded to allow for T1 equilibration. The remaining data were corrected for slice timing and realigned to the mean image of that sequence to compensate for head motion. Next, the structural image was co-registered to the mean functional image and segmented into three tissue classes (gray matter, white matter, and cerebrospinal fluid) in the standard Montreal Neurological Institute (MNI) space. Using associated parameters, the functional images were spatially normalized into the MNI space and resampled in a 2 × 2 × 2 mm grid. Finally, they were spatially smoothed using an isotropic Gaussian kernel of 8 mm full-width at half maximum (FWHM).

fNIRS Data Preprocessing

Prior to DOT analysis, the following preprocessing was applied to fNIRS signals.

(1) Convert voltage data into log-ratios using a base-10 logarithm.
(2) Calculate the coefficient of variation (CV, in%) of each channel for each wavelength, where CV = 100 × σ/μ, σ is the signal standard deviation, and μ is the mean signal level. Then, remove the bad channels which had CVs exceeding 15% (Piper et al., 2014) at least one of three wavelength or were saturated [the mean number of rejected channels was 13.0 ± 12.2 (SD)].
(3) Apply a high-pass filter (Butterworth filter of order 3, cutoff 0.009 Hz) and a low-pass filter (Butterworth filter of order 7, cutoff 0.08 Hz).
(4) Remove scalp hemodynamics from the filtered data, only in case of DOT image reconstruction with the MN and MN-WU algorithms. In this process, the global average of all the 'first' channels other than the bad channels is regarded as the scalp dynamics and regressed out. This process is omitted in case of DOT image construction with the HB algorithm.
(5) Remove the bad time points when absolute signal amplitudes exceeded more than three standard deviations from the mean at least one of the "first" channels [the mean number of removed time points was 590 ± 247 (SD) (roughly equal to 32 s)].

DOT Forward Model Construction

The DOT forward model was constructed in the following way. First, an individual head model was constructed by segmenting their T1 structural image into five tissue layers [scalp, skull, cerebrospinal fluid (CSF), gray matter, and white matter], using FreeSurfer software[2]. Positions of the fNIRS probes were then co-registered to the head model using an affine transformation. The rotation and translation parameters of the affine transformation were optimized so that a subject's facial surface measured by the laser scanner fitted that extracted from the T1 anatomical image. Next, the photon migration process inside the head was simulated with Monte Carlo simulation software MCX (Fang and Boas, 2009) with 10^9 photons. We used tissue optical parameters common to all three wavelengths (**Table 1**), as presented in a previous study (Fang, 2010). Finally, the sensitivity matrix, which relates the absorption changes in the head tissue voxels to the light intensity changes at the source-detector pairs, was computed with Rytov approximation to the MCX results (Shimokawa et al., 2012). For computation of the sensitivity matrix, the 1 × 1 × 1 mm voxel space was down-sampled to 4 × 4 × 4 mm voxel space in the reconstructed images. The image reconstruction region included the scalp and cortical voxels inside a 28-mm-deep cuboid, whose surface was a square along the scalp surface. This was obtained by extending the diagonals of the 5 × 5 NIRS probe square by a factor of 1.5.

DOT Image Reconstruction With the HB Algorithm

DOT image reconstruction with the HB algorithm has two steps. In the first step, DOT image is reconstructed from the preprocessed fNIRS signals, using the modified version of the depth-compensation minimum norm image reconstruction algorithm (MN). In the next step, the DOT image is refined using the iterative algorithm with the MN DOT image obtained in the first step as an initial value and a prior. Note that the preprocessed

[2]https://surfer.nmr.mgh.harvard.edu

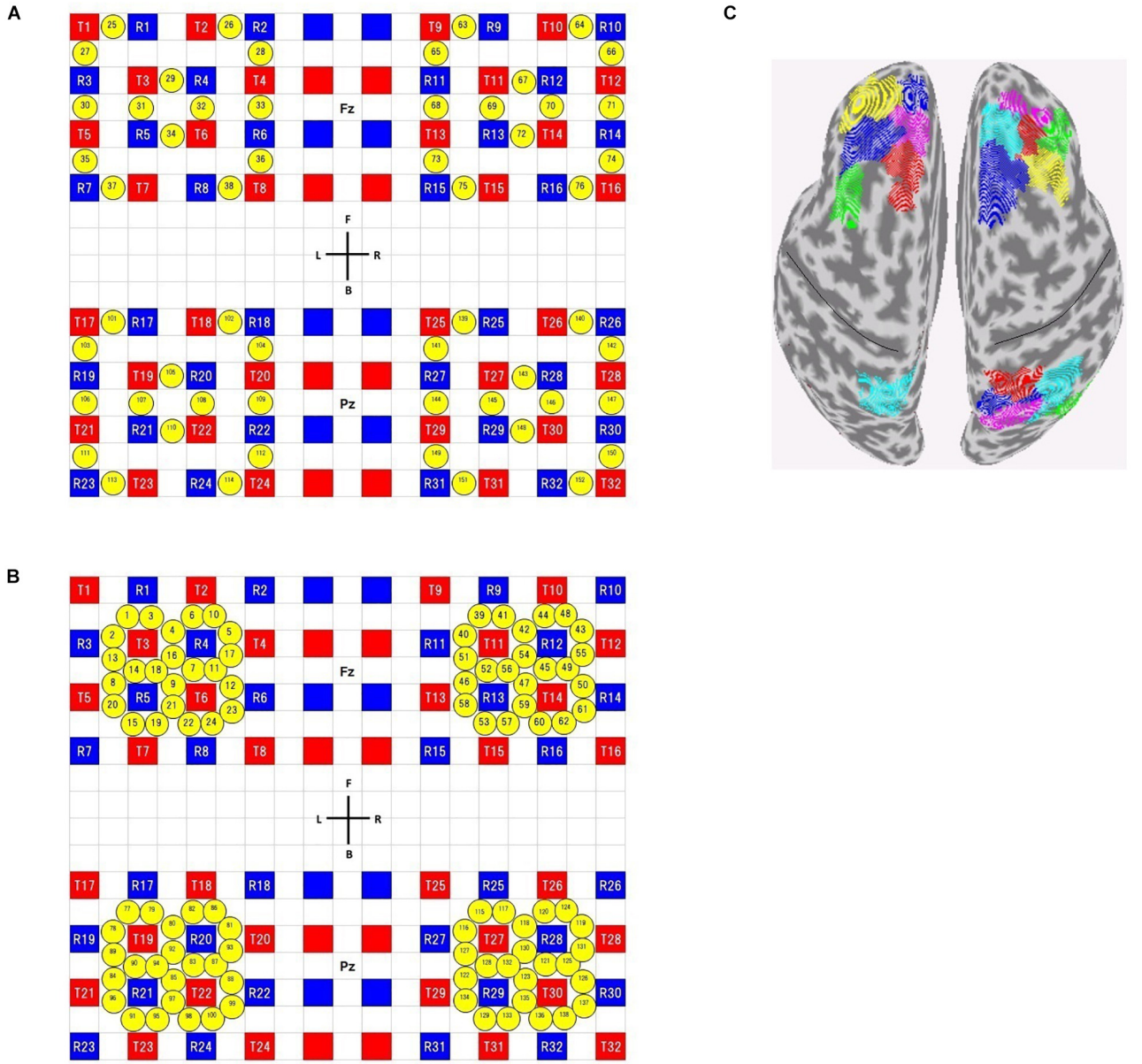

FIGURE 2 | Channel configuration **(A,B)** and *available* ROIs on the brain surface **(C)**. **(A)** Configuration of the short-distance channels, **(B)** configuration of the long-distance channels. Red and blue squares represent source and detector positions, respectively. Yellow circles represent measurement channel positions. Note that, in long-distance channels, some channels (for example, ch1 and ch3) overlap each other in real situation, though not precisely described as such. A custom-made holder was divided into two parts. One is used to cover frontal areas and its center positioned on Fz (according to the international 10–20 system). The other is used to cover parietal areas and its center positioned on Pz. **(C)** *available* ROIs for Shen's atlas (see section "**Calculation of Resting-State Connectivity**" for the definition of *available* ROIs). The black lines indicate the central sulci.

fNIRS signals used in both steps are not passed through the scalp hemodynamics removal (the 4th process in section "fNIRS data preprocessing").

For the HB DOT image reconstruction in the second step, we used the HB model presented in Yamashita et al. (2016). The hierarchical prior distribution has mean and confidence (or reliability) parameters. The mean parameter $\overline{\lambda_{0l}}$ were the mean square values of the solutions obtained from the MN DOT in the first step. The confidence parameter γ_0 controls the width of the hierarchical prior distribution (the variance of the hierarchical prior distribution is inversely proportional to the confidence parameter); large γ_0 narrows the hierarchical prior distribution around the mean value $\overline{\lambda_{0l}}$, and the estimation depends more critically on the solutions obtained from MN DOT in the first step. The confidence parameter γ_0 was set to L $\times$ 0.1, where L is data length, on the basis of our experience. But, we also tried the following settings; γ_0 = L $\times$ 0.01, L $\times$ 0.001, L $\times$ 0.0001. For the detail of the HB algorithm, see Yamashita et al. (2016).

TABLE 1 | Optical parameters in various head tissue types (common to all three wavelengths of 780, 805, and 830 nm).

Tissue types	Absorpt. Coeff. μ_a (mm^{-1})	Scattering Coeff. μ_s (mm^{-1})	Anisotropy (g)	Refract. Index (n)
Scalp and skull	0.019	7.8	0.89	1.37
CSF	0.004	0.009	0.89	1.37
Gray matter	0.02	9.0	0.89	1.37
White matter	0.08	40.9	0.84	1.37

DOT Image Reconstruction With the MN/MN-WU Algorithms

The DOT image with the MN algorithm and that with the MN-WU algorithm were also computed for comparison. As mentioned in section "fNIRS data preprocessing," in both MN and MN-WU algorithms, DOT image is reconstructed from the preprocessed fNIRS signals whose scalp hemodynamics were removed by regressing out the averaged 'first' channel data.

As for the MN-WU algorithm, the spatially variant parameter was set to $\beta = 0.1$ and the regularization parameter α was automatically determined by maximizing the marginal likelihood of each data set (see Culver et al., 2003).

As for the MN algorithms, the spatially variant parameter was set to $\beta = mean_{v\epsilon\ I_{20\ mm}}(\rho_2)_v$ where $I_{20\ mm}$ is a voxel index set whose depth from the scalp is around 20 mm. And the regularization parameter α was automatically determined by maximizing the marginal likelihood using all the measurements included in the I_{task}. See the Appendix of Yamashita et al. (2016) for the mathematical details.

Calculation of Resting-State Connectivity

Irrespective of the DOT algorithm, the reconstructed DOT image was passed through a spatial normalization into the standard MNI space and spatial smoothing with a Gaussian kernel of 8 mm full width at half maximum (FWHM), before calculation of resting-state functional connectivity (RSFC). These processes were done with SPM12.

The RSFC for both fMRI and DOT was obtained in the following way, using spatially normalized fMRI and DOT images, respectively. First, all cortical voxels were categorized into 278 regions of interest (ROI), based on functional-connectivity-based atlas (Shen et al., 2013). Then, voxels with sensitivity values of more than 0.5 for all subjects were regarded as *sensitive* voxels, and ROIs including more than or equal to 10 *sensitive* voxels were regarded as *available* ROIs (**Figure 2C** for Shen's atlas). Third, for each *available* ROI, timeseries of all *sensitive* voxels within the ROI were averaged. These mean timeseries were assumed to represent temporal activity of the corresponding ROI. Finally, partial correlations between all pairs of *available* ROIs were computed to make a correlation matrix. Partial correlation was used to reduce the influence of extra-neural components such as physiological noise signals due to spontaneous low-frequency oscillations, respiration and cardiac pulsation (Sakakibara et al., 2016). Note that all the following analyses were done for *sensitive* voxels and *available* ROIs.

The reason why we used Shen's atlas rather than the widely used Brodmann-based automatic anatomic labeling (AAL) atlas is as follows. The AAL atlas uses Brodmann areas which are based on cytoarchitecture. This atlas is not ideal because of its coarse-grained nature (116 regions for the AAL atlas whereas 278 regions for the Shen's atlas in our data) and the risk of including different functional areas within a single region, with the consequence that the resultant mean timeseries may not accurately represent any of the contributing timeseries. Shen's atlas is developed to avoid this pitfall and will provide meaningful nodes (Shen et al., 2013), and therefore is suitable for our case.

For reference, we will present the corresponding results for the AAL atlas in the **Supplementary Material**.

Comparison of Connectivity Matrices Among DOT Algorithms

In order to establish the superiority of the HB DOT in the estimation of RSFC, we compared correlation matrices among the DOT algorithms (HB, MN, MN-WU) in the following three ways.

Because it seems reasonable to use fMRI data as a reference, we first compared *similarity* of RSFCs between fMRI and DOT among three DOT algorithms, where correlation coefficient was used as a similarity measure. The comparison was done in the following way: (1) the lower triangular portion of correlation matrix, C_{low}, was transformed to $z(C_{low})$ by using Fisher's z-transformation, (2) correlation coefficient of $z(C_{low})$ between fMRI and DOT, $R_{fMRI\text{-}DOT}$, was calculated, (3) the correlation coefficient $R_{fMRI\text{-}DOT}$ was transformed to $z(R_{fMRI\text{-}DOT})$ by using Fisher's z-transformation, (4) differences in mean $z(R_{fMRI\text{-}DOT})$ among three DOT algorithms were tested using one-way analysis of variance (ANOVA) followed by multiple comparisons with the Tukey–Kramer correction.

Second, we compared inter-run *reproducibility* of RSFC estimation among three DOT algorithms. The comparison was done in the following way: (1) the lower triangular portion of correlation matrix, C_{low}, was transformed to $z(C_{low})$ by using Fisher's z-transformation, (2) correlation coefficient of $z(C_{low})$ between run1 and run2, $R_{ses1\text{-}ses2}$, was calculated, (3) the correlation coefficient $R_{ses1\text{-}ses2}$ was transformed to $z(R_{ses1\text{-}ses2})$ by using Fisher's z-transformation, (4) differences in mean $z(R_{ses1\text{-}ses2})$ among three DOT algorithms were tested using one-way analysis of variance (ANOVA) followed by multiple comparisons.

As a complementary metric to Pearson's correlation, intra-class correlation (ICC; McGraw and Wong, 1996) was also used for assessment of reproducibility across runs. Both single and average measures, i.e., ICC(C,1) and ICC(C,k), were calculated using MATLAB function *ICC* by Arash Salarian (available at MATLAB Central File Exchange).

Third, we performed additional analysis on intra-run test–retest reliability assessment. In this analysis, resting-state fNIRS data recorded in each 10 min run was firstly divided into two segments of equal length [i.e., first half (FH) and second half (SH)]. Note that duration of each half is 5 min at most (the mean is about 4 min and 44 s) because bad time points

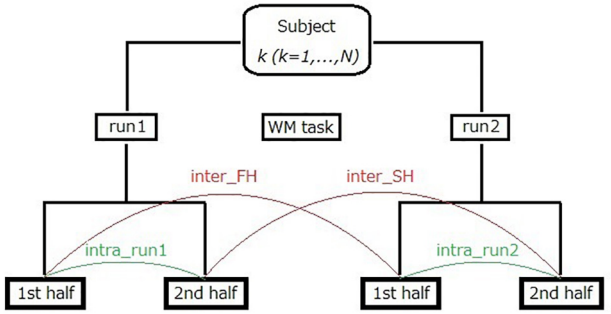

FIGURE 3 | Illustration of intra-run reproducibility and half-length inter-run reproducibility calculations for fNIRS data. The number of subjects, N, was 20.

were removed in the fNIRS data preprocessing (see section "fNIRS Data Preprocessing"). As shown in **Figure 3**, intra-run reproducibility was assessed using two pairs of datasets; run1-FH and run1-SH (intra_run1), as well as run2-FH and run2-SH (intra_run2). In addition, inter-run reproducibility (denoted by half-length inter-run reproducibility to distinguish it from the previous one using full-length data) was assessed with two pairs of datasets; run1-FH and run2-FH (inter_FH), as well as run1-SH and run2-SH (inter_SH). As measures for these reproducibilities, we used Pearson's correlation, ICC(C,1) and ICC(C,k) again.

We compared intra-run reliability among functional images (i.e., fMRI vs. HB vs. MN vs. MN-WU). More specifically, differences in mean measures for intra-run reliability were tested using one-way ANOVA followed by multiple comparisons.

In addition, we compared intra-run reproducibility and half-length inter-run reproducibility. Because resting-state fNIRS was acquired before and after a WM task, this comparison will serve to investigate whether the task affected the resting-state connectivity.

RESULTS

Similarity Between fMRI and DOT

Mean and SD maps for RSFCs of fMRI and DOT with HB, MN and MN-WU algorithms are shown in **Figures 4**, **5**, respectively. The mean map showed a common tendency between fMRI and fNIRS (i.e., HB, MN, and MN-WU) that most pairs between adjacent ROIs had positive correlations, though some of them (e.g., R.BA7.5-R.BA7.6) had negative correlations. Additional findings from the mean map is that some of frontal-parietal pairs (e.g., R.BA7.8-R.BA9.4) and contralateral counterpart pairs (e.g., R.BA9.4-L.BA10.1) had positive correlations in fMRI, whereas such a tendency was weak for the DOT cases. As for the SD maps, variability across subjects was little in fMRI, whereas it was relatively large especially for the pairs between adjacent ROIs in fNIRS regardless of the DOT algorithms.

Similarity of RSFCs between fMRI and DOT for each run and DOT algorithm is summarized in **Table 2**. One-way ANOVA applied to data combined between runs revealed a significant difference among three DOT algorithms for both oxy- and deoxy-Hb [$F_{(2,117)} = 4.27$, $p = 0.0162$ for oxy-Hb; $F_{(2,117)} = 7.69$, $p = 0.0007$ for deoxy-Hb]. The *post hoc* Tukey's HSD test revealed, for both oxy- and deoxy-Hb, that HB had significantly higher correlation values than both MN and MN-WU did ($p < 0.05$), but

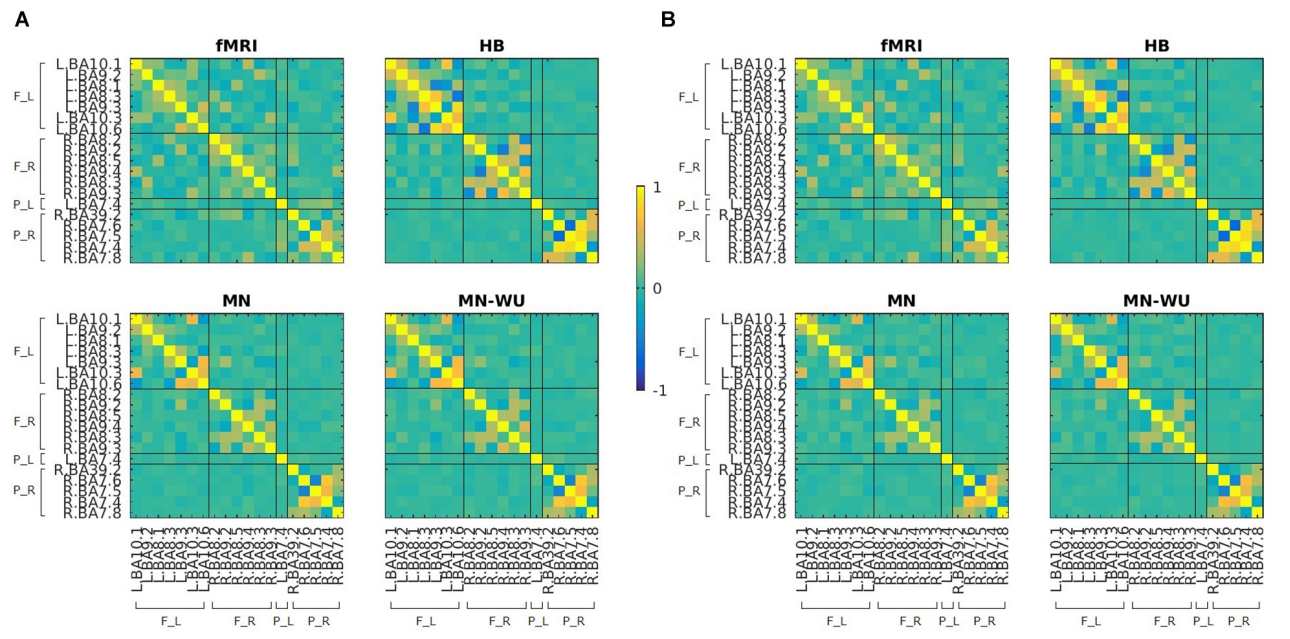

FIGURE 4 | Mean maps for RSFCs of fMRI and DOT with HB, MN and MN-WU algorithms. Correlation matrices were averaged across subjects and runs, for **(A)** oxy-Hb and **(B)** deoxy-Hb in the case of DOT. F_L, left frontal area; F_R, right frontal area; P_L, left parietal area; P_R, right parietal area.

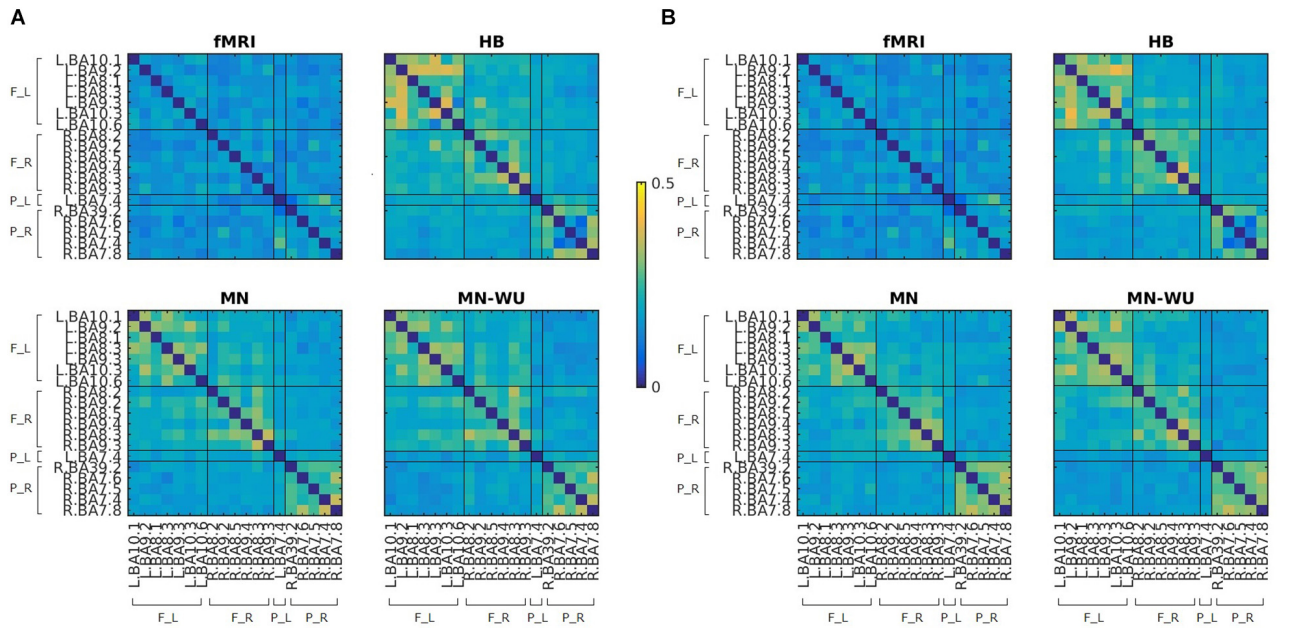

FIGURE 5 | SD maps for RSFCs of fMRI and DOT with HB, MN and MN-WU algorithms. SDs of correlation matrices were computed across subjects and runs, for **(A)** oxy-Hb and **(B)** deoxy-Hb in the case of DOT. F_L, left frontal area; F_R, right frontal area; P_L, left parietal area; P_R, right parietal area.

the difference of correlation values between MN and MN-WU was not significant.

Inter-Run Reproducibility, Intra-Run Reproducibility

Mean and SD maps for RSFCs are compared between runs in **Figures 6**, **7**, respectively. Mean ± SD of inter-run reproducibility (i.e., Pearson's correlation and inter-class correlation of correlation matrices between run 1 and 2) is summarized in **Table 3**.

As for Pearson's correlation, one-way ANOVA revealed a significant difference among three DOT algorithms for both oxy- and deoxy-Hb [$F_{(2,57)} = 11.0$, $p = 9.06 \times 10^{-5}$ for oxy-Hb; $F_{(2,57)} = 10.9$, $p = 9.89 \times 10^{-5}$ for deoxy-Hb]. The *post hoc* Tukey's HSD test revealed, for both oxy- and deoxy-Hb, that HB had significantly higher correlation values than both MN and MN-WU did ($p < 0.05$), but the difference of correlation values between MN and MN-WU was not significant.

As for the ICC metrices, the following results were obtained. First, for ICC(C,1), one-way ANOVA revealed a significant difference among three DOT algorithms for both oxy- and deoxy-Hb [$F_{(2,57)} = 11.0$, $p = 9.30 \times 10^{-5}$ for oxy-Hb; $F_{(2,57)} = 9.81$, $p = 0.0002$ for deoxy-Hb]. The *post hoc* Tukey's HSD test revealed, for both oxy- and deoxy-Hb, that HB had significantly higher ICC(C,1) values than both MN and MN-WU did ($p < 0.05$), but the difference of ICC(C,1) values between MN and MN-WU was not significant.

Then, for ICC(C,k), one-way ANOVA revealed a significant difference among three DOT algorithms for both oxy- and deoxy-Hb [$F_{(2,57)} = 10.5$, $p = 0.0001$ for oxy-Hb; $F_{(2,57)} = 8.61$, $p = 0.0005$ for deoxy-Hb]. The *post hoc* Tukey's HSD test revealed, for both oxy- and deoxy-Hb, that HB had significantly higher ICC(C,k) values than both MN and MN-WU did ($p < 0.05$), but the difference of ICC(C,k) values between MN and MN-WU was not significant.

Intra-run reproducibility (i.e., similarity of RSFCs between FH and SH) is summarized in **Table 4**.

One-way ANOVA revealed that Pearson's correlation value is significantly different among functional images [$F_{(3,136)} = 27.26$, $p = 7.25 \times 10^{-14}$ for oxy-Hb; $F_{(3,136)} = 23.84$, $p = 1.84 \times 10^{-12}$ for deoxy-Hb]. The *post hoc* Tukey's HSD test revealed, for both oxy- and deoxy-Hb, that HB had significantly higher Pearson's correlation than both MN and MN-WU did ($p < 0.05$), but the difference between HB and fMRI was not significant.

Similarly, according to one-way ANOVA, ICC(C,1) is significantly different among functional images [$F_{(3,136)} = 27.41$, $p = 6.28 \times 10^{-14}$ for oxy-Hb; $F_{(3,136)} = 24.59$, $p = 8.94 \times 10^{-13}$ for deoxy-Hb]. According to the Tukey's HSD test, for both oxy- and deoxy-Hb, HB had significantly higher ICC(C,1) than both MN and MN-WU did ($p < 0.05$), but HB was not significantly different from fMRI. In addition, one-way ANOVA and *post hoc*

TABLE 2 | Similarity of correlation matrices between fMRI and DOT.

		HB	MN	MN-WU
oxy-Hb	run 1	0.34 ± 0.09	0.29 ± 0.10	0.29 ± 0.10
	run 2	0.35 ± 0.08	0.30 ± 0.08	0.30 ± 0.09
deoxy-Hb	run 1	0.33 ± 0.08	0.25 ± 0.11	0.26 ± 0.12
	run 2	0.34 ± 0.08	0.27 ± 0.11	0.25 ± 0.10

Values of correlation coefficients are presented as mean ± standard deviation (SD).

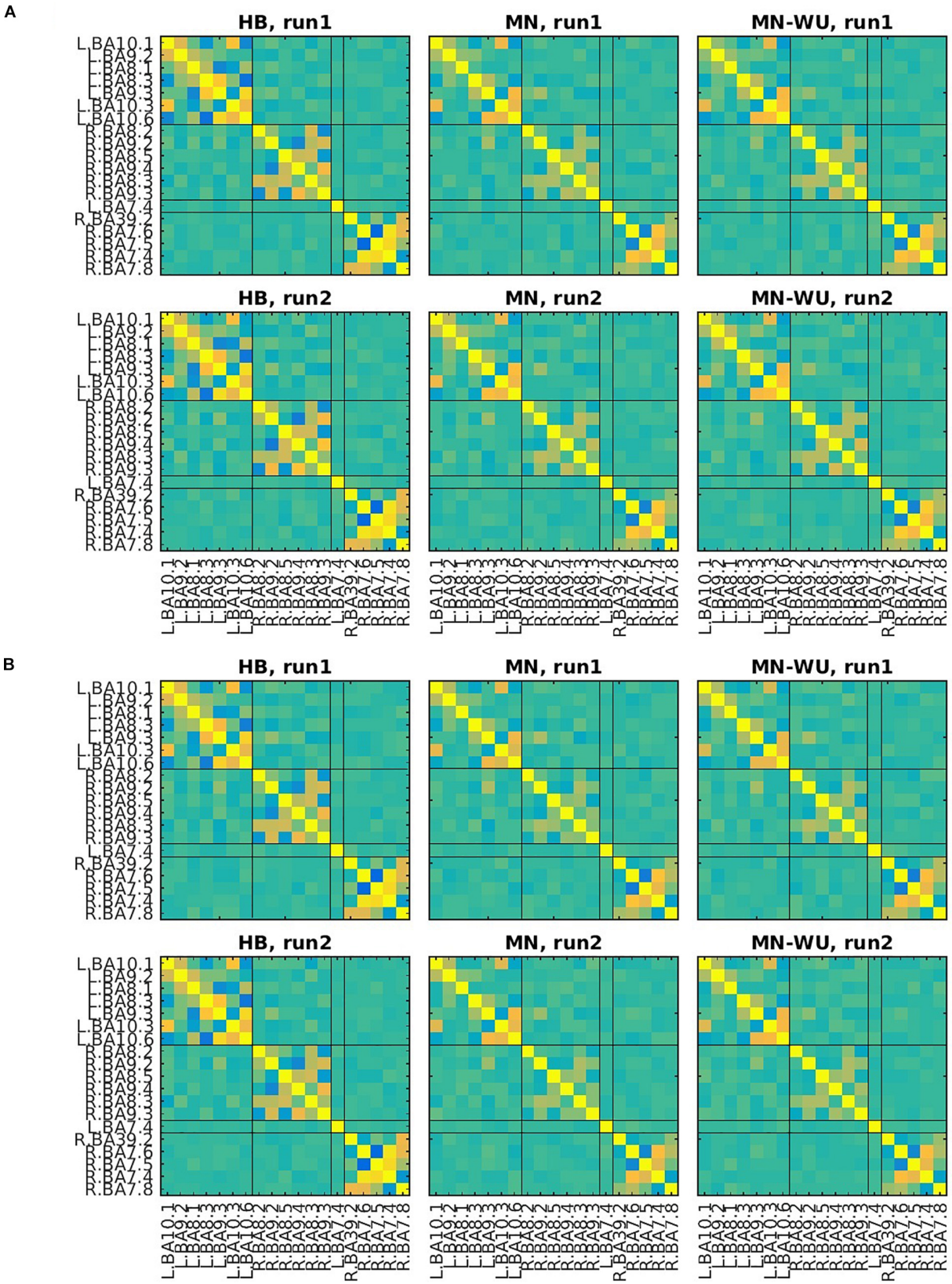

FIGURE 6 | Mean maps for RSFCs are compared between run 1 and run 2. Correlation matrices are averaged across subjects for **(A)** oxy-Hb and **(B)** deoxy-Hb. The upper and lower rows correspond to run 1 and run 2, respectively. ROIs are displayed in the same order as those in **Figures 4**, **5**.

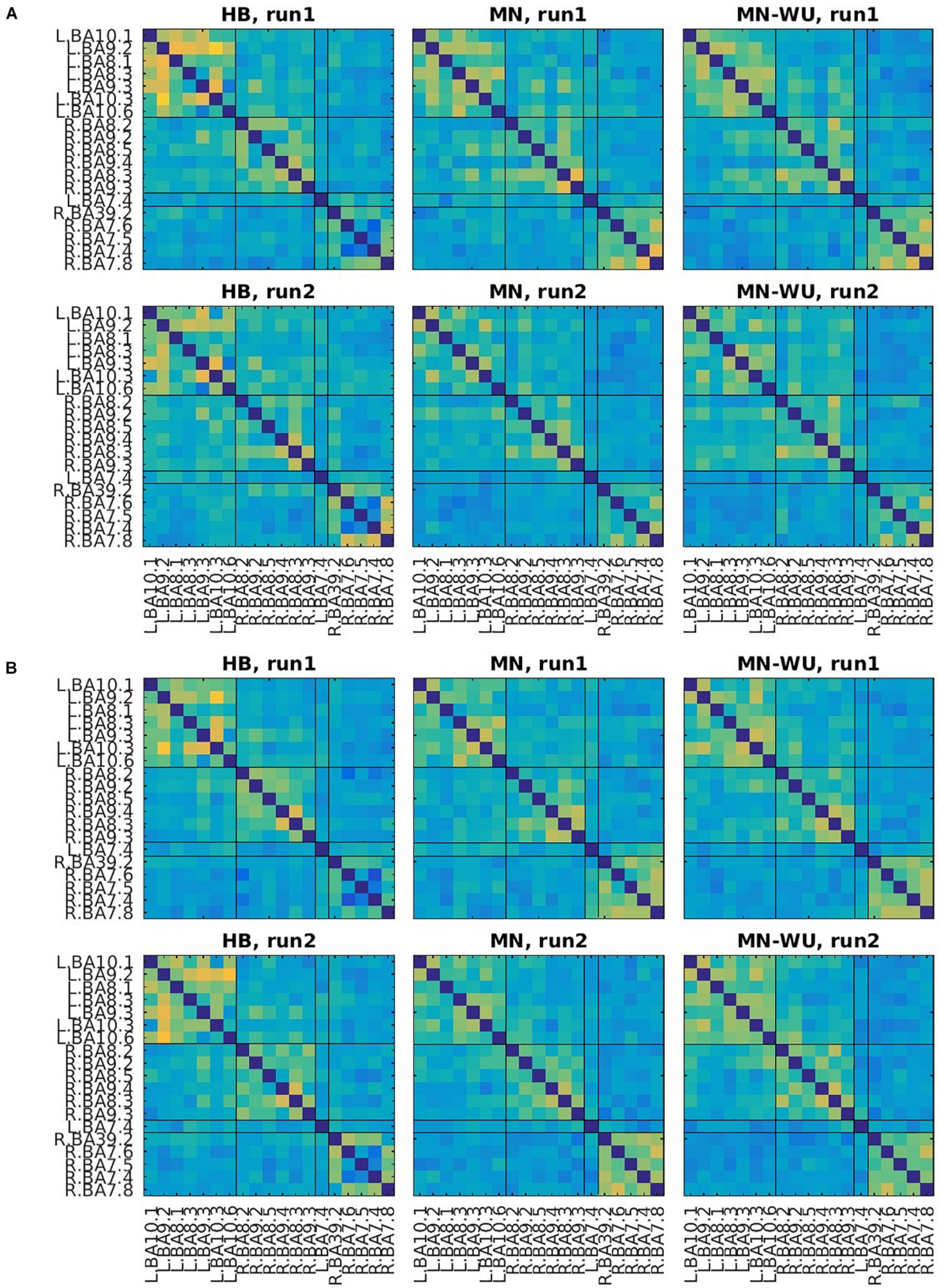

FIGURE 7 | SD maps of RSFCs for run 1 and run 2. SDs of correlation matrices are computed across subjects for **(A)** oxy-Hb and **(B)** deoxy-Hb. The upper and lower rows correspond to run 1 and run 2, respectively. ROIs are displayed in the same order as those in **Figure 6**.

TABLE 3 | Inter-run reproducibility.

		HB	MN	MN-WU
oxy-Hb	r	0.76 ± 0.06	0.61 ± 0.13	0.66 ± 0.12
	ICC(C,1)	0.76 ± 0.06	0.61 ± 0.13	0.65 ± 0.12
	ICC(C,k)	0.86 ± 0.04	0.75 ± 0.10	0.78 ± 0.09
deoxy-Hb	r	0.76 ± 0.07	0.60 ± 0.13	0.63 ± 0.15
	ICC(C,1)	0.75 ± 0.07	0.60 ± 0.13	0.62 ± 0.15
	ICC(C,k)	0.86 ± 0.04	0.74 ± 0.10	0.76 ± 0.12

Values of Pearson's correlation (r), ICC(C,1) and ICC(C,k) are presented as mean ± standard deviation (SD).

TABLE 4 | Intra-run reproducibility.

		fMRI	HB	MN	MN-WU
oxy-Hb	r	0.61 ± 0.08	0.57 ± 0.11	0.38 ± 0.16	0.41 ± 0.13
	ICC(C,1)	0.61 ± 0.08	0.56 ± 0.11	0.37 ± 0.15	0.40 ± 0.13
	ICC(C,k)	0.75 ± 0.06	0.71 ± 0.09	0.53 ± 0.16	0.56 ± 0.14
deoxy-Hb	r	0.61 ± 0.08	0.53 ± 0.10	0.38 ± 0.15	0.38 ± 0.15
	ICC(C,1)	0.61 ± 0.08	0.53 ± 0.10	0.37 ± 0.15	0.37 ± 0.15
	ICC(C,k)	0.75 ± 0.06	0.68 ± 0.09	0.52 ± 0.16	0.53 ± 0.15

Values of correlation coefficients (r), ICC(C,1) and ICC(C,k) are presented as mean ± standard deviation (across subjects for fMRI; across subjects and runs for DOT).

analysis revealed that ICC(C,k) had similar tendency [one-way ANOVA, $F_{(3,136)} = 25.00$, $p = 6.04 \times 10^{-13}$ for oxy-Hb; $F_{(3,136)} = 23.15$, $p = 3.61 \times 10^{-12}$ for deoxy-Hb].

For the HB case, intra-run reproducibility (i.e., similarity of RSFCs between FH and SH) was compared with half-length inter-run reproducibility (i.e., similarity of RSFCs between run 1 and run 2 for the corresponding half) in **Table 5**. Two-sample *t*-test revealed that intra-run reproducibility was not significantly different from half-length inter-run reproducibility for Pearson's correlation ($p = 0.31$ for oxy-Hb; $p = 0.42$ for deoxy-Hb), ICC(C,1) ($p = 0.36$ for oxy-Hb; $p = 0.47$ for deoxy-Hb), and ICC(C,k) ($p = 0.33$ for oxy-Hb; $p = 0.48$ for deoxy-Hb). Similar tendency was observed for both MN and MN-WU cases (detailed data not shown, but $p > 0.30$ in any case).

Effect of the Confidence Parameter γ_0 on Connectivity

As mentioned in the Materials and methods, in the HB algorithm, the confidence parameter, γ_0, represents the width of the hierarchical prior distribution, controlling how strong the HB method is affected by the prior information (the depth-weighted minimum norm estimation). In this subsection, the effect of the γ_0 value on the connectivity estimation was examined for only Pearson's correlation.

Similarity of RSFCs between fMRI and DOT for each run and γ_0 value is summarized in **Table 6**. One-way ANOVA applied to data combined between runs revealed no significant difference among five γ_0 values for both oxy- and deoxy-Hb [$F_{(4,195)} = 1.26$, $p = 0.287$ for oxy-Hb; $F_{(4,195)} = 1.40$, $p = 0.237$ for deoxy-Hb].

Mean ± SD of inter-run reproducibility (i.e., correlation values of correlation matrices between run 1 and 2) for each γ_0 value is summarized in **Table 7**. One-way ANOVA revealed no significant difference among five γ_0 values for both oxy- and deoxy-Hb [$F_{(4,95)} = 0.58$, $p = 0.679$ for oxy-Hb; $F_{(4,95)} = 0.49$, $p = 0.744$ for deoxy-Hb].

TABLE 5 | Comparison of reproducibility between intra-run and half-length inter-run for HB.

		Intra-run	Half-length inter-run
oxy-Hb	r	0.57 ± 0.11	0.55 ± 0.12
	ICC(C,1)	0.56 ± 0.11	0.54 ± 0.12
	ICC(C,k)	0.71 ± 0.09	0.69 ± 0.10
deoxy-Hb	r	0.53 ± 0.10	0.51 ± 0.10
	ICC(C,1)	0.53 ± 0.10	0.51 ± 0.10
	ICC(C,k)	0.68 ± 0.09	0.67 ± 0.09

Values are presented as mean ± standard deviation.

DISCUSSION

The aim of this study was to evaluate our proposed HB DOT algorithm in terms of its performance to estimate the resting-state functional connectivity among brain regions, not task-related brain responses. We used fMRI data as a reference. In addition, we compared our method with other DOT algorithms (the MN and MN-WU), which adopt the two-process approach. Similarity (i.e., correlation coefficient) of the RSFCs between fMRI and DOT showed higher for the HB than both the MN and MN-WU, suggesting that DOT with the HB algorithm is more appropriate to a substitute for fMRI than those with the MN and MN-WU in estimating the resting-state functional connectivity as well as the task-related cortical responses (Yamashita et al., 2016). In addition, inter-run reproducibility (i.e., Pearson's correlation and intra-class correlation coefficients of RSFCs between runs) showed higher for the HB than both the MN and MN-WU, suggesting that DOT with the HB algorithm is more reliable. In addition, mean values of both single- and average-measure ICC are far higher than 0.4, a criterion of sufficient reliability (Zhang et al., 2011), suggesting that DOT with the HB algorithm is highly reliable and comparable to fMRI. These results were true for not only deoxy-Hb but also oxy-Hb, which cannot be measured by fMRI.

We conducted additional analyses relating to intra-run reproducibility (i.e., similarity of RSFCs between FH and SH) for fNIRS data. As for the intra-run test-retest reliability, the HB had significantly higher intra-run reproducibility than both the MN and MN-WU for any intra-run reproducibility measure. In particular, both single- and average-measure ICC values for the HB were far higher than 0.4 and comparable to those for the fMRI. Thus, high reliability of DOT image with the HB algorithm was demonstrated in intra-run as well as inter-run analyses. Meanwhile, comparison of reproducibility between intra-run and half-length inter-run showed no significant difference. This result suggests that the WM task, conducted between the two resting-state fNIRS runs, did not affect RSFCs. According to Birn et al. (2013), the reliability of the resting-state fMRI connectivity estimates was low for the scan length less than 5 min. However, as described in section "Comparison of Connectivity Matrices Among DOT Algorithms," mean scan lengths of both first and second halves of resting-state fNIRS recording were slightly less

TABLE 6 | Effect of γ_0 value on similarity of correlation matrices between fMRI and DOT.

		$L \times 10^0$	$L \times 10^{-1}$	$L \times 10^{-2}$	$L \times 10^{-3}$	$L \times 10^{-4}$
oxy-Hb	run 1	0.34 ± 0.09	0.34 ± 0.09	0.33 ± 0.09	0.32 ± 0.10	0.30 ± 0.11
	run 2	0.35 ± 0.09	0.35 ± 0.08	0.35 ± 0.08	0.34 ± 0.09	0.32 ± 0.09
deoxy-Hb	run 1	0.33 ± 0.08	0.33 ± 0.08	0.32 ± 0.08	0.31 ± 0.09	0.29 ± 0.10
	run 2	0.35 ± 0.08	0.34 ± 0.08	0.34 ± 0.08	0.33 ± 0.08	0.31 ± 0.08

Values of correlation coefficients are presented as mean ± standard deviation (SD). Each column corresponds to $\gamma_0 = L \times 10^{-N}$, where L is the data length (L = 7774–8723, mean 8285). $\gamma_0 = L \times 10^{-1}$ is the default setting.

than 5 min in the present study. Thus, re-examination of results on intra-run analyses is desirable using data with sufficiently long scan lengths.

According to the SD maps for the RSFCs (i.e., **Figure 5**), variability across subjects was little in fMRI, whereas it was large in fNIRS regardless of the DOT algorithms. This difference suggests that the variability of the estimated DOT images across subjects is larger than that of the fMRI images. Such a large variability in DOT images may be due to errors in forward modeling such as probe coregistration error and head model error, variability in measurement condition (e.g., individual difference in a signal-to-noise ratio) and individual difference in optical parameters which cannot be precisely dealt in forward modeling. In addition, oxy-Hb or deoxy-Hb may not solely correspond to BOLD signals. Further work is required to explore the cause of this difference.

In the calculation of RSFCs, we used (1) Shen's atlas rather than the widely used AAL atlas and (2) timeseries averaged across all sensitive voxels within each region. This is because we considered that each region of the AAL includes different functional areas because of its coarse-grained nature [116 regions for a whole brain, but 9 *available* regions in our case (**Supplementary Figure S1**)], whereas that of the Shen's atlas includes a single functional area due to its fine-grained nature [order of 300 regions in a whole brain, but 19 *available* regions in our case (**Figure 2C**)] and therefore mean timeseries represent temporal activity of the ROI. In fact, as described in **Supplementary Material** (Section 3 Kendall's *W* analysis) the chi-squared test suggested that time courses of all voxels in each region of the Shen's atlas were concordant, supporting that the Shen's atlas provides functional subunits and therefore mean timeseries represent temporal activity of the ROI. In addition, the Kendall's *W* for the Shen's atlas is significantly larger than that for the AAL atlas, supporting the validity of using the Shen's atlas in the calculation of functional connectivity. These results are true, regardless of the DOT algorithms. Furthermore, the additional analysis with PCA (Section 4 Principal component analysis in **Supplementary Material**) also confirmed the validity of using both voxel-averaged timeseries and Shen's atlas.

As described in the previous paragraph, the AAL atlas is not ideal. However, the chi-squared test also failed to reject the null hypothesis that there is no concordance among all voxels in the region of the AAL atlas ($p < 0.05$ for all *available* ROIs). We therefore calculated the AAL counterpart on both (1) similarity between fMRI and DOT and (2) inter-run reproducibility, for your reference (see **Supplementary Material** for details). The similarity measure revealed no significant difference among three DOT algorithms (HB vs. MN vs. MN-WU), which is inconsistent with the Shen's case. On the contrary, the inter-run reproducibility for the HB tended to be higher than that for the MN and MN-WU, which is consistent with the Shen's case. Thus, the AAL counterpart was not always consistent with the Shen's results. Although we do not have evidence that each region of the AAL atlas includes different functional areas, it is obvious that the Shen's atlas is more suitable. Thus, the results for the Shen's atlas case seem to be more reliable.

The confidence parameter γ_0 in the HB DOT determines the balance between the data and the prior information. As far as we investigated in the present study, γ_0 did not significantly affected either similarity of RSFCs between fMRI and DOT or inter-run reproducibility of RSFCs. However, both correlation values slightly decreased by setting γ_0 the lowest value ($L \times 10^{-4}$). This may be consistent with the previous finding that a very low γ_0 results in incorrectly localized sparse DOT images in some subjects in real experimental data which has a low signal-to-noise ratio (Yamashita et al., 2016). At present, we do not have a technique to determine the optimal γ_0 value. Further work is required to find it. In the present study, we did not adopt the prevailing approach in the resting-state fMRI studies, spatial ICA. One of the reasons for this is that spatial ICA is suited for whole brain analysis whereas fNIRS data in the present study covered only frontal and parietal areas. Applying spatial ICA to whole brain DOT images will be a challenging future work.

TABLE 7 | Effect of γ_0 value on inter-run reproducibility.

	$L \times 10^0$	$L \times 10^{-1}$	$L \times 10^{-2}$	$L \times 10^{-3}$	$L \times 10^{-4}$
oxy-Hb	0.76 ± 0.06	0.76 ± 0.06	0.76 ± 0.06	0.75 ± 0.07	0.73 ± 0.09
deoxy-Hb	0.75 ± 0.07	0.76 ± 0.07	0.75 ± 0.08	0.74 ± 0.09	0.72 ± 0.10

Values of correlation coefficients are presented as mean ± standard deviation (SD). Each column corresponds to $\gamma_0 = L \times 10^{-N}$, where L is the data length. $\gamma_0 = L \times 10^{-1}$ is the default setting.

CONCLUSION

The present study showed that our HB algorithm can be used as an alternative to fMRI, in estimating resting-state functional connectivity as well as task-related responses. We also demonstrated its superiority over the current standard DOT algorithms. Although fNIRS data in the present study covered only frontal and parietal areas due to the experimental limitation of the high-density measurement, it is desired to cover wider areas of the cortex (ideally whole brain). Recently, we showed

that multi-directional measurement has the ability to accomplish DOT without requiring high-density measurement (Shimokawa et al., 2016). It would be interesting to estimate RSFC for more widespread cortical areas using multi-directional DOT in future work.

DATA AVAILABILITY STATEMENT

The raw data supporting the conclusions of this article will be made available by the authors, without undue reservation, to any qualified researcher.

ETHICS STATEMENT

The studies involving human participants were reviewed and approved by the ATR Review Board Ethics Committee. The patients/participants provided their written informed consent to participate in this study.

AUTHOR CONTRIBUTIONS

TA, TS, TO, YO, AI, YI, and OY designed the study. TA, TS, TO, YO, and OY collected the data. TA analyzed the data. TA, TS, and OY wrote and reviewed the manuscript.

FUNDING

This work was funded by the ImPACT Program of the Council for Science, Technology and Innovation (Cabinet Office, Government of Japan). This research was conducted under contract with the National Institute of Information and Communications Technology, entitled "Analysis of multi-modal brain measurement data and development of its application for BMI open innovation (grant #209)."

ACKNOWLEDGMENTS

Part of this work was presented at the fNIRS2018 conference in Tokyo, Japan, during October 2018 (Aihara et al., 2018). We thank Yoshiko Itakura for her assistance in data acquisition and Kaori Nakamura for her valuable support.

SUPPLEMENTARY MATERIAL

The Supplementary Material for this article can be found online at: https://www.frontiersin.org/articles/10.3389/fnins.2020.00032/full#supplementary-material

REFERENCES

Aihara, T., Shimokawa, T., Ogawa, T., Okada, Y., Ishikawa, A., Inoue, Y., et al. (2018). "Resting state functional connectivity with hierarchical Bayesian diffuse optical tomography," in *Proceedings of the Conference fNIRS2018*, Tokyo.

Birn, R. M., Molloy, E. K., Patriat, R., Parker, T., Meier, T. B., Kirk, G. R., et al. (2013). The effect of scan length on the reliability of resting-state fMRI connectivity estimates. *Neuroimage* 83, 550–558. doi: 10.1016/j.neuroimage.2013.05.099

Biswal, B., Yetkin, F. Z., Haughton, V. M., and Hyde, J. S. (1995). Functional connectivity in the motor cortex of resting human brain using echo-planar MRI. *Magn. Reson. Med.* 34, 537–541. doi: 10.1002/mrm.1910340409

Boas, D. A., Dale, A. M., and Franceschini, M. A. (2004). Diffuse optical imaging of brain activation: approaches to optimizing image sensitivity, resolution, and accuracy. *Neuroimage* 23(Suppl. 1), S275–S288.

Culver, J. P., Durduran, T., Furuya, D., Cheung, C., Greenberg, J. H., and Yodh, A. G. (2003). Diffuse optical tomography of cerebral blood flow, oxygenation, and metabolism in rat during focal ischemia. *J. Cereb. Blood Flow Metab.* 23, 911–924. doi: 10.1097/01.wcb.0000076703.71231.bb

Duan, L., Zhang, Y. J., and Zhu, C. Z. (2012). Quantitative comparison of resting-state functional connectivity derived from fNIRS and fMRI: a simultaneous recording study. *Neuroimage* 60, 2008–2018. doi: 10.1016/j.neuroimage.2012.02.014

Eggebrecht, A. T., Ferradal, S. L., Robichaux-Viehoever, A., Hassanpour, M. S., Dehghani, H., Snyder, A. Z., et al. (2014). Mapping distributed brain function and networks with diffuse optical tomography. *Nat. Photonics* 8, 448–454. doi: 10.1038/nphoton.2014.107

Fang, Q. (2010). Mesh-based Monte Carlo method using fast ray-tracing in Plcker coordinates. *Biomed. Opt. Express* 1, 165–175. doi: 10.1364/BOE.1.000165

Fang, Q., and Boas, D. A. (2009). Monte Carlo simulation of photon migration in 3D turbid media accelerated by graphics processing units. *Opt. Express* 17, 20178–20190. doi: 10.1364/OE.17.020178

Fox, M. D., Snyder, A. Z., Vincent, J. L., Corbetta, M., Van Essen, D. C., and Raichle, M. E. (2005). The human brain is intrinsically organized into dynamic, anticorrelated functional networks. *Proc. Natl. Acad. Sci. U.S.A.* 102, 9673–9678. doi: 10.1073/pnas.0504136102

Funane, T., Atsumori, H., Katura, T., Obata, A. N., Sato, H., Tanikawa, Y., et al. (2014). Quantitative evaluation of deep and shallow tissue layers' contribution to fNIRS signal using multi-distance optodes and independent component analysis. *Neuroimage* 85, 150–165. doi: 10.1016/j.neuroimage.2013.02.026

Gagnon, L., Cooper, R. J., Ycel, M. A., Perdue, K. L., Greve, D. N., and Boas, D. A. (2012). Short separation channel location impacts the performance of short channel regression in NIRS. *Neuroimage* 59, 2518–2528. doi: 10.1016/j.neuroimage.2011.08.095

Gagnon, L., Ycel, M. A., Boas, D. A., and Cooper, R. J. (2014). Further improvement in reducing superficial contamination in NIRS using double short separation measurements. *Neuroimage* 85, 127–135. doi: 10.1016/j.neuroimage.2013.01.073

Greicius, M. D., Krasnow, B., Reiss, A. L., and Menon, V. (2003). Functional connectivity in the resting brain: a network analysis of the default mode hypothesis. *Proc. Natl. Acad. Sci. U.S.A.* 100, 253–258. doi: 10.1073/pnas.0135058100

Guven, M., Yazici, B., Intes, X., and Chance, B. (2005). Diffuse optical tomography with a priori anatomical information. *Phys. Med. Biol.* 50, 2837–2858. doi: 10.1088/0031-9155/50/12/008

Jafri, M. J., Pearlson, G. D., Stevens, M., and Calhoun, V. D. (2008). A method for functional network connectivity among spatially independent resting-state components in schizophrenia. *Neuroimage* 39, 1666–1681. doi: 10.1016/j.neuroimage.2007.11.001

Kirilina, E., Jelzow, A., Heine, A., Niessing, M., Wabnitz, H., Brhl, R., et al. (2012). The physiological origin of task-evoked systemic artefacts in functional near infrared spectroscopy. *Neuroimage* 61, 70–81. doi: 10.1016/j.neuroimage.2012.02.074

Kohno, S., Miyai, I., Seiyama, A., Oda, I., Ishikawa, A., Tsuneishi, S., et al. (2007). Removal of the skin blood flow artifact in functional near-infrared spectroscopic imaging data through independent component analysis. *J. Biomed. Opt.* 12:062111. doi: 10.1117/1.2814249

Lu, C. M., Zhang, Y. J., Biswal, B. B., Zang, Y. F., Peng, D. L., and Zhu, C. Z. (2010). Use of fNIRS to assess resting state functional connectivity. *J. Neurosci. Meth.* 186, 242–249. doi: 10.1016/j.jneumeth.2009.11.010

McGraw, K. O., and Wong, S. P. (1996). Forming inferences about some intraclass correlation coefficients. *Psychol. Meth.* 1, 30–46. doi: 10.1037/1082-989x.1.1.30

Piper, S. K., Krueger, A. K., Koch, S. P., Mehnert, J., Habermehl, C., Steinbrink, J., et al. (2014). A wearable multi-channel fNIRS system for brain imaging in freely moving subjects. *Neuroimage* 85, 64–71. doi: 10.1016/j.neuroimage.2013.06.062

Rupawala, M., Dehghani, H., Lucas, S. J. E., Tino, P., and Cruse, D. (2018). Shining a light on awareness: a review of functional near-infrared spectroscopy for prolonged disorders of consciousness. *Front. Neurol.* 9:350. doi: 10.3389/fneur.2018.00350

Sakakibara, E., Homae, F., Kawasaki, S., Nishimura, Y., Takizawa, R., Koike, S., et al. (2016). Detection of resting state functional connectivity using parietal correlation analysis: a study using multi-distance and whole-head probe near-infrared spectroscopy. *Neuroimage* 142, 590–601. doi: 10.1016/j.neuroimage.2016.08.011

Sasai, S., Homae, F., Watanabe, H., Sasaki, A. T., Tanabe, H. C., Sadato, N., et al. (2012). A NIRS-fMRI study of resting state network. *Neuroimage* 63, 179–193. doi: 10.1016/j.neuroimage.2012.06.011

Sato, T., Nambu, I., Takeda, K., Aihara, T., Yamashita, O., Isogaya, Y., et al. (2016). Reduction of global interference of scalp-hemodynamics in functional near-infrared spectroscopy using short distance probes. *NeuroImage* 141, 120–132. doi: 10.1016/j.neuroimage.2016.06.054

Shen, X., Tokoglu, F., Papademetris, X., and Constable, R. T. (2013). Groupwise whole-brain parcellation from resting-state fMRI data for network node identification. *Neuroimage* 82, 403–415. doi: 10.1016/j.neuroimage.2013.05.081

Shimokawa, T., Ishii, T., Takahashi, Y., Sugawara, S., Sato, M.-A., and Yamashita, O. (2016). Diffuse optical tomography using multi-directional sources and detectors. *Biomed. Opt. Express* 7, 2623–2640. doi: 10.1364/BOE.7.002623

Shimokawa, T., Kosaka, T., Yamashita, O., Hiroe, N., Amita, T., Inoue, Y., et al. (2012). Hierarchical Bayesian estimation improves depth accuracy and spatial resolution of diffuse optical tomography. *Opt. Express* 20, 20427–20446. doi: 10.1364/OE.20.020427

Shimokawa, T., Kosaka, T., Yamashita, O., Hiroe, N., Amita, T., Inoue, Y., et al. (2013). Extended hierarchical Bayesian diffuse optical tomography for removing scalp artifact. *Biomed. Opt. Express* 4, 2411–2432. doi: 10.1364/BOE.4.002411

Takahashi, T., Takikawa, Y., Kawagoe, R., Shibuya, S., Iwano, T., and Kitazawa, S. (2011). Influence of skin blood blow on near-infrared spectroscopy signals measured on the forehead during a verbal fluency task. *Neuroimage* 57, 991–1002. doi: 10.1016/j.neuroimage.2011.05.012

van den Heuvel, M. P., and Hulshoff Pol, H. E. (2010). Exploring the brain network: a review on resting-state fMRI functional connectivity. *Eur. Neuropsychopharmacol.* 20, 519–534. doi: 10.1016/j.euroneuro.2010.03.008

White, B. R., Snyder, A. Z., Cohen, A. L., Petersen, S. E., Raichle, M. E., Schlaggar, B. L., et al. (2009). Resting-state functional connectivity in the human brain revealed with diffuse optical tomography. *Neuroimage* 47, 148–156. doi: 10.1016/j.neuroimage.2009.03.058

Yamashita, O., Shimokawa, T., Aisu, R., Amita, T., Inoue, Y., and Sato, M. (2016). Multi-subject and multi-task experimental validation of the hierarchical Bayesian diffuse optical tomography algorithm. *Neuroimage* 135, 287–299. doi: 10.1016/j.neuroimage.2016.04.068

Zeff, B. W., White, B. R., Dehghani, H., Schlaggar, B. L., and Culver, J. P. (2007). Retinotopic mapping of adult human visual cortex with high-density diffuse optical tomography. *Proc. Natl. Acad. Sci. U.S.A.* 104, 12169–12174. doi: 10.1073/pnas.0611266104

Zhang, H., Duan, L., Zhang, Y. J., Lu, C. M., Liu, H., and Zhu, C. Z. (2011). Test-retest assessment of independent component analysis-derived resting-state functional connectivity based on functional near-infrared spectroscopy. *Neuroimage* 55, 607–615. doi: 10.1016/j.neuroimage.2010.12.007

Zhang, H., Zhang, Y. J., Lu, C. M., Ma, S. Y., Zang, Y. F., and Zhu, C. Z. (2010). Functional connectivity as revealed by independent component analysis of resting-state fNIRS measurements. *Neuroimage* 51, 1150–1161. doi: 10.1016/j.neuroimage.2010.02.080

Zhang, Y., Brooks, D. H., Franceschini, M. A., and Boas, D. A. (2005). Eigenvector-based spatial filtering for reduction of physiological interference in diffuse optical imaging. *J. Biomed. Opt.* 10:11014.

Conflict of Interest: Although the authors AI and YI were employed by the company Shimadzu Corporation, they were not involved in the comparison of several DOT algorithms and therefore the results in the present study cannot be biased.

The remaining authors declare that the research was conducted in the absence of any commercial or financial relationships that could be construed as a potential conflict of interest.

Copyright © 2020 Aihara, Shimokawa, Ogawa, Okada, Ishikawa, Inoue and Yamashita. This is an open-access article distributed under the terms of the Creative Commons Attribution License (CC BY). The use, distribution or reproduction in other forums is permitted, provided the original author(s) and the copyright owner(s) are credited and that the original publication in this journal is cited, in accordance with accepted academic practice. No use, distribution or reproduction is permitted which does not comply with these terms.

frontiers in Human Neuroscience

ORIGINAL RESEARCH
published: 31 January 2020
doi: 10.3389/fnhum.2020.00003

Atypical Dynamic-Connectivity Recruitment in Attention-Deficit/Hyperactivity Disorder Children: An Insight Into Task-Based Dynamic Connectivity Through an fNIRS Study

Stephanie Sutoko[1,2], Yukifumi Monden[3,4], Tatsuya Tokuda[2], Takahiro Ikeda[3], Masako Nagashima[3], Tsukasa Funane[1], Hirokazu Atsumori[1], Masashi Kiguchi[1], Atsushi Maki[1], Takanori Yamagata[3] and Ippeita Dan[2]*

[1]*Hitachi, Ltd., Research & Development Group, Center for Exploratory Research, Tokyo, Japan,* [2]*Faculty of Science and Engineering, Applied Cognitive Neuroscience Laboratory, Chuo University, Tokyo, Japan,* [3]*Department of Pediatrics, Jichi Medical University, Shimotsuke, Japan,* [4]*Department of Pediatrics, International University of Health and Welfare Hospital, Nasushiobara, Japan*

OPEN ACCESS

Edited by:
Fenghua Tian, University of Texas at Arlington, United States

Reviewed by:
Yujin Zhang, Institute of Automation (CAS), China
Bo-yong Park, McGill University, Canada

***Correspondence:**
Stephanie Sutoko
stephanie.sutoko.tc@hitachi.com

Specialty section:
This article was submitted to Health, a section of the journal Frontiers in Human Neuroscience

Received: *22 September 2019*
Accepted: *07 January 2020*
Published: *31 January 2020*

Citation:
Sutoko S, Monden Y, Tokuda T, Ikeda T, Nagashima M, Funane T, Atsumori H, Kiguchi M, Maki A, Yamagata T and Dan I (2020) Atypical Dynamic-Connectivity Recruitment in Attention-Deficit/Hyperactivity Disorder Children: An Insight Into Task-Based Dynamic Connectivity Through an fNIRS Study. Front. Hum. Neurosci. 14:3. doi: 10.3389/fnhum.2020.00003

Connectivity between brain regions has been redefined beyond a stationary state. Even when a person is in a resting state, brain connectivity dynamically shifts. However, shifted brain connectivity under externally evoked stimulus is still little understood. The current study, therefore, focuses on task-based dynamic functional-connectivity (FC) analysis of brain signals measured by functional near-infrared spectroscopy (fNIRS). We hypothesize that a stimulus may influence not only brain connectivity but also the occurrence probabilities of task-related and task-irrelevant connectivity states. fNIRS measurement (of the prefrontal-to-inferior parietal lobes) was conducted on 21 typically developing (TD) and 21 age-matched attention-deficit/hyperactivity disorder (ADHD) children performing an inhibitory control task, namely, the Go/No-Go (GNG) task. It has been reported that ADHD children lack inhibitory control; differences between TD and ADHD children in terms of task-based dynamic FC were also evaluated. Four connectivity states were found to occur during the temporal task course. Two dominant connectivity states (states 1 and 2) are characterized by strong connectivities within the frontoparietal network (occurrence probabilities of 40%–56% and 26%–29%), and presumptively interpreted as task-related states. A connectivity state (state 3) shows strong connectivities in the bilateral medial frontal-to-parietal cortices (occurrence probability of 7–15%). The strong connectivities were found at the overlapped regions related the default mode network (DMN). Another connectivity state (state 4) visualizes strong connectivities in all measured regions (occurrence probability of 10%–16%). A global effect coming from cerebral vascular may highly influence this connectivity state. During the GNG stimulus interval, the ADHD children

tended to show decreased occurrence probability of the dominant connectivity state and increased occurrence probability of other connectivity states (states 3 and 4). Bringing a new perspective to explain neuropathophysiology, these findings suggest atypical dynamic network recruitment to accommodate task demands in ADHD children.

Keywords: dynamic functional connectivity, an inhibitory control task, functional near-infrared spectroscopy, connectivity states, frontoparietal network, attention-deficit/hyperactivity disorder

INTRODUCTION

Attention-deficit/hyperactivity disorder (ADHD) is one of the most prevalent neurodevelopmental disorders with continuous increases of prevalence rate (Akinbami et al., 2011; Hill et al., 2015). Due to the elevated demand for shifting the paradigm from qualitative behavior assessments to quantitative biomarker-based evaluations, the approach of neuroimaging (Fu and Costafreda, 2013; Hager and Keshavan, 2015) becomes very attractive for ADHD studies. Previous studies on ADHD suggest hypoactivation in task-dependent regions-of-interest (ROIs) while performing inhibition (Inoue et al., 2012; Monden et al., 2012b; Nagashima et al., 2014b), attention (Nagashima et al., 2014a,c), working memory (Ehlis et al., 2008), and verbal fluency (Schecklmann et al., 2008) tasks. Furthermore, ADHD subjects revealed abnormalities on the default mode network (DMN) and the sensory-motor network in a resting state (Castellanos et al., 2008; Choi et al., 2013), impaired the cingulo-frontoparietal (CFP) network and the cortico-striato-thalamocortical circuitry associated with attention (Bush, 2010, 2011) and more complex executive functions (Castellanos et al., 2006). ADHD adolescents showed weak connectivities within the inhibition network and failed to suppress irrelevant networks (e.g., DMN) during response inhibition (van Rooij et al., 2015). Both activation and network characteristics had been proposes as screening biomarkers (Monden et al., 2015; Uddin et al., 2017).

The conventional functional connectivity (FC) concept assumes static connectivity over temporal courses (Biswal et al., 1995). However, the assumption of stationarity dismisses the complexity of brain processes. FC analysis was progressing from concepts of static to dynamic temporal networks which several connectivity states were found to alternate (Liu and Duyn, 2013). Dynamic FC analysis provides the information of shifting connectivity states that are not addressed in the static FC analysis (for reviews, see Hutchison et al., 2013; Preti et al., 2017). The connectivity state depicts connectivity patterns, such as strong or weak associations between brain regions. For example, a connectivity state represented a positive correlation between posterior cingulate cortex (PCC) and anterior cingulate cortex (ACC) together with a negative correlation between PCC and right inferior frontal operculum. Furthermore, another connectivity state revealed the opposite correlation characteristics (Chang and Glover, 2010). Connectivity states and its characteristics are task-dependent that reveal distinct differences between resting-state (RS) and cognitive tasks (Gonzalez-Castillo et al., 2015; Gonzalez-Castillo and Bandettini, 2018). In order to accommodate cognitive flexibility, reconfiguration of frontal networks were evidenced by dynamic FC analysis (Braun et al., 2015). In addition, the connectivity state is one of essential information related to the pathophysiology of disorders; dynamic FC-based biomarkers for schizophrenia (Damaraju et al., 2014) and Alzheimer's disease (AD; Jones et al., 2012) may potentially surpass the benefits of static FC-based biomarkers.

Even though fMRI offers high spatial resolution (in the order of square millimeters) and is a well-established analysis method (Bandettini, 2012), another neuroimaging technique, namely, functional near-infrared spectroscopy (fNIRS; Maki et al., 1995; Strangman et al., 2002; Boas et al., 2014), provides better temporal resolution and motion tolerance (Hoshi, 2005). A critical issue facing fMRI is difficulty in measuring infants and children under an unnatural environment (i.e., a confined and noisy space that brings the risk of anxiety and claustrophobia; Byars et al., 2002). Measuring children with abnormal symptomatic behaviors is a challenging task for fMRI because of susceptible motion artifacts, which lead to low rates of successful measurement (Vaidya et al., 1998). For future clinical translational purposes, therefore, application of fNIRS in pediatric studies is inevitable. Several studies related to neurodevelopmental disorders [e.g., ADHD (Monden et al., 2012a), autism spectrum disorder (Ikeda et al., 2018a)] have been pursued using fNIRS.

FC analysis using fNIRS has been investigated, and the results of those investigations revealed that fNIRS detects similar networks to networks distinguished by fMRI (Duan et al., 2012; Sasai et al., 2012; Tak et al., 2015) and also achieves high reliability and reproducibility (Niu et al., 2011, 2013; Zhang et al., 2011). Furthermore, fNIRS is a valid method for quantifying characteristics of RS dynamic FCs (Li et al., 2015). RS dynamic FCs detected by fNIRS also revealed abnormalities of connectivity states in mild-cognitive-impairment and AD patients (Niu et al., 2019). The RS task was mainly studied due to its low task demand. However, test-retest reliability of the RS task was found to be insufficient (Lang et al., 2014) due to unavoidable ongoing cognitions at rest, such as inner experiences (i.e., speaking, seeing, thinking, sensory awareness, and feeling; Doucet et al., 2012; Hurlburt et al., 2015). Therefore, the task-based measurement with less-variant and controlled task-positive networks may be a potential approach. Task-based networks drawn from fNIRS measurements have been evaluated for an ADHD screening biomarker and showed a promising result of 88% accuracy (Sutoko et al., 2019a). However, to date, fNIRS has not been applied to study task-based dynamic FCs.

The current study, therefore, aims to explore and evaluate the feasibility of task-based dynamic FCs (measured by fNIRS) in particular data of typically developing children (TD) and children with ADHD during a task, such as an inhibition control task. The application of FC analysis using fNIRS to children also emphasizes the benefits of fNIRS measurement over less-practical fMRI measurement. By using task-based dynamic FC analysis, we addressed three questions: (1) Is shifting brain connectivity observed by fNIRS during the temporal task course? (2) How connectivity states within measured regions (i.e., ROIs) shift (and how frequently) during the temporal task course? While previous studies focus on particular networks over temporal courses, the dynamic FC analysis takes into account all networks within measured regions for categorizing them in connectivity states. This analysis becomes more robust compared to the fluctuation of connectivity strength during the temporal course. (3) What are the differences between TD and ADHD children in dynamically shifted connectivity states? Compared to the static FC analysis, the dynamic FC analysis is capable to resolve the mechanism of shifting connectivity state in response to the task. Brain connectivity states expectedly change during the temporal task course, and the changes may phase-lock with stimulus information (e.g., onset and end of the stimulus). We hypothesized that several connectivity states suggesting task-related and task-irrelevant networks may be alternated with different probabilities of occurrence. Brain-network impairment in ADHD subjects (as mentioned above) may also occur in atypical connectivity states and/or dynamic occurrence probabilities as implications of task demands. These results can provide ADHD neuropathophysiology from a noteworthy perspective and bring insights for clinical purposes.

MATERIALS AND METHODS

Subjects and Experimental Design

Subject data described here originally came from two different previously reported datasets: (1) 21 medication-naïve ADHD-children data (right-handed; 17 boys; 7.8 ± 1.7 years old; Tokuda et al., 2018; Sutoko et al., 2019b); and (2) 21 age-matching subjects selected from 30 TD control data (right-handed; 15 boys; 8.5 ± 1.8 years old; Monden et al., 2015). Both the TD and ADHD children were evaluated according to the Wechsler Intelligence Scale for Children—Third Edition (WISC-III). Full-scale IQ scores of the TD (105.5 ± 12.3 of IQ) and ADHD (92.8 ± 12.9 of IQ) groups were unmatched (two-sample t-test). The TD group had higher ($p < 0.01$; $t_{(40)} = 3.27$) full-scale IQ scores than those of the ADHD group. All subjects provided oral consent, and written consent was obtained from all subject's guardians according to the latest version of the Declaration of Helsinki. Previously related and current studies were approved by the Ethics Committees of Jichi Medical University Hospital, the International University of Health and Welfare, Chuo University, and Hitachi, Ltd. This study is collaboration research between Jichi Medical University Hospital, the International University of Health and Welfare, Chuo University, and Hitachi, Ltd. An ADHD-subject was excluded from further analysis because of an unexpected technical problem in data saving.

All subjects performed a visual inhibition control task. The block-design paradigm is described in detail elsewhere (Monden et al., 2012b; Nagashima et al., 2014b; Ikeda et al., 2018b). The paradigm involved two types of task blocks, namely, Go and Go/No-Go (GNG) blocks. The Go block was performed seven times and the GNG block was performed six times in turns in which the Go block always preceded the GNG block (i.e., baseline). In brief, the subjects were required to respond to any visual stimulus (e.g., tiger or lion pictures; 800 and 200 ms for display interval and between-picture waiting interval, respectively; 24 times) by pressing a designated button during the Go block. However, the subjects were asked to control their response and react only on selective visual stimulus (e.g., giraffe picture; 800 and 200 ms for display interval and between-picture waiting interval, respectively; 24 times with 50% occurrence of the selective stimulus) during the GNG block. The 3-s instruction was displayed prior to the Go and GNG blocks in order to guide the subjects in performing upcoming blocks (e.g., press the button for tiger or lion; do not press the button for elephant). This task lasted for about 5–6 min. Even though a previous experiment on a medication-naïve ADHD dataset adopted a randomized, double-blind, placebo-controlled, and crossover study, the current analysis incorporated only pre-administration data (neither medication nor placebo) in order to focus only on the nature of ADHD characteristics.

As conducting the measurement, three parameters of behavioral performance, such as accuracy of selective stimulus-response, accuracy of non-selective stimulus-response, and response time of selective stimulus-response, were measured. Behavioral performances have been reported in our previous publications. Inconsistent behavioral characteristics were found in term of group comparison (i.e., TD vs. ADHD; Monden et al., 2012b; Nagashima et al., 2014b). Despite these behavioral inconsistencies, hypoactivation in the right middle frontal gyrus (MFG) and inferior frontal gyrus (IFG) was constantly observed. In summary, the interpretation of behavioral performances is confounding, and brain dysfunctions prompt better understandings for inter-group differences. Consequently, the relationships between behavioral performances and brain parameters (i.e., connectivity states) were not subjected to the current analysis.

fNIRS Measurement

As the subjects were performing the task, a dual-wavelength fNIRS system (695 and 830 nm; ETG-4000, Hitachi Medical Corporation, Tokyo, Japan) was used to measure cerebral hemodynamic changes. Eight emitters and seven detectors were incorporated in a probe (in a 3 × 5 arrangement). The two probes were placed on the head of the subject according to the placement as described elsewhere (Monden et al., 2012a). The probe placement aimed to cover the bi-hemispheric lateral prefrontal-to-inferior parietal lobes (Garavan et al., 1999; Liddle et al., 2001; Rubia et al., 2003; Herrmann et al., 2004, 2005). The measured regions (also called "channels")

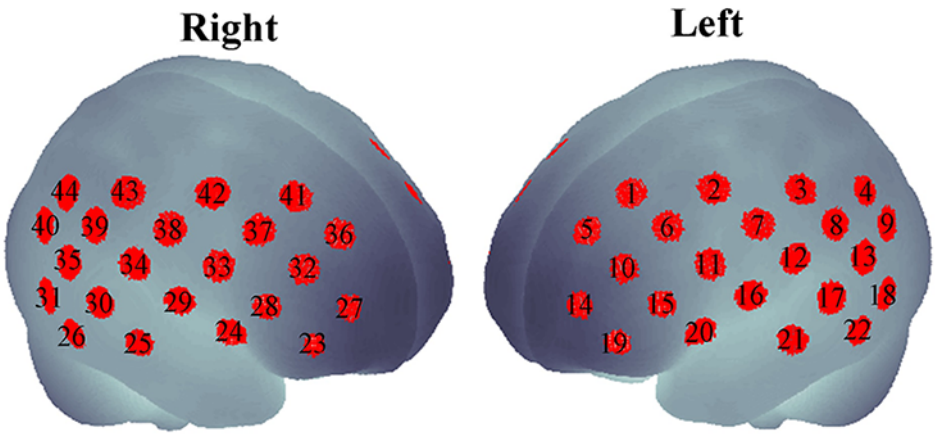

FIGURE 1 | Forty-four channels spatially registered on bilateral hemispheres.

were approximately estimated at the midpoint between an emitter and a detector. Therefore, measurements by 44 channels could be simultaneously obtained from the two probes. Emitter and detector positions was measured using a 3D digitizer, and the channel locations were spatially registered in the Montreal Neurological Institute (MNI) standard brain space by the probabilistic registration method (Tsuzuki et al., 2007, 2012; Tsuzuki and Dan, 2014) as shown in **Figure 1**.

Signal Processing

fNIRS signal processing was performed on the MATLAB-based software Platform for Optical Topography Analysis Tools (POTATo, Hitachi, Ltd, Research and Development; Sutoko et al., 2016). Optical density of transmitted NIR light was detected for two signal types, oxygenated and deoxygenated hemoglobin (O_2Hb and HHb) and converted into the product of hemoglobin-concentration change and optical-path length (ΔC_{O_2Hb}·L and ΔC_{HHb}·L in mM·mm units) according to the modified Beer-Lambert law (Delpy et al., 1988; Maki et al., 1995). A flow chart of the analysis of fNIRS data is summarized in **Figures 2**, **3**. The signal-processing steps are specified inside the dashed box in **Figure 2**. Signal processing was applied to ΔC_{O_2Hb}·L and ΔC_{HHb}·L signals of each subject and channel (**Figure 3A**). Channel signals with signal-to-noise ratio (SNR; power ratio of 0.01–0.15 Hz to 4.5–5 Hz) less than 10 dB were eliminated (about 5% of the total number of signals). To remove baseline drift and cardiac pulsation, basic processing including first-degree polynomial fitting and band-pass filtering (5th order Butterworth filtering at 0.01–0.8 Hz) was applied to remaining signals (92.0 ± 10.3% across subjects). Furthermore, sudden changes (> 0.1 mM·mm between two sampling points), also called "spikes" (i.e., a motion-artifact characteristic), were assessed. Data points affected by the spikes (together with one-second data points before and after the spikes) were then removed from a continuous signal (1.11 ± 1.69% of total data points across subjects), and the removed data points were estimated using cubic spline interpolation (third-order polynomials). An example result of spike removal and correction is shown in **Figure 3B**.

Analysis of Dynamic Connectivity

The five steps of the dynamic-connectivity analysis adapted from the sliding-window correlation (SWC) method (Hutchison et al., 2013; Preti et al., 2017), which follows the signal-processing steps shown in **Figure 2**, are detailed below.

In the first step, the channel-wise processed signals are correlated to each other ($ch \times ch$) with a window length of 12.0 s and window offset of one sampling point (0.1 s; see **Figure 3C**). The greater correlation coefficients (r) are computed, the stronger connectivities between regions are interpreted. The total number of connectivity maps (i.e., W) for each subject and signal type is given by the total data points (5–6 min; 3,000–3,600 points) minus the sliding-window points (12.0 s; 120 points). To monitor the transition of dynamic connectivity from baseline to task and vice versa, fifty percent of the stimulus interval (GNG block) was selected as the sliding window. Using a longer sliding window than the stimulus interval will neglect subtle connectivity changes during transitions.

In the second step, dynamic-connectivity maps obtained from all temporal points, subjects, and signal types are concatenated in 3D matrices (as shown in **Figure 3D**).

In the third step, because the number of connectivity states involved in the task is not presumed, it is determined by trial-and-error unsupervised clustering for all connectivity maps (starting from 2 to 10 clusters) by using the k-means clustering (**Figure 3E**). Each cluster produces a centroid map. Centroid maps characterize attribute centers with the shortest total Euclidean distances of within-cluster members to the centroids. Those clusters represent connectivity states. Low-SNR signals (which had been eliminated beforehand) formed incomplete

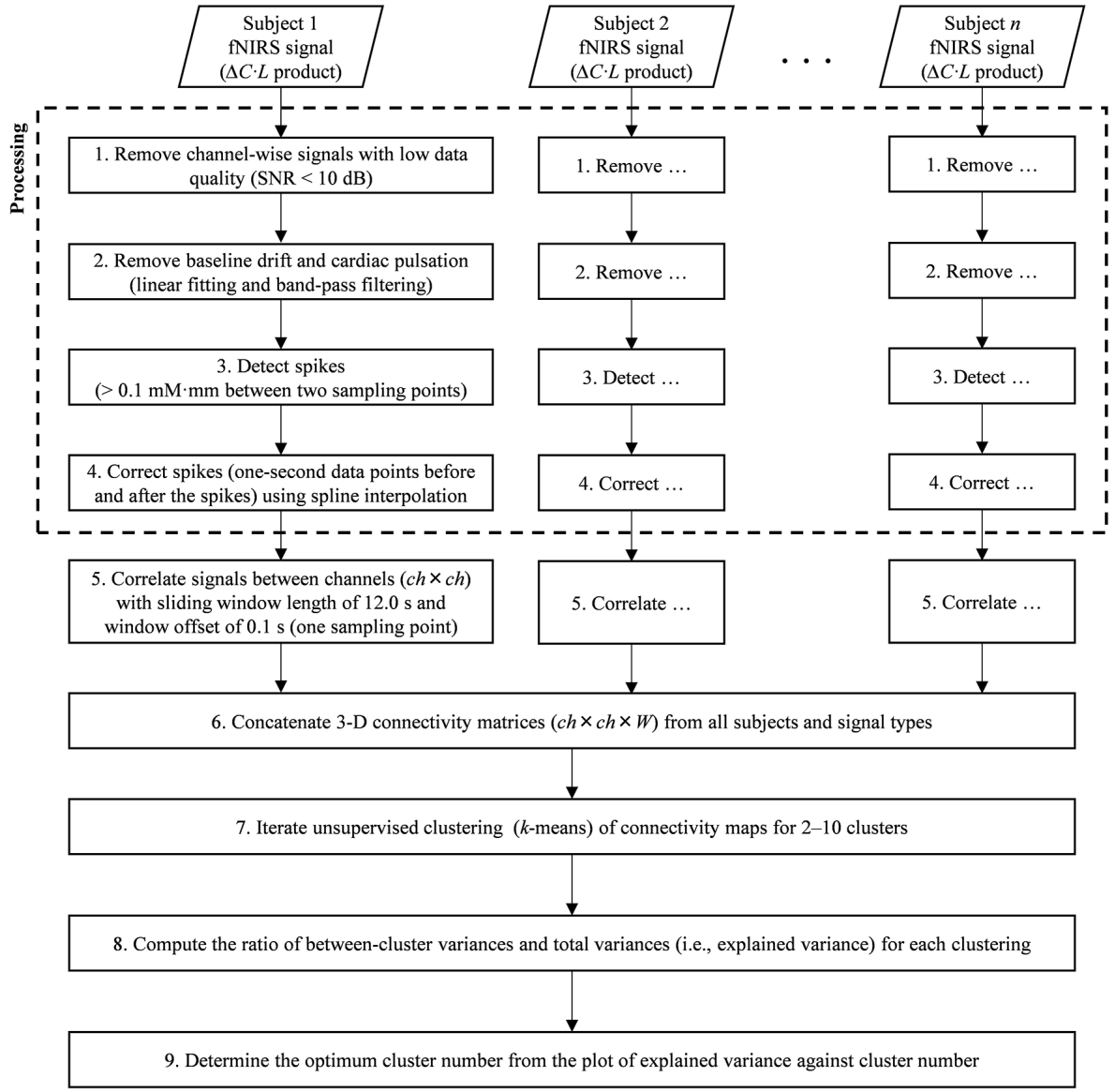

FIGURE 2 | Flow chart of signal processing (dashed square) and dynamic-functional-connectivity (FC) analysis.

connectivity maps, which were therefore temporarily rejected during the trial-and-error clustering.

In the fourth step, to evaluate the correctness of clustering, a parameter called "explained variance" is calculated. The explained variance (given as a percentage) indicates the ratio of between-cluster variances and total variances. As the cluster number increases, the between-cluster variance decreases, and the explained variance reaches approximately 100% (**Figure 3F**). Cluster number should be appropriately selected; that is, excessively low and high cluster numbers would result in mismatched clustering and overfitting, respectively.

In the fifth step, the elbow method was used to determine a threshold for cluster number, which, if surpassed, clustering is not effectively improved (Tibshirani et al., 2001). The threshold was then defined as the optimum cluster number (i.e., connectivity states). Thereafter, several centroid maps were obtained by clustering with the optimum cluster number. The incomplete connectivity maps previously disregarded were approximately classified into specific clusters according to the highest similarity among the remaining characteristics of connectivity maps and centroid maps.

Statistical Analysis

Subject-wise connectivity maps with labeled clusters were compartmentalized according to the block interval (13, 24, and 13 s) of the baseline (10 s Go block and 3 s instruction), stimulus (GNG block), and post-stimulus (3 s instruction and 10 s Go block) intervals. The temporal information of the connectivity

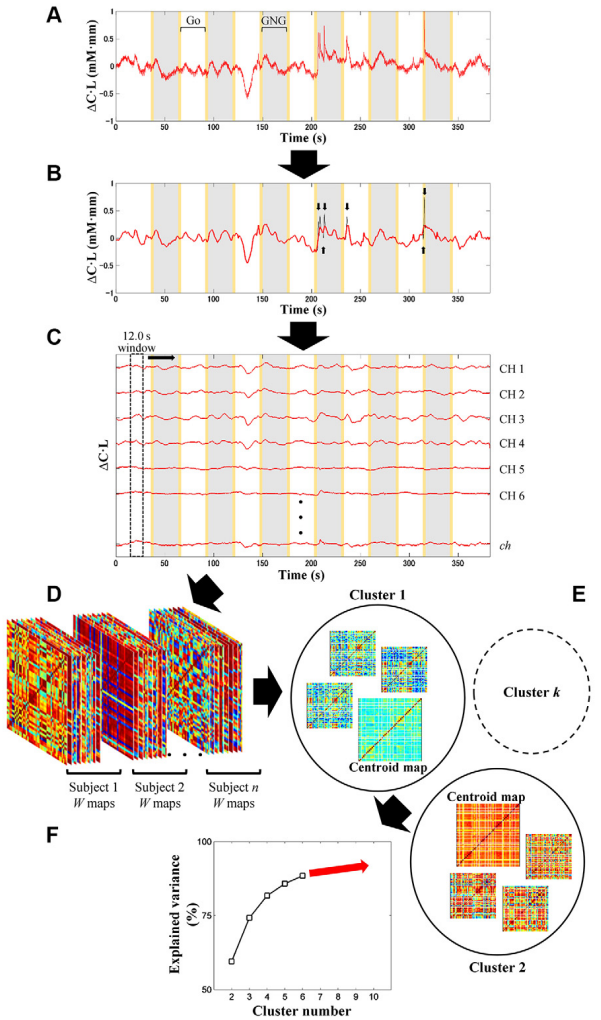

FIGURE 3 | Illustration of signal preprocessing **(A,B)** and dynamic-FC analysis **(C–F)**. Signal processing was applied to ΔC_{O_2Hb}·L and ΔC_{HHb}·L signals (i.e., signal type) of each subject and channel (*ch*) **(A)**. After linear fitting and band-pass filtering (5th order of Butterworth filtering; 0.01–0.8 Hz), motion artifacts with spike characteristics (black plot) were detected (black arrows) and corrected by spline interpolation **(B)**. Gray and yellow patches represent the Go/No-Go (GNG) block as stimulus intervals and the instruction intervals, respectively. Sliding-window-correlation analysis with 12.0-s window length and 0.1-s window offset between channels for each subject and signal type resulted in *W* (total measurement minus window lengths; in points) number of *ch* × *ch* maps **(C)**. Maps (*ch* × *ch* × *W*) obtained from all subjects and signal types were concatenated **(D)**. Cluster (i.e., connectivity state) number was optimized afterward (starting from 2 to 10 clusters) by *k*-means clustering **(E)**. In each clustering, a parameter called explained variance was computed. To determine the optimum cluster number, the relationship between cluster number and explained variance was then plotted **(F)** by using the elbow assessment method.

map was aligned to the onset of the connectivity window. The inter-stimulus interval was 30 s (including 24 s for the Go block and two 3-s instructions); thus, the connectivity maps in the post-stimulus and baseline intervals were unlikely to overlap. **Figure 4** shows an illustration of dynamic change for four connectivity states from an ADHD child over the temporal course. Subject-wise probability occurrence was defined as the probability of specific connectivity states occurring during six blocks. Because the occurrence probability follows the discrete probability distribution, statistical tests were performed according to non-parametric manners. Kruskal–Wallis *H* test was applied to median values of occurrence probability in order to evaluate the effect of connectivity state. The effect of connectivity state and signal type on median values of occurrence probability was determined by using Friedman test. Dunn-Šidák *post hoc* analysis was applied to significant effects given by the Kruskal–Wallis *H* test. Furthermore, the effect of signal type on median values of occurrence probability for each connectivity state was evaluated by using the Wilcoxon signed-rank test. The difference between the TD and ADHD groups (i.e., the effect of the group) in terms of occurrence probabilities of (O_2Hb and HHb) connectivity states was statistically analyzed by using Wilcoxon rank-sum test.

RESULTS

Selection of Optimum Cluster Number

The relationship between cluster numbers and explained variance is shown in **Figure 5**. As expected, a non-linear positive relationship was obtained. While two clusters could only address the explained variance of about 60%, unsupervised clustering with 10 clusters accommodated explained variance of approximately 93%. The "elbow" might not be empirically determined; thus, the optimum cluster number was selected on the basis of the longest distance between a first-order line (clusters two and 10) and other points. If there were two or more cluster numbers revealing a relatively similar distance, the less cluster number was preferred to minimize the risk of overfitting. Four clusters with an explained variance of 82% was selected as the optimum cluster number. Four centroid maps are shown in **Figure 6**. The centroid maps of clusters two and three are the least correlated (see **Figures 6B,C**; Pearson's correlation; $r = 0.40$), whereas the centroid maps of clusters one and two are the most correlated (see **Figures 6A,B**; Pearson's correlation; $r = 0.85$).

Connectivity States

Averages of within-cluster connectivity (Fisher's *z* transformed) for each state are shown in **Figure 7**. The five features highlighted from these results are explained as follows. First, the dynamic FC of state 1 shows specifically strong within-region connectivities in the bilateral IFG, bilateral MFG, bilateral supramarginal gyrus (SMG), and between-region connectivities in the left precentral gyrus (PrCG) and left postcentral gyrus (PoCG) and left IFG and left PrCG (**Figure 7A**; black-squared regions). Several channels within the right MFG and left IFG also reveals strong connectivities to channels in the regions of right IFG and left MFG (**Figure 7A**; magenta-squared regions). Furthermore, the strong within-region connectivity is observed in major channels of the right middle temporal gyrus (MTG) (**Figure 7A**; magenta-squared regions). Second, the dynamic FC pattern of state 2 (**Figure 7B**) is similar to that of state 1 (**Figure 7A**; Pearson's

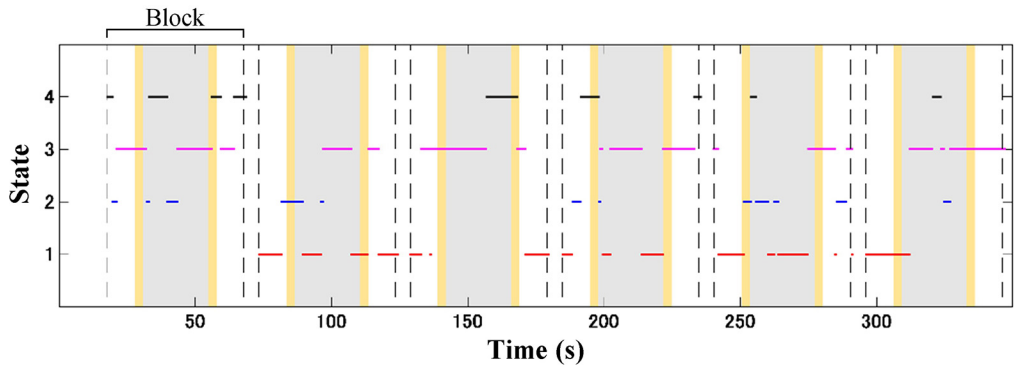

FIGURE 4 | Illustration of dynamic shifting between four connectivity states (red, blue, magenta, and black lines for connectivity states 1, 2, 3, and 4, respectively) in an attention-deficit/hyperactivity disorder (ADHD) child (a 7-years old boy) during the GNG task. Gray patches represent the GNG block as stimulus intervals, and yellow patches denote the instruction intervals. A block interval is specified by 13, 24, and 13 s of the baseline (10 s of Go block and 3 s of instruction), stimulus, and post-stimulus (10 s of Go block and 3 s of instruction) intervals, respectively. In one time measurement, six-block intervals were acquired according to the number of stimuli.

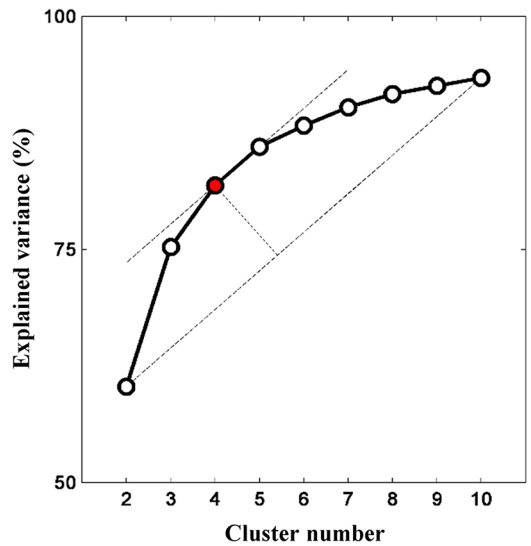

FIGURE 5 | Relationship between cluster number and explained variance. Increasing cluster number consequently increases the explained variance (given as a percentage). The explained variance gradually plateaus (or insignificant increase) as more clusters are added. The optimum cluster number is four clusters as determined by the elbow assessment method.

correlation; r = 0.87); however, the range of connectivity strength is stronger in the dynamic FC of state 2 (0.22–0.77 vs. −0.07–0.62). The significantly strong connectivities are found in the within-region of bilateral IFG – MFG and the between-region of left PrCG and left PoCG (**Figure 7B**; black-squared regions). Third, the dynamic FC of state 3 visualizes the strong (within- and between-region) connectivities in the midline vertex along the bilateral frontal to parietal cortices, such as the bilateral MFG, inter-hemispheric MFG (**Figure 7C**; black-squared regions), the upper part of bilateral and inter-hemispheric PrCG, SMG, and angular gyrus (ANG) (**Figure 7C**; magenta-squared regions). Fourth, similar to centroid maps, averages of within-cluster connectivity for states 2 and 3 are the least correlated (c.f. **Figures 7B,C**; Pearson's correlation; r = 0.34). The low correlation between two connectivity states may suggest differences of connectivity pattern. For example, strong connectivities between bilateral MTG and intra-hemispheric IFG were observed in the connectivity state 2. On the contrary, the connectivity state 3 revealed stronger connectivities of intra-hemispheric ANG and SMG. Fifth, the dynamic FC of state 4 (**Figure 7D**) represents massive and strong connectivity between all bi-hemispheric channels.

Characteristics of Connectivity State

Occurrence probability for each connectivity state (O_2Hb and HHb; **Figures 8A1–D1,A2–D2**) and group (TD and ADHD; red and blue plots) is shown in **Figure 8**. For the visualization purpose only, the plots were represented by mean values of occurrence probability across subjects. However, statistical tests were performed to test median values of occurrence probability between four states, two groups, and two signal types. The four features drawn from these results are explained as follows.

First, the highest occurrence probability was achieved in state 1 (mean of 56%; median of 67%; Dunn-Šidák *post hoc* analysis of Kruskal–Wallis H test; $\chi^2_{(3,160)} = 97.5$; $p < 10^{-20}$) for the dynamic HHb FC (**Figure 8A2**). For the dynamic O_2Hb FC, the occurrence probabilities of states 1 and 2 (**Figures 8A1,B1**; means of 40% and 29%; medians of 50% and 33%, respectively) were significantly higher (Dunn-Šidák *post hoc* analysis of Kruskal–Wallis H test; $\chi^2_{(3,160)} = 51.7$; $p < 10^{-10}$) than those of states 3 and 4 (**Figures 8C1,D1**).

Second, there was no significant difference between the occurrence probability of states 3 (mean of 7%–15%; median of 0%–17%) and state 4 (mean of 10%–16%; median of 0%–17%; see **Figures 8C,D**; Dunn-Šidák *post hoc* analysis of Kruskal-Wallis H test) for the dynamic O_2Hb and HHb FCs.

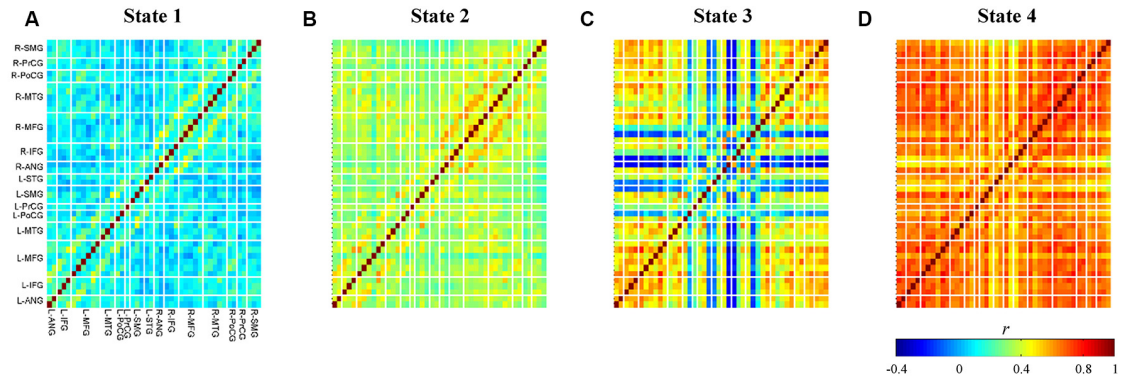

FIGURE 6 | Obtained centroid maps for each cluster **(A–D)**. Colors represent connectivity strength (*r*) between two channels. Channels are categorized and ordered according to spatially registered regions (L, left; R, right; ANG, angular gyrus; IFG, inferior frontal gyrus; MFG, middle frontal gyrus; MTG, middle temporal gyrus; PoCG, post-central gyrus; PrCG, pre-central gyrus; SMG, supramarginal gyrus; STG, superior temporal gyrus).

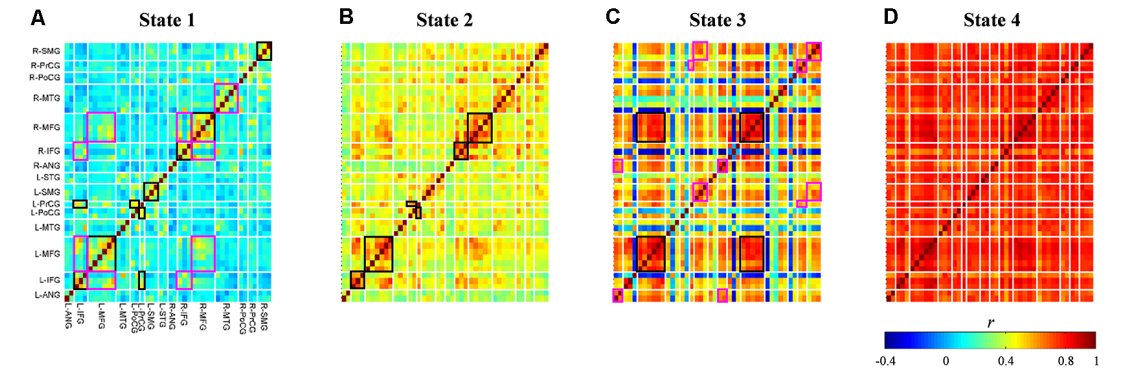

FIGURE 7 | Dynamic functional connectivity maps (Fisher's *z* transform) averaged across subjects and signal types for each connectivity state **(A–D)**. Colors represent connectivity strength ($\bar{r}$) between two channels. Channels are categorized and ordered according to spatially registered regions (L, left; R, right; ANG, angular gyrus; IFG, inferior frontal gyrus; MFG, middle frontal gyrus; MTG, middle temporal gyrus; PoCG, post-central gyrus; PrCG, pre-central gyrus; SMG, supramarginal gyrus; STG, superior temporal gyrus). Black and magenta rectangles identify regions with strong connectivities in the entire regions and in the several channels of regions, respectively.

Third, the occurrence probabilities of states 3 and 4 for the dynamic O_2Hb FC were significantly higher than those for the dynamic HHb FCs (see **Figures 8C1,C2,D1,D2**; Wilcoxon signed-rank test; $z = 2.95–3.08$; $p < 0.01$).

Fourth, the occurrence probability of state 1 for the dynamic HHb FC was significantly higher than that for the dynamic O_2Hb FC (see **Figures 8A1,A2**; Wilcoxon signed-rank test; $z = 4.80$; $p < 10^{-6}$).

These four points suggest that the connectivity states (Friedman test; $\chi^2_{(3)} = 145$; $p < 10^{-30}$) significantly affect occurrence probability. There was no evidence of the effect of signal type *per se* on occurrence probability (Friedman test; $\chi^2_{(1)} = 1.65$; $p > 0.05$). The statistical results are summarized in **Table 1**.

Occurrence Probabilities of Connectivity States for TD and ADHD Children

The effects of groups were found at different intervals for each connectivity state. For example, the ADHD group showed significant high occurrence probability (Wilcoxon rank-sum test; $z = 1.96–3.18$; $p < 0.05$) of states 3 (**Figure 8C**) and 4 (**Figure 8D**) at some points in the baseline, stimulus, and post-stimulus intervals. However, the ADHD group showed significant low occurrence probability of state 1 after the stimulus onset (blue plot in **Figure 8A1**; Wilcoxon rank-sum test; $z = -2.76$ to -1.99; $p < 0.05$) and in the post-stimulus interval (blue plots in **Figure 8A2**; Wilcoxon rank-sum test; $z = -1.99$; $p < 0.05$). The occurrence probabilities of state 2 for the dynamic O_2Hb and HHb FCs differed in the case of both groups. Significantly increased occurrence probabilities of state 2 (dynamic O_2Hb FC) were found at the baseline, transition of baseline-to-stimulus, and post-stimulus intervals for the TD group (**Figure 8B1**; Wilcoxon rank-sum test; $z = 1.96–2.68$; $p < 0.05$). On the other hand, occurrence probability of state 2 for the dynamic HHb FC in the case of the ADHD group (blue plot in **Figure 8B2**) significantly decreased at the baseline interval (Wilcoxon rank-sum test; $z = -2.46$ to -2.97; $p < 0.05$), but it increased at the end of the stimulus

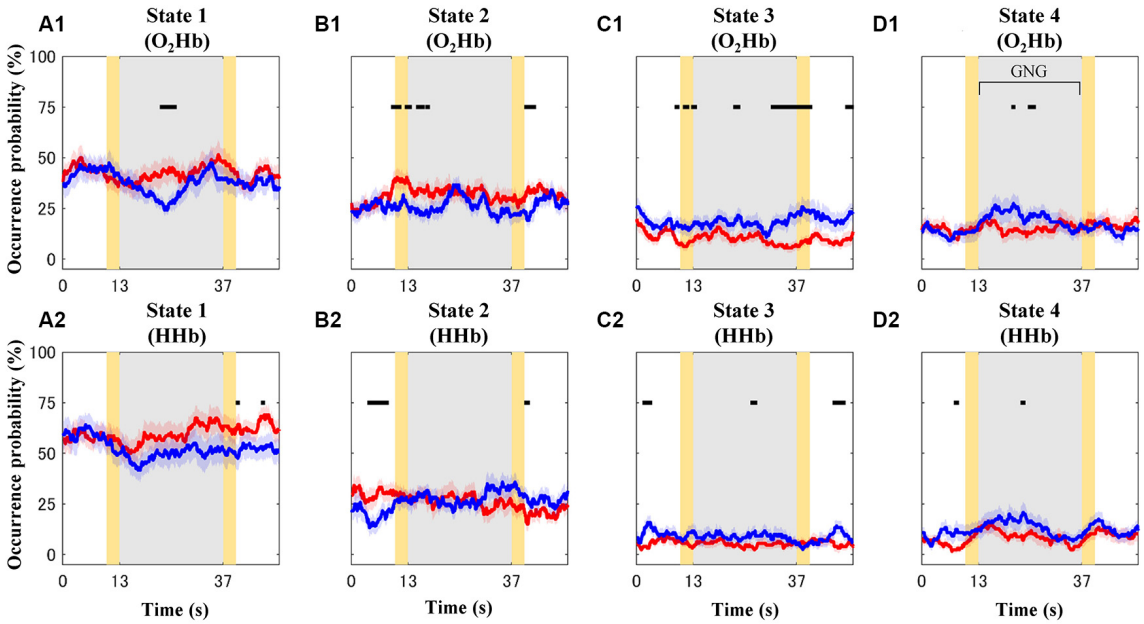

FIGURE 8 | Mean values of occurrence probability for each connectivity state [**A–D** for connectivity states 1–4; **(A1–D1)** and **(A2–D2)** for dynamic O_2Hb and HHb functional connectivities, respectively] in the case of the typically developing (TD; red plots) and ADHD (blue plots) groups. Gray and yellow patches represent the GNG block as stimulus intervals and the instruction intervals, respectively. Shaded red and blue patches around solid plots indicate within-group standard error. Black squares show significantly different occurrence probability between the TD and ADHD groups at particular time points.

TABLE 1 | Summary of occurrence probability for each connectivity state and statistical results of occurrence probability comparisons.

Signal type	State 1 (S1)	State 2 (S2)	State 3 (S3)	State 4 (S4)	Inter-state
O_2Hb	$\bar{x}$ = 40% $\tilde{x}$ = 50%	$\bar{x}$ = 29% $\tilde{x}$ = 33%	$\bar{x}$ = 15% $\tilde{x}$ = 17%	$\bar{x}$ = 16% $\tilde{x}$ = 17%	S1∼S2 > S3∼S4 $\chi^2_{(3,160)} = 51.7$; $p < 10^{-10}$
HHb	$\bar{x}$ = 56% $\tilde{x}$ = 67%	$\bar{x}$ = 26% $\tilde{x}$ = 17%	$\bar{x}$ = 7% $\tilde{x}$ = 0%	$\bar{x}$ = 10% $\tilde{x}$ = 0%	S1 > S2 > S3∼S4 $\chi^2_{(3,160)} = 97.5$; $p < 10^{-20}$
O_2Hb vs. HHb	$S1_{(O_2Hb)} < S1_{(HHb)}$ $z = -4.80$ $p < 10^{-6}$	$S2_{(O_2Hb)} \sim S2_{(HHb)}$ $z = 1.65$ $p > 0.1$	$S3_{(O_2Hb)} > S3_{(HHb)}$ $z = 2.95$ $p < 0.01$	$S4_{(O_2Hb)} > S4_{(HHb)}$ $z = 3.08$ $p < 0.01$	

$\bar{x}$: mean and $\tilde{x}$: median

near the post-stimulus interval (Wilcoxon rank-sum test; $z = 2.10$–2.26; $p < 0.05$).

DISCUSSION

In the current study, fNIRS signals were used for task-based dynamic FC analysis for the first time to the best of our knowledge. Without making any assumptions, we optimized the number of connectivity states. Four different connectivity states were found to shift while the GNG task was performed. The difference between connectivity states was caused by region-specific networks and their occurrence probabilities. A dominant connectivity state was frequently observed (averaged occurrence probability of 40%–56%). Occurrence probabilities of connectivity state dynamically fluctuated, but these fluctuations differed for the TD and ADHD groups. Furthermore, the chances of occurrence probability were seemingly stimulus-dependent. This result may explain atypical ADHD connectivity recruitment and be potentially useful as screening biomarkers.

Interpretations of Connectivity States

The current results of dynamic FC analysis show four alternating connectivity states during the execution of the GNG task. Even though connectivity states seemingly changed in random ways, strong connectivities within bilateral frontoparietal networks were apparently found in two dominant connectivity states (i.e., states 1 and 2). The frontoparietal network has been associated with attention control (Peers et al., 2005) showing extended activation of the inferior parietal cortex (including SMG and ANG) to accommodate attentional flexibility (Dodds et al., 2011). Since inhibitory control is a complex cognitive process, attention control may also be involved in sequential processes. Successful inhibition response should be able to recognize inhibitory cues that

also require intact attention control (Verbruggen et al., 2014; Hong et al., 2017). Moreover, attentional control sometimes correlates with behavioral performances such as omission-commission errors and response time (Murphy et al., 1999; Keilp et al., 2005; Reynolds et al., 2006). According to the above arguments, the relation between the frontoparietal network and complex cognitive processes of inhibition response is justifiably inferred (Dodds et al., 2011; Erika-Florence et al., 2014). It is therefore assumed that both dominant connectivity states are task-related states.

The differences between the two dominant connectivity states are still unclear unless the connectivity of state 2 was stronger and less frequently occurred than those of state 1. The framework of intrinsic-transient networks may explain the two connectivity states. Intrinsic networks should be at least maintained, whereas task-related (i.e., transient) networks may be associated with task demands (Braun et al., 2015). Transient networks are mainly constructed from intrinsic networks (Cole et al., 2014). However, we could not confirm that connectivity state 1 is a task-related intrinsic or transient network based only on connectivity strength and occurrence probability. Furthermore, in the current study, segregation of dynamic FCs for the Go and GNG blocks was insignificant. Even though previous studies evidenced functional differentiation within networks (Menon et al., 2001; Hong et al., 2017), the difficulty of functional differentiation has also been reported (Verbruggen and Logan, 2008). Our recent study also showed that the transitioned connectivity between baseline and stimulus intervals remained subtle particularly in the TD children compared to the ADHD children (Sutoko et al., 2019a).

The frontoparietal network is not specifically involved in the two other connectivity states (states 3 and 4). Thus, those two connectivity states are assumed to be task-irrelevant states. Strong connectivity affecting all regions (i.e., global) was detected in connectivity state 4. A global effect is propagated from cerebral vessels to the local regulation of neurovascular coupling (Roy and Sherrington, 1890; Devonshire et al., 2012). Furthermore, connectivity state 3 shows strong connectivities in overlapped DMN-related regions, particularly in the bilateral medial PFC and ANG (Raichle et al., 2001; Raichle and Snyder, 2007). However, it should be noted that the signal power was concentrated in the low-frequency range: the task-related frequency of interest (0.01–0.8 Hz) was wider than the usual low-frequency oscillations of DMN (<0.2 Hz). While the frontoparietal network is referred to as a task-positive network, the DMN network behaves in an opposite manner, showing deactivation of a task-negative network (Fox et al., 2005). The low occurrence probability of connectivity state 3 (7%–15% on average) happens during task performance, and it might be considered as the compensatory act of increased recruitment of task-positive networks (Cole et al., 2014).

Differences between occurrence probabilities for the O_2Hb and HHb dynamic FCs in connectivity states 1, 3, and 4 were observed. These differences might be caused by underlying characteristics of systemic effects (Franceschini et al., 2003) and blood-related change sensitivity (Hoshi et al., 2001; Hirasawa et al., 2015). Moreover, frequency-specific connectivity was also non-uniform. High coherence of HHb signals was found in a lower-frequency range than that of the O_2Hb signals (Sasai et al., 2011). Furthermore, as shown by the datasets used in this study, HHb signals have often been reported to have low SNR (Sasai et al., 2011; Fishburn et al., 2014). The current analysis (in which more HHb signals with low SNR were removed, and the clustering of connectivity state was approximated from remaining signals) may intensify these differences. Therefore, different O_2Hb and HHb FC behaviors are quite well-grounded.

Differences Between TD and ADHD Children

The current dynamic FC analysis offers a different perspective in defining differences between TD and ADHD children. Significant group effects were found to interlock with stimulus information, namely, baseline, stimulus, and post-stimulus intervals. Therefore, the task demand may suggest the mechanism of shifting states. The decreased occurrence probability of connectivity state 1 was shown by the ADHD children during the stimulus. Since the frontoparietal network is involved in connectivity state 1, this result may imply decreased effectiveness of task-related connectivity state recruitment in ADHD children. ADHD children revealed lower activation in the right MFG/IFG compared to the activation of the TD children during the GNG task (Monden et al., 2012b; Nagashima et al., 2014b). A meta-analysis of inhibitory control studies (i.e., GNG and SST) found extensive hypoactivation in the supplementary motor area (SMA), ACC, and striato-thalamic areas. This finding suggests impaired right-hemispheric fronto-basal ganglia networks (Hart et al., 2013). A further study is required to reveal relationships between hypoactivation and abnormal state recruitment during the stimulus.

Occurrence probability of connectivity state 2 significantly increases during the transitions between the baseline-stimulus and stimulus-post intervals, particularly in the case of TD children. The transition periods included 3-s instructions on performing the Go and GNG blocks. Therefore, the relationship between task-related state recruitment and task switching may be presumed. The essential role of the medial frontal cortex (including SMA/pre-SMA) in task switching has been demonstrated (Rushworth et al., 2002). Hypoactivation of ADHD children in the SMA/pre-SMA suggested task switching dysfunction (Tamm et al., 2004). Connectivity state 2 comprises strong connectivity between SMA/pre-SMA and other regions aligned within frontoparietal networks. Therefore, the change in occurrence probability of connectivity state 2 likely indicates a temporary condition of task switching that may be lacking in ADHD children.

Occurrence probabilities of assumed task-irrelevant states (i.e., connectivity states 3 and 4) were significantly higher in the case of the ADHD children than those in the TD children during sparse temporal task course. It was reported that the relationship between DMN connectivity and ADHD severity is positively correlated (van Rooij et al., 2015). That report addressed the incapability of ADHD subjects to suppress task-irrelevant networks during inhibition responses. Not only task-specific

networks but also other networks (e.g., frontostriatal, fronto-default, and sensory-motor networks) and its interactions among networks had been reported to have dysfunctionalities in ADHD subjects (Castellanos et al., 2006, 2008; Mennes et al., 2012; Choi et al., 2013). Both previous findings and our current results may propound the hypothesis of atypical dynamic state recruitment in ADHD children due to the incapability in accommodating task demands.

Advantages and Limitations

fNIRS measurement and task-based dynamic FC analysis simultaneously brought two advantages. First, the important finding of atypical dynamic state recruitment could be acquired from practical fNIRS measurement. In the current dataset, no subject was excluded from the analysis. Only 1.11 ± 1.69% of total data points were affected by spikes, and those spikes were corrected by a minimum amount of effort. Therefore, fNIRS provides superior data quality for children measurement compared to fMRI with 30%–50% failure rate (Vaidya et al., 1998; Durston et al., 2003). Second, the task-based dynamic FC analysis offers a controlled measurement environment and sensitive detection of connectivity state. While shifting connectivity states during the RS task may indicate numerous explanations of the conscious level (Barttfeld et al., 2015), performing a task controls common task-related and task-irrelevant connectivity states. Furthermore, a connectivity map was constructed from short signals (12 s) and could be regarded as one of the connectivity states. Therefore, shorter measurement time is feasibly performed, and subject inconveniences can be minimized. Besides confirming our hypothesis of atypical dynamic state recruitment, the current study highlighted clinical benefits. Since the characteristics of hypoactivation and static FC have been explored with the aim of discriminating between ADHD and TD children (Hart et al., 2014; Ishii-Takahashi et al., 2014; Monden et al., 2015; Sutoko et al., 2019a), evaluating the feasibility of dynamic-state recruitment behavior as screening biomarkers will be promising.

In spite of the current findings concerning task-based dynamic FCs and differences between TD-ADHD characteristics, the following two limitations of the current results should be addressed. First, computation methods are still confounding. Effects of SWC-analysis parameters, such as window length, offset, and edge treatment (e.g., tapered weight), have been reported (Shakil et al., 2016). Inappropriate selection of parameters would mislead findings. We tried different window lengths (e.g., 25, 50, and 100 s), and found that using longer window lengths did not significantly improve the explained variance for clustering (82%–83%; data not shown). Similar centroid maps were also obtained across different window lengths (r = 0.58–0.89). Even though the clustering analysis is reasonably robust, we have yet to confirm whether the selected window length was appropriate enough for the current task paradigm. The effect of stimulus lengths on window lengths needs to be addressed. Besides the SWC analysis, hidden Markov model has been proposed to reveal the probabilistic model of connectivity state (Vidaurre et al., 2017). There are still opportunities for further improvements in the analysis method. Second, the sample number was small, and the IQ characteristics of the TD and ADHD groups were unmatched. In previous studies, brain hypoactivation is commonly associated with ADHD neuropathophysiology due to good correlation between brain activation, symptomatic ADHD score (Rubia et al., 2005), and behavioral performance (Tamm et al., 2004). Therefore, the current findings should be verified by using a bigger dataset. The effects of fundamental traits (e.g., age, IQ and symptomatic score) and behavioral performances (e.g., omission/commission error and response time) on connectivity states (e.g., occurrence probability and FC strength) should be analyzed further.

CONCLUSION

To the best of our knowledge, the current study is the first to use fNIRS signals for investigating task-based dynamic FCs. Connectivity states shifted in alternate ways during the temporal task course. Four connectivity states, which likely represent two dominant task-related states and two task-irrelevant states, were found. Furthermore, the characteristics of TD and ADHD children could be distinguished by the occurrence probability of connectivity states. In the case of ADHD children, the occurrence probability of the dominant connectivity state decreased, and that of the assumed task-irrelevant states within the stimulus interval increased. These results provide a new perspective in explaining ADHD neuropathophysiology related to atypical dynamic state recruitment and promote clinical benefits.

DATA AVAILABILITY STATEMENT

All datasets generated for this study are included in the article.

ETHICS STATEMENT

The studies involving human participants were reviewed and approved by Ethics committees of Jichi Medical University, the International University of Health and Welfare, Chuo University, and Hitachi, Ltd. Written informed consent to participate in this study was provided by the participants' legal guardian/next of kin.

AUTHOR CONTRIBUTIONS

YM, MN, TI, and TT designed and performed the experiments. SS conceived the presented idea and performed the computation analysis. MK, HA, TT, and ID verified the analysis. YM, AM, TF, TY, and ID supervised the finding of this work. SS wrote the manuscript and ID elaborated it. All authors discussed the results and contributed to the final manuscript.

FUNDING

This work was supported in part by JST-RISTEX to ID.

REFERENCES

Akinbami, L. J., Liu, X., Pastor, P. N., and Reuben, C. A. (2011). *Attention Deficit Hyperactivity Disorder Among Children Aged 5–17 Years in the United States, 1998–2009*. Hyattsville, MD: U.S. Department of Health and Human Services.

Bandettini, P. A. (2012). Twenty years of functional MRI: the science and the stories. *NeuroImage* 62, 575–588. doi: 10.1016/j.neuroimage.2012.04.026

Barttfeld, P., Uhrig, L., Sitt, J. D., Sigman, M., Jarraya, B., and Dehaene, S. (2015). Signature of consciousness in the dynamics of resting-state brain activity. *Proc. Natl. Acad. Sci. U S A* 112, 887–892. doi: 10.1073/pnas.1418031112

Biswal, B., Yetkin, F. Z., Haughton, V. M., and Hyde, J. S. (1995). Functional connectivity in the motor cortex of resting human brain using echo-planar MRI. *Magn. Reson. Med.* 34, 537–541. doi: 10.1002/mrm.1910340409

Boas, D. A., Elwell, C. E., Ferrari, M., and Taga, G. (2014). Twenty years of functional near-infrared spectroscopy: introduction for the special issue. *NeuroImage* 85, 1–5. doi: 10.1016/j.neuroimage.2013.11.033

Braun, U., Schäfer, A., Walter, H., Erk, S., Romanczuk-Seiferth, N., Haddad, L., et al. (2015). Dynamic reconfiguration of frontal brain networks during executive cognition in humans. *Proc. Natl. Acad. Sci. U S A* 112, 11678–11683. doi: 10.1073/pnas.1422487112

Bush, G. (2010). Attention-deficit/hyperactivity disorder and attention networks. *Neuropsychopharmacology* 35, 278–300. doi: 10.1038/npp.2009.120

Bush, G. (2011). Cingulate, frontal, and parietal cortical dysfunction in attention-deficit/hyperactivity disorder. *Biol. Psychiatry* 69, 1160–1167. doi: 10.1016/j.biopsych.2011.01.022

Byars, A. W., Holland, S. K., Strawsburg, R. H., Schmithorst, V. K., Dunn, R. S., and Ball, W. S. (2002). Practical aspects of conducting large-scale fMRI studies in children. *J. Child Neurol.* 17, 885–890. doi: 10.1177/08830738020170122201

Castellanos, F. X., Marguilies, D. S., Kelly, C., Uddin, L. Q., Ghaffari, M., Kirsch, A., et al. (2008). Cingulate-precuneus interactions: a new locus of dysfunction in adult attention-deficit/hyperactivity disorder. *Biol. Psychiatry* 63, 332–337. doi: 10.1016/j.biopsych.2007.06.025

Castellanos, F. X., Sonuga-Barke, E. J. S., Milham, M. P., and Tannock, R. (2006). Characterizing cognition in ADHD: beyond executive dysfunction. *Trends Cogn. Sci.* 10, 117–123. doi: 10.1016/j.tics.2006.01.011

Chang, C., and Glover, G. H. (2010). Time-frequency dynamics of resting-state brain connectivity measured with fMRI. *NeuroImage* 50, 81–98. doi: 10.1016/j.neuroimage.2009.12.011

Choi, J., Jeong, B., Lee, S. W., and Go, H.-J. (2013). Aberrant development of functional connectivity among resting state-related functional networks in medication-naive ADHD children. *PLoS One* 8:e83516. doi: 10.1371/journal.pone.0083516

Cole, M. W., Bassett, D. S., Power, J. D., Braver, T. S., and Petersen, S. E. (2014). Intrinsic and task-evoked network architectures of the human brain. *Neuron* 83, 238–251. doi: 10.1016/j.neuron.2014.05.014

Damaraju, E., Allen, E. A., Belger, A., Ford, J. M., McEwen, S., Mathalon, D. H., et al. (2014). Dynamic functional connectivity analysis reveals transient states of dysconnectivity in schizophrenia. *NeuroImage Clin.* 5, 298–308. doi: 10.1016/j.nicl.2014.07.003

Delpy, D. T., Cope, M., van der Zee, P., Arridge, S., Wray, S., and Wyatt, J. (1988). Estimation of optical path length through tissue from direct time of flight measurement. *Phys. Med. Biol.* 33, 1433–1442. doi: 10.1088/0031-9155/33/12/008

Devonshire, I. M., Papadakis, N. G., Port, M., Berwick, J., Kennerley, A. J., Mayhew, J. E. W., et al. (2012). Neurovascular coupling is brain region-dependent. *NeuroImage* 59, 1997–2006. doi: 10.1016/j.neuroimage.2011.09.050

Dodds, C. M., Morein-Zamir, S., and Robbins, T. W. (2011). Dissociating inhibition, attention and response control in the frontoparietal network using functional magnetic resonance imaging. *Cereb. Cortex* 21, 1155–1165. doi: 10.1093/cercor/bhq187

Doucet, G., Naveau, M., Petit, L., Zago, L., Crivello, F., Jobard, G., et al. (2012). Patterns of hemodynamic low-frequency oscillations in the brain are modulated by the nature of free thought during rest. *NeuroImage* 59, 3194–3200. doi: 10.1016/j.neuroimage.2011.11.059

Duan, L., Zhang, Y.-J., and Zhu, C.-Z. (2012). Quantitative comparison of resting-state functional connectivity derived from fNIRS and fMRI: a simultaneous recording study. *NeuroImage* 60, 2008–2018. doi: 10.1016/j.neuroimage.2012.02.014

Durston, S., Tottenham, N. T., Thomas, K. M., Davidson, M. C., Eigsti, I. M., Yang, Y., et al. (2003). Differential patterns of striatal activation in young children with and without ADHD. *Biol. Psychiatry* 53, 871–878. doi: 10.1016/s0006-3223(02)01904-2

Ehlis, A. C., Bähne, C. G., Jacob, C. P., Herrmann, M. J., and Fallgatter, A. J. (2008). Reduced lateral prefrontal activation in adult patients with attention-deficit/hyperactivity disorder (ADHD) during a working memory task: a functional near-infrared spectroscopy (fNIRS) study. *J. Psychiatr. Res.* 42, 1060–1067. doi: 10.1016/j.jpsychires.2007.11.011

Erika-Florence, M., Leech, R., and Hampshire, A. (2014). A functional network perspective on response inhibition and attentional control. *Nat. Commun.* 5:4073. doi: 10.1038/ncomms5073

Fishburn, F. A., Norr, M. E., Medvedev, A. V., and Vaidya, C. J. (2014). Sensitivity of fNIRS to cognitive state and load. *Front. Hum. Neurosci.* 8:76. doi: 10.3389/fnhum.2014.00076

Fox, M. D., Snyder, A. Z., Vincent, J. L., Corbetta, M., Van Essen, D. C., and Raichle, M. E. (2005). The human brain is intrinsically organized into dynamic, anticorrelated functional networks. *Proc. Natl. Acad. Sci. U S A* 102, 9673–9678. doi: 10.1073/pnas.0504136102

Franceschini, M. A., Fantini, S., Thompson, J. H., Culver, J. P., and Boas, D. A. (2003). Hemodynamic evoked response of the sensorimotor cortex measured noninvasively with near-infrared optical imaging. *Psychophysiology* 40, 548–560. doi: 10.1111/1469-8986.00057

Fu, C. H. Y., and Costafreda, S. G. (2013). Neuroimaging-based biomarkers in psychiatry: clinical opportunities of a paradigm shift. *Can. J. Psychiatry* 58, 499–508. doi: 10.1177/070674371305800904

Garavan, H., Ross, T. J., and Stein, E. A. (1999). Right hemispheric dominance of inhibitory control: an event-related functional MRI study. *Proc. Natl. Acad. Sci. U S A* 96, 8301–8306. doi: 10.1073/pnas.96.14.8301

Gonzalez-Castillo, J., and Bandettini, P. A. (2018). Task-based dynamic functional connectivity: recent findings and open questions. *NeuroImage* 180, 526–533. doi: 10.1016/j.neuroimage.2017.08.006

Gonzalez-Castillo, J., Hoy, C. W., Handwerker, D. A., Robinson, M. E., Buchanan, L. C., Saad, Z. S., et al. (2015). Tracking ongoing cognition in individuals using brief, whole-brain functional connectivity patterns. *Proc. Natl. Acad. Sci. U S A* 112, 8762–8767. doi: 10.1073/pnas.1501242112

Hager, B. M., and Keshavan, M. S. (2015). Neuroimaging biomarkers for psychosis. *Curr. Behav. Neurosci. Rep.* 2, 102–111. doi: 10.1007/s40473-015-0035-4

Hart, H., Chantiluke, K., Cubillo, A. I., Smith, A. B., Simmons, A., Brammer, M. J., et al. (2014). Pattern classification of response inhibition in ADHD: toward the development of neurobiological markers for ADHD. *Hum. Brain Mapp.* 35, 3083–3094. doi: 10.1002/hbm.22386

Hart, H., Radua, J., Nakao, T., Mataix-Cols, D., and Rubia, K. (2013). Meta-analysis of functional magnetic resonance imaging studies of inhibition and attention in attention-deficit/hyperactivity disorder: exploring task-specific, stimulant medication, and age effects. *JAMA Psychiatry* 70, 185–198. doi: 10.1001/jamapsychiatry.2013.277

Herrmann, M. J., Ehlis, A. C., and Fallgatter, A. J. (2004). Bilaterally reduced frontal activation during a verbal fluency task in depressed patients as measured by near-infrared spectroscopy. *J. Neuropsychiatry Clin. Neurosci.* 16, 170–175. doi: 10.1176/jnp.16.2.170

Herrmann, M. J., Ehlis, A. C., Wagener, A., Jacob, C. P., and Fallgatter, A. J. (2005). Near-infrared optical topography to assess activation of the parietal cortex during a visuo-spatial task. *Neuropsychologia* 43, 1713–1720. doi: 10.1016/j.neuropsychologia.2005.02.011

Hill, H. A., Elam-Evans, L. D., Yankey, D., Singleton, J. A., and Kolasa, M. (2015). National, State, and selected local area vaccination coverage among childre aged 19–35 months—United States, 2014. *Morb. Mortal. Wkly. Rep.* 64, 889–896. doi: 10.15585/mmwr.mm6433a1

Hirasawa, A., Yanagisawa, S., Tanaka, N., Funane, T., Kiguchi, M., Sorensen, H., et al. (2015). Influence of skin blood flow and source-detector distance on near-infrared spectroscopy-determined cerebral oxygenation in humans. *Clin. Physiol. Funct. Imaging* 35, 237–244. doi: 10.1111/cpf.12156

Hong, X., Wang, Y., Sun, J., Li, C., and Tong, S. (2017). Segregating top-down selective attention from response inhibition in a spatial cueing Go/NoGo Task: an ERP and source localization study. *Sci. Rep.* 7:9662. doi: 10.1038/s41598-017-08807-z

Hoshi, Y. (2005). Functional near-infrared spectroscopy: potential and Limitations in neuroimaging studies. *Int. Rev. Neurobiol.* 66, 237–266. doi: 10.1016/s0074-7742(05)66008-4

Hoshi, Y., Kobayashi, N., and Tamura, M. (2001). Interpretation of near-infrared spectrosocopy signals: a study with a newly developed perfused rat brain model. *J. Appl. Physiol.* 90, 1657–1662. doi: 10.1152/jappl.2001.90.5.1657

Hurlburt, R. T., Alderson-Day, B., Fernyhough, C., and Kühn, S. (2015). What goes on in the resting-state? A qualitative glimpse into resting-state experinece in the scanner. *Front. Psychol.* 6:1535. doi: 10.3389/fpsyg.2015.01535

Hutchison, R. M., Womelsdorf, T., Allen, E. A., Bandettini, P. A., Calhoun, V. D., Corbetta, M., et al. (2013). Dynamic functional connectivity: promise, issues, and interpretations. *NeuroImage* 80, 360–378. doi: 10.1016/j.neuroimage.2013.05.079

Ikeda, T., Hirai, M., Sakurada, T., Monden, Y., Tokuda, T., Nagashima, M., et al. (2018a). Atypical neural modulation in the right prefrontal cortex during an inhibitory task with eye gaze in autism spectrum disorder as revealed by functional near-infared spectroscopy. *Neurophotonics* 5:035008. doi: 10.1117/1.nph.5.3.035008

Ikeda, T., Tokuda, T., Monden, Y., Hirai, M., Mizushima, S. G., Nagashima, M., et al. (2018b). Hypoactivation of the right prefrontal cortex underlying motor-related inhibitory deficits in children with Autism Spectrum Disorder: a functional near-infrared spectroscopy study. *Jpn. Psychol. Res.* 60, 251–264. doi: 10.1111/jpr.12204

Inoue, Y., Sakihara, K., Gunji, A., Ozawa, H., Kimiya, S., Shinoda, H., et al. (2012). Reduced prefrontal hemodynamic response in children with ADHD during the Go/NoGo task: a NIRS study. *Neuroreport* 23, 55–60. doi: 10.1097/wnr.0b013e32834e664c

Ishii-Takahashi, A., Takizawa, R., Nishimura, Y., Kawakubo, Y., Kuwabara, H., Matsubayashi, J., et al. (2014). Prefrontal activation during inhibitory control measured by near-infrared spectroscopy for differentiating between autism spectrum disorders and attention deficit hyperactivity disorder in adults. *NeuroImage Clin.* 4, 53–63. doi: 10.1016/j.nicl.2013.10.002

Jones, D. T., Vemuri, P., Murphy, M. C., Gunter, J. L., Senjem, M. L., Machuida, M. M., et al. (2012). Non-stationarity in the "resting brain's" modular architecture. *PLoS One* 7:e39731. doi: 10.1371/journal.pone.0039731

Keilp, J. G., Sackeim, H. A., and Mann, J. J. (2005). Correlates of trait impulsiveness in performance measures and neuropsychological tests. *Psychiatry Res.* 135, 191–201. doi: 10.1016/j.psychres.2005.03.006

Lang, S., Duncan, N., and Northoff, G. (2014). Resting-state functional magnetic resonance imaging: review of Neurosurgical applications. *Neurosurgery* 74, 453–464. doi: 10.1227/neu.0000000000000307

Li, Z., Liu, H., Liao, X., Xu, J., Liu, W., Tian, F., et al. (2015). Dynamic functional connectivity revealed by resting-state functional near-infrared spectroscopy. *Biomed. Opt. Express* 6, 2337–2352. doi: 10.1364/BOE.6.002337

Liddle, P. F., Kiehl, K. A., and Smith, A. M. (2001). Event-related fMRI study of response inhibition. *Hum. Brain Mapp.* 12, 100–109. doi: 10.1002/1097-0193(200102)12:2<100::aid-hbm1007>3.0.co;2-6

Liu, X., and Duyn, J. H. (2013). Time-varying functional network information extracted from brief instance of spontaneous brain activity. *Proc. Natl. Acad. Sci. U S A* 110, 4392–4397. doi: 10.1073/pnas.1216856110

Maki, A., Yamashita, Y., Ito, Y., Watanabe, E., Mayanagi, Y., and Koizumi, H. (1995). Spatial and temporal analysis of human motor activity using noninvasive NIR topography. *Med. Phys.* 22, 1997–2005. doi: 10.1118/1.597496

Mennes, M., Vega Potler, N., Kelly, C., Di Martino, A., Castellanos, F. X., and Milham, M. P. (2012). Resting state functional connectivity correlates of inhibitory control in children with attention-deficit/hyperactivity disorder. *Front. Psychiatry* 2:83. doi: 10.3389/fpsyt.2011.00083

Menon, V., Adleman, N. E., White, C. D., Glover, G. H., and Reiss, A. L. (2001). Error-related brain activation during a Go/NoGo response inhibition task. *Hum. Brain Mapp.* 12, 131–143. doi: 10.1002/1097-0193(200103)12:3<131::aid-hbm1010>3.0.co;2-c

Monden, Y., Dan, H., Nagashima, M., Dan, I., Kyutoku, Y., Okamoto, M., et al. (2012a). Clinically-oriented monitoring of acute effects of methylphenidate on cerebral hemodynamics in ADHD children using fNIRS. *Clin. Neurophysiol.* 123, 1147–1157. doi: 10.1016/j.clinph.2011.10.006

Monden, Y., Dan, H., Nagashima, M., Dan, I., Tsuzuki, D., Kyutoku, Y., et al. (2012b). Right prefrontal activation as a neuro-functional biomarker for monitoring acute effects of methylphenidate in ADHD children: an fNIRS study. *NeuroImage Clin.* 1, 131–140. doi: 10.1016/j.nicl.2012.10.001

Monden, Y., Dan, I., Nagashima, M., Dan, H., Uga, M., Ikeda, T., et al. (2015). Individual classification of ADHD children by right prefrontal hemodynamic responses during a go/no-go task as assessed by fNIRS. *Neuroimage Clin.* 9, 1–12. doi: 10.1016/j.nicl.2015.06.011

Murphy, F. C., Sahakian, B. J., Rubinsztein, J. S., Michael, A., Rogers, R. D., Robbins, T. W., et al. (1999). Emotional bias and inhibitory control processes in mania and depression. *Psychol. Med.* 29, 1307–1321. doi: 10.1017/s0033291799001233

Nagashima, M., Monden, Y., Dan, I., Dan, H., Mizutani, T., Tsuzuki, D., et al. (2014a). Neuropharmacological effect of atomoxetine on attention network in children with attention deficit hyperactivity disorder during oddball paradigms as assessed using functional near-infrared spectroscopy. *Neurophotonics* 1:025007. doi: 10.1117/1.nph.1.2.025007

Nagashima, M., Monden, Y., Dan, I., Dan, H., Tsuzuki, D., Mizutani, T., et al. (2014b). Acute neuropharmacological effects of atomoxetine on inhibitory control in ADHD children: a fNIRS study. *Neuroimage Clin.* 6, 192–201. doi: 10.1016/j.nicl.2014.09.001

Nagashima, M., Monden, Y., Dan, I., Dan, H., Tsuzuki, D., Mizutani, T., et al. (2014c). Neuropharmacological effect of methylphenidate on attention network in children with attention deficit hyperactivity disorder during oddball paradigms as assessed using functional near-infrared spectroscopy. *Neurophotonics* 1:015001. doi: 10.1117/1.nph.1.1.015001

Niu, H., Khadka, S., Tian, F., Lin, Z.-J., Lu, C., Zhu, C., et al. (2011). Resting-state functional connectivity assessed with two diffuse optical tomographic systems. *J. Biomed. Opt.* 16:046006. doi: 10.1117/1.3561687

Niu, H., Li, Z., Liao, X., Wang, J., Zhao, T., Shu, N., et al. (2013). Test-retest reliability of graph metrics in functional brain networks: a resting-state fNIRS study. *PLoS One* 8:e72425. doi: 10.1371/journal.pone.0072425

Niu, H., Zhu, Z., Wang, M., Li, X., Yuan, Z., Sun, Y., et al. (2019). Abnormal dynamic functional connectivity and brain states in Alzheimer's diseases: functional near-infrared spectroscopy study. *Neurophotonics* 6:025010. doi: 10.1117/1.nph.6.2.025010

Peers, P. V., Ludwig, C. J., Rorden, C., Cusack, R., Bonfiglioli, C., Bundesen, C., et al. (2005). Attentional functions of parietal and frontal cortex. *Cereb. Cortex* 15, 1469–1484. doi: 10.1093/cercor/bhi029

Preti, M. G., Bolton, T. A. W., and Van De Ville, D. (2017). The dynamic functional connectome: state-of-the-art and perspectives. *NeuroImage* 160, 41–54. doi: 10.1016/j.neuroimage.2016.12.061

Raichle, M. E., MacLeod, A. M., Snyder, A. Z., Powers, W. J., Gusnard, D. A., and Shulman, G. L. (2001). A default mode of brain function. *Proc. Natl. Acad. Sci. U S A* 98, 676–682. doi: 10.1073/pnas.98.2.676

Raichle, M. E., and Snyder, A. Z. (2007). A default mode of brain function: a brief history of an evolving idea. *NeuroImage* 37, 1083–1090. doi: 10.1016/j.neuroimage.2007.02.041

Reynolds, B., Ortengren, A., Richards, J. B., and de Wit, H. (2006). Dimensions of impulsive behavior: personality and behavioral measures. *Pers. Individ. Dif.* 40, 305–315. doi: 10.1016/j.paid.2005.03.024

Roy, C. S., and Sherrington, C. S. (1890). On the regulation of the blood-supply of the brain. *J. Physiol.* 11, 85–158. doi: 10.1113/jphysiol.1890.sp000321

Rubia, K., Smith, A. B., Brammer, M. J., and Taylor, E. (2003). Right inferior prefrontal cortex mediates response inhibition while medial prefrontal cortex is responsible for error detection. *NeuroImage* 20, 351–358. doi: 10.1016/s1053-8119(03)00275-1

Rubia, K., Smith, A. B., Brammer, M. J., Toone, B., and Taylor, E. (2005). Abnormal brain activation during inhibition and error detection in medication-naive adolescents with ADHD. *Am. J. Psychiatry* 162, 1067–1075. doi: 10.1176/appi.ajp.162.6.1067

Rushworth, M. F. S., Hadland, K. A., Paus, T., and Sipila, P. K. (2002). Role of the human medial frontal cortex in task switching: a combined fMRI and TMS study. *J. Neurophysiol.* 87, 2577–2592. doi: 10.1152/jn.2002.87.5.2577

Sasai, S., Homae, F., Watanabe, H., Sasaki, A. T., Tanabe, H. C., Sadato, N., et al. (2012). A NIRS-fMRI study of resting state network. *NeuroImage* 63, 179–193. doi: 10.1016/j.neuroimage.2012.06.011

Sasai, S., Homae, F., Watanabe, H., and Taga, G. (2011). Frequency-specific functional connectivity in the brain during resting state revealed by NIRS. *NeuroImage* 56, 252–257. doi: 10.1016/j.neuroimage.2010.12.075

Schecklmann, M., Ehlis, A. C., Plichta, M. M., Romanos, J., Heine, M., Boreatti-Hummer, A., et al. (2008). Diminished prefrontal oxygenation with normal and above-average verbal fluency performance in adult ADHD. *J. Psychiatr. Res.* 43, 98–106. doi: 10.1016/j.jpsychires.2008.02.005

Shakil, S., Lee, C.-H., and Keilholz, S. D. (2016). Evaluation of sliding window correlation performance for characterizing dynamic functional connectivity and brain states. *NeuroImage* 133, 111–128. doi: 10.1016/j.neuroimage.2016.02.074

Strangman, G., Boas, D. A., and Sutton, J. P. (2002). Non-invasive neuroimaging using near-infrared light. *Biol. Psychiatry* 52, 679–693. doi: 10.1016/s0006-3223(02)01550-0

Sutoko, S., Monden, Y., Tokuda, T., Ikeda, T., Nagashima, M., Funane, T., et al. (2019a). Exploring attentive task-based connectivity for screening attention deficit/hyperactivity disorder children: a functional near-infrared spectroscopy study. *Neurophotonics* 6:045013. doi: 10.1117/1.nph.6.4.045013

Sutoko, S., Monden, Y., Tokuda, T., Ikeda, T., Nagashima, M., Kiguchi, M., et al. (2019b). Distinct methylphenidate-evoked response measured using functional near-infrared spectroscopy during Go/No-Go task as a supporting differential diagnostic tool between attention-deficit/hyperactivity disorder and autism spectrum disorder comorbid children. *Front. Hum. Neurosci.* 13:7. doi: 10.3389/fnhum.2019.00007

Sutoko, S., Sato, H., Maki, A., Kiguchi, M., Hirabayashi, Y., Atsumori, H., et al. (2016). Tutorial on platform for optical topography analysis tools. *Neurophotonics* 3:010801. doi: 10.1117/1.nph.3.1.010801

Tak, S., Kempny, A. M., Friston, K. J., Leff, A. P., and Penny, W. D. (2015). Dynamic causal modelling for functional near-infrared spectroscopy. *NeuroImage* 111, 338–349. doi: 10.1016/j.neuroimage.2015.02.035

Tamm, L., Menon, V., Ringel, J., and Reiss, A. L. (2004). Event-related fMRI evidence of frontotemporal involvement in aberrant response inhibition and task switching in attention-deficit/hyperactivity disorder. *J. Am. Acad. Child Adolesc. Psychiatry* 43, 1430–1440. doi: 10.1097/01.chi.0000140452.51205.8d

Tibshirani, R., Walther, G., and Hastie, T. (2001). Estimating the number of clusters in a data set *via* the gap statistic. *J. R. Statist. Soc. B* 63, 411–423. doi: 10.1111/1467-9868.00293

Tokuda, T., Ikeda, T., Monden, Y., Mizushima, S. G., Inoue, T., Nagashima, M., et al. (2018). Methylphenidate-elicited distinct neuropharmacological activation patterns between medication-naive attention deficit hyperactivity disorder children with and without comorbid autism spectrum disorder: a functional near-infrared spectroscopy study. *Neuropsychiatry* 8, 917–929. doi: 10.4172/neuropsychiatry.1000418

Tsuzuki, D., Cai, D.-S., Dan, H., Kyutoku, Y., Fujita, A., Watanabe, E., et al. (2012). Stable and convenient spatial registration of stand-alone NIRS data through anchor-based probabilistic registration. *Neurosci. Res.* 72, 163–171. doi: 10.1016/j.neures.2011.10.008

Tsuzuki, D., and Dan, I. (2014). Spatial registration for functional near-infrared spectroscopy: from channel position on the scalp to cortical location in individual and group analyses. *NeuroImage* 85, 92–103. doi: 10.1016/j.neuroimage.2013.07.025

Tsuzuki, D., Jurcak, V., Singh, A. K., Okamoto, M., Watanabe, E., and Dan, I. (2007). Virtual spatial registration of stand-alone fNIRS data to MNI space. *NeuroImage* 34, 1506–1518. doi: 10.1016/j.neuroimage.2006.10.043

Uddin, L. Q., Dajani, D. R., Voorhies, W., Bednarz, H., and Kana, R. K. (2017). Progress and roadblocks in the search for brain-based biomarkers of autism and attention-deficit/hyperactivity disorder. *Transl. Psychiatry* 7:e1218. doi: 10.1038/tp.2017.164

Vaidya, C. J., Austin, G., Kirkorian, G., Ridlehuber, H. W., Desmond, J. E., Glover, G. H., et al. (1998). Selective effects of methylphenidate in attention deficit hyperactivity disorder: a functional magnetic resonance study. *Proc. Natl. Acad. Sci. U S A* 95, 14494–14499. doi: 10.1073/pnas.95.24.14494

van Rooij, D., Hartman, C. A., Mennes, M., Oosterlaan, J., Franke, B., Rommelse, N., et al. (2015). Altered neural connectivity during response inhibition in adolescents with attention-deficit/hyperactivity disorder and their unaffected siblings. *Neuroimage Clin.* 7, 325–335. doi: 10.1016/j.nicl.2015.01.004

Verbruggen, F., and Logan, G. D. (2008). Response inhibition in the stop-signal paradigm. *Trends Cogn. Sci.* 12, 418–424. doi: 10.1016/j.tics.2008.07.005

Verbruggen, F., Stevens, T., and Chambers, C. D. (2014). Proactive and reactive stopping when distracted: an attentional account. *J. Exp. Psychol. Hum. Percept. Perform.* 40, 1295–1300. doi: 10.1037/a0036542

Vidaurre, D., Smith, S. M., and Woolrich, M. W. (2017). Brain network dynamics are hierarchically organized in time. *Proc. Natl. Acad. Sci. U S A* 114, 12827–12832. doi: 10.1073/pnas.1705120114

Zhang, H., Duan, L., Zhang, Y.-J., Lu, C.-M., Liu, H., and Zhu, C.-Z. (2011). Test-retest assessment of independent component analysis-derived resting state functional connectivity based on functional near-infarred spectrosocopy. *NeuroImage* 55, 607–615. doi: 10.1016/j.neuroimage.2010.12.007

Conflict of Interest: SS, TF, HA, MK, and AM are employed by the Hitachi. Ltd.

The remaining authors declare that the research was conducted in the absence of any commercial or financial relationships that could be construed as a potential conflict of interest.

Copyright © 2020 Sutoko, Monden, Tokuda, Ikeda, Nagashima, Funane, Atsumori, Kiguchi, Maki, Yamagata and Dan. This is an open-access article distributed under the terms of the Creative Commons Attribution License (CC BY). The use, distribution or reproduction in other forums is permitted, provided the original author(s) and the copyright owner(s) are credited and that the original publication in this journal is cited, in accordance with accepted academic practice. No use, distribution or reproduction is permitted which does not comply with these terms.

frontiers in Human Neuroscience

ORIGINAL RESEARCH
published: 14 February 2020
doi: 10.3389/fnhum.2020.00006

Altered Functional Connectivity in the Motor and Prefrontal Cortex for Children With Down's Syndrome: An fNIRS Study

Shi-Yang Xu[1,2†], *Feng-Mei Lu*[1,3†], *Meng-Yun Wang*[1], *Zhi-Shan Hu*[1], *Juan Zhang*[4], *Zhi-Yi Chen*[5], *Paulo A. S. Armada-da-Silva*[6,7] *and Zhen Yuan*[1,2*]

[1] Faculty of Health Sciences, University of Macau, Macau, China, [2] Centre for Cognitive and Brain Sciences, University of Macau, Macau, China, [3] MOE Key Laboratory for Neuroinformation, The Clinical Hospital of Chengdu Brain Science Institute, University of Electronic Science and Technology of China, Chengdu, China, [4] Faculty of Education, University of Macau, Macau, China, [5] Department of Ultrasound Medicine, The Third Affiliated Hospital of Guangzhou Medical University, Guangzhou, China, [6] Faculty of Human Kinetics, University of Lisbon, Cruz Quebrada, Portugal, [7] Neuromechanics of Human Movement, Faculty of Human Kinetics, CIPER, University of Lisbon, Lisbon, Portugal

OPEN ACCESS

Edited by:
Fenghua Tian,
University of Texas at Arlington,
United States

Reviewed by:
Noman Naseer,
Air University, Pakistan
Xiaosu Hu,
University of Michigan, United States

***Correspondence:**
Zhen Yuan
zhenyuan@um.edu.mo

[†] These authors have contributed equally to this work

Specialty section:
This article was submitted to Motor Neuroscience, a section of the journal Frontiers in Human Neuroscience

Received: 22 September 2019
Accepted: 09 January 2020
Published: 14 February 2020

Citation:
Xu S-Y, Lu F-M, Wang M-Y, Hu Z-S, Zhang J, Chen Z-Y, Armada-da-Silva PAS and Yuan Z (2020) Altered Functional Connectivity in the Motor and Prefrontal Cortex for Children With Down's Syndrome: An fNIRS Study. Front. Hum. Neurosci. 14:6. doi: 10.3389/fnhum.2020.00006

Children with Down's syndrome (DS) might exhibit disrupted brain functional connectivity in the motor and prefrontal cortex. To inspect the alterations in brain activation and functional connectivity for children with DS, the functional near-infrared spectroscopy (fNIRS) method was applied to examine the brain activation difference in the motor and prefrontal cortex between the DS and typically developing (TD) groups during a fine motor task. In addition, small-world analysis based on graph theory was also carried out to characterize the topological organization of functional brain networks. Interestingly, behavior data demonstrated that the DS group showed significantly long reaction time and low accuracy as compared to the TD group ($p < 0.05$). More importantly, significantly reduced brain activations in the frontopolar area, the pre-motor, and the supplementary motor cortex ($p < 0.05$) were identified in the DS group compared with the TD group. Meanwhile, significantly high global efficiency (E_g) and short average path length (L_p) were also detected for the DS group. This pilot study illustrated that the disrupted connectivity of frontopolar area, pre-motor, and supplementary motor cortex might be one of the core mechanisms associated with motor and cognitive impairments for children with DS. Therefore, the combination of the fNIRS technique with functional network analysis may pave a new avenue for improving our understanding of the neural mechanisms of DS.

Keywords: fNIRS, cognition, Down's syndrome, brain connectivity, children

INTRODUCTION

Down's syndrome (DS) resulting from an extra 21st chromosome was first described in 1866 by John Langdon Down (Lott and Dierssen, 2010). Children who suffered from DS might exhibit disabled executive function (EF), impaired language comprehension (Martin et al., 2009), and poor learning ability and working memory (Jarrold and Baddeley, 2001). Together with cognitive dysfunctions, DS individuals also show the poor performance in motor tasks, particularly fine motor tasks involving the synchronization of hands and fingers that also require some degree

of executive functioning, such as response selection/inhibition, working memory and attention (Traverso et al., 2015). EF is denoted as a set of higher-order functions that organize and regulate goal-driven behavior, which involves several brain regions including the prefrontal cortex (PFC; Diamond, 2013). Interestingly, recent studies have illustrated that the motor performance shows a significant relationship with EF in children with atypical development (Piek et al., 2004; Wassenberg et al., 2005; Hartman et al., 2010; Cao et al., 2015; Yennu et al., 2016). For example, a close relationship between the motor skill competency and EF was identified for children with DS (Horvat et al., 2013; Schott and Holfelder, 2015). In particular, the motor cortex including premotor cortex (PMC), supplementary motor area (SMA) and primary motor cortex, and the somatosensory cortex (SMC), as well as the PFC (Seitz et al., 1990; Deiber et al., 1991; Shibasaki et al., 1993; Grafton et al., 1998; Nakamura et al., 1998; Li et al., 2001; Robertson et al., 2001; O'connor et al., 2004), play an essential role in motor and executive functions (Miyachi et al., 1997; Bloedel, 2004).

The technological and methodological developments in neuroimaging such as electroencephalography (EEG), functional magnetic resonance (fMRI) and functional near-infrared spectroscopy (fNIRS) enable us to better understand the neural mechanism associated with DS during cognitive and motor tasks or at rest. Differently from EEG, both fMRI and fNIRS are based on the detection of changes in regional cerebral blood flow or blood oxygen to infer brain activity. Compared to fMRI, fNIRS has the advantages of being a portable and comfortable technique for children development studies, in which brain imaging can be performed in a quiet environment with fewer body constraints (Cheng et al., 2015; Liu et al., 2016; Scarapicchia et al., 2017).

More importantly, it has been widely recognized that cognitive tasks involve multiple spatially distributed brain regions that integrate together to generate a functional network (Fries, 2005; Bassett and Bullmore, 2006). Specifically, it was discovered that brain functional networks tend to be more random and dispersed for DS patients (Drummond et al., 2013). For example, an fMRI study has been performed, indicating that compared to TD and autistic groups, the DS participants exhibited increased synchrony between various brain networks (Anderson et al., 2013). Additional work also provided solid evidence that within-network connectivity in DS individuals is more variable in patterns as compared to that of other neurodevelopmental disorders (Vega et al., 2015). Another fMRI study illustrated that DS individuals showed increased regional connectivity in the ventral brain regions and reduced functional connectivity across the dorsal executive network (Pujol et al., 2015). Besides, Imai et al. (2014) inspected the spontaneous brain activity of sleeping DS infants to reveal the highest short-range connectivity using fNIRS. Interestingly, EEG neuroimaging was also performed associated with DS, in which Ahmadlou et al. (2013) examined whether the global organization or topology of functional brain networks was affected, suggesting that the topology of DS individuals' brain activity resembled a random rather than a small-world network. However, although previous investigations revealed dysfunctional brain connectivity in DS, most of work are carried out using resting-state recordings and the neural mechanism for disrupted brain networks during task such as fine motor tasks still remains largely unclear. In particular, further study should also be conducted to explore the topological organization of task-evoked brain networks for DS children, which can be characterized by the small-world network analysis.

In this study, fNIRS was utilized to investigate the brain cortical hemodynamic changes in children with DS during the performance of a fine motor task involving both motor and executive functions. In addition, the small-world properties of functional networks in the prefrontal and motor cortex were carefully examined to show the significant difference between the DS and TD groups. Graph theoretical network analysis has allowed us to measure the topological properties of brain networks independently of *a priori* seeds. This method models the brain as a large-scale network composed of a series of nodes (brain regions) and edges (functional connectivity between pairs of nodes; Bullmore and Sporns, 2009). Using this approach, a network could be defined as small-world networks when the graphs were with higher clustering and similar shortest path length as compared with a random network (Watts and Strogatz, 1998). We hypothesized that the DS group would demonstrate altered small-world properties compared with the TD group and expected that the DS group would be characterized by a less small-worldness with a tendency toward randomization.

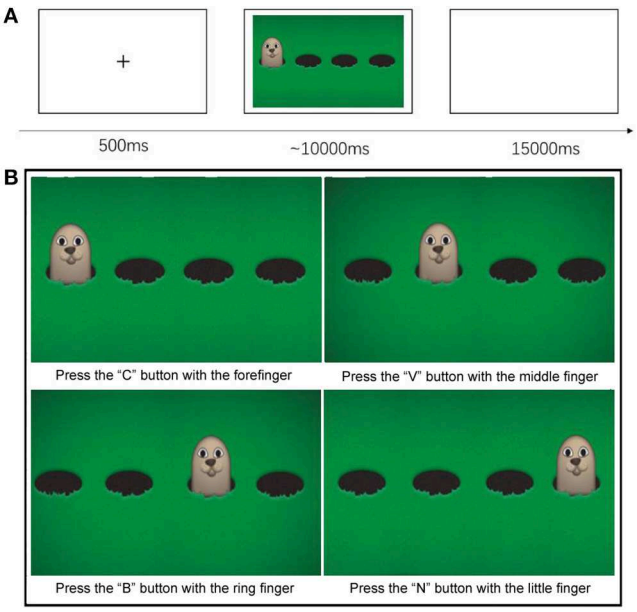

FIGURE 1 | (A) Trials' time sequence **(B)** Children from the TD group and the DS group had to catch the Hamster by pressing the key that corresponded to its position. There will be four hamsters, and one of them will appear randomly every time. The participant need use his or her forefinger, middle finger, ring finger, and little finger of right hand to press the "C" (the first position) button, "V" (the second position) button, "B" (the third position) button, and the "N" (the fourth position) button, respectively to indicate where the hamster appeared.

METHODS

Participants

Seven (three males, age 9.42 ± 1.61 years) DS and six (three males, age 9.00 ± 1.78 years) age- and gender-matched TD children were, respectively recruited from Guangdong Province or Macao Special Administrative Region (SAR), China to participate in this study. All children were right-handed, native Chinese speakers, and had a normal or corrected-to-normal vision. The children with DS all have their condition diagnosed by a medical doctor and confirmed by a karyotype test. All parents and caregivers were fully briefed about the study's aims and procedures and were required to give signed informed consent prior to the experiment. The study and its procedures were approved by the Ethics Committee of the University of Macau (Macao SAR, China).

Tasks and Procedures

Before data acquisition, children were invited to the lab and become familiar with the settings and the equipment used in this study. Since participants were children, their parents or caregivers were present for the whole procedure. When performing the task, children sat on a chair in front of a 23-inch monitor with 60 Hz refresh rate being told that they were going to play a computer game called "*Catch the Hamster.*"

During the task, participants need to press one of four keys of a computer keyboard using separate fingers of the right hand as fast as possible to indicate the correct hole where a hamster would come out. Each child was required to complete 32 trials in around 20 min. Each trial began with a warning signal consisting of a black cross showing at the center of the monitor for 500 ms. After this fixation period, a cartoon was displayed on the screen showing four hamsters' holes and a hamster coming out of one of these holes randomly every time. Children were asked to press the key matching the hole with a hamster using the index ("C key"—the first hole), middle ("V key"—the second hole), ring ("B key"—the third hole), or little ("N key"—the fourth hole) fingers of the right hand that was horizontally placed on the keyboard (**Figure 1**). Participants should press the corresponding key using one of four fingers as fast and accurately as possible within 10 s. Finally, a 15 s blank screen was shown between any two trials to allow hemodynamic responses to return to baseline.

The task for this experimental test was designed with the E-prime 2.0 software (Psychology Software Tools, Pittsburgh, PA), which was also used to access participants' response accuracy and reaction times automatically.

fNIRS Recordings and Processing

fNIRS Systems

The experiments were performed using a continuous wave (CW) fNIRS system (CW6 fNIRS system; TechEn Inc, Milford, MA), which consisted of 4 near-infrared light source emitters and 8 detectors, as shown in **Figure 2**. In this system, two CW lights at wavelengths of 690 nm and 830 nm are emitted at each source optic fiber providing sensitive detection for the changes of both HbO and HbR concentrations in the human brain cortex. The distance between each source and detector pair was set to 3 cm and the sampling rate for the CW fNIRS system was 50 Hz. Notably, our CW6 system only has four laser sources and eight detectors that cannot cover the whole motor and prefrontal cortex, so we only collected hemodynamic data from the left hemisphere motor areas in this pilot study.

The configuration of the four sources and eight detector pairs (**Figures 2**, **3**) was able to generate 13 channels over the hemisphere, covering most of the left frontal cortex and motor cortex (see **Table 1** for details about channels' location). The laser source four (the most anterior one) was located at Fcz according to the 10–20 standard system, serving as the reference point (Naseer and Hong, 2013). The three-dimensional (3D) positions of the optodes were measured by a 3D digitizer (PATRIOT, Polhemus, Colchester, Vermont, USA). Then the grand-averaged coordinates were processed by NIRS-SPM (Ye et al., 2009) to estimate the Montreal Neurological Institute (MNI) coordinates and associated brain regions of the optodes and channels together with the probability of the channels (**Table 1**). The probability is to describe how the estimated MNI coordinates are accurately corresponded to the specific brain regions processed by NIRS-SPM.

The fNIRS data were processed with HOMER 2 toolbox (Yang et al., 2010). To begin this process, the raw fNIRS data

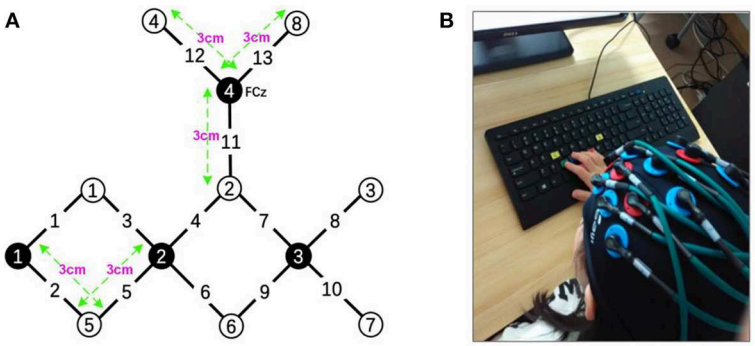

FIGURE 2 | (A) The layout of the fNIRS system: the fNIRS head patch consisting of 4 near-infrared light source emitters (black) and 8 detectors (white). **(B)** A child was performing the task.

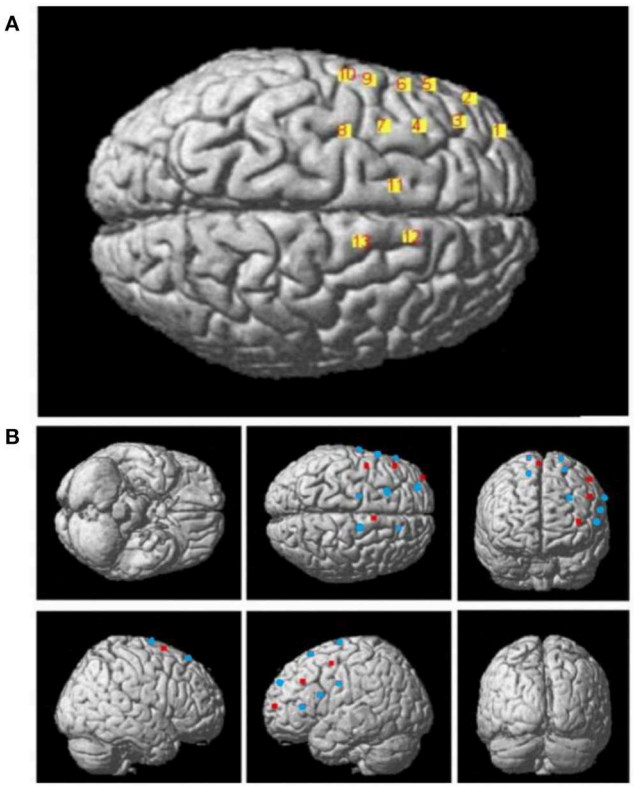

FIGURE 3 | (A) The 3D MNI coordinates of the 13 channels. **(B)** The 3D MNI coordinates of laser sources (red) and detectors (blue).

TABLE 1 | Mean channel locations for the fNIRS cap.

Channels	MNI coordinates (x,y,z)	Brodmann area	Probability
CH01	−35, 59, 22	46–Dorsolateral prefrontal cortex	0.844
CH02	−50, 46, 9	45–Pars triangularis broca's area	0.545
		46–Dorsolateral prefrontal cortex	0.454
CH03	−41, 43, 35	46–Dorsolateral prefrontal cortex	0.531
		45–Pars triangularis broca's area	0.310
CH04	−38, 26, 52	9–Dorsolateral prefrontal cortex	0.827
CH05	−55, 30, 23	45–Pars triangularis broca's area	0.920
CH06	−56, 21, 29	44–Pars opercularis, part of Broca's area	0.732
CH07	−39, 12, 61	6–Pre-motor and supplementary motor cortex	0.447
		8–Includes frontal eye fields	0.286
		9–Dorsolateral prefrontal cortex	0.266
CH08	−36, −4, 66	6–Pre-motor and supplementary motor cortex	0.978
CH09	−58, 5, 39	6–Pre-motor and supplementary motor cortex	0.733
CH10	−59, −5, 44	4–Primary motor cortex	0.321
		6–Pre-motor and supplementary motor cortex	0.430
CH11	−12, 16, 70	6–Pre-motor and supplementary motor cortex	0.763
CH12	10, 23, 67	5–Pre-motor and supplementary motor cortex	0.386
		8–Includes frontal eye fields	0.613
CH13	11, 1, 75	6–Pre-motor and supplementary motor cortex	1

were converted to optical density (OD) changes (Scholkmann and Wolf, 2013). Then, OD values were corrected for motion artifacts using a spline interpolation algorithm (Scholkmann et al., 2010). The data were further band-pass filtered by a low cut-off filter frequency of 0.1 Hz and a high cut-off filter frequency of 0.01 Hz in order to minimize the physiological noise due to heart pulsation (1∼1.5 Hz), respiration (0.2∼0.5 Hz), and blood pressure (Mayer) waves (∼0.1 Hz) as well as produce the data with the best signal-to-noise ratio. Finally, HbO concentration changes were generated using filtered OD values after normalized to zero mean and unit variance (z-scores; Zhang et al., 2010; Ding et al., 2013, 2014; Hu et al., 2018). The relative concentration changes of HbO were calculated according to the modified Beer-Lambert law (MBLL) (Lu et al., 2016) as follows:

$$\begin{bmatrix}\Delta[HbO]\\ \Delta[HbR]\end{bmatrix} = \frac{1}{SD}\begin{bmatrix}\varepsilon_{HbO}(\lambda_1)DPF(\lambda_1) & \varepsilon_{HbR}(\lambda_1)DPF(\lambda_1)\\ \varepsilon_{HbO}(\lambda_2)DPF(\lambda_2) & \varepsilon_{HbR}(\lambda_2)DPF(\lambda_2)\end{bmatrix}^{-1}\begin{bmatrix}\Delta A(\lambda_1)\\ \Delta A(\lambda_2)\end{bmatrix}$$

where SD is the separation distance between source and detector, ε is the absorption coefficient, and ΔA is the unitless total optical density variation between a time point and at a designated baseline (time $t = 0$). The DPF at each wavelength is the unitless differential path length factor, and in this study, this value is 6.0 for the two wavelengths (690 nm and 830 nm) which was deemed as an adequate value for the present work (Scholkmann and Wolf, 2013).

In this study, only HbO signals were analyzed, since they can serve as a more sensitive indicator of changes associated with regional cerebral blood flow (Fu et al., 2014).

Reconstruction and Characterization of the Brain Network

The nodes and edges are two crucial components in constructing brain networks. For the present study, the nodes were denoted as the channels, whereas the edges were defined as the correlation coefficient between any two-channel pair generated by Pearson correlation analysis (Lu et al., 2017a,b). To construct the functional brain networks, the matrix of correlation coefficients was first binarized by setting a threshold value T, and then the correlation matrix was converted into a binary undirected graph. When the Pearson correlation coefficient is smaller than T, the edges can be ignored in the network. By contrast, if the correlation coefficient is equal to or larger than T, the two channels or nodes were connected. The thresholds were defined by the *sparsity* procedure with the GRETNA toolbox, which guarantees the same number of nodes and edges in all network matrices, allowing the assessment of relative network organization (He et al., 2009; Wang et al., 2015). After generating the binary

connectivity matrix of nodes, the clustering coefficient (C_p), average characteristic path length (L_p), global efficiency (E_g) were computed.

The clustering coefficient (C_p) was defined (Watts and Strogatz, 1998),

$$C_p = \frac{1}{n}\sum_{i\in N} C_i = \frac{1}{n}\sum_{i\in N} \frac{2t_i}{k_i\left(k_i-1\right)} \quad (1)$$

in which C_i is the clustering coefficient of node i ($C_i = 0$ for $k_i < 2$), t_i stands for the number of triangles around node i, which is a basis for measuring segregation, and k_i is the number of links connected to a node i (Rubinov and Sporns, 2010).

The average of the characteristic path length L_p measured the overall routing efficiency of a network (Watts and Strogatz, 1998) and was written,

$$L = \frac{1}{n}\sum_{i\in N} L_i = \frac{1}{n}\sum_{i\in N} \frac{\sum_{j\in N, j\neq i} d_{ij}}{n-1} \quad (2)$$

in which N is the number of all node, L_i is the average distance between node i and all other nodes, and d_{ij} is the shortest path length between the node i and node j (Rubinov and Sporns, 2010).

The global efficiency (E_g) measured the functional integration over all nodes in the network (Latora and Marchiori, 2001) and was denoted as

$$Eg = \frac{1}{n}\sum_{i\in N} G_i = \frac{1}{n}\sum_{i\in N} \frac{\sum_{j\in N, j\neq i} d_{ij}^{-1}}{n-1} \quad (3)$$

in which N is the set of all nodes in the network and G_i is the efficiency of node i (Rubinov and Sporns, 2010).

In addition, the index σ of the small-world network was calculated as follows:

$$\sigma = \frac{C/C_{\text{rand}}}{L/L_{\text{rand}}} \quad (4)$$

in which C and C_{rand} represent the clustering coefficients, and L and L_{rand} denote the characteristic path lengths of the real brain network and the comparable random network, respectively. If the value of σ was larger than 1, the network possesses the small-world characteristics (Watts and Strogatz, 1998).

Statistical Analysis

For behavioral data, the IQ score, accuracy and reaction time were subjected to independent sample t-tests (two-tailed) to inspect the difference between the DS and TD groups. In particular, the children were required to perform a 32-trial task. For each trial, they need to press the button according to the position where the hamster showed up. If they press the right button, it will be counted as the right response. Otherwise, it is considered as a false response. The accuracy was determined by the number of trials with the right response divided by the whole trial number. The HbO signals and small-world properties between the two groups were also carefully examined using two-tailed paired t-tests.

The effect size of the t-test is estimated by Cohen's d and the p-value was corrected by the false discovery rate (FDR) (Storey, 2002). The relationship between the behavior data and the fNIRS data was generated by using Person correlation analysis. All statistical analyses were performed by SPSS 23.0 (SPSS Inc., Chicago, IL, USA) and the significance level was set to $p < 0.05$.

RESULTS

Behavioral Results

It was discovered that the difference in accuracy between the TD (0.958 ± 0.024) and DS groups (0.860 ± 0.030) was significant ($t = -2.475$, $p = 0.031$, *Cohen's d* = 0.14, power = 0.056). Likewise, the DS (3562.1 ± 485.7 ms) and TD (1202.4 ± 120.2 ms) groups also exhibited significant difference in the reaction time ($t = 4.716$, $p = 0.002$, *Cohen's d* = 2.53, power = 0.98; **Figure 4**).

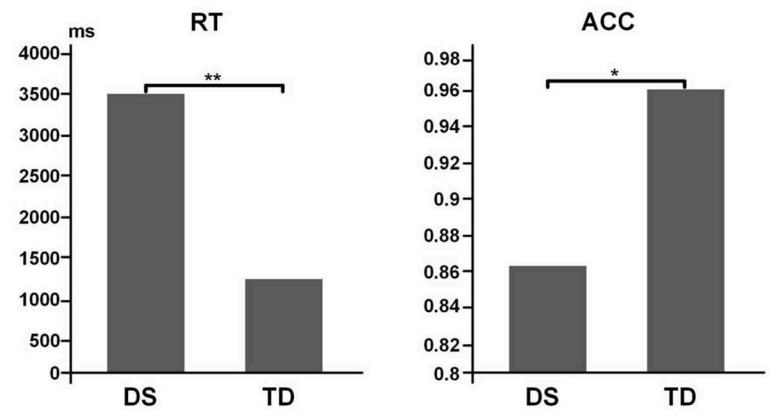

FIGURE 4 | Behavior results for task performance. Left, data for RT. Right, data for ACC. *$^{**}p < 0.01$; $^{*}p < 0.05$.

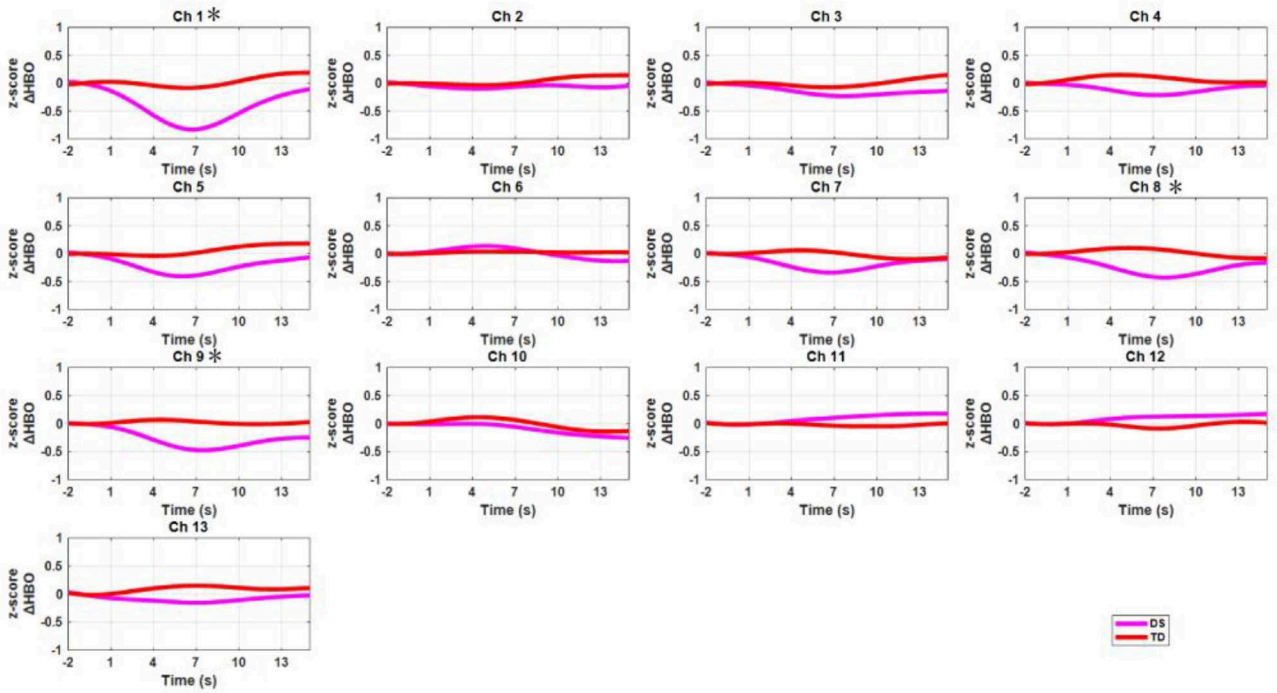

FIGURE 5 | The time courses of mean HbO signals (z-scores) for all channels across all participants. The red curves represent the DS group, and the pink curves denote the TD group. The X-axis and Y-axis denotes the time (second) and HbO concentration changes (z-scores), respectively. The star means the channels that two groups showed statistical significant differences.

Brain Activation and Its Relationship With Behavior Performance

The grand-averaged HbO data for all channels were displayed in **Figure 5** for both the DS and TD groups. After false discovery rate correction ($P_{FDR} < 0.05$), the two groups showed significant difference in HbO measurement in channel 1 [$t = -3.349$, $p = 0.006$, *Cohen's d* $= 1.89$, power $= 0.87$; dorsolateral prefrontal cortex (DLPFC), Brodmann area (BA)10], channel 8 ($t = -3.204$, $p = 0.008$, *Cohen's d* $=1.88$, power $= 0.86$; PMC, BA6), and channel 9 ($t = -3.072$, $p = 0.011$, *Cohen's d* $= 1.74$, power $= 0.81$; SMA, BA6).

As shown in **Figure 6**, the *t*-values of the HbO signal difference between the DS and TD groups were visualized on a brain cortex template by using the Xjview toolbox (http://www.alivelearn.net/xjview) and BrainNet Viewer toolbox (Xia et al., 2013).

To inspect the relationship between task performance and HbO data, the Pearson's correlation analysis was performed. It was discovered that only the TD group showed a significant positive correlation between the HbO measurement in channel 8 and task accuracy ($r = 0.827$, $p < 0.05$; **Figure 7**). However, it was not the case for the DS group, in which no significant correlation was identified.

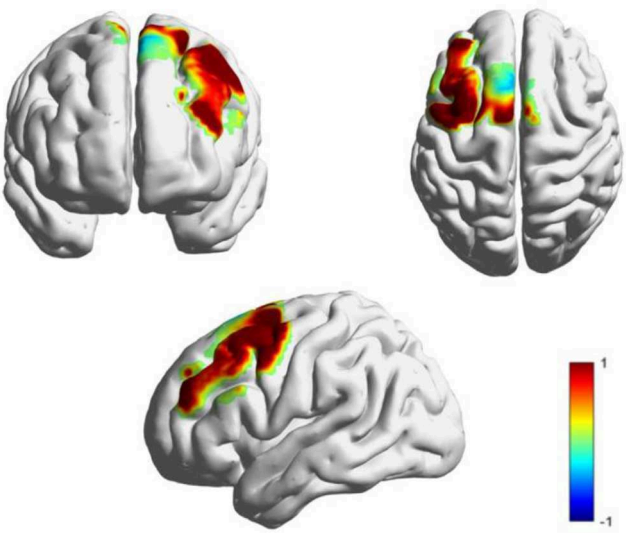

FIGURE 6 | T-maps for the cortical activation difference between the TD and DS groups.

Brain Network Analysis

The average path length (L_p), global efficiency (E_g) and the measure of small-worldness (σ) were, respectively calculated for both the DS and TD groups, which were provided in **Figure 8** as a function of the sparsity (i.e., threshold *T*). Since the σ of constructed brain functional networks for both groups was larger than 1 as compared to that of matched random

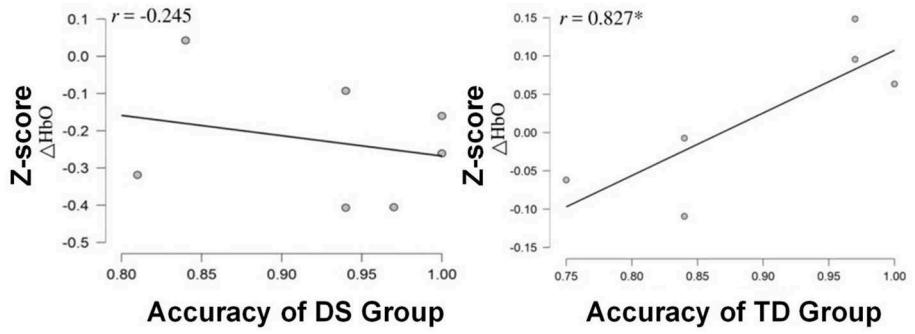

FIGURE 7 | Scatterplots and correlation coefficient (r) between the z-scores of HbO changes for channel 8 (the PMC) and ACC for each group of the children. *$p < 0.05$.

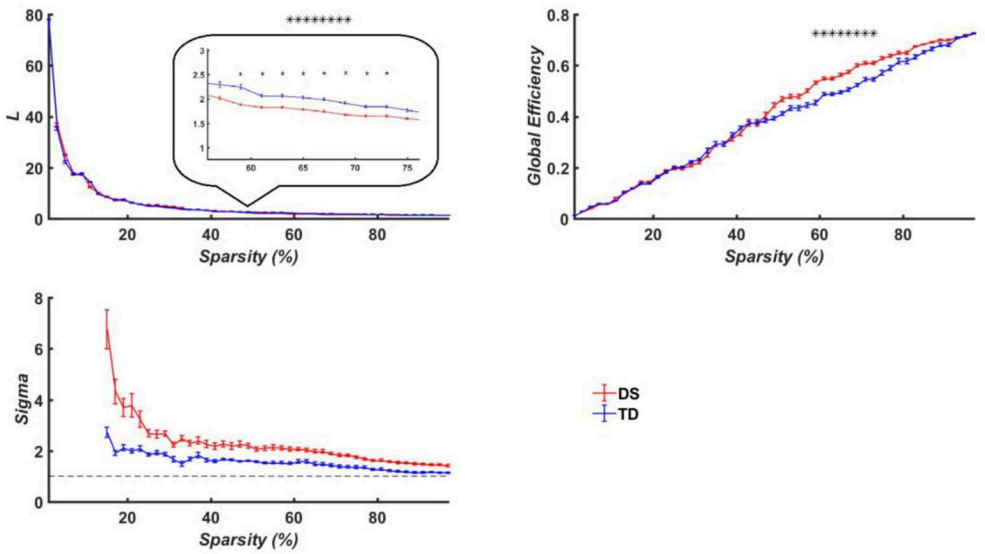

FIGURE 8 | Brain network properties of the TD the DS groups. Top left is for averaged path length (L_p); top right is the averaged node degree; bottom left is the measure of small-worldness, and the dashed curve is 1. The curves show the network indicators under different thresholds, in which the red represents the DS group while the blue denote the TD group. The horizontal axis denotes the threshold values while the vertical axis denotes the network properties indicators. Here the asterisks denote $p < 0.05$.

networks (**Figure 8**), the functional brain networks for the two groups exhibited small-world property. More importantly, we discovered that the DS group manifested significantly larger E_g and shorter L_p than the TD group when the threshold T was ranged between 0.59 and 0.73.

DISCUSSION

In this study, the small-world analysis combined with fNIRS recordings was conducted to inspect the differences in brain activation and networks along the motor and prefrontal cortex between the TD and DS children, which involves both the motor and cognitive functions, particularly the EF.

We discovered that the TD group exhibited significantly higher brain activation in the DLPFC and PMC (channels 1, 8, and 9) as compared to the DS group during a fine motor task (**Figure 5**). Interestingly, the DLPFC and the PMC are related to motor and executive functions (Haber, 2003; Leh et al., 2010; Stein et al., 2017). Previous studies employing similar fine motor tasks have also demonstrated that the DLPFC plays an essential role in performing these type of tasks that require EF in order to correctly plan the more complex motor actions (Robertson, 2007; Yogev-Seligmann et al., 2008; Sturm et al., 2016; Sachs et al., 2017).

In addition, no significant relationship was identified between fNIRS data and task performance in DS children. However, a strong positive correlation was revealed between the level of activation in channel 8 and task accuracy in TD children. Our new findings illustrated that the premotor cortex is vital for the performance of the task employed in this study. The impaired

ability to activate this cortical brain region might cause lower task performance in DS children.

Further, the motor and executive functions deficits in the DS group were demonstrated by altered brain functional connectivity. In particular, the functional brain networks of the DS group exhibited higher global efficiency and shorter path length as compared to those of the TD group, which demonstrated the tendency toward a more random connectivity. Consequently, the brain networks with higher E_g and shorter L_p might result in worse performance in the motor task for the DS group.

Besides the small sample size, only the DLPFC and the PMC was inspected in this study, thus limiting our ability to ascertain the impact from other brain regions. While this is a limitation of fNIRS neuroimaging technology, it will allow us to conduct a task-based study in DS children. This study offers some insight into the mechanism of the development of the fine motor function with the children with DS from the perspective of brain networks.

DATA AVAILABILITY STATEMENT

The datasets generated for this study are available on request to the corresponding author.

ETHICS STATEMENT

The studies involving human participants were reviewed and approved by Ethics Committee of the University of Macau (Macao SAR, China). Written informed consent to participate in this study was provided by the participants' legal guardian/next of kin.

AUTHOR CONTRIBUTIONS

ZY, F-ML, and S-YX designed research and wrote the paper. Z-SH and M-YW performed research and analyzed data. PA-S reviewed and discussed the data, proofread the manuscript, and co-wrote its final version. JZ and Z-YC provided the invaluable suggestion and revised this manuscript.

FUNDING

This study was supported by MYRG2019-00082-FHS and MYRG 2018-00081-FHS Grants from the University of Macau, as well as FDCT 025/2015/A1 and FDCT 0011/2018/A1 Grants from the Macau Government. PA-S was supported by a sabbatical grant SFRH/BSAB/150316/2019 from Fundação para a Ciência e a Tecnologia, Portugal.

REFERENCES

Ahmadlou, M., Gharib, M., Hemmati, S., Vameghi, R., and Sajedi, F. (2013). Disrupted small-world brain network in children with Down syndrome. *Clin. Neurophysiol.* 124, 1755–1764. doi: 10.1016/j.clinph.2013.03.004

Anderson, J. S., Nielsen, J. A., Ferguson, M. A., Burback, M. C., Cox, E. T., Dai, L., et al. (2013). Abnormal brain synchrony in Down syndrome. *NeuroImage Clin.* 2, 703–715. doi: 10.1016/j.nicl.2013.05.006

Bassett, D. S., and Bullmore, E. (2006). Small-world brain networks. *Neurosci.* 12, 512–523. doi: 10.1177/1073858406293182

Bloedel, J. R. (2004). Task-dependent role of the cerebellum in motor learning. *Progr. Brain Res.* 143, 319–329. doi: 10.1016/S0079-6123(03)43031-8

Bullmore, E., and Sporns, O. (2009). Complex brain networks: graph theoretical analysis of structural and functional systems. *Nat. Rev. Neurosci.* 10, 186–198. doi: 10.1038/nrn2575

Cao, J., Khan, B., Hervey, N., Tian, F., Delgado, M. R., Clegg, N. J., et al. (2015). "FNIRS-based evaluation of cortical plasticity in children with cerebral palsy undergoing constraint-induced movement therapy," in *Optical Techniques in Neurosurgery, Neurophotonics, and Optogenetics II,* eds H. Hirschberg, S. J. Madsen, E. D. Jansen, Q. Luo, S. K. Mohanty, and N. V. Thakor (San Francisco, CA: International Society for Optics and Photonics), 93050N. doi: 10.1117/12.2076995

Cheng, X., Li, X., and Hu, Y. (2015). Synchronous brain activity during cooperative exchange depends on gender of partner: a fNIRS-based hyperscanning study. *Hum. Brain Mapp.* 36, 2039–2048. doi: 10.1002/hbm.22754

Deiber, M.-P., Passingham, R. E., Colebatch, J. G., Friston, K. J., Nixon, P. D., and Frackowiak, R. S. J. (1991). Cortical areas and the selection of movement: a study with positron emission tomography. *Exp. Brain Res.* 84, 393–402. doi: 10.1007/BF00231461

Diamond, A. (2013). Executive functions. *Annu. Rev. Psychol.* 64:135. doi: 10.1146/annurev-psych-113011-143750

Ding, X. P., Gao, X., Fu, G., and Lee, K. (2013). Neural correlates of spontaneous deception: a functional near-infrared spectroscopy (fNIRS)study. *Neuropsychologia* 51, 704–712. doi: 10.1016/j.neuropsychologia.2012.12.018

Ding, X. P., Sai, L., Fu, G., Liu, J., and Lee, K. (2014). Neural correlates of second-order verbal deception: a functional near-infrared spectroscopy (fNIRS) study. *Neuroimage* 87, 505–514. doi: 10.1016/j.neuroimage.2013.10.023

Drummond, S. P. A., Walker, M., Almklov, E., Campos, M., Anderson, D. E., and Straus, L. D. (2013). Neural correlates of working memory performance in primary insomnia. *Sleep* 36, 1307–1316. doi: 10.5665/sleep.2952

Fries, P. (2005). A mechanism for cognitive dynamics: neuronal communication through neuronal coherence. *Trends Cogn. Sci.* 9, 474–480. doi: 10.1016/j.tics.2005.08.011

Fu, G., Mondloch, C. J., Ding, X. P., A., Short, L., Sun, L., et al. (2014). The neural correlates of the face attractiveness aftereffect: a functional near-infrared spectroscopy (fNIRS) study. *Neuroimage* 85, 363–371. doi: 10.1016/j.neuroimage.2013.04.092

Grafton, S. T., Hazeltine, E., and Ivry, R. B. (1998). Abstract and effector-specific representations of motor sequences identified with PET. *J. Neurosci.* 18, 9420–8. doi: 10.1523/JNEUROSCI.18-22-09420.1998

Haber, S. N. (2003). *Integrating Cognition and Motivation Into the Basal Ganglia Pathways of Action.* Totowa, NJ: Humana Press. 35–50. Available online at: https://link.springer.com/chapter/10.1007/978-1-59259-326-2_3#citeas

Hartman, E., Houwen, S., Scherder, E., and Visscher, C. (2010). On the relationship between motor performance and executive functioning in children with intellectual disabilities. *J. Intellect. Disabil. Res.* 54, 468–477. doi: 10.1111/j.1365-2788.2010.01284.x

He, Y., Dagher, A., Chen, Z., Charil, A., Zijdenbos, A., Worsley, K., et al. (2009). Impaired small-world efficiency in structural cortical networks in multiple sclerosis associated with white matter lesion load. *Brain.* 132, 3366–3379. doi: 10.1093/brain/awp089

Horvat, M., Croce, R., Tomporowski, P., and Barna, M. C. (2013). The influence of dual-task conditions on movement in young adults with and without Down syndrome. *Res. Dev. Disabil.* 34, 3517–3525. doi: 10.1016/j.ridd.2013.06.038

Hu, Z., Zhang, J., Couto, T. A., Xu, S., Luan, P., and Yuan, Z. (2018). Optical mapping of brain activation and connectivity in occipitotemporal cortex during chinese character recognition. *Brain Topogr.* 31, 1014–1028. doi: 10.1007/s10548-018-0650-y

Imai, M., Watanabe, H., Yasui, K., Kimura, Y., Shitara, Y., Tsuchida, S., et al. (2014). Functional connectivity of the cortex of term and preterm infants and infants with Down's syndrome. *Neuroimage* 85, 272–278. doi: 10.1016/j.neuroimage.2013.04.080

Jarrold, C., and Baddeley, A. (2001). Short-term memory in Down syndrome: applying the working memory model. *Down Syndr. Res. Pract.* 7, 17–23. doi: 10.3104/reviews.110

Latora, V., and Marchiori, M. (2001). Efficient behavior of small-world networks. *Phys. Rev. Lett.* 87:198701. doi: 10.1103/PhysRevLett.87.198701

Leh, S. E., Petrides, M., and Strafella, A. P. (2010). The neural circuitry of executive functions in healthy subjects and Parkinson's disease. *Neuropsychopharmacology* 35, 70–85. doi: 10.1038/npp.2009.88

Li, C. S., Padoa-Schioppa, C., and Bizzi, E. (2001). Neuronal correlates of motor performance and motor learning in the primary motor cortex of monkeys adapting to an external force field. *Neuron* 30, 593–607. doi: 10.1016/S0896-6273(01)00301-4

Liu, N., Mok, C., Witt, E. E., Pradhan, A. H., Chen, J. E., and Reiss, A. L. (2016). NIRS-based hyperscanning reveals inter-brain neural synchronization during cooperative jenga game with face-to-face communication. *Front. Hum. Neurosci.* 10:82. doi: 10.3389/fnhum.2016.00082

Lott, I. T., and Dierssen, M. (2010). Cognitive deficits and associated neurological complications in individuals with Down's syndrome. *Lancet Neurol.* 9, 623–633. doi: 10.1016/S1474-4422(10)70112-5

Lu, F.-M., Wang, Y.-F., and Yuan, Z. (2016). "Hemodynamic responses can modulate the brain oscillations in low frequency," in *Clinical and Translational Neurophotonics; Neural Imaging and Sensing; and Optogenetics and Optical Manipulation,* eds. S. J. Madsen, V. X. D. Yang, E. D. Jansen, Q. Luo, S. K. Mohanty, and N. V. Thakor (San Francisco, CA: International Society for Optics and Photonics), 96901U. doi: 10.1117/12.2211237

Lu, F. M., Dai, J., Couto, T. A., Liu, C. H., Chen, H., Lu, S. L., et al. (2017a). Diffusion tensor imaging tractography reveals disrupted white matter structural connectivity network in healthy adults with insomnia symptoms. *Front. Hum. Neurosci.* 11:583. doi: 10.3389/fnhum.2017.00583

Lu, F. M., Liu, C. H., Lu, S. L., Tang, L. R., Tie, C. L, Zhang, J., et al. (2017b). Disrupted topology of frontostriatal circuits is linked to the severity of insomnia. *Front. Neurosci.* 11:214. doi: 10.3389/fnins.2017.00214

Martin, G. E., Klusek, J., Estigarribia, B., and Roberts, J. E. (2009). Language characteristics of individuals with Down syndrome. *Top. Lang. Disord.* 29, 112–132. doi: 10.1097/TLD.0b013e3181a71fe1

Miyachi, S., Hikosaka, O., Miyashita, K., Kárádi, Z., and Rand, M. K. (1997). Differential roles of monkey striatum in learning of sequential hand movement. *Exp. Brain Res.* 115, 1–5. doi: 10.1007/PL00005669

Nakamura, K., Sakai, K., and Hikosaka, O. (1998). Neuronal activity in medial frontal cortex during learning of sequential procedures. *J. Neurophysiol.* 80, 2671–2687. doi: 10.1152/jn.1998.80.5.2671

Naseer, N., and Hong, K. S. (2013). Classification of functional near-infrared spectroscopy signals corresponding to the right- and left-wrist motor imagery for development of a brain-computer interface. *Neurosci. Lett.* 553, 84–89. doi: 10.1016/j.neulet.2013.08.021

O'connor, C., Manly, T., Robertson, I. H., Hevenor, S. J., and Levine, B. (2004). 1. An fmri study of sustained attention with endogenous and exogenous engagement. *Brain Cogn,.* 54, 113–135. doi: 10.1016/S0278-2626(03)00268-9

Piek, J., Dyck, M. J., Nieman, A., Anderson, M., Hay, D., et al. (2004). The relationship between motor coordination, executive functioning and attention in school aged children. *Arch. Clin. Neuropsychol.* 19, 1063–1076. doi: 10.1016/j.acn.2003.12.007

Pujol, J., del Hoyo, L., Blanco-Hinojo, L., de Sola, S., Macià, D., Martínez-Vilavella, G., et al. (2015). Anomalous brain functional connectivity contributing to poor adaptive behavior in Down syndrome. *Cortex* 64, 148–156. doi: 10.1016/j.cortex.2014.10.012

Robertson, E. M. (2007). The serial reaction time task: implicit motor skill learning? *J. Neurosci.* 27, 10073–10075. doi: 10.1523/JNEUROSCI.2747-07.2007

Robertson, E. M., Tormos, J. M., Maeda, F., and Pascual-Leone, A. (2001). The role of the dorsolateral prefrontal cortex during sequence learning is specific for spatial information. *Cereb. Cortex* 11, 628–635. doi: 10.1093/cercor/11.7.628

Rubinov, M., and Sporns, O. (2010). Complex network measures of brain connectivity: uses and interpretations. *Neuroimage* 52, 1059–1069. doi: 10.1016/j.neuroimage.2009.10.003

Sachs, M., Kaplan, J., Der Sarkissian, A., and Habibi, A. (2017). Increased engagement of the cognitive control network associated with music training in children during an fMRI Stroop task. *PLoS ONE* 12:e0187254. doi: 10.1371/journal.pone.0187254

Scarapicchia, V., Brown, C., Mayo, C., and Gawryluk, J. R. (2017). Functional magnetic resonance imaging and functional near-infrared spectroscopy: insights from combined recording studies. *Front. Hum. Neurosci.* 11:419. doi: 10.3389/fnhum.2017.00419

Scholkmann, F., Spichtig, S., Muehlemann, T., and Wolf, M. (2010). How to detect and reduce movement artifacts in near-infrared imaging using moving standard deviation and spline interpolation. *Physiol. Meas.* 31, 649–662. doi: 10.1088/0967-3334/31/5/004

Scholkmann, F., and Wolf, M. (2013). General equation for the differential pathlength factor of the frontal human head depending on wavelength and age. *J. Biomed. Opt.* 18:105004. doi: 10.1117/1.JBO.18.10.105004

Schott, N., and Holfelder, B. (2015). Relationship between motor skill competency and executive function in children with Down's syndrome. *J. Intellect. Disabil. Res.* 59, 860–872. doi: 10.1111/jir.12189

Seitz, R. J., Roland, P. E., Bohm, C., Greitz, T., and Stone-Elander, S. (1990). Motor learning in man. *Neuroreport* 1, 57–60. doi: 10.1097/00001756-199009000-00016

Shibasaki, H., Sadato, N., Lyshkow, H., Yonekura, Y., Honda, M., Nagamine, T., et al. (1993). Both primary motor cortex and supplementary motor area play an important role in complex finger movement. *Brain* 116, 1387–1398. doi: 10.1093/brain/116.6.1387

Stein, M., Auerswald, M., and Ebersbach, M. (2017). Relationships between motor and executive functions and the effect of an acute coordinative intervention on executive functions in kindergartners. *Front. Psychol.* 8:859. doi: 10.3389/fpsyg.2017.00859

Storey, J. D. (2002). A direct approach to false discovery rates. *J. R. Stat. Soc. Ser. B* 64, 479–498. doi: 10.1111/1467-9868.00346

Sturm, V. E., Haase, C. M., and Levenson, R. W. (2016). Emotional dysfunction in psychopathology and neuropathology: neural and genetic pathways. *Genom. Circ. Pathways Clin. Neuropsychiatr.* 345–364. doi: 10.1016/B978-0-12-800105-9.00022-6

Traverso, L., Viterbori, P., and Usai, M. C. (2015). Improving executive function in childhood: evaluation of a training intervention for 5-year-old children. *Front. Psychol.* 6:525. doi: 10.3389/fpsyg.2015.00525

Vega, J. N., Hohman, T. J., Pryweller, J. R., Dykens, E. M., Thornton-wells, T. A., Genetics, H., et al. (2015). Resting state functional connectivity in individuals with Down syndrome and Williams syndrome compared to typically developing controls. *Brain Connect.* 5, 461–75. doi: 10.1089/brain.2014.0266

Wang, J., Wang, X., Xia, M., Liao, X., Evans, A., and He, Y. (2015). GRETNA: a graph theoretical network analysis toolbox for imaging connectomics. *Front. Hum. Neurosci.* 9:386. doi: 10.3389/fnhum.2015.00458

Wassenberg, R., Feron, F. J. M., Kessels, A. G. H., Hendriksen, J. G. M., Kalff, A. C., Kroes, M., et al. (2005). Relation between cognitive and motor performance in 5- to 6-year-old children: results from a large-scale cross-sectional study. *Child Dev.* 76, 1092–1103. doi: 10.1111/j.1467-8624.2005.00899.x

Watts, D. J., and Strogatz, S. H. (1998). Collective dynamics of 'small-world' networks. *Nature* 393, 440–442. doi: 10.1038/30918

Xia, M., Wang, J., and He, Y. (2013). BrainNet viewer: a network visualization tool for human brain connectomics. *PLoS ONE* 8:e68910. doi: 10.1371/journal.pone.0068910

Yang, C., Tang, D., and Atluri, S. (2010). Three-dimensional carotid plaque progression simulation using meshless generalized finite difference method based on multi-year MRI patient-tracking data. *Comput. Model. Eng. Sci.* 57, 51–76.

Ye, J. C., Tak, S., Jang, K. E., Jung, J., and Jang, J. (2009). NIRS-SPM: statistical parametric mapping for near-infrared spectroscopy. *Neuroimage* 44, 428–447. doi: 10.1016/j.neuroimage.2008.08.036

Yennu, A., Tian, F., Smith-Osborne, A., J., Gatchel, R., Woon, F. L., et al. (2016). Prefrontal responses to Stroop tasks in subjects with post-traumatic stress disorder assessed by functional near infrared spectroscopy. *Sci. Rep.* 6:30157. doi: 10.1038/srep30157

Yogev-Seligmann, G., Hausdorff, J. M., and Giladi, N. (2008). The role of executive function and attention in gait. *Mov. Disord.* 23, 329–42. doi: 10.1002/mds.21720

Zhang, H., Zhang, Y.-J., Lu, C.-M., Ma, S.-Y., Zang, Y.-F., and Zhu, C.-Z. (2010). Functional connectivity as revealed by independent component analysis of resting-state fNIRS measurements. *Neuroimage* 51, 1150–1161. doi: 10.1016/j.neuroimage.2010.02.080

Conflict of Interest: The authors declare that the research was conducted in the absence of any commercial or financial relationships that could be construed as a potential conflict of interest.

Copyright © 2020 Xu, Lu, Wang, Hu, Zhang, Chen, Armada-da-Silva and Yuan. This is an open-access article distributed under the terms of the Creative Commons Attribution License (CC BY). The use, distribution or reproduction in other forums is permitted, provided the original author(s) and the copyright owner(s) are credited and that the original publication in this journal is cited, in accordance with accepted academic practice. No use, distribution or reproduction is permitted which does not comply with these terms.

frontiers in Neuroscience

ORIGINAL RESEARCH
published: 18 February 2020
doi: 10.3389/fnins.2020.00105

Assessing Time-Resolved fNIRS for Brain-Computer Interface Applications of Mental Communication

Androu Abdalmalak[1,2], Daniel Milej[1,2], Lawrence C. M. Yip[1,2], Ali R. Khan[1,3], Mamadou Diop[1,2], Adrian M. Owen[4] and Keith St. Lawrence[1,2]*

[1] Department of Medical Biophysics, Western University, London, ON, Canada, [2] Imaging Program, Lawson Health Research Institute, London, ON, Canada, [3] Imaging Research Laboratories, Robarts Research Institute, London, ON, Canada, [4] Brain and Mind Institute, Western University, London, ON, Canada

Brain-computer interfaces (BCIs) are becoming increasingly popular as a tool to improve the quality of life of patients with disabilities. Recently, time-resolved functional near-infrared spectroscopy (TR-fNIRS) based BCIs are gaining traction because of their enhanced depth sensitivity leading to lower signal contamination from the extracerebral layers. This study presents the first account of TR-fNIRS based BCI for "mental communication" on healthy participants. Twenty-one (21) participants were recruited and were repeatedly asked a series of questions where they were instructed to imagine playing tennis for "yes" and to stay relaxed for "no." The change in the mean time-of-flight of photons was used to calculate the change in concentrations of oxy- and deoxyhemoglobin since it provides a good compromise between depth sensitivity and signal-to-noise ratio. Features were extracted from the average oxyhemoglobin signals to classify them as "yes" or "no" responses. Linear-discriminant analysis (LDA) and support vector machine (SVM) classifiers were used to classify the responses using the leave-one-out cross-validation method. The overall accuracies achieved for all participants were 75% and 76%, using LDA and SVM, respectively. The results also reveal that there is no significant difference in accuracy between questions. In addition, physiological parameters [heart rate (HR) and mean arterial pressure (MAP)] were recorded on seven of the 21 participants during motor imagery (MI) and rest to investigate changes in these parameters between conditions. No significant difference in these parameters was found between conditions. These findings suggest that TR-fNIRS could be suitable as a BCI for patients with brain injuries.

Keywords: functional near-infrared spectroscopy, brain-computer interface, motor-imagery, disorders of consciousness, time-resolved measurement

OPEN ACCESS

Edited by:
Yasuyo Minagawa, Keio University, Japan

Reviewed by:
Benito de Celis Alonso, Meritorious Autonomous University of Puebla, Mexico
Kotaro Takeda, Fujita Health University, Japan

****Correspondence:***
Androu Abdalmalak
aabdalma@uwo.ca

Specialty section:
This article was submitted to Brain Imaging Methods, a section of the journal Frontiers in Neuroscience

Received: *16 October 2019*
Accepted: *27 January 2020*
Published: *18 February 2020*

Citation:
Abdalmalak A, Milej D, Yip LCM, Khan AR, Diop M, Owen AM and St. Lawrence K (2020) Assessing Time-Resolved fNIRS for Brain-Computer Interface Applications of Mental Communication. Front. Neurosci. 14:105. doi: 10.3389/fnins.2020.00105

INTRODUCTION

Brain-computer interfaces (BCIs) are devices that can be used to establish a communication pathway between the brain and external devices (Shih et al., 2012). For people with chronic paralysis following a severe spinal cord injury, surgical implants that record activity directly from the brain can provide a means of interacting with the environment, such as controlling a prosthetic

(Mak and Wolpaw, 2009; Shih et al., 2012). However, the need to implant electrodes limits the applications of this invasive approach (Waldert, 2016). The use of neuroimaging modalities as non-invasive BCI devices has garnered attention for applications such as assessing cognition in patients with disorders of consciousness (DOC), providing rudimentary communication for patients in a completely locked-in state, and as a feedback tool for stroke therapy (Naseer and Hong, 2015a; Kurz et al., 2018; Rupawala et al., 2018). The most frequently used portable BCI devices are based on electroencephalography (EEG). Although EEG provides excellent temporal resolution, making it ideal for real-time applications, the technology suffers from poor spatial resolution and an inherent sensitivity to motion artifacts (Padfield et al., 2019). Motion artifacts can have an impact on the spectral content of EEG in the frequency range below 20 Hz and lead to large spikes in the signal that may be difficult to correct (Mihajlovic et al., 2014). A promising alternative is functional near-infrared spectroscopy (fNIRS) (Rupawala et al., 2018) since it provides a good compromise between spatial and temporal resolution.

Analogous to functional magnetic resonance imaging (fMRI), fNIRS detects increases in neuronal activity through the hemodynamic response — that is, the change in blood oxygenation that occurs due to increased cerebral blood flow (Monti et al., 2010). By measuring light absorption at a minimum of two wavelengths, changes in concentrations of oxy- and deoxy-hemoglobin can be calculated (Strangman et al., 2002). A number of activation paradigms have been combined with fNIRS for BCI applications, including motor imagery (MI), mental arithmetic, working memory, and other mental activities (Naseer and Hong, 2015a; Rupawala et al., 2018). MI was the first task proposed for BCI applications, which requires participants to perform kinesthetic imagining, such as imagining squeezing a ball (Coyle et al., 2004), finger tapping (Sitaram et al., 2007), and hand grasping (Fazli et al., 2012). More recent fNIRS-BCI applications have focused on activation paradigms that involve the prefrontal cortex, such as mental arithmetic, to avoid signal loss due to the presence of hair and concerns regarding the quality of the NIRS signal for MI tasks (Shin et al., 2017; Qureshi et al., 2017). However, MI has proven extremely valuable in fMRI studies of DOC. Using tennis imagery as a mental task and focusing on activation in the supplementary motor area (SMA), fMRI was used to demonstrate residual brain function in a patient with a diagnosis of vegetative state (Owen et al., 2006) and in a subsequent study, to provide "yes" and "no" answers to a series of questions (Monti et al., 2010).

To improve the sensitivity of fNIRS to MI, time-resolved (TR) fNIRS has been investigated (Abdalmalak et al., 2017a, 2020). TR detection involves recording the arrival times of single photons, which can be used to enhance depth sensitivity since photons that interrogate superficial tissue are detected earlier than photons that travel farther (i.e., deeper). Consequently, improved sensitivity to the brain can be achieved by focusing on late-arriving photons (Diop and St Lawrence, 2013; Lange and Tachtsidis, 2019). This can be achieved by calculating the statistical moments of the recorded distribution of arrival times since higher moments are weighted toward late-arriving light (Liebert et al., 2004; Milej et al., 2015). Previous work has shown that the first moment (i.e., the mean time-of-flight, $<t>$) provided a good compromise between depth sensitivity and signal-to-noise for detecting MI activation from probes interrogating the SMA and premotor cortex (PMC) (Abdalmalak et al., 2017a). Using fMRI as a benchmark, the classification accuracy of TR NIRS based on $<t>$ analysis was 93% (Abdalmalak et al., 2017a). In a follow-up study, rudimentary communication was established with a locked-in patient who was instructed to use tennis imagery as affirmation to a series of questions (Abdalmalak et al., 2017b). The accuracy of the fNIRS-BCI responses was confirmed because the patient had regained sufficient eye movement to answer the same questions after the fNIRS study.

The promising results of the two previous studies suggest that time-resolved functional near-infrared spectroscopy (TR-fNIRS) combined with MI could be a suitable BCI for mental communication with DOC patients. The purpose of this study was therefore to evaluate the classification performance of this BCI approach on healthy volunteers. Each participant was asked a series of four questions requiring yes-or-no answers. They were instructed to imagine playing tennis to communicate "yes" and to stay relaxed if the answer was "no"(Monti et al., 2010). Linear discriminant analysis (LDA) and support vector machine (SVM) algorithms were evaluated for classification accuracy as these are the most commonly used machine-learning approaches used in fNIRS-BCI studies (Naseer and Hong, 2015a).

MATERIALS AND METHODS

BCI Study

Twenty-one healthy participants with no history of any neurological disease were recruited (6 females and 15 males, mean age of 29 ± 5 years, age range 24–40 years). All participants except one were right handed with no history of neurological condition or severe brain injury. Written informed consent was obtained from all participants and this study was approved by the Research Ethics Board at Western University, which complies with the guidelines of the Tri-Council Policy Statement (TCPS): Ethical Conduct for Research Involving Humans.

For each experiment, the participants were seated in a Fowler's position on a reclining chair with a cushioned pillow to support their neck. The TR system consisted of one emission and four detection fibers (see section "TR-NIRS System"), which were placed on the head in a cross pattern with the emission fiber over FCz (according to the international template for EEG electrode placement) in order to interrogate the SMA and PMC (Abdalmalak et al., 2016). The fibers were secured on the head using a 3D printed holder (TAZ 5, LulzBot, United States), which was covered by an EEG cap (EASYCAP GmbH, Germany). **Figure 1B** shows a picture of one of the participants wearing the cap with the TR-NIRS optodes inserted.

Each participant was asked the following four questions that could all be answered with a "yes" or "no" response:

1. Do you have any brothers?

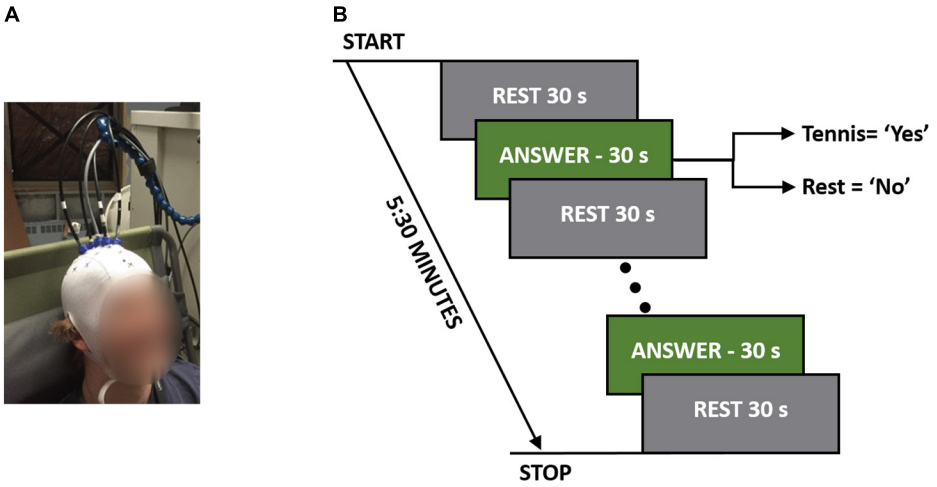

FIGURE 1 | (A) A participant wearing the TR-fNIRS cap with the probes positioned over the SMA and PMC. **(B)** Study protocol illustrating the rest and response periods. The total time per question was 5:30 min, which consisted of five 30-s answer periods.

2. Do you have any sisters?
3. Are you at St. Joseph's Hospital?
4. Are you feeling cold right now?

The order that questions were asked in was randomized between participants to avoid any biases that may exist based on the questions. These questions were chosen for their applicability to patient studies. For instance, the first two questions were factual with definitive known answers, while question 3 ("Are you at St. Joseph's Hospital?) served as a control since all participants were expected to answer "yes." The final question was chosen to simulate asking patients a question where only they would know the answer. Each question was asked five times in a block design consisting of a 30-s baseline rest period followed by five cycles of 30-s alternating blocks of "answer" and "rest" periods for a total duration of 5:30 min (**Figure 1A**). Answering all four questions took 22 min to complete. Each question was asked prior to the beginning of the run, and during the experiment the participants were cued to either "rest" or "answer." For a positive response, the participants were asked to imagine playing a game of tennis where they pictured themselves on a tennis court, swinging their arm back and forth trying to hit a tennis ball over and over again. For a negative response, the participants were asked to remain completely relaxed; i.e., a "no" response would result in 5:30 min of complete rest.

Physiological Monitoring Study

Since previous work has shown that changes in physiological variables such as heart rate (HR) and mean arterial pressure (MAP) can confound the fNIRS signal (Tachtsidis and Scholkmann, 2016), a subset (seven of the 21) of the participants were brought back for a separate session to investigate if the MI paradigm would elicit changes in HR and MAP. A non-invasive monitoring system was secured to the participant's left arm (Finapres Medical Systems, Netherlands) to record HR and MAP continuously (sampling rate = 200 Hz) during a 5:30 min experiment consisting of 30-s alternating blocks of rest and MI. The cues given to the participants were similar to those given in the BCI study, except in this experiment, the participants were asked to imagine playing tennis every time they heard the word "tennis."

For each participant, the Finapres data were subsequently down-sampled to 1 Hz and analyzed by averaging the data across each of the five MI and rest blocks. This resulted in five HR and five MAP values for each condition per participant. A paired t-test was used to determine if there was a significant difference between the two conditions across all participants while correcting for multiple comparisons using Bonferroni.

TR-NIRS System

Data were collected using an in-house built TR-fNIRS system (Milej et al., 2016b; Kewin et al., 2019). The system consisted of two lasers (λ = 760 and 830 nm) pulsing at 80 MHz and controlled by a Sepia laser driver (PicoQuant, Germany). The laser heads were coupled in a 2.5 m bifurcated fiber (φ = 0.4 mm, NA = 0.39, Thorlabs, United States) and four 1.5 m detection fiber bundles (φ = 3.6 mm, NA = 0.55, Fiberoptics Technology, United States) were used to deliver the diffusively reflected light from the scalp to one of four hybrid photomultiplier tubes (PMA Hybrid 50, PicoQuant, Germany). A time-correlated single-photon counting module (HydraHarp 400, PicoQuant, Germany) was used to record the distribution of times-of-flight (DTOF) of photons for each detector every 300 ms using in-house-developed LabVIEW (National Instruments, United States) software (Milej et al., 2016a).

TR-fNIRS Data Analysis

Data were analyzed in MATLAB (MathWorks Inc., United States) using the following processing steps. First, $<t>$ was calculated for every DTOF in a time series after truncating each DTOF at 10% of the ascending side and 1% of the descending side to reduce noise (Liebert et al., 2004). $<t>$ was chosen since previous work has

shown that it provided a good compromise between activation sensitivity and signal-to-noise ratio (Abdalmalak et al., 2017a). The change in mean time-of-flight ($\Delta <t>$) relative to the initial values was calculated, and these time series were corrected for motion artifacts using an algorithm based on a moving standard deviation and spline interpolation (Scholkmann et al., 2010; Metz et al., 2015). The time-courses were detrended to remove slow drifts by filtering with a high-pass filter with a cut-off period of 128 s and smoothed using a hemodynamic response function (full width half maximum = 4 s) to remove fast frequency components, such as those due to arterial pulsation. Next, the two $\Delta <t>$ time-courses for λ = 760 and 830 nm were converted into changes in concentration of oxy- and deoxy-hemoglobin using sensitivity factors obtained from Monte Carlo simulations. These simulations were generated based on a 10-layer model in which each layer was 0.2 cm thick. At each wavelength, the sensitivity factor for the brain was calculated as the sum of the sensitivity factors for all layers below 1 cm (i.e., layers 5–10) (Kacprzak et al., 2007; Abdalmalak et al., 2017b).

To calculate the changes in the concentrations of oxyhemoglobin (ΔC_{HbO_2}) and deoxyhemoglobin (ΔC_{Hb}), $\Delta <t>$ was first converted to the corresponding change in the absorption coefficient, $\Delta\mu_a(\lambda)$, for the two wavelengths (λ = 760 and 830 nm):

$$\Delta\mu_a(\lambda) = \frac{\Delta\langle t\rangle}{MTSF} = \frac{\langle t\rangle - \langle t\rangle_0}{MTSF} \quad (1)$$

where, MTSF is the sensitivity factor derived from Monte Carlo simulations for $\Delta <t>$ in the brain. Next, $\Delta\mu_a(\lambda)$ values determined at 760 and 830 nm were converted to ΔC_{HbO_2} and ΔC_{Hb} by:

$$\Delta\mu_a(\lambda) = \varepsilon_{HbO_2}(\lambda)\,\Delta C_{HbO_2} + \varepsilon_{Hb}(\lambda)\,\Delta C_{Hb} \quad (2)$$

where, $\varepsilon_{HbO_2}(\lambda)$ and $\varepsilon_{Hb}(\lambda)$ are the molar extinction coefficients for oxy- and deoxy-hemoglobin, respectively. After preprocessing, signals were averaged across all five trials and across all channels for each question; i.e., the response for each question was reduced to a single average time-course (60 s consisting of two 15 s rest periods and 30 s response period) for oxy- and deoxy-hemoglobin, respectively. Averaging was conducted to improve the signal-to-noise ratio and reduce the chance of detecting false positives based on the assumption that all four channels were interrogating motor-planning areas.

Features (listed in **Table 1**) were then extracted from the average time-courses for oxyhemoglobin only, since previous work has shown that oxyhemoglobin yields better performance for assessing task-induced brain activation (Mihara et al., 2012; Naseer and Hong, 2013). In order to investigate which combination of features produced the highest accuracy, an LDA and an SVM classifier were used to classify the result using the leave-one-out cross-validation method with all possible unique feature combinations (15 combinations in total). The classifier with the combination of feature(s) that yielded the highest accuracy was used to obtain all the results presented in this study. The code used for the analysis was developed in MATLAB (MathWorks Inc., United States) using functions implemented in the Statistical and Machine Learning Toolbox. Furthermore, a one-way ANOVA was used to determine if there was a significant difference in accuracy between questions (i.e., questions 1–4). Finally, to investigate the effect of the number of cycles on the overall accuracy, the analysis was initially conducted with only the first cycle and then repeated with increasing number of cycles until all five cycles were included.

TABLE 1 | Features extracted from the oxyhemoglobin time-courses and how each feature was calculated.

Feature	Calculation
Median change in signal (SM)	Difference between the median change during the task (excluding the first 10 s) and the preceding rest period
Signal slope (SS)	Slope of the first 16 s during the task period
Contrast-to-noise ratio (CNR)	Difference between the mean change during the task and the preceding rest period divided by the standard deviation of the rest period
Correlation coefficient (*r*)	Correlation coefficient between the change in the hemoglobin concentration time-courses and the theoretical activation model (i.e., box function convolved with a hemodynamic response function)

RESULTS

Of the 21 participants, three had to be excluded due to significant motion artifacts and overall low signal quality. The overall classification accuracy across all included subjects using LDA was 75% with a sensitivity of 83% and specificity of 58%. Similarly, the classification accuracy using SVM was 76% with a sensitivity of 79% and specificity of 71%. Individual classification accuracies using both classifiers are shown in **Table 2**. The combination of

TABLE 2 | Individual classification results for each participant.

Participant number	LDA Accuracy (%)	SVM Accuracy (%)
1	75	75
2	50	50
3	75	75
4	50	75
5	100	100
6	100	100
7	75	75
8	100	100
9	75	75
10	100	100
11	75	100
12	75	75
13	75	75
14	50	75
15	50	50
16	100	75
17	75	50
18	50	50

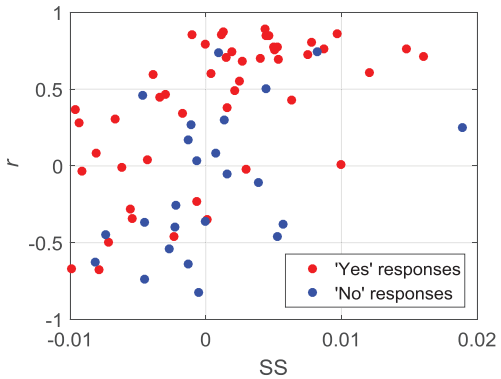

FIGURE 2 | 2D feature space showing the relationship between SS and *r* for all of the "yes" and "no" responses.

features that produced the highest accuracy using LDA was SM, CNR, and *r*, while SS and *r* contributed the most to the SVM model. Since SVM produced a higher accuracy, it was used for all further analyses. **Figure 2** shows the SS and *r* plotted in a 2D feature space for the "yes" and "no" responses in order to visualize the difference between the two responses.

The oxy- and deoxy-hemoglobin time-courses for one participant and for two different questions are shown in **Figure 3**. For the time-course shown on the left, which corresponded to the question: "Are you at St. Joseph's Hospital?," a clear increase in oxyhemoglobin and a concurrent, but smaller, decrease in deoxyhemoglobin can be observed during the response periods. For the second question in which the participant's response was "no," there were no noticeable changes in either ΔC_{HbO_2} or ΔC_{Hb}. As expected, these two questions were classified as "yes" and "no," respectively.

Average time courses of ΔC_{HbO_2} and ΔC_{Hb} for each consecutive question are presented in **Figure 4**. Since the order of the questions was randomized, each subplot does not represent the response to a particular question, but rather the response to all questions asked in one period. For each participant, the time courses were first averaged across trials and channels, resulting in a single time course per question. These time-courses were then averaged across all participants for the "yes" and "no" responses based on the classifier output. The "yes" responses show the expected hemodynamic changes in oxy-and deoxy-hemoglobin, which are absent in the "no" responses.

The overall accuracy of the SVM results is plotted as a function of the number of cycles in **Figure 5A**. As expected, increasing the number of cycles used for classification improved accuracy. The box-plot in **Figure 5A** shows variation in accuracy for each cycle for all unique combinations of features (15 in total), and the red circles represent the accuracy obtained using the optimum combination of features for SVM (i.e., SS and *r*). Since the best combination of features was optimized for five cycles, using only one, two or four cycles leads to different sets of optimum features. The classification accuracies for questions one to four are shown in **Figure 5B**. Once again, the accuracy presented is not for a particular question but based on the order of the questions asked. Although there appear to be differences in accuracy between questions, there were no statistically significant differences.

To further investigate the performance of the SVM classifier, the oxyhemoglobin signals that were classified as "yes" or "no" were averaged together for all trials, channels, participants, and questions. In other words, the oxyhemoglobin time-courses for the "yes" and "no" responses in **Figure 4** were averaged together to end up with one time-course for all "yes" responses and one time-course for all "no" responses. In addition, the oxyhemoglobin time-courses for the ground truth responses, i.e., based on the participants' responses recorded after the study, were averaged together to produce ground-truth "yes" and "no" oxyhemoglobin time-courses. The ground-truth "yes" signal represents the group average for all oxyhemoglobin signals for which participants answered "yes." Likewise, the ground-truth "no" is the group average for questions where participants

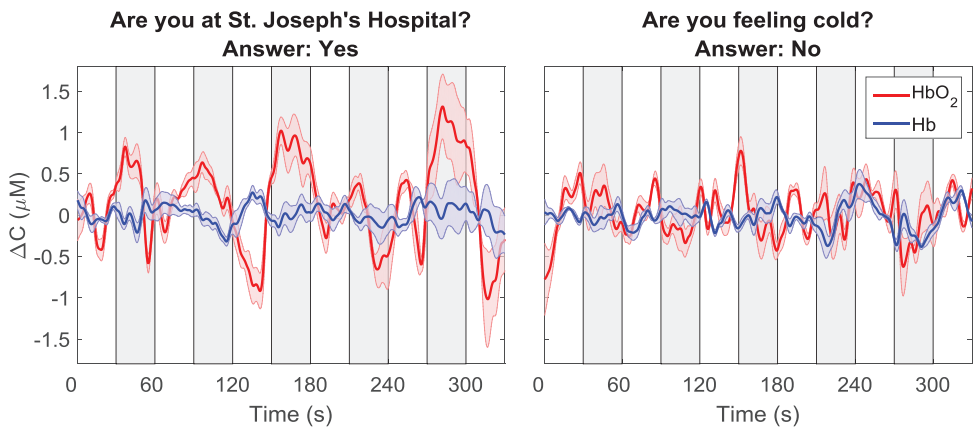

FIGURE 3 | Sample time courses of ΔC_{HbO_2} and ΔC_{Hb} for one participant and two questions. Each time course was averaged across data from all four channels. The time course on the left was classified as "yes" while the one on the right was classified as "no." The gray boxes indicate the response periods. The error bars represent the standard error of mean across channels.

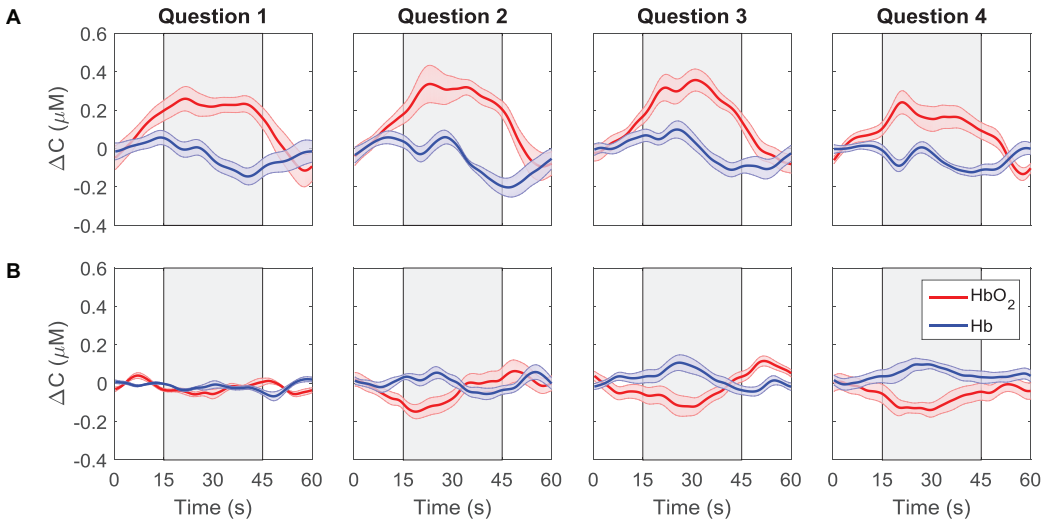

FIGURE 4 | ΔC_{HbO_2} (red) and ΔC_{Hb} (blue) for each question averaged across all trials, channels, and participants. Each column represents a different question. The first row **(A)** shows the signals that were classified as "yes" while the second row **(B)** shows the signals that were classified as "no." The gray boxes indicate the response period. The error bars represent the standard error of mean across participants (n = 18).

answered "no." These two sets are shown in **Figure 6**. As expected, the "yes" responses showed an increase in the signal during the response period. Interestingly, the ground truth "no" time-course also showed an unexpected increase in the signal during the response period upon visual inspection. This change was approximately 25% of the maximum change observed for the corresponding "yes" time-course.

The MAP and HR values averaged across the seven participants for MI and rest, respectively, are shown in **Table 3**. No significant difference between the two conditions was found.

DISCUSSION

The goal of this study was to assess the feasibility of TR-fNIRS as a BCI for mental communication. The study focused on a MI paradigm (i.e., imagine playing tennis) that has been used previously with fMRI to assess residual brain function in DOC patients and to provide rudimentary mental communication (Monti et al., 2010). Furthermore, the detection sensitivity of TR-fNIRS for this tennis imagery task was found to be comparable to fMRI in a cohort of healthy participants (Abdalmalak et al., 2017a). Based on these promising results, the motivation for this study was to evaluate the combination of TR-NIRS and MI for mental communication involving multiple closed-ended questions. A series of four questions was asked of each healthy participant and classification accuracy was assessed for two commonly used machine-learning algorithms (LDA and SVM) (Hong et al., 2018). Both algorithms produced similar accuracies (76% for SVM and 75% for LDA); however, SVM resulted in a better balance between sensitivity and specificity (79% and 71%, respectively) compared to LDA (83% and 58%, respectively). Overall, these estimates of classification accuracy are in-line with previous reports (Naseer and Hong, 2015a) and meet the minimum threshold of 70% for a BCI to be considered effective for communication (Proulx et al., 2018).

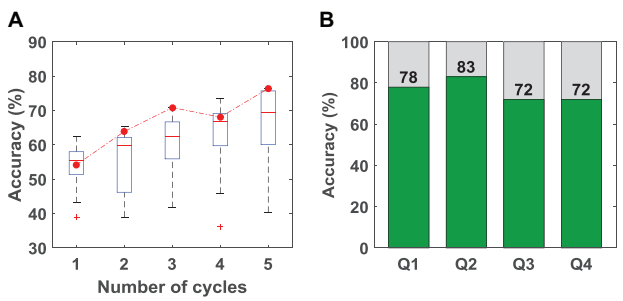

FIGURE 5 | (A) Classification accuracy obtained versus the number of cycles used for classification. The box plot shows the variation in accuracy for all 15 unique combinations of features. The red circles represent the accuracy for the set of features that was selected as optimum **(B)** Classification accuracy obtained for questions 1–4 using five cycles for classification.

Although the classification accuracy is comparable to results from other fNIRS studies involving various activation tasks for mental communication (Naseer and Hong, 2015b), it was less than the accuracy reported in an fMRI study involving the same tennis imagery task (Monti et al., 2010). One possible explanation is related to the challenges of detecting MI by fNIRS due to the presence of hair and the increased scalp-brain distance over the motor-planning areas relative to the frontal regions (Cui et al., 2011). The latter was likely compounded by the observation from fMRI studies that MI-related activation in the SMA frequently occurs at a greater distance from the cortical surface (Monti et al., 2010; Taube et al., 2015). TR detection will help compensate for activation at greater depths (Milej et al., 2019); however, these challenges reflect the lower classification accuracy generally

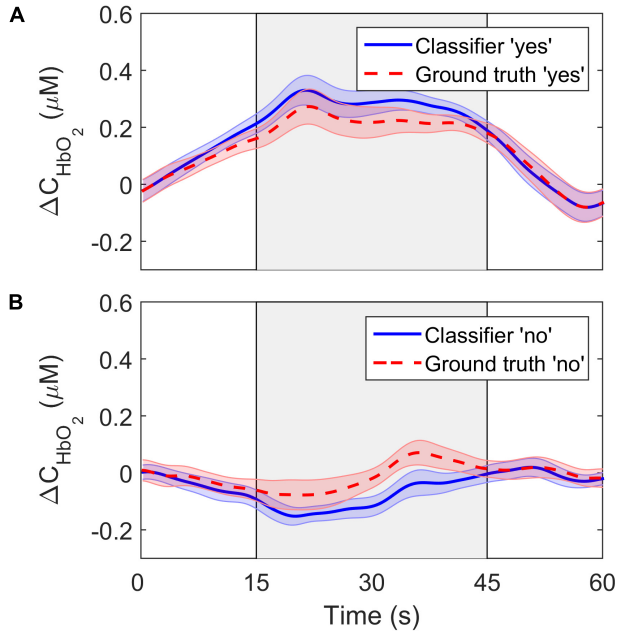

FIGURE 6 | ΔC_{HbO_2} averaged across channels, trials and participants for **(A)** the "yes" responses and **(B)** the "no" responses. The solid lines show the signals based on the SVM classifier output while the dashed lines represent the ground truth responses. The error bars represent the standard error of mean across participants (n = 18).

TABLE 3 | Physiological parameters obtained during motor imagery and rest.

	Rest	Change during MI	Range
MAP (mmHg)	77 ± 8	2 ± 1	−3, 5
HR (bpm)	70 ± 10	3 ± 2	−5, 5

MAP, Mean arterial pressure; HR, Heart rate.

reported for MI compared to tasks that activate the prefrontal cortex (Shin et al., 2017; Qureshi et al., 2017). It should also be noted that the activation contrast elicited by MI is less than for motor execution tasks (Batula et al., 2017), and activation for mental imagery tasks is not detectable in a small subset of participants, typically on the order of 10–15% (Fernández-Espejo et al., 2014). Unlike our previous study (Abdalmalak et al., 2017a), the current study did not include fMRI to confirm detectable MI activation for all participants. This would explain why the sensitivity in the current study (on the order of 80%) was lower than the sensitivity calculated previously when MI activation detected by TR-fNIRS was compared to fMRI results (Abdalmalak et al., 2017a).

While classification accuracy has been the most commonly used metric in fNIRS-BCI studies (Naseer and Hong, 2015a; Rupawala et al., 2018), sensitivity and specificity were also computed in the current study. These are important metrics in BCI applications for evaluating the confidence that can be placed on a measured response. This is relevant to applications involving DOC patients that are aimed at evaluating residual brain function and providing rudimentary mental communication (Peterson et al., 2015). The sensitivity of the LDA and SVM algorithms were similar (83% and 79%, respectively), but specificity was lower for both: 58% for LDA and 71% for SVM. Considering that specificity reflects the ability of the classifier to accurately detect a "no" response, the poorer results indicate that the inherent fluctuations in NIRS time courses were leading to false positives. This is confirmed by the average time courses shown in **Figure 6**. The ground truth "no" response showed an unexpected signal increase during the response period at approximately the 40-s mark. Similar artifacts are evident in other fNIRS-BCI studies that relied on a stable signal time-course to reflect a "no" response (Naseer et al., 2014), and reflect the challenges of removing all sources of noise in the pre-processing steps, particularly motion artifacts and low-frequency spontaneous oscillation.

There are a number of potential approaches that could be used to improve specificity. The first would be to use an active task for the "no" response as used in fMRI studies (Monti et al., 2010). For example, the "yes" response could be MI, while the "no" response could be a different task that activates brain areas other than the SMA (Bauernfeind et al., 2011). However, it is important to acknowledge that asking patients to perform two complex tasks, such as MI and mental arithmetic, could be challenging. Alternatively, "yes" and "no" responses could be decoded temporally instead of spatially. Bettina and colleagues demonstrated that healthy controls were able to encode at least four distinct answers on a single trial level by performing MI to the temporal prompt corresponding to the desired answer (Sorger et al., 2009; Nagels-Coune et al., 2017). Finally, participants could undergo some form of training to provide some familiarization with using MI for mental communication. None of the participants in this study received training prior to data collection, and it would be valuable to assess if classification accuracy would be improved on a return visit.

A variety of features have been investigated for fNIRS-BCI applications, including mean changes in concentration of oxy- and/or deoxy-hemoglobin, signal slope, the shape of the signal responses (i.e., skewness and kurtosis), et cetera (Naseer and Hong, 2015a). This study included similar features (SM, SS, CNR, see **Table 1**) as well as the correlation coefficient (r) between the HbO_2 time course and the model function obtained by convolving a box function representing task periods with the hemodynamic response function. For features such as the SS, there is some ambiguity regarding the appropriate period for calculating the signal slope. In this study, the slope was calculated over 16 s; however, a shorter period could have been selected based on the hemodynamic response function that peaks at 7 s. To investigate the potential impact of reducing the period, the analysis was repeated for a slope calculated over the first 7 s of the task period. This change resulted in a small reduction (4%) in the accuracy for the SVM algorithm, which is likely due to variability in the peak hemodynamic response between individuals (see **Figure 4** channel 2 for example).

A limitation with using features like r is the large amount of data required to obtain a reliable estimate. This was confirmed by the results presented in **Figure 5A**, showing the expected improvement in accuracy as the number of task cycles increased from one to five. The obvious disadvantage of using all five cycles

is that the approach is not suitable for real-time applications. However, for our goal of applying this methodology to helping evaluate consciousness in DOC patients, this is not a concern. Furthermore, *r* was the only feature common to both the final SVM and LDA algorithms, highlighting its value for optimizing classification accuracy.

One of the challenges with generic BCIs is inter-subject variability. Individual accuracies in this study varied from chance level to classifying all four questions correctly (**Table 2**). Psycho-physiological factors, such as attention and memory load, could contribute to the observed inter-subject variability. It has also been suggested that females, individuals over the age of 25, and those who play instruments are likely to perform better at mental imagery tasks (Randolph, 2012; Ahn and Jun, 2015). In this study, there was an imbalance between males and females; however, the total number of participants was not sufficient to assess if sex or age could have affected task performance. Additionally, it is known that task-induced changes in HR and MAP can potentially degrade the fNIRS signals, leading to false positives (Caldwell et al., 2016). To assess this potential source of error, HR and MAP were measured in seven participants performing MI in the same block design used in the BCI experiments, and no significant difference between the two conditions was found.

Another common challenge with most BCIs for mental communication is the trade-off between accuracy and the time delay before defining a response. In general, the greater the number of trials acquired prior to feature extraction and classifying the signals, the greater the SNR and hence the overall classification accuracy. BOLD-dependent modalities such as fMRI and fNIRS are inherently slow as the hemodynamic response peaks around 7 s post-stimulus. In contrast, EEG, which directly measures neuronal activity, can provide much faster responses. However, the majority of EEG-based BCIs do not display the results in real-time since most of these are classifier-based and often take time to judge and classify the signals to ensure accuracy. It is important to emphasize that the intended goal of our TR-fNIRS BCI is to assess residual awareness in DOC patients and therefore our protocol is intentionally long in order to maximize the confidence in the recorded responses.

In conclusion, this work highlights the potential of TR-fNIRS as a BCI for mental communication. Our approach focused on using a few detection channels that targeted specific brain regions known to be involved with MI. This is a relatively simple approach that is well suited for BCI applications without the need for training (Abdalmalak et al., 2017b). Our results indicate that the current method provides sufficient classification accuracy for clinical application. Since the technology is readily adaptable to other tasks/brain regions, incorporating separate active tasks for a "no" response could be considered to further improve the accuracy. In addition, the use of more sophisticated classifiers could be explored to further enhance performance.

DATA AVAILABILITY STATEMENT

The datasets generated for this study are available upon request to the corresponding author.

ETHICS STATEMENT

The studies involving human participants were reviewed and approved by the Research Ethics Board at Western University, which complies with the guidelines of the Tri-Council Policy Statement (TCPS): Ethical Conduct for Research Involving Humans. The patients/participants provided their written informed consent to participate in this study.

AUTHOR CONTRIBUTIONS

AA, AO, and KS contributed to the conception and design of the study. AA, LY, and DM developed the TR-fNIRS system used in this study. AA, DM, and KS contributed to the methodology and data acquisition. AA and DM with inputs from AK, MD, and KS carried out the fNIRS data analysis. AA wrote the manuscript with inputs from all the authors. DM, LY, AK, MD, AO, and KS contributed to critically revising the manuscript for important intellectual content. AO and KS secured funding for the study. All authors approved the final version of the manuscript for publication.

FUNDING

This work was supported by the Natural Sciences and Engineering Research Council (NSERC) grant R3592A02002 and Canada Excellence Research Chair (CERC) grant 215063. This research was additionally supported by the NSERC Canada Graduate Scholarships – Doctoral Program (AA), a Canadian Institutes of Health Research (CIHR) Postdoctoral Fellowship (DM, award number MFE-146770), and the Breast Cancer Society of Canada (LY).

REFERENCES

Abdalmalak, A., Milej, D., Cohen, D. J., Anazodo, U., Ssali, T., Diop, M., et al. (2020). Using fMRI to investigate the potential cause of inverse oxygenation reported in fNIRS studies of motor imagery. *Neurosci. Lett.* 714:134607. doi: 10.1016/j.neulet.2019.134607

Abdalmalak, A., Milej, D., Diop, M., Naci, L., Owen, A. M., and St. Lawrence, K. (2016). "Assessing the feasibility of time-resolved fNIRS to detect brain activity during motor imagery," in *Proceedings of the Clinical and Translational Neurophotonics; Neural Imaging and Sensing; and Optogenetics and Optical Manipulation*, San Francisco, CA.

Abdalmalak, A., Milej, D., Diop, M., Shokouhi, M., Naci, L., Owen, A. M., et al. (2017a). Can time-resolved NIRS provide the sensitivity to detect brain activity during motor imagery consistently? *Biomed. Opt. Express* 8:2162. doi: 10.1364/BOE.8.002162

Abdalmalak, A., Milej, D., Norton, L., Debicki, D. B., Gofton, T., Diop, M., et al. (2017b). Single-session communication with a locked-in patient by functional near-infrared spectroscopy. *Neurophotonics* 4:1. doi: 10.1117/1.NPh.4.4.040501

Ahn, M., and Jun, S. C. (2015). Performance variation in motor imagery brain-computer interface: a brief review. *J. Neurosci. Methods* 243, 103–110. doi: 10.1016/j.jneumeth.2015.01.033

Batula, A. M., Mark, J. A., Kim, Y. E., and Ayaz, H. (2017). Comparison of brain activation during motor imagery and motor movement using fNIRS. *Comput. Intell. Neurosci.* 2017:5491296. doi: 10.1155/2017/5491296

Bauernfeind, G., Scherer, R., Pfurtscheller, G., and Neuper, C. (2011). Single-trial classification of antagonistic oxyhemoglobin responses during mental arithmetic. *Med. Biol. Eng. Comput.* 49, 979–984. doi: 10.1007/s11517-011-0792-5

Caldwell, M., Scholkmann, F., Wolf, U., Wolf, M., Elwell, C., and Tachtsidis, I. (2016). Modelling confounding effects from extracerebral contamination and systemic factors on functional near-infrared spectroscopy. *Neuroimage* 143, 91–105. doi: 10.1016/j.neuroimage.2016.08.058

Coyle, S., Ward, T., Markham, C., and McDarby, G. (2004). On the suitability of near-infrared(NIR) systems for next-generation brain–computer interfaces. *Physiol. Measur.* 25, 815–822. doi: 10.1088/0967-3334/25/4/003

Cui, X., Bray, S., Bryant, D. M., Glover, G. H., and Reiss, A. L. (2011). A quantitative comparison of NIRS and fMRI across multiple cognitive tasks. *Neuroimage* 54, 2808–2821. doi: 10.1016/j.neuroimage.2010.10.069

Diop, M., and St Lawrence, K. (2013). Improving the depth sensitivity of time-resolved measurements by extracting the distribution of times-of-flight. *Biomed. Opt. Express* 4, 447–459. doi: 10.1364/BOE.4.000447

Fazli, S., Mehnert, J., Steinbrink, J., Curio, G., Villringer, A., Müller, K. R., et al. (2012). Enhanced performance by a hybrid NIRS-EEG brain computer interface. *Neuroimage* 59, 519–529. doi: 10.1016/j.neuroimage.2011.07.084

Fernández-Espejo, D., Norton, L., and Owen, A. M. (2014). The clinical utility of fMRI for identifying covert awareness in the vegetative state: a comparison of sensitivity between 3T and 1.5T. *PLoS One* 9:e95082. doi: 10.1371/journal.pone.0095082

Hong, K.-S., Khan, M. J., and Hong, M. J. (2018). Feature extraction and classification methods for hybrid fnirs-eeg brain-computer interfaces. *Front. Hum. Neurosci.* 12:246. doi: 10.3389/fnhum.2018.00246

Kacprzak, M., Liebert, A., Sawosz, P., Zolek, N., and Maniewski, R. (2007). Time-resolved optical imager for assessment of cerebral oxygenation. *J. Biomed. Opt.* 12:34019. doi: 10.1117/1.2743964

Kewin, M., Rajaram, A., Milej, D., Abdalmalak, A., Morrison, L., Diop, M., et al. (2019). Evaluation of hyperspectral NIRS for quantitative measurements of tissue oxygen saturation by comparison to time-resolved NIRS. *Biomed. Opt. Express* 10, 4789–4802. doi: 10.1364/boe.10.004789

Kurz, E. M., Wood, G., Kober, S. E., Schippinger, W., Pichler, G., Müller-Putz, G., et al. (2018). Towards using fNIRS recordings of mental arithmetic for the detection of residual cognitive activity in patients with disorders of consciousness (DOC). *Brain Cogn.* 125, 78–87. doi: 10.1016/j.bandc.2018.06.002

Lange, F., and Tachtsidis, I. (2019). Clinical brain monitoring with time domain NIRS: a review and future perspectives. *Appl. Sci.* 9:1612. doi: 10.3390/app9081612

Liebert, A., Wabnitz, H., Steinbrink, J., Obrig, H., Möller, M., Macdonald, R., et al. (2004). Time-resolved multidistance near-infrared spectroscopy of the adult head: intracerebral and extracerebral absorption changes from moments of distribution of times of flight of photons. *Appl. Opt.* 43, 3037–3047. doi: 10.1364/AO.43.003037

Mak, J. N., and Wolpaw, J. R. (2009). "Clinical applications of brain–computer interfaces: current state and future prospects," in *Proceedings of the IEEE Reviews in Biomedical Engineering*, Piscataway, NJ.

Metz, A. J., Wolf, M., Achermann, P., and Scholkmann, F. (2015). A new approach for automatic removal of movement artifacts in near-infrared spectroscopy time series by means of acceleration data. *Algorithms* 8, 1052–1075. doi: 10.3390/a8041052

Mihajlovic, V., Patki, S., and Grundlehner, B. (2014). "The impact of head movements on EEG and contact impedance: an adaptive filtering solution for motion artifact reduction," in *Proceedings of the 2014 36th Annual International Conference of the IEEE Engineering in Medicine and Biology Society (IEEE)*, Piscataway, NJ, 5064–5067. doi: 10.1109/EMBC.2014.6944763

Mihara, M., Miyai, I., Hattori, N., Hatakenaka, M., Yagura, H., Kawano, T., et al. (2012). Neurofeedback using real-time near-infrared spectroscopy enhances motor imagery related cortical activation. *PLoS One* 7:e32234. doi: 10.1371/journal.pone.0032234

Milej, D., Abdalmalak, A., Janusek, D., Diop, M., Liebert, A., and St. Lawrence, K. (2016a). Time-resolved subtraction method for measuring optical properties of turbid media. *Appl. Opt.* 55, 1507–1513. doi: 10.1364/AO.55.001507

Milej, D., Abdalmalak, A., McLachlan, P., Diop, M., Liebert, A., and St. Lawrence, K. (2016b). Subtraction-based approach for enhancing the depth sensitivity of time-resolved NIRS. *Biomed. Opt. Express* 7:4514. doi: 10.1364/BOE.7.004514

Milej, D., Janusek, D., Gerega, A., Wojtkiewicz, S., Sawosz, P., Treszczanowicz, J., et al. (2015). Optimization of the method for assessment of brain perfusion in humans using contrast-enhanced reflectometry: multidistance time-resolved measurements. *J. Biomed. Opt.* 20:106013. doi: 10.1117/1.JBO.20.10.106013

Milej, D., Rajaram, A., Abdalmalak, A., Khalid, M., Shahid, M., Kewin, M., et al. (2019). "Assessing extracerebral signal contamination in optical measurements of cerebral blood flow and oxygenation," in *Proceedingsof the Volume 11074, Diffuse Optical Spectroscopy and Imaging*, Munich.

Monti, M. M., Vanhaudenhuyse, A., Coleman, M. R., Boly, M., Pickard, J. D., Tshibanda, L., et al. (2010). Willful modulation of brain activity in disorders of consciousness. *N. Engl. J. Med.* 362, 579–589. doi: 10.1056/NEJMoa0905370

Nagels-Coune, L., Kurban, D., Reuter, N., Benitez, A., Gossé, L., Riecke, L., et al. (2017). "Yes or no? - Binary brain-based Communication utilizing motor imagery and fNIRS," in *Proceedings of the 7th Graz Brain-Computer Interface Conference 2017*, Graz.

Naseer, N., and Hong, K. S. (2013). Classification of functional near-infrared spectroscopy signals corresponding to the right- and left-wrist motor imagery for development of a brain-computer interface. *Neurosci. Lett.* 553, 84–89. doi: 10.1016/j.neulet.2013.08.021

Naseer, N., and Hong, K. S. (2015b). Decoding answers to four-choice questions using functional near infrared spectroscopy. *J. Near Infrared Spectrosc.* 23, 23–31. doi: 10.1255/jnirs.1145

Naseer, N., and Hong, K.-S. (2015a). fNIRS-based brain-computer interfaces: a review. *Front. Hum. Neurosci.* 9:3. doi: 10.3389/fnhum.2015.00003

Naseer, N., Hong, M. J., and Hong, K. S. (2014). Online binary decision decoding using functional near-infrared spectroscopy for the development of brain-computer interface. *Exp. Brain Res.* 232, 555–564. doi: 10.1007/s00221-013-3764-1

Owen, A. M., Coleman, M. R., Boly, M., Davis, M. H., Laureys, S., and Pickard, J. D. (2006). Detecting awareness in the vegetative state. *Science* 313, 1402–1402. doi: 10.1126/science.1130197

Padfield, N., Zabalza, J., Zhao, H., Masero, V., and Ren, J. (2019). EEG-based brain-computer interfaces using motor-imagery: techniques and challenges. *Sensors* 19:1423. doi: 10.3390/s19061423

Peterson, A., Cruse, D., Naci, L., Weijer, C., and Owen, A. M. (2015). Risk, diagnostic error, and the clinical science of consciousness. *Neuroimage Clin.* 7, 588–597. doi: 10.1016/j.nicl.2015.02.008

Proulx, N., Samadani, A.-A., and Chau, T. (2018). Online classification of the near-infrared spectroscopy fast optical signal for brain-computer interfaces. *Biomed. Phys. Eng. Express* 4:65010. doi: 10.1088/2057-1976/aada1a

Qureshi, N. K., Naseer, N., Noori, F. M., Nazeer, H., Khan, R. A., and Saleem, S. (2017). Enhancing classification performance of functional near-infrared spectroscopy- brain–computer interface using adaptive estimation of general linear model coefficients. *Front. Neurorobot.* 11:33. doi: 10.3389/fnbot.2017.00033

Randolph, A. B. (2012). "Not all created equal: individual-technology fit of brain-computer interfaces," in *Proceedings of the Annual Hawaii International Conference on System Sciences*, Maui, HI.

Rupawala, M., Dehghani, H., Lucas, S. J. E., Tino, P., and Cruse, D. (2018). Shining a light on awareness: a review of functional near-infrared spectroscopy for prolonged disorders of consciousness. *Front. Neurol.* 9:350. doi: 10.3389/fneur.2018.00350

Scholkmann, F., Spichtig, S., Muehlemann, T., and Wolf, M. (2010). How to detect and reduce movement artifacts in near-infrared imaging using moving standard deviation and spline interpolation. *Physiol. Measur.* 31, 649–662. doi: 10.1088/0967-3334/31/5/004

Shih, J. J., Krusienski, D. J., and Wolpaw, J. R. (2012). Brain-computer interfaces in medicine. *Mayo Clin. Proc.* 87, 268–279. doi: 10.1016/j.mayocp.2011.12.008

Shin, J., Von Luhmann, A., Blankertz, B., Kim, D. W., Jeong, J., Hwang, H. J., et al. (2017). "Open access dataset for EEG+NIRS single-trial classification," in *Proceedings of the IEEE Transactions on Neural Systems and Rehabilitation Engineering*, Piscataway, NJ.

Sitaram, R., Zhang, H., Guan, C., Thulasidas, M., Hoshi, Y., Ishikawa, A., et al. (2007). Temporal classification of multichannel near-infrared spectroscopy signals of motor imagery for developing a brain-computer interface. *Neuroimage* 34, 1416–1427. doi: 10.1016/j.neuroimage.2006.11.005

Sorger, B., Dahmen, B., Reithler, J., Gosseries, O., Maudoux, A., Laureys, S., et al. (2009). Another kind of "BOLD Response": answering multiple-choice questions via online decoded single-trial brain signals. *Prog. Brain Res.* 177, 275–292. doi: 10.1016/S0079-6123(09)17719-1

Strangman, G., Culver, J. P., Thompson, J. H., and Boas, D. A. (2002). A quantitative comparison of simultaneous BOLD fMRI and NIRS recordings during functional brain activation. *Neuroimage* 17, 719–731. doi: 10.1006/nimg.2002.1227

Tachtsidis, I., and Scholkmann, F. (2016). False positives and false negatives in functional near-infrared spectroscopy: issues, challenges, and the way forward. *Neurophotonics* 3:31405. doi: 10.1117/1.NPh.3.3.031405

Taube, W., Mouthon, M., Leukel, C., Hoogewoud, H. M., Annoni, J. M., and Keller, M. (2015). Brain activity during observation and motor imagery of different balance tasks: an fMRI study. *Cortex* 64, 102–114. doi: 10.1016/j.cortex.2014.09.022

Waldert, S. (2016). Invasive vs. non-invasive neuronal signals for brain-machine interfaces: will one prevail? *Front. Neurosci.* 10:295. doi: 10.3389/fnins.2016.00295

Conflict of Interest: The authors declare that the research was conducted in the absence of any commercial or financial relationships that could be construed as a potential conflict of interest.

Copyright © 2020 Abdalmalak, Milej, Yip, Khan, Diop, Owen and St. Lawrence. This is an open-access article distributed under the terms of the Creative Commons Attribution License (CC BY). The use, distribution or reproduction in other forums is permitted, provided the original author(s) and the copyright owner(s) are credited and that the original publication in this journal is cited, in accordance with accepted academic practice. No use, distribution or reproduction is permitted which does not comply with these terms.

frontiers in Human Neuroscience

HYPOTHESIS AND THEORY
published: 18 February 2020
doi: 10.3389/fnhum.2020.00030

Using the General Linear Model to Improve Performance in fNIRS Single Trial Analysis and Classification: A Perspective

Alexander von Lühmann[1,2]*, *Antonio Ortega-Martinez*[1], *David A. Boas*[1] and *Meryem Ayşe Yücel*[1]*

[1] Neurophotonics Center, Biomedical Engineering, Boston University, Boston, MA, United States, [2] Machine Learning Department, Berlin Institute of Technology, Berlin, Germany

Within a decade, single trial analysis of functional Near Infrared Spectroscopy (fNIRS) signals has gained significant momentum, and fNIRS joined the set of modalities frequently used for active and passive Brain Computer Interfaces (BCI). A great variety of methods for feature extraction and classification have been explored using state-of-the-art Machine Learning methods. In contrast, signal preprocessing and cleaning pipelines for fNIRS often follow simple recipes and so far rarely incorporate the available state-of-the-art in adjacent fields. In neuroscience, where fMRI and fNIRS are established neuroimaging tools, evoked hemodynamic brain activity is typically estimated across multiple trials using a General Linear Model (GLM). With the help of the GLM, subject, channel, and task specific evoked hemodynamic responses are estimated, and the evoked brain activity is more robustly separated from systemic physiological interference using independent measures of nuisance regressors, such as short-separation fNIRS measurements. When correctly applied in single trial analysis, e.g., in BCI, this approach can significantly enhance contrast to noise ratio of the brain signal, improve feature separability and ultimately lead to better classification accuracy. In this manuscript, we provide a brief introduction into the GLM and show how to incorporate it into a typical BCI preprocessing pipeline and cross-validation. Using a resting state fNIRS data set augmented with synthetic hemodynamic responses that provide ground truth brain activity, we compare the quality of commonly used fNIRS features for BCI that are extracted from (1) conventionally preprocessed signals, and (2) signals preprocessed with the GLM and physiological nuisance regressors. We show that the GLM-based approach can provide better single trial estimates of brain activity as well as a new feature type, i.e., the weight of the individual and channel-specific hemodynamic response function (HRF) regressor. The improved estimates yield features with higher separability, that significantly enhance accuracy in a binary classification task when compared to conventional preprocessing—on average +7.4% across subjects and feature types. We propose to adapt this well-established approach from neuroscience to the domain of single-trial analysis and preprocessing wherever the classification of evoked brain activity is of concern, for instance in BCI.

Keywords: fNIRS, BCI, GLM, preprocessing, classification, HRF, short-separation, nuisance regression

OPEN ACCESS

Edited by:
Chang-Hwan Im,
Hanyang University, South Korea

Reviewed by:
Noman Naseer,
Air University, Pakistan
Jaeyoung Shin,
Wonkwang University, South Korea

****Correspondence:***
Alexander von Lühmann
avolu@bu.edu
Meryem Ayse Yücel
mayucel@bu.edu

Specialty section:
This article was submitted to Brain-Computer Interfaces, a section of the journal Frontiers in Human Neuroscience

Received: *27 November 2019*
Accepted: *22 January 2020*
Published: *18 February 2020*

Citation:
von Lühmann A, Ortega-Martinez A, Boas DA and Yücel MA (2020) Using the General Linear Model to Improve Performance in fNIRS Single Trial Analysis and Classification: A Perspective. Front. Hum. Neurosci. 14:30. doi: 10.3389/fnhum.2020.00030

1. INTRODUCTION

Brain Computer Interface (BCI) research has gained momentum in the past two decades, fueled by the emergence of increasingly powerful Machine Learning based signal processing methods (Blankertz et al., 2008; Müller et al., 2008; Lemm et al., 2011) and advances in neuroimaging instrumentation. A BCI is an artificial system that bypasses the body's normal efferent pathways, which are the neuromuscular output channels. These systems aim to provide an active interface for communication and control (Birbaumer et al., 1999; Wolpaw et al., 2002) or aim to passively assess covert mental states (Müller et al., 2008; Blankertz et al., 2010) and monitor the "brain at work," as in the so-called field of Neuroergonomics (Parasuraman, 2003; Parasuraman and Wilson, 2008).

In noninvasive BCI, EEG is currently the primary modality used for both active and passive domains (Birbaumer et al., 1999; Blankertz et al., 2002, 2011; Wolpaw et al., 2002; Dornhege, 2007; Müller et al., 2008; Tomioka and Müller, 2010; Zander and Kothe, 2011; Van Erp et al., 2012; Haufe et al., 2014). However, more recently, an increasing number of studies have explored the suitability of functional Near-Infrared Spectroscopy for BCI and single trial classification of evoked brain activity (Matthews et al., 2008; Hong et al., 2018). fNIRS is a non-invasive, non-hazardous optical imaging technique that measures hemodynamic changes associated with brain metabolism (Villringer and Chance, 1997; Ferrari and Quaresima, 2012; Boas et al., 2014). It uses near-infrared light to measure concentration changes in oxygenated and deoxygenated hemoglobin (HbO and HbR, respectively) in the cerebral cortex and its signals are spatially and temporally comparable to blood oxygenation level dependent (BOLD) signals measured by functional Magnetic Resonance Imaging (fMRI) (Kleinschmidt et al., 1996; Huppert et al., 2005, 2006). The technique has found widespread use both in the research and clinical field despite its low penetration depth and spatial resolution, as it provides good portability, safety, and ecological validity at low-cost and is therefore well-suited for both experimental and real-life settings (Boas et al., 2014; Yücel et al., 2017). Similar to EEG, recent advances in fNIRS instrumentation have led to an increasing number of wearable, light weight, and fiberless systems (Scholkmann et al., 2014; von Lühmann et al., 2015; Zhao and Cooper, 2017) and wearable hybrid EEG-fNIRS systems (Safaie et al., 2013; von Lühmann et al., 2017; Kassab et al., 2018) that help translate BCI research from laboratory environments into real world applications.

Due to its dominance in the field, best practice preprocessing recipes exist for EEG to optimize BCI performance (Parra et al., 2005; Blankertz et al., 2008, 2011; Müller et al., 2008), but so far not for fNIRS. Along with the growing number of publications that have studied fNIRS-based BCI and single trial analysis over the course of the last several years (see for instance Naseer and Hong, 2015 for a review), a plethora of methods for optimal feature extraction and classification have been investigated (Matthews et al., 2008; Hong and Khan, 2017; Hong et al., 2018). Remarkably, however, well-established methodology from conventional fMRI and fNIRS neuroscience has so far rarely been adopted for fNIRS single trial signal preprocessing i.e., for removing systemic and non-systemic confounding factors from the signal (see **Figure 1**). One of these preferred approaches is to use a General Linear Model (GLM) (Friston et al., 1994; Cohen-Adad et al., 2007) which allows simultaneous extraction of the evoked Hemodynamic Response Functions (HRF) while filtering confounding signals with the help of nuisance regressors, for instance short-separation fNIRS measurements (Zhang et al., 2007; Saager and Berger, 2008; Gagnon et al., 2011). By this means, the contrast to noise ratio (CNR) of the evoked hemodynamic brain activity is increased, or in other words the ratio of the brain activity signal to any other physiological or non-physiological signal is increased, and the risk of falsely classifying task-evoked systemic physiology instead of brain activity is reduced. Adopting this approach can therefore significantly enhance accuracy, sensitivity, and specificity of fNIRS single trial classification.

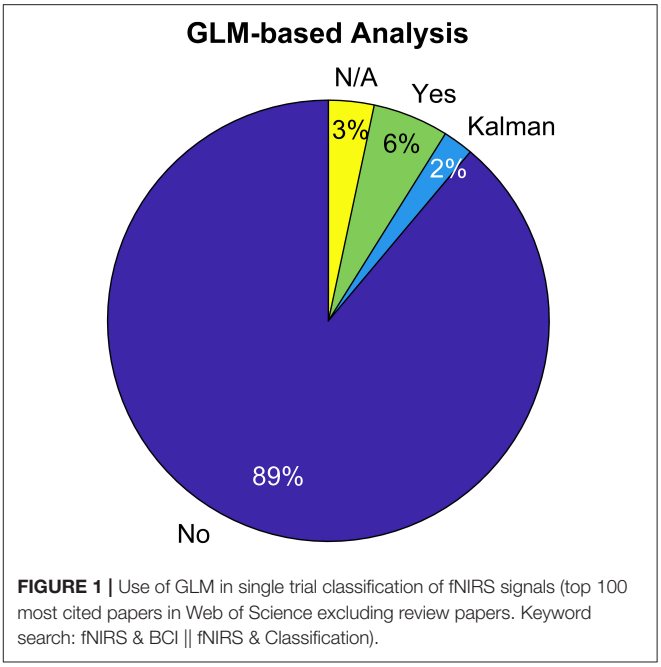

FIGURE 1 | Use of GLM in single trial classification of fNIRS signals (top 100 most cited papers in Web of Science excluding review papers. Keyword search: fNIRS & BCI || fNIRS & Classification).

In this manuscript, we first provide a brief overview of the most commonly applied preprocessing steps in the fNIRS-based BCI community, based on statistics obtained from a literature search of the top 100 most-cited papers in Web of Science within the field (search words: fNIRS & BCI or fNIRS & Classification). Then, we introduce the current state-of-the-art analysis in fNIRS neuroscience to fNIRS-based BCI researchers—the General Linear Model with Short-Separation regression (GLM with SS). Thirdly, we provide practical instructions on how to incorporate this approach into any preprocessing pipeline before feature extraction and how to use it within cross validation schemes. This is especially crucial, since learning statistics from the whole dataset by applying the GLM as a "preprocessing step" outside of cross-validation is methodologically wrong and will

lead to overfitting. Lastly, we perform a quantitative comparison between the quality of commonly used features when these are extracted from simulated ground truth fNIRS data that was preprocessed either (1) with a pipeline typical for current BCI studies or (2) with the GLM with SS. We show that the GLM-based approach provides better single trial estimates of brain activity, offers a new, more comprehensive feature type, and can significantly improve the classification accuracy in binary classification tasks.

2. PREPROCESSING IN fNIRS-BASED BCI: AN OVERVIEW AND PERSPECTIVE

While there have been major advances in fNIRS signal analysis methods since its first establishment, many of them have not yet found widespread use in the wider fNIRS community (Pfeifer et al., 2018). Specifically in single trial analysis and BCI, any fNIRS signal not properly corrected for confounding factors such as systemic interference or motion artifacts can be misleading. A common problem is that machine learning based classifiers exploit any type of task-related information in the signals, including movement artifacts and systemic physiological changes of non-neuronal origin. This can lead to improved discriminability within the designed study but also to a greatly reduced performance when applied outside of the exact same experiment, and is a known pitfall in EEG-based BCI (Müller et al., 2008; Blankertz et al., 2016).

fNIRS signals contain two types of noise that contaminate the underlying cerebral hemodynamics: physiological noise and non-physiological noise. Physiological noise involves the systemic interference which is driven by changes in blood pressure due to cardiac, respiration, Mayer waves, and low-frequency oscillations (Elwell et al., 1999; Saager and Berger, 2008; Gregg et al., 2010) or indirectly by head/body movements (von Lühmann et al., 2019), while non-physiological noise involves motion artifacts due to optode-scalp decoupling (Cooper et al., 2012; Brigadoi et al., 2014) and instrumental noise (**Figure 2**). In order to recover underlying brain activation pattern, one needs to carefully remove these confounding factors from the fNIRS signal. Such correction can either be applied prior to HRF estimation or, ideally, simultaneously with the HRF estimation as in the case of the General Linear Model (Friston et al., 1994; Cohen-Adad et al., 2007), which we will thoroughly discuss in this paper.

The majority of fNIRS-based BCI work performed so far relies on the first approach i.e., preprocessing steps such as channel pruning, removal of physiological noise, de-trending and motion artifact removal/correction are applied to the data prior to HRF estimation. The remaining signal is then assumed to represent the estimated hemodynamic brain response and features are extracted/selected from this signal for classification (Matthews et al., 2008; Hong et al., 2018). We summarize below the most commonly used preprocessing steps currently used in the fNIRS-based BCI field.

(1) *Signal quality check and pruning* is the first step in fNIRS preprocessing and is applied to the fNIRS signal regardless of whether the rest of the noise removal is performed prior to or during HRF estimation. In this step, the high frequency components in the signal that are due to non-physiological noise, such as instrumental noise, are typically filtered out and the channels that still have low SNR are removed from further analysis. Among the 100 most cited fNIRS-based BCI studies that we have investigated, ∼40% reported applying SNR pruning to their data (see **Supplementary Table 1**).

(2) *Motion artifact correction.* The majority of fNIRS-based BCI studies in our sample do not apply any motion artifact correction to their signal (∼80%, see **Supplementary Table 1**). The remaining studies apply motion correction algorithms typically used in the fNIRS field such as wavelet decomposition (Molavi and Dumont, 2012), spline interpolation (Scholkmann et al., 2010), tPCA (Yücel et al., 2014), CBSI (Cui et al., 2010), or SMAR (Ayaz et al., 2012).

(3) *Detrending.* Typically a linear detrending is applied to the relatively long fNIRS signals via high pass filtering or linear least squares fitting across long time windows.

(4) *Removal of physiological noise from the signal.* Bandpass filtering is the most commonly used approach in fNIRS-based BCI work to remove the physiological nuisance in the fNIRS signal, particularly very low frequency oscillations and cardiac. Thirty-six percent of the studies reported

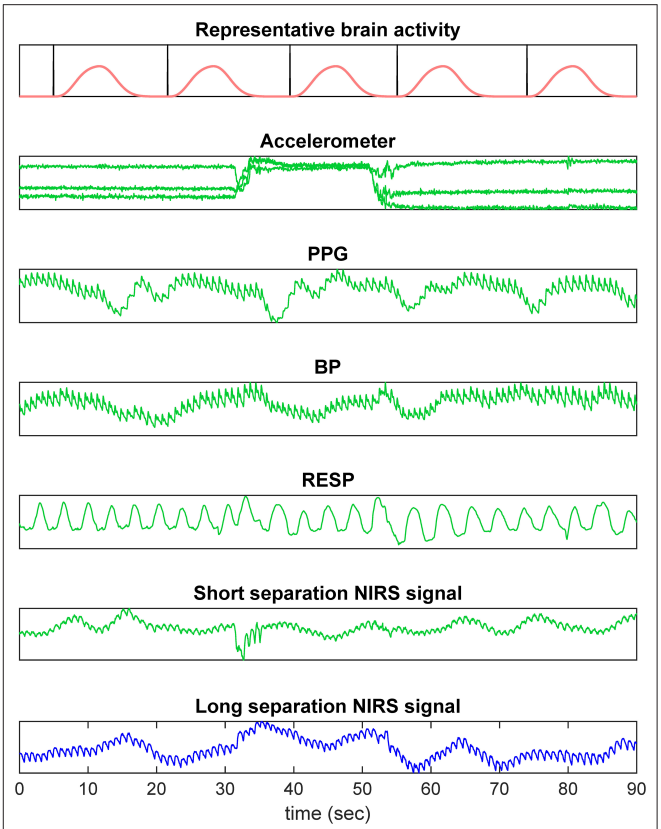

FIGURE 2 | fNIRS signal components. The fNIRS signal is generally a composition of motion related changes, cardiac pulse, blood pressure related changes, respiration, and hemodynamic changes in superficial layers.

using only a low-pass filter, 1% reported using only a high-pass filter and the majority reported using band-pass filtering (47%) (see **Supplementary Table 1**). Certain physiological oscillations such as respiration and Mayer waves fall into the same frequency band as the evoked brain activity in a typical fNIRS experiment, and can therefore not be removed via bandpass filtering without the risk of simultaneously removing signals of interest (Yücel et al., 2016). Thus, additional methods are being employed such as ICA (Independent Component Analysis), EMD (Empirical Mode Decomposition), and CWT (Continuous Wavelet Transform) which decompose the fNIRS signal into (latent) components, with the aim of identifying and removing those components that are due to systemic physiology. In our representative fNIRS-based BCI study sample, the most commonly applied methods for the removal of physiological nuisance signals aside from band-pass filtering (see **Figure 3**) are ICA (Comon, 1994), EMD (Huang et al., 1998), Transfer Function (TF) models (Pfurtscheller and Florian, 1997), Common Average Reference (CAR) (Pfurtscheller et al., 2010), CWT (Mallat, 1999), and Moving Average Convergence Divergence (MACD) (Appel, 2005). See Matthews et al. (2008), Scholkmann et al. (2014), Hong and Khan (2017), and Hong et al. (2018) for additional methods not mentioned here. ICA is a blind source separation method that assumes statistical independence between non-Gaussian components. The method has the risk of overcorrecting the signal by removing the frequency bands of interest. Results highly depend on the suitability of the applied ICA algorithm for fNIRS signals and methods that exploit sample dependence and higher order statistics are preferable (von Lühmann et al., 2019). EMD is an adaptive method that decomposes the signal into a set of nearly-orthogonal intrinsic mode functions in the time-domain (Huang et al., 1998). The intrinsic mode functions that correspond to the physiological noise in the signal such as cardiac or respiration are then removed from the original signal. Yin and colleagues not only reduce physiological noise using EMD, but also used the intrinsic mode functions as input features for their classifier (Yin et al., 2015). Similarly, CWT decomposes the signal into its components in the time-frequency domain, thus allowing removal of the components that lie in the frequency band of physiological noise. Abibullaev and An removed physiological noise using CWT and used the remaining "de-noised" wavelet coefficients as input features for their classifier (Abibullaev and An, 2012).

The above-mentioned methods can serve their purpose well when there is no additional information on physiological noise available. Ideally, however, independent measures of systemic physiology are acquired along with fNIRS recordings such as respiration or blood pressure variations. The majority of the physiological nuisance signals in fNIRS stems from the superficial layers i.e., scalp and skull (Zhang et al., 2007). Consequently, an independent measure of the hemodynamic changes in superficial layers using a short-separation detector measurement has been proposed (Saager and Berger, 2008).

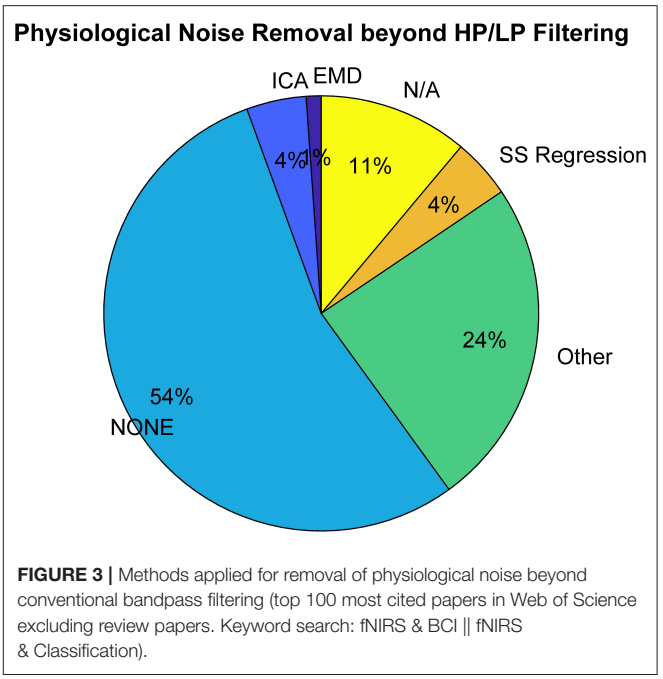

FIGURE 3 | Methods applied for removal of physiological noise beyond conventional bandpass filtering (top 100 most cited papers in Web of Science excluding review papers. Keyword search: fNIRS & BCI || fNIRS & Classification).

Using Monte Carlo simulations, Zhang and colleagues showed the benefit of using short-separation measurements as reference in an adaptive filter to remove the systemic interference in the long-separation measurements (Zhang et al., 2007). The short-separation measurements and other simultaneous and independent measurements can also be used as regressors to model systemic interference in a General Linear Model framework. This allows simultaneous estimation of brain activity and systemic interference and other nuisance terms in the signal without the risk of removing the underlying brain signal, thus providing a more accurate and robust unbiased estimate of the hemodynamic changes (Diamond et al., 2006; Tachtsidis et al., 2010). While the use of short-separation signals has been shown to significantly improve the robustness of the estimation of hemodynamic response emerging from brain (Gagnon et al., 2011; Yücel et al., 2015), only 4% of the recent fNIRS-based BCI studies used short-separation measurements in their work (see **Figure 3**) and none applied it in a GLM framework which is the standard approach in neuroscience research today. Some other works, on the other hand, applied the GLM, albeit without short-separation regression (such as Qureshi et al., 2017), and as a preprocessing step on the full dataset.

In the following section we give a brief introduction to the GLM and show how to correctly integrate it into a conventional BCI preprocessing pipeline (**Figure 4**) to improve classification performance while strictly avoiding overfitting pitfalls.

fNIRS BCI studies can benefit from the General Linear Model framework which allows simultaneous estimation of brain activity and concurrent physiological and non-physiological variations, providing a more accurate and robust recovery of the hemodynamic response.

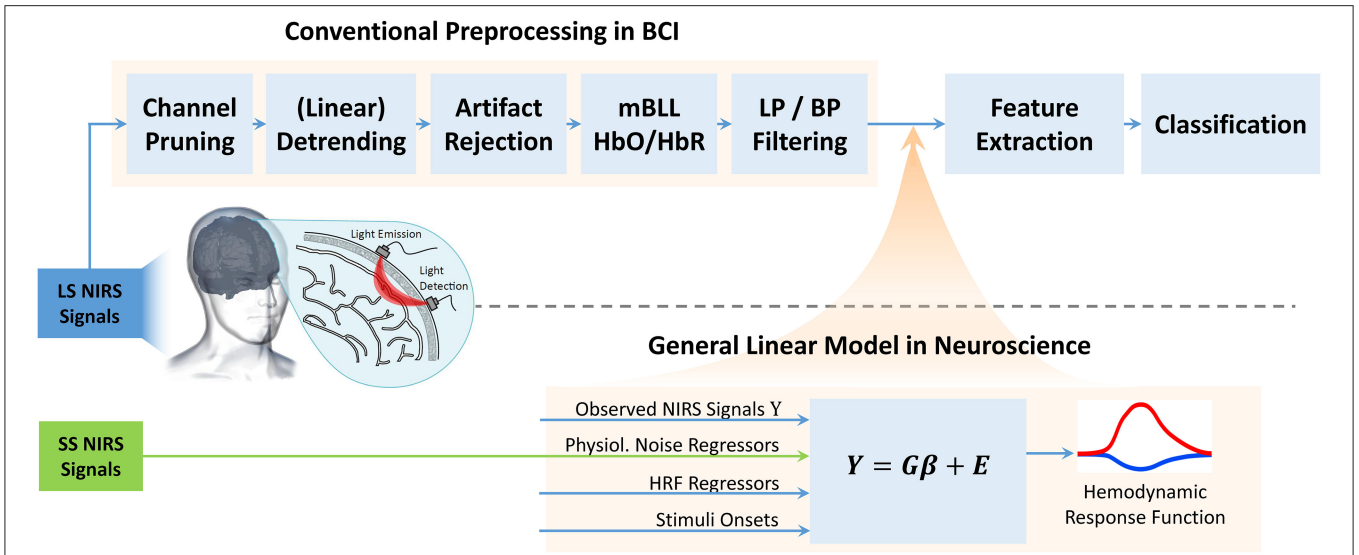

FIGURE 4 | Typical BCI preprocessing pipeline for fNIRS: Linear detrending, pruning of channels with low SNR, artifact rejection, conversion to HbO/HbR with modified Beer-Lambert Law (mBLL), low-pass (LP), or band-pass (BP) filtering. Sequence of blocks can deviate. (Down) established General Linear Model in fNIRS and fMRI Neuroscience using the current best practice: short-separation regression (GLM with SS). We propose to include the GLM into BCI approaches for enhanced performance by using better estimates of the hemodynamic response in fNIRS. Please note that drift removal (detrending) is part of the GLM when polynomial regressors are provided.

3. GLM BASED fNIRS PREPROCESSING (HRF REGRESSION)

In the following section, we provide a brief introduction to the GLM for fNIRS and show how one can incorporate physiological and non-physiological nuisance regressors into the GLM. This model is discussed in detail in Gagnon et al. (2011) and von Lühmann et al. (2020).

3.1. Introduction to the GLM

The General Linear Model represents measured data as a linear mixture of M functionally distinct processes (components). We express the GLM for fNIRS as

$$Y = G\,\beta + \mathrm{E} \tag{1}$$

where $Y \in \mathbb{R}^{T\times N}$ is the observation matrix with acquired fNIRS data from all time points T and recorded channels N. We will denote observed data samples of Y at time point t and channel n with scalars $y_n(t)$, the column vectors of the observation matrix as $y_n \in \mathbb{R}^T$ and its row vectors as $y(t) \in \mathbb{R}^N$. $G \in \mathbb{R}^{T\times M}$ is the *design matrix* that incorporates *a priori* knowledge about the expected shape of the evoked hemodynamic response, time structure of the experiment and regressors for drifts and/or physiological nuisance signals. $\beta \in \mathbb{R}^{M\times N}$ represents the set of weights for the regressors that model functional brain activity and physiological and non-physiological confounding components. These weights are to be estimated. Components that are not explained by the model are in the additional residual/noise term $E \in \mathbb{R}^{T\times N}$.

Under the GLM assumption, the observed hemodynamic signal $y_n(t)$ in each of the N channels is modeled by a combination of functional, physiological, and drift components plus the residual:

$$y_n(t) = y_n^{functional}(t) + y_n^{physiology}(t) + drift_n(t) + \varepsilon_n(t). \tag{2}$$

Both in BCI classification scenarios and conventional neuroscience, it is typically assumed that the evoked hemodynamic signal $y_n^{functional}$ is stationary across trials (stimuli δ_k) of the same condition within an experiment and subject. In the GLM, it is modeled either as a canonical HRF using a gamma-variant function (Abdelnour and Huppert, 2009) or with a weighted set of temporal basis functions $b_i(t)$ made from a linear combination of H normalized Gaussian functions $b_i = (\Delta t \cdot h, \sigma)$, with a standard deviation σ and means separated by Δt, both typically in the order of 0.5 s:

$$hrf\,(t) = \sum_{h=1}^{H} b_i\left(t - \Delta t \cdot h\right)\beta_h \tag{3}$$

and $hrf\,(t)$ is repeated at each stimulus onset δ_k

$$y_n^{functional}(t) = \sum_{k=0}^{K} hrf(t - \delta_k). \tag{4}$$

The current state-of-the-art fNIRS GLM approach uses polynomials to model $drift_n$ and short-separation (SS) fNIRS measurements as regressors to model systemic physiology: $y_n^{physiology}(t) = \sum_j^{Jss} \beta_{n,j}^{SS} y_j^{SS}(t)$. All regressors are combined to form the design Matrix G, which is visualized in **Figure 5**, and

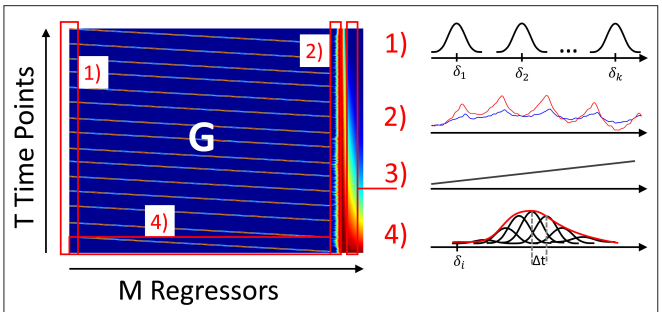

FIGURE 5 | Visualization of the GLM design matrix G. (1): HRF regressor (Gaussian basis function) repeated at each stimulus. (2) Short-separation regressor. (3) Drift regressor. (4) Example GLM solution with all M weighted Gaussian bases forming the estimated HRF across trials hrf(t), see equation (3).

the GLM Equation (1) is solved for each regressor's contribution, the coefficients $\hat{\beta}$, in a linear least squares approximation:

$$\hat{\beta} = \left(G^{\intercal}G\right)^{-1} G^{\intercal}\, Y. \tag{5}$$

The General Linear Model for fNIRS is an established supervised approach in neuroscience that combines a priori knowledge of experimental design and signal morphology. It provides the best linear unbiased estimate of the hemodynamic response to a series of stimuli in the presence of physiological nuisance signals.

3.2. How to Incorporate the GLM Into Cross Validation Schemes

In its conventional application in neuroscience, the fNIRS GLM is being applied as a supervised approach to recover hemodynamic responses to different task conditions across all available trials. Consequently, solving Equation (5) to obtain the weights ($\hat{\beta}$) for the HRF basis functions and nuisance regressors yields a best estimate across the whole dataset, and the estimate improves by increasing the number of trials provided. Here, we describe our proposed way of incorporating the GLM into a cross validation scheme, when fNIRS signals are to be analyzed on a *single-trial basis*, specifically for the prediction and classification in BCI scenarios. The proposed approach ensures that preprocessing, training of the HRF shape and training and testing of the classifier maintain the integrity and separation of training and unseen testing data. The overall implementation is schematically depicted in **Figure 6**.

3.2.1. Step 1: Learning the Individual and Channel-Specific HRF Shape From Training Trials

In each fold of an N-fold cross validation, the GLM is solved for each fNIRS channel n including all available training trials $trA = [tr1, \ldots trk]$ to find (1) weights $\hat{\beta}$ for the HRF basis functions $b_i(t)$ for each experimental condition c and (2) weights $\hat{\beta}$ for the regressors that model the physiological systemic nuisance signals y_{trA}^{SS} and the polynomial drift. The GLM solution minimizes the sum of squared residuals between the linear sum of these model terms and the continuous fNIRS time series of that channel $y_{n,trA}$. $y_{n,trA}$ is the original time series signal excluding all sample points within the testing interval *tst*. The rows of the design matrix that correspond to the testing interval *tst* are also set to zero. This way the time structure of the data is kept intact while the GLM solution is obtained without including any information from the testing data. The result is the best linear unbiased estimate of the individual and channel-specific HRF, denoted as $y_{n,c,tr}^{fnct}$, estimated across training trials of an experimental condition c. It is the sum of the individually weighted basis functions $b_i(t)$ and their corresponding weights $\hat{\beta}_{HRF,i}$. This across-trial estimate is now used as an *individually learned HRF regressor* to assess single trial responses in step 2.

3.2.2. Step 2: Obtaining Single Trial Estimates From Training and Testing Data

Using the learned HRF regressor $y_{n,c,tr}^{fnct}$ for each condition, the GLM is now set up and solved individually for each trial in the training splits tr, j and testing split *tst*. In each trial, aside from the individual and channel-specific HRF regressor obtained as described in Step 1, the physiological nuisance regressors, (linear) drift regressors and the measured fNIRS signals in the trial's interval are sole inputs to the model. Each individual GLM solution yields an unbiased trial by trial estimate of how pronounced the previously learned hemodynamic response to a condition is in the presence of nuisance signals. The resulting estimate is expressed by the HRF regressor weight $\hat{\beta}_{HRF,c}$ for each condition. In scenarios with multiple conditions, the GLM is solved c times for each trial using the c available HRF regressors.

3.2.3. Step 3: Feature Extraction, Training and Testing

Assuming stationarity, the estimated single trial HRF time signal can now be used for conventional feature extraction. If non-stationarities are to be taken into account for further identification and processing, the GLM's residual E can be added to the estimate. As an alternative to the extraction of conventional features from the estimated HRF time signal such as average or slope, the scalar regressor weight $\hat{\beta}_{HRF,c}$ itself can be used as a feature. Training and testing of the classifier is then performed conventionally using the single trial estimates for training and test trials, and steps 1–3 are repeated for each fold of the cross validation. Remarks: (1) Ideally, the individual HRF shape is learned in a training session previous to the actual BCI experiment. Step 1 can then be performed initially outside of the cross validation loop, which, however, requires more experimental data. (2) The described approach can easily be integrated into common existing offline-single trial analysis pipelines. To enable online single-trial analysis, e.g., online BCI, the GLM can be implemented in a state-space approach, for instance a Kalman filter, as was previously shown by Diamond et al. (2006) and Abdelnour and Huppert (2009). This approach will be briefly discussed in section Conclusion and Future Directions.

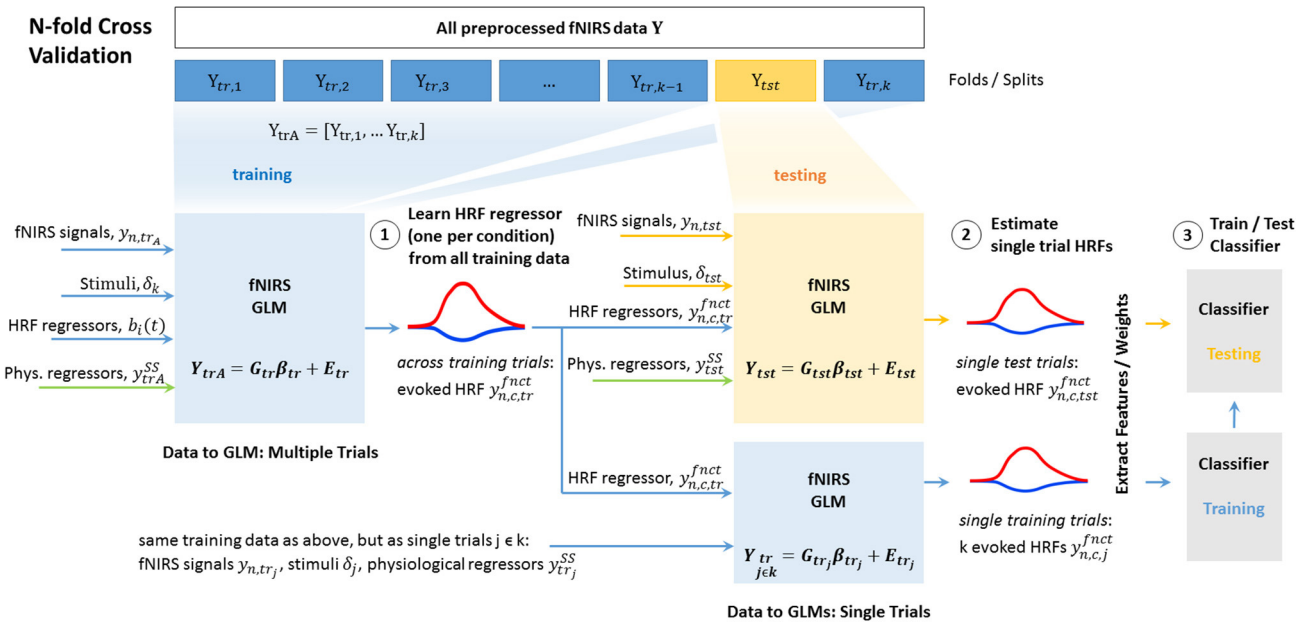

FIGURE 6 | GLM for single trial analysis embedded in a cross validation pipeline. Steps 1, 2, and 3 are described in detail in section 3.2.

To integrate the GLM into a conventional cross validation pipeline for single-trial analysis requires:

(1) *Learning the individual, channel and task specific HRF response across a set of training trials.*
(2) *Obtaining the unbiased estimate of this HRF's weight in each single trial for both training and testing data. The estimated single trial HRF signal can then be processed conventionally for feature extraction, training and testing of a classifier.*

3.3. Evaluation

Here we compare HRF recovery performance, feature quality and classification performance for typical fNIRS-based BCI pre-processing vs. GLM with SS. In order to do so, we generate ground truth data and apply processing pipelines as detailed below for each method for the estimation of the evoked hemodynamic signal. We use functions from the established HOMER2 fNIRS toolbox (Huppert et al., 2009) for signal processing. In sections 4 and 5, we provide a quantitative comparison between the performance of typical fNIRS-based BCI preprocessing (will be denoted as "no-GLM" from now on) and the proposed integration of the GLM with SS.

3.3.1. Synthetic HRF on Resting State Data

We generated ground truth data by augmenting fNIRS resting state data from 48 long-separation channels from 14 participants (see **Appendix**) with synthetic ground truth HRFs at randomized stimulus intervals. We generated a synthetic HRF following the *GAM* function in AFNI (Cox, 1996) which uses a gamma function convolved with a square wave. The resultant HRF has a time-to-peak of 6 s and a total duration of 15 s resulting in an increase in HbO of 0.66 μMol and a decrease in HbR of −0.23 μMol (**Figure 7**, right panel). The synthetic HRF is convolved with an onset vector with random inter-stimulus interval between 0 and 6 s and is then added onto a randomly selected half of the 48 available channels for the "STIM" condition. None of the channels were augmented with HRFs during the "REST" conditions. Overall, this yielded between 15 and 20 trials per condition.

3.3.2. Comparative Signal Pre-processing and HRF Estimation With and Without GLM

3.3.2.1. Common preprocessing for both methods

For both typical no-GLM (A) and GLM with SS (B), noisy fNIRS channels were identified and pruned using the HOMER2 function *hmrPruneChannels* (*dRange* = 10^4-10^7 (corresponding to 80 and 140 dB for a TechEn System) and *SNRthresh* = 5). All fNIRS data is then converted into optical density and low pass filtered at 0.5 Hz with a zero-phase Butterworth filter of effective order 6. Optical density is then converted into concentration changes using the modified Beer-Lambert law with a partial pathlength factor of 6 (Delpy et al., 1988; Boas et al., 2004).

3.3.2.2. Detrending

For training and testing splits of data, the signal was linearly detrended (A) for no-GLM by subtracting the linear least squares fit of each trial, and (B) by inserting a 1st order polynomial drift regressor term into the GLM with SS.

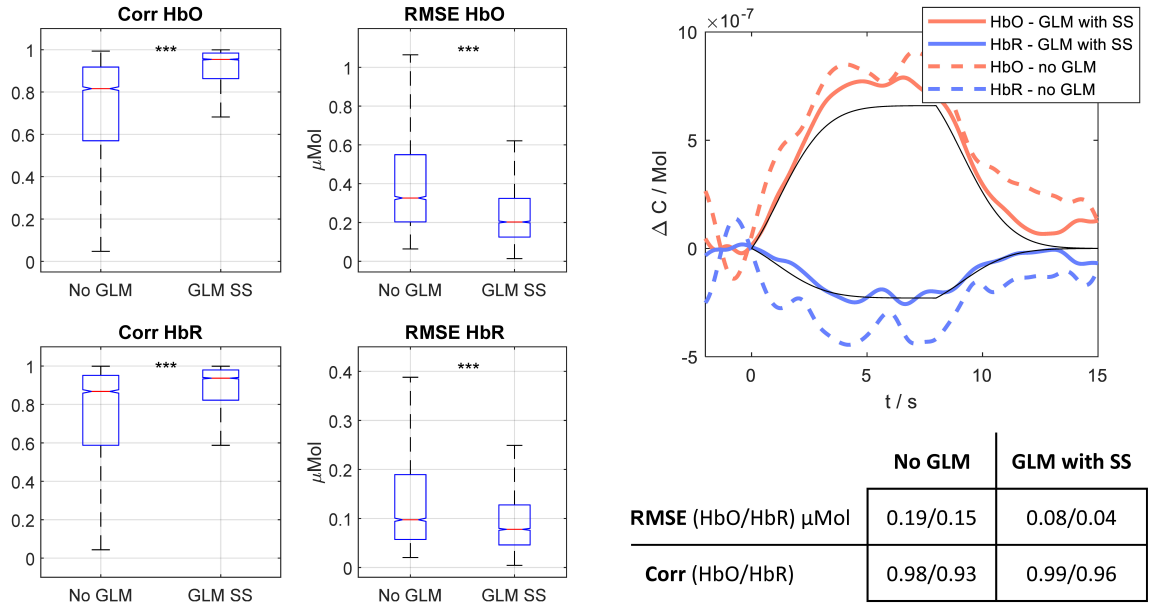

	No GLM	GLM with SS
RMSE (HbO/HbR) μMol	0.19/0.15	0.08/0.04
Corr (HbO/HbR)	0.98/0.93	0.99/0.96

FIGURE 7 | (Left) Correlation and RMSE boxplots for extracted single trial HRFs with both methodological approaches. Red line: median. Bottom/top box edges: 25th/75th percentile. Whiskers extend to most extreme data points that are not outliers. Significance for paired *t*-test $^{***}p << 10^{-3}$. **(Right)** Exemplary HRF recovered with both approaches. HbO/HbR (coral/blue) estimated via GLM with SS (solid) and no-GLM (dashed). Table provides the RMSE and Corr values for GLM with SS and no-GLM for the depicted HRFs.

3.3.2.3. HRF extraction

(A) The detrended concentration time course between the time period of 2 s prior to stimulus onset to 15 s after stimulus is used as the single trial HRF for no-GLM. (B) For the GLM with SS approach the HRF is modeled using a consecutive sequence of Gaussian functions with a standard deviation of 0.5 s and their means separated by 0.5 s (see section 3.1). The *hmrDeconvHRF_DriftSS* function in HOMER is then used to simultaneously estimate the HRF time signal together with the 1st order polynomial drift regressor term and one short-separation regressor term which corresponds to the signal at the fNIRS SS channel that has the highest correlation with the long-separation channel under investigation.

3.3.2.4. Baseline correction

The single trial HRF is then baseline corrected using the mean of the signal from 2 s prior to the onset of the stimulus to the onset of the stimulus for both no-GLM and GLM with SS.

4. PERFORMANCE IN HRF RECOVERY AND FEATURE EXTRACTION WITH AND WITHOUT GLM

With the ground truth data, we compare no-GLM and GLM with SS with respect to their recovery performance of fNIRS hemodynamic responses and feature quality. In the following, *recovered/estimated HRF* means the remaining fNIRS signal after preprocessing using these two approaches as detailed in section

TABLE 1 | 1st and 2nd order statistics of HRF recovery metrics Corr and RMSE.

	(Mean ± Std.)	No-GLM	GLM with SS
Corr	HbO	0.73 ± 0.25	0.90 ± 0.15
	HbR	0.75 ± 0.26	0.88 ± 0.17
RMSE (μMol)	HbO	0.47 ± 0.47	0.27 ± 0.29
	HbR	0.17 ± 0.21	0.10 ± 0.10

3.3.2. Single trial recovery performance across an observed trial length T is evaluated in terms of:

(1) the Pearson's correlation coefficient (Corr) between the estimated and ground truth HRF, obtained by using the "*corr*" function in MATLAB (MathWorks Inc., Natick, MA).
(2) the root mean squared error (RMSE) between the estimated ($\widehat{HRF}$) and ground truth HRF (HRF) time series is calculated as $RMSE = \sqrt{\frac{1}{T}\sum_{t=1}^{T}(HRF(t) - \widehat{HRF}(t))^2}$.

Figure 7 shows the boxplots and **Table 1** shows the 1st/2nd order statistics for both metrics and chromophores for no-GLM and GLM with SS. For both metrics and across all trials, subjects and channels (a total of 3,960 recovered hemodynamic responses per chromophore and method), the results of the GLM with SS are significantly closer to ground truth than those yielded without GLM ($p \ll 10^{-3}$, paired *t*-test).

Both preprocessing approaches can also be contrasted in terms of the absolute errors between features extracted from the preprocessed single trial HRFs and from the synthetic HRF ground truth. For this comparison, we investigate the features

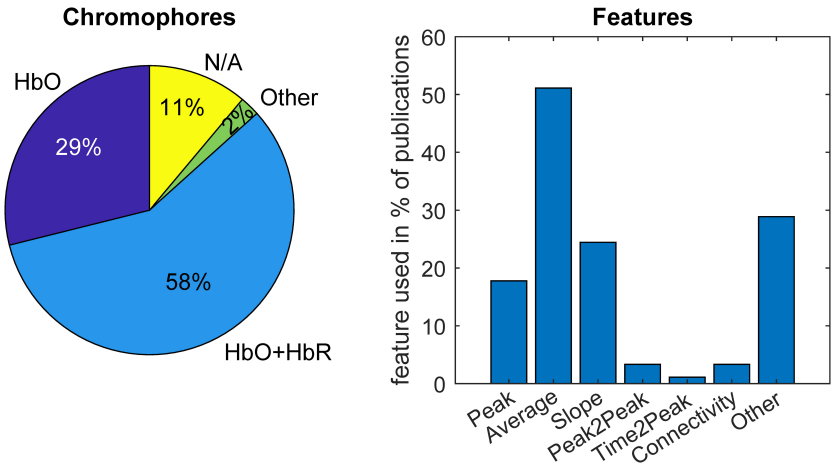

FIGURE 8 | Chromophores and features typically used in fNIRS-based BCI literature. Percentages from top 100 most cited papers in Web of Science excluding review papers. Keyword search: fNIRS & BCI || fNIRS & Classification.

most commonly used in BCI literature, also depicted in **Figure 8**. These are:

- Min/Max (Peak): Min (or max) is the minimum (or maximum) HbO (/HbR) amplitude within the estimated HRF time window.
- Peak to peak is the difference between the maximum and minimum HbO (/HbR) amplitude within the estimated HRF time window.
- Average is defined as the mean of HbO (/HbR) within the estimated HRF time window.
- Slope is the slope of a linear least squares fit to a pre-defined time window of the estimated HRF (HbO/HbR), here (0–4 s).

Other features include connectivity metrics, time to peak, and higher order statistics, such as skewness and kurtosis of the signal within an epoch.

Figure 9 shows boxplots of the errors between ground truth features and features extracted from the 3,960 estimated single trial HRFs using (A) the conventional pipeline (no-GLM) and (B) the GLM with SS. Across all trials, subjects and channels and for all feature types and chromophores, the error for GLM with SS is significantly smaller than for the no-GLM approach ($p \ll 10^{-3}$, paired t-test).

The GLM with SS recovers the evoked hemodynamic brain signal by simultaneously estimating the contributions of HRF, physiological nuisance, and drift. This approach leads to a better estimate of the HRF time signal than conventional single trial BCI preprocessing pipelines, and consequently also improves the quality of features.

5. SINGLE TRIAL HRF DETECTION AND CLASSIFICATION

Single trial analysis pipelines typically aim to detect evoked brain responses to single events—and to discriminate between events of different conditions. In BCI, where the recovered brain signals are used to predict the condition (class) of an event, a standard approach is to determine the signal's statistical properties with the help of machine learning to train classifiers for the prediction. Most common among recent fNIRS BCI studies are classifiers based on regularized Linear Discriminant Analysis (rLDA, 39%) and Support Vector Machines (SVM, 26%) (see **Figure 10**). While the performance of a classifier is strongly dependent on model and feature selection, it ultimately depends on the presence of discriminative characteristics that are to be extracted from the signal. Clearly, a preprocessing pipeline that increases the evoked signal's contrast to noise ratio can play a significant role in the achievable predictive performance. In this section we briefly compare the impact of the two preprocessing approaches (typical pipeline: no-GLM, and proposed approach: GLM with SS) on the discriminability of the most commonly used features in fNIRS-based BCI studies and the resulting classification accuracy.

Figure 11 shows the pooled distributions of the two most commonly applied feature types, average and slope, as well as our newly proposed feature type, the HRF regressor weight "β," across all subjects, channels and trials. We express the effect size of the distribution's mean differences by $Cohen's\ d := (\mu 1 - \mu 2)/s$ with s being the pooled stadard deviation. The effect size of the mean distance between the distributions for stimulus vs. rest conditions is significantly larger for features that were extracted after GLM with SS preprocessing, indicating a better separability compared to preprocessing without GLM.

A typical measure of separability of a feature is the point biserial correlation coefficient (r^2 value), which is defined as

$$r^2(x,y) = \frac{N_1 \cdot N_2}{(N_1+N_2)^2} \frac{(\mu_1 - \mu_2)^2}{var\langle x_i \rangle} \quad (6)$$

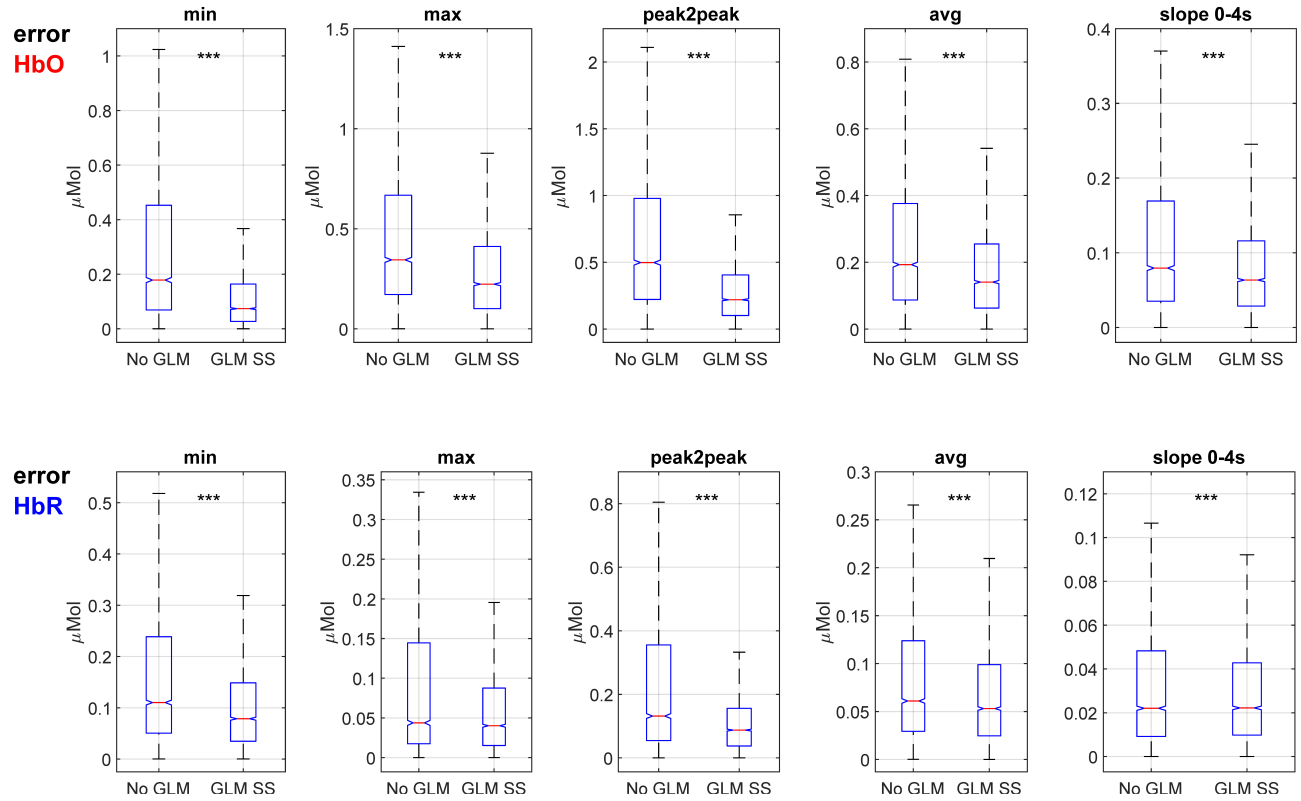

FIGURE 9 | Boxplots of errors between ground truth features and features extracted from fNIRS signals after conventional preprocessing (no-GLM) and GLM with SS. ***$p << 10^{-3}$.

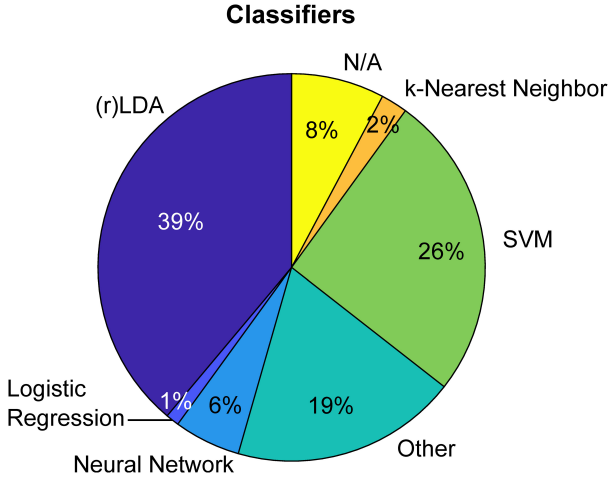

FIGURE 10 | Commonly applied classifiers in fNIRS BCI research (top 100 most cited papers in Web of Science excluding reviews. Keyword search: fNIRS & BCI || fNIRS & Classification).

with $\mu_i = mean\,\langle x_i \rangle_{y_i=1}$ being the class means and $N_k = |\{i \mid y_i = k\}|$ being the number of samples of class k, x_i the sample and y_i the class label of sample i.

For both preprocessing approaches, **Table 2** summarizes the across-subject average r^2 for each feature type and chromophore, each calculated across all augmented channels. GLM with SS preprocessing yields significantly higher biserial correlation coefficients for all compared features and chromophores ($p < 2 \times 10^{-3}$).

The enhanced separability of features from hemodynamic responses that are recovered with the GLM with SS naturally also improves classification performance. To exemplify this, we performed a typical classification approach, discriminating between resting vs. stimulation trials in a 10-fold cross validation using regularized Linear Discriminant Analysis with automatic shrinkage of the covariance matrices (Ledoit and Wolf, 2004; Blankertz et al., 2011). Within each fold, automatic feature selection was performed by choosing the 25 features with the highest r^2 value among the training data. The pipeline was repeated for each available single feature and common two-feature combinations, and each preprocessing method. **Figure 12** shows the resulting classification accuracies for each subject, feature and method, as well as the across-subject average performance.

Across all feature types and subjects, preprocessing the fNIRS data with the GLM with SS improved classification accuracy on average by 7.4% compared to the performance achieved with

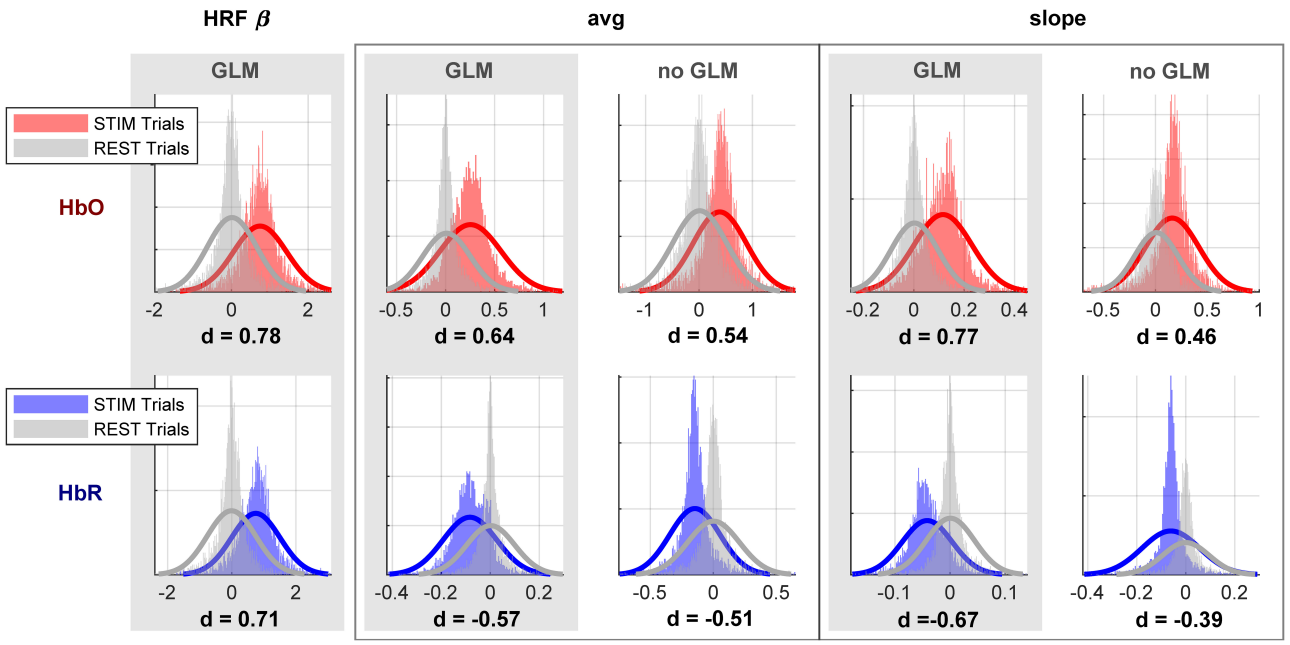

FIGURE 11 | Histograms and Gaussian fits of selected feature types for both conditions (stimulus and rest) extracted from fNIRS signals preprocessed with conventional pipeline (no-GLM) and GLM with SS. Features are pooled across all subjects, channels and trials of the same condition. (Top): HbO, (bottom): HbR. d is the effect size expressed through Cohen's d.

TABLE 2 | Across subject average point biserial correlation coefficient per feature and preprocessing approach.

r^2 Mean ± Std.		HRF β	Min.	Max.	Peak to peak	Avg.	Slope
No GLM	HbO		0.076 ± 0.058	0.068 ± 0.048	0.057 ± 0.054	0.107 ± 0.067	0.102 ± 0.068
	HbR		0.077 ± 0.072	0.081 ± 0.081	0.062 ± 0.070	0.110 ± 0.096	0.102 ± 0.081
GLM with SS	HbO	0.165 ± 0.097	0.108 ± 0.068	0.106 ± 0.075	0.132 ± 0.089	0.163 ± 0.101	0.166 ± 0.101
	HbR	0.166 ± 0.124	0.101 ± 0.071	0.112 ± 0.086	0.132 ± 0.112	0.166 ± 0.124	0.166 ± 0.124
Paired *t*-test (*p*-value)		N/A	$<2 \times 10^{-3}$	$<10^{-3}$	$<10^{-3}$	$\ll 10^{-3}$	$\ll 10^{-3}$

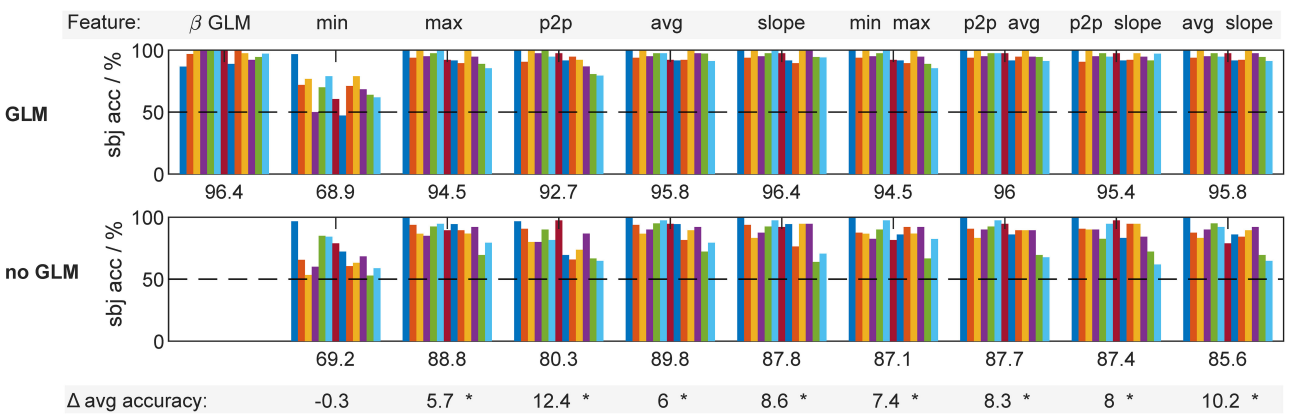

FIGURE 12 | Classification results for each feature type and preprocessing method. Single bars (colors) are individual subjects. Labels under each group are average accuracies across subjects. Bottom numbers highlighted by gray bar are average differences between methods. Asterisks (*) indicate significant difference (paired *t*-test, $p < 5\%$).

conventional preprocessing without GLM but otherwise identical classification pipeline and processing parameters. The new feature type, the HRF weight β, yielded the highest performance, identical to that achieved with the slope feature. It is notable that the HRF weight β inherently combines the characteristics of the other features, as it represents the strength of the individually trained whole HRF time course.

The improved Contrast to Noise Ratio of HRFs recovered with the GLM can significantly reduce noise in the feature space of both chromophores, leading to improved separability of features and better classification performance.

6. CONCLUSION AND FUTURE DIRECTIONS

With the concurrent advances in wearable imaging systems and active and passive Brain Computer Interfaces in the last two decades, the exploration of signal processing for a robust estimation of brain activity has become increasingly vital. A successful BCI application requires robust feature extraction from brain signals that accurately reflect the intent/state of the BCI user (He et al., 2012) and not physiological artifacts. In fNIRS-based BCIs, obtaining such features heavily depends on the robust estimation of the underlying cerebral hemodynamic changes associated with the brain activity. fNIRS measurements, though, can be heavily contaminated by signals of physiological and/or non-physiological origin, especially when acquired in environments with more ecological validity, recently enabled by new wearable systems. Despite the availability of dedicated preprocessing methods that can successfully filter such confounding signals, the fNIRS BCI field is still in an early stage in exploring and adapting these approaches from conventional neuroscience. In this paper, we aimed to highlight the importance of proper preprocessing of fNIRS signal, and showed how using the state-of-the-art approach, i.e., the General Linear Model with short-separation regression, can improve the discriminative power of features and the resultant classification accuracy.

6.1. GLM in Single Trial Analysis—Considerations and Caveats

The General Linear Model allows simultaneous extraction of the evoked HRF response and filtering out confounding signals with the help of nuisance regressors. Independent measures of such nuisance factors, such as short-separation fNIRS measurements, have been shown to be quite effective in modeling the systemic interference and allow a more robust estimation of brain activity (Gagnon et al., 2011; Yücel et al., 2015). We have shown that the single trial hemodynamic signals recovered with the GLM are significantly closer to ground truth compared to the ones obtained with conventional fNIRS-based BCI preprocessing pipelines in terms of both the correlation and the root mean squared error. We should note that our simulated data did not involve any task-evoked systemic changes in the short and long-separation measurements. In an actual scenario, the task at hand can produce hemodynamic changes in the superficial layers that are time-locked to the cerebral hemodynamic changes but are not brain signal. In such cases, discriminative systemic physiology can increase the classification accuracy, as the classifiers use all the information at hand to obtain highest discriminative power. However, they can dramatically reduce the performance in real world settings where systemic physiology is more susceptible to spontaneous changes outside of the constrained paradigm. Examples are increases in motion related artifacts in the signal while running, or changes in scalp hemodynamics during different emotional states. This issue further emphasizes the importance of proper cleaning of physiological and non-physiological confounding factors in the signal.

The improved HRF recovery performance of the proposed approach also impacts the discriminative power of the resultant features and classification accuracy. All commonly used features in the fNIRS BCI field, namely peak, average, slope, and peak-to-peak, extracted from HRFs obtained via GLM with SS were significantly closer to the ground truth and more discriminative between classes, as expressed by increased Cohen's d and biserial correlation coefficients. Expectably, the increased discriminability also resulted in an increased classification accuracy. Alongside with commonly used features in the BCI field, we introduced a new feature type by obtaining an individual and channel-specific hemodynamic response function from the training data which essentially incorporates the information of all commonly used features. The estimation of the contribution of this individual and channel-specific hemodynamic response function in each single trial, as performed by the GLM, yields one single comprehensive feature—the HRF weight β. Such an approach not only provides the highest classification accuracy but also reduces the risk of a biased or suboptimal choice of feature types among the many available.

One caveat of using individual and channel-specific HRF regressors is that the inclusion of channels that show no activation differences across conditions (e.g., STIM/REST) can result in a feature distribution that impairs classification accuracy. While without a GLM approach the features obtained from non-active channels during STIM and REST condition have a random distribution, using an individually learned HRF regressor in the GLM approach forces the single trial HRF estimates in these channels to have a fixed shape, varying only by amplitude between trials. An HRF regressor learned from random signals in the STIM condition applied to random signals in the REST condition can consequently yield more similar features than would have been obtained on a random signal without GLM. These "false positives" can reduce discriminative power and classification accuracy. A simple but important remedy is to perform channel and/or feature selection: Common approaches are (1) applying a statistical test on the training data and pick the channels that show significant difference between conditions,

thereby excluding inactive channels from the analysis. (2) Performing feature selection based on their separability, e.g., by means of a point biserial correlation coefficient, as done in this paper.

Accuracy and speed are two important performance measures in BCI applications, typically expressed together as the "information transfer rate" (ITR), in bits per minute or bits per trial (Wolpaw et al., 1998). The ITR naturally depends on the number of trials necessary (speed) for a robust estimation of the brain signal (accuracy). While using more than one trial improves the HRF estimation performance by better conditioning the design matrix in a GLM approach, here we showed that good performance and high classification accuracy can be achieved at the single trial level as well. By employing the GLM for single-trial analysis within cross validation as we propose in this manuscript, accuracy is increased by (1) obtaining the features from an individual and channel-specific HRF that was obtained from the training data which includes multiple trials and (2) properly removing the physiological and non-physiological nuisance from the test signal. Especially in passive BCI applications where speed can be less relevant and multiple trials can be analyzed simultaneously, it can be expected that the GLM approach improves accuracy even more beyond that achieved with conventional preprocessing.

6.2. Further Improved Nuisance Regression—Using the GLM With tCCA Regressors

We have recently shown that the presented state-of-the-art GLM using short-separation measurements as nuisance regressors can be further improved by incorporating temporally embedded Canonical Correlation Analysis (tCCA) (von Lühmann et al., 2020). tCCA enables the combination of any available auxiliary signals, including short-separation signals, accelerometer, respiration, blood pressure, and others, into more optimal nuisance regressors. By temporally embedding the auxiliary signals, a remedy to non-instantaneous and non-constant coupling between auxiliary and fNIRS signals is provided (von Lühmann et al., 2019). This makes the GLM solution less susceptible to errors from varying time delays between physiological nuisance signals in the measurement channels. The new approach models the physiological component in Equation (2) as $y_n^{physiology}(t) = \sum_j^{J_{CCA}} \beta_{n,j}^{CCA} \hat{s}_j^{CCA}(t)$, where $\hat{s}_j^{CCA}$ are the J_{CCA} regressors found by optimizing the tCCA objective function. The so found nuisance regressors improve GLM performance significantly in terms of the recovered HRF shape and Contrast to Noise Ratio as well as sensitivity and specificity, especially when the number of available trials are low (von Lühmann et al., 2020). tCCA regressors can be determined as a common set of multiple regressors for all fNIRS channels, or one individual tCCA regressor per fNIRS channel. The GLM with tCCA approach can be easily integrated into the proposed (cross validated) preprocessing pipeline for single-trial analysis in this manuscript. Instead of using J_{SS} short-separation channels y_j^{SS}, one simply employs the new J_{SS} tCCA regressors $\hat{s}_j^{CCA}$ for physiological regression in the GLM. There are two additional requirements: (1) The experimental setup has to include the acquisition of the additional auxiliary signals, with SS fNIRS channels and accelerometer being the most valuable, and (2) a few minutes of individual resting state data without evoked hemodynamic responses are required to train the tCCA projection filters. While the tCCA approach adds some complexity, it provides solutions for the challenges arising in real-world fNIRS application scenarios, such as BCI, neuroimaging and Neuroergonomics out of the lab, where physiological interference can otherwise be a major hindrance to robust single trial analysis (von Lühmann et al., 2019).

6.3. Real Time Implementation of the Proposed GLM Approach

In conventional fNIRS and fMRI neuroscience, the GLM is usually applied to supervised offline analysis of multiple trials at once. In this manuscript, we showed how to adapt it to single trial analysis within a cross validation scheme. Several ways exist to achieve real time capability of this approach. One way is to use a Kalman filter based state-space modeling approach. The Kalman filter method is a dynamic tracking scheme that estimates the state x_n of a process using a recursively updated regularized linear inversion routine. It has been successfully adapted for the fNIRS GLM by others and us in the past to adaptively estimate the GLM coefficients β for each time step (Diamond et al., 2006; Abdelnour and Huppert, 2009; Hu et al., 2010; Gagnon et al., 2011). Building on these previous adaptations allows the straight-forward integration of both the SS regression and tCCA-based noise regressors to achieve a robust real-time estimation of the GLM coefficients and evoked hemodynamic responses.

BCI and more integrative human-machine interfaces (HMI) that use both brain and body signals, have unprecedented potential to improve healthcare, work environments, efficiency, and security and can advance our understanding of brain function and cognition in general and especially under everyday life conditions. For the transition from well-controlled laboratory environments into real life applications, the robust separation of task-evoked brain activity from a wide range of confounding physiological and non-physiological nuisance factors is required. In fNIRS-based BCIs, a General Linear Model approach with short-separation regression and an individual and channel specific-HRF model obtained from a training data set can increase performance. By simultaneously estimating systemic physiology and evoked brain responses, it improves features separability and classification accuracy even at a single trial level.

DATA AVAILABILITY STATEMENT

All the relevant code is currently available on https://github.com/avolu/GLM-BCI with open public access. The data used

in this work is de-identified according the guidelines of the Institutional Review Board of Boston University and will be provided upon request.

ETHICS STATEMENT

The study has been reviewed and approved by the Institutional Review Board of Boston University. The patients/participants provided their written informed consent to participate in this study.

AUTHOR CONTRIBUTIONS

AL, MY, and AO-M developed the concept of this work, performed the analysis, designed the figures, and drafted the manuscript. DB provided critical feedback on the concept and results. AO-M created the database of 100 most cited fNIRS-BCI papers. All authors read and approved the final manuscript.

FUNDING

This work was funded by NIH R24NS104096.

ACKNOWLEDGMENTS

We would like to thank Natalie Gilmore with her help with the data acquisition.

SUPPLEMENTARY MATERIAL

The Supplementary Material for this article can be found online at: https://www.frontiersin.org/articles/10.3389/fnhum.2020.00030/full#supplementary-material

Supplementary Table 1 | Preprocessing steps applied by the top 100 most-cited papers in Web of Science within the fNIRS-BCI field (Search words: fNIRS & BCI or fNIRS & Classification, search year: 2019).

REFERENCES

Abdelnour, A. F., and Huppert, T. (2009). Real-time imaging of human brain function by near-infrared spectroscopy using an adaptive general linear model. *NeuroImage* 46, 133–143. doi: 10.1016/j.neuroimage.2009.01.033

Abibullaev, B., and An, J. (2012). Classification of frontal cortex haemodynamic responses during cognitive tasks using wavelet transforms and machine learning algorithms. *Med. Eng. Phys.* 34, 1394–1410. doi: 10.1016/j.medengphy.2012.01.002

Appel, G. (2005). *Technical Analysis Power Tools for Active Investors*, *1st Edn*. Upper Saddle River, NJ: Financial Times Prentice Hall.

Ayaz, H., Shewokis, P. A., Bunce, S., Izzetoglu, K., Willems, B., and Onaral, B. (2012). Optical brain monitoring for operator training and mental workload assessment. *NeuroImage* 59, 36–47. doi: 10.1016/j.neuroimage.2011.06.023

Birbaumer, N., Ghanayim, N., Hinterberger, T., Iversen, I., Kotchoubey, B., Kübler, A., et al. (1999). A spelling device for the paralysed. *Nature* 398:297.

Blankertz, B., Acqualagna, L., Dähne, S., Haufe, S., Schultze-Kraft, M., Sturm, I., et al. (2016). The Berlin brain-computer interface: progress beyond communication and control. *Front. Neurosci.* 10:530. doi: 10.3389/fnins.2016.00530

Blankertz, B., Curio, G., and Müller, K.-R. (2002). "Classifying single trial EEG: towards brain computer interfacing," in *Advances in Neural Information Processing Systems*, eds T. G. Dietterich, S. Becker, and Z. Ghahramani (Cambridge, MA: The MIT Press), 157–64.

Blankertz, B., Lemm, S., Treder, M., Haufe, S., and Müller, K. R. (2011). Single-trial analysis and classification of ERP components - a tutorial. *NeuroImage* 56, 814–825. doi: 10.1016/j.neuroimage.2010.06.048

Blankertz, B., Tangermann, M., Vidaurre, C., Fazli, S., Sannelli, C., Haufe, S., et al. (2010). The Berlin brain-computer interface: non-medical uses of BCI technology. *Front. Neurosci.* 4:198. doi: 10.3389/fnins.2010.00198

Blankertz, B., Tomioka, R., Lemm, S., Kawanabe, M., and Müller, K.-R. (2008). Optimizing spatial filters for robust EEG single-trial analysis. *Signal Proc. Mag. IEEE* 25, 41–56. doi: 10.1109/MSP.2008.4408441

Boas, D. A., Dale, A. M., and Franceschini, M. A. (2004). Diffuse optical imaging of brain activation: approaches to optimizing image sensitivity, resolution, and accuracy. *NeuroImage* 23 (Suppl. 1), S275–S288. doi: 10.1016/j.neuroimage.2004.07.011

Boas, D. A., Elwell, C. E., Ferrari, M., and Taga, G. (2014). Twenty years of functional near-infrared spectroscopy: introduction for the special issue. *NeuroImage* 85, 1–5. doi: 10.1016/j.neuroimage.2013.11.033

Brigadoi, S., Ceccherini, L., Cutini, S., Scarpa, F., Scatturin, P., Selb, J., et al. (2014). Motion artifacts in functional near-infrared spectroscopy: a comparison of motion correction techniques applied to real cognitive data. *NeuroImage* 85, 181–191. doi: 10.1016/j.neuroimage.2013.04.082

Cohen-Adad, J., Chapuisat, S., Doyon, J., Rossignol, S., Lina, J. M., Benali, H., et al. (2007). Activation detection in diffuse optical imaging by means of the general linear model. *Med. Image Anal.* 11, 616–629. doi: 10.1016/j.media.2007.06.002

Comon, P. (1994). Independent component analysis, a new concept? *Signal Process.* 36, 287–314. doi: 10.1016/0165-1684(94)90029-9

Cooper, R. J., Selb, J., Gagnon, L., Phillip, D., Schytz, H. W., Iversen, H. K., et al. (2012). A systematic comparison of motion artifact correction techniques for functional near-infrared spectroscopy. *Front. Neurosci.* 6:147. doi: 10.3389/fnins.2012.00147

Cox, R. W. (1996). AFNI: software for analysis and visualization of functional magnetic resonance neuroimages. *Comput. Biomed. Res.* 29, 162–173. doi: 10.1006/cbmr.1996.0014

Cui, X., Bray, S., and Reiss, A. L. (2010). Functional near infrared spectroscopy (NIRS) signal improvement based on negative correlation between oxygenated and deoxygenated hemoglobin dynamics. *NeuroImage* 49, 3039–3046. doi: 10.1016/j.neuroimage.2009.11.050

Delpy, D. T., Cope, M., van der Zee, P., Arridge, S., Wray, S., and Wyatt, J. (1988). Estimation of optical pathlength through tissue from direct time of flight measurement. *Phys. Med. Biol.* 33, 1433–1442.

Diamond, S. G., Huppert, T. J., Kolehmainen, V., Franceschini, M. A., Kaipio, J. P., Arridge, S. R., et al. (2006). Dynamic physiological modeling for functional diffuse optical tomography. *Neuroimage* 30, 88–101. doi: 10.1016/j.neuroimage.2005.09.016

Dornhege, G. (2007). *Toward Brain-Computer Interfacing*, eds G. Dornhege, J. R. Millán, T. Hinterberger, D. McFarland, and K.-R. Müller. Cambridge, MA: MIT Press.

Elwell, C. E., Springett, R., Hillman, E., and Delpy, D. T. (1999). Oscillations in cerebral haemodynamics. Implications for functional activation studies. *Adv. Exp. Med. Biol.* 471, 57–65.

Ferrari, M., and Quaresima, V. (2012). A brief review on the history of human functional near-infrared spectroscopy (FNIRS) development and fields of application. *NeuroImage* 63, 921–935. doi: 10.1016/j.neuroimage.2012.03.049

Friston, K. J., Holmes, A. P., Worsley, K. J., Poline, J.-P., Frith, C. D., and Frackowiak, R. S. J. (1994). Statistical parametric maps in functional imaging: a general linear approach. *Hum. Brain Map.* 2, 189–210. doi: 10.1002/hbm.460020402

Gagnon, L., Perdue, K., Greve, D. N., Goldenholz, D., Kaskhedikar, G., and Boas, D. A. (2011). Improved recovery of the hemodynamic response in diffuse optical imaging using short optode separations and state-space modeling. *Neuroimage* 56, 1362–1371. doi: 10.1016/j.neuroimage.2011.03.001

Gregg, N. M., White, B. R., Zeff, B. W., Berger, A. J., and Culver, J. P. (2010). Brain specificity of diffuse optical imaging: improvements from superficial signal regression and tomography. *Front. Neuroenerg.* 2:14. doi: 10.3389/fnene.2010.00014

Haufe, S., Kim, J. W., Kim, I. H., Sonnleitner, A., Schrauf, M., Curio, G., et al. (2014). Electrophysiology-based detection of emergency braking intention in real-world driving. *J. Neural Eng.* 11:56011. doi: 10.1088/1741-2560/11/5/056011

He, B., Gao, S., Yuan, H., and Wolpaw, J. (2012). *Brain–Computer Interfaces, 2nd Edn,* ed B. He. New York, NY: Springer.

Hong, K. S., and Khan, M. J. (2017). Hybrid brain–computer interface techniques for improved classification accuracy and increased number of commands: a review. *Front. Neurorobot.* 11:35. doi: 10.3389/fnbot.2017.00035

Hong, K. S., Khan, M. J., and Hong, M. J. (2018). Feature extraction and classification methods for hybrid FNIRS-EEG brain-computer interfaces. *Front. Hum. Neurosci.* 12:246. doi: 10.3389/fnhum.2018.00246

Hu, X. S., Hong, K. S., Ge, S. S., and Jeong, M. Y. (2010). Kalman estimator- and general linear model-based on-line brain activation mapping by near-infrared spectroscopy. *Bio Med. Eng. Online* 9, 1–15. doi: 10.1186/1475-925X-9-82

Huang, N., Shen, Z., Long, S., Wu, M., Shih, H., Zheng, Q., et al. (1998). The empirical mode decomposition and the hilbert spectrum for nonlinear and non-stationary time series analysis. *Proc. R. Soc. A Math. Phys. Eng. Sci.* 454, 303–995.

Huppert, T. J., Diamond, S. G., Franceschini, M. A., and Boas, D. A. (2009). HomER: a review of time-series analysis methods for near-infrared spectroscopy of the brain. *Appl. Opt.* 48, D280–298. doi: 10.1364/ao.48.00d280

Huppert, T. J., Hoge, R. D., Diamond, S. G., Franceschini, M. A., and Boas, D. A. (2006). A temporal comparison of BOLD, ASL, and NIRS hemodynamic responses to motor stimuli in adult humans. *NeuroImage* 29, 368–382. doi: 10.1016/j.neuroimage.2005.08.065

Huppert, T. J., Hoge, R. D., Franceschini, M. A., and Boas, D. A. (2005). A Spatial-temporal comparison of FMRI and NIRS hemodynamic responses to motor stimuli in adult humans. *Opt. Tomogr. Spectrosc. Tissue* 5693:191. doi: 10.1117/12.612143

Kassab, A., Le Lan, J., Tremblay, J., Vannasing, P., Dehbozorgi, M., Pouliot, P., et al. (2018). Multichannel wearable FNIRS-EEG system for long-term clinical monitoring. *Hum. Brain Mapp.* 39, 7–23. doi: 10.1002/hbm.23849

Kleinschmidt, A., Obrig, H., Requardt, M., Merboldt, K. D., Dirnagl, U., Villringer, A., et al. (1996). Simultaneous recording of cerebral blood oxygenation changes during human brain activation by magnetic resonance imaging and near-infrared spectroscopy. *J. Cereb. Blood Flow Metab.* 16, 817–826.

Ledoit, O., and Wolf, M. (2004). A well-conditioned estimator for large-dimensional covariance matrices. *J. Multivar. Anal.* 88, 365–411. doi: 10.1016/S0047-259X(03)00096-4

Lemm, S., Blankertz, B., Dickhaus, T., and Müller, K.-R. (2011). Introduction to machine learning for brain imaging. *NeuroImage* 56, 387–399. doi: 10.1016/j.neuroimage.2010.11.004

Mallat, S. (1999). *A Wavelet Tour of Signal Processing. 2nd Edn*. San Diego, CA: Academic Press.

Matthews, F., Pearlmutter, B. A., Ward,T. E., Soraghan, C., and Markham, C. (2008). Hemodynamics for brain-computer interfaces. *Signal Process. Mag. IEEE* 25, 87–94. doi: 10.1109/MSP.2008.4408445

Molavi, B., and Dumont, G. A. (2012). Wavelet-based motion artifact removal for functional near-infrared spectroscopy. *Physiol. Measure.* 33, 259–270. doi: 10.1088/0967-3334/33/2/259

Müller, K. R., Tangermann, M., Dornhege, G., Krauledat, M., Curio, G., and Blankertz, B. (2008). Machine learning for real-time single-trial EEG-analysis: from brain-computer interfacing to mental state monitoring. *J. Neurosci. Methods* 167, 82–90. doi: 10.1016/j.jneumeth.2007.09.022

Naseer, N., and Hong, K.-S. (2015). FNIRS-based brain-computer interfaces: a review. *Front. Hum. Neurosci.* 9:3. doi: 10.3389/fnhum.2015.00003

Parasuraman, R. (2003). Neuroergonomics: research and practice. *Theor. Issues Ergon. Sci.* 4, 5–20. doi: 10.1080/14639220210199753

Parasuraman, R., and Wilson, G. F. (2008). Putting the brain to work: neuroergonomics past, present, and future. *Hum. Factors* 50, 468–474. doi: 10.1518/001872008X288349

Parra, L. C., Spence, C. D., Gerson, A. D., and Sajda, P. (2005). Recipes for the linear analysis of EEG. *NeuroImage* 28, 326–341. doi: 10.1016/j.neuroimage.2005.05.032

Pfeifer, M. D., Scholkmann, F., and Labruyère, R. (2018). Signal processing in functional near-infrared spectroscopy (FNIRS): methodological differences lead to different statistical results. *Front. Hum. Neurosci.* 11:641. doi: 10.3389/fnhum.2017.00641

Pfurtscheller, G., Bauernfeind, G., Wriessnegger, S. C., and Neuper, C. (2010). Focal frontal (de)oxyhemoglobin responses during simple arithmetic. *Int. J. Psychophysiol.* 76, 186–192. doi: 10.1016/j.ijpsycho.2010.03.013

Pfurtscheller, G., and Florian, G. (1997). Elimination von atmungseffekten auf bewegungsinduzierte änderungen der herzrate. *Biomed. Technik* 42, 7–8.

Qureshi, N. K., Naseer, N., Noori, F. M., Nazeer, H., Khan, R. A., and Saleem, S. (2017). Enhancing classification performance of functional near-infrared spectroscopy-brain-computer interface using adaptive estimation of general linear model coefficients. *Front. Neurorobot.* 11:33. doi: 10.3389/fnbot.2017.00033

Saager, R., and Berger, A. (2008). Measurement of layer-like hemodynamic trends in scalp and cortex: implications for physiological baseline suppression in functional near-infrared spectroscopy. *J. Biomed. Opt.* 13:034017. doi: 10.1117/1.2940587

Safaie, J., Grebe, R., Abrishami Moghaddam, H., and Wallois, F. (2013). Toward a fully integrated wireless wearable EEG-NIRS bimodal acquisition system. *J. Neural Eng.* 10:56001. doi: 10.1088/1741-2560/10/5/056001

Scholkmann, F., Kleiser, S., Metz, A. J., Zimmermann, R., Pavia, J. M., Wolf, U., et al. (2014). A review on continuous wave functional near-infrared spectroscopy and imaging instrumentation and methodology. *NeuroImage* 85, 6–27. doi: 10.1016/j.neuroimage.2013.05.004

Scholkmann, F., Spichtig, S., Muehlemann, T., and Wolf, M. (2010). How to detect and reduce movement artifacts in near-infrared imaging using moving standard deviation and spline interpolation. *Physiol. Measure.* 31, 649–662. doi: 10.1088/0967-3334/31/5/004

Tachtsidis, I., Koh, P. H., Stubbs, C., and Elwell, C. E. (2010). Functional optical topography analysis using statistical parametric mapping (SPM) methodology with and without physiological confounds. *Adv. Exp. Med. Biol.* 662, 237–243. doi: 10.1007/978-1-4419-1241-1_34

Tomioka, R., and Müller, K. R. (2010). A regularized discriminative framework for eeg analysis with application to brain–computer interface. *NeuroImage* 49, 415–432. doi: 10.1016/j.neuroimage.2009.07.045

Van Erp, J., Lotte, F., and Tangermann, M. (2012). Brain-computer interfaces: beyond medical applications. *Computer* 45, 26–34. doi: 10.1109/MC.2012.107

Villringer, A., and Chance, B. (1997). Non-invasive optical spectroscopy and imaging of human brain function. *Trends Neurosci.* 20, 435–442. doi: 10.1016/S0166-2236(97)01132-6

von Lühmann, A., Boukouvalas, Z., Robert Müller, K., and Adali, T. (2019). A new blind source separation framework for signal analysis and artifact rejection in functional near-infrared spectroscopy. *NeuroImage* 200, 72–88. doi: 10.1016/j.neuroimage.2019.06.021

von Lühmann, A., Herff, C., Heger, D., and Schultz, T. (2015). Toward a wireless open source instrument: functional near-infrared spectroscopy in mobile neuroergonomics and BCI applications. *Front. Hum. Neurosci.* 9:617. doi: 10.3389/fnhum.2015.00617

von Lühmann, A., Li, X., Boas, D. A., and Yücel, M. A. (2020). Improved physiological noise regression in the FNIRS signal: a multimodal extension of the general linear model using temporally embedded canonical correlation analysis. *NeuroImage* 208:116472. doi: 10.1016/j.neuroimage.2019.116472

von Lühmann, A., Wabnitz, H., Sander, T., and Muller, K. R. (2017). M3BA: A mobile, modular, multimodal biosignal acquisition architecture for miniaturized eeg-nirs-based Hybrid BCI and Monitoring. *IEEE Trans. Biomed. Eng.* 64, 1199–1210. doi: 10.1109/TBME.2016.2594127

Wolpaw, J., Ramoser, H., Mcfarland, D., and Pfurtscheller, G. (1998). EEG-based communication: improved accuracy by response verification. *IEEE Trans. Rehabil. Eng. Publ. IEEE Eng. Med. Biol. Soc.* 6, 326–333. doi: 10.1109/86.712231

Wolpaw, J. R., Birbaumer, N., McFarland, D. J., Pfurtscheller, G., and Vaughan, T. M. (2002). Brain–computer interfaces for communication and control. *Clin. Neurophysiol.* 113, 767–791. doi: 10.1016/S1388-2457(02)00057-3

Yin, X., Xu, B., Jiang, C., Fu, Y., Wang, Z., Li, H., et al.. (2015). NIRS-based classification of clench force and speed motor imagery with the use of empirical mode decomposition for BCI. *Med. Eng. Phys.* 37, 280–286. doi: 10.1016/j.medengphy.2015.01.005

Yücel, M. A., Selb, J., Aasted, C. M., Lin, P. Y., Borsook, D., Becerra, L., et al. (2016). Mayer waves reduce the accuracy of estimated hemodynamic response functions in functional near-infrared spectroscopy. *Biomed. Opt. Express* 7:3078. doi: 10.1364/boe.7.003078

Yücel, M. A., Selb, J., Aasted, C. M., Petkov, M. P., Becerra, L., Borsook, D., et al. (2015). Short separation regression improves statistical significance and better localizes the hemodynamic response obtained by near-infrared spectroscopy for tasks with differing autonomic responses. *Neurophotonics* 2:035005. doi: 10.1117/1.NPh.2.3.035005

Yücel, M. A., Selb, J., Cooper, R. J., and Boas, D. A. (2014). Targeted principle component analysis: a new motion artifact correction approach for near-infrared spectroscopy. *J. Innov. Opt. Health Sci.* 7:1350066. doi: 10.1142/S1793545813500661

Yücel, M. A., Selb, J. J., Huppert, T. J., Franceschini, M. A., and Boas, D. A. (2017). Functional near infrared spectroscopy: enabling routine functional brain imaging. *Curr. Opin. Biomed. Eng.* 4, 78–86. doi: 10.1016/j.cobme.2017.09.011

Zander, T. O., and Kothe, C. (2011). Towards passive brain–computer interfaces: applying brain–computer interface technology to human–machine systems in general. *J. Neural Eng.* 8:25005. doi: 10.1088/1741-2560/8/2/025005

Zhang, Q., Brown, E. N., and Strangman, G. E. (2007). adaptive filtering for global interference cancellation and real-time recovery of evoked brain activity: a monte carlo simulation study. *J. Biomed. Opt.* 12:044014. doi: 10.1117/1.2754714

Zhao, H., and Cooper, R. J. (2017). Review of recent progress toward a fiberless, whole-scalp diffuse optical tomography system. *Neurophotonics* 5:1. doi: 10.1117/1.nph.5.1.011012

Conflict of Interest: The authors declare that the research was conducted in the absence of any commercial or financial relationships that could be construed as a potential conflict of interest.

Copyright © 2020 von Lühmann, Ortega-Martinez, Boas and Yücel. This is an open-access article distributed under the terms of the Creative Commons Attribution License (CC BY). The use, distribution or reproduction in other forums is permitted, provided the original author(s) and the copyright owner(s) are credited and that the original publication in this journal is cited, in accordance with accepted academic practice. No use, distribution or reproduction is permitted which does not comply with these terms.

A. APPENDIX

A.1. fNIRS Resting State Data

Ten minutes of fNIRS resting state data were collected from 13 healthy subjects (age: 30 ± 17 years; 7 male/5 female/1 not reported) who gave their signed written informed consent form prior to the experiment. The study was approved by and carried out in accordance with the regulations of the Institutional Review Board of Boston University. Subjects had no neurological or psychological disorders. A CW7 fNIRS system (TechEn Inc. MA, USA) with 32 frequency-encoded lasers (half at 690 and half at 830 nm) and 32 avalanche photo-diode detectors was used for data acquisition. The sample rate was 50 Hz.

Subjects were seated in a comfortable chair and an fNIRS probe was placed on their head. The head probe was consisted of an elastic cap (EasyCap, Herrsching, Germany) with 16 sources, 24 long-separation detectors (∼30 mm apart from the source) and 8 short separation detectors (∼8 mm apart from the source) providing, in total, 48 long-separation and 8 short-separation channels.

frontiers in Neuroscience

ORIGINAL RESEARCH
published: 04 March 2020
doi: 10.3389/fnins.2020.00168

Performance Improvement of Near-Infrared Spectroscopy-Based Brain-Computer Interface Using Regularized Linear Discriminant Analysis Ensemble Classifier Based on Bootstrap Aggregating

Jaeyoung Shin[1] *and Chang-Hwan Im*[2]*

[1] Department of Electronic Engineering, Wonkwang University, Iksan, South Korea, [2] Department of Biomedical Engineering, Hanyang University, Seoul, South Korea

OPEN ACCESS

Edited by:
Meryem Ayse Yücel,
Boston University, United States

Reviewed by:
Muhammad Jawad Khan,
National University of Sciences & Technology, Pakistan
Jan Mehnert,
University of Hamburg, Germany
Kiyohisa Natsume,
Kyushu Institute of Technology, Japan

***Correspondence:**
Chang-Hwan Im
ich@hanyang.ac.kr

Specialty section:
This article was submitted to Brain Imaging Methods, a section of the journal Frontiers in Neuroscience

Received: *20 July 2019*
Accepted: *14 February 2020*
Published: *04 March 2020*

Citation:
Shin J and Im C-H (2020) Performance Improvement of Near-Infrared Spectroscopy-Based Brain-Computer Interface Using Regularized Linear Discriminant Analysis Ensemble Classifier Based on Bootstrap Aggregating. Front. Neurosci. 14:168. doi: 10.3389/fnins.2020.00168

Ensemble classifiers have been proven to result in better classification accuracy than that of a single strong learner in many machine learning studies. Although many studies on electroencephalography-brain-computer interface (BCI) used ensemble classifiers to enhance the BCI performance, ensemble classifiers have hardly been employed for near-infrared spectroscopy (NIRS)-BCIs. In addition, since there has not been any systematic and comparative study, the efficacy of ensemble classifiers for NIRS-BCIs remains unknown. In this study, four NIRS-BCI datasets were employed to evaluate the efficacy of linear discriminant analysis ensemble classifiers based on the bootstrap aggregating. From the analysis results, significant (or marginally significant) increases in the bitrate as well as the classification accuracy were found for all four NIRS-BCI datasets employed in this study. Moreover, significant bitrate improvements were found in two of the four datasets.

Keywords: brain-computer interface, bootstrap aggregating, ensemble learning, near-infrared spectroscopy, pattern classification

INTRODUCTION

In general, brain-computer interface (BCI) systems (1) measure the brain signals in response to specific stimuli or mental tasks, (2) extract representative features from the acquired brain signals, (3) translate them by applying pattern recognition algorithms, and (4) control external devices or communicate with environments (Wolpaw et al., 2002; Schalk et al., 2004). In some cases, feedbacks are given to BCI users to improve the BCI performance (Lebedev and Nicolelis, 2006; Hwang et al., 2009; Kanoh et al., 2009; Blankertz et al., 2010). Among the aforementioned procedures, feature selection and pattern recognition are the most important parts that determine the overall performance of a BCI system (Nicolas-Alonso and Gomez-Gil, 2012). Particularly in the case of near-infrared spectroscopy (NIRS)-BCI, many different kinds of features have been tested to validate their suitability to various NIRS-BCI systems with different experimental paradigms and

environments (Hwang et al., 2014; Naseer et al., 2016). It was reported that the temporal mean, maximum, and slope yielded reasonable BCI performance (Naseer and Hong, 2015); however, there is no consensus on the most suitable features that can be generally applied to different NIRS-BCIs. In addition, various kinds of pattern recognition methods have also been proposed and tested with the aim to improve the performance of NIRS-BCI systems. Among them, linear discriminant analysis (LDA) classifier has been most widely used for NIRS-BCIs because of its excellent performance reflected by both a fast learning rate and a good classification performance (Holper and Wolf, 2011; Power et al., 2011, 2012a,b; Schudlo and Chau, 2014; Hong et al., 2015; Shin et al., 2016, 2018a; Hong and Khan, 2017). In applying the classifier, dimension reduction or feature selection methods are generally employed because the number of NIRS feature vectors is usually larger than that of training datasets and this might degrade the BCI performance due to the poor empirical sample covariance (Hwang et al., 2016; Hong et al., 2018; Sereshkeh et al., 2019). Regularization with a shrinkage parameter can be another option to alleviate the adverse effect of the large dimensionality (Fazli et al., 2012).

Ensemble learning can be considered a good substitute for further improving the overall BCI performance. Ensemble classifiers are grounded in the theory that a combination of multiple weak learners that barely exceed the chance level is capable of achieving better classification accuracy than that of a single strong leaner. It has been reported that ensemble classifiers can improve the performance of electroencephalography-BCIs. Sun et al. (2007); Ahangi et al. (2013), and Gao et al. (2016) employed various types of ensemble learning methods, e.g., bagging, boosting, and random subspace, etc., to evaluate the feasibility of ensemble learning for motor imagery EEG data. Fatourechi et al. (2008) stacked support vector machine (SVM) classifiers to classify finger flexion movement with a low false positive rate. Rakotomarnonjy and Guigue (2008) employed a majority voting system based on SVM for P300 signals by an oddball paradigm. Hassan and Bhuiyan (2017) demonstrated the automated identification of sleep stages by means of boosting methods, and Hosseini et al. (2018) exploited random subspace ensemble and majority voting for seizure detection. In the case of NIRS-BCIs, there have been a few studies that employed ensemble classifiers (Schudlo and Chau, 2015; Gurel et al., 2019), but they did not compare the performance of ensemble classifiers with that of conventional classifiers. To the best of our knowledge, no study has systematically investigated the performance improvement of NIRS-BCIs by the employment of ensemble classifiers. Specifically, because regularized linear discriminant of analysis (RLDA) alleviating the degradation of classification accuracy is generally known to be appropriate for the high dimensional NIRS dataset, we employed RLDA as a type of weak learner in the ensemble method. In the present study, for the first time, we explore whether the performance of NIRS-BCIs can be enhanced by using an ensemble of weak learners rather than a single strong learner through a systematic comparison of BCI performances with multiple NIRS datasets recorded with different experimental paradigms and/or under different recording environments.

MATERIALS AND METHODS

We employed four different NIRS datasets recorded by the first author of this paper. Datasets denoted by "dataset I" and "dataset II" can be freely downloaded at: http://doc.ml.tu-berlin.de/hBCI/ (Shin et al., 2017b) and "dataset III" can be downloaded at: http://dx.doi.org/10.14279/depositonce-5830 (Shin et al., 2018c). "Dataset IV" is a NIRS dataset used in the study of Shin et al. (2018b). All data processing was performed using MATLAB R2018b (Mathworks, MA, United States) and the BBCI toolbox[1] (Blankertz et al., 2016). A brief summary of the datasets I–IV is given in **Table 1**.

Datasets I and II

Data Recording

Near-infrared spectroscopy data were collected using NIRScout (NIRx GmbH, Berlin, Germany) at a sampling rate of 12.5 Hz. Adjacent source-detector distance was fixed to 30 mm. The locations of nine physical NIRS channels over the prefrontal area are depicted in **Figure 1A**.

Two Motor Imagery Tasks (Dataset I)

Twenty-nine participants were seated and performed two designated motor imagery (MI) tasks (kinesthetic motor imagery of grasping with either the left or the right hand at a rate of approximately 1 Hz) during the task period (0–10 s), 30 times each, in a randomized order.

Mental Arithmetic vs. Idle State (Dataset II)

The same participants who participated in the previously described MI experiment (dataset I) were asked to perform a mental arithmetic (MA) task. Starting with an initial problem of subtraction of a single digit between 6 and 9 from a three-digit number (e.g., 219 – 7), they continuously subtracted the given single-digit number from the result of the former

[1]https://github.com/bbci/bbci_public

TABLE 1 | Summary of the four datasets employed in this study.

Datasets	Duration of task period (s)	Post-task break (s)	The number of trials per task	Types of mental tasks
Dataset I	10	15–17	30	MI tasks (left- and right-hand grasping)
Dataset II	10	15–17	30	MA and IS
Dataset III	10	13–15	30	WG and IS
Dataset IV	10	16–18	30	MI (right-hand finger tapping), MA, and IS

MI, MA, WG, and IS represent mental imagery, mental arithmetic, word generation, and idle state, respectively.

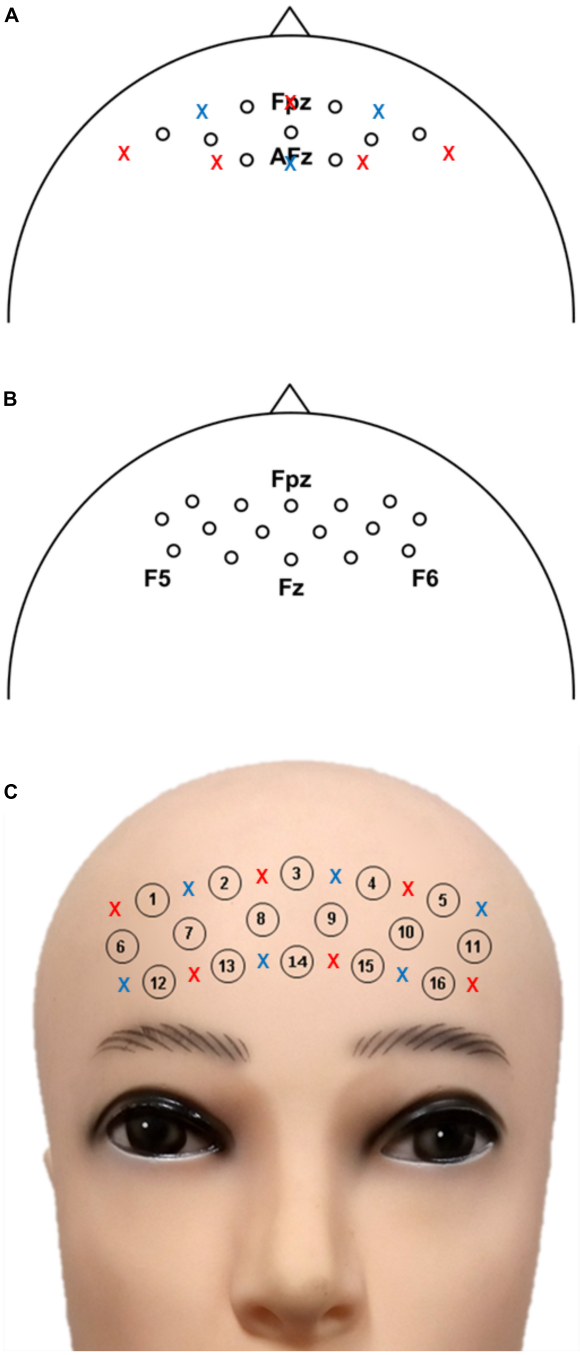

FIGURE 1 | Location of the NIRS channels for **(A)** datasets I-II, **(B)** dataset III, and **(C)** dataset IV. These figures were amended from Shin et al. (2017b; 2018b; 2018c). Blue and red crosses are the specific positions of source and detector, respectively. The specific source and detector positions for dataset II are not available.

calculation (e.g., 219 − 7 = 212, 212 − 7 = 205, 205 − 7 = 198,. . .) as fast as they could during the task period (0–10 s). For the idle state (IS), the participants relaxed and tried not to come up with any distractive thoughts during the task period (0–10 s). The MA and IS tasks were randomly repeated 30 times each.

Dataset III

Data Recording

Near-infrared spectroscopy data were acquired with NIRScout at a sampling rate of 10.4 Hz. Sixteen sources and 16 detectors were placed over the frontal area (around AFz), and sixteen NIRS channels with a source-detector separation of 30 mm were created. The NIRS channel locations are illustrated in **Figure 1B**.

Word Generation vs. Idle State

For the word generation (WG) task, twenty-six participants were seated and kept coming up with words beginning with a randomly given syllable as quickly as they could during the given task period (0–10 s). Repetition of the same word was not allowed for each trial to avoid potential adaptation. For the IS, the participants took a rest and tried not to think about anything for 10 s. The WG and IS tasks were randomly performed 30 times each.

Dataset IV

Data Recording

Near-infrared spectroscopy data were sampled at a sampling rate of 13.3 Hz using a portable NIRS acquisition system (LIGHTNIRS, Shimadzu Corp., Kyoto, Japan). Six sources and six detectors over the prefrontal area created 16 NIRS channels with a 30-mm source-detector separation. The locations of the 16 physical NIRS channels are illustrated in **Figure 1C**.

Mental Arithmetic vs. Motor Imagery vs. Idle State

For the MI task, seventeen participants were seated and imagined complex finger tapping at a rate of approximately 2 Hz for 10 s. The participants performed the MA task in the same way as with the dataset II, and for the IS, they relaxed without performing any specific mental task. The MI, MA, and IS tasks were randomly performed 30 times each.

Behavioral Data

Available behavioral data are stored in each repository for the datasets I–IV.

Preprocessing

In the original articles (Shin et al., 2017b, 2018b,c), the four datasets were preprocessed in different manners. For the sake of fair performance comparison, all datasets were preprocessed in the same manner. The hemodynamic changes in reduced and oxidized hemoglobin (ΔHbR and ΔHbO) were converted from the raw light intensity changes using the modified Beer–Lambert law, and were then band-pass filtered using a zero-phase Butterworth filter with a passband of 0.01–0.09 Hz to eliminate physiological noises (Matthews et al., 2008). Any trials were not excluded because the recorded data were minimally affected by motion artifacts.

Classification

The classification procedures were performed using the data from each of the participants separately.

Features

The baseline of the filtered data was corrected by subtracting the temporal mean of the data within [-1 0] s interval. The baseline-corrected data were then segmented to epochs ranging from 0 to 15 s, which contained part of the post-task break period, considering the hemodynamic delay in the order of several seconds (approximately 6–8 s) (Cui et al., 2010). Feature vectors consisted of the temporal mean values of ΔHbR and ΔHbO within two windows of [5 10] and [10 15] s. The number of features was [the number of NIRS channels] × [the number of NIRS chromophores (2)] × [the number of windows (2)].

Single Strong Learner

Three types of classifiers were considered, namely SVM, LDA, and RLDA. For SVM, the linear kernel was employed and the feature vectors were standardized by subtracting mean and dividing by standard deviation. Other parameters were default options given by MATLAB. For LDA, typical LDA was used. Normally, typical LDA classifier find the k^{th}class which maximize $\log \pi_k - \frac{1}{2}\mu_k^T \Sigma^{-1}\mu_k + x^T \Sigma^{-1}\mu_k$, where π_k, μ_k, and Σ are the *a prior* probability and the mean of samples in the k^{th}class, and the covariance matrix common to all classes, respectively. However, In the case of NIRS feature vectors, typical LDA is not likely to be adequate because of the degradation of classification accuracy due to the high-dimensionality, in other words, the number of features is greater than the number of samples. That is a reason why the RLDA classifier with a shrinkage parameter (γ) was employed to alleviate the adverse effects of large dimensionality on the BCI performance by replacing the empirical covariance matrix Σ with $(1-\gamma)\Sigma + \gamma I$, where I is the identity matrix. The optimal γ between 0 and 1 was determined individually based on the Ledoit and Wolf (2004), Schäfer and Strimmer (2005), Blankertz et al. (2011), Lemm et al. (2011). For the ternary classification, linear SVM and LDA with "one-versus-one" error-correcting output model were used, and the multi-class RLDA were applied.

Ensemble of Weak Learners

The bootstrap aggregating (Bagging) algorithm subsamples N_{learn} training sets of the same size with replacement (fraction of the training set to resample for every weak learner: 100% in this study), then builds N_{learn} classification models for each training set using a weak learner $h(\cdot)$. The final aggregate classification model based on a majority voting $H(x)$ is given by:

$$H(x) = \text{sign}\left(\sum_{n=1}^{N_{learn}} \text{sign}\left(h_n(x)\right)\right) \quad (1)$$

To verify the efficacy of LDA classifier, RLDA classifier was used as a weak learner and the value of λ was set to 0.1 as a rule of thumb. Stratified random sampling was applied to split the whole dataset into ten subsets, and a 10 × 10-fold cross-validation was performed for both the single strong learner and the ensemble of weak learners, resulting in the "strong classification accuracy (acc_{strong})" and the "Bagging classification accuracy (acc_{bag})," respectively.

Bitrate

Information transfer rate (ITR) is one of the most popular metrics to evaluate the performance of communication systems. The ITR per minute, called bitrate, is utilized to assess the performance of BCI systems, as follows (Dornhege et al., 2007):

$$bitrate = \frac{60}{T} \cdot \left[\log_2(n) + acc \cdot \log_2(acc) + (1-acc) \cdot \log_2\left(\frac{1-acc}{n-1}\right)\right] \ (bits/min), \quad (2)$$

where T, n, and acc are a single trial length (usually the length of the task period), the number of different types of mental tasks, and classification accuracy, respectively.

Statistical Test

Normality of data distribution was tested with Anderson–Darling test, and according to the test decision ($p < 0.05$), two-tailed paired t-test was performed to test the hypothesis that the average of acc_{bag} and acc_{strong} are different. The p-values were corrected by false positive rate (Benjamini and Yekutieli, 2001) unless otherwise noted.

RESULTS

Classification Accuracy

Figure 2 shows the grand average of the classification accuracy as a function of N_{learn}. As the N_{learn} increased, the classification accuracies improved irrespective of the type of NIRS datasets. Overall, the rate of increment rapidly decreased where $N_{\text{learn}} > 10$, and then the classification accuracy was almost converged where $N_{\text{learn}} = 50$. Comparisons of individual $acc_{\text{strong}}$and acc_{bag} are presented in **Figures 3**, **4**. In **Figure 3**, magenta dashed lines indicate the classification accuracy value (70%) generally known as a threshold for effective BCI control (Vidaurre and Blankertz, 2010). Black dashed lines denote the theoretical chance levels based on binomial distribution ($p < 0.05$) (Combrisson and Jerbi, 2015). For **Figures 3**, **4**, the values of N_{learn} to compute acc_{bag} are individually different and the optimal values of N_{learn} were chosen in the range of $10 \leq N_{\text{learn}} \leq 50$. For the dataset I, the grand average of acc_{bag} (62.6 ± 9.6%) was significantly higher than the averages of all three acc_{strong} (i.e., acc_{SVM} (59.6 ± 9.5%), acc_{LDA} (57.9 ± 9.5%), and acc_{RLDA} (59.1 ± 11.6%). For the dataset II, apart from the acc_{RLDA} (86.7 ± 8.6%), the grand average of acc_{bag} (88.5 ± 7.7%) was significantly higher than others. The grand average of acc_{bag} (74.8 ± 11.8%) for the dataset III was not significantly higher apart from the grand average of acc_{RLDA} (71.2 ± 12.4%) but the others. The bagging algorithm yielded the significant difference of ternary classification accuracy (71.2 ± 12.4%) compared to the other strong learners. The individual classification accuracies

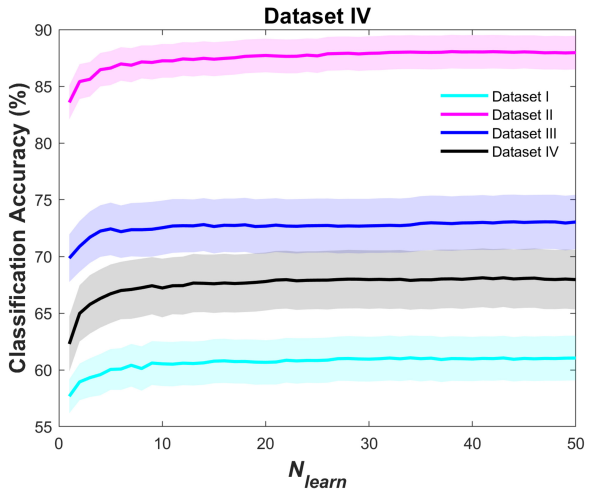

FIGURE 2 | Grand average of acc_{bag} as a function of N_{learn} for dataset I (cyan), dataset II (magenta), dataset III (blue), and dataset IV (black). The shaded area represents the standard error of the mean.

are provided in digits in the **Supplementary Information**. In **Figure 4**, symbols above the dashed diagonal line represent that the Bagging algorithm is more advantageous to improve the individual classification accuracy (i.e., $acc_{bag} > acc_{strong}$), while those below the diagonal line represent that $acc_{bag} < acc_{strong}$. It was revealed that acc_{bag} exceeded significantly acc_{strong} in nine cases out of 12 comparisons ($p < 0.05$). For the ternary classification (dataset IV), the improvement of bitrate was particularly significant in all cases.

Bitrate

Figure 5 shows comparisons of individual bitrates (bits/min), where the symbols above the dashed diagonal line represent that the Bagging algorithm resulted in higher bitrates than the single strong learner, and vice versa. In the case of the dataset I, significant (or marginally significant) bitrate improvements were observed and it was observed in over 70% of individual results in all three cases. The bagging highly significantly improved bitrates when it comes to the comparisons versus SVM or LDA (corrected-$p < 0.001$). For the dataset III, The bagging was significantly superior to RLDA when it came to bitrates (corrected-$p < 0.001$) unlikely the rest two cases. Note that the bagging always outperformed typical LDA in the ternary system (dataset IV).

DISCUSSION

Summary

In this study, we explored, for the first time, whether the performance of binary and ternary NIRS-BCI systems can be improved by using ensemble classifiers. We created ensembles of weak learners based on the Bagging algorithm. Four NIRS-BCI datasets recorded with different experimental paradigms were used for the quantitative performance comparisons between the Bagging algorithm and the conventional single stronger learner approach. Our results demonstrated that the Bagging algorithm significantly (or marginally significantly) outperformed the single strong learner in terms of classification accuracy and bitrate in all the cases of datasets.

Necessity of Using an Appropriate Ensemble Classifier

To create a better ensemble classifier, it is important to select an appropriate ensemble aggregation method, that is, a type of weak learner, and to determine the optimal hyperparameters, such as the number of ensemble learning cycles (N_{learn} in this study). For the optimization of the hyperparameters, various approaches can be employed, such as a grid search, random search (Bergstra and Bengio, 2012), and the Bayesian optimization (Mockus, 2012); however, since the optimized hyperparameters are generally dependent on the test set employed in the optimization, it is practically difficult to derive universally optimized hyperparameters. This implies that simply using ensemble classifiers does not always guarantee an enhanced performance in NIRS-BCIs and that a customized ensemble classifier appropriate for the given datasets needs to be employed. If the aggregation method and hyperparameters are not properly chosen or determined based on subjective assumptions, desired results might hardly be obtained. For example, when a binary decision tree was arbitrarily designated as a weak learner in this study, the classification accuracy was not enhanced at all compared to acc_{strong}. In addition, as shown in **Figure 2**, small values of N_{learn} resulted in low acc_{bag}, even lower than acc_{strong} because the small size of ensembles was not able to be trained sufficiently with various sample sets, causing to deteriorate classification accuracy. On the other hand, the bagging ensemble containing enough weak learners reduced effectively variance of estimates, which is consistent with the bagging ensemble theoretical background (Mayr et al., 2014). As mentioned above, the γ value for a weak learner was chosen as a rule of thumb. By changing the γ value from 0.001 to 0.5, in addition, we assessed whether the improvement of classification accuracy was possible. As a result, $\gamma = 0.1$ yielded significant difference in classification accuracies against N_{learn} (Bonferroni corrected-$p < 0.001$, not shown in the text) except the dataset I. This fact underpins the importance of proper parameter selection regarding ensemble learning methods as well. In this study, we could successfully achieve an enhanced BCI performance by using RLDA classifier with appropriate hyperparameters ($10 \leq N_{learn} \leq 50$ and $\gamma = 0.1$).

Limitation: Bitrate and Real Time Analysis

We improved the bitrate by successfully improving the classification accuracy in the present study. However, it is very difficult to reduce the trial length due to the inherent limitations of fNIRS-BCIs, such as slow response time due to hemodynamic delay. Recently, steady-state visually evoked potential (SSVEP)-BCI has shown the average performance of 701 bit/min (Nagel and Spüler, 2019). Even though many efforts have been devoted

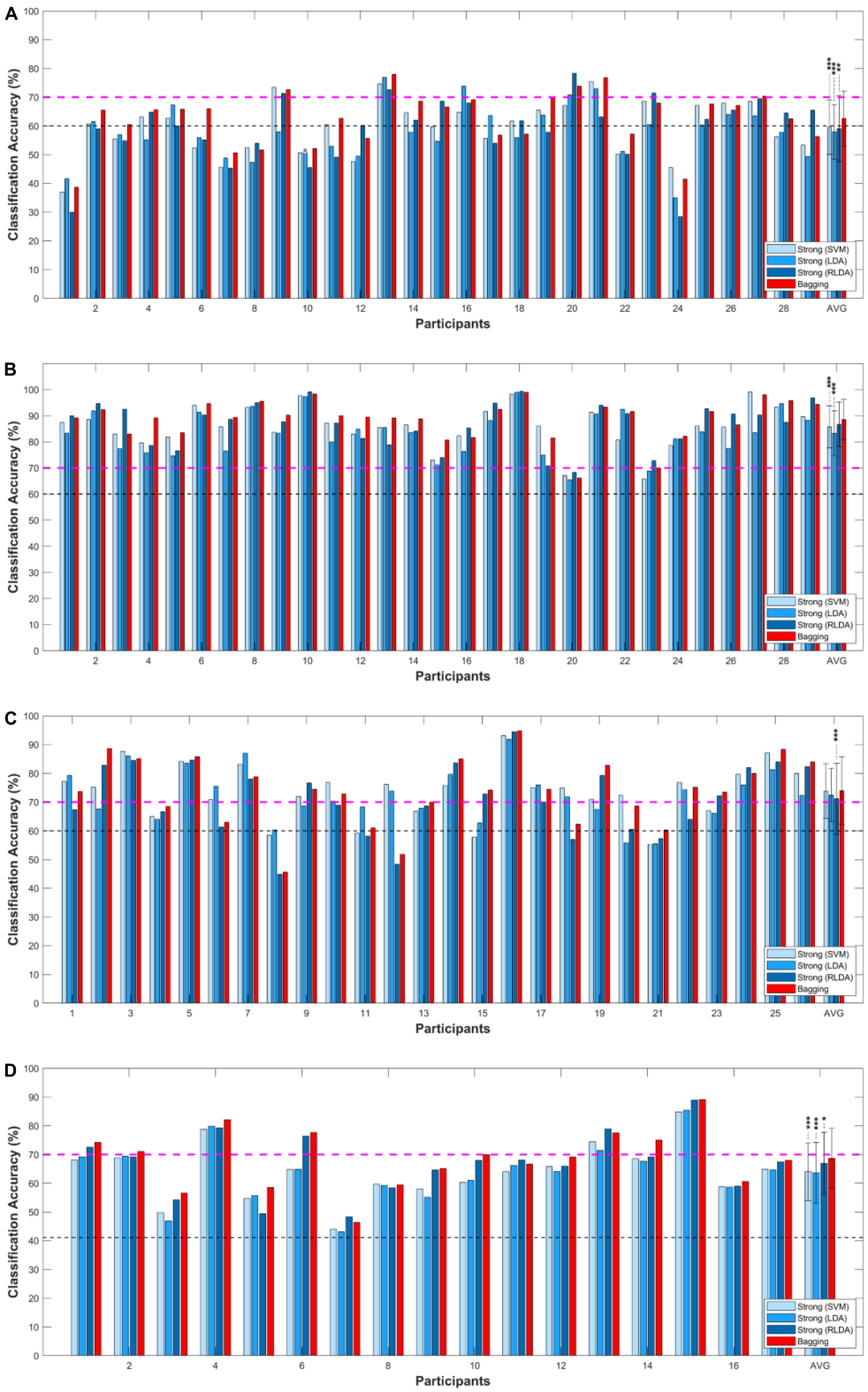

FIGURE 3 | Comparisons of individual acc_{strong} (blue) and acc_{bag} (red) for **(A)** dataset I, **(B)** dataset II, **(C)** dataset III, and **(D)** dataset IV. The error-bar indicates the standard deviation. The magenta dashed line represents the effective BCI threshold level (70.0%) indicating (Vidaurre and Blankertz, 2010). AVG represents the average of the classification accuracies across all participants. *Corrected-$p < 0.05$, **corrected-$p < 0.01$, and ***corrected-$p < 0.001$ (false discovery rate correction).

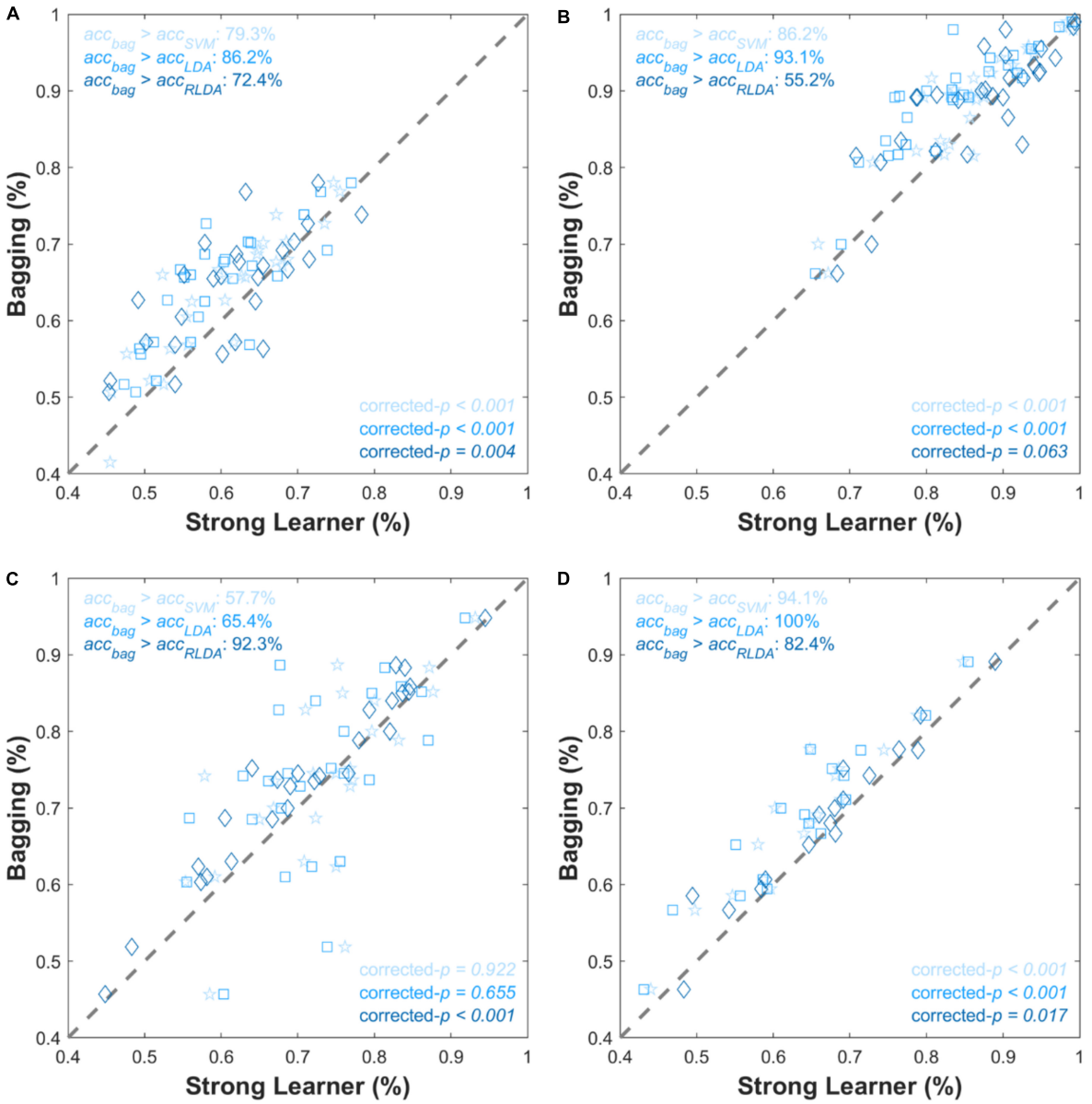

FIGURE 4 | Scatter plots comparing individual classification accuracies for **(A)** dataset I, **(B)** dataset II, **(C)** dataset III, and **(D)** dataset IV. The *x*- and *y*-axes correspond to acc_{strong} and acc_{bag}, respectively. Gray dashed lines are points where $acc_{strong} = acc_{bag}$. The corrected-*p*-values represent the significance of improvement of the classification accuracy by the bagging method. Pentagram, square, and diamond symbols are for SVM, LDA, and RLDA, respectively. Symbol color is in accordance with the bar color shown in **Figure 3**.

to improving the bitrate of fNIRS-BCIs (Cui et al., 2010; Zafar and Hong, 2017; Hong and Zafar, 2018), it is difficult to bridge the performance gap between fNIRS-BCIs and EEG-BCIs. However, for such SSVEP-BCI which is a type of exogenous BCIs, the need for an external stimulus causing user fatigue easily could be problematic.

This study dealt with the efficacy of the ensemble learning methods using the previously released open-access NIRS-BCI datasets. Since the experimental environment and analysis techniques for the implementation of real-time NIRS-BCIs are completely different from those for the implementation of offline NIRS-BCIs, it does not make sense to verify the feasibility of ensemble learning for online NIRS-BCIs with the offline NIRS-BCI datasets. Therefore, the efficacy of ensemble learning for online NIRS-BCIs should be validated in the future studies.

Efforts to Improve the Performance of NIRS-BCIs: Future Perspective

There have been many efforts to improve the overall performance of NIRS-BCIs. Recently, off-the-shelf NIRS systems adopting novel designs and form factors have been introduced to

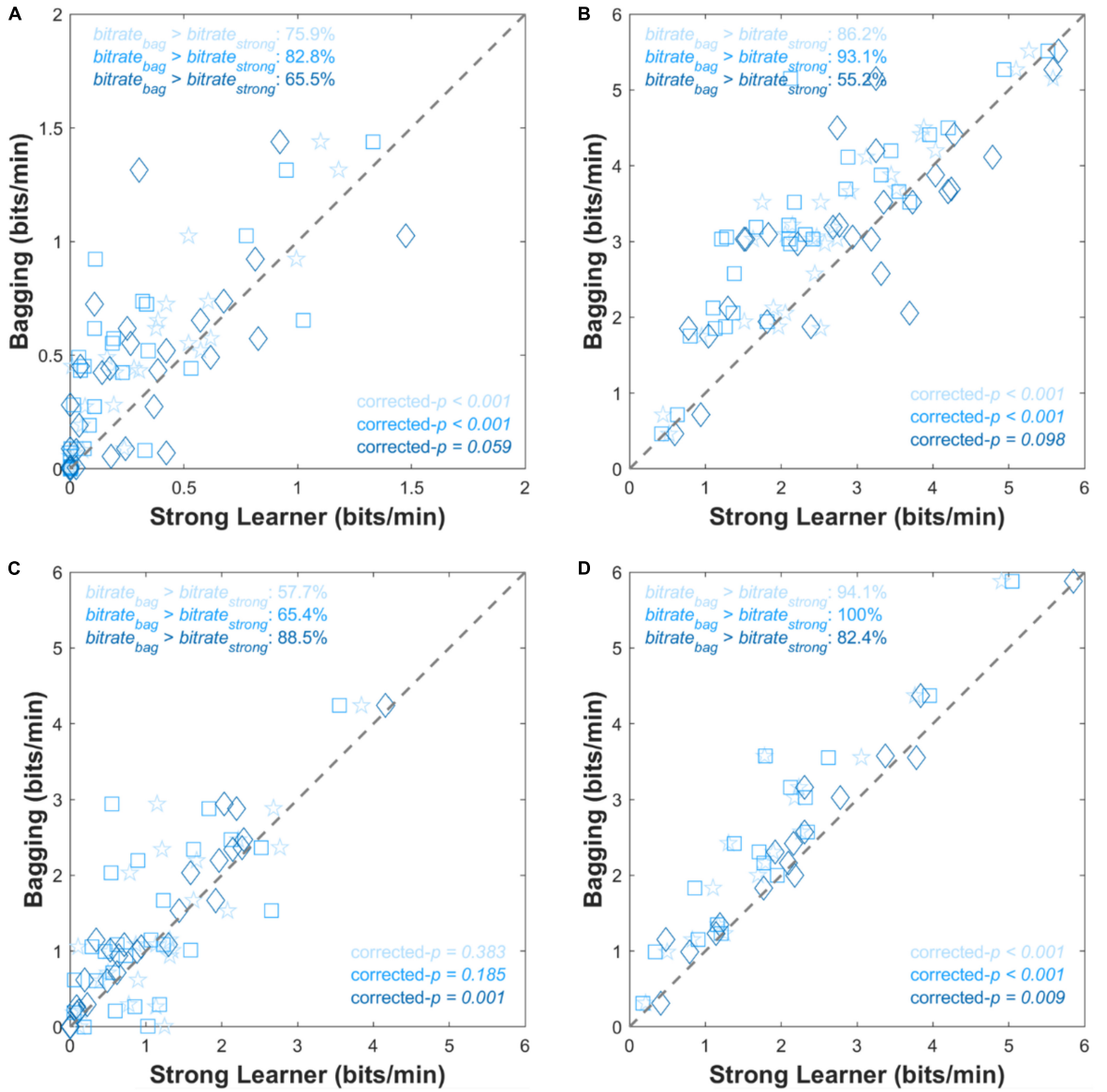

FIGURE 5 | Scatter plots comparing individual bitrates for **(A)** dataset I, **(B)** dataset II, **(C)** dataset III, and **(D)** dataset IV. The *x*- and *y*-axes correspond to $bitrate_{strong}$ and $bitrate_{bag}$, respectively. Gray dashed lines are points where $bitrate_{strong} = bitrate_{bag}$. The corrected-*p*-values represent the significance of improvement of the bitrate by the bagging method. Pentagram, square, and diamond symbols are for SVM, LDA, and RLDA, respectively. Symbol color is in accordance with the bar color shown in **Figure 3**.

the market and their usefulness in NIRS-BCIs has been verified (Shin et al., 2017a; Kim et al., 2018; Kwon et al., 2018; Lancia et al., 2018). However, most of the new form factors adopted by the recent NIRS systems do not possess general applicability because they are designed to record hemodynamic changes from the prefrontal area only. In addition, artificial intelligence methods based on deep learning have demonstrated their potential in enhancing the performance of BCI systems (Cecotti and Graser, 2011; Chiarelli et al., 2018; Lawhern et al., 2018; Nicholas et al., 2018; Sakhavi et al., 2018). Even though some studies have reported the superiority of the deep learning-based approach compared to the conventional machine learning methods (Trakoolwilaiwan et al., 2018), there still exist controversies regarding the employment of these opinions (Hennrich et al., 2015). Since deep learning techniques generally depend on human factors, such as how well the deep learning model structure is designed, objective and thorough investigations of deep learning models that can enhance the performance of NIRS-BCIs are necessary. Conversely, some recent studies showed the potential of the incorporated use of ensemble learning concepts with deep learning approaches (Xiao et al., 2018). The development of a novel ensemble classifier incorporated with deep learning techniques and its application

to NIRS-BCIs would be a promising topic, which we would like to pursue in future studies.

CONCLUSION

In this study, we demonstrated the effect of performance enhancement of NIRS-BCIs by the employment of a proper ensemble classifier, the RLDA ensemble classifier is based on the Bagging algorithm in this study, which has never been investigated before. As a result, the ensemble learning method employed was beneficial to improve the classification accuracies of all four datasets considered in this study. In our future studies, the ensemble classifier introduced in this study would be applied to new NIRS-BCI datasets to confirm its general availability, and new types of ensemble classifiers that can further enhance the performance of NIRS-BCI would also be tested.

DATA AVAILABILITY STATEMENT

Publicly available datasets were analyzed in this study. This data can be found here: http://dx.doi.org/10.14279/depositonce-5830, http://doc.ml.tu-berlin.de/hBCI/, and https://doi.org/10.6084/m9.figshare.9198932.

ETHICS STATEMENT

Ethical review and approval was not required for the study on human participants in accordance with the local legislation and institutional requirements. Written informed consent for participation was not required for this study in accordance with the national legislation and the institutional requirements.

AUTHOR CONTRIBUTIONS

JS planned the study and analyzed the data. C-HI supervised the work. Both authors wrote and reviewed the manuscript.

FUNDING

This work was supported in part by a grant from the Institute for Information and Communications Technology Promotion (IITP), funded by the Korea Government (MSIT) (2017-0-00432, Development of non-invasive integrated BCI SW platform to control home appliances and external devices by user's thought via AR/VR interface) and in part by grants from the Brain Research Program through the National Research Foundation of Korea, funded by the Ministry of Science and ICT (NRF-2015M3C7A1031969 and NRF-2017R1A6A3A01003543).

SUPPLEMENTARY MATERIAL

The Supplementary Material for this article can be found online at: https://www.frontiersin.org/articles/10.3389/fnins.2020.00168/full#supplementary-material

REFERENCES

Ahangi, A., Karamnejad, M., Mohammadi, N., Ebrahimpour, R., and Bagheri, N. (2013). Multiple classifier system for EEG signal classification with application to brain-computer interfaces. *Neural Comput. Appl.* 23, 1319–1327. doi: 10.1109/TBME.2013.2248153

Benjamini, Y., and Yekutieli, D. (2001). The control of the false discovery rate in multiple testing under dependency. *Ann. Stat.* 29, 1165–1188. doi: 10.1186/1471-2105-9-114

Bergstra, J., and Bengio, Y. (2012). Random search for hyper-parameter optimization. *J. Mach. Learn. Res.* 13, 281–305.

Blankertz, B., Acqualagna, L., Dähne, S., Haufe, S., Schultze-Kraft, M., Sturm, I., et al. (2016). The berlin brain-computer interface: progress beyond communication and control. *Front. Neurosci.* 10:530. doi: 10.3389/fnins.2016.00530

Blankertz, B., Lemm, S., Treder, M., Haufe, S., and Müller, K.-R. (2011). Single-trial analysis and classification of ERP components—a tutorial. *Neuroimage* 56, 814–825. doi: 10.1016/j.neuroimage.2010.06.048

Blankertz, B., Tangermann, M., Vidaurre, C., Fazli, S., Sannelli, C., Haufe, S., et al. (2010). The Berlin brain–computer interface: non-medical uses of BCI technology. *Front. Neurosci.* 4:00198. doi: 10.3389/fnins.2010.00198

Cecotti, H., and Graser, A. (2011). Convolutional neural networks for P300 detection with application to brain-computer interfaces. *IEEE Trans. Pattern Anal. Mach. Intell.* 33, 433–445. doi: 10.1109/TPAMI.2010.125

Chiarelli, A. M., Croce, P., Merla, A., and Zappasodi, F. (2018). Deep learning for hybrid EEG-fNIRS brain-computer interface: application to motor imagery classification. *J. Neural Eng.* 15:036028. doi: 10.1088/1741-2552/aaaf82

Combrisson, E., and Jerbi, K. (2015). Exceeding chance level by chance: the caveat of theoretical chance levels in brain signal classification and statistical assessment of decoding accuracy. *J. Neurosci. Methods* 250, 126–136. doi: 10.1016/j.jneumeth.2015.01.010

Cui, X., Bray, S., and Reiss, A. L. (2010). Speeded near infrared spectroscopy (NIRS) response detection. *PLoS One* 5:15474. doi: 10.1371/journal.pone.0015474

Dornhege, G., Millán, J. R., Hinterberger, T., Mcfarland, D., and Müller, K.-R. (2007). *Toward Brain-Computer Interfacing*. Cambridge, MA: MIT press.

Fatourechi, M., Ward, R. K., and Birch, G. E. (2008). A self-paced brain-computer interface system with a low false positive rate. *J. Neural Eng.* 5, 9–23. doi: 10.1088/1741-2560/5/1/002

Fazli, S., Mehnert, J., Steinbrink, J., Curio, G., Villringer, A., Müller, K.-R., et al. (2012). Enhanced performance by a hybrid NIRS-EEG brain computer interface. *Neuroimage* 59, 519–529. doi: 10.1016/j.neuroimage.2011.07.084

Gao, L., Cheng, W., Zhang, J. H., and Wang, J. (2016).). EEG classification for motor imagery and resting state in BCI applications using multi-class Adaboost extreme learning machine. *Rev. Sci. Instrum.* 87:085110. doi: 10.1063/1.4959983

Gurel, N. Z., Jung, H., Hersek, S., and Inan, O. T. (2019). Fusing near-infrared spectroscopy with wearable hemodynamic measurements improves classification of mental stress. *IEEE Sens. J.* 19, 8522–8531.

Hassan, A. R., and Bhuiyan, M. I. H. (2017). Automated identification of sleep states from EEG signals by means of ensemble empirical mode decomposition and random under sampling boosting. *Comput. Methods Programs Biomed.* 140, 201–210. doi: 10.1016/j.cmpb.2016.12.015

Hennrich, J., Herff, C., Heger, D., and Schultz, T. (2015). "Investigating deep learning for fNIRS based BCI," in *37th International Conference of the IEEE Engineering in Medicine and Biology Society (EMBC)*, (Milan), 2844–2847.

Holper, L., and Wolf, M. (2011). Single-trial classification of motor imagery differing in task complexity: a functional near-infrared spectroscopy study. *J. Neuroeng. Rehabi.* 8:34. doi: 10.1186/1743-0003-8-34

Hong, K.-S., and Khan, M. J. (2017). Hybrid brain-computer interface techniques for improved classification accuracy and increased number of commands: a review. *Front. Neurorobot.* 11:35. doi: 10.3389/fnbot.2017.00035

Hong, K.-S., Khan, M. J., and Hong, M. J. (2018). Feature extraction and classification methods for hybrid fNIRS-EEG brain-computer interfaces. *Front. Hum. Neurosci.* 12:246. doi: 10.3389/fnhum.2018.00246

Hong, K.-S., Naseer, N., and Kim, Y.-H. (2015). Classification of prefrontal and motor cortex signals for three-class fNIRS-BCI. *Neurosci. Lett.* 587, 87–92. doi: 10.1016/j.neulet.2014.12.029

Hong, K. S., and Zafar, A. (2018). Existence of initial dip for BCI: an illusion or reality. *Front. Neurorobot.* 12:69. doi: 10.3389/fnbot.2018.00069

Hosseini, M. P., Pompili, D., Elisevich, K., and Soltanian-Zadeh, H. (2018). Random ensemble learning for EEG classification. *Artif. Intell. Med.* 84, 146–158. doi: 10.1016/j.artmed.2017.12.004

Hwang, H. J., Choi, H., Kim, J. Y., Chang, W. D., Kim, D. W., Kim, K. W., et al. (2016). Toward more intuitive brain-computer interfacing: classification of binary covert intentions using functional near-infrared spectroscopy. *J. Biomed. Opt.* 21:091303. doi: 10.1117/1.JBO.21.9.091303

Hwang, H.-J., Kwon, K., and Im, C.-H. (2009). Neurofeedback-based motor imagery training for brain–computer interface (BCI). *J. Neurosci. Meth.* 179, 150–156.

Hwang, H.-J., Lim, J.-H., Kim, D.-W., and Im, C.-H. (2014). Evaluation of various mental task combinations for near-infrared spectroscopy-based brain-computer interfaces. *J. Biomed. Opt.* 19:077005. doi: 10.1117/1.JBO.19.7.077005

Kanoh, S.-I., Murayama, Y.-M., Miyamoto, K.-I., Yoshinobu, T., and Kawashima, R. (2009). "A NIRS-based brain-computer interface system during motor imagery: system development and online feedback training," in *31st Annual International Conference of the IEEE Engineering in Medicine and Biology Society (EMBC)*, (Minneapolis), 594–597.

Kim, J. M., Choi, J. K., Choi, M., Ji, M., Hwang, G., Ko, S. B., et al. (2018). Assessment of cerebral autoregulation using continuous-wave near-infrared spectroscopy during squat-stand maneuvers in subjects with symptoms of orthostatic intolerance. *Sci. Rep.* 8:13257. doi: 10.1038/s41598-018-31685-y

Kwon, H., Kim, K., Jo, Y., Park, M., Ko, S.-B., Kim, T., et al. (2018). Early detection of cerebral infarction with middle cerebral artery occlusion with functional near-infrared spectroscopy: a pilot study. *Front. Neurol.* 9:898. doi: 10.3389/fneur.2018.00898

Lancia, S., Choi, J., Baek, J., Mammarella, S., Bianco, D., Quaresima, V., et al. (2018). "Trail making test induces prefrontal cortex activation as revealed by a cw wearable-wireless fNIRS/DOT imager," in *Oxygen Transport to Tissue XL*, (Berlin: Springer), 139–144.

Lawhern, V. J., Solon, A. J., Waytowich, N. R., Gordon, S. M., Hung, C. P., and Lance, B. J. (2018). EEGNet: a compact convolutional neural network for EEG-based brain-computer interfaces. *J. Neural Eng.* 15:056013. doi: 10.1088/1741-2552/aace8c

Lebedev, M. A., and Nicolelis, M. A. L. (2006). Brain–machine interfaces: past, present and future. *Trends Neurosci.* 29, 536–546.

Ledoit, O., and Wolf, M. (2004). A well-conditioned estimator for large-dimensional covariance matrices. *J. Multivar. Anal.* 88, 365–411.

Lemm, S., Blankertz, B., Dickhaus, T., and Müller, K.-R. (2011). Introduction to machine learning for brain imaging. *Neuroimage* 56, 387–399. doi: 10.1016/j.neuroimage.2010.11.004

Matthews, F., Pearlmutter, B. A., Ward, T. E., Soraghan, C., and Markham, C. (2008). Hemodynamics for brain-computer interfaces. *IEEE Signal Process. Mag.* 25, 87–94.

Mayr, A., Binder, H., Gefeller, O., and Schmid, M. (2014). The Evolution of Boosting Algorithms From Machine Learning to Statistical Modelling. *Methods Inf. Med.* 53, 419–427. doi: 10.3414/ME13-01-0122

Mockus, J. (2012). *Bayesian Approach to Global Optimization: Theory and Applications*. Berlin: Springer Science & Business Media.

Nagel, S., and Spüler, M. (2019). World's fastest brain-computer interface: combining EEG2Code with deep learning. *PLoS One* 14:e0221909. doi: 10.1371/journal.pone.0221909

Naseer, N., and Hong, K.-S. (2015). fNIRS-based brain-computer interfaces: a review. *Front. Hum. Neurosci.* 9:00003.

Naseer, N., Noori, F. M., Qureshi, N. K., and Hong, K.-S. (2016). Determining optimal feature-combination for LDA classification of functional near-infrared spectroscopy signals in brain-computer interface application. *Front. Hum. Neurosci.* 10:237. doi: 10.3389/fnhum.2016.00237

Nicholas, W., Vernon, J. L., Javier, O. G., Jennifer, C., Josef, F., Paul, S., et al. (2018). Compact convolutional neural networks for classification of asynchronous steady-state visual evoked potentials. *J. Neural Eng.* 15:066031. doi: 10.1088/1741-2552/aae5d8

Nicolas-Alonso, L., and Gomez-Gil, J. (2012). Brain computer interfaces, a review. *Sensors* 12, 1211–1279. doi: 10.3390/s120201211

Power, S. D., Kushki, A., and Chau, T. (2012a). Automatic single-trial discrimination of mental arithmetic, mental singing and the no-control state from prefrontal activity: toward a three-state NIRS-BCI. *BMC Res. Notes* 5:141. doi: 10.1186/1756-0500-5-141

Power, S. D., Kushki, A., and Chau, T. (2011). Towards a system-paced near-infrared spectroscopy brain–computer interface: differentiating prefrontal activity due to mental arithmetic and mental singing from the no-control state. *J. Neural Eng.* 8:066004. doi: 10.1088/1741-2560/8/6/066004

Power, S. D., Kushki, A., and Chau, T. (2012b). Intersession consistency of single-trial classification of the prefrontal response to mental arithmetic and the no-control state by NIRS. *PLoS One* 7:0037791. doi: 10.1371/journal.pone.0037791

Rakotomarnonjy, A., and Guigue, V. (2008). BCI competition III: dataset II - ensemble of SVMs for BCI P300 speller. *IEEE Trans. Biomed. Eng.* 55, 1147–1154. doi: 10.1109/TBME.2008.915728

Sakhavi, S., Guan, C. T., and Yan, S. C. (2018). Learning temporal information for brain-computer interface using convolutional neural networks. *IEEE Trans. Neural Netw. Learn. Syst.* 29, 5619–5629. doi: 10.1109/TNNLS.2018.2789927

Schäfer, J., and Strimmer, K. (2005). A Shrinkage approach to large-scale covariance matrix estimation and implications for functional genomics. *Stat. Appl. Genet. Mol. Biol.* 4, 1175–1189.

Schalk, G., Mcfarland, D. J., Hinterberger, T., Birbaumer, N., and Wolpaw, J. R. (2004). BCI2000: A general-purpose, brain-computer interface (BCI) system. *IEEE Trans. Biomed. Eng.* 51, 1034–1043.

Schudlo, L. C., and Chau, T. (2014). Dynamic topographical pattern classification of multichannel prefrontal NIRS signals: II. Online differentiation of mental arithmetic and rest. *J. Neural. Eng.* 11:016003. doi: 10.1088/1741-2560/11/1/016003

Schudlo, L. C., and Chau, T. (2015). Towards a ternary NIRS-BCI: single-trial classification of verbal fluency task. Stroop task and unconstrained rest. *J. Neural Eng.* 12:066008. doi: 10.1088/1741-2560/12/6/066008

Sereshkeh, A. R., Yousefi, R., Wong, A. T., and Chau, T. (2019). Online classification of imagined speech using functional near-infrared spectroscopy signals. *J. Neural Eng.* 16:016005. doi: 10.1088/1741-2552/aae4b9

Shin, J., Kwon, J., Choi, J., and Im, C.-H. (2017a). Performance enhancement of a brain-computer interface using high-density multi-distance NIRS. *Sci. Rep.* 7:16545. doi: 10.1038/s41598-017-16639-0

Shin, J., Kwon, J., Choi, J., and Im, C. H. (2018a). Ternary near-infrared spectroscopy brain-computer interface with increased information transfer rate using prefrontal hemodynamic changes during mental arithmetic, breath-Holding, and idle State. *IEEE Access* 6, 19491–19498.

Shin, J., Kwon, J., and Im, C.-H. (2018b). A ternary hybrid EEG-NIRS brain-computer interface for the classification of brain activation patterns during mental arithmetic, motor imagery, and idle state. *Front. Neuroinform.* 12:5. doi: 10.3389/fninf.2018.00005

Shin, J., Von Lühmann, A., Blankertz, B., Kim, D.-W., Jeong, J., Hwang, H.-J., et al. (2017b). Open access dataset for EEG+NIRS single-trial classification. *IEEE Trans. Neural Syst. Rehabil. Eng.* 25, 1735–1745.

Shin, J., Von Lühmann, A., Kim, D.-W., Mehnert, J., Hwang, H.-J., and Müller, K.-R. (2018c). Simultaneous acquisition of EEG and NIRS during cognitive tasks for an open access dataset. *Sci. Data* 5:180003. doi: 10.1038/sdata.2018.3

Shin, J., Müller, K.-R., and Hwang, H.-J. (2016). Near-infrared spectroscopy (NIRS) based eyes-closed brain-computer interface (BCI) using prefrontal cortex activation due to mental arithmetic. *Sci. Rep.* 6:36203. doi: 10.1038/srep36203

Sun, S. L., Zhang, C. S., and Zhang, D. (2007). An experimental evaluation of ensemble methods for EEG signal classification. *Pattern Recognit. Lett.* 28, 2157–2163. doi: 10.1109/TNSRE.2015.2496334

Trakoolwilaiwan, T., Behboodi, B., Lee, J., Kim, K., and Choi, J. W. (2018). Convolutional neural network for high-accuracy functional near-infrared spectroscopy in a brain-computer interface: three-class classification of rest, right-, and left-hand motor execution. *Neurophotonics* 5:011008. doi: 10.1117/1.NPh.5.1.011008

Vidaurre, C., and Blankertz, B. (2010). Towards a cure for BCI illiteracy. *Brain Topogr.* 23, 194–198. doi: 10.1007/s10548-009-0121-6

Wolpaw, J. R., Birbaumer, N., Mcfarland, D. J., Pfurtscheller, G., and Vaughan, T. M. (2002). Brain-computer interfaces for communication and control. *Clin. Neurophysiol.* 113, 767–791.

Xiao, Y. W., Wu, J., Lin, Z. L., and Zhao, X. D. (2018). A deep learning-based multi-model ensemble method for cancer prediction. *Comput. Methods Programs Biomed.* 153, 1–9. doi: 10.1016/j.cmpb.2017.09.005

Zafar, A., and Hong, K.-S. (2017). Detection and classification of three-class initial dips from prefrontal cortex. *Biomed. Opt. Express* 8, 367–383. doi: 10.1364/BOE.8.000367

Conflict of Interest: The authors declare that the research was conducted in the absence of any commercial or financial relationships that could be construed as a potential conflict of interest.

The reviewer JM declared a past co-authorship with one of the authors JS to the handling editor.

Copyright © 2020 Shin and Im. This is an open-access article distributed under the terms of the Creative Commons Attribution License (CC BY). The use, distribution or reproduction in other forums is permitted, provided the original author(s) and the copyright owner(s) are credited and that the original publication in this journal is cited, in accordance with accepted academic practice. No use, distribution or reproduction is permitted which does not comply with these terms.

frontiers in Neuroscience

ORIGINAL RESEARCH
published: 10 March 2020
doi: 10.3389/fnins.2020.00167

Differences in Net Information Flow and Dynamic Connectivity Metrics Between Physically Active and Inactive Subjects Measured by Functional Near-Infrared Spectroscopy (fNIRS) During a Fatiguing Handgrip Task

*Elizabeth L. Urquhart[1], Xinlong Wang[1], Hanli Liu[1], Paul J. Fadel[2] and George Alexandrakis[1]**

[1] Bioengineering Department, University of Texas at Arlington, Arlington, TX, United States, [2] Department of Kinesiology, University of Texas at Arlington, Arlington, TX, United States

OPEN ACCESS

Edited by:
Yasuyo Minagawa, Keio University, Japan

Reviewed by:
Paola Pinti, University College London, United Kingdom
Satoshi Morimoto, Keio Advanced Research Centers (KARC), Japan

***Correspondence:**
George Alexandrakis
galex@uta.edu

Specialty section:
This article was submitted to Brain Imaging Methods, a section of the journal Frontiers in Neuroscience

Received: *18 September 2019*
Accepted: *14 February 2020*
Published: *10 March 2020*

Citation:
Urquhart EL, Wang X, Liu H, Fadel PJ and Alexandrakis G (2020) Differences in Net Information Flow and Dynamic Connectivity Metrics Between Physically Active and Inactive Subjects Measured by Functional Near-Infrared Spectroscopy (fNIRS) During a Fatiguing Handgrip Task. Front. Neurosci. 14:167. doi: 10.3389/fnins.2020.00167

Twenty-three young adults (4 Females, 25.13 ± 3.72 years) performed an intermittent maximal handgrip force task using their dominant hand for 20 min (3.5 s squeeze/6.5 s release, 120 blocks) with concurrent cortical activity imaging by functional Near-Infrared Spectroscopy (fNRIS; OMM-3000, Shimadzu Corp., 111 channels). Subjects were grouped as physically active (n = 10) or inactive (n = 12) based on a questionnaire (active- exercise at least four times a week, inactive- exercise less than two times a week). We explored how motor task fatigue affected the vasomotion-induced oscillations in ΔHbO as measured by fNIRS at each hemodynamic frequency band: endothelial component (0.003–0.02 Hz) associated to microvascular activity, neurogenic component (0.02–0.04 Hz) related to intrinsic neuronal activity, and myogenic component (0.04–0.15 Hz) linked to activity of smooth muscles of arterioles. To help understand how these three neurovascular regulatory mechanisms relate to handgrip task performance we quantified several dynamic fNIRS metrics, including directional phase transfer entropy (dPTE), a computationally efficient and data-driven method used as a marker of information flow between cortical regions, and directional connectivity (DC), a means to compute directionality of information flow between two cortical regions. The relationship between static functional connectivity (SFC) and functional connectivity variability (FCV) was also explored to understand their mutual dependence for each frequency band in the context of handgrip performance as fatigued increased. Our findings ultimately showed differences between subject groups across all fNIRS metrics and hemodynamic frequency bands. These findings imply that physical activity modulates neurovascular control mechanisms at the endogenic, neurogenic, and myogenic frequency bands

resulting in delayed fatigue onset and enhanced performance. The dynamic cortical network metrics quantified in this work for young, healthy subjects provides baseline measurements to guide future work on older individuals and persons with impaired cardiovascular health.

Keywords: fatigue, sensory-motor cortex, directional phase transfer entropy, directional connectivity, functional connectivity variability

INTRODUCTION

Cerebral autoregulation helps maintain a relatively constant oxygen supply to the brain during changes in arterial blood pressure, by maintaining cerebral blood flow (CBF) relatively constant. This occurs via vasoconstriction in response to increased blood pressure and vasodilation in response to decreased blood pressure. Regional CBF (rCBF) is flow-mediated vasodilation from distal to proximal vessels that occurs in activated brain regions which protects downstream microvascular pressure (Querido and Sheel, 2007; Peterson et al., 2011; Perrey, 2013; Tzeng and Ainslie, 2014; Peri-Okonny et al., 2015). There are overlapping regulatory mechanisms of rCBF that have been classified into contiguous ranges of hemodynamic frequencies as endogenic (0.003–0.02 Hz), neurogenic (0.02–0.04 Hz), and myogenic (0.04–0.15 Hz) (Cipolla, 2009; Li et al., 2012). These frequency oscillations reflect the influence of endothelial-related metabolic activity, intrinsic neuronal activity, and myogenic activity of the vascular smooth muscle, respectively (Cipolla, 2009; Li et al., 2012; Huo et al., 2018). Exercise may also modulate the regulatory mechanisms in each frequency band. Exercise is known to improve cardiovascular health (Myers, 2003) and brain health (Peri-Okonny et al., 2015; Mueller et al., 2017). Regular exercise produces beneficial alterations in the brain that maintain or improve cognition (Bosch et al., 2017; Mueller et al., 2017), and promote motor function (Perrey, 2013), known as exercise-dependent neuroplasticity.

The hemodynamic oscillations at these frequency bands can be measured using functional brain mapping using functional magnetic resonance image (fMRI) (Zhang et al., 2015), or functional near-infrared spectroscopy (fNIRS) (Li et al., 2012; Bosch et al., 2017; Andersen et al., 2018; Cao et al., 2018b). FNIRS measures non-invasively the change of oxyhemoglobin (ΔHbO) and deoxyhemoglobin (ΔHb) concentrations resulting from neurovascular coupling secondary to neuronal activation by utilizing light at near-infrared wavelengths (650–1000 nm). It is advantageous because of its relatively lower cost, portability, robustness to motion artifacts, and its higher temporal resolution compared to fMRI (Huppert et al., 2009; Naseer and Hong, 2015).

In recently completed work, we demonstrated interesting temporal evolution patterns for hemodynamic activation and static functional connectivity (SFC) changes that depended on the physical activity levels of subjects while they were trying to maintain maximal handgrip task performance (Urquhart et al., 2019). That work identified that physically active subjects experienced delayed fatigue onset as evident by their greater ability to maintain maximum voluntary contraction (MVC) force accompanied by longer-lasting and more spatially extended activation and SFC patterns in the primary motor (M1), premotor and supplementary motor areas (PMC/SMA) and the prefrontal cortex (PFC) (Urquhart et al., 2019). In contrast to the static networks explored in our previous work, the purpose of this work was to examine changes in dynamic cortical network patterns and how they relate to handgrip task performance for each hemodynamic frequency band, as a function of a subjects' physical activity level.

In this work we first applied directional phase transfer entropy (dPTE) analysis, a computationally efficient and data-driven method previously used in electroencephalography (EEG) research (Hillebrand et al., 2016), to estimate changes in the direction of information flow during the fatiguing handgrip task. It has been applied recently to fNIRS in one study (Cao et al., 2018b), but dPTE analysis has not been employed, to our knowledge, as yet to explore the effect of fatigue on the brain's networks. The net direction of information flow, or directional connectivity (DC), was also quantified between regions to better understand motor control regulation under fatiguing conditions (Hillebrand et al., 2016). A simultaneous multimodal neuroimaging study using fNIRS, fMRI, and EEG has previously examined directionality via Wiener-Granger causality on finger movement tasks, but their results were confined to the contralateral (i.e., left) hemisphere only and not broader cortical networks (Anwar et al., 2016). We also explored the relationship between SFC and functional connectivity variability (FCV), which represents spontaneous dynamic fluctuations of connectivity over time (Fong et al., 2019). This was motivated by the fact that SFC is known to increase with task performance (Jiang et al., 2012; Perrey, 2013; Urquhart et al., 2019), while FCV reflects resource availability during demanding tasks (Li et al., 2015; Fong et al., 2019). The aim of this work was to identify differences between subject groups across all of the aforementioned fNIRS metrics and hemodynamic frequency bands. In addition, we aimed to demonstrate the feasibility of using time-dependent fNIRS metrics to help understand how dynamic connectivity regulation of cortical networks relates to performance during a fatiguing motor task.

MATERIALS AND METHODS

Participants

Twenty-three young adults (4 females) between the ages 18 and 30 (mean age 25.13 $\pm$ 3.72) participated in this study. All subjects gave prior written informed consent for their participation in this study, which was approved by the Institutional Review Board of the University of Texas at Arlington (IRB# 2018-0686) and

performed in accordance with the Declaration of Helsinki. All but two subjects were right-handed, as determined by the Edinburgh handedness scale (Oldfield, 1971). All subjects were free of any neurological or psychiatric disorders (self-reported), and were non-smokers. Subjects self-reported as being physically inactive ($n = 12$, exercising less than twice a week for 30 min of moderately vigorous exercise), or active ($n = 11$, exercising at least four times a week for 30 min of moderately vigorous exercise).

Experimental Procedures

A continuous wave fNIRS imaging system (OMM-3000, Shimadzu Corp., Kyoto, Japan) was used in this experiment, which utilized near infrared light diode sources (780, 805, and 830 nm) and photomultiplier detectors at a sampling frequency of 10.101 Hz. The setup geometry consisted of 32 sources and 34 detectors with a separation of 3 cm, resulting in 111 source-detector channels (**Figure 1A**). This probe geometry covered cortical areas of the following 11 regions of interest (ROIs) (**Figure 1B**): left and right frontopolar prefrontal cortex (lFP; rFP), left and right dorsolateral prefrontal cortex (lDLPFC; rDLPFC), Broca's area, left and right premotor cortex (lPMC; rPMC), left and right primary motor and sensory cortical (lM1/S1; rM1/S1) areas, and left and right sensory association cortex (lSAC; rSAC). Anatomical cranial reference points (nasion, inion, left and right preauricular points and vertex) and optode locations were recorded for each subject using a 3D digitizer (FASTRAK, Polhemus VT, United States). Montreal Neurological Institute (MNI) coordinates for each source and detector locations were calculated using the statistical parametric mapping NIRS_SPM software, which provided the Brodmann area (BA) corresponding to each fNIRS channel as shown in **Supplementary Table S1** (Singh et al., 2005).

Subjects sat upright with their dominant arm at their side, elbow flexed at 90° and resting on a table. Subjects faced two screens that displayed protocol commands and visual feedback of handgrip performance (**Figure 1C**). Prior to starting the handgrip task, subjects performed three to five isometric MVCs with their dominant hand. All MVCs were recorded at a 1 kHz sampling rate using a handgrip dynamometer (BIOPAC, CA, United States). The pre-task MVCs were averaged for each subject and set as their maximum target of 100% MVC to reach during the subsequent handgrip task. The fNIRS data acquisition began with a 5 min resting period where subjects were asked to refrain from any movement or specific thoughts, followed immediately by a fatiguing handgrip task. The task required subjects to perform intermittent handgrip contractions for 3.5 s alternating with 6.5 s of rest for 120 blocks (**Figure 1D**) while attaining 100% MVC as closely as possible, as a means to induce fatigue in the forearm (Liu et al., 2007; Shibuya and Kuboyama, 2010; Jiang et al., 2012; Rhee and Mehta, 2018). The recorded force time-series data were low-pass filtered at 15 Hz and the maximum force for each block was calculated (Mehta and Shortz, 2014; Rhee and Mehta, 2018).

Data Preprocessing

This study used the open-source Homer2.0 to process (**Supplementary Table S2**) the collected fNIRS data (Huppert et al., 2009). Detrending was implemented using the least-squares fit of a line that was subtracted from the data (Xu et al., 2015). The data were then filtered for each respective frequency band. Following previously published work, frequency bands were defined as endogenic (0.003–0.02 Hz), neurogenic (0.02–0.04 Hz), and myogenic (0.04–0.15 Hz) (Aalkjaer et al., 2011; Cao et al., 2018b). Data in each of these three hemodynamic frequency bands were low-pass filtered by a third order and high-pass filtered by a fifth order Butterworth filter (Huppert et al., 2009). Channels were removed if signal standard deviations were greater than two times their mean signal amplitude (Cao et al., 2018b). Principal component analysis (PCA) was utilized to remove motion artifacts and global hemodynamic fluctuations that may overlap with the task-related hemodynamic response frequencies. The first two principal components were removed from all fNIRS channel data in order to remove these global artificats (Huppert et al., 2009; Naseer and Hong, 2015). To avoid signal contamination especially by branches from the middle cerebral artery or the superficial temporal artery and temporal muscle, channels located near these structures were also removed from analysis (Smielewski et al., 1997; Oldag et al., 2012). The resulting optical density data were then converted into changes in hemoglobin concentration relative to baseline (ΔHbO and ΔHb) using the Modified Beer-Lambert Law with an estimated differential pathlength factor of 6.0 for each wavelength, an estimate used in Homer 2.0 (Kohl et al., 1998). Only ΔHbO values were presented in the Result section below because ΔHb values were found to have similar and opposite qualitative trends, but with smaller amplitudes and lower signal-to-noise ratio as previously reported in other neuroimaging studies observing motor activation tasks (Anwar et al., 2013; Visani et al., 2015). Nevertheless, corresponding ΔHb results were included in the **Supplementary Material** section for completeness. Left-handed subjects' data was flipped to its mirror image on the brain for group averaging purposes and the subsequent interpretation for all data was right (r) for contralateral and left (l) for ipsilateral brain hemispheres relative to the arm performing the handgrip task.

Phase Transfer Entropy (PTE) and Directed PTE (dPTE) Data Analysis

The information flow between ROIs was estimated using phase transfer entropy (PTE) based on the same principle as Granger Causality (Siebenhuehner et al., 2013; Hillebrand et al., 2016; Cao et al., 2018b). It is calculated as the difference between the uncertainty of the target signal Y conditioned by its past and the uncertainty of the target signal conditioned on both its past and the source signal X (Hillebrand et al., 2016; Cao et al., 2018b):

$$PTE_{XY} = H\left(Y_{t+\delta}|Y_t\right) - H\left(Y_{t+\delta}|Y_t,\ X\right) \quad (1)$$

where PTE_{XY} is the PTE from source X to target signal Y. Shannon Entropy (H) is defines as:

$$H\left(Y_{t+\delta}\right) = -\sum_{i=0}^{n} p\left(Y_{t+\delta_i}\right) logp\left(Y_{t+\delta_i}\right) \quad (2)$$

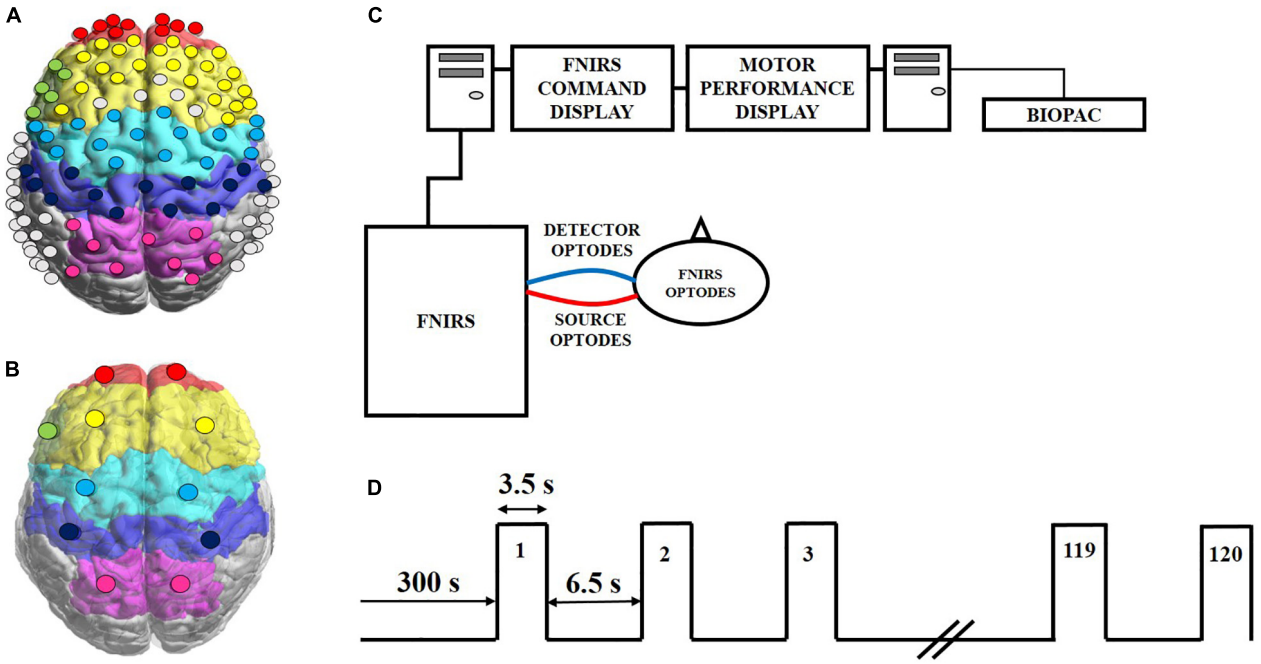

FIGURE 1 | Experimental set up and protocol timeline for the handgrip task. **(A)** FNIRS 111-channel layout with eleven regions of interest (ROIs) covered by the probe geometry: left and right frontopolar (lFP; rFP) (red), left and right pre-frontal cortex (lDLPFC; rDLPFC) (yellow), Broca's area (green), left and right pre-motor cortex (lPMC; rPMC) (light blue), left and right primary motor and sensory cortical (lM1/S1; rM1/S1) areas (purple), and left and right sensory association cortex (lSAC; rSAC) (pink). **(B)** Each circle shows the spatial average of the probe coordinates in each ROI, per brain hemisphere. These averaged probe locations served as reference points for plotting dPTE and DC between ROIs in this work. **(C)** Schematic of the experimental set-up of the fNIRS (LABNIRS) system and the BIOPAC handgrip force sensor system with one representative source-detector channel shown for simplicity. **(D)** The handgrip task protocol, starting with a 5-minute baseline. Subjects performed intermittent handgrip contractions for 3.5 s followed by 6.5 s of rest for 120 blocks at 100% MVC.

where the summation is performed for discrete time steps $t + \delta_i$ ($i = 0$, n), where n signifies the total number of time bins, defined by the product of the time interval duration (rest, or task period) in seconds and the data sampling frequency of 10.101 Hz. The delay between signal Y_t and $Y_{t+\delta_i}$ is expressed as δ_i. For a more complete description of how Shannon entropy is computed the reader is referred to relevant prior literature (Shannon, 1948; Schreiber, 2000; Hillebrand et al., 2016).

Due to PTE_{XY} lacking a meaningful upper bound and to reduce bias, a normalizing process is used (Hillebrand et al., 2016):

$$dPTE_{XY} = \frac{PTE_{XY}}{PTE_{XY} + PTE_{YX}}. \quad (3)$$

With a range between 0 and 1, if $0.5 < dPTE_{XY} < 1$ the information flow is preferentially from X to Y. But, if $0 < dPTE_{XY} < 0.5$, then the information flow is preferentially from Y to X. In the event that $dPTE_{XY} = 0.5$, there is no preferential direction of information flow (Hillebrand et al., 2016; Cao et al., 2018b).

Data Processing Steps for dPTE

Directed PTE analysis was applied to calculate information flow for the endogenic, neurogenic, and myogenic frequency bands at three periods: 5 min of resting state, 0–10 min, and 11–20 min of the handgrip task. Directed PTE for resting state requires a minimum of 5 min to attain stable computed values (Hillebrand et al., 2016) and in this work 10 min periods were used to account for the higher amount of hemodynamic variation during the handgrip paradigm (Urquhart et al., 2019). Firstly, PTE analysis was performed to quantify causality between every two channels among all 111 channels. Then PTE values were normalized into dPTE values, generating a 111×111 matrix. The value at Xth row and Yth column determined the scale of information flow from Y to X. If dPTE was between 0 and <0.5 the net information flow was from Y to X, whereas if dPTE $>$ 0.5 the net flow was from X to Y. If dPTE was equal to 0.5, within a rounding error of two decimals, no net information flow was assumed. Then the dPTE was averaged lengthwise by row, yielding a 1×111 matrix, which was the mean dPTE between each one channel and all other channels (Cao et al., 2018b). The two channels with the highest ROI percentage overlap relative to neighboring ROIs, as determined by NIRS_SPM, were averaged together and assigned to each ROI, yielding a 1×11 matrix. The high signal variability induced during the task, as demonstrated in our previous work (Urquhart et al., 2019), did not allow for identification of statistically significant changes in individual channels. Therefore, the dPTE channels were averaged from up to 11 channels to 2 per ROI in order to allow for comparisons between dPTE at rest and during the task that could lead to statistically significant differences. A one-sample t-test was then performed across subjects for significant differences in dPTE

across all possible pairs of ROIs ($p < 0.05$ and false discovery rate (FDR) corrected) (Singh and Dan, 2006). This test was used to determine significant net information flow into or out of each ROI by testing against the null hypothesis of no net flow, where positive *t*-values indicated outgoing net information flow ("source") and negative t-values indicated incoming net information flow ("sink"). Significant net information flow values for each ROI were visualized using BrainNet Viewer, an open-source software package (Xia et al., 2013), for each frequency band at each period per subject group. Dedicated software (G*Power v3.0.10, Franz Fual, Kiel University, Kiel, Germany) was used to perform *post hoc* statistical power (1-β) analysis (Faul et al., 2007).

Directional Connectivity (DC)

The dPTE values were first averaged to a single channel within each of the ROIs, generating an 11 × 11 matrix. A one-sample *t*-test was then performed across subjects for significant differences in dPTE across all possible pairs of ROIs ($p < 0.05$ and FDR corrected) (Singh and Dan, 2006). This test was used to determine directionality of significant information flow between each pair of ROIs by testing against the null hypothesis of no net flow ($dPTE_{XY} = 0.5$), where positive *t*-values indicated net information flow from ROI_1 to ROI_2 and conversely for negative *t*-values. Topographic images for DC were generated using BrainNet Viewer software (Xia et al., 2013) for each frequency band at each period per subject group.

Static FC (SFC) and FC Variability (FCV) Analysis

For each subject's data set, a static functional connectivity (SFC) matrix was generated by computing the Pearson's correlation coefficient (*r*) between the ROI-averaged channels per brain hemisphere (Li et al., 2015; Fong et al., 2019). Subsequently, dynamic functional connectivity (DFC) between pairs of ROIs was calculated using a sliding-window correlation (SWC) (Allen et al., 2014; Li et al., 2015; Fong et al., 2019). In this study, a 60 s time window was selected and shifted in 1 s increments along the entire time course as described in prior fNIRS studies (Hutchison et al., 2013; Li et al., 2015; Cao et al., 2018a). The FC within each time window was also calculated for each pair of ROIs via the Pearson's correlation coefficient. Then the functional connectivity variability (FCV) was calculated as the standard deviation of the correlation coefficient along time (Fong et al., 2019). For group analysis, the FCV of each correlation coefficient for each ROI was averaged across subjects in each group.

RESULTS

Relative Changes in MVC Over Time

The loss of handgrip force, expressed as the relative reduction in %MVC compared to the pre-task maximum value, was quantified as a proxy measure of fatigue (**Figure 2**). Force data was first averaged over 12 blocks for the 0–2 min period. An independent *t*-test, satisfying normality and equal variance assumptions, determined that there was no significant ($p > 0.05$) difference between groups (not shown), indicating subjects did not fatigue within this initial period. Force data were then averaged over 60 blocks resulting in two periods (0–10 min and 11–20 min) across the 120 contractions. As these data periods did not meet assumptions for independent *t*-tests, data was analyzed using the non-parametric Mann-Whitney *U* test (Marques, 2007). The absolute force produced by active subjects was significantly higher than inactive subjects at 0–10 min ($p < 0.01$) and 11–20 min ($p < 0.001$). Lastly, %MVC force decreased significantly between periods in both active ($p < 0.001$) and inactive ($p < 0.01$) subjects.

Frequency Band Analysis With Information Flow and Directional Connectivity

The net information flow among the eleven ROIs (lPF, rFP, lDLPFC, rDLPFC, Broca's, lPMC, rPMC, lM1/S1, rM1/S1, lSAC, and rSAC) during the three task periods (rest, 0–10 min, and 11–20 min) was computed by dPTE analysis for the endogenic, neurogenic, and myogenic hemodynamic frequency bands and plotted in color-coded maps. In these maps, blue ROIs indicate net incoming information flow (the channels at those cortical locations are a "sink") and red ROIs indicate net outgoing information flow (these channels are "sources"). Green ROIs indicate no statistically significant net flow.

The directionality of information flow (DC) was averaged within each of the eleven ROIs, so as to enable averaged, region-specific dPTE values that were amenable to statistical comparisons. The latter yielded differing spatial DC patterns between inactive and active subjects that are presented here for each hemodynamic frequency band. The unidirectional arrows originate from a source ROI and end in a sink ROI. Black arrows correspond to a significance of $p < 0.05$ and red arrows denote a significance of $p < 0.01$.

All one-sample *t*-tests satisfied normality assumptions for dPTE and DC analyses. While physiological interferences were minimized using band-pass filters and PCA filter for each frequency band, global mean removal was also applied, and results were effectively indistinguishable between the methods. A *post hoc* power analysis with $\alpha = 0.05$ yielded a statistical power of 80% for both groups.

Endogenic Frequency Band

Maps of net information flow in the endogenic frequency band are shown in **Figures 3A–C** (**Supplementary Figures S1A–C** for ΔHb) for inactive subjects and **Figures 3D–F** (**Supplementary Figures S1D–F** for ΔHb) for active subjects. Outgoing information (sources) differed between the groups at all time periods. Inactive subjects had a statistically significant sink at lM1/S1, whereas active subjects had a dPTE sink at lFP at rest in the endogenic frequency band (**Figures 3A,D**). For inactive subjects, rFP, lDLPFC, rDLPFC, and Broca's area were statistically significant sinks initially (**Figure 3B**) that later became more strongly unilateral at rFP, rDLPFC, and rPMC as the task progressed (**Figure 3C**). Additionally, inactive subjects

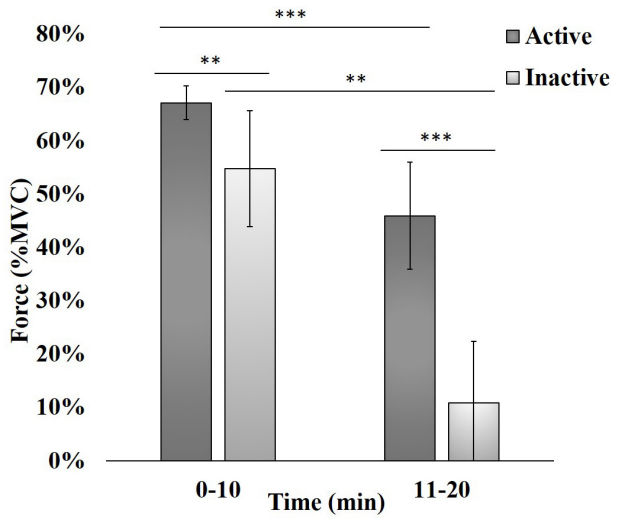

FIGURE 2 | Force produced during intermittent handgrip contractions while physically inactive and active subjects attempted to attain 100% MVC. Each bar represents an average of 60 consecutive trials, expressed as the Mean (bar height) ± Standard Error to the Mean (SEM; error bar). $^{**}p < 0.01$, $^{***}p < 0.001$.

had a statistically significant dPTE source at lPMC (**Figure 3C**). In contrast, active subjects had a significant sink at lDLPFC and rSAC initially (**Figure 3E**) that changed to lFP, rFP, and rDLPFC as the task progressed (**Figure 3F**).

In the endogenic frequency band, inactive subjects had notably more ROI pairs with significant DC than active subjects at rest (inactive: 6, active: 0), in the 0–10 min (inactive: 1, active: 0), and the 11–20 min intervals of the task (inactive: 8, active: 4) (**Figures 3G–L** and **Supplementary Figures S1G–L** for ΔHb). During the task, inactive subjects initially had statistically significant DC form rPMC to Broca's area (**Figure 3H**). However, as fatigue worsened in the second half of the task lM1/S1 became the primary functional area source connecting to bilateral FP, bilateral PFC, Broca's area, rPMC, and rSAC (**Figure 3I**). Additionally, inactive subjects had two DC pairs in the 11–20 min period (lM1/S1 to rFP and lM1/S1 to rSAC) that had higher statistical significance ($p < 0.01$) (**Figure 3I**).

In contrast, active subjects had an absence of significant net information flow between ROIs during rest and the 0–10 min periods (**Figures 3J,K**) and only exhibited significant net information flow between a few functional regions (from lPMC, rM1/S1, and rSAC to rDLPFC and rM1/S1 to lFP) in the 11–20 min period (**Figure 3L**).

Neurogenic Frequency Band

Information flow in the neurogenic frequency band is shown in **Figures 4A–C** (**Supplementary Figures S2A–C** for ΔHb) for inactive subjects and **Figures 4D–F** (**Supplementary Figures S2D–F** for ΔHb) for active subjects. At rest, inactive and active subject had dPTE sinks at the same ROIs, lFP and rFP (**Figures 4A,D**). These dPTE sinks persisted during the handgrip task while the number of dPTE sources increased between the 0–10 min and 11–20 min periods in both groups. In particular, inactive subjects had one dPTE source at rPMC in the first task period and none in the second period (**Figures 4B,C**). For active subjects, there were two sources at rPMC and lM1/S1 in the first period with two additional sources, at rDLPFC and lPMC, presenting in the second period (**Figures 4E,F**).

At the neurogenic frequency band, inactive subjects had more regions with significant net information flow than active subjects at resting state (inactive: 23, active: 10). However, active subjects had more significant regions with net information flow during the task at 0–10 min (inactive: 17, active: 25), and 11–20 min (inactive: 20, active: 26) (**Figures 4G–L** and **Supplementary Figures S2G–L** ΔHb). Additionally, both groups had several directed connections with higher statistical significance ($p < 0.01$) at the first half (inactive: 7, active: 3) and the second half (inactive: 7, active: 5) of the task. All but one of these connections were directed to the FP regions bilaterally (**Figures 4G–L**). At rest, inactive subjects had most ROIs connected to the FP regions bilateral (**Figure 4G**) whereas, active subjects' statistically significant ROIs primarily connected to the lFP (**Figure 4J**). During the task, inactive subjects' significant directional connections were more unilateral, favoring the contralateral hemisphere and primarily directed to the FP regions bilaterally (**Figures 4H,I**). In contrast, active subjects had more bilateral connections which were largely directed to the rFP, lFP, lDLPFC, and Broca's area (**Figures 4K,L**).

Myogenic Frequency Band

Information flow in the myogenic frequency band is shown in **Figures 5A–C** (**Supplementary Figures S3A–C** for ΔHb) for inactive subjects and **Figures 5D–F** (**Supplementary Figures S3D–F** for ΔHb) for active subjects for each task period. Notably, the myogenic frequency had no significant sources for both groups (**Figures 5A–F**). At rest, both groups had significant sinks at lFP, rFP, and lM1/S1 (**Figures 5A,D**). During the task, the number of ROIs with sinks increased from 9 to 10 in inactive subjects (**Figures 5B,C**) and from 8 to 10 in active subjects (**Figures 5E,F**).

At the myogenic frequency band, inactive subjects had more regions with significant net information flow than active subjects during the resting state (inactive: 21, active: 11), the 0–10 min (inactive: 5, active: 1), and the 11–20 min (inactive: 7, active: 1) task intervals (**Figures 5G–L** and **Supplementary Figures S3G–L** for ΔHb). During resting state, inactive subjects had five very significant ($p < 0.01$) directed connections originating from the rDLPFC, Broca's area, and rSAC, all ending at the FP regions bilaterally (**Figure 5G**). In contrast, active subjects had only one very significant directed connection from rM1/S1 to lM1/S1 (**Figure 5J**). During the task, inactive subjects initially had net information outflow from M1/S1 bilaterally (**Figure 5H**), however, as the task progressed surrounding ROIs such as rDLPFC, and lSAC became information outflow sources directed at the lPMC and lM1/S1 (**Figure 5I**). In contrast, active subjects demonstrated lM1/S1 as a net information outflow to lPMC during the first half of the task (**Figure 5K**) but later transitioned as a net informational inflow from lSAC at the second half of the task (**Figure 5L**).

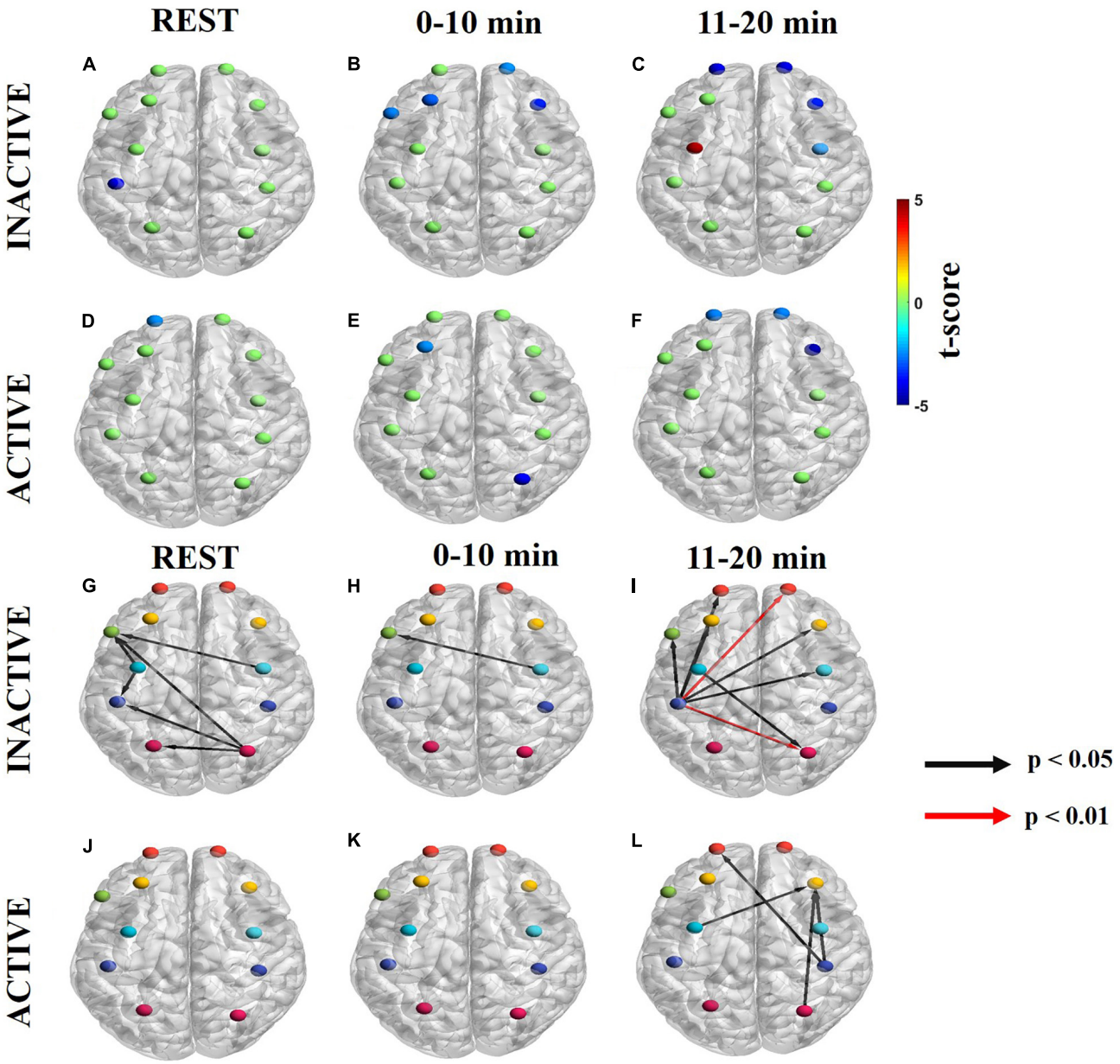

FIGURE 3 | Significant dPTE and DC in the endogenic frequency band for inactive and active subjects during the handgrip task for ΔHbO. Directed PTE *t*-values for each ROI as a color-coded map for inactive subjects **(A–C)** and active subjects **(D–F)**. Hot (yellow-reds) and cold (light blue-dark blue) colors indicate information outflow and inflow, respectively. Arrows indicate statistically significant information flow between functional regions for inactive **(G–I)** and active subjects **(J–L)**. Black arrows ($p < 0.05$); Red arrows ($p < 0.01$). Eleven regions of interest (ROIs) were mapped: left and right frontopolar (lFP; rFP) (red), left and right pre-frontal cortex (lDLPFC; rDLPFC) (yellow), Broca's area (green), left and right pre-motor cortex (lPMC; rPMC) (light blue), left and right primary motor and sensory cortical (lM1/S1; rM1/S1) areas (purple), and left and right sensory association cortex (lSAC; rSAC) (pink).

Correlations Between SFC and FCV

Correlation patterns between SFC and FCV were also explored for each frequency band and subject group, before and during the handgrip task (**Figure 6**). A representative pattern comparison between group-level SFC and FCV matrices and the resulting linear correlation plot are shown in **Figure 6A** as an example of how the subsequent correlation plots were generated. Correlation plots for endogenic (top), neurogenic (middle), and myogenic (bottom) frequency bands are shown for inactive subjects in **Figure 6B** and active subjects in **Figure 6C**.

In the endogenic frequency band, quantitative correlation analysis revealed a strongly significant ($p < 0.001$) negative correlation between SFC and FCV at resting state and for the 11–20 min task interval for inactive subjects (**Figure 6B**, top row). Similarly, strong negative correlations were found for all task periods for active subjects (**Figure 6C**, top row). The correlation

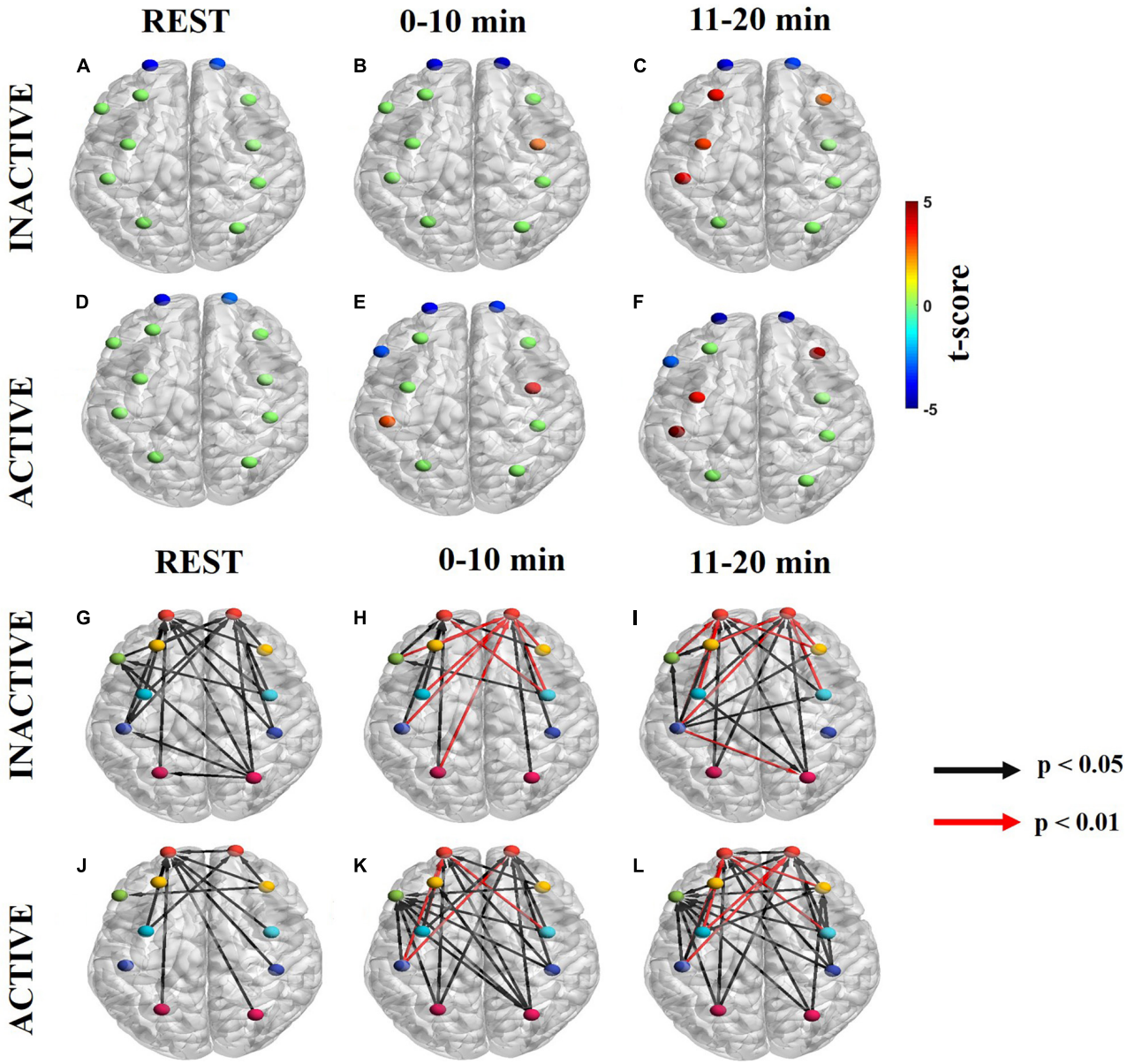

FIGURE 4 | Significant dPTE and DC in the neurogenic frequency band for inactive and active subjects during the handgrip task for ΔHbO. Directed PTE *t*-values for each ROI as a color-coded map for inactive subjects **(A–C)** and active subjects **(D–F)**. Hot (yellow-reds) and cold (light blue-dark blue) colors indicate information outflow and inflow, respectively. Arrows indicate statistically significant information flow between functional regions for inactive **(G–I)** and active subjects **(J–L)**. Black arrows ($p < 0.05$); Red arrows ($p < 0.01$). Eleven regions of interest (ROIs) were mapped: left and right frontopolar (lFP; rFP) (red), left and right pre-frontal cortex (lDLPFC; rDLPFC) (yellow), Broca's area (green), left and right pre-motor cortex (lPMC; rPMC) (light blue), left and right primary motor and sensory cortical (lM1/S1; rM1/S1) areas (purple), and left and right sensory association cortex (lSAC; rSAC) (pink).

between SFC and FCV at 0–10 min for inactive subjects was not significant but was marginally close to the significance criterion of $p = 0.05$ ($p = 0.07$).

Correlation analysis was significant ($p < 0.001$) in the neurogenic frequency band both for inactive (**Figure 6B**, middle row) and active subjects at 0–10 min period only (**Figure 6C**, middle row). Pearson's coefficient (r) values mostly indicated positive correlations, except for active subjects at resting state. Generally, the correlation trends were positive in contrast to the endogenic frequency band.

Quantitative correlation analysis at the myogenic frequency revealed significant ($p < 0.01$) negative correlation between SFC and FCV at 1–10 min and 11–20 min for inactive subjects (**Figure 6B**, bottom row) and at the 1–10 min period for active subjects (**Figure 6C**, bottom row). The correlation at the rest period for inactive subjects missed significance marginally ($p = 0.06$). The negative correlation trend in

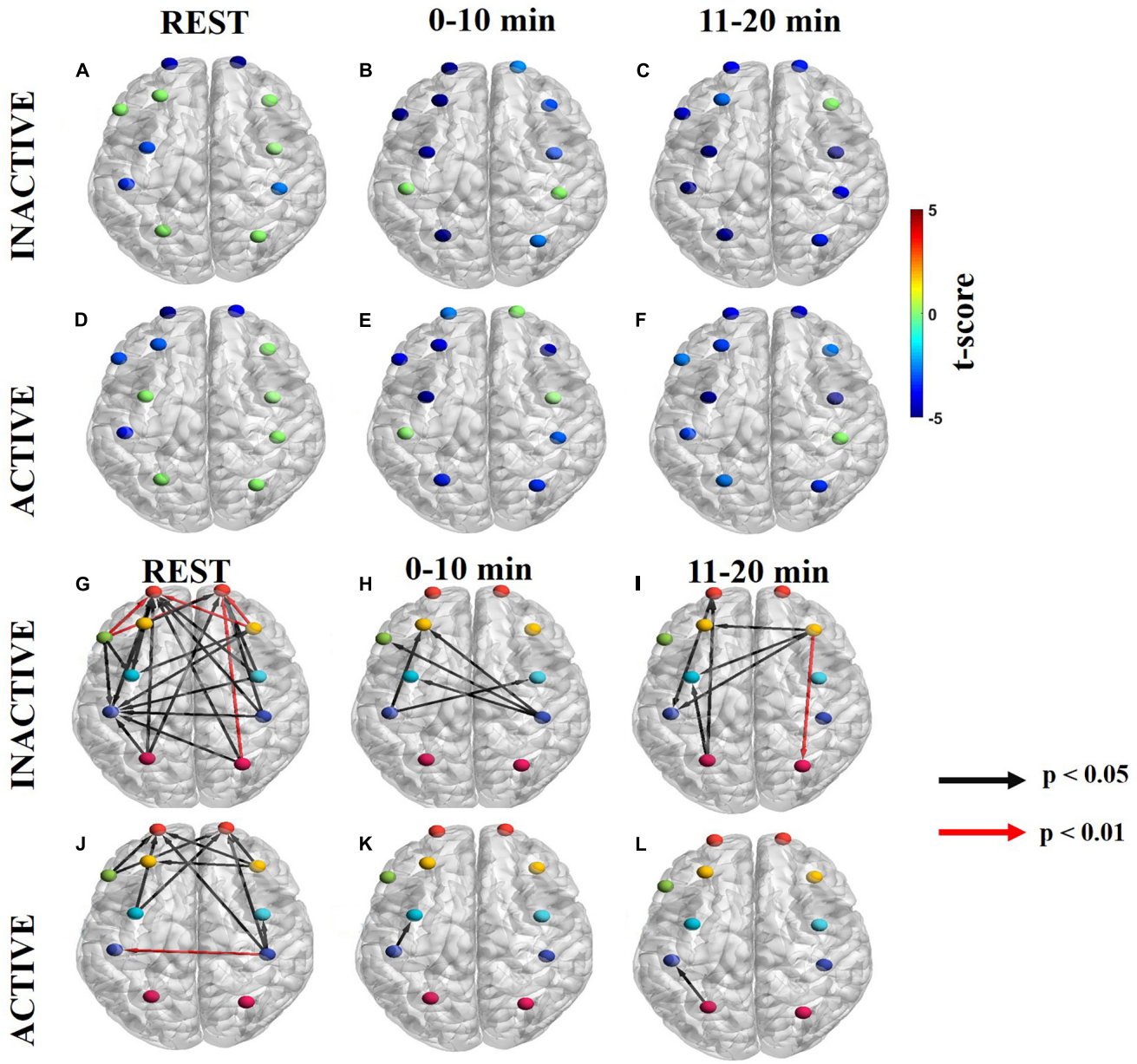

FIGURE 5 | Significant dPTE and DC in the myogenic frequency band for inactive and active subjects during the handgrip task for ΔHbO. Directed PTE *t*-values for each ROI as a color-coded map for inactive subjects **(A–C)** and active subjects **(D–F)**. Hot (yellow-reds) and cold (light blue-dark blue) colors indicate information outflow and inflow, respectively. Arrows indicate statistically significant information flow between functional regions for inactive **(G–I)** and active subjects **(J–L)**. Black arrows ($p < 0.05$); Red arrows ($p < 0.01$). Eleven regions of interest (ROIs) were mapped: left and right frontopolar (lFP; rFP) (red), left and right pre-frontal cortex (lDLPFC; rDLPFC) (yellow), Broca's area (green), left and right pre-motor cortex (lPMC; rPMC) (light blue), left and right primary motor and sensory cortical (lM1/S1; rM1/S1) areas (purple), and left and right sensory association cortex (lSAC; rSAC) (pink).

the myogenic frequency band was similar to that in the endogenic frequency band.

Overall, these plots illustrate a negative correlation trend in the endogenic and myogenic frequency bands and a positive correlation in the neurogenic frequency band, regardless of the physical activity levels of subjects. However, absolute *z*-values for inactive subjects were greater than active subjects for each frequency band, for both the positive and the negative trends, except for the 0–10 min and 11–20 min period in the endogenic frequency band.

DISCUSSION

Cerebral autoregulation is a multifactorial process of maintaining cerebral perfusion and brain tissue oxygenation against changes

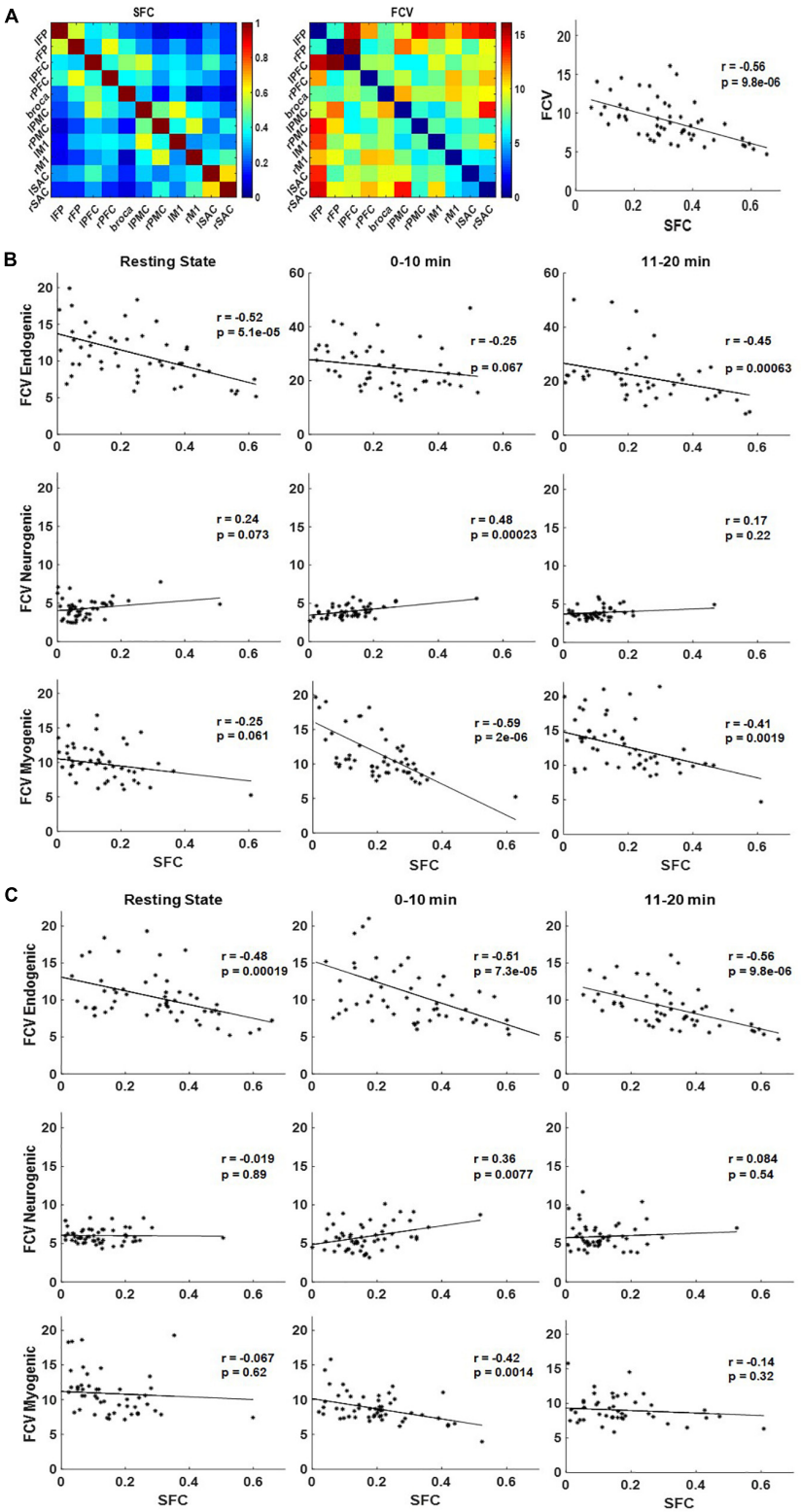

FIGURE 6 | Pattern comparison between static functional connectivity (SFC) and functional connectivity variability (FCV) at endogenic, neurogenic, and myogenic frequencies for inactive and active subjects during the handgrip task. **(A)** A representative example of the group-averaged SFC matrix (left), the FCV matrix (middle), and the linear relationship between them (right). **(B)** Correlation plots between SFC and FCV for inactive subjects and **(C)** active subjects at endogenic (top), neurogenic (middle), and myogenic (bottom) frequencies during resting state (left), 0–10 min (middle), and 11–20 min (right) of the handgrip task.

in arterial blood pressure that is challenged during exercise (Tzeng and Ainslie, 2014). The brain maintains relatively constant regional CBF (rCBF) through coordinated effort of endogenic, neurogenic and myogenic mechanisms that are known to be active in different hemodynamic frequency bands (Cipolla, 2009; Peterson et al., 2011; Tzeng and Ainslie, 2014; Peri-Okonny et al., 2015). The correspondence of each of these physiological mechanisms to distinct hemodynamic frequency bands enabled us to examine in this work how different fNIRS metrics could provide information about the interplay of these neurovascular coupling mechanisms during a fatiguing handgrip task.

Firstly, patterns of net information flow quantified by total dPTE-per-ROI (Hillebrand et al., 2016), calculated as the sum of all pair-wise contributions to each ROI, revealed which ROIs contributed to regulation (information sources) versus which were being regulated (information sinks) during the handgrip task (Huo et al., 2018). As the directionality of dominant contributions to net information flow is not evident in the total dPTE-per-ROI metric, the DC between ROIs was quantified also. The unidirectional connections indicate that one of the two ROIs serves as a functional source of coupling with a regulatory role over the connected sink region (Huo et al., 2018). While results for ΔHbO only were discussed above in detail, the corresponding ΔHb results were examined as well (**Supplementary Material**). In all, ΔHb signals yielded smaller dPTE values and fewer significant DC channel pairs due to smaller amplitudes and lower signal-to-noise ratio compared to ΔHbO signals, although the general trends were similar.

Furthermore, frequency band-based analyses were applied here to study the relationship between SFC, which measures coupling strength between ROIs and is known to increase with task performance (Jiang et al., 2012), and FCV, which reflects changes in spontaneous dynamic neural activity patterns between ROIs and relates to resource availability during demanding tasks (Li et al., 2015; Fong et al., 2019). The relationship between SFC and FCV was studied here for each hemodynamic frequency band to help understand their interdependence in the context of maintaining handgrip performance in the presence of fatigue. The latter was evident in the decline in %MVC (**Figure 2**) during a handgrip task. Our results showed differences between subject groups across all fNIRS metrics and hemodynamic frequency bands, suggesting that active subjects used different cortical activity strategies compared to inactive ones to maintain handgrip performance with increasing fatigue.

Endogenic Frequency Band

Subjects with different physical activity levels displayed different dPTE and DC patterns in the endogenic (0.003–0.02 Hz) frequency band (**Figure 3**). Physical exercise increases CBF, as a result of elevated shear stress in the arterial walls which subsequently facilitates endogenic involvement in the regulation of rCBF (Nosarev et al., 2015). The cerebrovascular endothelium releases vasoactive mediators, including nitric oxide (NO) and endothelium-derived hyperpolarizing factor, diffusing into vascular smooth muscle, which contribute to CBF regulation through vasodilation (Cipolla, 2009; Peterson et al., 2011).

At rest, the dPTE and DC patterns together resemble the default mode network (DMN) for inactive subjects with either incoming (sinks) and outgoing (source) information flow at PMC, lM1/S1, Broca's area, and rSAC. The DMN is highly engaged during rest and is involved in the emergence of spontaneous thought (van den Heuvel and Hulshoff Pol, 2010; Doucet et al., 2011, 2012; Raichlen et al., 2016). The DMN has previously been observed in the endogenic frequency for dPTE analysis (Cao et al., 2018b). and endogenic frequency specific FC maps (Bandettini and Bullmore, 2008). In this work active subjects did not exhibit any resting state dPTE network (indicating no net directional information flows) in the endogenic frequency band.

The handgrip task evoked significant dPTE and DC in the PFC and motor cortex in the endogenic frequency band, in particular for the inactive subjects. There was notable silencing of the ROIs associated with the DMN in dPTE and DC patterns once the task began, analogous to the DMN deactivation seen during tasks (Raichlen et al., 2016). For inactive subjects, the initial connection was from lPMC to Broca's area. However, as fatigue increased the source became more unilateral in the left hemisphere at the motor cortex (lPMC and lM1/S1) and connected more to sinks in the PFC (FP and DLPFC). These observations suggest that motor regions (PMC and lM1/S1), which are involved in motor preparation and execution respectively (Frackowiak, 2004) regulated the DLPFC, which is associated with cognitive activity, planning, motivation during goal-driven tasks, and inhibiting/excitatory control during exercise (Semendeferi et al., 2001; Frackowiak, 2004; Marek and Dosenbach, 2018). Inactive subjects had notably more significant dPTE and DC than active subjects in the endogenic frequency band particularly during the first period. We speculate that active subjects had limited dPTE (lDLPFC and rSAC) and no significant DC until the second half of the task because regular exercise training enhances performance and the physically active subjects would presumably be more efficient earlier in the exercise task.

Strength of SFC is known to correlate with performance and increases with difficulty or effort in prior neuroimaging studies (Jiang et al., 2012; Rhee and Mehta, 2018). On the other hand, FCV signifies a cortical region that dynamically changes its connectivity strength with other regions so as to tap into more neuronal network resources while already established connections may fade in strength as fatigue sets in Fong et al. (2019). In the endogenic frequency, there is a negative correlation between SFC and FCV both for inactive (**Figure 6B**, top row) and active subjects (**Figure 6C**, top row). Several prior FCV studies have also found similarly negative correlations between these two metrics (Allen et al., 2014; Li et al., 2015; Fong et al., 2019). It has been suggested that task performance may depend on more stable (less variable) connectivity strength between regions involved in the regulation of the task (Fong et al., 2019). The more significant *r*-value (which indicate less variable connectivity) and lower %MCV reduction seen in active subjects (higher performance) compared to inactive ones is consistent with this interpretation.

Overall, the endogenic frequency band may be related to fatigue levels, meaning that higher fatigue would result in more endogenic regulation. We speculate that active subjects likely did

not experience as much fatigue as inactive ones, as suggested by **Figure 2**, and supported by the difference in the amount of dPTE and DC between ROIs seen in **Figures 3F,L**.

Neurogenic Frequency Band

Subjects with different physical activity levels displayed different dPTE and DC patterns in the neurogenic (0.02–0.04 Hz) frequency band. The neurogenic mechanism integrates the high metabolic demands of neuronal tissue during a task with the neurovascular unit (endothelial cells, perivascular nerves, and astrocytes abducted to cortical microvessels) to release vasoactive neurotransmitters as a means of regulating rCBF based on neuronal demands (Cipolla, 2009; Peterson et al., 2011).

At rest, the dPTE and DC patterns together resemble the DMN and fronto-parietal network (FPN) for inactive and active subjects with either incoming (sinks) and outgoing (source) information flow at PMC and SAC, which integrates sensory information and forms connections between sensory and motor areas, for the DMN and FP and SAC for the FPN. The FPN is highly integrated with other brain networks, like the DMN and motor network (MN), and is involved in coordinating behavior in a rapid, accurate, and flexible goal-driven manner (Doucet et al., 2011, 2012; Marek and Dosenbach, 2018), including planning of motor control (Raichlen et al., 2016). Our FPN similarity findings are supported by a neuroimaging study indicating that endurance athletes had more significant FC in the FPN than non-athletes, although this fMRI study focused on a frequency range that mostly included the neurogenic frequency band (Raichlen et al., 2016).

The handgrip task evoked significant dPTE and DC globally in the neurogenic frequency band for both active and inactive subjects. During the handgrip task, the FPN was still engaged as evident by dPTE and DC patterns. In FC studies, the FPN is known to activate during motor tasks, such as the fatiguing handgrip in this study (Urquhart et al., 2019), to provide a functional back-bone for rapid and flexible modulation of other brain networks, such as the MN (Marek and Dosenbach, 2018). Inactive and active subjects also had similar, persistent dPTE and DC patterns during the handgrip task although, active subjects had more significant dPTE ROIs and DC connections. The neurogenic frequency band reflects the cortical resources available during the task, thus suggesting that active subjects have more cortical resources and exercise-altered neuroplasticity than inactive subjects (Mueller et al., 2017). Lastly, in the neurogenic frequency band, there were greater numbers of significant DC connections during the task than at rest, for all subjects, similar to prior neuroimaging studies (Liu et al., 2003, 2007; Benwell et al., 2005; White et al., 2009; Mehta and Shortz, 2014; Zhiguo et al., 2016; Rhee and Mehta, 2018). During the handgrip task itself, the FP was a common functional sink in all subjects, but active subjects also involved Broca's area. The FP region is associated with planning, cognitive branching, and monitoring importance of competing goal-driven tasks (Semendeferi et al., 2001; Frackowiak, 2004; Mansouri et al., 2017; Marek and Dosenbach, 2018). and Broca's area is involved with producing language and inner speech (Perrone-Bertolotti et al., 2014). The latter is likely related to the silent expression of conscious thought to oneself during handgrip task performance in our study. In our prior work, we demonstrated that active subjects reported utilizing self-talk to motivate themselves during the task (Urquhart et al., 2019).

The neurogenic frequency band was the only frequency band to have a positive correlation between SFC and FCV for both inactive (**Figure 6B**, middle row) and active (**Figure 6C**, middle row) subjects. Prior neuroimaging studies also noted a positive correlation between exercise duration and increased hemodynamic signal variance (Benwell et al., 2005), and task performance and increasing neurogenic signal (Bosch et al., 2017). The non-significant *r*-value (which indicate more variable connectivity) and the %MCV reduction over time suggest that subjects were likely trying to tap into more cortical networks as they gradually fatigued. The significant *r*-values seen initially (0–10 min) in both groups support the notion that task performance may depend on more stable connectivity strength. As fatigue increased (11–20 min) both subject groups had more variable connectivity (i.e., non-significant *r*-value), possibly indicating an effort to recruit previously untapped cortical network resources.

Overall the neurogenic frequency band reflects the cortical resources available during the handgrip task (Boyle et al., 2008). Similar to FC, as physical effort for the task increased, the number of dPTE ROIs and DC connections increased as well before reducing again as fatigue increased. We hypothesize that active subjects had more dPTE ROIs and DC connections than inactive ones because they could recruit more cortical network resources, as enabled by exercise-related neuroplasticity.

Myogenic Frequency Band

Subjects with different physical activity levels displayed different dPTE and DC patterns in the myogenic (0.04–0.15 Hz) frequency band. The myogenic regulatory mechanism plays an important role in stabilizing rCBF under differing physiological conditions, such as exercise (Cipolla, 2009). Exercise causes increased blood pressure resulting in depolarization of smooth muscle cell membrane and calcium influx and initiating the myogenic response, resulting in smooth muscles constricting during increased pressure (Cipolla, 2009; Peterson et al., 2011).

The resting state networks appeared to differ between inactive and active subjects in the myogenic frequency band based on dPTE and DC patterns. Inactive subjects' functional sinks at FP and most significant DC pair-wise connections (red arrows) resemble the FPN. As previously mentioned, the FPN is often interconnected with other resting state networks, such as the MN to facilitate motor task control (Marek and Dosenbach, 2018). In contrast, the active subjects' resting network was more reflective of the MN, with dPTE at M1/S1 and the most significant (red arrows) DC occurring between the M1/S1 areas as well as between the PMC areas bilaterally. The MN is a part of an extrinsic system of resting state networks that is typically driven by external sensory stimulation (Doucet et al., 2011). Active subjects appeared to have more active MN connectivity at rest than inactive subjects.

Inactive and active subjects also had different dPTE and DC patterns during the handgrip task in the myogenic frequency band. For inactive subjects, the lDLPFC was regulated by the

M1/S1 during the first half (0–10 min). The M1/S1 sources are involved in motor execution, in particular during hand movement (Anwar et al., 2016; Jiang et al., 2012, Rhee and Mehta, 2018; Mehta and Shortz, 2014; Bajaj et al., 2014, Michely et al., 2018) which we hypothesize is why the DC connections were directed toward these motor planning sink regions. The DC to lDLPFC is interesting due to its association with an approach reaction toward a goal (Ernst et al., 2013), such as maintaining task performance. As fatigued worsened for inactive subjects, the DC to lDLPFC was regulated by the rDLPFC instead that, especially during prolonged exercise, in known to purposely inhibit bodily afferences that arise with physical fatigue to preserve mental effort during exercise maintenance (Rupp et al., 2013; Radel et al., 2017).

For active subjects, the lPMC was regulated by the lM1/S1 in the first half of the task. Like the inactive subjects, the lM1/S1 source is directed toward the motor planning associated PMC sink region. As fatigue worsened, the lM1/S1 became a net receiver of information by the lSAC source instead. Similarly, a prior EEG study demonstrated substantial location shifts of focal regions during a fatiguing handgrip task from anterior to posterior regions as a means to maintain task performance (Liu et al., 2007).

Lastly, inactive subjects had nearly significant negative correlations between FCV and SFC at rest and significant negative correlations during the task (**Figure 6B**, bottom row). Many FCV studies have found similarly negative correlations between these two metrics (Allen et al., 2014; Li et al., 2015; Fong et al., 2019). As previously mentioned, the significant *r*-values suggest that improved task performance requires less variable connectivity in the regulation of the task (Fong et al., 2019). While active subjects also exhibited negative correlations between FCV and SFC, these were not significant except during 0–10 min. Active subjects likely experienced lower fatigue levels at 11–20 min, which could contribute to the non-significant *r*-value (**Figure 6C**, bottom row). Mayer waves could also possibly confound myogenic frequency band results due to their overlapping frequency at about 0.1 Hz (Yücel et al., 2016).

Overall the myogenic frequency band reflects the blood supply to the ROIs that is regulated by the arterioles (Cipolla, 2009). We hypothesize that active subjects were able to dilate arterioles more efficiently (Green et al., 2012), and as a result they had improved blood supply to motor areas compared to inactive subjects. The increased availability of resources locally to the ROIs of active subjects controlling the motor task is a possible explanation for the lower number of DC pairs seen for this group relative to inactive subjects, whose ROIs had to recruit more resources from other locations while trying to maintain task performance.

LIMITATIONS

There are several limitations to this study that should be addressed. This study did not incorporate multimodal monitoring of systemic hemodynamics, such as heart rate, blood pressure, and respiration, which could be used as regressors to improve fNIRS signals as well as provide information of the systemic physiology itself (Tachtsidis and Scholkmann, 2016). An alternative method would be to employ short-distance channels (<1 cm), which were not available in the commercial optode holder cap used, to remove by regression hemodynamic fluctuations that co-occur in the cortex as well as superficial scalp layers (Gagnon et al., 2012; Tachtsidis and Scholkmann, 2016). Although we used bandpass filters and PCA to remove physiological inferences and global hemodynamic fluctuations, there exists several other different computational methods including (i) independent component analysis, (ii) singular value decomposition (SVD) and Gaussian kernel smoothing, (iii) statistical correction methods, (iv) wavelet-based methods, or (v) a combination of these methods can be used for removal (Huppert et al., 2009; Jang et al., 2009; Tachtsidis and Scholkmann, 2016; Cao et al., 2018b; Duan et al., 2018; Klein and Kranczioch, 2019). Thus, a quantitative comparison using different global component removal methods is warranted in future studies.

CONCLUSION

This study presents a direct comparison of differences in dynamic fNIRS metrics (dPTE, DC, SFC, FCV) between physically active and inactive subjects as they tried to maintain performance despite fatigue during a maximal effort task. The results of our study demonstrate how physical activity improves the neurovascular regulation mechanisms at the endogenic, neurogenic, and myogenic frequency bands. This modulation allowed for active subjects to maintain higher %MVC longer and delay fatigue onset. In future work we propose to expand these analyses to study subject populations of older age and impaired cardiovascular health.

DATA AVAILABILITY STATEMENT

The datasets generated for this study are available on request to the corresponding author.

ETHICS STATEMENT

The studies involving human participants were reviewed and approved by the Institutional Review Board (IRB) at University of Texas at Arlington. The patients/participants provided their written informed consent to participate in this study.

AUTHOR CONTRIBUTIONS

EU, HL PF, and GA conceptualized and designed the study. EU acquired the data. EU and XW analyzed the data. EU and GA interpreted the results and wrote the manuscript. All authors read and approved the manuscript.

FUNDING

The authors acknowledge the financial support from the National Heart, Lung and Blood Institute with the award number NIH T32 HL134613 for Elizabeth L. Urquhart (née Lyde). The content is solely the responsibility of the authors and does not necessarily represent the official views of the National Institutes of Health.

SUPPLEMENTARY MATERIAL

The Supplementary Material for this article can be found online at: https://www.frontiersin.org/articles/10.3389/fnins.2020.00167/full#supplementary-material

FIGURE S1 | Significant dPTE and DC in the endogenic frequency band for inactive and active subjects during the handgrip task for ΔHb. Directed PTE *t*-values for each ROI as a color-coded map for inactive subjects **(A–C)** and active subjects **(D–F)**. Hot (yellow-reds) and cold (light blue-dark blue) colors indicate information outflow and inflow, respectively. Arrows indicate statistically significant information flow between functional regions for inactive **(G–I)** and active subjects **(J–L)**. Black arrows ($p < 0.05$); Red arrows ($p < 0.01$). Eleven regions of interest (ROIs) were mapped: left and right frontopolar (lFP; rFP) (red), left and right pre-frontal cortex (lDLPFC; rDLPFC) (yellow), Broca's area (green), left and right pre-motor cortex (lPMC; rPMC) (light blue), left and right primary motor and sensory cortical (lM1/S1; rM1/S1) areas (purple), and left and right sensory association cortex (lSAC; rSAC) (pink).

FIGURE S2 | Significant dPTE and DC in the neurogenic frequency band for inactive and active subjects during the handgrip task for ΔHb. Directed PTE *t*-values for each ROI as a color-coded map for inactive subjects **(A–C)** and active subjects **(D–F)**. Hot (yellow-reds) and cold (light blue-dark blue) colors indicate information outflow and inflow, respectively. Arrows indicate statistically significant information flow between functional regions for inactive **(G–I)** and active subjects **(J–L)**. Black arrows ($p < 0.05$); Red arrows ($p < 0.01$). Eleven regions of interest (ROIs) were mapped: left and right frontopolar (lFP; rFP) (red), left and right pre-frontal cortex (lDLPFC; rDLPFC) (yellow), Broca's area (green), left and right pre-motor cortex (lPMC; rPMC) (light blue), left and right primary motor and sensory cortical (lM1/S1; rM1/S1) areas (purple), and left and right sensory association cortex (lSAC; rSAC) (pink).

FIGURE S3 | Significant dPTE and DC in the myogenic frequency band for inactive and active subjects during the handgrip task for ΔHb. Directed PTE *t*-values for each ROI as a color-coded map for inactive subjects **(A–C)** and active subjects **(D–F)**. Hot (yellow-reds) and cold (light blue-dark blue) colors indicate information outflow and inflow, respectively. Arrows indicate statistically significant information flow between functional regions for inactive **(G–I)** and active subjects **(J–L)**. Black arrows ($p < 0.05$); Red arrows ($p < 0.01$). Eleven regions of interest (ROIs) were mapped: left and right frontopolar (lFP; rFP) (red), left and right pre-frontal cortex (lDLPFC; rDLPFC) (yellow), Broca's area (green), left and right pre-motor cortex (lPMC; rPMC) (light blue), left and right primary motor and sensory cortical (lM1/S1; rM1/S1) areas (purple), and left and right sensory association cortex (lSAC; rSAC) (pink).

TABLE S1 | Spatial registration of fNIRS channel positions on a standard brain fMRI atlas. MNI coordinates displayed as mean (SD); r-right contralateral brain hemisphere; l- left ipsilateral brain hemispheres.

TABLE S2 | Preprocessing input parameters used in Homer2.

REFERENCES

Aalkjaer, C., Boedtkjer, D., and Matchkov, V. (2011). Vasomotion - what is currently thought? *Acta Physiol.* 202, 253–269. doi: 10.1111/j.1748-1716.2011.02320.x

Allen, E. A., Damaraju, E., Plis, S. M., Erhardt, E. B., Eichele, T., and Calhoun, V. D. (2014). Tracking whole-brain connectivity dynamics in the resting state. *Cereb. Cortex* 24, 663–676. doi: 10.1093/cercor/bhs352

Andersen, A. V., Simonsen, S. A., Schytz, H. W., and Iversen, H. K. (2018). Assessing low-frequency oscillations in cerebrovascular diseases and related conditions with near-infrared spectroscopy: a plausible method for evaluating cerebral autoregulation? *Neurophotonics* 5:030901. doi: 10.1117/1.NPh.5.3.030901

Anwar, A. R., Muthalib, M., Perrey, S., Galka, A., Granert, O., Wolff, S., et al. (2013). Comparison of causality analysis on simultaneously measured fMRI and NIRS signals during motor tasks. *Conf. Proc. IEEE Eng. Med. Biol. Soc.* 2013, 2628–2631. doi: 10.1109/EMBC.2013.6610079

Anwar, A. R., Muthalib, M., Perrey, S., Galka, A., Granert, O., Wolff, S., et al. (2016). Effective connectivity of cortical sensorimotor networks during finger movement tasks: a simultaneous fNIRS, fMRI, EEG study. *Brain Topogr.* 29, 645–660. doi: 10.1007/s10548-016-0507-1

Bajaj, S., Drake, D., Butler, A. J., and Dhamala, M. (2014). Oscillatory motor network activity during rest and movement: an fNIRS study. *Front. Syst. Neurosci.* 8:13. doi: 10.3389/fnsys.2014.00013

Bandettini, P. A., and Bullmore, E. (2008). Endogenous oscillations and networks in functional magnetic resonance imaging. *Hum. Brain Mapp.* 29, 737–739. doi: 10.1002/hbm.20607

Benwell, N. M., Byrnes, M. L., Mastaglia, F. L., and Thickbroom, G. W. (2005). Primary sensorimotor cortex activation with task-performance after fatiguing hand exercise. *Exp. Brain Res.* 167, 160–164. doi: 10.1007/s00221-005-0013-2

Bosch, B. M., Bringard, A., Ferretti, G., Schwartz, S., and Iglói, K. (2017). Effect of cerebral vasomotion during physical exercise on associative memory, a near-infrared spectroscopy study. *Neurophotonics* 4:041404. doi: 10.1117/1.NPh.4.4.041404

Boyle, P. A., Wilson, R. S., Schneider, J. A., Bienias, J. L., and Bennett, D. A. (2008). Processing resources reduce the effect of Alzheimer pathology on other cognitive systems. *Neurology* 70:1534. doi: 10.1212/01.wnl.0000304345.14212.38

Cao, J., Liu, H., and Alexandrakis, G. (2018a). Modulating the resting-state functional connectivity patterns of language processing areas in the human brain with anodal transcranial direct current stimulation applied over the Broca's area. *Neurophotonics* 5:025002.

Cao, J., Wang, X., Liu, H., and Alexandrakis, G. (2018b). Directional changes in information flow between human brain cortical regions after application of anodal transcranial direct current stimulation (tDCS) over Broca's area. *Biomed. Opt. Express* 9, 5296–5317. doi: 10.1364/BOE.9.005296

Cipolla, M. J. (2009). *The Cerebral Circulation, Morgan and Claypool Life Sciences*. San Rafael CA: Morgan & claypool.

Doucet, G., Naveau, M., Petit, L., Delcroix, N., Zago, L., Crivello, F., et al. (2011). Brain activity at rest: a multiscale hierarchical functional organization. *J. Neurophysiol.* 105, 2753–2763. doi: 10.1152/jn.00895.2010

Doucet, G., Naveau, M., Petit, L., Zago, L., Crivello, F., Jobard, G., et al. (2012). Patterns of hemodynamic low-frequency oscillations in the brain are modulated by the nature of free thought during rest. *Neuroimage* 59, 3194–3200. doi: 10.1016/j.neuroimage.2011.11.059

Duan, L., Zhao, Z., Lin, Y., Wu, X., Luo, Y., and Xu, P. (2018). Wavelet-based method for removing global physiological noise in functional near-infrared spectroscopy. *Biomed. Opt. Express* 9, 3805–3820. doi: 10.1364/BOE.9.003805

Ernst, L. H., Plichta, M. M., Lutz, E., Zesewitz, A. K., Tupak, S. V., Dresler, T., et al. (2013). Prefrontal activation patterns of automatic and regulated approach–avoidance reactions – A functional near-infrared spectroscopy (fNIRS) study. *Cortex* 49, 131–142. doi: 10.1016/j.cortex.2011.09.013

Faul, F., Erdfelder, E., Lang, A. G., and Buchner, A. (2007). G*Power 3: a flexible statistical power analysis program for the social, behavioral, and biomedical sciences. *Behav. Res. Methods* 39, 175–191. doi: 10.3758/bf03193146

Fong, A. H. C., Yoo, K., Rosenberg, M. D., Zhang, S., Li, C. S. R., Scheinost, D., et al. (2019). Dynamic functional connectivity during task performance and rest predicts individual differences in attention across studies. *Neuroimage* 188, 14–25. doi: 10.1016/j.neuroimage.2018.11.057

Frackowiak, R. S. (2004). *Human Brain Function*. Amsterdam: Elsevier.

Gagnon, L., Cooper, R. J., Yücel, M. A., Perdue, K. L., Greve, D. N., and Boas, D. A. (2012). Short separation channel location impacts the performance of short channel regression in NIRS. *Neuroimage* 59, 2518–2528. doi: 10.1016/j.neuroimage.2011.08.095

Green, D. J., Spence, A., Rowley, N., Thijssen, H. D. J., and Naylor, L. H. (2012). Vascular adaptation in athletes: is there an 'athlete's artery'? *Exp. Physiol.* 97, 295–304. doi: 10.1113/expphysiol.2011.058826

Hillebrand, A., Tewarie, P., van Dellen, E., Yu, M., Douw, L., Gouw, A. A., et al. (2016). Direction of information flow in large-scale resting-state networks is frequency-dependent. *Proc. Natl. Acad. Sci. U.S.A.* 113, 3867–38672. doi: 10.1073/pnas.1515657113

Huo, C., Zhang, M., Bu, L., Xu, G., Liu, Y., Li, Z., et al. (2018). Effective connectivity in response to posture changes in elderly subjects as assessed using functional near-infrared spectroscopy. *Front. Hum. Neurosci.* 12:98. doi: 10.3389/fnhum.2018.00098

Huppert, T. J., Diamond, S. G., Franceschini, M. A., and Boas, D. A. (2009). HomER: a review of time-series analysis methods for near-infrared spectroscopy of the brain. *Appl. Opt.* 48, D280–D298.

Hutchison, R. M., Womelsdorf, T., Allen, E. A., Bandettini, P. A., Calhoun, V. D., Corbetta, M., et al. (2013). Dynamic functional connectivity: promise, issues, and interpretations. *Neuroimage* 80, 360–378. doi: 10.1016/j.neuroimage.2013.05.079

Jang, K. E., Tak, S., Jung, J., Jang, J., Jeong, Y., and Ye, Y. C. (2009). Wavelet minimum description length detrending for near-infrared spectroscopy. *J. Biomed. Opt.* 14:034004. doi: 10.1117/1.3127204

Jiang, Z., Wang, X. F., Kisiel-Sajewicz, K., Yan, J. H., and Yue, G. H. (2012). Strengthened functional connectivity in the brain during muscle fatigue. *Neuroimage* 60, 728–737. doi: 10.1016/j.neuroimage.2011.12.013

Klein, F., and Kranczioch, C. (2019). Signal processing in fNIRS: a case for the removal of systemic activity for single trial data. *Front. Hum. Neurosci.* 13:331. doi: 10.3389/fnhum.2019.00331

Kohl, M., Nolte, C., Heekeren, H. R., Horst, S., Scholz, U., Obrig, H., et al. (1998). Determination of the wavelength dependence of the differential pathlength factor from near-infrared pulse signals. *Phys. Med. Biol.* 43, 1771–1782. doi: 10.1088/0031-9155/43/6/028

Li, Z., Liu, H., Liao, X., Xu, J., Liu, W., Tian, F., et al. (2015). Dynamic functional connectivity revealed by resting-state functional near-infrared spectroscopy. *Biomed. Opt. Express* 6, 2337–2352. doi: 10.1364/BOE.6.002337

Li, Z., Zhang, M., Xin, Q., Chen, G., Liu, F., and Li, J. (2012). Spectral analysis of near-infrared spectroscopy signals measured from prefrontal lobe in subjects at risk for stroke. *Med. Phys.* 39, 2179–2185. doi: 10.1118/1.3696363

Liu, J. Z., Lewandowski, B., Karakasis, C., Yao, B., Siemionow, V., Sahgal, V., et al. (2007). Shifting of activation center in the brain during muscle fatigue: an explanation of minimal central fatigue? *Neuroimage* 35, 299–307. doi: 10.1016/j.neuroimage.2006.09.050

Liu, J. Z., Shan, Z. Y., Zhang, L. D., Sahgal, V., Brown, R. W., and Yue, G. H. (2003). Human brain activation during sustained and intermittent submaximal fatigue muscle contractions: an FMRI study. *J. Neurophysiol.* 90, 300–312. doi: 10.1152/jn.00821.2002

Mansouri, F. A., Koechlin, E., Rosa, M. G. P., and Buckley, M. J. (2017). Managing competing goals — a key role for the frontopolar cortex. *Nat. Rev. Neurosci.* 18, 645–657. doi: 10.1038/nrn.2017.111

Marek, S., and Dosenbach, U. F. N. (2018). The frontoparietal network: function, electrophysiology, and importance of individual precision mapping. *Dialog. Clin. Neurosci.* 20, 133–140.

Marques, J. P. (2007). *Applied Statistics Using SPSS, STATISTICA, MATLAB and R.* Berlin: Springer Publishing Company.

Mehta, R. K., and Shortz, A. E. (2014). Obesity-related differences in neural correlates of force control. *Eur. J. Appl. Physiol.* 114, 197–204. doi: 10.1007/s00421-013-2762-0

Michely, J., Volz, L. J., Hoffstaedter, F., Tittgemeyer, M., Eickhoff, S. B., Fink, G. R., et al. (2018). Network connectivity of motor control in the ageing brain. *Neuroimage* 18, 443–455. doi: 10.1016/j.nicl.2018.02.001

Mueller, P. J., Clifford, P. S., Crandall, C. G., Smith, S. A., and Fadel, P. J. (2017). Integration of central and peripheral regulation of the circulation during exercise: acute and chronic adaptations. *Compr. Physiol.* 8, 103–151. doi: 10.1002/cphy.c160040

Myers, J. (2003). Exercise and cardiovascular health. *Circulation* 107, e2–e5.

Naseer, N., and Hong, K. S. (2015). fNIRS-based brain-computer interfaces: a review. *Front. Hum. Neurosci.* 9:3. doi: 10.3389/fnhum.2015.00003

Nosarev, A. V., Smagliy, L. V., Anfinogenova, Y., Popov, S. V., and Kapilevich, L. V. (2015). Exercise and NO production: relevance and implications in the cardiopulmonary system. *Front. Cell Dev. Biol.* 2:73. doi: 10.3389/fcell.2014.00073

Oldag, A., Goertler, M., Bertz, M., Stoppel, C., Heinze, H. J., Kopitzki, K., et al. (2012). Assessment of cortical hemodynamics by multichannel near-infrared spectroscopy in steno-occlusive disease of the middle cerebral artery. *Stroke* 43, 2980–2985. doi: 10.1161/STROKEAHA.112.656710

Oldfield, R. C. (1971). The assessment and analysis of handedness: the Edinburgh inventory. *Neuropsychologia* 9, 97–113. doi: 10.1016/0028-3932(71)90067-4

Peri-Okonny, P., Fu, Q., Zhang, R., and Vongpatanasin, W. (2015). Exercise, the brain, and hypertension. *Curr. Hypertens. Rep* 17:82.

Perrey, S. (2013). Promoting motor function by exercising the brain. *Brain Sci.* 3, 101–122. doi: 10.3390/brainsci3010101

Perrone-Bertolotti, M., Rapin, L., Lachaux, J. P., Baciu, M., and Loevenbruck, H. (2014). What is that little voice inside my head? inner speech phenomenology, its role in cognitive performance, and its relation to self-monitoring. *Behav. Brain Res.* 261, 220–239. doi: 10.1016/j.bbr.2013.12.034

Peterson, E. C., Wang, Z., and Britz, G. (2011). Regulation of cerebral blood flow. *Int. J. Med.* 2011:823525. doi: 10.1155/2011/823525

Querido, J. S., and Sheel, A. W. (2007). Regulation of cerebral blood flow during exercise. *Sports Med.* 37, 765–782. doi: 10.2165/00007256-200737090-00002

Radel, R., Brisswalter, J., and Perrey, S. (2017). Saving mental effort to maintain physical effort: a shift of activity within the prefrontal cortex in anticipation of prolonged exercise. *Cogn. Affect. Behav. Neurosci* 17, 305–314. doi: 10.3758/s13415-016-0480-x

Raichlen, D. A., Bharadwaj, P. K., Fitzhugh, M. C., Haws, K. A., Torre, G. A., Trouard, T. P., et al. (2016). Differences in resting state functional connectivity between young adult endurance athletes and healthy controls. *Front. Hum. Neurosci.* 10:610. doi: 10.3389/fnhum.2016.00610

Rhee, J., and Mehta, R. K. (2018). Functional connectivity during handgrip motor fatigue in older adults is obesity and sex-specific. *Front. Hum. Neurosci.* 12:455. doi: 10.3389/fnhum.2018.00455

Rupp, T., Jubeau, M., Millet, G. Y., Wuyam, B., Levy, P., Verges, S., et al. (2013). Muscle, prefrontal, and motor cortex oxygenation profiles during prolonged fatiguing exercise. *Adv. Exp. Med. Biol.* 789, 149–155. doi: 10.1007/978-1-4614-7411-1_21

Schreiber, T. (2000). Measuring information transfer. *Phys. Rev. Lett.* 85, 461–464. doi: 10.1103/physrevlett.85.461

Semendeferi, K., Armstrong, E., Schleicher, A., Zilles, K., and Van Hoesen, G. W. (2001). Prefrontal cortex in humans and apes: a comparative study of area 10. *Am. J. Phys. Anthropol.* 114, 224–241. doi: 10.1002/1096-8644(200103)114:3<224::aid-ajpa1022>3.0.co;2-i

Shannon, C. E. (1948). A mathematical theory of communication. *Bell Syst. Tech. J.* 27, 379–423.

Shibuya, K., and Kuboyama, N. (2010). Decreased activation in the primary motor cortex area during middle-intensity hand grip exercise to exhaustion in athlete and nonathlete participants. *Percept. Mot. Skills* 111, 19–30. doi: 10.2466/15.25.26.pms.111.4.19-30

Siebenhuehner, F., Lobier, M., Palva, S., and Palva, M. (2013). Phase transfer entropy: a novel measure for effective connectivity among neuronal oscillations. *BMC Neurosci.* 14:305.

Singh, A. K., and Dan, I. (2006). Exploring the false discovery rate in multichannel NIRS. *Neuroimage* 33, 542–549. doi: 10.1016/j.neuroimage.2006.06.047

Singh, A. K., Okamoto, M., Dan, H., Jurcak, V., and Dan, I. (2005). Spatial registration of multichannel multi-subject fNIRS data to MNI space without MRI. *Neuroimage* 27, 842–851. doi: 10.1016/j.neuroimage.2005.05.019

Smielewski, P., Czosnyka, M., Pickard John, D., and Kirkpatrick, P. (1997). Clinical evaluation of near-infrared spectroscopy for testing cerebrovascular reactivity in patients with carotid artery disease. *Stroke* 28, 331–338. doi: 10.1161/01.str.28.2.331

Tachtsidis, I., and Scholkmann, F. (2016). False positives and false negatives in functional near-infrared spectroscopy: issues, challenges, and the way forward. *Neurophotonics* 3:031405. doi: 10.1117/1.NPh.3.3.031405

Tzeng, Y. C., and Ainslie, P. N. (2014). Blood pressure regulation IX: cerebral autoregulation under blood pressure challenges. *Eur. J. Appl. Physiol.* 114, 545–559. doi: 10.1007/s00421-013-2667-y

Urquhart, E. L., Wanniarachchi, H. I., Wang, X., Liu, H., Fadel, P. J., and Alexandrakis, G. (2019). Mapping cortical network effects of fatigue during a handgrip task by functional near-infrared spectroscopy in physically active and inactive subjects. *Neurophotonics* 6:045011. doi: 10.1117/1.NPh.6.4.045011

van den Heuvel, M. P., and Hulshoff Pol, H. E. (2010). Exploring the brain network: a review on resting-state fMRI functional connectivity. *Eur. Neuropsychopharmacol.* 20, 519–534. doi: 10.1016/j.euroneuro.2010.03.008

Visani, E., Canafoglia, L., Gilioli, I., Sebastiano, D. R., Contarino, V. E., Duran, D., et al. (2015). Hemodynamic and EEG time-courses during unilateral hand movement in patients with cortical myoclonus. An EEG-fMRI and EEG-TD-fNIRS Study. *Brain Topogr.* 28, 915–925. doi: 10.1007/s10548-014-0402-6

White, A. T., Lee, J. N., Light, A. R., and Light, K. C. (2009). Brain activation in multiple sclerosis: a BOLD fMRI study of the effects of fatiguing hand exercise. *Mult. Scler.* 15, 580–586. doi: 10.1177/1352458508100034

Xia, M., Wang, J., and He, Y. (2013). BrainNet viewer: a network visualization tool for human brain connectomics. *PLoS One* 8:e68910. doi: 10.1371/journal.pone.0068910

Xu, J., Liu, X., Zhang, J., Li, Z., Wang, X., Fang, F., et al. (2015). FC-NIRS: a functional connectivity analysis tool for near-infrared spectroscopy data. *Biomed. Res. Int.* 2015:248724. doi: 10.1155/2015/248724

Yücel, M. A., Selb, J., Aasted, C. M., Lin, P. Y., Borsook, D., Becerra, L., et al. (2016). Mayer waves reduce the accuracy of estimated hemodynamic response functions in functional near-infrared spectroscopy. *Biomed. Opt. Express* 7, 3078–3088. doi: 10.1364/BOE.7.003078

Zhang, H., Zhang, L., and Zang, Y. (2015). Fluctuation amplitude and local synchronization of brain activity in the ultra-low frequency band: an fMRI investigation of continuous feedback of finger force. *Brain Res.* 1629, 104–112. doi: 10.1016/j.brainres.2015.10.023

Zhiguo, J., Xiao-Feng, W., and Yue, G. H. (2016). Strengthened corticosubcortical functional connectivity during muscle fatigue. *Neural Plast.* 2016:172 6848.

Conflict of Interest: The authors declare that the research was conducted in the absence of any commercial or financial relationships that could be construed as a potential conflict of interest.

Copyright © 2020 Urquhart, Wang, Liu, Fadel and Alexandrakis. This is an open-access article distributed under the terms of the Creative Commons Attribution License (CC BY). The use, distribution or reproduction in other forums is permitted, provided the original author(s) and the copyright owner(s) are credited and that the original publication in this journal is cited, in accordance with accepted academic practice. No use, distribution or reproduction is permitted which does not comply with these terms.

frontiers in Neuroscience

REVIEW
published: 07 April 2020
doi: 10.3389/fnins.2020.00300

Frequency-Domain Techniques for Cerebral and Functional Near-Infrared Spectroscopy

Sergio Fantini and Angelo Sassaroli*

Department of Biomedical Engineering, Tufts University, Medford, MA, United States

This article reviews the basic principles of frequency-domain near-infrared spectroscopy (FD-NIRS), which relies on intensity-modulated light sources and phase-sensitive optical detection, and its non-invasive applications to the brain. The simpler instrumentation and more straightforward data analysis of continuous-wave NIRS (CW-NIRS) accounts for the fact that almost all the current commercial instruments for cerebral NIRS have embraced the CW technique. However, FD-NIRS provides data with richer information content, which complements or exceeds the capabilities of CW-NIRS. One example is the ability of FD-NIRS to measure the absolute optical properties (absorption and reduced scattering coefficients) of tissue, and thus the absolute concentrations of oxyhemoglobin and deoxyhemoglobin in brain tissue. This article reviews the measured values of such optical properties and hemoglobin concentrations reported in the literature for animal models and for the human brain in newborns, infants, children, and adults. We also review the application of FD-NIRS to functional brain studies that focused on slower hemodynamic responses to brain activity (time scale of seconds) and faster optical signals that have been linked to neuronal activation (time scale of 100 ms). Another example of the power of FD-NIRS data is related to the different regions of sensitivity featured by intensity and phase data. We report recent developments that take advantage of this feature to maximize the sensitivity of non-invasive optical signals to brain tissue relative to more superficial extracerebral tissue (scalp, skull, etc.). We contend that this latter capability is a highly appealing quality of FD-NIRS, which complements absolute optical measurements and may result in significant advances in the field of non-invasive optical sensing of the brain.

Keywords: near-infrared spectroscopy, diffuse optical imaging, frequency domain, cerebral hemodynamics, brain activation, fast optical signal, depth sensitivity

OPEN ACCESS

Edited by:
Ning Liu,
Stanford University, United States

Reviewed by:
Robert James Cooper,
University College London, United Kingdom
Felix Scholkmann,
University Hospital Zürich, Switzerland
Thomas D. O'Sullivan,
University of Notre Dame, United States

****Correspondence:***
Sergio Fantini
sergio.fantini@tufts.edu

Specialty section:
This article was submitted to Brain Imaging Methods, a section of the journal Frontiers in Neuroscience

Received: *10 December 2019*
Accepted: *16 March 2020*
Published: *07 April 2020*

Citation:
Fantini S and Sassaroli A (2020) Frequency-Domain Techniques for Cerebral and Functional Near-Infrared Spectroscopy. Front. Neurosci. 14:300. doi: 10.3389/fnins.2020.00300

INTRODUCTION

Diffuse optical imaging, in the near-infrared spectral band (wavelength range: 600–1000 nm), affords non-invasive sensing of the human brain through the intact scalp and skull. The associated instrumentation can be sufficiently lightweight and compact to be applicable at the bedside, in an ambulance, on the field (accident scene, sports venue, battlefield, etc.), in every-day settings, and even worn by subjects while they engage in normal activities. These enormous practical advantages of non-invasive diffuse optical imaging, combined with a strong sensitivity to cerebral hemodynamics and oxygenation, compensate intrinsic limitations in penetration depth and spatial resolution, and account for the large number of applications and the growing interest

in this technology. Several review articles cover a variety of topics in cerebral near-infrared spectroscopy (NIRS), including a historical overview (Ferrari and Quaresima, 2012), description of instrumentation and methodology (Scholkmann et al., 2014b), clinical applications (Irani et al., 2007; Smith, 2011; Obrig, 2014; Yang et al., 2019), brain oximetry in newborns and adults (Wolf et al., 2012; Nielsen, 2014; la Cour et al., 2018), and critical perspectives (Fantini et al., 2018; Quaresima and Ferrari, 2019).

NIRS can be performed using methods in continuous wave (CW) (constant illumination), time domain (TD) (pulsed illumination and time-resolved detection), or frequency domain (FD) (intensity-modulated illumination and phase-resolved detection). Review articles have been devoted to functional NIRS (fNIRS) based on CW methods (Scholkmann et al., 2014b), the most common technique and the one embraced by almost all commercial instruments, and TD methods (Torricelli et al., 2014). No review articles have been previously devoted specifically to cerebral and functional FD-NIRS, and this article intends to fill this gap. However, the general topic of FD-NIRS and its applications to biological tissue are covered in book chapters (Fantini et al., 1997; Cerussi and Tromberg, 2003; Srinivasan et al., 2011; Fantini and Sassaroli, 2016), review and tutorial articles (Chance et al., 1998b; O'Sullivan et al., 2012), and extended sections in biomedical optics books (Tuchin, 2007; Wang and Wu, 2007; Bigio and Fantini, 2016, Chapter 12).

As mentioned, CW techniques are by far the most commonly used, especially in the commercial space; in fact, to the best of our knowledge, while more than ten companies manufacture CW-NIRS systems worldwide, at the time of writing only one company (Hamamatsu Photonics, Japan) manufactures TD-NIRS systems, and only one company (ISS, Inc., United States) manufactures FD-NIRS systems. In the research arena, however, TD-NIRS and FD-NIRS are employed by several groups worldwide.

One question that is investigated in this article is the following: what is the advantage of using FD techniques for cerebral and functional NIRS, given its added instrumental complexity compared to CW-NIRS? This question will be explored by first describing the information content of FD data and how it enriches and differs from that of CW data, and then by describing the way in which FD data have been used in the field of NIRS studies of the brain. Following this description and a review of the literature, we will express our views on the potential role of FD techniques in cerebral and functional NIRS as this field is growing and evolving.

FREQUENCY-DOMAIN NEAR-INFRARED SPECTROSCOPY (FD-NIRS)

The FD-NIRS Data: DC Intensity, AC Amplitude, Phase

The basic idea of FD-NIRS is to use intensity-modulated illumination and phase-sensitive detection. Sinusoidal modulation, or a sinusoidal component of the modulated signal, at a given angular frequency ω is typical considered, so that the time-dependence of the FD-NIRS signal is described by $e^{-i\omega t}$. As a result, the optical signal measured in FD-NIRS consists of an average, or direct current (DC), intensity, and by a phasor described by an amplitude, or alternating current (AC) intensity, and a phase (φ):

$$FD\text{-}NIRS\ signal = DC + AC\ e^{i\varphi} e^{-i\omega t} \quad (1)$$

Typical modulation frequencies employed in the application of FD-NIRS to biological tissue are of the order of 100 MHz. Such a choice is related to the photon mean time of flight (t), which is of the order of nanoseconds for light propagation in typical biological tissues and for distances of centimeters between the illumination and detection points. Since the phase is related to the mean time of flight by the relationship $\varphi \approx \omega t$, a measurable phase of the order of 1 rad requires a modulation frequency [$f = \omega/(2\pi)$] of the order of 100 MHz. Lower modulation frequencies (say, 10 MHz or less) would cause a smaller phase shift that may be close to the limit of phase detectability. On the contrary, higher modulation frequencies (say, 1 GHz or more) would result in smaller AC amplitudes, possibly below the noise level, because of an increasing attenuation of the FD phasor at higher frequencies.

The solution of the diffusion equation in the frequency domain shows that the energy density distribution in turbid media resulting from intensity-modulated illumination can be described in terms of photon-density waves (PDWs) (Fishkin and Gratton, 1993; Tromberg et al., 1993). For a point-source in an infinite medium, PDWs are overdamped spherical waves. For typical optical properties of biological tissue in the near-infrared (absorption coefficient: $\mu_a = 0.1\ cm^{-1}$; reduced scattering coefficient: $\mu_s^{'} = 10\ cm^{-1}$), and for a typical modulation frequency of 100 MHz, the wavelength of the photon density waves is about 25 cm, while its attenuation length (i.e., the distance over which the energy density decreases by a factor of e) is about 0.6 cm. Therefore, PDWs are observable only over a fraction of their wavelength, rendering them analogous to near field waves (Bigio and Fantini, 2016, Section 12.4).

For typical modulation frequencies used in FD-NIRS and for typical optical properties of tissue in the near-infrared, DC intensity and AC amplitude carry a similar information content. For example, they feature a similar decay at increasing distances from the light source (although the AC attenuation is stronger than the DC attenuation), and a similar dependence to localized or homogeneous changes in the optical properties of tissue. However, the AC amplitude offers the practical advantage of being relatively insensitive to room light, or to any non-modulated stray light, so that it is often used instead of DC intensity when data are collected with FD-NIRS instruments.

Instrumentation for FD-NIRS

A review of basic instrumentation aspects of FD-NIRS can be found in Chance et al. (1998b) and in Bigio and Fantini (2016), Section 13.4.2). A description of FD-NIRS instruments used in a variety of applications is beyond the scope of this review article, which specifically focuses on non-invasive brain measurements. The interested reader is referred to the description of FD-NIRS instruments based on homodyne detection (Yang et al.,

1997; Ramanujam et al., 1998; Cheung et al., 2001; Yu et al., 2003), heterodyne detection (Fantini et al., 1995; Ramanujam et al., 1998; McBride et al., 2001; Nissilä et al., 2002, 2005), and on a radiofrequency network analyzer (Pham et al., 2000; Gulsen et al., 2006).

Recent developments in FD-NIRS instrumentation include implementations based on a compact frequency-sweeping circuit board (No et al., 2008), digital heterodyning (Arnesano et al., 2012), direct digital sampling (Roblyer et al., 2013; Zimmermann et al., 2016), frequency division multiplexing (Torjesen et al., 2017; Zhao et al., 2018), CMOS integrated circuitry (Sthalekar and Joyner Koomson, 2013; Yun and Joyner Koomson, 2013), and vertical cavity surface emitting lasers (VCSEL) (Sultan et al., 2013; Kitsmiller et al., 2018).

With regards to commercially available FD-NIRS instruments, they have only been made available by NIM, Inc. (Philadelphia, PA, United States), which operated from 1996 to 2009 (Ferrari and Quaresima, 2012), and by ISS, Inc. (Champaign, IL, United States), which introduced its first FD-NIRS instrument in the late 1990's and now offers FD-NIRS instruments for quantitative spectroscopy, oximetry, and imaging. Most non-invasive FD-NIRS studies of the brain are currently performed with ISS instruments, which operate by parallel multi-channel heterodyne detection and temporal multiplexing of light sources.

Measurement of Absolute Optical Properties With FD-NIRS

Diffusion theory yields analytical expressions of the FD-NIRS signals collected in a semi-infinite geometry. In this case, the light source and the optical detector are located on the tissue boundary, and the tissue is considered to be a uniform, semi-infinite medium, with optical properties described by an absorption coefficient (μ_a) and a reduced scattering coefficient (μ_s'). Such analytical solutions show that one can define functions of measured DC, AC, and phase signals (F_{DC}, F_{AC}, F_φ, respectively) that are linearly dependent on the distance (r) between the source and the detector [as one may derive, for example, from Eqs. (12.33), (12.35), and (12.36) in Bigio and Fantini (2016; Section 12.6)], even though actual measurements of such functions of DC, AC, and phase are also affected by instrumental terms associated with the source and the detector:

$$F_{DC}\left(DC, \rho, \mu_a, \mu_s'\right) = S_{DC}\left(\mu_a, \mu_s'\right)\rho + K_{DC-Source} + K_{DC-Detector} \quad (2)$$

$$F_{AC}\left(AC, \rho, \omega, \mu_a, \mu_s'\right) = S_{AC}\left(\omega, \mu_a, \mu_s'\right)\rho + K_{AC-Source} + K_{AC-Detector} \quad (3)$$

$$F_{\varphi}\left(\varphi, \rho, \omega, \mu_a, \mu_s'\right) = S_{\varphi}\left(\omega, \mu_a, \mu_s'\right)\rho + K_{\varphi-Source} + K_{\varphi-Detector} \quad (4)$$

In Eqs. (2–4), S_{DC}, S_{AC}, S_φ are the slopes of the linear functions of r, and the additive K terms indicate instrumental factors contributed by the source or the detector to the DC, AC, or phase measurement, as indicated by the subscripts. While the K terms are unknown, as they are determined by several instrumental factors as well as by the optical coupling of the source and the detector with tissue, the functions F and the slopes S are known from diffusion theory. The functions F can be approximated with $F_{DC}\left(DC, \rho, \mu_a, \mu_s'\right) = ln(\rho^2 DC)$, $F_{AC}\left(AC, \rho, \mu_a, \mu_s'\right) = ln(\rho^2 AC)$, and $F_\varphi\left(\varphi, \rho, \omega, \mu_a, \mu_s'\right) = \varphi$ if the condition $\rho\sqrt{3\mu_a\mu_s'} \gg 1$ is fulfilled (Fantini et al., 1999). Equations (2–4) provide a basic description of how FD-NIRS can accomplish absolute measurements of optical properties according to different methods that are described below.

Multi-Distance Methods

Multi-distance methods rely on measurements at multiple (at least two) source-detector distances (ρ), typically within a range of 1.5–4 cm. The goal is to measure the slopes [S_{DC}, S_{AC}, S_φ in Eqs. (2–4)], which only depend on the optical properties (and the known modulation frequency) through analytical expressions (at least for homogeneous media) that can be inverted to yield absolute values of μ_a and μ_s'. Two data types (either DC and φ, or AC and φ) are needed to determine the two optical coefficients (Fantini et al., 1994a). The solution of the diffusion equation for semi-infinite media with extrapolated boundary conditions (Haskell et al., 1994) has been used in an iterative approach that accounts for the presence of μ_a and μ_s' on the left-hand side of Eqs. (2–4) (Fantini et al., 1994b). As mentioned above, under the assumption $\rho\sqrt{3\mu_a\mu_s'} \gg 1$ one may use approximate expressions for F_{DC}, F_{AC}, and F_φ (namely $\ln\left(\rho^2 DC\right)$, $\ln\left(\rho^2 AC\right)$, and φ) that offer the advantage that μ_a and μ_s' do not appear on the left-hand side of Eqs. (2–4) (Fantini et al., 1999). We observe that in the case of non-invasive NIRS measurements of the brain (for which μ_a and μ_s' are of the order of 0.1 cm^{-1} and 8 cm^{-1}, respectively) the condition $\rho\sqrt{3\mu_a\mu_s'} \gg 1$ starts becoming fulfilled at source-detector distances ρ of about 2 cm, for which $\rho\sqrt{3\mu_a\mu_s'} \approx 2$, as we verified by comparing the results based on this approximation with those obtained with an iterative approach applied to the full solution of the diffusion equation.

Equations (2–4) clarify the importance of the source-detector configuration used in multi-distance methods. If the configuration uses a single detector and multiple sources placed at different distances from it, then the $K_{Detector}$ terms in Eqs. (2–4) are all independent of ρ (i.e., they are the same for all source-detector pairs) and therefore they cancel out in the determination of the slopes S. By contrast, the K_{Source} terms associated with each of the multiple sources are all different and must somehow be determined by a preliminary calibration on a tissue-like phantom with known optical properties. A reciprocal argument applies to the case of a configuration that uses a single source and multiple detectors (in which case, of course, it is the $K_{Detector}$ terms that are different for each source-detector pair). In a case

where one uses a single source and a single detector, so that multi-distance measurements are accomplished by scanning the source and/or detector relative to each other, no preliminary calibration is needed, since both K_{Source} and $K_{Detector}$ terms are the same for all measurements at different values of ρ (under the assumption that the optical coupling with tissue is kept constant throughout the scanning of source or detector). While this latter approach is the most robust for measurements in a lab setting, especially on tissue-like phantoms (Fantini et al., 1994b; Hallacoglu et al., 2013; Applegate and Roblyer, 2018), it is not practical for *in vivo* measurements, for which either multiple sources or multiple detectors are typically used. It is very important to observe that the multi-distance methods described above require that the optical coupling be the same in the calibration phantom and in tissue (for the method based on multiple sources or multiple detectors), or at the multiple source-detector distances considered (for the methods based on scanning the single source or single detector). This is an issue of high practical importance, and a potential limitation that can be addressed by the multi-distance method described next.

An ingenious, yet simple multi-distance method for absolute measurements of optical properties that does not require any preliminary calibration and does not require assumptions about optical coupling with tissue is the self-calibrating method (Hueber et al., 1999). This method uses two sources and two detectors that are arranged in such a way to generate data described by two sets of Eqs. (2–4) where the K_{Source} and $K_{Detector}$ terms have opposite signs, and thus can be canceled out by taking the average of the two sets of equations (Hueber et al., 1999). This method corrects for both instrumental and optical coupling contributions to the K_{Source} and $K_{Detector}$ terms, thus minimizing potential confounding effects related to instrumental drifts, variable optical coupling with tissue, and motion artifacts.

Single-Distance Methods

One possible approach to absolute measurements with single-distance FD-NIRS data is to perform a preliminary calibration on a phantom with known optical properties to determine the term $K_{Source} + K_{Detector}$ in Eqs. (2–4). While in principle this method is straightforward, it relies on a much more limiting assumption than the calibration methods for multi-distance measurements. While multi-distance calibrations assume that the *relative* optical coupling at the various distances is the same on the calibration phantom and on tissue, the single-distance calibration assumes that the *absolute* optical coupling is the same on phantom and tissue. This is a much stronger assumption that is difficult to realize in practice.

A more robust method for absolute single-distance measurements in the frequency domain is a multi-frequency approach. This method is also based on the solution of the diffusion equation represented by Eqs. (2–4). However, while in multi-distance methods the independent variable is the source-detector distance, ρ (i.e., FD-NIRS data are measured at several source-detector distances), in the multi-frequency approach the independent variable is the modulation frequency, ω (i.e., FD-NIRS data are measured at several modulation frequencies). Usually the modulation frequency is swept from tens to hundreds of MHz, while the source-detector distance is fixed at about 3 cm (Pham et al., 2000; Gulsen et al., 2006). Of course, any dependence on ω of the K_{Source} and $K_{Detector}$ terms must be considered through calibration measurements on a reference phantom or at multiple source-detector distances (Bevilacqua et al., 2000; Pham et al., 2000). Iterative methods based on non-linear least-squares fits have been used for the recovery of the optical properties in the multi-frequency approach (Haskell et al., 1994).

Measurement of Absorption Changes With FD-NIRS

Most non-invasive optical studies of the brain aim to detect absorption changes related to cerebral hemodynamic and oxygenation changes. One possible exception is the measurement of the fast optical signal, which will be presented in Section 3.6. In the case of a homogeneous absorption change, $\Delta\mu_a$, in a semi-infinite medium, one can translate relative changes in the DC Intensity ($\Delta I_{DC}/I_{DC0}$, where we indicate with I_{DC0} the detected DC intensity in a reference condition, say at baseline, and with ΔI_{DC} the intensity change with respect to the reference condition as a result of an absorption change $\Delta\mu_a$) and absolute changes in the phase ($\Delta\varphi$) into the corresponding absorption change as follows (Blaney et al., 2020; Fantini et al., 2020):

$$\Delta\mu_a\left(I_{DC}\right) = -\frac{2\left(1+\rho\sqrt{3\mu_{a0}\mu_{s0}^{'}}\right)}{3\rho^2\mu_{s0}^{'}}\left(\frac{\Delta I_{DC}}{I_{DC0}}\right) \tag{5}$$

$$\Delta\mu_a\left(\varphi\right) = -\left(\frac{1+\frac{\sqrt{\gamma+1}}{\gamma\rho}\sqrt{\frac{2}{3\mu_{a0}\mu_{s0}^{'}}}+\frac{1}{3\mu_{a0}\mu_{s0}^{'}\gamma\rho^2}}{\rho\frac{\sqrt{\gamma-1}}{2\gamma}\sqrt{\frac{3\mu_{s0}^{'}}{2\mu_{a0}}}}\right)\Delta\varphi \tag{6}$$

where the subscripts 0 indicate a reference condition for which $\mu_a = \mu_{a0}$, the changes with respect to this reference condition are $\Delta\mu_a = \mu_a - \mu_{a0}$, $\Delta I_{DC} = I_{DC} - I_{DC0}$, $\Delta\varphi = \varphi - \varphi_0$, and $\gamma = \sqrt{1+\left(\frac{\omega}{c_n\mu_{a0}}\right)^2}$, with c_n speed of light in tissue. Equation (5) represents the modified Beer-Lambert law that is extensively used in CW-NIRS (Delpy et al., 1988; Sassaroli and Fantini, 2004). A correction to Eq. (5) is needed for the AC amplitude of intensity (I_{AC}); such correction can be found in Sassaroli et al. (2019) and Blaney et al. (2020). The effect of localized absorption changes on the DC Intensity (and similarly on the AC amplitude) and on the phase can be described in terms of spatial regions of sensitivity, which are introduced in Section "The Spatial Region of Sensitivity of DC, AC, and Phase."

In the case of high modulation frequencies, such that $\omega \gg c_n\mu_a$, one can show that the term in parenthesis on the right-hand side of Eq. (6) becomes independent of μ_{a0} so that, under the further assumption that scattering is independent on wavelength, the ratio of phase changes at two wavelengths λ_1 and λ_2 equals the ratio of absorption changes at the same wavelengths:

$$\frac{\Delta\varphi\left(\lambda_1\right)}{\Delta\varphi\left(\lambda_2\right)} = \frac{\Delta\mu_a\left(\varphi,\lambda_1\right)}{\Delta\mu_a\left(\varphi,\lambda_2\right)} \tag{7}$$

In the ideal case of a baseline condition that features no absorption (i.e., $\mu_{a0} = 0$), $\Delta\mu_a = \mu_a$ and one can write (Sevick et al., 1991):

$$\frac{\Delta\varphi(\lambda_1)}{\Delta\varphi(\lambda_2)} = \frac{\mu_a(\varphi, \lambda_1)}{\mu_a(\varphi, \lambda_2)} \quad (8)$$

This result may be used to quantify the oxygen saturation of hemoglobin associated with an absorption change from baseline, but the condition $\omega \gg c_n\mu_a$ and the assumption $\mu_{s0}'(\lambda_1) \cong \mu_{s0}'(\lambda_2)$ are somewhat limiting. In fact, for $\mu_a = 0.05\ \mathrm{cm}^{-1}$, one would need to use a modulation frequency [$f = \omega/(2\pi)$] that is much greater than ∼170 MHz.

The Spatial Region of Sensitivity of DC, AC, and Phase

In this section, we describe the spatial region in tissue that is probed in FD-NIRS by a given source-detector pair that is placed on the tissue surface. This description requires several specifications. In fact, (1) different data types (DC, AC, φ) have different regions of sensitivity; (2) the sensitivity itself is not constant within the overall probed volume, so that a given optical perturbation in some portions of the probed region induce stronger changes in the optical signals than others; (3) the region of sensitivity can be different for different kinds of optical contrast, say for an absorption vs. a scattering perturbation. Here, we consider localized changes within a small region (conceptually a point-like region), in either the absorption coefficient or reduced scattering coefficient, in an otherwise optically homogeneous medium. The case of an absorption perturbation has been studied in two opposite regimes: in the limit of infinitely absorbing defects (Feng et al., 1995) and in the limit of infinitesimal changes in the absorption coefficient (Born approximation) (Boas, 1997). The relationship between these two extreme approaches has been recently investigated (Sassaroli et al., 2014). For the case of a scattering perturbation, only the Born approximation has been considered (Martelli et al., 2010). The region of sensitivity for a specific optical measurement with respect to a local change in optical properties also depends on the background optical properties, the shape of tissue and the nature of boundary conditions, and the spatial arrangements of source(s) and detector(s). If we denote with Y any optical measurement (for example, DC, AC, or phase in FD-NIRS), we define a dimensionless sensitivity of such a measurement to a point-like perturbation in a given optical coefficient μ (which may be either μ_a or μ_s') as follows:

$$S_{Y,\mu}(\mathbf{r}) = \frac{\left(\frac{\partial Y}{\partial \mu_{\mathbf{r}}}\right)}{\left(\frac{\partial Y}{\partial \mu}\right)} \quad (9)$$

where the derivative in the numerator is taken with respect to a point-like perturbation at position $\mathbf{r}$ ($\mu_{\mathbf{r}}$), whereas the derivative in the denominator is taken with respect to a uniform change, everywhere in the medium, in the optical property μ .

We have calculated the spatial sensitivity defined in Eq. (9) using diffusion theory for a semi-infinite medium of optical properties $\mu_a = 0.1\ cm^{-1}$ and $\mu_s' = 10\ cm^{-1}$, a single source-detector pair placed on the medium boundary at a source-detector distance of 35 mm, and an optical perturbation 1 mm^3 in size. The modulation frequency was 140 MHz. The results are reported in **Figure 1** for DC intensity (top panels) and phase (bottom panels), and for perturbations in absorption (left panels) or scattering (right panels). Positive sensitivity values at any position $\mathbf{r}$ mean that the considered data changes in the same direction (increase or decrease) as a result of a localized change at $\mathbf{r}$ or a homogeneous change in the considered optical property. **Figure 1** shows that the DC intensity sensitivity (i.e., the sensitivity in CW-NIRS) is always positive, for both absorption and scattering perturbations (with a possible exception of scattering defects near the source or the detector), and has a typical banana shape (Feng et al., 1995). Also, DC intensity sensitivity is especially high for optical perturbations close to the source and the detector. The phase sensitivity is more complex. In the case of absorption perturbations, it features a "double banana," a shallower one of negative sensitivity and a deeper one of positive sensitivity. In the case of scattering perturbations, the phase sensitivity is mostly positive, and also banana shaped, except for small regions close to the source and the detector. Based on **Figure 1**, one can appreciate the different nature of the optical sensitivity of intensity and phase data to absorption and scattering contrast.

USE OF FD-NIRS FOR NON-INVASIVE BRAIN STUDIES

Imaging With Phased Arrays

In Section "The FD-NIRS Data: DC Intensity, AC Amplitude, Phase," we mentioned that the photon-density waves generated by the intensity-modulated light sources in FD-NIRS are near-field waves. They are only measurable within a fraction of a wavelength. This is in contrast with the case of ultrasound imaging, where the ultrasound wavelength in soft tissue is typically of the order of hundreds of microns, and phased arrays are commonly used to focus and steer ultrasound beams. Nevertheless, phased arrays have also been proposed in FD-NIRS to exploit the interference of photon-density waves (Schmitt et al., 1992). In particular, it was proposed to achieve the accurate localization of small defects by scanning the null-plane generated by two light sources that are modulated in opposition of phase (Chance et al., 1993; Chance et al., 1996). This method has been applied to the study of sensorimotor (finger touching) and cognitive (backward spelling) activation in human subjects, demonstrating a high signal-to-noise ratio (>40) of phase measurements, resulting from the large (180 degrees) phase transition at the null plane (Chance et al., 1998a). The phased-array method has been used as a basis for diffuse optical tomography (Intes et al., 2002; Rajan et al., 2008), and it was proposed to implement it by post-processing CW-NIRS data (Liu et al., 2005a,b). The emphasis of the phased array approach is on an improvement of the spatial localization and resolution in diffuse optics. Because such an improvement comes

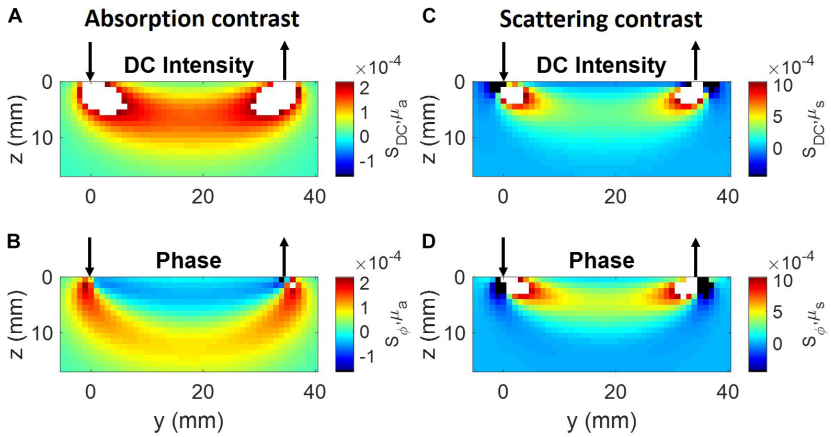

FIGURE 1 | Sensitivity maps in the (*y*,*z*) plane, where the tissue boundary is the *x*-*y* plane, the source (arrow pointing down) is at (0,0,0), and the detector (arrow pointing up) is at (0, 35 mm, 0). **(A)** DC Intensity, absorption contrast; **(B)** phase, absorption contrast; **(C)** DC intensity, scattering contrast, **(D)** phase, scattering contrast. The color bar labels in panels **(A, C)** indicate the sensitivity of DC intensity with respect to absorption (S_{DC,μ_a}) and reduced scattering coefficients (S_{DC,μ_s}), respectively. The color bar labels in panels **(B,D)** indicate the sensitivity of phase with respect to absorption (S_{ϕ,μ_a}) and reduced scattering coefficients (S_{ϕ,μ_s}), respectively. White and black in the color maps indicate values greater than the maximum or smaller than the minimum, respectively, of the color bars.

at the expense of a more complex instrumentation, targets specific classes of dynamic perturbations, and introduces some limitations to the field of view, it has not found broad applicability in diffuse optics. Of course, this does not mean that it may not be implemented in such a way to benefit specific applications in the near future.

Absolute Measurements With a Combination of Intensity and Phase Data

A common use of time-resolved NIRS, in either the time domain or the frequency domain, is toward measurements of absolute optical properties of tissue, namely its absorption (μ_a) and reduced scattering (μ_s') coefficients. Measurements at a minimum of two wavelengths, in conjunction with the Beer's law relationship between absorption and chromophores concentration, allow for the translation of absorption coefficients into cerebral concentrations of oxy-hemoglobin ([HbO_2]), deoxy-hemoglobin ([Hb]), total hemoglobin ([HbT] = [HbO_2] + [Hb]), and hemoglobin saturation (StO_2 = [HbO_2]/[HbT]). Here, the "t" in StO_2 indicates that the oxygen saturation of hemoglobin refers to an average over the investigated tissue. It is important to note that absolute measurements of StO_2 may still be obtained from absorption coefficients that are only known to within an unknown factor, because StO_2 depends on the ratio of absorption coefficients at multiple wavelengths (Bigio and Fantini, 2016, Section 15.1.3.1). This fact accounts for more robust absolute measurements of StO_2 with respect to [Hb] or [HbO_2], which instead rely on accurate absolute measurements of μ_a. For this reason, it is possible that FD and CW measurements of StO_2 (where the latter typically need to introduce some *ad hoc* assumptions on the scattering properties of tissue) may yield comparable results, as recently reported in a study on healthy human subjects during controlled hypoxia (Davies et al., 2017).

Multi-distance methods (see Section "Multi-Distance Methods") have been employed for absolute measurements of cerebral concentration and/or saturation of hemoglobin in newborn piglets (Fantini et al., 1999; Zhang et al., 2000), in rats (Culver et al., 2003), in newborn and infants (Franceschini et al., 2007; Grant et al., 2009; Roche-Labarbe et al., 2010, 2012; Lin et al., 2013b, Lin T.-Y. et al., 2016; Dehaes et al., 2014, 2015; Demel et al., 2014b, 2015; Farzam et al., 2017; Ferradal et al., 2017; Schwarz et al., 2018), and in adults under normal conditions (Fantini et al., 2003; Gatto et al., 2006, 2007; McIntosh et al., 2010; Hallacoglu et al., 2012, 2013; Scholkmann et al., 2013a; Clancy et al., 2015; Kainerstorfer et al., 2015; Yang and Dunn, 2015; Moreau et al., 2016; Davies et al., 2017; Blaney et al., 2019; Pham et al., 2019), under anesthesia (Paisansathan et al., 2007; Meng et al., 2012a,b), hypoxia (Davies et al., 2017), pathological conditions such as multiple sclerosis (Yang and Dunn, 2015), stroke (Moreau et al., 2016), traumatic brain injury (Davies et al., 2019), before and during electro-convulsive therapy (ECT) (Fabbri et al., 2003), during neurovascular surgery (Calderon-Arnulphi et al., 2007), and after death (Gatto et al., 2006). The absolute values of [Hb], [HbO_2], [HbT], and StO_2 reported in these studies are summarized in **Table 1** for piglets and rats, **Table 2** for neonates and infants, and **Table 3** for human adults. The absolute values of hemoglobin concentration and saturation reported in **Tables 1–3** represent typical reported values (thus no error is provided) under baseline conditions at rest (unless otherwise noted).

Some studies have also reported the optical coefficients (μ_a and μ_s') of brain tissue at discrete FD-NIRS wavelengths. This was done in newborn piglets (Fantini et al., 1999; Zhang et al., 2000), in neonates and infants (Zhao et al., 2005; Demel et al., 2014a; Farzam et al., 2017; Tian et al., 2017), and in adults (Hallacoglu et al., 2012; Blaney et al., 2019). Typically, optical properties were obtained by considering the tissue as homogeneous. However, a two-layer model has also been applied to analyze FD-NIRS

TABLE 1 | Absolute cerebral concentrations and oxygen saturation of hemoglobin in anesthetized newborn piglets and rats measured with non-invasive FD-NIRS *in vivo*.

References	Instr.	*f* (MHz)	Method	# of λ	[Hb] (μM)	[HbO_2] (μM)	[HbT] (μM)	StO_2 (%)	Age (days)	Animal model
Ntziachristos et al., 1997	NIM	200	SD (phase): ∼2 cm	2	–	–	–	80	1–5	Piglet
Fantini et al., 1999	ISS	110	MD: 1.5–3 cm	2	17	26	43	60	11 ± 1	Piglet
Zhang et al., 2000	ISS	110	MD: 1.5–3 cm	2	15	30	45	67	9 ± 2	Piglet
Culver et al., 2003	Own	70	MD: 0.3–1 cm	3	30	70	100	70	Adult	Rat

Instr., instrument; NIM, NIM (Near Infrared Monitoring), Inc. (Philadelphia, PA, United States); ISS, ISS, Inc. (Champaign, IL, United States); SD, single distance; MD, multi distance.

TABLE 2 | Absolute cerebral concentrations and oxygen saturation of hemoglobin in neonates, infants, and children measured with non-invasive FD-NIRS *in vivo*.

References	Instr.	*f* (MHz)	Method	# of λ	[Hb] (μM)	[HbO_2] (μM)	[HbT] (μM)	StO_2 (%)	Age
Watzman et al., 2000	NIM	200	SD: 3 or 4 cm	3	–	–	–	73	0–6 years
Zhao et al., 2005	Own	140	SD: 4 cm	2	16	24	40	59	1–17 days
Franceschini et al., 2007	ISS	110	MD: 1–2.5 cm	7	17	35	52	67	1 week
					14	19	33	57	6 weeks
					21	32	53	61	12 weeks
					24	49	73	67	52 weeks
Grant et al., 2009	ISS	110	MD: 1–2.5 cm	7	21	39	60	65	0–15 days
Roche-Labarbe et al., 2010	ISS	110	MD: 1–2.5 cm	6	12	28	40	70	1 week
					12	18	30	60	6 weeks
Roche-Labarbe et al., 2012	ISS	110	MD: 1–2.5 cm	6	15	40	55	73	1 week
					15	28	43	65	10 weeks
Lin et al., 2013b	ISS	110	MD: 1–2.5 or 1.5–3 cm	6	19	41	60	69	3.6 ± 1.7 weeks
Dehaes et al., 2014	ISS	110	MD: 1–2.5 cm	6	17	45	62	72	0–4 days
Demel et al., 2014b	ISS	110	MD: 1.5–3 cm	2	15	23	38	60	2 days
Dehaes et al., 2015	ISS	110	MD: 1.5–3 cm	6	16	35	51	69	33–71 h
Demel et al., 2015	ISS	110	MD: 1.5–3 cm	2	15	24	39	62	7–71 h (preterm)
					18	30	48	63	7–54 h (term)
Lin P. Y. et al., 2016	ISS	110	MD: 1–2.5 cm	6	–	–	–	50–70	3–14 weeks (preterm)
Farzam et al., 2017	ISS	110	MD: 1.5–3 cm	8	19	41	60	69	2.4 ± 0.8 days (males)
					16	33	50	65	2.6 ± 1.5 days (females)
Ferradal et al., 2017	ISS	110	MD: 1.5–3 cm	8	26	40	66	60	∼4 days (anesthesia)
Schwarz et al., 2018	ISS	110	MD: 1.5-3 cm	2	–	–	–	54	4–13 days

Instr., Instrument; NIM, NIM (Near Infrared Monitoring), Inc. (Philadelphia, PA, United States); ISS, ISS, Inc. (Champaign, IL, United States); SD, single distance; MD, multi distance.

data collected on adult human subjects to separately measure the optical properties of the superficial, extracerebral tissue (top layer) and the deeper brain tissue (bottom layer) (Hallacoglu et al., 2013). The absolute values of μ_a and μ_s' reported in these studies are summarized in **Table 4** and represent typical values (no error is provided) under baseline conditions.

The optical properties measured with multi-distance FD-NIRS on the forehead of sixteen elderly subjects (85 ± 6 years old) by Hallacoglu et al. (2012) are reported in **Figure 2** for different ranges of source-detector distance using diffusion theory for a homogeneous semi-infinite medium. Optical measurements were taken on the same group of subjects in two separate sessions separated in time by 5 months. The two measurement sessions are represented in **Figure 2** by gray and black blocks, respectively. The source-detector distances employed in the first session were 2, 2.5, 3, and 3.5 cm, whereas in the second session they were 0.8, 1.3, 1.8, 2.3, 2.8, 3.3, and 3.8 cm. The horizontal extent of the blocks in **Figure 2** indicates the distance range used for measurements of the optical properties according to the multi-distance method of Section "Multi-Distance Methods" (Fantini et al., 1999). The vertical extent of the blocks in **Figure 2** represent the mean value ± the standard error of measurements on different subjects. Because data collected at longer distances are more sensitive to deeper tissue, the strong decrease in scattering vs. distance (i.e., the lower scattering values associated with the blocks representing measurements at longer source-detector distances in the middle panels of **Figure 2**) suggests that brain tissue may be less scattering than superficial scalp and skull tissue, even though the low scattering of the cerebrospinal fluid layer may also contribute to this result. This finding of a lower scattering of deeper tissue (subarachnoid space, brain, etc.) vs. superficial tissue (scalp, skull, etc.) is confirmed by a study that considered diffusion theory for a two-layered medium, and found a significantly lower scattering coefficient in the bottom tissue layer compared to the top tissue layer, whose thickness was found to be about 13 mm (Hallacoglu et al., 2013) (see **Table 4**).

TABLE 3 | Absolute cerebral concentrations and oxygen saturation of hemoglobin in human adults measured with non-invasive FD-NIRS *in vivo*.

References	Instr.	*f* (MHz)	Method	# of λ	[Hb] (μM)	[HbO_2] (μM)	[HbT] (μM)	StO_2 (%)	Age (y)	Notes
Fabbri et al., 2003	ISS	110	MD: 1.5–3 or 1–2.5 cm	2	14	19	33	57	27–57	Before ECT
Fantini et al., 2003	ISS	110	MD:	2	14	20	34	59	29–44	Before sleep
Gatto et al., 2006	ISS	110	MD: 2–4 cm	2	13	24	37	64	36 ± 9	
Gatto et al., 2007	ISS	110	MD: 2–4 cm	2	15	28	43	65	20–39	
					13	22	35	63	40–60	
Calderon-Arnulphi et al., 2007	ISS	110	MD: 2–3.5 cm	2	16	16	32	50	58–81	Before surgery
Paisansathan et al., 2007	ISS	110	MD: 2–4 cm	2	13	19	32	59	44 ± 14	Anesth.
McIntosh et al., 2010	ISS	110	MD: 2–3.5 cm	2	19	26	45	58	20–53	
Meng et al., 2012a	ISS	110	MD: 2–3.5 cm	2	11	30	41	73	22–68	Anesth.
Meng et al., 2012b	ISS	110	MD: 2–3.5 cm	2	11	25	36	68	22–68	Anesth.
Hallacoglu et al., 2012	ISS	110	MD: 2.8–3.8 cm	2	20	39	59	66	28 ± 4	
					18	22	40	55	85 ± 6	
Hallacoglu et al., 2013	ISS	110	MD: 1.3–4.8 cm	2	11	15	26	42	29 ± 2	Superf. tissue
					31	51	82	64		Deep tissue
					17	30	47	64		Homog. tissue
Scholkmann et al., 2013a	ISS	110	MD: 2–4 cm	2	–	–	–	59	–	
Clancy et al., 2015	ISS	110	MD	2	11	29	40	72	–	
Yang and Dunn, 2015	ISS	110	MD: 2–3.5 cm	2	17	28	45	63	50 ± 8	
Kainerstorfer et al., 2015	ISS	110	MD: 2–3.5 cm	2	16	35	51	69	21–50	
Moreau et al., 2016	ISS	110	MD: 2–3.5 cm	2	20	35	56	63	42 ± 7	
Davies et al., 2017	ISS	110	MD	2	–	–	–	62	–	
Davies et al., 2019	ISS	110	MD: 3–4.5 cm	2				67	50 ± 17	TBI
Blaney et al., 2019	ISS	140	MD: 1.1–4 cm	2	18	24	42	56	25–53	
Pham et al., 2019	ISS	140	MD: 1.6–4 cm	2	11	39	50	78	22–33	

Measurements are for healthy subjects at rest and based on diffusion theory for homogeneous tissue, unless otherwise noted in the "Notes" column. Instr., Instrument; ISS, ISS, Inc. (Champaign, IL, United States); MD, multi distance; ECT, electro-convulsive therapy; TBI, Traumatic Brain Injury.

In some cases, absolute measurements of baseline optical properties and hemoglobin concentrations obtained with multi-distance FD-NIRS are not reported, as the focus was the investigation of quantitative changes in [Hb] and [HbO_2] associated with visual cortical activation in younger and older adults (McKernan Ward et al., 2015), brain activation with colored light (Scholkmann et al., 2017; Metz et al., 2017), a speech task (Scholkmann et al., 2013b, 2014a), or changes in cerebral blood flow (CBF) and StO_2 following intrathoracic pressure strains (Zhang et al., 2017). Even in cases like these, where the emphasis is on measuring relative rather than absolute concentrations of hemoglobin, the ability of FD-NIRS to provide absolute measures of baseline optical properties can be beneficial. In fact, one does not need to rely on assumptions associated with the modified Beer–Lambert law in CW-NIRS, namely the values of the differential pathlength factor (DPF) at the wavelengths used (since the DPF can be obtained from the absolute optical properties), and the lack of changes in the scattering properties of tissue (since absolute scattering measurements allows one to verify whether scattering stays constant).

The absolute measurements of [HbT] (units: mol/l) afforded by FD-NIRS can be translated into absolute measurements of cerebral blood volume (CBV) [units: ml/(100 g)] by taking into account the concentration of hemoglobin in large blood vessels (HGB) (units: mol/l), the molecular weight of hemoglobin (MW_{Hb}) (units: mol/g), the density of brain tissue (D_{bt}) (units: g/ml), and the small-to-large vessel hematocrit ratio, or Fårhaeus factor (F) (Franceschini et al., 2007; Meng et al., 2012a):

$$CBV = \frac{[HbT] \times MW_{Hb}}{HGB \times D_{bt} \times F} \tag{10}$$

Absolute measurements of StO_2 (dimensionless) with multi-distance FD-NIRS have been combined with measurements of a cerebral blood flow index (BFI) with diffuse correlation spectroscopy (DCS) to yield a relative cerebral metabolic rate of oxygen ($rCMRO_2$), with respect to a reference condition indicated by 0 subscripts (Roche-Labarbe et al., 2012):

$$rCMRO_2 = \frac{HGB \times BFI \times (SaO_2 - StO_2)}{HGB_0 \times BFI_0 \times (SaO_2 - StO_2)_0} \tag{11}$$

where SaO_2 is the oxygen saturation of hemoglobin in arterial blood, and under the assumption of a constant relative contribution of arterial and venous blood to the StO_2 measurement.

Using the approach of Eqs. (10) and (11), researchers have investigated the cerebral oxygen metabolism in neonates with intraventricular hemorrhage (Lin P. Y. et al., 2016) and the blood volume and metabolic responses to hand tactile stimulation in the somatosensory cortex of preterm neonates (Roche-Labarbe et al., 2014).

Single-distance methods (see Section "Single-Distance Methods") can also yield absolute measurements, as long as

TABLE 4 | Absolute cerebral absorption and reduced scattering coefficients measured with non-invasive FD-NIRS *in vivo*.

References	Instr.	*f* (MHz)	Method	λ (nm)	μ_a (cm^{-1})	μ_s' (cm^{-1})	Age	Brain investigated
Fantini et al., 1999	ISS	110	MD: 1.5–3 cm	758	0.15	9.3	11 ± 1 days	Piglets
				830	0.13	8.2		
Zhang et al., 2000	ISS	110	MD: 1.5–3 cm	758	–	7.8	9 ± 2 days	Piglets
				830	–	6.6		
Zhao et al., 2005	Own	140	SD(calib): 4 cm	788	0.078	9.2	1–17 days	Neonates/infants/children
				832	0.089	8.4		
Demel et al., 2014a	ISS	110	MD: 1.5–3 cm	692	0.07–0.11	5.9–9.4	1–71 days	Neonates/infants/children
				834	0.08–0.12	4.5–7.2		
Farzam et al., 2017	ISS	110	MD: 1.5–3 cm	672	0.160	8.7	2 ± 1 days	Neonates/infants/children
				689	0.127	8.5		
				701	0.115	8.5		
				724	0.110	8.2		
				771	0.140	7.5		
				783	0.126	7.2		
				803	0.121	6.8		
				829	0.141	6.5		
Tian et al., 2017	ISS	110	MD	785, 811	0.15–0.30	6–18	0–16 years (ECMO)	Neonates/infants/children
Hallacoglu et al., 2012	ISS	110	MD: 2.8–3.8 cm	690	0.14	7.2	28 ± 4 years	Adults (homogeneous tissue)
				830	0.12	6.0		
				690	0.10	5.3	85 ± 6 years	
				830	0.08	4.8		
Hallacoglu et al., 2013	ISS	110	MD: 1.3–4.8 cm	690	0.08	13	29 ± 2 years	Adults (superficial tissue, ∼13 mm)
				830	0.08	11		
				690	0.20	3		Adults (deep tissue, brain)
				830	0.20	2		
				690	0.11	7		Adults (homogeneous tissue)
				830	0.12	5		
Blaney et al., 2019	ISS	140	MD: 1.1–4 cm	690	0.10	9.8	25–53 years	Adults (homogeneous tissue)
				830	0.11	8.0		

Instr., Instrument; ISS, ISS, Inc. (Champaign, IL, United States); MD, multi distance; SD, single distance; ECMO, Extracorporeal Membrane Oxygenation.

they include a suitable calibration on a reference phantom with known optical properties. This method has been applied to the infant brain (Zhao et al., 2005).

Stand-Alone Use of DC Data

There are research studies in the literature that are performed with FD-NIRS instrumentation, but report results obtained exclusively with DC intensity, which is equivalent to what would be measured in CW-NIRS. For example, this is the case for studies on the cerebral hemodynamics associated with auditory stimulation [concurrently with electro-encephalography (EEG)] (Tong et al., 2005), motor stimulation [concurrently with functional magnetic resonance imaging (fMRI)] (Sassaroli et al., 2006), different levels of mental workload (Sassaroli et al., 2008), cognitive multitasking (Solovey et al., 2011), different sleep stages (Pierro et al., 2012), a cycling exercise (Lin et al., 2013a), arterial blood pressure oscillations (Tgavalekos et al., 2016) and transients (Kainerstorfer et al., 2015) induced by pneumatic cuffs on the subject's legs, electrical stimulation concurrent with voluntary movement (Lin T.-Y. et al., 2016), and fluctuations in intracranial pressure (Ruesch et al., 2019). One may wonder why the phase data was not considered in these studies. In some cases, it is possible that the most common objective of using phase data in FD-NIRS, namely their combination with intensity data to generate absolute measurements of optical properties, was not central to the study. In other cases, there may be reasons such as the lower signal-to-noise ratio of phase data, or uncertainties in how to exploit the added information content of phase data.

Some studies of brain functional activation have compared results obtained with stand-alone DC with those obtained with stand-alone phase (Sassaroli et al., 2004) or with combined DC and phase (Doulgerakis et al., 2019) to explore the importance of the additional information content of phase data. These studies concluded that phase data feature greater sensitivity to deeper, i.e., cerebral, tissue compared to DC data. This point is further explored in Section "Enhanced Depth Sensitivity Using Phase Data" on the depth sensitivity of stand-alone phase measurements.

Stand-Alone Use of AC Data

While the information content of AC data is essentially the same as for DC data, at least at modulation frequencies typically used in FD-NIRS (say, <150 MHz), the AC amplitude is weakly affected by room light or stray light, which instead may significantly

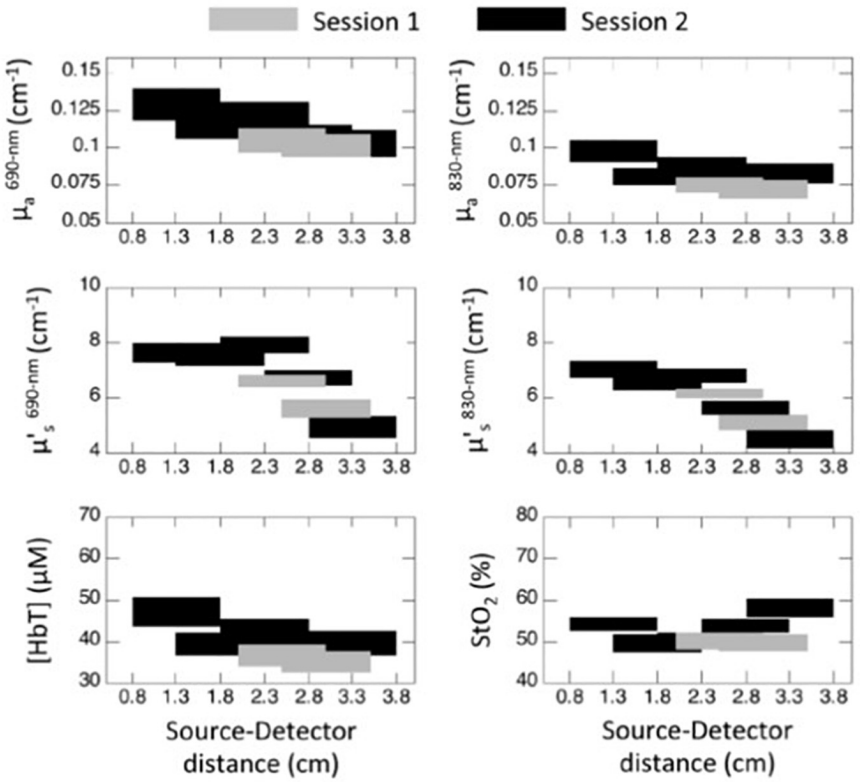

FIGURE 2 | Absolute absorption coefficients (μ_a: **top panels**) and reduced scattering coefficients (μ_s': **middle panels**) measured with multi-distance FD-NIRS at 690 nm **(left panels)** and 830 nm **(right panels)** on the forehead of 16 elderly subjects (85 ± 6 years old) using diffusion theory for a homogeneous semi-infinite medium. From the absorption coefficients at two wavelengths, absolute values of concentration of hemoglobin ([HbT]) and tissue saturation (StO_2) were obtained **(bottom panels)**. The blocks represent the mean ± standard error (vertical dimension) of the measurements performed at the range of distances corresponding to the horizontal range. The black and gray blocks correspond to two measurement sessions performed on the same group of 16 subjects 5 months apart. Reprinted with permission from Hallacoglu et al. (2012).

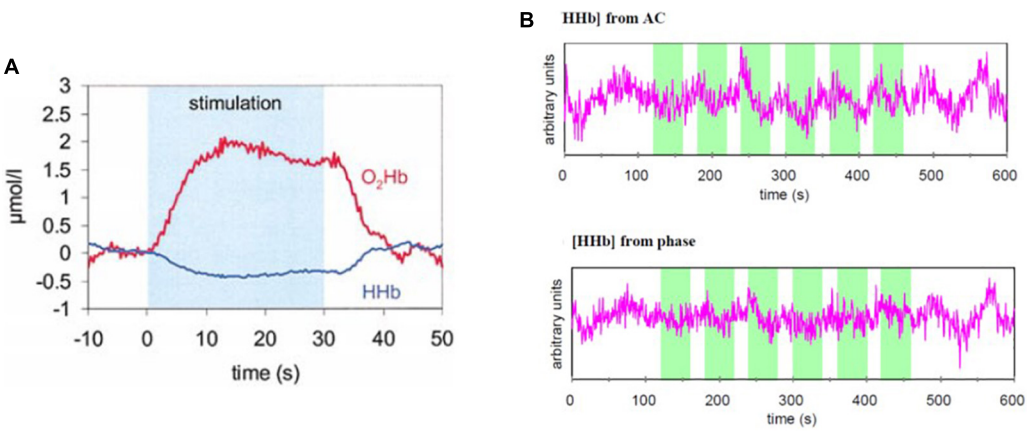

FIGURE 3 | Functional FD-NIRS on the human brain. **(A)** Hemodynamic response to visual stimulation (checkerboard reversing) measured in the human visual cortex with AC data at two wavelengths (758 and 830 nm) translated into concentration changes in oxyhemoglobin (O_2Hb) and deoxyhemoglobin (HHb). **(B)** Deoxyhemoglobin concentration ([HHb]) traces obtained from AC data (top) and phase data (bottom) in the human prefrontal cortex in a protocol involving arithmetic calculations (indicated by the green shaded areas in the two panels. **(A)** Reprinted with permission from Wolf et al. (2002b) Elsevier; **(B)** Reprinted with permission from Toronov et al. (2001) The Optical Society of America.

impact the DC intensity. For this reason, some researchers opted to use frequency-domain instrumentation to collect AC data that is then analyzed using data processing techniques typically associated with CW-NIRS (modified Beer–Lambert law with assumed values of DPF). This approach has been used for brain-computer interface research in the areas of decision making (Luu and Chau, 2009), classification of prefrontal activity (Power et al., 2010), for the assessment of independent component analysis (ICA) and principal component analysis (PCA) in removing extracerebral tissue contributions to the NIRS signal (Virtanen et al., 2009), and to investigate the hemodynamics in the prefrontal cortex during arithmetic calculations (Toronov et al., 2001), in the frontal cortex during breath holding, hyperventilation, and sleep (Noponen et al., 2003), in the motor and visual cortices during functional activation (Wolf et al., 2002a,b), and in the visual cortex under normo-, hypo-, and hypercapnia conditions (Noponen et al., 2005). **Figure 3A** shows the hemodynamic response to visual stimulation by checkerboard reversing in the human visual cortex measured with AC data, showing the typical increase in oxyhemoglobin and decrease in deoxyhemoglobin associated with the activation-induced increase in cerebral blood flow (Wolf et al., 2002b). The top panel of **Figure 3B** shows the decrease in deoxyhemoglobin concentration, measured with AC data, in the human prefrontal cortex as a result of arithmetic calculations (Toronov et al., 2001). Note the latency of several seconds for the hemodynamic response to brain activation.

While CW-NIRS data are conceptually equivalent to DC data in FD-NIRS, it is worth noting that it is common for CW-NIRS instruments to use frequency-encoding approaches to distinguish data from different light sources. While the modulation frequency in these cases is on a scale of kHz, thus inappropriate for FD-NIRS, it nevertheless results in a suppression of room light contributions, similarly to AC data in FD-NIRS.

Stand-Alone Use of Phase Data

While the signal-to-noise ratio associated with phase data in FD-NIRS is typically lower than that of DC and AC data, the unique information content of phase data and the different region of sensitivity of phase vs. DC or AC data (see **Figure 1**) justify a careful consideration of stand-alone phase. Regarding signal-to-noise ratio, it has been argued that higher modulation frequencies in the range 400–500 MHz may result in a significant improvement over phase measurements at the typical modulation frequencies of ∼100 MHz used in FD-NIRS (Toronov et al., 2004).

Stand-alone phase data have been used for quantitative brain oximetry (i.e., measurements of StO_2), after assuming values for the reduced scattering coefficient of tissue (Sevick et al., 1991; Wilson et al., 1992), or after calibration on known phantoms (Kurth and Thayer, 1999). These methods were applied to newborn piglets during a hypoxic challenge (Ntziachristos et al., 1997), and to human newborns and children with congenital heart disease (Watzman et al., 2000) (see **Tables 1**, **2**).

In the case of fNIRS, one is typically interested in hemodynamic changes associated with brain activation. Such hemodynamic changes affect both intensity and phase data and are mostly associated with absorption changes due to blood volume and blood oxygenation dynamics induced by brain activity. Under the assumption of negligible scattering changes, temporal phase data can be translated into measurements of $\Delta[\mathrm{Hb}]$ and $\Delta[\mathrm{HbO_2}]$ (concentration changes with respect to baseline) (Toronov et al., 2001; Blaney et al., 2020) [see Eq. (6)], similar to the way intensity changes are translated into $\Delta[\mathrm{Hb}]$ and $\Delta[\mathrm{HbO_2}]$ by the modified Beer-Lambert law in CW NIRS (Delpy et al., 1988; Sassaroli and Fantini, 2004) [see Eq. (5)]. Phase-only measurements on the human prefrontal cortex during a protocol involving arithmetic calculations (Toronov et al., 2001) and on the primary motor cortex during a finger-tapping task (Sassaroli et al., 2004) demonstrated the ability of stand-alone phase data to detect brain activation. The bottom panel of **Figure 3B** shows the decrease in deoxyhemoglobin concentration, measured with phase data, in the human prefrontal cortex as a result of arithmetic calculations (Toronov et al., 2001).

The Fast Optical Signal

FD-NIRS has been applied to the study of the so-called fast optical signal (occurring on a time scale of ∼100 ms), which is thought to be associated with scattering changes that are more directly representative of neuronal activation than the absorption changes associated with cerebral hemodynamic responses (occurring on a time scale of seconds). The fast optical signal was first reported with phase measurements in the human visual cortex under the name EROS, for "event-related optical signal" (Gratton et al., 1995a). Phase measurements, and sometimes AC measurements, were then used to investigate the fast optical signal in the visual (Gratton and Fabiani, 2003; Gratton et al., 2006; Maclin et al., 2007), auditory (Maclin et al., 2003), somatosensory (Maclin et al., 2004), motor (Gratton et al., 1995b; Parks et al., 2012), temporal/frontal (Tse et al., 2006, 2013; Tse and Penney, 2007), and prefrontal (Low et al., 2006, 2009; Gratton et al., 2009; Huang et al., 2013; Baniqued et al., 2013) cortices. Brain activation was reported to evoke a fast, transient phase increase of the order of 0.05° (sometimes extending to values of 0.1° or 0.2°) (see **Figure 4A**).

Stand-alone DC data, AC data, and phase data have been considered in the investigation of the fast optical signal. Some human studies on the motor cortex (Wolf et al., 2002a; Morren et al., 2004), visual cortex (Wolf et al., 2003), and prefrontal cortex (Proulx et al., 2018a,b) reported that DC and AC data can detect the fast signal more effectively than phase data. The fast optical signal was also investigated with CW-NIRS in the somatosensory cortex (Steinbrink et al., 2000), prefrontal cortex (Medvedev et al., 2010), temporal cortex (Kubota et al., 2008), visual cortex (Sun et al., 2014), and motor cortex (Zhang et al., 2012). However, given the small amplitude of the fast optical signal, questions were raised about its detectability (Steinbrink et al., 2005). In fact, the fast optical signal consists of a small transient decrease in the DC intensity (or AC amplitude), of the order of 0.05% or less (see **Figure 4B**). (We note that an animal study on the somatosensory cortex of marmosets found a transient *increase* of ∼0.08% in the CW intensity, in a method termed optoencephalography;

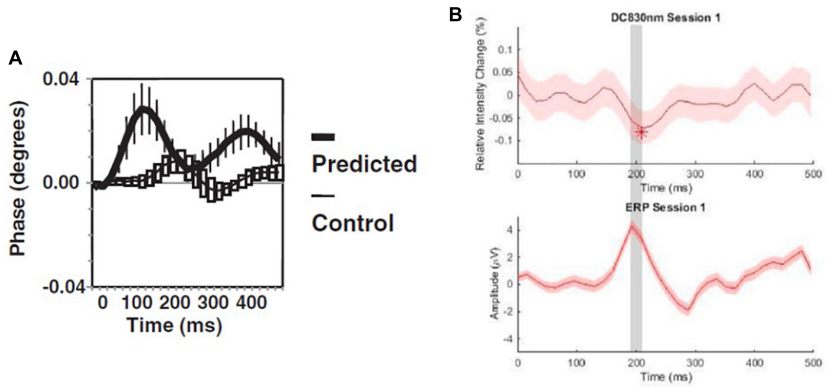

FIGURE 4 | Fast optical signal measured by FD-NIRS with **(A)** phase from the visual cortex of human subjects at the cortical location of predicted response and at a control location (EROS: event-related optical signal), and **(B)** DC Intensity from the prefrontal cortex (top) in comparison with the event-related potential (ERP) response. **(A)** Reprinted with permission from Gratton and Fabiani (2003)© Wiley; **(B)** Reprinted with permission from Proulx et al. (2018b)© Elsevier.

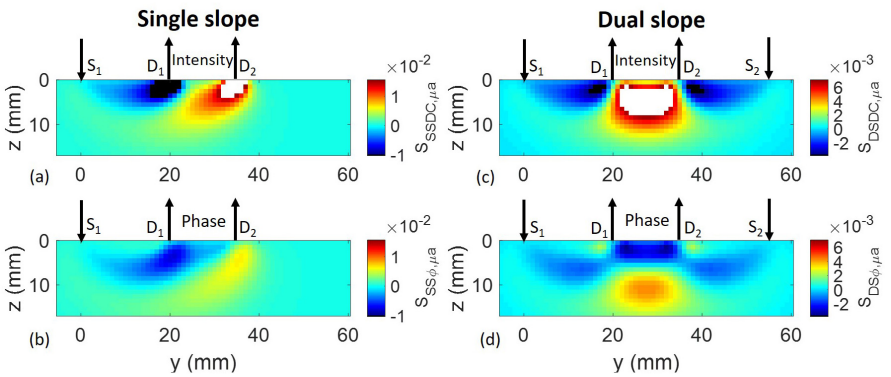

FIGURE 5 | Sensitivity maps for absorption contrast of **(A)** single-slope intensity, **(B)** single-slope phase, **(C)** dual-slope intensity, and **(D)** dual-slope phase. The arrows pointing down indicate the light sources (S_1, S_2), and the arrows pointing up indicate the optical detectors (D_1, D_2). The color bar labels in panels **(A,C)** indicate the sensitivity to absorption perturbations for single slope DC intensity (S_{SSDC,μ_a}) and dual slope DC intensity (S_{DSDC,μ_a}), respectively. The color bar labels in panels **(B,D)** indicate the sensitivity to absorption perturbations for single slope phase ($S_{SS\varphi,\mu_a}$) and dual slope phase ($S_{DS\varphi,\mu_a}$), respectively. White and black in the color maps indicate values greater than the maximum or smaller than the minimum, respectively, of the color bars. Adapted with permission from Sassaroli et al. (2019)© The Optical Society of America.

Hiwaki and Miyaguchi, 2018). The challenge of detecting the fast optical signal was further demonstrated in studies of the human motor cortex (Franceschini and Boas, 2004) and the primate visual cortex (Radhakrishnan et al., 2009).

Enhanced Depth Sensitivity Using Phase Data

A comparison of **Figures 1A,B** shows that single-distance phase measurements feature a sensitivity to absorption perturbations that extends deeper than single-distance intensity measurements. In fact, as already mentioned, it was observed that phase measurements provide deeper sensitivity, and thus a stronger sensitivity to cerebral tissue in non-invasive optical studies of the human brain (Sassaroli et al., 2004; Doulgerakis et al., 2019). In an effort to minimize the sensitivity to superficial tissue layers, multi-distance measurements were introduced in both CW and FD-NIRS, and implemented with either a single source and multiple detectors, or a single detector and multiple sources (Franceschini et al., 1998; Suzuki et al., 1999). Since these methods ultimately aimed at measuring a gradient, or slope, of optical signals versus source-detector distance, we refer to these methods as *single-slope* methods. These methods have been extensively used in both CW-NIRS and FD-NIRS, and have been implemented into several commercial NIRS instruments. While single-slope methods indeed feature a small sensitivity to uniform absorption changes in superficial layers, they may yield misleading results in the case of localized superficial perturbations. In fact, as shown in **Figures 5A,B**, the single-slope sensitivity of both intensity and phase feature double, asymmetrical banana-shaped regions with sensitivities of opposite sign (Sassaroli et al., 2019). This feature may be problematic in the case of localized superficial inhomogeneous changes in optical properties.

We have recently proposed to enhance depth sensitivity using a particular source-detector arrangement that was originally

introduced for self-calibrating, absolute measurements of optical properties with FD-NIRS (Hueber et al., 1999) (as described in Section "Multi-Distance Methods"). This particular arrangement involves at least two sources *and* at least two detectors to measure two paired gradients or slopes of optical signals versus source-detector distance, which are then averaged. Because it is based on the measurement of two slopes, this approach is referred to as a *dual-slope* method, and it can be applied separately to intensity and phase data. The region of sensitivity of dual slopes for intensity and phase, in the case of a linear arrangement of two sources and two detectors, is illustrated in **Figures 5C,D** for the same optical properties and modulation frequency of **Figure 1**. In this case, however, we considered a larger absorption perturbation having an axial size (along z) of 1 mm and a lateral size (across x and y) of 5 mm, which may represent a typical size of localized hemodynamic changes (as related to functional brain activation or extracerebral hemodynamics). A variety of other source-detector arrangements for dual-slope measurements, and the corresponding intensity and phase regions of sensitivity, have also been reported (Fantini et al., 2020). The dual-slope sensitivity features both positive and negative values, and takes maximum values deeper in the tissue than the single-distance sensitivity (in the case of **Figure 5**: ∼5 mm vs. ∼2 mm for intensity, and ∼11 mm vs. ∼5 mm for phase). Furthermore, it is evident from **Figures 5C,D** that the sensitivity of phase dual-slope extends deeper than the sensitivity of intensity dual-slope. An FD-NIRS study on human subjects showed the different information content of intensity and phase collected with single-distance, single-slope, and dual-slope arrangements, consistent with a deeper sensitivity of phase slope methods, and more robust dual-slope vs. single-slope data (Blaney et al., 2020).

The above observations about single-slope and dual-slope sensitivities have also been articulated in the time domain, where source-detector arrangements for self-calibrating absolute measurements have been shown to achieve a better depth sensitivity with the first and second moments of the photon time-of-flight distribution (the first moment is representative of the phase in the frequency domain), with respect to the 0th moment (which represents the CW intensity) (Sawosz and Liebert, 2019).

CRITICAL PERSPECTIVE: WHAT IS THE MAJOR PROMISE OF FD DATA IN CEREBRAL NIRS?

FD-NIRS provides data with richer information content than CW-NIRS. In this article, we have discussed how such additional information may be used in three broad areas: (1) absolute quantification of baseline optical properties and hemoglobin concentration in tissue; (2) minimization of sensitivity to room light and other potential sources of confounds (such as instrumental drifts, variable optical coupling with tissue, and motion artifacts) in practical measurements; (3) achievement of selective sensitivity to deeper tissue.

The ability to perform absolute baseline measurements is undoubtedly appealing, since it leads to the possibility of determining normative baseline values, performing comparisons across subjects, and conducting longitudinal studies over long periods of time. However, the accuracy of absolute measurements may be significantly affected by simplifying assumptions (on the tissue geometry, spatial distribution of optical properties, etc.), and by instrumental or experimental artifacts that are often difficult to avoid in real-life measurement conditions. These assumptions and experimental artifacts can be particularly limiting in the case of non-invasive brain studies because of the strong tissue heterogeneity, presence of hair, tissue rigidity due to the skull bone, etc. Furthermore, many applications of functional NIRS or cerebral oximetry do not need an absolute baseline characterization, but rather rely on relative changes during specific measurement protocols.

Practical advantages related to a lack of sensitivity to room light or other sources of instrumental artifacts are important, but may also be achieved with alternative methods.

In our opinion, the one aspect of FD-NIRS that holds the most promise to advance the field of non-invasive optical sensing of the brain is the ability to control the region of sensitivity by taking advantage of intensity and phase measurements collected with properly designed source-detector arrays. Such a capability is not available to CW-NIRS, and can help address one of the most critical open questions in the field, namely the minimization of confounding contributions from extracerebral tissue (scalp, skull, etc.) to non-invasive optical measurements of the brain. The possibility of achieving more selective sensitivity to brain tissue, while also providing access to valuable absolute measurements of optical properties and chromophore concentrations, renders FD-NIRS a powerful technique for non-invasive measurements of the human brain.

AUTHOR CONTRIBUTIONS

SF and AS: literature survey, analysis, and writing. SF: tables.

FUNDING

We acknowledge support from the US National Institutes of Health (NIH), Grant No. R01 NS095334.

REFERENCES

Applegate, M. B., and Roblyer, D. (2018). Multi-distance diffuse optical spectroscopy with a single optode via hypotrochoidal scanning. *Opt. Lett.* 43, 747–750. doi: 10.1364/OL.43.000747

Arnesano, C., Santoro, Y., and Gratton, E. (2012). Digital parallel frequency-domain spectroscopy for tissue imaging. *J. Biomed. Opt.* 17:096014.

Baniqued, P. L., Low, K. A., Fabiani, M., and Gratton, G. (2013). Frontoparietal traffic signals; a fast optical imaging study of preparatory dynamics in response mode switching. *J. Cogn. Neurosci.* 25, 887–902. doi: 10.1162/jocn_a_00341

Bevilacqua, F., Berger, A. J., Cerussi, A. E., Jakubowski, D., and Tromberg, B. J. (2000). Broadband absorption spectroscopy in turbid media by combined frequency-domain and steady-state methods. *Appl. Opt.* 39, 6498–6507.

Bigio, I. J., and Fantini, S. (2016). *Quantitative Biomedical Optics*. Cambridge: Cambridge University Press.

Blaney, G., Sassaroli, A., Pham, T., Fernandez, C., and Fantini, S. (2020). Phase dual slopes in frequency-domain near-infrared spectroscopy for enhanced sensitivity to brain tissue: first applications to human subjects. *J. Biophotonics* 13:e201960018. doi: 10.1002/jbio.201960018

Blaney, G., Sassaroli, A., Pham, T., Krishnamurthy, N., and Fantini, S. (2019). Multi-distance frequency-domain optical measurements of coherent cerebral hemodynamics. *Photonics* 6:83.

Boas, D. A. (1997). A fundamental limitation of linearized algorithms for diffuse optical tomography. *Opt. Express* 13, 404–413.

Calderon-Arnulphi, M., Alaraj, A., Amin-Hanjani, S., Mantulin, W. W., Polzonetti, C. M., Gratton, E., et al. (2007). Detection of cerebral ischemia in neurovascular surgery using quantitative frequency-domain near-infrared spectroscopy. *J. Neurosurg.* 106, 283–290.

Cerussi, A. E., and Tromberg, B. J. (2003). "Photon migration spectroscopy frequency-domain techniques," in *Biomedical Photonics Handbook*, ed. T. V. Dinh (Boca Raton, FL: CRC Press), 22/1–22/17.

Chance, B., Anday, E., Nioka, S., Zhou, S., Hong, L., Worden, K., et al. (1998a). A novel method for fast imaging of brain function, non-invasively, with light. *Opt. Express* 2, 411–423.

Chance, B., Cope, M., Gratton, E., Ramanujam, N., and Tromberg, B. (1998b). Phase measurement of light absorption and scatter in human tissue. *Rec. Sci. Instrum.* 69, 3457–3481.

Chance, B., Kang, K., He, L., Weng, J., and Sevick, E. (1993). Highly sensitive object location in tissue models with linear in-phase and anti-phase multi-element optical arrays in one and two dimensions. *Proc. Natl. Acad. Sci. U.S.A.* 90, 3423–3427.

Chance, B., Kang, K. A., He, L., Liu, H., and Zhou, S. (1996). Precision localization of hidden absorbers in body tissues with phased-array optical systems. *Rev. Sci. Instrum.* 67, 4324–4332.

Cheung, C., Culver, J. P., Takahashi, K., Greenberg, J. H., and Yodh, A. G. (2001). *In vivo* cerebrovascular measurement combining diffuse near-infrared absorption and correlation spectroscopies. *Phys. Med. Biol.* 46, 2053–2065.

Clancy, M., Belli, A., Davies, D., Lucas, S. J. E., Su, Z., and Dehghani, H. (2015). Comparison of neurological NIRS signals during standing Valsalva maneuvers, pre and post vasopressor injection. *Proc. SPIE* 9538:953817.

Culver, J. P., Durduran, T., Furuya, D., Cheung, C., Greenberg, J. H., and Yodh, A. G. (2003). Diffuse optical tomography of cerebral blood flow, oxygenation, and metabolism in rat during focal ischemia. *J. Cereb. Blood Flow Metab.* 23, 911–924.

Davies, D. J., Clancy, M., Dehghani, H., Lucas, S. J. E., Forcione, M., Yakoub, K. M., et al. (2019). Cerebral oxygenation in traumatic brain injury: can a non-invasive frequency domain near-infrared spectroscopy device detect changes in brain tissue oxygen tension as well as the established invasive monitor? *J. Neurotrauma* 36, 1175–1183. doi: 10.1089/neu.2018.5667

Davies, D. J., Clancy, M., Lighter, D., Balanos, G. M., Lucas, S. J. E., Dehghani, H., et al. (2017). Frequency-domain vs continuous-wave near-infrared spectroscopy devices: a comparison of clinically viable monitors in controlled hypoxia. *J. Clin. Monit. Comput.* 31, 967–974. doi: 10.1007/s10877-016-9942-5

Dehaes, M., Aggarwal, A., Lin, P. Y., Fortuno, C. R., Fenoglio, A., Roche-Labarbe, N., et al. (2014). Cerebral oxygen metabolism in neonatal hypoxic ischemic encephalopathy during and after therapeutic hypothermia. *J. Cereb. Blood Flow Metab.* 34, 87–94. doi: 10.1038/jcbfm.2013.165

Dehaes, M., Cheng, H. H., Buckley, E. M., Lin, P.-Y., Ferradal, S. L., Williams, K., et al. (2015). Perioperative cerebral hemodynamics and oxygen metabolism in neonates with single-ventricle physiology. *Biomed. Opt. Express* 6, 4749–4767. doi: 10.1364/BOE.6.004749

Delpy, D. T., Cope, M., van der Zee, P., Arridge, S., Wray, S., and Wyatt, J. (1988). Estimation of optical path length measurements on adult head, calf, and forearm and the head of newborn infants using phase resolved spectroscopy. *Phys. Med. Biol.* 40, 295–304.

Demel, A., Feilke, K., Schöning, M., Wolf, M., Poets, C. F., and Franz, A. R. (2015). Healthy term and moderately preterm infants have similar cerebral oxygen saturation and cerebral flow volumes during early post-natal transition. *Acta Paediatr.* 104, e330–e336. doi: 10.1111/apa.13023

Demel, A., Feilke, K., Wolf, M., Poets, C. F., and Franz, A. R. (2014a). Correlation between skin, bone, and cerebrospinal fluid layer thickness and optical coefficients measured by multidistance frequency-domain near-infrared spectroscopy in term and preterm infants. *J. Biomed. Opt.* 19:017004. doi: 10.1117/1.JBO.19.1.017004

Demel, A., Wolf, M., Poets, C. F., and Franz, A. R. (2014b). Effect of different assumptions for brain water content on absolute measures of cerebral oxygenation determined by frequency-domain near-infrared spectroscopy in preterm infants: an observational study. *BMC Pediatr.* 14:206. doi: 10.1186/1471-2431-14-206

Doulgerakis, M., Eggebrecht, A. T., and Dehghani, H. (2019). High-density functional diffuse optical tomography based on frequency-domain measurements improves image quality and spatial resolution. *Neurophotonics* 6:035007. doi: 10.1117/1.NPh.6.3.035007

Fabbri, F., Henry, M. E., Renshaw, P. F., Nadgir, S., Ehrenberg, B. L., Franceschini, M. A., et al. (2003). Bilateral near-infrared monitoring of the cerebral concentration and oxygen-saturation of hemoglobin during right unilateral electro-convulsive therapy. *Brain Res.* 992, 193–204.

Fantini, S., Aggarwal, P., Chen, K., Franceschini, M. A., and Ehrenberg, B. L. (2003). Near-infrared spectroscopy and polysomnography during all-night sleep in human subjects. *Proc. SPIE* 5068, 155–162.

Fantini, S., Barbieri, B., Franceschini, M. A., and Gratton, E. (1997). "Frequency-domain spectroscopy," in *Applications of Optical Engineering to the Study of Cellular Pathology*, ed. E. Kohen (Thiruvananthapuram: Research Signpost), 57–66.

Fantini, S., Blaney, G., and Sassaroli, A. (2020). Transformational change in the field of diffuse optics: from going bananas to going nuts. *J. Innov. Opt. Health Sci.* 13:1930013.

Fantini, S., Franceschini, M. A., Fishkin, J. B., Barbieri, B., and Gratton, E. (1994a). Quantitative determination of the absorption spectra of chromophores in strongly scattering media: a light-emitting-diode based technique. *Appl. Opt.* 33, 5204–5213. doi: 10.1364/AO.33.005204

Fantini, S., Franceschini, M. A., and Gratton, E. (1994b). Semi-infinite-geometry boundary problem for light migration in highly scattering media: a frequency-domain study in the diffusion approximation. *J. Opt. Soc. Am. B* 10, 2128–2138.

Fantini, S., Franceschini-Fantini, M. A., Maier, J. S., Walker, S. A., Barbieri, B., and Gratton, E. (1995). Frequency-domain multichannel optical detector for noninvasive tissue spectroscopy and oximetry. *Opt. Eng.* 34, 32–42.

Fantini, S., Frederick, B., and Sassaroli, A. (2018). Perspective: prospects of non-invasive sensing of the human brain with diffuse optical imaging. *APL Photonics* 3:110901. doi: 10.1063/1.5038571

Fantini, S., Hueber, D., Franceschini, M. A., Gratton, E., Rosenfeld, W., Stubblefield, P. G., et al. (1999). Non-invasive optical monitoring of the newborn piglet brain using continuous-wave and frequency-domain spectroscopy. *Phys. Med. Biol.* 44, 1543–1563.

Fantini, S., and Sassaroli, A. (2016). "Frequency-domain techniques for tissue spectroscopy and imaging," in *Handbook of Optical Biomedical Diagnostics: Light-Tissue Interactions*, 2nd Edn, Vol. 1, ed. V. V. Tuchin (Bellingham, WA: SPIE Press), 477–532.

Farzam, P., Buckley, E. M., Lin, P. Y., Hagan, K., Grant, P. E., Inder, T. E., et al. (2017). Shedding light on the neonatal brain: probing cerebral hemodynamics by diffuse optical spectroscopic methods. *Sci. Rep.* 7:15786.

Feng, S., Zeng, F., and Chance, B. (1995). Photon migration in the presence of a single defect: a perturbation analysis. *Appl. Opt.* 34, 3826–3837. doi: 10.1364/AO.34.003826

Ferradal, S. L., Yuki, K., Vyas, R., Ha, C. G., Yi, F., Stopp, C., et al. (2017). Non-invasive assessment of cerebral blood flow and oxygen metabolism in neonates during hypothermic cardiopulmonary bypass: feasibility and clinical implications. *Sci. Rep.* 7:44117. doi: 10.1038/srep44117

Ferrari, M., and Quaresima, V. (2012). A brief review on the history of human functional near-infrared spectroscopy (fNIRS) development and fields of application. *Neuroimage* 63, 921–935. doi: 10.1016/j.neuroimage.2012.03.049

Fishkin, J. B., and Gratton, E. (1993). Propagation of photon-density waves in strongly scattering media containing an absorbing semi-infinite plane bounded by a straight edge. *J. Opt. Soc. Am. A* 10, 127–140.

Franceschini, M. A., and Boas, D. A. (2004). Noninvasive measurement of neuronal activity with near-infrared optical imaging. *Neuroimage* 21, 372–386.

Franceschini, M. A., Fantini, S., Paunescu, L. A., Maier, J. S., and Gratton, E. (1998). Influence of a superficial layer in the quantitative spectroscopic study of strongly scattering media. *Appl. Opt.* 37, 7447–7458.

Franceschini, M. A., Thaker, S., Themelis, G., Krishnamoorthy, K. K., Bortfeld, H., Diamond, S. G., et al. (2007). Assessment of infant brain development with frequency-domain near-infrared spectroscopy. *Pediatr. Res.* 61, 546–551.

Gatto, R., Hoffman, W., Mueller, M., Flores, A., Valyi-Nagy, T., and Charbel, F. T. (2006). Frequency domain near-infrared spectroscopy technique in the assessment of brain oxygenation: a validation study in live subjects and cadaver. *J. Neurosci. Methods* 157, 274–277.

Gatto, R., Hoffman, W., Paisansathan, C., Mantulin, W., Gratton, E., and Charbel, F. T. (2007). Effect of age on brain oxygenation regulation during changes in position. *J. Neurosci. Methods* 164, 308–311.

Grant, P. E., Roche-Labarbe, N., Surova, A., Themelis, G., Selb, J., Warren, E. K., et al. (2009). Increased cerebral blood volume and oxygen consumption in neonatal brain injury. *J. Cereb. Blood Flow Metab.* 29, 1704–1713. doi: 10.1038/jcbfm.2009.90

Gratton, G., Brumback, C. R., Gordon, B. A., Pearson, M. A., Low, K. A., and Fabiani, M. (2006). Effects of measurements method, wavelength, and source-detector distance on the fast optical signal. *Neuroimage* 32, 1576–1590.

Gratton, G., Corballis, P. M., Cho, E., Fabiani, M., and Hood, D. C. (1995a). Shades of gray matter: noninvasive optical images of human brain responses during visual stimulation. *Psychophysiology* 32, 505–509.

Gratton, G., Fabiani, M., Friedman, D., Franceschini, M. A., Fantini, S., Corballis, P., et al. (1995b). Rapid changes of optical parameters in the human brain during a tapping task. *J. Cogn. Neurosci.* 7, 446–456. doi: 10.1162/jocn.1995.7.4.446

Gratton, G., and Fabiani, M. (2003). The event-related optical signal (EROS) in visual cortex: replicability, consistency, localization, and resolution. *Psychophysiology* 40, 561–571.

Gratton, G., Wee, E., Rykhlevskaia, E. I., Leaver, E. E., and Fabiani, M. (2009). Does white matter matter? Spatio-temporal dynamics of task switching in aging. *J. Cogn. Neurosci.* 21, 1380–1395. doi: 10.1162/jocn.2009.21093

Gulsen, G., Xiong, B., Birgul, O., and Nalcioglu, O. (2006). Design and implementation of a multifrequency near-infrared diffuse optical tomography system. *J. Biomed. Opt.* 11:014020.

Hallacoglu, B., Sassaroli, A., and Fantini, S. (2013). Optical characterization of two-layered turbid media for non-invasive, absolute oximetry in cerebral and extracerebral tissue. *PLoS One* 8:e64095. doi: 10.1371/journal.pone.0064095

Hallacoglu, B., Sassaroli, A., Wysocki, M., Guerrero-Berroa, E., Schnaider Beeri, M., Haroutunian, V., et al. (2012). Absolute measurement of cerebral optical coefficients, hemoglobin concentration and oxygen saturation in old and young adults with near-infrared spectroscopy. *J. Biomed. Opt.* 17:081406. doi: 10.1117/1.JBO.17.8.081406

Haskell, R. C., Svaasand, L. O., Tsay, T., Feng, T., McAdams, M. S., and Tromberg, B. J. (1994). Boundary conditions for the diffusion equation in radiative transfer. *J. Opt. Soc. Am. A* 10, 2727–2741.

Hiwaki, O., and Miyaguchi, H. (2018). Noninvasive measurement of dynamic brain signals using light penetrating the brain. *PLoS One* 13:e0192095. doi: 10.1371/journal.pone.0192095

Huang, J., Wang, S., Jia, A., Mo, D., and Chen, H.-C. (2013). Cortical dynamics of semantic processing during sentence comprehension: evidence from event-related optical signals. *PLoS One* 8:e70671. doi: 10.1371/journal.pone.0070671

Hueber, D. M., Fantini, S., Cerussi, A. E., and Barbieri, B. B. (1999). New optical design for absolute (self-calibrating) NIR tissue hemoglobin measurements. *Proc. SPIE* 3597, 618–631.

Intes, X., Ntziachristos, V., and Chance, B. (2002). Analytical model for dual-interfering sources diffuse optical tomography. *Opt. Express* 10, 2–14.

Irani, F., Platek, S. M., Bunce, S., Ruocco, A. C., and Chute, D. (2007). Functional near infrared spectroscopy (fNIRS): an emerging neuroimaging technology with important applications for the study of brain disorders. *Clin. Neuropsychol.* 21, 9–37.

Kainerstorfer, J. M., Sassaroli, A., Tgavalekos, K. T., and Fantini, S. (2015). Cerebral autoregulation in the microvasculature measured with near-infrared spectroscopy. *J. Cereb. Blood Flow Metab.* 35, 955–966.

Kitsmiller, V. J., Dummer, M. M., Johnson, K., Cole, G. D., and Sullivan, T. D. O. (2018). Frequency domain diffuse optical spectroscopy with a near-infrared tunable vertical cavity surface emitting laser. *Opt. Express* 26, 21033–21043. doi: 10.1364/OE.26.021033

Kubota, M., Inouchi, M., Dan, I., Tsuzuki, D., Ishikawa, A., and Scovel, T. (2008). Fast (100-175 ms) components elicited bilaterally by language production as measured by three-wavelength optical imaging. *Brain Res.* 1226, 124–133. doi: 10.1016/j.brainres.2008.05.079

Kurth, C. D., and Thayer, W. S. (1999). A multiwavelength frequency-domain near-infrared cerebral oximeter. *Phys. Med. Biol.* 44, 727–740.

la Cour, A., Greisen, G., and Hyttel-Sorensen, S. (2018). *In vivo* validation of cerebral near-infrared spectroscopy: a review. *Neurophotonics* 5:040901. doi: 10.1117/1.NPh.5.4.040901

Lin, P.-Y., Hagan, K., Fenoglio, A., Grant, P. E., and Franceschini, M. A. (2016). Reduced cerebral blood flow and oxygen metabolism in extremely preterm neonates with low-grade germinal matrix- intraventricular hemorrhage. *Sci. Rep.* 6:25903. doi: 10.1038/srep25903

Lin, T.-Y., Wu, J.-S., Lin, L. L., Ho, T.-C., Lin, P.-Y., and Chen, J.-J. (2016). Assessments of muscle oxygenation and cortical activity using functional near-infrared spectroscopy in healthy adults during hybrid activation. *IEEE Trans. Neural Syst. Rehabil. Eng.* 24, 1–9.

Lin, P.-Y., Chen, J. J., and Lin, S.-I. (2013a). The cortical control of cycling exercise in stroke patients: an fNIRS study. *Hum. Brain Mapp.* 34, 2381–2390.

Lin, P.-Y., Roche-Labarbe, N., Dehaes, M., Fenoglio, A., Grant, P. E., and Franceschini, M. A. (2013b). Regional and hemispheric asymmetries of cerebral hemodynamic and oxygen metabolism in newborns. *Cereb. Cortex* 23, 339–348. doi: 10.1093/cercor/bhs023

Liu, N., Sassaroli, A., and Fantini, S. (2005a). Two-dimensional phased-arrays of sources and detectors for depth discrimination in diffuse optical imaging. *J. Biomed. Opt.* 10:051801.

Liu, N., Sassaroli, A., Zucker, M. A., and Fantini, S. (2005b). Three-element phased-array approach to diffuse optical imaging based on post-processing of continuous-wave data. *Opt. Lett.* 30, 281–283.

Low, K. A., Leaver, E., Kramer, A. F., Fabiani, M., and Gratton, G. (2006). Fast optical imaging of frontal cortex during active and passive oddball tasks. *Psychophysiology* 43, 127–136.

Low, K. A., Leaver, E. E., Kramer, A. F., Fabiani, M., and Gratton, G. (2009). Share or compete? Load-dependent recruitment of prefrontal cortex during dual-task performance. *Psychophysiology* 46, 1069–1079.

Luu, S., and Chau, T. (2009). Decoding subjective preference from single-trial near-infrared spectroscopy signals. *J. Neural Eng.* 6:016003. doi: 10.1088/1741-2560/6/1/016003

Maclin, E. L., Gratton, G., and Fabiani, M. (2003). Optimum filtering for EROS measurements. *Psychophysiology* 40, 542–547.

Maclin, E. L., Low, K. A., Fabiani, M., and Gratton, G. (2007). Improving the signal-to-noise ratio of event-related optical signals. *IEEE Eng. Med. Biol. Mag.* 26, 47–51.

Maclin, E. L., Low, K. A., Sable, J. J., Fabiani, M., and Gratton, G. (2004). The event-related optical signal to electrical stimulation of the median nerve. *Neuroimage* 21, 1798–1804.

Martelli, F., Del Bianco, S., Ismaelli, A., and Zaccanti, G. (2010). *Light Propagation through Biological Tissues and Other Diffusive Media*. Bellingham, WA: SPIE press.

McBride, T. O., Pogue, B. W., Jiang, S., Österberg, U. L., and Paulsen, K. D. (2001). A parallel-detection frequency-domain near-infrared tomography system for hemoglobin imaging of the breast *in vivo*. *Rev. Sci. Instrum.* 72, 1817–1824.

McIntosh, M. A., Shahani, U., Boulton, R. G., and McCulloch, D. L. (2010). Absolute quantification of oxygenated hemoglobin within the visual cortex with functional near infrared spectroscopy (fNIRS). *Invest. Ophtalmol. Vis. Sci.* 51, 4856–4860. doi: 10.1167/iovs.09-4940

McKernan Ward, L., Aitchison, R. T., Tawse, M., Simmers, A. J., and Shahani, U. (2015). Reduced haemodynamic response in the ageing visual cortex measured by absolute fNIRS. *PLoS One* 10:e0125012. doi: 10.1371/journal.pone.0125012

Medvedev, A. V., Kainerstorfer, J. M., Borisov, S. V., Gandjbakhche, A. H., and VanMeter, J. (2010). 'Seeing' electroencephalogram through the skull: imaging prefrontal cortex with fast optical signal. *J. Biomed. Opt.* 15:061702.

Meng, L., Gelb, A. W., Alexander, B. S., Cerussi, A. E., Tromberg, B. J., Yu, Z., et al. (2012a). Impact of phenylephrine administration on cerebral tissue oxygen saturation and blood volume is modulated by carbon dioxide in anaesthesized patients. *Br. J. Anaesth.* 108, 815–822. doi: 10.1093/bja/aes023

Meng, L., Mantulin, W. W., Alexander, B. S., Cerussi, A. E., Tromberg, B. J., Yu, Z., et al. (2012b). Head-up tilt and hyperventilation produce similar changes in cerebral oxygenation and blood volume: an observational comparison study using frequency-domain near-infrared spectroscopy. *Can. J. Anesth.* 59, 357–365. doi: 10.1007/s12630-011-9662-8

Metz, A. J., Klein, S. D., Scholkmann, F., and Wolf, U. (2017). Continuous coloured light altered human brain haemodynamics, and oxygenation assessed by systemic physiology augmented functional near-infrared spectroscopy. *Sci. Rep.* 7:10027. doi: 10.1038/s41598-017-09970-z

Moreau, F., Yang, R., Nambiar, V., Demchuk, A. M., and Dunn, J. F. (2016). Near-infrared measurements of brain oxygenation in stroke. *Neurophotonics* 3:031403. doi: 10.1117/1.NPh.3.3.031403

Morren, G., Wolf, M., Lemmerling, P., Wolf, U., Choi, J. H., Gratton, E., et al. (2004). Detection of fast neuronal signals in the motor cortex from functional near infrared spectroscopy measurements using independent component analysis. *Med. Biol. Eng. Comput.* 42, 92–99.

Nielsen, H. B. (2014). Systematic review of near-infrared spectroscopy determined cerebral oxygenation during non-cardiac surgery. *Front. Physiol.* 5:93. doi: 10.3389/fphys.2014.00093

Nissilä, I., Kotilahti, K., Fallström, K., and Katila, T. (2002). Instrumentation for the accurate measurement of phase and amplitude in optical tomography. *Rev. Sci. Instrum.* 73, 3306–3312.

Nissilä, I., Noponen, T., Kotilahti, K., Fallström, K., Katila, T., Lipiäinen, L., et al. (2005). Instrumentation and calibration methods for the multichannel measurement of phase and amplitude in optical tomography. *Rev. Sci. Instrum.* 76:044302.

No, K.-S., Kwong, R., Chou, P. H., and Cerussi, A. (2008). Design and testing of a miniature broadband frequency domain photon migration instrument. *J. Biomed. Opt.* 13:050509. doi: 10.1117/1.2998473

Noponen, T., Kièiæ, D., Kotilahti, K., Kajava, T., Kähkönen, S., Nissilä, I., et al. (2005). Simultaneous diffuse near-infrared imaging of hemodynamic and oxygenation changes and electroencephalographic measurements of neuronal activity in the human brain. *Proc. SPIE* 5693, 179–190.

Noponen, T., Kotilahti, K., Toppila, J., Nissilä, I., Salmi, T., Kajava, T., et al. (2003). Near-infrared measurements of hemodynamic and oxygenation changes on the frontal cortex during breath holding, hyperventilation, and natural sleep. *Proc. SPIE* 4955, 124–133.

Ntziachristos, V., Brun, N., Feet, B., Greisen, G., and Chance, B. (1997). Oximetry with phase modulation NIR spectroscopy based on phase measurement only. *Proc. SPIE* 2979, 715–723.

Obrig, H. (2014). NIRS in clinical neurology: a 'promising' tool? *Neuroimage* 85, 535–546.

O'Sullivan, T. D., Cerussi, A. E., Cuccia, D. J., and Tromberg, B. J. (2012). Diffuse optical imaging using spatially and temporally modulated light. *J. Biomed. Opt.* 17:071311. doi: 10.1117/1.JBO.17.7.071311

Paisansathan, C., Hoffman, W. E., Gatto, R. G., Baughman, V. L., Mueller, M., and Charbel, F. T. (2007). Increased brain oxygenation during intubation-related stress. *Eur. J. Anaesthesiol.* 24, 1016–1020.

Parks, N. A., Maclin, E. L., Low, K. A., Beck, D. M., Fabiani, M., and Gratton, G. (2012). Examining cortical dynamics and connectivity with simultaneous single-pulse transcranial magnetic stimulation and fast optical imaging. *Neuroimage* 59, 2504–2510. doi: 10.1016/j.neuroimage.2011.08.097

Pham, T., Tgavalekos, K., Sassaroli, A., Blaney, G., and Fantini, S. (2019). Quantitative measurements of cerebral blood flow with near-infrared spectroscopy. *Biomed. Opt. Express* 10, 2117–2134. doi: 10.1364/BOE.10.002117

Pham, T. H., Coquoz, O., Fishkin, J. B., Anderson, E., and Tromberg, B. J. (2000). Broad bandwidth frequency domain instrument for quantitative tissue optical spectroscopy. *Rev. Sci. Instrum.* 71, 2500–2513.

Pierro, M., Sassaroli, A., Bergethon, P. R., Ehrenberg, B. L., and Fantini, S. (2012). Phase-amplitude investigation of spontaneous low-frequency oscillations of cerebral hemodynamics with near-infrared spectroscopy: a sleep study in human subjects. *Neuroimage* 63, 1571–1584. doi: 10.1016/j.neuroimage.2012.07.015

Power, S. D., Falk, T. H., and Chau, T. (2010). Classification of prefrontal activity due to mental arithmetic and music imagery using hidden Markov models and frequency domain near-infrared spectroscopy. *J. Neural Eng.* 7:026002. doi: 10.1088/1741-2560/7/2/026002

Proulx, N., Samadani, A. A., and Chau, T. (2018a). Online classification of the near-infrared spectroscopy fast optical signal for brain-computer interfaces. *Biomed. Phys. Eng. Express* 4:065010.

Proulx, N., Samadani, A. A., and Chau, T. (2018b). Quantifying fast optical signal and event-related potential relationships during a visual oddball task. *Neuroimage* 178, 119–128. doi: 10.1016/j.neuroimage.2018.05.031

Quaresima, V., and Ferrari, M. (2019). A mini-review on functional near-infrared spectroscopy (fNIRS): where do we stand, and where should we go? *Photonics* 6:87.

Radhakrishnan, H., Vanduffel, W., Deng, H. P., Ekstrom, L., Boas, D. A., and Franceschini, M. A. (2009). Fast optical signal not detected in awake behaving monkeys. *Neuroimage* 45, 410–419. doi: 10.1016/j.neuroimage.2008.12.014

Rajan, K., Vijayakumar, V., Biswas, S. K., and Vasu, R. M. (2008). Implementation of a phase array diffuse optical tomography imager. *Rev. Sci. Instrum.* 79:084301. doi: 10.1063/1.2963042

Ramanujam, N., Du, C., Ma, H. Y., and Chance, B. (1998). Sources of phase noise in homodyne and heterodyne phase modulation devices used for tissue oximetry studies. *Rec. Sci. Instrum.* 69, 3042–3054.

Roblyer, D., O'Sullvan, T. D., Warren, R. V., and Tromberg, B. (2013). Feasibility of direct digital sampling for diffuse optical frequency domain spectroscopy in tissue. *Meas. Sci. Technol.* 24:045501.

Roche-Labarbe, N., Carp, S. A., Surova, A., Patel, M., Boas, D. A., Grant, P. E., et al. (2010). Noninvasive optical measures of CBV, StO_2, CBF index, and $rCMRO_2$ in human premature neonates' brain in the first six weeks of life. *Hum. Brain Mapp.* 31, 341–352. doi: 10.1002/hbm.20868

Roche-Labarbe, N., Fenoglio, A., Aggarwal, A., Dehaes, M., Carp, S. A., Franceschini, M. A., et al. (2012). Near-infrared spectroscopy assessment of cerebral oxygen metabolism in the developing premature brain. *J. Cereb. Blood Flow Metab.* 32, 481–488. doi: 10.1038/jcbfm.2011.145

Roche-Labarbe, N., Fenoglio, A., Radhakrishnan, H., Kocienski-Filip, M., Carp, S. A., Dubb, J., et al. (2014). Somatosensory evoked changes in cerebral oxygen consumption measured non-invasively in premature neonates. *Neuroimage* 85, 279–286. doi: 10.1016/j.neuroimage.2013.01.035

Ruesch, A., Schmitt, S., Yang, J., Smith, M. A., and Kainerstorfer, J. M. (2019). Fluctuations in intracranial pressure can be estimated non-invasively using near-infrared spectroscopy in non-human primates. *J. Cereb. Blood Flow Metab.* doi: 10.1177/0271678X19891359 [Epub ahead of print].

Sassaroli, A., Blaney, G., and Fantini, S. (2019). Dual-slope method for enhanced depth sensitivity in diffuse optical spectroscopy. *J. Opt. Soc. Am. A* 36, 1743–1761. doi: 10.1364/JOSAA.36.001743

Sassaroli, A., deFrederick, B., Tong, Y., Renshaw, P. F., and Fantini, S. (2006). Spatially weighted BOLD signal for comparison of functional magnetic resonance imaging and near-infrared imaging of the brain. *Neuroimage* 33, 505–514.

Sassaroli, A., and Fantini, S. (2004). Comment on the modified Beer-Lambert law for scattering media. *Phys. Med. Biol.* 49, N255–N257.

Sassaroli, A., Pifferi, A., Contini, D., Torricelli, A., Spinelli, L., Wabnitz, H., et al. (2014). Forward solvers for photon migration in the presence of highly and totally absorbing objects embedded inside diffusive media. *J. Opt. Soc. Am. A* 31, 460–469. doi: 10.1364/JOSAA.31.000460

Sassaroli, A., Tong, Y., Fabbri, F., Frederick, B., Renshaw, P., and Fantini, S. (2004). Functional mapping of the human brain with near-infrared spectroscopy in the frequency-domain. *Proc. SPIE* 5312, 371–377.

Sassaroli, A., Zheng, F., Hirshfield, L. H., Girouard, A., Solovey, E. T., Jacob, R. J. K., et al. (2008). Discrimination of mental workload levels in human subjects with functional near-infrared spectroscopy. *J. Innov. Opt. Health Sci.* 1, 227–237. doi: 10.3389/fnhum.2013.00935

Sawosz, P., and Liebert, A. (2019). Method to improve the depth sensitivity of diffuse reflectance measurements to absorption changes in optically turbid medium. *Biomed. Opt. Express* 10, 5031–5041. doi: 10.1364/BOE.10.005031

Schmitt, J. M., Knûttel, A., and Knutson, J. R. (1992). Interference of diffusive light waves. *J. Opt. Soc. Am. A* 9, 1832–1843.

Scholkmann, F., Gerber, U., Wolf, M., and Wolf, U. (2013a). End-tidal CO2: an important parameter for a correct interpretation in functional brain studies using speech tasks. *Neuroimage* 66, 71–79. doi: 10.1016/j.neuroimage.2012.10.025

Scholkmann, F., Wolf, M., and Wolf, U. (2013b). The effect of inner speech on arterial CO_2, cerebral hemodynamics and oxygenation – A functional NIRS study. *Adv. Exp. Med. Biol.* 789, 81–87. doi: 10.1007/978-1-4614-7411-1_12

Scholkmann, F., Hafner, T., Metz, A. J., Wolf, M., and Wolf, U. (2017). Effect of short-term colored-light exposure on cerebral hemodynamics and oxygenation, and systemic physiological activity. *Neurophotonics* 4:045005. doi: 10.1117/1.NPh.4.4.045005

Scholkmann, F., Klein, S., Gerber, U., Wolf, M., and Wolf, U. (2014a). Cerebral hemodynamic and oxygenation changes induced by inner and heard speech: a study combining functional near-infrared spectroscopy and capnography. *J. Biomed. Opt.* 19:017002. doi: 10.1117/1.JBO.19.1.017002

Scholkmann, F., Kleiser, S., Jaakko Metz, A., Zimmermann, R., Mata Pavia, J., Wolf, U., et al. (2014b). A review on continuous wave functional near-infrared spectroscopy and imaging instrumentation and methodology. *Neuroimage* 85, 6–27.

Schwarz, C. E., Preusche, A., Wolf, M., Poets, C. F., and Franz, A. R. (2018). Prospective observational study on assessing the hemodynamic relevance of patent ductus arteriosus with frequency domain near-infrared spectroscopy. *BMC Pediatr.* 18:66. doi: 10.1186/s12887-018-1054-6

Sevick, E. M., Chance, B., Leigh, J., Nioka, S., and Maris, M. (1991). Quantitation of time- and frequency-resolved optical spectra for the determination of tissue oxygenation. *Anal. Biochem.* 195, 330–351.

Smith, M. (2011). Shedding light on the adult brain: a review of the clinical applications of near-infrared spectroscopy. *Philos. Trans. R. Soc. A* 369, 4452–4469. doi: 10.1098/rsta.2011.0242

Solovey, E. T., Lalooses, F., Chauncey, K., Weaver, D., Parasi, M., Scheutz, M., et al. (2011). "Sensing cognitive multitasking for a brain-based adaptive user interface," in *Proceedings of the ACM Conference on Human Factors in Computing Systems CHI'11*, (New York, NY: ACM Press), 383–392.

Srinivasan, S., Davis, S. C., and Carpenter, C. M. (2011). "Diffuse optical tomography using CW and frequency domain imaging systems," in *Handbook of Biomedical Optics*, eds D. A. Boas, C. Pitris, and N. Ramanujam (Boca Raton, FL: CRC Press), 373–394.

Steinbrink, J., Kempf, F. C. D., Villringer, A., and Obrig, H. (2005). The fast optical signal – Robust or elusive when non-invasively measured in the human adult? *Neuroimage* 26, 996–1008.

Steinbrink, J., Kohl, M., Obrig, H., Curio, G., Syré, F., Thomas, F., et al. (2000). Somatosensory evoked fast optical intensity changes detected non-invasively in the adult human head. *Neurosci. Lett.* 291, 105–108.

Sthalekar, C. C., and Joyner Koomson, V. (2013). A CMOS sensor for measurement of cerebral optical coefficients using non-invasive frequency domain near infrared spectroscopy. *IEEE Sens. J.* 13, 3166–3174.

Sultan, E., Najafizadeh, L., Gandjbakhche, A. H., Pourrezaei, K., and Daryoush, A. (2013). Accurate optical parameter extraction procedure for broadband near-infrared spectroscopy of brain matter. *J. Biomed. Opt.* 18:017008. doi: 10.1117/1.JBO.18.1.017008

Sun, B., Zhang, L., Gong, H., Sun, J., and Luo, Q. (2014). Detection of optical neuronal signals in the visual cortex using continuous wave near-infrared spectroscopy. *Neuroimage* 87, 190–198. doi: 10.1016/j.neuroimage.2013.11.003

Suzuki, S., Takasaki, S., Ozaki, T., and Kobayashi, Y. (1999). Tissue oxygenation monitor using NIR spatially resolved spectroscopy. *Proc. SPIE* 3597, 582–592.

Tgavalekos, K. T., Kainerstorfer, J. M., Sassaroli, A., and Fantini, S. (2016). Blood-pressure-induced oscillations of deoxy- and oxyhemoglobin concentrations are in-phase in the healthy breast and out-of-phase in the healthy brain. *J. Biomed. Opt.* 21:101410. doi: 10.1117/1.JBO.21.10.101410

Tian, F., Jenks, C., Potter, D., Miles, D., and Raman, L. (2017). Regional cerebral abnormalities measured by frequency-domain near-infrared spectroscopy in pediatric patients during extracorporeal membrane oxygenation. *ASAIO J.* 63, e52–e59. doi: 10.1097/MAT.0000000000000453

Tong, Y., Rooney, E. J., Bergethon, P. R., Martin, J. M., Sassaroli, A., Ehrenberg, B. L., et al. (2005). Studying brain function with near-infrared spectroscopy concurrently with electroencephalography. *Proc. SPIE* 5693, 444–449.

Torjesen, A., Istfan, R., and Roblyer, D. (2017). Ultrafast wavelength multiplexed broad bandwidth digital diffuse optical spectroscopy for *in vivo* extraction of tissue optical properties. *J. Biomed. Opt.* 22:036009. doi: 10.1117/1.JBO.22.3.036009

Toronov, V., D'Amico, E., Hueber, D., Gratton, E., Barbieri, B., and Webb, A. (2004). Optimization of the phase and modulation depth signal-to-noise ratio for near-infrared spectroscopy of the biological tissue. *Proc. SPIE* 5474, 281–284.

Toronov, V., Webb, A., Choi, J. H., Wolf, M., Safonova, L., Wolf, U., et al. (2001). Study of local cerebral hemodynamics by frequency-domain near-infrared spectroscopy and correlation with simultaneously acquired functional magnetic resonance imaging. *Opt. Express* 9, 417–427.

Torricelli, A., Contini, D., Pifferi, A., Caffini, M., Re, R., Zucchelli, L., et al. (2014). Time domain functional NIRS imaging for human brain mapping. *Neuroimage* 85, 28–50. doi: 10.1016/j.neuroimage.2013.05.106

Tromberg, B. J., Svaasand, L. O., Tsay, T. T., and Haskell, R. C. (1993). Properties of photon density waves in multiple-scattering media. *Appl. Opt.* 32, 607–616. doi: 10.1364/AO.32.000607

Tse, C.-Y., and Penney, T. B. (2007). Preattentive change detection using the event-related optical signal. *IEEE Eng. Med. Biol. Mag.* 26, 52–58.

Tse, C.-Y., Rinne, T., Ng, K. K., and Penney, T. B. (2013). The functional role of the frontal cortex in pre-attentive auditory change detection. *Neuroimage* 83, 870–879. doi: 10.1016/j.neuroimage.2013.07.037

Tse, C.-Y., Tien, K. R., and Penney, T. B. (2006). Event-related optical imaging reveals the temporal dynamics of right temporal and frontal cortex activation in pre-attentive change detection. *Neuroimage* 29, 314–320.

Tuchin, V. (2007). *Tissue Optics: Light Scattering Methods, and Instruments for Medical Diagnosis*, 2nd Edn. Bellingham, WA: SPIE Press, 463–482.

Virtanen, J., Noponen, T., and Meriläinen, P. (2009). Comparison of principal and independent component analysis in removing extracerebral interference from near-infrared spectroscopy signals. *J. Biomed. Opt.* 14:054032. doi: 10.1117/1.3253323

Wang, L. V., and Wu, H. I. (2007). *Biomedical Optics: Principles and Imaging*. Hoboken, NJ: Wiley, 253–275.

Watzman, H. M., Kurth, C. D., Montenegro, L. M., Rome, J., Steven, J. M., and Nicolson, S. C. (2000). Arterial and venous contributions to near-infrared cerebral oximetry. *Anesthesiology* 93, 947–953.

Wilson, B. C., Sevick, E. M., Patterson, M. S., and Chance, B. (1992). Time-dependent optical spectroscopy and imaging for biomedical applications. *Proc. IEEE* 80, 918–930.

Wolf, M., Naulaers, G., van Bel, F., Kleiser, S., and Greisen, G. (2012). A review of near infrared spectroscopy for term and preterm newborns. *J. Near Infrared Spectrosc.* 20, 43–55.

Wolf, M., Wolf, U., Choi, J. H., Gupta, R., Safonova, L. P., Paunescu, L. A., et al. (2002a). Functional frequency-domain near-infrared spectroscopy detects fast neuronal signal in the motor cortex. *Neuroimage* 17, 1868–1875.

Wolf, M., Wolf, U., Choi, J. H., Toronov, V., Paunescu, L. A., Michalos, A., et al. (2003). Fast cerebral functional signal in the 100-ms range detected in the visual cortex by frequency-domain near-infrared spectrophotometry. *Psychophysiology* 40, 521–528.

Wolf, M., Wolf, U., Toronov, V., Michalos, A., Paunescu, L. A., Choi, J. H., et al. (2002b). Different time evolution of oxyhemoglobin and deoxyhemoglobin concentration changes in the visual and motor cortices during functional stimulation: a near-infrared spectroscopy study. *Neuroimage* 16, 704–712.

Yang, M., Yang, Z., Yuan, T., Feng, W., and Wang, P. (2019). A systemic review of functional near-infrared spectroscopy for stroke: current application and future directions. *Front. Neurol.* 10:58. doi: 10.3389/fneur.2019.00058

Yang, R., and Dunn, J. F. (2015). Reduced cortical microvascular oxygenation in multiple sclerosis: a blinded, case-controlled study using a novel quantitative near-infrared spectroscopy method. *Sci. Rep.* 5:16477. doi: 10.1038/srep16477

Yang, Y., Liu, H., Li, X., and Chance, B. (1997). Low-cost frequency-domain photon migration instrument for tissue spectroscopy, oximetry, and imaging. *Opt. Eng.* 36, 1562–1569.

Yu, G., Durduran, T., Furuya, D., Greenberg, J. H., and Yodh, A. G. (2003). Frequency-domain multiplexing system for *in vivo* diffuse light measurements of rapid cerebral hemodynamics. *Appl. Opt.* 42, 2931–2939.

Yun, R., and Joyner Koomson, V. (2013). A novel CMOS frequency-mixing transimpedance amplifier for frequency domain near infrared spectroscopy. *IEEE Trans. Circuits Syst.* 60, 84–94.

Zhang, G., Katz, A., Alfano, R. R., Kofinas, A. D., Kofinas, D. A., Stubblefield, P. G., et al. (2000). Brain perfusion monitoring with frequency-domain and continuous-wave near-infrared spectroscopy: a cross-correlation study in newborn piglets. *Phys. Med. Biol.* 45, 3143–3158.

Zhang, Z., Bolz, N., Laures, M., Oremek, M., Schmidt, C., Qi, M., et al. (2017). Cerebral blood volume and oxygen supply uniformly increase following various intrathoracic pressure strain. *Sci. Rep.* 7:8344.

Zhang, Z., Sun, B., Gong, H., Zhang, L., Sun, J., Wang, B., et al. (2012). A fast neuronal signal-sensitive continuous-wave near-infrared imaging system. *Rev. Sci. Instrum.* 83:094301.

Zhao, J., Ding, H. S., Hou, X. L., Zhou, C. L., and Chance, B. (2005). *In vivo* determination of the optical properties of infant brain using frequency-domain near-infrared spectroscopy. *J. Biomed. Opt.* 10:024028.

Zhao, Y., Applegate, M. B., Istfan, R., Pande, A., and Roblyer, D. (2018). Quantitative real-time pulse oximetry with ultrafast frequency-domain diffuse optics and deep neural network processing. *Biomed. Opt. Express* 9, 5997–6008. doi: 10.1364/BOE.9.005997

Zimmermann, B. B., Fang, Q., Boas, D. A., and Carp, S. A. (2016). Frequency domain near-infrared multiwavelength imager design using high-speed, direct analog-to-digital conversion. *J. Biomed. Opt.* 21:016010.

Conflict of Interest: The authors declare that the research was conducted in the absence of any commercial or financial relationships that could be construed as a potential conflict of interest.

Copyright © 2020 Fantini and Sassaroli. This is an open-access article distributed under the terms of the Creative Commons Attribution License (CC BY). The use, distribution or reproduction in other forums is permitted, provided the original author(s) and the copyright owner(s) are credited and that the original publication in this journal is cited, in accordance with accepted academic practice. No use, distribution or reproduction is permitted which does not comply with these terms.

frontiers in Human Neuroscience

ORIGINAL RESEARCH
published: 15 April 2020
doi: 10.3389/fnhum.2020.00113

Brain-Based Binary Communication Using Spatiotemporal Features of fNIRS Responses

Laurien Nagels-Coune[1,2,3], Amaia Benitez-Andonegui[1,2], Niels Reuter[4,5], Michael Lührs[6], Rainer Goebel[1,2,6], Peter De Weerd[1,2,7], Lars Riecke[1,2] and Bettina Sorger[1,2]*

[1] Department of Cognitive Neuroscience, Maastricht University, Maastricht, Netherlands, [2] Maastricht Brain Imaging Center, Maastricht, Netherlands, [3] University Psychiatric Centre Sint-Kamillus, Bierbeek, Belgium, [4] Institute of Systems Neuroscience, Heinrich-Heine University, Düsseldorf, Germany, [5] Institute of Neuroscience and Medicine (INM-7), Research Centre Jülich, Jülich, Germany, [6] Brain Innovation B.V., Maastricht, Netherlands, [7] Maastricht Centre for Systems Biology (MaCSBio), Maastricht University, Maastricht, Netherlands

OPEN ACCESS

Edited by:
Yunjie Tong, Purdue University, United States

Reviewed by:
George Alexandrakis, University of Texas at Arlington, United States
Masashi Kiguchi, Hitachi, Japan

***Correspondence:**
Laurien Nagels-Coune laurien.nagels-coune@maastrichtuniversity.nl

Specialty section:
This article was submitted to Brain-Computer Interfaces, a section of the journal Frontiers in Human Neuroscience

Received: *22 December 2019*
Accepted: *12 March 2020*
Published: *15 April 2020*

Citation:
Nagels-Coune L, Benitez-Andonegui A, Reuter N, Lührs M, Goebel R, De Weerd P, Riecke L and Sorger B (2020) Brain-Based Binary Communication Using Spatiotemporal Features of fNIRS Responses. Front. Hum. Neurosci. 14:113. doi: 10.3389/fnhum.2020.00113

"Locked-in" patients lose their ability to communicate naturally due to motor system dysfunction. Brain-computer interfacing offers a solution for their inability to communicate by enabling motor-independent communication. Straightforward and convenient in-session communication is essential in clinical environments. The present study introduces a functional near-infrared spectroscopy (fNIRS)-based binary communication paradigm that requires limited preparation time and merely nine optodes. Eighteen healthy participants performed two mental imagery tasks, mental drawing and spatial navigation, to answer yes/no questions during one of two auditorily cued time windows. Each of the six questions was answered five times, resulting in five trials per answer. This communication paradigm thus combines both spatial (two different mental imagery tasks, here mental drawing for "yes" and spatial navigation for "no") and temporal (distinct time windows for encoding a "yes" and "no" answer) fNIRS signal features for information encoding. Participants' answers were decoded in simulated real-time using general linear model analysis. Joint analysis of all five encoding trials resulted in an average accuracy of 66.67 and 58.33% using the oxygenated (HbO) and deoxygenated (HbR) hemoglobin signal respectively. For half of the participants, an accuracy of 83.33% or higher was reached using either the HbO signal or the HbR signal. For four participants, effective communication with 100% accuracy was achieved using either the HbO or HbR signal. An explorative analysis investigated the differentiability of the two mental tasks based solely on spatial fNIRS signal features. Using multivariate pattern analysis (MVPA) group single-trial accuracies of 58.33% (using 20 training trials per task) and 60.56% (using 40 training trials per task) could be obtained. Combining the five trials per run using a majority voting approach heightened these MVPA accuracies to 62.04 and 75%. Additionally, an fNIRS suitability

questionnaire capturing participants' physical features was administered to explore its predictive value for evaluating general data quality. Obtained questionnaire scores correlated significantly (r = -0.499) with the signal-to-noise of the raw light intensities. While more work is needed to further increase decoding accuracy, this study shows the potential of answer encoding using spatiotemporal fNIRS signal features or spatial fNIRS signal features only.

Keywords: functional near infrared spectroscopy (fNIRS), brain computer interface, mental imagery, mental drawing, motor imagery, spatial navigation, binary communication, yes/no decoding

INTRODUCTION

Active human communication depends fully on the functional integrity of the motor system. When the motor system ceases to function, e.g., due to neuromuscular impairments, consequences can be detrimental for communication. Severe motor paralysis most often occurs through infarction of the pons (Patterson and Grabois, 1986) or in late stages of diseases such as amyotrophic lateral sclerosis (ALS) and multiple sclerosis. In some cases this leads to a state of being fully awake and aware (Laureys, 2005; Monti et al., 2009) but without any ability to communicate in a natural way, commonly referred to as the "locked-in" syndrome (LIS; see Plum and Posner, 1982; Laureys, 2005; Monti et al., 2009). In "classical" LIS, vertical eye movements and eye blinking are spared and can thus be used for basic communication. Nevertheless, in progressive motor-neuron disorders such as ALS, control of the eye muscles is lost in late stages of the disease, resulting in a "complete" or "total" LIS (Bauer et al., 1979).

In LIS patients, voluntarily evoked brain signals can be exploited to restore basic communication independent of motor function. This can be achieved through a brain-computer interface (BCI), which relies on intentionally generated brain signals that are measured with a functional neuroimaging method, e.g., electroencephalography (EEG; Farwell and Donchin, 1988; Leuthardt et al., 2004), magnetoencephalography (MEG; Mellinger et al., 2007; Reichert et al., 2017) or functional magnetic resonance imaging (fMRI; Sorger et al., 2009, 2012; Monti et al., 2010; Bardin et al., 2011; Naci and Owen, 2013). A BCI then processes these inputs such that they can be used for motor control, communication, neurofeedback, *etc*.

EEG is the most widely used neuroimaging method for BCI purposes. Encouraging communication results have been reported using EEG-based BCIs (Farwell and Donchin, 1988; Birbaumer et al., 1999; Leuthardt et al., 2004; Nijboer et al., 2008). Recent binary communication paradigms established accuracies consistently above 70% (Halder et al., 2010; Käthner et al., 2015), even reaching an accuracy of 87.5% in one patient (Han et al., 2019). EEG-based BCIs have been mainly tested with visual paradigms using event-related potentials that, at least partly, dependent on patients ability to fixate (Brunner et al., 2010; Treder and Blankertz, 2010). However, the population of LIS patients is heterogeneous, with varying degrees of visual impairment/oculomotor control (Riccio et al., 2012), cognitive impairment (Schnakers et al., 2008; Wilson et al., 2011) and brain areas affected. Given this patient heterogeneity, a wide range of neuroimaging methods should be explored as each has its limitations. In a recent hybrid EEG-functional near-infrared spectroscopy (fNIRS) study (Rezazadeh Sereshkeh et al., 2019) it was found that the EEG signal was detrimental in most healthy participants. Nevertheless, certain participants truly benefited from use of the fNIRS signal. The high spatial resolution of hemodynamic neuroimaging, such as fMRI and fNIRS, combined with the – typically used – auditorily guided imagery paradigms might be beneficial for certain BCI users.

A seminal fMRI paradigm (Monti et al., 2010) enabled binary communication in disorders of consciousness patients through the use of tennis imagery for encoding a "yes" response and spatial navigation imagery for a "no" response. In the 16 healthy control subjects, a decoding accuracy of 100% was obtained. Work from our lab has extended this type of paradigm to a four-choice BCI (Sorger et al., 2009), with an average accuracy of 94.9% (theoretical chance level being 25%), and a free-letter spelling BCI (Sorger et al., 2012), with an average accuracy of 82% (theoretical chance level: ca. 3.7%), successfully tested in healthy participants. Given the immobility of fMRI hardware, the current challenge is to transfer these fMRI-based paradigms to a mobile setup employing fNIRS, thereby enabling convenient BCI-based communication of patients in daily-life settings, e.g., in their home environments.

The use of fNIRS as a method to measure brain signals is gaining popularity, with the number of publications increasing rapidly (Boas et al., 2014) since its first use in 1993 (Chance et al., 1993; Hoshi and Tamura, 1993; Kato et al., 1993; Villringer et al., 1993). The mobility of fNIRS hardware makes it highly suited for bedside testing (Cutini et al., 2012; León-Carrión and León-Domínguez, 2012), hence its growing use in brain-computer interfacing (Zephaniah and Kim, 2014). However note that its mobility comes at the cost of a generally lower accuracy compared to fMRI-based paradigms. The reason for these relatively lower classification accuracies in fNIRS-based paradigms is threefold: (1) fNIRS possesses an inherently lower spatial resolution than fMRI (2) fNIRS has a limited spatial coverage and is thus only able to sample superficial regions of the cortex (3) fMRI has a higher signal-to-noise ratio (SNR) than fNIRS (Cui et al., 2011), as fNIRS suffers from global/physiological noise from extracranial tissue (Zhang et al., 2016).

In the context of communication, most hemodynamic BCI systems rely on mental imagery for intentional generation of brain signals. Commonly used mental imagery tasks (see

Abbreviations: COI, channel-of-interest; MD, mental drawing; SN, spatial navigation.

Naseer and Hong, 2015, for a more extensive review) include mental speech (Sorger et al., 2012; Rezazadeh Sereshkeh et al., 2018), mental calculation/counting (Naito et al., 2007; Power et al., 2012; Sorger et al., 2009, 2012) and motor imagery (Coyle et al., 2007; Sorger et al., 2009, 2012; Monti et al., 2010; Abdalmalak et al., 2017a). Most fNIRS based-BCI communication studies focus on binary communication, as multi-class fNIRS-based BCIs are not yet enabling effective BCI control (Power et al., 2012; Weyand and Chau, 2015).

In most binary fNIRS-communication paradigms, a "yes" answer is encoded through mental imagery, whereas a "no" answer is encoded by rest (Abdalmalak et al., 2017b; Nagels-Coune et al., 2017; Naito et al., 2007; Naseer et al., 2014). In healthy subjects, group average accuracies range between 62 and 82% (Naseer et al., 2014; Nagels-Coune et al., 2017). In a subset of 23 out of 40 patients, an average accuracy above 75% was found using tasks activating prefrontal cortex such as mental calculation or mental singing (Naito et al., 2007). Recently Abdalmalak et al. (2017b) asked a LIS patient to imagine playing tennis for encoding a "yes", while resting to encode a "no". An accuracy of 100% was reached over five repetitions of three questions. The drawback from previously mentioned studies is that one cannot distinguish a real "no" answer from possible disengagement from the task. This problem can be circumvented through the use of a different, active mental task for each answer option. The evoked spatially different brain-activation patterns can then be exploited for encoding two answer alternatives. Several studies have demonstrated the potential of spatial discernibility of mental tasks using fNIRS. For example, Sitaram et al. (2007) were able to distinguish left- from right- hand motor imagery with an accuracy of 73% using a support vector machine (SVM) classification. Furthermore, Hong et al. (2015) could distinguish mental calculation, right- and left-hand imagery with an accuracy of 75.6% using 3-class linear discriminant analysis (LDA). However, to our knowledge, no study has tested the use of two mental tasks directly in a communication experiment. In a recent study, participants imagined different mental speech content for answering yes/no questions intuitively, i.e., imagining saying "yes" or "no" repeatedly (Rezazadeh Sereshkeh et al., 2018). An average accuracy of 64.1% was attained over two experimental sessions. Note, however, that only a 3-class ("yes", "no" and "rest") accuracy was reported, thus the 2-class accuracy ("yes" vs. "no") cannot be inferred from the report.

The current study aimed to increase the feasibility and success of an fNIRS-BCI in healthy participants, thereby potentially increasing the applicability in LIS patients. We used an approach that combines temporal encoding (distinct time windows for encoding "yes" and "no") with spatial encoding (two channels, each coding for a distinct mental imagery task, here motor imagery for "yes" and spatial navigation for "no"), as has been done in Sorger et al. (2009, 2012) in fMRI-based communication BCIs. In mental drawing trials, participants were asked to imagine drawing small geometric shapes with their right hand. In spatial navigation trials, participants imagined walking through their home and visualized the visual scene in different rooms. Similar tasks were previously used in the seminal fMRI work of Monti et al. (2010) and have been suggested to be explored in the context of fNIRS-BCI (Abdalmalak et al., 2017a). We expected motor cortex activation during motor imagery (Sitaram et al., 2007), and parietal activation during spatial navigation imagery (Cabrera and Dremstrup, 2008; McKendrick et al., 2016; Abdalmalak et al., 2017a). To increase general fNIRS-BCI feasibility by decreasing setup time, we opted for a sparse fNIRS optode setup with nine optodes covering large parts of left-hemispheric fronto-parietal cortex.

The current study included 18 healthy participants who were briefly trained prior to undergoing the fNIRS recording session. Participants were asked six binary questions (e.g., "Do you have a driver's license?") which they answered by performing one of the two tasks in auditorily cued time windows. Conventional univariate analyses were employed in simulated real-time to decode the participants' answers from the recorded fNIRS data. Additionally, a multivariate approach was applied to explore the discernibility of the two tasks based on their spatial brain activation patterns only. Comfort ratings were obtained throughout the experiment as other studies have reported that participants may withdraw from fNIRS recordings due to headset discomfort (Suzuki et al., 2010; Cui et al., 2011; Rezazadeh Sereshkeh et al., 2018). In addition, we evaluated whether the presence of specific physical features of participants (e.g., hair thickness, root density, or color) affected fNIRS-signal quality and subsequent decoding results (Koizumi et al., 1999; Coyle et al., 2005; Cui et al., 2011; Khan et al., 2012; Fang et al., 2018). To this end, an in-house questionnaire was administered. Moreover, participants' experience with the mental tasks in terms of ease and pleasantness were assessed, since they are known to positively correlate with decoding accuracy (Weyand and Chau, 2015).

In summary, due to the unique combination of temporal and spatial encoding of mental tasks, and the use of an active mental task for each answer option, we expected that our paradigm would outperform the standard paradigms reviewed here.

MATERIALS AND METHODS

Participants

The current dataset was collected in the same session as the data published in a previous study by Nagels-Coune et al. (2017). Eighteen of the twenty participants performed the present paradigm in addition to the previously reported paradigm. The localizer runs (see sections Localizer Block 1 and Localizer Block 2) have already been used in the context of the earlier study (Nagels-Coune et al., 2017). All eighteen healthy participants (eight females, age = 26.00 ± 8.19 years [mean ± SD]) reported normal hearing. The participants' characteristics of relevance to the fNIRS measurements are shown in **Table 1**. Written informed consent was acquired from each participant before the experiment. The experimental procedure conformed to the Declaration of Helsinki and was approved by the local ethics committee. All participants were compensated with a gift voucher for their participation.

Participant Preparation

Introducing the Two Mental Tasks

Following the informed consent procedure, participants were introduced to two mental imagery tasks. For the mental drawing (MD) task, participants were instructed to imagine drawing simple geometric shapes with their right hand. The three left-handed participants were thus requested to imagine drawing with their non-dominant hand. For the spatial navigation (SN) task, participants imagined walking through their house while vividly visualizing the visual scene of each room (see **Supplementary Material** for the standardized mental task instructions). Participants chose objects they would like to imagine drawing and a familiar environment they would like to imagine navigating through.

Selection of Binary Questions

Prior to the experiment, participants answered 45 unobtrusive binary questions (see **Supplementary Material**), e.g., "Do you have a driver's license?" in a questionnaire. Six questions, three answered with "yes" and three answered with "no", were selected for the main fNIRS experiment to ensure an equal distribution of both answers.

fNIRS Suitability Questionnaire

Due to fNIRS being an optical neuroimaging method, participants' physical features may alter the penetration/absorption of light and consequently signal strength (Coyle et al., 2005). To evaluate whether this influenced our results, we created an in-house questionnaire that quantifies participants' suitability for fNIRS measurements. The questionnaire (see **Supplementary Material**) captured the following physical features that are thought to influence fNIRS signal strength via distortion of optical contact between the skin and optodes (distortion skin-optode contact) or via light absorption: hair length (distortion skin-optode contact), hair color (light absorption; Koizumi et al., 1999; Coyle et al., 2005; Lloyd-Fox et al., 2010; Khan et al., 2012), hair thickness (light absorption affected by hair follicle density; Coyle et al., 2005; Fang et al., 2018), hair density (distortion skin-optode contact; Lloyd-Fox et al., 2010; Orihuela-Espina et al., 2010), hair structure (distortion skin-optode contact; Lloyd-Fox et al., 2010); skin color (light absorption by melanin concentration; Orihuela-Espina et al., 2010), and head size (light absorption affected by altered inter-optode distance). Each feature was rated on a scale ranging from 0 (desirable feature) to a maximum of 4 (undesirable feature). Scores were summed with a maximum score of 21. The higher the suitability score, the less suitable for fNIRS measurement the participant was deemed.

Cap Placement and Mental Task Training

Participants' head circumference was measured and an appropriately sized cap was selected. Cap sizes used in this experiment ranged from 54 to 60 cm (see **Table 1**). Prior to placing the cap, participants were asked to moisten the left side of the head to aid the placement of the optodes. Similar to EEG cap placement, nasion-inion distance was measured to ensure proper cap positioning. Participants were then seated in a sound-attenuating cabin, which was kept entirely dark

TABLE 1 | Participant characteristics: Handedness, capsize (in cm) and fNIRS suitability score (max score = 21).

Participant	Handedness	Cap size	fNIRS suitability score	Mental drawing COI		Spatial navigation COI	
				HbO	HbR	HbO	HbR
01	Right	56	12	CP3-CP5	CP3-CP5	FC3-FC1	CP3-CP5
02	Right	56	14	FC3-FC1	C3-C1	C3-FC5	FC3-FC5
03	Right	56	13	FC3-FC5	CP3-CP5	CP3-CP5	FC3-C5
04	Right	56	10	C3-FC5	FC3-C5	FC3-C5	FC3-C5
05	Left	56	10	C3-FC5	FC3-FC1	CP3-CP5	CP3-CP5
06	Right	56	16	CP3-C5	C3-C5	CP3-C5	CP3-C5
07	Right	56	14	FC3-FC5	FC3-FC5	FC3-FC5	FC3-FC5
08	Right	56	1	C3-FC5	C3-FC5	FC3-C1	C3-FC1
09	Right	56	13	C3-CP5	CP3-CP1	C3-FC5	CP3-C1
10	Right	56	14	C3-C5	C3-CP5	FC3-FC1	FC3-FC1
11	Right	56	10	FC3-C5	CP3-CP1	CP3-CP5	C3-C1
12	Right	58	17	FC3-FC5	FC3-FC5	FC3-FC5	FC3-FC1
13	Right	56	13	C3-C1	C3-C1	FC3-FC5	FC3-FC5
14	Right	58	14	CP3-CP1	C3-C5	C3-C5	C3-C5
15	Right	60	17	C3-C5	C3-C5	FC3-FC5	C3-C1
16	Right	56	10	CP3-CP1	C3-C5	FC3-FC5	C3-C1
17	Left	56	13	FC3-FC5	CP3-CP5	FC3-FC1	FC3-FC1
18	Left	56	13	C3-CP1	C3-C1	FC3-C5	FC3-C5

The last four columns show the channels-of-interest (COIs), selected on the basis of the data of localizer runs in block 1. Abbreviations: HbO, oxygenated hemoglobin; HbR, deoxygenated hemoglobin.

during the fNIRS measurement as ambient light can influence near-infrared spectroscopy measurements (Kovalenko et al., 2014; Pinti et al., 2018). While the optodes were placed in optode holders, participants were given the opportunity to practice the two mental tasks. This procedure took on average 17 min (standard deviation: ± 8 min).

fNIRS-Based Communication Paradigm

We employed an auditorily cued encoding paradigm in which fNIRS signals were evoked through differently timed (temporal encoding) mental imagery tasks (spatial encoding). The auditory cues, i.e., concise spoken commands, guided participants' mental imagery by indicating the start and end of each encoding window. The cues and their accompanying time point triggers were presented using an in-house software (StimulGL; Gijsen, 2015). Our design encompassed two localizer runs (block 1), six encoding runs, and finally another two localizer runs (block 2).

Localizer Block 1

In the two localizer runs, participants performed the two tasks in a fixed order, with the MD run preceding the SN run. These localizer runs were conducted to gauge participant's hemodynamic responses to the mental tasks and select task-sensitive channels for answer decoding. In the first localizer run, participants performed 20 MD trials with a duration of 10 s each, interleaved with 20 s rest periods. The localizer started with an initial rest period of 20 s, after which the participants heard the auditory cue "start". This cue marked the start of the MD task, by which participants were instructed to perform the mental imagery task until they heard the cue "rest". They then halted the mental imagery and remained at rest for 20 s, until the next "start" cue urged them to commence the mental imagery again. This procedure was repeated 20 times, resulting in 20 MD trials. The second localizer followed the same protocol.

Six Answer Encoding Runs

In this stage of the experiment, participants were asked to answer binary questions by performing one of two mental tasks in a particular time window. Participants were informed that to encode a "yes" answer, they had to perform MD imagery when they heard "yes". In the "yes" encoding runs, participants were instructed to ignore the "no" cues and to not perform SN (or any other task). Conversely, to encode a "no" answer, they had to perform SN imagery when they heard "no". In this case, the "yes" cues were ignored (see **Figure 1**).

Six questions were asked, each at the start of a separate answer encoding run. The question was read aloud through a microphone by the experimentor. The fNIRS recording started when the participant reported having his/her answer, i.e., "yes" or "no", and the corresponding task, i.e., MD or SN, clearly in mind. The time intervals within which a "yes" or "no" answer could be given followed 20 s after termination of the question. The "yes" interval was initiated by the auditory "yes" cue and terminated 10 s later by an auditory "stop" cue. The "yes" interval always proceeded the "no" interval, which was marked by the auditory cue "no" and "stop" 10 s later. Hence, if participants had chosen to answer "yes", they started performing the MD. If participants had chosen to answer "no", they ignored the "yes" cue. The cue, "stop", indicated participants to stop the mental imagery. Again, if participants had chosen to answer "no", they also ignored this "stop" cue and remained at rest until they heard the cue "no". At this point they started performing the SN task until the "stop" cue was heard. This procedure was repeated five times per encoding run, resulting in five "yes" and five "no" trials.

Summarized, participants thus answered questions by performing the MD mental task within a first time interval marked by "yes" and "stop" cues, or the SN mental task within a second time interval marked by "no" and "stop" cues.

Localizer Block 2

The procedure in localizer block 1 was repeated to increase the amount of available data for classifier training. This repetition was warranted, as we were unsure with respect to the minimum amount of data necessary for effectively training the classifier in the multivariate approach.

Comfortability Ratings

In between the ten fNIRS runs, participants were allowed to take a short break to slightly adjust their body posture, or drink some water. After each run, participants were asked to give a comfortability rating between 0 and 10, with 0 meaning "very uncomfortable" and 10 being "very comfortable".

Ease and Pleasantness of the Mental Tasks

After the ten fNIRS runs, the cap was removed and participants were asked to rate the ease and pleasantness of the MD and SN tasks with a score from 0 to 10. An easiness rating of 0 indicated great difficulty of mental task execution, whereas a rating of 10 indicated extreme ease of task execution. A pleasantness rating of 0 indicated an extremely unpleasant experience when performing the mental task, whereas a score of 10 indicated an extremely pleasant experience.

fNIRS Data Acquisition

Hemodynamic signals were obtained using a continuous-wave fNIRS system (NIRScout-816 system, NIRx Medizintechnik GmbH, Berlin, Germany; RRID: SCR_002491) and NIRStar (v. 12.0) software (NIRx Medizintechnik GmbH, Berlin, Germany; RRID: SCR_014540). Three source optodes, LEDs emitting light with wavelengths of 760 and 850 nm, were used in combination with six detector optodes. These nine optodes were placed in optode holders on the cap according to the international 10-20 EEG system. The three sources optodes were positioned on FC3, C3, and CP3, whereas the six detector optodes were positioned on FC5, C5, CP5, FC1, C1, and CP1 (see **Figure 2**). Defining a channel as a unique source and detector optode pair, this setup resulted in 18 channels. Channels FC3-CP1, FC3-CP5, CP3-FC1, and CP3-FC5 were excluded from all analyses, as the spatial separation between the sources and detectors exceeded 60 mm in the largest cap size (60 cm) used in this experiment. An optode separation of that size was considered undesirable since it largely exceeds the recommended inter-optode distance of 30 mm and gives rise to noisy and unstable

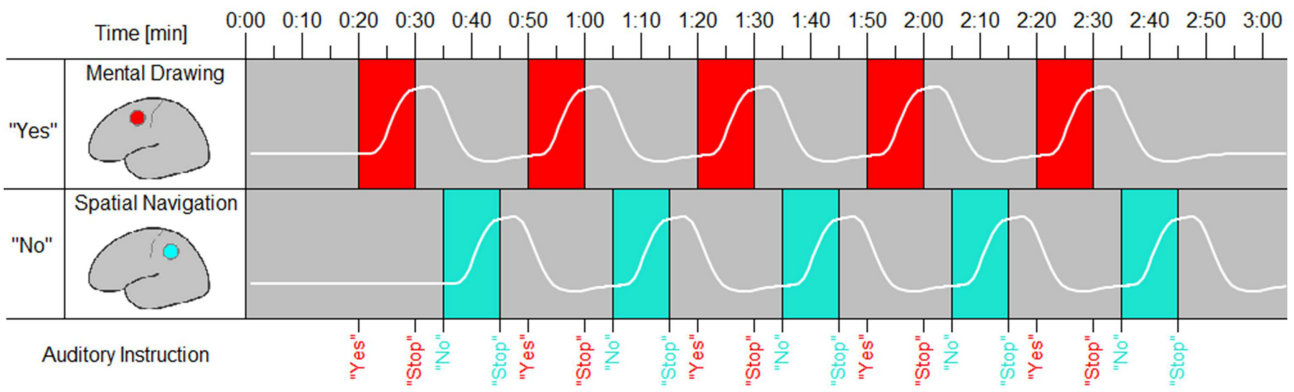

FIGURE 1 | Encoding scheme for answering a binary question. The red periods require mental drawing (MD) imagery, whereas the green periods required spatial navigation (SN) imagery. If participants chose to answer "yes", they started performing the MD task when they heard a "yes", halted their imagery when they heard the cue "stop", and ignored the auditory cues related to the "no" response. The hypothesized HbO response for a "yes" answer is shown by the upper white waveform. If participants chose to answer "no", they started performing the SN task when they heard a "no", halted their imagery when they heard the cue "stop", and ignored the auditory cues related to the "yes" response. The hypothesized HbO response for a "no" answer is shown by the lower white waveform.

signals (Gratton et al., 2006). The remaining 14 channels analyzed in this experiment are depicted by the red connecting lines in **Figure 2**. This optode montage covered a confined area above the left-hemispheric fronto-parietal (sensorimotor) cortex. The frontal optodes covered brain areas commonly associated with motor imagery, such as premotor cortex and possibly parts of the supplementary motor areas in certain head sizes (Sitaram et al., 2007; Koessler et al., 2009; Abdalmalak et al., 2016). The posterior optodes captured part of the parietal cortex, expected to be associated with SN imagery (Cabrera and Dremstrup, 2008; McKendrick et al., 2016; Abdalmalak et al., 2017a). Optical signals were recorded with a sampling rate of 12.5 Hz.

Data Analysis

Analyses of the fNIRS Signal

The main outcome of the spatiotemporal encoding paradigm, i.e., communication accuracy, was obtained with a General Linear Model (GLM) approach (univariate analysis). In addition, spatial discernibility of the two mental tasks was investigated using a SVM (multivariate analysis). See **Figure 3** for an illustration of the analyses workflow.

General data (pre)-processing

FNIRS time series were analyzed in simulated real-time using Turbo-Satori software (v1.2.8, Brain Innovation B.V., Maastricht, Netherlands). In the first pre-processing step, raw wavelengths were converted to optical densities. The optical density data were then converted to oxygenated hemoglobin (HbO) and deoxygenated hemoglobin (HbR) values using the modified Beer-Lambert law. Linear trend removal and moving average filtering (low-pass cut-off frequency: 0.3 Hz, filter order: 2; high-pass cut-off frequency: 0.01 Hz, filter order: 1) were applied. The low-pass filter aimed to remove high-frequency artifacts induced by heartbeat and breathing, whereas the high-pass filter served to remove low-frequency drifts.

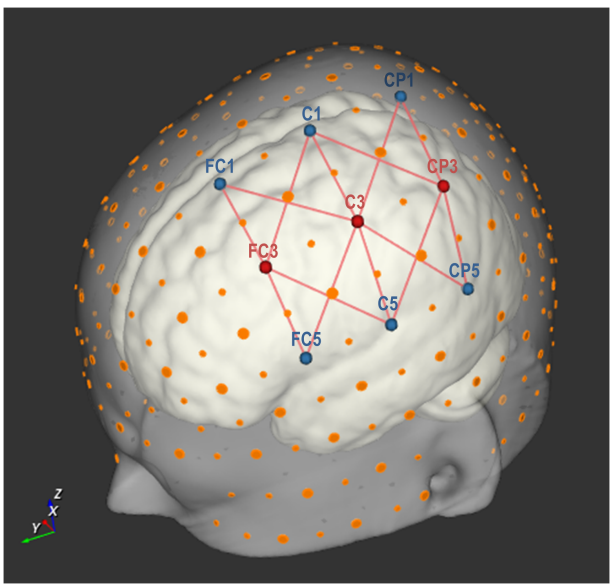

FIGURE 2 | Optode setup with three source and six detector optodes, placed on nine points according to the international 10-20 EEG system. Large orange dots represent reference points of the 10-20 system, whereas small orange dots represent reference points of the extended 10-10 EEG system (Oostenveld and Praamstra, 2001). The red lines represent 14 source-detector pairs (each forming an fNIRS channel). Image created using NIRSite (v.1) software (NIRx Medizintechnik GmbH, Berlin, Germany; RRID: SCR_002491).

Communication accuracy (univariate analysis)

Channel exclusion. To ensure proper signal quality, we excluded channels showing a signal-to-noise ratio below a given criterion value. To that aim, the channel-wise coefficient of variance percentage (CV%) was calculated on the unfiltered raw wavelength data by dividing the temporal standard deviation by the mean value (see Piper et al., 2014, for a detailed description).

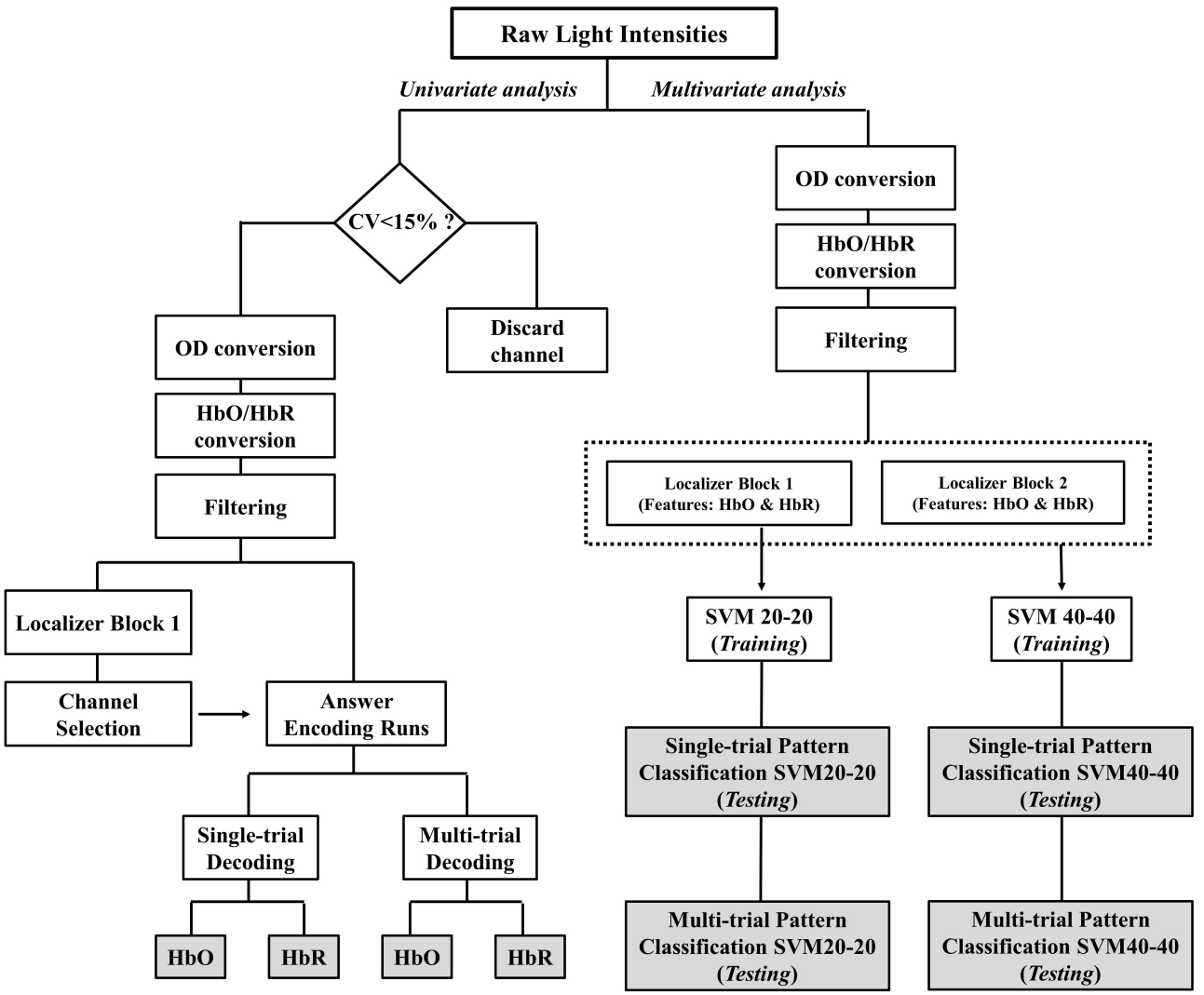

FIGURE 3 | Schematic depiction of the fNIRS signal analyses. The two main pipelines were univariate analysis and multivariate analysis. Each pipeline resulted in four accuracy outcomes. These outcome variables are represented in gray colored boxes. CV, coefficient of variance; OD, optical density; HbO, oxygenated hemoglobin; HbR, deoxygenated hemoglobin; SVM20-20, support vector machine with 20 training trials of each task; SVM40-40, support vector machine with 40 training trials of each task.

A CV% higher than 15 indicates insufficient signal-to-noise ratio (Schmitz et al., 2005; Schneider et al., 2011; Piper et al., 2014; Pfeifer et al., 2018). Consequently, all channels with a CV% higher than 15 for either one or both wavelengths in the first two localizers (block 1) were excluded from channel-of-interest selection. This channel-wise exclusion was also performed on the last set of localizers (block 2) to gauge the intra-individual variability in channel exclusion across all localizer runs.

Given the limited number of 14 channels in the current experiment, one runs the risk of excluding a potentially informative channel due to its high CV%. Therefore, all univariate analyses were repeated omitting the CV% criterion, thus allowing different channels to be selected for subsequent analyses (see **Supplementary Material**). Only when the overall accuracy differed significantly between both approaches, the accuracies of the analyses without the CV% criterion are also reported in the results section.

Channel selection. From the channels that were not excluded in the previous step, a single channel was chosen for each mental imagery task (MD and SN) based on the data of localizer block 1. HbO and HbR signals were analyzed separately. Four GLM analyses (HbO/HbR × MD/SN) were conducted with a predictor for the mental imagery trials and applying the contrast "MD/SN vs. rest". The four channels with the highest *t*-value in each of the four GLM analyses were coined "channels of interest" (COIs) and were considered for the following single- and multi-trial analyses of the answer encoding data.

Answer decoding. Participant's answers were decoded through comparison of the five individual trial pairs (single-trial

approach) or through comparison of the integrated five trials per answer option (multi-trial approach).

In the single-trial approach a GLM analysis was run with the statistical contrast "yes" vs. "no" for each yes/no trial pair (5 trial pairs per encoding run). This resulted in four *t*-values per trial pair, one for each COI (HbO/HbR × SN/MD), based on mental task predictors that encompassed two individual trials. These *t*-values were used to decode the participants' answer as follows: When the *t*-value of the MD COI was larger than the *t*-value of the SN COI, a "yes" answer was decoded. Whereas when the *t*-value of the MD COI was smaller than the *t*-value of the SN COI, a "no" answer was decoded. The single-trial approach resulted in 30 decoded answers (6 runs × 5 trial pairs) per participant. The decoded answers were compared to the originally encoded answers and each individual participant's accuracy was calculated.

In the multi-trial approach, a GLM analysis was run with the statistical contrast "yes" vs. "no". The five trials per answer option were used to infer a *t*-value for each COI (HbO/HbR × SN/MD). Decoding followed the same rationale of *t*-value comparison as in the single-trial approach. This procedure was repeated for all six answer-encoding runs for both the HbO and HbR signal separately. The decoded answers were compared to the originally encoded answers and each individual participant's accuracy was calculated. The multi-trial approach resulted in 6 decoded answers (6 runs) per participant. The decoded answers were compared to the originally encoded answers and each individual participant's accuracy was calculated.

To assess the significance of the participants' decoding accuracies in the univariate analyses, we determined the empirical chance level based on binomial distributions (Noirhomme et al., 2014). The following settings were determined: $\alpha = 0.05$, number of independent outcomes $k = 2$ and number of independent trials $n = 30$ or $n = 6$ for single- and multi-trial accuracies respectively. The resulting upper-bound empirical chance levels for evaluating single- and multi-trial accuracies were therefore 19 trials (63.33%) and 5 trials (83.33%) respectively. If 19 or more trials were decoded correctly in the single-trial approach, this was considered a significant result. If 5 or more trials were decoded correctly in the multi-trial approach, this was considered a significant result.

The rate of correct detection of "yes"/"no" answers was calculated by dividing the amount of correctly detected "yes"/"no" answers by the total amount of encoded "yes"/"no" answers per participant, i.e., 15 for the single-trial and 3 for the multi-trial analysis.

Multivariate analyses

Single-trial results. Two classifiers were trained to discriminate the spatial activation patterns in all 14 channels induced by the two different mental tasks. This was done using either 20 or 40 trials of each mental task. One classifier was trained on two runs: one for MD (MD1) and one for SN (SN1), with each 20 trials (SVM20-20). The other classifier was trained on four runs: two for MD (MD1 and MD2) and two for SN (SN1 and SN2), resulting in 40 trials for each task (SVM40-40). We considered a temporal window spanning -2 s to 20 s (where 0–10 s corresponds to the trial interval) and linearly fitted each HbO/HbR concentration channel time course separately with a design matrix consisting of a double-gamma hemodynamic response function per trial and an additional linear confound predictor. Resulting estimates were *t*-values which were stored in volume map files for each time course. These files were used as input for the classifier testing on an independent dataset, i.e., the six answer-encoding runs' data. Per answer-encoding run, the five "active" trials, i.e., trials in which we knew the participant was performing a task, were tested. The five "inactive" trials in which participants rested were not analyzed. This resulted into a total of thirty testing trials (6 runs × 5 "active" trials) per participant. The proportion of testing trials for which the decoded answer matched the true answer was subsequently calculated. Lastly, to determine the empirical chance level for each individual participant, permutation testing was performed with an in-house MATLAB script (ver. R2015a). To this end, task labels were randomly reassigned to each trial in the training dataset, on which the classifier was subsequently trained. Testing was then done on an independent, non-permuted testing dataset. This procedure was repeated 2000 times. Chance level was calculated as the proportion of permutations revealing accuracies lower or equal to the accuracy obtained using the real (non-permuted) dataset.

The rate of correct detection of MD/SN was calculated by dividing the amount of correctly detected MD/SN patterns by the total amount of encoded MD/SN trials, i.e., 15 per task.

Multi-trial results. Multi-trial accuracies were derived from the single-trial multivariate results reported above. The five yes/no decisions per run were integrated using majority voting (e.g., three answers encoded as "yes" and two answers encoded as "no" were considered as a "yes" answer, and vice versa). The proportion of decoded answers matching with the true answer was calculated for each participant. The upper-bound empirical chance level for each individual participant was 83.33%, based on binomial distributions.

The rate of correct detection of MD/SN was calculated by dividing the amount of correctly detected MD/SN patterns by the total amount of encoded MD/SN runs, i.e., 3 per task.

fNIRS Suitability Questionnaire and Signal Quality

The total fNIRS suitability score was obtained by summing all features, with a maximum score of 21 (see **Table 1** for suitability score per participant). This score was correlated with the number of channels with a CV under 15%, which is a metric for fNIRS signal quality (Balardin et al., 2017), through calculation of a one-tailed Pearson's *r* in SPPS (ver. 22). Furthermore linear regression analyses were performed using SPPS (ver. 22). FNIRS signal quality (i.e., SNR) was treated as predictor variable and the eight decoding accuracies obtained from the univariate analyses (single-/multi-trial × HbO/HbR) and multivariate analyses (single-/multi-trial × SVM20-20/SVM40-40) were treated as criterion variables.

Comfortability, Ease and Pleasantness Ratings

Mean and standard deviation are reported for comfortability, ease and pleasantness ratings. Pearson's r was calculated between ease and pleasantness and accuracy outcomes of all univariate (single-/multi-trial × HbO/HbR) and multivariate (single-/multi-trial × SVM20-20/SVM40-40) analyses. Statistical significance was evaluated using a criterion of $\alpha = 0.05$.

RESULTS

Communication Accuracy (Univariate Analysis)

Channel Exclusion

On average 37% of channels were excluded due to their low SNR in localizer block 1. Descriptively, the channels with a relatively longer source-detector distance, e.g., diagonal channels such as FC3-C1, as compared to the shorter optode distances, e.g., straight channels such as FC3-FC1, were excluded more often. Large variation was observed between individual participants, ranging from 0 to 13 excluded channels. In contrast, the SNR measure was highly consistent across the four localizer runs (block 1 and block 2) within individual participants (see **Supplementary Figure S1**).

Channel Selection

The four COIs selected for further data-analysis steps are reported per participant in **Table 1**. In the HbO selection, the same channel was selected for mental drawing and spatial navigation imagery in three participants, i.e., participant 6, 7, and 12. In the HbR selection the same channel was selected for both tasks in four participants, i.e., participant 1, 4, 7, and 14. Overall the channel selection was quite variable across participants (see **Table 2**). For the MD task, channels FC3-FC5 (HbO) and C3-C5 (HbR) were chosen most frequently. For the SN task, channels FC3-FC5 (HbO) and FC3-FC5, FC3-C5, FC3-CP1, and C3-CP3 (HbO) were chosen most frequently. The event-related averages of the four channels-of-interest are depicted for two exemplary participants, participant 4 and 17 (**Figures 4**, **5**).

Single-Trial Results

Univariate analysis of single-trial data resulted in an average decoding accuracy of 56.85% (*SD* = 11.17%) and 54.81% (*SD* = 13.58%) for HbO and HbR respectively (see **Figure 6**). Individual accuracies ranged from 33.33 to 90%. Two participants' HbO data decoding accuracy was significant (indicated with a ♦ symbol in **Figure 6**). The average rate of correct detection of "yes" answers in the HbO signal was 60.00%, whereas "no" answers were correctly detected 53.70% of the time. The HbR decoding accuracy was significant in four participants (indicated with a ♦ symbol in **Figure 6**). Participant 4 was the sole significant participant in both HbO and HbR accuracies. The average rate of correct detection of "yes" answers in the HbR signal was 62.22%, whereas "no" answers were correctly detected 47.41% of the time.

TABLE 2 | Frequency table of channel-of-interest selection in 18 participants.

Channel (source-detector) I	Absolute frequency			
	Mental drawing		Spatial navigation	
	HbO	HbR	HbO	HbR
FC3-FC5	4	2	5	3
FC3-C5	1	1	2	3
FC3-FC1	1	1	3	3
FC3-C1	0	0	1	0
C3-FC5	3	1	2	0
C3-C5	2	4	1	1
C3-CP5	1	1	0	0
C3-FC1	0	0	0	1
C3-C1	1	3	0	3
C3-CP1	1	0	0	0
CP3-C5	1	0	1	1
CP3-CP5	1	3	3	2
CP3-C1	0	0	0	1
CP3-CP1	2	2	0	0
Total	18	18	18	18

A channel is formed by the combination of two optodes (source-detector). Abbreviations: HbO, oxygenated hemoglobin; HbR, deoxygenated hemoglobin.

Multi-Trial Results

Univariate analysis of multi-trial decoding resulted in an average accuracy of 66.67% (*SD* = 20.6%) and 58.33% (*SD* = 32.96%) for HbO and HbR respectively (see **Figure 6**). The control analysis without channel exclusion yielded a significantly lower group average of 58.33% (*SD* = 25.73%) for the HbO data (paired samples t-test; $t = 2.70$; $p = 0.015$ (see **Supplementary Material** and **Supplementary Figure S2**). In the main analysis, i.e., with channel exclusion, individual accuracies ranged from 0 to 100%. Six participants' HbO data decoding accuracy was found to be significant (indicated with a * symbol in **Figure 6**). The answers by participants 4 and 9 were decoded with 100% accuracy. The average rate of correct detection of "yes" answers in the HbO signal was 83.33%, whereas "no" answers were correctly detected in 50.00% of the cases. The HbR decoding accuracy was significant in six participants (indicated with a * symbol in **Figure 6**), with 100% accuracy in participants 4, 8, 9, and 11. The answers of participants 4, 9, and 14 were significantly decoded in both HbO and HbR signal. For illustrative purposes the event-related averages of a "yes" and a "no" answer are depicted for participant 4 and 17 in **Figures 7**, **8**. The average rate of correct detection of "yes" answers in the HbR signal was 72.22%, whereas "no" answers were correctly detected 44.44% of the time.

Multivariate Analyses

Single-Trial Results

The SVM20-20 classifier achieved an accuracy of 58.33% (*SD* = 13.05%). Individual accuracies ranged from 33.33 to 76.67%. Spatial activation patterns could be distinguished significantly above chance level, assessed by permutation testing,

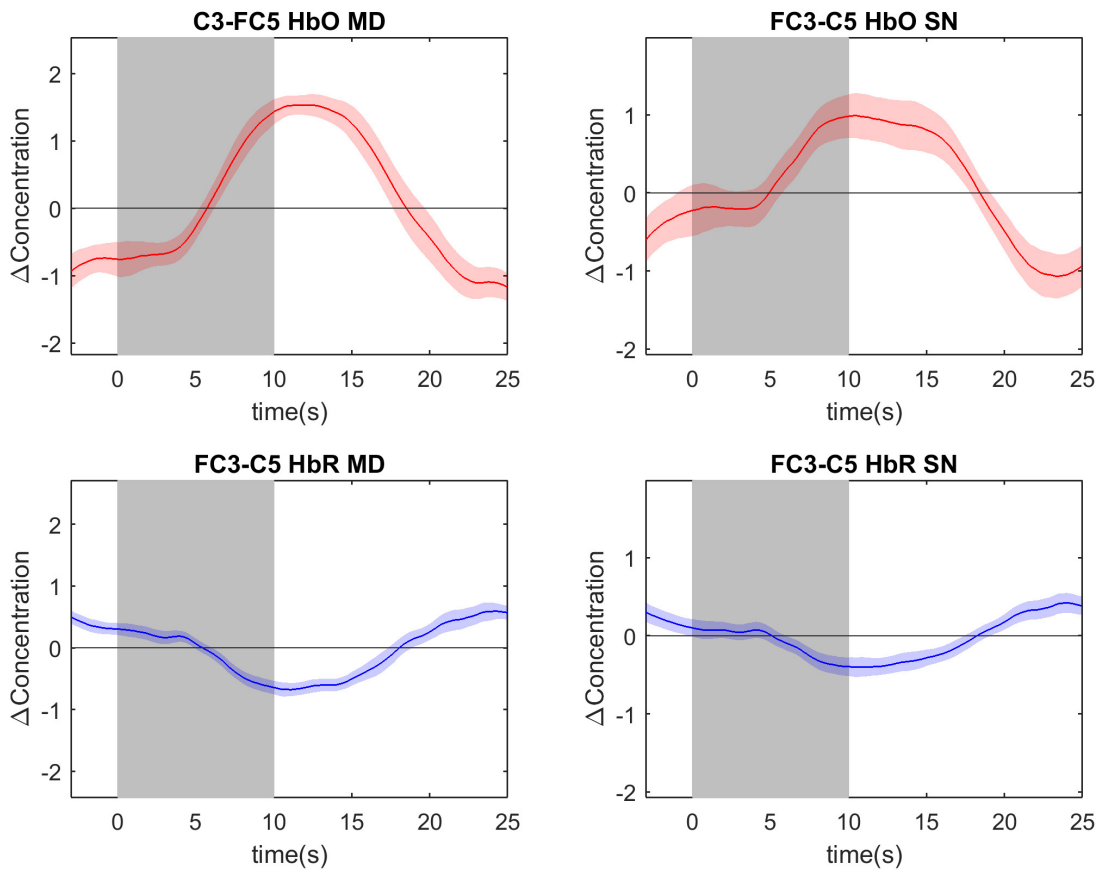

FIGURE 4 | Event-related averages of channels of interest in participant 4. The two graphs on the left are event-related averages from the first localizer run (mental drawing; MD). The two graphs on the right are event-related averages from the second localizer run (spatial navigation; SN). The top two graphs depict the oxygenated hemoglobin (HbO) response, whereas the bottom two graphs depict the deoxygenated hemoglobin (HbR) response. Each graph is the event-related average of 20 individual trials, with the darker average signal line and its standard deviation (lighter colored band surrounding the average signal line). Notice the clear and typical hemodynamic response during both tasks: a positive deflection in HbO and a negative deflection in HbR. The gray band from 0 to 10 s signifies the mental imagery time interval.

in four out of 18 participants (indicated with a ⌑ symbol in the top plot in **Figure 9**). The average rate of correct detection of MD was 52.59%, whereas SN was correctly detected 64.07% of the time.

The SVM40-40 classif ier achieved an accuracy of 60.56% (*SD* = 13.15). Individual accuracies ranged from 30.00 to 83.33%. Spatial activation patterns could be distinguished significantly above chance level, assessed by permutation testing, in seven out of 18 participants (indicated with a ⌑ symbol in the bottom plot in **Figure 9**). The average rate of correct detection of MD was 59.26%, whereas SN was correctly detected 62.59% of the time.

Multi-Trial Results

The SVM20-20 classifier achieved an accuracy of 62.04% (*SD* = 27.30%). Individual accuracies ranged from 0 to 100%. Spatial activation patterns discernibility was significant in eight out of 18 participants (indicated with a * symbol in the top plot in **Figure 9**). The average decoding accuracy of these eight participants was 85.42% (*SD* = 5.89%). The average rate of correct detection of MD was 59.26%, whereas SN was correctly detected 64.81% of the time.

The SVM40-40 classifier achieved an accuracy of 75.00% (*SD* = 21.58%). Individual accuracies ranged from 16.67 to 100%. Spatial activation patterns discernibility was significant in ten out of 18 participants (indicated with a * symbol in the bottom plot in **Figure 9**). The average rate of correct detection of MD was 72.22%, whereas SN was correctly detected 77.78% of the time.

fNIRS Suitability Questionnaire and Signal Quality

We found that SNR, as measured by the number of channels passing the CV% criterion, was significantly correlated with fNIRS suitability scores (r = -0.499, n = 18, p = 0.018; see **Supplementary Figure S3**). Participants with low fNIRS suitability scores (indicating highly suitable participants) thus typically had good fNIRS signal SNR.

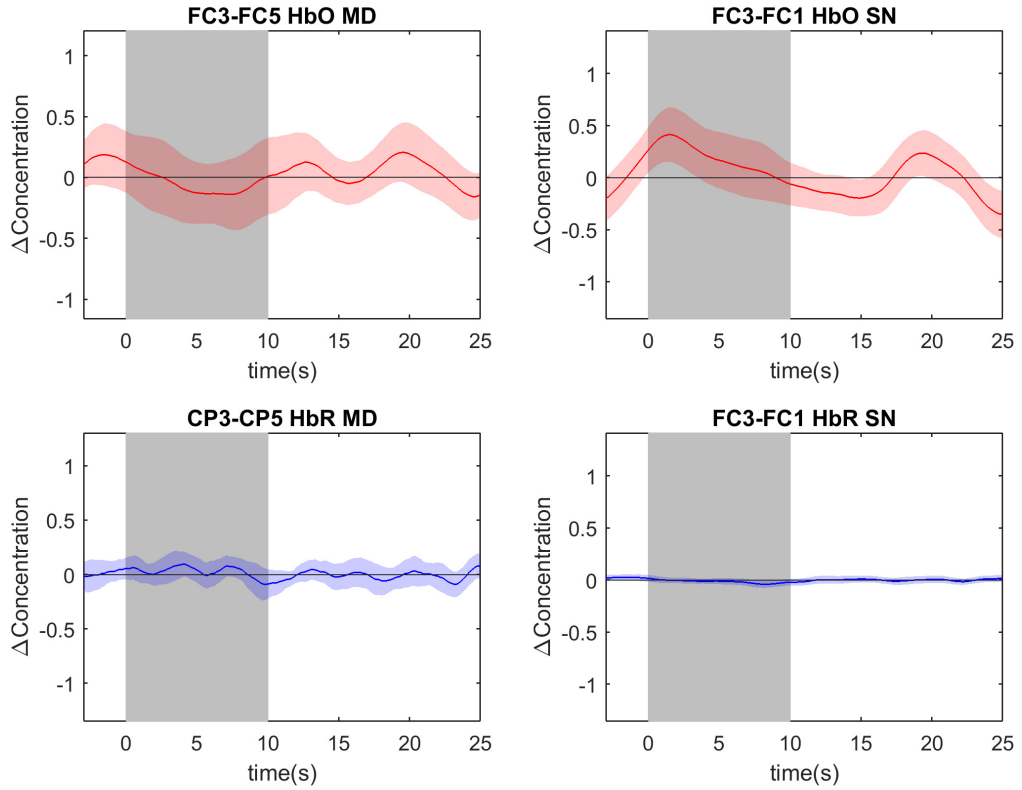

FIGURE 5 | Event-related averages of channels of interest in participant 17. The two graphs on the left are event-related averages from the first localizer run (mental drawing; MD). The two graphs on the right are event-related averages from the second localizer run (spatial navigation; SN). The top two graphs depict the oxygenated hemoglobin (HbO) response, whereas the bottom two graphs depict the deoxygenated hemoglobin (HbR) response. Each graph is the event-related average of 20 individual trials, with the darker average signal line and its standard deviation (lighter colored band surrounding the average signal line). Notice the absence of a typical hemodynamic response during both tasks: there is no clear positive deflection in HbO, nor a negative deflection in HbR. The gray band from 0 to 10 s signifies the mental imagery time interval.

Regression analyses with accuracy as the criterion variable and SNR as the predictor variable revealed the following results (see **Supplementary Figure S4**). Approximately 31% of the variation in HbR multi-trial accuracy could be attributed to the variation in SNR (R^2 = 0.309 with F_{17} = 7.165, p = 0.017). In contrast, SNR was no significant predictor for any other criterion variable: HbR single-trial accuracy (R^2 = 0.083 with F_{17} = 1.442, p = 0.247), HbO single-trial accuracy (R^2 = 0.045 with F_{17} = 0.755, p = 0.398), HbO multi-trial accuracy (R^2 = 0.029 with F_{17} = 0.480, p = 0.499), single-trial SVM20-20 (R^2 = 0.135 with F_{17} = 2.494, p = 0.134), multi-trial SVM20-20 (R^2 = 0.041 with F_{17} = 0.676, p = 0.423), single-trial SVM40-40 (R^2 = 0.009 with F_{17} = 0.144, p = 0.709) and multi-trial SVM40-40 (R^2 = 0.147 with F_{17} = 2.767, p = 0.116).

Comfortability, Easiness and Pleasantness

Participant's comfortability rating started out fairly high (8.03 ± 1.27) and then decreased over the remaining fNIRS runs (see **Figure 10**). The last run shows lowered although still acceptable comfort scores (6.53 ± 1.55). Not a single participant indicated a comfortability score lower than 5 during the experiment.

Overall both tasks were deemed easy and pleasant. On average the SN task was considered more difficult to perform (6.28 ± 1.32) and less pleasant (6.61 ± 1.45) than the MD task (7.94 ± 1.48; 7.28 ± 1.49). The difference between the two tasks in terms of ease was statistically significant (t = 4.70, p < 0.001). The difference in pleasantness showed a similar trend, yet it was not statistically significant (t = 1.86, p = 0.081). Ease and pleasantness ratings correlated significantly with the accuracy of the SVM40-40 analysis, whereas all other correlations were not significant (see **Table 3** for all correlations).

DISCUSSION

We presented a novel binary communication paradigm that aimed to exploit spatiotemporal characteristics of fNIRS signals evoked by differently timed mental imagery tasks. The paradigm involved minimal training and a sparse optode setup of only nine optodes (three sources, six detectors). Participants were

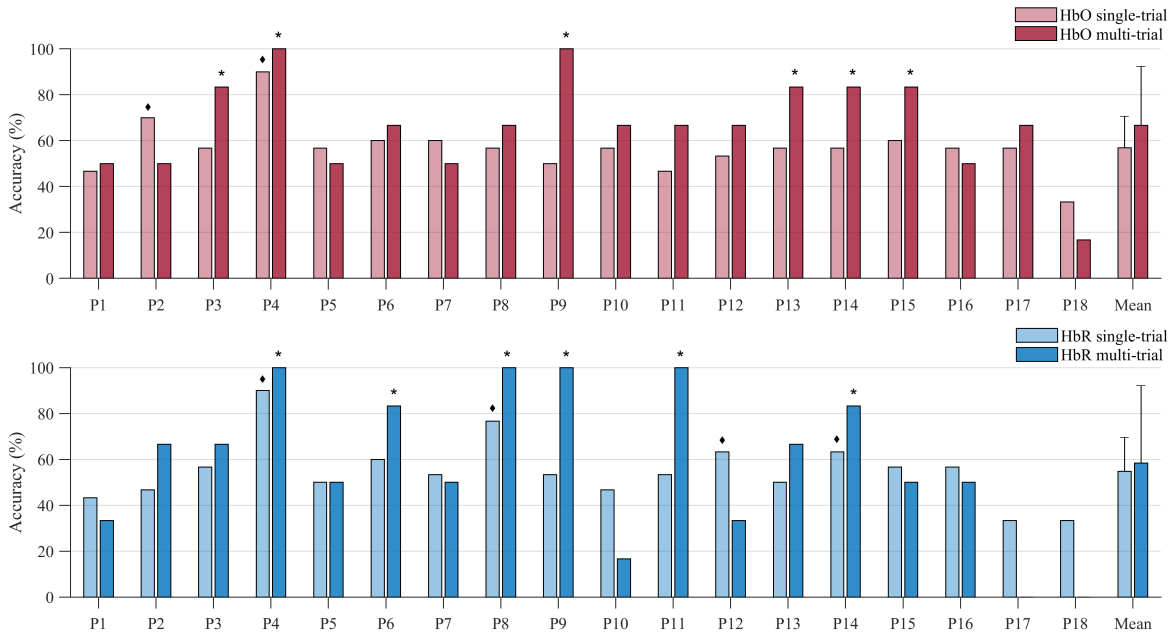

FIGURE 6 | Decoding accuracies of individual participants and the sample mean obtained with the single-trial (light-colored bars) and the multi-trial (dark-colored bars) univariate approach. Decoding accuracies were attained through channels-of-interest, preceded by a channel exclusion step. The upper plot show results based on analysis of HbO data (red bars), the lower plot is based on HbR data (blue bars). The ♦ symbol indicates participants whose single-trial accuracy was significant, whereas the * symbol indicates those participants whose multi-trial accuracy was significant.

TABLE 3 | Correlation table of ease and pleasantness ratings with the eight accuracy outcomes variables.

Pearson's p *p*-value	Multi-trial HbO	Multi-trial HbR	Single-trial HbO	Single-trial HbR	Single-trial SVM 20-20	Multi-trial SVM 20-20	Single-trial SVM 40-40	Multi-trial SVM40-40
Ease MD	0.288, 0.123	0.220, 0.190	0.101, 0.345	0.034, 0.447	0.010, 0.484	0.017, 0.945	0.508, 0.016*	0.383, 0.117
Ease SN	0.360, 0.071	0.147, 0.281	0.156, 0.268	0.041, 0.435	0.325, 0.094	0.364, 0.137	0.609, 0.004*	0.499, 0.035*
Pleasantness MD	0.320, 0.098	0.210, 0.202	0.127, 0.308	−0.051, 0.421	−0.116, 0.323	−0.208, 0.408	0.736, 0.000*	0.748, 0.000*
Pleasantness SN	0.295, 0.117	0.023, 0.464	0.023, 0.464	−0.163, 0.259	0.145, 0.283	0.076, 0.765	0.637, 0.002*	0.423, 0.080

*Abbreviations: MD, mental drawing; SN, spatial navigation; HbO, oxygenated hemoglobin; HbR, deoxygenated hemoglobin; SVM, support vector machine; * = correlation is significant at 0.05 level (1-tailed).*

asked to perform mental drawing (MD) for encoding a "yes" answer and spatial navigation (SN) for encoding a "no" answer in different auditorily cued time windows. The applied goal was to test decoding success and feasibility of the current paradigm compared to previous paradigms. Answers were decoded in simulated real-time using a set of predefined fNIRS channels and a univariate analysis approach. We also performed an explorative multivariate analysis on the data from all channels to investigate the differentiability of the two mental tasks based solely on spatial fNIRS signal features. In addition, the link between participants' physical characteristics and the fNIRS signal was explored with a novel fNIRS suitability questionnaire.

Univariate Analysis

Channel Selection

We hypothesized that relatively frontal optodes covered brain regions commonly associated with motor imagery, whereas posterior optodes covered brain areas associated with SN imagery (see section fNIRS Data Acquisition). On a group level, we found that frontal optodes were selected most often, irrespective of the type of task. However, note that a channel exclusion step was performed before the channel selection step, thus one should interpret these findings with caution. On an individual level, spatially different channels were selected as COI for each task in most participants. The absence of a spatial encoding aspect (i.e., selecting the same COI for both tasks) in a few participants (three in HbO and four in HbR; see **Table 1**) posed no decoding problem. Our paradigm aimed at exploiting spatial as well as temporal characteristics of fNIRS signals. Hence, in those few participants we solely relied on the temporal aspect, the fNIRS signal evoked by differently timed mental imagery tasks, to decode participant's answers. For example, participant 4 had the same COI for both tasks in the HbR signal but had a decoding accuracy clearly above chance level, with a single-trial accuracy of 90% and a multi-trial accuracy of 100%. The incorporation of both spatial and temporal features is an experimental safeguard in the presented fNIRS paradigm.

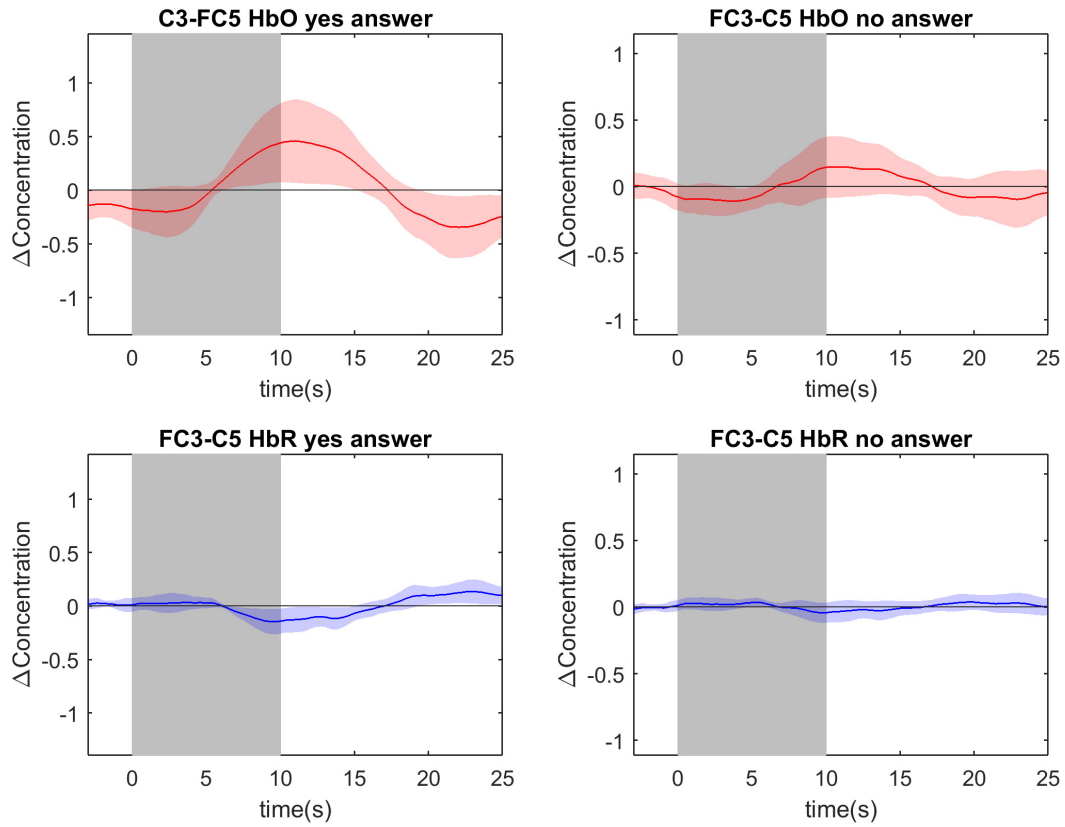

FIGURE 7 | Event-related averages of channels-of-interest in participant 4. The two graphs on the left are event-related averages from the first answer decoding run, in which the participant encoded a "yes" answer. The two graphs on the right are event-related averages from the sixth answer decoding run, in which the participant encoded a "no" answer. The top two graphs depict the oxygenated hemoglobin (HbO) response, whereas the bottom two graphs depict the deoxygenated hemoglobin (HbR) response. Each graph is the event-related average of five individual trials, with the darker average signal line and its standard deviation (lighter colored band surrounding the average signal line). Notice the clear and typical hemodynamic response function during both tasks: a positive deflection in HbO and a negative deflection in HbR. The gray band from 0 to 10 s signifies the mental imagery time interval.

Communication Accuracy

The single-trial GLM approach, with average decoding accuracies of 56.85% (HbO) and 54.81% (HbR), enabled effective communication in a limited subset of participants. In the fNIRS literature, no univariate single-trial accuracies have been previously reported. Multiple trials seem to be necessary at the current time, unfortunately at the cost of a lower information transfer rate. The multi-trial GLM approach resulted in higher group decoding accuracies in comparison to the single-trial approach. In four participants a 100% decoding accuracy was reached in the multi-trial approach, which was not attained in any participant using a single-trial approach. Average multi-trial decoding accuracy was higher in HbO (66.67%) than in HbR (58.33%), but on an individual level the same number of participants (six) reached significance. The similar individual decoding results across HbO and HbR were an unexpected finding. Generally, the lower amplitude and SNR of HbR, as compared to HbO, is thought to hinder detection of task-evoked changes (Leff et al., 2011). In line with this, it has been demonstrated that HbO signal is more robust than HbR for motor imagery specific activation (Mihara et al., 2012). Likewise, Rezazadeh Sereshkeh et al. (2018) reported that HbO signals yielded the highest accuracies in their 3-class BCI using imagined speech, and Hwang et al. (2016) reported that HbO features yield more discriminative information than HbR features in 2-class communication. Despite this previous work, here we find individual HbR multi-trial decoding accuracies that are similar to the ones seen in the HbO signal. It could be that the negative effect of the low SNR of the HbR signal is compensated by the relatively low sensitivity to physiological noise, i.e., systemic artifacts in both extra-cerebral and intra-cerebral compartments, as compared to HbO (Kirilina et al., 2012). In the current study we could not correct for physiological noise, which might have been a disadvantage for the HbO signal especially. Whether the differential sensitivity to physiological noise should influence researchers' decision to select either HbO or HbR for BCI purposes should be investigated further. Therefore, in line with Pinti et al. (2018), we encourage future studies to report both HbO and HbR results.

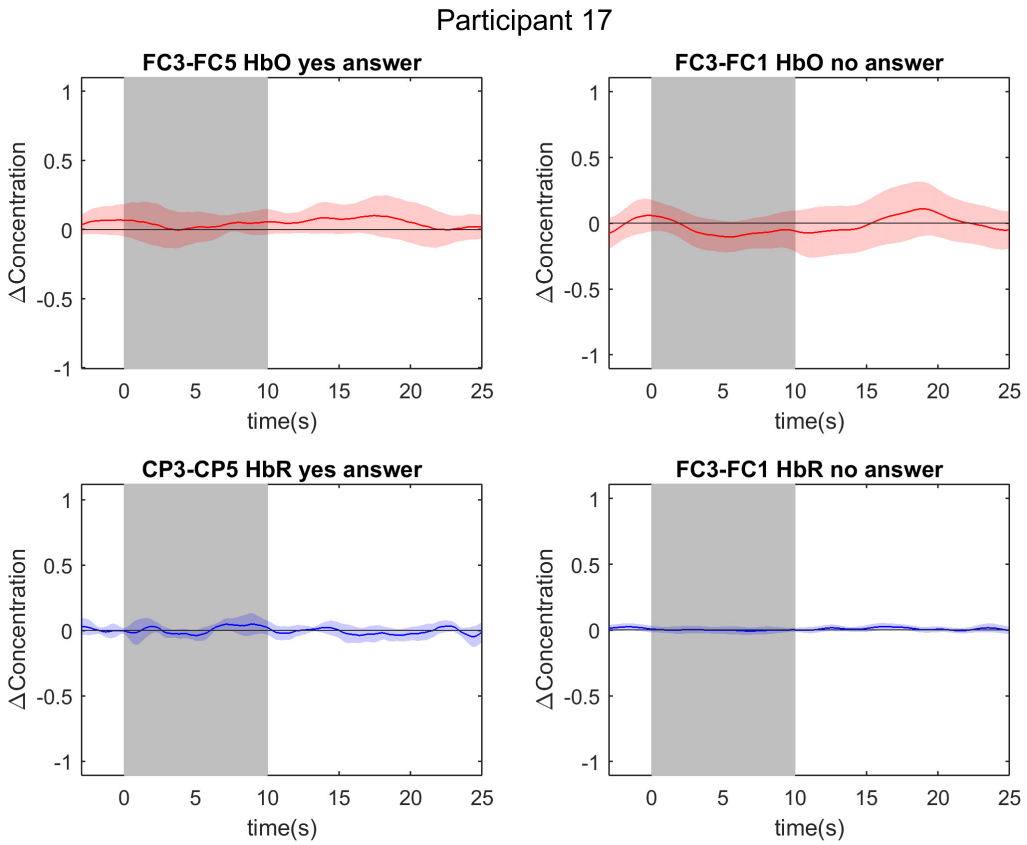

FIGURE 8 | Event-related averages of channels-of-interest in participant 17. The two graphs on the left are event-related averages from the fifth answer decoding run, in which the participant encoded a "yes" answer. The two graphs on the right are event-related averages from the sixth answer decoding run, in which the participant encoded a "no" answer. The top two graphs depict the oxygenated hemoglobin (HbO) response, whereas the bottom two graphs depict the deoxygenated hemoglobin (HbR) response. Each graph is the event-related average of five individual trials, with the darker average signal line and its standard deviation (lighter colored band surrounding the average signal line). Notice the absence of a typical hemodynamic response function during both tasks: there is no clear positive deflection in HbO, nor a negative deflection in HbR. The gray band from 0 to 10 s signifies the mental imagery time interval.

As in previous fNIRS-BCI studies, only a subset of our participants reached an acceptable criterion for communication (Naito et al., 2007; Nagels-Coune et al., 2017; Rezazadeh Sereshkeh et al., 2018). The multi-trial approach enabled effective communication in six participants in the HbO signal, i.e., participants 3, 4, 9, 13, 14, 15, and six participants in the HbR signal, i.e., participants 4, 6, 8, 9, 11, and 14. When taking the HbO and HbR results together, effective communication was reached in half of our participants. Therefore, as stated above, we recommend reporting BCI success for both HbO and HbR in future studies. Note that our use of the empirical chance level as a criterion is significantly stricter than the commonly used "70%" criterion that signifies a sufficient accuracy for communication in an individual user (Kubler et al., 2006). Our paradigm thus enables effective communication, greatly exceeding the common criterion of 70% for effective communication (Kubler et al., 2006), in a subset of participants.

Our multi-trial accuracies of 66.67% (HbO) and 58.33% (HbR) are low compared to those reported in other binary communication paradigms (Naseer et al., 2014; Rezazadeh Sereshkeh et al., 2018). This could be due to our sparse approach of a single session. Other studies encompassed multiple sessions (Rezazadeh Sereshkeh et al., 2018) or separate training sessions (Naseer et al., 2014). More training of our participants and more experimental trials could have resulted in better BCI performance (Kaiser et al., 2014) but would require more time investment, which in turn might affect the clinical applicability.

Our paradigm is the first to attempt using two active mental tasks to differentiate two answer options. However the low correct detection rate of the "no" answers, ranging from 44.44 to 53.70%, implies that the motor imagery task has mainly driven our univariate results. This finding questions the effective contribution of the spatial navigation task in our univariate analyses. Efforts have been made to investigate SN in naturalistic environments (McKendrick et al., 2016) and virtual reality environments (Kober et al., 2013) using fNIRS. However, to our knowledge no previous fNIRS study has explored the fNIRS signal in response to SN imagery. This study thus constitutes the first exploration of SN imagery in fNIRS. Future studies should investigate this mental task more thoroughly using an extended optode setup, as it is possible that our optode setup was not suited for SN. Alternatively, other promising mental

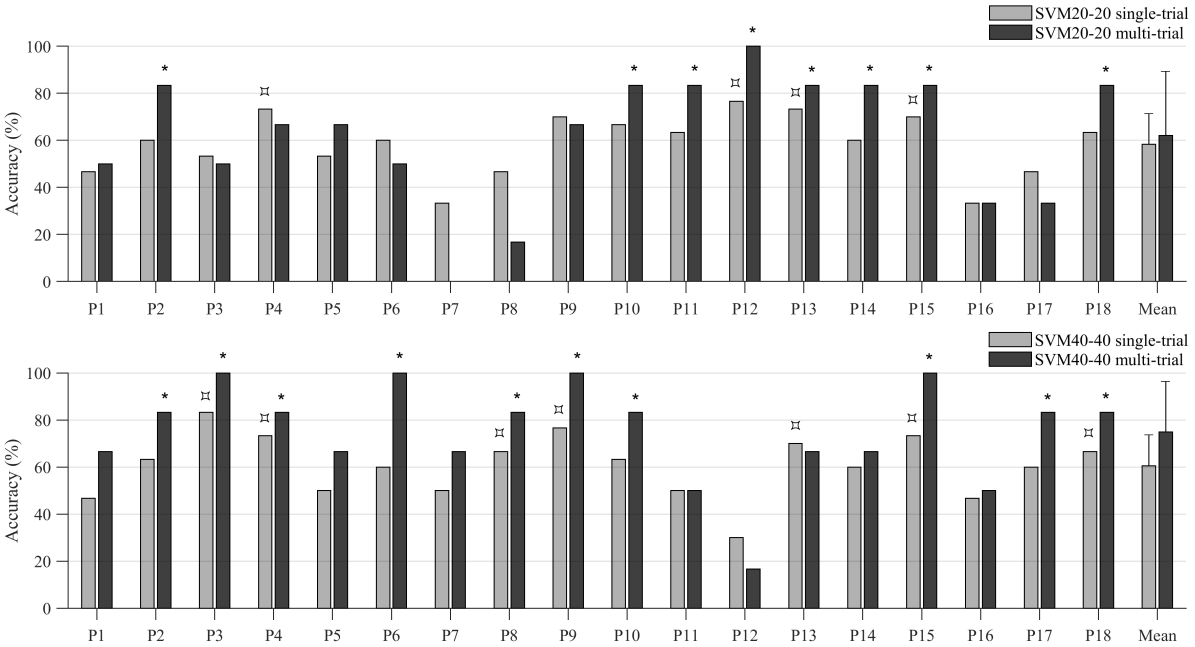

FIGURE 9 | Decoding accuracies of individual participants and the sample mean obtained with the single-trial (light-colored bars) and the multi-trial (dark-colored bars) multivariate approach. The upper plot shows decoding accuracies of the SVM20-20 classifier, the lower plot shows decoding accuracies of the SVM40-40 classifier. The ¤ symbol indicates participants whose accuracy reached significance, as tested with permutation testing (for evaluating single-trial accuracies), whereas the * symbol indicates those participants whose multi-trial accuracy was significant. Abbreviations: SVM20-20 = support vector machine with 20 training trials of each task; SVM40-40 = support vector machine with 40 training trials of each task.

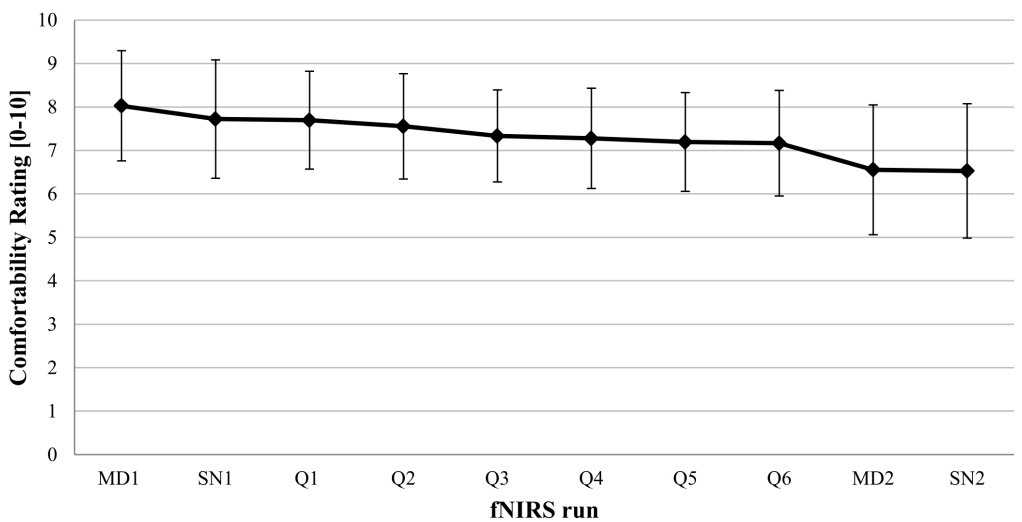

FIGURE 10 | Mean comfortability rating over time (fNIRS runs). A comfortability rating of 0 corresponds to "very uncomfortable" and 10 to "very comfortable". The ten fNIRS runs are depicted in the order they were conducted in the experiment. The first two runs, MD1 and SN2, were localizer runs (block 1) for mental drawing (MD) and spatial navigation (SN). The following six runs, Q1, Q2, Q3, Q4, Q5, Q6, represent the answer decoding runs, with a Q as an abbreviation for "question run". The last two runs, MD2 and SN2, were localizer runs (block 2). Error bars reflect standard deviations.

imagery tasks can be explored. With respect to the spatial encoding aspect of the current paradigm (two distinct mental tasks and associated channels-of-interest for encoding "yes" and "no" encoding), follow-up work is required to ensure effective and balanced contributions of both tasks.

Multivariate Analysis

The multivariate analysis explored the possibility of distinguishing the spatial patterns induced by MD vs. SN, disregarding any temporal information. From a clinical perspective, we compared the classifier results for both a limited

(localizer block 1) and a full (localizer block 1 and 2) training set. Both our single-trial decoding accuracies, 58.33% (SVM20-20) and 60.56% (SVM40-40), were rather low in comparison with previous studies. Classification results of 73% in two-class discrimination (Sitaram et al., 2007) and 64.1 to 75.6% in three-class discrimination (Hong et al., 2015; Rezazadeh Sereshkeh et al., 2018) are reported. However, the limited amount of trials in the current study should be noted, whereas other studies have trained and tested their classifiers on a significantly higher number of trials. In addition, our setup of nine optodes is quite sparse in comparison to previous work (Sitaram et al., 2007; Hong et al., 2015; Rezazadeh Sereshkeh et al., 2018). Note that the correct detection of the MD and SN tasks was more balanced, as compared to the univariate analyses. Correct detection of MD ranged from 52.59 to 72.22%, while correct detection of SN ranged from 62.59 to 77.78%. This implies effective contribution of both mental imagery tasks in our multivariate analyses.

Interestingly, in the current experiment, a simplistic majority voting approach applied on the single-trial SVM decisions, resulted in heightened accuracies of 62.04% (SVM20-20) and 75% (SVM40-40). This type of trial combination is rarely reported in BCI literature (Nagels-Coune et al., 2017), but it seems to affect the decoding accuracy in a positive manner and could potentially be useful in clinical BCI applications.

A limitation of our multivariate approach is that the two mental imagery tasks never co-occurred within localizer runs. Classifiers were thus trained on each distinctive task in one (SVM20-20) or two (SVM40-40) separate runs. In hindsight, it would have been better to perform both mental tasks within a run, as has been done by e.g., Valente et al. (2019) in an MVPA-based BCI control study using fMRI.

Uni- vs. Multivariate Results

Comparisons between the univariate and multivariate results should be drawn with caution given the fundamentally different nature of the methods. In the univariate analyses, the data from four channels-of-interest were considered, whereas all channels were considered in the multivariate analyses. Each analysis approach has its drawbacks for future BCI use, with the SVM approach requiring more measurement points and the GLM approach being dependent on a small subset of channels. There is no clear superiority of one approach over the other and one could think of these methods as two alternatives that can be explored depending on the BCI user's preferences and performance. Despite similar average decoding accuracies across uni- and multivariate analyses, accuracies varied largely within an individual participant. For example, the surprisingly low multi-trial decoding accuracy of 0% in HbR for participants 17 and 18 is in stark contrast with their MVPA accuracy. In **Figures 5**, **8**, one cannot recognize the expected hemodynamic response (positive HbO deflection and negative HbR deflection) or any other response in the signal of participant 17. The 0% finding in the HbR signal for the multivariate analyses is thus probably due to noisy signal in combination with a low number of trials (6 trials), as both participants attain an accuracy of 33.33% in the single-trial analysis. In addition, suboptimal channel selection due to our sparse optode setup might have contributed to these findings. Nevertheless, when looking at the multivariate results of participant 17 and 18, we see responses above chance level. These diverging results between uni- and multivariate analyses imply that our general linear model approach, with its focus on a single channel-of-interest for each task, was not well suited to disentangle the differential spatial features of the fNIRS signal in certain participants.

Inter-Subject Variability

The inter-subject variability in our sample was substantial, both in terms of signal quality and accuracy outcomes. The large variability between participants has been recognized in other fNIRS studies (Holper et al., 2011; Power et al., 2012; Rezazadeh Sereshkeh et al., 2018). We have explored a few subject-specific factors that potentially influence the fNIRS signal quality and accuracy, such as hair and skin features (fNIRS suitability questionnaire) and subjective ease and pleasantness ratings of the mental tasks.

fNIRS Suitability Questionnaire

We developed an fNIRS suitability questionnaire to explore whether physical features such as hair and skin could predict fNIRS signal quality. In the current study, we found that participants who were deemed less suitable for fNIRS (as measured by our in-house questionnaire), generally had less channels with a sufficient SNR (as operationalized by CV%). The resulting significant correlation constituted a first indicator of the questionnaire's usefulness. Furthermore, the variation in SNR across participants could explain approximately 31% of the variance in the HbR multi-trial accuracies (R^2 = 0.309 with F_{17} = 7.165, p = 0.017). Note however that the fNIRS suitability questionnaire administered in the current study is an exploratory instrument and further work is needed to establish its validity and reliability. In addition, it should be noted that we used common optode holders, as opposed to spring-loaded optode holders, in the current experiment. Common optode holders are thought to be more sensitive to signal disturbance due to hair than spring-loaded optode holders. It is thus expected that the established relationship between physical features and fNIRS signal quality will weaken in an experimental set-up with spring-loaded optode holders. However, given the participant discomfort they often cause (Lloyd-Fox et al., 2010), non-spring loaded optode holders will continue to be used in studies involving children, patients and other vulnerable populations. More extensive exploration of the effects of participants' hair, skin and head size on signal quality is required in the future. Ideally one would determine a suitability criterion that ensures sufficient SNR and thus enables detection of intentional brain activation.

Comfort, Ease, and Pleasantness

Our participants generally experienced the fNIRS setup as comfortable. Despite the average decrease of comfortability across time, participants still felt comfortable in the last fNIRS runs and not a single participant indicated discomfort at any point.

Participants considered the MD significantly easier to perform than the SN. In addition the SN task was considered less pleasant

than the MD task. Despite a clear trend, this difference did not reach significance. Ease and enjoyment have been shown to correlate with fNIRS decoding accuracy (Weyand and Chau, 2015). In line with these observations, ease and pleasantness correlated significantly with the SVM40-40 accuracies in the current study (see **Table 3**).

Unexplored User Characteristics

In half of our participants, the paradigm did not enable effective communication. While this may in part be due to the poor signal quality of the current data set, with on average 37% of channels rejected per participant, other studies have similarly identified subgroups of participants in which fNIRS-BCI failed to work (Naito et al., 2007; Rezazadeh Sereshkeh et al., 2018). Given the general recognition of substantial inter-subject variability, the current challenge in fNIRS-based BCI research is to investigate what enables certain participants to use the BCI successfully but also what factors are hindering BCI success in other participants. Given the known correlations between EEG-BCI success and user characteristics (Weyand and Chau, 2015), a systematic investigation of user characteristics in relation to fNIRS-BCI performance is due. Factors that are thought to influence fNIRS hemodynamic signatures are age (Zich et al., 2017), handedness (Kempny et al., 2016), user training (Kaiser et al., 2014), vividness of mental imagery (Cui et al., 2007), imagery content in combination with idiosyncratic cognitive abilities (Holper and Wolf, 2011) and mental fatigue (Sargent et al., 2018). Lastly, there is notable inter-subject variability in brain activation patterns elicited by certain mental tasks (Power et al., 2012; Weyand and Chau, 2015). Therefore, an individualized combination of two tasks may be most effective for controlling a binary BCI in individual users. A first effort to explore each participant's best discriminating subset of mental tasks has shown encouraging results (Weyand and Chau, 2015).

Limitations and Future Work

In the current study, three left-handed participants, i.e., participants 5, 17, and 18, were asked to perform motor imagery with their non-dominant hand. Given the established hemispheric asymmetry related to handedness (Maruff et al., 1999; Lee et al., 2019; Yokoyama et al., 2019), it is plausible that left hand imagery combined with right hemisphere fNIRS recordings would have resulted in heightened BCI decoding accuracies for these three participants. When excluding these three participants from our univariate analyses, single-trial accuracies rose to 58.44% (HbO) and 58.00% (HbR), previously 56.85 and 54.81%. Multi-trial accuracies rose to 70.83% (HbO) and 62.50% (HbR), previously 66.67 and 58.33% respectively.

The signal quality in the current data set may have been limited by our use of non-spring loaded optode holders. Recently the use of spring loaded optode holders is on the rise, as they are known to improve signal quality. Unfortunately the type of optode holders is not systematically reported in fNIRS studies, thereby limiting systematic comparison. Nevertheless, given the discomfort they often cause (Lloyd-Fox et al., 2010), non-spring loaded optode holders will continue to be used in patient studies. Therefore the current data might be representative for data we might encounter in patient population. It is known that the signal-to-noise ratio of fNIRS measurement remains a challenge in ecologically valid environments (Zephaniah and Kim, 2014; Pinti et al., 2017). Our presented fNIRS suitability questionnaire should be developed further and would ideally identify those participants with an insufficient SNR before the start of the experiment. Given this information, efforts can be made to ensure good signal quality by for example tracking the optode-to-scalp coupling in real-time (Pollonini et al., 2016).

Another drawback of the current study is the absence of additional physiological measures. Taking measures of blood pressure, respiration and heart rate (Bauernfeind et al., 2014), and regressing out these factors from our HbO and HbR signals might have improved our detection of task-specific activation. Moreover, given the absence of short-separation channels in the current study, we could not remove the influence of extra-cerebral tissue changes on the fNIRS signal (Brigadoi and Cooper, 2015). Methods such as the global component removal by Zhang et al. (2016) require optodes to cover a much larger area than the expected activated area and could thus not be applied. Mayer waves might thus have occurred in our dataset and have possibly reduced our decoding accuracies (Yucel et al., 2016). This might be especially the case for HbO as compared to HbR, given its higher sensitivity to physiological noise (Kirilina et al., 2012). Future studies should incorporate short-separation channels, as this can result in a significant improvement in both accuracy and reliability of fNIRS measurements (Brigadoi and Cooper, 2015). Such improvements are warranted for transference of fNIRS-BCI to clinical populations, as there is empirical evidence from EEG-based BCI that accuracies tend to be lower in patients as compared to healthy participants (Halder et al., 2010).

We advise future studies that employ a similar paradigm to focus on multi-trial decoding accuracies, as these proved most promising in our univariate analysis. This general linear model approach using a small set of fNIRS channels has enabled effective communication in half of our participants in either HbO or HbR signal. The good HbR decoding accuracies were an unexpected finding and we thus advise future experiments to report both HbO and HbR signal outcomes. In addition, future experiments should perform online, real-time, analysis. This would enable direct within-session feedback, which may heighten motivation in the participants and subsequently BCI performance (Kleih et al., 2010; Nijboer et al., 2010). Lastly, efforts to combine fNIRS with other modalities, such as EEG, have shown to improve classification accuracy significantly (Fazli et al., 2012; Zephaniah and Kim, 2014; Shin et al., 2018; Rezazadeh Sereshkeh et al., 2019) and are worth further investigation.

CONCLUSION

The presented binary communication paradigm aimed to exploit spatiotemporal characteristics of fNIRS-signals evoked by differently timed mental imagery tasks. In various univariate analyses, the group average decoding accuracy was limited and did not exceed previously reported paradigms. The mental drawing imagery mainly drove our decoding results in the

univariate analyses. Spatial navigation imagery should be explored more extensively in the context of fNIRS. Despite the rather low group average accuracies or number of participants exceeding chance level, it bears mention that those participants with a significant decoding accuracy performed excellent, with participants reaching decoding accuracies of 100%. The multivariate results showed potential spatial discernibility in a subset of participants. Integration of the single-trial multivariate outcomes using a majority voting approach resulted in encouraging decoding accuracies. The hypothesized link between participants' physical characteristics and the fNIRS signal was confirmed with our novel fNIRS suitability questionnaire.

DATA AVAILABILITY STATEMENT

The raw data supporting the conclusions of this article will be made available by the authors, without undue reservation, to any qualified researcher.

ETHICS STATEMENT

The study involved human participants and was reviewed and approved by the Ethische Commissie Psychologie (ECP), Faculty of Psychology and Neuroscience, Maastricht University. The participants provided their written informed consent to participate in this study.

AUTHOR CONTRIBUTIONS

NR and BS conceived and designed the study as well as obtained the data. LN-C performed the data analysis with the aid of AB-A, ML, and BS. BS, PD, LR, and RG oversaw the analyses. LN-C wrote the first draft of the manuscript. All authors contributed to manuscript revision, read and approved the submitted version.

FUNDING

This work was supported by the European Commission (7th Framework Program 2007-2013, DECODER project) and the Netherlands Organization for Scientific Research (Research talent grant 406-15-217 to LN-C).

ACKNOWLEDGMENTS

LN-C thanks her colleague Denizhan Kurban for the fruitful discussions.

SUPPLEMENTARY MATERIAL

The Supplementary Material for this article can be found online at: https://www.frontiersin.org/articles/10.3389/fnhum.2020.00113/full#supplementary-material

REFERENCES

Abdalmalak, A., Milej, D., Diop, M., Naci, L., Owen, A. M., and St. Lawrence, K. (2016). Assessing the feasibility of time-resolved fNIRS to detect brain activity during motor imagery. *SPIE* 9690:969002. doi: 10.1117/12.2209587

Abdalmalak, A., Milej, D., Diop, M., Shokouhi, M., Naci, L., Owen, A. M., et al. (2017a). Can time-resolved NIRS provide the sensitivity to detect brain activity during motor imagery consistently? *Biomed. Opt. Express* 8, 2162–2172. doi: 10.1364/BOE.8.002162

Abdalmalak, A., Milej, D., Norton, L., Debicki, D., Gofton, T., Diop, M., et al. (2017b). Single-session communication with a locked-in patient by functional near-infrared spectroscopy. *Neurophotonics* 4:040501. doi: 10.1117/1.NPh.4.4.040501

Balardin, J. B., Zimeo Morais, G. A., Furucho, R. A., Trambaiolli, L., Vanzella, P., Biazoli, C. Jr., et al. (2017). Imaging brain function with functional near-infrared spectroscopy in unconstrained environments. *Front. Hum. Neurosci.* 11:258. doi: 10.3389/fnhum.2017.00258

Bardin, J. C., Fins, J. J., Katz, D. I., Hersh, J., Heier, L. A., Tabelow, K., et al. (2011). Dissociations between behavioural and functional magnetic resonance imaging-based evaluations of cognitive function after brain injury. *Brain* 134, 769–782. doi: 10.1093/brain/awr005

Bauer, G., Gerstenbrand, F., and Rumpl, E. (1979). Varieties of the locked-in syndrome. *J. Neurol.* 221, 77–91.

Bauernfeind, G., Wriessnegger, S. C., Daly, I., and Müller-Putz, G. R. (2014). Separating heart and brain: on the reduction of physiological noise from multichannel functional near-infrared spectroscopy (fNIRS) signals. *J. Neural Eng.* 11:056010. doi: 10.1088/1741-2560/11/5/056010

Birbaumer, N., Ghanayim, N., Hinterberger, T., Iversen, I., Kotchoubey, B., Kübler, A., et al. (1999). A spelling device for the paralysed. *Nature* 398, 297–298. doi: 10.1038/18581

Boas, D. A., Elwell, C. E., Ferrari, M., and Taga, G. (2014). Twenty years of functional near-infrared spectroscopy: introduction for the special issue. *Neuroimage* 85(Pt 1), 1–5. doi: 10.1016/j.neuroimage.2013.11.033

Brigadoi, S., and Cooper, R. J. (2015). How short is short? Optimum source–detector distance for short-separation channels in functional near-infrared spectroscopy. *Neurophotonics* 2:025005. doi: 10.1117/1.NPh.2.2.025005

Brunner, P., Joshi, S., Briskin, S., Wolpaw, J. R., Bischof, H., and Schalk, G. (2010). Does the 'P300' speller depend on eye gaze? *J. Neural Eng.* 7:056013. doi: 10.1088/1741-2560/7/5/056013

Cabrera, A. F., and Dremstrup, K. (2008). Auditory and spatial navigation imagery in Brain–Computer Interface using optimized wavelets. *J. Neurosci. Methods* 174, 135–146. doi: 10.1016/j.jneumeth.2008.06.026

Chance, B., Zhuang, Z., UnAh, C., Alter, C., and Lipton, L. (1993). Cognition-activated low-frequency modulation of light absorption in human brain. *Proc. Natl. Acad. Sci. U.S.A.* 90, 3770–3774.

Coyle, S. M., Markham, C., and Ward, T. (2005). "A mechanical mounting system for functional near-infrared spectroscopy brain imaging studies," in *Proceedings of the SPIE 5826*, Dublin. doi: 10.1117/12.604823

Coyle, S. M., Ward, T. E., and Markham, C. M. (2007). Brain-computer interface using a simplified functional near-infrared spectroscopy system. *J. Neural Eng.* 4, 219–226. doi: 10.1088/1741-2560/4/3/007

Cui, X., Bray, S., Bryant, D. M., Glover, G. H., and Reiss, A. L. (2011). A quantitative comparison of NIRS and fMRI across multiple cognitive tasks. *Neuroimage* 54, 2808–2821. doi: 10.1016/j.neuroimage.2010.10.069

Cui, X., Jeter, C. B., Yang, D., Montague, P. R., and Eagleman, D. M. (2007). Vividness of mental imagery: individual variability can be measured objectively. *Vision Res.* 47, 474–478. doi: 10.1016/j.visres.2006.11.013

Cutini, S., Moro, S., and Bisconti, S. (2012). Review: functional near infrared optical imaging in cognitive neuroscience: an introductory review. *J. Near Infrared Spectrosc.* 20:75. doi: 10.1255/jnirs.969

Fang, X., Pan, B., Liu, W., Wang, Z., and Li, T. (2018). Effect of scalp hair follicles on NIRS quantification by monte carlo simulation and visible chinese human dataset. *IEEE Photon. J.* 10:3901110. doi: 10.1109/JPHOT.2018.2865427

Farwell, L. A., and Donchin, E. (1988). Talking off the top of your head: toward a mental prosthesis utilizing event-related brain potentials. *Electroencephalogr. Clin. Neurophysiol.* 70, 510–523. doi: 10.1016/0013-4694(88)90149-6

Fazli, S., Mehnert, J., Steinbrink, J., Curio, G., Villringer, A., Müller, K.-R., et al. (2012). Enhanced performance by a hybrid NIRS–EEG brain computer interface. *Neuroimage* 59, 519–529. doi: 10.1016/j.neuroimage.2011.07.084

Gijsen, S. (2015). *BrainStim*. Available online at: https://github.com/svengijsen/BrainStim (accessed November 3, 2019).

Gratton, G., Brumback, C. R., Gordon, B. A., Pearson, M. A., Low, K. A., and Fabiani, M. (2006). Effects of measurement method, wavelength, and source-detector distance on the fast optical signal. *Neuroimage* 32, 1576–1590.

Halder, S., Rea, M., Andreoni, R., Nijboer, F., Hammer, E. M., Kleih, S. C., et al. (2010). An auditory oddball brain–computer interface for binary choices. *Clin. Neurophysiol.* 121, 516–523. doi: 10.1016/j.clinph.2009.11.087

Han, C. H., Kim, Y. W., Kim, D. Y., Kim, S. H., Nenadic, Z., and Im, C. H. (2019). Electroencephalography-based endogenous brain-computer interface for online communication with a completely locked-in patient. *J. Neuroeng. Rehabil.* 16:18. doi: 10.1186/s12984-019-0493-0

Holper, L., Shalom, D. E., Wolf, M., and Sigman, M. (2011). Understanding inverse oxygenation responses during motor imagery: a functional near-infrared spectroscopy study. *Eur. J. Neurosci.* 33, 2318–2328. doi: 10.1111/j.1460-9568.2011.07720.x

Holper, L., and Wolf, M. (2011). Single-trial classification of motor imagery differing in task complexity: a functional near-infrared spectroscopy study. *J. Neuroeng. Rehabil.* 8, 34–34. doi: 10.1186/1743-0003-8-34

Hong, K.-S., Naseer, N., and Kim, Y.-H. (2015). Classification of prefrontal and motor cortex signals for three-class fNIRS–BCI. *Neurosci. Lett.* 587, 87–92. doi: 10.1016/j.neulet.2014.12.029

Hoshi, Y., and Tamura, M. (1993). Detection of dynamic changes in cerebral oxygenation coupled to neuronal function during mental work in man. *Neurosci. Lett.* 150, 5–8. doi: 10.1016/0304-3940(93)90094-2

Hwang, H.-J., Choi, H., Kim, J.-Y., Chang, W.-D., Kim, D.-W., Kim, K., et al. (2016). Toward more intuitive brain–computer interfacing: classification of binary covert intentions using functional near-infrared spectroscopy. *J. Biomed. Opt.* 21:091303. doi: 10.1117/1.JBO.21.9.091303

Kaiser, V., Bauernfeind, G., Kreilinger, A., Kaufmann, T., Kubler, A., Neuper, C., et al. (2014). Cortical effects of user training in a motor imagery based brain-computer interface measured by fNIRS and EEG. *Neuroimage* 85(Pt 1), 432–444. doi: 10.1016/j.neuroimage.2013.04.097

Käthner, I., Kübler, A., and Halder, S. (2015). Comparison of eye tracking, electrooculography and an auditory brain-computer interface for binary communication: a case study with a participant in the locked-in state. *J. Neuroeng. Rehabil.* 12:76. doi: 10.1186/s12984-015-0071-z

Kato, T., Kamei, A., Takashima, S., and Ozaki, T. (1993). Human visual cortical function during photic stimulation. *J. Cereb. Blood Flow Metab.* 13, 516–520.

Kempny, A. M., James, L., Yelden, K., Duport, S., Farmer, S., Playford, E. D., et al. (2016). Functional near infrared spectroscopy as a probe of brain function in people with prolonged disorders of consciousness. *Neuroimage Clin.* 12, 312–319. doi: 10.1016/j.nicl.2016.07.013

Khan, B., Wildey, C., Francis, R., Tian, F., Delgado, M. R., Liu, H., et al. (2012). Improving optical contact for functional near-infrared brain spectroscopy and imaging with brush optodes. *Biomed. Opt. Express* 3, 878–898. doi: 10.1364/BOE.3.000878

Kirilina, E., Jelzow, A., Heine, A., Niessing, M., Wabnitz, H., Brühl, R., et al. (2012). The physiological origin of task-evoked systemic artefacts in functional near infrared spectroscopy. *Neuroimage* 61, 70–81. doi: 10.1016/j.neuroimage.2012.02.074

Kleih, S. C., Nijboer, F., Halder, S., and Kübler, A. (2010). Motivation modulates the P300 amplitude during brain–computer interface use. *Clin. Neurophysiol.* 121, 1023–1031. doi: 10.1016/j.clinph.2010.01.034

Kober, S., Wood, G., and Neuper, C. (2013). "Measuring brain activation during spatial navigation in virtual reality: a combined EEG-NIRS study," in *Virtual Environments: Developments, Applications and Challenges*, eds S. Trautman, and F. Julien (Hauppauge, NY: NOVA), 1–24.

Koessler, L., Maillard, L., Benhadid, A., Vignal, J. P., Felblinger, J., Vespignani, H., et al. (2009). Automated cortical projection of EEG sensors: anatomical correlation via the international 10–10 system. *Neuroimage* 46, 64–72.

Koizumi, H., Yamashita, Y., Maki, A., Yamamoto, T., Ito, Y., Itagaki, H., et al. (1999). Higher-order brain function analysis by trans-cranial dynamic near-infrared spectroscopy imaging. *J. Biomed. Opt.* 4, 403–414.

Kovalenko, B., Roskosky, M., and Freedman, B. (2014). Effect of Ambient Light on Near Infrared Spectroscopy. *J. Trauma Treat.* 4:258. doi: 10.4172/2167-1222.1000258

Kubler, A., Mushahwar, V., Hochberg, L. R., and Donoghue, J. P. (2006). BCI meeting 2005-workshop on clinical issues and applications. *IEEE Trans. Neural Syst. Rehabil. Eng.* 14, 131–134.

Laureys, S. (2005). The neural correlate of (un)awareness: lessons from the vegetative state. *Trends Cogn. Sci.* 9, 556–559. doi: 10.1016/j.tics.2005.10.010

Lee, S. H., Jin, S. H., and An, J. (2019). The difference in cortical activation pattern for complex motor skills: a functional near-infrared spectroscopy study. *Sci. Rep.* 9:14066. doi: 10.1038/s41598-019-50644-9

Leff, D. R., Orihuela-Espina, F., Elwell, C. E., Athanasiou, T., Delpy, D. T., Darzi, A. W., et al. (2011). Assessment of the cerebral cortex during motor task behaviours in adults: a systematic review of functional near infrared spectroscopy (fNIRS) studies. *Neuroimage* 54, 2922–2936. doi: 10.1016/j.neuroimage.2010.10.058

León-Carrión, J., and León-Domínguez, U. (2012). "Functional near-infrared spectroscopy (fNIRS): principles and neuroscientific applications," in *Neuroimaging - Methods*, ed. P. Bright (Rijeka: InTech).

Leuthardt, E. C., Schalk, G., Wolpaw, J. R., Ojemann, J. G., and Moran, D. W. (2004). A brain–computer interface using electrocorticographic signals in humans. *J. Neural Eng.* 1, 63–71. doi: 10.1088/1741-2560/1/2/001

Lloyd-Fox, S., Blasi, A., and Elwell, C. E. (2010). Illuminating the developing brain: the past, present and future of functional near infrared spectroscopy. *Neurosci. Biobehav. Rev.* 34, 269–284. doi: 10.1016/j.neubiorev.2009.07.008

Maruff, P., Wilson, P. H., Fazio, J. D., Cerritelli, B., Hedt, A., and Currie, J. (1999). Asymmetries between dominant and non-dominanthands in real and imagined motor task performance. *Neuropsychologia* 37, 379–384.

McKendrick, R., Parasuraman, R., Murtza, R., Formwalt, A., Baccus, W., Paczynski, M., et al. (2016). Into the wild: neuroergonomic differentiation of hand-held and augmented reality wearable displays during outdoor navigation with functional near infrared spectroscopy. *Front. Hum. Neurosci.* 10:216. doi: 10.3389/fnhum.2016.00216

Mellinger, J., Schalk, G., Braun, C., Preissl, H., Rosenstiel, W., Birbaumer, N., et al. (2007). An MEG-based brain–computer interface (BCI). *Neuroimage* 36, 581–593. doi: 10.1016/j.neuroimage.2007.03.019

Mihara, M., Miyai, I., Hattori, N., Hatakenaka, M., Yagura, H., Kawano, T., et al. (2012). Neurofeedback using real-time near-infrared spectroscopy enhances motor imagery related cortical activation. *PLoS One* 7:e32234. doi: 10.1371/journal.pone.0032234

Monti, M. M., Coleman, M. R., and Owen, A. M. (2009). Neuroimaging and the vegetative state: resolving the behavioral assessment dilemma? *Ann. N. Y. Acad. Sci.* 1157, 81–89. doi: 10.1111/j.1749-6632.2008.04121.x

Monti, M. M., Vanhaudenhuyse, A., Coleman, M. R., Boly, M., Pickard, J. D., Tshibanda, L., et al. (2010). Willful modulation of brain activity in disorders of consciousness. *N. Engl. J. Med.* 362, 579–589. doi: 10.1056/NEJMoa0905370

Naci, L., and Owen, A. M. (2013). Making every word count for nonresponsive patients. *JAMA Neurol.* 70, 1235–1241. doi: 10.1001/jamaneurol.2013.3686

Nagels-Coune, L., Kurban, D., Reuter, N., Benitez, A., Gossé, L. K., Riecke, L., et al. (2017). Yes or no? Binary brain-based communiction utilizing motor imagery and fNIRS. *Paper Presented at the 7th Graz Brain-Computer Interface Conference*, Graz. doi: 10.3217/978-3-85125-533-1-65

Naito, M., Michioka, Y., Ozawa, K., Ito, Y., Kiguchi, M., and Kanazawa, T. (2007). A communication means for totally locked-in ALS patients based on changes in cerebral blood volume measured with near-infrared light. *IEICE Trans. Inf. Syst.* E90-D, 1028–1037. doi: 10.1093/ietisy/e90-d.7.1028

Naseer, N., and Hong, K. S. (2015). fNIRS-based brain-computer interfaces: a review. *Front. Hum. Neurosci.* 9:3. doi: 10.3389/fnhum.2015.00003

Naseer, N., Hong, M. J., and Hong, K. S. (2014). Online binary decision decoding using functional near-infrared spectroscopy for the development of brain-computer interface. *Exp. Brain Res.* 232, 555–564. doi: 10.1007/s00221-013-3764-1

Nijboer, F., Birbaumer, N., and Kübler, A. (2010). The influence of psychological state and motivation on brain–computer interface performance in patients with amyotrophic lateral sclerosis – a longitudinal study. *Front. Neurosci.* 4:55. doi: 10.3389/fnins.2010.00055

Nijboer, F., Sellers, E. W., Mellinger, J., Jordan, M. A., Matuz, T., Furdea, A., et al. (2008). A P300-based brain–computer interface for people with amyotrophic lateral sclerosis. *Clin. Neurophysiol.* 119, 1909–1916. doi: 10.1016/j.clinph.2008.03.034

Noirhomme, Q., Lesenfants, D., Gomez, F., Soddu, A., Schrouff, J., Garraux, G., et al. (2014). Biased binomial assessment of cross-validated estimation of

classification accuracies illustrated in diagnosis predictions. *Neuroimage Clin.* 4, 687–694. doi: 10.1016/j.nicl.2014.04.004

Oostenveld, R., and Praamstra, P. (2001). The five percent electrode system for high-resolution EEG and ERP measurements. *Clin. Neurophysiol.* 112, 713–719. doi: 10.1016/S1388-2457(00)00527-7

Orihuela-Espina, F., Leff, D., James, D., Darzi, A., and Yang, G. (2010). Quality control and assurance in functional near infrared spectroscopy (fNIRS) experimentation. *Phys. Med. Biol.* 55, 3701–3724. doi: 10.1088/0031-9155/55/13/009

Patterson, J. R., and Grabois, M. (1986). Locked-in syndrome: a review of 139 cases. *Stroke* 17, 758–764.

Pfeifer, M. D., Scholkmann, F., and Labruyère, R. (2018). Signal processing in functional near-infrared spectroscopy (fNIRS): methodological differences lead to different statistical results. *Front. Hum. Neurosci.* 11:641–641. doi: 10.3389/fnhum.2017.00641

Pinti, P., Aichelburg, C., Gilbert, S., Hamilton, A., Hirsch, J., Burgess, P., et al. (2018). A review on the use of wearable functional near-infrared spectroscopy in naturalistic environments().*Jpn. Psychol. Res.* 60, 347–373. doi: 10.1111/jpr.12206

Pinti, P., Merla, A., Aichelburg, C., Lind, F., Power, S., Swingler, E., et al. (2017). A novel GLM-based method for the Automatic IDentification of functional Events (AIDE) in fNIRS data recorded in naturalistic environments. *Neuroimage* 155, 291–304. doi: 10.1016/j.neuroimage.2017.05.001

Piper, S. K., Krueger, A., Koch, S. P., Mehnert, J., Habermehl, C., Steinbrink, J., et al. (2014). A wearable multi-channel fNIRS system for brain imaging in freely moving subjects. *Neuroimage* 85, 64–71. doi: 10.1016/j.neuroimage.2013.06.062

Plum, F., and Posner, J. B. (1982). *The Diagnosis of Stupor and Coma*, Vol. 19. Oxford: Oxford University Press.

Pollonini, L., Bortfeld, H., and Oghalai, J. S. (2016). PHOEBE: a method for real time mapping of optodes-scalp coupling in functional near-infrared spectroscopy. *Biomed. Opt. Express* 7, 5104–5119. doi: 10.1364/BOE.7.005104

Power, S. D., Kushki, A., and Chau, T. (2012). Automatic single-trial discrimination of mental arithmetic, mental singing and the no-control state from prefrontal activity: toward a three-state NIRS-BCI. *BMC Res. Notes* 5:141. doi: 10.1186/1756-0500-5-141

Reichert, C., Dürschmid, S., Heinze, H.-J., and Hinrichs, H. (2017). A comparative study on the detection of covert attention in event-related EEG and MEG signals to control a BCI. *Front. Neurosci.* 11:575. doi: 10.3389/fnins.2017.00575

Rezazadeh Sereshkeh, A., Yousefi, R., Wong, A. T., and Chau, T. (2018). Online classification of imagined speech using functional near-infrared spectroscopy signals. *J. Neural Eng.* 16:016005. doi: 10.1088/1741-2552/aae4b9

Rezazadeh Sereshkeh, A., Yousefi, R., Wong, A. T., Rudzicz, F., and Chau, T. (2019). Development of a ternary hybrid fNIRS-EEG brain–computer interface based on imagined speech. *Brain Comput. Interfaces* 1–13. doi: 10.1080/2326263X.2019.1698928

Riccio, A., Mattia, D., Simione, L., Belardinelli, M., and Cincotti, F. (2012). Eye-gaze independent EEG-based brain-computer interfaces for communication. *J. Neural Eng.* 9:045001. doi: 10.1088/1741-2560/9/4/045001

Sargent, A., Heiman-Patterson, T., Feldman, S., Shewokis, P. A., and Ayaz, H. (2018). "Chapter 92 - mental fatigue assessment in prolonged BCI use through EEG and fNIRS," in *Neuroergonomics*, eds H. Ayaz and F. Dehais (Cambridge, MA: Academic Press), 315–316.

Schmitz, C. H., Klemer, D. P., Hardin, R., Katz, M. S., Pei, Y., Graber, H. L., et al. (2005). Design and implementation of dynamic near-infrared optical tomographic imaging instrumentation for simultaneous dual-breast measurements. *Appl. Opt.* 44, 2140–2153.

Schnakers, C., Majerus, S., Goldman, S., Boly, M., Van Eeckhout, P., Gay, S., et al. (2008). Cognitive function in the locked-in syndrome. *J. Neurol.* 255, 323–330. doi: 10.1007/s00415-008-0544-0

Schneider, P., Piper, S., Schmitz, C., Schreiter, N., Volkwein, N., Lüdemann, L., et al. (2011). Fast 3D Near-infrared breast imaging using indocyanine green for detection and characterization of breast lesions. *Paper Presented at the RöFo-Fortschritte auf dem Gebiet der Röntgenstrahlen und der bildgebenden Verfahren*, New York, NY.

Shin, J., Kwon, J., and Im, C.-H. (2018). A ternary hybrid EEG-NIRS brain-computer interface for the classification of brain activation patterns during mental arithmetic, motor imagery, and idle state. *Front. Neuroinform.* 12:5. doi: 10.3389/fninf.2018.00005

Sitaram, R., Zhang, H., Guan, C., Thulasidas, M., Hoshi, Y., Ishikawa, A., et al. (2007). Temporal classification of multichannel near-infrared spectroscopy signals of motor imagery for developing a brain-computer interface. *Neuroimage* 34, 1416–1427. doi: 10.1016/j.neuroimage.2006.11.005

Sorger, B., Dahmen, B., Reithler, J., Gosseries, O., Maudoux, A., Laureys, S., et al. (2009). Another kind of 'BOLD Response': answering multiple-choice questions via online decoded single-trial brain signals. *Prog. Brain Res.* 177, 275–292. doi: 10.1016/S0079-6123(09)17719-1

Sorger, B., Reithler, J., Dahmen, B., and Goebel, R. (2012). A real-time fMRI-based spelling device immediately enabling robust motor-independent communication. *Curr. Biol.* 22, 1333–1338. doi: 10.1016/j.cub.2012.05.022

Suzuki, S., Harashima, F., and Furuta, K. (2010). Human Control Law and Brain Activity of Voluntary Motion by Utilizing a Balancing Task with an Inverted Pendulum. *Adv. Hum. Comput. Interact.* 2010:215825. doi: 10.1155/2010/215825

Treder, M. S., and Blankertz, B. (2010). (C) overt attention and visual speller design in an ERP-based brain-computer interface. *Behav. Brain Funct.* 6:28. doi: 10.1186/1744-9081-6-28

Valente, G., Kaas, A. L., Formisano, E., and Goebel, R. (2019). Optimizing fMRI experimental design for MVPA-based BCI control: combining the strengths of block and event-related designs. *Neuroimage* 186, 369–381. doi: 10.1016/j.neuroimage.2018.10.080

Villringer, A., Planck, J., Hock, C., Schleinkofer, L., and Dirnagl, U. (1993). Near infrared spectroscopy (NIRS): a new tool to study hemodynamic changes during activation of brain function in human adults. *Neurosci. Lett.* 154, 101–104. doi: 10.1016/0304-3940(93)90181-J

Weyand, S., and Chau, T. (2015). Correlates of near-infrared spectroscopy brain–computer interface accuracy in a multi-class personalization framework. *Front. Hum. Neurosci.* 9:536. doi: 10.3389/fnhum.2015.00536

Wilson, B. A., Hinchcliffe, A., Okines, T., Florschutz, G., and Fish, J. (2011). A case study of locked-in-syndrome: psychological and personal perspectives. *Brain Inj.* 25, 526–538. doi: 10.3109/02699052.2011.568034

Yokoyama, N., Ohtaka, C., Kato, K., Kubo, H., and Nakata, H. (2019). The difference in hemodynamic responses between dominant and non-dominant hands during muscle contraction and relaxation: an fNIRS study. *PLoS One* 14:e0220100. doi: 10.1371/journal.pone.0220100

Yucel, M. A., Selb, J., Aasted, C. M., Lin, P. Y., Borsook, D., Becerra, L., et al. (2016). Mayer waves reduce the accuracy of estimated hemodynamic response functions in functional near-infrared spectroscopy. *Biomed. Opt. Express* 7, 3078–3088. doi: 10.1364/BOE.7.003078

Zephaniah, P. V., and Kim, J. G. (2014). Recent functional near infrared spectroscopy based brain computer interface systems: developments, applications and challenges. *Biomed. Eng. Lett.* 4, 223–230. doi: 10.1007/s13534-014-0156-9

Zhang, X., Noah, J. A., and Hirsch, J. (2016). Separation of the global and local components in functional near-infrared spectroscopy signals using principal component spatial filtering. *Neurophotonics* 3:015004. doi: 10.1117/1.NPh.3.1.015004

Zich, C., Debener, S., Thoene, A. K., Chen, L. C., and Kranczioch, C. (2017). Simultaneous EEG-fNIRS reveals how age and feedback affect motor imagery signatures. *Neurobiol. Aging* 49, 183–197. doi: 10.1016/j.neurobiolaging.2016.10.011

Conflict of Interest: ML and RG are employed by the research company Brain Innovation B.V., Maastricht, Netherlands.

The remaining authors declare that the research was conducted in the absence of any commercial or financial relationships that could be construed as a potential conflict of interest.

Copyright © 2020 Nagels-Coune, Benitez-Andonegui, Reuter, Lührs, Goebel, De Weerd, Riecke and Sorger. This is an open-access article distributed under the terms of the Creative Commons Attribution License (CC BY). The use, distribution or reproduction in other forums is permitted, provided the original author(s) and the copyright owner(s) are credited and that the original publication in this journal is cited, in accordance with accepted academic practice. No use, distribution or reproduction is permitted which does not comply with these terms.

frontiers in Neuroscience

ORIGINAL RESEARCH
published: 17 April 2020
doi: 10.3389/fnins.2020.00347

Sleep State Modulates Resting-State Functional Connectivity in Neonates

Chuen Wai Lee[1,2†], Borja Blanco[3,4†], Laura Dempsey[1,3], Maria Chalia[1,2], Jeremy C. Hebden[1,3], César Caballero-Gaudes[4], Topun Austin[1,2,3] and Robert J. Cooper[1,3]*

[1] neoLAB, The Evelyn Perinatal Imaging Centre, The Rosie Hospital, Cambridge University Hospitals NHS Foundation Trust, Cambridge, United Kingdom, [2] Neonatal Intensive Care Unit, The Rosie Hospital, Cambridge University Hospitals NHS Foundation Trust, Cambridge, United Kingdom, [3] DOT-HUB, Department of Medical Physics and Biomedical Engineering, Faculty of Engineering Sciences, University College London, London, United Kingdom, [4] Basque Center on Cognition, Brain and Language, Donostia/San Sebastián, Spain

The spontaneous cerebral activity that gives rise to resting-state networks (RSNs) has been extensively studied in infants in recent years. However, the influence of sleep state on the presence of observable RSNs has yet to be formally investigated in the infant population, despite evidence that sleep modulates resting-state functional connectivity in adults. This effect could be extremely important, as most infant neuroimaging studies rely on the neonate to remain asleep throughout data acquisition. In this study, we combine functional near-infrared spectroscopy with electroencephalography to simultaneously monitor sleep state and investigate RSNs in a cohort of healthy term born neonates. During active sleep (AS) and quiet sleep (QS) our newborn neonates show functional connectivity patterns spatially consistent with previously reported RSN structures. Our three independent functional connectivity analyses revealed stronger interhemispheric connectivity during AS than during QS. In turn, within hemisphere short-range functional connectivity seems to be enhanced during QS. These findings underline the importance of sleep state monitoring in the investigation of RSNs.

Keywords: resting-state functional connectivity, functional near-infrared spectroscopy, sleep state, neonates, connectome, functional imaging

OPEN ACCESS

Edited by:
Yasuyo Minagawa, Keio University, Japan

Reviewed by:
Shuntaro Sasai, University of Wisconsin–Madison, United States
Silvina Ferradal, Indiana University, United States

****Correspondence:***
Borja Blanco
b.blanco@bcbl.eu

† These authors have contributed equally to this work

Specialty section:
This article was submitted to Brain Imaging Methods, a section of the journal Frontiers in Neuroscience

Received: *22 September 2019*
Accepted: *23 March 2020*
Published: *17 April 2020*

Citation:
Lee CW, Blanco B, Dempsey L, Chalia M, Hebden JC, Caballero-Gaudes C, Austin T and Cooper RJ (2020) Sleep State Modulates Resting-State Functional Connectivity in Neonates. Front. Neurosci. 14:347. doi: 10.3389/fnins.2020.00347

INTRODUCTION

In recent years, the number of studies investigating resting-state networks (RSNs) in neonates has grown immensely (Gao et al., 2016). While most of these studies utilize functional connectivity MRI (fcMRI) to identify RSNs (Fransson et al., 2007; Doria et al., 2010; Smyser et al., 2010; Damaraju et al., 2014), functional near-infrared spectroscopy (fNIRS) has emerged as a promising modality due to its practical advantages, which include portability, low-cost, and silent operation. fNIRS studies investigating resting-state functional connectivity in infants have demonstrated: (1) evidence of primary sensory RSNs such as the visual (White et al., 2012) and auditory RSNs in term neonates (Ferradal et al., 2016), (2) increasing interhemispheric connectivity between homotopic regions in the first 6 months of life (Homae et al., 2010), and (3) altered functional connectivity patterns in preterm born neonates at term age (Fuchino et al., 2013; Naoi et al., 2013).

A significant challenge in studying neonates, common to both fcMRI and optical modalities, is subject motion. To minimize motion, neonates are almost always scanned whilst asleep, or even under light sedation (Arthurs et al., 2012). However, the effect of sleep state on RSNs has not been

directly investigated in the neonatal population, despite evidence of altered activity in adults. In adults, networks associated with primary functions (such as the sensorimotor network) and cortico-cortical connectivity strength have both been shown to diminish during deep non-rapid eye movement (NREM) and slow wave sleep (Spoormaker et al., 2010; Watanabe et al., 2014), but are preserved in early, light NREM sleep (Horovitz et al., 2008; Larson-Prior et al., 2009). The different stages of NREM sleep can also have variable effects on higher cognitive function RSNs such as the default mode network (DMN), where different contributions from each region decrease with progressive sleep depth (Horovitz et al., 2009; Sämann et al., 2011). Furthermore, sedation is known to produce a variable effect on high-order cognitive RSNs in adults (Greicius et al., 2008; Martuzzi et al., 2010).

Monitoring arousal or sleep state in neonates is routinely performed with electroencephalography (EEG; Dereymaeker et al., 2017; Pillay et al., 2018). However, introducing additional neuro-monitoring equipment into a study of an already challenging population can be time consuming and problematic. Combining EEG and fcMRI is a significant technical challenge in any population, but particularly in neonates (Arichi et al., 2017). Because of the duration of the infant sleep cycle, if one wishes to investigate functional networks during multiple sleep states in a single neonate, it is necessary to monitor that subject for an extended period. Scanning for prolonged study durations can pose significant challenges for vulnerable neonates using modalities such as fcMRI. A more promising approach therefore is to combine EEG with multichannel fNIRS. Both modalities are portable and share a common set-up procedure that allows for simultaneous application of both devices to an infant subject. EEG offers the ability to distinguish sleep states in neonatal RSN studies. In the full-term neonate, the sleep cycle lasts between 30 and 70 min and comprises largely of so-called "active" and "quiet" sleep segments (Scher, 2008). The temporal order of active sleep (AS) and quiet sleep (QS) is variable in term neonates, and during a full sleep cycle, AS and QS can occur more than once. Typically, the sleep cycle starts with a period of mixed frequency AS, however, this only occurs in over 50% of infants. Short stages of transitional or indeterminate sleep patterns can also occur where physiology and behavior are not characteristic of either AS or QS (Scher, 2008). AS in infants is typically characterized by a continuous EEG background. Associated physiological observations include rapid eye movements, increased cardiorespiratory variability, low muscle tone, and frequent body movements. QS is characterized by either a continuous, slow, high-voltage EEG or a discontinuous EEG pattern also known as tracé alternant. The latter is defined by bursts of high amplitude slow-wave activity interspersed with low voltage activity. The absence of eye movements, reduced respiratory variability, increased muscle tone, and reduced body movements are also characteristic features.

In this study, we combined standard, neonatal clinical montage EEG with a multichannel fNIRS system with a source-detector (SD) array covering the temporal, parietal, and inferior frontal regions of the head in a relatively high-density arrangement. We measured spontaneous cortical hemodynamic activity with fNIRS in a group of healthy term born neonates during AS and QS. We employed three independent analysis methods to assess the influence of sleep state in resting-state functional connectivity. Using a seed-based correlation analysis we investigated the influence of sleep state in network structures such as the frontal, auditory, and sensorimotor RSNs which in this age group are expected to demonstrate a developing bilateral homotopic connectivity (Fransson et al., 2007; Doria et al., 2010; Homae et al., 2010; Smyser et al., 2010; Ferradal et al., 2016). By using two connectome-based approaches we also investigated the interaction between neonatal sleep state and the spatial organization of large-scale resting-state functional connectivity patterns.

MATERIALS AND METHODS

Subjects

Healthy term neonates (>37 weeks of gestation) were recruited from the postnatal ward of The Rosie Hospital (Cambridge University Hospitals NHS Foundation Trust). This study was approved by the National Research Ethics Service Committee East of England (REC reference 13/EE/0344), and written informed consent was obtained from parents for neonates to participate. A total of 30 neonates were recruited. Datasets from 10 neonates were excluded during data processing due to low data quality or insufficient duration of AS and QS data segments for subsequent RSN analysis. fNIRS data was analyzed from the remaining 20 subjects (11 males and 9 females; mean gestational age = 40 + 2 weeks; mean weight at birth = 3704 g; mean scan age = 2.65 days). Demographic details of the subjects are summarized in **Table 1**.

Data Collection

Neonates were imaged in a quiet, dimly lit room in The Evelyn Perinatal Imaging Centre (Cambridge University Hospitals NHS Foundation Trust). To promote sleep, a feed and wrap approach was used. As a full-sleep cycle in the neonatal period typically lasts for up to an hour (Scher, 2008), imaging sessions were performed for at least 1 h to capture both AS and QS. We used the NTS fNIRS System (Gowerlabs Ltd., United Kingdom), which is a continuous-wave multichannel fNIRS device (Everdell et al., 2005) with a sampling rate of 10 Hz. The system consists of 16 dual-wavelength laser-diode sources operating at near-infrared wavelengths of 780 nm and 850 nm, and 16 avalanche photodiode detectors. A SD array with 69 measurement channels consisting of SD separation distances ranging from 19 to 36 mm was designed to cover the inferior frontal, temporal, and parietal regions of the cortex (**Figure 1A**). A customized EEG head cap (EasyCap, GmbH) was adapted to hold the SD array in accordance with a subset of standard 10–5 positions (Oostenveld and Praamstra, 2001). Nasion, inion, and preauricular points were used as external head landmarks for cap positioning. A standard neonatal montage (Walls-Esquivel et al., 2007) consisting of 11 EEG electrodes (Fp1, Fp2, Fz, T3, T4, C3, C4, Cz, Pz,

TABLE 1 | Demographic details of the 20 subjects included in the fNIRS resting-state analysis.

Subject	GA at birth (weeks)	Scan age (days)	Weight (g)	Gender	AS recording duration (s)	QS recording duration (s)
1	38 + 0	3	2830	M	121	121
2	38 + 0	3	3165	M	126	182
3	41 + 5	2	3500	F	153	367
4	39 + 5	2	3890	F	124	124
5	40 + 6	1	3770	F	150	156
6	40 + 2	1	3440	M	155	153
7	40 + 6	2	3820	F	147	475
8	40 + 0	5	3585	F	161	180
9	41 + 6	3	3680	F	214	183
10	39 + 2	6	3450	M	590	534
11	39 + 0	2	3500	F	167	290
12	42 + 3	1	3960	M	148	171
13	39 + 0	4	3375	M	123	180
14	39 + 1	1	3980	M	136	654
15	40 + 4	1	3770	F	209	204
16	42 + 0	1	4270	F	141	333
17	41 + 2	2	4140	M	120	283
18	41 + 2	6	4180	M	121	150
19	41 + 0	2	4830	M	177	209
20	40 + 2	5	2935	M	128	225
					170.5 ± 102	259 ± 146

Recording duration for the analyzed AS and QS periods is also included. AS, active sleep; QS, quiet sleep; GA, gestational age; M, male; F, female.

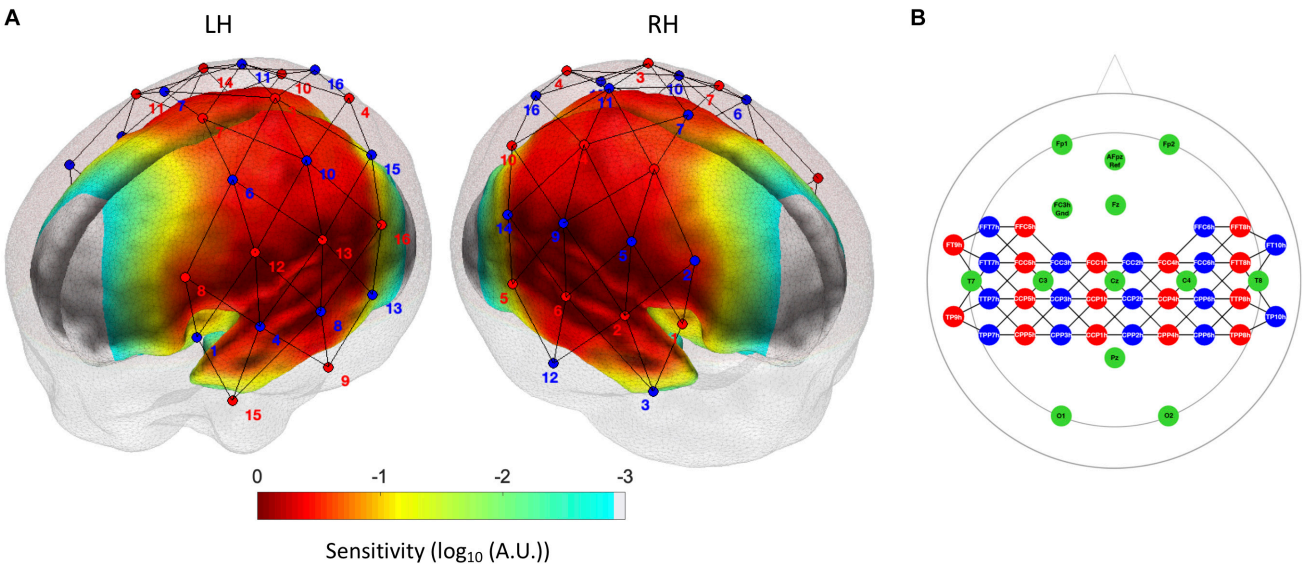

FIGURE 1 | (A) Optode localization (sources in red and detectors in blue) in the current experimental setup. The normalized sensitivity profile of this configuration is displayed on a neonate head model template (Brigadoi et al., 2014), where regions of higher sensitivity below the source-detector configuration are displayed in red color. **(B)** fNIRS optode and EEG electrode positions in the 10–5 system for the EasyCap montage employed in the current study. The fNIRS sources are indicated in red, the detectors in blue, and the EEG electrodes in green.

O1, and O2) with two of the electrodes assigned for ground (FC3h) and reference (AFpz) were incorporated into the EasyCap (**Figure 1B**). The cap was secured on the infant subject's head using a soft elastic chinstrap and a chest belt to maintain SD fiber coupling to the scalp (see **Figure 2** for an example of our cap arrangement on a representative participant). EEG abrasion gel and conduction paste were applied to minimize EEG electrode impedances to below 5 kΩ. The EEG setup also included electrocardiography (ECG), behavioral observation, and EEG video. To synchronize the fNIRS and EEG signals,

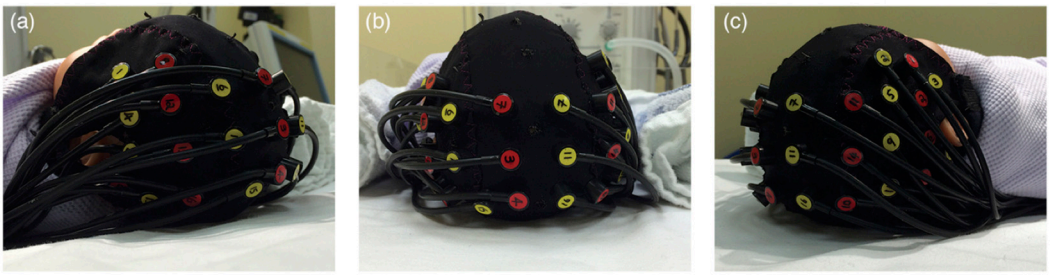

FIGURE 2 | fNIRS-EEG cap arrangement showing the positioning of fNIRS optodes (sources in red, detectors in yellow) on an infant head from **(a)** left, **(b)** top and **(c)** right views.

an external event generator device was used (Gowerlabs Ltd., United Kingdom).

EEG Sleep State Assessment

The EEG data were visualized offline using BrainVision Analyzer V.2.0.2 software (Brain Products GmbH, Germany), and the EEGLAB toolbox (Delorme and Makeig, 2004) for MATLAB (MathWorks, United States). Standard filtering was applied to the EEG signal using a high-pass filter at 0.5 Hz and a low-pass filter at 70 Hz with an added notch filter at 50 Hz (United Kingdom mains frequency). Each electrode was referenced to the common reference electrode positioned at AFpz.

The degree of continuity and amplitude of the EEG signal were used to visually categorize EEG segments into AS and QS using standard criteria (Scher, 2008; André et al., 2010; Grigg-Damberger, 2016). Segments of mixed frequency or low amplitude continuous EEG were labeled as AS. High-voltage continuous or tracé alternant segments were labeled as QS. ECG variability and infant movement observed and recorded on EEG video were used to complement the EEG signal in determining sleep state. Any segments in which sleep state was undetermined and those that contained motion artifacts were excluded from further analysis. Segments in which head movements were evident, as determined by visual inspection of the EEG video, were marked as motion in both EEG and fNIRS data. In addition, a 5-s mask was added at the beginning and at the end of each identified motion segment. Any other movement of the participant that was visible on EEG video was cross-referenced with the fNIRS signal and marked as motion if temporally correlated motion artifacts were observed. Sleep segments were also visually identified in a subset of infants by a second observer to confirm inter-rater agreement (Cohen's kappa = 0.833).

fNIRS Data Preprocessing

The fNIRS and EEG datasets for each subject were synchronized using the trigger events in both signals produced from the event generator device. The time markers for the labeled EEG sleep segments were transformed to the fNIRS time-base to enable the division of the fNIRS data into AS and QS segments. fNIRS data were excluded as noise if the measured light intensity was below 5e-4 a.u. (arbitrary units), as recommended by the manufacturer. On top of the data exclusion criteria described in the previous section we also excluded data segments based on the fNIRS signal using the *hmrMotionArtifact* function in Homer2, Huppert et al. (2009). Any change in measured optical density (OD) occurring within any 0.5 s period that was greater than 0.5 OD, or greater than 15 times the standard deviation of the entire time-course was considered motion artifact. Five seconds of data before the start and end of each segment marked as motion artifact were excluded. The longest motion-free segments from within each fNIRS sleep segment were extracted for the functional connectivity analyses. Previously reported infant RSN fNIRS studies used a minimum duration of 2 min of data (White et al., 2012; Bulgarelli et al., 2019, 2020), therefore the longest motion-free segment of at least 2 min duration was selected for AS and QS. The mean duration of fNIRS data segments was 215 s (AS = 170 ± 102 s; QS = 258 ± 146 s). From these segments, changes in OD were calculated from raw optical intensity data using the *hmrIntensity2OD* algorithm implemented in Homer2. OD data was converted into oxyhemoglobin (HbO) and deoxyhemoglobin (HbR) concentration changes (*hmrOD2Conc* in Homer2), using differential pathlength factors 5.3 and 4.2 (Scholkmann and Wolf, 2013). Temporal filtering and global signal regression were performed simultaneously in a unique regression model. Sine and cosine functions for frequencies above 0.08 Hz were included in the model to remove the contribution of physiological noise sources (e.g., respiration and cardiac pulsation), and up to 4th order Legendre polynomials (depending on dataset duration) were included to account for fluctuations at very low frequencies. The average fNIRS signal across channels was included in the regression model, for HbO and HbR independently, to remove globally occurring hemodynamic signals, which were assumed to largely reflect systemic changes (White et al., 2009; Mesquita et al., 2010; Tachtsidis and Scholkmann, 2016). Quality assurance figures for each participant at different steps of the pre-processing, are available as **Supplementary Material**.

Resting-State Functional Connectivity Analyses

All the analyses described below were performed for both HbO and HbR. First, a seed-based correlation analysis approach was adopted to create correlation maps for AS and QS conditions and for each infant. Seed channels for the left and right hemispheres were selected for the inferior frontal, auditory, and sensorimotor regions based on previously published reports (Doria et al., 2010;

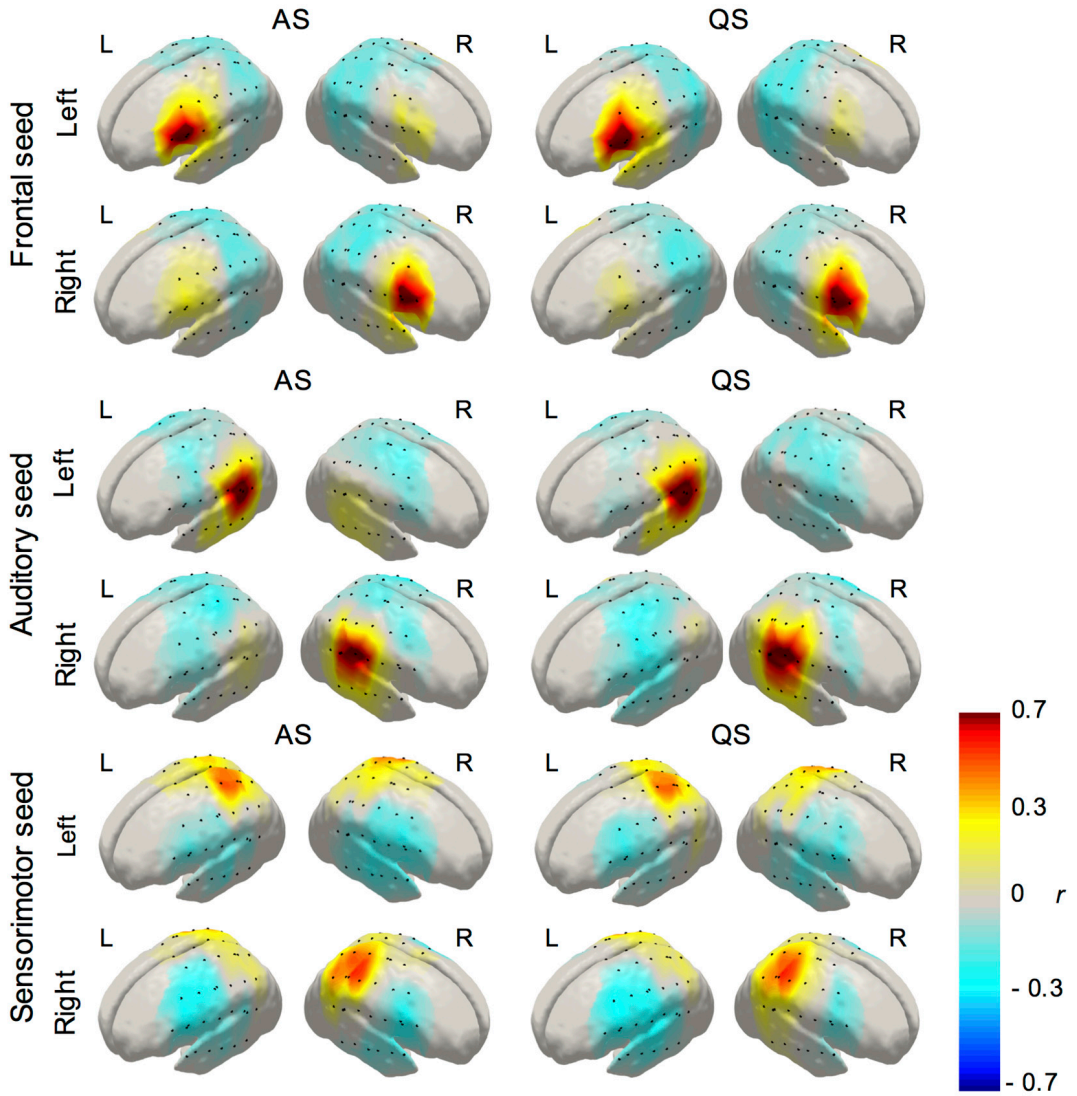

FIGURE 3 | Average correlation maps (HbO) derived from the seed-based correlation method for the left and right seeds in the inferior frontal, auditory, and sensorimotor regions (AS, active sleep, first column; QS, quiet sleep, second column). Due to its high similarity, and to avoid presenting redundant information, HbO maps are displayed in the main text and HbR maps are presented as **Supplementary Material**.

Smyser et al., 2010; Ferradal et al., 2016). A robust Pearson's correlation coefficient (Santosa et al., 2017) was calculated between each seed channel and every other channel in the array. Individual correlation values were normalized by Fisher's Z transformation before averaging across subjects. Average values were then transformed back to Pearson's correlation coefficients for the presentation of average correlation maps corresponding to each sleep state and for each region (**Figure 3**). For each seed region, group differences between sleep states were assessed by conducting channel-wise paired t-tests between AS and QS conditions, which were corrected for multiple comparisons using the false discovery rate (FDR; $q < 0.05$) method (Benjamini and Hochberg, 1995). For results visualization purposes, we computed the sensitivity profile of our fNIRS sensor setup. We registered our sensors to the MRI space of a neonate head model template (Brigadoi et al., 2014) and calculated the sensitivity matrix of our SD configuration using *Toast++* (Schweiger and Arridge, 2014). We summed the cortical sensitivity profiles of each channel, resulting in the aggregated sensitivity profile of our sensors. Channel positions were defined as the gray matter node which coordinates were closest to the central point of the maximum sensitivity path along each SD pair.

Between-group statistical comparisons of functional connectivity matrices were also performed using two connectome-based approaches. First, we followed a Network Based Statistic (NBS) approach, a widely employed method in fcMRI studies to perform group-level comparisons in structural and functional brain network organization (Zalesky et al., 2010, 2012; García-Pentón et al., 2014). In this approach, a statistical test of group differences (i.e., a t-test) is computed on

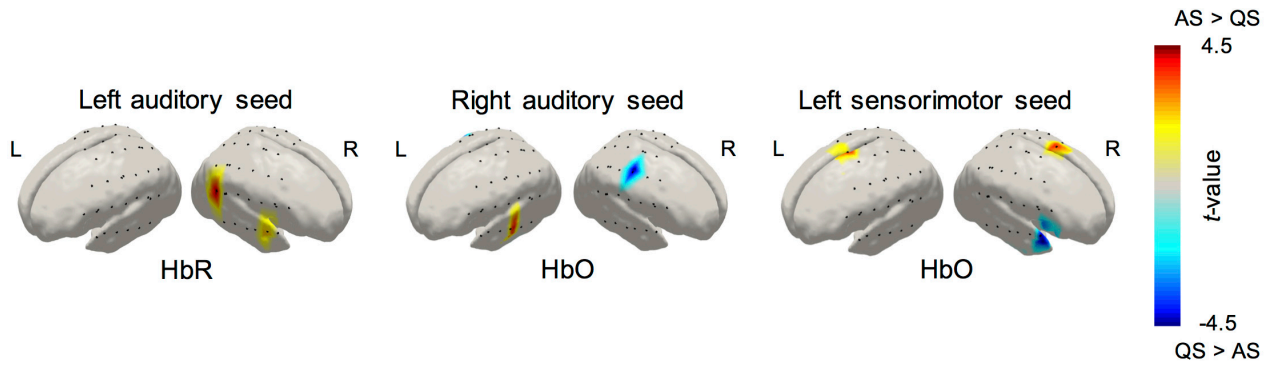

FIGURE 4 | Group differences in RSNs revealed by the paired *t*-tests of the seed-based correlation method between active and quiet sleep. Results for HbO and HbR are displayed for those statistical tests that survived the seed level FDR correction criterion ($q < 0.05$).

the subjects' functional connectivity matrices for each channel pair, and clusters of interconnected edges above a preselected statistical threshold are identified. In this study, we evaluated two thresholds (*t*-values) representing different levels of statistical significance: $t_1(19) = 2.6$, equivalent to $p = 0.01$ and $t_2(19) = 3.6$, equivalent to $p = 0.001$. These values represent the thresholds for which the null hypothesis will be rejected at each channel pair – same approach as a massive univariate analysis – and therefore have an impact on network size (i.e., total number of interconnected edges exceeding the statistical threshold), but not on the significance of the identified networks. This is tested using non-parametric permutation testing, controlling the family-wise error rate at the network level based on the network size. Second, we used connICA (Amico et al., 2017), a data-driven methodology based on independent component analysis (ICA), which can be used to extract group-level independent functional connectivity patterns from a set of individual functional connectivity matrices. This methodology also provides a framework to study potentially meaningful associations between a particular experimental variable (e.g., levels of consciousness in Amico et al., 2017) and the prominence of specific functional connectivity patterns representing distinct functional processes. We applied the NBS and connICA methods to HbO and HbR derived functional connectivity matrices, and the results for both chromophores are reported.

RESULTS

During EEG and fNIRS data processing, it was observed that AS data typically contain a larger number of motion artifacts, and were therefore shorter in duration compared to QS on average (mean duration for AS and QS were 170 ± 102 s and 258 ± 146 s, respectively). A paired two-tailed *t*-test revealed a significant difference; $t(19) = -2.8289$, $p = 0.0107$. This was expected as AS is associated with frequent body movements, while in QS body movements are reduced (Scher, 2008). However, we also assessed data quality across sleep states by comparing the amount of motion on each group, based on the kurtosis of wavelet coefficients of the selected segments (Chiarelli et al., 2015). This provides a measure of the abundance of outliers apparent in each dataset; outliers that are likely to represent transient noise sources, including any remaining motion artifact. No difference in wavelet kurtosis was evident between the AS and QS groups [$k_{AS} = 3.41 \pm 1.23$, $k_{QS} = 3.69 \pm 2.43$, $t(19) = -0.49$, $p = 0.6240$].

The average correlation maps produced from the seed-based correlation analysis illustrating functional connectivity for the left and right seeds in the inferior frontal, temporal, and parietal regions during AS and QS, are displayed in **Figure 3**. Connectivity maps for all the seed regions showed the expected spatial configuration in the two hemodynamic contrasts (i.e., HbO and HbR), with the strongest correlations being observed on channels surrounding the seed regions and in bilateral homologous seed-regions respectively. Qualitative assessment of group maps for the AS condition implied bilateral connectivity for both left and right seeds in the inferior frontal, auditory, and sensorimotor regions. In contrast, during QS bilateral connectivity appears reduced in the inferior frontal areas and absent in the auditory regions. Similar results were observed in the seed-based correlation analysis for HbR, which are available as **Supplementary Material**. The channel-wise paired *t*-tests results for the comparison between AS and QS for HbO and HbR are displayed in **Figure 4**. Only statistically significant differences that survived multiple comparison correction using the FDR criterion ($q < 0.05$) are reported. Overall these results show that the correlation between homologous channels across hemispheres is stronger in AS on the left and right auditory seeds and on the left sensorimotor seed. In turn, during QS, correlation was stronger within nearby channels on the right auditory seed, and between the left motor seed and channels on the right inferior frontal region.

The NBS analysis also revealed significant group differences between sleep states in global functional connectivity organization (**Figure 5A**). For HbO, and at the two statistical thresholds considered, we found a functional network showing higher synchronization in AS periods, as opposed to QS periods. This network was significant, evaluated using non-parametric permutation testing, for the two statistical thresholds considered (t_1, $p < 0.001$ and t_2, $p < 0.005$, corrected). The topological organization of this network demonstrates increased

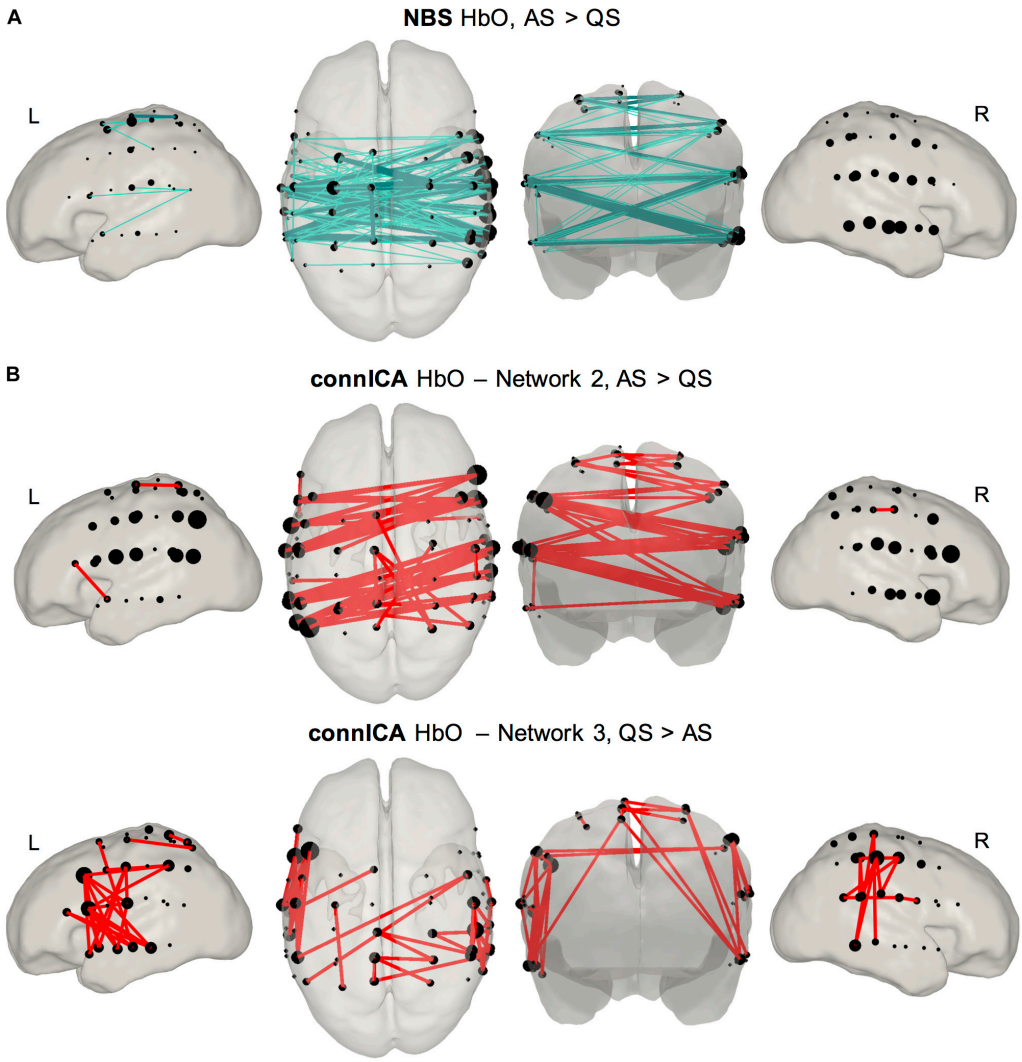

FIGURE 5 | Results of connectome based analyses revealing group differences between sleep states. **(A)** NBS method (top row) showed a network mainly characterized by interhemispheric connectivity which was stronger in AS compared to QS. Results are presented for two statistical thresholds (t_1, $p < 0.001$ empirical permutation test, light color, thin edges; t_2, $p < 0.005$ empirical permutation test, dark color, thick edges). This difference was only observed for HbO. **(B)** ConnICA method (second and third rows) revealed two networks showing significant differences between sleep states. Network 2 represents a functional connectivity pattern formed by interhemispheric edges showing a higher prominence during AS [$t(19) = 3.19$; $p = 0.0048$]. Network 3 is a RSN characterized by short-range unilateral edges displaying stronger connectivity during QS [$t(19) = -3.09$; $p = 0.006$]. These network level differences were observed for both HbO and HbR. Due to the high spatial similarity between the observed HbO and HbR networks only figures for HbO are presented in the main text, and HbR figures are presented as **Supplementary Material**.

interhemispheric connectivity during AS. The strongest connections (which are represented as dark colored, thick edges in **Figure 5A**) were observed along areas corresponding to bilateral auditory and sensorimotor regions. No significant network differences were observed for increased connectivity in QS as compared to AS for HbO, nor for the HbR analysis in either direction.

The modulation in functional connectivity resulting from variations in sleep state was also confirmed using connICA (**Figure 5B**). The connICA method revealed seven group-level functional connectivity patterns characterizing our set of individual functional connectivity matrices that included AS and QS. This method also provided a vector of values quantifying the presence of each group-level functional connectivity pattern within each individual. It is these values that were employed to assess statistical differences between our experimental groups. In both HbO and HbR, two of these independent functional connectivity patterns were associated with significant sleep state modulations. The first network, which demonstrated a high degree of overlap with that extracted in the NBS analysis, mainly involved interhemispheric connectivity and showed a significantly higher prominence in neonates during AS [$t(19) = 3.19$; $p = 0.0048$]. The second network, characterized by within hemisphere short-range connections between nearby

channels, showed a higher presence during QS [$t(19) = -3.09$; $p = 0.006$]. These two functional networks are threshold to show only positive connections (top 5% of connections), as the interpretation of negative correlations in functional connectivity analyses still remains contentious. The complete Figures – with positive and negative connections – of all the functional components calculated with connICA for HbO and HbR are available as **Supplementary Material**.

DISCUSSION

This study demonstrates the utility of combining multichannel fNIRS with EEG to simultaneously monitor sleep state and RSNs in neonates. The current work also represents the first demonstration of spatial pattern variations in RSNs between different sleep levels in neonates. We used three independent analysis methods to quantitatively compare resting-state functional connectivity between AS and QS in a cohort of healthy neonates, as each of them provides complementary information to investigate associations between sleep state and group-level network characteristics. NBS compares global network characteristics between experimental groups, but only networks showing differences between the groups are extracted. In contrast, connICA extracts multiple independent subcomponents from the functional connectivity patterns computed at the group-level, and then allows testing for statistical differences on the relevance of each component between groups. Our results for the three methods showed that interhemispheric long-range connectivity is stronger during periods of AS. In addition, the SBA and connICA methods revealed functional connectivity patterns in which local short-range connectivity is enhanced during QS.

These findings provide evidence that sleep state can modulate RSNs in the newborn brain and highlight the importance of monitoring sleep in studies of infant RSNs. Although prior studies have reported the presence of RSNs in neonates as early as 27 weeks of gestation (Smyser et al., 2010), several discrepancies exist in the observation of RSNs in the literature, both within and across imaging modalities (i.e., fcMRI or optical methods). For example, using fcMRI, Doria et al. (2010) observed complete RSNs (several of which were integrated with thalamic activity) in preterm infants scanned at term-equivalent age. These were indistinguishable from those observed in term-born infants. Smyser et al. (2010) also observed recognizable RSNs using fcMRI in preterm infants that developed with age. However, by term equivalent age, these RSNs demonstrated lower correlation, limited spatial distribution, and reduced thalamocortical connectivity as compared to term-born controls. Using diffuse optical tomography (DOT), White et al. (2012) reported interhemispheric connectivity in the occipital cortex reflecting visual RSNs in healthy term infants. On the other hand, in a RS fNIRS study, Homae et al. (2010) showed a reduced interhemispheric connectivity in their healthy term cohort, which was only observed across all brain regions at a later stage from 3 months of age, although these effects might be caused by contamination of the optical signal from physiological artifacts in the superficial layers of the head. However, none of these studies have formally monitored the sleep states of their subjects. This detail is particularly important since neuronal interactions as characterized by phase and amplitude dynamics in EEG have been reported to change significantly between sleep states in term born infants (Tokariev et al., 2016). While most RSN studies acquire data immediately within 30 min of sleep (Gao et al., 2016), the variability in sleep state and lack of sleep monitoring could also explain some of the inconsistencies observed across neonatal studies.

The stronger interhemispheric connectivity observed during AS may highlight the importance of sleep for neural development during the neonatal period, complementing the current understanding of the role of AS in early neural development. Sleep states emerge in the third trimester and become distinguishable electrographically from 30 weeks gestational age (Visser et al., 1987). While there is a significant increase in QS duration (Mulder et al., 1987; Curzi-Dascalova et al., 1988, 1993), AS remains the predominant sleep state until term (Mulder et al., 1987; Mirmiran, 1995). In full-term neonates, more than half of sleep time is spent in AS (Mirmiran et al., 2003). The long periods of AS in early infancy occur concurrently with periods of rapid cerebral maturation, suggesting neural activity during AS may be functionally important in early development. Animal studies demonstrate that cerebral blood flow and oxygen delivery is relatively higher in AS compared to QS (Morrison et al., 2005), and that cerebral metabolic rate of oxygen consumption is as high in AS as during wakefulness (Silvani et al., 2006). In rat pups, brain mass including the cerebral cortex and brainstem are significantly reduced after AS deprivation, with alterations in neurotransmitter sensitivity compared to typically developing rats (Mirmiran et al., 1983; Morrissey et al., 2004). In AS, movements that are anticipatory in nature such as eye movements, stretches, and sucking occur frequently, therefore AS may facilitate neural development by providing endogenous stimulation at a time when waking life is limited with little exogenous stimulation (Roffwarg et al., 1966; Denenberg and Thoman, 1981). Spontaneous cerebral activity represented by RSNs may therefore reflect the endogenous activity of the brain during AS.

The ability to monitor RSNs in neonates could become a valuable clinical tool to assess cerebral function and development in vulnerable neonatal patients. This is of great clinical importance as the incidence of neurodisability remains unchanged despite advances in neonatal care and improvements in survival rates (Costeloe et al., 2012). It has been shown that preterm neonates exhibit reduced network complexity, a quantitative measure of network amplitude and dimensionality (Smyser et al., 2016). Complications related to prematurity, such as white matter injury (Smyser et al., 2013), hemorrhagic parenchymal infarction (Arichi et al., 2014), and exposure to stress and painful procedures (Smith et al., 2011) may affect RSN development. Furthermore, the impact of prematurity on sleep maturation may also lead to complications in RSN development. Sleep is the predominant behavioral state in the neonate, however, the busy environment of the NICU can disrupt sleep organization in both preterm and sick term neonates (Scher et al., 1992, 2002). As the sleep cycle is largely made up of AS compared to QS, interruptions to sleep due to intensive care

are more likely to have an effect on the AS period therefore disrupting resting-state cerebral activity and potentially altering the development of RSNs.

While AS and QS can be broadly related to adult REM and NREM sleep respectively, comparisons between the sleep states of infants and adults need to be made with caution. In this study, the reduction in interhemispheric connectivity observed during QS is contrary to their preservation during NREM sleep in adults. This difference may be due to the significant maturational changes in sleep, especially of QS, in infants with advancing age (Mirmiran et al., 2003). Although standardized guidance is available for visual sleep scoring (Grigg-Damberger, 2016), the visual interpretation of AS and QS can vary between observers. A more objective approach could be to use quantitative EEG methods such as sleep state classifiers to identify sleep states (Paul et al., 2003; Piryatinska et al., 2009; Koolen et al., 2017). Extensive polysomnography is normally applied to formal clinical sleep studies, however, our set up (including ECG, behavioral observation, and EEG) was a practical one as it provided sufficient data to distinguish AS and QS with minimal handling of subjects.

It is difficult to capture a long continuous recording that is motion free in neonates, and this was one of the main limitations of this work. It is even more challenging if we are limited to a specific sleep state and even more so if there are segments of sleep states that are not easily identifiable as AS or QS. As a result of all this, the durations will inevitably be short. However, previous fNIRS resting-state functional connectivity studies reported using durations as short as 2 min on neonates (White et al., 2012), or 100 s in toddlers between 11 and 36 months of age (Bulgarelli et al., 2019, 2020). Wang et al. (2017) reported that 1-min recordings are enough to obtain accurate functional connectivity measures with fNIRS due its much faster temporal resolution. However, this study also confirmed that 7 min are necessary to obtain both accurate and stable measures. We also need to acknowledge the fact that, even with a higher sampling rate, the acquisition length will limit the spectral content of the fNIRS measurements. In particular, short acquisitions will fail to provide enough information in lower frequency ranges. In this study, and considering the need to allow at least one full cycle to resolve the lowest frequencies in the signal (Leonardi and Van De Ville, 2015), our 2 min measurements will lack enough information for robust estimation of functional connectivity at frequencies below 0.008 Hz (i.e., 1 full cycle/120 s). Although frequencies below 0.008–0.01 Hz are typically filtered out in resting-state functional connectivity analyses (Homae et al., 2010; White et al., 2012; Ferradal et al., 2016; Bulgarelli et al., 2020), longer recordings are still recommended, as they increase signal-to-noise ratio and reduce variability of the estimated functional connectivity (Hutchison et al., 2013). Another limitation of the current study is that the duration of AS and QS segments extracted for RSN analysis were significantly different. This was likely due to frequent subject motion associated with AS (Scher, 2008), which complicated the extraction of motion-free segments of sufficient duration. The presence of motion artifacts could lead to erroneous correlation results in RSN analysis (Santosa et al., 2017). However, this was not the case in the current study, as data quality was comparable across sleeps states.

Finally, the current fNIRS system uses a relatively dense SD array covering the temporal, parietal, and inferior frontal regions of the head. However, this limited us to investigating the inferior frontal, temporal, and sensorimotor RSNs. An ideal array configuration would achieve whole head coverage with a high sampling density and include short-distance channels to regress out systemic confounds. The shortest available SD distance in the current fNIRS setup was 19 mm, as we were limited to the physical size of the optodes (10 mm diameter) and we also allowed for placement of EEG electrodes. We acknowledge that 19 mm is already too large for short-separation regression, especially in infants (Brigadoi and Cooper, 2015). For this reason, we decided to follow a global signal regression approach to reduce physiological contamination (Pfeifer et al., 2018). With advances in technology, particularly the emergence of high-density, fiber-less DOT systems (Chitnis et al., 2016), it will soon be possible to produce high-quality, whole-cortex 3D images of cerebral hemodynamics at the cot-side, which will enable further investigation of neonatal RSNs.

CONCLUSION

We used simultaneous fNIRS and EEG to investigate whether RSNs in neonates are affected by sleep state. Our results show that resting-state functional connectivity is differentially modulated across AS and QS states. Increased interhemispheric connectivity during AS, that is consistently observed across three independent analyses, may reflect the importance of AS in the functional organization of the developing brain in the absence of sensory stimulation. The prominence of long-range connectivity during AS compared to short-range connectivity during QS may indicate that each sleep state fulfils a different role during the early development of functional networks (Ouyang et al., 2017). This work highlights the importance of monitoring sleep in studies of neonatal resting-state functional connectivity. Furthermore, the presence of sleep state-dependent functional connectivity may demonstrate the developmental importance of sleep in the neonatal period more generally. Further research in this field, and the combination of optical methods and EEG techniques, may become clinically valuable, particularly in the cot-side neurological assessment of neonatal patients vulnerable to sleep disruption, such as those born preterm or with brain injury.

DATA AVAILABILITY STATEMENT

The datasets presented in this article are not readily available because the NHS data ethics covering this protocol date back to 2014, and only permit anonymised data sharing only within the immediate research group.

ETHICS STATEMENT

The studies involving human participants were reviewed and approved by the National Research Ethics Service Committee

East of England (REC reference 13/EE/0344). Written informed consent to participate in this study was provided by the participants' legal guardian/next of kin.

AUTHOR CONTRIBUTIONS

CL conceived the study, designed the experiment, collected the data, performed the preliminary analyses, and wrote and edited the manuscript. BB designed and implemented the data analysis, determined the results, and wrote the manuscript. LD contributed to the design of the experiment and data collection, and edited the manuscript. MC contributed to the data collection, oversaw the EEG analysis, and edited the manuscript. JH oversaw the research collaboration, supervised LD, and edited the manuscript. CC-G supervised BB, oversaw the data analysis, and edited the manuscript. TA oversaw the research collaboration, supervised CL and MC, and edited the manuscript. RC oversaw the research collaboration, supervised CL, BB, and MC, and edited the manuscript.

FUNDING

This work was supported by the Medical Research Council (MR/L017490/1), Evelyn Trust (09/26 2013 RTF), EPSRC (EP/N025946/1), and the Basque Government (PRE_2018_2_0154).

ACKNOWLEDGMENTS

The authors would like to thank all the infants and the families who generously participated in this study. The authors would also like to thank ongoing support from the clinical staff of The Rosie Hospital, without whom this study would not be possible.

SUPPLEMENTARY MATERIAL

The Supplementary Material for this article can be found online at: https://www.frontiersin.org/articles/10.3389/fnins.2020.00347/full#supplementary-material

REFERENCES

Amico, E., Marinazzo, D., Di Perri, C., Heine, L., Annen, J., Martial, C., et al. (2017). Mapping the functional connectome traits of levels of consciousness. *Neuroimage* 148, 201–211. doi: 10.1016/j.neuroimage.2017.01.020

André, M., Lamblin, M. D., d'Allest, A. M., Curzi-Dascalova, L., Moussalli-Salefranque, F., and Nguyen, S. (2010). Electroencephalography in premature and full-term infants. Developmental features and glossary. *Neurophysiol. Clin.* 40, 59–124. doi: 10.1016/j.neucli.2010.02.002

Arichi, T., Counsell, S. J., Allievi, A. G., Chew, A. T., Martinez-Biarge, M., Mondi, V., et al. (2014). The effects of hemorrhagic parenchymal infarction on the establishment of sensorimotor structural and functional connectivity in early infancy. *Neuroradiology* 56, 985–994. doi: 10.1007/s00234-014-1412-5

Arichi, T., Whitehead, K., Barone, G., Pressler, R., Padormo, F., Edwards, A. D., et al. (2017). Localization of spontaneous bursting neuronal activity in the preterm human brain with simultaneous EEG-fMRI. *Elife* 6:e27814. doi: 10.7554/eLife.27814.001

Arthurs, O. J., Edwards, A., Austin, T., Graves, M. J., and Lomas, D. J. (2012). The challenges of neonatal magnetic resonance imaging. *Pediatr. Radiol.* 42, 1183–1194. doi: 10.1007/s00247-012-2430-2

Benjamini, Y., and Hochberg, Y. (1995). Controlling the false discovery rate: a practical and powerful approach to multiple testing. *J. R. Stat. Soc. B* 57, 289–300. doi: 10.1111/j.2517-6161.1995.tb02031.x

Brigadoi, S., Aljabar, P., Kuklisova-Murgasova, M., Arridge, S. R., and Cooper, R. J. (2014). A 4D neonatal head model for diffuse optical imaging of pre-term to term infants. *Neuroimage* 100, 385–394. doi: 10.1016/j.neuroimage.2014.06.028

Brigadoi, S., and Cooper, R. J. (2015). How short is short? Optimum source–detector distance for short-separation channels in functional near-infrared spectroscopy. *Neurophotonics* 2:025005. doi: 10.1117/1.NPh.2.2.025005

Bulgarelli, C., Blasi, A., de Klerk, C. C., Richards, J. E., Hamilton, A., and Southgate, V. (2019). Fronto-temporoparietal connectivity and self-awareness in 18-month-olds: a resting state fNIRS study. *Dev. Cogn. Neurosci.* 38:100676. doi: 10.1016/j.dcn.2019.100676

Bulgarelli, C., de Klerk, C. C. J. M., Richards, J. E., Southgate, V., Hamilton, A., and Blasi, A. (2020). The developmental trajectory of fronto-temporoparietal connectivity as a proxy of the default mode network: a longitudinal fNIRS investigation. *Hum. Brain Mapp.* 1–24. doi: 10.1002/hbm.24974

Chiarelli, A. M., Maclin, E. L., Fabiani, M., and Gratton, G. (2015). A kurtosis-based wavelet algorithm for motion artifact correction of fNIRS data. *Neuroimage* 112, 128–137. doi: 10.1016/j.neuroimage.2015.02.057

Chitnis, D., Cooper, R. J., Dempsey, L., Powell, S., Quaggia, S., Highton, D., et al. (2016). Functional imaging of the human brain using a modular, fibre-less, high-density diffuse optical tomography system. *Biomed Opt. Express* 7, 4275–4288. doi: 10.1364/BOE.7.004275

Costeloe, K. L., Hennessy, E. M., Haider, S., Stacey, F., Marlow, N., and Draper, E. S. (2012). Short term outcomes after extreme preterm birth in England: comparison of two birth cohorts in 1995 and 2006 (the EPICure studies). *BMJ* 345:e7976. doi: 10.1136/bmj.e7976

Curzi-Dascalova, L., Figueroa, J. M., Eiselt, M., Christova, E., Virassamy, A., d'Allest, A. M., et al. (1993). Sleep state organization in premature infants of less than 35 weeks' gestational age. *Pediatr. Res.* 34, 624–628. doi: 10.1203/00006450-199311000-00013

Curzi-Dascalova, L., Peirano, P., and Morel-Kahn, F. (1988). Development of sleep states in normal premature and full-term newborns. *Dev. Psychobiol.* 21, 431–444. doi: 10.1002/dev.420210503

Damaraju, E., Caprihan, A., Lowe, J. R., Allen, E. A., Calhoun, V. D., and Phillips, J. P. (2014). Functional connectivity in the developing brain: a longitudinal study from 4 to 9 months of age. *Neuroimage* 84, 169–180. doi: 10.1016/j.neuroimage.2013.08.038

Delorme, A., and Makeig, S. (2004). EEGLAB: an open source toolbox for analysis of single-trial EEG dynamics including independent component analysis. *J. Neurosci. Methods* 134, 9–21. doi: 10.1016/j.jneumeth.2003.10.009

Denenberg, V. H., and Thoman, E. B. (1981). Evidence for a functional role for active (REM) sleep in infancy. *Sleep* 4, 185–191.

Dereymaeker, A., Pillay, K., Vervisch, J., De Vos, M., Van Huffel, S., Jansen, K., et al. (2017). Review of sleep-EEG in preterm and term neonates. *Early. Hum. Dev.* 113, 87–103. doi: 10.1016/j.earlhumdev.2017.07.003

Doria, V., Beckmann, C. F., Arichi, T., Merchant, N., Groppo, M., Turkheimer, F. E., et al. (2010). Emergence of resting state networks in the preterm human brain. *Proc. Natl. Acad. Sci. U.S.A.* 107, 20015–20020. doi: 10.1073/pnas.1007921107

Everdell, N., Gibson, A., Tullis, D., Vaithianathan, T., Hebden, J., and Delpy, D. (2005). A frequency multiplexed near-infrared topography system for imaging functional activation in the brain. *Rev. Sci. Instrum.* 76:093705. doi: 10.1063/1.2038567

Ferradal, S. L., Liao, S. M., Eggebrecht, A. T., Shimony, J. S., Inder, T. E., Culver, J. P., et al. (2016). Functional Imaging of the developing brain at the bedside using diffuse optical tomography. *Cereb. Cortex* 26, 1558–1568. doi: 10.1093/cercor/bhu320

Fransson, P., Skiöld, B., Horsch, S., Nordell, A., Blennow, M., Lagercrantz, H., et al. (2007). Resting-state networks in the infant brain. *Proc. Natl. Acad. Sci. U.S.A.* 104, 15531–15536. doi: 10.1073/pnas.0704380104

Fuchino, Y., Naoi, N., Shibata, M., Niwa, F., Kawai, M., Konishi, Y., et al. (2013). Effects of preterm birth on intrinsic fluctuations in neonatal cerebral activity examined using optical imaging. *PLoS One* 8:e67432. doi: 10.1371/journal.pone.0067432

Gao, W., Lin, W., Grewen, K., and Gilmore, J. H. (2016). Functional connectivity of the infant human brain: plastic and modifiable. *Neuroscientist* 23, 169–184. doi: 10.1177/1073858416635986

García-Pentón, L., Fernández, A. P., Iturria-Medina, Y., Gillon-Dowens, M., and Carreiras, M. (2014). Anatomical connectivity changes in the bilingual brain. *Neuroimage* 84, 495–504. doi: 10.1016/j.neuroimage.2013.08.064

Greicius, M. D., Kiviniemi, V., Tervonen, O., Vainionpää, V., Alahuhta, S., Reiss, A. L., et al. (2008). Persistent default-mode network connectivity during light sedation. *Hum. Brain Mapp.* 29, 839–847. doi: 10.1002/hbm.20537

Grigg-Damberger, M. M. (2016). The visual scoring of sleep in infants 0 to 2 months of age. *J. Clin. Sleep Med.* 12, 429–445. doi: 10.5664/jcsm.5600

Homae, F., Watanabe, H., Otobe, T., Nakano, T., Go, T., Konishi, Y., et al. (2010). Development of global cortical networks in early infancy. *J. Neurosci.* 30, 4877–4882. doi: 10.1523/JNEUROSCI.5618-09.2010

Horovitz, S. G., Braun, A. R., Carr, W. S., Picchioni, D., Balkin, T. J., Fukunaga, M., et al. (2009). Decoupling of the brain's default mode network during deep sleep. *Proc. Natl. Acad. Sci. U.S.A.* 106, 11376–11381. doi: 10.1073/pnas.0901435106

Horovitz, S. G., Fukunaga, M., de Zwart, J. A., van Gelderen, P., Fulton, S. C., Balkin, T. J., et al. (2008). Low frequency BOLD fluctuations during resting wakefulness and light sleep: a simultaneous EEG-fMRI study. *Hum. Brain Mapp.* 29, 671–682. doi: 10.1002/hbm.20428

Huppert, T. J., Diamond, S. G., Franceschini, M. A., and Boas, D. A. (2009). HomER: a review of time-series analysis methods for near-infrared spectroscopy of the brain. *Appl. Opt.* 48, D280–D298. doi: 10.1364/AO.48.00D280

Hutchison, R. M., Womelsdorf, T., Allen, E. A., Bandettini, P. A., Calhoun, V. D., Corbetta, M., et al. (2013). Dynamic functional connectivity: promise, issues, and interpretations. *Neuroimage* 80, 360–378. doi: 10.1016/j.neuroimage.2013.05.079

Koolen, N., Oberdorfer, L., Rona, Z., Giordano, V., Werther, T., Klebermass-Schrehof, K., et al. (2017). Automated classification of neonatal sleep states using EEG. *Clin. Neurophysiol.* 128, 1100–1108. doi: 10.1016/j.clinph.2017.02.025

Larson-Prior, L. J., Zempel, J. M., Nolan, T. S., Prior, F. W., Snyder, A. Z., and Raichle, M. E. (2009). Cortical network functional connectivity in the descent to sleep. *Proc. Natl. Acad. Sci. U.S.A.* 106, 4489–4494. doi: 10.1073/pnas.0900924106

Leonardi, N., and Van De Ville, D. (2015). On spurious and real fluctuations of dynamic functional connectivity during rest. *Neuroimage* 104, 430–436. doi: 10.1016/j.neuroimage.2014.09.00

Martuzzi, R., Ramani, R., Qiu, M., Rajeevan, N., and Constable, R. T. (2010). Functional connectivity and alterations in baseline brain state in humans. *Neuroimage* 49, 823–834. doi: 10.1016/j.neuroimage.2009.07.028

Mesquita, R. C., Franceschini, M. A., and Boas, D. A. (2010). Resting state functional connectivity of the whole head with near-infrared spectroscopy. *Biomed Opt. Express* 1, 324–336. doi: 10.1364/BOE.1.000324

Mirmiran, M. (1995). The function of fetal/neonatal rapid eye movement sleep. *Behav. Brain Res.* 69, 13–22. doi: 10.1016/0166-4328(95)00019-p

Mirmiran, M., Maas, Y. G., and Ariagno, R. L. (2003). Development of fetal and neonatal sleep and circadian rhythms. *Sleep Med. Rev.* 7, 321–334. doi: 10.1053/smrv.2002.0243

Mirmiran, M., Scholtens, J., van de Poll, N. E., Uylings, H. B., van der Gugten, J., and Boer, G. J. (1983). Effects of experimental suppression of active (REM) sleep during early development upon adult brain and behavior in the rat. *Brain Res.* 283, 277–286. doi: 10.1016/0165-3806(83)90184-0

Morrison, J. L., Carmichael, L., Homan, J., White, S., and Richardson, B. S. (2005). Cerebral blood flow during spontaneous and cholinergically induced behavioral states in the sheep fetus. *Pediatr. Res.* 57, 667–673. doi: 10.1203/01.PDR.0000156210.27381.12

Morrissey, M. J., Duntley, S. P., Anch, A. M., and Nonneman, R. (2004). Active sleep and its role in the prevention of apoptosis in the developing brain. *Med. Hypotheses* 62, 876–879. doi: 10.1016/j.mehy.2004.01.014

Mulder, E. J., Visser, G. H., Bekedam, D. J., and Prechtl, H. F. (1987). Emergence of behavioural states in fetuses of type-1-diabetic women. *Early. Hum. Dev* 15, 231–251. doi: 10.1016/0378-3782(87)90082-x

Naoi, N., Fuchino, Y., Shibata, M., Niwa, F., Kawai, M., Konishi, Y., et al. (2013). Decreased right temporal activation and increased interhemispheric connectivity in response to speech in preterm infants at term-equivalent age. *Front. Psychol,* 4:94. doi: 10.3389/fpsyg.2013.00094

Oostenveld, R., and Praamstra, P. (2001). The five percent electrode system for high-resolution EEG and ERP measurements. *Clin. Neurophysiol.* 112, 713–719. doi: 10.1016/S1388-2457(00)00527-7

Ouyang, M., Kang, H., Detre, J. A., Roberts, T. P., and Huang, H. (2017). Short-range connections in the developmental connectome during typical and atypical brain maturation. *Neurosci. Biobehav. Rev.* 83, 109–122. doi: 10.1016/j.neubiorev.2017.10.007

Paul, K., Krajca, V., Roth, Z., Melichar, J., and Petranek, S. (2003). Comparison of quantitative EEG characteristics of quiet and active sleep in newborns. *Sleep Med.* 4, 543–552. doi: 10.1016/j.sleep.2003.08.008

Pfeifer, M. D., Scholkmann, F., and Labruyère, R. (2018). Signal processing in functional near-infrared spectroscopy (fNIRS): methodological differences lead to different statistical results. *Front. Hum. Neurosci.* 11:641. doi: 10.3389/fnhum.2017.00641

Pillay, K., Dereymaeker, A., Jansen, K., Naulaers, G., Van Huffel, S., and De Vos, M. (2018). Automated EEG sleep staging in the term-age baby using a generative modelling approach. *J. Neural Eng.* 15:036004. doi: 10.1088/1741-2552/aaab73

Piryatinska, A., Terdik, G., Woyczynski, W. A., Loparo, K. A., Scher, M. S., and Zlotnik, A. (2009). Automated detection of neonate EEG sleep stages. *Comput. Methods Programs* 95, 31–46. doi: 10.1016/j.cmpb.2009.01.006

Roffwarg, H. P., Muzio, J. N., and Dement, W. C. (1966). Ontogenetic development of the human sleep-dream cycle. *Science* 152, 604–619. doi: 10.1126/science.152.3722.604

Sämann, P. G., Wehrle, R., Hoehn, D., Spoormaker, V. I., Peters, H., Tully, C., et al. (2011). Development of the brain's default mode network from wakefulness to slow wave sleep. *Cereb. Cortex* 21, 2082–2093. doi: 10.1093/cercor/bhq295

Santosa, H., Aarabi, A., Perlman, S. B., and Huppert, T. J. (2017). Characterization and correction of the false-discovery rates in resting state connectivity using functional near-infrared spectroscopy. *J. Biomed. Opt.* 22:55002. doi: 10.1117/1.JBO.22.5.055002

Scher, M. S. (2008). Ontogeny of EEG-sleep from neonatal through infancy periods. *Sleep Med.* 9, 615–636. doi: 10.1016/B978-0-444-52006-7.00008-3

Scher, M. S., Steppe, D. A., Beggarly, M. E., Salerno, D. G., and Banks, D. L. (2002). Neonatal EEG- sleep disruption mimicking hypoxic-ischemic encephalopathy after intrapartum asphyxia. *Sleep Med.* 3, 411–415. doi: 10.1016/S1389-9457(02)00071-0

Scher, M. S., Steppe, D. A., Dahl, R. E., Asthana, S., and Guthrie, R. D. (1992). Comparison of EEG sleep measures in healthy full-term and preterm infants at matched conceptional ages. *Sleep* 15, 442–448. doi: 10.1093/sleep/15.5.442

Scholkmann, F., and Wolf, M. (2013). General equation for the differential pathlength factor of the frontal human head depending on wavelength and age. *J. Biomed. Opt.* 18:105004. doi: 10.1117/1.JBO.18.10.105004

Schweiger, M., and Arridge, S. R. (2014). The Toast++ software suite for forward and inverse modeling in optical tomography. *J. Biomed. Opt.* 19:040801. doi: 10.1117/1.JBO.19.4.040801

Silvani, A., Asti, V., Berteotti, C., Ferrari, V., Franzini, C., Lenzi, P., et al. (2006). Sleep-dependent changes in cerebral oxygen consumption in newborn lambs. *J. Sleep Res.* 15, 206–211. doi: 10.1111/j.1365-2869.2006.00521.x

Smith, G. C., Gutovich, J., Smyser, C., Pineda, R., Newnham, C., Tjoeng, T. H., et al. (2011). Neonatal intensive care unit stress is associated with brain development in preterm infants. *Ann. Neurol.* 70, 541–549. doi: 10.1002/ana.22545

Smyser, C. D., Inder, T. E., Shimony, J. S., Hill, J. E., Degnan, A. J., Snyder, A. Z., et al. (2010). Longitudinal analysis of neural network development in preterm infants. *Cereb. Cortex* 20, 2852–2862. doi: 10.1093/cercor/bhq035

Smyser, C. D., Snyder, A. Z., Shimony, J. S., Blazey, T. M., Inder, T. E., and Neil, J. J. (2013). Effects of white matter injury on resting state fMRI measures in prematurely born infants. *PLoS One* 8:e68098. doi: 10.1371/journal.pone.0068098

Smyser, C. D., Snyder, A. Z., Shimony, J. S., Mitra, A., Inder, T. E., and Neil, J. J. (2016). Resting-state network complexity and magnitude are reduced in prematurely born infants. *Cereb. Cortex* 26, 322–333. doi: 10.1093/cercor/bhu251

Spoormaker, V. I., Schroter, M. S., Gleiser, P. M., Andrade, K. C., Dresler, M., Wehrle, R., et al. (2010). Development of a large-scale functional brain network during human non-rapid eye movement sleep. *J. Neurosci.* 30, 11379–11387. doi: 10.1523/JNEUROSCI.2015-10.2010

Tachtsidis, I., and Scholkmann, F. (2016). False positives and false negatives in functional near-infrared spectroscopy: issues, challenges, and the way forward. *Neurophotonics* 3:031405. doi: 10.1117/1.NPh.3.3.031405

Tokariev, A., Videman, M., Palva, J. M., and Vanhatalo, S. (2016). Functional brain connectivity develops rapidly around term age and changes between vigilance states in the human newborn. *Cereb. Cortex* 26, 4540–4550. doi: 10.1093/cercor/bhv219

Visser, G. H., Poelmann-Weesjes, G., Cohen, T. M., and Bekedam, D. J. (1987). Fetal behavior at 30 to 32 weeks of gestation. *Pediatr. Res.* 22, 655–658. doi: 10.1203/00006450-198712000-00009

Walls-Esquivel, E., Vecchierini, M. F., Heberle, C., and Wallois, F. (2007). Electroencephalography (EEG) recording techniques and artefact detection in early premature babies. *Neurophysiol. Clin.* 37, 299–309. doi: 10.1016/j.neucli.2007.09.001

Wang, J., Dong, Q., and Niu, H. (2017). The minimum resting-state fNIRS imaging duration for accurate and stable mapping of brain connectivity network in children. *Sci. Rep.* 7:6461. doi: 10.1038/s41598-017-06340-7

Watanabe, T., Kan, S., Koike, T., Misaki, M., Konishi, S., Miyauchi, S., et al. (2014). Network-dependent modulation of brain activity during sleep. *Neuroimage* 98, 1–10. doi: 10.1016/j.neuroimage.2014.04.079

White, B. R., Liao, S. M., Ferradal, S. L., Inder, T. E., and Culver, J. P. (2012). Bedside optical imaging of occipital resting-state functional connectivity in neonates. *Neuroimage* 59, 2529–2538. doi: 10.1016/j.neuroimage.2011.08.094

White, B. R., Snyder, A. Z., Cohen, A. L., Petersen, S. E., Raichle, M. E., Schlaggar, B. L., et al. (2009). Resting-state functional connectivity in the human brain revealed with diffuse optical tomography. *Neuroimage* 47, 148–156. doi: 10.1016/j.neuroimage.2009.03.058

Zalesky, A., Cocchi, L., Fornito, A., Murray, M. M., and Bullmore, E. D. (2012). Connectivity differences in brain networks. *Neuroimage* 60, 1055–1062. doi: 10.1016/j.neuroimage.2012.01.068

Zalesky, A., Fornito, A., and Bullmore, E. T. (2010). Network-based statistic: identifying differences in brain networks. *Neuroimage* 53, 1197–1207. doi: 10.1016/j.neuroimage.2010.06.041

Conflict of Interest: RC has a financial interest in the UCL spin-out company Gowerlabs Ltd., which is a manufacturer of fNIRS technologies.

The remaining authors declare that the research was conducted in the absence of any commercial or financial relationships that could be construed as a potential conflict of interest.

Copyright © 2020 Lee, Blanco, Dempsey, Chalia, Hebden, Caballero-Gaudes, Austin and Cooper. This is an open-access article distributed under the terms of the Creative Commons Attribution License (CC BY). The use, distribution or reproduction in other forums is permitted, provided the original author(s) and the copyright owner(s) are credited and that the original publication in this journal is cited, in accordance with accepted academic practice. No use, distribution or reproduction is permitted which does not comply with these terms.

frontiers in Human Neuroscience

ORIGINAL RESEARCH
published: 21 April 2020
doi: 10.3389/fnhum.2020.00125

Cerebral Hemodynamic Responses to the Sensory Conflict Between Visual and Rotary Vestibular Stimuli: An Analysis With a Multichannel Near-Infrared Spectroscopy (NIRS) System

Nghia Trong Nguyen[1], Hiromasa Takakura[1], Hisao Nishijo[2], Naoko Ueda[1], Shinsuke Ito[1], Michiro Fujisaka[1], Katsuichi Akaogi[3] and Hideo Shojaku[1]*

[1]Department of Otorhinolaryngology, Head and Neck Surgery, Graduate School of Medicine and Pharmaceutical Sciences, University of Toyama, Toyama, Japan, [2]System Emotional Science Laboratory, Graduate School of Medicine and Pharmaceutical Sciences, University of Toyama, Toyama, Japan, [3]Department of Otorhinolaryngology, Toyama Red Cross Hospital, Toyama, Japan

OPEN ACCESS

Edited by:
Meryem Ayse Yücel, Boston University, United States

Reviewed by:
Chia-Cheng Lin, East Carolina University, United States
Jack Adam Noah, Yale University, United States
Yong Gu, Shanghai Institutes for Biological Sciences (CAS), China
Rainer Boegle, German Center for Vertigo and Balance Disorders (DSGZ), LMU Munich, Germany

***Correspondence:**
Hiromasa Takakura
hiromasa@med.u-toyama.ac.jp

Specialty section:
This article was submitted to Brain Imaging and Stimulation, a section of the journal Frontiers in Human Neuroscience

Received: *09 November 2019*
Accepted: *19 March 2020*
Published: *21 April 2020*

Citation:
Nguyen NT, Takakura H, Nishijo H, Ueda N, Ito S, Fujisaka M, Akaogi K and Shojaku H (2020) Cerebral Hemodynamic Responses to the Sensory Conflict Between Visual and Rotary Vestibular Stimuli: An Analysis With a Multichannel Near-Infrared Spectroscopy (NIRS) System. Front. Hum. Neurosci. 14:125. doi: 10.3389/fnhum.2020.00125

Sensory conflict among visual, vestibular, and somatosensory information induces vertiginous sensation and postural instability. To elucidate the cognitive mechanisms of the integration between the visual and vestibular cues in humans, we analyzed the cortical hemodynamic responses during sensory conflict between visual and horizontal rotatory vestibular stimulation using a multichannel near-infrared spectroscopy (NIRS) system. The subjects sat on a rotatory chair that was accelerated at 3°/s^2 for 20 s to the right or left, kept rotating at 60°/s for 80 s, and then decelerated at 3°/s^2 for 20 s. The subjects were instructed to watch white stripes projected on a screen surrounding the chair during the acceleration and deceleration periods. The white stripes moved in two ways; in the "congruent" condition, the stripes moved in the opposite direction of chair rotation at 3°/s^2 (i.e., natural visual stimulation), whereas in the "incongruent" condition, the stripes moved in the same direction of chair rotation at 3°/s^2 (i.e., conflicted visual stimulation). The cortical hemodynamic activity was recorded from the bilateral temporoparietal regions. Statistical analyses using NIRS-SPM software indicated that hemodynamic activity increased in the bilateral temporoparietal junctions (TPJs) and human MT+ complex, including the medial temporal (MT) area and medial superior temporal (MST) area in the incongruent condition. Furthermore, the subjective strength of the vertiginous sensation was negatively correlated with hemodynamic activity in the dorsal part of the supramarginal gyrus (SMG) in and around the intraparietal sulcus (IPS). These results suggest that sensory conflict between the visual and vestibular stimuli promotes cortical cognitive processes in the cortical network consisting of the TPJ, the medial temporal gyrus (MTG), and IPS, which might contribute to self-motion perception to maintain a sense of balance or equilibrioception during sensory conflict.

Keywords: NIRS, sensory conflict, vestibular cortices, temporoparietal junctions, medial superior temporal area, intraparietal sulcus

INTRODUCTION

Stability of self-motion perception is obtained through a composite of multimodal sensory inputs such as visual and nonvisual (e.g., vestibular and proprioceptive) information (Butler et al., 2010; Fetsch et al., 2010). Sensory mismatch (sensory conflict) among different sensory information during body motion induces vertigo and instability of posture (Brandt, 1999) as well as motion sickness and an undesirable illusion of body movements (Brandt, 1999; Keshavarz et al., 2015).

In mammalian species, the vestibular system in the inner ear has two sets of receptors, the semicircular canals and the otoliths (the utricle and saccule), which together sense angular and linear acceleration of the head, respectively, in three dimensions (Smith, 2017). This sensory system is critical to orientation and locomotion: the vestibular system is essential to maintain stable vision during unintentional head movements by generating rapid compensatory eye movements [i.e., the vestibulo-ocular reflexes (VORs)] that maintain stable visual images of the world in the retina (Smith, 2017). Acute elimination of unilateral vestibular inputs due to vestibular neuritis induces sudden ataxia and disturbance of postural stability (Horak, 2009; Peterka et al., 2011). It is suggested that sensory conflict is induced by differences between visual and vestibular information, where each information signal represents different spatial representations of the body and head based on stored experiences (Reason, 1978; Oman, 1982). Thus, coherent integration of multisensory inputs, especially visual and vestibular cues, is essential for appropriate self-motion perception.

Monkey neurophysiological studies reported visual and vestibular integration in several cortical regions including: (1) the dorsal medial superior temporal (MST) area that processes optic flow to induce motion and self-motion perception (Duffy, 1998; Gu et al., 2008); (2) the ventral intraparietal (VIP) area, in which neurons respond to visual and vestibular inputs and are sensitive to visual heading (Chen et al., 2011); and (3) the visual posterior Sylvian (VPS) area located at the posterior edge of the Sylvian fissure, in which neurons responded dominantly to vestibular inputs (Chen et al., 2011). Multisensory information including visual, vestibular, and proprioceptive signals also converges on the parieto-insular vestibular cortex (PIVC), which is essential for vestibular information processing (Guldin et al., 1992; Lewis and Van Essen, 2000).

Human functional magnetic resonance imaging (fMRI) studies using galvanic or caloric stimulation (Bucher et al., 1998; Fasold et al., 2002) reported that vestibular stimuli activated the regions involved in information processing of optic flow including the MST and VIP, suggesting that visual and vestibular information are converged and integrated in these cortical areas. Furthermore, various vestibular stimulations (e.g., caloric and galvanic stimulations as well as those to elicit vestibular evoked myogenic potentials) activated the posterior and anterior insula, temporoparietal junction (TPJ), posterior parietal cortex (PPC), somatosensory cortex, and other brain regions (Lopez and Blanke, 2011). The TPJ, which is a wide cortical region including the posterior superior temporal gyrus (pSTG), angular gyrus (AG), supramarginal gyrus (SMG), and the parietal operculum, receives multimodal information including vestibular as well as somatosensory and visual inputs (zu Eulenburg et al., 2012; Bzdok et al., 2013). The TPJ has been implicated in multimodal integration such as visual–vestibular interactions (Pfeiffer et al., 2014). Thus, the MST, the TPJ, and the PPC including the VIP might be crucial for the integration of visual and vestibular information in humans. However, it is unclear how these regions work during sensory conflict between visual and vestibular inputs in humans.

fMRI, positron emission tomography (PET), and magnetoencephalography (MEG) have often been used to investigate various human cognitive brain functions. However, these imaging techniques have a fundamental problem when applied to research on visual and vestibular integration: natural vestibular stimulation is usually induced by rotatory or linear acceleration movements of the subject's head, whereas fMRI, PET, and MEG require movements of the subject's head to be restricted (see below).

Recent studies using fMRI explored human brain activations when visual and vestibular cues were either complementary or in conflict (Roberts et al., 2017; Schindler and Bartels, 2018). Roberts et al. (2017) used horizontal optokinetic (visual) stimulation of black and white stripes and caloric (vestibular) stimulation; however, vestibular stimulation was artificial and without head movements because of the high restrictiveness of fMRI for head rotation. Schindler and Bartels (2018) used a special aircushion placed inside a head coil for fMRI, and subjects voluntarily rotated their heads from center to either approximately +30° or approximately −30° as vestibular stimulation. In this case, the vestibular stimulation was not artificial; however, the speed and angle of the rotation were not constant and were uncontrolled. Thus, fMRI is not suitable for experiments on vestibular stimulation because of the restricted movement of the head required during examination.

To circumvent these limitations, functional near-infrared spectroscopy (fNIRS) was used to investigate cortical hemodynamic responses during sensory conflict between visual and horizontal rotatory (vestibular) stimulations. fNIRS is a functional neuroimaging technique to detect task-related cortical activation by measuring oxygenated hemoglobin (Oxy-Hb) and deoxygenated hemoglobin (Deoxy-Hb) in the brain (Jöbsis, 1977; Colacino et al., 1981). The fNIRS system is more compact and robust against a subject's motion compared with fMRI, PET, and MEG and consequently is more suitable for analysis of task-related cortical activity during motion (Mihara et al., 2008; Takakura et al., 2015). fNIRS has been used to study visual and vestibular integration in previous studies. Some researchers investigated hemodynamic activity during the control of postural balance in computed dynamic posturography (CDP), which can create a sensory conflict situation among the visual, vestibular, and somatosensory inputs artificially, using a multichannel Near-Infrared Spectroscopy (NIRS) system (Karim et al., 2013; Takakura et al., 2015; Lin et al., 2017). These studies suggested that the TPJ including the SMG and superior temporal gyrus (STG), premotor cortex,

and supplementary motor area might be involved in visual and vestibular integration and postural control during CDP. However, these studies mainly applied linear acceleration (i.e., otolith stimulation) as the vestibular stimulation, whereas natural rotatory acceleration (i.e., semicircular canal stimulation) has not been used to investigate visual vestibular integration in previous human studies. We herein investigated cortical hemodynamic activities during sensory (vestibular and visual) integration in congruent and incongruent spinning paradigms using a rotatory chair and portable NIRS systems.

We hypothesized that vestibular and visual stimuli with sensory conflict would activate the cortical regions in and around the TPJ including the bilateral upper parts of the temporal lobe, the parietal lobe, and posterior parts of the frontal lobe. In the present study, to investigate cortical activity elicited by sensory conflict between rotatory vestibular stimuli (rotation of the body) and rotatory visual stimuli (moving white stripes on a screen surrounding a subject), we analyzed hemodynamic activity in and around the TPJ in the congruent condition without sensory conflict, in which visual stripes moved opposite the rotatory direction of the body, and the incongruent condition with sensory conflict, in which visual stripes moved in the same rotatory direction of the body.

MATERIALS AND METHODS

Subjects

Fourteen healthy men [aged 25.8 ± 8.2 (mean ± SD) years, all right-handed] participated in this study. None of the subjects had a medical history of ear diseases, vertigo, or head injury. They were treated in accordance with the Declaration of Helsinki and the U.S. Code of Federal Regulations for the protection of human subjects. Written consent was obtained from each subject, and the experiments were conducted according to a protocol approved by the ethical committee for human experiments of the University of Toyama.

In the present study, subjects sat on a chair that rotated to the left or right, and moving white stripes were projected on a screen in front of them. Portable NIRS systems were set on the backrest of the chair to record cortical hemodynamics. Head angular velocity and its acceleration/deceleration as vestibular stimulation were controlled by rotating the chair, whereas the stripes moved in two different conditions. In the congruent condition, the stripes moved in the opposite direction of chair rotation (natural visual stimulation), whereas in the incongruent condition, the stripes moved in the same direction of chair rotation (conflicted visual stimulation).

Setup and Tasks

In the present experiment, a visual–vestibular stimulator (OKN/VOR stimulator®; First Medicals Co. Ltd., Tokyo, Japan) consisting of a rotatory chair, cylindrical screen (diameter: 150 cm), and projector was used (**Figure 1A**). The axis of rotation of the rotatory chair was matched to the center of the cylindrical screen. Black (visual angle: 27.5°) and white (visual angle: 2.5°) stripes were projected on the screen. The stimulator could set and

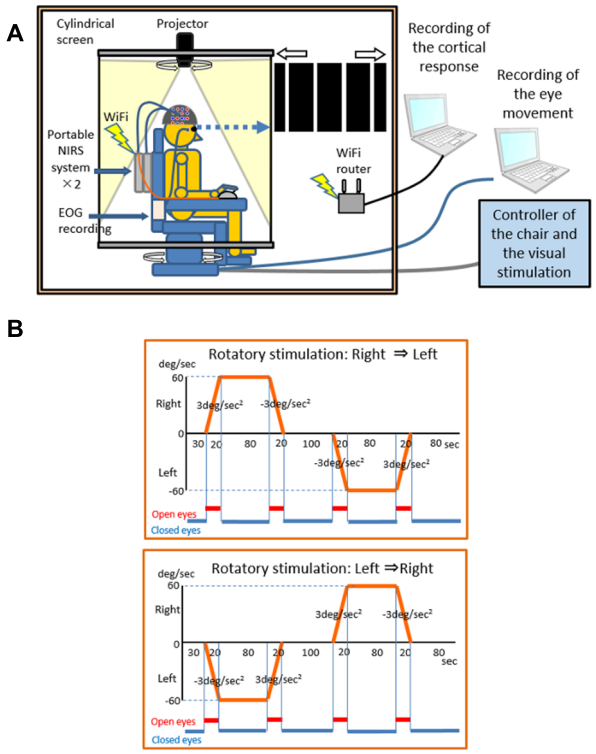

FIGURE 1 | An illustration of the laboratory instruments used in the experiment. The experimental system consists of two portable NIRS systems, an EOG recording unit, a rotary chair for rotary stimulation, a cylindrical screen, and a projector for OKN stimulation **(A)** and the rotatory stimulation protocol **(B)**.

control the angular velocity, acceleration, and deceleration of the rotatory chair and specify the direction of horizontal movements of the stripes, which was identical or opposite that of the rotatory chair, at the same speed. Each subject sat on the rotatory chair and kept his eyes closed except when he was requested to open his eyes. The timing of opening and closing of eyes was instructed by sounds, and thus, we could not use noise-cancelling earphones or earplugs. Thirty seconds after the onset of the task, the rotatory chair was accelerated to rotate to the left or right side at 3°/s^2 for 20 s and then rotated at a constant angular velocity (60°/s) for 80 s. After the constant rotation, the rotatory chair decelerated at 3°/s for 20 s and stopped for 100 s. Then, the rotatory chair was accelerated to the opposite side at 3°/s for 20 s, rotated in a constant angular velocity (60°/s) for 80 s, decelerated at 3°/s^2 for 20 s, and stopped for 80 s. Each subject was requested to open his eyes during acceleration or deceleration periods for 20 s to watch the movement of the strips (i.e., visual stimulations) projected on the cylindered screen. There were two kinds of the rotatory stimulations [a "right to-left" task (right rotation followed by left rotation) and a "left-to-right" task (left rotation followed by right rotation; **Figure 1B**)]. Each task included four acceleration/deceleration phases consisting of one acceleration phase to the right, one deceleration phase to the right, one acceleration phase to the left, and one deceleration phase to the left.

Two kinds of visual stimulation were applied. In the "congruent" visual stimulation, the stripes were accelerated or decelerated in the opposite rotatory direction of the rotatory chair at 3°/s^2 relative to the subject's head. In the "incongruent" visual stimulation, the stripes were accelerated or decelerated in the same rotatory direction of the rotatory chair at 3°/s^2 relative to the subject's head. We analyzed hemodynamic responses in the acceleration phases. Thus, there were four experimental conditions based on a combination of acceleration direction of the rotatory chair and visual stimulation: condition 1 (acceleration to the right and congruent visual stimulation), Condition 2 (acceleration to the left and congruent visual stimulation), Condition 3 (acceleration to the right and incongruent visual stimulation), and Condition 4 (acceleration to the left and incongruent visual stimulation). Each rotation task (i.e., "right-to-left" or "left-to-right" task in **Figure 1B**) was pseudo-randomly repeated four times in the congruent and incongruent visual stimulations, resulting in a total of four trials for each condition.

Self-assessment of the strength of an uncomfortable vertiginous sensation during the acceleration phase was performed after each rotation task using a visual analog scale (VAS), and mean VAS scores in the congruent and incongruent visual stimulations were calculated for each subject.

fNIRS Recording

Two portable continuous-wave (CW) fNIRS imaging systems (LIGHTNIRS®; Shimadzu Co., Ltd., Kyoto, Japan) were attached firmly on the backside of the backrest of the rotatory chair and used to measure cerebral hemodynamics (**Figure 1A**). LIGHTNIRS® has eight light sources and eight light detectors in one system. This commercial portable fNIRS system allows the use of two LIGHTNIRS® systems as one synchronized CW fNIRS system with 16 light sources and 16 light detectors by connecting the two systems with a SYNC cable. The lights at three different wavelengths (780, 805, and 830 nm) with a pulse width of 5 ms were emitted from the light-source optodes, and the lights were detected by the light-detector optodes. Signals from the light-detector optodes were processed based on a modified Lambert–Beer law to measure changes in Hb concentration [Oxy-Hb, Deoxy-Hb, and Total-Hb (Oxy Hb + Deoxy Hb)] (Seiyama et al., 1988; Wray et al., 1988).

After the subject sat on the chair, his body was tightly fixed in the chair to prevent falling during rotation of the chair, and he was fitted with a head cap for NIRS recording (FLASH-PLUS; Shimadzu Company Limited). The vertex position of the head cap was positioned at the vertex (Cz) in the 10–20 EEG system, and the 16 light-source optodes and 16 light-detector optodes were placed on the head cap, which has NIRS probe holders (**Figure 2A**), and the optodes were positioned crosswise from each other.

A 4 × 4 square arrangement of probe holders was used and set on the bilateral temporoparietal areas of the head as follows: a horizontal line connecting the probes and channels in the most upper part of the square holder was set 6 cm lateral from the sagittal midline of the head connecting the nasion, Cz, and inion, whereas the line running vertically through the center of the square holder was set to align with the coronal midline of the head connecting the right and left preauricular positions (AR and AL, respectively) and Cz in each hemisphere (**Figure 2A**).

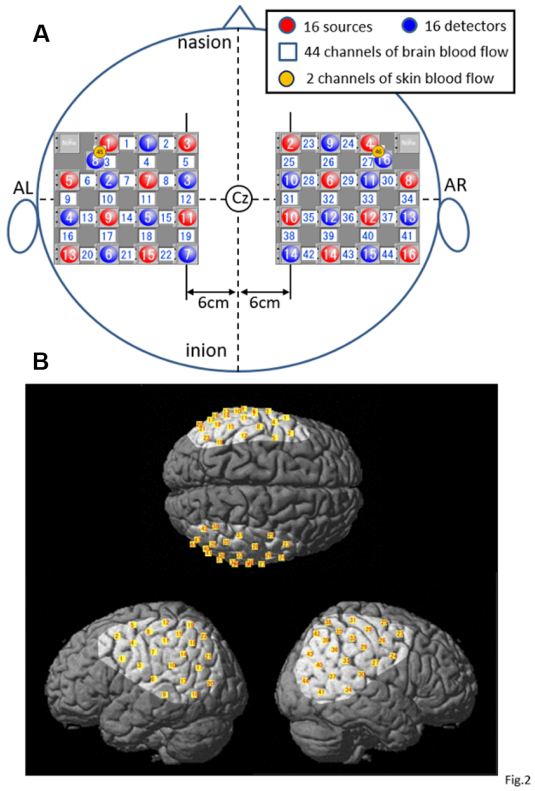

FIGURE 2 | Location of the NIRS optodes. **(A)** The arrangement of the optodes (sources and detectors) and recording channels. AL, left preauricular position; AR, right preauricular position; Cz, vertex in 10–20 EEG recording methods. **(B)** Highlighted areas indicate the recorded cortical regions covered with the optodes in the present study. Yellow small squares indicate the averaged coordinates of the NIRS channels among all subjects.

In the present study, the 15 detector optodes were placed 3 cm away from the 15 source optodes. The midpoints between the source and detector optodes were called "NIRS channels," which resulted in 44 channels in total. NIRS signals from the light-detector optodes are supposed to reflect hemodynamic activity under these channels. However, these NIRS signals (whole signals) include not only intracerebral (cerebral cortex) but also extracerebral (scalp, skull, and cerebrospinal fluid) components of hemodynamic activity (Niederer et al., 2008; Ishikuro et al., 2014). Therefore, another two detector optodes were placed 1.5 cm away from the source optodes to record the extracerebral signals (Niederer et al., 2008; Ishikuro et al., 2014), resulting in two channels and corresponding signals (**Figure 2A**). The probe holes at the anterior–inferior corner of the bilateral 4 × 4 probe holders were not used in both hemispheres. Three-dimensional coordinates of the optodes were measured by a 3-D digitizer (Nirtrack, Shimadzu Co., Limited; Takakura et al., 2011; Ishikuro et al., 2014; Nakamichi et al., 2018).

To determine the anatomical locations of the NIRS channels, we used the "spatial registration of NIRS channel

locations" function of the NIRS-SPM (statistical parametric mapping) Version 4_r1 software, which is an SPM5- or SPM8- and MATLAB-based software package for the statistical analysis of NIRS signals (Ye et al., 2009; downloadable from https://bispl.weebly.com/nirs-spm.html). Using the "stand-alone" option (without using MRI images), we estimated the locations of the NIRS channels on the normalized brain surface (Friston et al., 1995; Ashburner et al., 1997; Ashburner and Friston, 1999) using a Montreal Neurological Institute (MNI) brain template, which corresponds to the space identified by Talairach and Tournoux (1988). In each subject, the estimated locations of the NIRS channels were labeled using the 3-D digital brain atlas (Talairach daemon; Lancaster et al., 2000), which is incorporated into the NIRS-SPM. The averaged locations of the NIRS channels (yellow small squares) and covered cortical areas (highlighted on the standard brain) across all subjects are indicated on the standard brain in **Figure 2B**. The recording cortical areas included the bilateral ventral part of the supraparietal lobule (vSPL), infraparietal sulcus (IPS), SMG, AG, pSTG, parietal operculum (p-OP), frontal operculum (f-Op), ventral part of the precentral and postcentral gyrus (PrG and PoG), posterior middle temporal gyrus (pMTG), and ventral third visual association area (V3; **Figure 2B**).

Data Analysis

Analysis of Subjective Vertiginous Sensation

Shapiro–Wilk tests, initially performed to check normality of the distribution of the VAS scores in the congruent and incongruent visual stimulations, indicated normal distribution in the congruent visual stimulation ($p = 0.058$) and non-normal distribution in the incongruent visual stimulation ($p = 0.023$). Therefore, we applied nonparametric statistical analyses to the mean VAS scores: the Wilcoxon sign rank test was performed to compare the mean VAS scores between the congruent and incongruent visual stimulations. We also analyzed the correlation between the VAS scores and hemodynamic activity in the congruent and incongruent visual stimulations using Spearman's rank coefficient test.

Analysis of Hemodynamic Responses

The NIRS data consisted of four trials for each condition because each rotation task (i.e., "right-to-left" or "left-to-right" task in **Figure 1B**) was pseudo-randomly repeated four times in the congruent and incongruent visual stimulations. We analyzed increases in Oxy-Hb concentration and decreases in Deoxy-Hb concentrations as increases in neural activity because typical hemodynamic responses to neural activation consist of an increase in Oxy-Hb (Hoshi et al., 2001; Strangman et al., 2002; Yamamoto and Kato, 2002) and a decrease in Deoxy-Hb (Zhang et al., 2016, 2017) and amplitudes of Oxy-Hb signals are larger than those of Deoxy-Hb signals (Sato et al., 2016).

We analyzed only the data obtained during the acceleration periods (i.e., Conditions 1–4) and not that obtained during the deceleration periods, because our preliminary study indicated no significant hemodynamic responses during the deceleration periods. First, we computed the cerebral component of the NIRS signals by a simple-subtraction method (Schytz et al., 2009; Nakamichi et al., 2018), where the cerebral hemodynamic activity = (whole signals) minus (the extracerebral signals) located nearest to given whole signals. A band-pass filter (0.01–0.1 Hz) was used to eliminate long-term baseline drift and higher-frequency cardiac or respiratory activity from the cerebral component of the NIRS signals (Cordes et al., 2001; Lu et al., 2010). Second, to analyze the temporal changes of hemodynamics, the NIRS data for Oxy-Hb and Deoxy-Hb concentrations were summed and averaged for the onset of 20 s of acceleration in all conditions. The averaged responses were corrected for baseline activity from −10 to 0 s.

We also performed group analyses of the NIRS data based on the general linear model (GLM) using NIRS-SPM software[1] (Ye et al., 2009). After the subtraction and filtering (see above), we initially extracted two long data measurements, one each during the congruent and incongruent visual simulations, in each subject. The long data measurement in the congruent stimulation included the data in Condition 1 (acceleration to the right and congruent visual stimulation), Condition 2 (acceleration to the left and congruent visual stimulation), Deceleration Condition 1 (deceleration to the right and congruent visual stimulation), and Deceleration Condition 2 (deceleration to the left and congruent visual stimulation), whereas that in the incongruent stimulation included the data in Condition 3 (acceleration to the right and incongruent visual stimulation), Condition 4 (acceleration to the left and incongruent visual stimulation), Deceleration Condition 3 (deceleration to the right and incongruent visual stimulation), and Deceleration Condition 4 (deceleration to the left and incongruent visual stimulation). NIRS data in the congruent and incongruent stimulations were separately analyzed in each subject using GLM NIRS-SPM software for each acceleration condition (i.e., Conditions 1 and 2 in congruent visual stimulation and Conditions 3 and 4 in incongruent visual stimulation). In the GLM analyses, the rotatory acceleration periods with optokinetic visual stimulation were defined as the task periods, whereas the periods with no vestibular and no visual stimulation (periods with rotation at constant angular velocity with eyes closed and periods with no rotation and eyes closed) were defined as the baseline periods. Then, group statistical analyses were performed in each condition using the NIRS-SPM. The resultant T-statistic maps were superimposed on the standardized MNI brain in each condition. The statistical significance level was set at $p < 0.05$ as corrected by the false discovery rate (FDR; Benjamini and Hochberg, 1995).

Correlation Analysis Between Hemodynamic Cortical Activity and Subjective Vertiginous Sensation

We analyzed the correlation between hemodynamic activity and the strength of subjective vertiginous sensation (VAS scores) in each condition. Mean VAS scores in the congruent visual condition were used for the correlation analyses in Conditions 1 and 2, and those in the incongruent visual condition were used in the analyses in Conditions 3 and 4. Spearman's rank coefficient test between T-values and mean VAS scores was performed for

[1] https://bispl.weebly.com/nirs-spm.html

all MNI coordinates in each condition, and then p-value maps were superimposed on the standardized brain (MNI coordinate system). The statistical significance level was set at $p < 0.05$.

RESULTS

Statistical Analysis of Subjective Vertiginous Sensation

The results of the statistical analysis indicated that the strength of subjective vertiginous sensation was significantly larger in the incongruent than congruent conditions (**Figure 3A**; $p = 0.030$, Wilcoxon sign rank test). Furthermore, the VAS scores in the incongruent condition were significantly and positively correlated with those in the congruent condition (**Figure 3B**; $p = 0.000038$, Spearman's rank coefficient test), suggesting that the sensitivity of the subjects to the visual and vestibular stimulations to evoke vertigo was heterogeneous.

Hemodynamic Activity in Each Condition

Figure 4A depicts the 44 channel positions set on the bilateral temporoparietal cortical areas in a representative subject. **Figure 4B** shows the event-triggered average waveforms of Oxy-Hb and Deoxy-Hb of each channel in the bilateral ventral part of the SMG (vSMG), pMTG, and dorsal part of the SMG (dSMG) in each condition in a representative subject. Both increases in Oxy-Hb and decreases in Deoxy-Hb during the task period were observed in the left vSMG and bilateral pMTG in Condition 1; bilateral pMTG and right dSMG in Condition 2; bilateral pMTG, right vSMG, and dSMG in Condition 3; and bilateral vSMG and left pMTG in Condition 4. These results indicated that the activated cortical areas were different depending on the conditions.

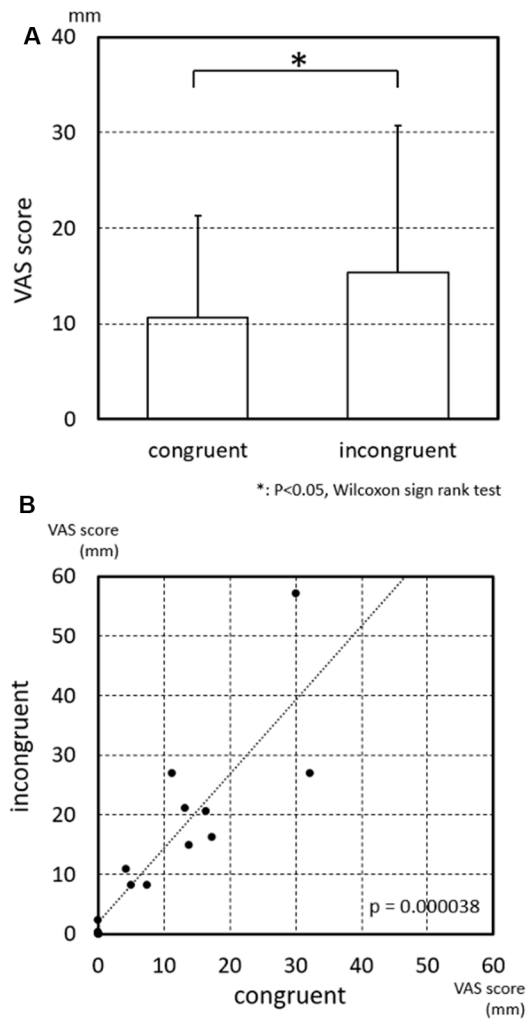

FIGURE 3 | Visual analog scale (VAS) scores of subjective vertiginous sensation in the congruent and incongruent conditions. **(A)** Comparison of VAS scores of subjective vertiginous sensation between the congruent and incongruent conditions. Subjective vertiginous sensation in the incongruent condition is significantly larger than that in the congruent condition by Wilcoxon sign rank test. Error bars indicate the standard deviation. $^*p < 0.05$. **(B)** Relationships of VAS scores of subjective vertiginous sensation between the congruent and incongruent conditions. A positive significant correlation of the strength of subjective vertiginous sensation is found between congruent and incongruent conditions with Spearman's rank coefficient test, with $R = 0.877353$ and $p = 0.000038$.

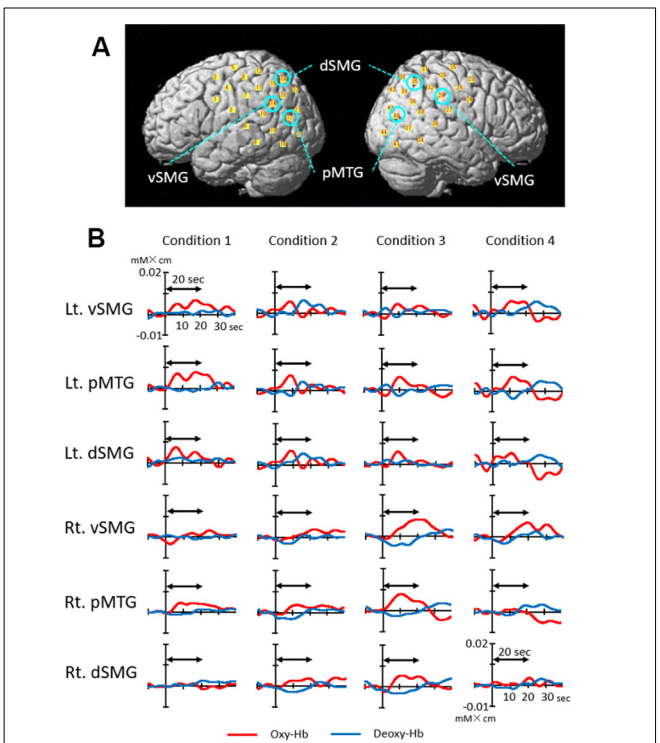

FIGURE 4 | Examples of cerebral hemodynamic activity in the bilateral ventral part of the supramarginal gyrus (vSMG), posterior part of the middle temporal gyrus (pMTG), and dorsal part of the SMG (dSMG). **(A)** Three-dimensional locations of six channels presented in B are indicated. **(B)** Cerebral hemodynamic activity during Condition 1 (congruent visual and right rotatory stimulation), Condition 2 (congruent visual and left rotatory stimulation), Condition 3 (incongruent visual and right rotatory stimulation), and Condition 4 (incongruent visual and left rotatory stimulation) is shown. Red and blue lines indicate Oxy-Hb and Deoxy-Hb, respectively. The data are derived from the same subject. The two-way arrow indicates the rotation period for 20 s. Rt., right; Lt., left.

Next, we performed the group analyses of the Oxy-Hb and Deoxy-Hb data using NIRS-SPM in each condition. However, the group statistical analyses of NIRS Deoxy-Hb data did not indicate significant changes (data not shown). The results of the group statistical analyses of NIRS Oxy-Hb data are shown in **Figures 5**, **6** (side view). The statistical results are also listed in **Table 1**. The topographical maps indicated significant activation in the left ventral primary somatosensory area (S1) and the right vSMG under Condition 1 (**Figure 5A**). In Condition 2, a small area in the left vSMG was activated (**Figure 5B**). In Condition 3, the bilateral vSMG, ventral part of the AG (vAG), and right pMTG were activated (**Figure 6A**). In Condition 4, the bilateral vSMG, bilateral pMTG, and right AG were activated (**Figure 6B**).

Correlation Between Hemodynamic Activity and Subjective Vertiginous Sensation

The results of the correlation analyses based on Spearman's rank coefficient test of the 14 subjects' data are shown in **Figures 7–9** (side and top views). The pixels with significant correlation (i.e., $p < 0.05$) are colored on the standard brain. The statistical results are also listed in **Table 2**. A negative correlation between *T*-values and subjective vertiginous sensation was found in the dorsal part of the left dSMG in Condition 1 ($p = 0.00327$; **Figure 7**) and Condition 3 ($p = 0.00328$; **Figure 8**). In Condition 4, a negative correlation was found in the right dSMG ($p = 0.0049$) and posterior part of the left STG (**Figure 9**). No significant correlation was found in Condition 2.

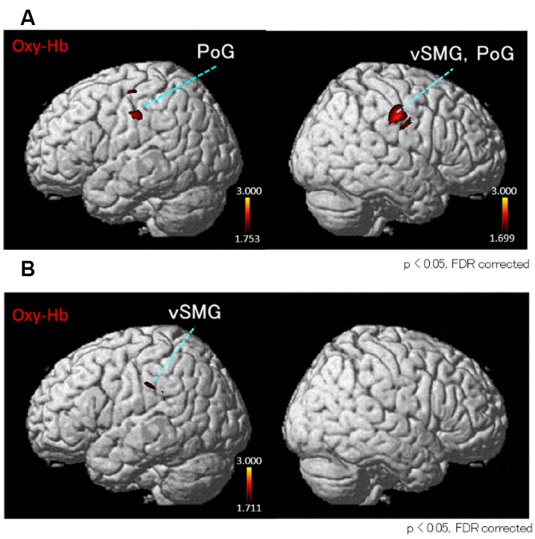

FIGURE 5 | *t*-Statistical maps of the group statistical analyses in Oxy-Hb data using NIRS-SPM in conditions with "congruent" visual stimulation. **(A)** In Condition 1 (acceleration to the right), small cortical regions in the bilateral ventral part of the postcentral gyrus (PoG) and the right ventral part of supramarginal gyrus (vSMG) are activated. **(B)** In Condition 2 (acceleration to the left), small cortical regions in the left vSMG are activated.

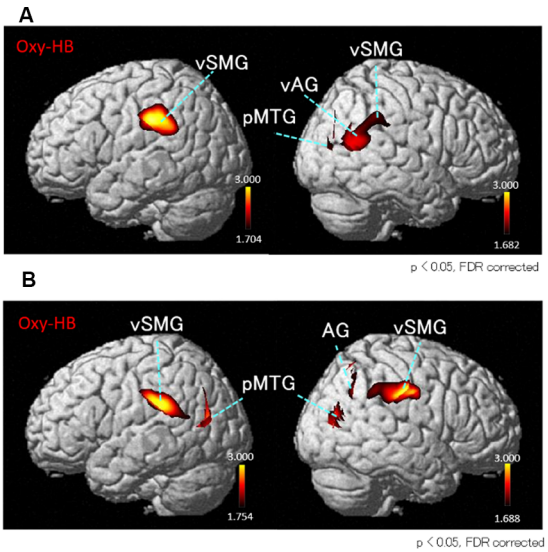

FIGURE 6 | *T*-statistical maps of the group statistical analyses in Oxy-Hb data using NIRS-SPM in conditions with "incongruent" visual stimulation. **(A)** In Condition 3 (acceleration to the right), cortical regions in the bilateral ventral parts of the vSMG, right ventral part of the angular gyrus (vAG), and right posterior part of the middle temporal gyrus (pMTG) are activated. **(B)** In Condition 4 (acceleration to the left), cortical regions in the bilateral vSMG, right AG, and bilateral pMTG are activated.

DISCUSSION

The present study indicated that sensory conflict strongly increased hemodynamic activity in a wide area including the bilateral vSMG and pSTG, which is called the TPJ, and pMTG. However, small activations in the bilateral primary somatosensory areas and vSMG were found under the congruent visual stimulation. Thus, the results indicated that sensory conflict between the visual and horizontal rotatory vestibular stimulations activated the bilateral TPJ and pMTG. In contrast, hemodynamic activity in the bilateral dSMG in and around the IPS was negatively correlated with subjective vertiginous sensation. These cortical regions are key structures of the cortical network for self-motion perception and visual–vestibular integration (Billington and Smith, 2015; Smith et al., 2017; Cheng and Gu, 2018).

Activation of the pMTG

In the present study, hemodynamic activity increased in the pMTG under incongruent visual stimulation (Conditions 3 and 4). The results suggest that these cortical regions are involved in information processing of sensory conflict between visual and rotatory vestibular stimulation. These cortical regions observed in our study may be homologous to the human MT+ complex, which are motion-sensitive visual areas and typically found on the bank of a limb of the inferior temporal sulcus (Huk et al., 2002). The human MT+ complex has been hypothesized to be homologous to those of monkeys and has two subdivisions, the MT and the MST (Huk et al., 2002). In monkeys, dorsal MST neurons responded to both optic flow

TABLE 1 | Significantly activated cortical regions in the four conditions in group analyses using NIRS-SPM.

Condition	Hemisphere	MNI coordinates			*T*-value	BA	Cortical regions	
Direction of Rotation Visual stimulation		***X***	***Y***	***Z***			**Anatomical**	**Functional**
Condition 1	L	−65	−16	39	1.9523	3, 1, 2	PoG	S1
Rotation: R								
Visual stimulation: C								
	R	68	−19	38	2.2803	40	vSMG	TPJ
		69	−15	31	1.6133	3, 1, 2	PoG	S1
Condition 2	L	−68	−27	33	1.8313	40	vSMG	TPJ
Rotation: L								
Visual stimulation: C								
Condition 3	L	−68	−27	33	2.7574	40	vSMG	TPJ
Rotation: R								
Visual stimulation: I								
	R	62	−63	21	2.0978	39	vAG	TPJ
		70	−35	29	1.6982	40	vSMG	TPJ
		49	−79	14	1.7484	19	pMTG	hMT+
Condition 4	L	−69	−33	26	2.6512	40	vSMG	TPJ
Rotation: L								
Visual stimulation: I								
		−59	−70	9	1.9816	19	pMTG	hMT+
	R	70	−26	33	2.7709	40	vSMG	TPJ
		58	−62	36	1.862	39	AG	TPJ
		54	−75	22	2.0687	19	pMTG	hMT+

R, right; L, left; C, congruent; I, incongruent; BA, Brodmann area; PoG, postcentral gyrus; vSMG, ventral part of the supramarginal gyrus; pMTG, posterior part of the medial temporal gyrus; vAG, ventral part of the angular gyrus; S1, primary somatosensory area; TPJ, temporoparietal junction; hMT+, human MT+ complex.

and translational movement (Duffy, 1998; Angelaki et al., 2011), suggesting MST involvement in the integration of visual and vestibular information in self-motion perception (Angelaki et al., 2011). Furthermore, monkey dorsal MST neurons preferentially responded to rotation with incongruent visual and vestibular inputs (Takahashi et al., 2007). In a human fMRI study, vestibular stimulation by galvanic vestibular stimulation activated the MST in the visual cortical areas in darkness, suggesting that visual and vestibular convergence might occur in the human MST during self-motion (Smith et al., 2012). Recent connectivity analyses using fMRI showed that the human MST may act as the relevant mediating network hub for the processing of conflicting visual–vestibular motion information (Rühl et al., 2018). These results suggest that the bilateral pMTG activated in the present study might correspond to the human MT+ complex, especially the human MST, and might be involved in detection of sensory conflict between visual and vestibular stimulations.

Activation of the TPJ

In the present study, bilateral activation of the vSMG, vAG, and pSTG around the limb of the Sylvian fissure was found in Conditions 3 and 4 with incongruent visual and vestibular stimulations. These areas correspond to the TPJ that surrounds the human homolog of the monkey PIVC (the PIVC in humans) in the mid-posterior Sylvian fissure (Lopez and Blanke, 2011; Frank and Greenlee, 2018). The TPJ is a large region including the pSTG, AG, SMG, and the parietal operculum (Pfeiffer et al., 2014) and receives outputs from the PIVC involved in visual–vestibular processing (see below).

The PIVC in humans is strongly interconnected with other vestibular cortical areas and is hypothesized to be a core region for vestibular information processing (Brandt and Dieterich, 1999; Eickhoff et al., 2006). Extensive functional imaging studies on vestibular processing suggest that the PIVC in humans spanning to the TPJ is a multisensory region that receives not only vestibular but also visual or somatosensory inputs (Lobel et al., 1998; Bense et al., 2001; Bottini et al., 2001; Deutschländer et al., 2002; Fasold et al., 2002; Dieterich et al., 2003; Eickhoff

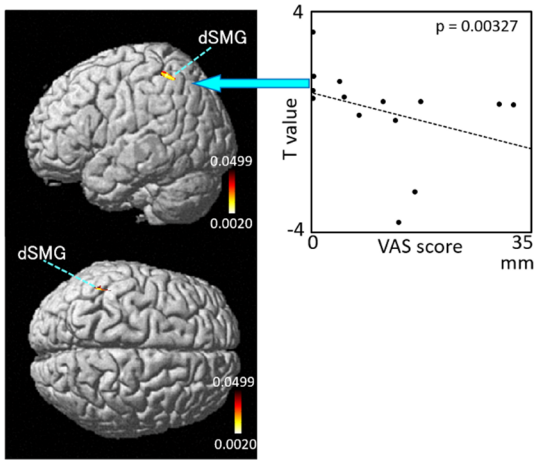

FIGURE 7 | Relationships between cortical hemodynamic activity (*T*-values) and subjective vertiginous sensation (VAS scores) in Condition 1. Left panel indicates statistical maps of the brain regions with significant correlation between cortical hemodynamic activity (*T*-value) and subjective vertiginous sensation (VAS score). A negative correlation is found in the left dorsal part of the SMG (dSMG) in Condition 1. Right panel indicates an example of the scatter plots (Spearman's rank coefficient test, $p = 0.00327$).

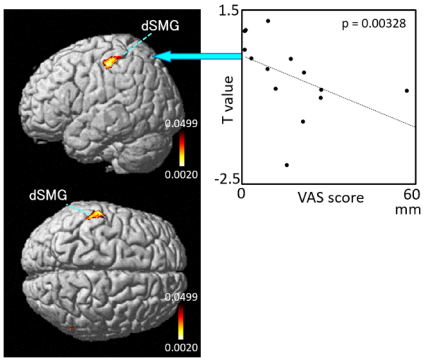

FIGURE 8 | Relationships between cortical hemodynamic activity (*T*-values) and subjective vertiginous sensation (VAS scores) in Condition 3. The left panel indicates statistical maps of the brain regions with a significant correlation between cortical hemodynamic activity (*T*-value) and subjective vertiginous sensation (VAS score). A negative correlation is found in the left dorsal part of the SMG (dSMG) as indicated on the scatter plot for Condition 3. The right panel indicates an example of the scatter plots (Spearman's rank coefficient test, $p = 0.00328$).

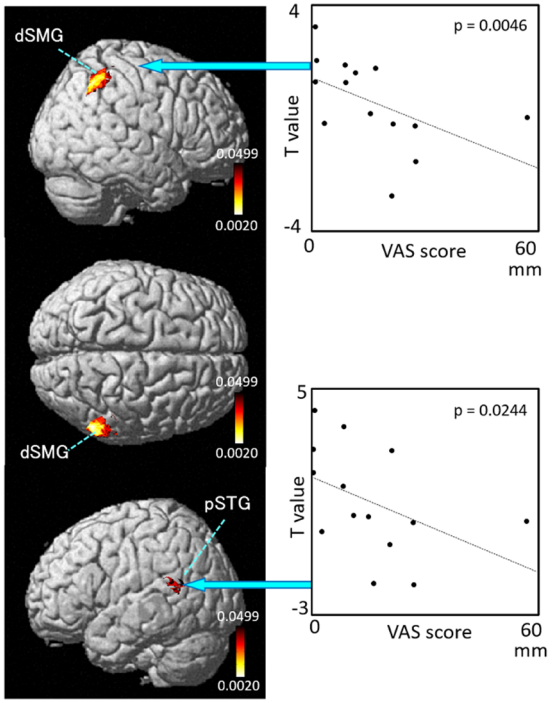

FIGURE 9 | Relationships between cortical hemodynamic activity (*T*-values) and subjective vertiginous sensation (VAS scores) in Condition 4. The left panel indicates statistical maps of the brain regions with a significant correlation between cortical hemodynamic activity (*T*-value) and subjective vertiginous sensation (VAS score). A negative correlation is found in the right dorsal part of the SMG (dSMG) and left posterior part of the superior temporal gyrus (pSTG) in Condition 4. The right panel indicates examples of the scatter plots in the dSMG (Spearman's rank coefficient test, $p = 0.0046$) and pSTG (Spearman's rank coefficient test, $p = 0.0244$).

et al., 2006; Dieterich and Brandt, 2008; zu Eulenburg et al., 2012; Bzdok et al., 2013).

A recent review article suggests that the PIVC reported in previous human imaging studies on vestibular processing contains two separate areas: the PIVC located in the parietal operculum and the posterior insular cortex (PIC) located in the retroinsular cortex (Frank and Greenlee, 2018). The authors named these two regions "PIVC+" as they are similar in some regard (both respond to vestibular stimuli) but dissimilar in others (PIVC is suppressed during visual processing, whereas the PIC is strongly activated; Frank et al., 2014, 2016; Frank and Greenlee, 2018). Recent fMRI studies using simultaneous visual (horizontal optokinetic stimulation) and vestibular (caloric irrigation or voluntary head rotation) stimulations reported activation in the PIC in incongruent visual–vestibular stimulation, suggesting that the PIC is involved in integration and disambiguation of visual–vestibular cues (Roberts et al., 2017; Schindler and Bartels, 2018). The PIVC may encode head and full-body movements and is involved in the estimation of heading direction through such movements, whereas the PIC may be involved in the estimation of heading direction by combining visual and vestibular cues and distinction between visual self-motion and visual object motion, which may be supported by neurons with incongruent visual–vestibular tuning (see a review by Frank and Greenlee, 2018).

The outputs of visual–vestibular processing from the PIVC+ are sent to the TPJ (Frank and Greenlee, 2018). fNIRS studies during postural balancing using the CDP also reported that the TPJ was activated in sensory conflict among vestibular, visual, and somatosensory inputs, consistent with the present results (Karim et al., 2013; Takakura et al., 2015; Lin et al., 2017).

It has been proposed that the vestibular system, especially the TPJ, is essential for representation of spatial aspects of bodily self-consciousness (Pfeiffer et al., 2014). Furthermore, a previous fMRI study using virtual reality reported that activity of the TPJ

TABLE 2 | Summary of the correlation analyses between cortical hemodynamic responses (*T*-value) and subjective vertiginous sensation (VAS score).

Hemisphere	Cortical regions	BA	Condition 1 Rotation: R Visual: C	Condition 2 Rotation: L Visual: C	Condition 3 Rotation: R Visual: I	Condition 4 Rotation: L Visual: I
Right	dSMG	40				Negative
	pSTG	22				
Left	dSMG	40	Negative		Negative	
	pSTG	22				Negative

Negative, negative correlation; R, right; L, left; C, congruent; I, incongruent; BA, Brodmann area; dSMG, dorsal part of the supramarginal gyrus; pSTG, posterior part of the superior temporal gyrus.

was associated with the sense of changes in self-location induced by incongruent visual–tactile stimulation (Ionta et al., 2011). These findings suggest that bilateral TPJ activation in the present study might reflect altered perception of head position and movements and neural process for an egocentric representation of the self in space in incongruent visual–vestibular conditions.

Correlation Between Hemodynamic Activity in the dSMG and Subjective Vertiginous Sensation

In the present study, hemodynamic activity in the bilateral dSMG in and around the IPS was negatively correlated with subjective vertiginous sensation. The IPS is implicated in sensorimotor integration. In monkeys, the VIP, located in the fundus of the IPS, receives multimodal information: (1) vestibular information from the PIVC (Guldin et al., 1992; Lewis and Van Essen, 2000); (2) vestibular and somatosensory information from the vestibular neck subregions in areas 3a and 2 (Guldin et al., 1992; Lewis and Van Essen, 2000); (3) visual information from the medial temporal (MT) and MST complex (Lewis and Van Essen, 2000); and (4) somatosensory information from the S1 area (Lewis and Van Essen, 2000). In humans, the IPS is involved in the representation of coherent body images during sensory stimulation of multimodal stimuli in incongruent (Hagura et al., 2007; Bufalari et al., 2014) and congruent (Ehrsson et al., 2004; Petkova et al., 2011) conditions.

The negative correlation between the hemodynamic activities in the dSMG and subjective vertiginous sensation indicates that greater activity in the dSMG induces a weaker subjective vertiginous sensation during visual–vestibular sensory conflict. This suggests that the subjects are heterogeneous in sensory reweighting during sensory conflict. A neurophysiological study reported that monkey VIP neurons represented vestibular heading in an egocentric (body-centered) reference frame in a body-fixed gaze condition that corresponds to the present experimental situation (Chen et al., 2018). The subjects with higher dSMG activity and less vertiginous sensation might tend to represent the body in an egocentric reference frame. That is, under the incongruent condition, the sensory weight of visual information might be decreased in these subjects, which leads to higher weight of the vestibular system as the reliable source of information, which might result in flexible transformation of the spatial reference frame to an egocentric (body-centered) one. Consistent with this idea, a computational model suggests that different reference frames could be used based on the agent's reliance in a specific reference frame and that the frame frequently switches between them (Oess et al., 2017). The subjects, who could not flexibly switch reference frames during sensory conflict, might feel a vertiginous sensation.

Possible Clinical Application of fNIRS

fNIRS has several advantages compared with other neuroimaging modalities such as fMRI, MEG, and PET. In particular, fNIRS can make measurements without preventing bodily movements, and the present apparatus is highly portable, being suitable for all possible subject populations from newborns to the elderly and for various experimental settings, both inside and outside the laboratory (Pinti et al., 2020). We could measure the cortical hemodynamic responses to rotatory stimulation using two portable NIRS systems mounted on the rotatory chair. The paradigm used in the present study has been used for clinical examination of patients with vertigo in general. The present results suggest that fNIRS could be applied to clinical use for simultaneous recording of cerebral hemodynamic activity and peripheral vestibular functions.

Furthermore, the present results indicated that hemodynamic activity in the dSMG adjacent to the IPS was negatively correlated with subjective vertiginous sensation. Recent studies reported that various neurofeedback therapies using NIRS were effective in patients with stroke (Mihara and Miyai, 2016), social anxiety disorder (Kimmig et al., 2018), and attention-deficit/hyperactivity disorder (Blume et al., 2017). These findings suggest that real-time neurofeedback training using fNIRS to increase hemodynamic activity in the dSMG adjacent to the IPS could be effective to treat motion sickness, visual vertigo, or intractable chronic dizziness such as persistent postural perceptual dizziness.

Limitations

There are several limitations in this study. First, the spatial resolution of NIRS is lower than that of fMRI, and it could not measure hemodynamics in the deeper brain regions including the insula, opercular regions, cerebellum, basal ganglia, or hippocampus. Furthermore, recorded cortical regions were limited in the present study: we recorded only the bilateral temporoparietal areas, whereas most parts of the frontal and parietal cortices were not measured. Further studies are required to investigate the roles of these brain regions in sensory conflict.

Second, the group statistical analyses of Deoxy-Hb signals did not indicate significant changes in the present study. As Oxy-Hb signals are more susceptible to systemic changes in blood circulation than are Deoxy-Hb, Oxy-Hb signals could yield false-positive data (Tachtsidis and Scholkmann, 2016). However, the signal-to-noise ratio of Deoxy-Hb signals is lower than that of Oxy-Hb signals (Sato et al., 2016), and Deoxy-Hb signals are sensitive not only to venous blood oxygenation but also to venous blood volume (Hoshi et al., 2001). Consequently, the direction of changes in Deoxy-Hb signals was variable across tasks and individuals, whereas the direction of changes in Oxy-Hb signals was consistent (Hoshi et al., 2001; Toichi et al., 2004; Sato et al., 2005). On the basis of these findings, we estimated Oxy-Hb data as cerebral hemodynamic activity in the present study. Future studies, which incorporate methods such as principal component spatial filtering to separate cerebral hemodynamic activity from the systemic component (Zhang et al., 2017), should be considered.

Third, we could not put foam rubber sheets between the rotatory chair and each subject's hip or back to reduce somatosensory inputs because we had to hold the subject's body tightly in the chair to prevent it from falling during rotation. Furthermore, we could not use ear plugs or noise-cancelling earphones to reduce auditory sounds (e.g., mechanical or wind noises) as we had to announce the timing of opening and closing of the subjects' eyes by sound cues. Thus, the subjects

could use these other inputs to recognize their orientation in space, and thus, we cannot completely deny the effect of sensory inputs other than visual and vestibular inputs (e.g., auditory and somatosensory inputs) during the rotatory task. However, previous studies reported that auditory information seems not to affect head postures (Thomas et al., 2018) and that trunk tactile cues did not affect the subjective sensation of rotation (Cheung and Hofer, 2007). Although the effects of these other sensory inputs seem to be low, further studies are required to assess the effects of the other sensory inputs on vertiginous sensation.

Fourth, the activated areas in the MST showed non-Gaussian distributions in Conditions 3 and 4. These regions were located in the posterior and inferior borders of the recording areas. Normalization of NIRS channel locations in individual subjects based on the MNI brain resulted in deviation of the NIRS channels from the MST in 3–4 subjects. The non-Gaussian distributions in and around the MST might be ascribed to a smaller number of NIRS channels over the MST due to the deviation of the channels. Further studies with a larger number of NIRS channels to record wider cortical regions are required to investigate the activity in the MST during sensory conflict.

Fifth, optokinetic visual stimuli usually elicit nystagmus. Therefore, nystagmus could affect cortical activation during the visual and rotatory tasks. In the present study, although the same optokinetic stimulations eliciting nystagmus were used in the congruent and incongruent visual conditions, the cortical areas activated were different between the two conditions. This suggests that differences in the areas activated might be attributed to factors other than nystagmus. Furthermore, a previous study reported that nystagmus itself activated mainly area V6A in the medial parieto-occipital sulcus (Konen et al., 2005), which is located outside the cortical areas recorded in the present study. These findings suggest that the effects of nystagmus itself on cortical activation might be small in the present study.

CONCLUSION

The present study indicated that sensory conflict in the incongruent visual–vestibular condition significantly increased hemodynamic activity in the bilateral pMTG (corresponding to human MT/MST) and TPJ. Human MT/MST and TPJ have been reported as the motion-sensitive visual cortex and vestibular cortices, respectively (Huk et al., 2002; Lopez and Blanke, 2011), but also receive multimodal information (Smith et al., 2012; zu Eulenburg et al., 2012; Bzdok et al., 2013; Pfeiffer et al., 2014). These findings suggest that human MT/MST and the TPJ might be crucial for the detection of sensory conflicts between visual and rotatory vestibular stimulations.

Furthermore, the hemodynamic activity in the dSMG in and around the IPS, which is implicated in the egocentric reference frame (Chen et al., 2018), was negatively correlated with subjective vertiginous sensation during the visual and vestibular stimulations. Activation of the dSMG in the subjects with less vertiginous sensation suggests both that these subjects might switch reference frames to an egocentric reference frame and that flexible changes in reference frames might be crucial to the reduction of subjective vertiginous sensation during sensory conflicts. Deficits in these flexible changes might induce motion sickness, visual vertigo, or persistent postural perceptual dizziness. Further studies are required to elucidate the neural mechanisms responsible for the flexible shift of spatial reference frames and subjective vertiginous sensation during sensory conflict.

DATA AVAILABILITY STATEMENT

The datasets generated for this study are available on request to the corresponding author.

ETHICS STATEMENT

The studies involving human participants were reviewed and approved by the ethical committee of the University of Toyama. The patients/participants provided their written informed consent to participate in this study.

AUTHOR CONTRIBUTIONS

NN, HT, and HS designed this research. NN, HT, NU, and SI performed the research. NN, HT, MF, and KA analyzed the data. NN, HT, HS, and HN wrote the manuscript.

FUNDING

This work was partially supported by JSPS Grant-in-Aid for Scientific Research C (JP17K11320 and JP17K11321) and a Grant-in-Aid from the Japan Agency for Medical Research and Development (JP19dk0310092).

REFERENCES

Angelaki, D. E., Gu, Y., and Deangelis, G. C. (2011). Visual and vestibular cue integration for heading perception in extrastriate visual cortex. *J. Physiol.* 589, 825–833. doi: 10.1113/jphysiol.2010.194720

Ashburner, J., and Friston, K. J. (1999). Nonlinear spatial normalization using basis functions. *Hum. Brain Mapp.* 7, 254–266. doi: 10.1002/(sici)1097-0193(1999)7:4>254::aid-hbm4>3.0.co;2-g

Ashburner, J., Neelin, P., Collins, D. L., Evans, A., and Friston, K. (1997). Incorporating prior knowledge into image registration. *NeuroImage* 6, 344–352. doi: 10.1006/nimg.1997.0299

Benjamini, Y., and Hochberg, Y. (1995). Controlling the false discovery rate—a practical and powerful approach to multiple testing. *J. R. Stat. Soc. B Method* 57, 289–300. doi: 10.1111/j.2517-6161.1995.tb02031.x

Bense, S., Stephan, T., Yousry, T. A., Brandt, T., and Dieterich, M. (2001). Multisensory cortical signal increases and decreases during vestibular galvanic stimulation (fMRI). *J. Neurophysiol.* 85, 886–899. doi: 10.1152/jn.2001.85.2.886

Billington, J., and Smith, A. T. (2015). Neural mechanisms for discounting head-roll-induced retinal motion. *J. Neurosci.* 35, 4851–4856. doi: 10.1523/JNEUROSCI.3640-14.2015

Blume, F., Hudak, J., and Dresler, T. (2017). NIRS-based neurofeedback training in a virtual reality classroom for children with attention-deficit/hyperactivity

disorder: study protocol for a randomized controlled trial. *Trials* 18:41. doi: 10.1186/s13063-016-1769-3

Bottini, G., Karnath, H. O., Vallar, G., Sterzi, R., Frith, C. D., Frackowiak, R. S., et al. (2001). Cerebral representations for egocentric space: functional-anatomical evidence from caloric vestibular stimulation and neck vibration. *Brain* 124, 1182–1196. doi: 10.1093/brain/124.6.1182

Brandt, T. (1999). *Vertigo: Its Multisensory Syndromes.* 2nd Edn. London: Springer.

Brandt, T., and Dieterich, M. (1999). The vestibular cortex. Its locations, functions, and disorders. *Ann. N Y Acad. Sci.* 871, 293–312. doi: 10.1007/978-1-4471-0527-5_13

Bucher, S. F., Dieterich, M., Wiesmann, M., Weiss, A., Zink, R., Yousry, T. A., et al. (1998). Cerebral functional magnetic resonance imaging of vestibular, auditory, and nociceptive areas during galvanic stimulation. *Ann. Neurol.* 44, 120–125. doi: 10.1002/ana.410440118

Bufalari, I., Di Russo, F., and Aglioti, S. M. (2014). Illusory and veridical mapping of tactile objects in the primary somatosensory and posterior parietal cortex. *Cereb. Cortex* 24, 1867–1878. doi: 10.1093/cercor/bht037

Butler, J. S., Smith, S. T., Campos, J. L., and Bülthoff, H. H. (2010). Bayesian integration of visual and vestibular signals for heading. *J. Vis.* 10:23. doi: 10.1167/10.11.23

Bzdok, D., Langner, R., Schilbach, L., Jakobs, O., Roski, C., Caspers, S., et al. (2013). Characterization of the temporo-parietal junction by combining data-driven parcellation, complementary connectivity analyses, and functional decoding. *NeuroImage* 81, 381–392. doi: 10.1016/j.neuroimage.2013.05.046

Chen, A., DeAngelis, G. C., and Angelaki, D. E. (2011). Representation of vestibular and visual cues to self-motion in ventral intraparietal cortex. *J. Neurosci.* 31, 12036–12052. doi: 10.1523/JNEUROSCI.0395-11.2011

Chen, X., DeAngelis, G. C., and Angelaki, D. E. (2018). Flexible egocentric and allocentric representations of heading signals in parietal cortex. *Proc. Natl. Acad. Sci. U S A* 115, 3305–3312. doi: 10.1073/pnas.1715625115

Cheng, Z., and Gu, Y. (2018). Vestibular system and self-motion. *Front. Cell. Neurosci.* 12:456. doi: 10.3389/fncel.2018.00456

Cheung, B., and Hofer, K. (2007). Tactile cueing vs. vestibular sensation and nystagmus during yaw rotation. *Aviat. Space Environ. Med.* 78, 756–763.

Colacino, J. M., Grubb, B., and Jöbsis, F. F. (1981). Infra-red technique for cerebral blood flow: comparison with 133Xenon clearance. *Neurol. Res.* 3, 17–31. doi: 10.1080/01616412.1981.11739590

Cordes, D., Haughton, V. M., Arfanakis, K., Carew, J. D., Turski, P. A., Moritz, C. H., et al. (2001). Frequencies contributing to functional connectivity in the cerebral cortex in "resting-state" data. *Am. J. Neuroradiol.* 22, 1326–1333. doi: 10.1093/cercor/bhr230

Deutschländer, A., Bense, S., Stephan, T., Schwaiger, M., Brandt, T., and Dieterich, M. (2002). Sensory system interactions during simultaneous vestibular and visual stimulation in PET. *Hum. Brain Mapp.* 16, 92–103. doi: 10.1002/hbm.10030

Dieterich, M., Bense, S., Lutz, S., Drzezga, A., Stephan, T., Bartenstein, P., et al. (2003). Dominance for vestibular cortical function in the non-dominant hemisphere. *Cereb. Cortex* 13, 994–1007. doi: 10.1093/cercor/13.9.994

Dieterich, M., and Brandt, T. (2008). Functional brain imaging of peripheral and central vestibular disorders. *Brain* 131, 2538–2552. doi: 10.1093/brain/awn042

Duffy, C. J. (1998). MST neurons respond to optic flow and translational movement. *J. Neurophysiol.* 80, 1816–1827. doi: 10.1152/jn.1998.80.4.1816

Ehrsson, H. H., Spence, C., and Passingham, R. E. (2004). That's my hand! Activity in premotor cortex reflects feeling of ownership of a limb. *Science* 305, 875–877. doi: 10.1126/science.1097011

Eickhoff, S. B., Weiss, P. H., Amunts, K., Fink, G. R., and Zilles, K. (2006). Identifying human parieto-insular vestibular cortex using fMRI and cytoarchitectonic mapping. *Hum. Brain Mapp.* 27, 611–621. doi: 10.1002/hbm.20205

Fasold, O., von Brevern, M., Kuhberg, M., Ploner, C. J., Villringer, A., Lempert, T., et al. (2002). Human vestibular cortex as identified with caloric stimulation in functional magnetic resonance imaging. *NeuroImage* 17, 1384–1393. doi: 10.1006/nimg.2002.1241

Fetsch, C. R., Deangelis, G. C., and Angelaki, D. E. (2010). Visual-vestibular cue integration for heading perception: applications of optimal cue integration theory. *Eur. J. Neurosci.* 10, 1721–1729. doi: 10.1111/j.1460-9568.2010.07207.x

Frank, S. M., Baumann, O., Mattingley, J. B., and Greenlee, M. W. (2014). Vestibular and visual responses in human posterior insular cortex. *J. Neurophysiol.* 112, 2481–2491. doi: 10.1152/jn.00078.2014

Frank, S. M., and Greenlee, M. W. (2018). The parieto-insular vestibular cortex in humans: more than a single area? *J. Neurophysiol.* 120, 1438–1450. doi: 10.1152/jn.00907.2017

Frank, S. M., Wirth, A. M., and Greenlee, M. W. (2016). Visual-vestibular processing in the human sylvian fissure. *J. Neurophysiol.* 116, 263–271. doi: 10.1152/jn.00009.2016

Friston, K. J., Ashburner, J., Frith, C. D., Poline, J. B., Heather, J. D., and Frackowiak, R. S. J. (1995). Spatial registration and normalization of images. *Hum. Brain Mapp.* 2, 165–189. doi: 10.1002/hbm.460030303

Gu, Y., Angelaki, D. E., and Deangelis, G. C. (2008). Neural correlates of multisensory cue integration in macaque MSTd. *Nat. Neurosci.* 11, 1201–1210. doi: 10.1038/nn.2191

Guldin, W. O., Akbarian, S., and Grüsser, O. J. (1992). Cortico-cortical connections and cytoarchitectonics of the primate vestibular cortex: a study in squirrel monkeys (*Saimiri sciureus*). *J. Comp. Neurol.* 326, 375–401. doi: 10.1002/cne.903260306

Hagura, N., Takei, T., Hirose, S., Aramaki, Y., Matsumura, M., Sadato, N., et al. (2007). Activity in the posterior parietal cortex mediates visual dominance over kinesthesia. *J. Neurosci.* 27, 7047–7053. doi: 10.1523/JNEUROSCI.0970-07.2007

Horak, F. B. (2009). Postural compensation for vestibular loss. *Ann. N Y Acad. Sci.* 1164, 76–81. doi: 10.1111/j.1749-6632.2008.03708.x

Hoshi, Y., Kobayashi, N., and Tamura, M. (2001). Interpretation of near-infrared spectroscopy signal: a study with a newly developed perfused rat brain model. *J. Appl. Physiol.* 90, 1657–1662. doi: 10.1152/jappl.2001.90.5.1657

Huk, A. C., Dougherty, R. F., and Heeger, D. J. (2002). Retinotopy and functional subdivision of human areas MT and MST. *J. Neurosci.* 22, 7195–7205. doi: 10.1523/JNEUROSCI.22-16-07195.2002

Ionta, S., Heydrich, L., Lenggenhager, B., Mouthon, M., Fornari, E., Chapuis, D., et al. (2011). Multisensory mechanisms in temporo-parietal cortex support self-location and first-person perspective. *Neuron* 70, 363–374. doi: 10.1016/j.neuron.2011.03.009

Ishikuro, K., Urakawa, S., Takamoto, K., Ishikawa, A., Ono, T., and Nishijo, H. (2014). Cerebral functional imaging using near-infrared spectroscopy during repeated performances of motor rehabilitation tasks tested on healthy subjects. *Front. Hum. Neurosci.* 8:292. doi: 10.3389/fnhum.2014.00292

Jöbsis, F. F. (1977). Noninvasive, infrared monitoring of cerebral and myocardial oxygen sufficiency and circulatory parameters. *Science* 198, 1264–1267. doi: 10.1126/science.929199

Karim, H., Fuhrman, S. I., Sparto, P., Furman, J., and Huppert, T. (2013). Functional brain imaging of multi-sensory vestibular processing during computerized dynamic posturography using near-infrared spectroscopy. *NeuroImage* 74, 318–325. doi: 10.1016/j.neuroimage.2013.02.010

Keshavarz, B., Riecke, B. E., Hettinger, L. J., and Campos, J. L. (2015). Vection and visually induced motion sickness: how are they related? *Front. Psychol.* 6:472. doi: 10.3389/fpsyg.2015.00472

Kimmig, A.-C. S., Dresler, T., Hudak, J., Haeussinger, F. B., Wildgruber, D., Fallgatter, A. J., et al. (2018). Feasibility of NIRS-based neurofeedback training in social anxiety disorder: behavioral and neural correlates. *J. Neural Transm.* 126, 1175–1185. doi: 10.1007/s00702-018-1954-5

Konen, C. S., Kleiser, R., Seitz, R. J., and Bremmer, F. (2005). An fMRI study of optokinetic nystagmus and smooth-pursuit eye movements in humans *Exp. Brain Res.* 165, 203–216.

Lancaster, J. L., Woldorff, M. G., Parsons, L. M., Liotti, M., Freitas, C. S., Rainey, L., et al. (2000). Automated Talairach atlas labels for functional brain mapping. *Hum. Brain Mapp.* 10, 120–131. doi: 10.1002/1097-0193(200007)10:3>120::aid-hbm30>3.0.co;2-8

Lewis, J. W., and Van Essen, D. C. (2000). Corticocortical connections of visual, sensorimotor, and multimodal processing areas in the parietal lobe

of the macaque monkey. *J. Comp. Neurol.* 428, 112–137. doi: 10.1002/1096-9861(20001204)428:1>112::aid-cne8>3.0.co;2-9

Lin, C. C., Barker, J. W., Sparto, P. J., Furman, J. M., and Huppert, T. J. (2017). Functional near-infrared spectroscopy (fNIRS) brain imaging of multi-sensory integration during computerized dynamic posturography in middle-aged and older adults. *Exp. Brain Res.* 235, 1247–1256. doi: 10.1007/s00221-017-4893-8

Lobel, E., Kleine, J. F., Bihan, D. L., Leroy-Willig, A., and Berthoz, A. (1998). Functional MRI of galvanic vestibular stimulation. *J. Neurophysiol.* 80, 2699–2709. doi: 10.1152/jn.1998.80.5.2699

Lopez, C., and Blanke, O. (2011). The thalamocortical vestibular system in animals and human. *Brain Res. Rev.* 67, 119–146. doi: 10.1016/j.brainresrev.2010.12.002

Lu, C. M., Zhang, Y. J., Biswal, B. B., Zang, Y. F., Peng, D. L., and Zhu, C. Z. (2010). Use of fNIRS to assess resting state functional connectivity. *J. Neurosci. Methods* 186, 242–249. doi: 10.1016/j.jneumeth.2009.11.010

Mihara, M., and Miyai, I. (2016). Review of functional near-infrared spectroscopy in neurorehabilitation. *Neurophotonics* 3:031414. doi: 10.1117/1.nph.3.3.031414

Mihara, M., Miyai, I., Hatakenaka, M., Kubota, K., and Sakoda, S. (2008). Role of the prefrontal cortex in human balance control. *NeuroImage* 43, 329–336. doi: 10.1016/j.neuroimage.2008.07.029

Nakamichi, N., Takamoto, K., Nishimaru, H., Fujiwara, K., Takamura, Y., Matsumoto, J., et al. (2018). Cerebral hemodynamics in speech-related cortical areas: articulation learning involves the inferior frontal gyrus, ventral sensory-motor cortex, and parietal-temporal sylvian area. *Front. Neurol.* 9:939. doi: 10.3389/fneur.2018.00939

Niederer, P., Mudra, R., and Keller, E. (2008). Monte Carlo simulation of light propagation in adult brain: influence of tissue blood content and indocyanine green. *Opto. Electron. Rev.* 16, 124–130. doi: 10.2478/s11772-008-0012-5

Oess, T., Krichmar, J. L., and Röhrbein, F. A. (2017). Computational model for spatial navigation based on reference frames in the hippocampus, retrosplenial, cortex and posterior parietal cortex. *Front. Neurorobot.* 11:4. doi: 10.3389/fnbot.2017.00004

Oman, C. M. (1982). A heuristic mathematical model for the dynamics of sensory conflict and motion sickness. *Acta Otolaryngol. Suppl.* 392, 1–44. doi: 10.3109/00016488209108197

Peterka, R. J., Statler, K. D., Wrisley, D. M., and Horak, F. B. (2011). Postural compensation for unilateral vestibular loss. *Front. Neurol.* 2:57. doi: 10.3389/fneur.2011.00057

Petkova, V. I., Björnsdotter, M., Gentile, G., Jonsson, T., Li, T. Q., and Ehrsson, H. H. (2011). From part- to whole-body ownership in the multisensory brain. *Curr. Biol.* 21, 1118–1122. doi: 10.1016/j.cub.2011.05.022

Pfeiffer, C., Serino, A., and Blanke, O. (2014). The vestibular system: a spatial reference for bodily self-consciousness. *Front. Integr. Neurosci.* 8:31. doi: 10.3389/fnint.2014.00031

Pinti, P., Tachtsidis, I., Hamilton, A., Hirsch, J., Aichelburg, C., Gilbert, S., et al. (2020). The present and future use of functional near-infrared spectroscopy (fNIRS) for cognitive neuroscience. *Ann. N Y Acad. Sci.* 1464, 5–29. doi: 10.1111/nyas.13948

Reason, J. T. (1978). Motion sickness adaptation. A neural mismatch model. *J. R. Soc. Med.* 71, 819–829. doi: 10.1177/014107687807101109

Roberts, R. E., Ahmad, H., Arshad, Q., Patel, M., Dima, D., Leech, R., et al. (2017). Functional neuroimaging of visuo-vestibular interaction. *Brain Struct. Funct.* 222, 2329–2343. doi: 10.1007/s00429-016-1344-4

Rühl, R. M., Bauermann, T., Dieterich, M., and Zu Eulenburg, P. (2018). Functional correlate and delineated connectivity pattern of human motion aftereffect responses substantiate a subjacent visual-vestibular interaction. *NeuroImage* 174, 22–34. doi: 10.1016/j.neuroimage.2018.02.057

Sato, H., Fuchino, Y., Kiguchi, M., Katura, T., Maki, A., Yoro, T., et al. (2005). Intersubject variability of near-infrared spectroscopy signals during sensorimotor cortex activation. *J. Biomed. Opt.* 10:44001. doi: 10.1117/1.1960907

Sato, T., Nambu, I., Takeda, K., Aihara, T., Yamashita, O., Isogaya, T., et al. (2016). Reduction of global interference of scalp-hemodynamics in functional near-infrared spectroscopy using short distance probes. *NeuroImage* 141, 120–132. doi: 10.1016/j.neuroimage.2016.06.054

Schindler, A., and Bartels, A. (2018). Integration of visual and non-visual self-motion cues during voluntary head movements in the human brain. *NeuroImage* 172, 597–607. doi: 10.1016/j.neuroimage.2018.02.006

Schytz, H. W., Wienecke, T., Jensen, L. T., Selb, J., Boas, D. A., and Ashina, M. (2009). Changes in cerebral blood flow after acetazolamide: an experimental study comparing near-infrared spectroscopy and SPECT. *Eur. J. Neurol.* 16, 461–467. doi: 10.1111/j.1468-1331.2008.02398.x

Seiyama, A., Hazeki, O., and Tamura, M. (1988). Noninvasive quantitative analysis of blood oxygenation in rat skeletal muscle. *J. Biochem.* 103, 419–424. doi: 10.1093/oxfordjournals.jbchem.a122285

Smith, P. F. (2017). The vestibular system and cognition. *Curr. Opin. Neurol.* 30, 84–89. doi: 10.1097/WCO.0000000000000403

Smith, A. T., Greenlee, K. W., DeAngelis, G. C., and Angelaki, D. E. (2017). Distributed visual-vestibular processing in the cerebral cortex of man and macaque. *Multisens. Res.* 30, 91–120. doi: 10.1163/22134808-00002568

Smith, A. T., Wall, M. B., and Thilo, K. V. (2012). Vestibular inputs to human motion-sensitive visual cortex. *Cereb. Cortex* 22, 1068–1077. doi: 10.1093/cercor/bhr179

Strangman, G., Culver, J. P., Thompson, J. H., and Boas, D. A. (2002). A quantitative comparison of simultaneous BOLD fMRI and NIRS recordings during functional brain activation. *NeuroImage* 17, 719–731. doi: 10.1006/nimg.2002.1227

Tachtsidis, I., and Scholkmann, F. (2016). False positives and false negatives in functional near-infrared spectroscopy: issues, challenges, and the way forward. *Neurophotonics* 3:031405. doi: 10.1117/1.NPh.3.3.031405

Takahashi, K., Gu, Y., May, P. J., Newlands, S. D., DeAngelis, G. C., and Angelaki, D. E. (2007). Multimodal coding of three-dimensional rotation and translation in area MSTd: comparison of visual and vestibular selectivity. *J. Neurosci.* 27, 9742–9756. doi: 10.1523/jneurosci.0817-07.2007

Takakura, H., Nishijo, H., Ishikawa, A., and Shojaku, H. (2015). Cerebral hemodynamic responses during dynamic posturography: analysis with a multichannel near-infrared spectroscopy system. *Front. Hum. Neurosci.* 9:620. doi: 10.3389/fnhum.2015.00620

Takakura, H., Shojaku, H., Takamoto, K., Urakawa, S., Nishijo, H., and Watanabe, Y. (2011). Cortical hemodynamic responses to intravenous thiamine propyldisulphide administration detected by multichannel near infrared spectroscopy (NIRS) system. *Brain Topogr.* 24, 114–126. doi: 10.1007/s10548-011-0179-9

Talairach, J., and Tournoux, P. (1988). *Co-Planar Stereotaxic Atlas of the Human Brain.* Stuttgart, NY: Thieme.

Thomas, E., Martines, F., Bianco, A., Messina, G., Giustino, V., Zangla, D., et al. (2018). Decreased postural control in people with moderate hearing loss. *Medicine* 97:e0244. doi: 10.1097/md.0000000000010244

Toichi, M., Findling, R. L., Kubota, Y., Calabrese, J. R., Wiznitzer, M., McNamara, N. K., et al. (2004). Hemodynamic differences in the activation of the prefrontal cortex: attention vs. higher cognitive processing. *Neuropsychologia* 42, 698–706. doi: 10.1016/j.neuropsychologia.2003.08.012

Wray, S., Cope, M., Delpy, D. T., Wyatt, J. S., and Reynolds, E. O. (1988). Characterization of the near infrared absorption spectra of cytochrome aa3 and haemoglobin for the non-invasive monitoring of cerebral oxygenation. *Biochim. Biophys. Acta* 933, 184–192. doi: 10.1016/0005-2728(88)90069-2

Yamamoto, Y., and Kato, T. (2002). Paradoxical correlation between signal in functional magnetic resonance imaging and deoxygenated haemoglobin content in capillaries: a new theoretical explanation. *Phys. Med. Biol.* 47, 1121–1141. doi: 10.1088/0031-9155/47/7/309

Ye, J. C., Tak, S., Jang, K. E., Jung, J., and Jang, J. (2009). NIRS-SPM: statistical parametric mapping for near-infrared spectroscopy. *NeuroImage* 44, 428–447. doi: 10.1016/j.neuroimage.2008.08.036

Zhang, X., Noah, J. A., Dravida, S., and Hirsch, J. (2017). Signal processing of functional NIRS data acquired during overt speaking. *Neurophotonics* 4:041409. doi: 10.1117/1.nph.4.4.041409

Zhang, X., Noah, J. A., and Hirsch, J. (2016). Separation of the global and local components in functional near-infrared spectroscopy signals using principal component spatial filtering. *Neurophotonics* 3:015004. doi: 10.1117/1.nph.3.1.015004

zu Eulenburg, P., Caspers, S., Roski, C., and Eickhoff, S. B. (2012). Meta-analytical definition and functional connectivity of the human vestibular cortex. *NeuroImage* 60, 162–169. doi: 10.1016/j.neuroimage.2011.12.032

Conflict of Interest: The authors declare that the research was conducted in the absence of any commercial or financial relationships that could be construed as a potential conflict of interest.

Copyright © 2020 Nguyen, Takakura, Nishijo, Ueda, Ito, Fujisaka, Akaogi and Shojaku. This is an open-access article distributed under the terms of the Creative Commons Attribution License (CC BY). The use, distribution or reproduction in other forums is permitted, provided the original author(s) and the copyright owner(s) are credited and that the original publication in this journal is cited, in accordance with accepted academic practice. No use, distribution or reproduction is permitted which does not comply with these terms.

frontiers in Human Neuroscience

ORIGINAL RESEARCH
published: 28 April 2020
doi: 10.3389/fnhum.2020.00149

Cortical Activation Patterns of Different Masking Noises and Correlation With Their Masking Efficacy, Determined by Functional Near-Infrared Spectroscopy

Qiyang Sun[1,2†], *Xianren Wang*[1,2†], *Bixue Huang*[1,2], *JinCangjian Sun*[1,2], *Jiahui Li*[1,2], *Huiwen Zhuang*[1,2] *and Guanxia Xiong*[1,2*]

[1]*Department of Otorhinolaryngology, The First Affiliated Hospital, Sun Yat-sen University, Guangzhou, China,* [2]*Institute of Otorhinolaryngology, Sun Yat-sen University, Guangzhou, China*

OPEN ACCESS

Edited by:
Meryem Ayse Yücel,
Boston University, United States

Reviewed by:
Xiaosu Hu,
University of Michigan, United States
Rebecca Susan Dewey,
University of Nottingham, United Kingdom
Sonja Rossi,
Innsbruck Medical University, Austria

***Correspondence:**
Guanxia Xiong
xgx001@163.com

[†]*These authors have contributed equally to this work*

Specialty section:
This article was submitted to Brain Imaging and Stimulation, a section of the journal Frontiers in Human Neuroscience

Received: *31 October 2019*
Accepted: *06 April 2020*
Published: *28 April 2020*

Citation:
Sun Q, Wang X, Huang B, Sun J, Li J, Zhuang H and Xiong G (2020) Cortical Activation Patterns of Different Masking Noises and Correlation With Their Masking Efficacy, Determined by Functional Near-Infrared Spectroscopy. Front. Hum. Neurosci. 14:149. doi: 10.3389/fnhum.2020.00149

Acoustic therapy in tinnitus treatment is poorly characterized, and efficacy assessment depends on subjective descriptions. Narrow-band noise, notched sound, and white noise have positive therapeutic effects on monotonous tinnitus. Considering the tonotopic characteristics of the auditory system and the spectral characteristics of these three masking sounds, the activation pattern of the auditory cortex and the mechanism of inhibiting tinnitus may be different. This study aimed to compare the activation patterns of three spectrally different masking noises and study the correlation between the masking effects and variational amplitude of oxygenated hemoglobin (HbO) in the corresponding cortical regions. We also assessed near-infrared spectroscopy brain function imaging (NIRS) as an objective assessment tool in acoustic therapy. Patients with persistent non-pulsatile tinnitus and control volunteers without tinnitus were enrolled in this study. The subjects were seated in a sound-proof room, with two optode arrays covering the bilateral temporal lobe. Auditory stimuli were presented; stimulation sequences followed the block design: different noises appeared randomly and repeated in five cycles. Tinnitus match and residual inhibition were performed in the tinnitus group. The data analyses were conducted using the NIRS_SPM toolbox. The group analysis results showed that the narrow-band noise caused a marginally significant decrease in HbO signal in the Brodmann 21 region (BA21), while white noise caused a significant increase in HbO signal in BA21. Notched sound did not cause significant changes in the HbO signal in the temporal cortex. And none of the three masking noises caused significant changes in the HbR signal in the temporal cortex. The depth of residual inhibition induced by the narrow-band noise and white noise significantly correlated with ΔHbO in the region of interest (ROI). However, neither the depth nor duration of the residual inhibition induced by notched sound correlated with the ΔHbO. Thus, NIRS showed three cortical activation patterns induced by three different masking noises, and correlations between residual inhibition effects and change of HbO amplitude were found. NIRS could therefore be applied in objective assessment of acoustic therapy.

Keywords: NIRS, tinnitus, acoustic therapy, masking noise, auditory cortex

INTRODUCTION

Tinnitus is defined as phantom sound perception in the absence of an external sound source and is experienced by 10–15% of the general population (Sereda et al., 2018). Tinnitus may cause anxiety, depression, sleep disorders, and deterioration of social function. The proportion of individuals who typically seek medical help for tinnitus is 1% to 2%. The mechanism of tinnitus remains unclear and likely involves a complex network comprising non-auditory centers including the posterior parietal, frontal, somatosensory, and limbic regions. Tinnitus is primarily a physio-pathological change in the auditory system; compensatory changes in the central auditory system triggered by peripheral hearing loss may be one of the key factors that underlie tinnitus (Noreña and Eggermont, 2003, 2005; Vanneste et al., 2010; Pape et al., 2014; Noreña, 2015).

To understand the mechanism of tinnitus and optimize its treatment, three key features of the normal functioning auditory system have to be considered. First, the spontaneous firing of neurons that occurs throughout the peripheral and central auditory nervous systems; even in the absence of sound in the environment, there is some level of nerve firing or spontaneous firing within the auditory nervous system (San Juan et al., 2017). Second, tonotopicity is maintained from the level of the basilar membrane of the cochlea to the central auditory structures and auditory cortex. Changes in tonotopicity with auditory system damage might be associated with tinnitus (Eggermont and Roberts, 2004). Third, neural synchrony, or the balance of excitatory and inhibitory neural firing within the central auditory system, must be maintained to preserve the neural coding of auditory input (Noreña and Farley, 2013). Excitation and inhibition are important neural functions within the auditory pathway (Pickles, 2008). When transduction occurs within the inner ear, all fibers of the auditory nerve are excited, with no inhibition. Once the fibers reach the central auditory nervous system, however, different groups of neurons respond differently to stimulation. Some groups of neurons are primarily excitatory whereas others are primarily inhibitory. Current theories of the origin of tinnitus-related to abnormalities in spontaneous firing rate, tonotopicity, and/or neural synchrony.

There are no effective drugs or surgical treatments for tinnitus; acoustic therapy has been broadly accepted as a safe and convenient choice. Besides the instant masking effect to the phantom sound, after a certain period of acoustic therapy, tinnitus loudness and negative emotion related to tinnitus reported by patients reduced (Roberts et al., 2015; Zenner et al., 2017; Schad et al., 2018; Brennan-Jones et al., 2019; Neff et al., 2019). These reports have led to the hypothesis that proper masking therapy can alter patients' tinnitus state by affecting the remapping of the auditory cortex (Pantev et al., 2012). However, the nature of subjective tinnitus makes it difficult to evaluate through objective and quantitative indicators. The symptom of tinnitus can only be reported by the patient, and physicians give their sound prescriptions depending on personal experience and feedback from patients. Thus, current tinnitus treatment largely involves trial and error.

Objective changes caused by tinnitus have been studied to some extent. Noreña and Eggermont (2005) found that the resting state network of the hypothalamus and the Heschl's gyrus was significantly enhanced in patients with tinnitus compared to healthy controls, and correlated with the reported tinnitus loudness. By applying Auditory Brainstem Response (ABR), Gu et al. (2012) found that the amplitudes of I and V waves in patients with tinnitus were significantly higher than those in healthy controls. Although these findings were based on strict matches between the tinnitus and control groups, and are not yet considered a diagnostic basis, they suggest the potential value of brain function study in the objective examination of tinnitus. We considered whether the effects of different masking noises could be distinguished and whether the therapeutic effects of such masking sounds could be evaluated by brain functional imaging.

According to a magnetoencephalography (MEG) study, patients with tinnitus receiving a one-year treatment of Tailor-Made Notched Music (TMNM), showed a reduction in tinnitus-related cortical activity that was significantly greater than that in the placebo-controlled patients (Okamoto et al., 2010). To date, brain functional imaging studies for masking noise have mainly focused on resting-state (Xu et al., 2015; San Juan et al., 2017). There have been no brain functional imaging studies to observe the activation patterns of different masking sounds. This could be because of incompatibility between existing brain functional imaging methods and auditory tasks, e.g., the profound noise of fMRI.

Compared with traditional brain function imaging technology, near-infrared spectroscopy brain function imaging equipment has the advantages of no ionizing radiation, electromagnetic compatibility, and low noise, which make it highly suited to application in auditory tasks (Sevy et al., 2010). Moreover, the good temporal and spatial resolution may prove useful in demonstrating the brain functional effect of acoustic therapy intuitively, which could, in turn, be applied as an objective indicator of acoustic therapy. This study aimed to use fNIRS to clarify whether different masking noises with contrasting spectra (e.g., narrow-band noise, notched sound, and white noise) induce distinguishable activation patterns and if the amplitude in the corresponding region of interest (ROI) correlates with clinical indicators (e.g., residual inhibition) in patients with tinnitus.

MATERIALS AND METHODS

Participants

Healthy subjects in the control group were volunteers from the Sun Yat-sen University. The tinnitus group consisted of patients with tinnitus from the otolaryngology clinic of the First Affiliated Hospital of Sun Yat-sen University. After tinnitus matching test and pure tone hearing threshold test, the subjects were included according to the following inclusion and exclusion criteria (**Table 1**). Our otologist conducted clinical evaluation among the recruited subjects by reviewing medical history and out-patient documentation. The patients' description of their tinnitus symptoms allowed us to determine whether they had

TABLE 1 | Inclusion and exclusion criteria for participants.

	Control group	Tinnitus group
Inclusion criteria	General population	Complaint of consistent tinnitus lasting for more than 3 months; tinnitus pitch falls between 4,000 Hz and 8,000 Hz
Exclusion criteria	Persistent tonal or pulse-like tinnitus; unstable hypertension; trauma history such as a temporal bone fracture; the history of middle-ear surgery; psychotic symptoms; neurological diseases such as stroke or epilepsy.	Unstable hypertension; a history of trauma such as a temporal bone fracture; the history of middle-ear surgery; psychotic symptoms; neurological disease such as stroke or epilepsy; pulse-like tinnitus; severe sensorineural or conductive hearing loss.

tonal tinnitus or a possible psychotic symptom, which is usually accompanied by other psychotic symptoms like delusion and sensory disturbance. This study was approved by the ethics committee of the First Affiliated Hospital of Sun Yat-sen University. All subjects gave written informed consent following the Declaration of Helsinki.

Audiometric Evaluation and Tinnitus Test

The hearing threshold was measured for both groups at a frequency range of 250–8,000 Hz with calibrated pure tone audiometry in a soundproof audio booth. For patients with tinnitus, tinnitus matching was performed to identify the tinnitus pitch and residual inhibition caused by three different masking sounds. The patients with tinnitus underwent tinnitus matching in a soundproof room, where the Tinnifit (Bozy Medical Technology Limited, Foshan, China) was used to play pure tones at different frequencies through headphones. We asked the patients if the exogenous sound was similar to their tinnitus, and thereby determined the tinnitus pitch of each patient. The residual inhibition, a temporary suppression of tinnitus after the termination of the external masking noise, was then determined. We played three masking sounds through the speaker directly in front of the patient at 70 dB SPL for 20 s. The patients were then asked whether they experienced a temporary suppression of tinnitus, and how long this suppression lasted. This information was used to determine residual inhibition. For example, if a patient reported that tinnitus was suppressed by 50% for 10 s, then the depth and duration of residual inhibition was recorded as "50%*10 s." Some patients could have a tinnitus rebound when the masking sound ended (e.g., 50% louder and lasted for 10 s; in this case, the residual inhibition was recorded as −50%*10 s).

Auditory Stimuli and Presenting Procedure

Three masking sounds, which are widely used in clinical practice, were chosen as auditory stimuli. The white noise was generated as a basic tone by using Adobe Audition, and the narrow-band noise and notched sound were created by band-passing and band-stopping the 4,000 Hz–8,000 Hz spectrum, respectively (**Figure 1**).

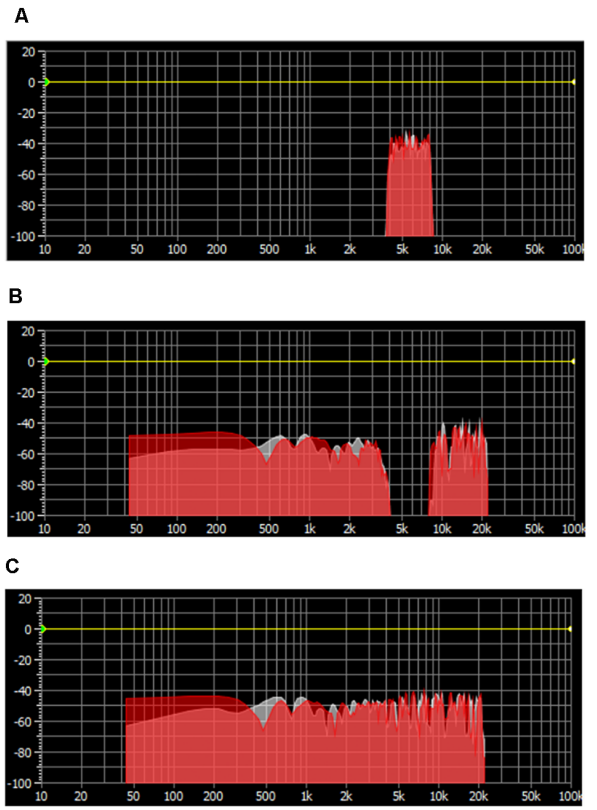

FIGURE 1 | Spectrum distribution of three masking noises. **(A)** Narrow-band noise with energy clustering around 6,000 Hz. **(B)** Notched sound with an "Energy Gap" centered at 6,000 Hz. **(C)** White noise with an equally distributed spectrum energy.

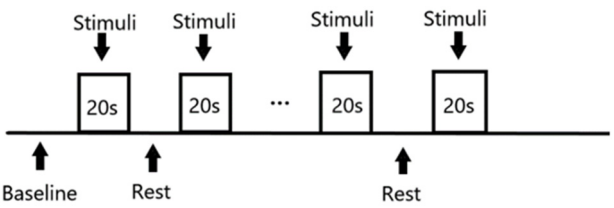

FIGURE 2 | Design of stimuli presentation.

The stimulation of the study were presented through the Eprime2.0 (Psychology Software Tools, Inc., Pittsburgh, PA, USA) tool. The stimulation sequence followed a block design (**Figure 2**): Each of the three masking sounds ran for five blocks, where one block consisted of 20 s stimulation alternating with 20 s silence. The program therefore comprised 15 blocks and a 20 s baseline, with a total duration of 620 s. Moreover, considering the effect of decreased attention and inadvertent motion of participants, these blocks were distributed randomly to avoid uneven influence upon the results of different masking sounds.

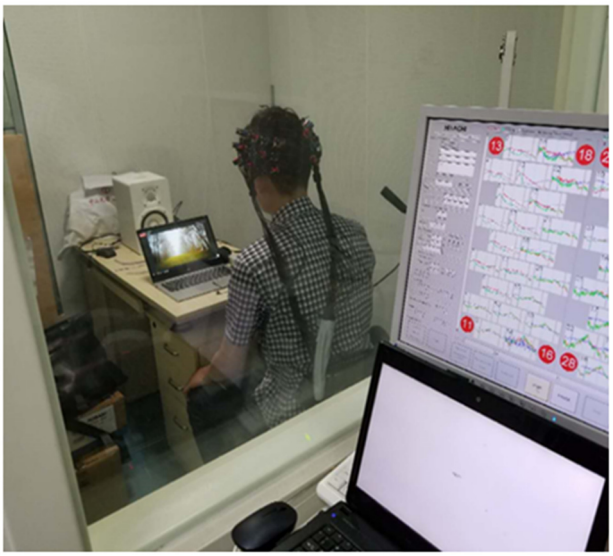

FIGURE 3 | Testing facility and environment.

During the auditory stimulation, the subjects were asked to listen to the masking noises passively; they were not required to make any response or remember the sequence of different noises.

Test Environment and Optode Localization

Experiments were conducted in a soundproof room (**Figure 3**) with background noise less than 30 dB SPL. Auditory stimuli were presented through a sound speaker placed 75 cm in the front of the subject. The sound intensity was coordinated at 70 dB SPL. All data were acquired on a Hitachi ETG4000 (Hitachi Medical Corporation, Tokyo, Japan) optical topography system with 30 optodes (16 sources and 14 detectors) arranged in two pre-defined 3*5 holder arrays, ensuring sources and detectors at fixed separations of 3 cm. These two arrays were placed over the left and right temporal regions aiming to mainly cover the bilateral auditory cortex, while the frontal and parietal lobe was involved. Infrared light was produced at two wavelengths (695 nm and 830 nm), and sampled with a frequency of 10 Hz. As shown in **Figure 4**, to standardize array placement, the optode arrays were placed with the central optode directly above the preauricular point on the line connecting T3/T4 and CZ using the 10-20 system (Niedermeyer and Lopes da Silva, 2005).

Considering the optical characteristics of the fNIRS device, poor contact between optodes and the skull is a major source of artifacts. To improve signal quality, we carefully removed unnecessary hair at contact points, adjusted the angle of optodes, and ran the signal check program pre-installed in the ETG 4000. We did not start the next step until all the channels passed the signal check. Another source of artifacts is motion (e.g., slight head moment) of the subject. This motion could cause changes in the blood flow, which leads to fluctuations in the measured hemodynamic response. A crude way to correct for motion artifacts is to average a certain number of experiments.

Data Preprocessing and Statistical Analyses

The fNIRS data analysis was performed using the NIRS_SPM toolbox (Tak and Ye, 2011; Bio Imaging Signal Processing Lab. Department of Bio and Brain Engineering, KAIST, Korea). Initially, optical density data were converted into concentration changes of oxy- and deoxy-hemoglobin by using the modified Beer–Lambert law (MBLL) with (Delpy et al., 1988). We then used the time series analysis routine, comprising temporal smoothing using canonical hemodynamic response function (hrf) and wavelet-MDL detrending algorithm (Jang et al., 2009), to remove unknown global trends due to breathing, cardiac, vaso-motion, or other experimental errors. After the definition of the onset point and duration of each stimulus block, the individual analysis ran automatically. The fNIRS response time courses were fit to a general linear model (GLM) of the stimulus time-course convolved with a canonical hemodynamic response function implemented in SPM 8 software (Wellcome Trust Centre for Neuroimaging, UCL, UK, 2009), resulting in the calculation of the optimal parameter estimate (beta value) of the contribution of the stimulus to the response. Beta value estimates were calculated for each participant, channel, and stimulus separately. Beta values were then averaged across each ROI and shown as ΔHbO, providing a measure of each participant's response to each of the three masking sounds. Group analyses were then conducted to obtain activation maps of the three different stimuli.

Statistical analysis was conducted using SPSS (version 20.0; SPSS Inc., Chicago, IL, USA). Multivariate linear regression was performed to determine the effect of age and hearing threshold on HbO response. Multivariate analysis of variance was performed to determine the main effect and interaction effect of factors such as masking noise, group, ROIs, and hemisphere. All these factors were integrated evenly, and the LSD's method was used to adjust the p-values for multiple comparisons. Pearson correlations were then computed between the activation levels and the residual inhibition data. In all analyses, $P < 0.05$ was taken to indicate statistical significance.

Definition of ROI

In this study, two ROIs were selected based on previous reports on the auditory cortex and the group analysis activation image. The ROIs were the bilateral STC and the bilateral BA21 zone. The bilateral STC is a classical audiology task interest area (including channels 7, 11, 12, 29, 33, and 34), and the BA21 area was drawn according to the activation pattern of different acoustic stimuli in this study (including channels 1, 2, 3, 23, 24, and 25).

RESULTS

Clinical Data

The relevant clinical data are presented in **Tables 2**, **3**, and **Figure 5**. There were significant differences in age and average

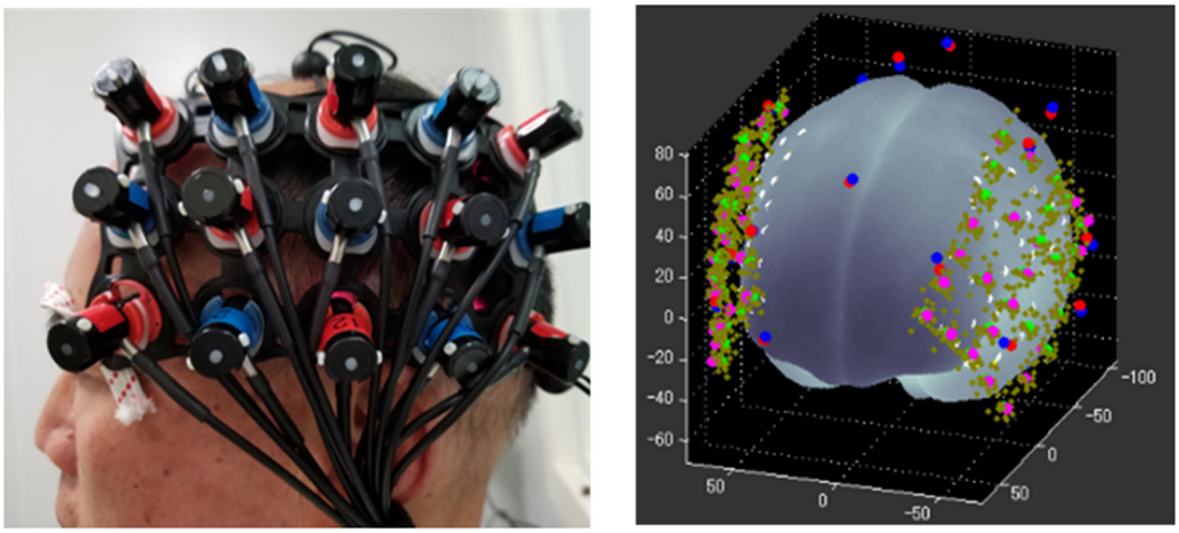

FIGURE 4 | Optode array and spatial registration.

TABLE 2 | Age and hearing threshold in the control and tinnitus groups.

Group	Control ($\bar{x} \pm SD$)	Tinnitus ($\bar{x} \pm SD$)	X^2	p
Age (year)	30.85 ± 5.68	36.77 ± 9.56	9.622	0.048
R500 Hz (dB HL)	15.75 ± 5.91	20.00 ± 4.56	5.629	0.235
R1000 Hz (dB HL)	13.75 ± 7.76	17.69 ± 5.25	3.475	0.667
R2000 Hz (dB HL)	15.25 ± 7.69	19.23 ± 5.72	3.683	0.882
R4000 Hz (dB HL)	16.25 ± 7.41	20.00 ± 8.17	4.515	0.508
R8000 Hz (dB HL)	14.25 ± 6.34	25.77 ± 8.38	13.182	0.036
L500 Hz (dB HL)	15.25 ± 4.13	18.85 ± 5.83	9.183	0.038
L1000 Hz (dB HL)	14.5 ± 4.84	15.39 ± 5.19	2.958	0.652
L2000 Hz (dB HL)	15.75 ± 5.45	18.46 ± 6.25	5.179	0.398
L4000 Hz (dB HL)	16.25 ± 5.82	21.54 ± 8.75	9.343	0.151
L8000 Hz (dB HL)	12.25 ± 6.38	24.23 ± 11.34	17.706	0.003

hearing threshold at 8,000 Hz between the control and tinnitus groups. However, multivariate linear regression results showed that the effect of age ($\beta = -0.24$, $t = -1.277$, $p = 0.212$) and average hearing threshold in 8,000 Hz (Left ear: $\beta = -0.069$, $t = -0.201$, $p = 0.842$; Right ear: $\beta = 0.229$, $t = 0.646$, $p = 0.523$) on HbO response were insignificant.

Multivariate Analysis of Variance

A global ANOVA with the factors masking noise, group, ROIs, and hemisphere was conducted. As shown in **Table 4**, only the type of masking noise showed significant main effects on the HbO signal ($df = 2$, $F = 11.759$, $P < 0.05$), and no significant interaction effects were found (not shown in the table). In this case, multiple comparisons between three different masking noises were conducted. As shown in **Table 6**, the HbO signal in selected ROIs induced by white noise was significantly larger than that induced by the other two masking noises, while the results between narrow-band noise and the notched sound did not show significant differences. The same procedure was also applied for HbR signal, as shown in **Table 5**, no significant main effect or interaction effect on HbO signal was found.

TABLE 3 | Tinnitus matching and residual inhibition.

Number	Tinnitus pitch	Sides	Duration (months)	Residual inhibition (Depth*Duration)		
				Narrow-band noise	Notched sound	White noise
Subject 1	6,000 Hz	B	12	30%*5s	−20%*1s	30%*4s
Subject 2	6,000 Hz	B	36	20%*3s	0	50%*4s
Subject 3	6,000 Hz	B	6	20%*5s	0	20%*1s
Subject 4	6,000 Hz	B	6	60%*2s	−10%*1s	20%*5s
Subject 5	6,100 Hz	B	6	30%*3s	−10%*1s	100%*2s
Subject 6	6,000 Hz	B	12	10%*1s	0	10%*1s
Subject 7	6,000 Hz	R	3	0	0	50%*4s
Subject 8	8,000 Hz	B	10	0	−20%*2s	20%*2s
Subject 9	8,000 Hz	L	60	10%*2s	0	10%*2s
Subject 10	6,000 Hz	B	48	10%*6s	0	20%*2s
Subject 11	6,000 Hz	B	3	10%*5s	0	30%*2s
Subject 12	6,000 Hz	R	5	0	0	0
Subject 13	7,336 Hz	R	5	10%*1s	−30%*1s	100%*2s

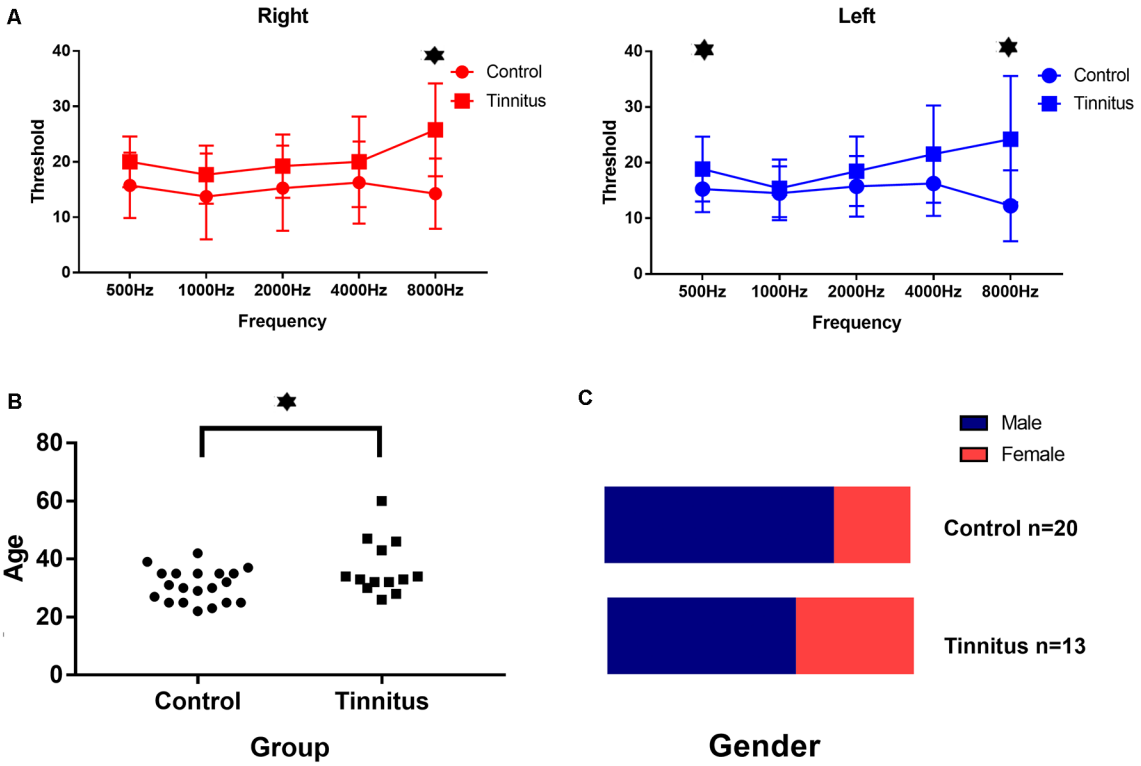

FIGURE 5 | Clinical data in both group. **(A)** The average hearing threshold at 8,000 Hz for both ears and at 500 Hz for the left ear in the tinnitus group was significantly higher than that in the control group. **(B)** The average age of the tinnitus group was 37 ± 9 years and the average age of the control group was 31 ± 6 years: the difference was significant. **(C)** There was no significant difference in the ratio of gender between both two groups. *Statistically significant/$p < 0.05$.

TABLE 4 | Results of multivariate analysis of variance (HbO).

Source of variation	SS	df	MS	F	*P*
Mask	10.303	2	5.151	11.759	0.000
Group	0.275	1	0.275	0.628	0.429
Hemisphere	0.000	0	.	.	.
ROI	0.025	2	0.012	0.028	0.972
Error	170.413	389	0.438		
Total	185.089	396			

TABLE 5 | Results of multivariate analysis of variance (HbR).

Source of Variation	SS	df	MS	F	*P*
Mask	0.066	2	0.033	1.993	0.138
Group	0.011	1	0.011	0.670	0.414
Hemisphere	0.000	0	.	.	.
ROI	0.035	2	0.018	1.060	0.347
Error	6.196	372	0.017		
Total	6.760	396			

Activation Patterns of the Three Different Masking Noises

The group analysis results from 33 individuals (**Figure 6A**) showed that the narrow-band noise caused a marginally significant decrease in HbO signal in the BA21 region of the bilateral temporal lobe, suggesting that the excitability of BA21 region decreased (F = 12.209, P = 0.055, Expected Euler characteristic corrected). White noise caused a significant increase in HbO signal in BA21 region, indicating that the excitability of the BA21 region increased (F = 12.543, $P < 0.05$, Expected Euler characteristic corrected). Notched sound did not cause significant changes in the HbO signal in the temporal cortex.

In terms of HbR results, the group analysis results from 33 individuals (**Figure 6B**) showed that narrow-band noise (F = 1.3932, $P > 0.05$, Expected Ec corrected), notched sound (F = 5.8659, $P > 0.05$, Expected Ec corrected) and white noise (F = 7.073, $P > 0.05$, Expected Ec corrected) did not cause significant changes in the HbR signal in the temporal cortex.

TABLE 6 | Multiple comparison between three different masking noises.

	(I) mask	(J) mask	Mean difference (I-J)	Standard error	*P*
LSD	1	2	−0.05466971	0.081471291	0.503
		3	−0.36620861*	0.081471291	0.000
	2	1	0.05466971	0.081471291	0.503
		3	−0.31153890*	0.081471291	0.000
	3	1	0.36620861*	0.081471291	0.000
		2	0.31153890*	0.081471291	0.000

*Mask 1, 2, and 3 indicate narrow-band noise, notched sound, and white noise, respectively. *Statistically significant/$p < 0.05$.*

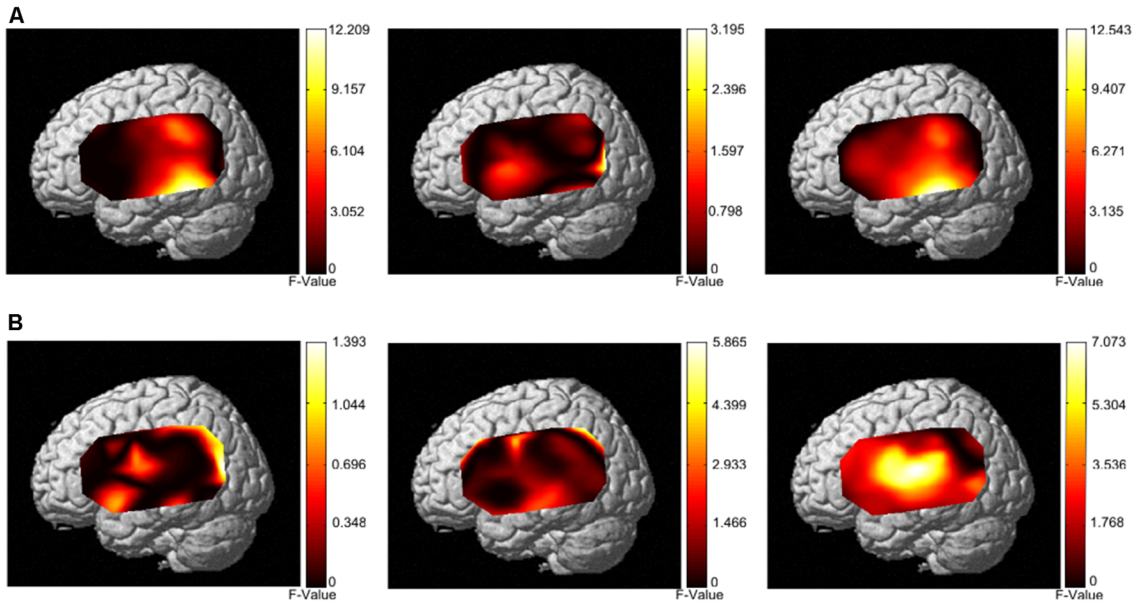

FIGURE 6 | Activation patterns of the three different masking noises. **(A)** Activation patterns based on HbO data from both the control group and tinnitus group under stimulation with narrow-band noise notched sound, and white noise. **(B)** Activation patterns based on HbR data from both the control group and tinnitus group under stimulation with narrow-band noise, notched sound, and white noise.

Correlation Between fNIRS Data And Residual Inhibition

Pearson correlation analysis was performed for the residual inhibition results and the amplitude of ΔHbO in each ROI (**Figure 7**). The depth of residual inhibition by narrow-band noise was negatively correlated with the ΔHbO in the bilateral STC ($r = -0.6209$, $p = 0.02$) and the BA21 ($r = -0.74$, $p = 0.01$). The duration was not significantly correlated with the ΔHbO amplitude in the bilateral STC ($r = -0.2$, $p = 0.5$) and BA21 ($r = -0.35$, $p = 0.23$). There was no significant correlation between the ΔHbO and depth of the residual inhibition caused by the notched sound in bilateral STC ($r = 0.07$, $p = 0.8$) and BA21 ($r = 0.06$, $p = 0.8$). The depth of the residual inhibition by white noise and the ΔHbO were positively correlated in the bilateral STC ($r = 0.65$, $p = 0.02$) and BA21 ($r = 0.57$, $p = 0.03$), and the duration of RI by the white noise showed a marginally significant correlation with the amplitude of ΔHbO in the bilateral STC ($r = 0.52$, $p = 0.06$) and BA21 areas ($r = 0.57$, $p = 0.05$).

DISCUSSION

Although the clinical effects of different types of masking noises have been extensively studied (Aytac et al., 2017; Rocha and Mondelli, 2017; Li et al., 2019; Tyler et al., 2020), there is no consensus on how to choose the optimal masking sound for specific therapy. Considering the clinical requirements for personalized and customized acoustic therapy, existing RCT studies on different masking sounds have limited value for clinical applications. Further studies on objective assessment for tinnitus and different masking sounds are needed to accurately predict the clinical outcome of different stimulations and conduct efficient acoustic therapy. In this study, we used a cross-sectional method to explore whether functional near-infrared spectroscopy technology could be used to detect different cortical activation characteristics of three representative masking sounds in the clinic and to determine whether the masking effect of different noises is related to the amplitude of ΔHbO in the corresponding cortical regions. Our results illustrate the potential of fNIRS technology in demonstrating the mechanism of different masking sounds and as an objective reference for clinical masking sound fitting.

There was a significant difference in mean age and the pure tone hearing threshold between the tinnitus group and the control group. Considering the control group in this study mostly comprised medical school students, the mean age and high-frequency hearing threshold failed to match. Previous studies have confirmed that different acoustic stimulation intensities (40 dB and 70 dB) induce different amplitudes of ΔHbO in the temporal cortex (Bauernfeind et al., 2016). To determine the effects of age and high-frequency hearing threshold mismatch on NIRS data, we performed multivariate linear regression analysis in this study and found no significant effect of age and hearing threshold (data not shown). Thus, although the mean age and high-frequency hearing threshold failed to match, the results of this study remain relevant.

Considering there is no significant change in HbR signal induced by three masking noise, it seems the HbO and HbR responses of three masking noise did not meet the classic definition of "activation," which refers to an increasing HbO signal along with a decreasing HbR signal. In another fNIRS study on tinnitus patients, the HbO signal was considered as

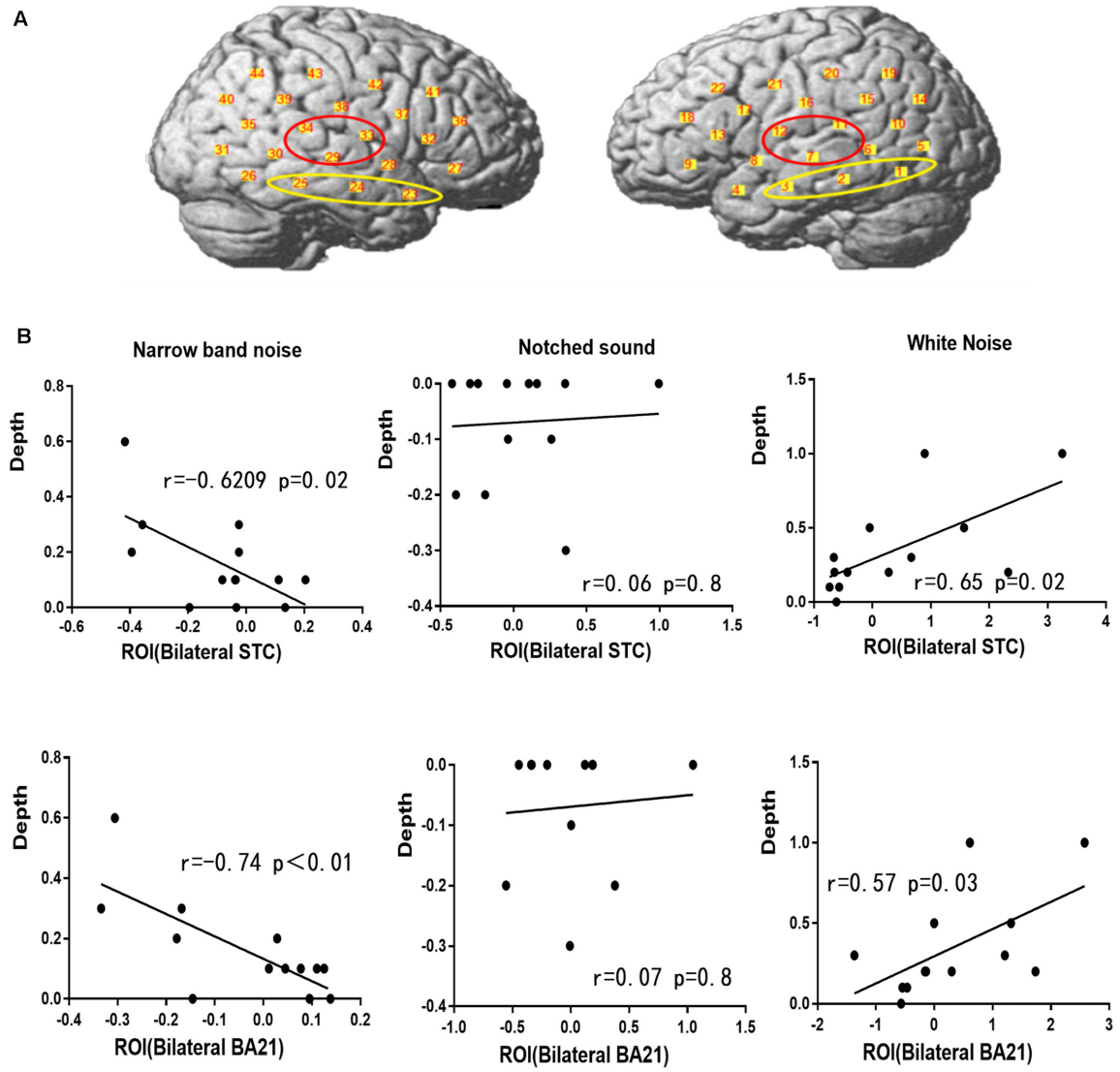

FIGURE 7 | Regions of interest (ROIs) and correlation between ΔHbO and residual inhibition. **(A)** The red circle represents the bilateral STC ROI and the yellow circle represents the BA21 ROI. **(B)** Correlation between ΔHbO and residual inhibition in BA21 and STC.

a more robust index of underlying neural activity, because of the correlations between the canonical model of the hemodynamic response function and models of HbO (vs. HbR) are consistently higher (Issa et al., 2016). Similar findings were reported from an fNIRS study on cochlear implant users, which involved only HbO data in correlation analysis with speech understanding ability (Zhou et al., 2018). Thus, the correlation analysis was based on HbO data in this study.

There has not been a detailed description and physiological explanation of the cortical activation patterns of different masking sounds. Previous functional magnetic resonance studies have shown that the area of the auditory cortex that typically responds to pure-tone stimulation of different frequencies is mainly located in the Heschl's gyrus. The typical phoneme arrangement is characterized as low frequency at both ends and high frequency at the center of the Heschl's gyrus (Moerel et al., 2018). However, our pre-test result showed that the high-low frequency pure tone stimulation did not yield a significant activation and the activation patterns were not completely consistent with the fMRI results (data not shown). Due to the large variance in temporal and spatial resolution between fNIRS and fMRI, and poor repeatability of cortical activation by auditory stimuli, fNIRS results cannot be directly compared to fMRI data. The inconsistency between the fNIRS and fMRI results needs further study, suggesting that the relevant activation patterns demonstrated by fNIRS should be interpreted more cautiously. Furthermore, while it is predictable that the white noise-induced activation response in the BA21, the "deactivation" induced by narrow-band noise was unexpected.

BA21 is part of the temporal cortex in the human brain. The region encompasses most of the lateral temporal cortex, a region believed to play a part in auditory processing and language. Several neural imaging studies have shown functional abnormalities in BA21 among patients with chronic tinnitus (Andersson et al., 2000; Farhadi et al., 2010). White noise is believed to induced "synchrony" in the auditory cortex due to its evenly distributed energy on the spectrum, which might gradually eliminates the perception of tonal tinnitus through rebalancing the excitatory and inhibitory neural interactions within the auditory cortex (Eggermont and Roberts, 2004). In our study, white noise led to a significant increased HbO signal in BA21, which is in line with the "synchrony" theory. As for the deactivation response, a PET study (Mirz et al., 1999) showed that complex auditory stimuli like semantic material and music activated BA21 in contrast with simple auditory stimuli (e.g., pure tone), and suggested that such deactivation responses might be a manifestation of a decrease in attentional resources allocated to brain structures irrelevant to the task. However, unlike the difference between semantic material and pure tone, the major difference between narrow-band noise and white noise is the energy distribution on the spectrum. How such differences can trigger the reallocation of attentional resources in BA21 remains unclear. Thus, we were unable to completely interpret the auditory cortex activation pattern of different masking sounds in this study but showed the potential of fNIRS for the discovery of different characteristics of masking sounds in the context of brain function.

Narrow-band noise, notched sound, and white noise are the most common clinically used sounds. The residual inhibition corresponding to notched sound in this study was significantly inferior to that of narrow-band noise and white noise, and some patients reported a brief increase in tinnitus loudness after listening to the notched sound. The Tinnitus Handicap Index (THI) of the patients decreased significantly after the application of notched sound therapy, which is not in agreement with the inferiority of notched sound in residual inhibition since it is widely accepted that residual inhibition is an indicator for predicting clinical outcome in acoustic therapy. The Zwicker effect describes a short-lived tinnitus-like feeling when a person listens to a sound with a narrow-band gap in a spectrum of energy (Franosch et al., 2003). This effect may explain why the notched sound did not induce residual inhibition and even caused tinnitus to rebound. Therefore, notched sound could be an exception in terms of residual inhibition.

A major feature of subjective tinnitus is the difficulty to perform an objective and quantitative assessment, which restricts the development of treatments. As shown in our study, fNIRS data is correlated with existing behavioral indicators such as residual inhibition. The depth of residual inhibition by narrow-band noise was negatively correlated with the ΔHbO in the bilateral STC and the depth of the residual inhibition by white noise and the ΔHbO in the bilateral STC and BA21 were positively correlated. These results reveal the potential value of fNIRS as an objective indicator of masking effects. In the future, we could use fNIRS data as an objective evaluation indicator to predict the clinical outcome of acoustic therapy. However, this cross-sectional study only demonstrated the correlation between fNIRS data and the residual inhibition, which is only an indirect indicator of long-term clinical outcomes. Moreover, the mechanism of tinnitus likely involves a complex network comprising non-auditory centers, including the posterior parietal, frontal, somatosensory, and limbic regions. In this study, although the optode positions covered some of these areas, we mainly focused on the temporal region. A prospective study is needed to determine the correlation between fNIRS results and clinical outcomes.

DATA AVAILABILITY STATEMENT

The datasets generated for this study are available on request to the corresponding author.

ETHICS STATEMENT

The studies involving human participants were reviewed and approved by The ethics committee of the First Affiliated Hospital of Sun Yat-sen University. The patients/participants provided their written informed consent to participate in this study.

AUTHOR CONTRIBUTIONS

QS and XW as the first authors contributed equally in the conception and design of the study and organized the database and performed the statistical analysis. QS wrote the first draft of the manuscript. BH, JL, and JS wrote sections of the manuscript. QS, XW, BH, JS, JL, HZ, and GX contributed to manuscript revision, read and approved the submitted version.

FUNDING

We disclose receipt of the following financial support for the research, authorship, and/or publication of this article: this research was supported by grants from the National Natural Science Fund of China (81200748), the Natural Science Fund of Guangdong Province (2018A030313112), and the Science Plan Fund of Guangzhou (201803010033).

REFERENCES

Andersson, G., Lyttkens, L., Hirvelä, C., Furmark, T., Tillfors, M., and Fredrikson, M. (2000). Regional cerebral blood flow during tinnitus: a PET case study with lidocaine and auditory stimulation. *Acta Otolaryngol.* 120, 967–972. doi: 10.1080/00016480050218717

Aytac, I., Baysal, E., Gulsen, S., Tumuklu, K., Durucu, C., Mumbuc, L. S., et al. (2017). Masking treatment and its effect on tinnitus parameters. *Int. Tinnitus J.* 21, 83–89. doi: 10.5935/0946-5448.20170017

Bauernfeind, G., Haumann, S., and Lenarz, T. (2016). fNIRS for future use in auditory diagnostics. *Curr. Dir. Biomed. Eng.* 2, 229–232. doi: 10.1515/cdbme-2016-0051

Brennan-Jones, C. G., Thomas, A., Hoare, D. J., and Sereda, M. (2019). Cochrane corner: sound therapy (using amplification devices and/or sound generators) for tinnitus. *Int. J. Audiol.* 59, 161–165. doi: 10.1080/14992027.2019.1643503

Delpy, D. T., Cope, M., van der Zee, P., Arridge, S., Wray, S., and Wyatt, J. (1988). Estimation of optical pathlength through tissue from direct time of flight measurement. *Phys. Med. Biol.* 33:1433.

Eggermont, J. J., and Roberts, L. E. (2004). The neuroscience of tinnitus. *Trends Neurosci.* 27, 676–682. doi: 10.1016/j.tins.2004.08.010

Farhadi, M., Mahmoudian, S., Saddadi, F., Karimian, A. R., Mirzaee, M., Ahmadizadeh, M., et al. (2010). Functional brain abnormalities localized in 55 chronic tinnitus patients: fusion of spect coincidence imaging and MRI. *J. Cereb. Blood Flow Metab.* 30, 864–870. doi: 10.1038/jcbfm.2009.254

Franosch, J. M. P., Kempter, R., Fastl, H., and van Hemmen, J. L. (2003). Zwicker tone illusion and noise reduction in the auditory system. *Phys. Rev. Lett.* 90:178103. doi: 10.1103/physrevlett.90.178103

Gu, J. W., Herrmann, B. S., Levine, R. A., and Melcher, J. R. (2012). Brainstem auditory evoked potentials suggest a role for the ventral cochlear nucleus in tinnitus. *J. Assoc. Res. Otolaryngol.* 13, 819–833. doi: 10.1007/s10162012-0344-1

Issa, M., Bisconti, S., Kovelman, I., Kileny, P., and Basura, G. J. (2016). Human auditory and adjacent nonauditory cerebral cortices are hypermetabolic in tinnitus as measured by functional near-infrared spectroscopy (fNIRS). *Neural Plast.* 2016:7453149. doi: 10.1155/2016/7453149

Jang, K. E., Tak, S., Jung, J., Jang, J., Jeong, Y., and Ye, J. C.. (2009). Wavelet-MDL detrending for near-infrared spectroscopy (NIRS). *J. Biomed. Opt.* 14, 1–13. doi: 10.1117/12.764141

Li, Y., Feng, G., Wu, H., and Gao, Z. (2019). Clinical trial on tinnitus patients with normal to mild hearing loss: broad band noise and mixed pure tones sound therapy. *Acta Otolaryngol.* 139, 284–293. doi: 10.1080/00016489.2019.1575522

Mirz, F., Ovesen, T., Ishizu, K., Johannsen, P., Madsen, S., Gjedde, A., et al. (1999). Stimulus-dependent central processing of auditory stimuli: a PET study. *Scand. Audiol.* 28, 161–169. doi: 10.1080/010503999424734

Moerel, M., De Martino, F., Kemper, V. G., Schmitter, S., Vu, A. T., Uğurbil, K., et al. (2018). Sensitivity and specificity considerations for fMRI encoding, decoding and mapping of auditory cortex at ultra-high field. *NeuroImage* 164, 18–31. doi: 10.1016/j.neuroimage.2017.03.063

Neff, P., Zielonka, L., Meyer, M., Langguth, B., Schecklmann, M., and Schlee, W. (2019). Comparison of amplitude modulated sounds and pure tones at the tinnitus frequency: residual tinnitus suppression and stimulus evaluation. *Trends Hear.* 23:2331216519833841. doi: 10.1177/2331216519833841

Niedermeyer, E., and Lopes da Silva, F. (2005). *Electroencephalography: Basic Principles, Clinical Applications, and Related Fields*. Philadelphia, USA; London, UK: Lippincott Williams & Wilkins.

Noreña, A. J. (2015). Revisiting the cochlear and central mechanisms of tinnitus and therapeutic approaches. *Audiol. Neurootol.* 20, 53–59. doi: 10.1159/000380749

Noreña, A. J., and Eggermont, J. J. (2003). Changes in spontaneous neural activity immediately after an acoustic trauma: implications for neural correlates of tinnitus. *Hear. Res.* 183, 137–153. doi: 10.1016/s0378-5955(03)00225-9

Noreña, A. J., and Eggermont, J. J. (2005). Enriched acoustic environment after noise trauma reduces hearing loss and prevents cortical map reorganization. *J. Neurosci.* 25, 699–705. doi: 10.1523/jneurosci.2226-04.2005

Noreña, A. J., and Farley, B. J. (2013). Tinnitus-related neural activity: theories of generation, propagation, and centralization. *Hear. Res.* 295, 161–171. doi: 10.1016/j.heares.2012.09.010

Okamoto, H., Stracke, H., Stoll, W., and Pantev, C. (2010). Listening to tailor-made notched music reduces tinnitus loudness and tinnitus-related auditory cortex activity. *Proc. Natl. Acad. Sci. U S A* 107, 1207–1210. doi: 10.1073/pnas.0911268107

Pantev, C., Okamoto, H., and Teismann, H. (2012). Music-induced cortical plasticity and lateral inhibition in the human auditory cortex as foundations for tonal tinnitus treatment. *Front. Syst. Neurosci.* 6:50. doi: 10.3389/fnsys.2012.00050

Pape, J., Paraskevopoulos, E., Bruchmann, M., Wollbrink, A., Rudack, C., and Pantev, C. (2014). Playing and listening to tailor-made notched music: cortical plasticity induced by unimodal and multimodal training in tinnitus patients. *Neural Plast.* 2014:516163. doi: 10.1155/2014/516163

Pickles, J. O. (2008). *An Introduction to the Physiology of Hearing*. UK: Emerald Group Publishing Limited.

Roberts, L. E., Bosnyak, D. J., Bruce, I. C., Gander, P. E., and Paul, B. T. (2015). Evidence for differential modulation of primary and nonprimary auditory cortex by forward masking in tinnitus. *Hear. Res.* 327, 9–27. doi: 10.1016/j.heares.2015.04.011

Rocha, A. V., and Mondelli, M. F. C. G. (2017). Gerador de som associado a aconselhamento no tratamento de zumbido: avaliação da eficácia. *Braz. J. Otorhinolaryngol.* 83, 249–255. doi: 10.1016/j.bjorl.2016.03.021

San Juan, J. S., Hu, X. S., Issa, M., Bisconti, S., Kovelman, I., Kileny, P., et al. (2017). Tinnitus alters resting state functional connectivity (RSFC) in human auditory and non-auditory brain regions as measured by functional near-infrared spectroscopy (fNIRS). *PLoS One* 12:e0179150. doi: 10.1371/journal.pone.0179150

Schad, M. L., McMillan, G. P., Thielman, E. J., Groon, K., Morse-Fortier, C., Martin, J. L., et al. (2018). Comparison of acoustic therapies for tinnitus suppression: a preliminary trial. *Int. J. Audiol.* 57, 143–149. doi: 10.1080/14992027.2017.1385862

Sereda, M., Xia, J., El Refaie, A., Hall, D. A., and Hoare, D. J. (2018). Sound therapy (using amplification devices and/or sound generators) for tinnitus. *Cochrane Database Syst. Rev.* 12:CD013094. doi: 10.1002/14651858.cd013094.pub2

Sevy, A. B. G., Bortfeld, H., Huppert, T. J., Beauchamp, M. S., Tonini, R. E., and Oghalai, J. S. (2010). Neuroimaging with near-infrared spectroscopy demonstrates speech-evoked activity in the auditory cortex of deaf children following cochlear implantation. *Hear. Res.* 270, 39–47. doi: 10.1016/j.heares.2010.09.010

Tak, S., and Ye, J. C. (2011). *NIRS-SPM: Statistical Parametric Mapping for Near-Infrared Spectroscopy*. User's guide. pp. 1–54. Available online at: https://www.nitrc.org/docman/view.php/621/1180/NIRS_SPM_UsersGuide_v4.pdf

Tyler, R. S., Perreau, A., Powers, T., Watts, A., Owen, R., Ji, H., et al. (2020). Tinnitus sound therapy trial shows effectiveness for those with tinnitus. *J. Am. Acad. Audiol.* 31, 6–16. doi: 10.3766/jaaa18027

Vanneste, S., Plazier, M., der Loo, E. V., de Heyning, P. V., Congedo, M., and De Ridder, D. (2010). The neural correlates of tinnitus-related distress. *NeuroImage* 52, 470–480. doi: 10.1016/j.neuroimage.2010.04.029

Xu, J., Liu, X., Zhang, J., Li, Z., Wang, X., Fang, F., et al. (2015). FC-NIRS : a functional connectivity analysis tool for near-infrared spectroscopy data. *Biomed Res. Int.* 2015:248724. doi: 10.1155/2015/248724

Zenner, H. P., Delb, W., Kröner-Herwig, B., Jäger, B., Peroz, I., Hesse, G., et al. (2017). A multidisciplinary systematic review of the treatment for chronic idiopathic tinnitus. *Eur. Arch. Otorhinolaryngol.* 274, 2079–2091. doi: 10.1007/s00405-016-4401-y

Zhou, X., Seghouane, A., Shah, A., Innes-brown, H., Cross, W., Litovsky, R., et al. (2018). Cortical speech processing in postlingually deaf adult cochlear implant users, as revealed by functional near-infrared spectroscopy. *Trends Hear.* 22:2331216518786850. doi: 10.1177/2331216518786850

Conflict of Interest: The authors declare that the research was conducted in the absence of any commercial or financial relationships that could be construed as a potential conflict of interest.

Copyright © 2020 Sun, Wang, Huang, Sun, Li, Zhuang and Xiong. This is an open-access article distributed under the terms of the Creative Commons Attribution License (CC BY). The use, distribution or reproduction in other forums is permitted, provided the original author(s) and the copyright owner(s) are credited and that the original publication in this journal is cited, in accordance with accepted academic practice. No use, distribution or reproduction is permitted which does not comply with these terms.

frontiers in Neuroscience

ORIGINAL RESEARCH
published: 28 April 2020
doi: 10.3389/fnins.2020.00346

An Augmented-Reality fNIRS-Based Brain-Computer Interface: A Proof-of-Concept Study

Amaia Benitez-Andonegui[1,2], Rodion Burden[1], Richard Benning[3], Rico Möckel[2], Michael Lührs[1,4] and Bettina Sorger[1]*

[1] Department Cognitive Neuroscience, Faculty of Psychology and Neuroscience, Maastricht Brain Imaging Center, Maastricht University, Maastricht, Netherlands, [2] Laboratory for Cognitive Robotics and Complex Self-Organizing Systems, Department of Data Science and Knowledge Engineering, Faculty of Science and Engineering, Maastricht University, Maastricht, Netherlands, [3] Instrumentation Engineering, Dean and Directors Office, Faculty of Psychology and Neuroscience, Maastricht University, Maastricht, Netherlands, [4] Research Department, Brain Innovation B.V., Maastricht, Netherlands

Augmented reality (AR) enhances the user's environment by projecting virtual objects into the real world in real-time. Brain-computer interfaces (BCIs) are systems that enable users to control external devices with their brain signals. BCIs can exploit AR technology to interact with the physical and virtual world and to explore new ways of displaying feedback. This is important for users to perceive and regulate their brain activity or shape their communication intentions while operating in the physical world. In this study, twelve healthy participants were introduced to and asked to choose between two motor-imagery tasks: mental drawing and interacting with a virtual cube. Participants first performed a functional localizer run, which was used to select a single fNIRS channel for decoding their intentions in eight subsequent choice-encoding runs. In each run participants were asked to select one choice of a six-item list. A rotating AR cube was displayed on a computer screen as the main stimulus, where each face of the cube was presented for 6 s and represented one choice of the six-item list. For five consecutive trials, participants were instructed to perform the motor-imagery task when the face of the cube that represented their choice was facing them (therewith temporally encoding the selected choice). In the end of each run, participants were provided with the decoded choice based on a joint analysis of all five trials. If the decoded choice was incorrect, an active error-correction procedure was applied by the participant. The choice list provided in each run was based on the decoded choice of the previous run. The experimental design allowed participants to navigate twice through a virtual menu that consisted of four levels if all choices were correctly decoded. Here we demonstrate for the first time that by using AR feedback and flexible choice encoding in form of search trees, we can increase the degrees of freedom of a BCI system. We also show that participants can successfully navigate through a nested menu and achieve a mean accuracy of 74% using a single motor-imagery task and a single fNIRS channel.

Keywords: hemodynamic brain-computer interface, augmented reality, motor imagery, real-time analysis, temporal information encoding, user-centered approach

OPEN ACCESS

Edited by:
Ning Liu,
Stanford University, United States

Reviewed by:
Andrea Soddu,
University of Western Ontario, Canada
Keum-Shik Hong,
Pusan National University,
South Korea

****Correspondence:***
Amaia Benitez-Andonegui
a.benitezandonegui@maastrichtuniversity.nl

Specialty section:
This article was submitted to Brain Imaging Methods, a section of the journal Frontiers in Neuroscience

Received: *03 October 2019*
Accepted: *23 March 2020*
Published: *28 April 2020*

Citation:
Benitez-Andonegui A, Burden R, Benning R, Möckel R, Lührs M and Sorger B (2020) An Augmented-Reality fNIRS-Based Brain-Computer Interface: A Proof-of-Concept Study. Front. Neurosci. 14:346. doi: 10.3389/fnins.2020.00346

INTRODUCTION

A brain-computer interface (BCI) is a system that enables users to send commands to the external world through brain signals in the absence of motor output (Wolpaw et al., 2002). BCI research has mainly focused on developing applications for (1) changing brain activation and associated behavior voluntarily through neurofeedback (Subramanian et al., 2011; Scharnowski et al., 2012; Shereena et al., 2018) and for (2) replacing (lost) motor functions through communication BCIs (Birbaumer et al., 1999; Nijboer et al., 2008; Sellers et al., 2010) and (e.g., wheelchair/robotic body-part) control systems (Galan et al., 2008; Muller-Putz and Pfurtscheller, 2008; Iturrate et al., 2009; Rebsamen et al., 2011; Murphy et al., 2017). Independent of the application, information is fed back to users about the success or failure of the intended act (Leeb et al., 2007). In communication and control BCIs, feedback may allow the BCI user to adapt the communication content (of a next encoding trial) in a sense of "back-and-forth communication," which enables users to communicate with or control a specific component of the external world.

The most common approach to provide feedback to users is through simplified unimodal (visual or auditory) representations of brain activation, such as bars or single tones (Sulzer et al., 2013). Alternative ways have emerged in the past years due to new technological developments in the areas of multimedia and entertainment, such as virtual reality (VR). VR is an immersive system that provides users with a sense of presence through potential interactions with a simulated virtual world rendered in real-time (Lécuyer et al., 2008). It has been suggested that VR environments can improve the BCI experience as it offers a richer and potentially more motivating feedback (Chin et al., 2010; Allison et al., 2012). Recent advances in VR research enabled the development of augmented reality (AR) systems. Unlike VR systems, AR enhances the environment the user is in by projecting virtual objects as overlays into the real world. This projection is called registration and it can be carried out using a camera that detects a number of fiducial markers placed in the real environment (Si-Mohammed et al., 2017). AR can be displayed using systems worn on the head (also known as head mounted displays, HMD) or visualized through a dedicated screen that the participant is not wearing (phone, computer screen, etc.). Depending on the augmentation type, AR systems can be divided into visual see-through (VST) and optical see-through (OST) systems. In VST-AR, real images are recorded in real-time by the camera of a device (tablet, phone, etc.) before being visualized through a screen, augmented with virtual information. In OST-AR, the virtual content is directly displayed in front of the user's eyes onto a semi-transparent screen.

The number of studies exploring the use of BCIs in AR applications remains relatively small (Si-Mohammed et al., 2017). Up until now, the majority of the AR-BCI literature has focused on electroencephalography (EEG)-based evoked potentials applied to a wide range of fields, namely robotics (Lenhardt and Ritter, 2010), medicine (Blum et al., 2012), home automation (Takano et al., 2011; Park et al., 2019), navigation (Faller et al., 2010), and neurofeedback (Chin et al., 2010; Mercier-Ganady et al., 2014). Importantly, some of these studies have assessed the impact of AR feedback in mental workload and engagement compared to traditional forms of feedback. For example, Chin et al. (2010) compared 3D-AR displays vs. traditional 2D feedback (both displayed on a computer screen) and found that despite the higher mental load experienced by the participants during the 3D-AR feedback, participants reported the 3D-AR feedback being more engaging and motivating.

AR-BCIs based on hemodynamic signals have also been explored, but to a smaller extent (Si-Mohammed et al., 2017). One way of measuring hemodynamic signals is using functional near-infrared spectroscopy (fNIRS), a portable, silent, and affordable counterpart to functional magnetic resonance imaging (fMRI) (Scarapicchia et al., 2017). Both EEG and fNIRS make use of sensors [electrodes and optode pairs (sources and detectors), respectively] placed on the scalp to measure signals which correlate with neural activity (Allison et al., 2012). While EEG measures the postsynaptic potentials of ensembles of neurons, fNIRS is based on the optical measurement of the hemodynamic response of both oxy- and deoxyhemoglobin (HbO and HbR, respectively) to neural activity (Lloyd-Fox et al., 2010). Although EEG offers a higher temporal resolution than fNIRS, the latter represents an interesting option as it provides higher spatial resolution and is less vulnerable to motion artifacts (Lloyd-Fox et al., 2010).

To our knowledge, only three fNIRS-based AR-BCIs have been reported. Hu et al. (2019) used an fNIRS-based AR-BCI in a simulated real-time environment aimed at clinicians to measure and visualize in real-time the ongoing cortical activity to determine when and where the patients were suffering from pain. For that, they placed fNIRS optodes over the patients' bilateral prefrontal cortex and primary somatosensory area and monitored brain activity while volunteers with hypersensitive teeth underwent a thermal stimulation session. The cortical activity was superimposed onto a participant's head in the real world in real-time through an OST-HMD (*HoloLens)* device the clinician was wearing. Afergan et al. (2015) developed an fNIRS-based BCI using OST-HMD called *Phylter*. They developed a control system connected to *Google Glass* that helped preventing the user from getting flooded by notifications. By monitoring users' mental workload in real-time with an fNIRS device, their system would only show notifications to the user if the mental workload was low enough. In the context of mental workload monitoring, McKendrick et al. (2016) assessed the cognitive differences between an AR wearable display (*Google Glass*) and a handheld display (smartphone) using a mobile fNIRS system covering the lateral PFC during an outdoor navigation task. They complimented it with two separate secondary tasks to assess differences in mental workload and situation awareness during navigation. They concluded that navigating with an AR wearable display produced the least workload during one of the working-memory task, and a trend for improved situational awareness in their measures of prefrontal hemodynamics. In this proof-of-concept study we tested whether healthy participants can use an AR fNIRS-based BCI paradigm motivated by the successful implementation in fNIRS-based BCIs, the increased engagement associated to the use of AR reported in previous

studies (Chin et al., 2010) and its ability to preserve the real world while blending digital components to it.

Generally speaking, the hemodynamic response to a given task execution/stimulus shows a specific and reproducible temporal behavior (Menon and Kim, 1999). Previous fMRI-based BCI work exploited this property and demonstrated that up to four distinctive BCI commands could be encoded/decoded by varying the temporal aspects (onset, offset and/or duration) of a (set of) mental task(s) (Sorger et al., 2009, 2012; Bardin et al., 2011). Despite its simplicity, so far no fNIRS-based BCI has implemented this temporal information encoding approach. This is probably because the temporal encoding approach is serial in its nature, which can make the encoding process lengthy depending on the experimental design. In addition, it has been used in combination with univariate information decoding approaches, while the hemodynamic BCI community has mostly adopted multivariate classification techniques such as Linear Discriminant Analysis, Support Vector Machines or Artificial Neural Networks that have been used to exploit the spatial features of fNIRS signals evoked by performing different mental-imagery tasks (Naseer and Hong, 2015b; Hong et al., 2018). However, with appropriate experimental designs, the temporal encoding approach offers a way to increase the degrees of freedom of a BCI using a single mental task. With this in mind, the present study aimed at transferring the fMRI-based temporal encoding approach mentioned above to fNIRS. For that, we used a selection paradigm where participants had to sift through a multi-leveled menu using a motor-imagery task. This menu consisted of four levels, in such a way that the choice options provided in each level (always six) were based on the decoded choice of the previous level. Thus, here we expanded the traditional four-choice temporal information encoding approach to include six options for choice selection in each of the levels comprising the menu, where an AR object guided the temporal encoding approach. We then used a univariate procedure for decoding participants' intention and used the same AR object to back-communicate the decoded answer of the participants' intention. Additionally, to account for potential mistakes during the decoding process, we implemented an active error-correction procedure to be applied by the participants. Importantly, this specific combination of temporal encoding and univariate decoding approaches allows participants' intentions to be decoded based on the information recorded from even a single fNIRS channel provided that this channel has enough signal quality. With this in mind, in the present study we used a single channel for decoding participants' choices.

Although the application of BCIs has been limited primarily to a laboratory setting, some of the studies mentioned above have examined the possibility of using BCI in everyday-life settings in different contexts (Takano et al., 2011; Blum et al., 2012; Afergan et al., 2015; Hu et al., 2019; Park et al., 2019). However, ecologically valid approaches are challenging to develop as, among other reasons, they should be as efficient, accurate and reliable as possible, but also easy to use, intuitive, and simple to (dis)assemble. This is probably the reason why most BCI research has focused predominantly on improving the technology (Liberati et al., 2015). There is a relevant body of work addressing that BCI design and development should become more user-centered in order to achieve successful everyday-life applications (Kübler et al., 2014; Liberati et al., 2015; Nijboer, 2015). Effort has been made to incorporate this aspect into various applications (Weyand and Chau, 2015, 2017; Weyand et al., 2015; Nagels-Coune et al., 2017; Si-Mohammed et al., 2018). While still in a laboratory setting, in the present study we worked toward a user-centered communication system by letting participants choose their preferred motor-imagery task and by selecting participant-specific (single) most-informative fNIRS channel for decoding their choices. Using a single channel constitutes the simplest setup to (dis)assemble. In addition, it should make the setup comfortable and thus prevent participants from withdrawing from fNIRS recordings due to setup-related discomfort (Suzuki et al., 2010; Cui et al., 2011; Rezazadeh Sereshkeh et al., 2018).

It is important to note that fNIRS measurements are contaminated by systemic interference of especially (but not limited to) extracerebral regions, which is mainly caused by cardiac pulsations, respiration, and blood-pressure variations (Boas et al., 2004; Tachtsidis and Scholkmann, 2016). Several approaches have been reported in the literature to reduce these noises: conventional band-pass filtering (Hocke et al., 2018; Pinti et al., 2019); modeling physiological noises as a sum of sinusoidal functions with known frequencies where their amplitudes are estimated by using the extended Kalman filter and regressed out using a general linear model (Prince et al., 2003); global signal-covariance removal by either principal/independent component analysis (Zhang et al., 2005; Aarabi and Huppert, 2016) or global average procedures (Batula et al., 2017); adaptive filters that use recursive least-squares estimation methods (Nguyen et al., 2018) or short-distance channel (SDC) regression (Saager and Berger, 2005; Saager et al., 2011; Goodwin et al., 2014). In fNIRS measurements these SDCs are channels that have reduced inter-optode separations such that the interrogated volume is confined primarily to extracerebral regions (Goodwin et al., 2014). The main assumption underlying their usability is that the same systemic physiological noise present in the normal-distance channels (NDCs) dominates the signal acquired with SDCs (Gagnon et al., 2012). Intuitively, SDCs can then be used to minimize/reduce unwanted physiological noise from the normal-distance channels. So far, not many fNIRS-based BCIs have employed them (but see Shin et al., 2017). This is partially because fNIRS equipment that allows such measurements has only recently become widely available. Here, SDC correction was used for the selection of the most-informative fNIRS channel as well as during the decoding process.

In this preliminary study participants achieved mean accuracy level of 74% (with a chance-level of 37.5% for six answer options), which shows that the temporal features of the fNIRS signal can be exploited in a temporal encoding paradigm to increase the degrees of freedom of a BCI using a single mental task. These accuracies also indicate that the proposed fNIRS-based AR-BCI setup can be successfully controlled, on average, by participants. Importantly, this work conveys the fundamental steps toward developing the first fNIRS-based AR-BCI system to be used as a communication device for bedside applications in a clinical setting.

MATERIALS AND METHODS

Participants

Twelve healthy volunteers [five males; mean age (*SD*) = 27.1 years (3.2 years)] with varying previous BCI/fNIRS/task experience participated in this study (see **Table 1**). Participants did not have a history of neurological disease and had a normal or corrected-to-normal vision. The experiment conformed to the *Declaration of Helsinki* and was approved by the ethics committee of the *Faculty of Psychology and Neuroscience*, *Maastricht University*. Informed consent was obtained from each participant before starting the measurements. Participants received financial compensation after the session.

Experimental Design and Stimulus Display

General Structure

The experiment consisted of a training session and an immediately following experimental fNIRS session. The training session was self-paced and ranged between 15 and 35 min across participants: we only switched to the experimental fNIRS session when participants felt comfortable with the stimuli and the motor-task performance.

In an attempt to follow a user-centered approach, participants were introduced to two motor imagery tasks during the training session and asked to choose between them: (option 1) mental drawing [of small geometrical figures (a square, circle, etc.) or contour drawings (a star, flower, boat, etc.) and (option 2) imagine to interact with the virtually presented AR cube (by, e.g., to imagine to hit/squeeze it)]. Participants were asked to choose the mental task (mental drawing or imagining interacting with the cube), the specific strategy (drawing a square or imagining hitting the cube) they expected would work best and would interfere the least with the stimuli and to perform the motor-imagery task with their right hands. They were instructed to keep their eyes open throughout the experiment and to look at the computer screen while staying as still as possible during the runs.

The experimental fNIRS session lasted around 1.5 h. Participants first performed a functional localizer run, during which the participants were presented with a gray AR cube that contained specific symbols (5/6 = crosses, 1/6 = checkmark). For twelve consecutive times, they performed the selected motor imagery task when the checkmark was facing them (for 6 s) and had to rest for the remaining faces (for 30 s, see **Figure 1**). There was an initial baseline period of 36 s indicated by a blue rotating cube, in which participants rested. We chose a baseline period of 36 s to guarantee a stable baseline measure for real-time conversion of raw data into hemoglobin (Hb) concentration changes. After the twelve trials, the cube stopped rotating and became blue again, indicating the end of the run. This run was used to select a user-specific most-informative ("best") fNIRS channel to decode participants' choices in the eight subsequent choice-encoding runs (here on referred to as choice runs).

Each choice run aimed at selecting one option from a six-item list (menu). These runs differed from the functional localizer run in (1) the number of active motor imagery trials [five trials (choice runs) vs. twelve (functional localizer run)] and (2) the fact that the AR cube was color-coded and numbered (choice runs) vs. the AR cube was gray and contained geometrical shapes (functional localizer run). Importantly, the task duration remained at 6 s during the choice runs. During each choice run, participants selected one choice from a six-item list provided before the start of the run and performed the motor imagery task only when the number corresponding to their choice was facing them (temporal information encoding), for five consecutive times. There was an additional baseline period of 18 s after the last trial to ensure that the hemodynamic response goes back to baseline. After the run, the cube unfolded and the decoded choice (based on real-time analysis of the fNIRS data) was highlighted in red (see **Figure 1**).

AR Stimulus Display

In this experiment, we used a variation of a VST-AR system, where a rotating AR cube displayed on a computer screen embodied the menu and each face of the cube represented one

TABLE 1 | Participant characteristics.

	Age range	fNIRS Cap Size (cm)	Previous experience			
			BCI	fNIRS	Task	
					Mental drawing	Interacting with cube
P01	20–25	56	First time	<5 times	< 5times	First time
P02	20–25	56	<5 times	5–10 times	5–10 times	First time
P03	20–25	56	<5 times	< 5times	<5 times	First time
P04	25–30	56	>10 times	> 10 times	>10 times	First time
P05	35–40	58	First time	First time	First time	First time
P06	25–30	56	<5 times	<5times	5–10 times	First time
P07	25–30	58	<5 times	5–10 times	<5 times	First time
P08	25–30	58	First time	First time	First time	First time
P09	25–30	56	<5 times	< 5times	<5 times	First time
P10	25–30	56	5–10 times	5–10 times	5–10 times	First time
P11	25–30	56	>10 times	>10 times	>10 times	First time
P12	25–30	58	First time	<5 times	<5times	First time

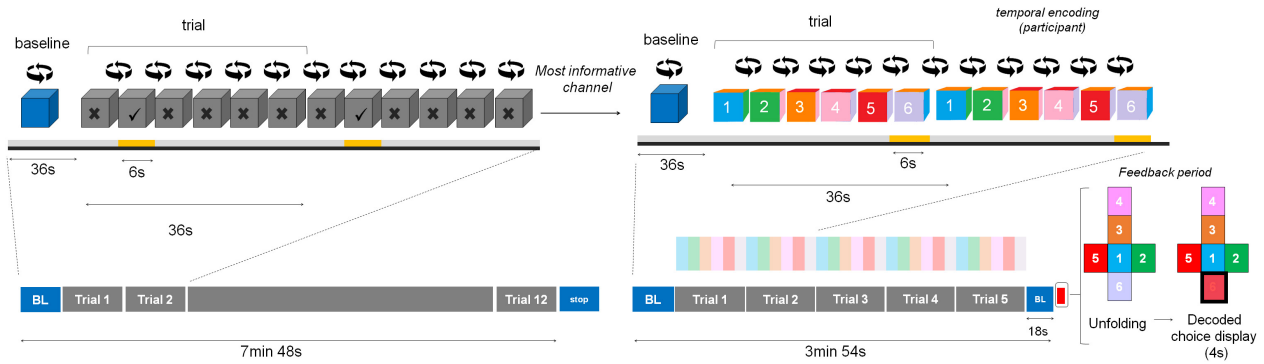

FIGURE 1 | Experimental design. During the training session participants chose between two motor imagery tasks. Then, during the functional localizer run, participants performed the chosen task for twelve consecutive trials when the checkmark was facing them (indicated in yellow, below the face showing a checkmark) and had to rest for the remaining faces. There was an initial baseline (BL) period indicated by a blue rotating cube, in which participants rested. After the twelve trials the cube stopped rotating and became blue again, indicating signaling the end of the run (indicated with the word stop in the figure). The user-specific most-informative channel from this run was used to decode participants' choices during the choice runs. Participants were asked to perform the mental task when the number corresponding to their choice was facing them (temporal information encoding), for five consecutive trials (in this example it corresponded to choice number 6, again underlined in yellow). After each run the feedback period started (indicated by the red square), where the cube unfolded and the decoded choice was highlighted in red (for visualization purposes, we added a black thick square in this schematic representation). After the choice runs, participants were asked to fill in several questionnaires.

choice of the list (see **Figure 2A** for an example of a user's view). In the presented AR system, a white A4 cardboard was used to represent the real-world stimulus that also served as a spatial point of reference necessary for the visualization of the AR cube. The A4 cardboard was placed on the desk, between the computer screen and the participants. The left half of the board was wrapped in transparent wrapping paper and served as a whiteboard, where choice options were handwritten (and modified after each run). The right half of the board contained a marker (a 2D-image, see hand-icon in top-left image of **Figure 2A**) that, when detected by the HD webcam (Logitech C270 HD, which was fixated on the participant's forehead using an elastic band and recording the cardboard), triggered the visualization of the AR cube on a standard computer screen. The AR cube was placed relative to the marker as seen in the camera image (see top-left image in **Figure 2A**) with the help of Vuforia (v7.1.34), an AR software development kit (SDK) that was running in Unity3D. This SDK makes it possible to detect the marker and to place the virtual cube on it, creating the effect of augmented reality. The marker was motor imagery task-specific and reminded participants of the task to be performed (mental drawing or virtual interaction with the cube). After each run, an unfolded AR cube was displayed on the computer screen highlighting the decoded choice of the participant (see top-right image, **Figure 2A**).

Nested Menu and Error-Correction Approach

The menu presented during choice runs consisted of four levels that were interconnected in such a way that the choice options provided in each level were based on the decoded choice of the previous run. The provided answer options became more specific throughout the levels. An example transition of provided options from level one to level four would be: listen to music > choose a genre > choose a band/artist > choose a song. Displaying the selected choice of the fourth level (a song, a picture, a movie, etc., depending on the choice in the first level) indicated the end of the navigation round, and participants were directed back to the first level of the menu (see **Figure 2A**). This structure allowed participants to go through a four-level nested menu twice if all choices were correctly decoded.

Importantly, it could be that the decoded choice of any given level of the nested menu did not match the encoded option by the participant. To account for such decoding mistakes and in a first attempt to correct for it, participants were instructed to choose the "Error" option in the next run. This "Error" option was part of the choice list in levels > 1 and the position this option appeared on the menu list was balanced across the different levels. If "Error" was decoded, they were provided with the same option lists they saw before the decoding mistake was made (see first Level 2 trial in **Figure 2B**).

fNIRS Data Acquisition

fNIRS data was recorded using a continuous-wave system (NIRScout-816, NIRx, Medizintechnik GmbH, Berlin, Germany). The optode setup consisted of nine sources and eight detectors which were placed on the left hemisphere that cover areas commonly associated with motor imagery, i.e., premotor cortex and part of the supplementary motor area, primary motor cortex, somatosensory motor cortex and part of the parietal cortex following the extended 10/10 EEG system (see **Figure 3**; Sorger et al., 2012; Abdalmalak et al., 2016; Batula et al., 2017; Klein and Kranczioch, 2019; Erdogan et al., 2019). An in-house SDC was created by placing source S9 as close as the optodes would allow (~13 mm away) to detector D5 on the same sagittal plane that connects D5 and source S6 (see **Figure 3**). The signal measured by the SDC should be influenced by the mid-sagittal sinus and other large vascular structures commonly found in this region (Duvernoy et al., 1981), which have been

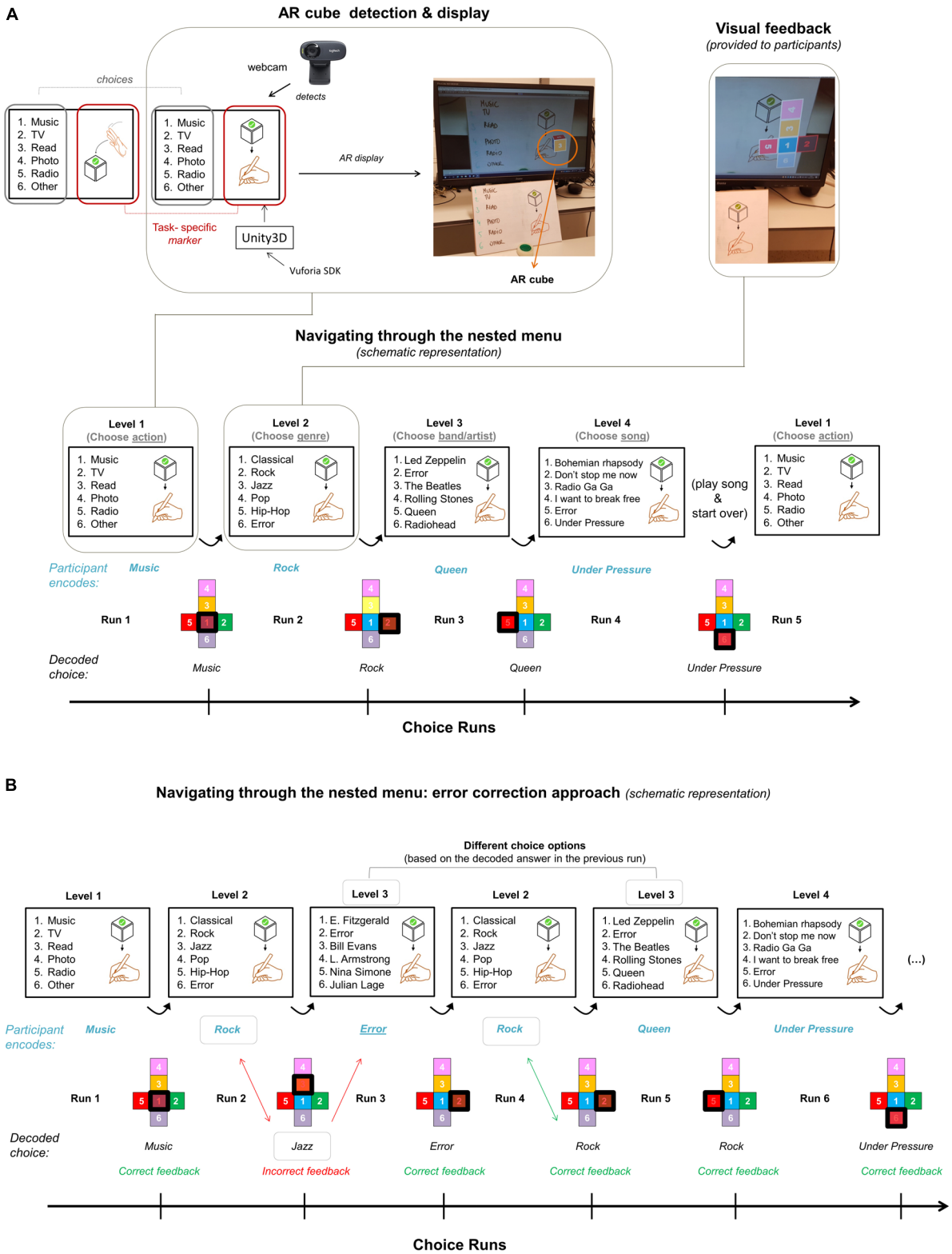

FIGURE 2 | AR display and example of a full cycle of the nested menu. **(A)** A task-specific marker in the right-side of the A4 cardboard served as the spatial point of reference necessary for the visualization of the AR cube. This cube was used to navigate through a four-level nested menu with six options in each level. The choice options encoded by the participant are written in blue, while the decoded answers are written in black and highlighted in red with a black thick square in the schematic representation of the unfolded cube. The choice options provided in each level were based on the decoded choice of the previous run. **(B)**

(Continued)

FIGURE 2 | Continued
If the decoded choice was incorrect, they were asked to choose the "Error" option in the next run. If "Error" was decoded, they were provided with the same option list they saw before the error occurred. In this example, the participant chose to perform a mental drawing task, as indicated by the markers under "Navigating through the nested menu". In the first level, we provided participants with keywords that responded to the question "What would you like to do?" Since the decoded choice [Listen to] Music (highlighted in red only in the actual run; highlighted in red and with a black thick square in the schematic view) was correct, the next run summarized music-genre options (Level 2). Here, the participant chose "Rock" [music] but the decoded choice was "Jazz". Thus, the participant was provided with Jazz-band options in the next run (Level 3), where (s)he encoded the "Error" option. Since the "Error" option was correctly decoded (see displayed choice after Run 3), the participant was provided again with Level 2 choice options. The procedure went on until the participant reached the last level of the nested menu. At the end of the run, we played the decoded song ("Under pressure" in this example) to the participant and (s)he was directed back to the first level of the menu.

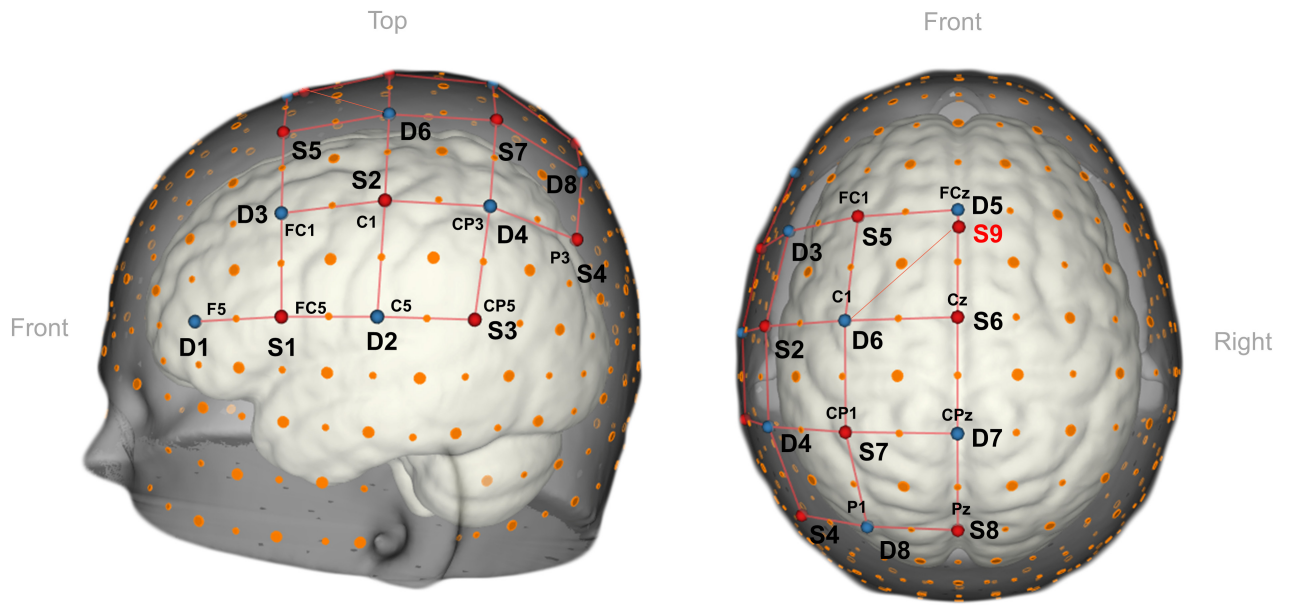

FIGURE 3 | 3D view of the fNIRS-optode arrangement. The setup consisted of nine sources (in red), eight detectors (in blue) placed over the left-hemipsheric motor and premotor regions. In total the setup contained one SDC (S9-D5) and 24 NDC. For the 3D representation we used NIRSite v1.0 software (NIRx Medizitechnik GmbH, Berlin, Germany; RRID: SCR_002491).

shown to be affected by low frequency oscillations and cardiac signals (Tong and Frederick, 2012). We used this information as a proxy to account for physiological noise in the region covered by the optode setup.

In total, the setup contained 24 NDCs and one SDC. The mean inter-optode distance of the standard channels spanned from 26.1 to 36.5 mm. Sources emitted light at wavelengths 760 and 850 nm, and the light intensity acquired at the detector side was sampled at 6.94 Hz. Besides the standard cap fixation (using the chin band), the fNIRS cap (EasyCap 128Ch ActiCap, EasyCap GmbH, Herrsching, Germany) was fixated onto the participants' head with three medical tape stripes (connecting the cap and the participant's forehead) to assure the cap would not shift during the measurements. In addition, a black, plastic overcap was placed on top of the fNIRS cap to additionally prevent the light in the room from reaching the optodes.

Apparatus

The session took place in a lab that consisted of two rooms, i.e., an inner and an outer room, where the hardware and materials comprising the setup were distributed (see **Figure 4**). We used NIRStar 15.2 (NIRx, Medizintechnik GmbH, Berlin, Germany) for recording the data and Turbo-Satori (TSI) 1.4.2 (BrainInnovation B.V., Maastricht, the Netherlands; Lührs and Goebel, 2017) and Matlab 2017a (The MathWorks Inc., Natick, Massachusetts, United States) for real-time preprocessing and decoding the participants' choices, respectively (see Data Analysis section). The three programs ran on the data-recording and -analysis laptop (depicted with number 6 in **Figure 4**). NIRStar 15.2 was connected to the NIRScout system via USB and to TSI via Lab Streaming Layer (LSL). TSI and Matlab were connected via the TSI-Matlab interface, a self-designed network interface enabling real-time access to raw and preprocessed fNIRS data as well as protocol and statistical information (Lührs and Goebel, 2017; BrainInnovationSupport, 2019). In addition, Matlab was used to log the different experimental conditions by sending triggers to the fNIRS system via LSL and to control the stimulus display in that was running in Unity 3D software (v2018.3.2.f1, Unity Technologies, San Francisco, California, United States), which was running in the stimulus laptop (number 5 in **Figure 4**). During choice-encoding runs Matlab sent to Unity3D the following commands via TCP/IP: ("a") start of the run, which initiated the rotation of the inactive (blue) AR cube; ("b"), start of the encoding period,

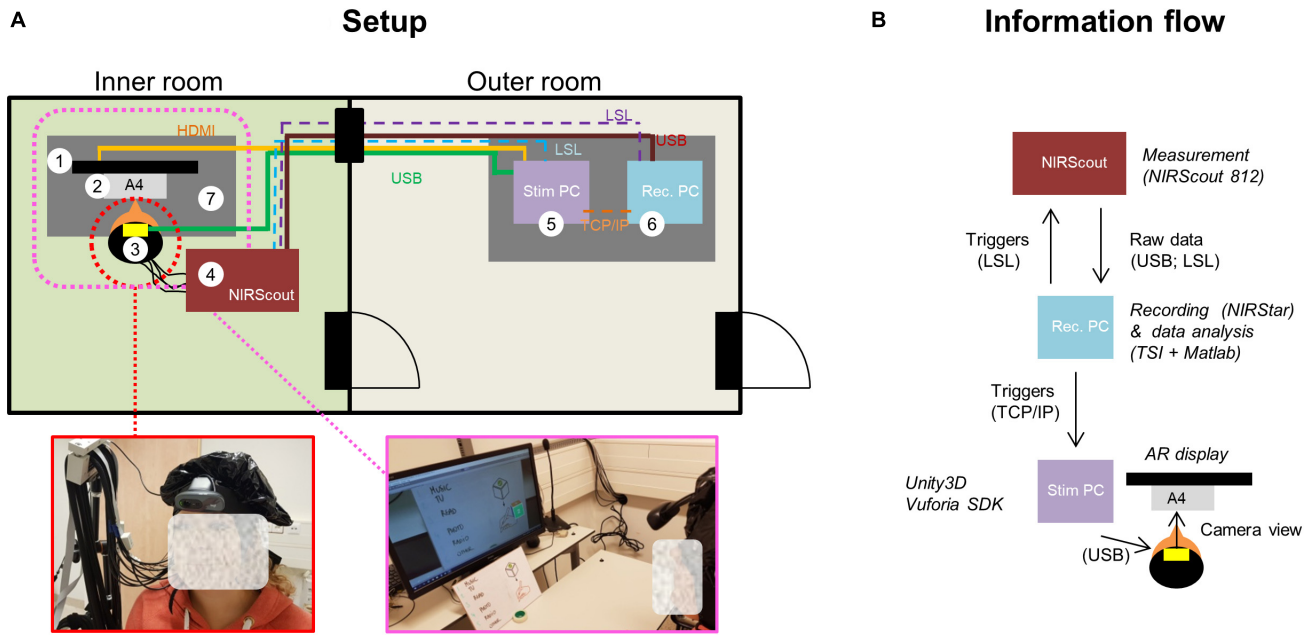

FIGURE 4 | Summary of the technical setup and connections between its different components. **(A)** Setup. The inner room, where participants were measured while seated (see (3) and enlarged picture), contained the fNIRS system (4), a computer screen (1), an HD webcam (3), the A4 cardboard (2) and a desk (7). The outer room, where the experimenter was located, hosted the two laptops, i.e., the data-recording and -analysis laptop (6) and the stimulus laptop (5). Physical connections (wires) are depicted with continuous lines, while non-physical connections [Lab Stream Layer (LSL), TCP/IP] connections are depicted with dashed lines. **(B)** Information flow. NIRStar 15.2 was connected to the NIRScout system via USB and to Turbo-Satori (TSI) viaLSL. TSI and Matlab were connected via the TSI-Matlab interface. Matlab was used to send triggers back to the fNIRS system via LSL and to control the stimulus display in Unity3D software (via TCP/IP).

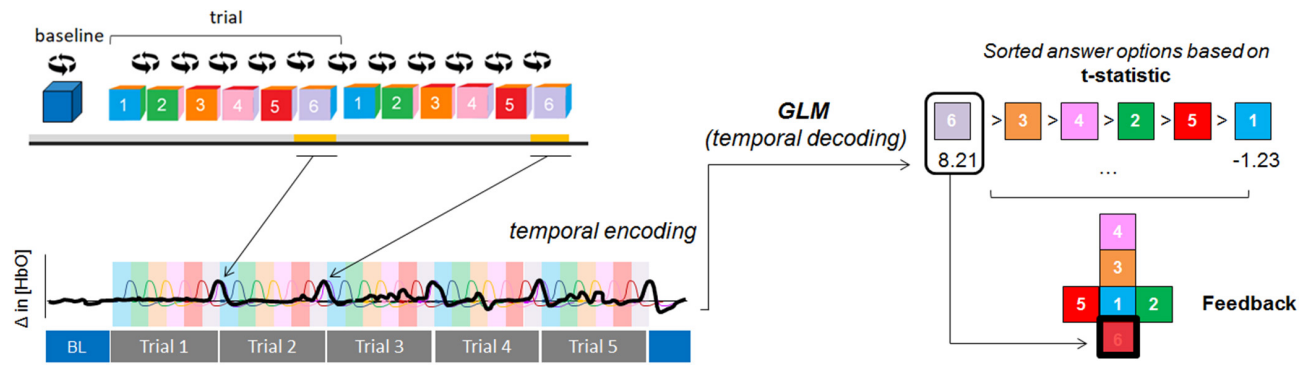

FIGURE 5 | Temporal-decoding approach. A GLM was fitted to the HbX data (from five repeated trials) to decode the participants' intentions. In this example, the participant encoded option #6 (represented by the black, thick line) and HbO signal was used for decoding. Each colored area represents the encoding time (the period where participants were instructed to perform the mental task) for each of the cube faces. Each colored HRF represents the expected fNIRS response for each of the options. After the run the cube unfolded and feedback was provided by highlighting in red the decoded intention (which was the condition that led to the highest *t*-statistic [option 6, *t*-value = 8.21]). For visualization purposes, we added a black thick square in this schematic representation).

which turned the inactive cube into an active one by changing the blue-colored faces into color-coded faces; ("c") last rest period, which turned the face of the AR cube back to blue, indicating the last rest period of the run; ("1–6") decoded choice, which unfolded the cube and highlighted in red the decoded choice. All commands except for those pertaining to the decoded choice were used for the functional localizer run. The computer screen in the inner room was connected to the stimulus laptop through an HDMI cable. The HD webcam in the inner room (number 3 in **Figure 4**) was connected to the stimulus laptop via USB.

Subjective Ratings and Previous Experience Report

After the completion of the experiment, participants first rated how comfortable the setup (optodes and webcam) felt throughout the session according to a Likert-scale ranging from 0 (extremely

uncomfortable) to 10 (extremely comfortable). We predicted that comfortability ratings would decrease over time due to the presence of local pressure on the head surface caused by optodes (Nagels-Coune et al., 2017) and the webcam. Then participants rated the general easiness, pleasantness and vividness of the two motor imagery tasks they were trained on using another Likert-scale ranging from 0 (extremely difficult/unpleasant/not vivid at all) to 10 (extremely easy/pleasant/very vivid). In addition, participants were asked to report on their previous motor imagery task, fNIRS and BCI experience (first time, less than five, five to ten times or more than ten experiments).

Data Analysis

Real-Time Analysis

Data preprocessing

Raw fNIRS data were first converted into optical-density data and then into changes in Hb concentration through the modified Beer-Lambert law in real-time, using differential path-length factors of λ_{760} = 6.40 and λ_{850} = 5.85 (Essenpreis et al., 1993) and a baseline calculation period of 15 s (10–25 s after run onset). Data were filtered using a first-order moving-average high-pass filter with a cutoff of 0.01 Hz and a second-order moving-average low-pass filter with a cutoff of 0.25 Hz. No motion correction was applied.

Channel selection

The channel and Hb-type selection per participant was based on the result of the general linear model (GLM) analysis. Specifically, the selection was based on the chromophore and channel that led to the highest *t*-statistic of the task vs. rest contrast in the functional localizer run. The design matrix included one task predictor convolved with a standard hemodynamic response function (HRF). The default HRF from SPM12 was used (two Gamma HRF, the onset of response and undershoot 6 and 16 s, respectively, dispersion 1 s, response to undershot ratio 6) and the same amplitudes were used for the HbO and HbR task predictors. In addition, a constant term and the SDC time course were used as confound predictors should the latter satisfy the coefficient of variation criterion (CV $<$ 7.5%, which was the case for all participants). The pre-whitening approach implemented in TSI was used to remove serial correlations (Lührs and Goebel, 2017).

Temporal decoding

During choice runs the time course of the selected channel was read in real-time in Matlab using the TSI-Matlab interface. Participants' choices were decoded by fitting a GLM in Matlab using *glmfit* to all five trials in each choice run (see **Figure 5**). The design matrix differed from the functional localizer run in that it included six task predictors (one for each choice option, i.e., choice period) instead of one convolved with the HRF. Importantly, the SDC time course was used as a confound predictor during choice runs only if it was used as a confound predictor during the channel selection process. No pre-whitening was applied. The condition that led to the highest *t*-estimate of the task vs. rest contrast was considered the selected choice (see **Figure 5**). It should be noted that this analysis was re-computed offline using a simulated real-time approach for participants P01–P07 due to a technical mistake during these sessions.

Offline Analysis

Channel-selection assessment

We evaluated the effect (on choice-decoding accuracies) of using a predefined Hb type for the channel selection vs. selecting the most informative HbX channel (where HbX ε {HbO, HbR}). Importantly, and despite following a single-channel decoding approach, we kept all channels in place to carry out this assessment.

Besides, we evaluated the effect (on choice-decoding accuracies) of using the SDC as confound predictor in the channel-selection process. Differences across Hb-type and usage of SDC were tested for significance using a two-way ANOVA with factors SDC (with SDC, without SDC) × Hb-type (HbX, HbO, HbR), followed by paired *t*-tests.

Effect of the number of trials in the decoding process

We used the same univariate choice-decoding approach as described in section Temporal decoding to evaluate the effect of the number of trials in a given run on decoding accuracies (based on the most informative HbX channel). For that, we computed the accuracies of all consecutive trial combinations for every trial number (1:*n* trials, where *n* = {1,2,3,4,5}). For example, to compute the decoding accuracy of three trials, trial combinations 1-2-3, 2-3-4, and 3-4-5 were used. We then quantified the effect of the number of repetitions in the decoding accuracy at the group level using Spearman's rho correlation coefficient. The effect of number of trials was additionally evaluated using information transfer rate (ITR), defined as in Allison et al. (2012):

$$ITR = (log_2 N + P^* log_2 P + (1-P)^* log_2(\frac{1-P}{N-1}))^* \frac{60}{\tau} \quad (1)$$

where N is the number of classes, P is the classification accuracy and τ is the duration of task and rest period, in seconds.

Decoding accuracy of error-correction trials

We incorporated an error-correction mechanism in our decoding process by including an "Error" option in levels $>$ 1 of the menu. We assessed the accuracy of the error-correction approach with a confusion matrix. For that, we pooled all encoded answers across participants and divided them into "Error" and "Non-Error" instances, depending on whether the participant intended to encode "Error" or not, respectively. The encoded choices were then compared to the decoded ones. Four measures were extracted from the confusion matrix, namely accuracy, recall, precision and specificity, which were calculated as follows:

- Accuracy = (TP + TN)/(TP + TN + FP + FN)
- Recall = TP/(TP + FN)
- Precision = TP/(TP + FP)
- Specificity = TN/(TN + FP)

where TP = True positive or correctly detected "Error" trials; TN = True negative or correctly detected "Non-Error" trials; FP = False Positive or incorrectly detected "Error" trials; FN = False negative or incorrectly undetected "Error" trial.

Chance-level definition

A quantile function of a multinomial distribution was used to define the upper bound of the chance-level (37.5% for N = eight runs, c = six classes and a $p < 0.05$).

Subjective ratings

Mean and SE of normalized subjective comfortability ratings was computed by calculating the mean (of eight runs) for each subject and subtracting the subject's mean to each item. The effect of the duration of the experiment (number of runs) on the comfortability score was quantified using Pearson's correlation. In addition, the relation between previous BCI/fNIRS/task experience on task accuracies reached by each participant was assessed using Spearman's correlation coefficient. Finally, to evaluate the perceptual differences the mental tasks elicit on each participant, normalized absolute mean differences between the preferred and non-preferred mental task ratings were assessed. First, each item was normalized following the same approach as for the comfortability ratings. Next, the three scores (easiness, pleasantness and vividness) were averaged for each mental task and participant. Then, absolute differences between mental tasks were computed and a right-tailed *t*-test was used in Matlab.

RESULTS

Choice-Decoding Results Obtained in (Simulated) Real-Time

Figure 6 shows the individual and group accuracies achieved in the experiment. In addition, it shows that half of the participants chose to perform the mental-drawing task and that HbR was selected for seven out of twelve participants. All participants but P04 exceeded the upper bound of the chance-level (37.50%, orange dashed line). It should be noted that accuracies from participants P01-P07 were computed offline using a simulated real-time approach due to a technical mistake during these sessions, while accuracies from participants P08-P12 were calculated online based on real-time results. On average, participants reached an accuracy of 73.96% (*SD* = 20.96), as depicted by the left-most gray bar of the group plots. Mean decoding accuracies with different grouping factors were also computed and descriptively did not differ substantially within each group (see **Figure 6**).

Evaluation of Error-Correction Procedure

In total, participants had to encode the "Error" option 22 times (see **Figures 7A,B**). Out of the 22 instances, the error option was correctly detected 14 times, missed eight times, and incorrectly labeled once, as indicated in the confusion matrix (**Figure 7A**). Overall, the accuracy of the error-correction trials was 90.6% (upper bound of the chance level was 58.88%, assessed by the quantile function of a multinomial distribution with $n = 96$ trials, $c = 2$ classes and alpha = 0.05).

Assessment of the Effect of Number of Trial Repetitions

To assess how the number of trial repetitions affects the decoding process, we sequentially reduced the number of trial repetitions we used for decoding. **Table 2** summarizes the individual and group decoding accuracies for a decreasing number of repetitions and **Figure 8A** shows that the number of repetitions used to decode each run influences the decoding process. Specifically, we observed a significant negative correlation between the accuracies and the number of repetitions, as assessed by Spearman's rho correlation coefficient ($\rho = -0.639$, $p < 0.0001$). Importantly, mean- and several single-subject accuracies (7 out of 12 participants) remain above chance level even when using a single trial. As for the ITR computation, **Figure 8B** indicates that slightly higher ITR values can be reached, on average, when using four trials (0.34 bits/min) instead of five (0.29 bits/min).

Assessment of Channel Selection

Although our channel selection approach was based on selecting the most informative HbX channel for each participant, it is not uncommon to have a predefined Hb-type before the data acquisition (Naseer and Hong, 2015b). In this context, we looked at whether the selected channel would change had we decided to focus on only one chromophore. In addition, since we used the SDC time course as a confound predictor, we assessed whether applying SDC correction (or not) influences the channel selection. **Table 3** shows that for some participants, the channel selection approach does not affect the selected channel (see P01, P02, P07 and P11 across all columns), while for other participants it does. Descriptively speaking, SDC correction slightly reduced the mean accuracy for the most-informative HbX-channel approach. The reason behind this observation is that the increased accuracy for some participants (P03, P06, P09, P11, and P12) was smaller than the decrease in accuracies for other participants (P04, P05, P08, and P10). The mean decoding accuracy increased for the most-informative HbO and HbR channel approaches (although to a considerably lesser extent for the latter).

A repeated measures 2-way ANOVA with factors SDC (with SDC, without SDC) × Hb-type (HbX, HbO, HbR) showed that the mean accuracies were different across Hb-types [main effect of Hb-types; $F_{(2, 66)} = 3.494$, $p = 0.036$; no significant interaction], but not across SDC. Subsequent paired *t*-tests showed that HbX and HbR performed better than HbO [$t_{(23)} = 3.83$; p(FDR [$q = 0.05$]) = 0.001, and $t_{(23)} = 2.736$; p(FDR [$q = 0.05$]) = 0.008].

Previous Experience and Subjective Reports

Due to the (novel) AR component, the participants were enthusiastic about the research study. Independent of the achieved accuracies participants rated the setup positively and considered the experiment as "fun," "engaging," and "motivating." The setup became uncomfortable over the runs as indicated by a significant negative correlation ($r = -0.991$, $p < 0.0001$). Participants reported the main source of discomfort to be the pressure caused by the webcam on their foreheads and to a lesser

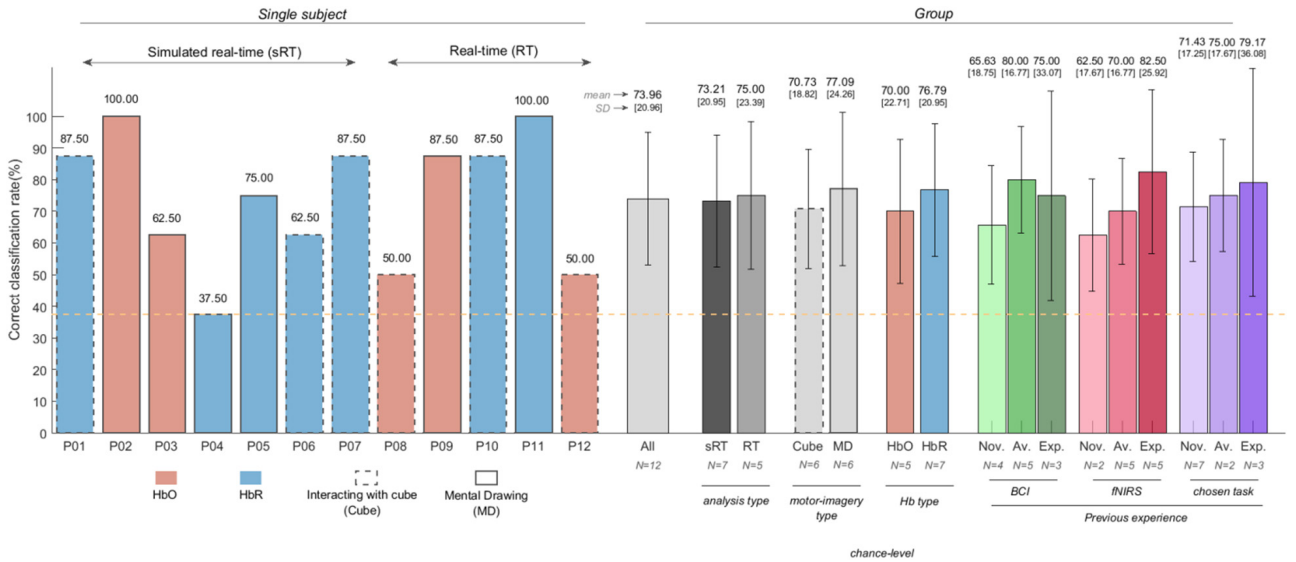

FIGURE 6 | Choice-decoding accuracies obtained in (simulated) real-time (individual and group results) using HbX channel selection and SDC correction. All participants but P04 reached accuracies higher than chance-level (orange, dashed line). The face colors and line pattern of the bar plots of each subject (left-half of the figure) represent the selected Hb-type and strategy participants chose to perform, respectively. Mean decoding accuracies and standard deviation of all participants and with different grouping factors can be found on the right-half of the figure. Groupings were based on the analysis type (simulated real-time vs. real-time), the motor imagery participants chose [interacting with the cube (cube) vs. mental drawing (MD)], the selected chromophore (HbO vs. HbR) and previous BCI experience (novices, average and experts). Participants with no previous BCI/fNIRS/task experience were considered *novices*; *expert* participants were those who had participated in more than five BCI experiments; the remaining participants were considered *average* (see **Table 2**). The integer after "*N* = " indicates the number of participants employed in each computation.

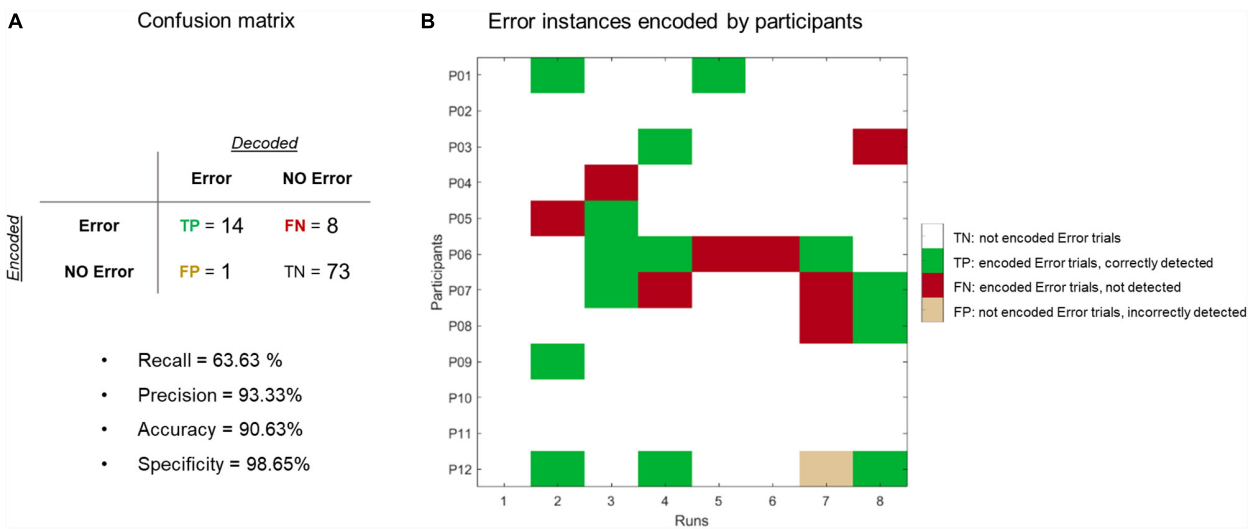

FIGURE 7 | Evaluation of error-correction procedure. **(A)** Confusion matrix. We reached an accuracy of 90.62% (72/96 trials were correctly labeled as "Error" or "NoError") and a recall level of 65.22% (out of 22 error trials, 8 trials were missed). **(B)** Summary matrix of when participants encoded the "Error" option (marked in dark gray). Green (red) cells represent trials where the "Error" option was correctly (incorrectly) detected. Beige cells indicate a false positive trial.

extent the optodes on the head surface. We observed that the preferred motor imagery task was rated significantly higher than the non-preferred task [$t_{(11)} = 5.240$, $p < 0.001$]. In addition, we observed that previous BCI/fNIRS/task experience correlated positively with individual accuracies, but none of them reached significance ($\rho_{task} = 0.429$, $\rho_{BCI} = 0.360$, $\rho_{fNIRS} = 0.566$, $p > 0.05$).

DISCUSSION

The present proof-of-concept study combined AR technology and an fNIRS-based BCI to apply it in a communication context, where twelve healthy participants were asked to navigate in real-time through a nested six-choice menu while following a

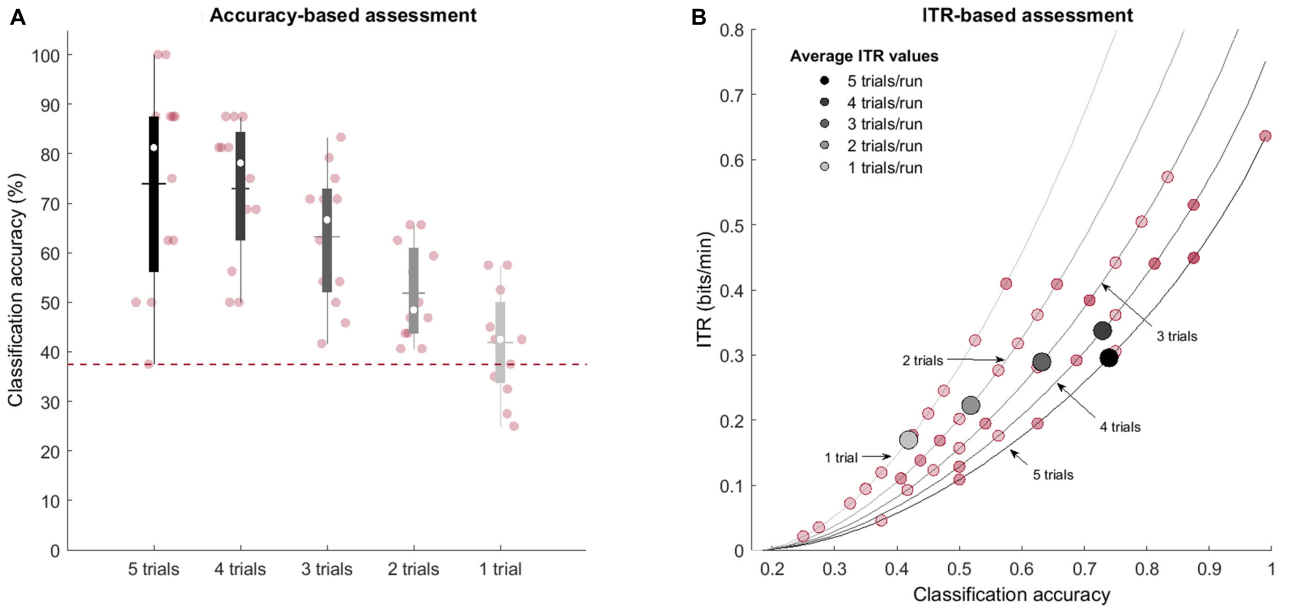

FIGURE 8 | Effect of the number of trial repetitions on obtained decoding accuracy (individual and group results). **(A)** The box-plot shading depicts the number of repetitions used for decoding: from five trials (black) to a single trial (light gray). Median values are represented by the white circles, while the mean values are indicated with the horizontal lines. The y-axis represents the accuracy (%) achieved by the participant. The red, dashed line shows the chance-level defined by the cumulative multinomial distribution. The number of trials used to decode each run influences the decoding process, but mean- and several single-subject accuracies remain above chance level even with a single trial. **(B)** Average (gray-scale markers) and single-subject (red markers) ITR values (bits/min) for different number of trials as a function of achieved classification accuracies. Lines represent the theoretical values the ITR can take as a function of the number of classes, trial duration and accuracy.

TABLE 2 | Individual and group decoding accuracies over decreasing number of repetitions (for HbX with SDC regression analysis).

	Accuracies (%)				
	5 trials	**4 trials**	**3 trials**	**2 trials**	**1 trials**
P01	87.50	81.25	70.83	65.63	47.50
P02	100.00	81.25	70.83	59.38	57.50
P03	62.50	75.00	54.17	56.25	45.00
P04	37.50	50.00	54.17	43.75	37.50
P05	75.00	50.00	50.00	50.00	42.50
P06	62.50	68.75	41.67	46.88	27.50
P07	87.50	87.50	79.17	65.63	57.50
P08	50.00	56.25	45.83	40.63	32.50
P09	87.50	81.25	75.00	43.75	35.00
P10	87.50	87.50	83.33	62.50	52.50
P11	100.00	87.50	62.50	46.88	42.50
P12	50.00	68.75	70.83	40.63	25.00
Group (SD)	73.96 (20.96)	72.92 (14.19)	63.19 (13.74)	51.82 (9.56)	41.88 (11.83)

temporal information encoding approach. The decoded choice was defined for each participant based on the time course of the most-informative channel in the setup. In case the decoded choice was incorrect, an active error correction procedure was used. We achieved mean accuracy levels of 73.96% (with a chance-level of 37.5% for six answer options) and error detection accuracies of 90.6%. The following sections discuss the general implications of this study, together with its limitations and prospects for the future.

The Temporal Information Encoding Approach – A Powerful Paradigm for fNIRS-Based BCIs

In this experiment, we applied for the first time a temporal information encoding approach and a GLM-based decoding scheme previously reported in fMRI-based BCIs (Sorger et al., 2009, 2012; Bardin et al., 2011) to an fNIRS-based BCI system to distinguish between six options using a single channel and

TABLE 3 | Most informative channel for different channel selection approaches and (individual and mean) accuracies reached with each approach.

	Accuracies (%)											
	Best HbX				Best HbO				Best HbR			
	SDC		No SDC		SDC		No SDC		SDC		No SDC	
P01	[S3-D2]	87.50 (=)	[S3-D2]	87.50	[S3-D2]	75.00 (↑)	[S3-D2]	25.00	[S3-D2]	87.50 (=)	[S3-D2]	87.50
P02	[S9-D6]	100.00 (=)	[S9-D6]	100.00	[S9-D6]	100.00 (=)	[S9-D6]	100.00	[S9-D6]	87.50 (=)	[S9-D6]	87.50
P03	[S6-D5]	62.50 (↑)	[S2-D6]	37.50	[S6-D5]	62.50 (↑)	[S9-D6]	25.00	[S2-D6]	62.50 (↑)	[S2-D6]	37.50
P04	[S1-D3]	37.50 (↓)	[S9-D6]	100.00	[S1-D3]	25.00 (↓)	[S9-D6]	100.00	[S1-D3]	37.50 (↓)	[S5-D6]	75.00
P05	[S2-D4]	75.00 (↓)	[S2-D4]	87.50	[S7-D8]	25.00 (↑)	[S6-D7]	12.50	[S2-D4]	75.00 (↓)	[S2-D4]	87.50
P06	[S2-D6]	62.50 (↑)	[S3-D2]	25.00	[S2-D6]	62.50 (↑)	[S2-D6]	12.50	[S2-D6]	62.50 (↑)	[S3-D2]	25.00
P07	[S2-D4]	87.50 (=)	[S2-D4]	87.50	[S2-D4]	75.00 (↑)	[S2-D4]	37.50	[S2-D4]	87.50 (=)	[S2-D4]	87.50
P08	[S1-D2]	50.00 (↓)	[S2-D2]	100.00	[S1-D2]	50.00 (↓)	[S1-D2]	62.50	[S2-D2]	100.00 (=)	[S2-D2]	100.00
P09	[S2-D3]	87.50 (↑)	[S2-D3]	75.00	[S2-D3]	87.50 (↑)	[S2-D3]	75.00	[S1-D3]	75.00 (=)	[S5-D6]	75.00
P10	[S1-D2]	87.50 (↓)	[S1-D2]	100.00	[S1-D2]	87.50 (↑)	[S3-D2]	75.00	[S1-D2]	87.50 (↓)	[S1-D2]	100.00
P11	[S1-D3]	100.00 (↑)	[S1-D3]	62.50	[S1-D3]	50.00 (↑)	[S1-D3]	37.50	[S1-D3]	100.00 (↑)	[S1-D3]	62.50
P12	[S5-D5]	50.00 (↑)	[S2-D4]	37.50	[S5-D5]	50.00 (↑)	[S2-D4]	37.50	[S2-D3]	12.50 (↓)	[S2-D4]	37.50
Group (SD)	73.96 (20.96) (↓)		75.00 (27.70)		62.50 (23.84) (↑)		50.00 (31.53)		72.92 (26.02) (↑)		71.88 (25.63)	

Note 1: Red (blue) cells indicate that the selected chromophore was HbO (HbR) Note 2: The different symbols summarize the effect in decoding accuracy (↑ [increased], ↓ [decreased], = [maintained]) when SDC was used as a confound predictor vs. when it was not.

mental task. An advantage of using this procedure is that a single channel may be sufficient for decoding participants' intentions without hampering our decoding ability. Intuitively, using a single channel should also make the setup more comfortable. It should be mentioned that although we assessed the feasibility of the single-channel approach and recorded participants' comfortability scores over time, we kept all channels in place for *post hoc* analyses. Another advantage is that, theoretically, this approach could allow including a considerably high number of conditions. In the present work we have further advanced previous applications by going from four (Sorger et al., 2009; Bardin et al., 2011) to now six temporally different but still differentiable encoding phases. Importantly, future work should explore the upper limit of the included number of conditions that would yield a sufficiently high decoding accuracy. In any case, increasing the number of conditions would inevitably rise the duration of the run, but this could be solved by reducing the task duration to a certain extent. Until now the biggest body of hemodynamic BCI applications has used a task duration of 10 s (Naseer and Hong, 2013; Herff et al., 2013; Hong and Santosa, 2016; Nagels-Coune et al., 2017; Shin et al., 2017; Snipes et al., 2017) or longer (Bardin et al., 2011; Bauernfeind et al., 2011; Batula et al., 2017), and very few studies have used task durations under 10 s: for example, Sorger et al. (2009) and Shin and Jeong (2014) used variable task durations of 5/10/15 s and 6/8/10/15 s, respectively. To maintain the single-trial duration as low as possible without hindering the ability to distinguish between conditions, we opted to use 6 s task duration per condition for our experiment. However, the considerable inter-subject variability in accuracies suggests that user-tailored task durations should be considered in future studies.

Using a Single fNIRS Channel – A Promising Approach in the Context of Temporal Information Encoding

Selected Feature

Feature selection varies across studies, but in general, previous work has focused on either using only HbO signal (Stangl et al., 2013; Erdoğan et al., 2014; Hong et al., 2015; Koo et al., 2015; Hong and Santosa, 2016; Lapborisuth et al., 2017; Noori et al., 2017; Liu et al., 2018) or the combination of different chromophores (computing the mean or the difference of HbO and HbR, Naseer and Hong, 2015b). A few fNIRS-BCI applications have used/explored HbR on its own (Cui et al., 2010; Naseer and Hong, 2015a; Hwang et al., 2016). The main reason is that HbO is considered to exhibit larger and more pronounced concentration changes than HbR in response to mental tasks (Stangl et al., 2013; Sato et al., 2016). Besides, it has been reported that HbO signals are more discriminative and perform more robustly than HbR signals (Mihara et al., 2012; Naseer and Hong, 2015a). However, Cui et al. (2010) and Hwang et al. (2016) found that HbO and HbR performed similarly in terms of accuracy. In the present work the channel selection approach led to selecting HbR for 7/12 participants. In addition, our *post hoc* analysis revealed that at the group level channel selection using either HbX approach or HbR performed better than only HbO channel selection. Despite having lower SNR, these results point at the usefulness of the HbR signal for the classification of motor imagery (at least) in a GLM-based decoding approach.

SDC Correction

SDCs are used to minimize/reduce unwanted physiological noise contained in NDCs (Goodwin et al., 2014). In the current work,

a custom-built SDC was used as a GLM confound predictor during both, the selection of the most informative channel and the decoding process. Offline, we evaluated the effect of using SDC for channel selection and choice decoding. As derivable from **Table 3**, when using the HbX approach, SDC correction did not affect the channel selection in seven out of twelve participants (P01, P02, P05, P07, P09, P10, and P11). The selected channels for the remaining participants differed either in location only (P06) or in location and Hb-type (P03, P04, P08, and P12). This suggests that the former group of participants had a relatively stable signal compared to the latter ones. Interestingly, the mean accuracies were higher for the former group, too [89.29% (*SD* = 8.63) vs. 58.33% (17.08)]. Although the accuracy did not significantly change on average when SDC correction was used vs. when it was not, a clear divergence between both approaches was observed in some participants. For example, the accuracy reached by P04 and P08 was considerably reduced after SDC correction (100–37.5% and 100–50%, respectively), while it improved for P06 and P11 (25–62.5% and 62.5–100%, respectively). It is not straightforward to attribute this opposing and seemingly irregular effect across participants to an isolated cause. Instead, it may be the result of an interaction between the spatial relation of the SDC and the selected channel, which suggests that the location of the SDC matters even in a relatively small setup. In addition, the selected chromophore (whether it is HbO or HbR) may influence the effect of SDC correction. Indeed, unlike for the HbX (and the HbR) approach, we observed a clear improvement before/after SDC correction when selecting channels based on HbO (see **Table 3**, "Best HbO"). Specifically, the mean decoded accuracy increased from 50 to 62.5% after SDC correction. This is expected, as HbO signal is more affected by global systemic artifacts in both extracerebral and intracerebral compartments than HbR (Kirilina et al., 2012).

T-Statistic for Channel Selection and Decoding

Different approaches for channel selection have been reported in the literature. Hu et al. (2013) compared the difference between the maximum value during the task and rest periods, and considered the channel to be active if the difference was positive. Hong and Naseer (2016) and Khan and Hong (2017) suggested selecting channels where the initial dip could be reliably detected. For that, a vector-based phase analysis with a threshold circle as a decision criterion was employed. Previous fNIRS studies have also followed a *t*-value (Hong and Santosa, 2016; Nagels-Coune et al., 2017) or beta-value criterion (Klein and Kranczioch, 2019) between the measured and expected hemodynamic response by the given stimulation for channel selection.

In the present study we selected the most informative channel and Hb-type combination based on the highest *t*-statistic of the task vs. rest contrast of the functional localizer data. We ensured correct *t*-value estimation during channel selection by removing serial correlations generally present in the fNIRS data (Huppert, 2016). The decoded answer option was based on the choice that led to the highest *t*-statistic of the choice$_i$ vs. rest contrasts, where i = {1,2,3,4,5,6}. No pre-whitening was used during decoding since the ranking of the *t-estimate* should not change across choices. The reason for this is that, as a single channel was used for decoding, each *t-estimate* was affected by the same amount of serial correlations (Lührs et al., 2019).

Necessity of Trial Repetition

Sorger et al. (2009) and Bardin et al. (2011) used an fMRI-based temporal-encoding and decoding approach to carry out five and two communication runs (respectively) with four answer options; while Sorger et al. (2012) used it in a letter speller context with 27 letter options to encode words between 7 and 13 characters. They reached single-trial mean accuracies of 94.9% (Sorger et al., 2009), 100% (Bardin et al., 2011), and 82% (Sorger et al., 2012) in healthy participants. As for fNIRS-based BCIs, previous work has addressed classification problems using multivariate approaches that maximally distinguished between five mental tasks with an average single-trial accuracy of 37.2% (Weyand and Chau, 2015), or four commands involving motor-execution (Shin and Jeong, 2014) and motor imagery tasks (Batula et al., 2014; Naseer and Hong, 2015a; Weyand and Chau, 2015) that reached mean single-trial accuracies of 82.46, 45.6, 73.3, and 46.7%, respectively. In the present work, participants encoded the same choice five consecutive times in each of the eight choice runs, and we achieved mean (multi-trial/repetition) accuracy levels of 74%.

To assess whether five consecutive trials were actually necessary to successfully decode their choice, the effect of reducing the repetitions on the decoding accuracy was evaluated *post hoc*. We observed a significant negative correlation between the accuracies and decreasing the number of repetitions ($\rho = -0.639$, $p < 0.0001$). Interestingly, encoding the same choice only once maintained the mean group accuracies above chance level although with considerably lower values than with five trials (73.96% vs. 41.88%). In line with the observed accuracies, the mean ITR value was considerably reduced when a single trial is used (ITR_1 = 0.17 bits/min) compared to when five trials were used (ITR_5 = 0.30 bits/min). In addition, we observed that reducing the number of repetitions to four slightly improves the mean ITR, with 0.34 bits/min. To put these values in a broader context, the average ITR of the studies mentioned above were calculated and can be compared to the present study in **Figure 9**. This figure shows that the ITR_1 is closely related to the ITR values from Batula et al. (2014) and Weyand and Chau (2015) and that with the approach employed in this study (ITR_5) considerably higher accuracies are reached, while maintaining the ITR value. This figure also depicts that ITR_5 is considerably lower than in Shin and Jeong (2014) and Naseer and Hong (2015a).

Lower decoding accuracies compared to fMRI studies are expected since fMRI has a higher spatial resolution (Valente et al., 2019), fMRI signals have stronger signal-to-noise ratio (Cui et al., 2011) and because unlike fMRI, the brain signal measured with fNIRS also contains (unwanted) superficial scalp information (Erdoğan et al., 2014). This is because light traveling from a source to a detector to reach the brain must pass through scalp and skull tissues twice (Brigadoi and Cooper, 2015). Lower decoding accuracies compared to fNIRS-BCI studies employing multivariate approaches may require further explanation. Multivariate approaches are pattern-classification algorithms used to decode the information that is represented in a given pattern of activity (Norman et al., 2006). They

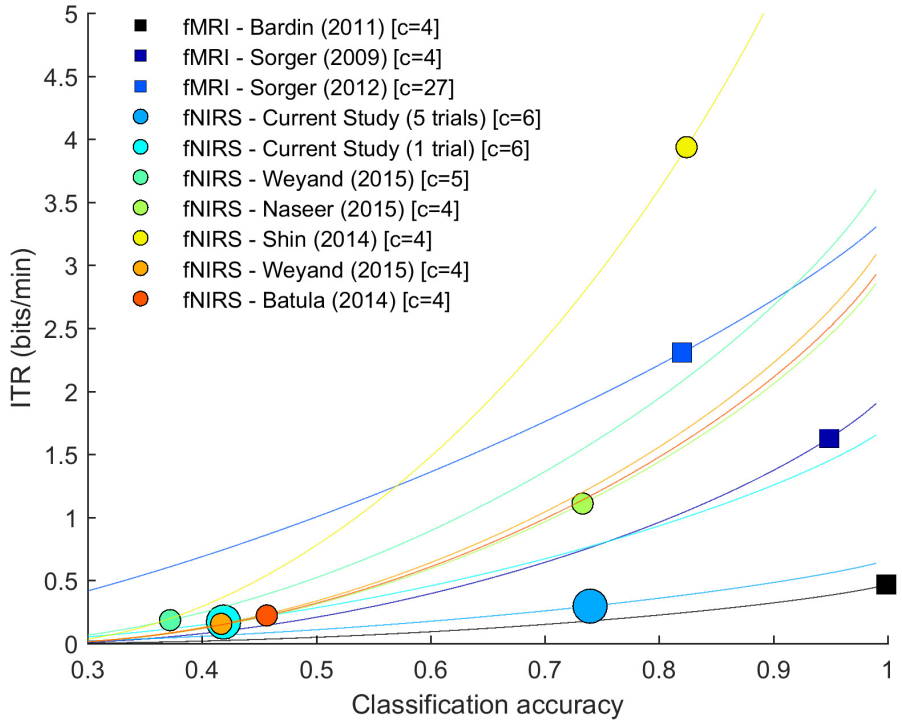

FIGURE 9 | Average ITR values from relevant hemodynamic-BCI literature. Square markers represent fMRI-based BCIs, while circular markers represent fNIRS-based BCIs. Lines depict the theoretical values the ITR (bits/min) can take as a function of the number of classes (c), trial duration and accuracy.

integrate information of multiple voxels/electrodes/channels by optimizing their weights and theoretically should provide higher sensitivity to disentangle overlapping distributed activation patterns than univariate approaches (Valente et al., 2019). The fundamental steps comprising multivariate approaches are, generally speaking, feature extraction, feature selection, model learning and validation (Norman et al., 2006). The available number of trials/examples for model learning and feature extraction influences the performance of multivariate approaches, as estimating a model based on few examples may not be sufficiently reliable or may not capture the differences between classes in a relatively high-dimensional space (Valente et al., 2019). Thus, it is expected that a model trained on a sufficient number of examples should be able to accurately classify examples never seen by the model. Naseer and Hong (2015a) and Shin and Jeong (2014) employed multivariate approaches and both used > 100 trials to train their models, collected over four separate sessions and a single session, respectively. In addition, their classification problem aimed at distinguishing between different task patterns, which we suspect may elicit more discernible patterns than classification problems aimed at detecting the presence or absence of a task-related information (i.e., task vs. rest scenario). It should be noted that Batula et al. (2014) and Weyand and Chau (2015) also applied multivariate approaches that aimed at distinguishing between different motor imagery tasks, but employed less total number of trials to address the classification problem, which can partially explain the lower accuracies reported in these studies. The temporal approach employed in this study did not require any model learning, but relied on a time course extracted from a single channel with certain degree of trial-to-trial variability that was not constant across participants. Indeed, in some participants (see P03, P04, P06, P08, or P12), we did not observe a linear decrease in the decoding performance with reducing the number of repetitions as in the group results, which suggests that for some participants the inter-trial variability is higher than for others. Altogether, we believe these are the main reasons that could explain the divergence in the mean single-trial accuracies observed in the present study and in the literature.

In the future, a multivariate temporal approach could be tested that would also only require a single localizer run. Specifically, instead of selecting and using a single (most-informative) channel for decoding participants' intentions, a task-specific activation pattern would be defined after the localizer session (based on a univariate approach over each channel comprising the setup), here called as "*base-pattern*." For each of the communication runs a new activation pattern for each condition would be calculated and compared to the *base-pattern* as in Monti et al. (2010). The answer option leading to the highest correlation or the smallest distance between the patterns would be the selected option. Importantly, the number of optodes comprising the setup should be optimized to guarantee participants' comfort and a good accuracy level. In addition, due to the existing trial-to-trial variability within and across participants, a subject-specific number of trials could be considered instead of seeking a group-based criterion. This could be achieved, for example, by

implementing an evidence accumulation process with a stopping criterion that trades speed and accuracy for each participant (Mattout et al., 2015).

Feasibility of Error-Correction Approach

Automatic recognition of error potentials has been successfully used in EEG-based BCIs that focus on sensorimotor rhythms and event-related potentials, since evoked responses by the feedback differ depending on whether the feedback is correct or not (Chavarriaga et al., 2014; Mattout et al., 2015). Hemodynamic signals do not show such distinct patterns, which makes direct forms of error-correction mechanisms more challenging to implement. Here we developed an active error-correction approach where participants were asked to indicate a decoding error by encoding the "Error" option in the next choice run if the decoded choice they received did not correspond to what they intended to encode. This approach assumes that we can correctly detect the "Error" option when participants encode it. We built a confusion matrix by pooling all encoded answers across participants to evaluate the performance of our proposed error detection approach. In an ideal scenario, the number of "Error" trials comprising this matrix should be zero or close to zero, which would indicate that no decoding mistakes were made. The fact that participants reached an average of ∼74% accuracy indicates that participants had to encode "Error" several times, but importantly, this number differed across participants. **Figure 7** (right side) shows that for example, P06 had to encode "Error" 5/8 times, while P02 did not have to encode any. The figure also indicates that the number of "Error" trials was lower than "not Error" trials (thus making the confusion matrix unbalanced). The confusion matrix shows that we reached an accuracy of 90.62% (72/96 trials were correctly labeled as "Error" or "not Error"). However, we only reached a recall level of 63.63% (out of 22 error trials, 8 trials were missed), which indicates that this approach did not always work.

It is also important to note that the number of encoded errors does not directly represent the accuracy of the BCI setup. This is due to three reasons: first of all, owing to a technical mistake, data from P01-P07 were reanalyzed offline. In turn, some trials that were incorrectly decoded in real-time were correctly decoded offline (and *vice versa*), which misplaced the presence of "Error" encoding runs (and disrupted the semantic link between the encoded and decoded choices). This means that in the former case (after offline analysis the choice was correctly decoded), a subsequent error-encoding run became unnecessary, while for the latter case (after offline analysis the choice run was incorrectly decoded) a following "Error" encoding run should have occurred (see **Supplementary Data Sheet S1**). Second, our experimental design did not include an error option in the first level of the nested menu. This implies that if choices were wrongly decoded in the fourth level of the menu, participants were no longer able to encode the "Error" option in the next run. Third, and similarly, if a decoding error occurred in the last run of the experiment (run number eight), participants were no longer able to encode the "Error" option. These two scenarios could be addressed in the future by using additional short runs (under a minute) where the participant would verify if the decoded answer was correct or not. The run would consist of an initial and final baseline periods of 20 and 10 s, respectively, with a single full rotation of the AR cube presented in between. Specifically, the AR cube would show faces corresponding to yes/no answers, alternated with rest periods, i.e., YES-NO-REST-YES-NO-REST (6 s per face, 36 s in total). This would allow participants to encode twice whether the decoding option was correct or not in 66 s, while leaving enough time for the hemodynamic response to get back to baseline.

In this experiment participants navigated through a four-level, nested menu. After completing one full round (i.e., reaching level four), participants were directed back to the first level of the menu. Since participants performed eight choice runs, this structure allowed them to maximally go through the menu twice. Due to the technical mistake mentioned above, the following lines will only discuss results pertaining P08–P12: P11 completed two full rounds (100% accuracy), while P09 and P10 completed one full round (both participants reached a 87.5% accuracy); P08 and P12 did not manage to complete a single round (the decoding accuracy for both participants was 50%). These results clearly show that *statistically* significant accuracy is a necessary but not sufficient prerequisite to achieve a *functionally* significant accuracy. Indeed, the accuracy that would be necessary to use the system in a convenient way requires the accuracy to be much higher. Future work should include the "Error" option in each level of the nested menu. It should also consider an additional measure besides the magnitude of the t-statistic for decoding participants' choices, such as a confidence measure based on the absolute differences in the t-estimate across conditions. We expect that a more informed decision helps improving the decoding and the error-detection processes.

Task Selection Based on Participants' Preference and Previous Experience

In the present study, we first trained participants to perform two different motor imagery tasks and subsequently let them choose their preferred option. However, unlike previous work, we did not test whether user preference leads to better performance compared to an experimenter-based task selection approach (Weyand and Chau, 2017).

Intuitively, experienced BCI users may have a more realistic idea of which mental strategy works best for them and thus choose the task that has worked well in the past. Although we asked participants to choose the task they felt most comfortable with in the given setup independent of their previous experience, P02, P04, P05, and P11 chose to use mental drawing for this very reason. In contrast, participants P07 and P10, who also reported being familiar with the mental drawing task (and unfamiliar to the interacting with the cube task), chose to use interacting with the cube as it felt more natural for them given the AR stimuli.

Previous experience with the mental task, BCI setups and fNIRS systems did not show significant correlation with obtained accuracies. However, differences in decoding accuracies between (1) novices and (2) average and more experienced BCI/fNIRS users were considerably high [65.63% vs. 80% (average) and 75% (more experienced) for BCI and 62.5% vs. 70% (average) and 82.5% (more experienced) for fNIRS]. Similarly, we

observed differences between the same groups but to a lower extent regarding previous task experience. Specifically, novices reached a mean accuracy of 71.73%, while average and more experienced users reached 75 and 79.17%, respectively. These observations suggest that participants with a certain level of experience with a BCI/fNIRS system or a given mental task may have enough introspective information to make an adequate and informed decision on their preferred task after a single training session.

Using AR in BCIs Offers a Great Flexibility

Recent work has shown that EEG-based BCIs can successfully be used in combination with new technological developments such as AR to improve real-world practicality by offering a richer, more direct, and intuitive interface (Kansaku et al., 2010; Takano et al., 2011; Borges et al., 2016; Faller et al., 2017). However, very few fNIRS applications have explored this option (Afergan et al., 2015; McKendrick et al., 2016; Si-Mohammed et al., 2018; Hu et al., 2019). In the present study, we employed an AR cube to guide the temporal-encoding approach and to display the decoded answer of participants' intentions. For that, we used a relatively simple and flexible setup from the hardware point of view: we made use of two laptops, one additional computer screen, an HD webcam, and home-made A4 cardboards. The home-made A4 cardboards served as whiteboards and triggered the display of the AR cube in Unity3D on an additional computer screen. Importantly, a whiteboard offers a high degree of flexibility and individuality as anyone (a caretaker, family member, experimenter, etc.) could write potential choice options based on previous knowledge of the user and/or the social context (although we used the same choice options for all participants in this experiment, see **Supplementary Data Sheet S2**). Also, a whiteboard provides a degree of proximity to the setup and interaction between the user and the experimenter as new choice options need to be written down after each run. Besides, handwriting may offer a sense of familiarity to the user. It is important to note that participants were instructed to look at the computer screen at all times throughout the runs, which makes the chosen location of the cardboard (on the desk, between the computer screen and the participant) not intuitive from a pure AR setup perspective. Indeed, the cardboard could have been placed in a different location (behind the screen, for example) as long as the webcam's placement would change accordingly. However, we chose consciously to place the cardboard between the screen and the participants exclusively to exploit the cardboards' interactive and proximity features mentioned above.

Altogether, this relatively simple setup has the potential to be successfully implemented in a more ecologically valid environment such as a hospital room or a rehab center. From the setup point of view, we picture a situation where the user would be placed comfortably in a Fowler's position (head is placed at a 45-degree angle), while wearing the optodes, fNIRS cap and overcap. The fNIRS system would be located next to the bed. A removable desk would be attached to the structure of the bed, above the user's thighs, slightly tilted toward the user's head. A tablet fixated almost perpendicular to the desk could be used instead of the additional computer screen to display the AR cube. To maximize comfort, the rotation of the desk would be adjusted to ensure the tablet was placed at the same height as the user's eye gaze. The webcam would be integrated into the tablet or a separate camera would be placed on a stable structure such as a tripod located right next to the participant and it would be recording the contents of the whiteboard. Alternatively, smart glasses with an integrated camera could be used. These glasses would then also replace the tablet and could display the cube directly on the glasses.

From the data analysis point of view, the current decoding process could be improved to increase the performance of the BCI (as discussed in previous sections). Importantly, as the majority of the analysis steps have been streamlined (through scripts written in Matlab and Unity3D), a single BCI operator would be sufficient to perform the measurements. However, to assure that the channel selection procedure is properly done (i.e., the selected channel is sufficiently informative and not corrupted extensively by noise), an experienced researcher or a trained medical professional in understanding the fNIRS signal would be necessary. Of course, caretakers and family members should be encouraged at all times to assist the experimenter in selecting the most appropriate options to be presented to the user through the whiteboard.

CONCLUSION AND OUTLOOK

In the present study, we showed that fNIRS-based BCIs can be successfully combined with AR technology to address a six-class problem using a single mental task and fNIRS channel. AR technology allows for a seamless real-world interaction that future studies should explore in more detail. The high inter-subject variability observed in this study not only in achieved accuracies but also in task preference and channel selection, points at the need of shifting the BCI field toward a true user-centered approach. Future studies should consider pursuing individualized approaches to bridge the gap from research to real-world applications.

DATA AVAILABILITY STATEMENT

The raw data supporting the conclusions of this article will be made available by the authors, without undue reservation, to any qualified researcher.

ETHICS STATEMENT

The studies involving human participants were reviewed and approved by ethics committee of the Faculty of Psychology and Neuroscience, Maastricht University, The Netherlands. The

patients/participants provided their written informed consent to participate in this study.

AUTHOR CONTRIBUTIONS

RBu, AB-A, and BS conceived the idea and designed the experiment. RBe and RBu prepared the Unity3D environment. RBe developed the dynamic object control functions. RBu, ML, and AB-A optimized the hardware setup. RBu and AB-A measured pilot participants. BS and AB-A adapted the design based on pilot measurements. AB-A carried out the fNIRS measurements, analyzed the data, and wrote the manuscript. BS, ML, and RM assisted on the interpretation of results and data analysis. AB-A, BS, and ML structured the manuscript. RBu, BS, RM, ML, RM, and RBe revised the manuscript critically.

FUNDING

This research was supported by The Luik 3 grant for joint research between Cognitive Neuroscience and Knowledge Engineering Departments, Maastricht University, on advanced brain-robot interfaces, 2015-9999 (to RM and BS).

ACKNOWLEDGMENTS

We would like to thank Giancarlo Valente and Andrew Morgan for their advice on data analysis; to Anita Tursic and Laurien Nagels-Coune for their advice on the experimental setup; the Instrumentation department for their timely assistance; and to all the participants for their time and effort.

SUPPLEMENTARY MATERIAL

The Supplementary Material for this article can be found online at: https://www.frontiersin.org/articles/10.3389/fnins.2020.00346/full#supplementary-material

DATA SHEET S1 | Encoded and decoded choices.

DATA SHEET S2 | Menu choices presented to participants.

REFERENCES

Aarabi, A., and Huppert, T. J. (2016). Characterization of the relative contributions from systemic physiological noise to whole-brain resting-state functional near-infrared spectroscopy data using single-channel independent component analysis. *Neurophotonics* 3:025004. doi: 10.1117/1.NPh.3.2.025004

Abdalmalak, A., Milej, D., Diop, M., Naci, L., Owen, A., and St. Lawrence, K. (2016). *Assessing the Feasibility of Time-Resolved fNIRS to Detect Brain Activity During Motor Imagery*. Bellingham, WA: SPIE.

Afergan, D., Hincks, S. W., Shibata, T., and Jacob, R. J. K. (2015). "Phylter: a system for modulating notifications in wearables using physiological sensing," in *Foundations of Augmented Cognition: 9th International Conference, AC*, Los Angeles, CA.

Allison, B., Dunne, S., Leeb, R., Millán, J. D. R., and Nijholt, A. (2012). *Towards Practical Brain-Computer Interfaces; Bridging the Gap from Research to Real-World Applications*. Berlin: Springer.

Bardin, J. C., Fins, J. J., Katz, D. I., Hersh, J., Heier, L. A., Tabelow, K., et al. (2011). Dissociations between behavioural and functional magnetic resonance imaging-based evaluations of cognitive function after brain injury. *Brain* 134(Pt 3), 769–782. doi: 10.1093/brain/awr005

Batula, A. M., Ayaz, H., and Kim, Y. E. (2014). "Evaluating a four-class motor-imagery-based optical brain-computer interface," in *2014 36th Annual International Conference of the IEEE Engineering in Medicine and Biology Society*, Chicago, IL, 2000–2003.

Batula, A. M., Mark, J. A., Kim, Y. E., and Ayaz, H. (2017). Comparison of brain activation during motor imagery and motor movement using fNIRS. *Comput. Intell, Neurosci.* 2017, 5491296–5491296. doi: 10.1155/2017/5491296

Bauernfeind, G., Scherer, R., Pfurtscheller, G., and Neuper, C. (2011). Single-trial classification of antagonistic oxyhemoglobin responses during mental arithmetic. *Med. Biol. Eng. Comput.* 49:979. doi: 10.1007/s11517-011-0792-5

Birbaumer, N., Ghanayim, N., Hinterberger, T., Iversen, I., Kotchoubey, B., Kübler, A., et al. (1999). A spelling device for the paralysed. *Nature* 398, 297–298. doi: 10.1038/18581

Blum, T., Stauder, R., Euler, E., and Navab, N. (2012). "Superman-like X-ray vision: Towards brain-computer interfaces for medical augmented reality," in *2012 IEEE International Symposium on Mixed and Augmented Reality (ISMAR)*, Atlanta, GA, 271–272.

Boas, D. A., Dale, A. M., and Franceschini, M. A. (2004). Diffuse optical imaging of brain activation: approaches to optimizing image sensitivity, resolution, and accuracy. *NeuroImage* 23, S275–S288. doi: 10.1016/j.neuroimage.2004.07.011

Borges, L., Martins, F., Naves, E., Freire, T., and Lucena, V. Jr. (2016). Multimodal System for training at distance in a virtual or augmented reality environment for users of electric-powered wheelchairs. *IFACPapersOnLine* 49, 156–160. doi: 10.1016/j.ifacol.2016.11.146

BrainInnovationSupport (2019). *Matlab Network Interface*. Available: https://support.brainvoyager.com/turbo-satori/getting-started/393-matlab-network-interface (accessed Septembe 19, 2019).

Brigadoi, S., and Cooper, R. J. (2015). How short is short? Optimum source-detector distance for short-separation channels in functional near-infrared spectroscopy. *Neurophotonics* 2:025005. doi: 10.1117/1.NPh.2.2.025005

Chavarriaga, R., Sobolewski, A., and Millán, J. D. R. (2014). Errare machinale est: the use of error-related potentials in brain-machine interfaces. *Fron. Neurosci.* 8:208. doi: 10.3389/fnins.2014.00208

Chin, Z. Y., Ang, K. K., Wang, C., and Guan, C. (2010). "Online performance evaluation of motor imagery BCI with augmented-reality virtual hand feedback," in *2010 Annual International Conference of the IEEE Engineering in Medicine and Biology*, Berlin, 3341–3344.

Cui, X., Bray, S., Bryant, D. M., Glover, G. H., and Reiss, A. L. (2011). A quantitative comparison of NIRS and fMRI across multiple cognitive tasks. *NeuroImage* 54, 2808–2821. doi: 10.1016/j.neuroimage.2010.10.069

Cui, X., Bray, S., and Reiss, A. L. (2010). Speeded near infrared spectroscopy (NIRS) response detection. *PLoS One* 5:e15474. doi: 10.1371/journal.pone.0015474

Duvernoy, H. M., Delon, S., and Vannson, J. L. (1981). Cortical blood vessels of the human brain. *Brain Res. Bull.* 7, 519–579. doi: 10.1016/0361-9230(81)90007-1

Erdogan, S. B., Özsarfati, E., Dilek, B., Soğukkanlı Kadak, K., Hanoğlu, L., and Akin, A. (2019). Classification of motor imagery and execution signals with population-level feature sets: Implications for probe design in fNIRS based BCI. *J. Neural Eng.* 16:026029. doi: 10.1088/1741-2552/aafdca

Erdoğan, S. B., Yücel, M. A., and Akın, A. (2014). Analysis of task-evoked systemic interference in fNIRS measurements: insights from fMRI. *NeuroImage* 87, 490–504. doi: 10.1016/j.neuroimage.2013.10.024

Essenpreis, M., Cope, M., Elwell, C. E., Arridge, S. R., van der Zee, P., and Delpy, D. T. (1993). "Wavelength dependence of the differential pathlength factor and the log slope in time-resolved tissue spectroscopy," in *Optical Imaging of Brain Function and Metabolism*, eds U. Dirnagl, A. Villringer, and K. M. Einhäupl (Boston, MA: Springer US), 9–20.

Faller, J., Allison, B. Z., Brunner, C., Scherer, R., Schmalstieg, D., Pfurtscheller, G., et al. (2017). A feasibility study on SSVEP-based interaction with motivating

and immersive virtual and augmented reality. *arXiv.org*. [Preprint]. Available online at: https://arxiv.org/abs/1701.03981 (accessed January 6, 2020).

Faller, J., Leeb, R., Pfurtscheller, G., and Scherer, R. (2010). "Avatar navigation in virtual and augmented reality environments using an SSVEP BCI," in *Proceeding. of the 1st International Conference on Apllied Bionics and Biomechanics(ICABB)*, Venice.

Gagnon, L., Cooper, R. J., Yücel, M. A., Perdue, K. L., Greve, D. N., and Boas, D. A. (2012). Short separation channel location impacts the performance of short channel regression in NIRS. *NeuroImage* 59, 2518–2528. doi: 10.1016/j.neuroimage.2011.08.095

Galan, F., Nuttin, M., Lew, E. W., Ferrez, P., Vanacker, G., Philips, J., et al. (2008). A Brain-actuated wheelchair: asynchronous and non-invasive brain-computer interfaces for continuous control of robots. *Clin. Neurophysiol.* 119, 2159–2169. doi: 10.1016/j.clinph.2008.06.001

Goodwin, J. R., Gaudet, C. R., and Berger, A. J. (2014). Short-channel functional near-infrared spectroscopy regressions improve when source-detector separation is reduced. *Neurophotonics* 1:015002. doi: 10.1117/1.NPh.1.1.015002

Herff, C., Heger, D., Putze, F., Hennrich, J., Fortmann, O., and Schultz, T. (2013). Classification of mental tasks in the prefrontal cortex using fNIRS. *Conf. Proc. IEEE Eng. Med. Biol. Soc.* 2013, 2160–2163. doi: 10.1109/EMBC.2013.6609962

Hocke, M. L., Oni, K. I., Duszynski, C. C., Corrigan, V. A., Frederick, D. B., and Dunn, F. J. (2018). Automated processing of fNIRS Data—A visual guide to the pitfalls and consequences. *Algorithms* 11:67. doi: 10.3390/a11050067

Hong, K.-S., Khan, M. J., and Hong, M. J. (2018). Feature extraction and classification methods for hybrid fNIRS-EEG brain-computer interfaces. *Front. Hum. Neurosci.* 12:246. doi: 10.3389/fnhum.2018.00246

Hong, K.-S., and Naseer, N. (2016). Reduction of delay in detecting initial dips from functional near-infrared spectroscopy signals using vector-based phase analysis. *Int. J. Neural Syst.* 26:1650012. doi: 10.1142/S0129065716500124

Hong, K.-S., Naseer, N., and Kim, Y.-H. (2015). Classification of prefrontal and motor cortex signals for three-class fNIRS–BCI. *Neurosci. Lett.* 587, 87–92. doi: 10.1016/j.neulet.2014.12.029

Hong, K.-S., and Santosa, H. (2016). Decoding four different sound-categories in the auditory cortex using functional near-infrared spectroscopy. *Hear. Res.* 333, 157–166. doi: 10.1016/j.heares.2016.01.009

Hu, X.-S., Hong, K.-S., and Ge, S. S. (2013). Reduction of trial-to-trial variability in functional near-infrared spectroscopy signals by accounting for resting-state functional connectivity. *J. Biomed. Opt.* 18:17003.

Hu, X.-S., Nascimento, T. D., Bender, M. C., Hall, T., Petty, S., O'Malley, S., et al. (2019). Feasibility of a real-time clinical augmented reality and artificial intelligence framework for pain detection and localization from the brain. *J. Med. Internet Res.* 21:e13594. doi: 10.2196/13594

Huppert, T. J. (2016). Commentary on the statistical properties of noise and its implication on general linear models in functional near-infrared spectroscopy. *Neurophotonics* 3:010401. doi: 10.1117/1.NPh.3.1.010401

Hwang, H.-J., Choi, H., Kim, J.-Y., Chang, W.-D., Kim, D.-W., Kim, K., et al. (2016). Toward more intuitive brain–computer interfacing: classification of binary covert intentions using functional near-infrared spectroscopy. *J. Biomed. Opt.* 21:091303.

Iturrate, I., Antelis, J., Kübler, A., and Minguez, J. (2009). A noninvasive brain-actuated wheelchair based on a P300 neurophysiological protocol and automated navigation. *Rob. IEEE Trans.* 25, 614–627. doi: 10.1109/TRO.2009.2020347

Kansaku, K., Hata, N., and Takano, K. (2010). My thoughts through a robot's eyes: an augmented reality-brain-machine interface. *Neurosci. Res.* 66, 219–222. doi: 10.1016/j.neures.2009.10.006

Khan, M. J., and Hong, K.-S. (2017). Hybrid EEG-fNIRS-based eight-command decoding for BCI: application to quadcopter control. *Front. Neurorobot.* 11:6. doi: 10.3389/fnbot.2017.00006

Kirilina, E., Jelzow, A., Heine, A., Niessing, M., Wabnitz, H., Brühl, R., et al. (2012). The physiological origin of task-evoked systemic artefacts in functional near infrared spectroscopy. *NeuroImage* 61, 70–81. doi: 10.1016/j.neuroimage.2012.02.074

Klein, F., and Kranczioch, C. (2019). Signal Processing in fNIRS: a case for the removal of systemic activity for single trial data. *Front. Hum. Neurosci.* 13:331. doi: 10.3389/fnhum.2019.00331

Koo, B., Lee, H.-G., Nam, Y., Kang, H., Koh, C. S., Shin, H.-C., et al. (2015). A hybrid NIRS-EEG system for self-paced brain computer interface with online motor imagery. *J. Neurosci. Methods* 244, 26–32. doi: 10.1016/j.jneumeth.2014.04.016

Kübler, A., Holz, E. M., Riccio, A., Zickler, C., Kaufmann, T., Kleih, S. C., et al. (2014). The user-centered Design as novel perspective for evaluating the usability of bci-controlled applications. *PLoS One* 9:e112392. doi: 10.1371/journal.pone.0112392

Lapborisuth, P., Zhang, X., Noah, A., and Hirsch, J. (2017). Neurofeedback-based functional near-infrared spectroscopy upregulates motor cortex activity in imagined motor tasks. *Neurophotonics* 4:021107. doi: 10.1117/1.NPh.4.2.021107

Lécuyer, A., Lotte, F., Reilly, R. B., Leeb, R., Hirose, M., and Slater, M. (2008). Brain-computer interfaces, virtual reality, and videogames. *Computer* 41, 66–72.

Leeb, R., Friedman, D., Müller-Putz, G. R., Scherer, R., Slater, M., and Pfurtscheller, G. (2007). Self-paced (asynchronous) BCI control of a wheelchair in virtual environments: a case study with a tetraplegic. *Comput. Intell. Neurosci.* 2007, 79642–79642. doi: 10.1155/2007/79642

Lenhardt, A., and Ritter, H. (2010). "An augmented-reality based brain-computer interface for robot control," in *Neural Information Processing. Models and Applications*, eds K. W. Wong, B. S. U. Mendis, and A. Bouzerdoum (Berlin: Springer), 58–65.

Liberati, G., Pizzimenti, A., Simione, L., Riccio, A., Schettini, F., Inghilleri, M., et al. (2015). Developing brain-computer interfaces from a user-centered perspective: assessing the needs of persons with amyotrophic lateral sclerosis, caregivers, and professionals. *Appl. Ergon.* 50, 139–146. doi: 10.1016/j.apergo.2015.03.012

Liu, X., Kim, C.-S., and Hong, K.-S. (2018). An fNIRS-based investigation of visual merchandising displays for fashion stores. *PLoS ONE* 13:e0208843. doi: 10.1371/journal.pone.0208843

Lloyd-Fox, S., Blasi, A., and Elwell, C. E. (2010). Illuminating the developing brain: the past, present and future of functional near infrared spectroscopy. *Neurosci. Biobehav. Rev.* 34, 269–284. doi: 10.1016/j.neubiorev.2009.07.008

Lührs, M., and Goebel, R. (2017). Turbo-Satori: a neurofeedback and brain-computer interface toolbox for real-time functional near-infrared spectroscopy. *Neurophotonics* 4:041504. doi: 10.1117/1.NPh.4.4.041504

Lührs, M., Riemenschneider, B., Eck, J., Andonegui, A. B., Poser, B. A., Heinecke, A., et al. (2019). The potential of MR-Encephalography for BCI/Neurofeedback applications with high temporal resolution. *NeuroImage* 194, 228–243. doi: 10.1016/j.neuroimage.2019.03.046

Mattout, J., Perrin, M., Bertrand, O., and Maby, E. (2015). Improving BCI performance through co-adaptation: applications to the P300-speller. *Ann. Phys. Rehabil. Med.* 58, 23–28. doi: 10.1016/j.rehab.2014.10.006

McKendrick, R., Parasuraman, R., Murtza, R., Formwalt, A., Baccus, W., Paczynski, M., et al. (2016). Into the wild: neuroergonomic differentiation of hand-held and augmented reality wearable displays during outdoor navigation with functional near infrared spectroscopy. *Front. Hum. Neurosci.* 10:216. doi: 10.3389/fnhum.2016.00216

Menon, R. S., and Kim, S.-G. (1999). Spatial and temporal limits in cognitive neuroimaging with fMRI. *Trends Cogn. Sci.* 3, 207–216. doi: 10.1016/S1364-6613(99)01329-7

Mercier-Ganady, J., Lotte, F., Loup-Escande, E., Marchal, M., and Lécuyer, A. (2014). "The Mind-Mirror: See your brain in action in your head using EEG and augmented reality," in *2014 IEEE Virtual Reality (VR)*, Minneapolis, MN, 33–38.

Mihara, M., Miyai, I., Hattori, N., Hatakenaka, M., Yagura, H., Kawano, T., et al. (2012). Neurofeedback using real-time near-infrared spectroscopy enhances motor imagery related cortical activation. *PLoS One* 7:e32234. doi: 10.1371/journal.pone.0032234

Monti, M. M., Vanhaudenhuyse, A., Coleman, M. R., Boly, M., Pickard, J. D., Tshibanda, L., et al. (2010). Willful modulation of brain activity in disorders of consciousness. *New England J. Med.* 362, 579–589. doi: 10.1056/NEJMoa0905370

Muller-Putz, G. R., and Pfurtscheller, G. (2008). Control of an electrical prosthesis With an SSVEP-Based BCI. *IEEE Trans. Biomed. Eng.* 55, 361–364. doi: 10.1109/TBME.2007.897815

Murphy, D. P., Bai, O., Gorgey, A. S., Fox, J., Lovegreen, W. T., Burkhardt, B. W., et al. (2017). Electroencephalogram-based brain-computer interface and lower-limb prosthesis control: a case study. *Front. Neurol.* 8:696. doi: 10.3389/fneur.2017.00696

Nagels-Coune, L., Kurban, D., Reuter, N., Benitez, A., Gossé, L., Riecke, L., et al. (2017). "Yes or no? binary brain-based communication utilizing motor imagery and fNIRS," in *Proceedings of the 7th Graz Brain-Computer Interface*, Graz.

Naseer, N., and Hong, K.-S. (2013). Classification of functional near-infrared spectroscopy signals corresponding to the right- and left-wrist motor imagery for development of a brain–computer interface. *Neurosci. Lett.* 553, 84–89. doi: 10.1016/j.neulet.2013.08.021

Naseer, N., and Hong, K.-S. (2015a). Decoding answers to four-choice questions using functional near infrared spectroscopy. *J. Near Infrar. Spectrosc.* 23, 23–31. doi: 10.1255/jnirs.1145

Naseer, N., and Hong, K.-S. (2015b). fNIRS-based brain-computer interfaces: a review. *Front. Hum. Neurosci.* 9:3. doi: 10.3389/fnhum.2015.00003

Nguyen, H.-D., Yoo, S.-H., Bhutta, M. R., and Hong, K.-S. (2018). Adaptive filtering of physiological noises in fNIRS data. *BioMed. Eng. Online* 17:180. doi: 10.1186/s12938-018-0613-2

Nijboer, F. (2015). Technology transfer of brain-computer interfaces as assistive technology: barriers and opportunities. *Ann. Phys. Rehabil. Med.* 58, 35–38. doi: 10.1016/j.rehab.2014.11.001

Nijboer, F., Sellers, E. W., Mellinger, J., Jordan, M. A., Matuz, T., Furdea, A., et al. (2008). A P300-based brain-computer interface for people with amyotrophic lateral sclerosis. *Clin. Neurophysio.* 119, 1909–1916. doi: 10.1016/j.clinph.2008.03.034

Noori, F. M., Naseer, N., Qureshi, N. K., Nazeer, H., and Khan, R. A. (2017). Optimal feature selection from fNIRS signals using genetic algorithms for BCI. *Neurosci. Lett.* 647, 61–66. doi: 10.1016/j.neulet.2017.03.013

Norman, K. A., Polyn, S. M., Detre, G. J., and Haxby, J. V. (2006). Beyond mind-reading: multi-voxel pattern analysis of fMRI data. *Trends Cogn. Sci.* 10, 424–430. doi: 10.1016/j.tics.2006.07.005

Park, S., Cha, H., and Im, C. (2019). Development of an online home appliance control system using augmented reality and an SSVEP-based brain–computer interface. *IEEE Access* 7, 163604–163614. doi: 10.1109/ACCESS.2019.2952613

Pinti, P., Scholkmann, F., Hamilton, A., Burgess, P., and Tachtsidis, I. (2019). Current status and issues regarding Pre-processing of fNIRS neuroimaging data: an investigation of diverse signal filtering methods within a general linear model framework. *Front. Hum. Neurosci.* 1 2:505. doi: 10.3389/fnhum.2018.00505

Prince, S., Kolehmainen, V., Kaipio, J. P., Franceschini, M. A., Boas, D., and Arridge, S. R. (2003). Time-series estimation of biological factors in optical diffusion tomography. *Phys. Med. Biol.* 48, 1491–1504. doi: 10.1088/0031-9155/48/11/301

Rebsamen, B., Guan, C., Zhang, H., Wang, C., Teo, M. Jr., et al. (2011). a brain controlled wheelchair to navigate in familiar environments. *Neural Syst. Rehabil. Eng. IEEE Trans.* 18, 590–598. doi: 10.1109/TNSRE.2010.2049862

Rezazadeh Sereshkeh, A., Yousefi, R., Wong, A. T., and Chau, T. (2018). Online classification of imagined speech using functional near-infrared spectroscopy signals. *J. Neural Eng.* 16:12.

Saager R. B., and Berger, A. J. (2005). Direct characterization and removal of interfering absorption trends in two-layer turbid media. *J. Opt. Soc. Am. A* 22, 1874–1882. doi: 10.1364/JOSAA.22.001874

Saager, R. B., Telleri, N. L., and Berger, A. J. (2011). Two-detector Corrected Near Infrared Spectroscopy (C-NIRS) detects hemodynamic activation responses more robustly than single-detector NIRS. *NeuroImage* 55, 1679–1685. doi: 10.1016/j.neuroimage.2011.01.043

Sato, T., Nambu, I., Takeda, K., Aihara, T., Yamashita, O., Isogaya, Y., et al. (2016). Reduction of global interference of scalp-hemodynamics in functional near-infrared spectroscopy using short distance probes. *NeuroImage* 141, 120–132. doi: 10.1016/j.neuroimage.2016.06.054

Scarapicchia, V., Brown, C., Mayo, C., and Gawryluk, J. R. (2017). Functional magnetic resonance imaging and functional near-infrared spectroscopy: insights from combined recording studies. *Front. Hum. Neurosci.* 11:419. doi: 10.3389/fnhum.2017.00419

Scharnowski, F., Hutton, C., Josephs, O., Weiskopf, N., and Rees, G. (2012). Improving visual perception through neurofeedback. *J. Neurosci.* 32, 17830–17841. doi: 10.1523/JNEUROSCI.6334-11.2012

Sellers, E. W., Vaughan, T. M., and Wolpaw, J. R. (2010). A brain-computer interface for long-term independent home use. *Amyotrophic Lateral Scler.* 11, 449–455. doi: 10.3109/17482961003777470

Shereena, E. A., Gupta, R. K., Bennett, C. N., Sagar, K. J. V., and Rajeswaran, J. (2018). EEG neurofeedback training in children with attention deficit/hyperactivity disorder: a cognitive and behavioral outcome study. *Clin. EEG Neurosci.* 50, 242–255. doi: 10.1177/1550059418813034

Shin, J., and Jeong, J. (2014). Multiclass classification of hemodynamic responses for performance improvement of functional near-infrared spectroscopy-based brain–computer interface. *J. Biomed. Opt.* 19:067009.

Shin, J., Kwon, J., Choi, J., and Im, C.-H. (2017). Performance enhancement of a brain-computer interface using high-density multi-distance NIRS. *Sci. Rep.* 7:16545.

Si-Mohammed, H., Argelaguet, F., Casiez, G., Roussel, N., and Lécuyer, A. (2017). "Brain-computer interfaces and augmented reality: a state of the art," in *Proceedings of the 7th Graz Brain-Computer Interface*, Graz.

Si-Mohammed, H., Petit, J., Jeunet, C., Argelaguet, F., Spindler, F., Évain, A., et al. (2018). Towards BCI-based interfaces for augmented reality: feasibility, design and evaluation. *IEEE Trans. Vis. Comput. Graphics* 26, 1608–1621. doi: 10.1109/TVCG.2018.2873737

Snipes, S., Kurban, D., Accascina, S., Poser, B., and Sorger, B. (2017). "A whole-word encoding paradigm for fMRI-based communication: a divide-and-conquer approach," in *Poster session presented at Organization for Human Brain Mapping*.

Sorger, B., Dahmen, B., Reithler, J., Gosseries, O., Maudoux, A., Laureys, S., et al. (2009). Another kind of 'BOLD Response': answering multiple-choice questions via online decoded single-trial brain signals. *Prog. Brain Res.* 177, 275–292. doi: 10.1016/S0079-6123(09)17719-1

Sorger, B., Reithler, J., Dahmen, B., and Goebel, R. (2012). A real-time fMRI-based spelling device immediately enabling robust motor-independent communication. *Curr. Biol.* 22, 1333–1338. doi: 10.1016/j.cub.2012.05.022

Stangl, M., Bauernfeind, G., Kurzmann, J., Scherer, R., and Neuper, C. (2013). A haemodynamic brain–computer interface based on real-time classification of near infrared spectroscopy signals during motor imagery and mental arithmetic. *J. Near Infrared Spectrosc.* 21, 157–171. doi: 10.1255/jnirs.1048

Subramanian, L., Hindle, J. V., Johnston, S., Roberts, M. V., Husain, M., Goebel, R., et al. (2011). Real-time functional magnetic resonance imaging neurofeedback for treatment of Parkinson's disease. *J. Neurosci.* 31, 16309–16317. doi: 10.1523/JNEUROSCI.3498-11.2011

Sulzer, J., Haller, S., Scharnowski, F., Weiskopf, N., Birbaumer, N., Blefari, M. L., et al. (2013). Real-time fMRI neurofeedback: progress and challenges. *NeuroImage* 76, 386–399. doi: 10.1016/j.neuroimage.2013.03.033

Suzuki, S., Harashima, F., and Furuta, K. (2010). Human control law and brain activity of voluntary motion by utilizing a balancing task with an inverted pendulum. *Adv. in Hum. Comput. Interact.* 2010:16. doi: 10.1155/2010/215825

Tachtsidis, I., and Scholkmann, F. (2016). False positives and false negatives in functional near-infrared spectroscopy: issues, challenges, and the way forward. *Neurophotonics* 3:031405. doi: 10.1117/1.NPh.3.3.031405

Takano, K., Hata, N., and Kansaku, K. (2011). Towards intelligent environments: an augmented reality-brain-machine interface operated with a see-through head-mount display. *Front. Neurosci.* 5:60. doi: 10.3389/fnins.2011.00060

Tong, Y., and Frederick, B. D. (2012). Concurrent fNIRS and fMRI processing allows independent visualization of the propagation of pressure waves and bulk blood flow in the cerebral vasculature. *NeuroImage* 61, 1419–1427. doi: 10.1016/j.neuroimage.2012.03.009

Valente, G., Kaas, A. L., Formisano, E., and Goebel, R. (2019). Optimizing fMRI experimental design for MVPA-based BCI control: combining the strengths of block and event-related designs. *NeuroImage* 186, 369–381. doi: 10.1016/j.neuroimage.2018.10.080

Weyand, S., and Chau, T. (2015). Correlates of near-infrared spectroscopy brain–computer interface accuracy in a multi-class personalization framework. *Front. Hum. Neurosci.* 9:536. doi: 10.3389/fnhum.2015.00536

Weyand, S., and Chau, T. (2017). Challenges of implementing a personalized mental task near-infrared spectroscopy brain–computer interface for a non-verbal young adult with motor impairments. *Dev. Neurorehabil.* 20, 99–107. doi: 10.3109/17518423.2015.1087436

Weyand, S., Schudlo, L., Takehara-Nishiuchi, K., and Chau, T. (2015). Usability and performance-informed selection of personalized mental tasks for an online near-infrared spectroscopy brain-computer interface. *Neurophotonics* 2:025001.

Wolpaw, J. R., Birbaumer, N., McFarland, D. J., Pfurtscheller, G., and Vaughan, T. M. (2002). Brain–computer interfaces for communication and control. *Clin. Neurophysiol.* 113, 767–791. doi: 10.1016/S1388-2457(02)00057-3

Zhang, Y., Brooks, D., Franceschini, M., and Boas, D. (2005). Eigenvector-based spatial filtering for reduction of physiological interference in diffuse optical imaging. *J. Biomed. Opt.* 10:011014.

Conflict of Interest: The authors declare that the research was conducted in the absence of any commercial or financial relationships that could be construed as a potential conflict of interest.

Copyright © 2020 Benitez-Andonegui, Burden, Benning, Möckel, Lührs and Sorger. This is an open-access article distributed under the terms of the Creative Commons Attribution License (CC BY). The use, distribution or reproduction in other forums is permitted, provided the original author(s) and the copyright owner(s) are credited and that the original publication in this journal is cited, in accordance with accepted academic practice. No use, distribution or reproduction is permitted which does not comply with these terms.

frontiers in Human Neuroscience

ORIGINAL RESEARCH
published: 03 June 2020
doi: 10.3389/fnhum.2020.00201

Joint Attention During Live Person-to-Person Contact Activates rTPJ, Including a Sub-Component Associated With Spontaneous Eye-to-Eye Contact

*Swethasri Dravida[1], J. Adam Noah[2], Xian Zhang[2] and Joy Hirsch[2,3,4,5]**

[1] Interdepartmental Neuroscience Program, Yale School of Medicine, New Haven, CT, United States, [2] Brain Function Laboratory, Department of Psychiatry, Yale School of Medicine, New Haven, CT, United States, [3] Department of Neuroscience, Yale School of Medicine, New Haven, CT, United States, [4] Department of Comparative Medicine, Yale School of Medicine, New Haven, CT, United States, [5] Department of Medical Physics and Biomedical Engineering, University College London, London, United Kingdom

OPEN ACCESS

Edited by:
Xianchun Li,
East China Normal University, China

Reviewed by:
Takahiko Koike,
National Institute for Physiological Sciences, Japan
Takayuki Nozawa,
Tokyo Institute of Technology, Japan

***Correspondence:**
Joy Hirsch
joy.hirsch@yale.edu

Specialty section:
This article was submitted to Cognitive Neuroscience, a section of the journal Frontiers in Human Neuroscience

Received: *26 November 2019*
Accepted: *05 May 2020*
Published: *03 June 2020*

Citation:
Dravida S, Noah JA, Zhang X and Hirsch J (2020) Joint Attention During Live Person-to-Person Contact Activates rTPJ, Including a Sub-Component Associated With Spontaneous Eye-to-Eye Contact. Front. Hum. Neurosci. 14:201. doi: 10.3389/fnhum.2020.00201

Eye-to-eye contact is a spontaneous behavior between interacting partners that occurs naturally during social interactions. However, individuals differ with respect to eye gaze behaviors such as frequency of eye-to-eye contacts, and these variations may reflect underlying differences in social behavior in the population. While the use of eye signaling to indicate a shared object of attention in joint attention tasks has been well-studied, the effects of the natural variation in establishing eye contact during joint attention have not been isolated. Here, we investigate this question using a novel two-person joint attention task. Participants were not instructed regarding the use of eye contacts; thus all mutual eye contact events between interacting partners that occurred during the joint attention task were spontaneous and varied with respect to frequency. We predicted that joint attention systems would be modulated by differences in the social behavior across participant pairs, which could be measured by the frequency of eye contact behavior. We used functional near-infrared spectroscopy (fNIRS) hyperscanning and eye-tracking to measure the neural signals associated with joint attention in interacting dyads and to record the number of eye contact events between them. Participants engaged in a social joint attention task in which real partners used eye gaze to direct each other's attention to specific targets. Findings were compared to a non-social joint attention task in which an LED cue directed both partners' attention to the same target. The social joint attention condition showed greater activity in right temporoparietal junction than the non-social condition, replicating prior joint attention results. Eye-contact frequency modulated the joint attention activity, revealing bilateral activity in social and high level visual areas associated with partners who made more eye contact. Additionally, when the number of mutual eye contact events was used to classify each pair as either "high eye contact" or "low eye contact" dyads, cross-brain coherence

analysis revealed greater coherence between high eye contact dyads than low eye contact dyads in these same areas. Together, findings suggest that variation in social behavior as measured by eye contact modulates activity in a subunit of the network associated with joint attention.

Keywords: joint attention, eye-to-eye contact, two-person neuroscience, live dyadic interactions, fNIRS, hyperscanning, eye tracking, neural coherence

INTRODUCTION

Eye contact is one of the most basic and prevalent behaviors that can occur between two individuals. Mutual eye contact can be used to indicate anything from attraction, attention, or aggression. The frequency of eye contacts can vary naturally based on the interaction; for example, partners who are comfortable with the topic they are discussing tend to make more eye contact than those who are uncomfortable (Argyle and Dean, 1965). Groups of individuals also make different amounts of eye contact; individuals with autism tend to make less eye contact than neurotypical individuals (Kanner, 1943, 1944) and tend to focus more on the mouth than the eyes when viewing faces (Klin et al., 2002; Neumann et al., 2006). While eye contact has been studied in social contexts (Hirsch et al., 2017; Koike et al., 2019b), few studies have focused on individual differences in eye contact behavior and the potential effect of these differences on known mechanisms of joint attention.

Joint Attention refers to the shared focus of two or more individuals on an object. A joint attention "event" refers to the alignment of attention due to a cue provided by an "initiator," that is followed by one or more "responders." Joint attention behaviors develop in early childhood, and the ability to engage in joint attention early in life is thought to be crucial to the development of language (Tomasello and Todd, 1983; Tomasello, 1988). Problems with initiating joint attention or responding to nonverbal joint attention initiated by another person (usually a parent) are some of the earliest observable deficits in children with autism (Dawson et al., 2004). Gaze-based joint attention between two people is a fundamental social communication, and the neural mechanisms of joint attention serve as an important clinical target in social disorders.

The majority of prior neuroimaging work in joint attention has focused on the neural mechanisms of single subjects in an fMRI scanner as they engage in joint attention tasks with an experimenter who is outside the scanner. These studies have identified a number of brain networks activated during joint attention tasks, including social cognitive networks as well as traditional attentional networks. In studies of social cognition, areas including the right temporoparietal junction (rTPJ) and medial prefrontal cortex (mPFC) show activity in response to mentalizing (Castelli et al., 2000; Frith and Frith, 2003) and other types of social perception and cognition (Hampton et al., 2008; Van Overwalle, 2009). Attentional tasks that do not involve a live partner show activity in parietal areas, and cardiovascular damage to these areas results in neglect, or the inability to direct the attention to one side of the visual field (Corbetta et al., 1995; Colby and Goldberg, 1999; Behrmann et al., 2004). A joint attention fMRI study using a virtual partner to direct and respond to the participant's gaze showed increased activity in the mPFC when participants initiated joint attention with the virtual partner (Schilbach et al., 2010). Similar findings were observed in another fMRI study of participants engaging in joint attention with an experimenter where greater activity was observed in mPFC as well as right posterior superior temporal sulcus (pSTS), left pSTS, left inferior parietal lobe, right anterior insula, and right inferior frontal gyrus (Redcay et al., 2013). In these studies, data were acquired either from single individuals viewing a confederate or virtual avatar, or from two individuals who viewed videos of each other in real-time while lying in fMRI scanners. Here, we introduce both a live interaction paradigm to investigate joint attention and technology in which subjects can interact directly in a naturalistic environment with additional behavioral measurements of eye gaze.

Advancements in neuroimaging enable simultaneous acquisition of neural signals as well as behavioral measurements from interacting individuals who are seated face to face (Jiang et al., 2012; Pfeiffer et al., 2013; Babiloni and Astolfi, 2014; Hirsch et al., 2017, 2018; Piva et al., 2017). Functional near-infrared spectroscopy (fNIRS) is a neuroimaging tool that measures a blood oxygenation signal as a proxy for direct neuronal responses, similar to the BOLD signal of functional magnetic resonance imaging. However, the head-mounted optodes of fNIRS and the relative tolerance to small movements compared to fMRI enable simultaneous acquisition, hyperscanning, of neural signals from two face-to-face individuals as they interact. Hyperscanning using fNIRS permits investigation of theoretical questions under the framework of the Social Brain Hypothesis and the Dynamic Neural Coupling Hypothesis. The Social Brain hypothesis states that brains in interaction show different activity than brains performing the same task without live interaction (Di Paolo and De Jaegher, 2012; De Jaegher et al., 2016). In the context of joint attention, these hypotheses provoke the question: how do brains engaging in social joint attention with a partner differ from brains engaging in the same attentional task without live interaction? The Dynamic Neural Coupling hypothesis posits that brain areas across partners show covariation as they engage in tasks together that are due to the exchange of social information (Hasson and Frith, 2016). Thus, social joint attention is expected to engage unique cross-brain correlations compared to conditions in which both partners engage in non-social joint attention.

Many studies have looked at neural coherence between partners engaged in a task (Saito et al., 2010; Cui et al., 2012; Konvalinka and Roepstorff, 2012; Tanabe et al., 2012; Schilbach et al., 2013; Scholkmann et al., 2013; Hirsch et al.,

2017, 2018). Hasson et al. (2012) have proposed that the mechanism of coherence between the brains of interacting individuals is driven by shared information; that is, some aspect of the interaction triggers similar activity in the two brains (Hasson and Frith, 2016). Measurement of neural coherence along with behavioral measures can serve as evidence that specific aspects of the interactions between partners leads to synchrony between their brain signals (Saito et al., 2010; Jiang et al., 2012, 2015). By recording the frequency of mutual eye contact events, we can relate "socialness" of joint attention, as measured by the numbers of mutual eye contact events, to coherence differences. Based on the neural coupling hypothesis that cross-brain neural synchrony reflects shared information between dyads, we hypothesize that these differences are driven, not just by the interaction, but by the number of eye contact events during the joint attention task.

Prior fMRI joint attention studies involve tasks in which subjects are explicitly asked to make direct gaze with a partner on a video screen prior to directing their attention. In this way, joint attention has typically been thought of as an extension of eye contact-based communication between the initiator of joint attention and the responder. In this conceptualization of a traditional joint attention event, the first step is direct eye gaze, followed by the initiator transferring his/her gaze to the attentional target. The final step occurs when the responder follows the initiator's gaze to direct his/her attention to the target as well, resulting in joint attention. However, joint attention can also be achieved without initial direct eye gaze, as long as the responder follows the initiator's gaze to focus on the target. Take the example of a passerby who notices someone else standing on the street and looking up at the sky. The first individual can follow the second's gaze to look up at the sky as well, without having to first make eye contact. The extent to which individuals make eye contact without explicit instruction when engaging in joint attention may be related to their innate social behavior. Joint attention with and without un-instructed eye contact has not been investigated.

Here, we examine the role of social eye-to-eye contact behavior as a modulator of joint attention mechanisms to test the hypothesis that the two mechanisms are synergistic. Based on prior studies of eye contact, we have previously shown that direct, mutual eye contact engages the visual and social systems during social interaction (Hirsch et al., 2017; Noah et al., 2020). This predicts increased social exchange between participants who engage in increased eye contact, and these participants may recruit these areas more than in less social participants who make fewer eye contacts during a social joint attention task.

Pairs of participants were instructed to engage in joint attention tasks in which one person was assigned the role of initiator and the other person was the responder. The participants were not explicitly told to make eye contact, allowing for variation in the amount of eye contact across dyads. Importantly, performance on the joint attention task was at ceiling levels regardless of the number of mutual eye contact events between the partners, indicating that joint eye gaze was not required to correctly orient the attention. The effects of engaging in social joint attention were compared with non-social joint attention, in which both participants directed their attention to the same object without exchanging visual cues. Further, we examined how the number of eye contact events that occurred during the social runs modified the brain activity associated with social joint attention. In addition, cross-brain coherence between areas of the brain involved in face-processing was compared between high and low eye contact dyads. Our hypothesis was two-fold: first, that increased engagement in mutual eye contact would result in the modulation of social and high-level visual areas distinct from the neural responses to the joint attention task itself; and second, that pairs who engaged in more mutual eye contact would show greater cross-brain coherence between these areas.

MATERIALS AND METHODS

Participants

Twenty-eight pairs of participants (mean age 29.4, 35 females) took part in the joint attention experiment. All participants completed the Edinborough Handedness Inventory (Oldfield, 1971), and fifty-four of the fifty-six participants were right-handed. There were twelve female-female, five male-male, and ten female-male pairs. One participant declined to report gender information. Participants had no known neurologic or psychiatric conditions. All participants provided written informed consent in accordance with the guidelines approved by the Yale University Human Investigation Committee (HIC # 1501015178) and were compensated for participating. Data were collected at the Yale School of Medicine, New Haven, Connecticut, United States. Prior to taking part in the joint attention experiment, each participant underwent a finger-thumb tapping procedure at a previous date.

Paradigm

Participants were seated at a table across from each other, approximately 140 cm apart. Between them, on the table, was a transparent panel with two LEDs to the right side of each participant (**Figure 1A**). Each participant's LEDs were not visible to their partner. The higher LED was either off or illuminated yellow, while the lower LED was either off or illuminated in red, green, or blue during the experiment. In the center of the panel were three circular stickers, equally spaced, one red, one green, and one blue. Importantly, the position of each color was the same in space for each participant; for example, if the red sticker was to the right for Subject 1, it was to the left for Subject 2 sitting across from Subject 1, so that when both subjects looked at the red sticker, they were looking at the same point in space. Below the stickers was a white bar with a magnet on which the Tobii x3-120 eye tracker was mounted (see **Figure 1A**). The panel did not obstruct the partners' view of each other's faces. A scene camera was positioned on a camera mount attached to an articulated arm behind each participant and aimed to record what the participant was seeing during the experiment. LEDs were controlled by serial port commands sent from a Python script to an Arduino board that was pre-programmed to recognize commands as "on" and "off" for each color.

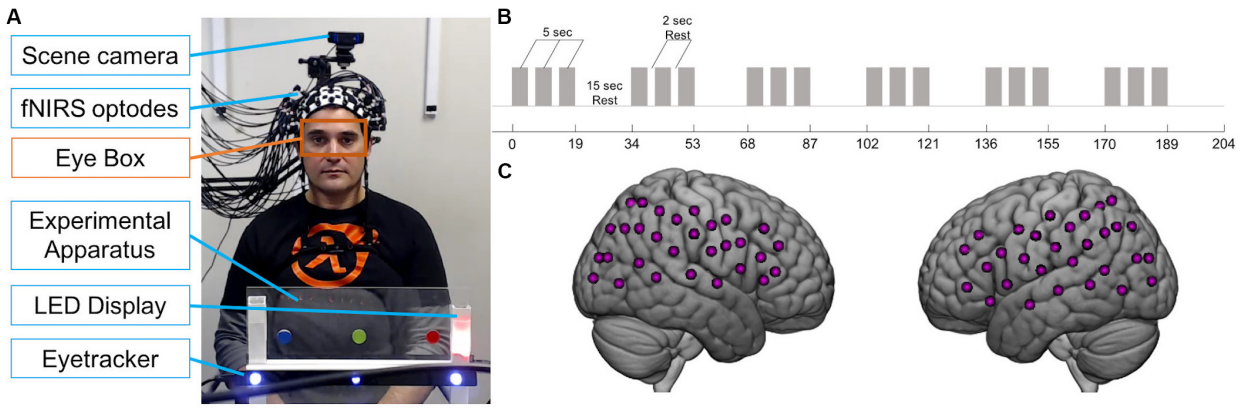

FIGURE 1 | Joint attention experiment. **(A)** Example view of experimental apparatus during social trial in which partner seen in photo is the responder. Black bar with blue lights is the eye tracker. For each participant, an eye tracker was used to record eye movements and a scene camera was used to record what the participant saw. Orange box indicates eye box used to calculate mutual eye contact events. Photograph used with permission. **(B)** Paradigm time course. Gray bars represent 5-s trials. Task blocks consisted of three 5-s trials interspersed with 2-s of rest. 19-s task blocks alternated with 15-s rest blocks. **(C)** Example fNIRS 60-channel layout covering bilateral frontal, temporal, and parietal areas on one participant.

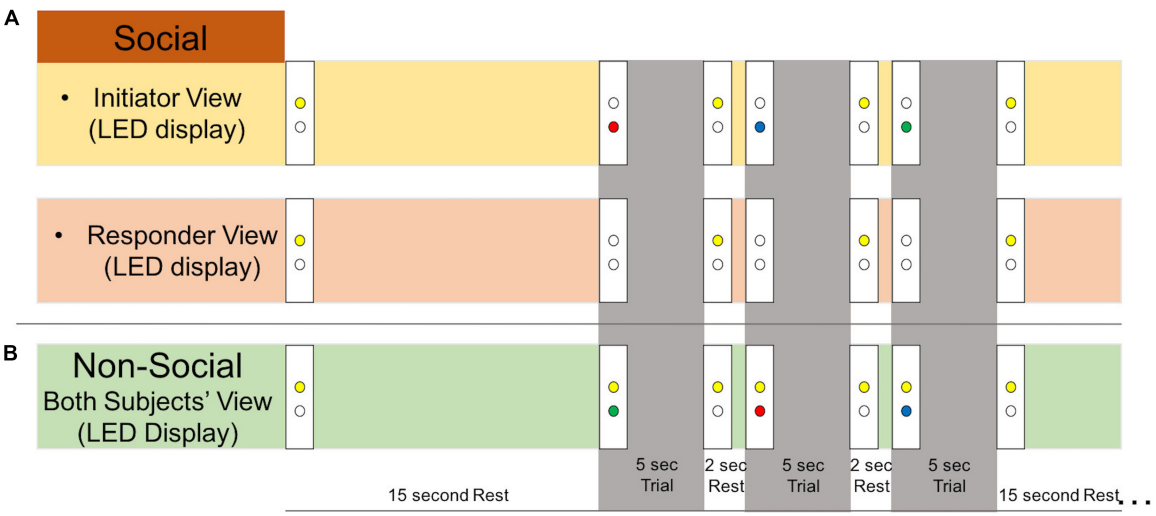

FIGURE 2 | Experimental stimuli. Example LED display as viewed by each subject during social and non-social runs. During all rest periods, participants were instructed to look at the lit yellow LED. An auditory tone indicated to both participants that the trial was over and to look back at the yellow LED rest cue. **(A)** During 5-s social trials, the initiator would receive an LED cue (green, blue, or red) and use his/her eye gaze to indicate the location of the correct target to the responder. The responder would not receive an LED cue during the trial. **(B)** During 5-s non-social trials, both participants received an LED cue (green, blue, or red) indicating the correct gaze target. The yellow LED remained on during the whole run to remind participants that it was non-social.

Task

There were two types of runs: "social runs" in which one subject initiated the joint attention events and the other subject responded, and "non-social runs" in which both subjects received an LED cue that directed their attention. Subjects were told that as a dyad, the goal of the task was for both participants to gaze at the correct target. For the social runs, the initiator was told that his/her goal was to show his/her partner the correct target using only eye movements. The responder was told to use his/her partner's gaze to find the correct target. For the non-social runs, subjects were told to look at the correct target, shown by the LED color. Runs began with both yellow LEDs illuminated for the first 5 s, during which each participant focused their gaze on their yellow LED. Each run consisted of six 19-s task blocks and six 15-s rest blocks (**Figure 1B**). Task blocks included three 5-s attention trials interspersed with 2-s of rest. Example LED displays during the rest and task blocks are shown in **Figure 2**. During the joint attention trials in the social runs, a colored LED to the right of the apparatus indicated the target to the initiator. The initiator was instructed to communicate the location of the target to the responder non-verbally, using only eye movements. Importantly, the initiator was not told to first make eye contact with the responder before directing his/her gaze to the target. An auditory beep indicated the trial was over and both participants

should return their gaze to the yellow LED, which was illuminated during rest periods. When the next trial started, the yellow LEDs would become unlit and the initiator would see the colored LED with the next target, while the responder would not see any LED cue. During all rest periods, participants were instructed to focus their gaze on the lit, yellow LED to the right of the apparatus. The yellow LED was also illuminated during the entirety of the non-social joint attention runs. During these runs, both participants received the same colored LED light cueing them to the correct target.

There were four social runs total: two runs in which Subject A was the initiator and two runs in which Subject B was the initiator. There were also two non-social joint attention runs with no initiator or responder; therefore, there were six runs total. The order of the runs was randomized and each type was completed once before any were repeated. For example, one possible run order was: Subject A initiates, Subject B initiates, non-social, Subject A initiates, Subject B initiates, non-social. Prior to the start of the recording, participants engaged in a "practice run," in which they experienced two blocks of each type (Subject A initiating, Subject B initiating, non-social). The experimenter observed and talked to the participants during the practice run, ensuring that both participants understood the task and could see the targets, the LED and each other, and reminding them to keep their heads as still as possible. Once the experiment began, participants wore the instruments the entire time but had about a 15-s break between runs, when the fNIRS and eye tracking recordings were stopped and re-started.

Eye Tracking

Eye tracking data were acquired using two Tobii Pro x3-120 eye trackers (Tobii Pro, Stockholm, Sweden), one per participant, at a sampling rate of 120 Hz. Eye trackers were mounted on the experimental apparatus facing each subject (**Figure 1A**). Each subject was calibrated using a three-point calibration on their partner's face prior to the start of the experiment. The partner was instructed to stay still and look straight ahead while the subject was told to look first at the partner's right eye, then left eye, then the tip of the chin.

UDP signals were used to synchronize the triggers from the stimulus presentation program to a custom virtual keyboard interpretation tool written in Python to the Tobii Pro Lab software. When a joint attention trial started and ended, UDP triggers were sent wirelessly from the paradigm computer to the eye tracking computers, and the virtual keyboard "typed" a letter that marked the events in the eye tracking data recorded in Tobii Pro Lab.

Functional Near-Infrared Spectroscopy Acquisition

Functional NIRS signals were acquired from two participants simultaneously using a continuous wave Shimadzu LABNIRS system (Shimadzu Corp., Kyoto, Japan) with eighty optodes. Three wavelengths of light (780, 805, and 830 nm) were emitted by each emitter and the temporal resolution of acquisition was 27 ms. Light absorption measured by each detector was converted to concentrations of oxyhemoglobin (oxyHb) and deoxyhemoglobin (deoxyHb) using a modified Beer-Lambert equation. Twenty emitters and twenty detectors were placed on each participant to cover bilateral frontal, temporal, and parietal areas (**Table 1**) resulting in 60 channels per head (**Figure 1C**). Participants were fitted with custom caps with optode separation distances of either 2.75 or 3 cm for participants with head circumferences less than 56.5 cm or greater than 56.5 cm, respectively. Caps were placed such that the front-most optodes were approximately 1 cm above nasion, to maximize similar positioning across participants. A lighted fiberoptic probe (Daiso, Hiroshima, Japan) was used to remove hair from each optode holder before placing the optode to ensure contact with the skin. A TTL triggering system was used to synchronize triggers sent from the Python stimulus presentation script to the fNIRS system.

Digitization

A Polhemus Patriot digitizer (Polhemus, Colchester, VT, United States) was used to record the position of each optode relative to each subject's anatomical landmarks (nasion, inion, Cz, left pre-auricular point, right pre-auricular point). Coordinates were converted into Montreal Neurological Institute (MNI) space using NIRS-SPM (Ye et al., 2009). MNI coordinates and anatomical labels for the median channel locations across all subjects are listed in **Table 1**.

Analysis of Eye Gaze Position

Tobii Pro Lab software (Tobii Pro, Stockholm, Sweden) was used to create areas of interest for subsequent eye tracking analyses run in MATLAB 2014a (Mathworks, Natick, MA, United States). The first area of interest was the "eye box" (see **Figure 1A**), which covered the portion of the face of the partner in the video to which the participant's eye tracking was targeted during initiation and response to joint attention events. The second area of interest was the "target box" which covered the part of the scene where the participant's gaze rested on the red, blue, and green targets. Areas of interest were created manually based on watching the eye tracking videos. Data were exported from Tobii and custom scripts in MATLAB were used calculate the behavioral measures of mutual eye contact events, accuracy, and latency to targets. An "eye hit" was defined when the participant's gaze was directed to the eye box of his/her partner. A mutual eye contact event was defined as simultaneous eye hits for both partners lasting at least 10 frames (83 ms). The videos of each participant recorded using the eye tracking software were also viewed to confirm that the participants' head movement was minimal during the task.

The median number of eye contact events for all participant pairs was used to categorize dyads into two groups: "high eye contact pairs" and "low eye contacts pairs" whose number of mutual eye contact events were above and below the median, respectively. The interaction between groups (high and low eye contact pairs) and behavioral measures (latency to target and duration on target) was examined using a two-way repeated measures ANOVA. *Post hoc* tests applied Tukey's multiple comparisons test with Bonferroni correction. The amount of cross-brain coherence between dyads in the high and low

TABLE 1 | Median channel MNI coordinates for each of the 60 channels with anatomical labels and probabilities.

Channel	*X*	*Y*	*Z*	BA	Anatomical Area	Probability
1	−43.67	−57.33	59.33	7	Somatosensory Association Cortex	0.305
				40	Supramarginal gyrus part of Wernicke's area	0.683
2	−51.67	−52.00	56.00	40	Supramarginal gyrus part of Wernicke's area	1.000
3	−47.33	−74.67	42.33	19	V3	0.237
				39	Angular gyrus, part of Wernicke's area	0.644
4	−49.67	26.67	38.67	9	Dorsolateral prefrontal cortex	0.677
5	−59.00	2.00	40.67	6	Pre-Motor and Supplementary Motor Cortex	0.832
6	−61.33	−20.67	47.67	1	Primary Somatosensory Cortex	0.257
				2	Primary Somatosensory Cortex	0.268
				6	Pre-Motor and Supplementary Motor Cortex	0.217
7	−61.33	−40.67	49.67	40	Supramarginal gyrus part of Wernicke's area	0.989
8	−56.33	−65.33	39.33	39	Angular gyrus, part of Wernicke's area	0.625
				40	Supramarginal gyrus part of Wernicke's area	0.375
9	−49.00	37.67	27.33	46	Dorsolateral prefrontal cortex	0.947
10	−60.33	13.33	25.33	9	Dorsolateral prefrontal cortex	0.476
				44	pars opercularis, part of Broca's area	0.231
				45	pars triangularis Broca's area	0.231
11	−64.67	−9.67	36.67	6	Pre-Motor and Supplementary Motor Cortex	0.720
12	−66.00	−30.67	41.67	40	Supramarginal gyrus part of Wernicke's area	0.627
13	−62.00	−55.33	35.67	40	Supramarginal gyrus part of Wernicke's area	0.837
14	−49.67	−81.33	23.33	19	V3	0.464
				39	Angular gyrus, part of Wernicke's area	0.536
15	−58.33	25.67	14.67	45	pars triangularis Broca's area	0.709
16	−65.00	0.67	20.33	6	Pre-Motor and Supplementary Motor Cortex	0.592
17	−68.00	−19.33	27.67	2	Primary Somatosensory Cortex	0.234
				40	Supramarginal gyrus part of Wernicke's area	0.228
18	−67.00	−43.33	29.67	40	Supramarginal gyrus part of Wernicke's area	0.962
19	−54.00	−76.00	19.00	19	V3	0.495
				39	Angular gyrus, part of Wernicke's area	0.505
20	−55.33	35.67	5.67	45	pars triangularis Broca's area	0.393
				46	Dorsolateral prefrontal cortex	0.290
				47	Inferior prefrontal gyrus	0.281
21	−61.67	5.33	1.67	22	Superior Temporal Gyrus	0.638
22	−68.00	−11.33	13.33	22	Superior Temporal Gyrus	0.259
				42	Primary and Auditory Association Cortex	0.316
				43	Subcentral area	0.378
23	−69.33	−34.33	16.67	22	Superior Temporal Gyrus	0.558
				42	Primary and Auditory Association Cortex	0.242
24	−66.00	−56.33	11.67	21	Middle Temporal gyrus	0.381
				22	Superior Temporal Gyrus	0.576
25	−48.00	−86.67	7.00	19	V3	0.873
26	−53.67	17.33	−9.33	38	Temporopolar area	0.566
				47	Inferior prefrontal gyrus	0.315
27	−67.67	−6.33	−10.67	21	Middle Temporal gyrus	1.000
28	−71.00	−24.67	−1.67	21	Middle Temporal gyrus	0.627
				22	Superior Temporal Gyrus	0.264
29	−69.67	−46.00	2.00	21	Middle Temporal gyrus	0.585
				22	Superior Temporal Gyrus	0.405
30	−60.00	−69.00	0.00	19	V3	0.306
				37	Occipito-temporal cortex	0.516
31	46.67	−62.33	55.67	7	Somatosensory Association Cortex	0.491
				40	Supramarginal gyrus part of Wernicke's area	0.509

(Continued)

TABLE 1 | Continued

Channel	*X*	*Y*	*Z*	BA	Anatomical Area	Probability
32	48.00	−74.67	40.00	19	V3	0.351
				39	Angular gyrus, part of Wernicke's area	0.570
33	54.67	−53.33	54.33	40	Supramarginal gyrus part of Wernicke's area	1.000
34	56.67	−65.33	37.67	39	Angular gyrus, part of Wernicke's area	0.673
				40	Supramarginal gyrus part of Wernicke's area	0.327
35	61.67	−42.33	50.67	40	Supramarginal gyrus part of Wernicke's area	1.000
36	63.67	−19.67	48.33	1	Primary Somatosensory Cortex	0.259
				2	Primary Somatosensory Cortex	0.204
				3	Primary Somatosensory Cortex	0.208
				6	Pre-Motor and Supplementary Motor Cortex	0.223
37	61.00	3.67	41.67	6	Pre-Motor and Supplementary Motor Cortex	0.750
38	52.00	28.67	37.67	9	Dorsolateral prefrontal cortex	0.672
				46	Dorsolateral prefrontal cortex	0.229
39	46.67	−84.67	19.67	19	V3	0.852
40	62.67	−57.67	33.33	39	Angular gyrus, part of Wernicke's area	0.287
				40	Supramarginal gyrus part of Wernicke's area	0.713
41	68.00	−32.00	42.00	40	Supramarginal gyrus part of Wernicke's area	0.694
42	67.33	−6.67	34.67	6	Pre-Motor and Supplementary Motor Cortex	0.854
43	62.67	14.33	25.67	9	Dorsolateral prefrontal cortex	0.528
				45	pars triangularis Broca's area	0.260
44	51.33	38.33	28.33	46	Dorsolateral prefrontal cortex	0.867
45	54.00	−75.33	19.33	19	V3	0.386
				39	Angular gyrus, part of Wernicke's area	0.614
46	68.67	−44.00	27.00	40	Supramarginal gyrus part of Wernicke's area	0.821
47	70.00	−20.67	28.33	2	Primary Somatosensory Cortex	0.209
				40	Supramarginal gyrus part of Wernicke's area	0.348
48	67.67	2.67	21.33	6	Pre-Motor and Supplementary Motor Cortex	0.618
49	60.67	26.67	17.33	45	pars triangularis Broca's area	0.638
				46	Dorsolateral prefrontal cortex	0.299
50	48.00	−86.33	3.33	18	Visual Association Cortex (V2)	0.254
				19	V3	0.746
51	66.00	−57.33	10.67	21	Middle Temporal gyrus	0.387
				22	Superior Temporal Gyrus	0.470
52	72.00	−33.67	15.33	22	Superior Temporal Gyrus	0.541
				42	Primary and Auditory Association Cortex	0.325
53	70.00	−10.67	12.33	22	Superior Temporal Gyrus	0.319
				42	Primary and Auditory Association Cortex	0.300
				43	Subcentral area	0.322
54	62.67	11.67	5.67	22	Superior Temporal Gyrus	0.364
				44	pars opercularis, part of Broca's area	0.358
55	58.00	35.33	9.67	45	pars triangularis Broca's area	0.440
				46	Dorsolateral prefrontal cortex	0.467
56	59.00	−69.67	−2.67	19	V3	0.460
				37	Occipito-temporal cortex	0.507
57	71.00	−46.33	0.33	21	Middle Temporal gyrus	0.623
				22	Superior Temporal Gyrus	0.335
58	73.00	−23.67	−0.33	21	Middle Temporal gyrus	0.458
				22	Superior Temporal Gyrus	0.399
59	69.00	−4.67	−7.33	21	Middle Temporal gyrus	0.921
60	57.67	22.67	−1.33	45	pars triangularis Broca's area	0.237
				47	Inferior prefrontal gyrus	0.595

Negative x-coordinate indicates the left side. MNI coordinates were converted to Tailarach coordinates to generate cluster labels. Note that for the first ten pairs of participants, optodes were arranged in a 58 channel layout. The layout was switched to cover more of the higher-level visual cortex.

eye contact groups was compared using wavelet coherence analysis (see below).

Functional Near-Infrared Spectroscopy Analysis

Analysis methods for fNIRS data were similar to those previously reported and are explained in detail elsewhere (Dravida et al., 2017; Hirsch et al., 2017, 2018; Noah et al., 2017, 2020). The signal used for the analysis was the combined hemoglobin signal, the sum of the oxyhemoglobin and the inverted deoxyhemoglobin signals. Briefly, wavelet detrending was used to remove baseline drift. Noisy channels were removed automatically if the root mean square of the signal was more than 10 times the average for that participant. A principal component analysis (PCA) spatial filter was used to remove physiologic, non-neural components from the signal (Zhang et al., 2016, 2017). For each run, a general linear model (GLM) of the joint attention task paradigm (**Figure 1B**) convolved with a canonical hemodynamic response function was used to generate beta values for each channel. Data from each participant were then registered to the median channel locations for all participants and reshaped into 3D voxel-based images with 3,753 standard 2x2x2 mm^3 voxels. Thus, the beta values in each channel for each participant represent the fit of the individual participant's data to the model. The first-level model resulted in contrast images for the Social > Non-social joint attention contrast, Initiation of joint attention > Non-social joint attention, and Response to joint attention > Non-social joint attention for each participant.

SPM8 (Wellcome Trust, London, United Kingdom) was used for second-level, group contrast analysis and *t*-tests were used to generate statistical maps of brain activity, using a threshold of $p < 0.01$. For each of the contrasts above, in the second-level group analysis, the average number of eye contacts in all four social runs for each participant was added as a covariate. Thus the Social>Non-Social main effect contrast is the result of the canonical regressor with all ones in the design matrix. The contrast with the covariate regressor answers the question of how the activity due to social joint attention changes more in participants who made more eye contact than in participants who made less eye contact (modulatory effect of eye contact on joint attention).

An alternate analysis was run using only the main effect regressor. Separating the participants into "high eye contact dyads" and "low eye contact dyads," the contrast of High eye contact (Social > Non-social) > Low eye contact (Social > Non-social) was computed to further illustrate the effect of the high eye contact dyads' behavior on the activity due to the joint attention task.

Wavelet Coherence Analysis

Coherence analyses were performed on the deoxyhemoglobin signals rather than the oxyhemoglobin or combined signals due to the increased sensitivity of the oxyhemoglobin to systemic signal components (Franceschini et al., 2004; Huppert et al., 2006; Kirilina et al., 2012; Tachtsidis and Scholkmann, 2016; Zhang et al., 2016) which affect residual signals used in the analysis. Details on this method can be found in Hirsch et al. (2017, 2018), Piva et al. (2017). Briefly, channels were grouped into 12 anatomical regions and wavelet coherence analysis was evaluated between all groups across participants in a pair exhaustively. The wavelet coherence analysis decomposes time-varying signals into their frequency components. Here, the wavelet kernel used was a complex Gaussian ("Cgau2") provided in MATLAB. The residual signal from the entire data trace was used, with the activity due to the task removed, similar to traditional PPI analysis (Friston et al., 1997). Sixteen scales were used and the range of frequencies was 0.1 to 0.025 Hz. Based on prior work, we restricted the wavelengths used to only those that reflect fluctuations in the range of the hemodynamic response function; coherence results in the range higher than 0.1 Hz have been shown to be due to non-neural physiologic components (Nozawa et al., 2016; Zhang et al., 2020). Therefore, 11 wavelengths total were used for the analysis. Complex coherence values were averaged because averaging complex coherence values results in greater correlation between measured and expected coherence compared to averaging the absolute value of coherence over time (Zhang et al., 2020).

Cross-brain coherence is the correlation between the corresponding frequency components across interacting partners, averaged across all time points and represented as a function of the wavelength of the frequency components. The difference in coherence between dyads in the high eye contact group and dyads in the low eye contact group was measured using *t*-tests for each frequency component. Only wavelengths shorter than 30 s were considered. All four social runs were used to find pairs of areas across participants in a dyad that showed significant coherence difference between the high and low eye contact groups. An analysis on shuffled pairs of participants who did not do the task together was conducted in order to report coherence that was specific to the pair interaction and not due to engagement in a similar task. Results that showed increased coherence in the group of high eye contact dyads relative to the group of low eye contact dyads for at least three consecutive wavelengths are reported.

RESULTS

Behavioral Eye Tracking Results

All mutual eye contact events that occurred from the start to the end of the run were counted. Most eye contact events occurred before joint attention to the target; however, for some dyads, some eye contact events occurred during the trial but after joint gaze on the target was achieved, resulting in greater than 18 events. No eye contact events occurred during rest periods. Dyads were ordered (**Figure 3**, *x*-axis) from least to most number of eye contact events (**Figure 3**, *y*-axis). The median number of mutual eye contact events across all dyads was 10.5. Pairs with greater than 10.5 eye contact events were classified as "high eye contact dyads" (orange circles) and pairs with lower than 10.5 eye contact events were classified as "low eye contact dyads" (blue circles). Onset of eye contact events during one social run for an example high eye contact dyad (**Figure 4A**) and a low eye contact dyad (**Figure 4B**) are shown. During social runs, the high eye contact

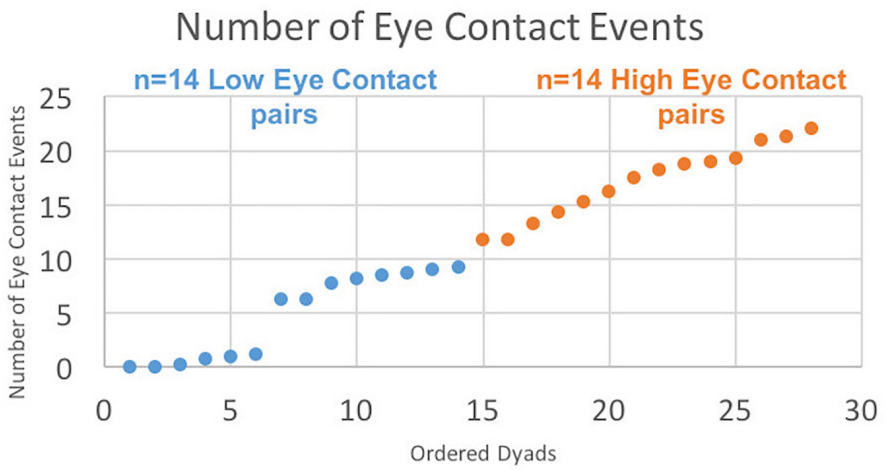

FIGURE 3 | Number of eye contact events for each pair ordered. "Eye contact event" is defined when both subjects' eye gaze is located in the partner's eye box (see **Figure 1B**) for at least 10 frames (83 ms). Twenty-eight dyads are ordered on the *x*-axis from least to most number of eye contact events, with median number of eye contact events = 10.5. Blue points constitute the "Low Eye Contact Dyads;" orange points constitute the "High Eye Contact Dyads." For the within-brain, general linear model analysis, the number of eye contact events for each participant was included as a second-level covariate in the group analysis, regardless of participant group. For the cross-brain coherence, the high and low eye contact groupings were used.

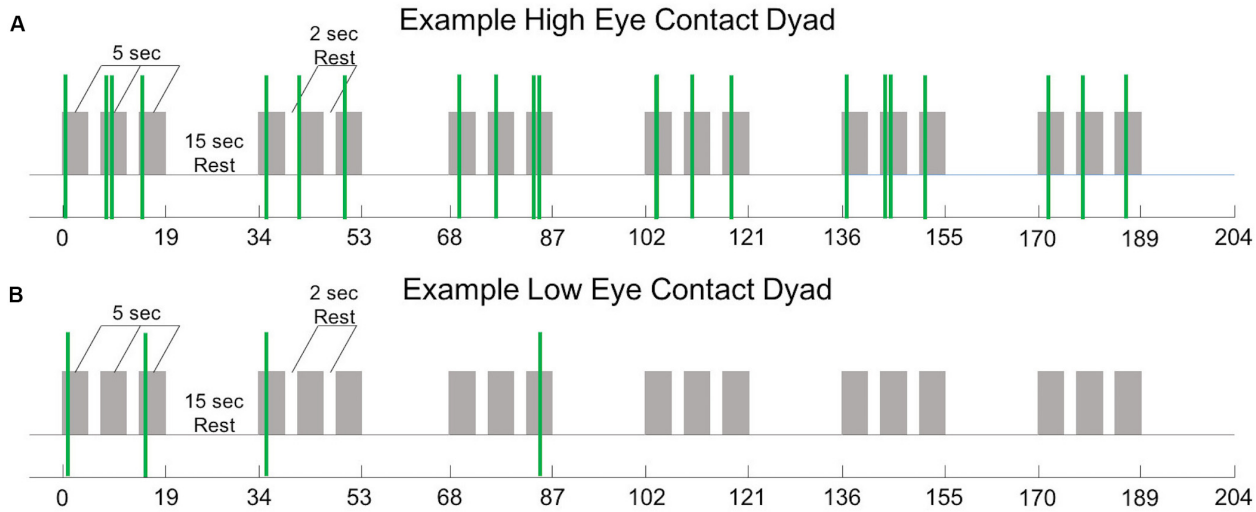

FIGURE 4 | (A) Experiment time course (see **Figure 1A**) with 22 mutual eye contact events (green bars) from one social run from one "high eye contact" dyad. **(B)** Experiment time course with 4 mutual eye contact events (green bars) from one social run from one "low eye contact" dyad.

dyads had an average of 17.1 eye contacts events, while the low eye contact dyads had an average of 4.8 eye contact events. There were no mutual eye contact events during the non-social runs for any of the dyads. High eye contact dyads consisted of 7 female-female pairs, 2 male-male pairs, and 5 male-female pairs. Low eye contact dyads consisted of 5 female-female pairs, 3 male-male pairs, 5 male-female pairs, and one pair in which a participant declined to report gender information. Thus the differences that are reported between the high and low eye contact dyads cannot be explained by the demographic compositions of the groups.

Eye tracking data were used to quantify the latency to targets, accuracy, and number of eye hits on the partner's face for each participant. The average latency to target was 952.6 ms. Average latency to target was lowest during the non-social attention trials, when the subject's attention was directed using an LED. There was no difference in latency to target between the three colored targets regardless of condition. Accuracy to target was 100% in both groups regardless of condition; only one subject made an error on one non-social trial by failing to redirect their attention on the next trial at the auditory cue.

The effect of the interaction between groups (high and low eye contact pairs) and conditions (initiation, response, and non-social attention) on the latency to target was determined using a two-way repeated measures ANOVA, with *post hoc*

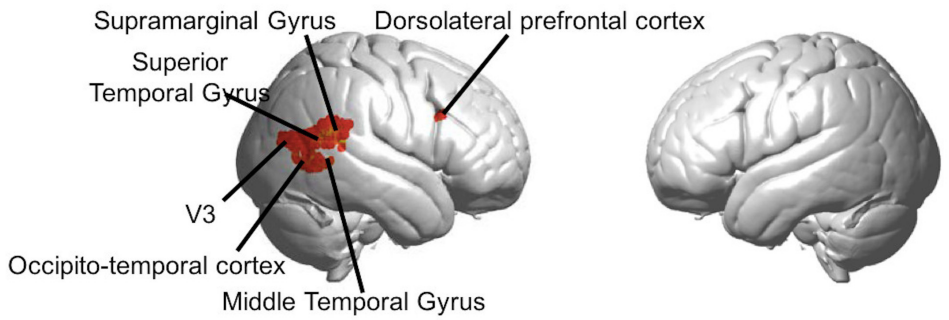

FIGURE 5 | Group GLM Results: Social joint attention effect. Whole brain rendered images showing greater activity for Social > Non-social joint attention ($p < 0.01$, uncorrected). Social conditions include all runs in which one subject was an initiator and one was a responder. Results are combined across all participants ($n = 56$).

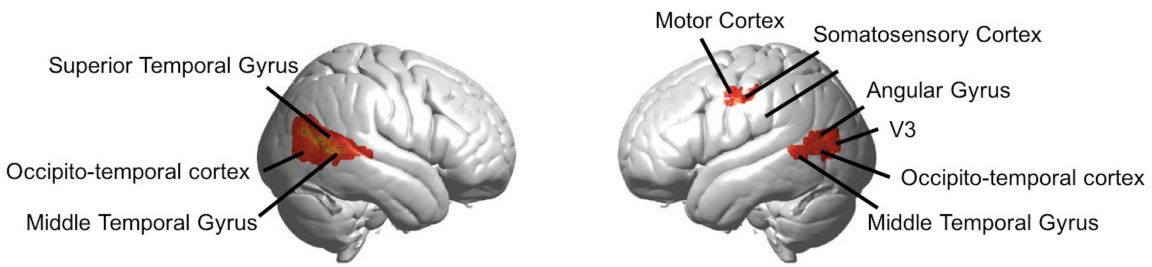

FIGURE 6 | Group GLM Results: Social joint attention modulated by eye contact. Red-yellow areas on whole brain rendered images indicate greater activity in the Social > Non-social joint attention with greater activity in participants who made more eye contact ($p < 0.01$, uncorrected; $n = 56$).

tests using Tukey's multiple comparisons test with Bonferroni correction. As expected, there was a significant effect of condition ($p < 0.0001$); i.e., latency to target was significantly slower when the participant was the responder than during he/she was the initiator or when he/she was in a non-social run (**Supplementary Figure S1**). There was also a significant effect of group, with higher latencies in the high eye contact group than the low eye contact group ($p = 0.0092$). There was no significant group by condition interaction.

Each video was watched by an examiner who recorded the location of the eye box and whether or not the location of the eyes moved from the start to the end of the video. Minimal head movement was observed during the task in all eye tracking videos, regardless of whether the participant was part of the low or high eye contact pairs.

Within-Subject General Linear Model Results

Results of the joint attention contrasts are presented with and without the effect of the mutual eye contact events between partners. The GLM main effect figure (**Figure 5**) represents the results of the main task effect for the Social joint attention> Non-social joint attention contrast. This is the result of the main effect of the canonical regressor from the column of ones in the design matrix. The results are also presented using the covariate regressor of the number of eye contact events in the second-level analysis for the Social > Non-social joint attention contrast (**Figure 6**). In other words, **Figure 5** displays the result of the social joint attention task for all pairs, while **Figure 6** represent the results of the modulatory effect of eye contact on joint attention.

The Social > Non-social main effect (orthogonal to the modulatory effect of mutual eye contact) revealed activity in the following clusters ($p < 0.01$; **Figure 5**): right superior temporal gyrus/supramarginal gyrus (n of voxels = 160, peak T = 3.87, peak MNI coordinate of (70, −42, 14)), right occipito-temporal cortex (n of voxels = 18, peak T = 3.05, peak MNI coordinate at (58, −70,6)), and right dorsolateral prefrontal cortex (n of voxels = 14, peak T = 2.89, peak MNI coordinate of (58, 18, 28)). These findings are in line with expected result for joint attention tasks.

The rendered hemodynamic results of the Social > Non-social contrast with the group-level eye contact covariate regressor are

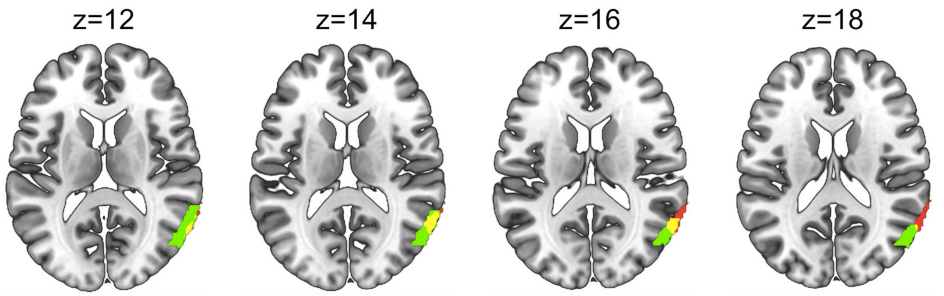

FIGURE 7 | Overlap (yellow) between the area showing greater activity for the Social>Non-social joint attention main effect in **Figure 5** (red) and the Social > Non-social joint attention modulated by eye contact in **Figure 6** (green). Areas and overlap are displayed on four axial slices using a template brain.

shown in **Figure 6**, with red-yellow clusters denoting higher activity with more eye contact events ($p < 0.01$). This resulted in a cluster on the left consisting of angular gyrus, middle temporal gyrus, occipito-temporal cortex, and V3 (n of voxels = 147, peak t = 3.76, peak MNI coordinate of (−58, −70, 12)) and a cluster on the right comprised of the superior temporal gyrus, middle temporal gyrus, and occipito-temporal cortex (n of voxels = 671, peak t = 3.81, peak MNI coordinate of (62, −50, 6)), as well as smaller clusters in the left motor cortex (see **Table 2** for details). There are 61 voxels in the right superior temporal gyrus/middle temporal gyrus/occipito-temporal cortex area that overlap between the results shown in **Figures 5**, **6**. The area of overlap is shown in **Figure 7** and the brain regions covered by this area are listed in **Table 3**. The contrast of the social joint attention task relative to rest resulted in similar areas as above, with and without the modulation of eye contact, respectively (**Supplementary Figure S2**).

To further elucidate the effects of eye contact on initiating and responding to joint attention, results are presented using brain activity for the "initiation of joint attention > non-social joint attention" contrast, and for the "response to joint attention > non-social joint attention" contrast. For the "initiation > non-social" contrast, for each subject only the social runs in which that subject was the initiator were used, as well as the non-social runs. For the "response > non-social" contrast, for each subject only the social runs in which that subject was the responder were used, as well as the non-social runs. These analyses were possible because in each run, only one subject was the initiator for the entire duration of the run and the other subject was the responder. A contrast image was generated with these contrasts for each participant in the first-level analysis.

In the second level analysis, the modulatory effect of eye contact was calculated using the covariate regressor. Here, we present the result of the eye contact covariate regressor on the contrasts of Initiation > Non-social joint attention and Response > Non-social joint attention. The following clusters represent higher activity with greater eye contact for initiation of joint attention relative to the non-social condition (**Figure 8A**): the right angular gyrus [n of voxels = 443, t = 3.81, peak MNI coordinate of (48, −68, 16)], left somato-motor area [n of voxels = 112, t = 3.24, peak MNI coordinate of (−56, −20, 42)], and bilateral superior parietal areas [right: n of voxels = 17, peak t = 2.69, peak MNI coordinate of (42, −56, 58); left: n of voxels = 284, peak t = 3.43, peak MNI coordinate of (−32, −56, 56)]. The following clusters showed greater activity with higher amount of eye contact for the response to joint attention relative to the non-social condition (**Figure 8B**): right superior temporal gyrus [n of voxels = 413, peak t = 4.98, peak MNI coordinate of (64, −56, 16)], left angular gyrus [part of Wernicke's area; n of voxels = 394, peak t = 4.43, peak MNI coordinate of (−58, −70, 10)], and bilateral parietal areas [right: n of voxels = 27, peak t = 2.89, peak MNI coordinate of (58, −56, 32); left: n of voxels = 12, peak t = 2.62, peak MNI coordinate of (−34, −70, 48)], along with smaller clusters in bilateral motor cortex. All whole-brain clusters are listed in **Table 2**. The results of the contrast of initiation of joint attention > response to joint attention with the group-level eye contact regressor are shown in the **Supplementary Figure S3**.

The results above using the eye contact covariate regressor were calculated using the average number of eye contacts for each participant. We also split the participants into "high" and "low" eye contact dyads (blue and orange dots in **Figure 3**) to further illustrate the increase in the joint attention activity in participants who made more eye contact. The contrast of the social joint attention > non-social joint attention in the high eye contact dyads versus the low eye contact dyads resulted in an area of increased activity in the right superior and middle temporal gyrus (**Figure 9**), similar to the result of the eye contact frequency covariate on social > non-social joint attention for all dyads (**Figure 6**).

Wavelet Coherence Results

One advantage of the dynamic two-person paradigm is the measure of neural coupling, which enables a test of the shared information hypothesis (Hasson and Frith, 2016). Cross-brain coherence was compared between high eye contact and low eye contact pairs for the social runs to test the specific hypothesis that increased frequency of eye-to-eye contacts will be associated with increased coherence between neural signals in regions that process face information. Coherence (**Figure 10**) is represented as the correlation between frequency components (y-axis) as a function of component wavelength (x-axis), with coherence between the high eye contact pairs in red and coherence between low eye contact pairs in blue. Coherence was increased ($p < 0.05$)

TABLE 2 | Group-level general linear model contrast results ($p < 0.01$).

Peak MNI coordinates	Peak T	*P*	# Voxels	BA	Anatomical Area	Probability
Social > Non-social Joint Attention (Task effect)						
(70, −42, 14)	3.87	0.00015	160	22	Superior Temporal Gyrus	0.636
				40	Supramarginal Gyrus	0.171
(64, −60, 4)	3.38	0.00068	31	37	Occipito-temporal cortex	0.337
				21	Middle Temporal Gyrus	0.300
				22	Superior Temporal Gyrus	0.180
(58, −70, 6)	3.05	0.00177	18	19	V3	0.426
				37	Occipito-temporal cortex	0.220
				39	Angular Gyrus	0.206
(58, 18, 28)	2.89	0.0028	14	9	Dorsolateral prefrontal cortex	0.506
				45	pars triangularis, Broca's area	0.238
				46	Dorsolateral prefrontal cortex	0.141
Social > Non-social Joint Attention (Eye Contact effect)						
(62, −50, 6)	3.81	0.00018	671	22	Superior Temporal Gyrus	0.479
				21	Middle Temporal Gyrus	0.382
				37	Occipito-temporal cortex	0.111
(−58, −70, 12)	3.76	0.00021	147	19	V3	0.335
				39	Angular Gyrus	0.314
				37	Occipito-temporal cortex	0.179
(−64, −48, 4)	2.76	0.00397	21	21	Middle Temporal Gyrus	0.512
				22	Superior Temporal Gyrus	0.429
(−60, −10, 40)	3.09	0.00159	32	6	Pre-motor and supplementary motor cortex	0.664
				3	Primary somatosensory cortex	0.135
(−48, −8, 40)	2.62	0.00574	16	6	Pre-motor and supplementary motor cortex	0.906
Initiation of Joint Attention > Non-social Joint Attention (Eye Contact effect)						
(48, −68, 16)	3.81	0.00018	443	39	Angular Gyrus	0.607
				19	V3	0.367
(42, −56, 58)	2.69	0.0048	17	7	Somatosensory Association Cortex	0.460
				40	Supramarginal Gyrus	0.441
(−32, −56, 56)	3.43	0.00059	284	7	Somatosensory Association Cortex	0.717
				40	Supramarginal Gyrus	0.242
(−56, −20, 42)	3.24	0.00103	112	6	Pre-motor and supplementary motor cortex	0.298
				2	Primary somatosensory cortex	0.243
				3	Primary somatosensory cortex	0.176
				1	Primary somatosensory cortex	0.165
(−58, 0, −4)	2.59	0.00615	13	21	Middle Temporal Gyrus	0.470
				22	Superior Temporal Gyrus	0.407
Response to Joint Attention > Non-social Joint Attention (Eye Contact effect)						
(64, −56, 16)	4.98	0	413	22	Superior Temporal Gyrus	0.380
				39	Angular Gyrus	0.241
				21	Middle Temporal Gyrus	0.170
				40	Supramarginal Gyrus	0.147
(58, −56, 32)	2.89	0.00279	27	40	Supramarginal Gyrus	0.605
				39	Angular Gyrus	0.351
(−58, −70, 10)	4.43	0.00002	394	19	V3	0.368
				39	Angular Gyrus	0.252
				37	Occipito-temporal cortex	0.196
				21	Middle Temporal Gyrus	0.103
(−58, −14, 12)	2.56	0.00668	21	22	Superior Temporal Gyrus	0.342

(Continued)

TABLE 2 | Continued

Peak MNI coordinates	Peak T	*P*	# Voxels	BA	Anatomical Area	Probability
				42	Primary and Auditory Association Cortex	0.310
				43	Subcentral area	0.285
(−34, −70, 48)	2.62	0.00572	12	7	Somatosensory Association Cortex	0.735
				19	V3	0.203

Clusters of positive activity for each contrast are listed. Horizontal lines separate results from each contrast (in bold). Negative x-coordinate indicates the left side. BA, Brodmann's area. For each cluster in each contrast, the peak MNI coordinates, T-value, p-Value, anatomical labels, and probabilities are presented. MNI coordinates were converted to Tailarach coordinates to generate cluster labels.

between bilateral occipito-temporal cortex and middle temporal gyrus in the high eye contact group relative to the low eye contact group for wavelet components between 16 and 28 s. This was the only pair of areas that showed greater coherence for the high eye contact pairs than the low eye contact pairs. When the pairs were shuffled such that coherence was measured between people who did not do the task together, there was no significant difference between the coherence in the high eye contact versus low eye contact group.

DISCUSSION

Although the neural mechanisms of initiating and responding to joint attention have been previously studied using human neuroimaging techniques, few studies have examined the relationship between social joint attention and eye contact in a live, social context. Here we test the role of eye contact in joint attention. In the present study, simultaneous fNIRS hyperscanning and dual eye tracking were used to acquire neural signals in face-to-face interacting dyads, and to classify these dyads into groups based on the number of mutual eye contacts made prior to the direction of attention. Analyzing brain activity using frequency of eye contact as a covariate resulted in clusters of increased activity in the right superior temporal gyrus, middle temporal gyrus, and lateral occipito-temporal area, and in the left

TABLE 3 | Areas represented by the overlap (yellow area in **Figure 7**) of **Figures 5**, **6**.

BA	Anatomical Area	Probability
39	Angular Gyrus	0.246
37	Occipito-temporal cortex	0.243
21	Middle Temporal gyrus	0.193
19	V3	0.177
22	Superior Temporal Gyrus	0.141

Broadmann areas, anatomical labels and probabilities assigned using the Tailarach atlas.

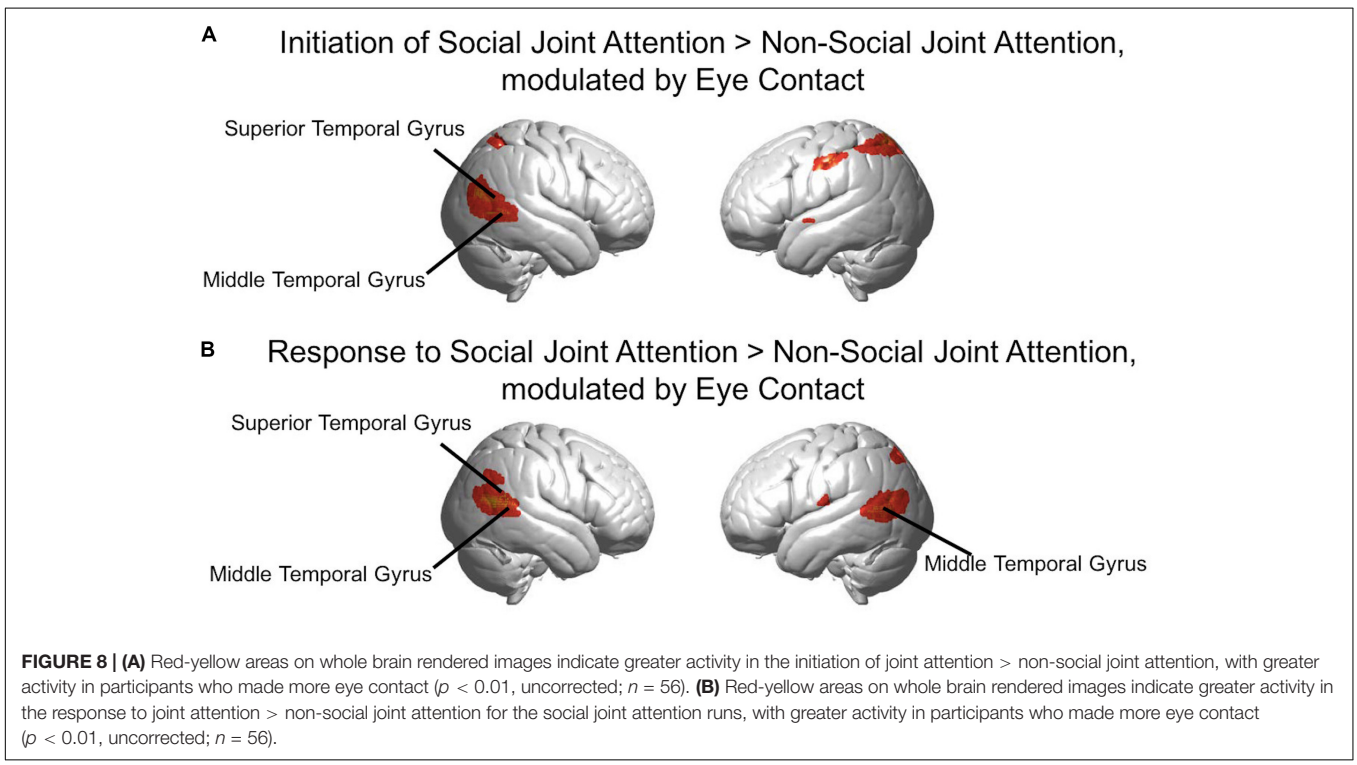

FIGURE 8 | (A) Red-yellow areas on whole brain rendered images indicate greater activity in the initiation of joint attention > non-social joint attention, with greater activity in participants who made more eye contact ($p < 0.01$, uncorrected; $n = 56$). **(B)** Red-yellow areas on whole brain rendered images indicate greater activity in the response to joint attention > non-social joint attention for the social joint attention runs, with greater activity in participants who made more eye contact ($p < 0.01$, uncorrected; $n = 56$).

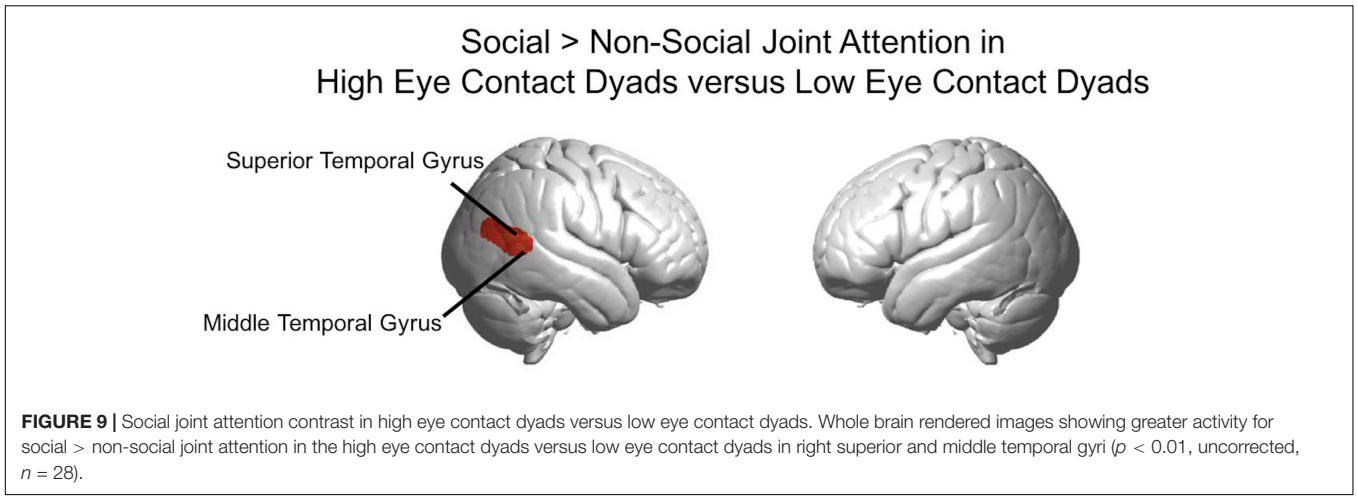

FIGURE 9 | Social joint attention contrast in high eye contact dyads versus low eye contact dyads. Whole brain rendered images showing greater activity for social > non-social joint attention in the high eye contact dyads versus low eye contact dyads in right superior and middle temporal gyri ($p < 0.01$, uncorrected, $n = 28$).

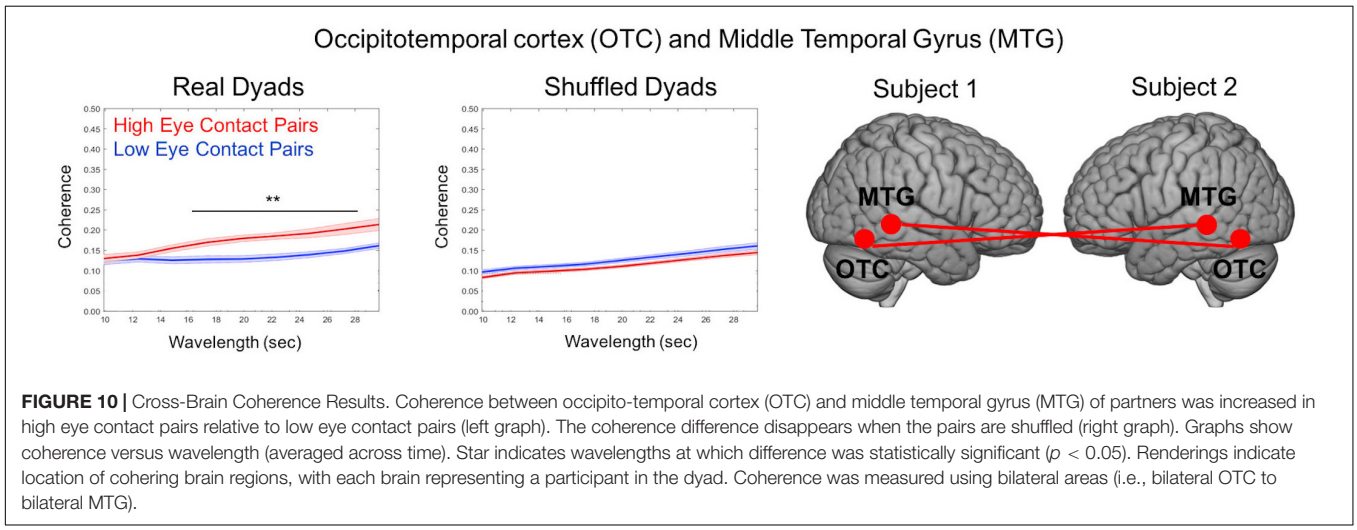

FIGURE 10 | Cross-Brain Coherence Results. Coherence between occipito-temporal cortex (OTC) and middle temporal gyrus (MTG) of partners was increased in high eye contact pairs relative to low eye contact pairs (left graph). The coherence difference disappears when the pairs are shuffled (right graph). Graphs show coherence versus wavelength (averaged across time). Star indicates wavelengths at which difference was statistically significant ($p < 0.05$). Renderings indicate location of cohering brain regions, with each brain representing a participant in the dyad. Coherence was measured using bilateral areas (i.e., bilateral OTC to bilateral MTG).

angular gyrus and lateral occipito-temporal cortex (**Figure 6**). In addition, coherence was greater across the middle temporal gyrus and occipito-temporal cortex in high eye contact dyads compared to low eye contact dyads.

Although the neural mechanisms of joint attention are well−studied, the relationship between joint attention with and without eye contact has not been investigated. Most studies of joint attention begin with eye contact between the initiator and responder, before the initiator shifts his/her gaze and the responder follows. However, in real world contexts, joint attention can be achieved with or without mutual eye contact as the initiating step. In fact, averted eye gaze is known to be a salient cue for directing the attention (Kleinke, 1986; Von Grünau and Anston, 1995; Senju et al., 2005; Conty et al., 2006). The main difference between joint attention that involves eye contact and joint attention that does not is whether the initiator's eye gaze is first directed toward the responder or averted toward the target, respectively. The responder must always look at the initiator's eyes in order to follow the gaze and achieve a joint attention event on the correct target. Additionally, some initiators made eye contact briefly with the responders again even after joint attention was achieved and before redirecting their attention to the object. Here, we show that accounting for this initiator behavior by analyzing the frequency of eye-to-eye contact is enough to replicate prior findings of increased activity in social and high-level visual networks. This is consistent with studies of direct versus averted eye gaze (Puce et al., 1998; Hoffman and Haxby, 2000; Pelphrey et al., 2004; Akiyama et al., 2006; Calder et al., 2007), further supporting the important role of the initiator in this behavior.

Direct gaze has also been shown in EEG studies to affect coherence between partners engage in interaction (Leong et al., 2017). In this study, joint gaze between infants and adults increased the neural coherence between them, is consistent with our coherence findings using functional NIRS. Here, we use wavelet coherence to relate the signals of interacting partners (Cui et al., 2012; Hirsch et al., 2017, 2018), which is done on the residual signals, after the task-related activity has been removed. Here, the task-related activity was due to the joint attention task, and this activity was removed prior to the cross-brain coherence analysis. We hypothesized that the residual fluctuations in the time series would be due behavioral

events related to eye contact, and tested this by comparing the groups that made more eye contact with those who made less. Wavelet coherence assumes that sparse behavioral events result in similar short bursts of brain activity with a delay between interacting partners. Thus the finding of increased coherence between social and face-processing areas across high eye contact dyads compared to low eye contact dyads may indicate that some feature of eye contact modulates these small, sporadic neural events. For example, eye movements or eye blinks (Koike et al., 2019a) that occur during the eye contact events may be triggers of neural synchrony or social attention. The involvement of the middle temporal gyrus in the inter-brain coherence is consistent with the activity in this area in joint attention tasks (Redcay et al., 2012) as well as in eye contact experiments (Koike et al., 2016). The finding in the high eye contact group of increased coherence between the occipito-temporal cortex with the middle temporal gyrus is consistent with prior work showing that the occipito-temporal cortex is sensitive to eye contact and social interactions (Koike et al., 2016, 2019b; Piva et al., 2017). Koike et al. (2019a) have shown that occipito-temporal areas show greater inter-brain synchronization across partners making live eye contact compared to viewing a pre-recorded video (Koike et al., 2019b). A study in which participants played a game against a partner or against a computer showed greater cross-brain synchrony between the angular gyrus and the occipito-temporal area specific to the human-to-human interaction, where eye-to-eye contact contained relevant information (Piva et al., 2017). The findings of the current investigation contribute to this emerging literature consistent with increased neural coherence between social and high-level visual brain areas.

The right temporal parietal junction is an area that has been associated with many social functions, including theory of mind (Saxe and Kanwisher, 2003; Saxe and Wexler, 2005; Aichhorn et al., 2006; Perner et al., 2006), biological motion perception (Grossman et al., 2005; Pelphrey et al., 2005), and processing of dynamic faces and eyes (Puce et al., 1998; Langton et al., 2000; Pitcher et al., 2011). A functionally defined region, the TPJ subsumes aspects of the posterior superior temporal gyrus, angular gyrus, and supramarginal gyrus. Meta-analyses of functional imaging studies have shown that distinct parts of the TPJ may be responsible for different functions, and that eye gaze and social cognition in particular may be more restricted to the superior temporal gyrus (Carter and Huettel, 2013). The joint attention task described here involved direction of attention via eye gaze, and accounting for the initial mutual eye contact events in the analysis resulted in activity in different aspects of the right TPJ. Analysis of the task-related interaction activity resulted in a cluster that included the supramarginal gyrus. This is consistent with evidence showing that TPJ activity can be separated into anterior portion, including the supramarginal gyrus, that is more responsive to attention-direction, while the posterior portion is more sensitive to social cognition (Carter and Huettel, 2013). In the current study, activity in the supramarginal gyrus was not present when eye contact frequency was regressed in the group analysis; rather, the superior temporal and middle temporal gyri, and the lateral occipito-temporal cortex showed more eye contact-specific activity. These same areas also showed increased coherence across participants who made more eye contact, supporting the idea that eye contact was the driver of the cross-brain coherence.

The presented results are consistent with prior hyperscanning fMRI studies of interpersonal coherence in joint attention, eye contact, and other social tasks. Many of these studies have shown involvement and synchronization of both right superior temporal gyrus/sulcus and right inferior frontal gyrus. In one study, right posterior STS showed greater coherence across partners during both cooperation and competition, while right IFG showed more coherence with greater competition, modulated by empathy (Liu et al., 2017). Another study found increased cross-brain connectivity between the TPJ of partners during a cooperative task involving grip coordination (Abe et al., 2019). Studies using hyperscanning fMRI and joint attention tasks have also reported inter-brain coherence in the right TPJ (Bilek et al., 2015; Goelman et al., 2019), while another recent study demonstrated increased activity in the right anterior insular cortex (Koike et al., 2019a), an area from which signals can not be measured using fNIRS. Our findings of increased right STG/MTG activity in a cooperative joint attention task are consistent with this prior work. Other studies have demonstrated the importance of the right inferior frontal gyrus (IFG) alongside the right STG in studies of joint attention and eye contact (Saito et al., 2010; Tanabe et al., 2012; Caruana et al., 2015; Koike et al., 2016, 2019a). Here, we did not find right IFG activity, which may be due to the fewer number of uninstructed eye contact events that occurred during the task. It may be that if every pair had made eye contact during the joint attention task, this area would have shown more activity due to the eye contact itself or due to the inherent social traits of the participants. Further research is necessary to confirm how right IFG activity relates to eye contact in joint attention, especially in pairs who naturally make more eye contact.

These findings present a unique clinical significance in the study of disorders of social interaction, such as autism. It is well known that people with autism have difficulty both with initiating eye contact, as well as with joint attention. Results of neuroimaging on people with autism show decreased or altered neural activity when they engage in these behaviors (Senju and Johnson, 2009; Philip et al., 2012; Redcay et al., 2013). Our results indicate that if eye contact modulates the neural activity elicited by joint attention, the lack of spontaneous eye contact in this population may explain altered neural findings in joint attention.

Finally, we refer to the "social runs" as those in which there was an initiator and a responder of joint attention, and the responder had to follow the eye gaze of the initiator to direct their attention to the correct object. However, it could be argued that even during these runs, the low eye-contact dyads failed to engage in true social interaction or did not possess social traits present in the higher eye contact dyads, as measured by the frequency of eye contact. The responder in the low eye contact dyads essentially performed the task similarly during both run types, using the eye gaze as a cue in the social

condition rather than the LED in the non-social condition. High eye contact dyads showed greater neural activity in social and visual areas during the social joint attention runs, in which they made eye contact, compared to the non-social joint runs, in which no eye contact was made. Performance did not differ in interaction or non-social runs but the interaction involved eye contact for this group. True social interaction could be defined as engagement of both individuals with each other, and it may be that the high eye contact dyads naturally interacted more as a result of individual trait differences. With this perspective, it is not surprising that the high eye contact dyads showed more recruitment of hemodynamic activity to social and high-level visual brain regions, as well as more coherence between these same networks across interacting partners, as these dyads engaged in true social interaction.

In this study, amount of eye contact was used as a measure of social behavior that varied between dyads. We assume that this behavior is largely driven by differences in individual traits, that are amplified by the social context. For example, a naturally shy person would most likely not make as much uninstructed eye contact when initiating joint attention trials with his/her partner. We did not collect behavioral measures of socialness and comfort with social interactions, such as self-reported standardized social anxiety scales, from the participants. It is possible that the individual trait differences drove the number of eye contacts made during the interaction and the subsequent increases in neural activity in social and high-level visual brain areas. In addition to individual traits, other aspects of the interaction may also have influenced the brain activity of the participants. For example, some pairs of participants may have found each other mutually attractive, or felt more engaged with each other for some reason than other pairs. Further work including behavioral measures of "socialness" within individuals and "interactivity" between participants is needed to elucidate the specific traits and behaviors of "more social" people and "more connected" partners, and how these traits and behaviors affects neural activity during joint attention with a partner.

Using optical imaging methods and computational techniques for dual-brain and multi-modal imaging, we show that eye contact modulates the social system that engages in the neural activity related to joint attention, and that interacting partners who engage in more eye contact show more coherence between social and eye-gaze processing brain regions. These results suggest that some aspect of eye contact may contribute to the interaction involved in directing another person's gaze toward an object. Further studies using hyperscanning as well as simultaneous acquisition of behavioral measures are necessary to confirm whether eye movements or some other aspect of face or eye-processing drives this brain activity, and how it relates to the observation of coherence across individuals that is specific to pairs who make more eye contact.

Limitations

A common finding in neuroimaging studies of joint attention is activity in the medial prefrontal cortex (Schilbach et al., 2010; Redcay et al., 2012, 2013) and in reward-related regions in the basal ganglia (Schilbach et al., 2010) when participants engage in joint attention. Hemodynamic activity acquired by fNIRS can only be detected from the superficial cortex. It is likely that we did not detect joint attention-related activity in the mPFC and basal ganglia due to our inability to record from these areas.

While the results reported here are consistent with a large body of prior work exploring the neural mechanisms of joint attention, it should be noted that no multiple comparisons correction was applied to either the intra-brain GLM or the inter-brain coherence analysis. By using a combination of the oxyhemoglobin and deoxyhemoglobin signals and restricting the number of wavelengths in the coherence analysis, we reduce the likelihood of false positive results. However, this possibility cannot be ruled out with the thresholds reported here; further work is necessary to confirm and validate these descriptive findings of the modulatory effect of live eye contact on joint attention.

The small area of overlap (**Figure 7**) between the brain regions represented in **Figures 5**, **6** may represent an area of the brain sensitive to both the mechanisms of social joint attention as well as the modulation of eye contact on these mechanisms. A future study using separate eye contact and joint attention tasks could confirm whether this region is significantly activated by both tasks.

Finally, we report the modulatory effect of eye contact on social joint attention using the average number of mutual eye contact events across all social runs for each participant. An important question arises from this work is what is the direct effect of a mutual eye contact event that precedes a joint attention event? While the answer to this question is beyond the scope of this manuscript, it is an important future direction of this work.

DATA AVAILABILITY STATEMENT

The datasets generated for this study are available on request to the corresponding author.

ETHICS STATEMENT

The studies involving human participants were reviewed and approved by the Yale University Human Investigation Committee (HIC # 1501015178). The patients/participants provided their written informed consent to participate in this study. Written informed consent was obtained from the individual(s) for the publication of any potentially identifiable images or data included in this article.

AUTHOR CONTRIBUTIONS

SD designed and performed the experiment, and analyzed the data. SD and JH wrote the manuscript. JN and XZ assisted with planning, data acquisition, and analysis.

FUNDING

This research was partially supported by the National Institute of Mental Health of the National Institutes of Health under award numbers R01MH107513 (PI JH), R01MH111629 (PI JH), R01MH119430 (PI JH), F30MH116626 (PI SD), and R37 HD 090153; and the NIH Medical Scientist Training Program Training Grant T32GM007205. The content is solely the responsibility of the authors and does not necessarily represent the official views of the National Institutes of Health. All data reported in this manuscript are available upon request from the corresponding author.

SUPPLEMENTARY MATERIAL

The Supplementary Material for this article can be found online at: https://www.frontiersin.org/articles/10.3389/fnhum.2020.00201/full#supplementary-material

REFERENCES

Abe, M. O., Koike, T., Okazaki, S., Sugawara, S. K., Takahashi, K., Watanabe, K., et al. (2019). Neural correlates of online cooperation during joint force production. *Neuroimage* 191, 150–161. doi: 10.1016/j.neuroimage.2019.02.003

Aichhorn, M., Perner, J., Kronbichler, M., Staffen, W., and Ladurner, G. (2006). Do visual perspective tasks need theory of mind? *Neuroimage* 30, 1059–1068. doi: 10.1016/j.neuroimage.2005.10.026

Akiyama, T., Kato, M., Muramatsu, T., Saito, F., Nakachi, R., and Kashima, H. (2006). A deficit in discriminating gaze direction in a case with right superior temporal gyrus lesion. *Neuropsychologia* 44, 161–170. doi: 10.1016/j.neuropsychologia.2005.05.018

Argyle, M., and Dean, J. (1965). Eye-contact, distance and affiliation. *Sociometry* 28, 289–304.

Babiloni, F., and Astolfi, L. (2014). Social neuroscience and hyperscanning techniques: past, present and future. *Neurosci. Biobehav. Rev.* 44, 76–93. doi: 10.1016/j.neubiorev.2012.07.006

Behrmann, M., Geng, J. J., and Shomstein, S. (2004). Parietal cortex and attention. *Curr. Opin. Neurobiol.* 14, 212–217.

Bilek, E., Ruf, M., Schäfer, A., Akdeniz, C., Calhoun, V. D., Schmahl, C., et al. (2015). Information flow between interacting human brains: identification, validation, and relationship to social expertise. *Proc. Natl. Acad. Sci. U.S.A.* 112, 5207–5212. doi: 10.1073/pnas.1421831112

Calder, A. J., Beaver, J. D., Winston, J. S., Dolan, R. J., Jenkins, R., Eger, E., et al. (2007). Separate coding of different gaze directions in the superior temporal sulcus and inferior parietal lobule. *Curr. Biol.* 17, 20–25. doi: 10.1016/j.cub.2006.10.052

Carter, R. M., and Huettel, S. A. (2013). A nexus model of the temporal–parietal junction. *Trends Cognit. Sci.* 17, 328–336.

Caruana, N., Brock, J., and Woolgar, A. (2015). A frontotemporoparietal network common to initiating and responding to joint attention bids. *Neuroimage* 108, 34–46. doi: 10.1016/j.neuroimage.2014.12.041

Castelli, F., Happé, F., Frith, U., and Frith, C. (2000). Movement and mind: a functional imaging study of perception and interpretation of complex intentional movement patterns. *Neuroimage* 12, 314–325. doi: 10.1006/nimg.2000.0612

Colby, C. L., and Goldberg, M. E. (1999). Space and attention in parietal cortex. *Annu. Rev. Neurosci.* 22, 319–349.

Conty, L., Tijus, C., Hugueville, L., Coelho, E., and George, N. (2006). Searching for asymmetries in the detection of gaze contact versus averted gaze under different head views: a behavioural study. *Spat. Vision* 19, 529–546. doi: 10.1163/156856806779194026

Corbetta, M., Shulman, G. L., Miezin, F. M., and Petersen, S. E. (1995). Superior parietal cortex activation during spatial attention shifts and visual feature conjunction. *Science* 270, 802–805. doi: 10.1126/science.270.5237.802

Cui, X., Bryant, D. M., and Reiss, A. L. (2012). NIRS-based hyperscanning reveals increased interpersonal coherence in superior frontal cortex during cooperation. *Neuroimage* 59, 2430–2437. doi: 10.1016/j.neuroimage.2011.09.003

Dawson, G., Toth, K., Abbott, R., Osterling, J., Munson, J., Estes, A., et al. (2004). Early social attention impairments in autism: social orienting, joint attention, and attention to distress. *Dev. Psychol.* 40:271. doi: 10.1037/0012-1649.40.2.271

De Jaegher, H., Di Paolo, E., and Adolphs, R. (2016). What does the interactive brain hypothesis mean for social neuroscience? A dialogue. *Philos. Trans. R. Soc. B Biol. Sci.* 371, 20150379. doi: 10.1098/rstb.2015.0379

Di Paolo, E. A., and De Jaegher, H. (2012). The interactive brain hypothesis. *Front. Hum. Neurosci.* 6:163. doi: 10.3389/fnhum.2012.00163

Dravida, S., Noah, J. A., Zhang, X., and Hirsch, J. (2017). Comparison of oxyhemoglobin and deoxyhemoglobin signal reliability with and without global mean removal for digit manipulation motor tasks. *Neurophotonics* 5:011006. doi: 10.1117/1.NPh.5.1.011006

Franceschini, M. A., Andre, J., Huppert, T. J., Joseph, D., Stott, J. J., and Boas, D. A. (2004). Diffuse optical imaging of the whole head. *Neuroimage* 22, e2341–e2342. doi: 10.1117/1.NPh.2.3.035002

Friston, K., Buechel, C., Fink, G., Morris, J., Rolls, E., and Dolan, R. J. (1997). Psychophysiological and modulatory interactions in neuroimaging. *Neuroimage* 6, 218–229. doi: 10.1006/nimg.1997.0291

Frith, U., and Frith, C. D. (2003). Development and neurophysiology of mentalizing. *Philos. Trans. R. Soc. Lon. Ser. B Biol. Sci.* 358, 459–473. doi: 10.1098/rstb.2002.1218

Goelman, G., Dan, R., Stößel, G., Tost, H., Meyer-Lindenberg, A., and Bilek, E. (2019). Bidirectional signal exchanges and their mechanisms during joint attention interaction–A hyperscanning fMRI study. *Neuroimage* 198, 242–254. doi: 10.1016/j.neuroimage.2019.05.028

Grossman, E. D., Battelli, L., and Pascual-Leone, A. (2005). Repetitive TMS over posterior STS disrupts perception of biological motion. *Vision Res.* 45, 2847–2853. doi: 10.1016/j.visres.2005.05.027

Hampton, A. N., Bossaerts, P., and O'Doherty, J. P. (2008). Neural correlates of mentalizing-related computations during strategic interactions in humans. *Proc. Natl. Acad. Sci. U.S.A.* 105, 6741–6746. doi: 10.1073/pnas.0711099105

Hasson, U., and Frith, C. D. (2016). Mirroring and beyond: coupled dynamics as a generalized framework for modelling social interactions. *Philos. Trans. R. Soc. B Biol. Sci.* 371:20150366. doi: 10.1098/rstb.2015.0366

Hasson, U., Ghazanfar, A. A., Galantucci, B., Garrod, S., and Keysers, C. (2012). Brain-to-brain coupling: a mechanism for creating and sharing a social world. *Trends Cognit. Sci.* 16, 114–121. doi: 10.1016/j.tics.2011.12.007

Hirsch, J., Adam Noah, J., Zhang, X., Dravida, S., and Ono, Y. (2018). A cross-brain neural mechanism for human-to-human verbal communication. *Soc. Cognit. Affect. Neurosci.* 13, 907–920. doi: 10.1093/scan/nsy070

Hirsch, J., Zhang, X., Noah, J. A., and Ono, Y. (2017). Frontal temporal and parietal systems synchronize within and across brains during live eye-to-eye contact. *Neuroimage* 157, 314–330. doi: 10.1016/j.neuroimage.2017.06.018

Hoffman, E. A., and Haxby, J. V. (2000). Distinct representations of eye gaze and identity in the distributed human neural system for face perception. *Nat. Neurosci.* 3:80. doi: 10.1038/71152

Huppert, T. J., Hoge, R. D., Diamond, S. G., Franceschini, M. A., and Boas, D. A. (2006). A temporal comparison of BOLD, ASL, and NIRS hemodynamic responses to motor stimuli in adult humans. *Neuroimage* 29, 368–382. doi: 10.1016/j.neuroimage.2005.08.065

Jiang, J., Chen, C., Dai, B., Shi, G., Ding, G., Liu, L., et al. (2015). Leader emergence through interpersonal neural synchronization. *Proc. Natl. Acad. Sci. U.S.A. U.S.A.* 112, 4274–4279. doi: 10.1073/pnas.1422930112

Jiang, J., Dai, B., Peng, D., Zhu, C., Liu, L., and Lu, C. (2012). Neural synchronization during face-to-face communication. *J. Neurosci.* 32, 16064–16069. doi: 10.1523/JNEUROSCI.2926-12.2012

Kanner, L. (1943). Autistic disturbances of affective contact. *Nervous Child* 2, 217–250.

Kanner, L. (1944). Early infantile autism. *J. Pediatr.* 25, 211–217.

Kirilina, E., Jelzow, A., Heine, A., Niessing, M., Wabnitz, H., Brühl, R., et al. (2012). The physiological origin of task-evoked systemic artefacts in functional near infrared spectroscopy. *Neuroimage* 61, 70–81. doi: 10.1016/j.neuroimage.2012.02.074

Kleinke, C. L. (1986). Gaze and eye contact: a research review. *Psychol. Bull.* 100:78.

Klin, A., Jones, W., Schultz, R., Volkmar, F., and Cohen, D. (2002). Visual fixation patterns during viewing of naturalistic social situations as predictors of social competence in individuals with autism. *Arch. Gen. Psychiatry* 59, 809–816. doi: 10.1001/archpsyc.59.9.809

Koike, T., Sumiya, M., Nakagawa, E., Okazaki, S., and Sadato, N. (2019a). What makes eye contact special? Neural substrates of on-line mutual eye-gaze: a hyperscanning fMRI study. *eNeuro* 6:ENEURO.284. doi: 10.1523/ENEURO.0284-18.2019

Koike, T., Tanabe, H. C., Adachi-Abe, S., Okazaki, S., Nakagawa, E., Sasaki, A. T., et al. (2019b). Role of the right anterior insular cortex in joint attention-related identification with a partner. *Soc. Cognit. Affect. Neurosci.* 14, 1131–1145. doi: 10.1093/scan/nsz087

Koike, T., Tanabe, H. C., Okazaki, S., Nakagawa, E., Sasaki, A. T., Shimada, K., et al. (2016). Neural substrates of shared attention as social memory: a hyperscanning functional magnetic resonance imaging study. *Neuroimage* 125, 401–412. doi: 10.1016/j.neuroimage.2015.09.076

Konvalinka, I., and Roepstorff, A. (2012). The two-brain approach: how can mutually interacting brains teach us something about social interaction? *Front. Hum. Neurosci.* 6:215. doi: 10.3389/fnhum.2012.00215

Langton, S. R., Watt, R. J., and Bruce, V. (2000). Do the eyes have it? Cues to the direction of social attention. *Trends Cognit. Sci.* 4, 50–59. doi: 10.1016/s1364-6613(99)01436-9

Leong, V., Byrne, E., Clackson, K., Georgieva, S., Lam, S., and Wass, S. (2017). Speaker gaze increases information coupling between infant and adult brains. *Proc. Natl. Acad. Sci. U.S.A.* 114, 13290–13295. doi: 10.1073/pnas.1702493114

Liu, T., Saito, G., Lin, C., and Saito, H. (2017). Inter-brain network underlying turn-based cooperation and competition: a hyperscanning study using near-infrared spectroscopy. *Sci. Rep.* 7, 1–12. doi: 10.1038/s41598-017-09226-w

Neumann, D., Spezio, M. L., Piven, J., and Adolphs, R. (2006). Looking you in the mouth: abnormal gaze in autism resulting from impaired top-down modulation of visual attention. *Soc. Cognit. Affect. Neurosci.* 1, 194–202. doi: 10.1093/scan/nsl030

Noah, J. A., Dravida, S., Zhang, X., Yahil, S., and Hirsch, J. (2017). Neural correlates of conflict between gestures and words: a domain-specific role for a temporal-parietal complex. *PLoS ONE* 12:e0173525. doi: 10.1371/journal.pone.0173525

Noah, J. A., Zhang, X., Dravida, S., Ono, Y., Naples, A., McPartland, J. C., et al. (2020). Real-time eye-to-eye contact is associated with cross-brain neural coupling in angular gyrus. *Front. Hum. Neurosci.* 14:19. doi: 10.3389/fnhum.2020.00019

Nozawa, T., Sasaki, Y., Sakaki, K., Yokoyama, R., and Kawashima, R. (2016). Interpersonal frontopolar neural synchronization in group communication: an exploration toward fNIRS hyperscanning of natural interactions. *Neuroimage* 133, 484–497. doi: 10.1016/j.neuroimage.2016.03.059

Oldfield, R. C. (1971). The assessment and analysis of handedness: the Edinburgh inventory. *Neuropsychologia* 9, 97–113. doi: 10.1016/0028-3932(71)90067-4

Pelphrey, K. A., Morris, J. P., Michelich, C. R., Allison, T., and McCarthy, G. (2005). Functional anatomy of biological motion perception in posterior temporal cortex: an fMRI study of eye, mouth and hand movements. *Cereb. Cortex* 15, 1866–1876. doi: 10.1093/cercor/bhi064

Pelphrey, K. A., Viola, R. J., and McCarthy, G. (2004). When strangers pass: processing of mutual and averted social gaze in the superior temporal sulcus. *Psychol. Sci.* 15, 598–603. doi: 10.1111/j.0956-7976.2004.00726.x

Perner, J., Aichhorn, M., Kronbichler, M., Staffen, W., and Ladurner, G. (2006). Thinking of mental and other representations: the roles of left and right temporo-parietal junction. *Soc. Neurosci.* 1, 245–258. doi: 10.1080/17470910600989896

Pfeiffer, U. J., Vogeley, K., and Schilbach, L. (2013). From gaze cueing to dual eye-tracking: novel approaches to investigate the neural correlates of gaze in social interaction. *Neurosci. Biobehav. Rev.* 37, 2516–2528. doi: 10.1016/j.neubiorev.2013.07.017

Philip, R. C., Dauvermann, M. R., Whalley, H. C., Baynham, K., Lawrie, S. M., and Stanfield, A. C. (2012). A systematic review and meta-analysis of the fMRI investigation of autism spectrum disorders. *Neurosci. Biobehav. Rev.* 36, 901–942. doi: 10.1016/j.neubiorev.2011.10.008

Pitcher, D., Dilks, D. D., Saxe, R. R., Triantafyllou, C., and Kanwisher, N. (2011). Differential selectivity for dynamic versus static information in face-selective cortical regions. *Neuroimage* 56, 2356–2363. doi: 10.1016/j.neuroimage.2011.03.067

Piva, M., Zhang, X., Noah, J. A., Chang, S. W., and Hirsch, J. (2017). Distributed neural activity patterns during human-to-human competition. *Front. Hum. Neurosci.* 11:571. doi: 10.3389/fnhum.2017.00571

Puce, A., Allison, T., Bentin, S., Gore, J. C., and McCarthy, G. (1998). Temporal cortex activation in humans viewing eye and mouth movements. *J. Neurosci.* 18, 2188–2199. doi: 10.1523/JNEUROSCI.18-06-02188.1998

Redcay, E., Dodell-Feder, D., Mavros, P. L., Kleiner, M., Pearrow, M. J., Triantafyllou, C., et al. (2013). Atypical brain activation patterns during a face-to-face joint attention game in adults with autism spectrum disorder. *Hum. Brain Mapp.* 34, 2511–2523. doi: 10.1002/hbm.22086

Redcay, E., Kleiner, M., and Saxe, R. (2012). Look at this: the neural correlates of initiating and responding to bids for joint attention. *Front. Hum. Neurosci.* 6:169. doi: 10.3389/fnhum.2012.00169

Saito, D. N., Tanabe, H. C., Izuma, K., Hayashi, M. J., Morito, Y., Komeda, H., et al. (2010). "Stay tuned": inter-individual neural synchronization during mutual gaze and joint attention. *Front. Integr. Neurosci.* 4:127. doi: 10.3389/fnint.2010.00127

Saxe, R., and Kanwisher, N. (2003). People thinking about thinking people: the role of the temporo-parietal junction in "theory of mind". *Neuroimage* 19, 1835–1842. doi: 10.1016/s1053-8119(03)00230-1

Saxe, R., and Wexler, A. (2005). Making sense of another mind: the role of the right temporo-parietal junction. *Neuropsychologia* 43, 1391–1399. doi: 10.1016/j.neuropsychologia.2005.02.013

Schilbach, L., Timmermans, B., Reddy, V., Costall, A., Bente, G., Schlicht, T., et al. (2013). Toward a second-person neuroscience 1. *Behav. Brain Sci.* 36, 393–414.

Schilbach, L., Wilms, M., Eickhoff, S. B., Romanzetti, S., Tepest, R., Bente, G., et al. (2010). Minds made for sharing: initiating joint attention recruits reward-related neurocircuitry. *J. Cogn. Neurosci.* 22, 2702–2715. doi: 10.1162/jocn.2009.21401

Scholkmann, F., Holper, L., Wolf, U., and Wolf, M. (2013). A new methodical approach in neuroscience: assessing inter-personal brain coupling using functional near-infrared imaging (fNIRI) hyperscanning. *Front. Hum. Neurosci.* 7:813. doi: 10.3389/fnhum.2013.00813

Senju, A., Hasegawa, T., and Tojo, Y. (2005). Does perceived direct gaze boost detection in adults and children with and without autism? The stare-in-the-crowd effect revisited. *Visual Cognit.* 12, 1474–1496.

Senju, A., and Johnson, M. H. (2009). Atypical eye contact in autism: models, mechanisms and development. *Neurosci. Biobehav. Rev.* 33, 1204–1214. doi: 10.1016/j.neubiorev.2009.06.001

Tachtsidis, I., and Scholkmann, F. (2016). False positives and false negatives in functional near-infrared spectroscopy: issues, challenges, and the way forward. *Neurophotonics* 3:031405. doi: 10.1117/1.NPh.3.3.039801

Tanabe, H. C., Kosaka, H., Saito, D. N., Koike, T., Hayashi, M. J., Izuma, K., et al. (2012). Hard to "tune in": neural mechanisms of live face-to-face interaction with high-functioning autistic spectrum disorder. *Front. Hum. Neurosci.* 6:268. doi: 10.3389/fnhum.2012.00268

Tomasello, M. (1988). The role of joint attentional processes in early language development. *Lang. Sci.* 10, 69–88.

Tomasello, M., and Todd, J. (1983). Joint attention and lexical acquisition style. *First Lang.* 4, 197–211.

Van Overwalle, F. (2009). Social cognition and the brain: a meta-analysis. *Hum. Brain Mapp.* 30, 829–858. doi: 10.1002/hbm.20547

Von Grünau, M., and Anston, C. (1995). The detection of gaze direction: a stare-in-the-crowd effect. *Perception* 24, 1297–1313. doi: 10.1068/p241297

Ye, J. C., Tak, S., Jang, K. E., Jung, J., and Jang, J. (2009). NIRS-SPM: statistical parametric mapping for near-infrared spectroscopy. *Neuroimage* 44, 428–447. doi: 10.1016/j.neuroimage.2008.08.036

Zhang, X., Noah, J. A., Dravida, S., and Hirsch, J. (2017). Signal processing of functional NIRS data acquired during overt speaking. *Neurophotonics* 4:041409. doi: 10.1117/1.NPh.4.4.041409

Zhang, X., Noah, J. A., Dravida, S., and Hirsch, J. (2020). Optimization of wavelet coherence analysis as a measure of neural synchrony during hyperscanning using functional near-infrared spectroscopy. *Neurophotonics* 7:015010. doi: 10.1117/1.NPh.7.1.015010

Zhang, X., Noah, J. A., and Hirsch, J. (2016). Separation of the global and local components in functional near-infrared spectroscopy signals using principal component spatial filtering. *Neurophotonics* 3:015004. doi: 10.1117/1.NPh.3.1.015004

Conflict of Interest: The authors declare that the research was conducted in the absence of any commercial or financial relationships that could be construed as a potential conflict of interest.

Copyright © 2020 Dravida, Noah, Zhang and Hirsch. This is an open-access article distributed under the terms of the Creative Commons Attribution License (CC BY). The use, distribution or reproduction in other forums is permitted, provided the original author(s) and the copyright owner(s) are credited and that the original publication in this journal is cited, in accordance with accepted academic practice. No use, distribution or reproduction is permitted which does not comply with these terms.

frontiers in Neuroscience

REVIEW
published: 03 June 2020
doi: 10.3389/fnins.2020.00476

Applications of Resting-State fNIRS in the Developing Brain: A Review From the Connectome Perspective

*Zhishan Hu, Guangfang Liu, Qi Dong and Haijing Niu**

State Key Laboratory of Cognitive Neuroscience and Learning, Beijing Normal University, Beijing, China

Early brain development from infancy through childhood is closely related to the development of cognition and behavior in later life. Human brain connectome is a novel framework for describing topological organization of the developing brain. Resting-state functional near-infrared spectroscopy (fNIRS), with a natural scanning environment, low cost, and high portability, is considered as an emerging imaging technique and has shown valuable potential in exploring brain network architecture and its changes during the development. Here, we review the recent advances involving typical and atypical development of the brain connectome from neonates to children using resting-state fNIRS imaging. This review highlights that the combination of brain connectome and resting-state fNIRS imaging offers a promising framework for understanding human brain development.

Keywords: connectome, graph theory, functional connectivity, development, NIRS

OPEN ACCESS

Edited by:
Fenghua Tian,
University of Texas at Arlington,
United States

Reviewed by:
Hui-Jie Li,
Chinese Academy of Sciences, China
Gao-Xia Wei,
Chinese Academy of Sciences, China

****Correspondence:***
Haijing Niu
niuhjing@bnu.edu.cn

Specialty section:
This article was submitted to Brain Imaging Methods, a section of the journal Frontiers in Neuroscience

Received: *02 December 2019*
Accepted: *16 April 2020*
Published: *03 June 2020*

Citation:
Hu Z, Liu G, Dong Q and Niu H (2020) Applications of Resting-State fNIRS in the Developing Brain: A Review From the Connectome Perspective. Front. Neurosci. 14:476. doi: 10.3389/fnins.2020.00476

INTRODUCTION

The human brain undergoes rapid development during the first few years (Gao et al., 2015a; Xiao et al., 2016). Non-invasive techniques such as functional MRI (fMRI) have shed light on neural development across the life span (Bunge et al., 2002; Zuo et al., 2017; Mohammadi-Nejad et al., 2018; Koen and Rugg, 2019). Combined with the newly developed connectomics framework, it characterizes the changes in neural network architecture during typical development or network dysfunctions underlying neurological disorders (Cao et al., 2017b). For example, small-world structure with efficient information segregation and integration is enhanced during development (Supekar et al., 2009; Wu et al., 2013; Cao et al., 2014). Furthermore, brain networks exhibit region-specific development, in which the primary sensorimotor and auditory regions develop first, followed by the visual, attention, default mode, and executive control networks in sequence (Gao et al., 2015a,b; Cao et al., 2017a).

Despite the remarkable fMRI findings, the operation cost, and extreme body confinement during the scan limit its use in neural developmental studies. Hence, the functional near-infrared spectroscopy (fNIRS) has been increasingly used for neuroimaging research in children. Compared with fMRI, fNIRS can be operated in a more economic, comfortable, quiet, and portable way, which is highly suitable for children participants (Cao et al., 2015). Moreover, fNIRS measures concentration changes in both oxyhemoglobin (HbO) and deoxyhemoglobin (HbR) with a much higher time resolution than fMRI, which provides more information about the neurovascular changes in the developing brain.

Resting-state fNIRS measures spontaneous hemodynamic fluctuations in the cortex and does not require explicit cognitive processes and task performance. This technique is feasible

(Niu et al., 2012), reliable (Niu et al., 2013; Wang et al., 2019), and reproducible (Niu et al., 2011) in characterizing brain connectivity network at a spontaneous state. In the last decade, resting-state fNIRS has been increasingly utilized to delineate typical and atypical development in cortical functional connectivity and network topological characteristics, from neonates to adolescents.

The current review aims to summarize the current advances in the application of resting-state fNIRS in neural developmental research and is organized into three main sections. First, fundamentals of the fNIRS brain connectome is introduced. Second, typical and atypical development of fNIRS brain connectome was summarized. Specifically, we demonstrate the development of functional connectivity, network topologies, and network asymmetry in typical development children, as well as the brain connectome in preterm infants and children with neurological disorders. Finally, we discuss the remaining challenges and highlight future directions in this field.

LITERATURE SELECTION

In this review, we conducted a literature search on *PubMed, psychINFO, Embase,* and *Web of Science* databases using the following search items: [(NIRS OR fNIRS) OR optical] AND [(resting-state AND functional connectivity) OR (resting-state AND functional networks)]. We selected the studies that (a) used resting-state functional near-infrared spectroscopy; (b) recruited participants under 18 years old; and (c) characterized brain connectome patterns. With this procedure, 16 studies were identified for the systematic review. In addition, three articles were retrieved by manually checking the references in these studies and other relevant reviews. Details of the study selection are provided in **Figure 1**, and the included studies are summarized in **Table 1**.

FUNDAMENTALS OF THE FNIRS BRAIN CONNECTOME

fNIRS Imaging and Brain Connectome Construction

fNIRS measures hemodynamic changes in the cerebral cortex induced by neural activity. In specific, NIR light emits from light source probes that can penetrate through the scalp and skull and arrive at cerebral cortex tissue. The reflected lights from the cortex tissue can be received and quantified by the detectors placed on the surface of the

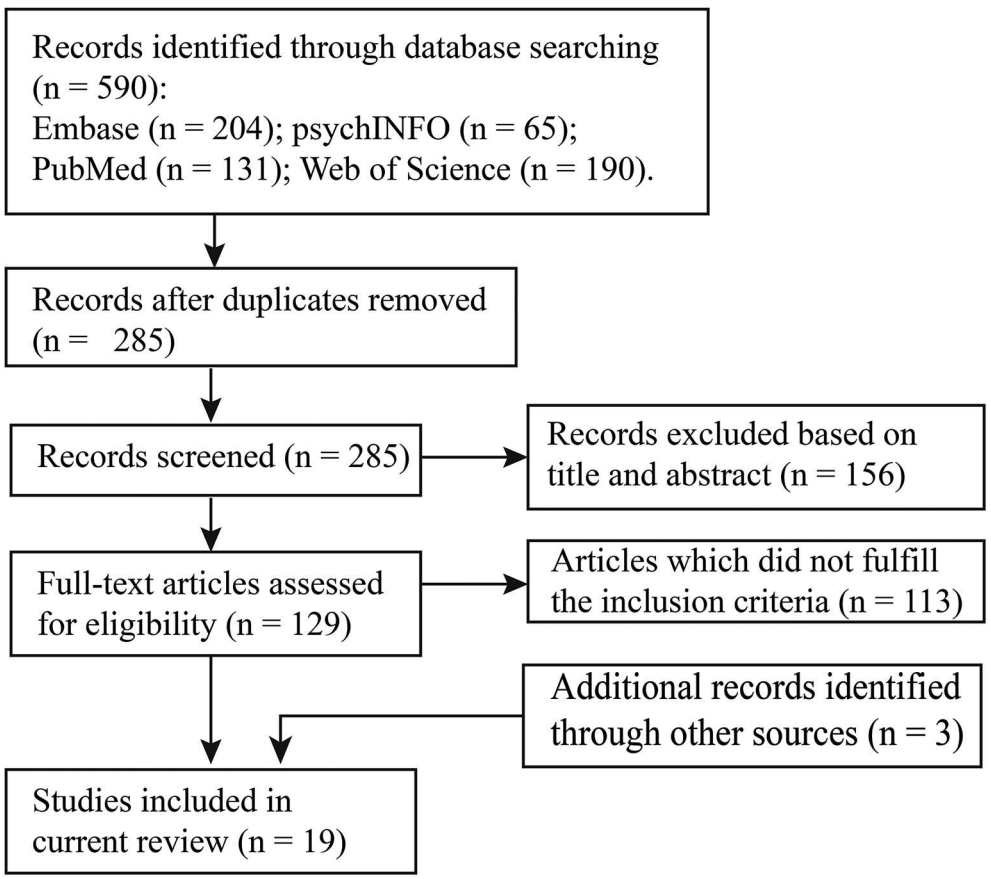

FIGURE 1 | Flowchart of study selection.

TABLE 1 | Overview of the included studies.

	Study	Subjects	Age	N	Brain regions	State	Duration (min)	Instrument	Sources/ detectors	#CH	Metrics
Typical	Ferradal et al. (2016)	Infant	<2 D	9	Temporal, occipital, inferior parietal	Sleep	20 – 60	HD-DOT	32 S/34 D	NR	FC
	Homae et al. (2010)	Neonate Infant Infant	2 – 11 D 102 – 123 D 180 – 206 D	15 21 16	Frontal, temporal, parietal, occipital	Sleep	3	ETG-7000	30 S/30 D	94	FC
	Taga et al. (2018)	Infant Infant Infant Infant	71 – 100 D 101 – 130 D 131 – 170 D 291 – 330 D	25 28 24 14	Frontal, temporal, occipital	Sleep	10	ETG-100	8 S/64 D	48	FC
	Homae et al. (2011)	Infant	104 – 123 D	21	Frontal, temporal, occipital, temporoparietal	Sleep	3	ETG-7000	30 S/30 D	94	FC
	Funane et al. (2014)	Infant	113 D	9	Temporal	Sleep	2.5	ETG-100	2 S/8 D	8	FC
	Blanco et al. (2018)	Infant	124.6 ± 3.76 D	24	Frontal, temporal, parietal, occipital	Sleep	11 – 21	NIRScout	14 S/19 D	46	FC
	Bulgarelli et al. (2019)	Toddler	553.11 ± 12.17 D	43	Frontal, temporoparietal	Fixation	1.5	UCL-NIRS	12 S/12 D 16 S/16 D	30 44	FC
	Gallagher et al. (2016)	Early childhood Late childhood Adolescence	3 – 6 Y 7 – 10 Y 11 – 16 Y	6 8 11	Frontal, temporal	Fixation	5	Imagent	8 S/64 D	NR	FC
	Wang et al. (2017)	Children	6.9 – 8.21 Y	53	Frontal, temporal, parietal, occipital	Awake, eyes closed	11	CW6	12 S/24 D	46	Topology
	Cai et al. (2019)	Children	7.0 – 8.9 Y	30	Frontal, temporal, parietal, occipital	Awake, eyes closed	11	CW6	12 S/24 D	46	Topology
	Cai et al. (2018)	Children Adolescent	7.0–8.9 Y 11.0–12.9 Y	30 30	Frontal, temporal, parietal, occipital	Awake, eyes closed	11	CW6	12 S/24 D	46	Topology
	Koen and Rugg (2019)	Children	9.0 ± 1.5 Y	12	Frontal, temporal	Awake, eyes closed	8	FOIRE-3000	16 S/16 D	44	FC
Atypical	White et al. (2012)	Preterm Preterm (stroke)	30 – 39 W (GA) 40 W (GA)	4 1	Occipital	Sleep	10 – 20	HD-DOT	18 S/16 D	108	FC
	Imai et al. (2014)	Preterm Down's	28.9 ± 3.0 W (GA) 38.0 ± 1.6 W (GA)	15 5	Frontal, temporal, occipital	Sleep	6	ETG-100	6 S/6 D	10	FC
	Fuchino et al. (2013)	Preterm	23.1 – 36.7 (GA)	25	Frontal, temporal, parietal, occipital	Sleep	3 – 6.5	ETG-7000	30 S/30 D	94	FC
	Li and Yu (2018)	ASD	2.0 – 8.9 Y	46	Frontal, temporal, occipital	Fixation	10	LABNIRS	16 S/16 D	44	Topology
	Zhu et al. (2014)	ASD	9.0 ± 1.3 Y	10	Frontal, temporal	Awake, eyes closed	8	FOIRE-3000	16 S/16 D	44	FC
	Li et al. (2016)	ASD	9.3 ± 1.4 Y	25	Temporal	Awake, eyes closed	8	FOIRE-3000	16 S/16 D	44	FC
	Cao et al. (2015)	Cerebral palsy	10.2 ± 2.1 Y	6	Sensorimotor	Awake, eyes open	3	CW6	16 S/32 D	84	FC

For typical and atypical developmental trajectories, the studies are listed in ascending order of the mean age of the youngest group, respectively. For preterm infants, the gestational age (GA) is reported.

ASD, autism spectrum disorder; D, days; Y, years; N, sample size; S, sources; D, detectors; #CH, number of channels; FC, functional connectivity.

scalp (**Figure 2A**, Niu et al., 2010). Based on the Beer-Lambert law, the optical signals can be transformed into the concentration changes of the oxygenated hemoglobin (HbO) and deoxygenated hemoglobin (HbR) (**Figure 2B**, Delpy et al., 1988). To measure the hemodynamics emanating from spontaneous neural activity, the hemoglobin concentration signal is filtered with a bandpass filter which usually ranges from 0.009 to 0.08 Hz (Niu et al., 2012). Subsequently, spontaneous functional connectivity is calculated with Pearson correlation between the time series of every pair of nodes (i.e., measurement channels), which results in a correlation matrix. The correlation matrix is then thresholded into a binary matrix that describes the topological organization of the functional networks (**Figure 2C**). Of note, there are other approaches used to get brain connectivity networks, such as clustering (Homae et al., 2010; Blanco et al., 2018) and independent component analysis (White et al., 2012; Ferradal et al., 2016; ICA).

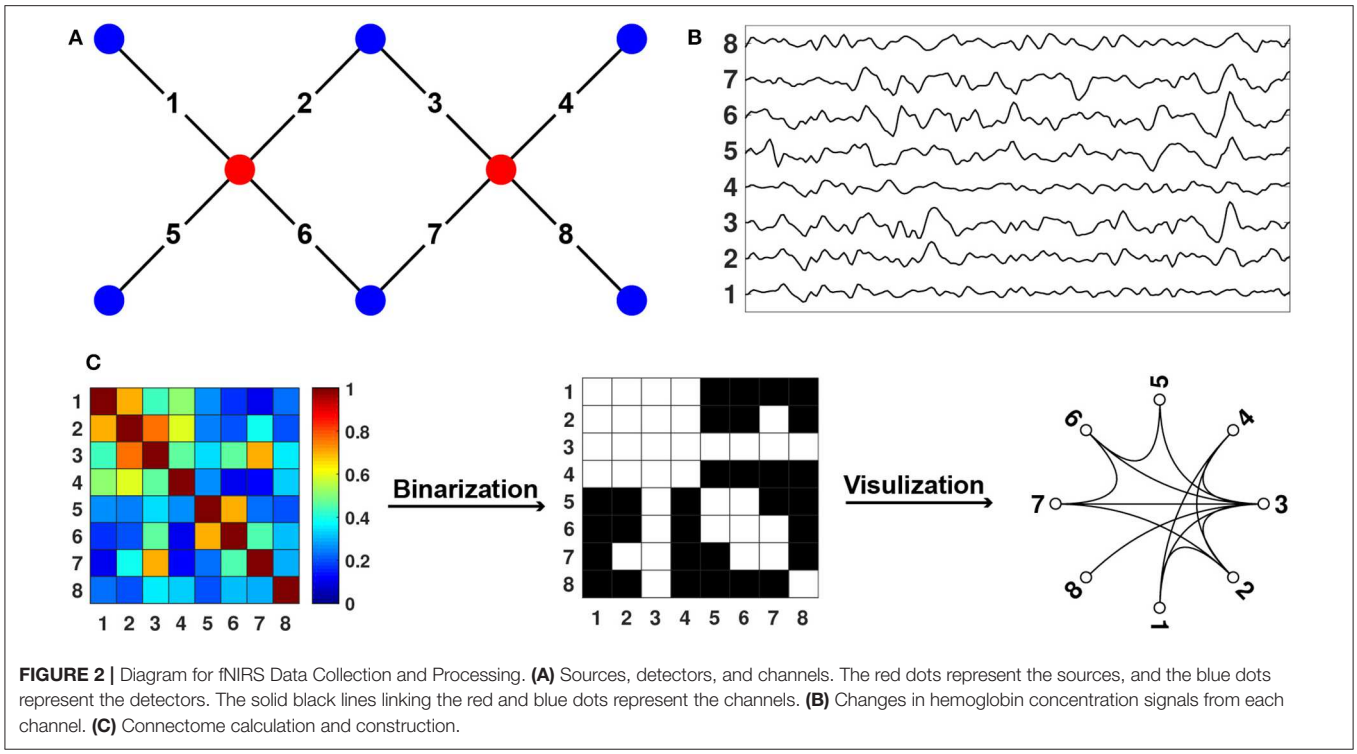

FIGURE 2 | Diagram for fNIRS Data Collection and Processing. **(A)** Sources, detectors, and channels. The red dots represent the sources, and the blue dots represent the detectors. The solid black lines linking the red and blue dots represent the channels. **(B)** Changes in hemoglobin concentration signals from each channel. **(C)** Connectome calculation and construction.

Graph-Theoretical Topology Analysis of the fNIRS Brain Connectome

Graph-theoretical topology analysis is an ideal tool for characterizing network structure at global and regional levels (Cao et al., 2017b). At the global level, it has been well-established that human brain networks exhibit small-world topology (Watts and Strogatz, 1998), which are both locally and globally efficient, reflecting optimized information segregation and integration. At the regional level, regional nodal properties are usually evaluated by nodal degree and nodal efficiency (Niu and He, 2014; Cao et al., 2017b; Cai et al., 2018). For more details about graph metrics, see (Niu et al., 2012; Niu and He, 2014). For the analysis of fNIRS brain network, please see the freely downloaded software, FC-NIRS (http://www.nitrc.org/projects/fcnirs; Xu et al., 2015).

fNIRS Brain Connectome Asymmetry

Hemispheric asymmetry is an important characteristic of the human brain. Recent studies have showed the topological asymmetry of structural or functional hemispheric networks in the human brain. The construction and topological analysis of the hemispheric network are conducted within each brain hemisphere, using the same methods applied to the whole-brain network. Usually, a brain asymmetry index (*AI*) is utilized to quantify the asymmetry in topological properties between two brain hemispheres (Cai et al., 2019). Specifically, the *AI* was defined using the following formula:

$$AI = \frac{ML - MR}{ML + MR} \quad (1)$$

where the *ML* denotes the averaged measures in the left hemisphere and *MR* denotes the averaged measures in the right hemisphere. Therefore, the *AI* changes from −1 to +1, with a positive value denoting a leftward asymmetry and a negative value denoting a rightward asymmetry.

PERFORMANCE EVALUATION OF THE FNIRS BRAIN CONNECTOME

The performance of the fNIRS brain connectome has been evaluated by comparing its stability between different scanning time and by comparing its spatial patterns with other neuroimaging modality.

In specific, the length of data acquisition time may affect the results in resting state imaging. Wang et al. (2017) explored its effect on the stability of fNIRS brain network on children participants. They found that FC was stable after 1 min fNIRS imaging duration, and both accurate and stable after 7 min duration. For network metrics, the minimum scanning duration of 2.5 min could achieve both accurate and stable performance (**Figure 3B**). This research provides direct evidence for the choice of the resting-state fNIRS imaging time in children in brain FC and network topology study.

In addition, the fNIRS brain connectome is often validated by fMRI imaging, ICA results, and task-evoked activation. For example, Ferradal et al. (2016) showed that spatial patterns in the functional connectivity in visual, middle temporal, and auditory areas were consistent with those obtained from resting-state fMRI imaging data. They also found that functional connectivity in these areas exhibited similar spatial patterns to those identified

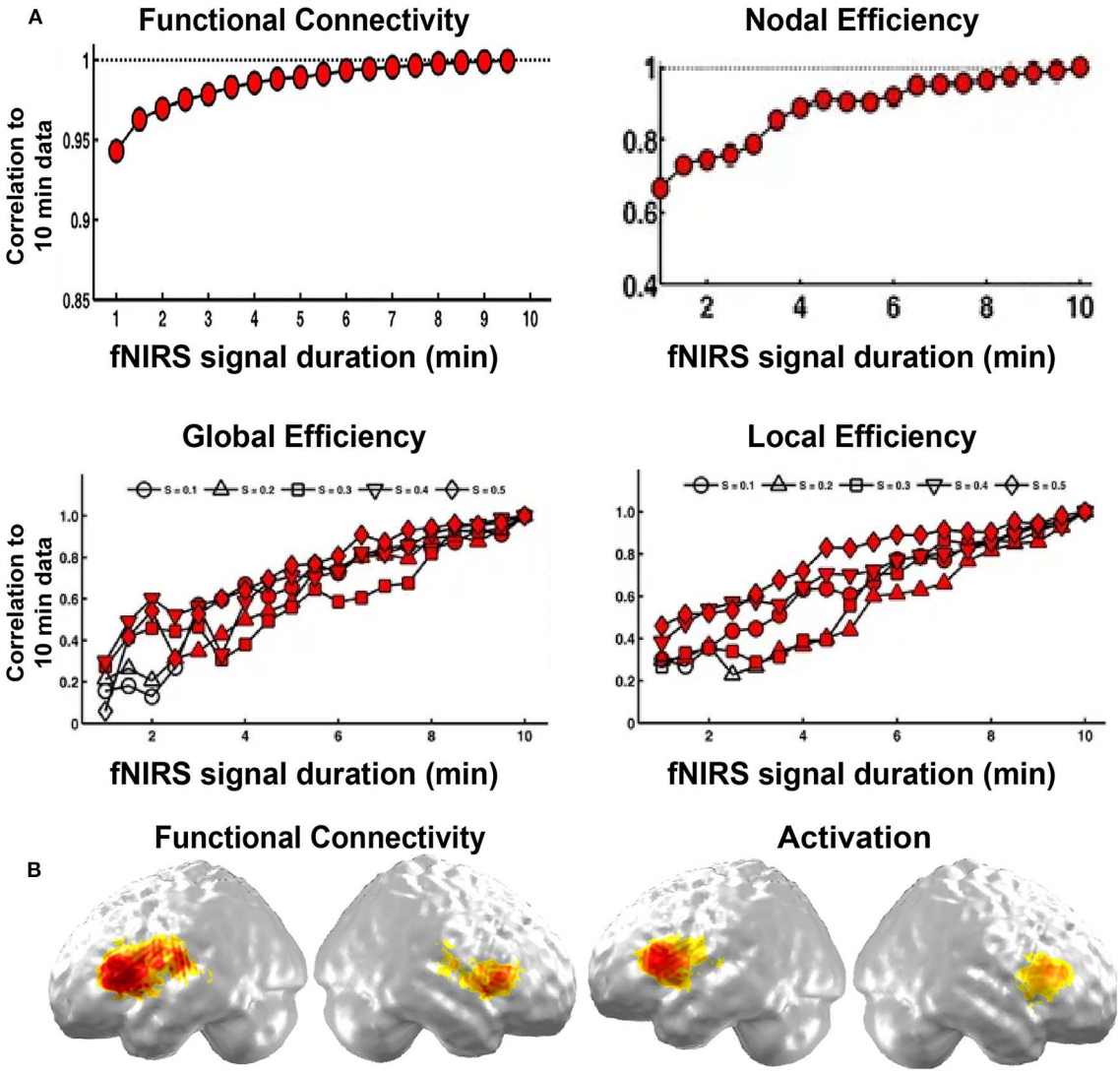

FIGURE 3 | Validity and reliability of the brain connectome. **(A)** Correlations in network metrics, including functional connectivity, nodal efficiency, global efficiency, and local efficiency, between different short recording durations and 10 min of recording duration. The red-filled shapes represent significant correlations. **(B)** Functional connectivity and activation. **(A,B)** are adapted from Wang et al. (2017) and Gallagher et al. (2016), respectively, under a Creative Commons Attribution 4.0 International License (CC BY 4.0, http://creativecommons.org/licenses/by/4.0/).

by ICA, and the networks were sensitive to neuronal injury identified by structure MRI (Ferradal et al., 2016). In addition, the functional connectivity map in the language network was also consistent with the task-evoked activation map (**Figure 3A**; Gallagher et al., 2016). These results validate the fNIRS brain connectome as a promising tool to characterize the brain network structure.

TYPICAL DEVELOPMENT OF THE BRAIN CONNECTOME

The typical development of fNIRS-derived brain connectome is summarized in terms of functional connectivity, topological network characteristics, and the asymmetry between hemispheric brain networks.

Development of Functional Connectivity

Functional connectivity is a potential biomarker of brain development and has been frequently used in the fNIRS community recently. For example, Ferradal et al. (2016) used a high-density diffuse optical tomography imaging system to record the spontaneous brain activity in healthy, full-term neonates within the first 2 days of their life. Seed-based correlation analysis was used to identify intrinsic functional connectivity in infants. In their study, strong connectivity was found between homotopic counterparts of each region of interest (e.g., visual, middle temporal visual area, and auditory cortices),

indicating a well-developed functional connectivity in infants. These results also highlight the fNIRS imaging system as a powerful and practical method for quantitative mapping of the early functional brain development in neonates. With the development of the brain, functional connectivity undergoes substantial changes, which demonstrate the strengthening and pruning of brain connectivity between different cortical regions (Damaraju et al., 2014; Cao et al., 2017b). For example, during the first 6 months of life, Homae et al. (2010) presented that the cortical network organization showed region-dependent and dynamic changes (**Figures 4A–C**). Specifically, the functional connectivity between homologs regions was identified in three- and four-month-old infants (Homae et al., 2010, 2011; Funane et al., 2014; Blanco et al., 2018). Homae et al. (2010) further identified the age-related enhanced homolog functional connectivity in the bilateral temporal, parietal, and occipital cortices (**Figures 4A,B**) and in the temporal and posterior regions (**Figure 4C**). This implies the strengthening and pruning of connections between different cortical regions during the development of the infant brain (**Figure 4**). Notably, an "*U*-shaped" developmental pattern for edges connecting frontal and occipital regions during development was also observed. For example, frontoposterior long-connectivity interactions decreased from the neonatal period to the age of 3 months and increased from the age of 3 months to the age of 6 months (**Figure 4C**; Homae et al., 2010). By contrast, the functional connectivity within the temporal regions, which was enhanced from 0 to 6 months in Homae et al.'s study, exhibited obviously decreased in 4- to 10-months-old infants compared to that in infants aged 2 to 3 months old (Taga et al., 2018).

The dynamic changes in brain network may benefit the cognition and behavior. As was pointed out by Li and Qiu et al., 9-years-old children exhibited significantly decreased functional connectivity in language areas when compared to adults, which demonstrates that functional connectivity in children remains immature (Li and Qiu, 2014). By examining 18-months-old toddlers, Bulgarelli et al. (2019) showed that infants who developed good self-awareness exhibited increased functional connectivity between frontal and temporoparietal regions. Note that such connectivity between frontal region and posterior region has been identified in infants aged as early as 4 months old (Blanco et al., 2018).

Development of Brain Network Topologies

Global and local network properties are often used to characterize integration and segregation of the developing brain. For example, Cai et al. (2018) found that global and local network efficiency in children and adolescents was significantly lower than that in adults (**Figure 5A**), demonstrating immature global information processing and local information transformation in children and adolescents. Intriguingly, children showed a significantly lower global efficiency, but comparable local efficiency, compared to early adolescents, which indicates enhance integration and steady segregation of the functional network from childhood to adolescence. Furthermore, it was found that the small-worldness and modularity showed no significant differences across developmental stages (**Figure 5A**), demonstrating maturity of these important functional brain network organization properties in the early stage of childhood.

For the regional nodal metrics, it was found that nodes with a significant increase in nodal efficiency during development

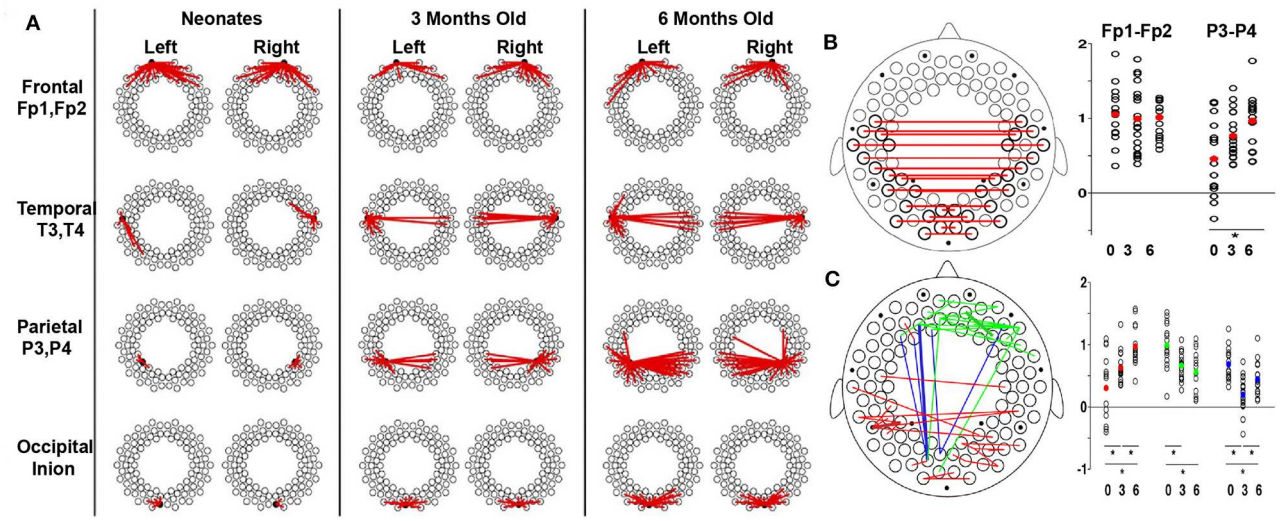

FIGURE 4 | Developmental trajectories of functional connectivity. **(A)** Development of the connectome with seeds in different brain regions. The dots represent the measurement channels, and the red lines represent correlations higher than 0.5. **(B)** Development of the connectome in homologous channels. Red lines represent the connections exhibiting significant changes. The scatter plots show *z* scores in frontal (Fp1–Fp2) and parietal (P3–P4) pairs, with the red dot indicating the average values. **(C)** Increase (red), decrease (green), and *U*-shaped (blue) changes in the connectome across development. The normalized connectivity grouped by the change patterns are displayed next to the brain template, in which the dots with corresponding colors represent the average connectivity of corresponding change patterns. For **(B,C)**, the significant differences are labeled with asterisks ($p < 0.05$, *post-hoc* tests, Tukey's HSD). These figures are adapted from Homae et al. (2010) under a Creative Commons Attribution-Non-commercial-Share Alike 3.0 Unported License (CC BY-NC-SA 3.0, https://creativecommons.org/licenses/by-nc-sa/3.0/).

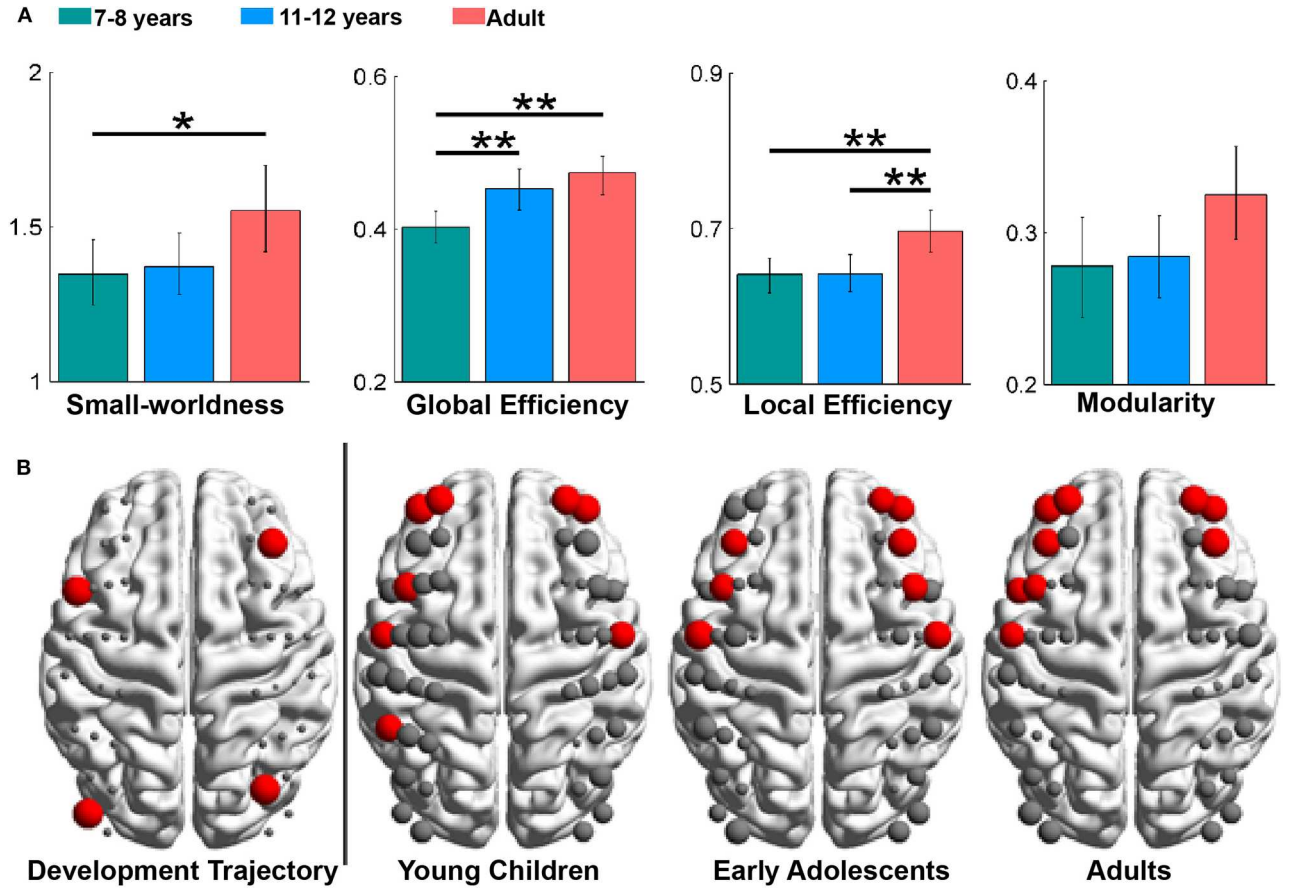

FIGURE 5 | Developmental trajectories of brain network topologies and asymmetry. **(A)** Group differences in the global network metrics, with significance indicated by asterisks (*$p < 0.05$, **$p < 0.01$). **(B)** The developmental trajectory (left) and hub distributions (right). In the developmental trajectory, nodes exhibiting age-related increases in nodal efficiency are shown in red. In the hub distributions, hubs are also shown in red, and the node size represents the values in the nodal properties. These figures are adapted from Cai et al. (2018) under an Attribution-Non-Commercial-NoDerivatives 4.0 International License (CC BY-NC-ND 4.0, https://creativecommons.org/licenses/by-nc-nd/4.0/).

were mainly distributed in frontal brain regions (**Figure 5B**), and the number of frontal hubs increased with development. Consistent with previous studies showing late developed and enhanced functional connectivity in the frontal regions (Gao et al., 2015a,b), this result provides additional biomarkers for the increasing cognitive capacity during the development.

Development of Brain Network Asymmetry

Cerebral asymmetry is a fundamental characteristic of the human brain and an important marker of brain development. Gallagher et al. (2016) compared resting-state functional connectivity identified in language regions to the activation maps of language tasks in 25 children. They found good agreement between these two approaches for language localization and hemispheric language dominance (**Figure 3A**). These results provide preliminary evidence that the fNIRS-derived functional connectivity is a valuable tool for language localization.

In addition, Cai et al. (2019) investigated the asymmetry of the brain network properties and their development from childhood to adulthood. They found the leftward asymmetry in global but not local efficiency in children (**Figure 6A**). For the adults, both hemispheric global and local efficiency showed a significant leftward asymmetry (**Figure 6A**). It was further revealed by asymmetry index (AI) that the leftward asymmetry in local (but not global) network efficiency significantly increased with development (**Figure 6B**). At the regional level, increased leftward asymmetry in nodal efficiency with development was mainly observed in the frontal, parietal–occipital junction, and occipital regions. Collectively, these developmental patterns of topological asymmetries suggest that the maturation of functional segregation in the left hemisphere plays a more important role than the right hemisphere in the cognitive development from childhood to adulthood.

ATYPICAL DEVELOPMENT OF THE BRAIN CONNECTOME

In this part, we introduce the findings regarding abnormal brain networks in preterm infants and children with neural

developmental disorders (e.g., cerebral palsy, Down's syndrome, and autism spectrum disorder) using the resting-state fNIRS brain connectome.

Brain Connectome in Preterm Infants

In 2012, White et al. showed that functional connectivity could be obtained at the bedside using fNIRS imaging. They identified functional connectivity in the visual cortex in both healthy and preterm infants (**Figure 7A**). Interestingly, Fuchino et al. (2013) noted that preterm infants showed enhanced connectivity between bilateral temporal regions and parietal regions compared to that in postmenstrual age-matched full-term infants (**Figure 7B**). However, preterm infants' functional connectivity between the left temporal and left parietal regions

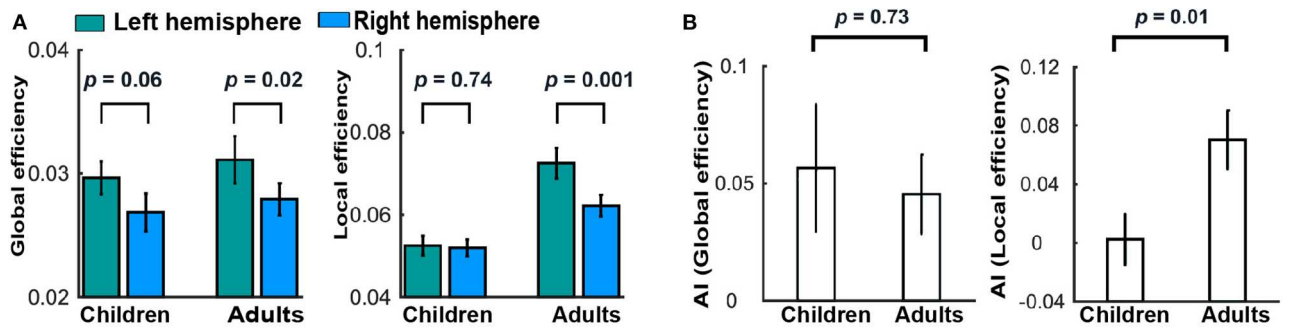

FIGURE 6 | Development of brain asymmetry. **(A)** Differences between the hemispheres in global and local efficiency for each group. **(B)** Group differences in the AI of global and local efficiency. These figures were adapted from Cai et al. (2018) under a CC BY-NC-ND 4.0 license.

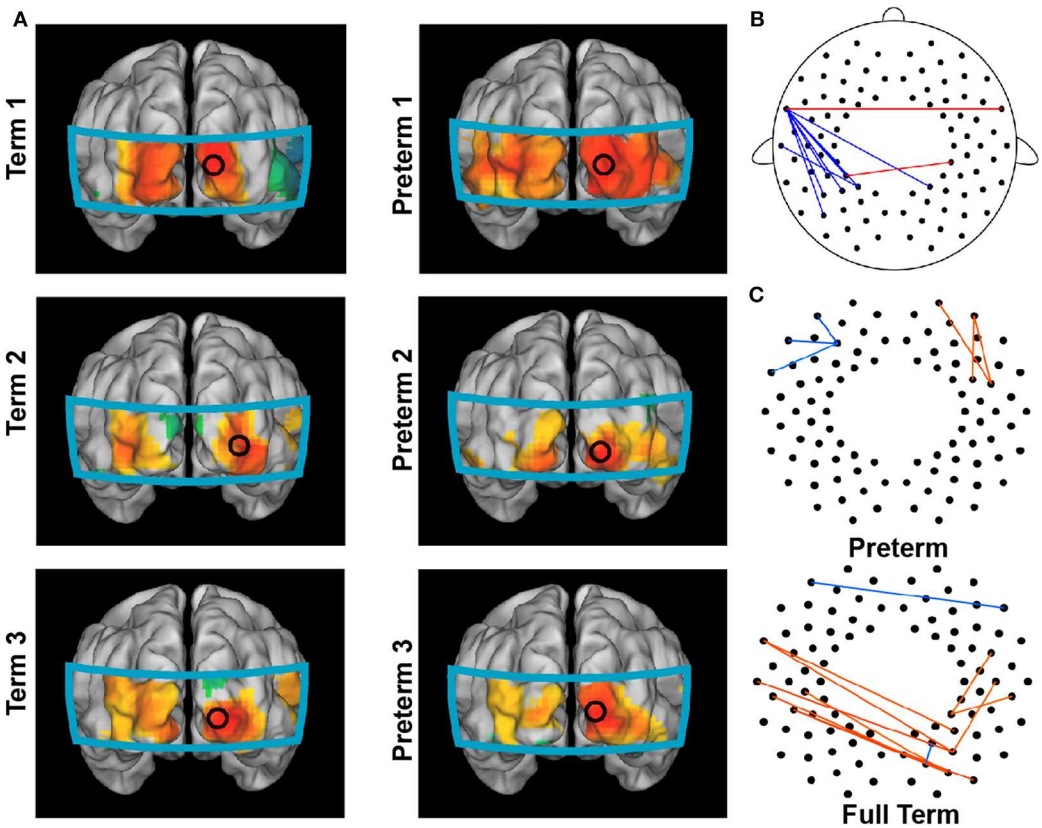

FIGURE 7 | Brain connectome in preterm infants. **(A)** Functional connectivity maps in full-term infants (left column) and preterm infants (right column) with the seed located in the right occipital region. **(B)** Group differences between preterm and full-term infants in functional connectivity. Red lines indicate the enhanced connections of preterm infants, and blue lines indicate the decreased connections of preterm infants compared to those of full-term infants. **(C)** Connections exhibiting significant correlations between normalized functional connectivity and postmenstrual age at the time of the scan in preterm (up) and full-term (bottom) infants. **(A)** is adapted from White et al. (2012) with permission from Elsevier; **(B,C)** are adapted from Fuchino et al. (2013) under a CC BY 4.0 license.

was much lower than full-term infants (**Figure 7B**). These findings imply that preterm infants have developed sufficient connectivity between homologous language-related regions (i.e., temporal cortex). However, their language development was still influenced by the immature connectivity between the temporal cortex and posterior regions, which should have increased with age (**Figure 4C**, Homae et al., 2010). This interpretation was further confirmed by the developmental trajectories of preterm and full-term infants (**Figure 7C**), in which the age-related development mainly occurred in frontal areas in the preterm infants, while changes in connectivity were mainly identified between the left temporal and posterior regions in the full-term infants (Fuchino et al., 2013).

Brain Connectome in Children With Neurological Disorders

It is well-established that disruptions in functional connectivity and topological network organization underlie various neurological disorders (Suo et al., 2015; Li et al., 2018; Wang et al., 2020). Meanwhile, resting-state fNIRS has been widely used to capture network dysfunctions in the early stage and to aid diagnosis of many pediatric neurological conditions. For example, 10-years-old children with cerebral palsy exhibited increased functional connectivity between sensorimotor centers, which was back to normal immediately after physical therapy but then relapsed after 6 months (**Figure 8A**; Cao et al., 2015). White et al. (2012) examined the functional connectivity pattern in an infant with unilateral occipital stroke and found that the functional connectivity in the visual cortex was unilateral and nonsymmetrical (**Figure 8B**). For healthy infants, the connectivity displayed a strong and bilaterally symmetrical pattern in the occipital network. In addition, for infants with Down's syndrome, the authors found decreased functional connectivity in the frontal, temporal, and occipital regions compared to that in full-term and preterm infants (**Figure 8C**; Imai et al., 2014). Decreased functional connectivity was also observed in the bilateral temporal cortices of children with autism spectrum disorder (ASD) compared to that in typically developing children (Zhu et al., 2014; Li et al., 2016). Furthermore, children's autistic behaviors were associated with decreased network efficiency (**Figure 8D**; Li and Yu, 2018). These findings support that resting-state networks, as characterized by resting-state fNIRS, are sensitive to neural dysfunctions. Therefore, disruptions in the fNIRS-based brain connectome could serve as a biomarker in diagnosis and in the evaluation of rehabilitation.

CONCLUDING REMARKS AND FURTHER CONSIDERATIONS

The current review clearly demonstrates the validity of the fNIRS-based brain connectome. By using this technique, a lot of studies have illustrated the typical and atypical development in resting-state functional connectivity and topological organization of brain networks from the neonatal period to adolescence. More specifically, functional brain connectivity was identified in neonates (Ferradal et al., 2016), and it changed dynamically with development, which reflects

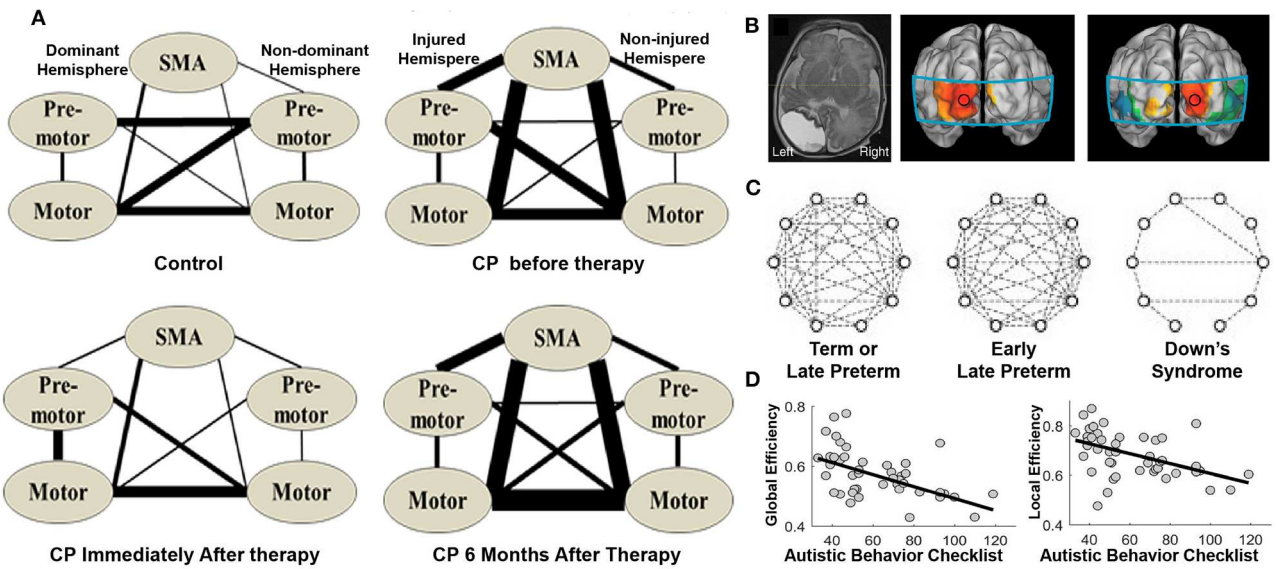

FIGURE 8 | Brain connectome in children with neurological disorders. **(A)** Brain connectome changes in cerebral palsy patients (CP) before, immediately after, and 6 months after the therapy. The thickness of the lines indicates the percentage of subjects with significant connectivity. **(B)** Structural MRI of a preterm infant with stroke and its functional connectivity maps with seeds in the left and right occipital cortex, respectively. **(C)** Brain connectome in each group. The dashed lines indicate correlation coefficients higher than 0.5. **(D)** Scatter plot illustrating the relationship between autistic behaviors and network efficiency (i.e., global and local efficiency). **(A)** is adapted from Cao et al. (2015) under a CC BY 4.0 license; **(B,C)** is adapted from White et al. (2012) and Imai et al. (2014), respectively, with permission from Elsevier; **(D)** is adapted from Li and Yu (2018) under a CC BY 4.0 license.

the strengthening and pruning of brain connectivity during development. Several topological properties of the functional networks in children were similar to those of adults, e.g., in small-world and modularity characteristics, which indicated the developmental maturity in the network organization in childhood. However, it should be noted that some specific network properties, e.g., global efficiency and local efficiency, are still being optimized during the development (i.e., both increased segregation and integration; Cai et al., 2018). Interestingly, from the view of hemispheric lateralization, local efficiency also showed a significant increase in the topological left asymmetry with development from childhood to adulthood (Cai et al., 2019). These accumulated evidence highlights that the maturation of functional segregation in the left hemisphere plays a more important role than the right hemisphere in the cognitive development from childhood to adulthood. Furthermore, resting-state fNIRS can also capture network dysfunctions in the atypically developing brain, which often leads to different neurological disorders such as autism (Li and Yu, 2018), Down's syndrome (Imai et al., 2014), and cerebral palsy (Cao et al., 2015). The abovementioned findings illustrate that fNIRS-derived connectome can serve as a promising tool for mapping neural development and as a biomarker for neurological diagnosis and rehabilitation evaluation.

However, several issues still need to be addressed in the future. First, these findings were derived from cross-sectional data, which could be influenced by inter-subject variability and unmatched cohort distributions. No longitudinal studies regarding the fNIRS connectome development have been conducted, which should be conducted in the future to reveal the nature of developmental changes.

Second, topological development has not been fully explored by these studies, and other network properties, such as network variability (Li et al., 2015), betweenness centrality (Zhao et al., 2018), and causality (Hu et al., 2019), await further investigation. Additionally, more methodological work should be performed to validate these analytical approaches.

Third, we have not combined the fNIRS with other imaging modalities such as electroencephalograph (EEG) to achieve a more comprehensive understanding of the developing brain network. The simultaneous EEG-fNIRS recording has been used in clinical monitoring (Kassab et al., 2018) and addiction research (Ieong and Yuan, 2019). It should be used in the investigation of the developing brain to depict the developmental trajectories of neurovascular coupling.

Fourth, most developmental studies did not investigate the relationship between brain connectome metrics (e.g., functional connectivity, cerebral asymmetry, and network characteristics) and behavioral performance. It remains largely unknown regarding to the underlying physiological basis of behavior performances at different stages of brain development. Further studies employing multimodal imaging and longitudinal data should be conducted to ascertain the brain-behavior relationship during development.

Fifth, the infant participants included in these studies were always in a sleeping state, while children in other age stages were in an awake state. Since, Taga et al. (2018) found that stimuli during wakefulness and sleep elicited different cortical response, the states during the resting-recording may also influence the resting-state networks, which also deserve further investigation.

Sixth, resting-state fNIRS imaging should be included in routine introspection in clinical psychiatric practice. Because of the convenient operating procedure, fNIRS is among the best candidates for clinical use. The quickly accumulating neurological data from this technique combined with the emerging deep learning technology (Hennrich et al., 2015; Marblestone et al., 2016; Cole et al., 2017; Shen et al., 2017; Vieira et al., 2017; Zhou et al., 2018) could help to diagnose neurological diseases precisely.

CONCLUSION

This review summarizes current advances in resting-sate fNIRS in characterizing the development of the brain connectome. By illustrating the brain connectome structure and quantifying the topological properties, dozens of fNIRS studies have suggested that fNIRS is an ideal alternative to resting-state fMRI for demonstrating the developmental trajectories of spontaneous cortical connectome. Despite the fruitful achievements in this field, we suggest that future studies pay more attention to the longitudinal data, expand the methodological approaches and measure modalities, ascertain the brain-behavior relationship, compare the brain states, increase the sample size, and make the best use of deep learning technology. As such, resting-state fNIRS could pave a new way toward a better understanding of brain network development.

AUTHOR CONTRIBUTIONS

ZH, QD, and HN designed the framework of this review. ZH and GL conducted the search, selected the relevant literature, and made the tables and figures. ZH wrote the manuscript. All authors reviewed the manuscript and made significant contributions to this manuscript.

FUNDING

This study was supported by the National Natural Science Foundation of China (81761148026 and 81571755).

REFERENCES

Blanco, B., Molnar, M., and Caballero-Gaudes, C. (2018). Effect of prewhitening in resting-state functional near-infrared spectroscopy data. *Neurophotonics* 5:040401. doi: 10.1117/1.NPh.5.4.040401

Bulgarelli, C., Blasi, A., De Klerk, C., Richards, J. E., Hamilton, A., and Southgate, V. (2019). Fronto-temporoparietal connectivity and self-awareness in 18-month-olds: a resting state fNIRS study. *Dev. Cogn. Neurosci.* 38:100676. doi: 10.1016/j.dcn.2019.100676

Bunge, S. A., Dudukovic, N. M., Thomason, M. E., Vaidya, C. J., and Gabrieli, J. D. (2002). Immature frontal lobe contributions to cognitive control in children: evidence from fMRI. *Neuron* 33, 301–311. doi: 10.1016/S0896-6273(01)00583-9

Cai, L., Dong, Q., and Niu, H. (2018). The development of functional network organization in early childhood and early adolescence: a resting-state fNIRS study. *Dev. Cogn. Neurosci.* 30, 223–235. doi: 10.1016/j.dcn.2018.03.003

Cai, L., Dong, Q., Wang, M., and Niu, H. (2019). Functional near-infrared spectroscopy evidence for the development of topological asymmetry between hemispheric brain networks from childhood to adulthood. *Neurophotonics* 6:025005. doi: 10.1117/1.NPh.6.2.025005

Cao, J., Khan, B., Hervey, N., Tian, F., Delgado, M. R., Clegg, N. J., et al. (2015). Evaluation of cortical plasticity in children with cerebral palsy undergoing constraint-induced movement therapy based on functional near-infrared spectroscopy. *J. Biomed. Opt.* 20:046009. doi: 10.1117/1.JBO.20.4.046009

Cao, M., He, Y., Dai, Z., Liao, X., Jeon, T., Ouyang, M., et al. (2017a). Early development of functional network segregation revealed by connectomic analysis of the preterm human brain. *Cereb. Cortex* 27, 1949–1963. doi: 10.1093/cercor/bhw038

Cao, M., Huang, H., and He, Y. (2017b). Developmental connectomics from infancy through early childhood. *Trends Neurosci.* 40, 494–506. doi: 10.1016/j.tins.2017.06.003

Cao, M., Wang, J. H., Dai, Z. J., Cao, X. Y., Jiang, L. L., Fan, F. M., et al. (2014). Topological organization of the human brain functional connectome across the lifespan. *Dev. Cogn. Neurosci.* 7, 76–93. doi: 10.1016/j.dcn.2013.11.004

Cole, J. H., Poudel, R. P. K., Tsagkrasoulis, D., Caan, M. W. A., Steves, C., Spector, T. D., et al. (2017). Predicting brain age with deep learning from raw imaging data results in a reliable and heritable biomarker. *NeuroImage* 163, 115–124. doi: 10.1016/j.neuroimage.2017.07.059

Damaraju, E., Caprihan, A., Lowe, J. R., Allen, E. A., Calhoun, V. D., and Phillips, J. P. (2014). Functional connectivity in the developing brain: a longitudinal study from 4 to 9 months of age. *Neuroimage* 84, 169–180. doi: 10.1016/j.neuroimage.2013.08.038

Delpy, D. T., Cope, M., Van Der Zee, P., Arridge, S., Wray, S., and Wyatt, J. (1988). Estimation of optical pathlength through tissue from direct time of flight measurement. *Phys. Med. Biol.* 33, 1433–1442. doi: 10.1088/0031-9155/33/12/008

Ferradal, S. L., Liao, S. M., Eggebrecht, A. T., Shimony, J. S., Inder, T. E., Culver, J. P., et al. (2016). Functional imaging of the developing brain at the bedside using diffuse optical tomography. *Cereb. Cortex* 26, 1558–1568. doi: 10.1093/cercor/bhu320

Fuchino, Y., Naoi, N., Shibata, M., Niwa, F., Kawai, M., Konishi, Y., et al. (2013). Effects of preterm birth on intrinsic fluctuations in neonatal cerebral activity examined using optical imaging. *PLoS ONE* 8:e67432. doi: 10.1371/journal.pone.0067432

Funane, T., Homae, F., Watanabe, H., Kiguchi, M., and Taga, G. (2014). Greater contribution of cerebral than extracerebral hemodynamics to near-infrared spectroscopy signals for functional activation and resting-state connectivity in infants. *Neurophotonics* 1:025003. doi: 10.1117/1.NPh.1.2.025003

Gallagher, A., Tremblay, J., and Vannasing, P. (2016). Language mapping in children using resting-state functional connectivity: comparison with a task-based approach. *J. Biomed. Opt.* 21:125006. doi: 10.1117/1.JBO.21.12.125006

Gao, W., Alcauter, S., Elton, A., Hernandez-Castillo, C. R., Smith, J. K., Ramirez, J., et al. (2015a). Functional network development during the first year: relative sequence and socioeconomic correlations. *Cereb. Cortex* 25, 2919–2928. doi: 10.1093/cercor/bhu088

Gao, W., Alcauter, S., Smith, J. K., Gilmore, J. H., and Lin, W. (2015b). Development of human brain cortical network architecture during infancy. *Brain Struct. Funct.* 220, 1173–1186. doi: 10.1007/s00429-014-0710-3

Hennrich, J., Herff, C., Heger, D., and Schultz, T. (2015). Investigating deep learning for fNIRS based BCI. *Conf. Proc. IEEE Eng. Med. Biol. Soc.* 2015, 2844–2847. doi: 10.1109/EMBC.2015.7318984

Homae, F., Watanabe, H., Nakano, T., and Taga, G. (2011). Large-scale brain networks underlying language acquisition in early infancy. *Front Psychol.* 2:93. doi: 10.3389/fpsyg.2011.00093

Homae, F., Watanabe, H., Otobe, T., Nakano, T., Go, T., Konishi, Y., et al. (2010). Development of global cortical networks in early infancy. *J. Neurosci.* 30, 4877–4882. doi: 10.1523/JNEUROSCI.5618-09.2010

Hu, Z., Lam, K. F., Xiang, Y. T., and Yuan, Z. (2019). Causal cortical network for arithmetic problem-solving represents brain's planning rather than reasoning. *Int. J. Biol. Sci.* 15, 1148–1160. doi: 10.7150/ijbs.33400

Ieong, H. F.-H., and Yuan, Z. (2019). Desynchronized lower alpha rhythms were associated with functional ischemia in the prefrontal cortex in heroin patients after protracted abstinence: a concurrent EEG-fNIRS study. *Biol. Psychiatry* 85, S295–S296. doi: 10.1016/j.biopsych.2019.03.749

Imai, M., Watanabe, H., Yasui, K., Kimura, Y., Shitara, Y., Tsuchida, S., et al. (2014). Functional connectivity of the cortex of term and preterm infants and infants with down's syndrome. *Neuroimage* 85, 272–278. doi: 10.1016/j.neuroimage.2013.04.080

Kassab, A., Le Lan, J., Tremblay, J., Vannasing, P., Dehbozorgi, M., Pouliot, P., et al. (2018). Multichannel wearable fNIRS-EEG system for long-term clinical monitoring. *Hum. Brain Mapp.* 39, 7–23. doi: 10.1002/hbm.23849

Koen, J. D., and Rugg, M. D. (2019). Neural dedifferentiation in the aging brain. *Trends Cogn. Sci.* 23, 547–559. doi: 10.1016/j.tics.2019.04.012

Li, J., and Qiu, L. (2014). Temporal correlation of spontaneous hemodynamic activity in language areas measured with functional near-infrared spectroscopy. *Biomed. Opt. Express* 5, 587–595. doi: 10.1364/BOE.5.000587

Li, J., Qiu, L., Xu, L., Pedapati, E. V., Erickson, C. A., and Sunar, U. (2016). Characterization of autism spectrum disorder with spontaneous hemodynamic activity. *Biomed. Opt. Express* 7, 3871–3881. doi: 10.1364/BOE.7.003871

Li, Y., and Yu, D. (2018). Variations of the functional brain network efficiency in a young clinical sample within the autism spectrum: a fNIRS investigation. *Front. Physiol.* 9:67. doi: 10.3389/fphys.2018.00067

Li, Z., Chen, R., Guan, M., Wang, E., Qian, T., Zhao, C., et al. (2018). Disrupted brain network topology in chronic insomnia disorder: a resting-state fMRI study. *Neuroimage Clin.* 18, 178–185. doi: 10.1016/j.nicl.2018.01.012

Li, Z., Liu, H., Liao, X., Xu, J., Liu, W., Tian, F., et al. (2015). Dynamic functional connectivity revealed by resting-state functional near-infrared spectroscopy. *Biomed. Opt. Express* 6, 2337–2337. doi: 10.1364/BOE.6.002337

Marblestone, A., Wayne, G., and Kording, K. (2016). Towards an integration of deep learning and neuroscience. *Front. Comput. Neurosci.* 10:94. doi: 10.3389/fncom.2016.00094

Mohammadi-Nejad, A. R., Mahmoudzadeh, M., Hassanpour, M. S., Wallois, F., Muzik, O., Papadelis, C., et al. (2018). Neonatal brain resting-state functional connectivity imaging modalities. *Photoacoustics* 10, 1–19. doi: 10.1016/j.pacs.2018.01.003

Niu, H., and He, Y. (2014). Resting-state functional brain connectivity: lessons from functional near-infrared spectroscopy. *Neuroscientist* 20, 173–188. doi: 10.1177/1073858413502707

Niu, H., Khadka, S., Tian, F., Lin, Z. J., Lu, C., Zhu, C., et al. (2011). Resting-state functional connectivity assessed with two diffuse optical tomographic systems. *J. Biomed. Opt.* 16:046006. doi: 10.1117/1.3561687

Niu, H., Li, Z., Liao, X., Wang, J., Zhao, T., Shu, N., et al. (2013). Test-retest reliability of graph metrics in functional brain networks: a resting-state fNIRS study. *PLoS ONE* 8:e72425. doi: 10.1371/journal.pone.0072425

Niu, H., Lin, Z. J., Tian, F., Dhamne, S., and Liu, H. (2010). Comprehensive investigation of three-dimensional diffuse optical tomography with depth compensation algorithm. *J. Biomed. Opt.* 15:046005. doi: 10.1364/BIOMED.2010.BWA8

Niu, H., Wang, J., Zhao, T., Shu, N., and He, Y. (2012). Revealing topological organization of human brain functional networks with resting-state functional near infrared spectroscopy. *PLoS ONE* 7:e45771. doi: 10.1371/journal.pone.0045771

Shen, D., Wu, G., and Suk, H.-I. (2017). Deep learning in medical image analysis. *Annu. Rev. Biomed. Eng.* 19, 221–248. doi: 10.1146/annurev-bioeng-071516-044442

Suo, X., Lei, D., Li, K., Chen, F., Li, F., Li, L., et al. (2015). Disrupted brain network topology in pediatric posttraumatic stress disorder: a resting-state fMRI study. *Hum. Brain Mapp.* 36, 3677–3686. doi: 10.1002/hbm.22871

Supekar, K., Musen, M., and Menon, V. (2009). Development of large-scale functional brain networks in children. *PLoS Biol.* 7:e1000157. doi: 10.1371/journal.pbio.1000157

Taga, G., Watanabe, H., and Homae, F. (2018). Developmental changes in cortical sensory processing during wakefulness and sleep. *Neuroimage* 178, 519–530. doi: 10.1016/j.neuroimage.2018.05.075

Vieira, S., Pinaya, W. H. L., and Mechelli, A. (2017). Using deep learning to investigate the neuroimaging correlates of psychiatric and neurological disorders: methods and applications. *Neurosci. Biobehav. Rev.* 74, 58–75. doi: 10.1016/j.neubiorev.2017.01.002

Wang, J., Dong, Q., and Niu, H. (2017). The minimum resting-state fNIRS imaging duration for accurate and stable mapping of brain connectivity network in children. *Sci. Rep.* 7:6461. doi: 10.1038/s41598-017-06340-7

Wang, M., Hu, Z., Liu, L., Li, H., Qian, Q., and Niu, H. (2020). Disrupted functional brain connectivity networks in children with attention-deficit/hyperactivity disorder: evidence from resting-state functional near-infrared spectroscopy. *Neurophotonics* 7:015012. doi: 10.1117/1.NPh.7.1.015012

Wang, M., Yuan, Z., and Niu, H. (2019). Reliability evaluation on weighted graph metrics of fNIRS brain networks. *Quant. Imag. Med. Surg.* 9, 832–841. doi: 10.21037/qims.2019.05.08

Watts, D. J., and Strogatz, S. H. (1998). Collective dynamics of 'small-world' networks. *Nature* 393, 440–442. doi: 10.1038/30918

White, B. R., Liao, S. M., Ferradal, S. L., Inder, T. E., and Culver, J. P. (2012). Bedside optical imaging of occipital resting-state functional connectivity in neonates. *Neuroimage* 59, 2529–2538. doi: 10.1016/j.neuroimage.2011.08.094

Wu, K., Taki, Y., Sato, K., Hashizume, H., Sassa, Y., Takeuchi, H., et al. (2013). Topological organization of functional brain networks in healthy children: differences in relation to age, sex, and intelligence. *PLoS ONE* 8:e55347. doi: 10.1371/journal.pone.0055347

Xiao, Y., Friederici, A. D., Margulies, D. S., and Brauer, J. (2016). Longitudinal changes in resting-state fMRI from age 5 to age 6 years covary with language development. *Neuroimage* 128, 116–124. doi: 10.1016/j.neuroimage.2015.12.008

Xu, J., Liu, X., Zhang, J., Li, Z., Wang, X., Fang, F., et al. (2015). FC-NIRS: a functional connectivity analysis tool for near-infrared spectroscopy data. *BioMed. Res. Int.* 2015, 100875–100875. doi: 10.1155/2015/248724

Zhao, T., Xu, Y., and He, Y. (2018). Graph theoretical modeling of baby brain networks. *NeuroImage* 185, 711–727. doi: 10.1016/j.neuroimage.2018.06.038

Zhou, Y., Li, G., Wen, D., Zhang, X., Han, W., and Wei, Z. (2018). Deep learning methods to process fMRI data and their application in the diagnosis of cognitive impairment: a brief overview and our opinion. *Front. Neuroinform.* 12:23. doi: 10.3389/fninf.2018.00023

Zhu, H., Fan, Y., Guo, H., Huang, D., and He, S. (2014). Reduced interhemispheric functional connectivity of children with autism spectrum disorder: evidence from functional near infrared spectroscopy studies. *Biomed. Opt. Express* 5, 1262–1274. doi: 10.1364/BOE.5.001262

Zuo, X. N., He, Y., Betzel, R. F., Colcombe, S., Sporns, O., and Milham, M. P. (2017). Human connectomics across the life span. *Trends Cogn. Sci.* 21, 32–45. doi: 10.1016/j.tics.2016.10.005

Conflict of Interest: The authors declare that the research was conducted in the absence of any commercial or financial relationships that could be construed as a potential conflict of interest.

Copyright © 2020 Hu, Liu, Dong and Niu. This is an open-access article distributed under the terms of the Creative Commons Attribution License (CC BY). The use, distribution or reproduction in other forums is permitted, provided the original author(s) and the copyright owner(s) are credited and that the original publication in this journal is cited, in accordance with accepted academic practice. No use, distribution or reproduction is permitted which does not comply with these terms.

frontiers in Human Neuroscience

ORIGINAL RESEARCH
published: 24 June 2020
doi: 10.3389/fnhum.2020.00169

Interpersonal Neural Synchronization During Cooperative Behavior of Basketball Players: A fNIRS-Based Hyperscanning Study

*Lin Li[1,2], Huiling Wang[1,2], Huiyu Luo[3], Xiaoyou Zhang[1,2], Ruqian Zhang[4] and Xianchun Li[4]**

[1] Key Laboratory of Adolescent Health Assessment and Exercise Intervention of Ministry of Education, East China Normal University, Shanghai, China, [2] College of Physical Education and Health, East China Normal University, Shanghai, China, [3] Shanghai Yucai Junior High School, Shanghai, China, [4] School of Psychology and Cognitive Science, Shanghai Changning-ECNU Mental Health Center, East China Normal University, Shanghai, China

Accumulating evidence has consistently shown that team-based sports (such as basketball) are beneficial to interpersonal cooperation. However, its neural correlate remains to be discovered, especially in the perspective of two-person neuroscience. In this study, 12 dyads of basketball players and 12 dyads of college students who had no experience of team-based sports training were asked to perform joint-drawing task and control task. During task performance, neural activities were recorded in frontal area by the functional near-infrared spectroscopy (fNIRS)-based hyperscanning approach. The results demonstrated that dyads of basketball players were faster to finish joint-drawing task and showed higher subjective cooperativeness than dyads of college students. Meanwhile, significant interpersonal neural synchronization (INS) was observed in the dorsolateral prefrontal area only when pairs of basketball players performed joint-drawing task, but not control task. Therefore, we provide the first piece of inter-brain evidence for enhanced cooperative behavior in the individuals with team-based sports training, which could make us deeply understand exact neural correlate for experience-dependent changes of cognitions in humans.

Keywords: cooperation, basketball, hyperscanning, brain synchronization, fNIRS

OPEN ACCESS

Edited by:
Xiaolin Zhou,
Peking University, China

Reviewed by:
Naama Mayseless,
Stanford University, United States
Dan Zhang,
Tsinghua University, China

***Correspondence:**
Xianchun Li
xcli@psy.ecnu.edu.cn

Specialty section:
This article was submitted to Cognitive Neuroscience, a section of the journal Frontiers in Human Neuroscience

Received: *13 October 2019*
Accepted: *20 April 2020*
Published: *24 June 2020*

Citation:
Li L, Wang H, Luo H, Zhang X, Zhang R and Li X (2020) Interpersonal Neural Synchronization During Cooperative Behavior of Basketball Players: A fNIRS-Based Hyperscanning Study. Front. Hum. Neurosci. 14:169. doi: 10.3389/fnhum.2020.00169

INTRODUCTION

Cooperation is a joint action between individuals or groups that enables achievement of common goals while people collaborate with each other (Fantasia et al., 2014). There are two main types of cooperation: one is joint action and the other is joint decision-making. The researcher proposes that joint action refers to the coordination of individuals' respective behaviors in the time and space dimensions in order to achieve a common goal (Sebanz et al., 2006), such as synchronized dance, synchronized singing, and imitation. While joint decision-making refers to two or more people making decisions separately in the same situation, and their respective decisions will affect the results of themselves and their partners (Hasson et al., 2012). A wide range of sports contain cooperative behaviors, such as basketball, table tennis doubles, and so on, in which two or more

people cooperatively work together to achieve common goals. Thus, performance in those sports should be linked with the level of interpersonal cooperation during the game.

Basketball is a highly competitive team sport between two teams that requires multiple people to participate in. The main characteristic of basketball is that the team's goal is achieved by the tacit interaction and cooperation between athletes in a highly tense and rapidly changing environment (Li, 2015). In this game, the players of the offensive team pass the ball, cooperate with one another to cover each other, and break through the opponent's defense. The defense also needs coordination through zone or man-to-man defense to block the offense from scoring. No matter joint action or joint decision-making in offensive and defensive processes, both of them can be regarded as interpersonal cooperation. The characteristics of basketball suggest that it can improve people's cooperation and prosocial behaviors. A questionnaire study assessed 16 personality factors of 103 Chinese male (Sheng, 1999) and 77 female basketball players (Hou and Sheng, 2001). They found that basketball players were more passionate and courageous, as well as more cooperative and adaptable. Another questionnaire study found that compared with students who did not play basketball regularly, those who often played it were more obedient and got along better with others. Furthermore, basketball could promote handicapped people's mental health and social skills (Fiorilli et al., 2013). All these findings consistently indicate the positive effects of basketball on cooperative behaviors in the perspective of personality. However, hitherto, the neural mechanism underlying basketball players' cooperation still remains to be clarified.

Hyperscanning refers to simultaneous neural recording from two or more socially interacting individuals (Montague et al., 2002). It can provide inter-brain evidence for cognitions enriched with interactions. The interpersonal neural synchronization (INS) has been proven to be an important neural marker for various social interactions, such as joint action (Bilek et al., 2015, 2017; Osaka et al., 2015), teaching (Holper et al., 2013; Dikker et al., 2017; Zheng et al., 2018; Pan et al., 2020; Sun et al., 2020), imitation (Dumas et al., 2010; Holper et al., 2012; Pan et al., 2018), and communication (Stephens et al., 2010; Jiang et al., 2012; Dai et al., 2018). Many types of paradigms have been employed in exploring cooperation in the hyperscanning studies, including key-pressing task (Cui et al., 2012; Pan et al., 2017), collaborative mapping (Cheng et al., 2019), and collaborative decision making tasks such as prisoner's dilemma (Hu et al., 2018) and ultimatum game (Tang et al., 2016). In these studies, the INS in prefrontal area or temporal-parietal junction is consistently observed to be much higher when dyads of subjects perform a cooperation task, not control task (Lindenberger et al., 2009; Metzger et al., 2017). Moreover, INS is positively correlated with cooperative performance (Cui et al., 2012; Pan et al., 2017).

Therefore, we attempt to explore the effect of basketball training on cooperation in the framework of two-person neuroscience. Dyads of basketball players or college students (as control) were asked to perform a joint-drawing task and control task, during which prefrontal activities were simultaneously recorded from each dyad of subjects. Based on previous findings, we hypothesized that basketball players should have better performance in the cooperative task, which should be associated with higher INS in the prefrontal cortex.

MATERIALS AND METHODS

Subjects

Twelve dyads of basketball players (experimental group) and 12 dyads of college students (control group) who had no experience of sports training were recruited in this study. They were all males, and at the age of around 20 (experimental group, 19.95 $\pm$ 1.43; control group, 19.7 $\pm$ 1.87). Participants in the experimental group were Chinese national second-level athletes, while participants in the control group had no experience of team-based sports training. All dyads were right-handed, with normal or corrected-to-normal vision. None of the participants had color blindness or any physical or mental illness.

In order to control the influence of intimacy on results, the dyads were required to get to know each other for at least three months before the experiment. All participants fully understood the tasks and signed the informed consent form before the experiment. The experiment was approved by the Ethics Committee of Human Experiments of East China Normal University. All participants received the remuneration after the experiment.

Procedures and Tasks

Once participants arrived in the laboratory, they filled in a questionnaire about basic information, such as age, gender, training years, and completed interpersonal intimacy scale (Aron et al., 1992) (**Supplementary Figure S1**). The participants were then told about the experimental procedures and tasks. Once both of them fully understood the tasks, the experiment formally began. The participants sat across the table, with two monitors in the middle (**Figure 1A**). After 1-min rest, the joint or single drawing task (described below) began. After finishing the tasks, participants were required to complete a task participation scale (**Supplementary Figure S2**) to measure the subjective cooperativeness of oneself and the partner during the task. The items were rated on a seven-point Likert-scale with one ("very low") to seven ("very high").

The study adopted a joint drawing task designed to measure cooperative behaviors (Arueti et al., 2013). The task required participants to control the direction (top, bottom, left, and right) of a brush on a computer screen to trace a target graphic. In the cooperative task, participant 1 controlled the vertical movement of the brush by pressing the up ("↑') and down ("↓") arrow keys, and participant 2 controlled the horizontal movement of the brush by pressing the left ("←") and right ("→") arrow keys. However, in the single task, two participants should control the up, down, left, and right directions to trace the target graphics, respectively. Participant 1 pressed the arrow keys ("↑," "↓," "←," "→"), and participant 2 pressed the keys of "W," "A," "S," and "D." Each participant could only see his own movements presented on the screen in the single task.

The specific process of each trial was as follows. First, a fixation appeared in the center of the screen. Then, a prompt

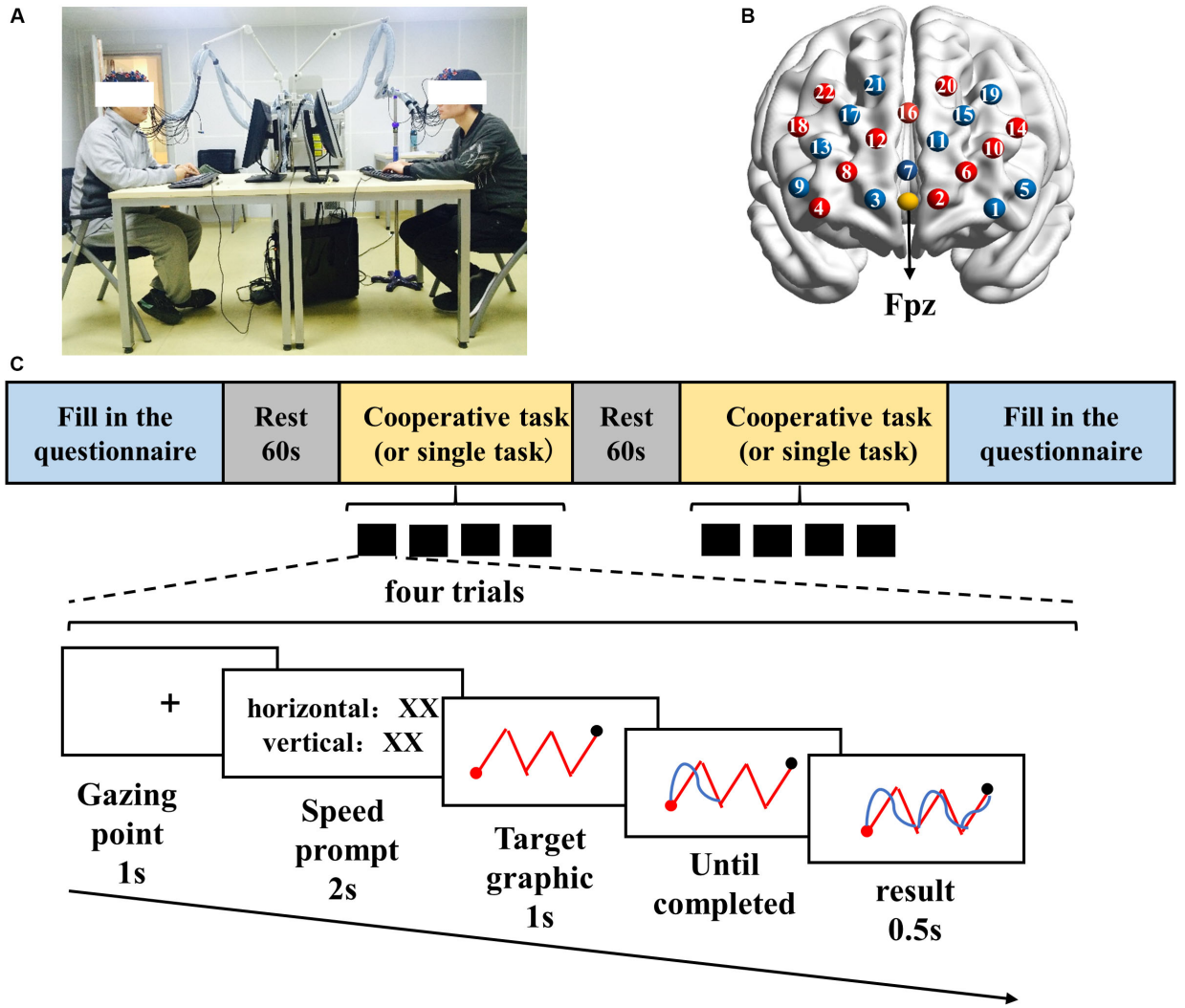

FIGURE 1 | Experimental design. **(A)** Experimental scene. **(B)** Channel location. **(C)** Task procedure.

(i.e., "speed prompt") was presented to indicate the moving speed of the brush in the present trial. The speed prompt could help participants adjust their key pressing speed more effectively, but it did not function as a variable in the current study. After that, the screen presented a red target graphic to the participants. In the process of drawing, the target graphic always appeared on the screen. The participants had to control the brush to move along the given path, from the starting point (the red point) to the end point (the black point). When the brush reached the end point, the screen automatically jumped to the next target graphic. With each key pressing, participants could clearly see the trajectory of the brush movement (blue curves) which helped them adjust their movement directions according to this real-time feedback (**Figure 1C**).

To balance the effect of order of the task, for both experimental and control groups, half of the dyads completed the cooperative task first and then performed the single task, while the other half completed the single task first and then performed the cooperative task. Each task had four trials; thus, each participant had eight trials to complete. There was no time limit to complete a trial, and the next trial did not begin until the brush moved to the end point.

Data Collection

The joint drawing task was written and run on the MATLAB platform using Psychotoolbox (The Math Works, Inc.[1], Psychophysics Toolbox Version 3[2]). The screen resolution of the computer monitor was 1920 × 1080 pixels, and the refresh rate was 60 Hz.

The ETG-7100 optical topography system (Hitachi Medical Corporation, Japan) was adopted to record concentration changes of oxy-hemoglobin (Hbo) and deoxy-hemoglobin (Hbr) for each dyad of participants. The 3 × 5 probe patch, inlaid

[1]https://www.mathworks.com/products/matlab.html

[2]http://psychtoolbox.org/

in a swimming cap, was placed on each participant's forehead, covering the prefrontal cortex. Each probe patch was composed of eight emitters and seven detectors, 3 cm apart and forming 22 channels. According to the 10-20 international system, the center detector of the middle row was placed at Fpz position (**Figure 1B**). The probes of the middle column were aligned to the midline, from the Nasion to the Inion. The spatial location of each channel referenced to the template provided by Jichi University[3] (**Supplementary Table S1**). The wavelength of the near infrared light was 695 and 830 nm, and the sampling frequency was 10 Hz.

Data Processing and Analysis

Behavioral Data Analysis

The Psychtoolbox recorded the time spent on each trial and the location of the brush in relation to the tracing line. Completion time referred to the time length required for the brush to move from the red point to the black point, and deviation area referred to the area that the brush trajectory deviated from the original target graphic (**Figure 1C**). The deviation area was calculated as follows: (Monitor area × the number of pixels that the trajectory deviated from the original shape)/screen resolution. The unit was cm^2. The reciprocal of the deviation area was used to indicate the "completion effect" of the drawing task. The greater reciprocal of the deviation area, the better the completion effect. What is more, another indicator was also established to measure the quality of the performance, namely, completion efficiency, referring to the completion effect per unit time (Completion efficiency = Completion effect/Completion time) (Cheng et al., 2019).

Through SPSS Statistics 19, we conducted independent sample *t*-tests on the intimacy and task participation, and conducted 2 (Group: experimental group, control group) × 2 (Condition: single task, cooperative task) repeated measures analysis of variance on completion time and completion efficiency. In order to more objectively and accurately reflect the level of cooperation and exclude the interference of unrelated variables, we took the single-person task as the baseline, thus subtracting completion time and completion efficiency of the single-person task from those of the cooperative task. The difference values, defined as cooperation time and cooperation efficiency, were used as criteria for evaluating the quality of cooperation. A large difference corresponded to better cooperation.

fNIRS Data Analysis

Functional near-infrared spectroscopy (fNIRS) data were processed by MATLAB 2014a. Given that compared with Hbr, Hbo is a better indicator of changes in the cerebral blood flow (Hoshi, 2003, 2007), only Hbo signals were analyzed in the study. In order to eliminate the global components, the principal component spatial filtering (PCA) algorithm (Zhang et al., 2016) was adopted. To obtain the INS, we performed wavelet transform coherence (WTC) analysis (Grinsted et al., 2004). To identify the task-related frequency band, we calculated the time-averaged coherence at each frequency from 0.02 to 0.2 Hz as previous studies (Nozawa et al., 2016; Pan et al., 2018, 2020; Zheng et al., 2018; Liu et al., 2019). The INS of the baseline (30 s rest) was subtracted from that of the task session. After that, a series of one-sample *t*-tests were conducted on all channels. Given that this analysis was only used to identify the task-related frequency range rather than obtaining final results, therefore, no multiple comparison correction was performed. Significantly increased INS was found in the frequency band ranging from 0.048 to 0.068 Hz (14.8–21 s, **Supplementary Figure S3**). Combined with visual inspection on pictures of WTC for two different tasks (**Supplementary Figure S4**), finally, the frequency band between 0.039 and 0.078 Hz (12.8–25.6 s) was chosen as the frequency band of interest in the current study. The average coherence in this band of each task was calculated by subtracting the average coherence in the rest session from that in the task session. After converting coherence values into z-scores, we performed one-sample *t*-tests with FDR correction (Benjamini and Hochberg, 1995) to find significantly synchronized channels in each task for two different groups separately. For channels with significant INS increase in at least one condition, we performed the 2 (Group: experimental group, control group) × 2 (Condition: single-person task, cooperative task) repeated measures ANOVA. At last, the contrasts between cooperative task and single task of the experimental and control groups were compared through independent sample *t*-test.

RESULTS

Behavioral Results

The differences of intimacy and task participation between two groups were examined by independent sample *t*-tests. The results showed that there was no significant difference of intimacy between two groups [$t_{(46)} = 1.629$, $p = 0.11$, Cohen's $d = 0.470$; **Figure 2A**]. However, task participation in the experimental group was significantly higher than that in the control group [$t_{(46)} = 2.023$, $p = 0.049$, Cohen's $d = 0.584$; **Figure 2B**].

The 2 (Group: experimental group, control group) × 2 (Condition: single task, cooperative task) repeated measures ANOVA on the completion time revealed significant main effects of group [$F_{(1,22)} = 4.834$, $p = 0.039$, $\eta^2 = 0.18$] and condition [$F_{(1,22)} = 17.675$, $p < 0.001$, $\eta^2 = 0.446$]. The interaction effect reached to the edge of a significant level [$F_{(1,22)} = 3.966$, $p = 0.059$, $\eta^2 = 0.153$]. The simple effect analysis found that the completion time of the single task in the experimental group was longer than that of the control group, $p = 0.034$. There was no significant difference of the completion time between two groups for the cooperative task, $p = 0.156$. The analysis on completion efficiency showed that the main effect of group [$F_{(1,22)} = 0.056$, $p = 0.815$, $\eta^2 = 0.003$], the main effect of condition [$F_{(1,22)} = 0.03$, $p = 0.865$, $\eta^2 = 0.001$] and the interaction effect [$F_{(1,22)} = 0.222$, $p = 0.642$, $\eta^2 = 0.01$] were not significant.

In order to examine the differences between two groups, we used the single-person task as a baseline, and performed

[3]http://www.jichi.ac.jp/brainlab/virtual_registration/Result3x5_E.html

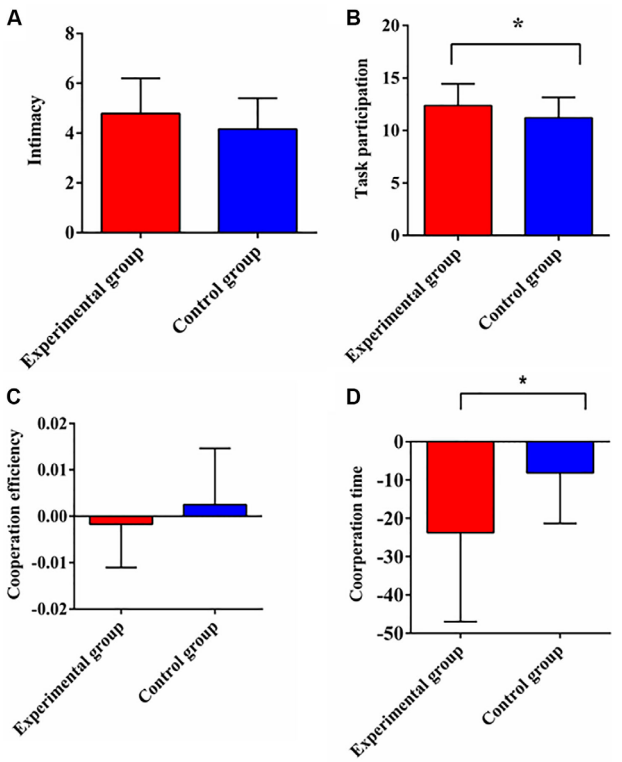

FIGURE 2 | The comparisons of intimacy **(A)**, task participation **(B)**, cooperation efficiency **(C)**, and cooperation time **(D)** between experimental group and control group. Cooperation efficiency and cooperation time are the difference of completion efficiency and the difference of completion time between two tasks respectively. Note: Error bars represent standard error; *designates $p < 0.05$.

independent sample *t*-tests on the difference of completion time and efficiency between two tasks, namely, cooperation time and cooperation efficiency. The result indicated that group had the marginal significant effect on the cooperation time [$t_{(22)} = -1.991$, $p = 0.059$, Cohen's $d = 0.813$], with the cooperation time of the experimental group being shorter than that of the control group (**Figure 2D**). But there was no significant difference of the cooperation efficiency [$t_{(22)} = -0.47$, $p = 0.642$, Cohen's $d = 0.186$; **Figure 2C**].

fNIRS Results

We first examined the INS of the experimental group in the cooperative task. A series of one sample *t*-tests found that for channel 12 [Frontopolar, $t_{(11)} = 4.021$, $p = 0.002$, Cohen's $d = 1.161$], channel 15 [Dorsolateral prefrontal cortex, $t_{(11)} = 3.745$, $p = 0.003$, Cohen's $d = 1.081$], and channel 22 [Dorsolateral prefrontal cortex, $t_{(11)} = 3.320$, $p = 0.007$, Cohen's $d = 0.958$], there was significant INS (**Figure 3A**). After FDR correction, these three channels still reached significant level ($p < 0.05$). With respect to the single task, no channel with significant INS was found. The same analysis was conducted for the control group, and no significant INS was detected in two tasks.

Then the 2 (Group: experimental group, control group) × 2 (Condition: single task, cooperative task) repeated measures ANOVA was performed for channel 12, channel 15, and channel 22. With respect to channel 12, the results showed that there were no significant main effects [group: $F_{(1,22)} = 0.763$, $p = 0.392$, $\eta^2 = 0.034$; condition: $F_{(1,22)} = 3.006$, $p = 0.097$, $\eta^2 = 0.12$] or interaction effect [$F_{(1,22)} = 0.679$, $p = 0.419$, $\eta^2 = 0.030$]. For channel 15, the results showed that the main effect of group was not significant [$F_{(1,22)} = 0.746$, $p = 0.397$, $\eta^2 = 0.033$], but the main effect of condition [$F_{(1,22)} = 12.64$, $p = 0.002$, $\eta^2 = 0.365$] and the interaction effect were significant [$F_{(1,22)} = 6.49$, $p = 0.018$, $\eta^2 = 0.228$]. Further simple effect analysis found that the INS of the experimental group in the cooperative task was significantly stronger than that of the control group, $p = 0.047$. However, such difference was not observed in the single task, $p = 0.346$ (**Figure 3B**). As for channel 22, only the main effect of condition was significant [group: $F_{(1,22)} = 2.552$, $p = 0.124$, $\eta^2 = 0.104$; condition: $F_{(1,22)} = 5.55$, $p = 0.028$, $\eta^2 = 0.201$; interaction: $F_{(1,22)} = 0.406$, $p = 0.531$, $\eta^2 = 0.018$; **Figure 3C**].

To clear the effects of group on INS, we took the single-person task as a baseline, and performed an independent sample *t*-test on the INS difference between cooperative task and single task of channel 15 and channel 22. In channel 15, the analysis revealed a significant difference between two groups [$t_{(22)} = 2.548$, $p = 0.018$, Cohen's $d = 1.04$], with the experimental group having significantly stronger INS increase than the control group. But the comparison for the INS increase in channel 22 did not showed such difference [$t_{(22)} = 0.637$, $p = 0.531$, Cohen's $d = 0.26$; **Figure 3D**].

Furthermore, to make clear the relationship between INS and behavioral performance, Pearson correlation coefficients were calculated. However, for both groups, no statistically correlations were found between task-related INS in channel 12, 15, or 22 and completion efficiency (experimental group: $ps > 0.10$; control group: $ps > 0.653$, FDR controlled), deviation area (experimental group: $ps > 0.507$; control group: $ps > 0.783$, FDR controlled), and completion time (experimental group: $ps > 0.782$; control group: $ps > 0.159$, FDR controlled).

DISCUSSION

To explore the inter-brain neural mechanism of basketball players during interpersonal cooperation, the present study combined the joint drawing task and fNIRS-based hyperscanning. During the task, two participants needed to adjust their key-pressing speed and brush directions through real-time feedback presented on the screen to trace the given graphics. The behavioral results showed that although two groups performed comparatively in the cooperative task, the subjective cooperation of the experimental group was significantly higher than that of the control group. Furthermore, there was significant INS in the dorsolateral prefrontal cortex during the cooperative task for basketball players.

The paradigm used in this study was the joint drawing task. To trace the target graphics as accurately as possible, two partners needed to continuously adjust their speed of key pressing and

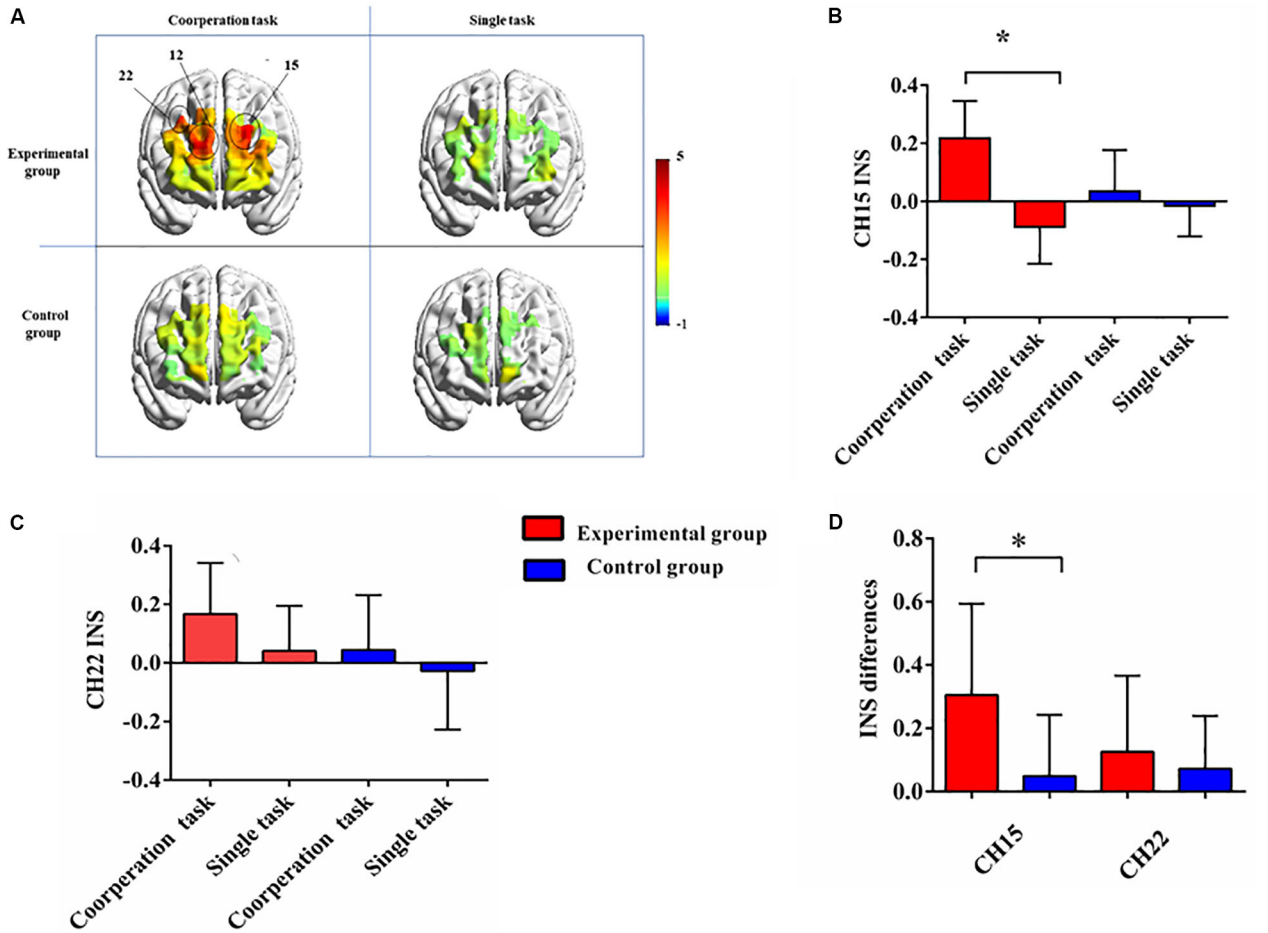

FIGURE 3 | (A) T-maps of interpersonal neural synchronization of two groups in different conditions. For the experimental group, channel 12, channel 15, and channel 22 showed significant INS increase in the cooperative task. **(B)** The task-related INS in channel 15 of two groups in different tasks. **(C)** The task-related INS in channel 22 of two groups in different tasks. **(D)** The INS contrasts (cooperative task—single task) of two groups in channel 15 and 22. Error bars are standard errors. *designates $p < 0.05$.

the direction of the brush based on their partner's performance during the task. In basketball games, for perfect cooperation, athletes not only pay attention to the situation of themselves, but also pay attention to the situation of their teammates. In this sense, interpersonal cooperation of the joint drawing task was similar to that in basketball games. Therefore, the experimental paradigm in current study was suitable for explore the difference of cooperation between basketball athletes and normal persons.

The fNIRS results showed that the basketball athletes had stronger INS in the dorsolateral prefrontal area in the cooperative task. Previous studies have shown that the dorsolateral prefrontal lobe is involved in cognitive control (Sanfey et al., 2003; Gabay et al., 2014; Feng et al., 2015), and plays an important role in cooperation-related decision-making (Fermin et al., 2016; Lukinova and Myagkov, 2016; Macoveanu et al., 2016). When dyads choose to cooperate, the dorsolateral prefrontal area is more sensitive. Using fNIRS-based hyperscanning, increased INS between two interacting persons has been observed in superior frontal cortex and dorsolateral prefrontal cortex when they performed a cooperation task (Cui et al., 2012; Pan et al., 2017). Using transcranial magnetic stimulation technology to inhibit the activity of the dorsolateral prefrontal area could reduce the cooperative behavior of the subjects (Soutschek et al., 2015). What is more, compared with cooperating with strangers, the INS of parent–child interactions was greater in the dorsolateral prefrontal area and the frontal pole cortex (FPC) in the cooperative game, which was not found in the competitive task (Reindl et al., 2018). Similar to the results of aforementioned literature, our study also found that basketball players showed significant INS in the dorsolateral prefrontal area in cooperative tasks.

In our study, we did not find significant correlation between the behavioral indicators and INS. We speculate that during the cooperation tasks, the nerves activated faster than muscles in the nerve-muscle system, and cooperation consciousness was faster than cooperative behavior. Once basketball players began to cooperate, the brain would quickly get into a cooperative state. But due to inexperience in the experimental paradigm, the

cooperation level of the basketball players in behavior was not perfectly reflected. We also analyzed the task participation of the experimental group and the control group, and found that the task participation of the experimental group was significantly better than that of the control group. This also showed that the sense of cooperation of basketball players was stronger than college students who had no experience of team-based sports training.

This study also has some limitations. First, the experimental paradigm did not perfectly reflect the characteristics of basketball and the level of cooperation of basketball players was not fully displayed. Second, the fNIRS probe board was too small to cover the entire brain, leading to incomplete observation of the brain. Finally, gender is also an important factor influencing cooperation. In this study, only men were included as participants. This is an avenue for future research.

This research is the first study on cooperation in the field of sports using fNIRS-based hyperscanning technology. It attempted to observe the relationship between sports and cooperation from the perspective of cognitive neuroscience. Future research should adopt a task paradigm combined with sports scenarios, which can better reflect the ecological nature of athlete cooperation.

DATA AVAILABILITY STATEMENT

The datasets generated for this study are available on request to the corresponding author.

ETHICS STATEMENT

The studies involving human participants were reviewed and approved by the University Committee on Human Research Protection, East China Normal University. The patients/participants provided their written informed consent to participate in this study.

AUTHOR CONTRIBUTIONS

LL and XL designed the research. HW and HL finished the experiment. HL, HW, and RZ analyzed the data. LL, XL, HW, and XZ wrote the draft. All authors reviewed the manuscript.

ACKNOWLEDGMENTS

We would like to thank all the participants. We would also thank for the equipment and technical support provided by the School of Psychology and Cognitive Science, East China Normal University.

SUPPLEMENTARY MATERIAL

The Supplementary Material for this article can be found online at: https://www.frontiersin.org/articles/10.3389/fnhum.2020.00169/full#supplementary-material

REFERENCES

Aron, A., Aron, E. N., and Smollan, D. (1992). Inclusion of other in the self scale and the structure of interpersonal closeness. *J. Pers. Soc.Psychol.* 63, 596–612. doi: 10.1037/0022-3514.63.4.596

Arueti, M., Perach-Barzilay, N., Tsoory, M. M., Berger, B., Getter, N., Shamay-Tsoory, S. G., et al. (2013). When two become one: the role of oxytocin in interpersonal coordination and cooperation. *J. Cogn. Neurosci.* 25, 1418–1427. doi: 10.1162/jocn_a_00400

Benjamini, Y., and Hochberg, Y. (1995). controlling the false discovery rate: a practical and powerful approach to multiple testing. *J. R. Statist. Soc. Ser. B* 57, 289–300. doi: 10.1111/j.2517-6161.1995.tb02031.x

Bilek, E., Ruf, M., Schaefer, A., Akdeniz, C., Calhoun, V. D., Schmahl, C., et al. (2015). Information flow between interacting human brains: identification, validation, and relationship to social expertise. *Proc. Natl. Acad. Sci. U.S.A.* 112, 5207–5212. doi: 10.1073/pnas.1421831112

Bilek, E., Stoessel, G., Schaefer, A., Clement, L., Ruf, M., Robnik, L., et al. (2017). State-dependent cross-brain information flow in borderline personality disorder. *JAMA Psychiatr.* 74, 949–957. doi: 10.1001/jamapsychiatry.2017.1682

Cheng, X., Pan, Y., Hu, Y., and Hu, Y. (2019). coordination elicits synchronous brain activity between co-actors: frequency ratio matters. *Front. Neuro.Sci.* 13:1071. doi: 10.3389/fnins.2019.01071

Cui, X., Bryant, D. M., and Reiss, A. L. (2012). Nirs-based hyperscanning reveals increased interpersonal coherence in superior frontal cortex during cooperation. *Neuroimage* 59, 2430–2437. doi: 10.1016/j.neuroimage.2011.09.003

Dai, B., Chen, C., Long, Y., Zheng, L., Zhao, H., Bai, X., et al. (2018). Neural mechanisms for selectively tuning in to the target speaker in a naturalistic noisy situation. *Nat. Commun.* 9:4819. doi: 10.1038/s41467-018-04819-z

Dikker, S., Wan, L., Davidesco, I., Kaggen, L., Oostrik, M., McClintock, J., et al. (2017). Brain-to-brain synchrony tracks real-world dynamic group interactions in the classroom. *Curr. Biol.* 27, 1375–1380. doi: 10.1016/j.cub.2017.04.002

Dumas, G., Nadel, J., Soussignan, R., Martinerie, J., and Garnero, L. (2010). Inter-brain synchronization during social interaction. *PLoS One* 5:12166. doi: 10.1371/journal.pone.0012166

Fantasia, V., De Jaegher, H., and Fasulo, A. (2014). We can work it out: an enactive look at cooperation. *Front. Psychol.* 5:874. doi: 10.3389/fpsyg.2014.00874

Feng, C., Luo, Y., and Krueger, F. (2015). Neural signatures of fairness-related normative decision making in the ultimatum game: a coordinate-based meta-analysis. *Hum. Brain Mapp.* 36, 591–602. doi: 10.1002/hbm.22649

Fermin, A. S. R., Sakagami, M., Kiyonari, T., Li, Y., Matsumoto, Y., Toshio Yamagishi, T., et al. (2016). Representation of economic preferences in the structure and function of the amygdala and prefrontal cortex. *Sci. Rep.* 6:20982. doi: 10.1038/srep20982

Fiorilli, G., Iuliano, E., Aquino, G., Battaglia, C., Giombini, A., and di Cagno, A. (2013). Mental health and social participation skills of wheelchair basketball players: a controlled study. *Res. Develop. Disb.* 34, 3679–3685. doi: 10.1016/j.ridd.2013.08.023

Gabay, A. S., Radua, J., Kempton, M. J., and Mehta, M. A. (2014). The ultimatum game and the brain: a meta-analysis of neuroimaging studies. *Neurosci. Biobehav. Rev.* 47, 549–558. doi: 10.1016/j.neubiorev.2014.10.014

Grinsted, A., Moore, J., and Jevrejeva, S. (2004). Application of the cross wavelet transform and wavelet coherence to geophysical time series. *Nonlin. Proces. Geophys.* 11, 561–566. doi: 10.5194/npg-11-561-2004

Hasson, U., Ghazanfar, A. A., Galantucci, B., Garrod, S., and Keysers, C. (2012). Brain-to-brain coupling: a mechanism for creating and sharing a social world. *Trends Cogn. Sci.* 16, 114–121. doi: 10.1016/j.tics.2011.12.007

Holper, L., Goldin, A. P., Shalom, D. E., Battro, A. M., Wolf, M., and Mariano, S. (2013). The teaching and the learning brain: a cortical hemodynamic marker of

teacher-student interactions in the socratic dialog. *Intern. J. Educ. Res.* 59, 1–10. doi: 10.1016/j.ijer.2013.02.002

Holper, L., Scholkmann, F., and Wolf, M. (2012). Between-brain connectivity during imitation measured by fnirs. *Neuroimage* 63, 212–222. doi: 10.1016/j.neuroimage.2012.06.028

Hoshi, Y. (2003). Functional near-infrared optical imaging: utility and limitations in human brain mapping. *Psychophysiology* 40, 511–520. doi: 10.1111/1469-8986.00053

Hoshi, Y. (2007). Functional near-infrared spectroscopy: current status and future prospects. *J. Biomed. Opt.* 12:911. doi: 10.1117/1.2804911

Hou, B., and Sheng, S. (2001). The determination and analysis on 16PF Norm for women basketball players in China. *China Sports Technol.* 37, 26–28. doi: 10.3969/j.issn.1002-9826.2001.06.009

Hu, Y., Pan, Y., Shi, X., Cai, Q., Li, X., and Cheng, X. (2018). Inter-brain synchrony and cooperation context in interactive decision making. *Biol. Psychol.* 133, 54–62. doi: 10.1016/j.biopsycho.2017.12.005

Jiang, J., Dai, B., Peng, D., Zhu, C., Liu, L., and Lu, C. (2012). Neural synchronization during face-to-face communication. *J. Neuro. Sci.* 32, 16064–16069. doi: 10.1523/Jneurosci.2926-12.2012

Li, X. (2015). On the interpretation and thinking of whole basketball. *J. Cheng. Sport Univer.* 41, 85–89.

Lindenberger, U., Li, S., Gruber, W., and Müller, V. (2009). Brains swinging in concert: cortical phase synchronization while playing guitar. *BMC Neurosci.* 10:22. doi: 10.1186/1471-2202-10-22

Liu, J., Zhang, R., Geng, B., Zhang, T., Yuan, D., Otani, S., et al. (2019). Interplay between prior knowledge and communication mode on teaching effectiveness: interpersonal neural synchronization as a neural marker. *Neuroimage* 193, 93–102. doi: 10.1016/j.neuroimage.2019.03.004

Lukinova, E., and Myagkov, M. (2016). Impact of short social training on prosocial behaviors: an fmri study. *Front. Syst. Neuro. Sci.* 10:60. doi: 10.3389/fnsys.2016.00060

Macoveanu, J., Ramsoy, T. Z., Skov, M., Siebner, H. R., and Fosgaard, T. R. (2016). The neural bases of framing effects in social dilemmas. *J. Neuro. Sci.Psychol. Econ.* 9, 14–28. doi: 10.1037/npe0000050

Metzger, F. G., Ehlis, A., Haeussinger, F. B., Schneeweiss, P., Hudak, J., Fallgatter, A. J., et al. (2017). Functional brain imaging of walking while talking-an fnirs study. *Neuroscience* 343, 85–93. doi: 10.1016/j.neuroscience.2016.11.032

Montague, P. R., Berns, G. S., Cohen, J. D., McClure, S. M., Pagnoni, G., Dhamala, M., et al. (2002). Hyperscanning: simultaneous fmri during linked social interactions. *Neuroimage* 16, 1159–1164. doi: 10.1006/nimg.2002.1150

Nozawa, T., Sasaki, Y., Sakaki, K., Yokoyama, R., and Kawashima, R. (2016). Interpersonal frontopolar neural synchronization in group communication: an exploration toward fnirs hyperscanning of natural interactions. *Neuroimage* 133, 484–497. doi: 10.1016/j.neuroimage.2016.03.059

Osaka, N., Minamoto, T., Yaoi, K., Azuma, M., Shimada, Y. M., and Osaka, M. (2015). How two brains make one synchronized mind in the inferior frontal cortex: fnirs-based hyperscanning during cooperative singing. *Front. Psychol.* 6:1811. doi: 10.3389/fpsyg.2015.01811

Pan, Y., Cheng, X., Zhang, Z., Li, X., and Hu, Y. (2017). Cooperation in lovers: an fnirs-based hyperscanning study. *Hum. Brain Mapp.* 38, 831–841. doi: 10.1002/hbm.23421

Pan, Y., Dikker, S., Goldstein, P., Zhu, Y., Yang, C., and Hu, Y. (2020). Instructor-learner brain coupling discriminates between instructional approaches and predicts learning. *Neuroimage* 211:657. doi: 10.1016/j.neuroimage.2020.116657

Pan, Y., Novembre, G., Song, B., Li, X., and Hu, Y. (2018). Interpersonal synchronization of inferior frontal cortices tracks social interactive learning of a song. *Neuroimage* 183, 280–290. doi: 10.1016/j.neuroimage.2018.08.005

Reindl, V., Gerloff, C., Scharke, W., and Konrad, K. (2018). Brain-to-brain synchrony in parent-child dyads and the relationship with emotion regulation revealed by fnirs-based hyperscanning. *Neuroimage* 178, 493–502. doi: 10.1016/j.neuroimage.2018.05.060

Sanfey, A. G., Rilling, J. K., Aronson, J. A., Nystrom, L. E., and Cohen, J. D. (2003). The neural basis of economic decision-making in the ultimatum game. *Science* 300, 1755–1758. doi: 10.1126/science.1082976

Sebanz, N., Bekkering, H., and Knoblich, G. (2006). Joint action: bodies and minds moving together. *Trends Cogn. Sci.* 10, 70–76. doi: 10.1016/j.tics.2005.12.009

Sheng, S. (1999). 16PF norm calibration and personality analysis of national male basketball players. *China Sports Sci. Technol.* 35, 24–27. doi: 10.16470/j.csst.1999.12.009

Soutschek, A., Sauter, M., and Schubert, T. (2015). The importance of the lateral prefrontal cortex for strategic decision making in the prisoner's dilemma. *Cogn. Affect. Behav. Neurosci.* 15, 854–860. doi: 10.3758/s13415-015-0372-5

Stephens, G. J., Silbert, L. J., and Hasson, U. (2010). Speaker-listener neural coupling underlies successful communication. *Proc. Natl. Acad. Sci. U.S.A.* 107, 14425–14430. doi: 10.1073/pnas.1008662107

Sun, B., Xiao, W., Feng, X., Shao, Y., Zhang, W., and Li, W. (2020). Behavioral and brain synchronization differences between expert and novice teachers when collaborating with students. *Brain Cogn.* 139:e0105513. doi: 10.1016/j.bandc.2019.105513

Tang, H., Mai, X., Wang, S., Zhu, C., Krueger, F., and Liu, C. (2016). Interpersonal brain synchronization in the right temporo-parietal junction during face-to-face economic exchange. *Soc. Cogn. Affect. Neurosci.* 11, 23–32. doi: 10.1093/scan/nsv092

Zhang, D., Liu, R., Zhang, G., Zhang, Y., Xiong, Y., Zhang, C. Y., et al. (2016). Nir-sers spectra detection of cytidine on nano-silver films. *Spectrosc. Spect. Analy.* 36, 743–748. doi: 10.3964/j.issn.1000-0593(2016)03-0743-06

Zheng, L., Chen, C., Liu, W., Long, Y., Zhao, H., Bai, X., et al. (2018). Enhancement of teaching outcome through neural prediction of the students' knowledge state. *Hum. Brain Mapp.* 39, 3046–3057. doi: 10.1002/hbm.24059

Conflict of Interest: The authors declare that the research was conducted in the absence of any commercial or financial relationships that could be construed as a potential conflict of interest.

Copyright © 2020 Li, Wang, Luo, Zhang, Zhang and Li. This is an open-access article distributed under the terms of the Creative Commons Attribution License (CC BY). The use, distribution or reproduction in other forums is permitted, provided the original author(s) and the copyright owner(s) are credited and that the original publication in this journal is cited, in accordance with accepted academic practice. No use, distribution or reproduction is permitted which does not comply with these terms.

frontiers in Human Neuroscience

ORIGINAL RESEARCH
published: 30 June 2020
doi: 10.3389/fnhum.2020.00252

Functional Near-Infrared Spectroscopy Indicates That Asymmetric Right Hemispheric Activation in Mental Rotation of a Jigsaw Puzzle Decreases With Task Difficulty

*Murat Can Mutlu[1], Sinem Burcu Erdoğan[2], Ozan Cem Öztürk[3], Reşit Canbeyli[4] and Hale Saybaşılı[1]**

[1] Institute of Biomedical Engineering, Boğaziçi University, Istanbul, Turkey, [2] Department of Medical Engineering, Acıbadem Mehmet Ali Aydınlar University, Istanbul, Turkey, [3] School of Sport Exercise and Health Sciences, Loughborough University, Leicestershire, United Kingdom, [4] Department of Psychology, Boğaziçi University, Istanbul, Turkey

OPEN ACCESS

Edited by:
Fenghua Tian,
University of Texas at Arlington,
United States

Reviewed by:
Summer Sheremata,
Florida Atlantic University,
United States
George Alexandrakis,
University of Texas at Arlington,
United States

***Correspondence:**
Hale Saybaşılı
saybasil@boun.edu.tr

Specialty section:
This article was submitted to Cognitive Neuroscience, a section of the journal Frontiers in Human Neuroscience

Received: 26 November 2019
Accepted: 08 June 2020
Published: 30 June 2020

Citation:
Mutlu MC, Erdoğan SB, Öztürk OC, Canbeyli R and Saybaşılı H (2020) Functional Near-Infrared Spectroscopy Indicates That Asymmetric Right Hemispheric Activation in Mental Rotation of a Jigsaw Puzzle Decreases With Task Difficulty. Front. Hum. Neurosci. 14:252. doi: 10.3389/fnhum.2020.00252

Mental rotation (MR) is a cognitive skill whose neural dynamics are still a matter of debate as previous neuroimaging studies have produced controversial results. In order to investigate the underlying neurophysiology of MR, hemodynamic responses from the prefrontal cortex of 14 healthy subjects were recorded with functional near-infrared spectroscopy (fNIRS) during a novel MR task that had three categorical difficulty levels. Hemodynamic activity strength (HAS) parameter, which reflects the ratio of brain activation during the task to the baseline activation level, was used to assess the prefrontal cortex activation localization and strength. Behavioral data indicated that the MR requiring conditions are more difficult than the condition that did not require MR. The right dorsolateral prefrontal cortex (DLPFC) was found to be active in all conditions and to be the dominant region in the easiest task while more complex tasks showed widespread bilateral prefrontal activation. A significant increase in left DLPFC activation was observed with increasing task difficulty. Significantly higher right DLPFC activation was observed when the incongruent trials were contrasted against the congruent trials, which implied the possibility of a robust error or conflict-monitoring process during the incongruent trials. Our results showed that the right DLPFC is a core region for the processing of MR tasks regardless of the task complexity and that the left DLPFC is involved to a greater extent with increasing task complexity, which is consistent with the previous neuroimaging literature.

Keywords: fNIRS, lateralization, mental rotation, puzzle, DLPFC, prefrontal cortex

INTRODUCTION

In recent years, the number of studies conducted with functional near-infrared spectroscopy (fNIRS) has increased due to several advantages it has over other functional imaging techniques such as electroencephalography (EEG), functional magnetic resonance imaging (fMRI), and positron emission tomography (PET). fNIRS technology offers a more cost-effective and

user-friendly alternative to fMRI and PET in measuring cerebral energy metabolism besides having the major advantage of being field-deployable. Furthermore, its portability allows recordings of the functional cerebral hemodynamics induced by cortical activation in daily life environments. Numerous studies have demonstrated the reliability of fNIRS in measuring cortical hemodynamic responses during various lateralized cognitive tasks involving language (Herff et al., 2013; Jasinska and Petitto, 2013; Sugiura et al., 2015; Fu et al., 2016), visual/visuospatial (Herff et al., 2013; Baker et al., 2018; Curtin et al., 2019) and mathematic processing (Herff et al., 2013; Artemenko et al., 2018). However, studies that have investigated visuospatial processing with fNIRS is limited in number, particularly for mental rotation (MR) tasks, the decoding of which might have crucial importance in the design of fNIRS based brain-computer interfaces.

Mental rotation is a spatial cognitive ability that involves mentally rotating two or three-dimensional objects. Since the development of the first mental rotation test by Shepard and Metzler (1971), mental rotation skill has been widely investigated by numerous research groups employing different behavioral and neuroimaging methods. While initial studies depended mostly on behavioral responses and usually measured reaction time as a metric of cognitive workload and difficulty (Shepard and Metzler, 1971; Cooper and Shepard, 1975), more recent studies have employed neuroimaging methods such as fMRI (Jordan et al., 2001; Halari et al., 2006; Seydell-Greenwald et al., 2017), fNIRS (Shimoda et al., 2008) and PET (Harris et al., 2000) to understand the neurophysiological processes underlying MR skill. In these studies, hemispheric dominance in mental rotation skill has been a major scope of the investigation, but the results still remain to be a matter of debate. While a majority of the studies claimed a right-hemispheric superiority in mental rotation with different imaging modalities (Ratcliff, 1979; Papanicolaou et al., 1987; Deutsch et al., 1988), others found a left-hemispheric dominance (Mehta and Newcombe, 1991; Alivisatos and Petrides, 1997) or a bilateral activation (Cohen et al., 1996; Vingerhoets et al., 2002; Hugdahl et al., 2006; Shimoda et al., 2008). While various factors may contribute to the discrepancy in these results, variations in task complexity and the resultant cognitive effort appear to be the first and foremost issue to be addressed. Mehta and Newcombe (1991) found that left hemispheric lesions affected the mental rotation of 3D-shapes, while Ratcliff (1979) and Ditunno and Mann (1990) found that right hemispheric lesions impaired the mental rotation of 2D-shapes. It is claimed that left-hemispheric activity increases with the complexity or difficulty of the task possibly because of two factors: applied rotation strategy (piecemeal vs. holistic) and involvement of other cognitive elements such as verbalization (Corballis, 1997). Corballis (1997) claimed that simpler shapes are being rotated in more holistic fashion, while more complex shapes are being rotated in more piecemeal fashion during which the subjects focus on certain features or attributes of the shapes. For the latter factor, increased task complexity requires various additional cognitive resources to be utilized during the task.

Since findings regarding the hemodynamic activation patterns observed during mental rotation tasks are not consistent in terms of lateralization, the present study aimed to assess whether MR elicits a lateralized neural response in the prefrontal cortex regions and, if so, where the hemodynamic activity is localized. Another aim was to investigate the effect of task difficulty on prefrontal cortex activation. Overall, the study was designed to show that fNIRS is reliably capable of capturing the cerebral hemodynamics during mental rotation tasks, and thus can be used in decoding of cognitive abilities. For these purposes, a novel mental rotation task based on jigsaw puzzle piece-template pairs with various categorical difficulty was designed, and fNIRS data were collected during execution of these tasks in a daily life environment rather than inside an MRI or PET apparatus. Several fNIRS studies have derived spatial and temporal features from hemodynamic responses during mental rotation tasks for fNIRS-Brain Computer Interface (BCI) applications (Herff et al., 2013; Banville et al., 2017; Qureshi et al., 2017). However, to the best of our knowledge, no fNIRS study has examined the spatial and temporal features of the cerebral hemodynamics of mental rotation tasks of varying difficulty at a group level in detail to reveal the underlying physiological mechanisms in the prefrontal cortex.

MATERIALS AND METHODS

Participants

Fifteen healthy volunteer subjects, ages 21–35, participated in the study. One subject was excluded from analysis due to poor signal to noise ratio in fNIRS recordings. The remaining subjects were eight females and six males (11 right-handed and 3 left-handed). All subjects were informed before the experiment and gave written consent. The study was approved by the local ethical committee, Human Research Ethical Committee of Boğaziçi University.

fNIRS Data Acquisition

A NIRSport system (NIRx Medical Technologies, LLC, Berlin, Germany) with a set-up of 22 channels consisting of 8 light sources (emitting near-infrared light at 760 and 850 nm) and 7 detectors covering the frontal cortex was used to collect hemodynamic data (**Figure 1A**). The sampling rate of the signal was 7.8125 Hz and the source-detector distance was 3 cm. Probe sensitivity profile was computed with the Atlas Viewer toolbox (Aasted et al., 2015) of Homer2 Software (Huppert et al., 2009). AtlasViewer provides wavelength-specific sensitivity maps of photon propagation for each. In **Figure 1A**, the optical sensitivity profile of the probe is mapped on a standard brain template with a 10/5 global EEG electrode system. The sensitivity of the probe for detecting brain hemodynamics was calculated with the method explained in Aasted et al. (2015) and presented as a temperature plot ranging from 0 (red) to -2 (blue) in log10 units. The channel locations are coregistered onto a standard brain in MNI space using the NIRS_SPM toolbox in **Figure 1B** (Singh et al., 2005; Jang et al., 2009; Ye et al., 2009). The percentage of Brodmann areas covered by each channel was computed with the spatial registration toolbox of NIRS_SPM according to the Rorden's brain atlas (Rorden and Brett, 2001) and are presented in **Table 1**.

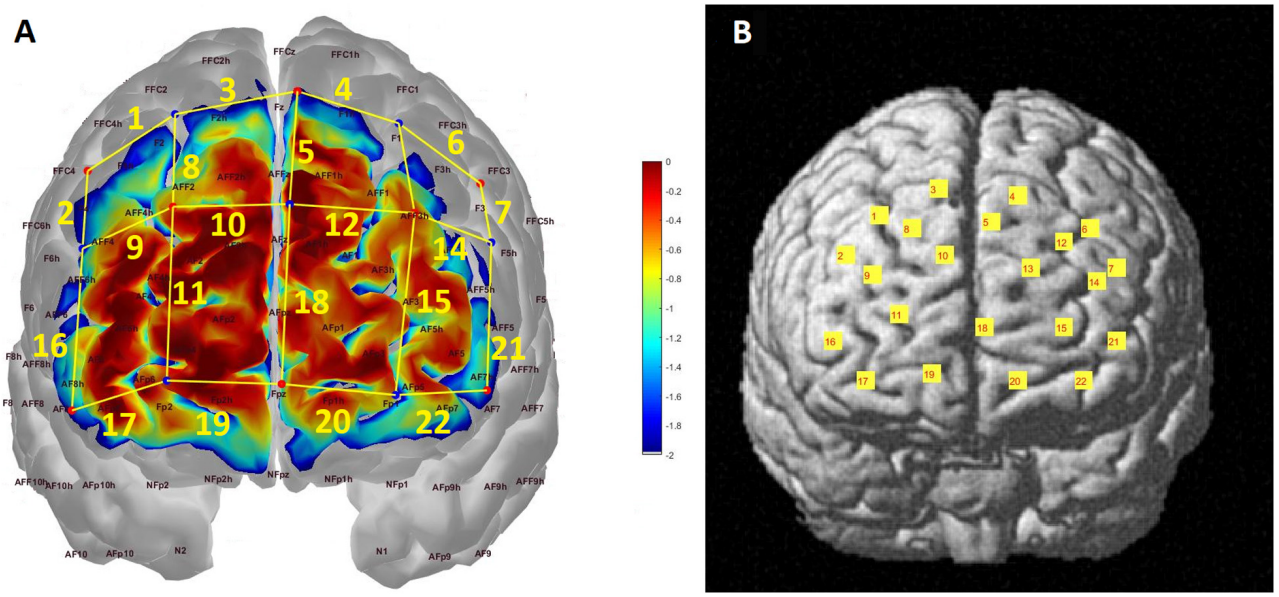

FIGURE 1 | (A) Probe configuration and photon sensitivity profile. Each red dot corresponds to a light source while each blue dot represents a detector. Channels are formed between adjacent source-detector pairs and represented with yellow lines and labeled accordingly. The sensitivity of the probe to detecting brain hemodynamics is presented as a heat map in log10 units. **(B)** Channel locations projected onto a standard brain template in MNI space.

Experimental Design

The study was carried out in a silent and dimly lit room. The temperature of the room was controlled with an air conditioning system and set approximately at 23°C. Subjects sat in front of a computer screen with a 50 cm eye-to-screen distance and all experimental cues were presented on a 24-inch computer monitor. After the acquisition of demographic data, the experimental protocol was explained in detail to each subject. During the experiment, subjects had to decide whether a puzzle piece shown on the screen could fit the gap in the middle of a puzzle template, shown after the puzzle piece, by pressing either the "S" or "K" key on the keyboard, indicating a "Yes" ("Congruent") or "No" ("Incongruent") answer respectively. There were three conditions: (1) Perfect Match (PM) condition in which the piece can fit into the template without requiring a mental rotation, (2) Match (M) condition in which the piece would fit into the template only if the subject mentally rotated the piece, and (3) a Non-Match (NM) condition in which the piece could not fit into the template (**Figure 2**). Each subject made decisions for 24 trials consisting of 6 PM, 6 M, and 12 NM conditions presented in random order. All of the Perfect Match and Match trials formed a "congruent" condition and required a "Yes" answer, while Non-Match trials formed an "incongruent" condition requiring a "No" answer. Each experiment began with a baseline fNIRS recording of 30 s, after which the subject pressed the "Space" key on the keyboard to start the experiment. At the beginning of each trial, a plus sign ("+") was presented for 500 ms to briefly alert the subject to the onset of a new trial. Then, a puzzle piece was presented for 500 ms, followed by a white noise masking image presentation for 750 ms to eliminate the after-image effect of the puzzle piece. Subsequently, the template was shown for 3 s during which the subject had to give a "Yes" or "No" answer by pressing "S" or "K" on the keyboard, respectively. Afterward, a white noise masking was shown for another 750 ms. All of the visual cues and images were rendered at the center of the screen in order to eliminate a possible visual field effect. The total duration of a trial was 5.5 s and the inter-trial interval was set randomly for each trial, ranging from 9 to 12 s, in order to prevent subjects' anticipatory hemodynamic responses (**Figure 3**). The experiment was designed with PsychoPy 3.0.6 (Peirce et al., 2019). Reaction times and accuracy rates for each trial were collected as behavioral data with PsychoPy software. fNIRS data were collected continuously during the experiment.

Data Preprocessing and Feature Selection

Data preprocessing was performed with a combination of nirsLAB (a free analysis software that comes with the NIRSport system), Homer2 and custom-made scripts written in MATLAB R2017B. Raw intensity data were first visually examined in nirsLAB. Then, the coefficients of variation (CV) method (Hocke et al., 2018; Pfeifer et al., 2018) was employed to eliminate the channels with poor signal quality. The threshold for CV was set to 7.5% as used by Hocke et al. (2018). A preprocessing pipeline based on HOMER2 functions was constructed. The raw intensity data were converted into optical density (OD) data with *hmrIntensity2OD* function. Data segments that included motion artifacts were identified by using *hmrMotionArtifact.m* function with the following parameters: tMotion = 0.5,

TABLE 1 | The MNI coordinates and the percentage of Brodmann areas covered by each projected channel.

Channels	MNI coordinates	Brodmann's areas	Percentage of overlap
	x y z		
CH1	29 46 45	BA9	0.99
		BA46	0.01
CH2	41 49 32	BA9	0.08
		BA45	0.2
		BA46	0.72
CH3	11 48 52	BA8	0.16
		BA9	0.84
CH4	−12 48 50	BA8	0.05
		BA9	0.95
CH5	−4 57 41	BA9	0.89
		BA10	0.11
CH6	−33 44 40	BA9	0.64
		BA46	0.36
CH7	−42 48 28	BA45	0.42
		BA46	0.58
CH8	20 56 41	BA9	0.96
		BA46	0.04
CH9	31 60 27	BA9	0.01
		BA10	0.28
		BA46	0.71
CH10	11 66 31	BA9	0.21
		BA10	0.79
CH11	23 71 14	BA10	1
CH12	−27 53 37	BA9	0.50
		BA46	0.50
CH13	−16 65 28	BA9	0.16
		BA10	0.79
		BA46	0.05
CH14	−36 56 25	BA10	0.01
		BA46	0.99
CH15	−27 68 10	BA10	0.89
		BA11	0.11
CH16	44 60 6	BA10	0.54
		BA46	0.46
CH17	34 67 −6	BA10	0.26
		BA11	0.61
		BA46	0.03
		BA47	0.10
CH18	−2 69 11	BA10	1
CH19	13 73 −4	BA10	0.50
		BA11	0.50
CH20	−13 73 −5	BA10	0.37
		BA11	0.63
CH21	−43 57 5	BA10	0.37
		BA46	0.63
CH22	−32 66 −6	BA10	0.32
		BA11	0.54
		BA46	0.04
		BA47	0.10

tMask = 1, STDEVthresh = 10, and AMPthresh = 1. PCA filtering was applied for motion artifact removal by using *hmrMotionCorrectPCA.m* with the parameter nSV set to 0.8. Motion corrected OD data were filtered with a third-order Butterworth bandpass filter with high and low cut-off frequencies of 0.01 and 0.2 Hz, respectively. Lastly, oxygenated hemoglobin (HBO) and deoxygenated hemoglobin (HBR) concentrations were calculated from filtered optical density data by using *hmrOD2Conc.m* function. Only HBO data were used in the analysis as it was shown that HBO is a more reliable indicator of cortical activation (Watanabe et al., 2002; Dravida et al., 2017).

Data Analysis

Behavioral Data Analysis

Accuracy was calculated by dividing the number of successfully answered trials by the total number of trials for each subject. In the reaction time dataset, for the trials during which the subject could not give a valid answer within the 3 s response period, reaction time was set at 3 s, the maximum. Due to the unbalanced number of trials among conditions, we calculated the average reaction time and accuracy per condition for each subject. Therefore 14 × 3 matrices (number of subjects × conditions) were created for reaction time and accuracy separately and were subjected to one-way repeated measures ANOVA.

fNIRS Data Analysis

For each trial, 14 s long block segments were created which spanned a 2 s pre-stimulus baseline interval and a 12 s long duration after the onset of stimulus presentation. Each segment was detrended and classified as a Perfect Match, Match or Non-Match condition trial. We defined a new parameter, called Hemodynamic Activity Strength (HAS), for hemodynamic time series as in the following: First, the time point corresponding to the maximum concentration value between 4.5 and 12 s period after the onset of a trial is determined. Then, a mean peak value (MPV) is calculated within a window, which spans 1.5 s before and after that peak. The mean value of the 2 s pre-stimulus baseline window is calculated (MB) and subtracted from the MPV. Lastly, this value is divided by the standard deviation of the pre-stimulus baseline window.

Hemispheric lateralization analysis

At the single subject level, whether a channel was deemed significant was tested for each condition as follows: (1) Single-trial HAS parameter of each trial ($n = 6$ for PM and M conditions; $n = 12$ for NM condition) was computed separately for each condition and channel with the abovementioned method. (2) One sample student t-tests were performed on the vector of HAS parameters belonging to each condition and channel separately. (3) Channels having statistical significance ($p < 0.05$) were considered as active channels.

Hemispheric Lateralization (HL) parameter was calculated for each subject and condition with the following formula:

$$\mathrm{HL}_{sub,con} = \frac{N_{RC} - N_{LC}}{N_C}$$

where N_{RC} denotes the number of active channels in the right hemisphere; N_{LC} denotes the number of active channels in the left hemisphere; N_C is the total number of channels in a hemisphere (i.e., N_C equals to 10); and $HL_{sub,con}$ denotes the hemispheric difference parameter for a subject and condition. With this formula, the hemispheric lateralization parameter is normalized between -1 and 1, where positive values denote right hemispheric lateralization and the negative values denote left hemispheric lateralization.

To assess whether there is a statistically significant hemispheric lateralization in a condition, 14 × 1 vectors of hemispheric lateralization parameters belonging to each condition were subjected to a one-sample student *t*-test. Furthermore, to assess whether there is a difference between conditions in terms of lateralization, hemispheric lateralization vectors were subjected to one-way ANOVA with the condition as the main effect.

Hemodynamic activity analysis

To localize the hemodynamic activity, group level HAS parameter was computed as follows: (1) For each channel and subject, the trial time series of each condition were block averaged, resulting in a single time-series data for each condition and channel in a subject (see section fNIRS Data Analysis). (2) A HAS parameter was calculated on this block-averaged time series with the abovementioned method. (3) Lastly, 14 × 3 matrices (subject × condition) were generated with group level HAS parameters for each channel.

To localize the statistically significant hemodynamic activity at the group level, one sample student *t*-test was performed on group level HAS parameter separately for each channel and condition. To assess contrasts among different conditions, a channel based one-way repeated measure ANOVA was performed with the condition as the main effect. *Post hoc* *t*-tests with Bonferroni correction were performed for pairwise comparisons for the following contrasts: Match > Perfect Match, Non-Match > Perfect Match and Non-Match > Match. Thresholded t-statistics depicting significant activation were mapped onto a standard head template for each condition and contrast. Including channels as a main factor in ANOVA analyses should be avoided in fNIRS studies because of the systematic bias caused by variations in optical properties of different brain regions, as suggested in the works of Yanagisawa et al. (2010) and Kujach et al. (2018). Thus channel was not included as a main factor in ANOVA. All statistical analyses were conducted with IBM SPSS Statistics 2015 and MATLAB R2017B.

RESULTS

Behavioral Data

Reaction time and accuracy data are summarized in **Table 2**.

Reaction Time

We found a significant difference among conditions in terms of reaction time [$F(2, 39) = 4.931$, $p = 0.015$]. Bonferroni corrected *post hoc* analysis of paired *t*-test results showed that reaction times for the Match trials were significantly longer than those for the Perfect Match trials ($p = 0.02$), while no significant difference was found between the Non-Match and the Match ($p = 0.272$) or between the Non-Match and the Perfect Match ($p = 0.99$) conditions, even though Non-Match required slightly longer reaction times than Perfect Match condition.

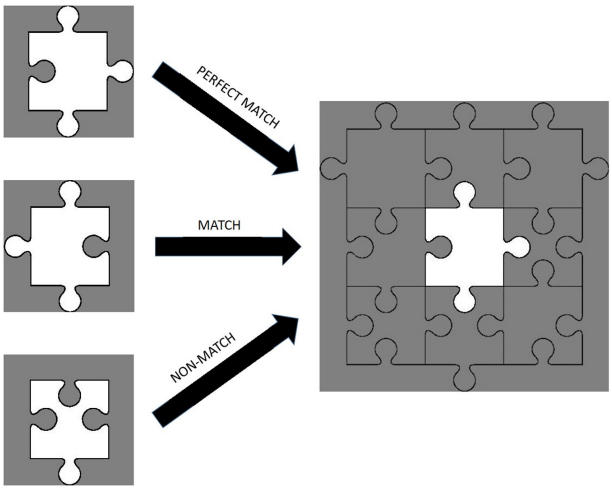

FIGURE 2 | Examples of perfect match, match, and non-match trials.

Accuracy

One way repeated measure ANOVA results did not show any significant difference among conditions for accuracy data [$F(2, 39) = 0.236$, $p = 0.791$].

Reaction Time vs. Accuracy

We calculated Pearson's correlation between accuracy and reaction time for each condition. A negative correlation between the two behavioral metrics was found for each condition but only Match ($p = 0.012$, $R = -0.648$) and Non-Match ($p = 0.026$, $R = -0.591$) conditions surpassed a statistically significant threshold while Perfect Match condition did not ($p = 0.165$, $R = -0.393$).

fNIRS Data

Hemispheric Lateralization Analysis

Hemispheric lateralization data are listed in **Table 3**. One sample student *t*-test results showed that Perfect Match condition had a statistically significant right hemispheric lateralization (HL = 0.071 ± 0.029, $p = 0.027$), while Match (HL = 0.029 ± 0.049, $p = 0.566$) and Non-Match (HL = 0.036 ± 0.064, $p = 0.588$) conditions did not present statistical significance even though they show a right hemispheric lateralization. Besides, 57% of the total number of active channels from all subjects were located on the right hemisphere in Perfect Match condition, while only 39% of active channels were located on the left hemisphere. One way repeated measure ANOVA revealed that there was no significant difference among conditions in terms of hemispheric lateralization [$F(2, 39) = 0.22$, $p = 0.806$].

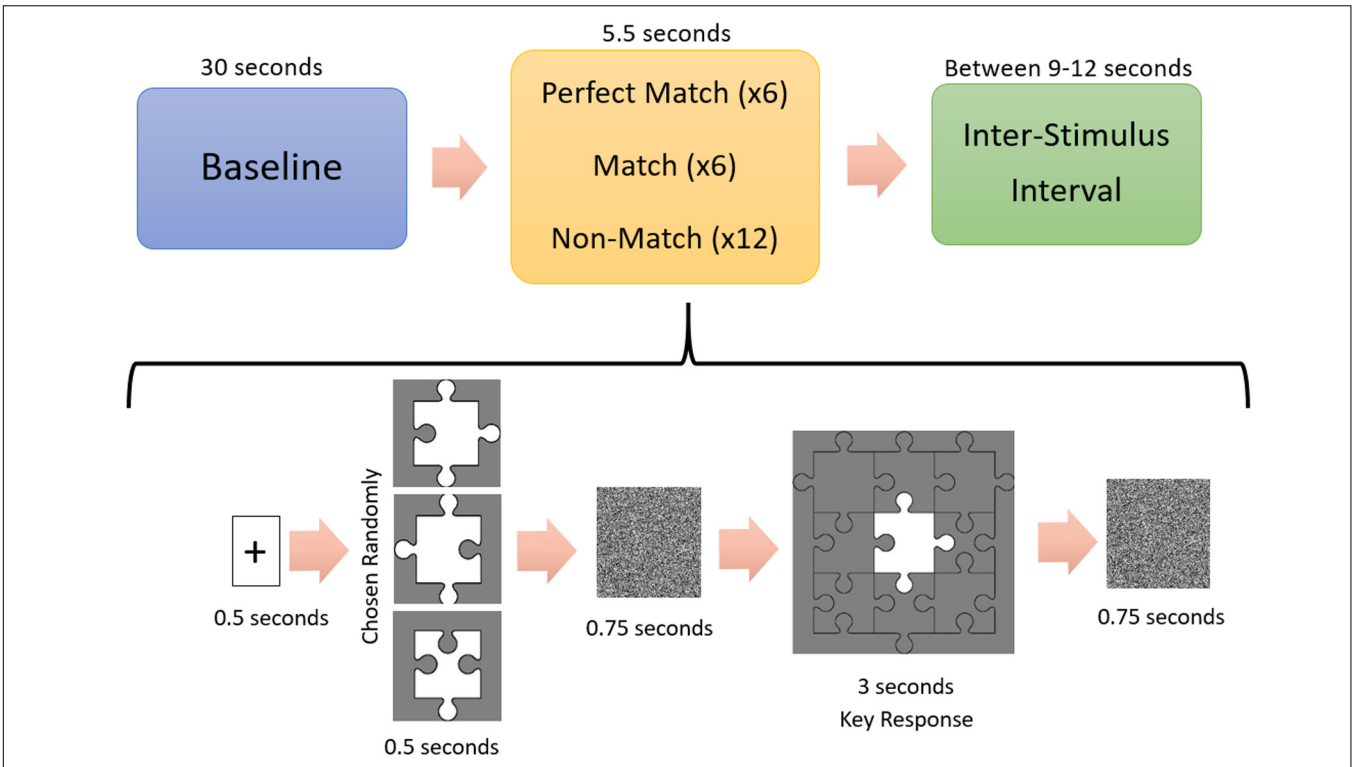

FIGURE 3 | Experimental procedure. A 30 s long-baseline recording was followed by a 0.5 s long fixation point shown in the center of the computer screen. After turning off the fixation point, subjects saw a randomly chosen jigsaw puzzle piece, followed by 0.75 s long white noise masking image. Subsequently, the puzzle template was shown on the screen for 3 s during which the subjects had to give a "Yes" ("Matched") or "No" ("Unmatched") answer. Another 0.75 s long white noise masking image was followed by an inter-stimulus interval randomly chosen from the range of 9–12 s.

TABLE 2 | Summary of the behavioral data in mean ± standard error.

	Perfect match	Match	Non-match	Overall
Accuracy	0.952 ± 0.102	0.941 ± 0.106	0.964 ± 0.063	0.952 ± 0.09
Reaction time (s)	1.146 ± 0.327	1.394 ± 0.486	1.21 ± 0.287	1.25 ± 0.382

TABLE 3 | Hemispheric Lateralization (HL) parameter of each subject.

	S1	S2	S3	S4	S5	S6	S7	S8	S9	S10	S11	S12	S13	S14	Mean ± Std
PM	0.2	−0.1	0	0	0	0	0	0.1	0	0.1	0.1	0.3	0.1	0.2	0.071 ± 0.029
M	0	0	0	0.3	0	0.3	−0.2	0	0	0	0.4	−0.1	−0.2	−0.1	0.029 ± 0.049
NM	−0.1	−0.2	0.4	−0.3	0.3	0.1	0.1	0.2	0.3	−0.1	−0.1	0.2	0.1	−0.4	0.036 ± 0.064

Positive values indicate right lateralization and negative values indicate left lateralization.

Hemodynamic Activity Analysis

The *p*-values obtained from one-sample *t*-tests for each channel showed that significant hemodynamic changes occurred in 8 out of 22 channels for Perfect Match condition; 18 channels for Match condition; and 19 channels for Non-Match condition ($p < 0.05$). **Figure 4** depicts the thresholded t-statistics parameter for each condition on a head model. In Perfect Match condition, neural activity was localized mainly in the right hemisphere (2 left, 5 right, 1 medial) while a bilateral neural activity was observed during Match (9 left, 8 right and 1 medial) and Non-Match (9 left, 8 right and 2 medial) conditions (**Table 4**).

One-way repeated measure ANOVA revealed significant hemodynamic activity differences among conditions in two channels: Channel 9 [$F(2, 26) = 6.500$, $p = 0.024$] and Channel 14 [$F(2, 24) = 4.059$, $p = 0.039$]. These channels correspond to the right Brodmann Area (BA) 9, 10, 46, and left BA 10, 46, respectively. However, the majority of the signal collected by these channels come from right and left DLPFC, respectively (**Table 1**). *Post hoc t*-tests with Bonferroni correction showed that HAS of Match condition was stronger than Perfect Match condition only in the left DLPFC ($p = 0.014$); HAS of Non-Match condition was stronger than Match condition only in the

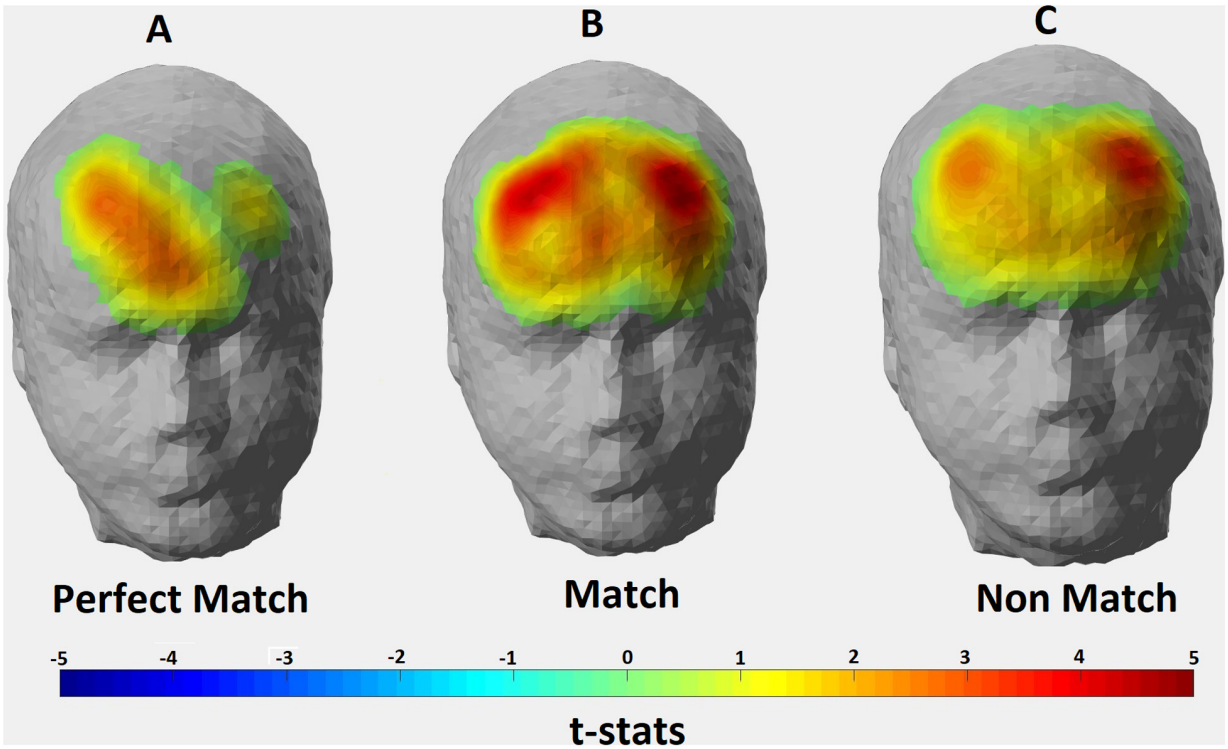

FIGURE 4 | Hemodynamic activity strength parameter map for **(A)** Perfect Match; **(B)** Match; and **(C)** Non Match conditions. Channels depicting statistically significant activation ($p < 0.05$) were mapped onto a standard head model with their thresholded t-statistics score for each condition.

TABLE 4 | Significantly active channels and corresponding brain regions for each condition at the group level.

		PM	M	NM
Left	# of active channels	2	9	9
	Channel #	14, 20	4, 6, 7, 12, 13, 14, 15, 21, 22	6, 7, 12, 13, 14, 15, 20, 21, 22
Medial	# of active channels	1	1	2
	Channel #	18	18	5, 18
Right	# of active channels	5	8	8
	Channel #	1, 9, 10, 11, 19	2, 3, 8, 9, 10, 16, 17, 19	1, 2, 9, 10, 11, 16, 17, 19

right DLPFC ($p = 0.005$); and HAS of Non-Match condition was stronger than Perfect Match condition in only right DLPFC ($p = 0.004$) (**Figure 5**).

DISCUSSION

The aim of this study was to investigate the neural activity lateralization in the prefrontal cortex in response to mental rotation tasks with varying complexity and to demonstrate the reliability of fNIRS for capturing the neurophysiological mechanisms underlying mental rotation. For this purpose, a novel mental rotation task based on mentally fitting a jigsaw puzzle piece into a template was designed. Our results demonstrated a right hemispheric activation in all mental rotation tasks while recruitment of the left hemisphere with increasing task complexity.

Behavioral Data

Assuming task difficulty is accompanied by longer reaction times as demonstrated by Shepard and Metzler (1971), the reaction time data revealed task difficulty as Match > Non-Match > Perfect Match. Perfect Match condition requires no mental rotation of the puzzle piece, thus it shows similarity to simple delayed match-to-sample task (DMTS). However, for the Match and Non-Match conditions, subjects needed to recruit further cognitive processes such as mental rotation, inner speech, and verbalization to make a judgment. Therefore, it can be assumed that in perfect match trials subjects only maintain the relevant information, but in the other two conditions, they had to manipulate it as well. The maintaining and manipulating processes will be discussed later in this report.

High accuracy rates (>%94 ± 1.5) observed in all three conditions indicated that all subjects actively participated in the tasks (**Table 2**). Even though no statistically significant

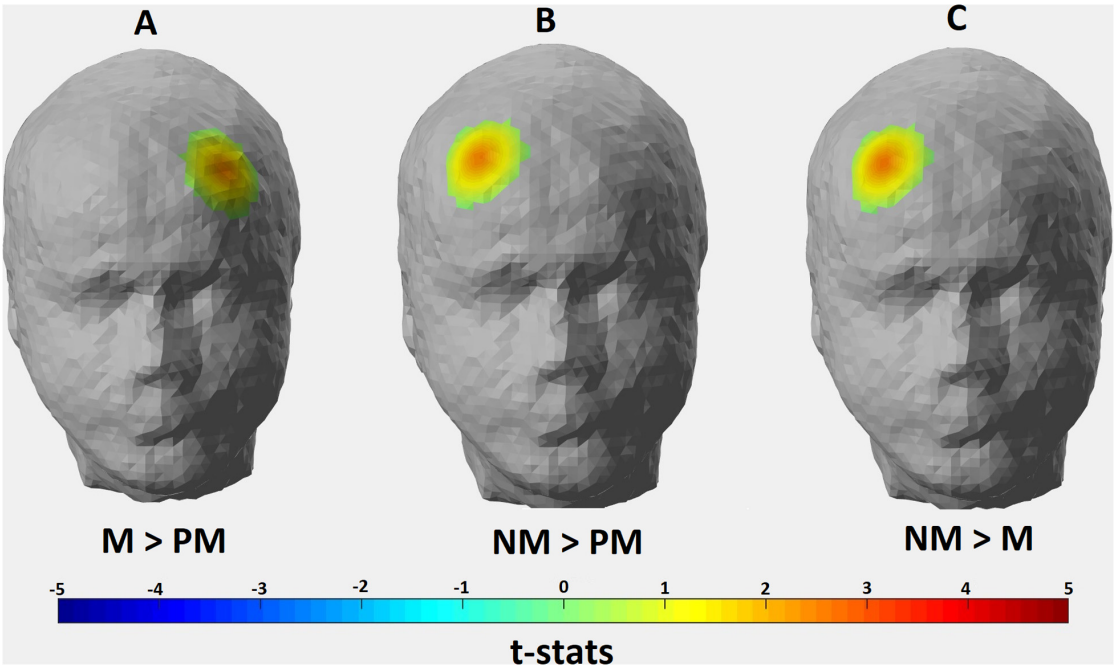

FIGURE 5 | Hemodynamic activity strength parameter map depicting the contrasts for **(A)** Match > Perfect Match; **(B)** Non Match > Perfect Match; and **(C)** Non Match > Match conditions. Channels depicting statistically significant contrast ($p > 0.05$) were mapped onto a standard head model with their thresholded t-statistics score for each condition pair.

difference was found in terms of the accuracy values among the three conditions, the Match condition had the lowest accuracy rate (%94.1 ± 2.8) suggesting that it was the most cognitively demanding task. On the other hand, negative correlations between reaction time and accuracy for all three conditions indicated that increased reaction time was associated with increased task difficulty (Shepard and Metzler, 1971; Cooper and Shepard, 1975).

fNIRS Data

When the hemodynamic activity localization was analyzed at the group level for three conditions in terms of hemispheric lateralization parameter, a right hemisphere dominant activation was found for the Perfect Match condition whereas bilateral activations were found for Non-Match and Match conditions (**Figure 4**). Right DLPFC was found to be activated in all three conditions which was in accordance with many studies reporting right hemispheric activity during mental rotation tasks (Ditunno and Mann, 1990; Corballis, 1997; Harris et al., 2000; Hugdahl et al., 2006). Subjects had to keep the shape of the puzzle piece in their mind until the template is shown and manipulate it where necessary in order to arrive at a judgment. Therefore, visual working memory is essential for all three conditions. It is shown that right DLPFC is involved in visual working memory processes (Leung et al., 2002; Slotnick and Moo, 2006; Daniel et al., 2016) which was supported by our findings. As mentioned above, perfect match trials have a similarity with the simplest form of DMTS tasks. Daniel et al. (2016) described this type of DMTSs as having three phases: cue, delay, and response. In this type of DMTSs, subjects need only to maintain the relevant information in their visual working memory without further manipulation. Thus, activating only the right DLPFC might provide adequate neural sources for solving the perfect match trials. On the other hand, in match and non-match conditions, subjects had to manipulate the information stored in visual working memory in order to arrive at the correct answer. D'Esposito et al. (1999) demonstrated that mental tasks requiring the manipulation of the information stored in working memory are more difficult than tasks requiring only maintaining the relevant information. It is likely that the recruitment of left-hemispheric resources during Match and Non-Match conditions was because of the additional mental strategies (manipulations) employed as the task becomes more difficult. Feedback from subjects revealed that they tended to employ complex strategies during Match and Non-Match conditions such as focusing on local attributes (i.e., number and position of the protrusions) of the shapes rather than global attributes, and/or verbalization and inner speech. Multiple studies have also shown left hemispheric dominance in the processing of local features of complex shapes while right hemispheric dominance in processing global features regardless of the stimuli type (Christie et al., 2012; Brederoo et al., 2017). Language related brain activities are mostly localized in the left hemisphere (Frost et al., 1999) and inner speech is known to be regulated by the left hemisphere (Scholkmann et al., 2013). Another study by Hugdahl et al. (2006) suggested that verbalization might be one of the strategies used by subjects during mental rotation tasks and may explain the left-hemispheric activity. Significantly active channels found

in the left hemisphere for Match and Non-Match conditions cover the BA 8, 9, 45, and 46 which are known to be involved in language processing. Hence, mental strategies deployed by subjects during Match and Non-Match tasks might explain the bilateral activation found in the prefrontal regions (**Figure 4**).

The location of the significant activation found for Match > Perfect Match contrast corresponds to the left DLPFC (**Figure 5**). As mentioned above, subjects used additional mental strategies (i.e., verbalization/inner speech) in Match condition compared to the Perfect Match condition due to the increased complexity of the task. It was shown that left DLPFC is involved in the processing of various linguistic tasks (Hugdahl et al., 1999; Abrahams et al., 2003). Hugdahl et al. (2006) also claimed that verbalization strategy might be the reason for left-hemispheric activity during the processing of mental rotation tasks. Therefore, we assume that stronger left DLPFC activity in Match condition compared to Perfect Match condition in our experimental design might be due to the use of inner speech and verbalization of local attributes of the stimuli in order to complete the Match trials. For the contrasts depicting Non-Match > Match and Non-Match > Perfect Match, the location of significant activation covered DLPFC of the right hemisphere (**Figure 5**). A stronger activation localized in the left hemisphere would be expected for Non-Match > Perfect Match and Match > Non-Match contrasts due to the increasing task complexity as revealed by behavioral metrics. However, a dominant right hemispheric activity observed in Non-Match compared to the other two conditions leads us to interpret the results from another perspective. In the Non-Match condition, subjects were exposed to incongruent stimuli and they were expected to correctly reject the unmatching piece-template pair. It is possible that this correct rejection mechanism may require strong conflict monitoring. Chevrier et al. (2007) used event-related fMRI to investigate the neural response for successful and unsuccessful inhibition of incongruent trials during the Stroop test and found that the right DLPFC is one of the active regions. A meta-analysis of Go/No-Go tasks carried out by Simmonds et al. (2008) also demonstrated that the right DLPFC is one of the brain regions found to be in association with successful inhibitions of No-Go trials. In our task, subjects had to recognize that the piece could not fit into the template in the Non-Match condition in contrast to the Perfect Match and Match conditions, thus replying with a "No" response in order to successfully reject the trial.

Top-Down vs. Bottom-Up Modulation

In a meta-analysis review, Tomasino and Gremese (2016) explored the impact of the employed strategy (i.e., top-down modulation) and stimulus type (i.e., bottom-up modulation) on brain activation during mental rotation tasks. They included studies where the specific motor or visual imagery strategy instructions were given at the onset of the experiment. Their findings indicated that the mental rotation network included activations in the inferior frontal and middle frontal gyrus bilaterally, regardless of the stimulus type and type of strategy followed.

Our results indicated that the right DLPFC activation was common for all trial types. Right DLPFC activation is associated with visual working memory processes and may not necessarily be influenced by the type of strategy. As previous literature suggests (Corballis, 1997; Hugdahl et al., 2006), subjects may also employ secondary cognitive processes during mental rotation tasks such as local feature processing and inner speech, which are known to be regulated by left DLPFC resources. We propose that the bilateral activations observed during Match and Non-Match conditions in our experimental design are likely to be related to the use of secondary cognitive processes. It should be noted that Tomasino and Gremese (2016) excluded the studies in which the subjects were not instructed with a specific mental rotation strategy. In our study, we did not give any specific instructions to our subjects on whether to follow motor or visual imagery strategies at the onset of the experiment. Nonetheless, regarding the top-down regulation consensus reported in Tomasino and Gremese (2016), we may speculate that the bilateral DLPFC activation observed during the match and non-match conditions might be due to the usage of motor imagery-based strategy in addition to the abovementioned secondary cognitive processes.

Regarding the frontal cortex regions for mental rotation of non-bodily objects, Tomasino and Gremese (2016) reported activation in inferior frontal gyrus bilaterally and middle frontal gyrus. Our design included only non-bodily stimuli. Bilaterally activated frontal regions observed during Match and Non-Match conditions are in accordance with the findings of Tomasino and Gremese (2016). Our findings indicate that the left hemispheric activation increases with task difficulty for non-bodily stimuli.

Recommendation for Future Work

In our protocol, the Match condition was the most cognitively demanding condition as supported by both behavioral and hemodynamic metrics (**Table 2** and **Figure 4**). Post-experimental feedback from subjects suggested that their decision-making strategy involved counting the number of protrusions and recesses and/or a mental rotation strategy involving the dynamic spatial transformation of the puzzle piece. Seepanomwan et al. (2015) stated that the task difficulty increases with the number of distinctive features of stimuli. There are two distinctive features in our stimulus design: (i) the number of local features (i.e., protrusions and recessions), and (ii) their orientation. During the non-match conditions, checking either of the distinctive features would be sufficient to arrive at a decision. Subjects may prefer either counting the local features or rotating the puzzle piece. The Match conditions were more challenging than the Non-Match conditions because the subjects had to check both distinctive features, as checking only the number of local features would not be sufficient to make a correct decision (e.g., both the piece and the template may have two protrusions and recesses, yet the protrusions and recesses might be on the consecutive edges for the piece, while they might be located on the opposite edges for the template. Therefore, they had to check the second distinctive feature as well.). However, we should note that more challenging protocols involving match and non-match conditions can also be designed where it will be necessary to consider a mental rotation in all non-match trials (Seepanomwan et al., 2015). In

future designs, different strategies might be employed to make the non-match condition more cognitively demanding, such as using unusual rotation angles (e.g., 15, 145, 20, 220 degrees) instead of multiples of 90 degrees, designing the puzzle piece and template with asymmetrical distinctive features.

Removal of instrumental, systemic, and motion artifacts in fNIRS signals generally consist of a combination of three steps: (1) motion correction; (2) bandpass filtering; and (3) low-frequency systemic noise removal. While numerous detailed signal processing methods have been developed for each step, there is still no consensus in literature for a standardized preprocessing pipeline (Pinti et al., 2019). Several methods have been proposed in the literature to eliminate the common systemic noise in fNIRS signals. Regarding data-driven approaches, global signal regression (Carbonell et al., 2011; Hocke et al., 2018), time-delayed global signal subtraction (Erdogan et al., 2016), ICA (Kohno et al., 2007; Santosa et al., 2013), and PCA based methods (Zhang et al., 2005) have been the most widely used methods. However, modeling systemic effects with regressors derived from short separation channel measurements that monitor only scalp hemodynamics are considered as the gold standard for global noise removal (Saager et al., 2011). Data-driven methods have limitations and the potential to distort the signals of interest which are extensively reviewed in Hocke et al. (2018) and Pinti et al. (2019). Our system did not have short separation channels for monitoring scalp hemodynamics. Hence; we decided to use minimal preprocessing practices to avoid possible signal distortion. For future work, we plan to compare the impact of the data-driven noise removal strategies with short channel removal methods for a better understanding of the noise characteristics of the signals collected from the prefrontal cortex region during cognitive tasks. We also plan to monitor frontal and parietal areas with a system equipped with a higher number of channels to investigate functional connectivity measures among different brain regions.

CONCLUSION

Our findings indicate that the right DLPFC is one of the core brain regions activated during mental rotation regardless of the task difficulty. Our results also showed that left hemisphere activity becomes profound with increased task difficulty and the fact that the left hemispheric involvement does not depend on the dimension (2D or 3D) of the stimuli but on task difficulty. The present study showed that fNIRS is a reliable neuroimaging method to be utilized in mental rotation studies, or in general lateralization studies. It is of vital importance to show that fNIRS technology can be used in assessing various cognitive skills for two reasons. First, it allows for investigating the brain dynamics during cognitive tests in daily, natural environments rather than the noisy, stress-inducing artificial MR or PET settings. Secondly, due to its great ease of use when compared with EEG, fNIRS is a good candidate for new generation BCI systems.

DATA AVAILABILITY STATEMENT

The datasets generated for this study are available on request to the corresponding author.

ETHICS STATEMENT

The studies involving human participants were reviewed and approved by the Human Research Ethical Committee of Boğaziçi University. The patients/participants provided their written informed consent to participate in this study.

AUTHOR CONTRIBUTIONS

MCM, SE, RC, and HS designed the experiments. MCM and OÖ carried out the experiments. MCM and SE analyzed the data, wrote the manuscript, and prepared the figures. All authors reviewed the manuscript.

FUNDING

This research was financially supported by the Boğaziçi University Research Fund Grant Number 14663.

ACKNOWLEDGMENTS

We thank Asst. Prof. İnci Ayhan for her help in experimental design and during the interpretation of the findings.

REFERENCES

Aasted, C. M., Yücel, M. A., Cooper, R. J., Petkov, M. P., Boas, D. A., Cooper, R. J., et al. (2015). Anatomical guidance for functional near-infrared spectroscopy: atlasviewer tutorial. *Neurophoton* 2:020801. doi: 10.1117/1.NPh.2.2.020801

Abrahams, S., Goldstein, L., Simmons, A., Brammer, M., Williams, S., Giampietro, V., et al. (2003). Functional magnetic resonance imaging of verbal fluency and confrontation naming using compressed image acquisition to permit overt responses. *Hum. Brain Mapp.* 20, 29–40. doi: 10.1002/hbm.10126

Alivisatos, B., and Petrides, M. (1997). Functional activation of the human brain during mental rotation. *Neuropsychologia* 35, 111–118. doi: 10.1016/s0028-3932(96)00083-8

Artemenko, C., Coldea, A., Soltanlou, M., Dresler, T., Nuerk, H., and Ehlis, A. (2018). The neural circuits of number and letter copying: an fNIRS study. *Exp. Brain Res.* 236, 1129–1138. doi: 10.1007/s00221-018-5204-8

Baker, J., Bruno, J., Gundran, A., Hosseini, S., and Reiss, A. (2018). fNIRS measurement of cortical activation and functional connectivity during a visuospatial working memory task. *PLoS One* 13:e0201486. doi: 10.1371/journal.pone.0201486

Banville, H., Gupta, R., and Falk, T. (2017). Mental task evaluation for hybrid NIRS-EEG brain-computer interfaces. *Comput. Intell. Neurosci.* 2017, 1–24. doi: 10.1155/2017/3524208

Brederoo, S., Nieuwenstein, M., Lorist, M., and Cornelissen, F. (2017). Hemispheric specialization for global and local processing: a direct comparison of linguistic

and non-linguistic stimuli. *Brain Cogn.* 119, 10–16. doi: 10.1016/j.bandc.2017.09.005

Carbonell, F., Bellec, P., and Shmuel, A. (2011). Global and system-specific resting-state fmri fluctuations are uncorrelated: principal component analysis reveals anti-correlated networks. *Brain Connect.* 1, 496–510. doi: 10.1089/brain.2011.0065

Chevrier, A., Noseworthy, M., and Schachar, R. (2007). Dissociation of response inhibition and performance monitoring in the stop signal task using event-related fMRI. *Hum. Brain Mapp.* 28, 1347–1358. doi: 10.1002/hbm.20355

Christie, J., Ginsberg, J., Steedman, J., Fridriksson, J., Bonilha, L., and Rorden, C. (2012). Global versus local processing: seeing the left side of the forest and the right side of the trees. *Front. Hum. Neurosci.* 6:28. doi: 10.3389/fnhum.2012.00028

Cohen, M., Kosslyn, S., Breiter, H., DiGirolamo, G., Thompson, W., Anderson, A., et al. (1996). Changes in cortical activity during mental rotation A mapping study using functional MRI. *Brain* 119, 89–100. doi: 10.1093/brain/119.1.89

Cooper, L., and Shepard, R. (1975). Mental transformation in the identification of left and right hands. *J. Exp. Psychol. Hum. Percept. Perform.* 1, 48–56. doi: 10.1037/0096-1523.1.1.48

Corballis, M. (1997). Mental rotation and the right hemisphere. *Brain Lang.* 57, 100–121. doi: 10.1006/brln.1997.1835

Curtin, A., Sun, J., Zhao, Q., Onaral, B., Wang, J., Tong, S., et al. (2019). Visuospatial task-related prefrontal activity is correlated with negative symptoms in schizophrenia. *Sci. Rep.* 4:9575. doi: 10.1038/s41598-019-45893-7

Daniel, T. A., Katz, J. S., and Robinson, J. L. (2016). Delayed match-to-sample in working memory: a brainmap meta-analysis. *Biol Psychol.* 120, 10–20. doi: 10.1016/j.biopsycho.2016.07.015

D'Esposito, M., Postle, B. R., Ballard, D., and Lease, J. (1999). Maintenance versus manipulation of information held in working memory: an event-related fMRI study. *Brain Cogn.* 41, 66–86. doi: 10.1006/brcg.1999.1096

Deutsch, G., Bourbon, W., Papanicolaou, A., and Eisenberg, H. (1988). Visuospatial tasks compared via activation of regional cerebral blood flow. *Neuropsychologia* 26, 445–452. doi: 10.1016/0028-3932(88)90097-8

Ditunno, P., and Mann, V. (1990). Right hemisphere specialization for mental rotation in normals and brain damaged subjects. *Cortex* 26, 177–188. doi: 10.1016/s0010-9452(13)80349-8

Dravida, S., Noah, J., Zhang, X., and Hirsch, J. (2017). Comparison of oxyhemoglobin and deoxyhemoglobin signal reliability with and without global mean removal for digit manipulation motor tasks. *Neurophotonics* 5:011006. doi: 10.1117/1.nph.5.1.011006

Erdogan, S. B., Tong, Y., Hocke, L. M., Lindsey, K. P., and deB Frederick, B. (2016). Correcting for blood arrival time in global mean regression enhances functional connectivity analysis of resting state fmri-bold signals. *Front. Hum. Neurosci.* 10:311. doi: 10.3389/fnhum.2016.00311

Frost, J. A., Binder, J. R., Springer, J. A., Hammeke, T. A., Bellgowan, P. S., Rao, S. M., et al. (1999). Language processing is strongly left lateralized in both sexes: evidence from functional MRI. *Brain* 122, 199–208. doi: 10.1093/brain/122.2.199

Fu, G., Wan, N., Baker, J., Montgomery, J., Evans, J., and Gillam, R. (2016). A proof of concept study of function-based statistical analysis of fNIRS Data: syntax comprehension in children with specific language impairment compared to typically-developing controls. *Front. Behav. Neurosci.* 10:108. doi: 10.3389/fnbeh.2016.00108

Halari, R., Sharma, T., Hines, M., Andrew, C., Simmons, A., and Kumari, V. (2006). Comparable fMRI activity with differential behavioural performance on mental rotation and overt verbal fluency tasks in healthy men and women. *Exp. Brain Res.* 169, 1–14. doi: 10.1007/s00221-005-0118-7

Harris, I. M., Egan, G. F., Sonkkila, C., Tochon-Danguy, H. J., and Watson, J. D. G. (2000). Selective right parietal lobe activation during mental rotation. *Brain* 123, 65–73. doi: 10.1093/brain/123.1.65

Herff, C., Heger, D., Putze, F., Hennrich, J., Fortmann, O., and Schultz, T. (2013). "Classification of mental tasks in the prefrontal cortex using fNIRS," in *2013 35Th Annual International Conference of the IEEE Engineering in Medicine and Biology Society (EMBC)*, Osaka.

Hocke, L. M., Oni, I. K., Duszynski, C. C., Corrigan, A. V., deB Frederick, B., and Dunn, J. (2018). Automated processing of fNIRS Data—A visual guide to the pitfalls and consequences. *Algorithms* 11:67. doi: 10.3390/a11050067

Hugdahl, K., Brønnick, K., Kyllingsbrk, S., Law, I., Gade, A., and Paulson, O. (1999). Brain activation during dichotic presentations of consonant-vowel and musical instrument stimuli: a 15 O-PET study. *Neuropsychologia* 37, 431–440. doi: 10.1016/s0028-3932(98)00101-8

Hugdahl, K., Thomsen, T., and Ersland, L. (2006). Sex differences in visuo-spatial processing: an fMRI study of mental rotation. *Neuropsychologia* 44, 1575–1583. doi: 10.1016/j.neuropsychologia.2006.01.026

Huppert, T., Diamond, S., Franceschini, M., and Boas, D. (2009). HomER: a review of time-series analysis methods for near-infrared spectroscopy of the brain. *Appl. Opt.* 48:D280. doi: 10.1364/ao.48.00d280

Jang, K. E., Tak, S., Jung, J., Jang, J., Jeong, Y., and Ye, J. C. (2009). Wavelet-MDL detrending for near-infrared spectroscopy. *J. Biomed. Opt.* 14, 1–13. doi: 10.1117/1.3127204

Jasinska, K., and Petitto, L. (2013). How age of bilingual exposure can change the neural systems for language in the developing brain: a functional near infrared spectroscopy investigation of syntactic processing in monolingual and bilingual children. *Dev. Cogn. Neurosci.* 6, 87–101. doi: 10.1016/j.dcn.2013.06.005

Jordan, K., Heinze, H., Lutz, K., Kanowski, M., and Jäncke, L. (2001). Cortical activations during the mental rotation of different visual objects. *Neuroimage* 13, 143–152. doi: 10.1006/nimg.2000.0677

Kohno, S., Miyai, I., Seiyama, A., Oda, I., Ishikawa, A., Tsuneishi, S., et al. (2007). Removal of the skin blood flow artifact in functional near-infrared spectroscopic imaging data through independent component analysis. *J. Biomed. Opt.* 12:062111. doi: 10.1117/1.2814249

Kujach, S., Byun, K., Hyodo, K., Suwabe, K., Fukuie, T., Laskowski, R., et al. (2018). A transferable high-intensity intermittent exercise improves executive performance in association with dorsolateral prefrontal activation in young adults. *Neuroimage* 169, 117–125. doi: 10.1016/j.neuroimage.2017.12.003

Leung, H., Gore, J., and Goldman-Rakic, P. (2002). Sustained mnemonic response in the human middle frontal gyrus during on-line storage of spatial memoranda. *J. Cogn. Neurosci.* 14, 659–671. doi: 10.1162/08989290260045882

Mehta, Z., and Newcombe, F. (1991). A role for the left hemisphere in spatial processing. *Cortex* 27, 153–167. doi: 10.1016/s0010-9452(13)80121-9

Papanicolaou, A., Deutsch, G., Bourbon, W., Will, K., Loring, D., and Eisenberg, H. (1987). Convergent evoked potential and cerebral blood flow evidence of task-specific hemispheric differences. *Electroencephalogr. Clin. Neurophysiol.* 66, 515–520. doi: 10.1016/0013-4694(87)90098-8

Peirce, J. W., Gray, J. R., Simpson, S., MacAskill, M. R., Höchenberger, R., Sogo, H., et al. (2019). PsychoPy2: experiments in behavior made easy. *Behav. Res. Methods* 51, 195–201. doi: 10.3758/s13428-018-01193-y

Pfeifer, M., Scholkmann, F., and Labruyère, R. (2018). Signal processing in functional near-infrared spectroscopy (fNIRS): methodological differences lead to different statistical results. *Front. Hum. Neurosci.* 11:641. doi: 10.3389/fnhum.2017.00641

Pinti, P., Scholkmann, F., Hamilton, A., Burgess, P., and Tachtsidis, I. (2019). Current status and issues regarding pre-processing of fNIRS neuroimaging data: an investigation of diverse signal filtering methods within a general linear model framework. *Front. Hum. Neurosci.* 12:505. doi: 10.3389/fnhum.2018.00505

Qureshi, N., Naseer, N., Noori, F., Nazeer, H., Khan, R., and Saleem, S. (2017). Enhancing classification performance of functional near-infrared spectroscopy-brain–computer interface using adaptive estimation of general linear model coefficients. *Front. Neurorobot.* 11:33. doi: 10.3389/fnbot.2017.00033

Ratcliff, G. (1979). Spatial thought, mental rotation and the right cerebral hemisphere. *Neuropsychologia* 17, 49–54. doi: 10.1016/0028-3932(79)90021-6

Rorden, C., and Brett, M. (2001). Stereotaxic display of brain lesions. *Behav. Neurol.* 12, 191–200. doi: 10.1155/2000/421719

Saager, R. B., Telleri, N. L., and Berger, A. J. (2011). Two-detector corrected near infrared spectroscopy (C-NIRS) detects hemodynamic activation responses more robustly than single-detector NIRS. *Neuroimage* 55, 1679–1685. doi: 10.1016/j.neuroimage.2011.01.043

Santosa, H., Hong, M. J., Kim, S.-P., and Hong, K.-S. (2013). Noise reduction in functional near-infrared spectroscopy signals by independent component analysis. *Rev. Sci. Instrum.* 84:73106. doi: 10.1063/1.4812785

Scholkmann, F., Wolf, M., and Wolf, U. (2013). "The effect of inner speech on arterial co2 and cerebral hemodynamics and oxygenation: a functional NIRS study," in *Oxygen Transport to Tissue XXXV. Advances in Experimental Medicine*

and Biology, Vol. 789, eds S. Van Huffel, G. Naulaers, A. Caicedo, D. F. Bruley, and D. K. Harrison (New York, NY: Springer).

Seepanomwan, K., Caligore, D., Cangelosi, A., and Baldassarre, G. (2015). Generalization, decision making, and embodiment effects in mental rotation: a neurorobotic architecture tested with humanoid robot. *Neural Networks* 72, 31–47. doi: 10.1016/j.neunet.2015.09.010

Seydell-Greenwald, A., Ferrara, K., Chambers, C. E., Newport, E. L., and Landau, B. (2017). Bilateral activations for complex visual-spatial functions: evidence from a visual-spatial construction task. *Neuropsychologia* 106, 194–206. doi: 10.1016/j.neuropsychologia.2017.10.005

Shepard, R., and Metzler, J. (1971). Mental rotation of three-dimensional objects. *Science* 171, 701–703. doi: 10.1126/science.171.3972.701

Shimoda, N., Takeda, K., Imai, I., Kaneko, J., and Kato, H. (2008). Cerebral laterality differences in handedness: a mental rotation study with NIRS. *Neurosci. Lett.* 430, 43–47. doi: 10.1016/j.neulet.2007.10.016

Simmonds, D., Pekar, J., and Mostofsky, S. (2008). Meta-analysis of Go/No-go tasks demonstrating that fMRI activation associated with response inhibition is task-dependent. *Neuropsychologia* 46, 224–232. doi: 10.1016/j.neuropsychologia.2007.07.015

Singh, A. K., Okamoto, M., Dan, H., Jurcak, V., and Dan, I. (2005). Spatial registration of multichannel multi-subject fNIRS data to MNI space without MRI. *NeuroImage* 27, 842–851. doi: 10.1016/j.neuroimage.2005.05.019

Slotnick, S., and Moo, L. (2006). Prefrontal cortex hemispheric specialization for categorical and coordinate visual spatial memory. *Neuropsychologia* 44, 1560–1568. doi: 10.1016/j.neuropsychologia.2006.01.018

Sugiura, L., Ojima, S., Matsuba-Kurita, H., Dan, I., Tsuzuki, D., Katura, T., et al. (2015). Effects of sex and proficiency in second language processing as revealed by a large-scale fNIRS study of school-aged children. *Hum. Brain Mapp.* 36, 3890–3911. doi: 10.1002/hbm.22885

Tomasino, B, and Gremese, M. (2016). Effects of stimulus type and strategy on mental rotation network: an activation likelihood estimation meta-analysis. *Front. Hum. Neurosci.* 9:693. doi: 10.3389/fnhum.2015.00693

Vingerhoets, G., de Lange, F., Vandemaele, P., Deblaere, K., and Achten, E. (2002). Motor imagery in mental rotation: an fMRI study. *Neuroimage* 17, 1623–1633. doi: 10.1006/nimg.2002.1290

Watanabe, A., Kato, N., and Kato, T. (2002). Effects of creatine on mental fatigue and cerebral hemoglobin oxygenation. *Neurosci. Res.* 42, 279–285. doi: 10.1016/s0168-0102(02)00007-x

Yanagisawa, H., Dan, I., Tsuzuki, D., Kato, M., Okamoto, M., Kyutoku, Y., et al. (2010). Acute moderate exercise elicits increased dorsolateral prefrontal activation and improves cognitive performance with Stroop test. *Neuroimage* 50, 1702–1710. doi: 10.1016/j.neuroimage.2009.12.023

Ye, J. C., Tak, S., Jang, K. E., Jung, J., and Jang, J. (2009). NIRS-SPM: statistical parametric mapping for near-infrared spectroscopy. *NeuroImage* 44, 428–447. doi: 10.1016/j.neuroimage.2008.08.036

Zhang, Y., Brooks, D. H., Franceschini, M. A., and Boas, D. A. (2005). Eigenvector-based spatial filtering for reduction of physiological interference in diffuse optical imaging. *J. Biomed. Opt.* 10:11014. doi: 10.1117/1.1852552

Conflict of Interest: The authors declare that the research was conducted in the absence of any commercial or financial relationships that could be construed as a potential conflict of interest.

Copyright © 2020 Mutlu, Erdoğan, Öztürk, Canbeyli and Saybaşılı. This is an open-access article distributed under the terms of the Creative Commons Attribution License (CC BY). The use, distribution or reproduction in other forums is permitted, provided the original author(s) and the copyright owner(s) are credited and that the original publication in this journal is cited, in accordance with accepted academic practice. No use, distribution or reproduction is permitted which does not comply with these terms.

frontiers in Neuroscience

ORIGINAL RESEARCH
published: 10 July 2020
doi: 10.3389/fnins.2020.00694

Using a Data-Driven Approach to Estimate Second-Language Proficiency From Brain Activation: A Functional Near-Infrared Spectroscopy Study

Miaomei Lei[1], Toshinori Miyoshi[1], Ippeita Dan[2] and Hiroki Sato[3]*

[1] Research & Development Group, Hitachi, Ltd., Tokyo, Japan, [2] Research and Development Initiatives, Applied Cognitive Neuroscience Laboratory, Chuo University, Tokyo, Japan, [3] Department of Bioscience and Engineering, College of Systems Engineering and Science, Shibaura Institute of Technology, Saitama, Japan

While non-invasive brain imaging has made substantial contributions to advance human brain science, estimation of individual state is becoming important to realize its applications in society. Brain activations were used to classify second-language proficiencies. Participants in functional near-infrared spectroscopy (fNIRS) experiment were 20/20 native Japanese speakers with high/low English abilities and 19/19 native English speakers with high/low Japanese abilities. Their cortical activities were measured by functional near-infrared spectroscopy while they were conducting Japanese/English listening comprehension tests. The data-driven method achieved classification accuracy of 77.5% in the case of Japanese speakers and 81.9% in the case of English speakers. The informative features predominantly originated from regions associated with language function. These results bring an insight of fNIRS neuroscience and its applications in society.

Keywords: machine learning, language proficiency, brain activation, feature selection, native Japanese speakers, native English speakers

OPEN ACCESS

Edited by:
Ning Liu,
Stanford University, United States

Reviewed by:
Hendrik Santosa,
University of Pittsburgh, United States
Keum-Shik Hong,
Pusan National University,
South Korea

****Correspondence:***
Miaomei Lei
miaomei.lei.jt@hitachi.com

Specialty section:
This article was submitted to Brain Imaging Methods, a section of the journal Frontiers in Neuroscience

Received: *21 October 2019*
Accepted: *08 June 2020*
Published: *10 July 2020*

Citation:
Lei M, Miyoshi T, Dan I and Sato H (2020) Using a Data-Driven Approach to Estimate Second-Language Proficiency From Brain Activation: A Functional Near-Infrared Spectroscopy Study. Front. Neurosci. 14:694. doi: 10.3389/fnins.2020.00694

INTRODUCTION

Language, which differentiates human beings from other living species, plays an important role in our daily lives. The neural basis of language has been investigated with various techniques for functional neuroimaging (Price, 2012; Quaresima et al., 2012). Functional near-infrared spectroscopy (fNIRS) is an optical neuroimaging technique that measures brain activity by monitoring the hemodynamic changes in cerebral cortex response of brain activation. Its main advantages are relatively low cost, portability, safety, low acoustic noise (compared to functional magnetic resonance imaging), and easiness to operate (Scholkmann et al., 2014; Hong and Yaqub, 2019). In the context of fNIRS community, hemodynamic changes (which represent brain activation) have been used as a useful indicator to demonstrate speech perception in infants (Pena et al., 2003; Bortfeld et al., 2009; Sato et al., 2012) and language comprehension in adults

(Sato et al., 1999; Schecklmann et al., 2008; Lei et al., 2018). Since conventional analysis of fNIRS data has focused on human brain activity at the group level, these studies have traditionally drawn a population-level conclusion about general patterns across a large number of participants. Knowledge from these studies has important implications for advancing our understanding of how the human brain processes language. To further translate this knowledge into practical applications in society, individual estimation or classification of language ability (e.g., speech-comprehension level and second-language proficiency) on the basis of neuroimaging data across participants is a topic of interest.

Research interest in estimating the state of an individual by applying machine learning using fNIRS data has been increasing. fNIRS data with corresponding labels/classes are used to train a machine-learning classifier/model. The trained classifier is applied to the unknown data to estimate the labels. For example, in previous studies, mental arithmetic and music imagery (Power et al., 2010) motor imagery (Naseer and Hong, 2013), and subjective preference (Luu and Chau, 2008) were estimated. These studies showed the feasibility of establishing a predictive machine-learning model based on the state of individuals and their underlying brain activity. However, they focused on categorical discrimination to estimate the state of a participant using data of the participant. It is still a challenge to estimate the state of individuals on the basis of neuroimaging data of others, namely, estimation of state across participants. Clinical studies focusing on classification of diseases or disorders have made progresses in such estimation across participants (Hosseini et al., 2018; Sutoko et al., 2019) however, estimation of, for example, language ability, which may subtly differ across groups, remains unstudied.

The major difficulty concerning estimation across participants based on neuroimaging data is the relatively small data sample with individual differences. Individual differences refer to the variations across participants even though they have the same label in the same population group, for example, patients who have the same disease. It has been recognized that the brain structure and its corresponding function show high individual variability even among a healthy population group (Raz et al., 2005; Qin et al., 2014; Finn et al., 2015). From the viewpoint of machine learning, if input patterns have high individual differences, data in the feature space will be almost impossible to separate according to the label. It is thus difficult to construct a machine-learning classifier and model for the estimation, that is, separating feature vectors based on the information of the label. On the other hand, estimation with a small number of data samples is also a challenge; that is, the data dimensionality is usually much higher than the number of samples available for classifier training (Fan et al., 2007; An et al., 2017). This typical problem is known in machine-learning literature as the "curse of dimensionality" (Bellman, 2015). It may make the model unstable or cause the problem of overfitting (Guyon and Elisseeff, 2003), which is the condition that model fits accurately to the training data (including inherent noise) but fits poorly to unknown test data. In addition, in a practical situation, increasing the number of data samples is not always possible, for example, when the number of patients with a particular disease is limited. To solve this unbalance between number of features and sample size with the aim of increasing classification accuracy, various methods of feature selection (to extract a subset of most-informative features) have been proposed (Saeys et al., 2007; Pereira et al., 2009; Hu et al., 2013; Mwangi et al., 2014; Hong et al., 2018). Common methods of feature selection include using *t*-test (De Martino et al., 2008) ANOVA (analysis of variance) (Akama et al., 2014; Lei et al., 2014) Pearson correlation coefficient (Fan et al., 2007) and prior knowledge (Chu et al., 2012). Recently, sparse-feature selection has become one of the choices for data-driven feature selection (Tibshirani, 1996). Sparse techniques combine both machine learning and feature-reduction steps by enlisting a L1-norm regularization, resulting in a reduced subset of relevant features (Zou and Hastie, 2005).

In our previous study, we reported significant differences between brain-activity patterns in regard to correct responses and incorrect responses of a second language at group level (Lei et al., 2018). A reliable quantitative tool for evaluating second-language proficiency based on brain-activation patterns may help people to learn a second language more efficiently. In the present study, we aimed to estimate second-language proficiency using functional brain activity provided by fNIRS data applying machine learning methods. fNIRS data were collected from native Japanese speakers with high/low second-language (English) proficiency and native English speakers with high/low second-language (Japanese) proficiency. Brain activities were recorded by fNIRS when the subjects (speakers) were doing listening-comprehension tasks in English, Japanese, and an unknown language (Chinese). High second-language proficiency and low second-language proficiency is estimated cross participants. To overcome difficulties with estimation across participants and further improve classification performance, the informative features were extracted by using a method of sparse-feature selection. The generalization capability of the machine-learning methods was confirmed by analyzing two independent-validation population groups of native Japanese speakers and native English speakers. In addition, using the label of second-language proficiency classification of the first language and an incomprehensible unknown language was also conducted.

MATERIALS AND METHODS

Participants

All participants in the present study, categorized as native Japanese speakers and native English speakers, were right-handed. The native Japanese speakers were 65 healthy adults (mean age ± SD: 28.5 ± 2.8; range: 24–33; 35 males and 30 females). Based on their TOEIC® Listening & Reading scores, two groups with different English proficiency were recruited. The high-proficiency group contained 32 participants (mean age ± SD: 27.8 ± 2.6; range: 24–32; 18 males and 14 females) with TOEIC® Listening & Reading scores above 700. The low-proficiency group contained 33 participants (mean age ± SD: 29.2 ± 2.8; range: 24–33; 17 males and 16 females) with TOEIC® Listening & Reading scores under 500.

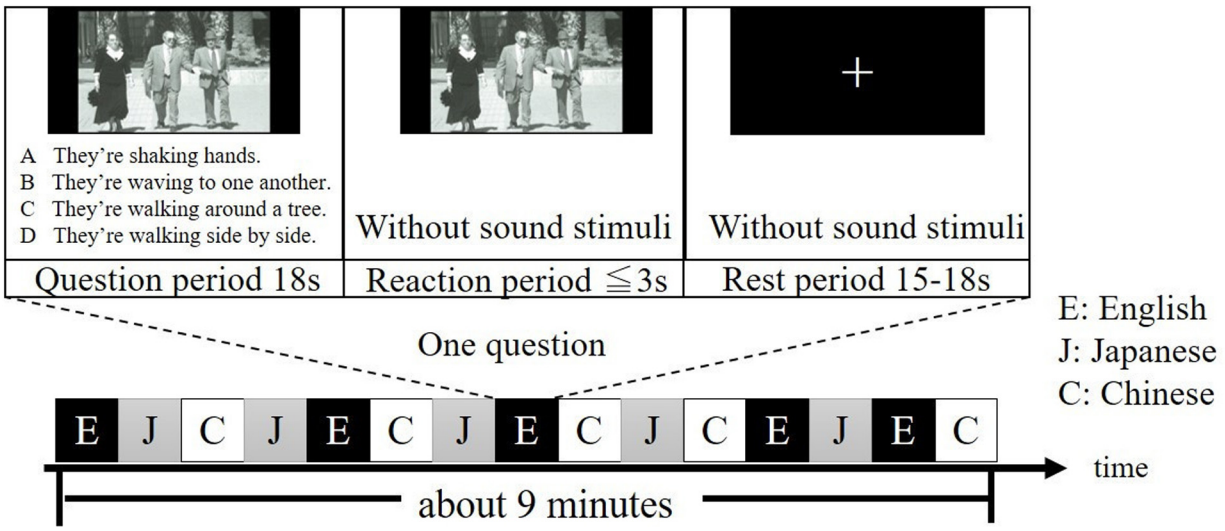

FIGURE 1 | Example of one run of the experiment. Questions in English, Japanese, and Chinese are denoted as E, J, and C, respectively. It takes about 9 min for one run. Questions were selected from the TOEIC® Test New Official Preparation Guide.

The native English speakers were 66 healthy adults (mean age ± SD: 28.7 ± 2.9; range: 24–33; 34 males and 32 females). They included nationals from Australia, Canada, New Zealand, the United Kingdom, and the United States, who were temporarily staying in Japan for periods ranging from 0.2 to 12 years (mean years ± SD: 3.4 ± 2.6). On the basis of their self-assessments of Japanese proficiency, namely, whether they can speak Japanese or not, the participants were categorized into the high-proficiency group or the low-proficiency group. The high-proficiency group was composed of 31 people (mean age ± SD: 29.3 ± 3.1; range: 24–33; 15 males and 16 females), and low-proficiency group was composed of 35 people (mean age ± SD: 28.1 ± 2.7; range: 24–33; 19 males and 16 females). In addition, all participants did not have experience of learning Chinese.

Data were obtained according to the standards of the internal review board of Research & Development Group, Hitachi, Ltd. Data from volunteers were obtained according to the standards of internal review board on Research & Development Group, Hitachi, Ltd., following receipt of written informed consent.

Auditory Stimuli and Task Design

Listening comprehension questions from "TOEIC® Listening Test Part 1: Photographs"[1] were used (ETS, 2005, 2007, 2008, 2012). Each question relates to a photograph with four short explanations. The explanation that most accurately describes the photograph is to be chosen. These listening-comprehension questions were respectively translated into Japanese and Chinese by the native speakers. Sound stimuli were created from the recorded voice of a professional female announcer who is bilingual in Japanese and English, and has learned Chinese as a third language.

All participants were given two runs, each of which contained 15 different questions. During each run, questions in Japanese, English and Chinese were presented five times, respectively, in a pseudo-randomized order (**Figure 1**). Note that questions in the same language were not given continuously. For each question, a period of 18 s was for presenting the question (question period), a period of less than or equal to 3 s was for answering the question (reaction period) and an arbitrary period between 15 to 18 s was for resting (rest period). The experimental session was conducted in a quiet, dimly lit room. Participants were instructed to look at the photograph on the screen and listen to the four explanations in the question period, answer the question in the reaction period and look at a fixation cross on the screen in the rest period. Specifically, after listening the four explanations of the question, participants were asked to press the button as quick as possible during the reaction period. After pressing the button, the photograph will disappear, and a fixation cross will be shown. Finally, the participants were instructed to silently fix their eyes on the cross and no response was required during the rest period, when they were also asked to think nothing as possible as they can. To ensure that each participant clearly understood the experiment procedure during the on-line tasks, the participants did practice tasks similar to experimental tasks in advance.

fNIRS Measurement

An optical-topography system (ETG-4000; Hitachi Medical, Japan) was used to measure change in concentration of cerebral

[1]Written pledge was submitted to copyright owner IIBC (The Institute for International Business Communication) and permission was obtained from the copyright owner. Questions were selected from the TOEIC® Test New Official Preparation Guide vol. 1 (2005), vol. 2 (2007), vol. 3 (2008), and vol. 5 (2012) published by IIBC, and copyrighted by Educational Testing Service (ETS). TOEIC is a registered trademark of ETS. This publication is not endorsed or approved by ETS.

cortical hemoglobin. Absorption of near-infrared light at two wavelengths (695 and 830 nm) was measured with a sampling rate of 10 Hz. Two 3 × 5 optode probe sets were placed over the bilateral frontal and temporal areas by referring to the international 10–20 system of electrode placement. Each optode-probe set consists of eight emitters and seven detectors, resulting in 22 measurement channels. The source-detector distance was fixed at 3 cm. For spatial registration, virtual registration (Tsuzuki et al., 2007) was used to register the channel positions in relation to the Montreal Neurological Institute (MNI) standard brain space (Collins et al., 1994; Brett et al., 2002). The anatomical estimation is based on LBPA40 (Shattuck et al., 2008) and Brodmann's atlas (Rorden and Brett, 2000). The channel positions include regions related to auditory language processing (Friederici et al., 2000; Obrig et al., 2010; Price, 2012; Hall et al., 2013).

fNIRS Data Preprocessing

For analyzing the fNIRS data, Mathematica (Version 10.0, Wolfram Research, Inc., IL, United States) and Matlab (Version 2017a, Mathworks Inc., Natick, MA, United States) were used. Based on the modified Lambert–Beer law, concentration changes in oxygenated hemoglobin (oxy-Hb) and deoxygenated hemoglobin (deoxy-Hb) on each measurement channel were obtained (Maki et al., 1995). A band-pass filter (0.01–0.8 Hz) was then applied for noise reduction as in a previous study (Sasai et al., 2012; Santosa et al., 2013; Tak and Ye, 2014). The time-continuous data were divided into 33-s language blocks, which consisted of the 18-s question period, the reaction period (less than or equal to 3 s) and the rest period (between 15 and 18 s). After all language blocks were extracted, the baseline was corrected by using linear fitting to a mean signal over 5 s before the task and over the last 5 s of the task. Since optical measurements correspond to the hemodynamic signals, which are an indirect measure of neuronal activity. The hemodynamic signals (representing blood flow) are delayed in relation to the actual neuronal activity (Dehaene-Lambertz et al., 2002). Therefore, in consideration of the delay, the most-informative part of the comprehension during the task period (that is, the amplitude between 5 and 18 s averaged over each extracted language block on each measurement channel) was used to calculate brain activation.

The activation indicator used as an input feature is based on the significant differences between the oxy-Hb and deoxy-Hb signals (Cui et al., 2010). Since fNIRS simultaneously measures the concentration changes of oxy-Hb and deoxy-Hb, this indicator reflects activation strength. For each measurement channel of each participant, the activation indicator is defined as

$$\text{Activation indicator} = \frac{\overline{oxy} - \overline{deoxy}}{\sqrt{\frac{S_{oxy^2}}{n} + \frac{S_{deoxy^2}}{m}}} \quad (1)$$

where $\overline{oxy}$ and $\overline{deoxy}$ are sample means, S_{oxy} and S_{deoxy} are sample standard deviations, and n and m are sample sizes.

Since there are 44 measurement channels, the number of activation indicators for one participant is 44, and the input feature can be represented as a vector, A = $(a_{1,\ldots},a_{44})$. The number of dimensions of the original input feature is 44.

TABLE 1 | Details of participants after participant selection.

	Native Japanese speakers		Native English speakers	
	High-proficiency group	Low-proficiency group	High-proficiency group	Low-proficiency group
N	20	20	19	19
Female/male	8/12	10/10	6/13	8/11
Age (mean ± SD)	28.1 ± 2.6	29.4 ± 2.9	29.2 ± 2.9	28.5 ± 2.4

The label of the participants was re-examined. As a matter of fact, the participants in the high-proficiency group showed a low rate of correct answers, and the participants in the low-proficiency group showed a high rate of correct answers; that is, label proficiency group and label rate of correct answers contradict. To remove ambiguous data, participants whose measurement data did not contradict were further selected from both the native Japanese speakers and native English speakers. After those participants were selected, as for the native Japanese speakers, 20 participants were left in the high-proficiency group, and 20 participants were left in the low-proficiency group; and as for native English speakers, 19 participants were left in the high-proficiency group, and 19 participants were left in the low-proficiency group. The details about number, sex and age are shown in **Table 1**. As for both the native Japanese speakers and native English speakers, the high- and low-language proficiency groups were age-gender matching groups.

Algorithm Evaluation

The following conventional methods, which were shown to be promising by various classification studies, were used to classify the language proficiency into the high or low group.

- Support Vector Machine (SVM)
- Sparse Logistic Regression (Yamashita, 2009) (SLR)
- K-Nearest-Neighbors based on Euclidean distance of original input features (KNN, $K = 5$).

Using brain-activation vectors [for example, A = $(a_{1,\ldots},a_{44})$] for classifying each participant into the high or low groups was evaluated. Concretely, a support-vector machine (SVM) is considered to be a promising and popular algorithm among those used in classification studies, and it has been used in a variety of fNIRS studies (Li et al., 2016; Hosseini et al., 2018). Moreover, a SVM has already been used to examine the diagnostic potential of neuroimaging for a range of psychiatric disorders (Nieuwenhuis et al., 2012; Orrù et al., 2012). A SVM with a linear kernel was adopted for the binary-classification problem. The algorithm known as sparse logistic regression (SLR) (Yamashita, 2009) is an extension of logistic regression to automatically select features related to a label. Logistic regression is extended to a Bayesian framework by using a technique known as automatic relevance determination (ARD) from the neural-network literature. By combining logistic regression with ARD, SLR is obtained. SLR

is effective for removing irrelevant features, such that their associated weights are automatically set to zero, leading to a sparse weight vector for classification. In the implementation of this study, default values in the SLR toolbox were used to do the classification. K-nearest neighbor(s) (KNN) using majority voting (Duda et al., 2012) was used for classification. In this study, K was fixed to 5. K-nearest neighbors defines the label of test data by looking at the K-closest training data in the feature space. And it is sensitive to the local structure of the data.

Leave-one-out cross validation (LOOCV) was applied for cross validation. In detail, the data are divided into N folds (N = 40 for the native Japanese speakers; N = 38 for the native English speakers). In each leave-one-out cross-validation fold, all except one participant (N-1) were used as training data; the one participant left out was used as test data to determine which group the participant came from. This process is repeated once for each participant.

The classification accuracy of second language proficiency was computed to verify the estimation performance of the algorithm. A confusion matrix contains information about actual and predicted classifications done by a classification system. Performance of such a system is commonly evaluated using the data in the matrix.

$$\text{Accuracy} = \frac{TP + TN}{TP + TN + FP + FN}, \tag{2}$$

where TP is the number of true positives, TN is the number of true negatives, FP is the number of false positives, and FN is the number of false negatives.

Informative-Feature Selection

Given the small number of data sets and the high dimensions of the data, to further improve classification accuracy, feature selection or feature extraction is necessary (Guyon and Elisseeff, 2003; Akama et al., 2014). By selecting informative features, the machine-learning algorithm can give stable results and the physical interpretations of selected features are also important and worth discussing by means of neuroscience.

In this study, sparse canonical correlation analysis (SCCA) is applied to select the informative features. SCCA identifies sparse linear combinations of two sets of highly correlated variables (Witten et al., 2009). It has been shown to be useful in the analysis of high-dimensional neuroimaging data, namely, when two sets of variables are available for the same set of samples (Yahata et al., 2016).

Specifically, N observations (participants) of paired variables $X \in R^{d1}$ and $Y \in R^{d2}$ are given, X is an N × d1 matrix comprising the first set of variables, and Y is an N × d2 matrix comprising the second set of variables. L1-norm SCCA can be formulated as

$$\max_{v_X, v_Y} v_X^T X^T Y v_Y \text{ subject to } ||v_X||_1^2 \le \lambda_X, ||v_Y||_1^2 \le \lambda_Y, \\ ||v_X||_2^2 \le 1, ||v_Y||_2^2 \le 1, \tag{3}$$

where hyperparameters λ_X and λ_Y indicate the sparseness of projection vectors v_X and v_Y, respectively. The projection matrices are $v_X \in R^{d1 \times m}$ and $v_Y \in R^{d2 \times m}$, where m = min (d1, d2). In this study, X is the input feature, and Y is the label for language proficiency. Before input to SCCA, the training set is centered to have zero mean and scaled to have unit variance.

To select the common informative feature, the data sets for the second language were applied, and the LOOCV described above was used for cross validation. A feature selected from more than 95% of participants during the leave-one-out procedure was defined as a common informative feature. That is, a feature was selected when it was shown more than 38 times by the Japanese speakers (N = 40) and more than 36 times by the English speakers (N = 38). After the common informative features were selected, machine-learning methods were used to classify language proficiency to confirm that classification accuracy has been improved.

RESULTS

Classification Performance

Classification performance for the native Japanese speakers and the native English speakers is shown in **Figure 2**. Classification accuracies of the SVM for the native Japanese speakers were 55.0%, 52.5%, and 55.0% in terms of first language (L1), second language (L2) and third (unknown) language (L3), respectively, which show low classification accuracy. When SLR was used, classification accuracies were 66.0%, 65.0%, and 42.5% for the three languages, respectively; namely, classification of L1 and L2 showed higher accuracy than that for L3. When KNN was used, classification accuracies were 52.5%, 60.0%, and 37.5%; that is, only classification of L2 showed higher accuracy. For the native English speakers, classification accuracies of SVM were 68.4%, 76.3%, and 44.7% for L1, L2, and L3, respectively; that is, classification of L2 showed higher accuracy. When SLR was used, classification accuracies were 71.1%, 68.4%, and 47.4% for the three languages, respectively. When KNN was used, classification accuracies were 50.0%, 63.2%, and 36.8%, respectively. SLR showed the highest classification accuracy for the second language in the case of the Japanese speakers, and SVM showed the highest classification accuracy for the second language in the case of the English speakers.

The SVM showed unstable classification results: it cannot classify language proficiency in the case of the native Japanese speakers. SLR showed unexpected high classification accuracy when classifying L1. Using the label of second-language proficiency, SLR showed the highest classification accuracy for L1 in the case of both the native Japanese speakers and native English speakers. K-nearest neighbor showed reasonable classification results; namely, classification accuracy for L2 is higher, and that for L1 and L3 is near to chance level.

Informative Features Shared Between High- and Low-Language-Proficiency Groups

To extract informative features that can improve classification accuracy, sparse canonical correlation analysis was used. The same leave-one-out cross validation (LOOCV) procedure was

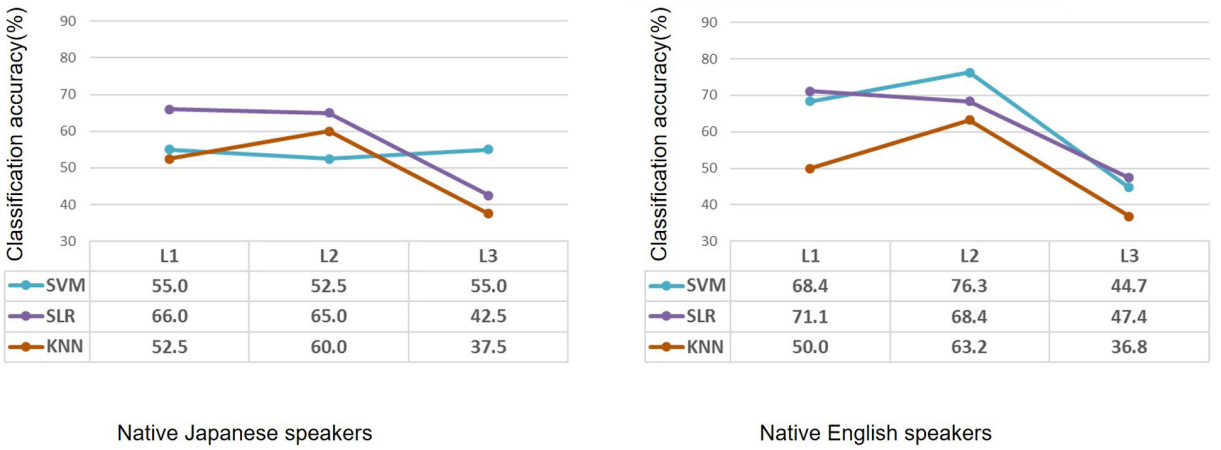

FIGURE 2 | Performance of classification by using machine learning methods of participants with high or low second-language proficiency in the case of native Japanese speakers and native English speakers. Based on the same second-language-proficiency label, classification results of the first language and third (unknown) language are also shown. L1: first language; L2: second language; L3: third (unknown) language.

adopted to select the features. Common informative features were defined as features selected from more than 95% of the participants. Spatial distribution of informative features is shown in **Figure 3**, and anatomical information about the features is listed in **Table 2**. As for the native Japanese speakers, the selected common informative features correspond to channel 1, channel 6, and channel 22 on the left hemisphere and channel 16 on the right hemisphere. The anatomical information about these features indicate the pars opercularis, part of Broca's area, left precentral gyrus, left inferior temporal gyrus and right superior temporal gyrus. As for the native English speakers, the selected common informative features correspond to channel 2, channel 9, channel 15, and channel 17 on the left hemisphere and channel 19 on the right hemisphere. The anatomical information about these features indicate the left postcentral gyrus, left angular gyrus, part of Wernickes's area, left superior and middle temporal gyrus and right middle temporal gyrus.

After feature selection, the informative features were used to classify each participant into the high-proficiency group or the low-proficiency group. Classification accuracy for L1, L2, and L3 in the case of the native Japanese speakers and the native English speakers is shown in **Figure 4**. As for the native Japanese speakers, when SVM was used, classification accuracy for L2 was the highest, i.e., 75%. When SLR was used, classification accuracies were 70.0%, 75.0%, and 55.0% for L1, L2, and L3, respectively; similarly, the accuracy was highest for L2. When KNN was used, classification accuracies were 55.0%, 77.5%, and 65.0%. As for the native English speakers, when SVM was used, classification accuracies for L1, L2, and L3 were 76.3%, 81.9%, and 57.9%, respectively. When SLR was used, classification accuracies were 68.4%, 79.0%, and 63.2% for L1, L2, and L3, respectively. When KNN was used, classification accuracies were 63.2%, 73.7%, and 63.2%; namely, classification accuracy was highest for L2.

After feature selection, as expected, classification accuracy for the second language was improved; meanwhile, classification accuracies for the first and unknown languages tend to be at the chance level. On the other hand, the SVM showed higher accuracy for L3 in the case of the native Japanese speakers and for L1 in the case of the native English speakers. SLR also showed higher accuracies for L1 in both cases. When K-nearest neighbor was used, classification accuracy tended to be reasonable; that is, it showed higher classification accuracy for L2. After feature selection, all the algorithms showed higher classification accuracy for L2. These results suggest that the informative features, which are related to second-language proficiency, are important for improving classification accuracy.

DISCUSSION

In this study, machine-learning methods—using activation patterns in fNIRS data— were used to classify individuals with high second-language proficiency or low second-language proficiency, in the case of both native Japanese speakers and native English speakers. After feature selection, all methods showed higher classification accuracy for the second language, suggesting that the validity of feature selection. Also, the activation patterns of frontal-temporal region are important indicators to estimate individual language proficiency.

In the field of neuroimaging studies applying machine learning, it is believed that to achieve better classification accuracy, informative features must be extracted (Norman et al., 2006; De Martino et al., 2008; Pereira et al., 2009; An et al., 2017). The higher classification performance demonstrated in this study indicates the validity of feature selection. Optimal feature extraction avoids over-fitting and eliminates the effects of noisy variables that are irrelevant to the classification problem. How to extract intrinsic features is an important research focus. SCCA was used as one of the methods for extracting informative features for individual estimation (Yahata et al., 2016). CCA can derive projection vectors that have maximum correlation with desired labels (e.g., a label for

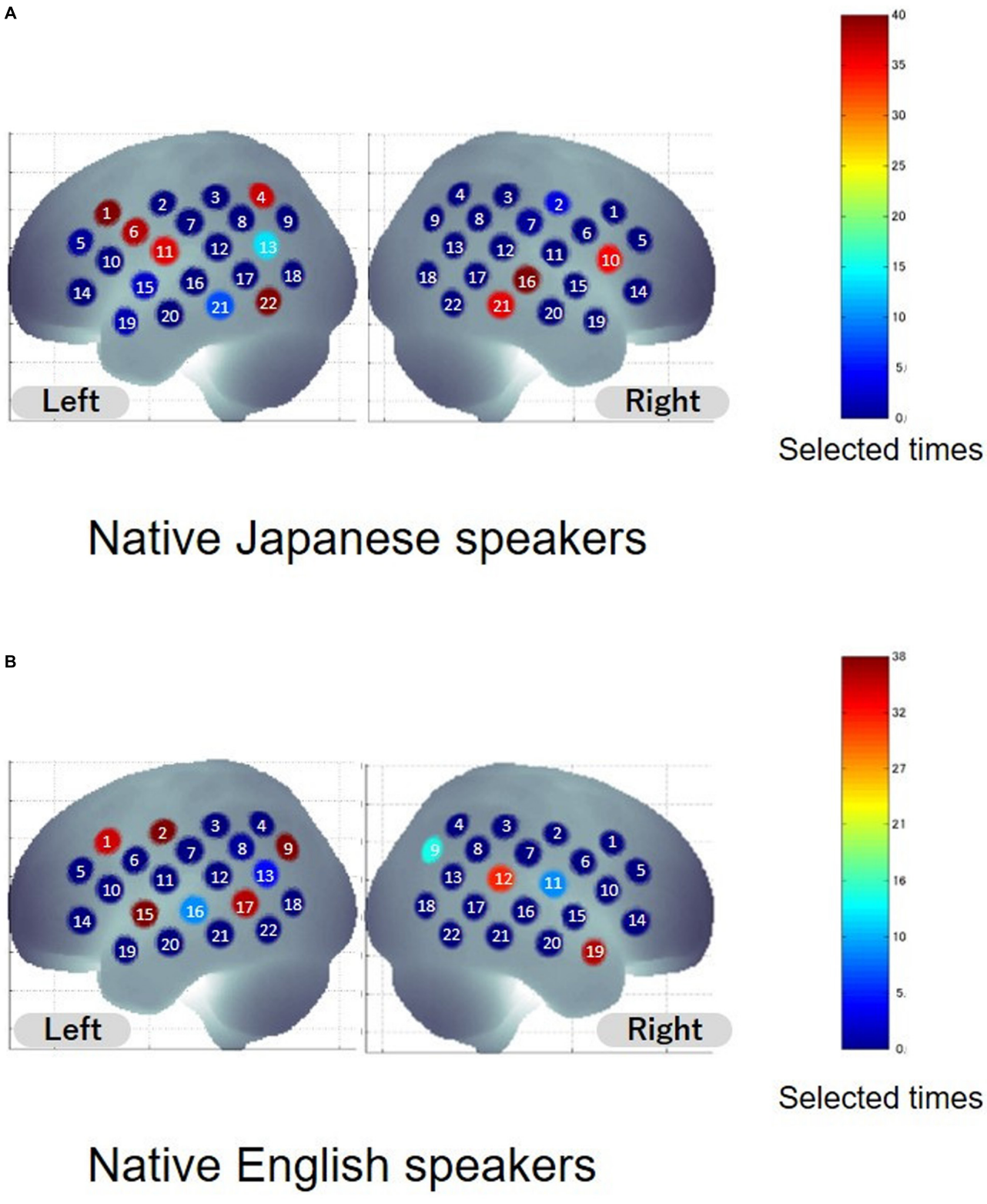

FIGURE 3 | Distribution of selected features. Colors indicate the number of times the channel was selected as the feature. The number on the channel indicates the channel number. **(A,B)** Show the results for native Japanese speakers and native English speakers, respectively.

TABLE 2 | Spatial and anatomical information of selected features.

	Channels	MNI coordinates x,y,z	Anatomical information
Japanese speakers	Left Ch 1	−50, 22, 38	Left middle frontal gyrus (BA 44)
	Ch 6	−61, 7, 28	Left precentral gyrus (BA 6)
	Ch 22	−61, −62, −8	Left inferior temporal gyrus (BA 37)
	Right Ch 16	71, −25, 4	Right superior temporal gyrus (BA 21)
English speakers	Left Ch 2	−60, −7, 43	Left postcentral gyrus (BA 4)
	Ch 9	−52, −72, 35	Left angular gyrus (BA 39)
	Ch 15	−62, 2, 1	Left superior temporal gyrus (BA 48)
	Ch 17	−67, −50, 6	Left middle temporal gyrus (BA 21)
	Right Ch 19	58, 10, −18	Right middle temporal gyrus (BA 21)

language proficiency). Using L1-norm regularization will lead to sparse solutions. As a result, features only related to desired labels can be extracted, so label-unrelated variables can be eliminated. Conventional methods of feature selection need careful engineering and considerable domain expertise to design a feature extractor that transforms raw data into an appropriate feature vector. SCCA allows an input to be composited from raw data; thus, it makes it possible to automatically extract the informative features required for the classification task.

Analyzing the most-discriminative features shared between high- and low-language-proficiency groups revealed that native Japanese speakers and native English speakers utilize different specific brain regions, but they show the same tendency, that is, Broca' s area, Wernicke' s area and the temporal cortex. The reason for activation of different specific brain regions may be due to the differences between brain shapes of native Japanese speakers and native English speakers; consequently, specific brain regions may deviate during spatial registration of measurement channels (Chee et al., 2011). Previous studies have found evidence that the two languages extensively overlap in regard to the classical language areas, namely Broca's area and Wernicke's area. Specifically, a variety of regions, including the left frontal region (Price et al., 1999; Lehtonen et al., 2005; Abutalebi and Green, 2008) and the bilateral supramarginal gyri (Price et al., 1999) have been observed to be involved in bilingual language comprehension and processing. Those studies also suggested that no single region is responsible for language comprehension and processing. Moreover, multiple studies have suggested that the bilateral temporal-frontal network is involved in processing during auditory language comprehension (Friederici, 2002; Price, 2012; Fengler et al., 2016). Concretely, syntactic and semantic information are processed predominately by the left hemisphere, while processing of prosodic information occurs predominately in the right hemisphere (Friederici et al., 2000; Friederici, 2002). Studies on sentence-comprehension tasks also reported left laterality plays a primary and significant role in language comprehension (Harrington et al., 2006; Sanjuán et al., 2010; Niskanen et al., 2012). In the present study, the brain region of selected features are consistent with the previous findings; namely, multiple cortical regions in a temporal-frontal network were observed to be related to language comprehension irrespective of native language, and the informative features in these brain regions play an important role in improving classification accuracy.

Using the label of second-language proficiency, classification of L1 and L3 results in a higher classification accuracy than the chance level. One possible explanation of this result is the relation between the second-language ability and the native-language ability (Brevik et al., 2016; Guo, 2018). In addition, during the fNIRS-measurement experiment, the psychological stressors of the high-language-proficiency group and the low-language-proficiency group may differ. Since all the languages

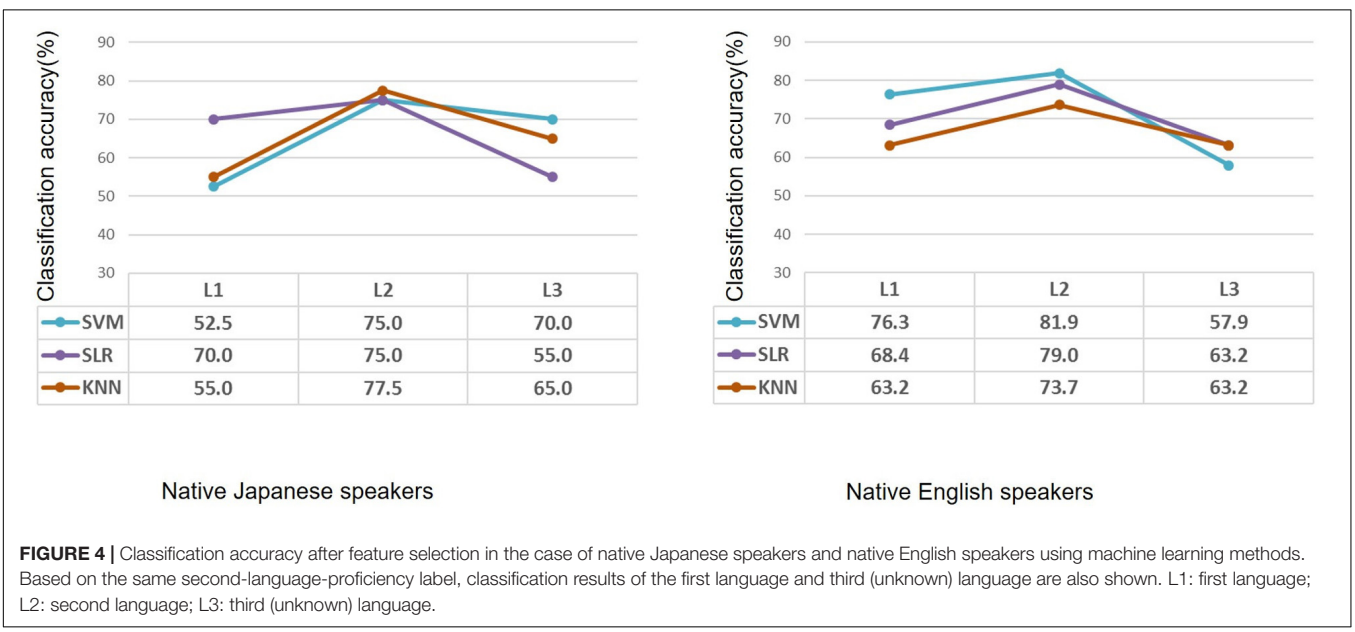

FIGURE 4 | Classification accuracy after feature selection in the case of native Japanese speakers and native English speakers using machine learning methods. Based on the same second-language-proficiency label, classification results of the first language and third (unknown) language are also shown. L1: first language; L2: second language; L3: third (unknown) language.

were randomly presented, the tests for L1 and L3 may be affected by the different psychological stressors.

CONCLUSION

Machine-learning methods were used for distinguishing second-language proficiency individually for both native Japanese speakers and native English speakers. By extracting informative features, the machine-learning methods showed higher classification accuracy for the second language. The informative features showed the effectiveness of feature selection in improving classification accuracy. Moreover, brain-activation patterns measured by fNIRS have the potential to serve as biomarkers for identifying language proficiency. Finally, the same approach could potentially be used with other biological data with similar characteristic to those of fNIRS data.

DATA AVAILABILITY STATEMENT

The datasets generated for this study are available on request to the corresponding author.

ETHICS STATEMENT

The studies involving human participants were reviewed and approved by internal review board on Research & Development Group, Hitachi, Ltd. The patients/participants provided their written informed consent to participate in this study.

AUTHOR CONTRIBUTIONS

HS, ID, and TM conceived and designed the study. HS, TM, ID, and ML conducted the experiment. ML, TM, and HS carried out the analysis of the data. ML wrote the manuscript. All the authors reviewed the manuscript.

ACKNOWLEDGMENTS

We thank Yoshiki Niwa, Yukiko Hirabayashi, Tsukasa Funane, Stephanie Sutoko, and Takashi Numata for their technical assistance in the fNIRS measurement experiment.

REFERENCES

Abutalebi, J., and Green, D. W. (2008). Control mechanisms in bilingual language production: neural evidence from language switching studies. *Lang. Cogn. Process.* 23, 557–582. doi: 10.1080/01690960801920602

Akama, H., Murphy, B., Lei, M. M., and Poesio, M. (2014). Cross-participant modelling based on joint or disjoint feature selection: an fMRI conceptual decoding study. *Appl. Inform.* 1:1.

An, L., Adeli, E., Liu, M., Zhang, J., Lee, S.-W., and Shen, D. (2017). A hierarchical feature and sample selection framework and its application for Alzheimer's disease diagnosis. *Sci. Rep.* 7:45269.

Bellman, R. E. (2015). *Adaptive Control Processes: a Guided Tour*. Princeton, NJ: Princeton university press.

Bortfeld, H., Fava, E., and Boas, D. A. (2009). Identifying cortical lateralization of speech processing in infants using near-infrared spectroscopy. *Dev. Neuropsychol.* 34, 52–65. doi: 10.1080/87565640802564481

Brett, M., Johnsrude, I. S., and Owen, A. M. (2002). Opinion: the problem of functional localization in the human brain. *Nat. Rev. Neurosci.* 3, 243–249. doi: 10.1038/nrn756

Brevik, L. M., Olsen, R. V., and Hellekjær, G. O. (2016). The complexity of second language reading: investigating the L1-L2 relationship. *Read. Foreign Lang.* 28, 161–182.

Chee, M. W. L., Zheng, H., Goh, J. O. S., Park, D., and Sutton, B. P. (2011). Brain structure in young and old East Asians and Westerners: comparisons of structural volume and cortical thickness. *J. Cogn. Neurosci.* 23, 1065–1079. doi: 10.1162/jocn.2010.21513

Chu, C., Hsu, A.-L., Chou, K.-H., Bandettini, P., Lin, C., and Initiative, A. S. D. N. (2012). Does feature selection improve classification accuracy? Impact of sample size and feature selection on classification using anatomical magnetic resonance images. *Neuroimage* 60, 59–70. doi: 10.1016/j.neuroimage.2011.11.066

Collins, D. L., Neelin, P., Peters, T. M., and Evans, A. C. (1994). Automatic 3D intersubject registration of MR volumetric data in standardized Talairach space. *J. Comput. Assist. Tomogr.* 18, 192–205. doi: 10.1097/00004728-199403000-00005

Cui, X., Bray, S., and Reiss, A. L. (2010). Functional near infrared spectroscopy (NIRS) signal improvement based on negative correlation between oxygenated and deoxygenated hemoglobin dynamics. *Neuroimage* 49, 3039–3046. doi: 10.1016/j.neuroimage.2009.11.050

De Martino, F., Valente, G., Staeren, N., Ashburner, J., Goebel, R., and Formisano, E. (2008). Combining multivariate voxel selection and support vector machines for mapping and classification of fMRI spatial patterns. *Neuroimage* 43, 44–58. doi: 10.1016/j.neuroimage.2008.06.037

Dehaene-Lambertz, G., Dehaene, S., and Hertz-Pannier, L. (2002). Functional neuroimaging of speech perception in infants. *Science* 298, 2013–2015. doi: 10.1126/science.1077066

Duda, R. O., Hart, P. E., and Stork, D. G. (2012). *Pattern Classification*. Hoboken, NJ: John Wiley & Sons.

ETS (2005). *TOEIC® Test New Official Preparation Guide*, Vol. 1. Tokyo: The Institute for International Business Communication.

ETS (2007). *TOEIC® Test New Official Preparation Guide*, Vol. 2. Tokyo: The Institute for International Business Communication.

ETS (2008). *TOEIC® Test New Official Preparation Guide*, Vol. 3. Tokyo: The Institute for International Business Communication.

ETS (2012). *TOEIC® Test New Official Preparation Guide*, Vol. 5. Tokyo: The Institute for International Business Communication.

Fan, Y., Rao, H., Hurt, H., Giannetta, J., Korczykowski, M., Shera, D., et al. (2007). Multivariate examination of brain abnormality using both structural and functional MRI. *Neuroimage* 36, 1189–1199. doi: 10.1016/j.neuroimage.2007.04.009

Fengler, A., Meyer, L., and Friederici, A. D. (2016). How the brain attunes to sentence processing: relating behavior, structure, and function. *Neuroimage* 129, 268–278. doi: 10.1016/j.neuroimage.2016.01.012

Finn, E. S., Shen, X., Scheinost, D., Rosenberg, M. D., Huang, J., Chun, M. M., et al. (2015). Functional connectome fingerprinting: identifying individuals using patterns of brain connectivity. *Nat. Neurosci.* 18, 1664–1671. doi: 10.1038/nn.4135

Friederici, A. D. (2002). Towards a neural basis of auditory sentence processing. *Trends Cogn. Sci.* 6, 78–84. doi: 10.1016/s1364-6613(00)01839-8

Friederici, A. D., Meyer, M., and Von Cramon, D. Y. (2000). Auditory language comprehension: an event-related fMRI study on the processing of syntactic and lexical information. *Brain Lang.* 74, 289–300. doi: 10.1006/brln.2000.2313

Guo, L. (2018). Modeling the relationship of metacognitive knowledge, L1 reading ability, L2 language proficiency and L2 reading. *Read. Foreign Lang.* 30, 209–231.

Guyon, I., and Elisseeff, A. (2003). An introduction to variable and feature selection. *J. Mach. Learn. Res.* 3, 1157–1182.

Hall, M., Chaudhary, U., Rey, G., and Godavarty, A. (2013). Fronto-temporal mapping and connectivity using NIRS for language-related paradigms. *J. Neurolinguistics* 26, 178–194. doi: 10.1016/j.jneuroling.2012.06.002

Harrington, G. S., Buonocore, M., and Farias, S. T. (2006). Intrasubject reproducibility of functional MR imaging activation in language tasks. *Am. J. Neuroradiol.* 27, 938–944.

Hong, K.-S., Khan, M. J., and Hong, M. J. (2018). Feature extraction and classification methods for hybrid fNIRS-EEG brain-computer interfaces. *Front. Hum. Neurosci.* 12:246. doi: 10.3389/fnhum.2018.00246

Hong, K.-S., and Yaqub, M. A. (2019). Application of functional near-infrared spectroscopy in the healthcare industry: a review. *J. Innov. Opt. Health Sci.* 12:1930012. doi: 10.1142/s179354581930012x

Hosseini, R., Walsh, B., Tian, F., and Wang, S. (2018). An fNIRS-based feature learning and classification framework to distinguish hemodynamic patterns in children who stutter. *IEEE Trans. Neural Syst. Rehabil. Eng.* 26, 1254–1263. doi: 10.1109/tnsre.2018.2829083

Hu, X.-S., Hong, K.-S., and Ge, S. S. (2013). Reduction of trial-to-trial variability in functional near-infrared spectroscopy signals by accounting for resting-state functional connectivity. *J. Biomed. Opt.* 18:017003. doi: 10.1117/1.jbo.18.1.017003

Lehtonen, M. H., Laine, M., Niemi, J., Thomsen, T., Vorobyev, V. A., and Hugdahl, K. (2005). Brain correlates of sentence translation in Finnish-Norwegian bilinguals. *Neuroreport* 16, 607–610. doi: 10.1097/00001756-200504250-00018

Lei, M., Akama, H., and Murphy, B. (2014). Neural basis of language switching in the brain: fMRI evidence from Korean-Chinese early bilinguals. *Brain Lang.* 138, 12–18. doi: 10.1016/j.bandl.2014.08.009

Lei, M., Miyoshi, T., Niwa, Y., Dan, I., and Sato, H. (2018). Comprehension-dependent cortical activation during speech comprehension tasks with multiple languages: functional near-infrared spectroscopy study. *Jpn. Psychol. Res.* 60, 300–310. doi: 10.1111/jpr.12218

Li, J., Qiu, L., Xu, L., Pedapati, E. V., Erickson, C. A., and Sunar, U. (2016). Characterization of autism spectrum disorder with spontaneous hemodynamic activity. *Biomed. Opt. Express* 7, 3871–3881.

Luu, S., and Chau, T. (2008). Decoding subjective preference from single-trial near-infrared spectroscopy signals. *J. Neural Eng.* 6:016003. doi: 10.1088/1741-2560/6/1/016003

Maki, A., Yamashita, Y., Ito, Y., Watanabe, E., Mayanagi, Y., and Koizumi, H. (1995). Spatial and temporal analysis of human motor activity using noninvasive NIR topography. *Med. Phys.* 22, 1997–2005. doi: 10.1118/1.597496

Mwangi, B., Tian, T. S., and Soares, J. C. (2014). A review of feature reduction techniques in neuroimaging. *Neuroinformatics* 12, 229–244. doi: 10.1007/s12021-013-9204-3

Naseer, N., and Hong, K.-S. (2013). Classification of functional near-infrared spectroscopy signals corresponding to the right-and left-wrist motor imagery for development of a brain–computer interface. *Neurosci. Lett.* 553, 84–89. doi: 10.1016/j.neulet.2013.08.021

Nieuwenhuis, M., Van Haren, N. E., Pol, H. E. H., Cahn, W., Kahn, R. S., and Schnack, H. G. (2012). Classification of schizophrenia patients and healthy controls from structural MRI scans in two large independent samples. *Neuroimage* 61, 606–612. doi: 10.1016/j.neuroimage.2012.03.079

Niskanen, E., Könönen, M., Villberg, V., Nissi, M., Ranta-Aho, P., Säisänen, L., et al. (2012). The effect of fMRI task combinations on determining the hemispheric dominance of language functions. *Neuroradiology* 54, 393–405. doi: 10.1007/s00234-011-0959-7

Norman, K. A., Polyn, S. M., Detre, G. J., and Haxby, J. V. (2006). Beyond mind-reading: multi-voxel pattern analysis of fMRI data. *Trends Cogn. Sci.* 10, 424–430. doi: 10.1016/j.tics.2006.07.005

Obrig, H., Rossi, S., Telkemeyer, S., and Wartenburger, I. (2010). From acoustic segmentation to language processing: evidence from optical imaging. *Front. Neuroenergetics* 2:13. doi: 10.3389/fnene.2010.00013

Orrù, G., Pettersson-Yeo, W., Marquand, A. F., Sartori, G., and Mechelli, A. (2012). Using support vector machine to identify imaging biomarkers of neurological and psychiatric disease: a critical review. *Neurosci. Biobehav. Rev.* 36, 1140–1152. doi: 10.1016/j.neubiorev.2012.01.004

Pena, M., Maki, A., Kovacic, D., Dehaene-Lambertz, G., Koizumi, H., Bouquet, F., et al. (2003). Sounds and silence: an optical topography study of language recognition at birth. *Proc. Natl. Acad. Sci. U.S.A.* 100, 11702–11705. doi: 10.1073/pnas.1934290100

Pereira, F., Mitchell, T., and Botvinick, M. (2009). Machine learning classifiers and fMRI: a tutorial overview. *Neuroimage* 45, S199–S209.

Power, S. D., Falk, T. H., and Chau, T. (2010). Classification of prefrontal activity due to mental arithmetic and music imagery using hidden Markov models and frequency domain near-infrared spectroscopy. *J. Neural Eng.* 7:26002.

Price, C. J. (2012). A review and synthesis of the first 20 years of PET and fMRI studies of heard speech, spoken language and reading. *Neuroimage* 62, 816–847. doi: 10.1016/j.neuroimage.2012.04.062

Price, C. J., Green, D. W., and Von Studnitz, R. (1999). A functional imaging study of translation and language switching. *Brain* 122(Pt 12), 2221–2235. doi: 10.1093/brain/122.12.2221

Qin, S., Young, C. B., Duan, X., Chen, T., Supekar, K., and Menon, V. (2014). Amygdala subregional structure and intrinsic functional connectivity predicts individual differences in anxiety during early childhood. *Biol. Psychiatry* 75, 892–900. doi: 10.1016/j.biopsych.2013.10.006

Quaresima, V., Bisconti, S., and Ferrari, M. (2012). A brief review on the use of functional near-infrared spectroscopy (fNIRS) for language imaging studies in human newborns and adults. *Brain Lang.* 121, 79–89. doi: 10.1016/j.bandl.2011.03.009

Raz, N., Lindenberger, U., Rodrigue, K. M., Kennedy, K. M., Head, D., Williamson, A., et al. (2005). Regional brain changes in aging healthy adults: general trends, individual differences and modifiers. *Cereb. Cortex* 15, 1676–1689. doi: 10.1093/cercor/bhi044

Rorden, C., and Brett, M. (2000). Stereotaxic display of brain lesions. *Behav. Neurol.* 12, 191–200. doi: 10.1155/2000/421719

Saeys, Y., Inza, I., and Larrañaga, P. (2007). A review of feature selection techniques in bioinformatics. *Bioinformatics* 23, 2507–2517. doi: 10.1093/bioinformatics/btm344

Sanjuán, A., Bustamante, J.-C., Forn, C., Ventura-Campos, N., Barrós-Loscertales, A., Martínez, J.-C., et al. (2010). Comparison of two fMRI tasks for the evaluation of the expressive language function. *Neuroradiology* 52, 407–415. doi: 10.1007/s00234-010-0667-8

Santosa, H., Jiyoun Hong, M., Kim, S.-P., and Hong, K.-S. (2013). Noise reduction in functional near-infrared spectroscopy signals by independent component analysis. *Rev. Sci. Instrum.* 84:073106. doi: 10.1063/1.4812785

Sasai, S., Homae, F., Watanabe, H., Sasaki, A. T., Tanabe, H. C., Sadato, N., et al. (2012). A NIRS–fMRI study of resting state network. *Neuroimage* 63, 179–193. doi: 10.1016/j.neuroimage.2012.06.011

Sato, H., Hirabayashi, Y., Tsubokura, H., Kanai, M., Ashida, T., Konishi, I., et al. (2012). Cerebral hemodynamics in newborn infants exposed to speech sounds: a whole-head optical topography study. *Hum. Brain Mapp.* 33, 2092–2103. doi: 10.1002/hbm.21350

Sato, H., Takeuchi, T., and Sakai, K. L. (1999). Temporal cortex activation during speech recognition: an optical topography study. *Cognition* 73, B55–B66.

Schecklmann, M., Ehlis, A. C., Plichta, M. M., and Fallgatter, A. J. (2008). Functional near-infrared spectroscopy: a long-term reliable tool for measuring brain activity during verbal fluency. *Neuroimage* 43, 147–155. doi: 10.1016/j.neuroimage.2008.06.032

Scholkmann, F., Kleiser, S., Metz, A. J., Zimmermann, R., Pavia, J. M., Wolf, U., et al. (2014). A review on continuous wave functional near-infrared spectroscopy and imaging instrumentation and methodology. *Neuroimage* 85, 6–27. doi: 10.1016/j.neuroimage.2013.05.004

Shattuck, D. W., Mirza, M., Adisetiyo, V., Hojatkashani, C., Salamon, G., Narr, K. L., et al. (2008). Construction of a 3D probabilistic atlas of human cortical structures. *Neuroimage* 39, 1064–1080. doi: 10.1016/j.neuroimage.2007.09.031

Sutoko, S., Monden, Y., Tokuda, T., Ikeda, T., Nagashima, M., Kiguchi, M., et al. (2019). Distinct methylphenidate-evoked response measured using functional near-infrared spectroscopy during Go/No-Go task as a supporting differential diagnostic tool between attention-deficit/hyperactivity disorder and autism spectrum disorder comorbid children. *Front. Hum. Neurosci.* 13:7. doi: 10.3389/fnhum.2019.00007

Tak, S., and Ye, J. C. (2014). Statistical analysis of fNIRS data: a comprehensive review. *Neuroimage* 85, 72–91. doi: 10.1016/j.neuroimage.2013.06.016

Tibshirani, R. (1996). Regression shrinkage and selection via the lasso. *J. R. Stat. Soc. Ser. B* 58, 267–288. doi: 10.1111/j.2517-6161.1996.tb02080.x

Tsuzuki, D., Jurcak, V., Singh, A. K., Okamoto, M., Watanabe, E., and Dan, I. (2007). Virtual spatial registration of stand-alone fNIRS data to MNI space. *Neuroimage* 34, 1506–1518. doi: 10.1016/j.neuroimage.2006.10.043

Witten, D. M., Tibshirani, R., and Hastie, T. (2009). A penalized matrix decomposition, with applications to sparse principal components and canonical correlation analysis. *Biostatistics* 10, 515–534. doi: 10.1093/biostatistics/kxp008

Yahata, N., Morimoto, J., Hashimoto, R., Lisi, G., Shibata, K., Kawakubo, Y., et al. (2016). A small number of abnormal brain connections predicts adult autism spectrum disorder. *Nat. Commun.* 7:11254.

Yamashita, O. (2009). *Sparse Logistic Regression ToolBox*. Available online at: https://bicr.atr.jp/~oyamashi/SLR_WEB.html (accessed June 17, 2020).

Zou, H., and Hastie, T. (2005). Regularization and variable selection via the elastic net. *J. R. Stat. Soc. Ser. B* 67, 301–320. doi: 10.1111/j.1467-9868.2005.00503.x

Conflict of Interest: ML and TM was employed by the company Hitachi, Ltd.

The remaining authors declare that the research was conducted in the absence of any commercial or financial relationships that could be construed as a potential conflict of interest.

Copyright © 2020 Lei, Miyoshi, Dan and Sato. This is an open-access article distributed under the terms of the Creative Commons Attribution License (CC BY). The use, distribution or reproduction in other forums is permitted, provided the original author(s) and the copyright owner(s) are credited and that the original publication in this journal is cited, in accordance with accepted academic practice. No use, distribution or reproduction is permitted which does not comply with these terms.

frontiers in Neuroscience

ORIGINAL RESEARCH
published: 28 July 2020
doi: 10.3389/fnins.2020.00746

Integration of Spatial Information Increases Reproducibility in Functional Near-Infrared Spectroscopy

Sergio Luiz Novi[1,2†], Edwin Johan Forero[1,2*†], Jose Angel Ivan Rubianes Silva[2,3], Nicolas Gabriel S. R. de Souza[1,2], Giovani Grisotti Martins[1,2], Andres Quiroga[1,2], Shin-Ting Wu[2,3] and Rickson C. Mesquita[1,2*]*

[1] "Gleb Wataghin" Institute of Physics, University of Campinas, Campinas, Brazil, [2] Brazilian Institute of Neuroscience and Neurotechnology, Campinas, Brazil, [3] School of Electrical and Computer Engineering, University of Campinas, Campinas, Brazil

OPEN ACCESS

Edited by:
Fenghua Tian,
The University of Texas at Arlington,
United States

Reviewed by:
Benito de Celis Alonso,
Meritorious Autonomous University of Puebla, Mexico
Luca Pollonini,
University of Houston, United States

***Correspondence:**
Sergio Luiz Novi
novisl@ifi.unicamp.br
Edwin Johan Forero
edwinjo@ifi.unicamp.br
Rickson C. Mesquita
rickson@ifi.unicamp.br

[†] These authors have contributed equally to this work

Specialty section:
This article was submitted to Brain Imaging Methods, a section of the journal Frontiers in Neuroscience

Received: 05 February 2020
Accepted: 24 June 2020
Published: 28 July 2020

Citation:
Novi SL, Forero EJ, Rubianes Silva JAI, de Souza NGSR, Martins GG, Quiroga A, Wu S-T and Mesquita RC (2020) Integration of Spatial Information Increases Reproducibility in Functional Near-Infrared Spectroscopy. Front. Neurosci. 14:746. doi: 10.3389/fnins.2020.00746

As functional near-infrared spectroscopy (fNIRS) is developed as a neuroimaging technique and becomes an option to study a variety of populations and tasks, the reproducibility of the fNIRS signal is still subject of debate. By performing test–retest protocols over different functional tasks, several studies agree that the fNIRS signal is reproducible over group analysis, but the inter-subject and within-subject reproducibility is poor. The high variability at the first statistical level is often attributed to global systemic physiology. In the present work, we revisited the reproducibility of the fNIRS signal during a finger-tapping task across multiple sessions on the same and different days. We expanded on previous studies by hypothesizing that the lack of spatial information of the optodes contributes to the low reproducibility in fNIRS, and we incorporated a real-time neuronavigation protocol to provide accurate cortical localization of the optodes. Our proposed approach was validated in 10 healthy volunteers, and our results suggest that the addition of neuronavigation can increase the within-subject reproducibility of the fNIRS data, particularly in the region of interest. Unlike traditional approaches to positioning the optodes, in which low intra-subject reproducibility has been found, we were able to obtain consistent and robust activation of the contralateral primary motor cortex at the intra-subject level using a neuronavigation protocol. Overall, our findings support the hypothesis that at least part of the variability in fNIRS cannot be only attributed to global systemic physiology. The use of neuronavigation to guide probe positioning, as proposed in this work, has impacts to longitudinal protocols performed with fNIRS.

Keywords: fNIRS, test–retest, neuronavigation, reproducibility, within-subject analysis, data analysis

INTRODUCTION

Functional near-infrared spectroscopy (fNIRS) has emerged as a promising tool to measure brain function over the years (Ferrari and Quaresima, 2012; Boas et al., 2014; Strait and Scheutz, 2014; Herold et al., 2018; Quaresima and Ferrari, 2019). fNIRS relies on the fact that near-infrared light (∼700–900 nm) is absorbed by oxy- (HbO) and deoxy-hemoglobin (HbR), which allows one to

estimate HbO/HbR concentration changes in biological tissue. In the brain, changes in HbO and HbR reflect (at least partially) neural activity due to neurovascular coupling (Obrig et al., 2002; Devor et al., 2005; Rovati et al., 2007; Mesquita et al., 2009; Ou et al., 2009; Phillips et al., 2015). Due to its high temporal resolution, portability, and versatility, fNIRS has become a suitable choice to investigate brain function non-invasively over a variety of populations, ranging from neonates to adults, both in the healthy and in the diseased brain (Tsuji et al., 2000; Brown et al., 2002; Terborg et al., 2004; Kim et al., 2010, 2014; Dehaes et al., 2015; de Oliveira et al., 2017, 2019; Forero et al., 2017; He et al., 2018; Forti et al., 2019). More recently, wearable technologies have expanded fNIRS protocols to study activities in natural and unconstrained environments (Piper et al., 2014; McKendrick et al., 2016; Pinti et al., 2018). These novel technologies afford new application scenarios never thought before, such as learning, training, and rehabilitation (Hatakenaka et al., 2007; Sitaram et al., 2009).

The reliability of fNIRS to answer questions in several fields, however, depends highly on the reproducibility of the results derived from the optical signal. From a scientific perspective, reproducibility is one of the cores of progress. Test–retest protocols have been previously applied to investigate the variability of fNIRS data. Due to the increased interest of the neuroscience community in functional connectivity, several studies have attempted to characterize the reliability of resting-state networks extracted from the fNIRS signal during the resting state (Mesquita et al., 2010; Zhang et al., 2011; Niu et al., 2013; Novi et al., 2016). Zhang et al. (2011) concluded that fNIRS connectivity maps are highly robust at the group level and fairly reliable at the individual level. Niu et al. (2013) and Novi et al. (2016) independently showed that graph-theoretical approaches can extract reliable features from fNIRS data despite greater intra-individual variability in functional connectivity experiments.

The reproducibility of fNIRS data in functional protocols has also been investigated. Most of the studies agree that the fNIRS signal is reproducible over group analysis, while within-subject fNIRS reproducibility has been shown to be poor (Watanabe et al., 2003; Kono et al., 2007; Plichta et al., 2007; Schecklmann et al., 2008; Kakimoto et al., 2009; Blasi et al., 2014; Dravida et al., 2017). By longitudinally measuring infants, Blasi et al. (2014) observed that HbO concentration changes were highly reproducible over group analysis yet just acceptable within subjects. More recently, Wiggins et al. (2016) analyzed speech protocols on healthy adults and found that the fNIRS signal is highly variable within subjects during speech-based protocols.

Several aspects related to the fNIRS technique can contribute to the increase in variability. Previous studies have suggested that systemic physiology plays an important role in the fNIRS signal (Joseph et al., 2006; Kirilina et al., 2012; Caldwell et al., 2016). Motion artifacts can also influence fNIRS results if not properly corrected (Huppert et al., 2009a; Cooper et al., 2012; Brigadoi et al., 2014; Novi et al., 2020). In addition, lack of spatial information may also be an important factor to decrease subject reproducibility. In typical fNIRS experiments, fNIRS optodes are placed on the scalp of the volunteers with little known information regarding the brain structure below the surface. To maximize accuracy in fNIRS measurements, one often decides to cover a broad surface with as many sources and detectors as possible. The 10–20 system localization (Klem et al., 1958) has also been widely used in fNIRS protocols, but this procedure is subjected to systematic errors of measurement and does not account for subject variation. Currently, the use of fNIRS probes with standard layouts in fixed positions is the best procedure to minimize spatial variation across multiple measurements.

In the present work, we hypothesized that the lack of precise anatomical information could contribute to a further increase in the within-subject variability in fNIRS. To test our hypothesis, we devised a protocol consisting of two sequences of measurements: with and without a real-time neuronavigation system to guide the placement of the fNIRS optodes. We assessed within-subject reproducibility by performing motor stimulation in three to five independent sessions in 10 subjects, both at the same day and in subsequent days. Extra-cortical contributions and systemic physiological parameters [i.e., heart rate (HR) and arterial blood pressure] were also included in the analysis.

MATERIALS AND METHODS

Subjects and Experimental Protocol

We acquired data from 10 young healthy male, right-handed volunteers with ages ranging from 19 to 34 years [mean (standard deviation) age = 22 (5) years]. We excluded subjects from the study when they presented any history of neurological or vascular disease, magnetic resonance imaging (MRI) contraindications (e.g., metal implants), or lack of a palpable inion because of neuronavigation constraints (see section "Real-Time Neuronavigation"). All participants provided signed informed consent prior to the experiment protocol. The study protocol is in accordance with the Declaration of Helsinki, and it was approved by the local Ethics Committee at the University of Campinas, where the experiments were carried out.

All subjects were required to perform the same experimental protocol at different times (i.e., sessions). For each session, participants performed a right-hand finger-tapping block-designed protocol consisting of 30 blocks of 2-s stimulation interleaved with a rest period that varied between 10 and 20 s. [Note that the rest period was randomized to decrease the probability of task synchronization with periodic physiological noise, such as Mayer waves (Yücel et al., 2016).] Since we wanted to investigate the effect of spatial information on the fNIRS reproducibility, we attempted to minimize the effects of circadian cycle in the measurements. Therefore, we acquired three independent sessions at the same time of the day over three different days for all subjects. For five of the 10 subjects, we additionally performed fNIRS measurements in three different periods of the day in one of the 3 days. In the latter case, measurements were taken in the morning (∼9 a.m.), in the afternoon (∼2 p.m.), and in the evening (∼6 p.m.). This approach allowed us to investigate how differences in systemic physiology (induced by different times of the circadian cycle) affect fNIRS reproducibility. In all sessions, we independently measured the subject's HR and arterial blood pressure with a

commercial automated blood pressure monitor before and after the experimental protocol.

fNIRS Signal Acquisition

All measurements were performed with a commercial continuous-wave (CW) NIRS system (NIRScout, NIRx Medical Systems, New York, NY, United States). We designed an optical probe with 14 sources (each source has two LEDs centered at 760 and 850 nm, ∼5 mW light power emission each) and 32 detectors, allowing 64 source-detector combinations (i.e., channels) at 3 cm and four source-detector pairs (i.e., short-channels) at 0.8 cm. This setup allowed an acquisition frequency of 8.9 Hz. We fixed the optodes with a 10–20 standard head cap. **Figure 1A** shows the location of each source and detector for an arbitrary volunteer. The optodes were placed symmetrically with respect to the brain hemispheres, and the probe was designed to be sensitive to the primary and secondary motor cortices, covering most of the parietal and the frontal lobes. **Figure 1B** shows the sensitivity profile for the optical setup, which was obtained with Monte Carlo simulations via the AtlasViewer package (Aasted et al., 2015). The position of the short channels is also highlighted in **Figure 1B**; they were located in the frontal lobe, with one close to the primary motor cortex and another one more anterior. The table in **Figure 1C** shows the projection of each channel onto the brain cortex, following the nomenclature from **Figure 1A**.

To position the probe on the subjects' head, we followed two different approaches: half of the subjects performed a standard approach and the other half followed a guided approach. In the standard approach, we adjusted the cap with a measuring tape following the standard metric procedure that considered the subject's head circumference, nasion–inion, and ear-to-ear

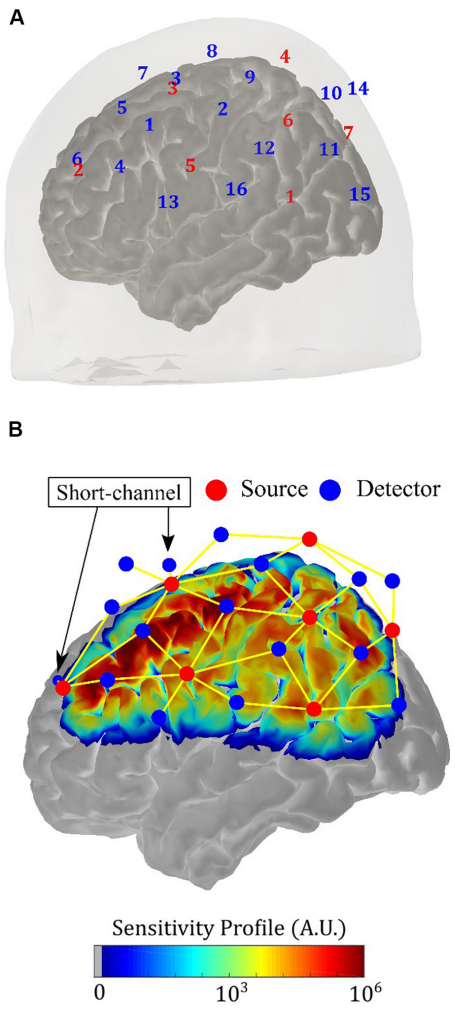

C

Src	Det	MNI	Gyrus
1	11	-38 -49 26	Angular
1	12	-41 -36 28	SupraMarginal
1	15	-49 -54 20	SupraMarginal
1	16	-56 -26 21	SupraMarginal
2	1	-42 28 33	Frontal_Mid
2	4	-46 37 30	Frontal_Mid
2	5	-41 38 44	Frontal_Mid
3	1	-44 8 57	Frontal_Mid
3	2	-45 -6 60	Precentral
3	5	-21 4 48	Frontal_Sup
3	7	-19 3 52	Frontal_Sup
3	8	-25 -10 65	Precentral
3	9	-30 -15 58	Precentral
4	8	-15 -30 66	Postcentral
4	9	-22 -34 57	Postcentral
4	10	-28 -48 62	Parietal_Inf
4	14	-27 -62 71	Parietal_Sup
5	1	-32 6 31	Frontal_Inf_Oper
5	2	-37 -12 38	Postcentral
5	4	-52 16 31	Frontal_Inf_Oper
5	12	-60 -17 40	Postcentral
5	13	-57 11 28	Precentral
5	16	-54 -6 32	Precentral
6	2	-36 -26 41	Postcentral
6	9	-50 -36 61	Parietal_Inf
6	10	-33 -48 48	Parietal_Inf
6	11	-34 -47 35	Angular
6	12	-51 -36 46	Parietal_Inf
7	10	-35 -66 49	Angular
7	11	-38 -63 39	Angular
7	14	-30 -70 45	Parietal_Inf
7	15	-37 -66 30	Angular

FIGURE 1 | Details of the anatomical positioning of the fNIRS probe. **(A)** Source-detector configuration of the optical probe used in the study, with 14 sources (red) and 32 detectors (blue), allowing 64 channels with source-detector separation of 3 cm and four short channels with source-detector separation of 0.8 cm. Since the probe is symmetric, the right hemisphere was omitted in the figure. **(B)** Sensitivity profile of the optical probe on the left hemisphere obtained with Monte Carlo simulation, considering all channels (yellow lines). The position of the short channels is indicated by the arrows. **(C)** Projections of the channels onto the brain cortex, with MNI coordinates and the associated gyrus, following the specifications of source (Src) and detector (Det) shown in **(A)**.

distances (Chatrian et al., 1985; Pfeifer et al., 2018). In the guided approach, the positioning of the fNIRS cap was based on the cortical anatomy. With a real-time neuronavigation system (section "Real-Time Neuronavigation"), a subset of optodes was first placed above the primary contralateral motor cortex. The position of the remaining optodes of the probe was constrained by the head cap. In both cases (i.e., standard and guided approaches), the position of each optode was captured with a commercial digitizer (Fastrak, Polhemus, Colchester, VT, United States). These positions were used for Monte Carlo simulations and for properly registering the position of optodes on a standard brain atlas. Due to time constraints, the subjects that were submitted to the guided approach performed three independent sessions in three different days, always at the same time of the day. In the standard approach, subjects performed five independent sessions: three sessions in three different days (to match the guided approach) and two extra sessions in one of the 3 days, at different times of the day (section "Subjects and Experimental Protocol").

Real-Time Neuronavigation

To perform the neuronavigation protocol in real time, we employed an in-house visualization system developed for this specific purpose (Rubianes Silva, 2017). A version runnable on Windows is freely available on our website[1]. First, subjects underwent an MRI session on a 3 T MRI scanner (Philips Achieva). The structural MRI image (T1-weighted with $1 \times 1 \times 1$ mm^3 resolution, TE = 3.2 s, TR = 7 ms, TI = 900 ms, 8° flip angle) was used as *a priori* information to guide the movements of the commercial digitizer on the subjects' scalp during the fNIRS sessions. For this, a rigid transformation matrix that aligns the scanned volume with the corresponding physical head must be computed. Eight pairs of anatomical points (i.e., points from the physical head and its correspondence on the rendered scanned volume) must be provided manually. In this study, we used the inion, right outer corner of eye, nasion, preauricular left, preauricular right, glabella, left alar, and right alar as the anatomical references (Sforza and Ferrario, 2006; Ibrahim et al., 2016). The singular value decomposition (SVD) technique was applied to find the elements of the transformation matrix.

During the fNIRS sessions, the visualization system captures the position of the digitizer on the physical head, transforms it to the anatomical space of the MRI volume using the computed transformation matrix, and displays it as a triad cursor on the visible head's surface. The setup to calibrate the neuronavigation space employs eight pairs of anatomical points (i.e., points from the physical head and its correspondence on the rendered scanned volume) that must be provided manually. In this study, we used the inion, right outer corner of eye, nasion, preauricular left, preauricular right, glabella, left alar, and right alar as the anatomical references (Sforza and Ferrario, 2006; Ibrahim et al., 2016). The depthmap-based picking algorithm was implemented to afford 3D interactions with rendered images (Wu et al., 2003, 2011). The reproducibility of the procedure was assessed through a one-way analysis of variance (ANOVA) of a series of measurements of randomly chosen seven points on different heads at different instants of time. It only failed when the subject did not have palpable inion.

With the visualization system described above, we used the MRI image to guide the placement of the digitizer over the primary motor cortex at all sessions of each subject (Yousry et al., 1997). In the first session of measurements, we saved the position of the fNIRS optodes that were located above the motor cortex. In the subsequent sessions, small spheres with a radius of less than 6 mm were displayed on these saved positions to guide the placement of optodes. This ensured that all the optodes were placed very close on the head across different sessions.

NIRS Preprocessing

After the fNIRS data collection, we first removed channels with a low signal-to-noise ratio (SNR), defined as SNR < 8. We computed the SNR as the mean intensity of each channel divided by the standard deviation of the same channel, and the threshold was chosen based on previous works (de Oliveira et al., 2017, 2019; Forero et al., 2017; Novi et al., 2018). Next, we converted light intensity at each wavelength of each channel to optical density (OD) and removed motion artifacts with spline interpolation followed by wavelet decomposition (Scholkmann et al., 2010; Molavi and Dumont, 2012; Di Lorenzo et al., 2019; Novi et al., 2020). Hemoglobin concentration changes were estimated using the modified Beer–Lambert law with a pathlength factor equal to six for both wavelengths (Huppert et al., 2009b). Finally, we filtered the concentration changes with a bandpass filter between 0.005 and 0.5 Hz in order to remove low-frequency drifts, HR, and other high-frequency physiological noise (Joseph et al., 2006; Pinti et al., 2019).

Test–Retest Reliability Analyses

To investigate the reproducibility of the fNIRS signal, each channel was classified as activated or not activated. A channel was assigned as activated if it presented a characteristic hemodynamic response (i.e., significant increase in oxy-hemoglobin and decrease in deoxy-hemoglobin during the task period compared to the baseline period). The dynamics of the hemodynamic response was inferred by a general linear model (GLM) with a gamma function (Santosa et al., 2019). For each long fNIRS channel, the closest short-channel measurement was incorporated in the GLM model as a regressor to remove extra-cortical hemodynamics (Gagnon et al., 2012; Goodwin et al., 2014; Yücel et al., 2015; Sato et al., 2016). The GLM was solved with an iterative algorithm introduced by Barker et al. (2013). The algorithm uses an autoregressive model based on pre-whitening filter and robust regression to remove both serially correlated errors and remaining motion artifacts. Channels that presented significant responses ($p < 0.05$) for *both* oxy-hemoglobin and deoxy-hemoglobin were classified as activated (Huppert, 2016; Pinti et al., 2017) with the additional constrain that the coefficient β associated with the gamma function needed to be positive for HbO ($\beta_{HbO} > 0$) and negative for HbR ($\beta_{HbR} < 0$). By simultaneously analyzing HbO and HbR time series and using the pre-whitening filter, we decreased false-positive rates in the

[1] http://www.light4brain.com

hemodynamic response function (HRF) (Kirilina et al., 2012; Barker et al., 2013).

Standard group analysis was performed with the coefficients (β_{HbO} and β_{HbR}) found after solving the GLM model for each channel of each volunteer. To compute the beta coefficients for a given group of volunteers (β^g_{HbO} and β^g_{HbR}, where g stands for group), we performed a weighted-linear regression to correct different errors of β-values of each channel and each measurement.

To assess the reproducibility across different sessions, we obtained a binary vector, B^s, for each session of each subject from the GLM. The jth element of the B^s vector, B^s_j, was assigned to 1 if the jth channel from a session s had a characteristic hemodynamic response ($\beta_{HbO} > 0$ and $\beta_{HbR} < 0$ with $p < 0.05$); otherwise, the element was set to 0. With the binary vectors, we assessed the spatial within-subject reproducibility of a given joint of channels with two metrics that have been previously used in the fNIRS literature (Plichta et al., 2007; Schecklmann et al., 2008; Blasi et al., 2014). The metrics compare the size (R_q) and the overlap (R_o) of the evoked hemodynamic response over different sessions:

$$R_q^{i,j} = 1 - \frac{\left|A_{s_i} - A_{s_j}\right|}{A_{s_i} + A_{s_j}},$$

$$R_o^{i,j} = 2 \times \frac{A_{overlap}^{i,j}}{A_{s_i} + A_{s_j}},$$

where A_{s_i} is the number of activated channels of session i and $A_{overlap}^{i,j}$ is the number of common activated channels in sessions i and j. To verify the channel-wise within-subject reproducibility, we created frequency vectors that show the number of times that each channel was activated over different sessions for a given subject (de Oliveira et al., 2017, 2019; Novi et al., 2020). A high frequency of a given channel means that this channel was recruited over different sessions repeatedly.

RESULTS

Group Results Evidence Robust Contralateral Activation

Figure 2A shows the group response to the right finger-tapping stimulation in the five subjects acquired with the standard protocol (i.e., without the neuronavigation system and with a total of 25 measurements). As expected for a motor stimulation, the right finger-tapping task induced significant hemodynamic changes in the channels located on the contralateral motor cortex (Obrig et al., 2000; Franceschini et al., 2003). In addition to the spatial analysis, we also computed the measured HRF of the activated channels by averaging the concentration changes across all trials for the same subject, and then averaging the subject HRF across all volunteers (**Figure 2B**). As compared to the baseline, the measured HRF of each activated channel is temporally well-behaved, presenting a clear increase in oxy-hemoglobin (HbO) and a decrease in deoxy-hemoglobin (HbR) concentration synchronized with the period of stimulation. These results show that we were able to recover the expected response to a simple motor stimulation task even with a small sample size. However, this result does not inform about the consistency of activation across different subjects or the reproducibility of the activation for the same subject.

Individual fNIRS Response Is Highly Variable in the Standard Approach

To analyze the reproducibility of the fNIRS response at the within-subject level, we quantified the frequency of activation of each channel for each subject acquired with the standard approach. The first interesting finding that contrasts with the group analysis concerns the location of the hemodynamic response. Although the HRF was well localized in the contralateral primary motor cortex for the group, the number of channels that were activated at least once across all sessions for the same subject ranged from 0 to 65% of the whole probe. Despite the fact that the probe was entirely located around the somatomotor cortex, the heterogeneity of the response evidences the individual variability of the fNIRS results, as pointed by previous studies (Plichta et al., 2007).

The low reproducibility of the fNIRS signal in the standard approach was quantified by the values of R_q and R_o (**Table 1**). To evaluate these two parameters for the data acquired with the standard approach, we separated the sessions performed on the same day and the sessions performed across different days. For the sessions acquired on the same day, the median R_q and R_o across all subjects were 0.73 and 0.36, respectively. The reproducibility was lower for the sessions acquired across different days: 0.66 and 0.04 for R_q and R_o, respectively.

Specifically in the contralateral primary motor cortex, which is the expected activated region for the motor task, channels in this region were activated in all sessions for only one subject, regardless of the protocol (i.e., sessions on the same day or sessions across different days). Although most of the channels of the probe were activated at least once over the different sessions, the left brain hemisphere was not activated in eight out of the 25 sessions for the data acquired with the standard approach.

Systemic Physiology Does Not Explain All Variability in fNIRS Data

From Section "Individual fNIRS Response Is Highly Variable in the Standard Approach," it appears that the reproducibility of the fNIRS response is slightly higher for sessions acquired at different times on the same day, compared to the sessions performed at the same time of the day for different days. This led us to further investigate the extent to how much of the within-subject variability could be associated with systemic physiology (and, in particular, the circadian cycle) for the data acquired with the standard approach. **Figure 3** shows the activated fNIRS channels along with the systemic physiological parameters for a representative subject in each session with the standard approach. As expected, both HR and mean arterial blood pressure (MAP) oscillated during the different measures taken over a single day, likely due to the circadian cycle (**Figure 3A**). For the

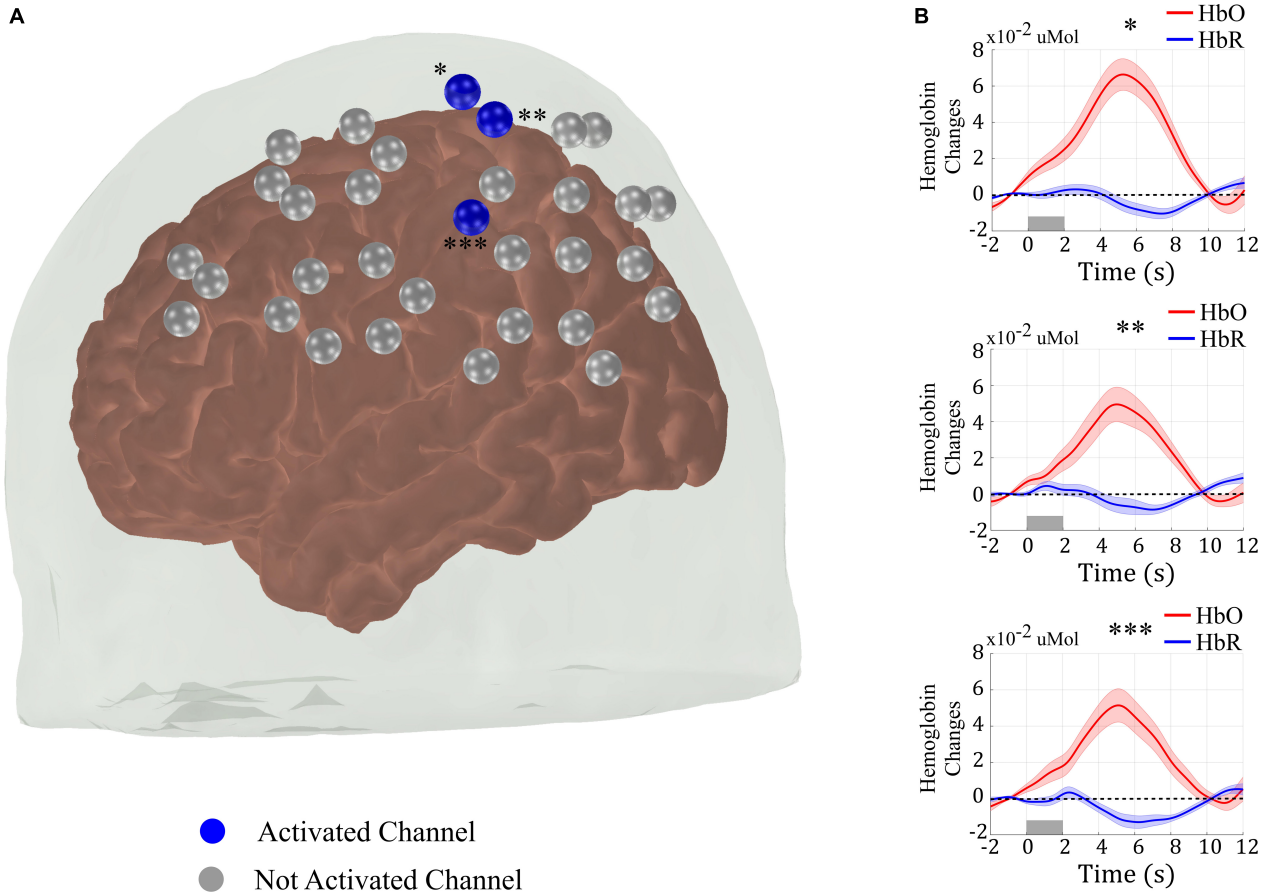

FIGURE 2 | (A) Results from the group analysis using the measures from all five sessions of the five subjects acquired with the standard approach (i.e., without the assistance of a neuronavigation system) to position the optical probe. The right-brain hemisphere did not have any activated channel in the group analysis. **(B)** Evoked hemodynamic response of the activated channels in **(A)**. The hemodynamic response was computed by block-averaging the measured fNIRS signal across all sessions for all volunteers of the blue channels shown in **(A)** and marked with asterisks.

TABLE 1 | Reproducibility parameters (R_q and R_o) for the data acquired with the standard protocol, along with variations in heart rate (ΔHR) and mean arterial pressure (ΔMAP).

	Same day				Across days			
Subject	**ΔMAP (%)**	**ΔHR (%)**	R_q	R_o	**ΔMAP (%)**	**ΔHR (%)**	R_q	R_o
1	3.1	11.8	0.00	0.00	8.3	8.9	0.00	0.00
2	14.2	12.5	0.41	0.17	5.1	6.8	0.13	0.00
3	5.5	20.7	0.73	0.45	8.3	14.5	0.66	0.31
4	13.2	6.8	0.89	0.36	8.3	4.0	0.71	0.04
5	4.7	9.5	0.9	0.68	5.1	9.0	0.94	0.71
Median	5.5	11.8	0.73	0.36	8.3	9.0	0.66	0.04

Both R_q and R_o were computed for the whole probe.

subject in **Figure 3**, HR and MAP varied 12.5 and 14.2% across morning, afternoon, and evening measurements, respectively. The fNIRS activation pattern also varied within the sessions of the same day. The average (standard error) fNIRS reproducibility indexes were R_q = 0.41 (0.31) and R_o = 0.17 (0.20) for this specific subject. A significant fNIRS response in the contralateral primary motor cortex was found in two out of the three sessions performed on the same day. Considering all subjects, the median HR and MAP variations in the same day were 11.8 and 5.5%, respectively, while the median R_q and R_o were 0.73 and 0.36, respectively.

For the measurements performed at the same time of the day in different days, the circadian cycle is expected to have less influence on systemic physiology; therefore, variations in

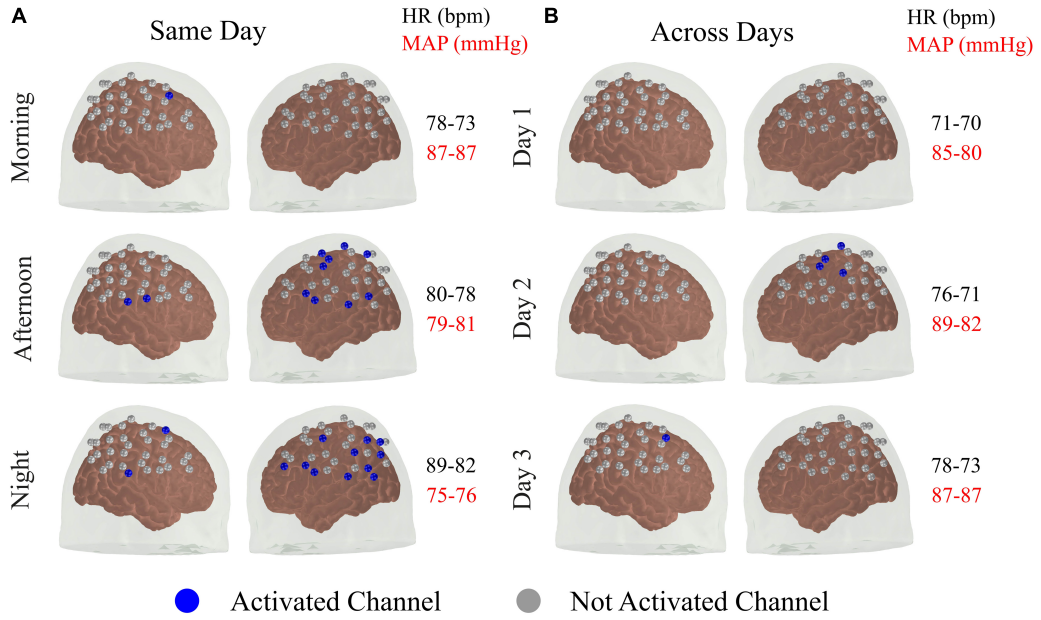

FIGURE 3 | Activated brain regions for one representative subject over different sessions **(A)** within the same day and **(B)** across subsequent days. A channel was classified as activated for a $p < 0.05$ for both HbO and HbR with the additional constrain that the coefficient associated with HbO and HbR needed to be positive and negative, respectively. In addition to the activated brain regions in each session, the values of heart rate (HR) and mean arterial blood pressure (MAP) acquired immediately before and after the fNIRS measurements are shown.

HR and MAP are expected to be smaller. For the subject in **Figure 3**, the average changes in HR and MAP were 6.8 and 5.1%, respectively, while the average (standard error) fNIRS reproducibility indexes were R_q = 0.13 (0.16) and R_o = 0.00 (**Figure 3B**). Considering all subjects, we observed a median HR and MAP change by 9.0 and 8.3%, respectively, with median R_q and R_o of 0.66 and 0.04, respectively. **Table 1** summarizes the reproducibility metrics and variations in HR and MAP for all subjects.

Interestingly, although the variations of HR and MAP were similar for measurements on the same day compared to inter-day measurements, the size and spatial overlap of the hemodynamic responses were more reproducible on the same day rather than across different days. This last finding, along with the fact that we performed short-channel regression, suggests that part of the variability in the fNIRS signal may not come from global physiological noise.

As an attempt to quantify the effects of systemic physiology in the variability of the fNIRS signal, we further computed the complement of R_q (i.e., $v_q \equiv 1 - R_q$) as a measure of variability instead of reproducibility of the fNIRS results. By assuming a linear relationship between fNIRS variability and both HR and MAP changes (i.e., $< v_q >= \alpha + \beta \Delta HR + \gamma \Delta MAP$), we performed a regression analysis to quantify the degree of dependency of the fNIRS variability on the systemic variables. We found that neither HR nor MAP changes can predict fNIRS variability. The fit estimates (standard error, p-value) for α, β, and γ were, respectively, 0.62 (0.47, p = 0.23), −0.37 (3.0, p = 0.90), and −1.6 (3.8, p = 0.61). The low significance of the contribution of HR and MAP to the fNIRS variability suggests that there may be other confounding factors that drive the intra-subject variability in fNIRS data.

Guided fNIRS Experiments Present Lower Within-Subject Variability

Last, we hypothesized that the variation on the spatial location of the fNIRS optodes across different sessions may contribute to the fNIRS variability. To reduce the spatial variation in probe positioning, we employed a real-time neuronavigation system to reliably position the fNIRS optodes above the motor cortex and to ensure the reproducibility across the sessions (see section "Real-Time Neuronavigation"). To properly compare the reproducibility of the guided and the standard approaches, we considered only the sessions that were acquired at the same time across different days. Each subject performed three independent sessions with this condition in both approaches.

Figure 4 shows the frequency maps of activation on the left hemisphere for each subject. The differences in reproducibility between the two approaches are clear. Most of the subjects acquired with the standard approach did not have activated channels in the contralateral hemisphere with frequency higher than 1/3 (**Figure 4A**). On the other hand, the guided approach showed robust and consistent activation maps in the contralateral motor cortex. Activation on the same channels was repeated at least twice for all subjects that performed the guided protocol. In addition, at least one channel in the contralateral motor cortex was activated at all sessions in four of the five subjects.

We also compared the inter-session measures of size (R_q) and spatial overlap (R_o) from both approaches. **Table 2**

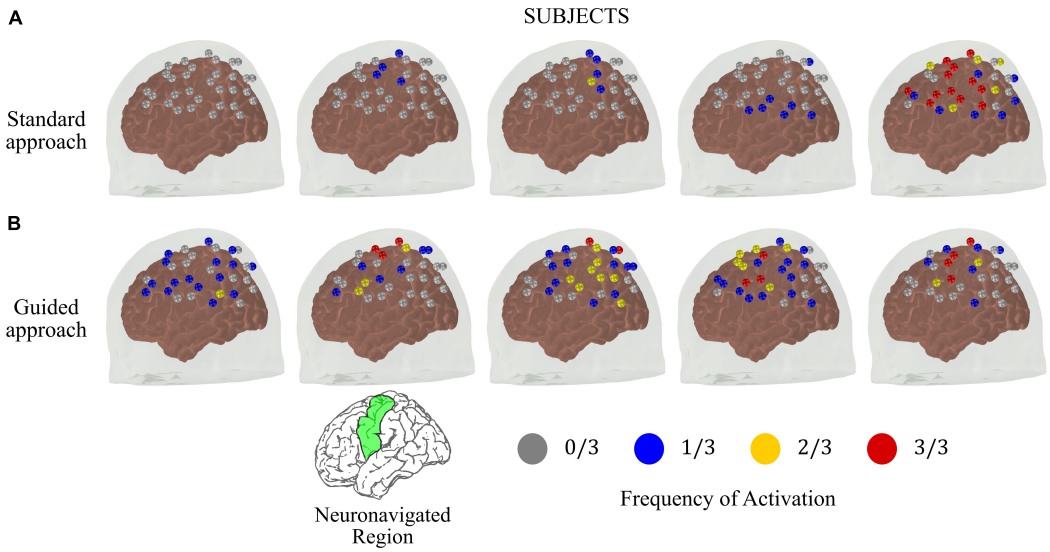

FIGURE 4 | Frequency of activated brain regions at the contralateral brain hemisphere due to right finger-tapping at the subject level for the measurements performed at the same time across different days (total of three sessions) for the **(A)** standard and **(B)** guided approaches. The green region in the reference brain (located at the bottom of the figure) corresponds to the targeted brain region that we used as reference to position the optical probe in the guided approach.

TABLE 2 | Comparison of the fNIRS signal reproducibility for the data acquired with the standard and guided approaches.

	Whole probe				Left hemisphere				Neuronavigated region			
Subject	***Standard***		***Guided***		***Standard***		***Guided***		***Standard***		***Guided***	
	R_q	R_o	R_q	R_o	R_q	R_o	R_q	R_o	R_q	R_o	R_q	R_o
1	0.00	0.00	0.54	0.08	0.00	0.00	0.69	0.07	0.00	0.00	0.13	0.00
2	0.13	0.00	0.71	0.51	0.13	0.00	0.63	0.56	0.17	0.00	0.70	0.70
3	0.66	0.31	0.34	0.32	0.11	0.11	0.39	0.37	0.17	0.17	0.44	0.44
4	0.71	0.04	0.75	0.36	0.29	0.00	0.82	0.43	0.00	0.00	0.85	0.59
5	0.94	0.71	0.9	0.49	0.94	0.77	0.83	0.65	0.89	0.89	0.87	0.73
Median	0.66	0.04	0.71	0.36	0.13	0.00	0.69	0.43	0.17	0.00	0.70	0.59

The numbers show the size (R_q) and the overlap (R_o) of the evoked hemodynamic response for all channels (whole probe), for the left hemisphere, and for the neuronavigated region. In all situations, the reproducibility of the guided approach was higher than the standard approach.

summarizes the results obtained for all volunteers when R_q and R_o were calculated for the whole probe, for the left hemisphere, and for the neuronavigated region. The reproducibility of the guided approach exceeded the standard approach in all situations. When considering all channels of the probe, we observed reproducibility medians of 0.66 (R_q) and 0.04 (R_o) with the standard approach, while the guided approach yielded 0.71 (R_q) and 0.36 (R_o). If one considers only the contralateral brain hemisphere (i.e., left hemisphere), the size and the overlap of the evoked hemodynamic response decrease in the standard approach (R_q = 0.13 and R_o = 0.00) while they both remained approximately constant in the guided approach (R_q = 0.69 and R_o = 0.43). These trends continue as one analyzes the activation reproducibility more locally. Considering only the neuronavigated brain region, we observed median R_q equals to 0.17 and 0.70, and R_o equals to 0.00 and 0.59 for the standard and guided approaches, respectively. On average, the neuronavigation system increased the reproducibility in size and spatial overlap of the fNIRS signal by a factor of two.

DISCUSSION

In this work, we aimed to investigate the reproducibility of fNIRS measures. Since fNIRS has rapidly expanded its applications in functional neuroscience, the importance of obtaining reproducible results has also grown. Therefore, test–retest studies have become a topic of debate in the fNIRS community. Here, by collecting functional motor stimulation data from 10 healthy subjects across multiple sessions on different days and during the same day, we characterized the inter- and intra-subject reproducibility of a simple and predictive task: block-designed finger tapping.

In line with previous reports, our results show that finger-tapping stimulation induces a robust fNIRS response in the

contralateral primary motor cortex with the standard approach of positioning the optodes, even for a small group of subjects (**Figure 2**). Compared to baseline, HbO (HbR) significantly increased (decreased) in the region of interest during stimulation, just as expected. However, when we compared the individual responses to the task, it is possible to observe a wide variation in the activation maps (**Figures 3**, **4**). The low reproducibility of fNIRS was also quantified by measuring the size and spatial overlap of the evoked hemodynamic responses over different sessions (**Tables 1**, **2**). For the three independent sessions performed in the same day, the median R_q and R_o were 0.73 and 0.36, respectively, considering all volunteers. Independent sessions performed during the same time of the day at different days yielded an even lower reproducibility (R_q = 0.66 and R_o = 0.04) across all volunteers, despite the smaller variations in global systemic physiology under this condition.

Several factors can influence the reproducibility of fNIRS results. From the methodological perspective, it is important to combine oxy- and deoxy-hemoglobin data to decide whether a channel presented a characteristic hemodynamic response (i.e., an increase in oxy-hemoglobin and a decrease in deoxy-hemoglobin during the period of stimulation compared to the baseline period). Although this is the most basic approach in order to minimize false-positive rates of activation, most studies still report only changes in one of the chromophores. Specially for the HbO change, it is highly susceptible to arteriolar vessels, which are more responsive to systemic physiological changes (Huppert et al., 2009b; Tachtsidis and Scholkmann, 2016). For example, an increase in cerebral blood volume can induce an increase in both oxy- and deoxy-hemoglobin; motion artifacts can also change HbO and HbR concentrations. In our data, we verified that if we did not evaluate both HbO and HbR, we would have incorporated false positives to our analysis, which increases the variability at both the inter- and intra-subject levels. Since these contributions are expected to be random across sessions and subjects, they tend to average out at the group level, which explains the higher reproducibility of the fNIRS-based results for a group of subjects.

Another confounding factor in the fNIRS signal comes from hemodynamic contaminations from the extra-cortical layers and systemic physiology. In this work, we proposed to remove extra-cortical contributions by performing additional measurements with four short channels located on the primary and secondary motor cortices (Gagnon et al., 2012). Recent studies have demonstrated that removal of global noise leads to a more accurate localization in the hemodynamic response (Yücel et al., 2015; Dravida et al., 2017). While the localization of the hemodynamic response reduces the number of activated brain regions due to a single task, it does not decrease the spatial variability of the fNIRS signal at the channel level. In fact, the reduction in the number of activated channels may increase the channel inter- and intra-subject variability due to the lack of accuracy in repositioning the optical probe at several sessions. Therefore, a channel-wise comparison (such as the ones performed with GLM) may fail to find real activated regions.

Although short-channel regression can reduce the influence of global systemic physiology in the fNIRS signal, previous studies have shown that it is not completely effective (Kirlilna et al., 2013). Indeed, our data suggest that there is a weak to moderate correlation between fNIRS variability and global systemic physiology (as measured by HR and MAP) even after removing extra-cortical contributions (**Figure 3** and **Table 1**). In our work, we observed that the highest variation of systemic physiology occurred in the measurements performed on the same day (as expected due to the circadian cycle). However, the values of the metrics of reproducibility (R_q and R_o) were on average twice as high for the data acquired on the same day than for the data acquired in different days with the standard approach. This result suggests that part of the variability in the fNIRS signal does not come from physiological contamination, only. Unfortunately, in this work, we measured HR and MAP at the beginning and end of each session. Continuous monitoring of systemic physiology simultaneous with fNIRS may evidence a greater relationship between HR/MAP and fNIRS variability than the ones reported in this work (Caldwell et al., 2016).

The proper positioning of fNIRS sources and detectors are usually neglected with the argument that the intrinsic spatial resolution of the technique is poor by itself. By neglecting this uncertainty, it has been widely assumed that systemic and extra-cortical physiological noise triggered by the task can explain all variability presented in the fNIRS data (Blasi et al., 2014; Dravida et al., 2017). In this work, we provide a robust methodological approach to constrain the spatial variability in fNIRS protocols and to acquire missing anatomical information with a real-time navigation procedure. Our approach requires *a priori* information from a high spatial resolution imaging that carries brain anatomy information of each volunteer. Here, we opted to use structural MRI images, but other neuronavigation systems (as well as ours) can also work with computed tomography (CT) scans (Rubianes Silva, 2017; Souza et al., 2018, 2019). The validation of our approach shows that by adding spatial information to the protocol, we were able to improve the within-subject reproducibility of the fNIRS results by an average factor of almost three in the region of interest (**Table 2**). More importantly, the guided approach with the neuronavigator was sensitive to functional activation in every session of every subject. Although the low number of subjects limited statistical inferences, results obtained with our proposed neuronavigation protocol suggest that imprecise positioning of fNIRS optodes is an important source of variability in fNIRS that needs to be taken into account.

CONCLUSION

In the present work, we observed that guided measurements with real-time anatomical information can significantly improve the within-subject reproducibility of the fNIRS results. By performing a functional finger-tapping protocol, we found that the within-subject fNIRS reproducibility increased by a factor of two on average. The guided approach also increased the sensitivity of fNIRS measurements to detect the evoked hemodynamic response induced by the finger-tapping task. While the standard experimental approach yielded

heterogeneous activation patterns that vary across subjects and sessions for the same subject, every session acquired with the assistance of the neuronavigation system presented a characteristic hemodynamic response in the contralateral brain hemisphere for all subjects. Although more data are needed to extend the validity of the observed results, the present work brings attention to the fact that proper probe positioning may play an important role in the intra-subject reproducibility of the fNIRS signal.

DATA AVAILABILITY STATEMENT

The datasets generated for this study are available on request to the corresponding author.

ETHICS STATEMENT

The studies involving human participants were reviewed and approved by the Ethics Committee at the University of Campinas. The patients/participants provided their written informed consent to participate in this study.

AUTHOR CONTRIBUTIONS

SN and EF performed the data acquisition, analyzed the data, and wrote and edited the manuscript. NS performed the data acquisition and contributed to the data analysis. JR and S-TW edited the manuscript and contributed to the design and development of the neuronavigation system. AQ and GM contributed on designing the experimental protocol. RM conceived the main idea of the work (including the hypothesis), supervised the data analysis, and edited and wrote the manuscript. All authors discussed the results and contributed to the final edition of the manuscript.

FUNDING

This work was supported by the São Paulo Research Foundation (FAPESP) through 2013/07559-3, 2012/02500-8, 2016/22990-0, 2013/07559-3, and 2019/21962-1; the National Council for Scientific and Technological Development (CNPq) through 142018/2017-1; and the Improvement of Higher Education Personnel (CAPES) through 88882.329008/2019-01.

REFERENCES

Aasted, C. M., Yücel, M. A., Cooper, R. J., Dubb, J., Tsuzuki, D., Becerra, L., et al. (2015). Anatomical guidance for functional near-infrared spectroscopy: atlasviewer tutorial. *Neurophotonics* 2:020801. doi: 10.1117/1.NPh.2.2.020801

Barker, J. W., Aarabi, A., and Huppert, T. J. (2013). Autoregressive model based algorithm for correcting motion and serially correlated errors in fNIRS. *Biomed. Opt. Express* 4, 1366–1379. doi: 10.1364/boe.4.001366

Blasi, A., Lloyd-Fox, S., Johnson, M. H., and Elwell, C. (2014). Test–retest reliability of functional near infrared spectroscopy in infants. *Neurophotonics* 1:025005. doi: 10.1117/1.NPh.1.2.025005

Boas, D. A., Elwell, C. E., Ferrari, M., and Taga, G. (2014). Twenty years of functional near-infrared spectroscopy: introduction for the special issue. *Neuroimage* 85, 1–5. doi: 10.1016/j.neuroimage.2013.11.033

Brigadoi, S., Ceccherini, L., Cutini, S., Scarpa, F., Scatturin, P., Selb, J., et al. (2014). Motion artifacts in functional near-infrared spectroscopy: a comparison of motion correction techniques applied to real cognitive data. *Neuroimage* 85, 181–191. doi: 10.1016/j.neuroimage.2013.04.082

Brown, D. W., Picot, P. A., Naeini, J. G., Springett, R., Delpy, D. T., and Lee, T.-Y. (2002). Quantitative near infrared spectroscopy measurement of cerebral hemodynamics in newborn piglets. *Pediatr. Res.* 51, 564–570. doi: 10.1203/00006450-200205000-00004

Caldwell, M., Scholkmann, F., Wolf, U., Wolf, M., Elwell, C., and Tachtsidis, I. (2016). Modelling confounding effects from extracerebral contamination and systemic factors on functional near-infrared spectroscopy. *Neuroimage* 143, 91–105. doi: 10.1016/j.neuroimage.2016.08.058

Chatrian, G. E., Lettich, E., and Nelson, P. L. (1985). Ten percent electrode system for topographic studies of spontaneous and evoked EEG activities. *Am. J. EEG Technol.* 25, 83–92. doi: 10.1080/00029238.1985.11080163

Cooper, R. J., Selb, J., Gagnon, L., Phillip, D., Schytz, H. W., Iversen, H. K., et al. (2012). A systematic comparison of motion artifact correction techniques for functional near-infrared spectroscopy. *Front. Neurosci.* 6:147. doi: 10.3389/fnins.2012.00147

de Oliveira, S. R., de Paula Machado, A. C. C., de Paula, J. J., de Moraes, P. H. P., Nahin, M. J. S., Magalhães, L., et al. (2017). Association between hemodynamic activity and motor performance in six-month-old full-term and preterm infants: a functional near-infrared spectroscopy study. *Neurophotonics* 5:011016. doi: 10.1117/1.NPh.5.1.011016

de Oliveira, S. R., Machado, A. C. C. P., de Paula, J. J., Novi, S. L., Mesquita, R. C., de Miranda, D. M., et al. (2019). Changes of functional response in sensorimotor cortex of preterm and full-term infants during the first year: an fNIRS study. *Early Hum. Dev.* 133, 23–28. doi: 10.1016/j.earlhumdev.2019.04.007

Dehaes, M., Cheng, H. H., Buckley, E. M., Lin, P.-Y., Ferradal, S., Williams, K., et al. (2015). Perioperative cerebral hemodynamics and oxygen metabolism in neonates with single-ventricle physiology. *Biomed. Opt. Express* 6, 4749–4767. doi: 10.1364/BOE.6.004749

Devor, A., Ulbert, I., Dunn, A. K., Narayanan, S. N., Jones, S. R., Andermann, M. L., et al. (2005). Coupling of the cortical hemodynamic response to cortical and thalamic neuronal activity. *Proc. Natl. Acad. Sci. U.S.A.* 102, 3822–3827. doi: 10.1073/pnas.0407789102

Di Lorenzo, R., Pirazzoli, L., Blasi, A., Bulgarelli, C., Hakuno, Y., Minagawa, Y., et al. (2019). Recommendations for motion correction of infant fNIRS data applicable to data sets acquired with a variety of experimental designs and acquisition systems. *Neuroimage* 200, 511–527. doi: 10.1016/j.neuroimage.2019.06.056

Dravida, S., Noah, J. A., Zhang, X., and Hirsch, J. (2017). Comparison of oxyhemoglobin and deoxyhemoglobin signal reliability with and without global mean removal for digit manipulation motor tasks. *Neurophotonics* 5:011006. doi: 10.1117/1.NPh.5.1.011006

Ferrari, M., and Quaresima, V. (2012). A brief review on the history of human functional near-infrared spectroscopy (fNIRS) development and fields of application. *Neuroimage* 63, 921–935. doi: 10.1016/j.neuroimage.2012.03.049

Forero, E., Novi, S., Avelar, W., Anjos, C., Menko, J., Forti, R., et al. (2017). Use of near-infrared spectroscopy to probe occlusion severity in patients diagnosed with carotid atherosclerotic disease. *Med. Res. Arch.* 5, 1–22. doi: 10.18103/mra.v5i6.1240

Forti, R. M., Favilla, C. G., Cochran, J. M., Baker, W. B., Detre, J. A., Kasner, S. E., et al. (2019). Transcranial optical monitoring of cerebral hemodynamics in acute stroke patients during mechanical thrombectomy. *J. Stroke Cerebrovasc. Dis.* 28, 1483–1494. doi: 10.1016/j.jstrokecerebrovasdis.2019.03.019

Franceschini, M. A., Fantini, S., Thompson, J. H., Culver, J. P., and Boas, D. A. (2003). Hemodynamic evoked response of the sensorimotor cortex measured noninvasively with near-infrared optical imaging. *Psychophysiology* 40, 548–560. doi: 10.1111/1469-8986.00057

Gagnon, L., Cooper, R. J., Yücel, M. A., Perdue, K. L., Greve, D. N., and Boas, D. A. (2012). Short separation channel location impacts the performance of

short channel regression in NIRS. *Neuroimage* 59, 2518–2528. doi: 10.1016/j.neuroimage.2011.08.095

Goodwin, J. R., Gaudet, C. R., and Berger, A. J. (2014). Short-channel functional near-infrared spectroscopy regressions improve when source-detector separation is reduced. *Neurophotonics* 1:015002. doi: 10.1117/1.nph.1.1.015002

Hatakenaka, M., Miyai, I., Mihara, M., Sakoda, S., and Kubota, K. (2007). Frontal regions involved in learning of motor skill-A functional NIRS study. *Neuroimage* 34, 109–116. doi: 10.1016/j.neuroimage.2006.08.014

He, L., Baker, W. B., Busch, D. R., Jiang, J. Y., Lawrence, K. S., Kofke, W. A., et al. (2018). Noninvasive continuous optical monitoring of absolute cerebral blood flow in critically ill adults. *Neurophotonics* 5:045006. doi: 10.1117/1.nph.5.4.045006

Herold, F., Wiegel, P., Scholkmann, F., and Müller, N. (2018). Applications of functional near-infrared spectroscopy (fNIRS) neuroimaging in exercise–cognition science: a systematic, methodology-focused review. *J. Clin. Med.* 7:466. doi: 10.3390/jcm7120466

Huppert, T. J. (2016). Commentary on the statistical properties of noise and its implication on general linear models in functional near-infrared spectroscopy. *Neurophotonics* 3:010401. doi: 10.1117/1.NPh.3.1.010401

Huppert, T. J., Diamond, S. G., Franceschini, M. A., and Boas, D. A. (2009a). HomER: a review of time-series analysis methods for near-infrared spectroscopy of the brain. *Appl. Opt.* 48, 280–298. doi: 10.1016/j.drugalcdep.2008.02.002.A

Huppert, T. J., Jones, P. B., Devor, A., Dunn, A. K., Teng, I. C., Dale, A. M., et al. (2009b). Sensitivity of neural-hemodynamic coupling to alterations in cerebral blood flow during hypercapnia. *J. Biomed. Opt.* 14:044038. doi: 10.1117/1.3210779

Ibrahim, A., Suttie, M., Bulstrode, N. W., Britto, J. A., Dunaway, D., Hammond, P., et al. (2016). Combined soft and skeletal tissue modelling of normal and dysmorphic midface postnatal development. *J. Craniomaxillofac. Surg.* 44, 1777–1785. doi: 10.1016/j.jcms.2016.08.020

Joseph, D. K., Huppert, T. J., Franceschini, M. A., and Boas, D. A. (2006). Diffuse optical tomography system to image brain activation with improved spatial resolution and validation with functional magnetic resonance imaging. *Appl. Opt.* 45, 8142–8151. doi: 10.1364/AO.45.008142

Kakimoto, Y., Nishimura, Y., Hara, N., Okada, M., Tanii, H., and Okazaki, Y. (2009). Intrasubject reproducibility of prefrontal cortex activities during a verbal fluency task over two repeated sessions using multi-channel near-infrared spectroscopy. *Psychiatry Clin. Neurosci.* 63, 491–499. doi: 10.1111/j.1440-1819.2009.01988.x

Kim, M. N., Durduran, T., Frangos, S., Edlow, B. L., Buckley, E. M., Moss, H. E., et al. (2010). Noninvasive measurement of cerebral blood flow and blood oxygenation using near-infrared and diffuse correlation spectroscopies in critically brain-injured adults. *Neurocrit. Care* 12, 173–180. doi: 10.1007/s12028-009-9305-x

Kim, M. N., Edlow, B. L., Durduran, T., Frangos, S., Mesquita, R. C., Levine, J. M., et al. (2014). Continuous optical monitoring of cerebral hemodynamics during head-of-bed manipulation in brain-injured adults. *Neurocrit. Care* 20, 443–453. doi: 10.1007/s12028-013-9849-7

Kirilina, E., Jelzow, A., Heine, A., Niessing, M., Wabnitz, H., Brühl, R., et al. (2012). The physiological origin of task-evoked systemic artefacts in functional near infrared spectroscopy. *Neuroimage* 61, 70–81. doi: 10.1016/j.neuroimage.2012.02.074

Kirlilna, E., Yu, N., Jelzow, A., Wabnitz, H., Jacobs, A. M., and Tachtsidis, L. (2013). Identifying and quantifying main components of physiological noise in functional near infrared spectroscopy on the prefrontal cortex. *Front. Hum. Neurosci.* 7:864. doi: 10.3389/fnhum.2013.00864

Klem, G. H., Lüders, H. O., Jasper, H. H., and Elger, C. (1958). The ten twenty electrode system: international federation of societies for electroencephalography and clinical neurophysiology. *Electroencephalogr. Clin. Neurophysiol.* 10, 370–375.

Kono, T., Matsuo, K., Tsunashima, K., Kasai, K., Takizawa, R., Rogers, M. A., et al. (2007). Multiple-time replicability of near-infrared spectroscopy recording during prefrontal activation task in healthy men. *Neurosci. Res.* 57, 504–512. doi: 10.1016/j.neures.2006.12.007

McKendrick, R., Parasuraman, R., Murtza, R., Formwalt, A., Baccus, W., Paczynski, M., et al. (2016). Into the wild: neuroergonomic differentiation of hand-held and augmented reality wearable displays during outdoor navigation with functional near infrared spectroscopy. *Front. Hum. Neurosci.* 10:216. doi: 10.3389/fnhum.2016.00216

Mesquita, R. C., Franceschini, M. A., and Boas, D. A. (2010). Resting state functional connectivity of the whole head with near infrared spectroscopy. *Biomed. Opt. Express* 1, 324–336. doi: 10.1364/BOE.1.000324

Mesquita, R. C., Huppert, T. J., and Boas, D. A. (2009). Exploring neuro-vascular and neuro-metabolic coupling in rat somatosensory cortex. *Phys. Med. Biol.* 54, 175–185. doi: 10.1088/0031-9155/54/2/001

Molavi, B., and Dumont, G. A. (2012). Wavelet-based motion artifact removal for functional near-infrared spectroscopy. *Physiol. Meas.* 33, 259–270. doi: 10.1088/0967-3334/33/2/259

Niu, H., Li, Z., Liao, X., Wang, J., Zhao, T., Shu, N., et al. (2013). Test-retest reliability of graph metrics in functional brain networks: a resting-state fNIRS study. *PLoS One* 8:e72425. doi: 10.1371/journal.pone.0072425

Novi, S. L., Aparecido da Rocha, W. A., Carvalho, A. D. C., Scavariello, G. H., Forti, R. M., Guiroga Soto, A. F., et al. (2018). Desenvolvimento de novos métodos para investigação do cérebro durante o estado de repouso. *Rev. Bras. Fís. Méd.* 11:33. doi: 10.29384/rbfm.2017.v11.n3.p33

Novi, S. L., Roberts, E., Spagnuolo, D., Spilsbury, B. M., Price, D. C., Imbalzano, C. A., et al. (2020). Functional near-infrared spectroscopy for speech protocols: characterization of motion artifacts and guidelines for improving data analysis. *Neurophotonics* 7:015001. doi: 10.1117/1.NPh.7.1.015001

Novi, S. L., Rodrigues, R. B. M. L., and Mesquita, R. C. (2016). Resting state connectivity patterns with near-infrared spectroscopy data of the whole head. *Biomed. Opt. Express* 7, 2524–2537. doi: 10.1364/BOE.7.002524

Obrig, H., Israel, H., Kohl-Bareis, M., Uludag, K., Wenzel, R., Muüller, B., et al. (2002). Habituation of the visually evoked potential and its vascular response: implications for neurovascular coupling in the healthy adult. *Neuroimage* 17, 1–18. doi: 10.1006/nimg.2002.1177

Obrig, H., Wenzel, R., Kohl, M., Horst, S., Wobst, P., Steinbrink, J., et al. (2000). Near-infrared spectroscopy: does it function in functional activation studies of the adult brain? *Int. J. Psychophysiol.* 35, 125–142. doi: 10.1016/s0167-8760(99)00048-3

Ou, W., Nissilä, I., Radhakrishnan, H., Boas, D. A., Hämäläinen, M. S., and Franceschini, M. A. (2009). Study of neurovascular coupling in humans via simultaneous magnetoencephalography and diffuse optical imaging acquisition. *Neuroimage* 46, 624–632. doi: 10.1016/j.neuroimage.2009.03.008

Pfeifer, M. D., Scholkmann, F., and Labruyère, R. (2018). Signal processing in functional near-infrared spectroscopy (fNIRS): methodological differences lead to different statistical results. *Front. Hum. Neurosci.* 11:641. doi: 10.3389/fnhum.2017.00641

Phillips, A. A., Chan, F. H., Zheng, M. M. Z., Krassioukov, A. V., and Ainslie, P. N. (2015). Neurovascular coupling in humans: physiology, methodological advances and clinical implications. *J. Cereb. Blood Flow Metab.* 36, 647–664. doi: 10.1177/0271678X15617954

Pinti, P., Aichelburg, C., Gilbert, S., Hamilton, A., Hirsch, J., Burgess, P., et al. (2018). A review on the use of wearable functional near-infrared spectroscopy in naturalistic environments. *Jpn. Psychol. Res.* 60, 347–373. doi: 10.1111/jpr.12206

Pinti, P., Merla, A., Aichelburg, C., Lind, F., Power, S., Swingler, E., et al. (2017). A novel GLM-based method for the automatic identification of functional events (AIDE) in fNIRS data recorded in naturalistic environments. *Neuroimage* 155, 291–304. doi: 10.1016/j.neuroimage.2017.05.001

Pinti, P., Scholkmann, F., Hamilton, A., Burgess, P., and Tachtsidis, I. (2019). Current status and issues regarding pre-processing of fNIRS neuroimaging data: an investigation of diverse signal filtering methods within a general linear model framework. *Front. Hum. Neurosci.* 12:505. doi: 10.3389/fnhum.2018.00505

Piper, S. K., Krueger, A., Koch, S. P., Mehnert, J., Habermehl, C., Steinbrink, J., et al. (2014). A wearable multi-channel fNIRS system for brain imaging in freely moving subjects. *Neuroimage* 85, 64–71. doi: 10.1016/j.neuroimage.2013.06.062

Plichta, M. M., Herrmann, M. J., Baehne, C. G., Ehlis, A. C., Richter, M. M., Pauli, P., et al. (2007). Event-related functional near-infrared spectroscopy (fNIRS)

based on craniocerebral correlations: reproducibility of activation? *Hum. Brain Mapp.* 28, 733–741. doi: 10.1002/hbm.20303

Quaresima, V., and Ferrari, M. (2019). Functional near-infrared spectroscopy (fNIRS) for assessing cerebral cortex function during human behavior in natural/social situations: a concise review. *Organ. Res. Methods* 22, 46–68. doi: 10.1177/1094428116658959

Rovati, L., Salvatori, G., Bulf, L., and Fonda, S. (2007). Optical and electrical recording of neural activity evoked by graded contrast visual stimulus. *Biomed. Eng. Online* 6:28. doi: 10.1186/1475-925X-6-28

Rubianes Silva, J. A. I. (2017). *Multimodal Visualization of Electrophysiological Signals and Anatomical Magnetic Resonance Images*. Available online at: http://repositorio.unicamp.br/jspui/handle/REPOSIP/330733 (accessed July 10, 2020).

Santosa, H., Huppert, T. J., Santosa, H., Fishburn, F., Zhai, X., and Huppert, T. J. (2019). Investigation of the sensitivity-specificity of canonical- and deconvolution-based linear models in evoked functional near-infrared spectroscopy. *Neurophotonics* 6:025009. doi: 10.1117/1.NPh.6.2.025009

Sato, T., Nambu, I., Takeda, K., Aihara, T., Yamashita, O., Isogaya, Y., et al. (2016). Reduction of global interference of scalp-hemodynamics in functional near-infrared spectroscopy using short distance probes. *Neuroimage* 141, 120–132. doi: 10.1016/j.neuroimage.2016.06.054

Schecklmann, M., Ehlis, A.-C., Plichta, M. M., and Fallgatter, A. J. (2008). Functional near-infrared spectroscopy: a long-term reliable tool for measuring brain activity during verbal fluency. *Neuroimage* 43, 147–155. doi: 10.1016/j.neuroimage.2008.06.032

Scholkmann, F., Spichtig, S., Muehlemann, T., and Wolf, M. (2010). How to detect and reduce movement artifacts in near-infrared imaging using moving standard deviation and spline interpolation. *Physiol. Meas.* 31, 649–662. doi: 10.1088/0967-3334/31/5/004

Sforza, C., and Ferrario, V. (2006). Soft-tissue facial anthropometry in three dimensions: from anatomical landmarks to digital morphology in research, clinics and forensic anthropology. *J. Anthropol. Sci.* 84, 97–124.

Sitaram, R., Caria, A., and Birbaumer, N. (2009). Hemodynamic brain-computer interfaces for communication and rehabilitation. *Neural Netw.* 22, 1320–1328. doi: 10.1016/j.neunet.2009.05.009

Souza, V., Matsuda, R., Peres, A., Amorim, P., Moraes, T., Silva, J., et al. (2019). InVesalius navigator, a free and open-source software for navigated transcranial magnetic stimulation. *Brain Stimul.* 12:571. doi: 10.1016/j.brs.2018.12.894

Souza, V. H., Matsuda, R. H., Peres, A. S. C., Amorim, P. H. J., Moraes, T. F., Silva, J. V. L., et al. (2018). Development and characterization of the InVesalius navigator software for navigated transcranial magnetic stimulation. *J. Neurosci. Methods* 309, 109–120. doi: 10.1016/j.jneumeth.2018.08.023

Strait, M., and Scheutz, M. (2014). What we can and cannot (yet) do with functional near infrared spectroscopy. *Front. Neurosci.* 8:117. doi: 10.3389/fnins.2014.00117

Tachtsidis, I., and Scholkmann, F. (2016). False positives and false negatives in functional near-infrared spectroscopy: issues, challenges, and the way forward. *Neurophotonics* 3:031405. doi: 10.1117/1.NPh.3.3.031405

Terborg, C., Bramer, S., Harscher, S., Simon, M., and Witte, O. W. (2004). Bedside assessment of cerebral perfusion reductions in patients with acute ischaemic stroke by near-infrared spectroscopy and indocyanine green. *J. Neurol. Neurosurg. Psychiatry* 75, 38–42.

Tsuji, M., Saul, J. P., du Plessis, A., Eichenwald, E., Sobh, J., Crocker, R., et al. (2000). Cerebral intravascular oxygenation correlates with mean arterial pressure in critically Ill premature infants. *Pediatrics* 106, 625–632. doi: 10.1542/peds.106.4.625

Watanabe, A., Matsuo, K., Kato, N., and Kato, T. (2003). Cerebrovascular response to cognitive tasks and hyperventilation measured by multi-channel near-infrared spectroscopy. *J. Neuropsychiatry Clin. Neurosci.* 15, 442–449. doi: 10.1176/jnp.15.4.442

Wiggins, I. M., Anderson, C. A., Kitterick, P. T., and Hartley, D. E. H. (2016). Speech-evoked activation in adult temporal cortex measured using functional near-infrared spectroscopy (fNIRS): are the measurements reliable? *Hear. Res.* 339, 142–154. doi: 10.1016/j.heares.2016.07.007

Wu, S. T., Abrantes, M., Tost, D., and Batagelo, H. C. (2003). "Picking and snapping for 3D input devices," in *Proceedings of the Brazilian Symposium of Computer Graphic and Image Processing*, Brazil. doi: 10.1109/SIBGRA.2003.1241002

Wu, S. T., Vidalón, J. E. Y., and De Souza Watanabe, L. (2011). "Snapping a cursor on volume data," in *Proceedings of the 24th SIBGRAPI Conference on Graphics, Patterns and Images*, Brazil. doi: 10.1109/SIBGRAPI.2011.32

Yousry, T. A., Schmid, U. D., Alkadhi, H., Schmidt, D., Peraud, A., Buettner, A., et al. (1997). Localization of the motor hand area to a knob on the precentral gyrus. A new landmark. *Brain* 120, 141–157. doi: 10.1093/brain/120.1.141

Yücel, M. A., Selb, J., Aasted, C. M., Lin, P.-Y., Borsook, D., Becerra, L., et al. (2016). Mayer waves reduce the accuracy of estimated hemodynamic response functions in functional near-infrared spectroscopy. *Biomed. Opt. Express* 7, 3078–3088. doi: 10.1364/BOE.7.003078

Yücel, M. A., Selb, J., Aasted, C. M., Petkov, M. P., Becerra, L., Borsook, D., et al. (2015). Short separation regression improves statistical significance and better localizes the hemodynamic response obtained by near-infrared spectroscopy for tasks with differing autonomic responses. *Neurophotonics* 2:035005. doi: 10.1117/1.NPh.2.3.035005

Zhang, H., Duan, L., Zhang, Y.-J., Lu, C.-M., Liu, H., and Zhu, C.-Z. (2011). Test-retest assessment of independent component analysis-derived resting-state functional connectivity based on functional near-infrared spectroscopy. *Neuroimage* 55, 607–615. doi: 10.1016/j.neuroimage.2010.12.007

Conflict of Interest: The authors declare that the research was conducted in the absence of any commercial or financial relationships that could be construed as a potential conflict of interest.

Copyright © 2020 Novi, Forero, Rubianes Silva, de Souza, Martins, Quiroga, Wu and Mesquita. This is an open-access article distributed under the terms of the Creative Commons Attribution License (CC BY). The use, distribution or reproduction in other forums is permitted, provided the original author(s) and the copyright owner(s) are credited and that the original publication in this journal is cited, in accordance with accepted academic practice. No use, distribution or reproduction is permitted which does not comply with these terms.

frontiers in Human Neuroscience

ORIGINAL RESEARCH
published: 08 October 2020
doi: 10.3389/fnhum.2020.523456

Prefrontal Responses to Odors in Individuals With Autism Spectrum Disorders: Functional NIRS Measurement Combined With a Fragrance Pulse Ejection System

*Mingdi Xu[1,2], Yasuyo Minagawa[1,2,3], Hirokazu Kumazaki[4], Ken-ichi Okada[5] and Nozomi Naoi[3,6]**

[1] Faculty of Letters, Keio University, Tokyo, Japan, [2] Center of Life-Span Development of Communication Skills, Keio University, Yokohama, Japan, [3] Global Centre for Advanced Research on Logic and Sensibility, Keio University, Tokyo, Japan, [4] National Center of Neurology and Psychiatry, Tokyo, Japan, [5] Faculty of Science and Technology, Keio University, Yokohama, Japan, [6] Division of Arts and Sciences, College of Liberal Arts, International Christian University, Tokyo, Japan

Individuals with autism spectrum disorders (ASD) are impaired not only in social competencies but also in sensory perception, particularly olfaction. The olfactory ability of individuals with ASD has been examined in several psychophysical studies, but the results have been highly variable, which might be primarily due to methodological difficulties in the control of odor stimuli (e.g., the problem of lingering scents). In addition, the neural correlates of olfactory specificities in individuals with ASD remain largely unknown. To date, only one study has investigated this issue using functional magnetic resonance imaging (fMRI). The present study utilized a sophisticated method—a pulse ejection system—to present well-controlled odor stimuli to participants with ASD using an ASD-friendly application. With this advantageous system, we examined their odor detection, identification, and evaluation abilities and measured their brain activity evoked by odors using functional near-infrared spectroscopy (fNIRS). As the odor detection threshold (DT) of participants with ASD was highly variable, these participants were divided into two groups according to their DT: an ASD-Low DT group and an ASD-High DT group. Behavioral results showed that the ASD-High DT group had a significantly higher DT than the typically developing (control) group and the ASD-Low DT group, indicating their insensitivity to the tested odors. In addition, while there was no significant difference in the odor identification ability between groups, there was some discrepancy between the groups' evaluations of odor pleasantness. The brain data identified, for the first time, that neural activity in the right dorsolateral prefrontal cortex (DLPFC) was significantly weaker in the ASD-High DT group than in the control group. Moreover, the strength of activity in the right DLPFC was negatively correlated with the DT. These findings suggest that participants with ASD have impairments in the higher-order function of olfactory processing, such as olfactory working memory and/or attention.

Keywords: autism spectrum disorders (ASD), olfactory function, working memory, attention, detection threshold, dorsolateral prefrontal cortex (DLPFC), functional near-infrared spectroscopy (fNIRS)

OPEN ACCESS

Edited by:
Filippo Brighina, University of Palermo, Italy

Reviewed by:
Eleonora Vecchio, University of Bari Aldo Moro, Italy
Pengfei Han, Southwest University, China

***Correspondence:**
Nozomi Naoi
nnaoi@icu.ac.jp

Specialty section:
This article was submitted to Cognitive Neuroscience, a section of the journal Frontiers in Human Neuroscience

Received: *29 December 2019*
Accepted: *16 September 2020*
Published: *08 October 2020*

Citation:
Xu M, Minagawa Y, Kumazaki H, Okada K and Naoi N (2020) Prefrontal Responses to Odors in Individuals With Autism Spectrum Disorders: Functional NIRS Measurement Combined With a Fragrance Pulse Ejection System. Front. Hum. Neurosci. 14:523456. doi: 10.3389/fnhum.2020.523456

INTRODUCTION

Individuals with autism spectrum disorders (ASD) generally have unusual sensory awareness, showing either hyper- or hypo-responsiveness to various sensory modalities, including olfaction (Kientz and Dunn, 1997; Rogers et al., 2003; Rogers and Ozonoff, 2005; Schreck and Williams, 2006; Ben-Sasson et al., 2009; Wiggins et al., 2009). Accumulating evidence indicates that individuals with ASD experience more sensory disturbances than typically developing (TD) individuals or individuals with intellectual disabilities (Leekam et al., 2007; Tomchek and Dunn, 2007). Particularly, an aberrant response to smell has been repeatedly reported in the ASD population (Schecklmann et al., 2013; Martin and Daniel, 2014; Rozenkrantz et al., 2015; Endevelt-Shapira et al., 2018) and has been suggested as a prominent criterion for distinguishing individuals with ASD from those with other developmental disorders (Rogers et al., 2003; Leekam et al., 2007; Schoen et al., 2009).

Sensory Psychophysical Studies of Olfactory Perception in ASD

Previous studies have found that over 50% of sampled children with ASD had unusual smell and/or taste sensitivity (Schoen et al., 2009; Lane et al., 2010). Moreover, olfactory problems have been suggested to be a good predictor of social deficiency in individuals with ASD (Liss et al., 2006; Bennetto et al., 2007; Hilton et al., 2007; Lane et al., 2010), and olfactory alterations have been suggested as an early marker for ASD (Brewer et al., 2006; Hrdlicka et al., 2011).

Odor is a very powerful sensory modality, capable of eliciting strong emotional reactions (Soudry et al., 2011) and episodic memory (Saive et al., 2014) in humans and can serve as a potent cue for both social and cognitive development in children with ASD (Parma et al., 2013; Woo et al., 2015). Despite its importance, relatively few studies have investigated the sense of smell in individuals with ASD. Moreover, these studies have reported conflicting results across a variety of domains. Specifically, several studies found that individuals with ASD are impaired in the ability to identify odors (Suzuki et al., 2003; Bennetto et al., 2007; May et al., 2011; Galle et al., 2013; Wicker et al., 2016) compared with TD individuals, while other studies did not find a significant difference between the two groups (Brewer et al., 2008; Dudova et al., 2011; Addo et al., 2017). Similarly, some studies suggested preserved odor sensitivity in individuals with ASD (Suzuki et al., 2003; Tavassoli and Baron-Cohen, 2012; Galle et al., 2013; Addo et al., 2017), whereas other studies reported either enhanced (Ashwin et al., 2014) or decreased odor sensitivity (Dudova et al., 2011; Kumazaki et al., 2016). In addition, Hrdlicka et al. (2011) found atypical hedonic responses to odor stimuli in individuals with ASD; however, Galle et al. (2013) and Addo et al. (2017) did not find such responses. Likewise, while Kumazaki et al. (2019) demonstrated decreased odor adaptation in children with ASD as compared to TD children, Tavassoli and Baron-Cohen (2012) reported similar odor adaptation in adults with ASD and TD adults. This is in contrast to the well-established literature on abnormalities in vision (Simmons et al., 2009), audition (O'Connor, 2012), and touch (Puts et al., 2014) in individuals with ASD.

The discrepancies between studies might be due to many factors including large variability in participants' age (from childhood to adulthood) and ASD subtype [e.g., high functioning autism (HFA), Asperger's syndrome (AS), and pervasive developmental disorder (PDD)], as well as in tests [e.g., Sniffin' Sticks (Hummel et al., 1997), University of Pennsylvania Smell Identification Test (UPSIT; Doty et al., 1984b), alcohol sniff test (AST; Davidson and Murphy, 1997), and custom-made tests] and/or odors used (e.g., n-butanol, alcohol, custom-made), making direct comparison difficult.

Neuroimaging Studies of Olfaction in ASD

Studies of sensory perception in ASD have predominantly investigated auditory and visual differences in individuals with ASD while olfactory differences are least studied (Martin and Daniel, 2014; Kumazaki et al., 2019), particularly at the neural level.

Non-invasive neuroimaging modalities such as magnetic resonance imaging (MRI) have expanded the knowledge of olfactory dysfunction in humans (Han et al., 2019). Anatomically, dysfunction in areas often implicated in ASD, such as the orbitofrontal and medial temporal areas including the amygdala, may be responsible for olfactory deficits (Amaral et al., 2008; Stanfield et al., 2008; Tonacci et al., 2017). In addition, a bioinformatics study exploring the genetic heterogeneity of olfaction in individuals with ASD suggested that four brain regions are critically related to ASD pathogenesis: the olfactory bulb, occipital lobe, prefrontal cortex, and pituitary (Kumar et al., 2011).

Functional neuroimaging studies investigating the neural basis of olfactory processing in individuals with ASD are scarce. To the best of our knowledge, only two recent functional MRI (fMRI) studies have probed the neural responses of individuals with ASD to odors (Koehler et al., 2018; Stickel et al., 2019). Koehler et al. (2018) examined the neural response of participants with ASD (18 participants aged 29.5 $\pm$ 2.51 years with HFA and AS; two women) to odor detection and identification in the olfactory cortex including the piriform cortex, amygdala, and orbitofrontal cortex (OFC). They found impaired odor detection and odor identification in participants with ASD and reported, for the first time, significantly attenuated odor-induced brain response in the piriform cortex as well as a trend toward decreased activity in the OFC in participants with ASD compared to TD controls. Stickel et al. (2019) did not directly examine brain function in individuals with ASD in response to odors; instead, they investigated olfactory- and auditory-visual integration (essentially multisensory integration). Similar neural networks, including the medial and inferior frontal cortices, were found to be involved in the multisensory integration processes, which were not significantly different between participants with ASD and their matched TD counterparts.

With functional near-infrared spectroscopy (fNIRS), much knowledge has been accumulated about sensory perception,

including olfactory processing (Ishimaru et al., 2004a,b; Harada et al., 2006; Kobayashi et al., 2009; Takakura et al., 2011). For example, Ishimaru et al. (2004a,b), Harada et al. (2006), and Kobayashi et al. (2009) reported activation (increased oxy-Hb concentration) of the most anterior part of the prefrontal areas in response to olfactory stimuli and suggested that such hemodynamic responses might reflect activity in the OFC corresponding to the secondary olfactory cortex (Zatorre et al., 1992; Saive et al., 2014). Similar prefrontal activity, primarily in the frontal pole (FP) and dorsolateral prefrontal cortex (DLPFC), was reported by Takakura et al. (2011) and was suggested to indicate attention and working memory related to the odor detection task. Nevertheless, an important knowledge gap remains, in that none of these fNIRS studies included individuals with ASD in spite of its amenability to the ASD population.

Considering abnormality in executive functions including attention and working memory in individuals with ASD (Russell, 1997; Hill, 2004; Kenworthy et al., 2008; Travers et al., 2011), it is possible that their brain activity in the region responsible for these functions (i.e., the DLPFC; Duncan and Owen, 2000; Levy and Goldman-Rakic, 2000) is different from that of TD individuals in tasks requiring executive functions. This possibility might also partially account for the olfactory hyposensitivity in younger individuals with ASD, which was found in the meta-analysis of Larsson et al. (2017). This analysis has suggested that younger individuals with ASD (<30 years) tend to show olfactory hyposensitivity, whereas older individuals with ASD (>35 years) do not. Since the development of prefrontal region continues until early adulthood (Diamond, 2002), the immaturity of this region in younger individuals with ASD may result in their olfactory hyposensitivity.

Heterogeneity in Odor Sensitivity in Individuals With ASD and Methodological Obstacles to Olfactory Stimulation

Autism spectrum disorders is characterized by a high degree of heterogeneity across individuals (Jeste and Geschwind, 2014). In addition to the large variability in individuals' intelligence and their sensory and attentional capacities, neuroimaging studies have demonstrated heterogeneity in both structural and functional brain abnormalities among individuals with ASD (Anagnostou and Taylor, 2011; Dichter, 2012). It is possible that, apart from methodological discrepancies, divergent findings among studies investigating olfactory perception in individuals with ASD might be due to a complex blend of these factors. When assessing odor-evoked neural responsiveness in individuals with ASD, it is fundamental to assess whether and to what degree the used odors can be actually perceived. Thus, to evaluate functionality of the olfactory system, it is critical to examine the odor detection threshold (DT) of each participant. In fact, Koehler et al. (2018) tested odor detection and identification abilities in ASD participants before scanning sessions but did not directly correlate these datasets.

As mentioned above, the investigation of olfactory perception in individuals with ASD has yielded inconsistent results, and methodological obstacles might be one of the most significant reasons for such results. Most of these studies have used UPSIT, AST, and Sniffin' Sticks, for which control of odor granularity is challenging due to the problem of lingering scents (Fukasawa et al., 2013). As olfaction is a highly adaptable sensory modality, measurements of olfactory ability can be compromised when the odor stimuli remain in the air (Kumazaki et al., 2016). In addition, prolonged odor exposure will lead to odor adaptation, which decreases the measurement accuracy (Dalton and Wysocki, 1996). To solve these problems, we developed the Fragrance Jet for Medical Checkup (Keio University) that uses a pulse ejection system (Fukasawa et al., 2013) and which has been reliably standardized and successfully used in our previous work (Kumazaki et al., 2016, 2018a,b, 2019). It employs an identical technique as a basic inkjet printer, using a very small quantity of an odorant to emit tiny droplets of scent. This technique can be fine-tuned with respect to the amount and time of exposure to reduce lingering scents, allowing precise assessment of the olfactory function. More specifically, by modulating the number of simultaneous ejections (NSE), the ejection quantity per unit time (EQUT) can be adjusted, which, together with the ejection time (ET), determines the intensity of ejected odor (please see Fukasawa et al., 2013 for details). Instead of preparing various concentrations of scent beforehand as in conventional olfactory measurement techniques, our approach makes measurement by only changing the NSE. Using a very small quantity of an odor reduces lingering scents and avoids odor adaptation (Sato et al., 2008), which is an important confounding factor during the assessment of olfaction. However, because many parts of the instrument are metal, this type of instrument cannot be used with fMRI scanning but can be combined with fNIRS.

To address the aforementioned issues, the present study uses fNIRS to investigate cerebral activation in olfactory processing in young adults with ASD and TD young adults. The primary aim of this study was to examine the feasibility of combined usage of a fragrance pulse ejection system for presenting odor stimuli with fNIRS system. The secondary aim was to reveal differential functions of the prefrontal region in odor processing in participants with ASD and TD participants by carefully examining the relationship between odor sensitivity and associated neuronal responses in participants with ASD. We predict that both odor perception and odor-induced neural function are impaired in participants with ASD and that their brain activity is correlated with their odor sensitivity.

MATERIALS AND METHODS

Participants

The present study was approved by the ethics committee of the Keio University, Faculty of Letters (No. 16028). The participants were young adults with ASD and TD young adults. Twenty-five participants with ASD (19 males, 18–24 years old, mean age: 20.50 years) and 16 TD participants (13 males, 19–24 years old, mean age: 21.33 years) volunteered for the study. The exclusion criteria for both participants with ASD and TD participants included organic smell disturbance, nasal problems, diagnosed psychiatric conditions, and a history of head injury. After a

complete explanation of the study, all volunteers and their parents agreed to participate in the study and provided written informed consent.

The participants with ASD were diagnosed by psychiatrists using the Diagnostic and Statistical Manual of Mental Disorders (DSM-5; American Psychiatric Association, 2013) criteria and the standardized criteria taken from the Diagnostic Interview for Social and Communication Disorders (DISCO; Leekam et al., 2002) at the time of enrollment in the study. The TD participants had no history or evidence of ASD, but they were tested for autism traits using autism spectrum quotient (AQ; Baron-Cohen et al., 2001). The psychiatrists also categorized participants with ASD into three subtypes based on DISCO: AS, autistic disorder (AD), and pervasive developmental disorder not otherwise specified (PDD-NOS; see **Table 1**).

To assess autistic traits of participants with ASD, the Childhood Autism Rating Scale-Tokyo Version (CARS-TV) was used. The CARS-TV is the Japanese version of the CARS (Schopler et al., 1980)—one of the most widely used scales to evaluate the degree and profiles of autism in children—which has been shown to have satisfactory reliability and validity (Kurita et al., 1989; Tachimori et al., 2003). We did not use AQ for participants with ASD because it chiefly examines autistic tendency in neurotypical individuals. In addition, as CARS data for the ASD groups had been provided to us, we refrained from applying further questionnaires to them to avoid taking them too much time.

Intelligence testing in both participants with ASD and TD participants was performed using the Wechsler Intelligence Scale for Children—Fourth Edition (WISC-IV; Wechsler, 2003) or Wechsler Adult Intelligence Scale—Third Edition (WAIS-III; Dumont and Willis, 2008). We did not obtain IQ from one participant with ASD due to his low motivation. In addition, both participants with ASD and TD participants were tested for their perceptual traits using a sensory profile (Dunn et al., 1999). The participants' demographic information is shown in **Table 1**.

Procedure

Both the participants with ASD and the TD participants completed an olfactory measurement session that included assessment of odor DT, odor identification, and odor evaluation. The participants subsequently received an fNIRS assessment, after which they underwent odor identification and evaluation again. The details of the procedure can be seen in **Figure 1**.

Olfactory Measurement

Odor Presentation

Two types of odors were used for each olfactory measurement: a simple chemical β-phenylethyl alcohol that smells like rose and a natural fragrance of mint. Odorants were diluted to 5% using water and little ethanol to adjust their adhesiveness. In our preliminary experiment, we tried many odors and found that the odors of rose and mint were most suitable for obtaining consistent brain responses from participants, which is important for the success of the fNIRS experiment. The experiment room was well-ventilated to prevent lingering scents. Olfactory measurements were performed using an olfactory display (**Figure 2A**), which uses a pulse ejection system (Fukasawa et al., 2013) and can measure and quantify odor DT with high precision. It uses an ejection head to produce scent droplets from tiny holes. The device has one large tank and three small tanks. We used the large tank for DT measurement and the small tanks for odor identification and odor evaluation measurements. There are 255 tiny holes in the ejection head connected to the large tank and 127 tiny holes in the head connected to the small tanks. These tiny holes can emit scents simultaneously. The average ejection quantity from a single hole was referred to as the unit average ejection quantity, which is 7.3 pL for the large tank and 4.7 pL for the small tanks. The intensity of ejected odor is determined by two parameters: EQUT and ET. The EQUT can be adjusted by modulating the NSE ($0 \sim 255$ for the large tank, and $0 \sim 127$ for the small tanks). Ejections can be controlled in pulses of 667 μs; ET determines the number of ejected pulses (ET/667; please see Fukasawa et al., 2013 for details). Participants sat in front of the pulse ejection system from a distance of approximately 20 cm (**Figure 3B**).

Odor DT

The task was designed to be as simple as possible so that participants with ASD could concentrate and complete the measurement without making verbal responses. To this end, we used a game-like application developed in our previous work (Matsuura et al., 2014) to perform the experiment using a touch panel (**Figure 2B**). In each trial, three boxes were shown on the display of the touch panel, each of which contained an odor stimulus. The three stimuli were arranged pseudo-randomly; one stimulus was scented while the other two were odorless. When the participants clicked one of the three boxes, an odor was emitted 3.0 s later. The participants were allowed to click each box up to two times and were asked to identify the box that contained the odor stimulus (triple forced-choice). Before measurement, we confirmed that all participants understood the instructions. Based on the results of preliminary tests and our earlier studies (Fukasawa et al., 2013; Kumazaki et al., 2016), we began the measurement with an NSE of 60 and an ET of 200 ms. A specific measurement algorithm that employs a binary search (Fukasawa et al., 2013; Kumazaki et al., 2019) was used to determine the participants' DT (**Supplementary Figure 1**). For the first trial, when a participant made an error (selecting a box that contained an odorless stimulus), the NSE increased by 50%; once two consecutive trials were successful, the NSE decreased by 50%. For the rest of the trials, the increment or decrement unit of the NSE was 10. The maximum and minimum values of NSE were 120 and 10, respectively. These values were also based on the results of preliminary tests and our earlier study on olfaction in individuals with ASD using the same odor presentation device (Kumazaki et al., 2019). All participants' measurements were completed in approximately 5 min. The DT was generated after the procedure was completed. This odor DT test was conducted once for both rose and mint odors.

Odor Identification and Odor Evaluation

There were two sessions for measuring odor identification and odor evaluation: the olfactory measurement session and the

TABLE 1 | Descriptive characteristics of the ASD and control (TD) groups.

Characteristics	ASD-Low DT (n = 12) (ME, SD)	ASD-High DT (n = 13) (ME, SD)	Control (n = 13) (ME, SD)	Statistics
Age in years	19.8 (1.7)	19.9 (2.0)	20.6 (1.7)	$F(2,35) = 0.889$, $p = 0.42$
Gender (M:F)	9:3	10:3	10:3	χ^2 (2) = 0.017, $p = 0.99$
Type of ASD	1 AD, 7 AS, 4 PDD-NOS	3AD, 1 AS, 9 PDD-NOS		
Full scale IQ	77.8 (10.8)	65.2 (12.7)	115.9 (7.6)	$F(2,35) = 79.83$, $p < 0.001$ Control vs. ASD-Low DT: $p < 0.001$ Control vs. ASD-High DT: $p < 0.001$ ASD-Low DT vs. ASD-High DT: $p = 0.018$
AQ-J			17.5 (9.6)	
CARS-TV	32.7 (2.0)	31.8 (2.7)		t (23) = 0.945, $p = 0.36$
DT				See section "Behavior Results"
Rose	49.2 (7.0)	108.5 (6.7)	39.2 (6.7)	
Mint	27.5 (16.0)	82.3 (49.9)	28.5 (17.7)	
Mean	38.3 (9.4)	95.4 (20.4)	33.9 (15.8)	
				Two-way ANOVA: Main effect of odor: $F(1,35) = 6.51$, $p = 0.02$ Rose > Mint Main effect of group: $F(2,35) = 59.24$, $p < 0.001$ ASD-High DT > Control ($p < 0.001$) ASD High-DT > ASD Low-DT ($p < 0.001$) No interaction: $F(2,35) = 0.37$, $p = 0.70$

ASD, autism spectrum disorders; TD, typical development; DT, odor detection threshold; ME, mean; SD, standard deviation; Parentheses indicate SD. M, male; F, female; AD, autistic disorder; AS, Asperger's syndrome; PDD-NOS, pervasive developmental disorder not otherwise specified; IQ, intelligence quotient. We did not obtain IQ from one participant with ASD due to his low motivation; AQ-J, autism spectrum quotient, Japanese version. Higher scores indicate a greater number of ASD-specific behaviors; CARS-TV, Childhood Autism Rating Scale-Tokyo Version. Higher scores indicate high autistic symptoms.

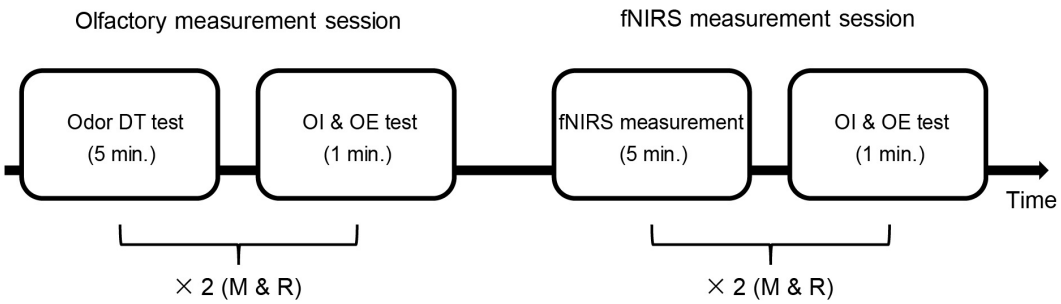

FIGURE 1 | Time sequence of the whole experiment. There were two sessions: the olfactory measurement session and the fNIRS measurement session. The olfactory measurement session included an odor detection threshold (DT) test and an odor identification (OI) and odor evaluation (OE) test. First, the odor DT test was performed for each odor (rose and mint, as shown with "×2"). Then, both odors were used once in the OI and OE test. In the fNIRS measurement session, the OI and OE test was performed after the fNIRS measurement using each odor (two sets of fNIRS measurement). The time used is shown in minute (min.) M, mint; R, rose.

fNIRS measurement session (see **Figure 1**). Both rose and mint odors were presented to the participants once in each session, and the sequence of the two odors in each session was randomized among participants. In the olfactory measurement session, an odor stimulus at an intensity of 120 NSE was presented to a participant for an ET of 200 ms. Subsequently, the participant was asked to verbally answer what kind of odor he/she smelt (odor identification) and how pleasant they thought the smell was (odor evaluation) if he/she had perceived it. For the odor identification test, we used a free identification paradigm in which no odor descriptor was provided to the participants. The participants got 3 points if they explicitly named the odor (i.e., rose or mint). They got 2 points if they answered flower or herb. They got 1 point if they generalized the odor as sweet or cooling. Otherwise, they got 0 points. For odor evaluation, the participants were asked to verbally rate the pleasantness of the odor from 1 (very pleasant) to 5 (very unpleasant) for each trial. The details of the odor identification and odor evaluation tests in the fNIRS measurement session are provided in the following subsection.

fNIRS Measurement

Hemodynamic responses in the prefrontal region were recorded using a multichannel NIRS system (ETG-7000, Hitachi Medical Co., Japan). The system emits continuous near-infrared lasers with fixed wavelengths of approximately 780 and 830 nm. Lasers are modulated at different frequencies depending on the

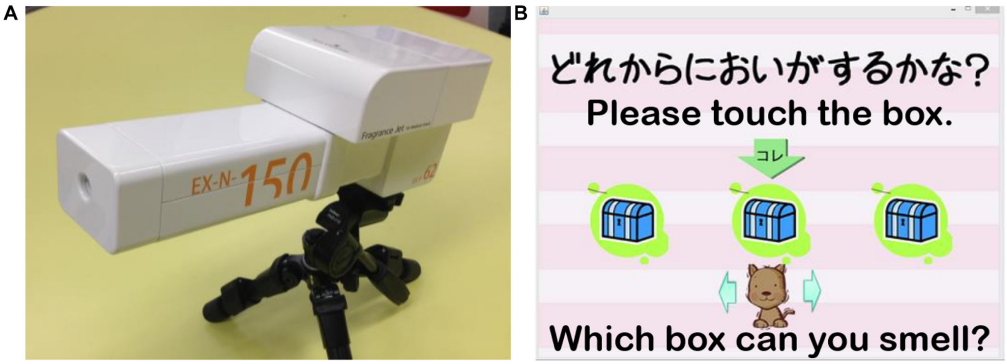

FIGURE 2 | (A) The olfactory display using a pulse ejection system. **(B)** A screenshot of the application for odor detection threshold (DT) measurement designed for participants with ASD (Matsuura et al., 2014).

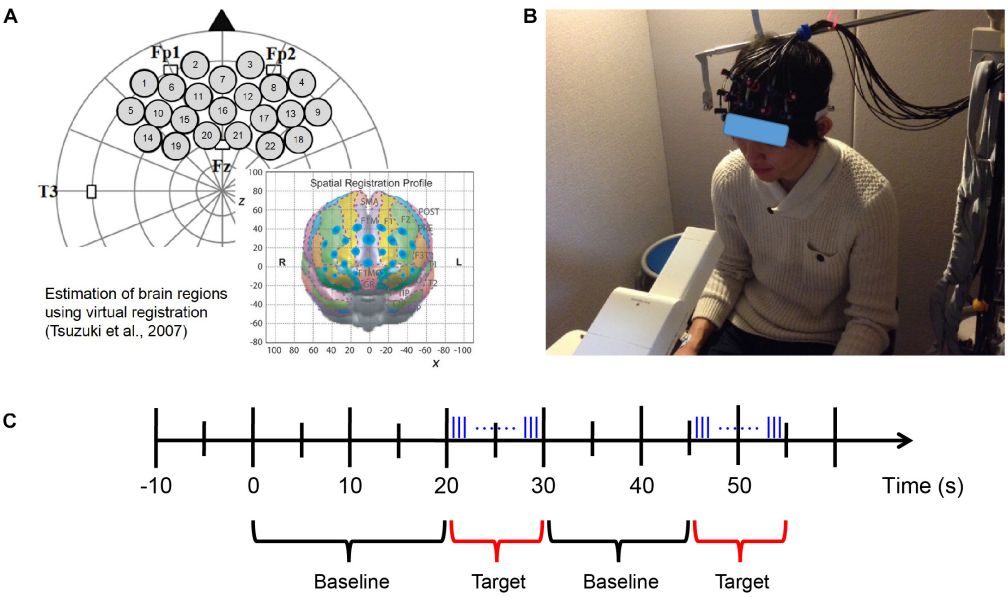

FIGURE 3 | fNIRS measurement. **(A)** Probe set and position on the brain (Xu et al., 2017). **(B)** fNIRS experimental environment (informed consent was obtained from the participant shown in the figure). **(C)** Block design of fNIRS measurement. Odor stimuli were emitted during the 10 s of the target period. The blue vertical lines represent the pulses of odor stimuli presented by the fragrance pulse ejection system. The odor stimuli were emitted for 200 ms (200/0.667 = 300 pulses) at a time, and the inter-stimulus interval was 80 ms.

wavelengths and the channels and are detected using lock-in amplifiers (Watanabe et al., 1996). The device provides estimates of changes in hemoglobin (Hb) concentrations and oxygenation levels of the optical paths in the underlying brain regions between the nearest pairs of emitter and detector probes.

A silicon probe pad was used to arrange eight emitters and seven detector probes in a 3 × 5 rectangular lattice, forming 22 recording channels. Each pair of emitter and detector probes was separated by 30 mm. The 3 × 5 probe pad was placed on the participants' prefrontal region (**Figure 3A**; Xu et al., 2017). Specifically, the bottom edge of the probes was placed in a direction horizontal to the line connecting T3, Fp1, Fp2, and T4 on the international 10–20 system, and the center of the channels was positioned across the nasion–inion line (Klem et al., 1999). This probe arrangement enabled the spatial estimation of localized cerebral activity based on the virtual registration method (Tsuzuki et al., 2007). After probe placement, the experimenter verified that each probe was in adequate contact with the scalp. Only after this verification were fNIRS recordings initiated.

During the fNIRS measurement, the participants were shown a silent video of running trains to help them keep their head position stable as much as possible while the odor was presented at a random time using a block design (**Figure 3B**). We aimed to use this approach (1) to maintain the distance from the odor emitting instrument to the participants' nose and (2) to reduce motion artifact caused by head movement in the fNIRS data as has been used in neuroimaging experiments with

passive task for young population (e.g., Dehaene-Lambertz, 2000; Minagawa-Kawai et al., 2009). These are important factors for evaluation of neural responses elicited by olfaction. Moreover, since the video was silent and monotonous, we presume that even if it would occupy the participants' attention to some extent, the degree would not vary much among participants and stimulus conditions.

The length of the baseline period was randomized from 15 to 25 s; the target period was 10 s, within which the odor stimuli were emitted for 200 ms (200/0.667 = 300 pulses) at a time, and the inter-stimulus interval was 80 ms (**Figure 3C**). The fNIRS measurement also used the odors of mint and rose and executed eight blocks of odor stimulation for each odor. After completing the fNIRS measurement session using each odor, the participants were required to identify and evaluate the odor.

To minimize the influence of individual difference in breathing, we asked the participants to breathe at a fixed pace (inhale for 2 s and exhale for 3 s) in the preliminary experiment. We found that pace-controlled breathing led to so much physiological noise that it even concealed the neural responses induced by the odor stimulus itself. We therefore used various lengths of baseline period (15–25 s) to avoid the influence of regular breathing cycle and let the participants breathe at their normal pace during the target period of each block to minimize the impact of breathing as much as possible. In addition, the odor stimulus was presented to the participants continuously during the 10-s target period of each block and there were eight blocks in total. We chose a 10-s target period because natural breathing occurs once within 3–4 s in human adults (Dishman et al., 2000; Ragnarsdóttir and Kristinsdóttir, 2006) and this combined with a total of eight blocks enables all the participants to have inhaled the odor stimulus for several times during the fNIRS session.

Behavioral Data Analysis

First, the participants with ASD were divided into two groups using a median split according to their DT scores. The participants with ASD with DT < 60 were labeled as the "ASD-Low DT" group and those with DT ≥ 60 were labeled as the "ASD-High DT" group. Next, their performance in odor identification and odor evaluation was also grouped. Two-way repeated measures analysis of variance (ANOVA) with the groups used as between-subject factors (control, ASD-Low DT, ASD-High DT) and the odors used as within-subject factors (mint, rose) was applied to the DT using IBM SPSS Statistics 25. For odor identification and evaluation, two-way repeated ordinal regression with cumulative link mixed models (CLMM; Christensen, 2015) was applied using R (R Core Team, 2018).

NIRS Data Analysis

The NIRS data were preprocessed using Platform for Optical Topography Analysis Tools (POTATo) developed by Research and Development Group, Hitachi, Ltd., in a Matlab 7.7 environment (The MathWorks, Inc., Natick, MA, United States). Changes in the concentration of oxygenated (oxy-) Hb and deoxygenated (deoxy-) Hb were calculated from absorbance changes of 780 and 830 nm laser beams sampled at 10 Hz. For each participant, the raw oxy- and deoxy-Hb data in each channel were high-pass filtered at 0.0167 Hz to remove components originating from systematic fluctuations (Naoi et al., 2012). Blocks with motion artifacts were excluded [signal variations larger than two standard deviations (SD) from the mean over 0.2 s]. Any block containing oxy-Hb changes larger than 0.15 mM/mm within 0.2 s was discarded. The oxy-Hb and deoxy-Hb concentrations of the remaining baseline and target blocks were smoothened with a moving average of 5 s. To eliminate long-term signal trends due to systemic vascular factors, a first-degree baseline fit was estimated for each channel using the first 5 s and last 5 s of the analysis block.

For each group (control, ASD-Low DT, and ASD-High DT), the block analysis focused on a 25-s epoch composed of a 5-s prestimulus baseline period, a 10-s target period with odor stimulation, and a 10-s poststimulus period. The Hb concentrations of all artifact-free trials were averaged. Subsequently, a time course of the mean change in oxy-Hb and deoxy-Hb concentrations was compiled for each channel of each participant. These time courses for all the participants in each group were subsequently averaged to form time-dependent waveforms of the hemodynamic responses in each channel. Considering the slow characteristics of neural hemodynamic responses, a 10-s period starting 5 s after stimulus onset was regarded as the analysis window (10 $\sim$ 20 s of each block). A 5-s period immediately before stimulus onset was regarded as the time window for the baseline (0 $\sim$ 5 s of each block). A two-way repeated measures ANOVA with the group as the between-subject factor and odor as the within-subject factor was analyzed for the oxy-Hb concentration changes (the mean of oxy-Hb during the analysis window vs. the mean of oxy-Hb during the baseline) in each channel. A Bonferroni *post hoc* test was used to further evaluate any significant main effects. In addition, the means of oxy-Hb during the analysis window and the baseline period in each channel were analyzed by a paired *t*-test to identify the activated regions in response to the olfactory stimuli for each group. The brain regions underlying each channel were estimated using the virtual registration method for NIRS channels (Tsuzuki et al., 2007). For activated channels showing significant main effect of group, latency of the oxy-Hb peaks and mean amplitude of the deoxy-Hb and latency of the deoxy-Hb peaks within the analysis window were analyzed as well. Lastly, correlations between the oxy-Hb concentration changes and behavioral data (odor DT, odor identification, and odor evaluation), as well as the scores in the sensory profile, were assessed using Pearson correlation.

RESULTS

Behavioral Results

There were 12 participants with ASD in the "ASD-Low DT" group and 13 participants in the "ASD-High DT" group. Three control participants were excluded from further data analysis because of technical problems with the odor presentation device.

The results of DT (**Figure 4A**) showed higher DT for rose than for mint, and higher DT in the ASD-High DT group. This tendency was supported by two-way repeated measures

ANOVA using odor (rose vs. mint) as the within-subject factor and group (control vs. ASD-Low DT vs. ASD-High DT) as the between-subject factor. Specifically, this analysis showed significant main effects of odor [$F(1,35) = 6.51$, $p = 0.02$] and group [$F(2,35) = 59.24$, $p < 0.001$]. There was no significant interaction effect between odor and group [$F(2,35) = 0.37$, $p = 0.70$]. For the significant main effect of odor, the DT (mean ± SD) for rose (66.05 ± 39.08) was significantly higher than for mint (46.58 ± 40.82). A Bonferroni *post hoc* analysis for the significant main effect of group revealed that the DT was significantly higher in the ASD-High DT group (95.38 ± 42.35) than in the control group (33.85 ± 22.29; $p < 0.001$) and the ASD-Low DT group (38.33 ± 18.10; $p < 0.001$), indicating significantly lower odor sensitivity in the ASD-High DT group (**Figure 4A**).

Two-way repeated ordinal regression with CLMM was applied to the performance of odor identification and odor evaluation. For odor evaluation, a higher rate indicates unpleasantness while a lower rate indicates pleasantness. After comparisons of a series of models with different fixed and random effects, the most appropriate model evaluated by the likelihood ratio test was accepted. For odor identification, there were no significant main effects or interactions (**Figure 4B**). For odor evaluation (rating of pleasantness; **Figure 4C**), the most appropriate model included the odor (rose vs. mint) and group (control vs. ASD-Low DT vs. ASD-High DT) as fixed effects, and the intercepts for odor and NIRS (with or without NIRS measurement) and by-subject random slopes as random effects. Both odor [χ^2 (1) = 6.03, $p = 0.014$] and group [χ^2 (2) = 7.02, $p = 0.030$] significantly affected odor evaluation. Specifically, the odor of mint (2.14 ± 0.81) was rated as significantly more pleasant than that of rose (2.46 ± 0.83). *Post hoc* analysis revealed that the odor evaluation was significantly different between the control group (2.73 ± 0.62) and the ASD-High DT group (2.04 ± 0.94) [coefficient estimate: 2.34, standard error (SE): 0.89, $p = 0.009$], and a tendency of significant difference between the control group and the ASD-Low DT group (2.13 ± 0.74) (coefficient estimate: 1.85, SE: 1.05, $p = 0.08$).

The odor identification test after the fNIRS measurement session indicated that almost all participants recognized the odor, except three participants in the ASD-High DT group.

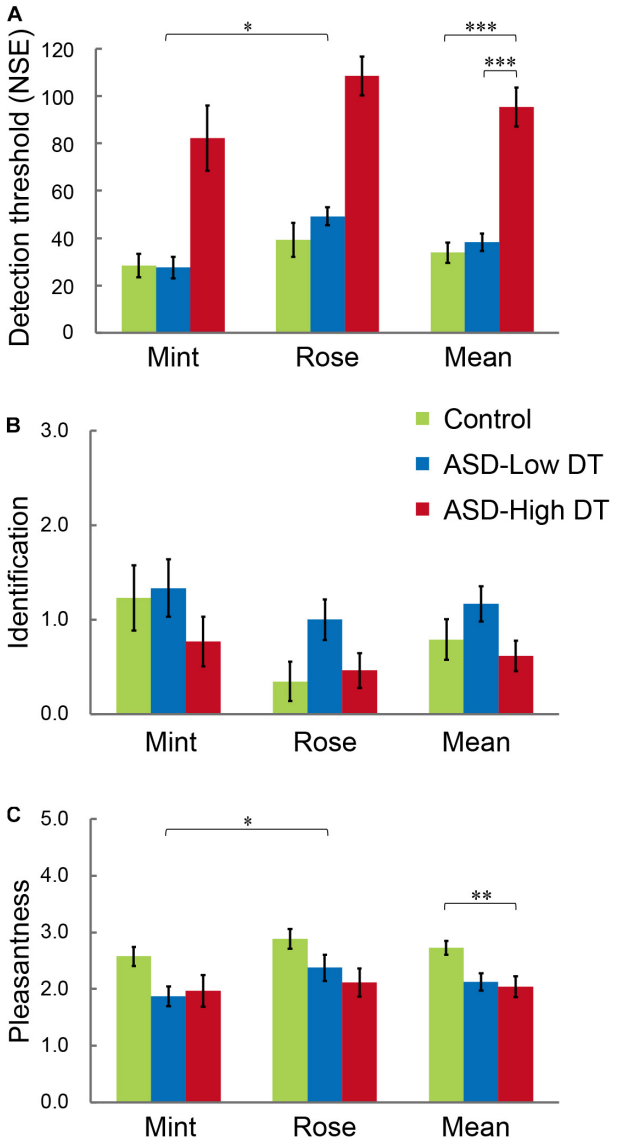

FIGURE 4 | Performance of participants with ASD and TD control participants in the **(A)** odor detection threshold (DT), **(B)** odor identification, and **(C)** odor evaluation (pleasantness) tests. The ASD group was divided into "ASD-Low DT" (those DT < 60, 12 participants) and "ASD-High DT" (those DT ≥ 60, 13 participants) subgroups. Error bars represent 1 standard error. *$p < 0.05$; **$p < 0.01$; ***$p < 0.001$.

NIRS Results

The concentration changes in oxy-Hb and deoxy-Hb were analyzed for each group. Since two-way repeated measures ANOVA with group and odor as factors revealed almost no significant odor effect except for CH6 [$F(1,35) = 4.32$, $p < 0.05$], and no interaction for any channel, the trials in the mint and rose conditions were combined to identify the activated channels in each group (**Figure 5**) and to create the time course of Hb changes in all channels for each group (**Supplementary Figures 2–4**). More channels were activated in the control group than in the ASD-Low DT group while there were no activated channels in the ASD-High DT group (**Figure 5**). Specifically, according to the virtual registration method (Tsuzuki et al., 2007), multiple channels chiefly covering the DLPFC were activated in the control group (CH9, right DLPFC 100%; CH10, left DLPFC 91.7%, FP 8.3%; CH13, right DLPFC 78.9%, FP 21.1%; CH14, left DLPFC 100%; CH17, right DLPFC 50.5%, left DLPFC 39.8%; CH19, left DLPFC 95.1%, FP 4.9%). Similar channels covering the DLPFC were also activated in the ASD-Low DT group (CH10 and CH17). However, no active channel was found for the ASD-High DT group. Among these DLPFC channels, CH9 [$F(2,35) = 3.49$, $p = 0.042$] and CH13 [$F(2,35) = 3.39$, $p = 0.047$] showed a significant main effect of group according to the results of two-way repeated measures ANOVA with group and odor as factors. Particularly, activity of CH13 (right DLPFC) was significantly weaker in the ASD-High DT group than in the control group ($p = 0.046$, Bonferroni correction; **Figure 6**).

The time series of Hb changes in CH13 (right DLPFC) with significant main effect of group (control > ASD-High DT) are shown in **Figure 7**. The pattern of brain activity of the ASD-High DT group was different from that of the other two groups, and the level of brain activity of this group was weaker than that of the control group. One-way ANOVA showed that there was no significant main effect of group for latency of the oxy-Hb peaks [$F(2,35) = 0.47$, $p = 0.63$], mean amplitude of the deoxy-Hb [$F(2,34) = 2.41$, $p = 0.11$], and latency of the deoxy-Hb peaks [$F(2, 34) = 1.45$, $p = 0.25$]. To exclude the possible influence of perception of odor pleasantness on the observed discrepancy in neural activity between the control and the ASD groups, the rating score of odor pleasantness was included as a covariate of no interest. The results were largely consistent with the analysis without this covariate. Specifically, significant main effect of group was found in CH13 [$F(2,69) = 3.953$, $p = 0.024$], and *post hoc* comparisons with Bonferroni's correction revealed a significant difference between the control group and the ASD-High DT group ($p = 0.020$). Hence, the group difference in odor-elicited neural activity does not likely come from the difference in perception of odor pleasantness.

To examine whether there was a relationship between odor detection sensitivity and the fNIRS data, the correlation between the oxy-Hb response to the odor in CH13 and the DT of all participants was assessed using Pearson correlation. The result revealed a significant negative correlation ($r = -0.41$, $p = 0.012$; **Figure 8**), indicating that participants with lower odor detection sensitivity might show reduced brain activity to a certain level of odor stimulation. The relationship between brain activity and other olfactory perception abilities (odor identification and odor evaluation), as well as other sensory characteristics observed from the sensory profile battery, was also evaluated, but no significant correlations were found.

DISCUSSION

The present study aimed to investigate the neural underpinnings of olfactory processing in individuals with ASD by combining a precise and ASD-friendly olfactory measurement system, which consists of a pulse ejection system, with fNIRS measurement. Significant differences were found between ASD and control groups not only at the behavioral level but also at the neural level. The ASD group with hyposensitivity (ASD-High DT group) to olfactory stimuli was found to be significantly different from the control group with respect to the olfactory DT and pleasant feelings to the used odors. The brain activity in the right DLPFC of the ASD-High DT group was significantly weaker than that of the control group. In addition, the strength of brain activity in the right DLPFC was significantly correlated with the DT in all participants.

Combined Use of a Sophisticated System for Olfactory Examination and fNIRS

The present study successfully utilized a pulse ejection system in combination with fNIRS to examine neural dysfunction related to olfactory processing in individuals with ASD. The system is unique in that it can precisely control the interval of odor stimulation and, therefore, significantly reduce the potential confounding effect lingering scents have on olfactory perception. Together with an ASD-friendly game-like application for odor detection test, the system is feasible for gauging the olfactory ability of not only high functioning individuals with ASD but also individuals with ASD who have intellectual impairment. While this system has been successfully used for olfactory assessment in children with ASD (Kumazaki et al., 2016, 2018c, 2019), the present study, for the first time tried combining it with fNIRS.

Since some parts of the pulse ejection system were made of metal, it could not be used in fMRI scanning; however, it could be used during fNIRS measurement. Our study verified the feasibility of the combination of this olfactory test system and a highly ecologically valid neuroimaging method such as fNIRS to localize the brain functions of olfactory processing in ASD. The system facilitated the examination of not only high functioning individuals with ASD but also of individuals with ASD who have relatively low intellectual abilities, which has not been well established. This olfactory neuroimaging experimental paradigm is friendly for individuals with mental disorders who have olfactory differences, such as individuals with ASD and schizophrenia, and may also be useful for the future diagnosis of these disorders.

Olfactory Sensitivity in Individuals With ASD

Our findings showed that participants with ASD with high DT were significantly impaired in their sensitivity and hedonic response to olfactory stimuli but not in their odor identification ability. Previous literature has suggested atypical olfactory function in ASD, but the pattern of findings shows much heterogeneity. This is particularly true for investigations of sensory-driven olfactory function, such as odor detection. Thus, while some studies reported either enhanced (Ashwin et al., 2014) or decreased odor sensitivity (Dudova et al., 2011; Kumazaki et al., 2016) in ASD, most studies reported no significant differences between individuals with ASD and controls in DT (Suzuki et al., 2003; Tavassoli and Baron-Cohen, 2012; Galle et al., 2013; Addo et al., 2017). The discrepancy in findings might come from a complex blend of variance in participants' demography (age and gender), subtype of ASD (AS, HFA, PDD, etc.), sample size, and the study design/test method used. For instance, most of these studies recruited participants with AS and HFA (Suzuki et al., 2003; Galle et al., 2013; Addo et al., 2017), generally having a higher cognitive functioning than the general ASD population. Therefore, individuals with these subtypes of ASD may have comparable odor sensitivity to that of age-matched TD controls. In addition, though it is common for these studies to include more male participants with ASD (as males are more susceptible to ASD; Baron-Cohen, 2002), their ages varied from children, to teenagers (Dudova et al., 2011; Kumazaki et al., 2016), to young adults around twenties (Galle et al., 2013), to adults in their thirties or forties (Suzuki et al., 2003; Tavassoli and Baron-Cohen, 2012; Ashwin et al., 2014; Addo et al., 2017). While prior

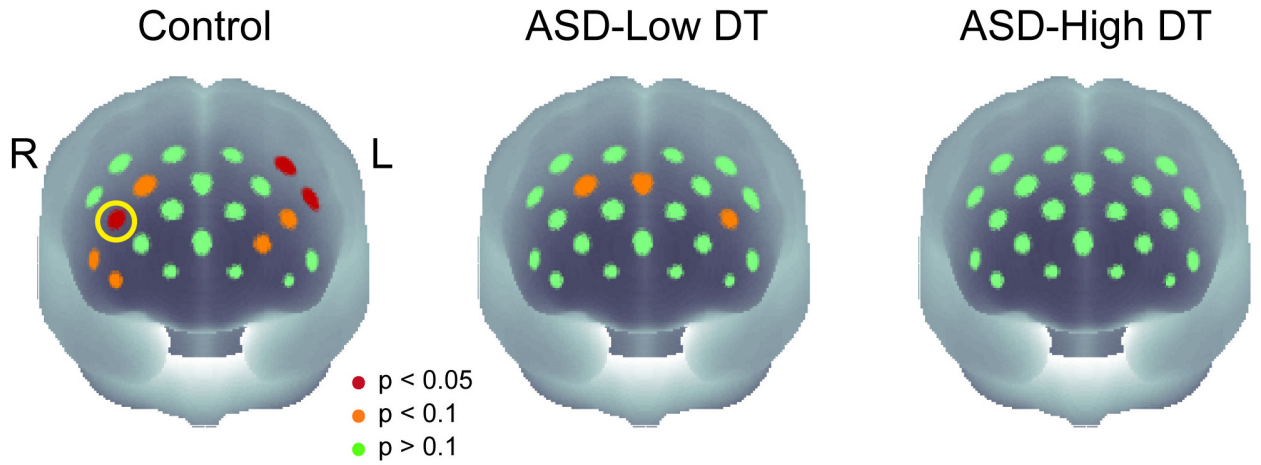

FIGURE 5 | The *p*-maps of the averaged concentration changes in oxy-Hb for the three groups. CH13 that showed significant difference in response between the control group and the ASD-High DT group was marked using a yellow circle. The corresponding brain region of CH13 was estimated as right dorsolateral prefrontal cortex (DLPFC) using virtual spatial registration (Tsuzuki et al., 2007).

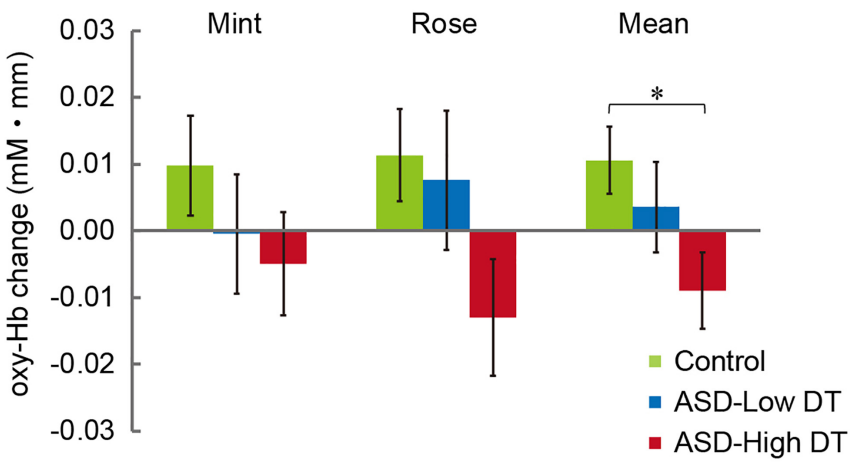

FIGURE 6 | Averaged oxy-Hb responses in CH13 to mint and rose stimuli for the three groups. The results of two-way repeated measures ANOVA showed a significant main effect of group (Control > ASD-High DT). *$p < 0.05$.

evidence reveals that females have higher olfactory functioning (primarily olfactory sensitivity and identification) than males in TD population (e.g., Doty et al., 1984a; Lehrner, 1993; Barber, 1997), the above-mentioned olfactory studies in ASD consistently enrolled more male participants and the gender ratio is therefore not likely to be the source of the discrepancy between studies, instead, age is more likely the source. It is well known that olfactory sensitivity substantially declines due to aging in healthy individuals (e.g., Cain et al., 1995; Schiffman, 1997; Larsson et al., 2000). However, while younger individuals with ASD (<30 years) tend to show lower olfactory sensitivity than TD individuals, older individuals with ASD (>35 years) do not (Larsson et al., 2017). In addition, it is suggested that in TD individuals, olfactory sensitivity develops earlier in life while odor identification ability is acquired later, during adolescence (Tonacci et al., 2017), but this timing could be more heterogeneous and/or shifted in individuals with ASD (Dudova et al., 2011). As for young adults with ASD, who are within our scope, Galle et al. (2013) reported no significant differences in DT between them and TD controls; however, they did show large variability in DT. In addition, this study's sample size was very small (five individuals with ASD and five controls), which may be the cause of the inconsistencies with our findings.

Considering the similar sample size (over 20) and sampled population (ASD also including individuals with AS and HFA, 10–20 years old), our findings of impaired odor detection ability in young adults with ASD are consistent with the observations of Kumazaki et al. (2016). The observed impaired odor sensitivity in these individuals with ASD might be attributed to age. It is possible that young individuals with ASD might be compromised in their olfactory sensitivity, but the impairment may be alleviated with maturation. This is an open question that warrants further

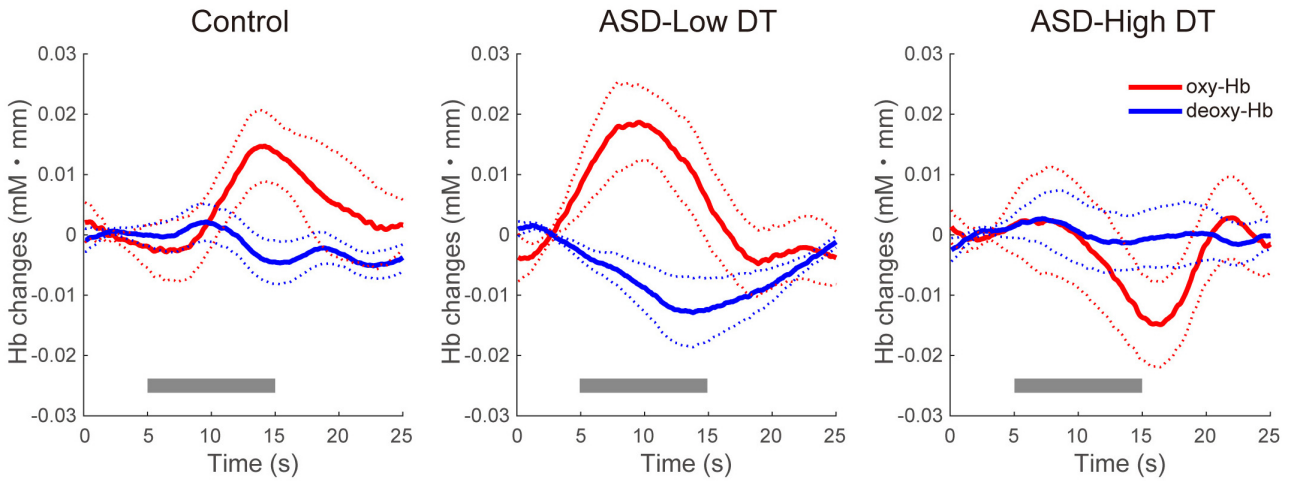

FIGURE 7 | Time series of the averaged concentration changes in oxy-Hb and deoxy-Hb (mM mm) in CH13 for the three groups. The gray bars represent the target period (5 ∼ 15 s). The thick red and blue lines represent the mean concentration changes of oxy-Hb and deoxy-Hb, respectively. The thin dotted red and blue lines represent 1 standard error of concentration changes in oxy-Hb and deoxy-Hb, respectively.

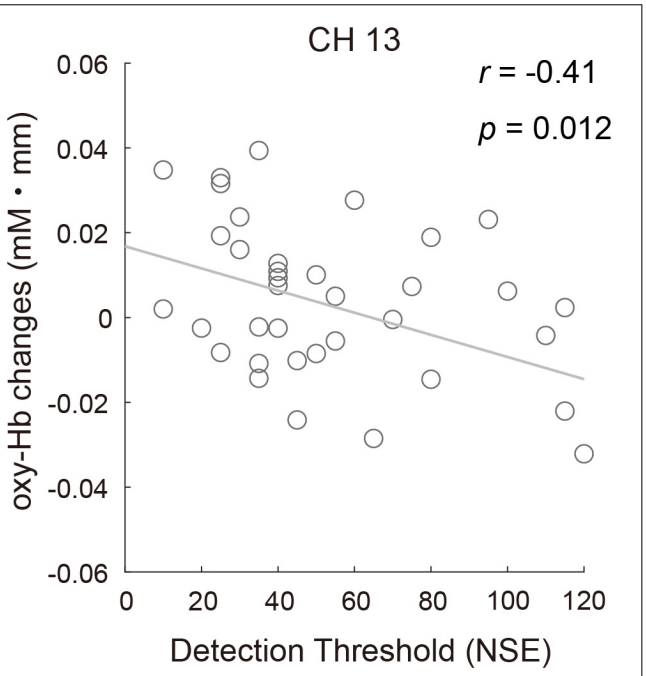

FIGURE 8 | Correlation between the mean concentration changes in oxy-Hb in CH13 and odor detection thresholds for all participants (r = –0.41, p = 0.012).

research using longitudinal methods. However, the substantial heterogeneity across studies with respect to odor DT in ASD is in accord with the idea that ASD may be associated with both hyposensitivity and hypersensitivity in olfaction. As such, it is necessary to treat individuals with ASD differently when investigating their relevant brain functions. Therefore, in the present study, we divided participants with ASD into two groups—ASD-Low DT and ASD-High DT—according to their DT and compared their brain responses elicited by odor stimuli with those of age-matched TD controls.

With respect to odor identification, our task did not provide written label alternatives (one target and several foils), as do UPSIT (Doty et al., 1984b) and Sniffin' Sticks (Hummel et al., 1997), and it was somewhat difficult for the participants to give an answer without any reference information. Even the control group had poor performance in this aspect. This might be the reason for non-significant difference between the groups. Although some previous studies have reported decreased odor identification ability in ASD (Suzuki et al., 2003; Bennetto et al., 2007; Galle et al., 2013; Wicker et al., 2016), there is also evidence of no significant difference compared with TD controls (Brewer et al., 2008; Dudova et al., 2011; Luisier et al., 2015; Addo et al., 2017).

With respect to the hedonic responses to odor stimuli (i.e., pleasantness), the ASD-High DT participants were significantly different from TD controls. This finding is consistent with a previous study on the estimation of odor pleasantness in approximately 10-year-old children with ASD (Hrdlicka et al., 2011). One possibility is that the ASD-High DT group could not process the odor stimuli at a metacognitive level, i.e., self-knowledge of one's cognitive process (Shimamura, 2008), to rate the pleasantness. In other words, the participants in ASD-High DT group cannot properly rate the pleasantness of odor maybe because they were not fully aware of their cognition of an odor so that they were not able to evaluate the odor as good as the TD controls did. In fact, impaired metacognitive function has been reported in individuals with ASD during perceptual processing of several domains (e.g., Grainger et al., 2016; McMahon et al., 2016). Considering their impaired social capabilities including emotion (Legisa et al., 2013), another possibility could be that participants with ASD had difficulty in emotionally rating an odor.

Weaker Prefrontal Activity in Individuals With ASD

With respect to the prefrontal fNIRS data, we found significantly weaker hemodynamic responses in the right DLPFC of participants with ASD with lower olfactory sensitivity (the ASD-High DT group) compared to the TD participants. Although there was no significant difference in neural activity between the participants with ASD with relatively higher olfactory sensitivity (the ASD-Low DT group) and the TD participants, the ASD-Low DT group did not show significant right DLPFC activity compared to the control group. These results indicate that individuals with ASD generally have different neuronal basis for processing odor stimuli compared to TD individuals. Such discrepancies may be related to impaired olfactory processing in ASD. More specifically, considering the important role of the DLPFC in executive functions including attention (Duncan and Owen, 2000) and working memory (Levy and Goldman-Rakic, 2000), reduced activity in this region may reflect the general abnormality in attention and working memory in individuals with ASD (Russell, 1997; Travers et al., 2011) during olfactory processing.

In the fNIRS measurement session, although the task requirement was passive perception (i.e., olfaction), the participants were instructed that there could or could not be an odor stimulus during the fNIRS measurement and that they would be asked to report whether they had smelt something after the fNIRS measurement. Therefore, the participants might have attentively monitored their sense of smell, which demanded some degree of attention and working memory. In addition, right DLPFC activation was found to be significantly related to odor sensitivity, which was assessed in the odor DT test that required attention and working memory as well. Thus, it is possible that odor sensitivity indirectly reflects the participants' attention and working memory, and consequently correlates with the level of brain activity in the region responsible for these functions. From this perspective, the weaker response in the DLPFC of participants with ASD with lower sensitivity (the ASD-High DT group) may be attributed to their deficits in attention and working memory. The neural correlates of olfactory attention and olfactory working memory have been suggested to be in the olfactory bulb or the piriform cortex (Keller, 2011) and in the primary olfactory cortex (Zelano et al., 2009), respectively. On the other hand, robust involvement of the DLPFC in olfactory working memory has been demonstrated in one positron emission tomography (PET) study (Dade et al., 2001), while another fNIRS study also reported the engagement of the bilateral DLPFC and FP in response to an olfactory task requiring attention and working memory (Takakura et al., 2011). Similarly, the significant channel (CH13, virtually covering DLPFC 78.9% and FP 21.1%) of our study also partially covered the FP, which is suggested to function as "gateway" that biases attention (Burgess et al., 2005; Gilbert et al., 2006; Takakura et al., 2011).

The question remains as to how altered working memory and attention in ASD are associated with the olfactory anomaly. There are two possible explanations, one is at the perceptual level and the other is at the cognitive level. The perceptual explanation is that individuals with ASD may have impairments in sensory processors such as in the olfactory bulb and/or olfactory cortex, which produce weakened perceptual signals, which may then be reflected as impaired olfactory working memory. The cognitive explanation posits that perceptual processing of individuals with ASD may not be problematic; instead, perceptual signals may not be processed efficiently to be held as explicit meta-cognitive signals in the DLPFC. In other words, even if individuals with ASD may have unconsciously processed the odors to a similar sensory degree as TD individuals, they may not consciously process the odors due to the problems of attention and/or working memory. This imprecise operation may lead to compromised olfactory processing in ASD.

The cognitive explanation may, however, be the most likely. One reason is that the DLPFC may not activate as a function of the intensity of olfactory stimulation, instead, it may primarily encode the presence or the type of olfactory stimuli at the conscious (i.e., cognitive) level. During the fNIRS measurement, we used an odor stimulus with an intensity of 120 NSE, which is higher than the DT of almost all participants and, therefore, should have been perceived. This is also validated by the participants' performance in the post-experiment odor identification task: none of the 12 participants in the ASD-Low DT group failed to recognize the odor, and only 3 of the 13 participants in the ASD-High DT group failed to explicitly recognize the odor. Thus, the significant difference in neural responses between the ASD-High DT group and the control group is not likely caused by low-level sensory processing of odor stimuli but might possibly be due to higher-order olfactory processing, such as executive function, which has been shown to be impaired in ASD (Hill, 2004; Kenworthy et al., 2008). Moreover, while there was no statistically significant difference in brain activity between the ASD-Low DT group and the control group, the brain activity of the ASD-Low DT group showed a similar but weaker pattern compared to the control group (**Figure 5**). Considering that the two groups have almost equivalent olfactory sensitivity, the odor used should have stimulated their olfactory system to a comparable degree. However, the ASD-Low DT group showed weaker neural responses. This group may have a problem in odor processing in more complicated social situations that require a higher load of olfactory working memory and/or attention.

A precise definition of the DLPFC's contribution to olfactory working memory and attention is not established. On the one hand, participants with ASD might not be able to activate the DLPFC in response to olfactory stimuli as efficiently as the control group. On the other hand, they may recruit brain regions other than the DLPFC in situations requiring olfactory working memory and/or attention. A future systematic examination of the relationship between working memory and attention and DLPFC activity in individuals with ASD is necessary to investigate these possibilities. In any case, DLPFC deficit as a cause of olfactory processing plausibly explains age dependent olfactory sensitivity for individuals with ASD: Prefrontal cortex develops rapidly during adolescence and that facilitates matured DLPFC function, resulting in unimpaired olfactory function in adults with ASD.

There are also some other DLPFC-related issues worth considering. For instance, a recent genetic study reported decreased olfactory receptor expression in the DLPFC of individuals with chronic schizophrenia (Ansoleaga et al., 2015). The authors suggested that the deregulation of olfactory receptors is associated with olfactory alterations in these patients. Whether there is a similar mechanism in individuals with ASD remains unclear and would be interesting to investigate in future studies. Additionally, while the present study found a significant group difference in the DLPFC of the right hemisphere only, it does not necessarily indicate that the right DLPFC is predominantly involved in olfactory working memory; however, it may contribute to the ongoing research on the lateralization of the working memory of various modalities in the DLPFC (Smith et al., 1996; Murphy et al., 1998) and the lateralization of olfaction-related processing (Zatorre et al., 1992; Brand et al., 2001; Ishimaru et al., 2004b). Nevertheless, the interpretation of reduced DLPFC activity as a result of impaired odor sensitivity should be treated with caution, since the olfactory task in the odor DT test session and fNIRS recording session differed due to their respective purpose.

Finally, differences in IQ among groups in relation to fNIRS results and DT should be discussed. As for the fNIRS results, one may ask whether the weaker prefrontal activity of the participants with ASD is due to their impaired ability, as reflected by IQ, to properly engage in the fNIRS experiment. Although the participants with ASD had lower IQ than the TD control group (**Table 1**), they had no problem in participating in the experiment at any stage as confirmed by their proper verbal responses to the odor identification and evaluation questions after each fNIRS measurement session. In addition, they did not have any difficulty in performing the odor DT task, which was more complicated than the fNIRS task. Another IQ-related issue is that perceptual sensitivity to odor may directly relate to IQ as our ASD-Low DT group had higher IQ than ASD-high DT group. However, this is not likely because no correlation between IQ and olfactory processing has been reported in the general population (Hedner et al., 2010). On the other hand, since performance on IQ tests depends on executive functions including attention, the lower IQ of the participants with ASD may indirectly reflect their deficits in directing attention toward odor stimuli, which may have led to their impaired olfactory processing and weaker/absence of prefrontal activity.

Limitations

Although our sample size was comparable to that of previous studies on olfactory function in ASD, considering the high degree of heterogeneity of ASD, it was still not sufficiently large. This may be one of the reasons why we did not have robust statistical results. Another limitation is that the present study included individuals with ASD with several different subtypes (i.e., AS, AD, and PDD-NOS). Therefore, we did not reveal subtype-specific olfactory traits in ASD. However, since most previous studies on olfactory dysfunction in individuals with ASD predominantly included individuals with AS and HFA, who are more capable of performing experimental tasks, the present study contributes to the limited evidence on behavioral and neural impairments in individuals with ASD with moderate to severe intellectual difficulties, who can also undergo both psychophysical and neuroimaging measurements with our ASD-friendly system. A more systematic study of olfactory processing in ASD with a larger sample size and taking into account various subtypes of ASD is warranted. In addition, we used odor of mint, an olfactory-trigeminal stimulus, while we did not assess the intranasal trigeminal sensitivity of the participants. We tried using many odors in the preliminary experiments and odors of rose and mint were found to be the most suitable for obtaining consistent brain responses from participants as measured with fNIRS. The present findings with the usage of odor of mint should not be simply generalized to odor stimuli as a whole. For instance, the mint odor induced relatively smaller difference in brain activation between the ASD-Low DT and the control groups regardless of their comparable DT values, although these are not statistically significant. Future study could examine odor-type-dependent cerebral responses, particularly the difference in responsiveness to odors stimulating the trigeminal nerve or not.

CONCLUSION

The present study verified the feasibility of combining a precise and easy-to-use system for olfactory measurement—the odor pulse ejection system—with fNIRS. Using this ASD-friendly system, we successfully measured olfactory function in individuals with ASD, including those with moderate to severe intellectual impairment. Compared to TD controls, participants with ASD with lower odor sensitivity showed blunted activity in the right DLPFC in response to odor stimulation. Even in participants with ASD with normal odor sensitivity, DLPFC activities were not as significant as in the control group. In addition, the strength of olfaction-evoked neural activity in the right DLPFC was correlated with DT. These findings indicate that differential DLPFC function for olfactory processing, particularly olfactory working memory and/or attention, is related to odor-processing anomaly in ASD. The present study provides insight into the neural mechanisms of specific olfactory malfunctions associated with ASD by revealing deficit in the cognitive brain function as a possible cause. Future establishment of fNIRS-based biomarkers might facilitate the use of a non-invasive technique in identifying olfactory difficulties in individuals with ASD.

DATA AVAILABILITY STATEMENT

The dataset generated for this study are available, under the restriction of ethic permission obtained from our university, on request to the corresponding author.

ETHICS STATEMENT

The studies involving human participants were reviewed and approved by the ethics committee of the Keio University, Faculty

of Letters (No. 16028). The patients/participants provided their written informed consent to participate in this study.

AUTHOR CONTRIBUTIONS

NN and MX analyzed the data. NN, MX, and YM interpreted the data. MX and YM wrote the manuscript. NN, YM, HK, and KO designed the study. NN and YM performed the experiment. All authors contributed to the article and approved the submitted version.

FUNDING

This work was supported by MEXT Supported Program for the Strategic Research Foundation at Private Universities, the Japan Science and Technology (JST), CREST (JPMJCR14E2, JPMJCR19A2), and the Japan Society for the Promotion of Science (JSPS) Kakenhi (Grant No. 19H05594).

ACKNOWLEDGMENTS

The authors thank all the participants of the experiment; Ms. E. Matsuura and other graduate students of Okada's Lab for their assistance in using the fragrance pulse ejection system; Ms. Yasui, A. and Mr. Ishikawa, T. for their help with the experiments; and Dr. Kawahara, S. and Dr. Hoshino, E. for their help with the analyses.

SUPPLEMENTARY MATERIAL

The Supplementary Material for this article can be found online at: https://www.frontiersin.org/articles/10.3389/fnhum.2020.523456/full#supplementary-material

REFERENCES

Addo, R. N., Wiens, S., Nord, M., and Larsson, M. (2017). Olfactory functions in adults with autism spectrum disorders. *Perception* 46, 530–537. doi: 10.1177/0301006616686100

Amaral, D. G., Schumann, C. M., and Nordahl, C. W. (2008). Neuroanatomy of autism. *Trends Neurosci.* 31, 137–145. doi: 10.1016/j.tins.2007.12.005

American Psychiatric Association (2013). *Diagnostic and Statistical Manual of Mental Disorders (DSM-5®)*. Washington, DC: American Psychiatric Publication.

Anagnostou, E., and Taylor, M. J. (2011). Review of neuroimaging in autism spectrum disorders: what have we learned and where we go from here. *Mol. Autism* 2:4. doi: 10.1186/2040-2392-2-4

Ansoleaga, B., Garcia-Esparcia, P., Pinacho, R., Haro, J. M., Ramos, B., and Ferrer, I. (2015). Decrease in olfactory and taste receptor expression in the dorsolateral prefrontal cortex in chronic schizophrenia. *J. Psychiatr. Res.* 60, 109–116. doi: 10.1016/j.jpsychires.2014.09.012

Ashwin, C., Chapman, E., Howells, J., Rhydderch, D., Walker, I., and Baron-Cohen, S. (2014). Enhanced olfactory sensitivity in autism spectrum conditions. *Mol. Autism* 5:53. doi: 10.1186/2040-2392-5-53

Barber, C. E. (1997). Olfactory acuity as a function of age and gender: a comparison of African and American samples. *Int. J. Aging Hum. Dev.* 44, 317–334. doi: 10.2190/81EE-CKJD-REDM-FJ9G

Baron-Cohen, S. (2002). The extreme male brain theory of autism. *Trends Cogn. Sci.* 6, 248–254. doi: 10.1016/S1364-6613(02)01904-6

Baron-Cohen, S., Wheelwright, S., Skinner, R., Martin, J., and Clubley, E. (2001). The autism-spectrum quotient (AQ): evidence from Asperger syndrome/high-functioning autism, males and females, scientists and mathematicians. *J. Autism Dev. Disord.* 31, 5–17. doi: 10.1023/a:1005653411471

Bennetto, L., Kuschner, E. S., and Hyman, S. L. (2007). Olfaction and taste processing in autism. *Biol. Psychiatry* 62, 1015–1021. doi: 10.1016/j.biopsych.2007.04.019

Ben-Sasson, A., Hen, L., Fluss, R., Cermak, S. A., Engel-Yeger, B., and Gal, E. (2009). A meta-analysis of sensory modulation symptoms in individuals with autism spectrum disorders. *J. Autism Dev. Disord.* 39, 1–11. doi: 10.1007/s10803-008-0593-3

Brand, G., Millot, J. L., and Henquell, D. (2001). Complexity of olfactory lateralization processes revealed by functional imaging: a review. *Neurosci. Biobehav. Rev.* 25, 159–166. doi: 10.1016/s0149-7634(01)00005-7

Brewer, W. J., Brereton, A., and Tonge, B. J. (2008). Dissociation of age and ability on a visual analogue of the University of Pennsylvania Smell Identification Test in children with autism. *Res. Autism Spectr. Disord.* 2, 612–620. doi: 10.1016/j.rasd.2008.01.003

Brewer, W. J., Pantelis, C., De Luca, C., and Wood, S. J. (2006). *Olfactory Processing and Brain Maturation. Olfaction and the Brain*, 103-118. London: Cambridge University Press.

Burgess, P. W., Simons, J. S., Dumontheil, I., and Gilbert, S. J. (2005). "The gateway hypothesis of rostral prefrontal cortex (area 10) function," in *Measuring the Mind: Speed, Control and Age*, eds J. Duncan, L. Phillips, and P. Mcleod (Oxford: Oxford University Press), 217–248.

Cain, W. S., Stevens, J. C., Nickou, C. M., Giles, A., Johnston, I., and Garcia-Medina, M. R. (1995). Life-span development of odor identification, learning, and olfactory sensitivity. *Perception* 24, 1457–1472. doi: 10.1068/p241457

Christensen, R. H. B. (2015). Analysis of Ordinal Data with Cumulative Link Models–Estimation with the R-Package Ordinal. R-Package Version, 1-31.

Dade, L. A., Zatorre, R. J., Evans, A. C., and Jones-Gotman, M. (2001). Working memory in another dimension: functional imaging of human olfactory working memory. *Neuroimage* 14, 650–660. doi: 10.1006/nimg.2001.0868

Dalton, P., and Wysocki, C. J. (1996). The nature and duration of adaptation following long-term odor exposure. *Percept. Psychophys.* 58, 781–792. doi: 10.3758/bf03213109

Davidson, T. M., and Murphy, C. (1997). Rapid clinical evaluation of anosmia. The alcohol sniff test. *Arch. Otolaryngol. Head Neck Surg.* 123, 591–594. doi: 10.1001/archotol.1997.01900060033005

Dehaene-Lambertz, G. (2000). Cerebral specialization for speech and non-speech stimuli in infants. *J. Cognitive Neurosci.* 12, 449–460. doi: 10.1162/089892900562264

Diamond, A. (2002). "Normal development of prefrontal cortex from birth to young adulthood: cognitive functions, anatomy, and biochemistry," in *Principles of Frontal Lobe Function*, eds D. T. Stuss and R. T. Knight (Oxford: Oxford University Press), 466–503.

Dichter, G. S. (2012). Functional magnetic resonance imaging of autism spectrum disorders. *Dialogues Clin. Neurosci.* 14, 319–351.

Dishman, R. K., Nakamura, Y., Garcia, M. E., Thompson, R. W., Dunn, A. L., and Blair, S. N. (2000). Heart rate variability, trait anxiety, and perceived stress among physically fit men and women. *Int. J. Psychophysiol.* 37, 121–133. doi: 10.1016/S0167-8760(00)00085-4

Doty, R. L., Shaman, P., Applebaum, S. L., Giberson, R., Sikorski, L., and Rosenberg, L. (1984a). Smell identification ability: changes with age. *Science* 226, 1441–1443. doi: 10.1126/science.6505700

Doty, R. L., Shaman, P., and Dann, M. (1984b). Development of the University of Pennsylvania smell identification test: a standardized microencapsulated test of olfactory function. *Physiol. Behav.* 32, 489–502. doi: 10.1016/0031-9384(84)90269-5

Dudova, I., Vodicka, J., Havlovicova, M., Sedlacek, Z., Urbanek, T., and Hrdlicka, M. (2011). Odor detection threshold, but not odor identification, is impaired in

children with autism. *Eur. Child Adolesc. Psychiatry* 20, 333–340. doi: 10.1007/s00787-011-0177-1

Dumont, R., and Willis, J. O. (2008). "Wechsler adult intelligence scale–third edition," in *Encyclopedia of Special Education*, eds C. R. Reynolds and E. Fletcher-Janzen (Hoboken, NJ: John Wiley & Sons), 2129–2130. doi: 10.1002/9780470373699.speced2203

Duncan, J., and Owen, A. M. (2000). Common regions of the human frontal lobe recruited by diverse cognitive demands. *Trends Neurosci.* 23, 475–483. doi: 10.1016/S0166-2236(00)01633-7

Dunn, W., Collier, T., Ziegler, J., and Alexander, K. (1999). "Sensory profile: a measure of sensory experiences in natural environments," in *Proceedings 1999 Autism Society of America National Conference on Autism: Up-to-Date in Kanasas City*, (Bethesda, MD: Autism Society of America), 9–10.

Endevelt-Shapira, Y., Perl, O., Ravia, A., Amir, D., Eisen, A., Bezalel, V., et al. (2018). Altered responses to social chemosignals in autism spectrum disorder. *Nat. Neurosci.* 21, 111–119. doi: 10.1038/s41593-017-0024-x

Fukasawa, A., Suzuki, R., and Okada, K. (2013). "Olfactory measurement system to quantify the ability to smell using pulse ejection," in *Proceedings of the 2013 IEEE International Conference on Healthcare Informatics*, (Philadelphia, PA: IEEE), 99–106. doi: 10.1109/ICHI.2013.19

Galle, S. A., Courchesne, V., Mottron, L., and Frasnelli, J. (2013). Olfaction in the autism spectrum. *Perception* 42, 341–355. doi: 10.1068/p7337

Gilbert, S. J., Spengler, S., Simons, J. S., Steele, J. D., Lawrie, S. M., Frith, C. D., et al. (2006). Functional specialization within rostral prefrontal cortex (area 10): a meta-analysis. *J. Cogn. Neurosci.* 18, 932–948. doi: 10.1162/jocn.2006.18.6.932

Grainger, C., Williams, D. M., and Lind, S. E. (2016). Metacognitive monitoring and control processes in children with autism spectrum disorder: diminished judgement of confidence accuracy. *Conscious. Cogn.* 42, 65–74. doi: 10.1016/j.concog.2016.03.003

Han, P. F., Zang, Y. P., Akshita, J., and Hummel, T. (2019). Magnetic resonance imaging of human olfactory dysfunction. *Brain Topogr.* 32, 987–997. doi: 10.1007/s10548-019-00729-5

Harada, H., Tanaka, M., and Kato, T. (2006). Brain olfactory activation measured by near-infrared spectroscopy in humans. *J. Laryngol. Otol.* 120, 638–643. doi: 10.1017/S002221510600123X

Hedner, M., Larsson, M., Arnold, N., Zucco, G. M., and Hummel, T. (2010). Cognitive factors in odor detection, odor discrimination, and odor identification tasks. *J. Clin. Exp. Neuropsychol.* 32, 1062–1067. doi: 10.1080/13803391003683070

Hill, E. L. (2004). Evaluating the theory of executive dysfunction in autism. *Dev. Rev.* 24, 189–233. doi: 10.1016/j.dr.2004.01.001

Hilton, C., Graver, K., and Lavesser, P. (2007). Relationship between social competence and sensory processing in children with high functioning autism spectrum disorders. *Res. Autism Spectr. Disord.* 1, 164–173. doi: 10.1016/j.rasd.2006.10.002

Hrdlicka, M., Vodicka, J., Havlovicova, M., Urbanek, T., Blatny, M., and Dudova, I. (2011). Brief report: significant differences in perceived odor pleasantness found in children with ASD. *J. Autism Dev. Disord.* 41, 524–527. doi: 10.1007/s10803-010-1084-x

Hummel, T., Sekinger, B., Wolf, S. R., Pauli, E., and Kobal, G. (1997). 'Sniffin' sticks': olfactory performance assessed by the combined testing of odor identification, odor discrimination and olfactory threshold. *Chem. Senses* 22, 39–52. doi: 10.1093/chemse/22.1.39

Ishimaru, T., Yata, T., and Hatanaka-Ikeno, S. (2004a). Hemodynamic response of the frontal cortex elicited by intravenous thiamine propyldisulphide administration. *Chem. Senses* 29, 247–251. doi: 10.1093/chemse/bjh029

Ishimaru, T., Yata, T., Horikawa, K., and Hatanaka, S. (2004b). Near-infrared spectroscopy of the adult human olfactory cortex. *Acta Otolaryngol. Suppl.* 124, 95–98. doi: 10.1080/03655230410017751

Jeste, S. S., and Geschwind, D. H. (2014). Disentangling the heterogeneity of autism spectrum disorder through genetic findings. *Nat. Rev. Neurol.* 10, 74–81. doi: 10.1038/nrneurol.2013.278

Keller, A. (2011). Attention and olfactory consciousness. *Front. Psychol.* 2:380. doi: 10.3389/fpsyg.2011.00380

Kenworthy, L., Yerys, B. E., Anthony, L. G., and Wallace, G. L. (2008). Understanding executive control in autism spectrum disorders in the lab and in the real world. *Neuropsychol. Rev.* 18, 320–338. doi: 10.1007/s11065-008-9077-7

Kientz, M. A., and Dunn, W. (1997). A comparison of the performance of children with and without autism on the sensory profile. *Am. J. Occup. Ther.* 51, 530–537. doi: 10.5014/ajot.51.7.530

Klem, G. H., Luders, H. O., Jasper, H. H., and Elger, C. (1999). The ten-twenty electrode system of the International Federation. The International federation of clinical neurophysiology. *Electroencephalogr. Clin. Neurophysiol. Suppl.* 52, 3–6.

Kobayashi, E., Karaki, M., Kusaka, T., Kobayashi, R., Itoh, S., and Mori, N. (2009). Functional optical hemodynamic imaging of the olfactory cortex in normosmia subjects and dysosmia subjects. *Acta Otolaryngol. Suppl.* 562, 79–84. doi: 10.1080/00016480902964325

Koehler, L., Foumel, A., Albertowski, K., Roessner, V., Gerber, J., Hummel, C., et al. (2018). Impaired odor perception in autism spectrum disorder is associated with decreased activity in olfactory cortex. *Chem. Senses* 43, 627–634. doi: 10.1093/chemse/bjy051

Kumar, A., Croft Swanwick, C., Johnson, N., Menashe, I., Basu, S. N., Bales, M. E., et al. (2011). A brain region-specific predictive gene map for autism derived by profiling a reference gene set. *PLoS One* 6:e28431. doi: 10.1371/journal.pone.0028431

Kumazaki, H., Kikuchi, M., Yoshimura, Y., Miyao, M., Okada, K.-I., Mimura, M., et al. (2018a). Relationship between odor identification and visual distractors in children with autism spectrum disorders. *J. Autism Dev. Disord.* 48, 2590–2592. doi: 10.1007/s10803-018-3511-3

Kumazaki, H., Muramatsu, T., Fujisawa, T. X., Miyao, M., Matsuura, E., Okada, K.-I., et al. (2016). Assessment of olfactory detection thresholds in children with autism spectrum disorders using a pulse ejection system. *Mol. Autism* 7:6. doi: 10.1186/s13229-016-0071-2

Kumazaki, H., Muramatsu, T., Miyao, M., Okada, K. I., Mimura, M., and Kikuchi, M. (2019). Brief report: olfactory adaptation in children with autism spectrum disorders. *J. Autism Dev. Disord.* 49, 3462–3469. doi: 10.1007/s10803-019-04053-6

Kumazaki, H., Okamoto, M., Kanzaki, S., Okada, K. I., Mimura, M., Minabe, Y., et al. (2018b). Approaches for assessing olfaction in children with autism spectrum disorder. *Methods Mol. Biol.* 1820, 221–228. doi: 10.1007/978-1-4939-8609-5_16

Kumazaki, H., Okamoto, M., Yoshimura, Y., Ikeda, T., Hasegawa, C., Saito, D. N., et al. (2018c). Brief report: odour awareness in young children with autism spectrum disorders. *J. Autism Dev. Disord.* 50, 1809–1815. doi: 10.1007/s10803-018-3710-y

Kurita, H., Miyake, Y., and Katsuno, K. (1989). Reliability and validity of the childhood autism rating scale-Tokyo version (CARS-TV). *J. Autism Dev. Disord.* 19, 389–396. doi: 10.1007/BF02212937

Lane, A. E., Young, R. L., Baker, A. E., and Angley, M. T. (2010). Sensory processing subtypes in autism: association with adaptive behavior. *J. Autism Dev. Disord.* 40, 112–122. doi: 10.1007/s10803-009-0840-2

Larsson, M., Finkel, D., and Pedersen, N. L. (2000). Odor identification: influences of age, gender, cognition, and personality. *J. Gerontol B Psychol.* 55, 304–310. doi: 10.1093/geronb/55.5.P304

Larsson, M., Tirado, C., and Wiens, S. (2017). A meta-analysis of odor thresholds and odor identification in autism spectrum disorders. *Front. Psychol.* 8:679. doi: 10.3389/fpsyg.2017.00679

Leekam, S. R., Libby, S. J., Wing, L., Gould, J., and Taylor, C. (2002). The diagnostic interview for social and communication disorders: algorithms for ICD-10 childhood autism and Wing and Gould autistic spectrum disorder. *J. Child Psychol. Psychiatry* 43, 327–342. doi: 10.1111/1469-7610.00024

Leekam, S. R., Nieto, C., Libby, S. J., Wing, L., and Gould, J. (2007). Describing the sensory abnormalities of children and adults with autism. *J. Autism Dev. Disord.* 37, 894–910. doi: 10.1007/s10803-006-0218-7

Legisa, J., Messinger, D. S., Kermol, E., and Marlier, L. (2013). Emotional responses to odors in children with high-functioning autism: autonomic arousal, facial behavior and self-report. *J. Autism Dev. Disord.* 43, 869–879. doi: 10.1007/s10803-012-1629-2

Lehrner, J. P. (1993). Gender differences in long-term odor recognition memory: verbal versus sensory influences and consistency of label use. *Chem. Senses* 18, 17–26. doi: 10.1093/chemse/18.1.17

Levy, R., and Goldman-Rakic, P. S. (2000). Segregation of working memory functions within the dorsolateral prefrontal cortex. *Exp. Brain Res.* 133, 23–32. doi: 10.1007/s002210000397

Liss, M., Saulnier, C., Fein, D., and Kinsbourne, M. (2006). Sensory and attention abnormalities in autistic spectrum disorders. *Autism* 10, 155–172. doi: 10.1177/1362361306062021

Luisier, A. C., Petitpierre, G., Ferdenzi, C., Clerc Berod, A., Giboreau, A., Rouby, C., et al. (2015). Odor perception in children with autism spectrum disorder and its relationship to food neophobia. *Front. Psychol.* 6:1830. doi: 10.3389/fpsyg.2015.01830

Martin, G. N., and Daniel, N. (2014). Autism spectrum disorders and chemoreception: dead-end or fruitful avenue of inquiry? *Front. Psychol.* 5:42. doi: 10.3389/fpsyg.2014.00042

Matsuura, E., Suzuki, R., Homma, S., and Okada, K. (2014). "Application of olfactory measurement for children to detect autism spectrum disorder early," in *Multimedia, Distributed, Cooperative, and Mobile (DICOM) symposium*, (Fukushima: AHC), 1428–1435.

May, T., Brewer, W. J., Rinehart, N. J., Enticott, P. G., Brereton, A. V., and Tonge, B. J. (2011). Differential olfactory identification in children with autism and Asperger's disorder: a comparative and longitudinal study. *J. Autism Dev. Disord.* 41, 837–847. doi: 10.1007/s10803-010-1101-0

McMahon, C. M., Henderson, H. A., Newell, L., Jaime, M., and Mundy, P. (2016). Metacognitive awareness of facial affect in higher-functioning children and adolescents with autism spectrum disorder. *J. Autism Dev. Disord.* 46, 882–898. doi: 10.1007/s10803-015-2630-3

Minagawa-Kawai, Y., Naoi, N., Kikuchi, N., Yamamoto, J. I., Nakamura, K., and Kojima, S. (2009). Cerebral laterality for phonemic and prosodic cue decoding in children with autism. *Neuroreport* 20, 1219–1224. doi: 10.1097/WNR.0b013e32832fa65f

Murphy, D. G. M., Daly, E. M., Van Amelsvoort, T., Robertson, D., Simmons, A., and Critchley, H. D. (1998). Functional neuroanatomical dissociation of verbal, visual and spatial working memory. *Schizophr. Res.* 29, 105–106. doi: 10.1016/S0920-9964(97)88566-0

Naoi, N., Minagawa-Kawai, Y., Kobayashi, A., Takeuchi, K., Nakamura, K., Yamamoto, J., et al. (2012). Cerebral responses to infant-directed speech and the effect of talker familiarity. *Neuroimage* 59, 1735–1744. doi: 10.1016/j.neuroimage.2011.07.093

O'Connor, K. (2012). Auditory processing in autism spectrum disorder: a review. *Neurosci. Biobehav. Rev.* 36, 836–854. doi: 10.1016/j.neubiorev.2011.11.008

Parma, V., Bulgheroni, M., Tirindelli, R., and Castiello, U. (2013). Body odors promote automatic imitation in autism. *Biol. Psychiatry* 74, 220–226. doi: 10.1016/j.biopsych.2013.01.010

Puts, N. A. J., Wodka, E. L., Tommerdahl, M., Mostofsky, S. H., and Edden, R. A. E. (2014). Impaired tactile processing in children with autism spectrum disorder. *J. Neurophysiol.* 111, 1803–1811. doi: 10.1152/jn.00890.2013

R Core Team (2018). *R: A Language and Environment for Statistical Computing*. Vienna: R Foundation for Statistical Computing.

Ragnarsdóttir, M., and Kristinsdóttir, E. K. (2006). Breathing movements and breathing patterns among healthy men and women 20–69 years of age. *Respiration* 73, 48–54. doi: 10.1159/000087456

Rogers, S. J., Hepburn, S., and Wehner, E. (2003). Parent reports of sensory symptoms in toddlers with autism and those with other developmental disorders. *J. Autism Dev. Disord.* 33, 631–642. doi: 10.1023/b:jadd.0000006000.38991.a7

Rogers, S. J., and Ozonoff, S. (2005). Annotation: what do we know about sensory dysfunction in autism? A critical review of the empirical evidence. *J. Child Psychol. Psychiatry* 46, 1255–1268. doi: 10.1111/j.1469-7610.2005.01431.x

Rozenkrantz, L., Zachor, D., Heller, I., Plotkin, A., Weissbrod, A., Snitz, K., et al. (2015). A mechanistic link between olfaction and autism spectrum disorder. *Curr. Biol.* 25, 1904–1910. doi: 10.1016/j.cub.2015.05.048

Russell, J. E. (1997). *Autism as An Executive Disorder*. Oxford: Oxford University Press.

Saive, A. L., Royet, J. P., and Plailly, J. (2014). A review on the neural bases of episodic odor memory: from laboratory-based to autobiographical approaches. *Front. Behav. Neurosci.* 8:240. doi: 10.3389/fnbeh.2014.00240

Sato, J., Ohtsu, K., Bannai, Y., and Okada, K. I. (2008). "Pulse ejection technique of scent to create dynamic perspective," in *Proceedings of the 18th International Conference on Artificial Reality and Telexistence*, (Ota city: Canon Inc), 167–174.

Schecklmann, M., Schwenck, C., Taurines, R., Freitag, C., Warnke, A., Gerlach, M., et al. (2013). A systematic review on olfaction in child and adolescent psychiatric disorders. *J. Neural Transm.* 120, 121–130. doi: 10.1007/s00702-012-0855-2

Schiffman, S. S. (1997). Taste and smell losses in normal aging and disease. *JAMA* 278, 1357–1362. doi: 10.1001/jama.1997.03550160077042

Schoen, S. A., Miller, L. J., Brett-Green, B. A., and Nielsen, D. M. (2009). Physiological and behavioral differences in sensory processing: a comparison of children with autism spectrum disorder and sensory modulation disorder. *Front. Integr. Neurosci.* 3:29. doi: 10.3389/neuro.07.029.2009

Schopler, E., Reichler, R. J., DeVellis, R. F., and Daly, K. (1980). Toward objective classification of childhood autism: Childhood Autism Rating Scale (CARS). *J. Autism Dev. Disord.* 10, 91–103. doi: 10.1007/BF02408436

Schreck, K. A., and Williams, K. (2006). Food preferences and factors influencing food selectivity for children with autism spectrum disorders. *Res. Dev. Disabil.* 27, 353–363. doi: 10.1016/j.ridd.2005.03.005

Shimamura, A. P. (2008). A neurocognitive approach to metacognitive monitoring and control. *Handb. Metamem. Mem.* 11, 373–390.

Simmons, D. R., Robertson, A. E., Mckay, L. S., Toal, E., Mcaleer, P., and Pollick, F. E. (2009). Vision in autism spectrum disorders. *Vision Res.* 49, 2705–2739. doi: 10.1016/j.visres.2009.08.005

Smith, E. E., Jonides, J., and Koeppe, R. A. (1996). Dissociating verbal and spatial working memory using PET. *Cereb. Cortex* 6, 11–20. doi: 10.1093/cercor/6.1.11

Soudry, Y., Lemogne, C., Malinvaud, D., Consoli, S. M., and Bonfils, P. (2011). Olfactory system and emotion: common substrates. *Eur. Ann. Otorhinolaryngol. Head Neck Dis.* 128, 18–23. doi: 10.1016/j.anorl.2010.09.007

Stanfield, A. C., McIntosh, A. M., Spencer, M. D., Philip, R., Gaur, S., and Lawrie, S. M. (2008). Towards a neuroanatomy of autism: a systematic review and meta-analysis of structural magnetic resonance imaging studies. *Eur. Psychia.* 23, 289–299. doi: 10.1016/j.eurpsy.2007.05.006

Stickel, S., Weismann, P., Kellermann, T., Regenbogen, C., Habel, U., Freiherr, J., et al. (2019). Audio-visual and olfactory-visual integration in healthy participants and subjects with autism spectrum disorder. *Hum. Brain Map.* 40, 4470–4486. doi: 10.1002/hbm.24715

Suzuki, Y., Critchley, H. D., Rowe, A., Howlin, P., and Murphy, D. G. (2003). Impaired olfactory identification in Asperger's syndrome. *J. Neuropsychiatry Clin. Neurosci.* 15, 105–107. doi: 10.1176/jnp.15.1.105

Tachimori, H., Osada, H., and Kurita, H. (2003). Childhood autism rating scale—Tokyo version for screening pervasive developmental disorders. *Psychiatry Clin. Neurosci.* 57, 113–118. doi: 10.1046/j.1440-1819.2003.01087.x

Takakura, H., Shojaku, H., Takamoto, K., Urakawa, S., Nishijo, H., and Watanabe, Y. (2011). Cortical hemodynamic responses to intravenous thiamine propyldisulphide administration detected by multichannel near infrared spectroscopy (NIRS) system. *Brain Topogr.* 24, 114–126. doi: 10.1007/s10548-011-0179-9

Tavassoli, T., and Baron-Cohen, S. (2012). Olfactory detection thresholds and adaptation in adults with autism spectrum condition. *J. Autism Dev. Disord.* 42, 905–909. doi: 10.1007/s10803-011-1321-y

Tomchek, S. D., and Dunn, W. (2007). Sensory processing in children with and without autism: a comparative study using the short sensory profile. *Am. J. Occup. Ther.* 61, 190–200. doi: 10.5014/ajot.61.2.190

Tonacci, A., Billeci, L., Tartarisco, G., Ruta, L., Muratori, F., Pioggia, G., et al. (2017). Olfaction in autism spectrum disorders: a systematic review. *Child Neuropsychol.* 23, 1–25. doi: 10.1080/09297049.2015.1081678

Travers, B. G., Klinger, M. R., and Klinger, L. G. (2011). "Attention and working memory in ASD," in *The Neuropsychology of Autism*, ed. D. Fein (Oxford: Oxford University Press), 161–184.

Tsuzuki, D., Jurcak, V., Singh, A. K., Okamoto, M., Watanabe, E., and Dan, I. (2007). Virtual spatial registration of stand-alone MRS data to MNI space. *Neuroimage* 34, 1506–1518. doi: 10.1016/j.neuroimage.2006.10.043

Watanabe, E., Yamashita, Y., Maki, A., Ito, Y., and Koizumi, H. (1996). Non-invasive functional mapping with multi-channel near infra-red spectroscopic topography in humans. *Neurosci. Lett.* 205, 41–44. doi: 10.1016/0304-3940(96)12376-4

Wechsler, D. (2003). *Wechsler Intelligence Scale for Children, 4th Edn (WISC-IV)*. San Antonio: The Psychological Corporation.

Wicker, B., Monfardini, E., and Royet, J. P. (2016). Olfactory processing in adults with autism spectrum disorders. *Mol. Autism* 7:4. doi: 10.1186/s13229-016-0070-3

Wiggins, L. D., Robins, D. L., Bakeman, R., and Adamson, L. B. (2009). Breif report: sensory abnormalities as distinguishing symptoms of autism spectrum disorders in young children. *J. Autism Dev. Disord.* 39, 1087–1091. doi: 10.1007/s10803-009-0711-x

Woo, C. C., Donnelly, J. H., Steinberg-Epstein, R., and Leon, M. (2015). Environmental enrichment as a therapy for autism: a clinical trial replication and extension. *Behav. Neurosci.* 129, 412–422. doi: 10.1037/bne0000068

Xu, M., Hoshino, E., Yatabe, K., Matsuda, S., Sato, H., Maki, A., et al. (2017). Prefrontal function engaging in external-focused attention in 5-to 6-month-old infants: a suggestion for default mode network. *Front. Hum. Neurosci.* 10:676. doi: 10.3389/fnhum.2016.00676

Zatorre, R. J., Jones-Gotman, M., Evans, A. C., and Meyer, E. (1992). Functional localization and lateralization of human olfactory cortex. *Nature* 360, 339–340. doi: 10.1038/360339a0

Zelano, C., Montag, J., Khan, R., and Sobel, N. (2009). A specialized odor memory buffer in primary olfactory cortex. *PLoS One* 4:e4965. doi: 10.1371/journal.pone.0004965

Conflict of Interest: The authors declare that the research was conducted in the absence of any commercial or financial relationships that could be construed as a potential conflict of interest.

Copyright © 2020 Xu, Minagawa, Kumazaki, Okada and Naoi. This is an open-access article distributed under the terms of the Creative Commons Attribution License (CC BY). The use, distribution or reproduction in other forums is permitted, provided the original author(s) and the copyright owner(s) are credited and that the original publication in this journal is cited, in accordance with accepted academic practice. No use, distribution or reproduction is permitted which does not comply with these terms.

frontiers in Human Neuroscience

ORIGINAL RESEARCH
published: 05 November 2020
doi: 10.3389/fnhum.2020.519171

Acute Effects of Two Types of Dumbbell Exercise on Oxygenated Hemodynamic Concentration of Cerebral Activation in Healthy Young Male Adults: A Functional Near-Infrared Spectroscopy Study

Yana Wang[1,2], Jiaojiao Lü[1], Jifeng Rong[2], Linjie Song[1], Wei Wang[1], Yifan Jiang[1], Yu Liu[1] and Lingyan Huang[1]**

[1]Key Laboratory of Exercise and Health Science of Ministry of Education, Shanghai University of Sport, Shanghai, China, [2]Department of Rehabilitation Medicine, Shanghai First Rehabilitation Hospital, Shanghai, China

OPEN ACCESS

Edited by:
Fenghua Tian,
University of Texas at Arlington, United States

Reviewed by:
Tao Liu,
Zhejiang University, China
Hada Fong-ha Ieong,
Yale University, United States

***Correspondence:**
Yu Liu
yuliu@sus.edu.cn
Lingyan Huang
alice37yn@163.com

Specialty section:
This article was submitted to Brain Imaging and Stimulation, a section of the journal Frontiers in Human Neuroscience

Received: *13 December 2019*
Accepted: *01 September 2020*
Published: *05 November 2020*

Citation:
Wang Y, Lü J, Rong J, Song L, Wang W, Jiang Y, Liu Y and Huang L (2020) Acute Effects of Two Types of Dumbbell Exercise on Oxygenated Hemodynamic Concentration of Cerebral Activation in Healthy Young Male Adults: A Functional Near-Infrared Spectroscopy Study. Front. Hum. Neurosci. 14:519171. doi: 10.3389/fnhum.2020.519171

Purpose: To examine cerebral cortical activation differences in the frontal cortex and parietal lobe during the performance of two types of dumbbell exercise.

Methods: A total of 22 young healthy male adults (mean age, 23.8 ± 2.05 years; height, 1.75 ± 0.06 m; weight, 71.4 ± 8.80 kg) participated in a crossover design study that involved two experimental exercise conditions: momentum dumbbell and conventional dumbbell. Performance tasks included 10, 10-s sets of single-arm dumbbell exercise, with a rest interval of 60 s between sets and a 5-min washout period between conditions. The primary outcome was the cerebral concentrations of oxygenated hemoglobin (HbO_2) in the frontal cortex and parietal lobe assessed during performance of both exercises using functional near-infrared spectroscopy (fNIRS). The secondary outcome was upper-limb muscle activation measured using surface electromyography (sEMG). Outcome data were ascertained during exercise.

Results: A significant between-condition difference in HbO_2 was observed in the frontal and parietal regions with an increase in HbO_2 during momentum, relative to conventional, dumbbell exercise ($p < 0.05$). Compared to conventional dumbbell exercise, performing a momentum dumbbell exercise led to a higher level of muscle activation in the anterior and posterior deltoids of the upper arm and in the flexor carpi radialis and extensor carpi radialis longus of the forearm ($p < 0.05$). However, no between-condition differences were found in the biceps and triceps brachii ($p > 0.05$).

Conclusion: Dynamic, compared with conventional, dumbbell exercise resulted in higher hemodynamic responses and greater upper-limb muscle activation in young healthy

Abbreviations: fNIRS, functional near infrared spectroscopy; HbO_2, oxygenated hemoglobin; MANOVA, multivariate analysis of variance; sEMG, surface electromyography.

adults. The findings of this study showed differential cortical hemodynamic responses during performance of the two types of dumbbell exercise with a higher activation level produced during momentum-based dumbbell exercise.

Keywords: momentum dumbbell, conventional dumbbell, strengthening exercise, functional near infrared spectroscopy (fNIRS), surface electromyography (sEMG)

INTRODUCTION

There is now irrefutable scientific evidence showing the health benefits of various exercise modalities such as aerobic, resistance and balance training and flexibility exercise in improving cardiovascular fitness (Fletcher et al., 2018), cognitive function (Northey et al., 2018), musculoskeletal health (Hagen et al., 2012), and the metabolic system (Park and Larson, 2014). Among the most common exercise modalities, resistance training, which causes the muscles to contract against an external resistance, has been shown to be therapeutically effective in improving muscular strength (Grgic et al., 2018), balance (Orr et al., 2008), bone health (Hong and Kim, 2018), and cognitive function (Li et al., 2018) among younger and older adults. In addition, resistance training regimens such as free-weight dumbbells were also shown to elicit changes in the hemodynamic concentration of the primary motor cortex in healthy adults (Bai et al., 2016).

Using a novel momentum dumbbell exercise type that involved self-initiated spinning of a handheld dumbbell with a built-in pendulum to generate momentum for training upper-limb strength and core stability, Lü et al. (2015) evaluated the effects of this motor–cognitive integrated dynamic exercise on cognitive function among older adults with mild cognitive impairment. Findings of the study showed that, compared with a no-exercise control condition, 12 weeks of momentum dumbbell training resulted in significant improvement in cognitive ability and physical performance. Thus, while conventional dumbbell exercise was shown to increase brain oxygenation (Bai et al., 2016), the augmented momentum dumbbell exercise has also shown potential for enhancing cognition.

Therefore, by extending the studies of conventional (Bai et al., 2016) and momentum (Lü et al., 2015) dumbbell exercises on brain activity and cognitive function, this study aims to examine cerebral cortical activation differences in the regions of the frontal cortex and parietal lobe during the performance of conventional dumbbell and momentum dumbbell exercises using functional near infrared spectroscopy (fNIRS) among young healthy adults. We specifically targeted the frontal cortex and parietal lobe because of their functional (motor and sensory) roles intrinsically linked with exercise performance (Bai et al., 2016). We hypothesized that, compared with conventional dumbbell exercise, momentum dumbbell exercise would lead to a higher level of oxygenated hemoglobin (HbO_2) concentration in the frontal cortex and parietal lobe. As secondary outcomes, we also examined the differences between these two exercises on upper-arm muscle activation patterns.

MATERIALS AND METHODS

Study Design and Participants

The study used a crossover design in which 22 male adults completed two different dumbbell-based exercise conditions: momentum dumbbell exercise and conventional dumbbell exercise, consecutively administered in each participant. Eligibility criteria included being male, age $\geq$20 years, absence of neurological disorders, and physical fitness. Subjects were recruited through public promotion and word of mouth among college students studying at the Shanghai University of Sport (SUS) in Shanghai, China. All participants provided written consent to participate in the study, and the study procedures were approved by the Ethics Committee at SUS and conformed to the Declaration of Helsinki.

Experimental Tasks

Participants were instructed to stand straight with their feet hip-width apart, toes facing forward, and handhold a dumbbell (in a horizontal position) using the dominant hand with palms facing up, positioned on the lateral side of the body. Participants were asked to stand quietly for 60 s and, upon receiving a "Go" signal light (placed in front of them), to begin performing the single-arm dumbbell curl exercises at their self-selected speed for 10 s. Each dumbbell exercise session consisted of 10 10-s sets of exercise with a 60-s resting break in between. A 5-min interval (wash out) between the two dumbbell exercise conditions was provided. **Figure 1** describes the flow of the current study.

The momentum dumbbell used in this study was a handheld device with two built-in eccentric pendulums (approximately 9 cm in length) at each end, with dimensions of 32 cm in length and 22 cm in diameter and weighing 1.92 kg (Lü et al., 2015). During the exercise, participants were instructed to perform a continuous spinning motion by having the pendulums inside the dumbbell spinning in a clockwise direction around the frontal axis for up to 10 s. For the conventional single dumbbell exercise, participants were instructed to engage in bicep curls performed in the sagittal plane at their own pace without moving the upper arm by bending the elbow joint and curling the dumbbell at approximately 90 angles, then allowing the dumbbell to return to the starting position. A brief cool-down period was provided at the end of the exercise experiment.

Experimental Procedure

The experiment was conducted at a research laboratory located in an academic setting. Participants reported to the laboratory twice, at an interval of at least 24 h. To control for the potential influence of cerebral hemodynamic responses resulting from stimulant intake, participants were required

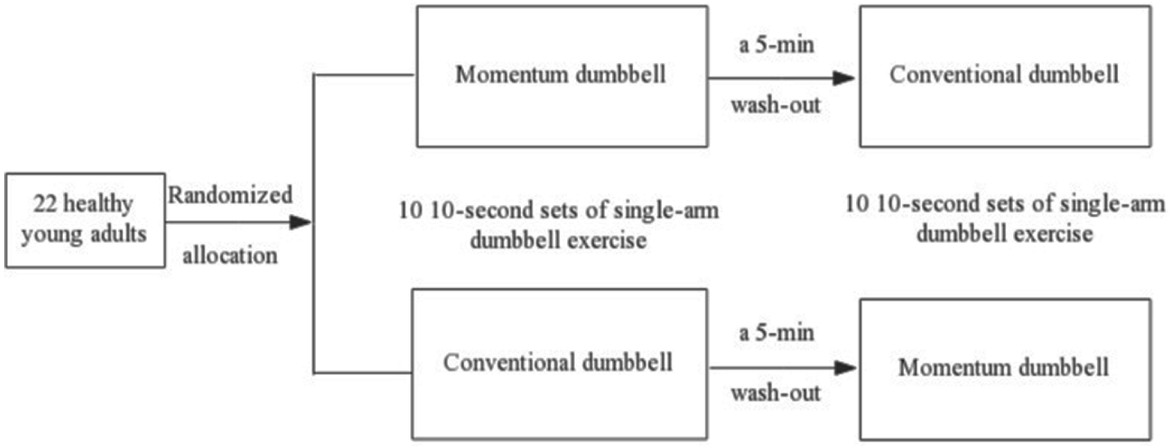

FIGURE 1 | Flow of the cross-over study design.

to refrain from alcohol and caffeine intake for 24 h before data acquisition (Orihuela-Espina et al., 2010). During the first visit, participants were provided with an orientation of the experimental task protocol, including an introduction to each of the dumbbell exercise techniques and a brief warm-up practice for each exercise to acclimatize themselves to the performance protocol. On the second visit, the exercise protocol was reiterated to all participants, who were then allowed sufficient warm-up time before performing the experimental tasks. After the warm-up, the experimenter placed the surface electrodes over the targeted muscle belly for collecting the surface electromyography (sEMG) data, and the fNIRS probes were placed on the participants' heads. Participants were then instructed to complete the two types of dumbbell exercise tasks per the instructions provided.

Randomization and Blinding

The order of exercise conditions was randomized, and the experimenters were blinded to the order of conditions until the experimental visit.

Outcome Assessment

Primary Outcome

Cerebral concentrations of HbO_2 in the anterior frontal cortex and parietal lobe of the brain during the performance of the two exercises were the primary outcome measures. HbO_2 was assessed during the exercise using fNIRS (NIRScout, NIRX Medical Technologies, Minneapolis, MN, USA). Participants were fitted with the fNIRS cap on their head, secured with conductive paste in the areas corresponding to their anterior frontal cortex and parietal lobe for each hemisphere (consisting of 20 channels on each side with an interoptode distance of 30 mm), and were asked to perform the exercise described in the Experimental Tasks section. Necessary adjustments, corresponding to the 10-20 system, were made to the probe for each participant (Jurcak et al., 2007). Headgear was fitted on the top of the optodes to prevent detectors from interfering with the movement. The device emitted light at two wavelengths (780 and 830 nm), with a sampling rate of 3.91 Hz. **Figure 2** describes the spatial arrangement of the fNIRS probes used during the experiment.

Surface Electromyography

We used the Delsys data acquisition system (Trigno Wireless EMG System, Delsys, Natick, MA, USA) to record surface electromyographic signals (electrical activity) of the upper-limb muscles in response to the dumbbell exercises. The targeted muscles of the dominant arm included the anterior deltoid, posterior deltoid, biceps brachii and triceps brachii of the upper arm, and flexor carpi radialis and extensor carpi radialis longus of the forearm. Before placing the Delsys electrodes over the bellies of the targeted muscle fibers, excessive hair was shaved, and the skin was cleaned with an alcohol preparation pad and allowed time to try. After confirming signal quality, the electrodes were secured with adhesive tape and elastic straps or net bandages (Hermens et al., 2000). Raw sEMG signals were amplified, simultaneously digitized, and acquired at a sample rate of 2,000 Hz.

Data Acquisition, Processing, and Reductions

To synchronize data acquisition, a customized synchronization box was prepared that connected the sEMG to the functional near infrared computer's input and to the "Go" signal light.

Because HbO_2 signals can reflect changes in the local brain blood flow better, only oxygenated concentration data were processed and analyzed (Hoshi, 2005) using the HomER2 toolbox (MGH-Martinos Center for Biomedical Imaging, Boston, MA, USA) based on MATLAB (Mathworks, Natick, MA, USA; Huppert et al., 2009). As part of the quality control, we first inspected the signal quality of the individual channels by means of the coefficient of variation, with the exclusion value set at 25% (Schneider et al., 2011). Using a movement artifact reduction algorithm, a detection of

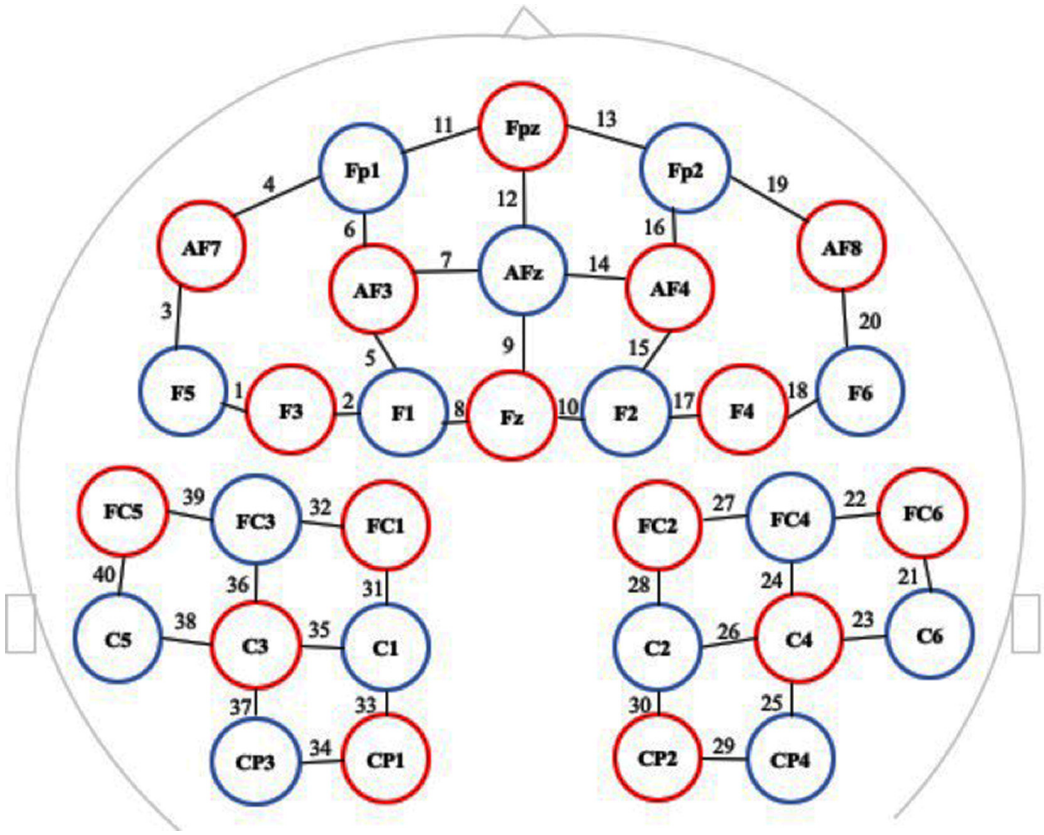

FIGURE 2 | Spatial arrangement of the functional near infrared spectroscopy (fNIRS) probes in which red circles indicate the 16 optical sources, blue circles indicate the 15 detectors, and black numbers (1–40) indicate the fNIRS channels. The optical sources and detectors were positioned on the international 10-20 system.

sampling points greater than 50 standard deviations from the mean was used as a rejection point for movement correction (Scholkmann et al., 2010). The data were band-pass filtered (0.01–0.1 Hz) to remove physiological noise and baseline drift (Huppert et al., 2009; Tong et al., 2012). We transformed the optical data into hemoglobin signals with mol/l based on the modified Beer–Lambert Law (Cope et al., 1988). In each channel, HbO_2 concentration ascertained from the two dumbbell exercises was corrected by baseline (i.e., 2 s before trial onset) and then averaged for all participants (Niu et al., 2019). The mean HbO_2 concentration for each channel was arranged in descending order with the top 25% of channels (with greatest values) defined as the channels of interest (Chen et al., 2018). The fNIRS space was converted into the standard Montreal Neurological Institute coordinate space. These channels of interest corresponded to two regions of interest (ROI) as shown in **Table 1**, i.e., the frontal cortex and parietal lobe.

The sEMG signals were recorded during the entire exercise at 2,000 Hz using a Delsys amplifier and data acquisition system. The measurement of sEMG signals was initially band-pass filtered at 10–400 Hz, and their means were processed using the Delsys 4.3 analysis software. For analysis purposes, we calculated the root mean square on each of the targeted muscles within 10 s.

Statistical Analysis

Descriptive statistics were used to describe the demographic characteristics of the study participants, including age, height, weight, and frequency of weekly habitual physical activity. Differences in HbO_2 between momentum dumbbell and conventional dumbbell exercises were assessed on the basis of the within-subject difference between the two exercise conditions with regard to the two ROIs. Accordingly, one-way repeated-measures multivariate analysis of variance (MANOVA) was conducted. In the presence of an omnibus *F*-test statistic in MANOVA, a follow-up univariate repeated-measures ANOVA was performed for each dependent variable. Statistical significance was set at $p \leq 0.05$. A similar analytic approach was used for the six muscle outcome measures derived from the sEMG. Effect sizes are presented as partial eta-square (η^2). Given the multiple dependent variables in our sEMG data, the *p*-value was adjusted for multiple testing (0.05/6 = 0.008). All data are presented as mean ± standard deviation. Statistical analyses were performed with SPSS version 25 (IBM Corp., Armonk, NY, USA).

Sample Size and Power

We calculated the sample size that compared the expected difference on the primary outcome of HbO_2 in both ROIs

TABLE 1 | Two regions of interest (ROI).

ROI	Channel	Hemisphere	Location	Brodmann area
1	6	Left	AFp3	10-Frontopolar area
	13	Right	Fp2h	11-Orbitofrontal area
	21	Right	FCC6	43-Subcentral area
	23	Right	C6h	1-Primary somatosensory cortex
	29	Right	CP4h	2-Primary somatosensory cortex 40-Supramarginal gyrus, part of Wernicke's area
	30	Right	CCP2	4-Primary motor cortex
2	34	Left	CP3h	2-Primary somatosensory cortex & 40-Supramarginal gyrus, part of Wernicke's area
	38	Left	C5h	1-Primary somatosensory cortex
	39	Left	FC5h	44-Pars opercularis, part of Broca's area & 6-Pre-motor and supplementary motor cortex
	40	Left	FCC5	43-Subcentral area

ROI, region of interest.

between the two experimental (momentum dumbbell vs. conventional dumbbell exercises) conditions. On the basis of prior research (Lü et al., 2015), we determined that a sample size of 20 participants would provide 80% power (at a two-tailed α-level of 0.05, a correlation of 0.50) for detecting a medium effect size (Cohen's $d = 0.65$) in HbO_2 between the two experimental conditions in either of the ROIs. Assuming a 10% attrition rate, the study was planned for a total of 22 participants.

RESULTS

Compliance and Adverse Events

A total of 23 participants were recruited and completed the experiment. There were no exercise-induced side effects observed during the study. The fNIRS data of one participant were unusable and were removed from the analysis. Thus, the data of the remaining 22 participants were analyzed and reported. Demographic characteristics of the participants are presented in **Table 2**.

Primary Outcomes

The MANOVA results showed a significant experimental condition effect on HbO_2 across the two ROIs, $F_{(2,20)} = 19.70$, $p < 0.001$. Results from the follow-up ANOVAs showed that a significant experimental condition effect existed for both the frontal cortex ($F_{(1,21)} = 41.34$, $p < 0.001$, partial $\eta^2 = 0.66$) and the parietal lobe ($F_{(1,21)} = 16.96$, $p < 0.001$, partial $\eta^2 = 0.45$). An inspection of the difference in means between the two experimental conditions indicated that a statistically significant higher level of HbO_2 concentration was observed for the momentum dumbbell exercise relative to the conventional dumbbell exercise in the frontal cortex (11.603×10^{-7} mol/l $\pm$ 8.159×10^{-7} mol/l vs. 0.257×10^{-7} mol/l $\pm$ 4.128×10^{-7} mol/l, $p < 0.05$) and in the parietal lobe (6.373×10^{-7} mol/l $\pm$ 4.521×10^{-7} mol/l vs. 1.978×10^{-7} mol/l $\pm$ 2.962×10^{-7} mol/l, $p < 0.05$). **Figure 3** displays the differences in HbO_2 concentrations in the frontal cortex and parietal lobe between the momentum and conventional dumbbell exercises.

TABLE 2 | Demographic characteristics of study participants ($N = 22$).

Profile	Descriptive statistics
Age, mean (years; SD)	23.8 (2.05)
Height, mean (m; SD)	1.75 (0.06)
Weight, mean (kg; SD)	71.4 (8.80)
Habitual physical activity (days/week; SD)	4.09 (1.70)

SD, standard deviation.

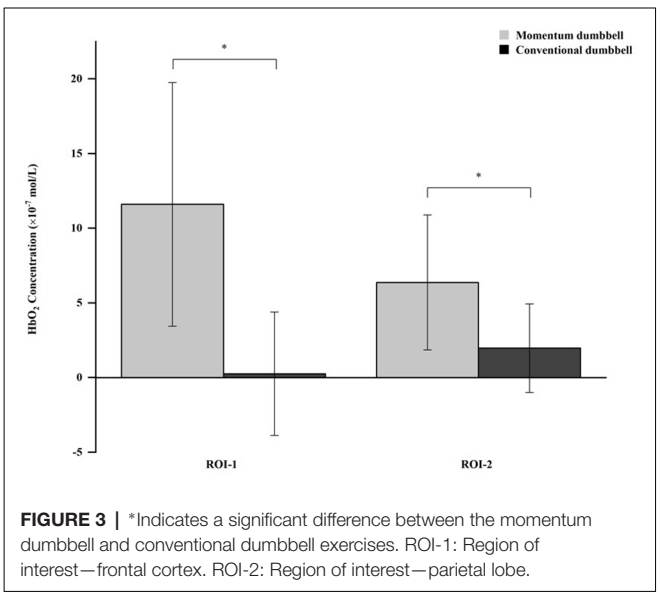

FIGURE 3 | *Indicates a significant difference between the momentum dumbbell and conventional dumbbell exercises. ROI-1: Region of interest—frontal cortex. ROI-2: Region of interest—parietal lobe.

Secondary Outcomes

The MANOVA results indicated a significant experimental condition effect on the six muscles studied, $F_{(6,16)} = 20.65$, $p < 0.001$. Of the six ANOVAs conducted, four were statistically significant ($p \leq 0.003$). Compared to the conventional dumbbell exercise, momentum dumbbell exercise was shown to involve a higher level of electrical activity in the muscles of the anterior and posterior deltoids of the upper arm and the flexor carpi radialis and extensor carpi radialis longus of the forearm ($p < 0.05$). There was, however, no significant difference in the biceps brachii ($p = 0.06$) and triceps brachii ($p = 0.37$). Estimates on sEMG are presented in **Figure 4**.

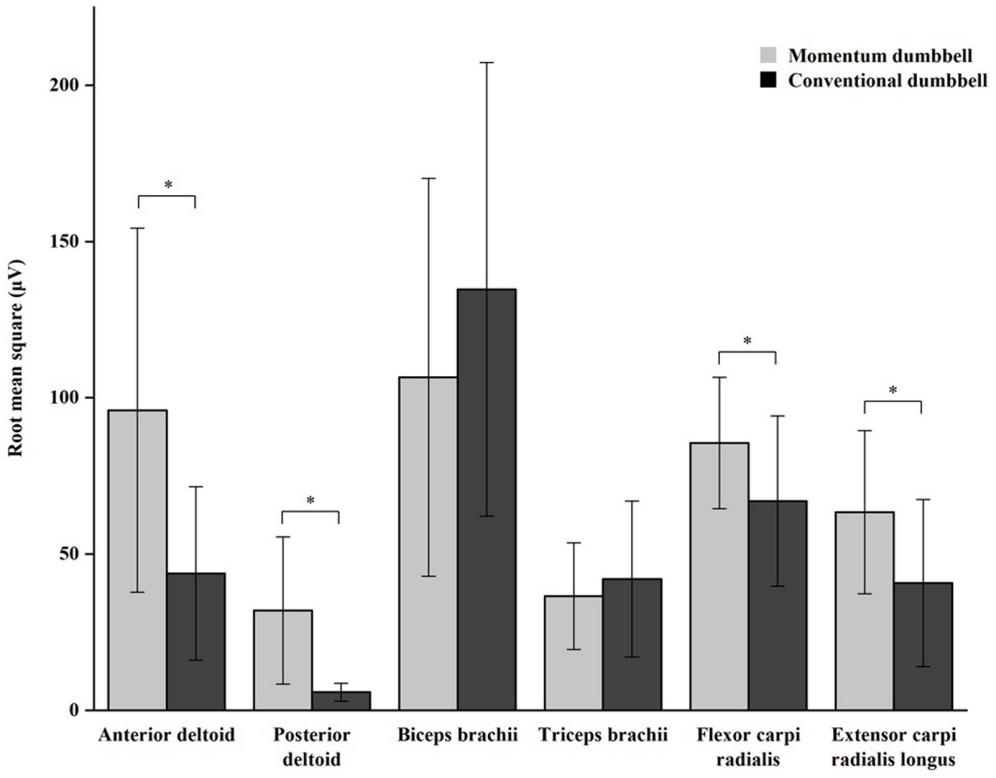

FIGURE 4 | *Indicates a significant difference between the momentum dumbbell and conventional dumbbell exercises.

DISCUSSION

In this study, we compared the acute effects of two resistance-based dumbbell training exercises on cerebral cortical activation among healthy young male adults. Through quantification of fNIRS, we found that, although both the momentum and conventional dumbbell exercises elicited oxygenated hemodynamic responses in the frontal cortex and parietal lobe, the momentum dumbbell exercise produced a higher level of acute cerebral response than the conventional exercise. In addition, relative to the conventional exercise, performing the momentum exercise led to a higher level of muscle activation in the anterior and posterior deltoids of the upper arm and flexor carpi radialis and extensor carpi radialis longus of the forearm.

The results regarding the hemodynamic responses observed during both dumbbell exercises in this study are consistent with findings showing hemodynamic responses during walking (Miyai et al., 2001), running (Suzuki et al., 2004), cycling (Lin et al., 2012, 2013; Tempest and Reiss, 2019), and video game-based dynamic balancing exercise (Karim et al., 2012) among healthy adults and patients with stroke. However, this was the first study that compared two active but different resistance training regimens, with the results showing a higher level of hemodynamic responses elicited from the momentum-based dumbbell exercise. Using the fNIRS neuroimaging tool, the study extended the findings of a previous momentum dumbbell intervention study (Lü et al., 2015) by showing that the momentum dumbbell exercise was also associated with hemodynamic alterations as evidenced in both the frontal cortex and parietal lobe, areas in the brain that are considered important for cognitive functioning and the executive control of arm movement (Rossi et al., 2009).

The exact mechanisms by which the momentum dumbbell exercise elicits the hemodynamic response are unclear. One plausible explanation is the challenging movement characteristics of this novel exercise modality. The exercise requires that an individual perform with a high level of coordination between upper-extremity strength and core control, as well as attention necessary to maintain the spinning action of the dumbbell (i.e., spinning of the pendulum inside the dumbbell). This dual-tasking feature may have been responsible for the increased level of HbO_2 observed in the frontal cortex and parietal lobe, findings that align with the hemodynamic responses observed in aerobic-based exercise with dual tasking (Mirelman et al., 2014). In contrast, conventional dumbbell exercise primarily involves a single (elbow) joint arm extension/flexion mechanical movement performed in a single (sagittal) plane. Naturally, we cannot exclude the possibility that performance of the momentum, relative to the conventional, dumbbell exercise may require higher effort by the participants, inducing higher work load and thus increasing activation. Nevertheless, the current findings provide impetus for future inquiries regarding the mechanisms by which resistance-based exercises induce cerebrovascular changes.

In addition to the increase in the level of HbO_2 in response to the dynamic dumbbell exercises, our EMG analyses showed high levels of muscle activity involving the shoulder and forearm during dumbbell performance. The differences in muscle activation patterns between the two exercise formats may have been due to the high speed and frequency of movements occurring during the momentum dumbbell exercise, resulting in high muscle recruitment, whereas for the conventional dumbbell exercise, the elbow joint of the performing arm was relatively fixed while engaging in bicep curls (flexion-extension), with limited active engagement of the proximal (shoulder) and distal (wrist) joints. Collectively, these EMG data provide additional support for the hemodynamic responses observed because they indicate concomitant activities occurring both at the cortical level and in the working muscles involved in the performance of the experimental dumbbell task, with higher levels of muscle activity observed in the momentum dumbbell exercise. Such a co-occurring event, however, does not necessarily imply that one is the cause of the other (i.e., that cortical activation causes the muscle activities in question). We observed no difference between the two exercise methods in the biceps and triceps brachii of the upper arm. While the dumbbell exercise movement predominantly involves bicep curls, our results suggest that there is an equal amount of involvement or firing in the biceps brachii while performing the exercises with either type of dumbbell.

This study adds new knowledge regarding a novel momentum-based dumbbell exercise, compared to a conventional dumbbell exercise, in inducing change in cerebral cortical activation, which will allow us to advance exercise-cognition research (Erickson et al., 2007; Voss et al., 2010). With the use of neuroimaging techniques, such as fNIRS, the findings of this study provide a premise to explore the neural correlates of exercise, establish a bridge between brain activity and cognitive and motor functions, and elucidate the neural systems associated with exercise and cognition. From an exercise-enhancing perceptive, future research may focus on examining the potential value of the momentum dumbbell exercise on altering brain neural activity using complex movement configurations and different exercise intensities to enhance brain function (Lü et al., 2015).

Strengths and Limitations

A notable strength of our study is the use of fNIRS for the real-time examination of cerebral cortical activation induced by the momentum-based dumbbell exercise. The study, however, has some limitations. First, the participants in the study were healthy male college students, rendering generalization of the results to women and other populations difficult; this is especially relevant for older adults whose brain health may benefit most from this type of exercise (Lü et al., 2015). Second, the current study design only involved experimental conditions (dumbbell exercises) without evaluation at two different time points (e.g., pre- and post-activity evaluation), thus limiting the ability to make an inference regarding changes in hemodynamic responses from baseline. Third, although we ensured that the performance time and workload were constant across the two conditions (10, 10-s sets of exercise), we did not measure the intensity of either exercise during the experiment. It is likely that given the novelty of and performance difficulties in maintaining the momentum dumbbell spinning, more effort may have been exerted by the participants while performing the momentum dumbbell task. This may have resulted in higher intensity for the momentum, relative to the conventional, dumbbell exercise, leading to increased activation. Finally, given the lack of measures of cognitive function in the current study, it was impossible to evaluate the associations between exercise-induced brain activation and cognitive performance.

CONCLUSIONS

A momentum, compared to a conventional, dumbbell exercise was shown to be effective in eliciting hemodynamic responses and muscle activation of the upper limbs among healthy young male adults. Future investigators analyzing this form of exercise should focus on exploring the therapeutic value of this new exercise modality in clinical populations (i.e., patients with cognitive and/or movement impairment), examining the long-term effects, and investigating the link between hemodynamic responses and cognitive function.

DATA AVAILABILITY STATEMENT

All datasets generated for this study are included in the article.

ETHICS STATEMENT

The studies involving human participants were reviewed and approved by Shanghai University of Sport. The patients/participants provided their written informed consent to participate in this study. Written informed consent was obtained from the individual(s) for the publication of any potentially identifiable images or data included in this article.

AUTHOR CONTRIBUTIONS

YW, LH, and YL: study concept and design. YW, LS, WW, and YJ: acquisition of data. YW, JL, and JR: analysis and interpretation. YW: drafting of manuscript. LH and YL: critical revision of manuscript and study supervision. LH: obtain funding. All authors contributed to the article and approved the submitted version.

FUNDING

This study was supported by the National Natural Science Foundation of China (31701041) and the Shanghai City Committee of Science and Technology Key Project (No. 17080503200).

ACKNOWLEDGMENTS

We would like to express our gratitude to all volunteers who participated in this study.

REFERENCES

Bai, X., Zhang, Q., Zhang, P., Zhou, S., Liu, Y., Song, X., et al. (2016). Comparison of motor execution and motor imaging brain activation modes based on fNIRS (in Chinese). *Acta Psychol. Sin.* 48, 495–508. doi: 10.3724/SP.J.1041.2016.00495

Chen, Y., Yu, Y., Niu, R., and Liu, Y. (2018). Selective effects of postural control on spatial vs. nonspatial working memory: a functional near-infrared spectral imaging study. *Front. Hum. Neurosci.* 12:243. doi: 10.3389/fnhum.2018.00243

Cope, M., Delpy, D. T., Reynolds, E. O., Wray, S., Wyatt, J., and van der Zee, P. (1988). Methods of quantitating cerebral near infrared spectroscopy data. *Adv. Exp. Med. Biol.* 222, 183–189. doi: 10.1007/978-1-4615-9510-6_21

Erickson, K. I., Colcombe, S. J., Wadhwa, R., Bherer, L., Peterson, M. S., Scalf, P. E., et al. (2007). Training-induced functional activation changes in dual-task processing: an FMRI study. *Cereb. Cortex* 17, 192–204. doi: 10.1093/cercor/bhj137

Fletcher, G. F., Landolfo, C., Niebauer, J., Ozemek, C., Arena, R., and Lavie, C. J. (2018). Reprint of: promoting physical activity and exercise: JACC health promotion series. *J. Am. Coll. Cardiol.* 72, 3053–3070. doi: 10.1016/j.jacc.2018.10.025

Grgic, J., Schoenfeld, B. J., Davies, T. B., Lazinica, B., Krieger, J. W., and Pedisic, Z. (2018). Effect of resistance training frequency on gains in muscular strength: a systematic review and meta-analysis. *Sports Med.* 48, 1207–1220. doi: 10.1007/s40279-018-0872-x

Hagen, K. B., Dagfinrud, H., Moe, R. H., Østerås, N., Kjeken, I., Grotle, M., et al. (2012). Exercise therapy for bone and muscle health: an overview of systematic reviews. *BMC Med.* 10:167. doi: 10.1186/1741-7015-10-167

Hermens, H. J., Freriks, B., Disselhorst-Klug, C., and Rau, G. (2000). Development of recommendations for SEMG sensors and sensor placement procedures. *J. Electromyogr. Kinesiol.* 10, 361–374. doi: 10.1016/s1050-6411(00)00027-4

Hong, A. R., and Kim, S. W. (2018). Effects of resistance exercise on bone health. *Endocrinol. Metab.* 33, 435–444. doi: 10.3803/EnM.2018.33.4.435

Hoshi, Y. (2005). Functional near-infrared spectroscopy: potential and limitations in neuroimaging studies. *Int. Rev. Neurobiol.* 66, 237–266. doi: 10.1016/S0074-7742(05)66008-4

Huppert, T. J., Diamond, S. G., Franceschini, M. A., and Boas, D. A. (2009). HomER: a review of time-series analysis methods for near-infrared spectroscopy of the brain. *Appl. Opt.* 48, D280–D298. doi: 10.1364/ao.48.00d280

Jurcak, V., Tsuzuki, D., and Dan, I. (2007). 10/20, 10/10 and 10/5 systems revisited: their validity as relative head-surface-based positioning systems. *NeuroImage* 34, 1600–1611. doi: 10.1016/j.neuroimage.2006.09.024

Karim, H., Schmidt, B., Dart, D., Beluk, N., and Huppert, T. (2012). Functional near-infrared spectroscopy (fNIRS) of brain function during active balancing using a video game system. *Gait Posture* 35, 367–372. doi: 10.1016/j.gaitpost.2011.10.007

Li, Z., Peng, X., Xiang, W., Han, J., and Li, K. (2018). The effect of resistance training on cognitive function in the older adults: a systematic review of randomized clinical trials. *Aging. Clin. Exp. Res.* 30, 1259–1273. doi: 10.1007/s40520-018-0998-6

Lin, P. Y., Chen, J. J., and Lin, S. I. (2013). The cortical control of cycling exercise in stroke patients: an fNIRS study. *Hum. Brain Mapp.* 34, 2381–2390. doi: 10.1002/hbm.22072

Lin, P.-Y., Lin, S.-I., and Chen, J.-J. (2012). Functional near infrared spectroscopy study of age-related difference in cortical activation patterns during cycling with speed feedback. *IEEE Trans. Neural Syst. Rehabil. Eng.* 20, 78–84. doi: 10.1109/TNSRE.2011.2170181

Lü, J., Sun, M., Liang, L., Feng, Y., Pan, X., and Liu, Y. (2015). Effects of momentum-based dumbbell training on cognitive function in older adults with mild cognitive impairment: a pilot randomized controlled trial. *Clin. Interv. Aging* 11, 9–16. doi: 10.2147/CIA.S96042

Mirelman, A., Maidan, I., Bernad-Elazari, H., Nieuwhof, F., Reelick, M., Giladi, N., et al. (2014). Increased frontal brain activation during walking while dual tasking: an fNIRS study in healthy young adults. *J. Neuroeng. Rehabil.* 11:85. doi: 10.1186/1743-0003-11-85

Miyai, I., Tanabe, H. C., Sase, I., Eda, H., Oda, I., Konishi, I., et al. (2001). Cortical mapping of gait in humans: a near-infrared spectroscopic topography study. *NeuroImage* 14, 1186–1192. doi: 10.1006/nimg.2001.0905

Niu, R., Yu, Y., Li, Y., and Liu, Y. (2019). Use of fNIRS to characterize the neural mechanism of inter-individual rhythmic movement coordination. *Front. Physiol.* 10:781. doi: 10.3389/fphys.2019.00781

Northey, J. M., Cherbuin, N., Pumpa, K. L., Smee, D. J., and Rattray, B. (2018). Exercise interventions for cognitive function in adults older than 50: a systematic review with meta-analysis. *Br. J. Sports Med.* 52, 154–160. doi: 10.1136/bjsports-2016-096587

Orihuela-Espina, F., Leff, D. R., James, D. R., Darzi, A. W., and Yang, G. Z. (2010). Quality control and assurance in functional near infrared spectroscopy (fNIRS) experimentation. *Phys. Med. Biol.* 55, 3701–3724. doi: 10.1088/0031-9155/55/13/009

Orr, R., Raymond, J., and Fiatarone Singh, M. (2008). Efficacy of progressive resistance training on balance performance in older adults: a systematic review of randomized controlled trials. *Sports Med.* 38, 317–343. doi: 10.2165/00007256-200838040-00004

Park, S. K., and Larson, J. L. (2014). The relationship between physical activity and metabolic syndrome in people with chronic obstructive pulmonary disease. *J. Cardiovasc. Nurs.* 29, 499–507. doi: 10.1097/JCN.0000000000000096

Rossi, A. F., Pessoa, L., Desimone, R., and Ungerleider, L. G. (2009). The prefrontal cortex and the executive control of attention. *Exp. Brain Res.* 192, 489–497. doi: 10.1007/s00221-008-1642-z

Schneider, P., Piper, S., Schmitz, C. H., Schreiter, N. F., Volkwein, N., Lüdemann, L., et al. (2011). Fast 3D near-infrared breast imaging using indocyanine green for detection and characterization of breast lesions. *Rofo* 183, 956–963. doi: 10.1055/s-0031-1281726

Scholkmann, F., Spichtig, S., Muehlemann, T., and Wolf, M. (2010). How to detect and reduce movement artifacts in near-infrared imaging using moving standard deviation and spline interpolation. *Physiol. Meas.* 31, 649–662. doi: 10.1088/0967-3334/31/5/004

Suzuki, M., Miyai, I., Ono, T., Oda, I., Konishi, I., Kochiyama, T., et al. (2004). Prefrontal and premotor cortices are involved in adapting walking and running speed on the treadmill: an optical imaging study. *NeuroImage* 23, 1020–1026. doi: 10.1016/j.neuroimage.2004.07.002

Tempest, G. D., and Reiss, A. L. (2019). The utility of functional near-infrared spectroscopy for measuring cortical activity during cycling exercise. *Med. Sci. Sports Exerc.* 51, 979–987. doi: 10.1249/MSS.0000000000001875

Tong, Y., Hocke, L. M., Licata, S. C., and Frederick, B. D. (2012). Low-frequency oscillations measured in the periphery with near-infrared spectroscopy are strongly correlated with blood oxygen level-dependent functional magnetic resonance imaging signals. *J. Biomed. Opt.* 17:106004. doi: 10.1117/1.JBO.17.10.106004

Voss, M. W., Erickson, K. I., Prakash, R. S., Chaddock, L., Malkowski, E., Alves, H., et al. (2010). Functional connectivity: a source of variance in the association between cardiorespiratory fitness and cognition? *Neuropsychologia* 48, 1394–1406. doi: 10.1016/j.neuropsychologia.2010.01.005

Conflict of Interest: The authors declare that the research was conducted in the absence of any commercial or financial relationships that could be construed as a potential conflict of interest.

Copyright © 2020 Wang, Lü, Rong, Song, Wang, Jiang, Liu and Huang. This is an open-access article distributed under the terms of the Creative Commons Attribution License (CC BY). The use, distribution or reproduction in other forums is permitted, provided the original author(s) and the copyright owner(s) are credited and that the original publication in this journal is cited, in accordance with accepted academic practice. No use, distribution or reproduction is permitted which does not comply with these terms.

Advantages of publishing in Frontiers

OPEN ACCESS
Articles are free to read for greatest visibility and readership

FAST PUBLICATION
Around 90 days from submission to decision

HIGH QUALITY PEER-REVIEW
Rigorous, collaborative, and constructive peer-review

TRANSPARENT PEER-REVIEW
Editors and reviewers acknowledged by name on published articles

Frontiers
Avenue du Tribunal-Fédéral 34
1005 Lausanne | Switzerland

Visit us: www.frontiersin.org
Contact us: frontiersin.org/about/contact

REPRODUCIBILITY OF RESEARCH
Support open data and methods to enhance research reproducibility

DIGITAL PUBLISHING
Articles designed for optimal readership across devices

FOLLOW US
@frontiersin

IMPACT METRICS
Advanced article metrics track visibility across digital media

EXTENSIVE PROMOTION
Marketing and promotion of impactful research

LOOP RESEARCH NETWORK
Our network increases your article's readership